



# *XIV International Conference on Thermoelectrics*

*June 27 - 30, 1995, St.Petersburg, Russia*

19960229 079

DISTRIBUTION STATEMENT A  
Approved for public release;  
Distribution Unlimited

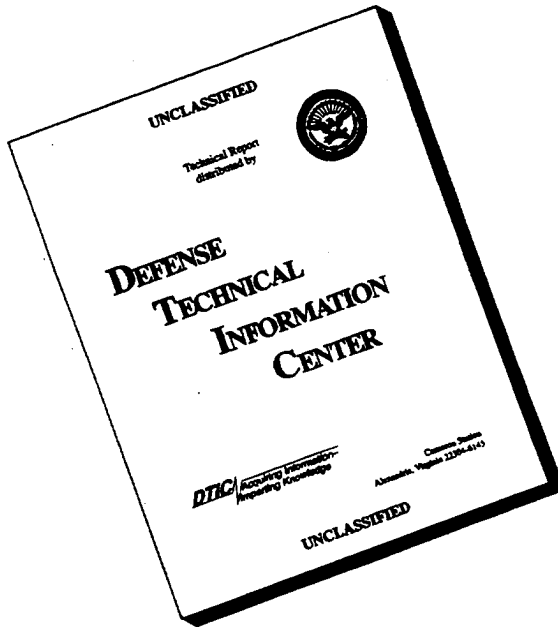


Supervising Organization:  
International Thermoelectric Society



Host Organization:  
A.F.Ioffe Physical-Technical Institute

# **DISCLAIMER NOTICE**



**THIS DOCUMENT IS BEST  
QUALITY AVAILABLE. THE  
COPY FURNISHED TO DTIC  
CONTAINED A SIGNIFICANT  
NUMBER OF PAGES WHICH DO  
NOT REPRODUCE LEGIBLY.**

# **Proceedings**

of the

## **XIV International Conference on Thermoelectrics**

*June 27 - 30, 1995, St.Petersburg, Russia*

---

*Chief Editor: M.V. Vedernikov*

*Associate Editors: M.I. Fedorov, A.E. Kalazin*

**A.F. Ioffe Physical-Technical Institute, St.Petersburg, Russia  
1995**

**Proceedings of the XIV International Conference on  
Thermoelectrics  
© 1995. A.F.Ioffe Physical-Technical Institute,  
St.Petersburg, Russia**

**Request by authors for copyright release should be directed to:**

**M. V. Vedernikov**  
*Head of Laboratory for Physics of Thermoelements*  
*A.F.Ioffe Physical-Technical Institute,*  
*Polytekhnicheskaya, 26*  
*194021, St.Petersburg,*  
*Russia*  
**FAX: (812) 515-6747, 247-1017**

**ISBN 5-86763-081-1**

## Preface

The 14th International Conference on Thermoelectrics (ICT'95) has been held in Saint Petersburg, Russia from June 27 to June 30, 1995. It was organized by the Laboratory for Physics of Thermoelements of the A.F.Ioffe Physical-Technical Institute according to the decision of the International Thermoelectric Society. Traditionally, this annual conference was devoted to all aspects of thermoelectric energy conversion and thermoelectrics. Scientific, engineering, production problems were discussed. Researchers, engineers, managers, businessmen from different countries could discuss the latest news in thermoelectricity and see some examples of thermoelectric production at the Conference technical exhibition.

There were 195 registered attendees from 23 countries including 86 from abroad (17 countries) and 109 from 6 countries of the former USSR. The greatest national delegations were: Russia - 92 persons (including 41 from St.Petersburg), USA - 28, Japan - 23, Ukraine - 14, Korea - 6, Germany - 5. The ICT'95 Organizing Committee received 181 abstracts of possible papers. Of these 132 papers were presented at the conference. Abstracts and, later, full texts of the papers presented were considered by the ICT'95 Program Committee. After this, 123 were included in the ICT'95 Proceedings. They are published here by phototypesetting from the authors' camera ready manuscripts.

All papers at the conference were divided in 7 sections:

- A — Thermoelectrics for low temperatures**
- B — Thermoelectrics for moderate temperatures**
- C — Thermoelectrics for high temperatures**
- D — Basic aspects of thermoelectrics & thermoelectricity**
- E — Measurements**
- F — Thermoelectric generators**
- G — Thermoelectric coolers**

Each paper is placed here in its section (see Contents), whether it was presented orally or at poster session.

ICT'95 is a special case among the other ICT's because ICT was held for the first time in Russia. Modern semiconductor thermoelectricity was initiated in this country by Abram Ioffe in 1931, and there still exists a wide thermoelectric community in the countries of the former USSR. This is why the Organizing Committee tried to attract as many participants from these countries as possible for effective contact with their foreign colleagues. Another consequence of the situation is our decision to honour the pioneering contribution of A.F.Ioffe to thermoelectricity by including a special page to this volume with his portrait and short personal information.

It was extremely important for the success of the Conference to find significant additional financial support. I am happy that we may write out here, on separate page, all sponsors of ICT'95.

I am happy too to thank the people without whose assistance it would have been impossible to organize and conduct the conference: Drs. C.B.Vining (President) and B.Mathiprakasam (treasurer) International Thermoelectric Society; Drs. M.I.Fedorov, V.L.Kuznetsov and Mr. A.E.Kalazin (the Organizing Committee) - Ioffe Institute; Drs. V.A.Kutasov, Yu.I.Ravich and V.K.Zaitsev (the Program Committee) - Ioffe Institute.



M.V. Vedernikov,  
Head of the Laboratory for Physics of Thermoelements,  
A.F.Ioffe Physical-Technical Institute,  
Chief Editor, ICT'95 Proceedings.

*The Organizing Committee is very grateful  
to organizations and firms, listed below chronologically, for financial  
support of XIV International Conference on Thermoelectrics:*

*Main sponsors*

Osterm — St.Petersburg, Russia

Russian Foundation for Basic Research

US Department of Energy,  
Radioisotopic Power Systems

United Energy System of Russia

European Research Office of US Army

*Sponsors*

Supercool AB — Göteborg, Sweden

Nord — Moscow, Russia

Mobicool International — Hong Kong

MJ Research — Watertown, MA, USA

Cryotherm — St.Petersburg, Russia

## Abram Fedorovich Ioffe (1880-1960)



<b>1880</b> , October 27	- born in Romny, near Poltava (Russia, now Ukraine);
<b>1902</b>	- graduated from St.Petersburg Techological Institute;
<b>1902-1905</b>	- post-graduate student of Prof. W.Röntgen in Munich;
<b>1906-1917 (before the October Revolution)</b>	- teacher, lecturer and professor of physics in St.Petersburg;
<b>1918 (after the October Revolution)</b>	- organized the Physical-Technical Institute in St.Petersburg (Petrograd);
<b>1918-1920</b>	- was elected as corresponding member and, later, full member of the Russian Academy of Sciences;
<b>1919</b>	- organized the Physical-Technical Department at the St.Petersburg Polytechnical Institute;
<b>1931</b>	- initiated study of semiconductors at the Physical-Technical Institute, predicted their great prospects for technical applications, particularly for thermoelectric conversion of heat to electrical energy;
<b>1939-1945</b>	- first semiconductor thermoelectric generators were constructed at the Physical-Technical Institute;
<b>1950</b>	- published the theory of application of semiconductors for thermoelectric energy conversion
<b>1950</b>	- the first semiconductor thermoelectric cooler was tested under the direction of Ioffe;
<b>1960</b> , October 14	- died in St.Petersburg (Leningrad).

# Contents

Section A – Thermoelectrics for low temperatures	<i>pages</i>
<b>Verification of a transport model for p-type <math>(\text{Bi}_{0.5}\text{Sb}_{0.5})_2\text{Te}_3</math> and <math>(\text{Bi}_{0.25}\text{Sb}_{0.75})_2\text{Te}_3</math> mixed crystals by means of temperature dependent thermoelectric properties below room temperature</b> Süßmann H., Müller E. Martin-Luther-Universität Halle-Wittenberg, Fachgruppe Angew. Physik, Germany	1
<b>Functional-Gradient Material for Thermoelectric Energy Converters</b> Anatychuk L.I., Vikhor L.N., Kuznetsov A.V., Letiuchenko S.D. Institute of thermoelectricity, Chernovtsy, Ukraine	7
<b>Thermoelectric properties of doped single crystals of solid solutions based on bismuth telluride</b> Svechnikova T.E., Maksimova N.M., Süßmann H., Reinshaus P. A.A.Baikov institute of metallurgy RAS, Moscow, Russia Martin-Luther-Universität Halle-Wittenberg, Germany	10
<b>Application of scanning thermo-probe technique for homogeneity determination of <math>\text{Bi}_{0.5}\text{Sb}_{1.5}\text{Te}_3</math> single crystals</b> Ivanova L.D., Süßmann H., Reinshaus P., Dietrich Th. A.A.Baikov institute of metallurgy RAS, Moscow, Russia Martin-Luther-Universität Halle-Wittenberg, Germany	13
<b>A simplified theory of phonon boundary scattering in solid solutions</b> Goldsmid H.J., Lyon H.B. Jr., Volckmann E.H. Marlow Industries, Inc., USA	16
<b>Thermoelectric properties of solid solutions based on <math>\text{Bi}_2\text{Te}_3</math> at 300 K</b> Kutasov V.A., Luk'yanova L.N. A.F.Ioffe Physical-Technical Institute RAS, St.Petersburg, Russia	20
<b>Composition dependence on thermoelectric properties of undoped polycrystal <math>(\text{Bi}_2\text{Te}_3)_{1-x}(\text{Sb}_2\text{Te}_3)_x</math> prepared by PIES method</b> Ohta T., Yamamoto A., Tanaka T., Fujimaki T., Kamisako K. Electrotechnical Lab., AIST, MITI Tsukuba, Japan Tokyo University of Agriculture and Technology, Tokyo, Japan	24
<b><math>(\text{BiSb})_2\text{Te}_3</math> and <math>\text{Bi}_2(\text{TeSe})_3</math> films prepared by vacuum-arc plasma method: characterization and application</b> Gasenkova I.V., Tochitsky E.I. Institute of Electronics Belarus AS, Minsk, Republic of Belarus Engineering Center "Plasmoteg", Belarus AS, Minsk, Republic of Belarus	29
<b>Structure and properties of large-diameter zone-melt grown thermoelectric crystals</b> Bublik V.T., Karatajev V.V., Osvensky V.B., Sagalova T.B., Frolov A.M., Jouravlev O. Institute of Chemical Problems in Microelectronics, Moscow, Russia Atramat Co., New York, USA	33
<b>Mechanical properties of Bi-Sb single crystal solid solutions grown by Czochralsky method</b> Belaya A.D., Zayakin S.A., Zemskov V.S. A.A.Baikov institute of metallurgy RAS, Moscow, Russia	37
<b>On the durability of doped <math>\text{Bi}_2\text{Te}_3</math> single crystals</b> Korzhuev M.A., Chizhevskaya S.N., Svechnikova T.E., Maksimova N.M., Kulakova E.A. A.A.Baikov institute of metallurgy RAS, Moscow, Russia	42

## VIII

<b>Inversion of the Hall coefficient in Bi<sub>2</sub>Te<sub>3-x</sub>S<sub>x</sub> crystals</b>	<b>45</b>
<i>Kulbachinckii V.A., Horak J., Lošťák P.</i>	
Moscow State University, Moscow, Russia	
University of Pardubice, Pardubice, Czech Republic	
<b>Obtaining semiconductor systems alloys at super-rapid rates of cooling</b>	<b>49</b>
<i>Glasov V.M., Poyarkov K.B.</i>	
Moscow Institute of Electronic Engineering (Technical University), Moscow, Russia	
<b>Transport phenomena peculiarities caused of intervalley scattering of charge carries in bismuth type crystals</b>	<b>52</b>
<i>Grabov V.M., Bondarenko M.G., Uryupin O.N.</i>	
Herzen Russian State Pedagogical University, St.Petersburg, Russia	
A.F.Ioffe Physical-Technical Institute RAS, St.Petersburg, Russia	
<b>Thermoelectrical properties and energy band spectrum p-Bi<sub>2</sub>Te<sub>3</sub> doped with element of II or IV group</b>	<b>56</b>
<i>Zhitinskaya M.K., Nemov S.A., Abaidulina T.G., Svechnikova T.E.</i>	
State technical university, St.Petersburg, Russia	
A.A.Baikov institute of metallurgy RAS, Moscow, Russia	
<b>Experimental investigation of Nernst-Ettingshausen effect in antimony telluride</b>	<b>60</b>
<i>Zhitinskaya M.K., Nemov S.A., Rykov S.A., Ivanova L.D.</i>	
State technical university, St.Petersburg, Russia	
A.A.Baikov institute of metallurgy RAS, Moscow, Russia	
<b>Statistical micro-inhomogeneities in (Bi,Sb)<sub>2</sub>Te<sub>3</sub> solid solutions grown from melt with excess content of tellurium</b>	<b>65</b>
<i>Anukhin A.I., Skipidarov S.Ya., Sokolov O.B.</i>	
Telvis Co., Moscow, Russia	
Nord Co., Moscow, Russia	
<b>Thermoelectric properties of n-Bi<sub>2</sub>Te<sub>3</sub>.Se<sub>x</sub> (x&lt;0.4) solid solutions in the temperature range from 80 to 300 K</b>	<b>72</b>
<i>Alekseeva G.T., Vedernikov M.V., Konstantinov P.P., Kutasov V.A., Luk'yanova L.N.</i>	
A.F.Ioffe Physical-Technical Institute RAS, St.Petersburg, Russia	
<b>Heterovalent replacement in Bi<sub>2</sub>Te<sub>3</sub>(Sn,Pb,In) solid solutions</b>	<b>75</b>
<i>Alekseeva G.T., Vedernikov M.V., Konstantinov P.P., Kutasov V.A., Luk'yanova L.N., Ravich Yu.</i>	
A.F.Ioffe Physical-Technical Institute RAS, St.Petersburg, Russia	
<b>Phonon thermal conductivity of the thermoelectric Bi-Sb alloys</b>	<b>78</b>
<i>Kagan V.D., Red'ko N.A.</i>	
A.F.Ioffe Physical-Technical Institute RAS, St.Petersburg, Russia	
<b>Thermoelectric efficiency of semiconducting Bi-Sb alloys</b>	<b>82</b>
<i>Red'ko N.A.</i>	
A.F.Ioffe Physical-Technical Institute RAS, St.Petersburg, Russia	
<b>Transport properties and electronic structure of bismuth-antimony single crystals doped by tellurium at 80-530 K temperature range</b>	<b>85</b>
<i>Grabov V.M., Kolgunov D.A., Uryupin O.N.</i>	
Herzen Russian State Pedagogical University, St.Petersburg, Russia	
A.F.Ioffe Physical-Technical Institute RAS, St.Petersburg, Russia	
<b>The influence of titanium doping on thermoelectric properties of Sb-riched bismuth-antimony tellurides</b>	<b>88</b>
<i>Navrátil J., Starý Z., Lošťák P., Plecháček T.</i>	
Joint Laboratory of Solid State Chemistry, Czech Academy of Sciences and University Pardubice, Pardubice, Czech Republic	
University Pardubice, Pardubice, Czech Republic	

<b>Interdiffusion and some transport properties of cold pressed composite materials on the basis of Bi<sub>2</sub>Te<sub>3</sub>, Sb<sub>2</sub>Te<sub>3</sub> and Bi<sub>2</sub>Se<sub>3</sub> with addition of Indium</b>	92
Starý Z., Navrátil J., Novotný R., Plecháček T.	
Joint Laboratory of Solid State Chemistry, Czech Academy of Sciences and University Pardubice, Pardubice, Czech Republic	
<b>Highest figure of merit in undoped Bi<sub>1-x</sub>Sb<sub>x</sub> alloys</b>	96
Lenoir B., Cassart M., Dauscher A., Ravich Yu.I., Scherrer H.	
Laboratoire de Métallurgie Physique et Science des Matériaux, Ecole des Mines, Nancy, France	
Unité de Physico-Chimie et de Physique des Matériaux, Louvain-la-Neuve, Belgique	
A.F.Ioffe Physical-Technical Institute RAS, St.Petersburg, Russia	
<b>Thermal expansion coefficient in Bi<sub>0.5</sub>Sb<sub>1.5</sub>Te<sub>3</sub></b>	100
Tamaki N., Onodera A., Ido M., Fukuda K., Imaizumi H., Ishii T.	
Department of Physics, Faculty of Science, Hokkaido University, Sapporo, Japan	
Advanced Research Laboratory, Komatsu Ltd., Hiratsuka, Japan	
<b>Thermoelectric properties and segregation behaviors of n-type Bi<sub>2</sub>Te<sub>3</sub> - Bi<sub>2</sub>Se<sub>3</sub> solid solution</b>	104
Ha H.P., Hyun D.B., Cho Y.W., Shim J.D.	
Korea Institute of Science and Technology, Seoul, Korea	
<b>Thermoelectric properties of Sb<sub>2</sub>Te<sub>3</sub>-SnTe and Sb<sub>2</sub>Te<sub>3</sub>-PbTe pseudo-eutectic alloys</b>	108
Jang Kyung-Wook, Lee Dong-Hi	
Department of Metallurgical Engineering, Yonsei University, Seoul, Korea	
<b>Influence of electric current flowing during crystallization process on thermoelectric properties of materials</b>	112
Liaschenok V.I., Strekopytova N.I.	
St.Petersburg Academy of air-space Instrument Making, St.Petersburg, Russia	
<b>Thermoelectric figure of merit of horizontal zone-leveling prepared bismuth-antimony single crystals</b>	115
Grabov V.M., Ivanov G.A., Naletov V.L., Bondarenko M.G., Uryupin O.N.	
Herzen Russian State Pedagogical University, St.Petersburg, Russia	
A.F.Ioffe Physical-Technical Institute RAS, St.Petersburg, Russia	
<b>Service properties of doped Bi-Sb single crystals</b>	119
Belya A.D., Zayakin S.A., Zemskov V.S., Ponomarev Y.G.	
A.A.Baikov institute of metallurgy RAS, Moscow, Russia	
M.I.Lomonosov Moscow State University, Moscow, Russia	
<b>Microstructure Bi<sub>2</sub>Te<sub>3</sub>-Sb<sub>2</sub>Te<sub>3</sub> alloys grown by zone melting technique</b>	125
Anukhin A.I., Skipidarov S.Ya., Sokolov O.B., Aivazov A.A.	
Telvis Co., Moscow, Russia	
Nord Co., Moscow, Russia	
Moscow Institute of Electronic Engineering (Technical University), Moscow, Russia	
<b>Mechanical alloying behavior and thermoelectric properties of (Bi,Sb)<sub>2</sub>Te<sub>3</sub></b>	130
Jung B.Y., Choi J.S., Oh T.S., Hyun D.B., Ha H.P., Shim J.D.	
Department of Metallurgy and Material Science, Hong Ik University, Seoul, Korea	
Metals Research Division, Korea Institute of Science and Technology, Seoul, Korea	
<b>Orientational distribution in hot pressed n-type Bi<sub>2</sub>Te<sub>3</sub></b>	135
Fukuda K., Imaizumi H., Ishii T., Toyoda F., Yamanashi M., Kibayashi Y.	
Research Center, Komatsu Ltd., Hiratsuka, Japan	
Komatsu Electronics Inc., Hiratsuka, Japan	
<b>A new-type thermoelectric module composed of hamburger-type elements</b>	140
Tanji Y., Nakagawa Y., Kaneko T., Ido H., Kuboki M., Kogo M., Masumoto T., Sato R.	
M & D Division, Tohoku Technobrains Corporation, Sendai, Japan	
Faculty of Engineering, Tohoku Institute of Technology, Sendai, Japan	
Institute for materials Research, Tohoku University, Sendai, Japan	
Faculty of Engineering, Tohoku Gakuin University, Tagaio, Japan	

**X**

<b>Effects of thickness and processing variables of the performance of (Bi,Sb)<sub>2</sub>(Te,Se)<sub>3</sub>-based film type thermoelectric modules</b>	<b>145</b>
<i>Kim Il-Ho, Min Byong-Gue, Lee Dong-Hi</i> Department of Metallurgical Engineering, Yonsei University, Seoul, Korea	
<b>Transient Thermoelectric Effect in Sb<sub>2</sub>In<sub>x</sub>Te<sub>3</sub> and Sb<sub>2</sub>Te<sub>3-y</sub>Se<sub>y</sub></b>	<b>151</b>
<i>Kulbachinckii V.A., Inoue M., Sasaki M., Negishi H., Gao W.X.</i> Physics Faculty, M.I.Lomonosov Moscow State University, Moscow, Russia Faculty of Science, Hiroshima University, Higashi-Hiroshima, Japan	
<b>Seebeck coefficient and electrical conductivity of Bi<sub>2</sub>Te<sub>3</sub>-Sb<sub>2</sub>Te<sub>3</sub> alloys prepared using powder metallurgy</b>	<b>156</b>
<i>Rowe D.M., Gao Min</i> School of Engineering, University of Wales, Cardiff, UK	
<b>Optimization of bismuth telluride based alloys for thermoelectric power generation using "waste" heat</b>	<b>159</b>
<i>Rowe D.M., Gao Min, Williams S.G.K.</i> School of Engineering, University of Wales, Cardiff, UK	
<b>Thermoelectric cooling modules based on bismuth telluride alloys: technique and use in the world patent documentation</b>	<b>163</b>
<i>Malkovitch B.Sh.</i> Engineering & Production Firm "Cryotherm", St.Petersburg, Russia	
<hr/> <b>Section B – Thermoelectrics for moderate temperatures</b> <hr/>	
<b>The metallisation of the thermoelement branches by ionic sputtering of the nickel and cobalt</b>	<b>166</b>
<i>Kuznetsov G.D., Polystanskiy Yu.G., Evseev V.A.</i> State Institute of Steel and Alloys, Moscow, Russia	
<b>The film structures on the A<sup>IV</sup>B<sup>VI</sup> compounds-base for thermoelectric transformers</b>	<b>168</b>
<i>Polystanskiy Yu.G., Kuznetsov G.D., Evseev V.A.</i> State Institute of Steel and Alloys, Moscow, Russia	
<b>Investigation of energy spectrum and properties of lead chalcogenides implanted by oxygen</b>	<b>171</b>
<i>Veis A.N., Suvorova N.A.</i> St.Petersburg State technical university, St.Petersburg, Russia	
<b>Thermoelectric properties of PbTe thin films: Dependence from surface layer conductance</b>	<b>174</b>
<i>Boikov Yu.A., Danilov V.A., Gribanova O.S., Derjagina I.M.</i> A.F.Ioffe Physical-Technical Institute RAS, St.Petersburg, Russia	
<b>Electrical contact for galena thermoelements</b>	<b>178</b>
<i>Aloke Kumar Das, Acharya H.N., Choudhary R.N.P., Chatterjee S.</i> Department of Physics & Meteorology, Indian Institute of Technology, Kharagpur, India R & D Division, Mecon (India) Ltd., Ranchi, India	
<b>Reliability and defects in PbTe-based materials</b>	<b>182</b>
<i>Fano V., Ortalli I., Pozela K., Meletti G.</i> Istituto di Scienze Fisiche, Parma, Italy World Laboratory, Vilnius, Lithuania Maspec Institute, Parma, Italy	
<b>From ore to thermoelectric generators: a study on indian galena</b>	<b>185</b>
<i>Chatterjee S., Acharya H.N.</i> R & D Division, Mecon (India) Ltd., Ranchi, India Department of Physics & Meteorology, Indian Institute of Technology, Kharagpur, India	

<b>Development of Thermoelements from dross galena</b>	<b>189</b>
<i>Shannigrahi S.R., Acharya H.N., Choudhary R.N.P., Singh A.K., Chatterjee S.</i>	
Department of Physics & Meteorology, Indian Institute of Technology, Kharagpur, India	
R & D Division, Mecon (India) Ltd., Ranchi, India	
<b>Na-doping of lead-tin chalcogenides</b>	<b>193</b>
<i>Alekseeva G.T., Gurieva E.A., Konstantinov P.P., Prokof'eva L.V.</i>	
A.F.Ioffe Physical-Technical Institute RAS, St.Petersburg, Russia	
<hr/>	
<i>Section C - Thermoelectrics for high temperatures</i>	
<b>Preparation and investigation of thermoelectrical and electrical properties of CuInSe<sub>2</sub> bulk and thin films crystals</b>	<b>198</b>
<i>Abdullaev M.A., Gadjeva R.M., Magomedova I.Kh., Khochlachov P.P., Khasbulatov A.M.</i>	
Institute of physics, Dagestan Sc. Center RAS, Makhachkala, Russia	
<b>On the valence band negative non-parabolicity in Cu<sub>2-x</sub>Se superionic conductor</b>	<b>201</b>
<i>Korzhuev M.A., Laptev A.V.</i>	
A.A.Baikov institute of metallurgy RAS, Moscow, Russia	
<b>Structure and Transport Properties in Amorphous and Nanocrystalline Re<sub>1</sub>-Si<sub>1-x</sub> Thin Films at High Temperatures</b>	<b>206</b>
<i>Burkov A.T., Gladun C., Heinrich A., Pischke W., Schumann J.</i>	
A.F.Ioffe Physical-Technical Institute RAS, St.Petersburg, Russia	
Institute of Solid State and Materials Science Dresden e.V., Dresden, Germany	
<b>Thermoelectric properties of small mobility materials in the hopping regime</b>	<b>210</b>
<i>Zaitsev V.K., Ktitorov S.A., Kalazin A.E., Fedorov M.I.</i>	
A.F.Ioffe Physical-Technical Institute RAS, St.Petersburg, Russia	
<b>Thermoelectric waves in anisotropic crystal of Higher Manganese Silicide (HMS)</b>	<b>212</b>
<i>Ordin S.V.</i>	
A.F.Ioffe Physical-Technical Institute RAS, St.Petersburg, Russia	
<b>Electrochemical deposition of metallic films on transition metal silicides</b>	<b>215</b>
<i>Solomkin F.Yu., Fedorov M.I., Zaitsev V.K.</i>	
A.F.Ioffe Physical-Technical Institute RAS, St.Petersburg, Russia	
<b>Thermoelectrical properties of new intermetallic compounds M<sup>I</sup>M<sup>II</sup>Sn</b>	<b>217</b>
<i>Marchuk N.D., Skolozdra R.V., Stadnyk Y.V.</i>	
Institute for Nuclear Research NUAS, Kiev, Ukraine	
Lviv State University, Lviv, Ukraine	
<b>Effective medium analysis and equi-Z-contour map for porosity controlled SiC:B<sub>4</sub>C system</b>	<b>222</b>
<i>Okamoto Y., Miyakawa T., Morimoto J., Aruga A., Fujimoto S.</i>	
Department of material Science and Engineering, National Defense Academy, Yokosuka, Kanagawa, Japan	
<b>Effect of Intergrain Defects on Thermoelectric Properties of β-FeSi<sub>2</sub> - Electron Spin Resonance Study</b>	<b>227</b>
<i>Miki T., Teraoka Y., Kishimoto K., Matsubara K.</i>	
Department of Electrical and Electronic Engineering, Yamaguchi University, Yamaguchi, Japan	
Yamaguchi College, Tokyo Science University, Yamaguchi, Japan	
<b>Thermoelectric materials with the skutterudite structure: New results</b>	<b>231</b>
<i>Fleurial J.-P., Caillat Th., Borshchevsky A.</i>	
Jet Propulsion Laboratory, California Institute of Technology, Pasadena, USA	
<b>New thermoelectric materials based on IrSb<sub>3</sub></b>	<b>236</b>
<i>Nolas G.S., Slack C.A., Tritt T.M., Morelli D.T.</i>	
Department of Physics, Rensselaer Polytechnic Institute, Troy, NY, USA	
Material Science Branch, US Naval Research Laboratory, Washington, DC, USA	
Physics Department, General Motors Research and Development Center, Warren, Michigan, USA	

<b>Low Temperature Transport Properties of IrSb:</b>	<b>240</b>
Tritt T.M., Gillespie D.J., Ehrlich A.C., Nolas G., Slack G.A., Cohn J.L. Material Science Branch, US Naval Research Laboratory, Washington, DC, USA Department of Physics, Rensselaer Polytechnic Institute, Troy, NY, USA Department of Physics, University of Miami, Coral Gables, FL, USA	
<b>Thermoelectric performance of ZnO-based mixed oxides as a promising high-temperature material</b>	<b>245</b>
Ohtaki M., Tsubota T., Eguchi K., Arai H. Department of Materials Science and Technology, Graduate School of Engineering Science, Kyushu University, Kasuga, Fukuoka, Japan	
<b>Microstructure analysis of Thermoelectric TiNiSn Alloy</b>	<b>249</b>
Tan Z.S., Jesser W.A. Department of Materials Science and Engineering, University of Virginia, Charlottesville, VA, USA	
<b>Prospects of various thermoelectric use in thermoelectric generators</b>	<b>254</b>
Fedorov M.I., Gurieva E.A., Prokof'eva L.V., Zaitsev V.K. A.F.Ioffe Physical-Technical Institute RAS, St.Petersburg, Russia	
<b>Thermopower and electrical resistivity of <math>\beta</math>-FeSi<sub>2</sub> single crystals doped with Co, Cr and Mn</b>	<b>259</b>
Heinrich A., Gladun C., Burkov A., Tomm Y., Brehme S., Lange H. Institute of Solid State and Materials Science Dresden e.V., Dresden, Germany A.F.Ioffe Physical-Technical Institute RAS, St.Petersburg, Russia Hann-Meitner-Institute Berlin GmbH, Berlin, Germany	
<b>Investigation of dopants for ruthenium silicide</b>	<b>264</b>
Yamamoto A., Ohta T., Sawade Y., Tanaka T., Kamisako K. Electrotechnical Laboratory, AIST, MITI, Ibaraki, Japan Tokyo university of Agriculture and Technology	
<b>Temperature dependence of thermoelectric properties of SiC/Al</b>	<b>269</b>
Okamoto Y., Aruga A., Tashiro H., Morimoto J., Miyakawa T., Fujimoto S. Department of material Science and Engineering, National Defense Academy, Yokosuka, Kanagawa, Japan	
<b>Thermoelectric properties of SiGe ceramics sintered with germane or silane plasma processed micrograins</b>	<b>274</b>
Kishimoto K., Nagamoto Y., Miki T., Koyanagi T., Matsubara K. Yamaguchi University, Ube, Yamaguchi, Japan	
<b>Effective thermal conductivity of porous oxides at temperatures <math>T \geq 1000</math> K</b>	<b>277</b>
Sher E.M. A.F.Ioffe Physical-Technical Institute RAS, St.Petersburg, Russia	
<hr/> <b>Section D – Basic aspects of thermoelectrics &amp; thermoelectricity</b> <hr/>	
<b>Cluster superlattice as 3D-array of thermoionic energy converters</b>	<b>280</b>
Bogomolov V.N., Kurdyukov D.A., Prokofiev A.V., Ravich Yu.I., Samoilovich L.A., Samoilovich S.M. A.F.Ioffe Physical-Technical Institute RAS, St.Petersburg, Russia Almaztechnocrystal Co., Aleksandrov, Russia M.I.Lomonosov Moscow State University, Moscow, Russia	
<b>Multilayer thin film thermoelectrics produced by sputtering</b>	<b>283</b>
Wagner A.V., Foreman R.J., Summers L.J., Barbee T.W.Jr., Farmer J.C. Chemistry and Materials Science Department, Lawrence Livermore National Laboratory, Livermore, CA, USA	
<b>Estimation of the maximum electrical power factor of thermoelectric materials using <math>\alpha</math>-ln<math>\sigma</math> plot</b>	<b>288</b>
Rowe D.M., Min G., Williams S.G.K. School of Engineering, University of Wales, Cardiff, UK	

### XIII

<b>Improving the power output and conversion efficiency of Peltier modules when used as generators</b>	<b>291</b>
Rowe D.M., Min G., Williams S.G.K.	
School of Engineering, University of Wales, Cardiff, UK	
<b>Problems and Perspectives for Thermoelectrics</b>	<b>295</b>
Anatychuk L.I.	
Institute of thermoelectricity, Chernovtsy, Ukraine	
<b>The extrinsic Thomson effect (ETE)</b>	<b>301</b>
Buist R.J.	
TE Technology, Inc., Traverse City, Michigan, USA	
<b>The Distributed Peltier effect and its influence on cooling devices</b>	<b>305</b>
Ball C.A.B., Jesser W.A., Maddux J.	
Department of Materials Science and Engineering, University of Virginia, Charlottesville, VA, USA	
Department of Physics, University of Port Elizabeth, Port Elizabeth, South Africa	
<b>gradT = const, is it correct?</b>	<b>310</b>
Bulat L.P.	
St.Petersburg State Academy of Refrigeration, St.Petersburg, Russia	
<b>Experimental Testing of the Deformation of Thermoelectrical Field in Anisotropic Inhomogeneous Semiconductors</b>	<b>314</b>
Bochegov V.I.	
Kurgan State Pedagogical Institute, Kurgan, Russia	
<b>Programming of the Distribution of Impurity in the Continuum of Semiconductor by the Method of Crystallization</b>	<b>315</b>
Podgorbunskih S.A., Bochegov V.I., Ovsjanov V.M.	
Kurgan State Pedagogical Institute, Kurgan, Russia	
<b>Thermoelectric figure of merit of nondegenerate semiconductor submicron layers</b>	<b>316</b>
Gurevich Yu.G., Logvinov G.N., Titov O.Yu.	
Centro de Investigación y de Estudios Avanzados del Instituto Politécnico Nacional, Mexico D.F., Mexico	
Institute of Thermoelectricity, Chernovtsy, Ukraine	
<b>Computer Modeling of Thermoelectric Material Anisotropic Powder Structures</b>	<b>319</b>
Anatychuk L.I., Melnichuk S.V., Kosyachenko S.V.	
Institute of thermoelectricity, Chernovtsy, Ukraine	
<b>Thermoelectric Phenomena in Randomly Inhomogeneous Solid State Systems</b>	<b>324</b>
Fishchuk I.I., Marchuk N.D.	
Institute for nuclear research NUAS, Kiev, Ukraine	
<b>Enhanced thermoelectric efficiency of submicron-thick structures</b>	<b>327</b>
Yurchenko V.B.	
Institute of radiophysics and electronics NUAS, Kharkov, Ukraine	
<b>The thermoelectrical and electrical properties of the system Au/p-CdTe/Au</b>	<b>331</b>
Vacková S., Racko J., Donoval D., Gurevich Yu.G.	
Department of Semiconductors, Charles University, Prague, Czech Republic	
Microelectronics Department, Slovak Technical University, Bratislava, Slovakia	
Centro de Investigación y de Estudios Avanzados del Instituto Politécnico Nacional, Mexico D.F., Mexico	
<b>Thermoelectromotive force of hot carriers arising in metal-p-Ge and GaAs contacts</b>	<b>334</b>
Ašmontas S.P., Sužiedelis A.	
Semiconductor Physics Institute, Vilnius, Lithuania	

---

<i>Section E – Measurements</i>	
<b>Thermoelectric modules quality testing by a manufacturer</b>	338
<i>Babin V.P., Gorodetskyi S.M.</i>	
Engineering & Production Firm "Cryotherm", St.Petersburg, Russia	
<b>High-Precise Thermoelectric AC Converters</b>	341
<i>Anatychuk L.I., Bodnaruc V.I., Shcherbina L.A.</i>	
Institute of thermoelectricity, Chernovtsy, Ukraine	
<b>Precise Determination of Metal-Thermoelectric Material Contact Resistance</b>	344
<i>Anatychuk L.I., Luste O.J., Pervozvansky S.V.</i>	
Institute of thermoelectricity, Chernovtsy, Ukraine	
<b>The device for precise thermoelectric material parameters measurement in the range of 100-400 K</b>	349
<i>Razinkov V.V., Khabrenko A.A., Shevchukovich Ya.A.</i>	
Institute of thermoelectricity, Chernovtsy, Ukraine	
<b>Information System for Thermoelectric Material Parameters Exact Determination</b>	351
<i>Razinkov V.V., Pervozvansky S.V., Shchedrin A.A.</i>	
Institute of thermoelectricity, Chernovtsy, Ukraine	
<b>A new kind of gradient heating for thermopower measurements at low temperatures and high magnetic fields</b>	354
<i>Resel R., Bauer E., Nakama T., Higa M., Yagasaki K., Burkov A.T.</i>	
Institute for Experimental Physics, Technical University Vienna, Vienna, Austria	
College of Science, University of the Ryukyus, Okinawa, Japan	
A.F.Ioffe Physical-Technical Institute RAS, St.Petersburg, Russia	
<b>Evaluation of commercially available Peltier modules for use in a hot-water driven thermoelectric generator</b>	357
<i>Rowe D.M., Williams S.G.K., Min G.</i>	
School of Engineering, University of Wales, Cardiff, UK	
<b>Application of Laser Doppler anemometry for experimental investigation of thermoelectric elements dynamic deformation</b>	363
<i>Sidorenko N.A., Soutorshin V.N.</i>	
Institute for Problems in Mechanics, Moscow, Russia	
<i>Section F – Thermoelectric generators</i>	
<b>Thermoelectric linear motor</b>	367
<i>Bulat L.P.</i>	
St.Petersburg State Academy of Refrigeration, St.Petersburg, Russia	
<b>Stage Thermoionic and Thermoelectric Energy Converter</b>	369
<i>Anatychuk L.I., Vikhor L.N., Nikolayev Yu.V.</i>	
Institute of thermoelectricity, Chernovtsy, Ukraine	
SIA-Lutch, Podolsk, Moscow region, Russia	
<b>Optimal Control in Stage Thermoelectric Generator Design</b>	372
<i>Anatychuk L.I., Vikhor L.N.</i>	
Institute of thermoelectricity, Chernovtsy, Ukraine	
<b>Peculiarities of Fuel Combustion Process Control in Catalytic Heat Sources for TEGs</b>	376
<i>Mikhailovsky V.Ja., Strutinskaya L.T.</i>	
Institute of thermoelectricity, Chernovtsy, Ukraine	
<b>Multichannel thermoelectric flame detector</b>	380
<i>Razinkov V.V., Gritsai V.V., Opyr L.A., Gromko E.D.</i>	
Institute of thermoelectricity, Chernovtsy, Ukraine	

<b>Optimum design of a thermoelectric generating module for use of a waste heat thermoelectric generator</b>	<b>382</b>
<i>Tsuyoshi A., Kagawa Sh., Engo I., Hino M., Matsuura K.</i>	
Kobe City College of Technology, Japan	
KUBOTA Corporation, Japan	
Osaka University, Japan	
<b>Large scale thermoelectric conversion of waste heat and its use in the production of hydrogen</b>	<b>386</b>
<i>Matsuura K., Rowe D.M.</i>	
Osaka University, Osaka, Japan	
School of Engineering, University of Wales, Cardiff, UK	
<b>Catalytic thermoelectric generators(CATEG) for systems of cathode protection and telemechanic devices of gas mains</b>	<b>391</b>
<i>Pustovalov A.A., Rybkin N.N., Gusev V.V., Nebera L.P., Cubanok I.I., Lavrukhin V.K.</i>	
BIAPOS Scientific-Production Enterprise, Moscow, Russia	
Severgazprom Production Association, Ukhta, Komi Republic, Russia	
<b>Application of silicon germanium thermoelectric devices for electrical power production in space</b>	<b>394</b>
<i>Braun James F.</i>	
Lockheed Martin AstroSpace, King of Prussia, PA, USA	
<b>Comparison of thermoelectric space power system with alternative conversion options</b>	<b>401</b>
<i>Schock A.</i>	
Orbital Science Corporation, Germantown, MD, USA	
<b>Elaboration of New Concept on Creation of Transport Nuclear Reactor - Thermoelectric Generator</b>	<b>415</b>
<i>Marchuk N.D.</i>	
Institute for Nuclear Research NUAS, Kiev, Ukraine	
<b>Thermoelectric Batteries for Low-Powered Radionucleide Thermogenerators (RTG) with Long Service Life in Space</b>	<b>424</b>
<i>Ahatychuk L.I., Demchuk B.N., Pustovalov A.A., Makhorin O.I., Zhabin V.N.</i>	
Institute of thermoelectricity, Chernovtsi, Ukraine	
BIAPOS Scientific-Production Enterprise, Moscow, Russia	

---

*Section G – Thermoelectric coolers*

---

<b>Thermoelectric metal base module</b>	<b>428</b>
<i>Lushkina T.L., Blagorodov A.M., Dubov V.I.</i>	
"IMPULS" Joint-Stock Company, Moscow, Russia	
<b>Evaporation cooling of the elements of the thermoelectric heat pumps</b>	<b>430</b>
<i>Serebryanyi G.L.</i>	
Prived Individual Enterprise "COMFORT", Moscow, Russia	
<b>Example of application of thermoelectric cooler with high T<sub>c</sub> superconducting elements</b>	<b>438</b>
<i>Sidorenko N.A.</i>	
Institute for Problems in Mechanics, Moscow, Russia	
<b>A generalized procedure to study multistage thermoelectric coolers operated in the regime of maximum energy efficiency</b>	<b>442</b>
<i>Calperin V.L.</i>	
MGNPP "OSTERM", St.Petersburg, Russia	
<b>Non-steady cooling processes in pulsed-mode thermoelectric devices</b>	<b>446</b>
<i>Calperin V.L.</i>	
MGNPP "OSTERM", St.Petersburg, Russia	

<b>Optimization of the thermoelectric air chillers construction</b>	<b>449</b>
<i>Aivazov A.A., Stern Y.I., Makhratchov K.B.</i>	
Moscow institute of electronic engineering (Technical University), Moscow, Russia	
Terif Ltd., Russia	
<b>New approach to thermoelectric air-cooled subunit configuration</b>	<b>453</b>
<i>Sulin A.B.</i>	
Research Institute of Industrial and Marine Medicine, St.Petersburg, Russia	
<b>Thermoelectric fin</b>	<b>455</b>
<i>Zorin I.V.</i>	
A.F.Ioffe Physical-Technical Institute RAS, St.Petersburg, Russia	
<b>Preliminary thermoelectric cooling of cryogenic flux in microcryogenic vessel systems</b>	<b>459</b>
<i>Uryupin O.N., Bondarenko M.G., Grabov V.M., Ovchinnikov S.G.</i>	
A.F.Ioffe Physical-Technical Institute RAS, St.Petersburg, Russia	
<b>Optimal functions of magnetic field for the Peltier coolers</b>	<b>461</b>
<i>Anatychuk L.I., Vikhor L.N.</i>	
Institute of thermoelectricity, Chernovtsy, Ukraine	
<b>Thermoelectric Microcalorimetry of Biological Objects</b>	<b>464</b>
<i>Anatychuk L.I., Demchuk B.N., Luste O.J.</i>	
Institute of thermoelectricity, Chernovtsy, Ukraine	
<b>Microcalorimeter for Chemical Current Sources</b>	<b>467</b>
<i>Gavrilyuk N.V., Demchuk B.N., Petrenko N.S., Khmelevskaya Yu.S.</i>	
Institute of thermoelectricity, Chernovtsy, Ukraine	
<b>Thermoelectric cooling of semiconductor lasers under extreme temperature conditions</b>	<b>469</b>
<i>Semeniouk V.A., Pilipenko T.V.</i>	
Termion Co., Odessa, Ukraine	
<b>A novel thermally-driven thermoelectric heat pump</b>	<b>474</b>
<i>Nakahara Y., Tsutsumi A., Yoshida K.</i>	
Department of Chemical System Engineering, University of Tokyo, Tokyo, Japan	
<b>Thermoelectric regulation for electric cabinets</b>	<b>478</b>
<i>Redondo J.M., Sanchez J.M., Pascual I., Noriega G.</i>	
G.D.F. Department de Fisica Aplicada, Universitat Politecnica de Catalunya, Barselona, Spain	
BEROTZA, Pamplona, Navarra, Spain	
<b>The potential for improved cycle efficiency by combining thermoelectric coolers with vapor compression cycles in hybrid systems</b>	<b>481</b>
<i>Lyon H.B. Jr., Bierschenk J.</i>	
Marlow Industries, Inc., Dallas, TX, USA	
<b>Single stage thermoelectric coolers with temperature difference of 80 K</b>	<b>485</b>
<i>Semeniouk V.A., Svechnikova T.E., Ivanova L.D.</i>	
Termion Co., Odessa, Ukraine	
A.A.Baikov Institute of Metallurgy RAS, Moscow, Russia	
<hr/> <b>XIII ICT</b> <hr/>	
<b>MOCVD growth of Bi<sub>2</sub>Te<sub>3</sub> and related materials and their superlattice structures for high-ZT thermoelectric cooling devices</b>	<b>490</b>
<i>Venkatasubramanian R., Colpitts T.S., Malta D., Mantini M.</i>	
Research Triangle Institute, USA	
<b>Author Index</b>	<b>496</b>

**VERIFICATION OF A TRANSPORT MODEL  
FOR P-TYPE  $(\text{Bi}_{0.5}\text{Sb}_{0.5})_2\text{Te}_3$  AND  $(\text{Bi}_{0.25}\text{Sb}_{0.75})_2\text{Te}_3$  SOLID SOLUTIONS  
BY MEANS OF TEMPERATURE DEPENDENT THERMOELECTRIC PROPERTIES  
BELOW ROOM TEMPERATURE**

H. Süßmann, E. Müller  
*Martin-Luther-Universität Halle-Wittenberg*  
*Fachgruppe Angew. Physik, Germany*

Assuming a non-parabolic 1-valence band/6-valley structure and mixed carrier scattering, a model of the charge transport in p-type  $(\text{Bi}_{0.5}\text{Sb}_{0.5})_2\text{Te}_3$  and  $(\text{Bi}_{0.25}\text{Sb}_{0.75})_2\text{Te}_3$  has been established in the 100..300 K temperature range. From thermoelectric, galvanomagnetic and optical measurements on a single sample of elevated carrier density, resp., model parameters have been determined. The applicability of the model to a wide carrier concentration range, containing optimized material from high to low temperature conditions, has been proved by an extended data basis (temperature dependencies of thermoelectric properties for sample sets of varying carrier density).

### Introduction

Though solid solutions of the system  $(\text{Bi}_{1-x}\text{Sb}_x)_2\text{Te}_3$  have been the subject of investigation for almost forty years and have found a wide field of application, the transport properties especially for compositions near antimony telluride haven't been satisfactorily described yet. This results from a complex combination of effects like strong crystal anisotropy, non-parabolic bands, mixed scattering, the occurrence of two valence bands... One way to obtain interpretations by means of convenient models implies the restriction on pure scattering with introduction of a real scattering exponent [1],[2]. Another approach gives an interpretation of selected sets of transport properties basing on simplified model assumptions [3]. On the other hand, more sophisticated models with a growing number of parameters have to be involved in order to get a consistent interpretation of a larger number of measured properties by means of numeric parameter fits. Whereas the temperature dependence of the galvanomagnetic low-field coefficients of  $\text{Bi}_2\text{Te}_3$  could be described by means of pure isotropic acoustic phonon scattering and non-parabolic bands, this was found to be inadequate for  $(\text{Bi}_{0.25}\text{Sb}_{0.75})_2\text{Te}_3$ , even by assuming anisotropic mixed scattering including ionized impurities [4]. Usually the implication of parallel main axes systems of the tensors of effective mass and relaxation time has been used.

This work gives an interpretation of galvanomagnetic and infra-red optical measurements on p-type  $(\text{Bi}_{0.5}\text{Sb}_{0.5})_2\text{Te}_3$  and  $(\text{Bi}_{0.25}\text{Sb}_{0.75})_2\text{Te}_3$  assuming a non-parabolic six-valley valence band structure, non-parallel main axes of the co-ordinate systems of effective mass and relaxation time as well as anisotropic mixed scattering in consideration of several mechanisms including an inelastic one.

The availability of a transport model is of practical importance especially for materials, which properties are essentially influenced by material inhomogeneities. In [5] a concept has been developed to reach a cold end temperature below 130 K by a multi-stage PELTIER cooler with the aim of a pure thermoelectric cooling of high temperature superconductors. Because of the increased mobility expected at lower temperatures,  $(\text{Bi}_{1-x}\text{Sb}_x)_2\text{Te}_3$  with a composition  $x < 0.75$  has been estimated there as a promising p-type material for the coldest stage(s) ("low temperature material" - LTM). Therefore the carrier density has to be diminished below the optimal value for room temperature application. This amplifies the deteriorating influence of local carrier density variation. At this point, the technologic-empirical approach to material optimization finds its limits, because it doesn't permit a distinction between single crystal properties and inhomogeneity influence. Then, a transport model with parameters determined from homogeneous samples of elevated carrier concentration allows the estimation of the maximal figure of merit (FOM) of a homogeneous single crystal, if the validity of extrapolation to lower carrier density values can be assured.

### The non-parabolic 1-VB/6-valley model für p-type $(\text{Bi}_{1-x}\text{Sb}_x)_2\text{Te}_3$ ( $x=0.5, 0.75$ )

**Specimens:** Large single crystals of  $(\text{Bi}_{0.5}\text{Sb}_{0.5})_2\text{Te}_3$  and  $(\text{Bi}_{0.25}\text{Sb}_{0.75})_2\text{Te}_3$  with a carrier concentration of about  $2 \cdot 10^{19} \text{ cm}^{-3}$  and  $3.5 \cdot 10^{19} \text{ cm}^{-3}$ , resp., have been grown by CZOCHRALSKI method [6]. The homogeneity of the

specimens was ascertained by a locally resolving measurement of the SEEBECK coefficient [15]. The temperature dependencies of the thermoelectric properties have been recorded between 100..400 K along and across the crystallographic c-axis; furthermore the HALL coefficients  $\rho_{123}$  and  $\rho_{312}$ , the longitudinal magneto-resistances  $\rho_{1111}, \rho_{3333}$  and the transverse magneto-resistances  $\rho_{1122}, \rho_{1133}, \rho_{3311}$  have been measured between 110..350 K using a magnetic field of about 1 T. Infra-red reflectivity of polished crystal surfaces perpendicular to the cleavage planes was investigated. Reflectance spectra within 300..5000  $\text{cm}^{-1}$  have been obtained on a Fourier spectrometer between 40 K and 300 K for an electric field polarization parallel and perpendicular to the c-axis, resp.

**Fundamental:** The quantitative interpretation of the galvanomagnetic low-field transport properties can be given from the solution tensor of the BOLTZMANN equation. The model functions of all galvanomagnetic quantities are determined by the tensor of the energy dependent mobility of charge carriers  $u_i(y)$  and the FERMI level. Infra-red reflectivity is calculated from the frequency dependence of the dielectric susceptibility, which is obtained from the frequency dependent relaxation time [7]. Carrier scattering on lattice vibrations has been confirmed to be the most important scattering mechanism for  $(\text{Bi}_{1-x}\text{Sb}_x)_2\text{Te}_3$  in the 100 to 300 K temperature range. In multi-valley semiconductors an inelastic carrier transition from one energy minimum into another may occur during scattering processes. Defect scattering can be expected as well. The high carrier concentration of  $10^{18}..10^{20} \text{ cm}^{-3}$  due to the strong disorder of the crystal lattice [8] should be accompanied by the occurrence of ionized impurities to the same extent. Therefore in qualitative discussions, discrepancies between experiment and simplified interpretation models have often been attributed to ionized impurity scattering.

With more than one independent mechanism involved, the inverse relaxation times have to be added. When intervalley scattering (IVS) on acoustic phonons occurs, the electron-phonon-interaction (absorption or emission of a phonon) is accompanied by a non-negligible change of the carrier energy, i.e. strongly inelastic [9]. The scattering rate is isotropic and a relaxation time  $\tau(E)$  can be introduced.

The calculation of transport coefficients from given values of the band structure and carrier scattering parameters, FERMI level and temperature was executed by the following procedure:

- Construction of the tensors of the inverse effective mass  $a_{ij}^A$  and the relaxation time tensor  $\tau_{ij}^A$  in their main axes' systems from given values
- Transformation into the basal plane across the crystallographic c-axis ( $a_{ij}^B, \tau_{ij}^B$ )
- Calculation of the energy-dependent mobility tensor  $u_{ik}^B \sim a_{ij}^B \tau_{jk}^B$  in the basal system B
- Evaluation of the orientation of the main axes system H of microscopic mobility at the current carrier energy y:  $u_{ij}^H(y)$
- Construction of the energy-dependent integrands for the components of the conductivity and thermodiffusion tensor
- Main axes' transformation of the integrands to the crystal system K and summation over the six valleys using the transformation equations given in the DRABBLE and WOLFE model [10]
- Numerical integration over all carrier energy values in the crystal system. Thus, the conductivity, HALL- and magneto-conductivity and the thermodiffusion tensor are obtained

- Calculation of the HALL- and magneto-resistance coefficients from the conductivity components (after [10,7]), calculation of the SEEBECK coefficients.

**Fitting procedure:** The parameter fit was based on temperature dependences of 13 experimental quantities: SEEBECK coefficients, resistivity and HALL coefficients for two independent crystallographic directions each, two longitudinal and three transverse magneto-resistance coefficients and the parameter  $p/m_x^*$  for the two directions of field polarization obtained from infra-red reflectivity. A set of 12 fitting parameters has been chosen: three components of the relaxation time constant along the main axes directions of the dominating scattering mechanism and the tilt angle of its co-ordinate system, three components of the inverse effective mass tensor  $a_{ii}^A$  along its main axes directions and the tilt angle of the isoenergy ellipsoids, three constant mixing parameters along the main axes directions of the relaxation time as well as the parameter of non-parabolicity  $\beta$  at 300 K. In order to evaluate the influence of various scattering mechanisms, six versions of the model with different scattering types have been tested: Acoustic deformation potential scattering either as single process or mixed with another elastic (scattering on linear dislocations/neutral/ionized impurities, alloy scattering) or inelastic mechanism (IVS on acoustic phonons). In order to exclude the temperature range of intrinsic effects, the fitting process has been restricted to 100..300 K for  $(Bi_{0.5}Sb_{0.5})_2Te_3$  and 100..360 K for  $(Bi_{0.25}Sb_{0.75})_2Te_3$ .

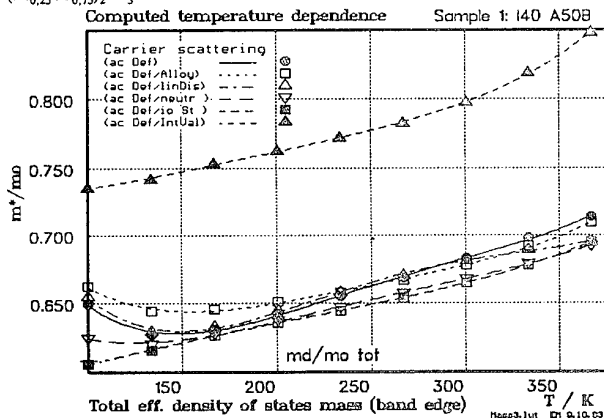


Fig. 1 Comparison of competing versions of carrier scattering: mixed scattering including intervalley processes leads to modified model values. The weak slope causes higher FOM at LT

**Fit results:** For both samples very small mixing parameters for scattering with contribution of alloy scattering or linear dislocations have been found. The temperature dependencies of the parameters differ only insignificantly from those obtained in the case of pure acoustic deformation potential scattering. The mixing parameters for neutral and ionized impurity scattering partly adopted negative values. Hence, these model versions have to be rejected.

The exclusion of the assumption of ionized impurity scattering at temperatures above 100 K is in correspondence with measurements of the electrical conductivity on p-type  $(Bi_{1-x}Sb_x)_2Te_3$  [11], which showed a continued increase with falling temperature until about 5 K. In coincidence, the values of the parameter  $\tau_{op}$  derived from reflectivity spectra increase with decreasing temperature down to less than 20 K. However, if impurity scattering should have any importance above 100 K, it ought to become dominant at somewhat lower temperatures.

A qualitative improvement of the model fit has been obtained by assuming a contribution of inelastic scattering. This becomes evident especially for the curvature of the HALL coefficients and the magneto-resistance in the lower part of the temperature range as well as by the capability to reproduce partly the slight anisotropy of the SEEBECK coefficient, which has been experimentally proved for  $(Bi_{0.25}Sb_{0.75})_2Te_3$ . For the assumption of a contribution of IVS an essential shift of the fitting parameters and deduced quantities has been observed: higher values of the effective mass and relaxation time components, lower non-parabolicity and FERMI level. Then, the parameter of non-parabolicity at 300 K is 0.015 for both compositions. The total carrier density calculated from the fitting parameters remains constant within 10 % ( $(Bi_{0.5}Sb_{0.5})_2Te_3$ ) or is varying within 30 % depending on the scattering assumed ( $(Bi_{0.25}Sb_{0.75})_2Te_3$ ). The FERMI level shows a strong almost linear decrease with temperature due to the temperature dependence of the FERMI function. At room temperature a

strong anisotropy of the effective mass tensor has been found in qualitative agreement with STORDEUR [3]. The  $a_{ii}^A$  are falling by about 20..30 % over the temperature range. The tilt angle shows very little variation with temperature. The total d.o.s. mass calculated from this data increases with temperature (Fig. 1, Fig. 2). The slope at low temperature is higher for  $(Bi_{0.25}Sb_{0.75})_2Te_3$ , which brings along a mobility decrease (i. e. FOM degradation).

The anisotropy of the relaxation time constant has been obtained to be small. The maximum deviation between the components at room temperature is about 30 %. The largest component has been found along the 22 direction. Similar to the findings of [4,7] the relaxation time constants exhibit a noticeable decrease with temperature.

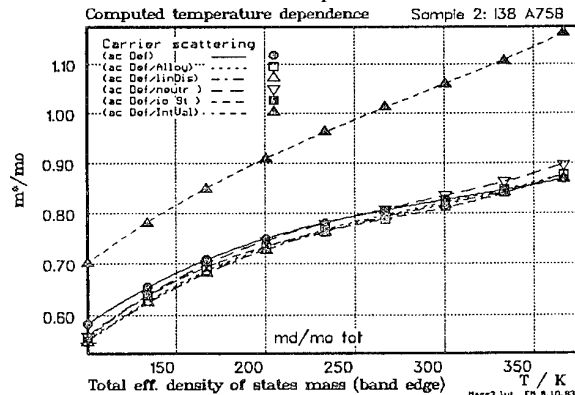


Fig. 2 Comparison of versions of carrier scattering: An analogous shift of model parameters and dependent quantities is observed due to the change to mixed elastic/inel. scattering for  $x=0.5$  and  $x=0.75$

The dependence of the calculated carrier density on the assumed scattering version gives a further experimental confirmation to IVS: The saturation value of the high field HALL coefficient yields the experimental carrier density independently from any model assumption. On the  $(Bi_{0.25}Sb_{0.75})_2Te_3$  sample this value has been ascertained [11]. At room temperature it coincides to the calculated value for mixed acoustic phonon/IVS scattering within the experimental errors.

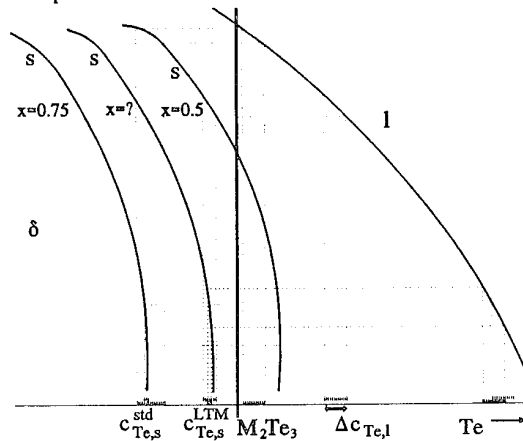


Fig. 3 Variation of the Te concentration in the range of solubility for several material compositions (std/LTM) for a given value of variation of the liquid Te concentration at the phase boundary (schematically)

### Influence of local carrier density variation on LTM

The production of homogeneous  $(Bi_{1-x}Sb_x)_2Te_3$  LTM makes extreme demands on crystal growth. Because doping brings along the risk of mobility restriction, the necessary reduced carrier density is tuned by growth with excess tellurium in the melt. A strong tendency to segregation along the growth direction results from the small distribution coefficient of Te. The radial dependence of heat conduction inside the growing solid inhibits the forming of a plane phase boundary and leads to radial gradients of the Te concentration. As a consequence, gradients or a local variation of the properties over scales of the crystal dimension are observed (macro-inhomogeneity). Hydrodynamic instabilities near the phase boundary due to solutal density convection generate a variation of the Te concentration

over a mm to  $\mu\text{m}$  scale (micro-inhomogeneity). High Te enrichment near the crystallization front lets arise the assumption of the formation of Te incorporations in the solid [12]. A reduction of the FOM  $Z$  is related to a carrier density variation due to the inhomogeneous Te incorporation or electrically conducting precipitations: The occurrence of circular thermo-electric currents diminishes the effective SEEBECK coefficient and causes an additional contribution to heat conduction. The  $Z$  reduction is essentially influenced by the material composition  $x$  and the average value of the carrier density  $p$ : The Te content in the liquid  $c_{\text{Te},l}$  changes insignificantly over the whole range of the solid concentration  $c_{\text{Te},s}$  inside the homogeneous  $\delta$ -phase due to its small width [13]. With a given state of inhomogeneity in the liquid near the phase boundary (mean variation:  $\Delta c_{\text{Te},l}$ ), the variation in the solid  $\Delta c_{\text{Te},s}$  is determined by the slope of the *solidus* line at the Te-rich side of the  $\delta$ -phase in the quasibinary phase diagram (Bi,Sb)-Te (Fig. 3). Due to the composition dependence of the deviation from stoichiometry at the dystectic point,  $\Delta c_{\text{Te},s}$  will be influenced for a given  $p$  by the choice of the material composition.

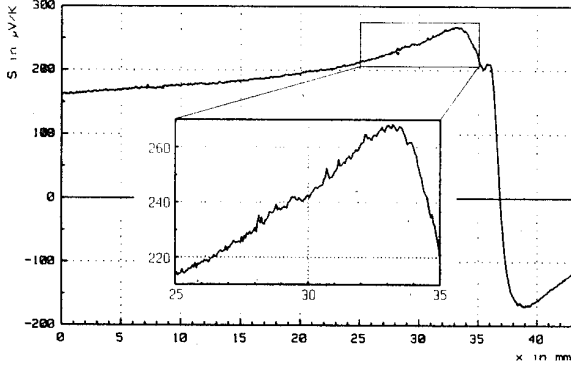


Fig. 4 SEEBECK-scan along a BRIDGMAN-grown ingot of  $(\text{Bi}_{0.5}\text{Sb}_{0.5})_2\text{Te}_3$ . The Te segregation leads to the conversion to n-type. The box magnifies the part of maximal  $S$

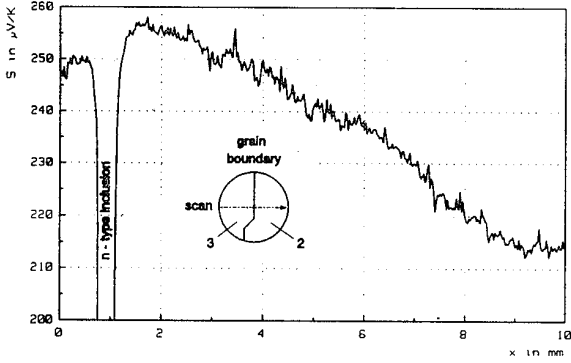


Fig. 5 Scan of the SEEBECK-coefficient over the cross section of a cylindric sample of  $(\text{Bi}_{0.5}\text{Sb}_{0.5})_2\text{Te}_3$  with a n-type inclusion.

Fig. 3 presents the situation schematically for the investigated compositions  $x=0.5, 0.75$  and an intermediate value: For LTM ( $x=0.5$ ) the stoichiometry line ( $\text{M}_2\text{Te}_3$ ) intersects the range of existence;  $c_{\text{Te},s}$  can be increased until n-conduction is reached. For an intended carrier concentration  $p$ , i. e. for a given  $c_{\text{Te},s}$  the *solidus* line is less inclined than for standard material ("std",  $x=0.75$ ). Hence, the inhomogeneity content increases. N-type inclusions are easily formed for macro-inhomogeneous material of low average carrier density. If the material composition is chosen in a manner, that the reduced carrier concentration necessary for LTM is just reached for the steepest range of the *solidus* line (and the  $\delta$ -phase doesn't touch the stoichiometry line), most favorable conditions for the generation of homogeneous material exist. With drawing advantage from the Te segregation, [14] investigated samples of different carrier density from one zone melted  $(\text{Bi}_{0.5}\text{Sb}_{0.5})_2\text{Te}_3$  ingot. From the stabilization of the material properties near the end of the ingot at low carrier density values can be concluded, that an inversion to n-type is still possible for  $x<0.6$ . Their

maximum values of the temperature dependencies of the HARMAN FOM are in qualitative agreement with our computed curves  $Z_{\max}(T)$  (see Fig. 10).

A locally resolving thermo probe technique [15] allows an exemplary characterization of the inhomogeneity state (line and planar scans on the sample surface) down to a resolution of  $20..50 \mu\text{m}$ . Fig. 4 shows a line scan along the axis of a  $(\text{Bi}_{0.5}\text{Sb}_{0.5})_2\text{Te}_3$  BRIDGMAN ingot. The small extension of the area with LTM properties is recognizable. This area is located in a section of strong gradients of the SEEBECK coefficient and in near neighborhood to the pn-transition. Therefore a preparation of LTM samples with satisfactory homogeneity from this ingot cannot be expected. Fig. 5 presents a scan along the radial direction near the pn-transition containing a n-type inclusion as a typical (and fatal) example of macro-inhomogeneity.

With decreasing amount of the carrier density the reduction of the FOM due to a given variation  $\Delta c_{\text{Te},s}$  grows drastically. With a FOURIER series approach after [16] for micro-inhomogeneity of small amplitude, formulae for the estimation of the effective material properties have been developed in [17]. In the longitudinal layer case (i. e. for parallel connection of regions with different properties) the expressions

$$\begin{aligned} \text{Thermoel. circular currents: } S_{\text{eff}} &\propto, \kappa_{\text{eff}} \rightarrow Z_{\text{eff}} \\ S_{\text{eff}} &= \langle S \rangle \left\{ 1 + \left( \frac{\Delta P}{P} \right)^2 \left( -\frac{1}{2} \frac{k_B/e_o}{\langle S \rangle} \right) \right\} \quad \langle \dots \rangle - \text{local average} \\ \kappa_{\text{eff}} &= \langle \kappa \rangle \left\{ 1 + \left( \frac{\Delta P}{P} \right)^2 \left( \frac{k_B/e_o}{\langle S \rangle} \right)^2 Z T \right\} \\ Z_{\text{eff}} &= \langle Z \rangle \left\{ 1 + \left( \frac{\Delta P}{P} \right)^2 \left( -\frac{k_B/e_o}{\langle S \rangle} \right) \left( 1 + Z T \frac{k_B/e_o}{\langle S \rangle} \right) \right\} \end{aligned} \quad (1)$$

are valid. For optimized material (SEEBECK coefficient  $S_{\text{opt}}=S(Z_{\max})$ ), the approximation  $k_B/e_o/S_{\text{opt}} \approx 1/3$  can be applied independently from temperature (compare Fig. 6,7: temperature dependence  $S_{\text{opt}}(T)$ ). Hence, for the reduction of the FOM results

$$\delta = 1 - \frac{Z_{\text{eff}}}{\langle Z \rangle} \propto \left( \frac{\Delta c_{\text{Te},s}}{P} \right)^2 \left( 1 + \frac{Z T}{3} \right), \quad \text{Low temp.: } \delta \propto \frac{1}{P^2} \quad (2)$$

An estimation for the increase of the inhomogeneity influence when changing from standard ("std") to LTM can be deduced from the ratio of the conductivity values (see Fig. 8):

$$\text{Exp. } (\text{Bi}_{0.5}\text{Sb}_{0.5})_2\text{Te}_3: \quad \frac{P_{\text{opt}}^{\text{std}}}{P_{\text{opt}}^{\text{LTM}}} \approx 3 \rightarrow \frac{\delta^{\text{LTM}}}{\delta^{\text{std}}} \approx 6 \cdot 10 \left( \frac{\Delta c_{\text{Te},s}^{\text{LTM}}}{\Delta c_{\text{Te},s}^{\text{std}}} \right)^2 \quad (3)$$

The empirical search for optimal LTM therefore meets systematical obstacles.

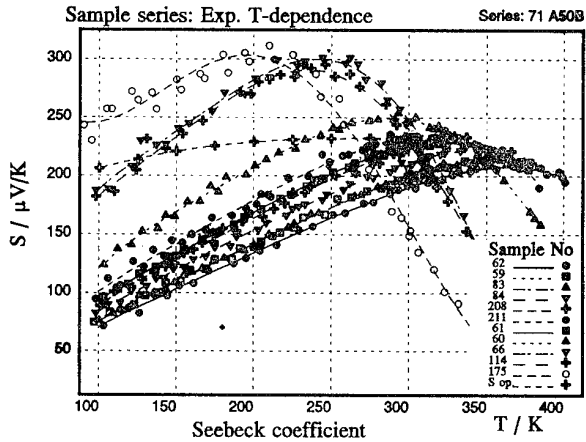


Fig. 6 Sample series of a BRIDGMAN ingot ( $x=0.5$ ).  $S_{\text{opt}}$  - calculated value at maximum FOM (one-carrier model)

### Temperature dependent properties

Cylindrical specimens of 1..3 mm in length were cut from a BRIDGMAN-

grown  $(\text{Bi}_{0.5}\text{Sb}_{0.5})_2\text{Te}_3$  single crystalline ingot ( $\varnothing$  10 mm). The temperature dependence of thermoelectric properties (SEEBECK coefficient  $S$ , electrical and thermal conductivity  $\sigma$ ,  $\kappa$ , figure of merit (HARMAN)  $Z_H$ , 100..400 K) along the ingot axis (across the crystallographic  $c$ -axis) are presented in Fig. 6,8,9,10. For comparison, measurements will be discussed for a set of selected samples of the composition  $(\text{Bi}_{0.25}\text{Sb}_{0.75})_2\text{Te}_3$  with differing carrier density values (Fig. 7,11).

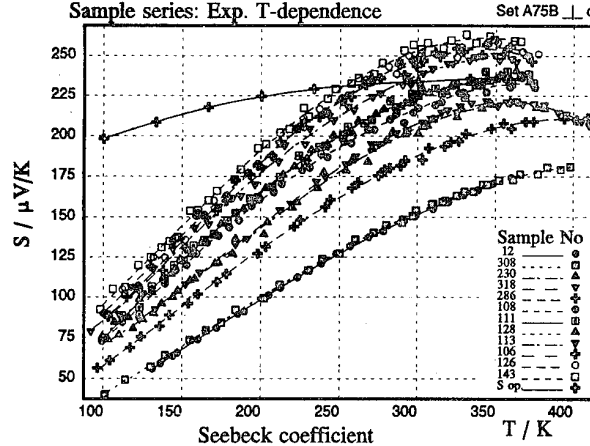


Fig. 7 Set of samples ( $x=0.75$ ) with different carrier density: The highest reachable  $S$  values are limited by Te solubility.  $S_{\text{opt}}$  - calculated value at maximum FOM (one-carrier model)

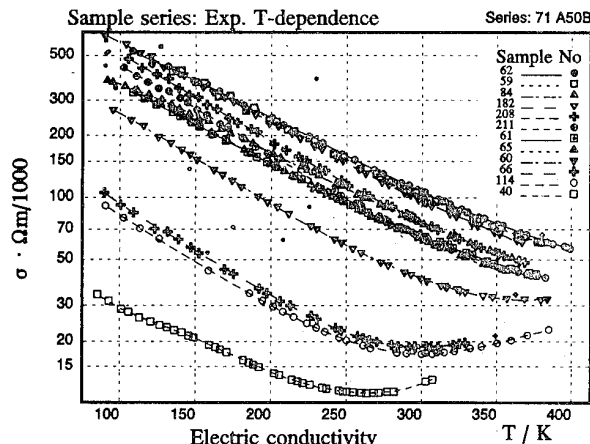


Fig. 8 Sample series of a BRIDGMAN ingot ( $x=0.5$ ): The conductivity can be diminished down to the intrinsic level by increasing the Te concentration

The consideration of Fig. 6 and Fig. 10 reveals, that the shift of the  $Z(T)$  maximum below room temperature begins for values of the SEEBECK coefficient  $S(300 \text{ K}) > 230 \mu\text{V/K}$ , i. e. about 8 mm away from the pn-transition (look Fig. 4). The maximum room temperature value of the SEEBECK coefficient at the transition from one-carrier conduction to mixed conduction is equivalent to the location of the  $Z(T)$  maximum in the 150..200 K range. The zoom in Fig. 4 shows in this region of the ingot increasing inhomogeneity (upcoming gradients). Samples with a maximum in their  $Z(T)$  dependence below 150 K exhibit at room temperature SEEBECK coefficient values falling below 200  $\mu\text{V/K}$  due to a growing portion of electron conduction. In the considered ingot this region is very small and disturbed by a steep gradient. Therefore greatly reduced values of the HARMAN FOM had to be expected from an integral measurement of this part (sample N° 40).

In comparison to the temperature dependencies of the SEEBECK coefficient of both compositions (Fig. 6:  $x=0.5$ , Fig. 7:  $x=0.75$ ) a significant curvature and a steeper slope of the  $(\text{Bi}_{0.25}\text{Sb}_{0.75})_2\text{Te}_3$  curves is recognizable especially at low temperatures, whereas  $S(T)$  for  $(\text{Bi}_{0.5}\text{Sb}_{0.5})_2\text{Te}_3$  in the extrinsic range has an essentially linear shape. This is caused by the differences of the temperature dependence of the band shape and can be understood in context with the calculated dependencies of d.o.s. mass (Fig. 1:  $x=0.5$ , Fig. 2:  $x=0.75$ ), if a temperature constant carrier density is implied: The stronger decrease of the effective mass towards lower

temperatures for  $(\text{Bi}_{0.25}\text{Sb}_{0.75})_2\text{Te}_3$  is equivalent to a narrowing of the energy extrema and leads to a higher FERMI level.

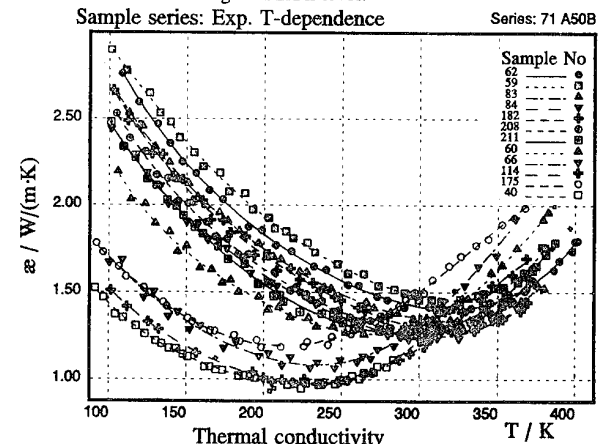


Fig. 9 Sample series of a BRIDGMAN ingot ( $x=0.5$ ): The increasing inhomogeneity towards decreasing conductivity lifts the lowest curves and causes intersections

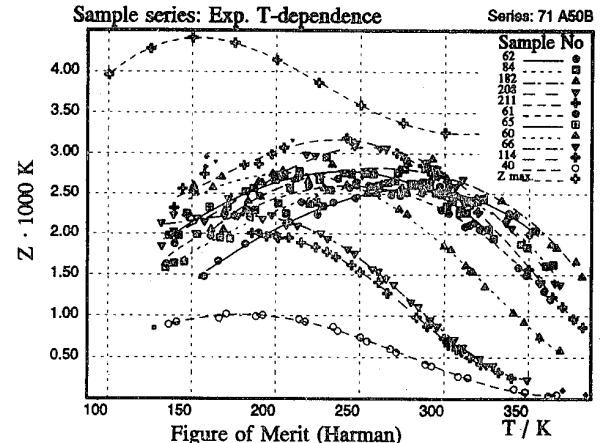


Fig. 10 Sample series of a BRIDGMAN ingot ( $x=0.5$ ): Strong inhomogeneity leads to reduced experimental values at low temperatures;  $Z_{\text{max}}$  - calculated maximum value (one-carrier model)

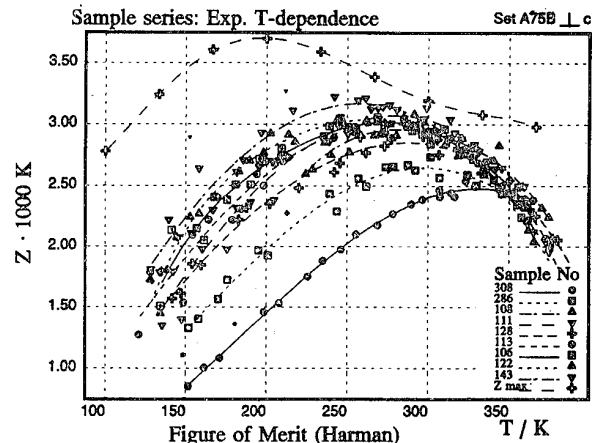


Fig. 11 Sample set ( $x=0.75$ ): The limited Te solubility prevents that the theoretical maximum values are reached at low temperature.  $Z_{\text{max}}$  - calculated maximum value (one-carrier model)

The smaller band gap of  $(\text{Bi}_{0.5}\text{Sb}_{0.5})_2\text{Te}_3$  brings along a significant degradation of the FOM at room temperature, whereas this becomes apparent for  $(\text{Bi}_{0.25}\text{Sb}_{0.75})_2\text{Te}_3$  still above about 320 K. For this reason the HARMAN experimental values of  $(\text{Bi}_{0.5}\text{Sb}_{0.5})_2\text{Te}_3$  reach their best approximation to the computed maximum values (extrinsic model) below room temperature (Fig. 10), whereas  $(\text{Bi}_{0.25}\text{Sb}_{0.75})_2\text{Te}_3$  nearly reproduces the calculated values near 300 K (Fig. 11). The maximum 300 K SEEBECK coefficient reaches amounts about 260..270  $\mu\text{V/K}$  for both sample sets. The restriction arises

for  $(Bi_{0.5}Sb_{0.5})_2Te_3$  from the beginning intrinsic processes, for  $(Bi_{0.25}Sb_{0.75})_2Te_3$  on the other hand from the limited solubility of Te. The latter results in the fact, that the optimization condition can no more be fulfilled for  $(Bi_{0.25}Sb_{0.75})_2Te_3$  without admixtures below about 250 K. This is in agreement to the limitation of the diminution of electrical and thermal conductivity for  $(Bi_{0.25}Sb_{0.75})_2Te_3$ . The descend of the HARMAN FOM below the theoretical maximum values at low temperatures for  $(Bi_{0.5}Sb_{0.5})_2Te_3$  is on the other hand connected to the strong inhomogeneity of the available LT samples. An indication for that are the moderated temperature dependence of the electrical conductivity (sample № 40) as well as an increase of the thermal conductivity (formation of thermoelectric circular currents). The thermal conductivity reacts most sensitive of all quantities to both the appearance of a second carrier type and material inhomogeneity. Hence, a direct experimental proof for inhomogeneity is accessible: Similar to the electrical conductivity the thermal conductivity depends for a fixed temperature and a given material composition monotonously on the majority carrier concentration, both for the electronic and the bipolar component. Intersections of the temperature dependencies of a sample series can solely be caused by the uplift of single curves due to additional contributions of thermal conductivity. In agreement to the above discussion this concerns especially the LTM samples. Hence, for homogeneously prepared LTM a significantly higher FOM than from our ingot should be expected. The electrical conductivity exhibits the lowest sensitivity to the occurrence of a second carrier type. Its influence becomes apparent still for lowest conductive  $(Bi_{0.5}Sb_{0.5})_2Te_3$  samples. The greatly inhomogeneous sample № 40 has a clearly moderated slope compared to the parallelity of all other conductivity curves in the extrinsic range. In the logarithmic diagram the nearly linear dependencies  $\sigma(T)$  for  $(Bi_{0.5}Sb_{0.5})_2Te_3$  contrast with the slightly curved ones for  $(Bi_{0.25}Sb_{0.75})_2Te_3$ .

#### Determination of properties of homogeneous LTM

The computation of the optimal carrier density and the reachable maximum FOM for given values of composition and operational temperature was based on the model of charge transport discussed above. Macro-homogeneous single crystals of high quality with higher than room temperature optimal carrier density were used. In this way the influence of local variation of the Te concentration is reduced and the evaluable extrinsic range is extended towards higher temperature. Model parameters are obtained from the fit to an extensive data set. For a given value  $S(T_o)$  they provide computed temperature dependencies of relevant quantities of charge transport ( $S(T)$ ,  $\sigma(T)$ ,  $p(T)$ ,  $L(T)$ ). The lattice contribution of the thermal conductivity was separated from the experimental values and used for the calculation of the FOM. The reachable maximum FOM  $Z_{max}$  for an operational temperature  $T_o$  and the belonging to it optimal concentration  $p_{opt}$  was obtained from the maximization of the function  $Z(p, T=T_o)$ . Then,  $S_{opt}=S(p_{opt}, T=T_o)$ . The execution of this procedure for a sufficiently close grid of composition values  $x$  yields a function  $Z_{max}(x, T)$ , from which a function of the optimal composition  $x_{opt}(T)$  can be built.

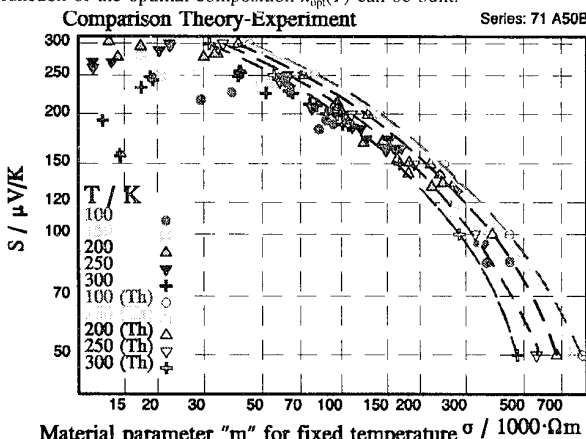


Fig. 12 ( $x=0.5$ ): The calculated curves yield a monotonous increasing parameter  $m$  with falling temperature. Small  $\sigma$ : intrinsic effects reduce the experimental values

#### Theory and experiment: $S(\sigma)$

The reliability of such limit functions can only be assumed, if the applicability of the transport model can be assured over the whole range of relevant carrier density values. This is possible by means of comparison of the  $S(\sigma)$  dependence for a set of samples with different carrier density values at a fixed temperature. For each sample, one point is formed from interpolation values of the experimental temperature dependencies  $S(T)$  and  $\sigma(T)$ . This points array on parameter curves, which location is a quality parameter for the maximum FOM  $Z_{max}(T_o)$ . (For simplifying model assumptions - isotropic scattering - values of the material parameter  $m=\mu_o(m_0/m_0)^{3/2}$  can be determined from the curve;  $\mu_o$  - carrier mobility in the case of BOLTZMANN statistics.) The curves can immediately used for material comparison between different compositions with equal lattice thermal conductivity. This comparison is more meaningful for the properties of homogeneous single crystals than the immediate consideration of HARMAN FOM, since the SEEBECK coefficient and the electrical conductivity are the least sensitive to material inhomogeneity quantities.

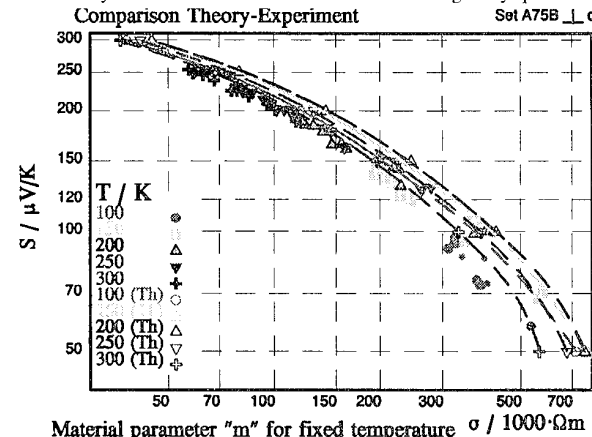


Fig. 13 Parameter curves  $S(\sigma)$  ( $x=0.75$ ): The highest values  $m$  are calculated for 200 K. The experimental values show a weak variation (weak inhomogeneity)

If the range of smallest conductivity for  $(Bi_{0.5}Sb_{0.5})_2Te_3$  (Fig. 12) is left aside (where no comparison between theory and experiment is possible due to systematical reasons since the model implication (one carrier type) is not fulfilled), the calculated  $S(\sigma)$  curves practically coincide with the experimental dependencies above 200 K. Merely for the lowest temperatures the experimental values remain slightly smaller. The model reproduces the experimental result of a monotonous increasing parameter  $m$  with falling temperature. For  $(Bi_{0.25}Sb_{0.75})_2Te_3$  (Fig. 13), the model yields the highest  $m$  values near 200 K. The sorting of the experimental curves is weaker, the 100 K values remain slightly behind the calculated ones and those for  $(Bi_{0.5}Sb_{0.5})_2Te_3$ .

As a further criterium for the applicability of the transport model can be checked, whether the used calculation procedure provides a lattice thermal conductivity value independently from the carrier concentration of the sample. At 100 and 300 K nearly identical values have been found for sample sets of both compositions. Hence, the comparison of the  $S(\sigma)$  curves shows the material with higher  $Z_{max}$  at these temperatures. The plot over electrical conductivity yields practically constant values, merely above 250 K a weak sorting appears for  $(Bi_{0.25}Sb_{0.75})_2Te_3$ . Hence, the suggested model can be evaluated as applicable for specimens down to low carrier density values.

#### Conclusions

The proposed charge transport model gave for both  $(Bi_{0.5}Sb_{0.5})_2Te_3$  and  $(Bi_{0.25}Sb_{0.75})_2Te_3$  a satisfying fit of the experimental temperature dependences. The fitting parameters of the effective mass are comparable to literature values by magnitude and component's ratio. Their variation with temperature remains weak. The scattering on acoustic deformation potential shows small anisotropy nearly parallel to the crystal's axes. The relaxation time constants are decreasing with temperature. A satisfying fit is obtained for pure acoustic phonon scattering, which is not significantly improved for mixed elastic scattering. The consideration of inelastic

scattering yields a qualitatively better reproduction of the temperature dependencies, especially of the galvanomagnetic coefficients between 100..150 K and could explain the small anisotropy of the SEEBECK coefficient measured. The mixing parameters are small.

The applicability of the model to the relevant range of carrier concentration could be confirmed. The assumption of intervalley scattering between equivalent energy extrema of the six-valley structure is emphasized by a high field HALL experiment. It could be shown, that homogeneous  $(\text{Bi}_{0.5}\text{Sb}_{0.5})_2\text{Te}_3$  material possesses more favorable features for low temperature application compared to  $(\text{Bi}_{0.25}\text{Sb}_{0.75})_2\text{Te}_3$  due to its band structure and higher Te solubility. Nevertheless, its strong tendency to inhomogeneity aggravates the preparation of sufficiently homogeneous material and presents a challenge to the growth techniques, which are less complicated to control in the composition range  $0.5 < x < 0.75$ .

### References

- [1] H. Kaibe, Y. Tanaka, M. Sakata, I. Nishida, J. Phys. Chem. Solids, Vol. 50 No. 9 (1989) 945-950.
- [2] V. A. Kutasov, L. N. Luk'yanova, Sov. Phys. Solid State, **26** (1984) 1515.
- [3] M. Stordeur, phys. stat. sol. (b) **150** (1988) 165
- [4] Th. Eick, Dissertation, Martin-Luther-Universität Halle-Wittenberg (1987)
- [5] M. V. Vedernikov et. al., Proc. of the XIII. Conf. on Thermoel., Kansas City (1994)
- [6] L. D. Ivanova, J. V. Granatkina, H. Süßmann, E. Müller, Int. Conf. "Crystal Growth", Novosibirsk (1992)
- [7] M. Stordeur, Dissertation B, Martin-Luther-Universität Halle-Wittenberg (1987)
- [8] B. M. Golman, V. A. Kudinov, I. A. Smirnov, "Poluprovodnikovye termoelektricheskie materialy na osnove  $\text{Bi}_2\text{Te}_3$ ", Izd. Nauka Moscow (1972)
- [9] B. R. Nagi, "Electron transport in compound semiconductors", Springer-Verlag Berlin Heidelberg New York (1980)
- [10] J. R. Drabble, R. Wolfe, Proc. Phys. Soc. **69B** (1956) 1101.
- [11] Ch. Baier, D. Elefant, Proc. of the 2nd Symp. on Thermoel., Dresden (1994)
- [12] P. Reinshaus, Dissertation A, Martin-Luther-Universität Halle-Wittenberg (1990)
- [13] R. F. Brebrick, J. Phys. Chem. Solids, **30** (1969) 712.
- [14] A. A. Ajvasov, A. I. Anukhin, A. I. Mazina, N. A. Boboshko, Neorganicheskie materialy, **27** № 10 (1991) 2072-2078.
- [15] H. Süßmann, M. Bohm, P. Reinshaus, Proc. of the XII. Int. Conf. on Thermoel., Yokohama (1993)
- [16] C. Herring, Bell Syst. Tech. J. **34** (1955) 237.
- [17] V. A. Kudinov, B. Ya. Moizhes, Fizika tverd. tela, **7** № 8 (1965) 2309-2317.

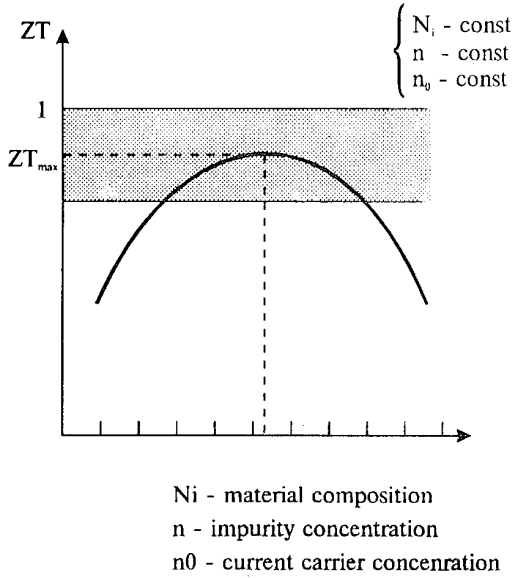
## FUNCTIONAL-GRADIENT MATERIALS FOR THERMOELECTRIC ENERGY CONVERTORS

Anatychuk L.I., Vikhor L.N., Kuznetsov A.V., Letiuchenko S.D.

*Institute of ThermoElectricity, General Post-Office, Box 86, 274000, Chernivtsi, Ukraine*

It is well-known that progress in thermoelectrics occurs mainly due to the progress in thermoelectric material science. For last 30 - 40 years the scientists worked hardly on finding the optimal parameters of the homogeneous thermoelectric material. These are the composition, dopants concentration determining the current carriers concentration in materials (fig. 1). It was silently said that the object for study is homogeneous thermoelectric material. Success of this approach coming true is undoubtable.

*Fig.1. Homogeneous thermoelements optimal parameters*



But there are no material changes in figure of merit increase during last decades. Value of  $zT$  is around the magic for thermoelectrics magnitude of  $zT \approx 1$ . Our institute has made the analysis for maximum possibilities of homogeneous materials. From this it follows that the further essential improvement of the figure of merit for the known electron and phonon substance structures will maybe not occur.

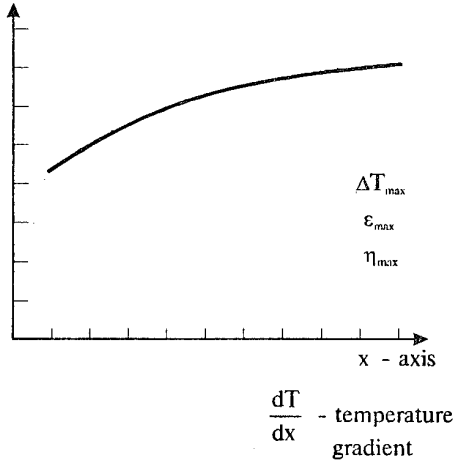
At the same time it gets more and more obvious that the further progress in thermoelectric materials is connected with inhomogeneous materials. In these substances the three-dimensional thermoelectric effects can occur. First these effects were mentioned almost simultaneously by Samoilovich A.G., Korenblit L.L. [1] (Ukraine, Chernivtsi) and Dominicali [2]. Experimentally the presence of three-dimensional gradient effect was firstly proved using Ge samples by P.I. Baransky (Ukraine)

in 1958 [3]. Possibilities for practical usage the three-dimensional effect for thermoelectric cooling efficiency increase are shown in american patent [4] where authors are not said, unfortunately. Reich A.D. in 1972 reported of getting the temperature difference more than 80 degrees using the inhomogeneous thermoelement [5]. The big contributions to the inhomogeneous thermoelements development were paid by Semeniuk V.A. [6-11], Vainer A.L., Lukishker E.M., Kolomoets N.V. [12], Rivkin A.S. [13]. Most of the encouraging results were gotten by them for the first time, and this was the reason for more active investigations in this area. Generalization for three-dimensional effects study and their combined analysis are given in the book "Optimal control of thermoelectric materials and devices characteristics" by Anatychuk L.I. and Semeniuk V.A. [14].

Three-dimensional effects realization in combination with material properties temperature dependences leads to the necessity of using more complex methods for substance optimization, namely optimization by functions instead of optimization by parameter (fig.2).

*Fig.2. Inhomogeneous material optimal functions*

Ni - material composition  
 n - impurity concentration  
 n<sub>0</sub> - current carrier concentration



Mathematically the problem of finding the optimal function of material inhomogeneity is formulated as follows. Let's examine the thermoelement comprising *n*- and *p*-type legs where the material properties are being changed with the coordinate because of parameters are

dependent on temperature and charge carriers concentration.

One-dimensional stationary temperature  $T$  distribution in thermoelement legs is being determined by the differential equations system of non-equilibrium thermodynamics

$$\begin{aligned} \frac{d}{dx} \left( \kappa_n \frac{dT}{dx} \right) + \frac{j^2}{\sigma_n} - T \frac{\partial \alpha_n}{\partial T} i \frac{dT}{dx} - T \frac{\partial \alpha_n}{\partial x} i = 0 \\ \frac{d}{dx} \left( \kappa_p \frac{dT}{dx} \right) + \frac{j^2}{\sigma_p} - T \frac{\partial \alpha_p}{\partial T} i \frac{dT}{dx} - T \frac{\partial \alpha_p}{\partial x} i = 0 \end{aligned} \quad (1)$$

therewith Seebeck coefficients  $\alpha$ , electric conductance  $\sigma$  and thermal conductance  $\kappa$  are functions of electron concentration  $n(x)$  in  $n$ -leg, or holes concentration  $p(x)$  in  $p$ -leg, and the temperature, namely

$$\alpha_n = \alpha_n(n(x), T); \sigma_n = \sigma_n(n(x), T); \kappa_n = \kappa_n(n(x), T); \quad (2)$$

$$\alpha_p = \alpha_p(p(x), T); \sigma_p = \sigma_p(p(x), T); \kappa_p = \kappa_p(p(x), T);$$

Power efficiency of thermoelement in cooling mode is determined by coefficient of performance

$$\varepsilon = \frac{Q_c}{Q_b - Q_c}. \quad (3)$$

Efficiency of thermoelement generating the electricity is determined by its efficiency value

$$\eta = \frac{Q_b - Q_c}{Q_b}. \quad (4)$$

Heat fluxes  $Q_h$  and  $Q_c$  between the thermoelement and the external sources at fixed temperatures  $T_h$  and  $T_c$  are defined from the equations system (1) solution on the thermoelement legs edges at the boundary conditions

in the cooling mode

$$T_{n,p}(0) = T_h, \quad T_{n,p}(l) = T_c \quad (5)$$

in the generation mode

$$T_{n,p}(0) = T_c, \quad T_{n,p}(l) = T_h \quad (6)$$

The problem is to find such an optimal current carriers distribution in both thermoelement legs  $n(x)$  and  $p(x)$  and such parameters of current density  $i_n$ ,  $i_p$ , so they could provide the maximum  $COP$  (3) value or generation efficiency (4) at differential bonds (1) and boundary conditions (5) or (6).

Optimal function search is pretty difficult mathematical problem we decided to solve by optimal control theory, although the other mathematical methods can be used as well.

By now the problems of optimal inhomogeneity finding are being solved step by step in the Institute of Thermoelectricity both for cooling and energy generation modes, and the possibilities for efficiency increase by using functional-gradient materials are brightly demonstrated. Results for these problems solving are in the table. It is seen that using functional-gradient materials improves a lot the thermoelectric conversion efficiency in both cooling and energy generation modes.

That's why it is necessary to create the technology for these materials.

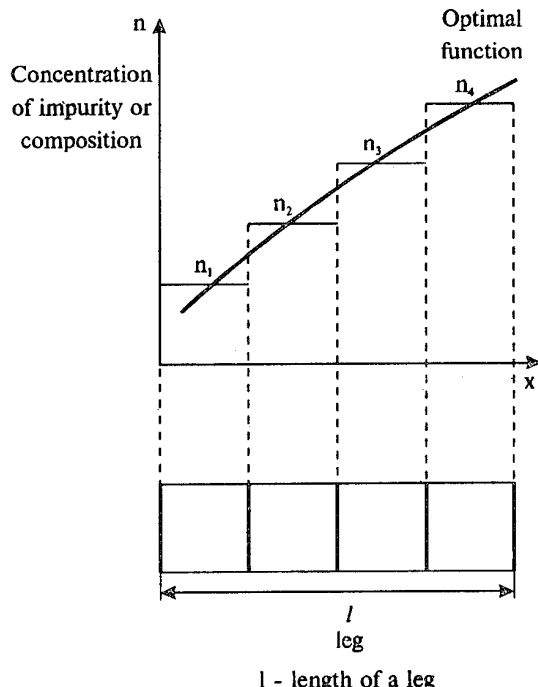
Table

Optimal functions	Obtained results
1. The material optimal inhomogeneity for a cooling thermoelement of $Bi - Te$ [14]	$\Delta T_{max}$ increase by 17% $\varepsilon_{max}$ 0.5 - 6 times
2. The magnetic field optimal inhomogeneity for low-temperature thermoelement of $Bi - Sb$ [15]	$\varepsilon_{max}$ increase 1.1 - 1.2 times
3. The magnetic field optimal inhomogeneity for stage coolers thermoelement of $Bi - Sb$ [16]	$\varepsilon_{max}$ increase 1.5 - 3 times
4. The material optimal inhomogeneity for generating thermo-element of $Bi - Te$ [17]	Efficiency increase 1.25 times

Getting the functional-gradient materials is possible in different ways.

The simplest one is to use piece-homogeneous material. Model of this structure is given in fig.3. Such experiments were conducted by many scientists [8-10, 12]. The calculations were also made, and from them it was found how many homogeneous pieces should one take to have good approximation to the needed inhomogeneity. It occurred that 3-4 pieces is enough.

Fig.3. Model of partially homogeneous structure



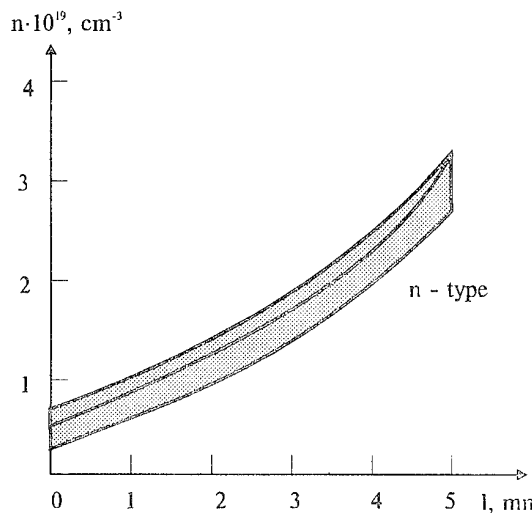
$l$  - length of a leg

But using such combined legs will lead to losses on the contacts and this will decrease the structure efficiency.

It is attractive to create the inhomogeneous structure by modification the known methods for thermoelectric materials obtaining.

In fig.4 there are the results of these investigations for thermoelectric material of *n*-type of *Bi-Te* aimed to thermoelectric cooling. Full line is the needed optimal current carriers concentration. The shaded area corresponds to experimental materials homogeneity value (materials are obtained by compacting and Chokhralsky methods). Similar results are gotten also for *p*-type materials.

*Fig.4. Functional-gradient Bi-Te of n-type*



Results demonstrate the possibility to get the materials with prescribed inhomogeneity and, therefore, creating the thermoelectric battery of improved quality using the functional-gradient materials.

#### References

- [1]. Samoilovich A.G., Korenblit L.L. Modern state of thermoelectric and thermomagnetic phenomena theory in semiconductors. УФН. -1953. -E.49, N2, p.243-272.
- [2]. Domenicali C.A. Irreversible Thermodynamics of Thermoelectricity, Rev. Mod. Phys., 1954, Vol. 26, N2, p. 237 - 275.
- [3]. Barabsky P.I. Three-dimensional Peltier effect in germanium. ЖТФ, 1958, 28, N2, p. 225 - 230.
- [4]. Peltier thermoelectric couple with non-homogeneous elements. USA patent specification No. 586486, 13.09.1966.
- [5]. Reich A.D. The Distributed Peltier Effect, Bull. Amer. Phys. Soc. - 1972, Vol. 17, N3, P. 282.
- [6]. Semeniuk V.A. Real limits for temperature decrease when using inhomogeneous thermoelements. Tes. Docl. on Soviet Union Conf. Tashkent, 25 - 27 oct., 1977. - Tashkent, ТАШПИ, 1977, v.4, p. 42 - 44.
- [7]. Anatychuk L.I., Semeniuk V.A. Optimal control of thermoelectric material inhomogeneity. Докл. АН УССР. Сер. А, Физ. -мат. и техн. науки,, 1987, N6, p. 58 - 61.
- [8]. Semeniuk V.A., Nechiporuk O.L. Maximum temperature drop in combined semiconductor thermocouples. Изв. высш. учеб. завед. Энергетика, 1976, N2, p. 105 - 110.
- [9]. Semeniuk V.A. Semiconductive material choice for combined thermocouples. Изв. высш. учеб. завед. Энергетика, 1978, N4, p. 146 - 151.
- [10]. Semeniuk V.A., Nechiporuk O.L. Real limits for temperature decrease in combined thermocouples. Study of the direct heat conversion into electricity. Сб. науч. трудов, Киев, Наукова думка, 1978, p. 114 - 117.
- [11]. Semeniuk V.A. Possibilities for thermoelectric cooling efficiency increase when using inhomogeneous thermoelements. Теплофизика и теплотехника, Респ. межвед. сб., Киев, Наукова думка, 1978, N.35, p.80- 84.
- [12]. Vainer A.L., Kolomoets N.V., Lukishker E.M., Rzhevsky V.M. To the theory of combined thermoclement. ФТП, 1977, - v.11, N. 3, p. 546-552.
- [13]. Ivanova K.F., Rivkin A.S. Optimal current carriers distribution along the thermoelement legs height. ЖТФ, 1982, v. 52, N. 7, p. 1406-1411.
- [14]. L.I.Anatychuk, V.A.Semenyuk. Optimal Control for the Thermoelectric Material and Device Properties. Chernovtsi, Prut, 1992, p.264.
- [15]. Anatychuk L.I., Vikhor L.N., Ivanov G.A. The Optimal Control Theory for Thermoelectric Cooler Design. In Proceedings for Twelfth International Conference on Thermolectrics, Japan, Nov., pp.412-415.
- [16]. Anatychuk L.I.,Vikhor L.N. Study On Cooler Design In Magnetic Field For Low Themperature Cascades. In Proceedings of the Thirteenth International Conference on Thermolectrics, Cansas, Aug., 1994.
- [17]. Anatychuk L.I., Bulat V.P., Semeniuk V.A. Thermoelectric material for thermogenerators as the object of optimal control. Докл. АН УССР. Сер. А, Физ.- мат. и техн. науки, 1988, N10, p. 48 - 51.

# Thermoelectric Properties of Doped Single Crystal Solid Solutions Based on Bismuth Telluride

T.E.Svechnikova, N.M.Maksimova <sup>1</sup>, H.Sussmann, P.Reinshaus <sup>2</sup>

<sup>1</sup> Baikov Institute of Metallurgy RAN, Moscow, 117334, Russia

<sup>2</sup> Martin Luther University, Halle, Germany

Single crystal solid solutions based on Bi<sub>2</sub>Te<sub>3</sub> doped with various additions were grown by the Czochralski technique. The influence of doping on thermoelectric and mechanical properties of these solutions was studied. The effective segregation coefficients for the dopants were determined. Homogeneity of single crystals up to 40 mm in diameter was investigated.

## Introduction

The bismuth telluride based solid solutions are used in a negative leg of thermoelectric coolers in the temperature range of 220 to 350 K. In search of more efficient low-temperature materials we have conducted investigations of multi-component solid solutions. The basic composition was solid solution Bi<sub>2</sub>Te<sub>2.85</sub>Se<sub>0.15</sub>. CdTe, In<sub>2</sub>Te<sub>3</sub>, Sb<sub>2</sub>Se<sub>3</sub>, Bi<sub>2</sub>S<sub>3</sub>, Ge, and Cu, having restricted solubility region, were used as impurities. As an addition ensuring the n-type conductivity in the material antimony iodide SbI<sub>3</sub> was used.

Our objective was to estimate the influence of doping on thermoelectric and mechanical properties of the solid solutions and to determine the dopants effective segregation coefficients, for these give an indication of distribution of the elements along the crystal length.

## Experimental

The single crystals were grown by the Czochralski technique with the replenishment of the melt using a double crucible (floating crucible) technique [1]. They were grown in a direction [10̄10] normal to the main crystallographic axis *c*. The starting charge was prepared from the previously synthesized compounds Bi<sub>2</sub>Te<sub>3</sub>, Bi<sub>2</sub>Se<sub>3</sub>, In<sub>2</sub>Te<sub>3</sub>, Sb<sub>2</sub>Se<sub>3</sub>, CdTe, Bi<sub>2</sub>S<sub>3</sub> and elements Cu and Ge. These materials were of 4N purity. The crystals grown had the form of platelets up to 120 mm long, to 25 mm wide, and to 15 mm thick. Single crystals of the following compositions were investigated:

Bi<sub>2</sub>Te<sub>2.85</sub>Se<sub>0.15</sub> - x mol % CdTe for x = 0.5 to 3,  
 Bi<sub>2</sub>Te<sub>2.85</sub>Se<sub>0.15</sub> - x mol % In<sub>2</sub>Te<sub>3</sub> for x = 0.2 to 2,  
 Bi<sub>2</sub>Te<sub>2.85</sub>Se<sub>0.15</sub> - x mol % Sb<sub>2</sub>Se<sub>3</sub> for x = 1 to 3,  
 Bi<sub>2</sub>Te<sub>2.85</sub>Se<sub>0.15</sub> - x at. % Cu for x = 0.05 to 0.3,  
 Bi<sub>2</sub>Te<sub>2.85</sub>Se<sub>0.15</sub> - x at. % Ge for x = 0.2 to 1,  
 Bi<sub>2</sub>Te<sub>3-z</sub>S<sub>z</sub> for z = 0.06 to 0.09,  
 Bi<sub>2</sub>Te<sub>3-y</sub>Se<sub>y</sub>S<sub>z</sub> for y = 0.09, z = 0.06 and y = 0.09, z = 0.09.  
 For each composition the specified growth conditions providing high perfection of single crystals were determined.

The content of the dopants Cu, In, Ge, and Se was determined by plasma absorption spectroscopy by using a spectrophotometer of the Perkin-Elmer type (model 403), and the sulphur content was measured by a computerized BINOS gas

analyzer (model CSA-2003). The both methods permit to measure the concentration of the analysed elements to a high precision. The measurements yielded the dopants effective segregation coefficients displayed in Table 1 [2 - 4]. The maximum segregation coefficients correspond to S and Se (see Table 1) which are situated in the same group as the host elements are (Group VI).

**Table 1.** The effective segregation coefficients for the dopants in Bi<sub>2</sub>Te<sub>2.85</sub>Se<sub>0.15</sub>

Group of the Periodic table	Dopant	Form of the dopant	Effective segregation coefficient K <sub>eff</sub>
I	Cu	Cu	0.17
II	Cd	CdTe	0.21
III	In	In <sub>2</sub> Te <sub>3</sub>	0.51
IV	Ge	Ge	0.13
VI	S	Bi <sub>2</sub> S <sub>3</sub>	0.8
	Se	Sb <sub>2</sub> Se <sub>3</sub> , Bi <sub>2</sub> Se <sub>3</sub>	1.3

The thermoelectric properties of single crystals of the basic solid solution Bi<sub>2</sub>Te<sub>2.85</sub>Se<sub>0.15</sub> with a variety of current carrier concentration (Fig. 1) and of this solid solution doped with various impurities (Fig. 2) were measured over the temperature range of 100 to 400 K. The value of thermoelectric figure of merit of Bi<sub>2</sub>Te<sub>2.85</sub>Se<sub>0.15</sub> single crystals changes from 2.8 to 3.1x10<sup>-3</sup> K<sup>-1</sup> in the temperature range 220 to 310 K (curves 1 and 2 in Fig. 1). Several types of miniature coolers were manufactured from these single crystals and withstood tests [6]. Doping of the solid solution with Ge, Bi<sub>2</sub>S<sub>3</sub>, Sb<sub>2</sub>Se<sub>3</sub>, and CdTe results in increase in material's figure of merit compared to Bi<sub>2</sub>Te<sub>2.85</sub>Se<sub>0.15</sub> at the same carrier concentration and in expansion of the temperature range in which high values of Z are held. In the temperature range 200 to 270 K the figure of merit Z = (2.8 - 3.2)x10<sup>-3</sup> K<sup>-1</sup>, and in the range 270 to 320 K Z = (3.1 - 3.2)x10<sup>-3</sup> K<sup>-1</sup> (curves 1 and 2 in Fig. 2).

**Fig. 1.** Thermoelectric figure of merit of  $\text{Bi}_{2}\text{Te}_{2.85}\text{Se}_{0.15}$  single crystals with different coefficients of thermoelectric e.m.f. at 300 K: (1) -206 microV/K, (2) -240 microV/K, and (3) -273 microV/K as a function of temperature.

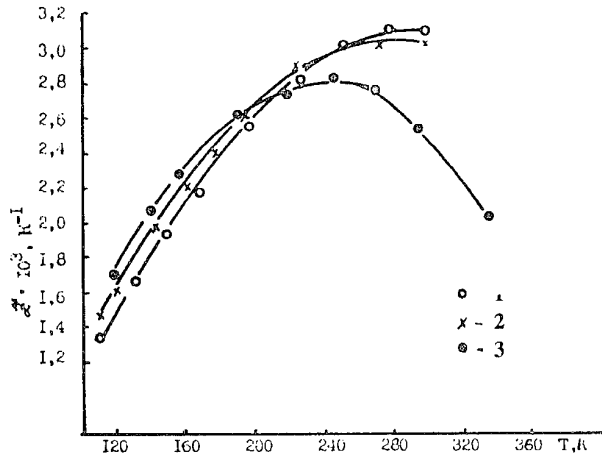
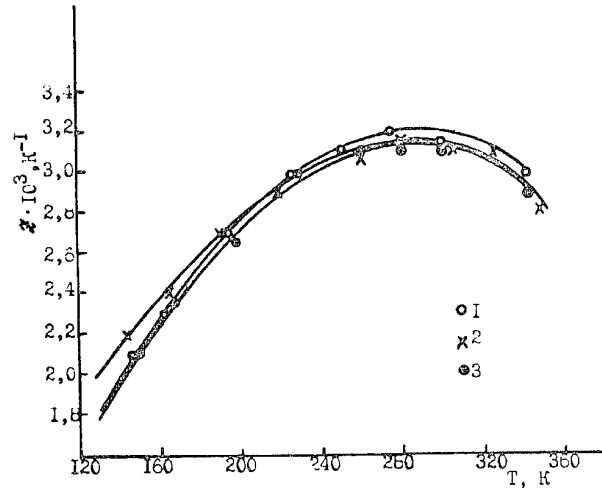


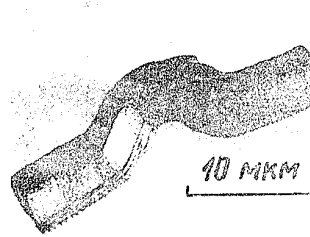
**Fig. 2.** Thermoelectric figure of merit of the single crystal compounds: (1)  $\text{Bi}_{2}\text{Te}_{2.85}\text{Se}_{0.15} + 0.5$  at. % Ge, (2)  $\text{Bi}_{2}\text{Te}_{2.85}\text{Se}_{0.15} + 2$  mol %  $\text{Sb}_2\text{Se}_3$ , and (3)  $\text{Bi}_{2}\text{Te}_{2.82}\text{Se}_{0.09}\text{Sb}_{0.09}$  with the same values of coefficient of thermoelectric e.m.f. at 300 K as a function of temperature.



Single crystals doped with the above-mentioned additions were used for investigation of mechanical properties (bending strength) of these solid solutions [3, 5, 7]. A knowledge of these properties is important since mechanical and thermal stresses appearing at various stages of manufacture and operation of devices made of these materials may lead to their destruction. The mechanism of plastic deformation of the single crystals has been studied. The doping causes strengthening of chemical bonding between layers in solid solutions based on  $\text{Bi}_2\text{Te}_3$  [8]. These tests show that doping with  $\text{Bi}_2\text{S}_3$ ,  $\text{Sb}_2\text{Se}_3$ ,  $\text{CdTe}$ ,  $\text{Cu}$ , and  $\text{Ge}$  in specified amounts causes increase in  $Z$  and also enhancement of mechanical strength of the material. Figure 3 shows a sample of single crystal compound

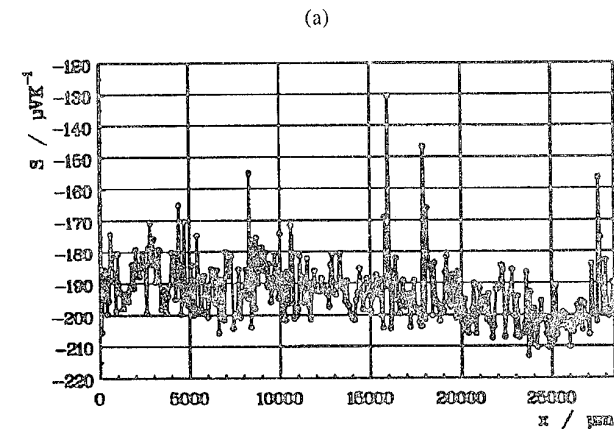
$\text{Bi}_{2}\text{Te}_{2.85}\text{Se}_{0.15} + 2$  mol %  $\text{CdTe}$  after bend tests. The sample is deformed by interlayer shears of basic planes which pass mainly through the medium part of the sample.

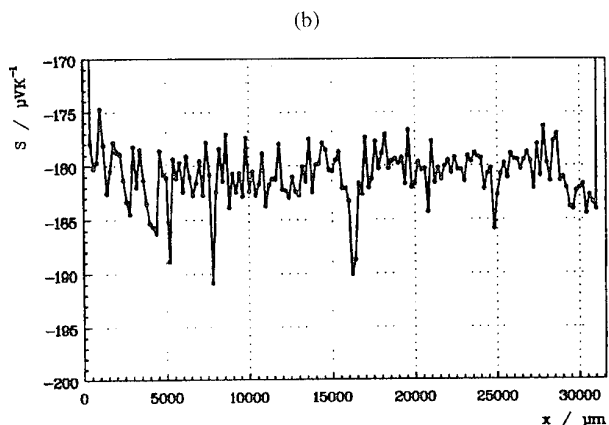
**Fig. 3.** A sample of single crystal compound  $\text{Bi}_{2}\text{Te}_{2.85}\text{Se}_{0.15} + 2$  mol %  $\text{CdTe}$  after bend tests.



The Czochralski technique allows one to grow large-sized single crystals up to 50 mm in diameter. Therefore, a study of axial and radial homogeneity of single crystals as a function of crystal diameter, pull rate, and purity of source materials was conducted [9]. From this study the conditions of growth of homogeneous along the length and cross-section  $\text{Bi}_{2}\text{Te}_{2.85}\text{Se}_{0.15}$  single crystals up to 35 mm in diameter were determined. Figure 4 illustrates the distribution of coefficient of microthermoelectric e.m.f. across the cross-section of plates cut from the initial part of the crystal (about 30 mm from the seed) (Fig. 4a) and from the end of the crystal (about 140 mm from the seed) (Fig. 4b) which was grown in accordance with the determined conditions. Variation of coefficient of microthermoelectric e.m.f. across the cross-section in both cases lies within  $\pm 5$  microV/K.

**Fig. 4.** Variation of coefficient of microthermoelectric e.m.f. across the cross-section of a plate cut from (a) the initial part (about 30 mm from the seed) and (b) from the end (about 140 mm from the seed) of the single crystal.





### Summary

Single crystals of  $\text{Bi}_2\text{Te}_{2.85}\text{Se}_{0.15}$  solid solutions with various dopants were grown by the Czochralski technique. The effective segregation coefficients for Cu, Cd, In, Ge, S, and Se are determined. It is established that doping of the solid solutions with specified amounts of  $\text{Bi}_2\text{S}_3$ , Ge, and  $\text{Sb}_2\text{Se}_3$  causes increase in figure of merit of the material in the temperature range 200 to 270 K as well as enhancement of its mechanical strength. The conditions of growth of homogeneous crystals up to 35 mm in diameter are determined.

### References

- [1]. N.Kh.Abrikosov, L.D.Ivanova, O.G.Karpinskii, T.E. Svechnikova et al., Growth and Investigation of Lamellar Single Crystals of  $\text{Sb}_2\text{Te}_3$  and  $\text{Bi}_2\text{Te}_3$  Based Solid Solutions, *Izv. Akad. Nauk, ser. Neorg. Mater.*, 1977, v.13, No.4, pp.641-643.
- [2]. T.E.Svechnikova, S.N.Chizhevskaya, N.V.Polikarpova, Doping of Single Crystals of  $\text{Bi}_2\text{Te}_{2.85}\text{Se}_{0.15}$  Solid Solution with In, *Izv. Akad. Nauk, ser. Neorg. Mater.*, 1987, v.23, No.7, pp.1128-1131.
- [3]. T.E.Svechnikova, S.N.Chizhevskaya, N.V.Polikarpova, P.P. Konstantinov et al., Influence of CdTe on Thermoelectric and Mechanical Properties of  $\text{Bi}_2\text{Te}_{2.85}\text{Se}_{0.15}$  Single Crystals, *Izv. Akad. Nauk, sér. Neorg. Mater.*, 1992, v.28, No.2, pp.316-320.
- [4]. T.E.Svechnikova, S.N.Chizhevskaya, N.M.Maksimova, N.V.Polikarpova, Effective Segregation Coefficients for Selenium and some other Impurities in Bismuth Telluride Based Solid Solutions, Properties of Doped Semiconducting Materials, Ed. V.S.Zemskov, N.Y., 1993, pp.117-122.
- [5]. T.E.Svechnikova, S.N.Chizhevskaya, N.M.Maksimova et al., Doping of  $\text{Bi}_2\text{Te}_{2.85}\text{Se}_{0.15}$  Solid Solution with Germanium, *Izv. Akad. Nauk, ser. Neorg. Mater.*, 1994, v.30, No.2, pp.168-171.
- [6]. V.A.Semenyuk, T.E.Svechnikova, L.D.Ivanova, Single Crystals of Solid Solutions of Chalcogenides of Bismuth and Antimony and Miniature Coolers Based on Them., *J. Advanced Materials*, 1994, No1(5), pp. 428-434.
- [7]. S.N.Chizhevskaya, M.A.Korzhuev, T.E.Svechnikova, On the Peculiar Plastic Deformation of  $\text{Bi}_2\text{Te}_3$  Single Crystals and Based on them Solid Solutions under Bend Tests, *Izv. Akad. Nauk, ser. Neorg. Mater.*, 1994, v.30, No.4, pp.474-478.
- [8]. M.A.Korzhuev, S.N.Chizhevskaya, T.E.Svechnikova, O.G. Karpinskii, Mechanical Properties of Single and Polycrystals of  $\text{Bi}_2\text{Te}_3$  and  $\text{Bi}_2\text{Te}_{2.85}\text{Se}_{0.15}$  Doped with Copper, *Izv. Akad. Nauk, ser. Neorg. Mater.*, 1992, v.28, No.7, pp.1383-1388.
- [9]. T.E.Svechnikova, N.M.Maksimova, H.Sussmann, P. Reinshaus, Investigation of Homogeneity of  $\text{Bi}_2\text{Te}_{2.85}\text{Se}_{0.15}$  Single Crystals Prepared by the Czochralski Technique, *Izv. Akad. Nauk, ser. Neorg. Mater.*, 1995, v.31, No.1, pp.23-31.

## APPLICATION OF A SCANNING THERMO-PROBE TECHNIQUE FOR HOMOGENEITY DETERMINATION OF $\text{Bi}_{0.5}\text{Sb}_{1.5}\text{Te}_3$ SINGLE CRYSTALS

L. D. Ivanova<sup>1</sup>, H. Süßmann<sup>2</sup>, P. Reinshaus<sup>2</sup>, Th. Dietrich<sup>2</sup>  
 1.) A. A. Baikov Institute of Metallurgy RAS, Moscow, 117911, Russia  
 2.) Martin-Luther-Universität Halle-Wittenberg, Germany

**The dependence of the axial and radial homogeneity of single crystals grown by CZOCHRALSKI technique on the growth conditions by means of a local thermo-probe technique was investigated.**

Single crystals based on solid solutions of bismuth and antimony chalcogenides grown by CZOCHRALSKI technique are used for manufacturing solid-state thermoelectric devices, working at temperatures of 250..350 K. Using single crystals in miniature thermocooling devices increases the output-rate of effective devices, expands the range of achievable temperatures and increases the figure of merit of thermoelectric cooling compared with devices based on polycrystalline materials [1]. Currently p- and n-type crystals of solid solutions of bismuth and antimony chalcogenides are grown at A. A. Baikov Institute of Metallurgy of Russian Academy of Sciences by using a CZOCHRALSKI method with replenishment of the liquid phase and using a floating crucible. The diameter of the grown crystals is 35 to 50 mm, their length is up to 100 mm and their weight is about 1 kg. The use of an automatic weight gauge allows to change the temperature during the growth process. In this way an accuracy of  $\pm 1$  mm of the diameter of the crystal can be obtained. Selenium and tellurium doped p-type crystals of  $\text{Bi}_{0.5}\text{Sb}_{1.5}\text{Te}_3$  with a carrier concentration of 1.8 to  $8 \cdot 10^{-19} \text{ cm}^{-3}$  and a corresponding Seebeck coefficient of 260 to  $150 \mu\text{V/K}$  at 300 K reach optimum thermoelectric properties in the temperature range of 250 to 350 K. One of the main tasks is to increase the homogeneity of crystals. In order to assess the homogeneity of crystals a scanning thermo-probe technique is used to measure the Seebeck coefficient along the crystal axis or on a cross section of the crystal. The Seebeck coefficient is very sensitive to changes of the carrier concentration, which is determined by the deviation from stoichiometric composition in a solid solution of  $\text{Bi}_{0.5}\text{Sb}_{1.5}\text{Te}_3$ . As it was shown in [2] for equilibrium alloys, a change in the content of tellurium by no more than 0.2 at.% causes a change of the Seebeck coefficient by about  $100 \mu\text{V/K}$  (from 120 up to  $230 \mu\text{V/K}$ ), i.e. very small deviations of the content of tellurium lead to a significant change of the Seebeck coefficient. During the growth process the feeding melt contained a surplus of tellurium of 1 up to 2.5 at.%. The composition of the melt and conditions of growth were determined according to the aspired carrier concentration (value of the Seebeck coefficient) of a crystal. The growth velocity was 0.1 to 0.3 mm/min. During the growth the concentration of excess tellurium in the floating crucible increased and when it exceeded 3 at.%, the growth was terminated, because a polycrystalline structure began to be formed. Thus the lateral surface of a crystal was deformed and became rough. As a rule, the Seebeck coefficient in this crystal area exceeds  $210 \mu\text{V/K}$  at room temperature. The investigation of the microstructure shows the presence of eutectic lamellas in this area.

The used scanning thermo-probe method had been developed at the department of Physics of Martin-Luther-Universität, Halle (Germany) [3]. This method reaches a local resolution of  $10 \mu\text{m}$ . The accuracy of measurement is better than  $5 \mu\text{V/K}$ . Raster scans of samples for investigation of a two-dimensional distribution of the Seebeck coefficient are performed automatically. The analysis of homogeneity of  $\text{Bi}_{0.5}\text{Sb}_{1.5}\text{Te}_3$  single crystals doped with selenium, grown at various technological conditions, is necessary in order to

find the optimal growth conditions for uniform crystals. The Seebeck coefficient along the axial direction of crystals, grown at various growth velocities has been investigated. It was found that in the initial area, at the beginning of the growth, crystals exhibit lower values of the Seebeck coefficient. After the begin of melt feeding from the main crucible containing surplus tellurium the carrier concentration of the growing crystal is decreasing. Simultaneously the Seebeck coefficient is increasing because of decreasing deviation of the crystal composition from stoichiometry. After reaching a constant crystal diameter the speed of growth remains constant. In these parts of crystals with a diameter of 40 mm the variation of the Seebeck coefficient along 150 mm crystal length is lower than  $30 \dots 40 \mu\text{V/K}$ . The macrohomogeneity of the crystals can be improved by reducing of the growth velocity. Crystals with an axial variation of the Seebeck coefficient of lower than  $10 \mu\text{V/K}$  over a length of 100 mm have been obtained (fig. 1 curve 3).

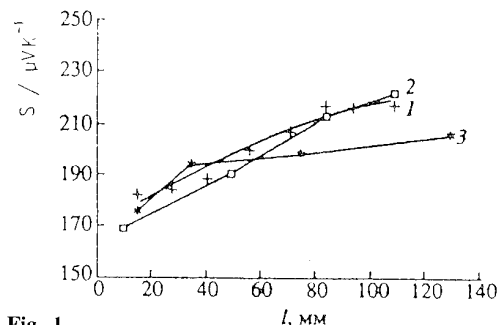


Fig. 1

The evaluation of the distribution of the Seebeck coefficient on sections cut from various crystal areas (at the start of growth / 40 mm from the seed / at the end of the crystal, at a distance of 80 mm from the seed) has shown that the most inhomogeneous area is that of the start of growth: at 2 to 5 mm from the crystal periphery the Seebeck coefficient  $S$  is  $165 \dots 170 \mu\text{V/K}$ , then follows a region with higher  $S$  ( $180 \dots 190 \mu\text{V/K}$ ). In the central area  $S=165 \dots 170 \mu\text{V/K}$  is found. From the growth with constant diameter the distribution of the Seebeck coefficient over the cross section becomes more uniform. However, the outer areas of the crystal have lower  $S$  values in comparison with the central part. Towards the end of a crystal, when polycrystalline structure is formed, a significant spread of the Seebeck coefficient values is observed ( $\delta S=20 \mu\text{V/K}$ ). The occurrence of crystal areas with a lowered Seebeck coefficient is obviously linked to the presence of antistructural defects according to the deviation from the stoichiometric composition of the solid solution towards surplus Bi and Sb atoms. During the growth of a crystal with constant diameter, tellurium is evaporated from the free surface of the melt in the floating crucible. This is compensated by feeding of melt from the main crucible. Therefore, the peripheral areas of the crystals have a lower Seebeck coefficient than the central area. The influence of the rotational frequency of crucible and seed on the homogeneity state of the crystals was investigated. A consideration of the

properties was carried out on slices of 10 mm thickness parallel to the cross section. Plates cut from the ends of a crystal with 40 mm in diameter, where the strongest inhomogeneity occurs, possessed uniform values of the Seebeck coefficient of  $220 \pm 5 \mu\text{V/K}$ .

The influence of the rotational frequency of the crucible was investigated on crystals, grown at a crucible rotation  $f_c = 15, 10, 5 \text{ min}^{-1}$  and a seed rotation  $f_s = 30 \text{ min}^{-1}$ . The studies have shown that due to a reduction of the crucible rotation down to  $5 \text{ min}^{-1}$  the difference between the minimum and maximum values of the Seebeck coefficient  $\delta S$  increases by a factor of 2.3: from 10 up to  $23 \mu\text{V/K}$ .

The influence of the seed rotation on the distribution of the Seebeck coefficient was studied on crystals grown at a seed rotation of 40, 30 and  $20 \text{ min}^{-1}$  (crucible rotation of  $10 \text{ min}^{-1}$ ). It turned out that an increase of the seed rotation in this range increases homogeneity of crystals to a smaller degree than a change of crucible rotation:  $\delta S = 17 \mu\text{V/K}$  at  $f_s = 20 \text{ min}^{-1}$ ;  $\delta S = 15 \mu\text{V/K}$  at  $f_s = 40 \text{ min}^{-1}$ .

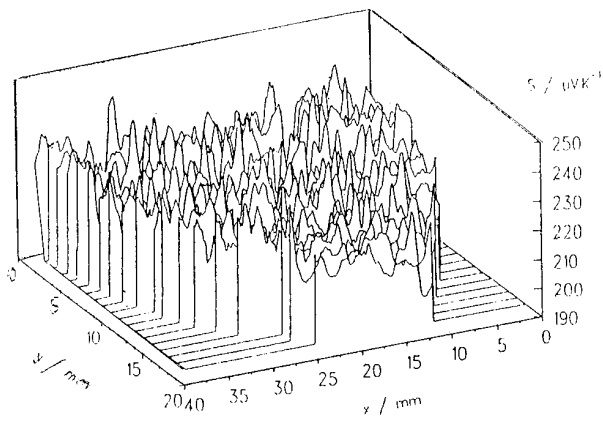


Fig. 2

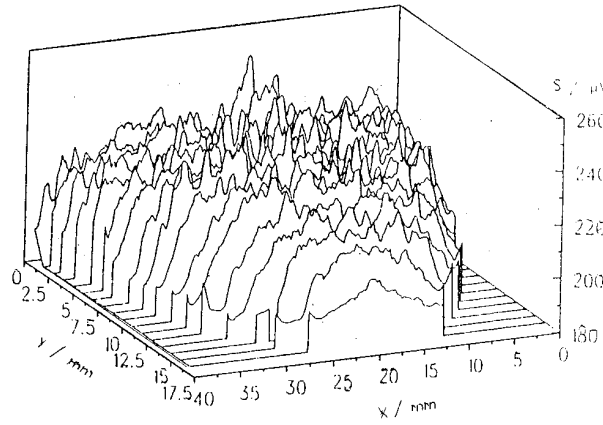


Fig. 3

In Fig. 2 and 3 isometric distribution images of the Seebeck coefficient over sections of crystals grown at the following conditions are adduced:  $f_s = 30 \text{ min}^{-1}$ ,  $f_c = 10 \text{ min}^{-1}$  (Fig. 2) and  $f_s = 15 \text{ min}^{-1}$ ,  $f_c = 6 \text{ min}^{-1}$  (Fig. 3).

It is visible that at low rotational frequency of crucible and seed an area of lowered Seebeck coefficient of 3 to 7 mm in width is observed whereas for other crystals this area does not exceed 1-2 mm. The occurrence of areas with a lower Seebeck coefficient near the periphery of the crystal mentioned above can be explained by the evaporation of tellurium from the free surface of the melt. A

reduction of the rotational frequency of crucible and seed reduces the intermixing of the melt. As a result, the width of the area with lower Seebeck coefficient increases (Fig. 3). The uniformity of crystals of this solid solution of various diameters (from 15 up to 47 mm) grown under the same technological conditions ( $f_s = 30 \text{ min}^{-1}$ ,  $f_c = 10 \text{ min}^{-1}$ ) is demonstrated on distribution images of the Seebeck coefficient on cross sectional planes.

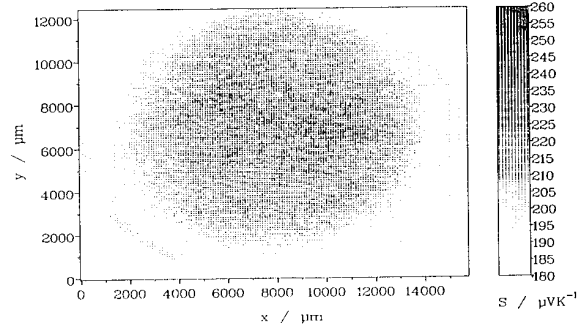


Fig. 4

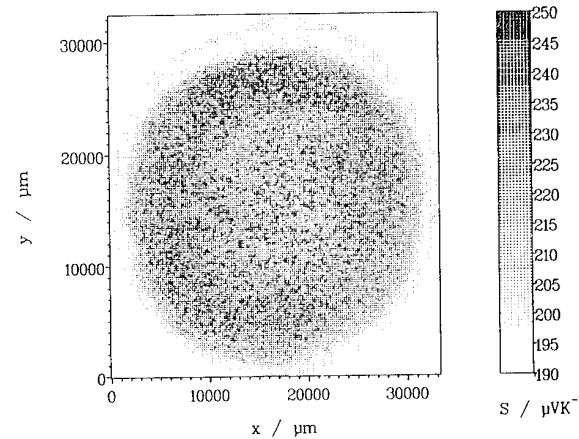


Fig. 5

For example, Fig. 4 and 5 show the distribution of the Seebeck coefficient of the overall cross section of crystals with a diameter of 15 mm (Fig. 4) and 35 mm (Fig. 5). Fig. 6..8 demonstrate the variation of the Seebeck coefficient along the x-axis through the central part of cross sections for crystals with diameters of 15 mm (Fig. 6), 35 mm (Fig. 7) and 40 mm (Fig. 8). The most inhomogeneous crystal was this of the least diameter, because the width of the excess tellurium area is 5 mm here (Fig. 4 and 6), the same as for the crystal with a diameter of 47 mm. For the crystal of 35 mm in diameter, the area of lowered Seebeck coefficient was 1..2 mm in width (Fig. 5 and 7). The most uniform distribution of the Seebeck coefficient was obtained for the 40 mm thick crystal (Fig. 8).

## Conclusion

Axial and radial homogeneity of crystals on the basis of  $\text{Bi}_{0.5}\text{Sb}_{1.5}\text{Te}_3$  grown by CZOCHRALSKI technique with feeding of the liquid phase has been investigated by means of a scanning thermoprobe technique. The study of axial homogeneity showed that during the growth the degree of deviation from the stoichiometric composition decreases, which results in an increase of the Seebeck coefficient towards the end of the crystal. A decrease in axial inhomogeneity was reached by gradual reduction of the growth velocity. The heaviest radial inhomogeneity was found in the start

area of the growth and at the end, where a polycrystalline structure is formed and eutectic precipitations on the basis of tellurium appear at the basis planes. Reduction of radial inhomogeneity of the crystals is possible by an increase of rotation frequency of the crucible to 6 up to 15 min<sup>-1</sup>. The change of the frequency of seed rotation from 20 to 40 min<sup>-1</sup> has an effect on homogeneity of crystals to a smaller extent. Homogeneity investigation of crystals of different diameter (from 15 up to 47 mm) grown under equal conditions has shown that the most uniform distribution of the Seebeck coefficient is reached for a crystal with 40 mm in diameter, the least for a crystal of 15 mm in diameter.

### References

- [1] V. A. Semenyuk, T. E. Svechnikova, L. D. Ivanova, Neorgan. mat. 31 № 1 (1995) 32-36.
- [2] N. Ch. Abrikosov, V. F. Bankina, L. A. Kolomoets, N. V. Dgarmachvili, Izv. AN SSSR, Neorgan. mat. 13 № 5 (1977) 827-831.
- [3] H. Süßmann, M. Bohm, P. Reinshaus, Proc of the XII. Int. Conf. on Thermoel., Yokohama (1993)

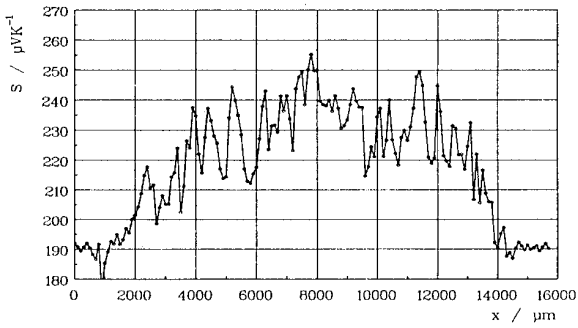


Fig. 6

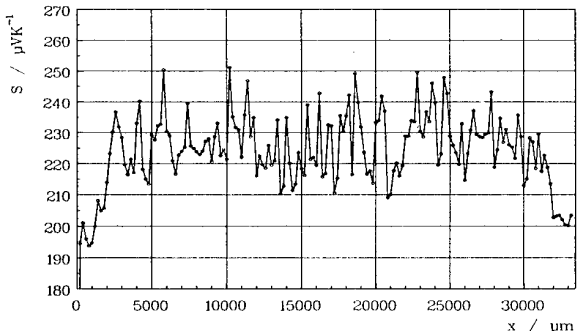


Fig. 7

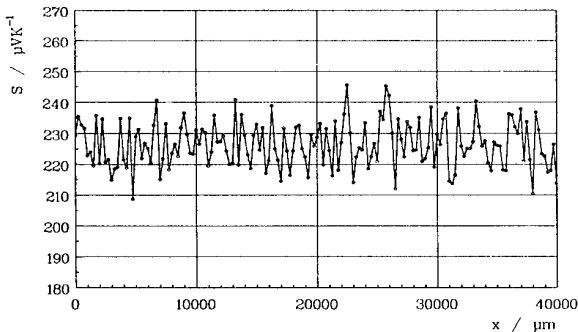


Fig. 8

## A SIMPLIFIED THEORY OF PHONON BOUNDARY SCATTERING IN SOLID SOLUTIONS

H.J.Goldsmid, H.B.Lyon Jr., E.H.Volkmann  
Marlow Industries Inc.  
10451 Vista Park Road, Dallas, TX 75238-1645

The conditions for high temperature boundary scattering are determined in the general case and applied to predict the thermal conductivity of the Bi<sub>88</sub>Sb<sub>12</sub> system and incidentally, to the Bi<sub>2</sub>Te<sub>3</sub> alloy system as well. Essentially what happens is that strong scattering of the high frequency phonons by the point defects occurs in the solid solution, leaving most of the heat to be carried by the low frequency phonons that have very long free path lengths. The phonons are, thus, much more susceptible to boundary scattering.

### Introduction

It has recently been reported<sup>1</sup> that the thermal conductivity of Bi<sub>88</sub>Sb<sub>12</sub> produced by the sintering of fine particles is much less than that of a single crystal. The authors attribute this to phonon scattering at the grain boundaries. Such scattering at relatively high temperatures is known to occur in Si-Ge alloys but has not really been established for any other substances although, of course, boundary scattering at low temperatures is a well known phenomenon.

The theoretical basis for high temperature boundary scattering was first established by Goldsmid and Penn<sup>2</sup>. It was shown that such scattering would be much more pronounced in a solid solution than in a pure crystal. This is in spite of the fact that the mean free path of the phonons is less in a solid solution than in a pure element or compound. Essentially what occurs is the strong scattering of the high frequency phonons by the point defects in the solid solution, leaving most of the heat to be carried by the low frequency phonons that have very long free path lengths. Therefore these phonons are much more susceptible to boundary scattering.

In order for high temperature boundary scattering to take place at a relatively large grain size, it is desirable that the mean free path length for the phonons should be rather large in the absence of point defect scattering and that the reduction of thermal conductivity through point defect scattering should be substantial. These conditions are met in the Si-Ge system. Here we shall endeavor to determine the conditions for high temperature boundary scattering in the general case and then apply our predictions to the Bi-Sb system (and incidentally, to the Bi<sub>2</sub>Te<sub>3</sub> alloy system as well)

### Theoretical Principles

Any precise calculation of the effect of boundary scattering would require considerable computation using a large number of parameters that would have to be determined separately for each material. Often, the detailed knowledge of the phonon spectrum and the phonon scattering mechanisms would not exist. However, by making a number of simplifying assumptions, an approximate theory may be developed and this should be adequate for predicting the order of magnitude of the maximum grain size for boundary scattering to be significant. Moreover, as we shall show, this approximate theory leads to simple predictions that can readily be applied to all solid solutions.

The simple theory is based on the Debye model for the phonon spectrum and the specific heat. It is supposed that there are just three mechanisms for the phonon scattering which depend on the (angular) frequency  $\omega$  in the following way:

<i>Umklapp Scattering</i>	$\tau_u = \frac{A_u}{\omega^2}$
<i>Point Defect Scattering</i>	$\tau_p = \frac{A_p}{\omega^4}$
<i>Boundary Scattering</i>	$\tau_L = \frac{L}{v}$

Equation (1)

where  $\tau$  is the relaxation time (time between collisions) and  $A_u$  and  $A_p$  are constants and for any particular solid solution.  $L$  is the grain size and  $v$  is the speed of sound. We also note that the contribution to the specific heat from the phonons with frequencies  $\omega$  to  $\omega + d\omega$  is proportional to  $\omega^2 d\omega$  up to the Debye frequency limit  $\omega_D$ .

Because the dependencies upon frequency of the three forms of scattering are quite different, it is a good approximation to suppose that only one mechanism be considered at a particular frequency. This being so the contribution  $\lambda(\omega)d\omega$  to the thermal conductivity  $\lambda$  from the various frequencies may be represented as in Figure 1.

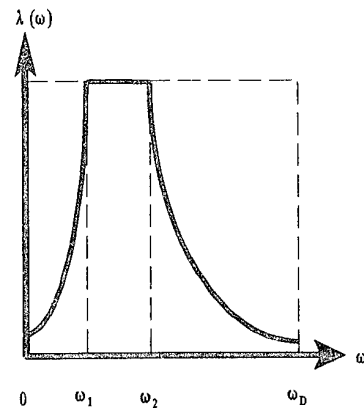


Figure 1

Boundary scattering predominates in the frequency range 0 to  $\omega_1$ , while between  $\omega_1$  and  $\omega_2$  umklapp scattering is the dominant mechanism. Above  $\omega_2$ , up to the limit  $\omega_D$ , point defect scattering takes over.

The contribution to the thermal conductivity from the frequency interval  $\omega$  to  $\omega + d\omega$  is

$$\lambda(\omega) d\omega = \frac{1}{3} C(v)^2 \tau(\omega) d\omega = \frac{C v^2 \tau(\omega)}{\omega_D^3} \omega^2 d\omega$$

Equation (6)

Thence:

$$\frac{A_u}{\omega_2^2} = \frac{A_p}{\omega_2^4}$$

and

$$A_p = A_u \omega_2^2$$

Equation (2)

where  $C$  is the total specific heat per unit volume. Thus, for our simplified model,

$$\begin{aligned} \lambda &= \int_0^{\omega_D} \lambda(\omega) d\omega = \\ &= \frac{C v^2}{\omega_D^3} \left\{ \int_0^{\omega_1} \frac{L \omega^2}{v} d\omega + \int_{\omega_1}^{\omega_2} A_u d\omega + \int_{\omega_2}^{\omega_D} \frac{\omega_2 A_p}{\omega^2} d\omega \right\} \\ &= \frac{C v^2}{\omega_D^3} \left\{ \frac{L \omega_1^3}{3v} + A_u (\omega_2 - \omega_1) + A_p \left( \frac{1}{\omega_2} - \frac{1}{\omega_D} \right) \right\} \end{aligned}$$

Equation (7)

In the absence of boundary scattering,  $\lambda = \lambda_s$  and  $\omega_1 = 0$ . Thus:

$$\lambda_s = \frac{\lambda_o \omega_2}{\omega_D} \left( 2 - \frac{\omega_2}{\omega_D} \right)$$

Equation (8)

At the frequency  $\omega_1$ , the scattering times  $\tau_L$  and  $\tau_u$  are equal, so that:

$$\frac{L}{v} = \frac{A_u}{\omega_1^2} = \frac{\omega_D^2 \lambda_o}{C v^2 \omega_1^2}$$

Equation (9)

By expressing the thermal conductivity  $\lambda_o$  in terms of the mean free path  $\bar{\tau}$  in the absence of point defect scattering, we can put

$$\omega_1^2 = \frac{1}{3} \omega_D^2 \frac{L}{\bar{\tau}}$$

Equation (10)

Equation (4)

and

$$\lambda_s = \frac{C v^2}{\omega_D^3} \left[ A_u \omega_2 + A_p \left( \frac{1}{\omega_2} - \frac{1}{\omega_D} \right) \right]$$

Equation (5)

We see, then, that  $A_u$  can be replaced by  $\omega_D^2 \lambda_o / Cv^2$ . Also we determine that the frequency  $\omega_2$  as being that for which  $\tau_p = \tau_u$ , so that:

We then find that the thermal conductivity of the fine grained solid solution is given by:

$$\begin{aligned}\lambda &= \frac{\omega_1}{3\omega_D} \lambda_o + \lambda_o \frac{\omega_2}{\omega_D} \left( 2 - \frac{\omega_1}{\omega_2} - \frac{\omega_2}{\omega_D} \right) \\ &= \lambda_s - \frac{2}{3} \frac{\omega_1}{\omega_D} \lambda_o\end{aligned}$$

Equation (11)

or

$$\lambda = \lambda_s - \frac{2}{3} \lambda_o \sqrt{\frac{l}{3L}}$$

Equation (12)

This equation shows clearly that the reduction of the thermal conductivity ( $\lambda_s - \lambda$ ) depends on the ratio of the mean free path  $T$  in the virtual crystal to the grain size  $L$ , but, because of the square root function, the second term on the right hand side of the equation (12) can become significant even if  $L$  is much greater than  $T$ . Also, this term is the more significant as  $\lambda_s$  becomes smaller, that is the stronger the point defect scattering.

Finally, we can estimate the value of  $T$  from the thermal conductivity  $\lambda_o$  using the expressions for the Debye theory for the speed of sound  $v$  and the specific heat  $C$ . We have  $v = 2 k_B a \Theta_D / h$  where  $k_B$  is the Boltzmann constant,  $a^3$  is the mean atomic or molecular volume,  $\Theta_D$  is the Debye temperature and  $h$  is the Planck constant. Also,  $C = 3 k_B / a^3$ . Then, if  $\Theta_D$  is expressed in degrees Kelvin and  $a$  is in meters, we find:

$$C v = 1.72 \times 10^{-12} \frac{\Theta_D}{a^2}$$

Equation (13)

and

$$\bar{l} = \frac{3 \lambda_o}{Cv} = 1.74 \times 10^{12} \frac{\lambda_o a^2}{\Theta_D}$$

Equation (14)

Also,  $a^3 = Z/\zeta N_A$  where  $Z$  is the atomic weight,  $\zeta$  is the density and  $N_A$  is Avogadro's number.

#### Application to Si-Ge

We may test the validity of this simplified theory for the case of Si-Ge alloys. Savvides and Goldsmid<sup>3</sup> found that the thermal conductivity of  $\text{Si}_{70}\text{Ge}_{30}$  at 300 K fell from 8.2 W/m K to 4.3 W/m K when the grain size was reduced to 2  $\mu\text{m}$ . Si and Ge have, respectively, Debye temperatures of 640 K and 370 K and lattice

thermal conductivities of 124 W/mK and 64 W/mK. Furthermore, the atomic weights are 28 and 72 and the densities are  $2.33 \times 10^3$  Kg/m<sup>3</sup> and  $5.35 \times 10^3$  Kg/m<sup>3</sup> respectively. If, then, we interpolate for the alloy, we find  $\lambda_o = 106$  W/m K,  $\Theta_D = 559$  K and  $Z/\zeta = 12.5 \times 10^{-3}$  Kg/m<sup>3</sup>. Putting  $N_A = 6.02 \times 10^{26}$  mols/Kg atom,  $a = 2.75 \times 10^{-10}$  m. The mean free path in the virtual crystal turns out to be  $2.5 \times 10^{-8}$  m.

If we use equation (12) to predict the thermal conductivity of  $\text{Si}_{70}\text{Ge}_{30}$  with a grain size of 2  $\mu\text{m}$ , taking  $\lambda_s$  to be 8.2 W/m K, we find :

$$\lambda = 8.2 - 4.6 = 3.6 \frac{W}{mK}$$

Equation (15)

This is in remarkably good agreement with the observed effect which, itself, is consistent with the predictions of the more rigorous theory.

#### Applications to BiSb

Having ascertained that the effect for Si-Ge is in reasonable agreement with our simple theory, we now turn to  $\text{Bi}_{88}\text{Sb}_{12}$ , the composition studied by Suse et al. Since the alloy lies close to the Bi end of the range, we may use without much error, values corresponding to Bi for the virtual crystal. From the work of Uher and Goldsmid<sup>4</sup>  $\lambda_o = 9.8$  W/mK at 155 K and 19.1 W/m K at 80 K. The recent work of Lenoir<sup>5</sup> gives a value of  $\lambda_s = 3.0$  W/m K observed at 80 K. Measured without magnetic field. All these measurements refer to the heat flow in the binary direction and we take into no account the anisotropy of Bi or its alloys here.

First we have to estimate the thermal conductivity of a large crystal of the alloy at 155 K. This we do by making use of Matthiessen's rule, whereby we may treat the resistivity due to point defect scattering and umklapp scattering as additive. We also take the point defect component to be independent of temperature. Thence, we find that at 155 K  $\lambda_s = 2.6$  W/m K.

Taking the values for Bi of the density equal to  $9.80 \times 10^3$  Kg/m<sup>3</sup> and the atomic weight of 209, we obtain  $Z/\zeta = 21.3 \times 10^{-3}$  m<sup>3</sup> Kg and,  $a^3 = 35.4 \times 10^{-30}$  m<sup>3</sup>, with  $a$  then being  $3.3 \times 10^{-10}$  m. Using a Debye temperature of 118 K we find the mean free path in Bi to be  $1.57 \times 10^{-8}$  m.

Using equation (12),

$$\lambda = 2.6 - 6.53 \sqrt{\frac{0.523 \times 10^{-8}}{L}} \frac{W}{mK}$$

Equation (16)

According to Suse et al., their materials were made from particles of "1 to 5  $\mu\text{m}$  in diameter". If we substitute  $L = 1 \mu\text{m}$ . We obtain  $\lambda = (2.6 - 0.47)$  W/m K. This is certainly a significant reduction in

the thermal conductivity (it amounts to about 18%) but it is not nearly so great as that claimed by Suse and his colleagues which they stated was two thirds of that of the single crystal. Actually, Suse's thermal conductivity of 1.2 W/m K is not quite as small as one-third of 2.6 W/m K but it is still much smaller than the theory would predict.

Perhaps the effective grain size in Suse's material is smaller than the stated 1 to 5  $\mu\text{m}$ . Let us consider, then, what value of grain size  $L$  might be needed for, say, a 50% reduction in the thermal conductivity. Again using equation (12), we find that  $L$  would have to be 0.13  $\mu\text{m}$ . In other words, it would seem to be quite possible to obtain really large reductions in the thermal conductivity of Bi-Sb if the effective grain size could be reduced to a fraction of a micrometer.

#### Bismuth Telluride Alloys

Boikov et al.<sup>6</sup> Reported a boundary scattering effect for phonons in  $\text{Bi}_{0.5}\text{Sb}_{1.5}\text{Te}_3$  in thin film form. Let us see, then, what sort of grain size might be needed for a worthwhile reduction in thermal conductivity in this material.

Here we are interested in applications at room temperature or not much lower. The thermal conductivity of phonons in  $\text{Bi}_2\text{Te}_3$  at room temperature is 1.5 W/m K and this is reduced by about 20% in  $\text{Bi}_2\text{Te}_3 - \text{Sb}_2\text{Te}_3$  solid solutions. The molecular weight of  $\text{Bi}_2\text{Te}_3$  is 801 and its density is  $7.86 \times 10^3 \text{ Kg/m}^3$  giving  $Z/\zeta = 101.9 \times 10^{-3} \text{ m}^3/\text{Kg}$  and,  $a = 5.5 \times 10^{-10} \text{ m}$ . Using a Debye temperature of 155 K, we find a phonon mean free path of  $0.51 \times 10^{-8} \text{ m}$ . Substituting in equation (12),

$$\lambda = \lambda_0 \left( 0.8 + \frac{2}{3} \sqrt{\frac{L}{3L}} \right)$$

#### Equation (17)

Here we see that to produce, say, a 10% reduction in the lattice thermal conductivity we need,

$$\frac{2}{3} \sqrt{\frac{L}{3L}} = 0.08$$

#### Equation (18)

which leads to a grain size of  $L$  of  $11.8 \times 10^{-8} \text{ m}$ . Thus, even if the grain size is reduced to only one-tenth of a micrometer, the resultant effect on the thermal conductivity is rather small. It would, therefore, seem to be rather difficult to make use the boundary scattering effect to improve the figure of merit in the  $\text{Bi}_2\text{Te}_3$  system.

#### Conclusions

The theory presented here makes it a simple matter to predict the effect of boundary scattering on the thermal conductivity of fine grained solid solutions. The results agree well with experiment for Si-Ge alloys and this gives us confidence in applying the theory to other systems. It would seem that there would be as significant (on

the order of 20%) reduction in the thermal conductivity of Bi-Sb alloys for a grain size of about 1  $\mu\text{m}$ . Through the effects reported by Suse et al. would probably need a grain size at least an order of magnitude smaller than this. There seems little prospect of using the effect to advantage for the  $\text{Bi}_2\text{Te}_3$  system of alloys.

#### References

- (1) Suse, Y., Lee, Y.H. Morimoto, H., Koyanagi, T., Matsubara, K. And Kawamoto. In *Proceedings for 12th International Conference on Thermoelectrics Yokohama*, 243, 1993
- (2) Goldsmid, H.J., Penn, A.W. *Phys. Lett. A* **27**, 523, 1968
- (3) N. Savvides, and H.J.Goldsmid *J. Phys. C*, **13**, 4657, 1980
- (4) C. Uher and H.J. Goldsmid, *Phys Status Solidi B*, **65** 765 1974
- (5) B. Lenoir, "Elaboration d'alliages bismuth-antimone contribution à l'étude des propriétés de transport" These L'Institute National Polytechnique de Lorraine, May 1994.
- (6) Y. Boikov, B. Gol'tsman, V. Kntasov, *Sov. Phys. Solid State*, **20**, 757, 1978

**THERMOELECTRIC PROPERTIES OF SOLID SOLUTIONS BASED ON Bi<sub>2</sub>Te<sub>3</sub>  
AT 300 K**

Kutasov V.A., Luk'yanova L.N.

*A.F. Ioffe Physical-Technical Institute of RAS, St. Petersburg, 194021, Russia.*

Thermoelectric properties of the many-components of n-type solid solutions based on bismuth telluride were studied at 300 K. Dependences of  $(m^*/m)^{3/2} \mu_0$  expression and thermoconductivity of the crystal lattice ( $\kappa_i$ ), that calculated from experimental data on electroconductivity ( $\sigma$ ), thermoelectric power ( $\alpha$ ) and thermoconductivity ( $\kappa$ ), defining the figure of merit Z were considered.

The most well-known solid solutions of n-type based on bismuth telluride (Bi<sub>2</sub>Te<sub>3-x</sub>Se<sub>x</sub>) have been used in energy converters intended for different purposes. Moreover some references have been published about more complicated compositions of solid solutions which is formed by substitution atoms in anion and cation sublattice of bismuth telluride [1-3]. These compositions have a high value of figure of merit at 300 K [1,2] and also in the range of less temperatures [3]. As a rule, it is not discussed peculiarities of thermoelectric properties of these many-components solid solutions for more wide range of compositions than considered materials.

In the present investigation many-components of n-type solid solutions based on bismuth telluride were studied on the range of existence of these solid solutions [4-6]. The next system of solid solutions were studied: Bi<sub>2</sub>Te<sub>3-x,y</sub>Se<sub>x</sub>S<sub>y</sub> (x = y and x = 2y, 0 ≤ x+y ≤ 0.9), Bi<sub>2-z</sub>Sb<sub>z</sub>Te<sub>3-x,y</sub>Se<sub>x</sub>S<sub>y</sub> (x = y, x = 2y, 0 ≤ x+y ≤ 0.9, 0 ≤ z ≤ 0.6), and also two solid solutions without selenium Bi<sub>2-z</sub>Sb<sub>z</sub>Te<sub>3-y</sub>S<sub>y</sub> (0 ≤ y ≤ 0.3, z ≤ 0.2) and Bi<sub>2</sub>Te<sub>3-y</sub>S<sub>y</sub> (0 ≤ y ≤ 0.3).

Ingots of the solid solutions were grown by directed crystallization method in the conditions excluding a concentration overcooling [7]. A rate of crystallization was no more than 0.5 mm/min, the temperature gradient on the front of crystallization was about 200 K/cm. Cleavage plane in the samples provided a possibility of cutting single crystals by electroerosian method for studying anisotropy of thermoelectric properties. But majority measurements of electroconductivity, thermocconductivity and thermoelectric power were made on cylindrical samples with diameter 8 ± 10mm and length l = 10 ± 12mm. Thermal flow and electrical current were oriented along cleavage planes. All measurements were made at the room temperature. The figure of merit Z for thermoelectric materials is given by expression:

$$Z = \frac{\alpha^2 \sigma}{\kappa} \quad (1)$$

The expression for Z without account of the electron part of thermoconductivity may be also given in another form:

$$Z \approx \frac{(m^*/m)^{3/2} \mu_0}{\kappa_i} \quad (2)$$

where m\* - density of states effective mass,  $\mu_0$  - charge carrier mobility with account of degeneracy of electron gas, m - mass of free electron.

The expression (2) connects the figure of merit Z with values, which are defined by scattering of electrons and phonons, and also peculiarities of the band structure of the material.

The value of  $(m^*/m)^{3/2} \mu_0$  may be calculated from experimental  $\alpha$  and  $\sigma$  using some assumption about scattering mechanism of charge carriers. It is supposed in many published data, that acoustic scattering mechanism of charge carriers is main. The value of scattering parameter for acoustic mechanism is equal to r = -0.5 (r-the index of a power in the dependence of relaxation time  $\tau$  on energy:  $\tau = \tau_0 E^r$ ). A value of r = -0.5 may be used for qualitative estimations. In this case influence of impurity scattering and interband scattering is neglected. And for more detailed analysis of the thermoelectric properties is required to use the effective scattering parameter  $r_{ef}$  [8]. The value of  $(m^*/m)^{3/2} \mu_0$  may be obtained from the expressions [9]:

$$n = \frac{4(2\pi m^* k_0 T)^{3/2} F_{1/2}(\eta)}{\sqrt{\pi} h^3} \quad (3)$$

$$\alpha = \frac{k_0 (2r+5) F_{r+3/2}(\eta)}{e (2r+3) F_{r+1/2}(\eta)} - \eta \quad (4)$$

$$\sigma = en\mu \quad (5)$$

where n - charge carrier concentration,  $F_r(\eta)$  is the Fermi function:

$$F_r(\eta) = \int_0^\infty x^r [\exp(x-\eta) + 1]^{-1} dx \quad (6)$$

Then the experimental dependence of  $\alpha = f(\sigma)$  in the impurity of charge carriers is considered (Fig.1). The value of  $\sigma$  for  $\alpha = \text{const}$  is decreased with growth of atoms concentrations of the second component at all values of x,y,z and the parameter  $(m^*/m)^{3/2} \mu_0$  is also decreased with growth of x,y,z (Fig.2).

As seen from Fig.2 the most strong changes of  $(m^*/m)^{3/2} \mu_0$  on composition of solid solution were observed in the range of a small concentration of the second component.

The same analysis was also made for another solid solutions. The dependences of  $(m^*/m)^{3/2}\mu_0$  on composition of the solid solution  $\text{Bi}_2\text{Te}_{3-x-y}\text{Se}_x\text{S}_y$  are shown in Fig.3.

From comparison of Fig.2 and 3 it is shown, that the addition of Sb atoms for equal values of  $x+y$  leads to decreasing of  $(m^*/m)^{3/2}\mu_0$  parameter. This decreasing may be explained as a change of the effective mass, as the charge carrier mobility.

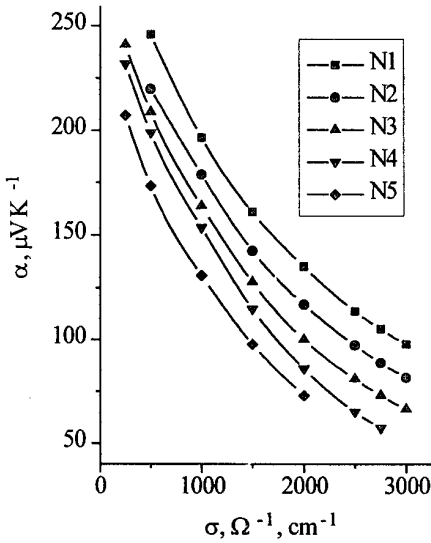


Fig.1 Dependence of the thermoelectric power on electroconductivity in solid solutions  $\text{Bi}_{2-x}\text{Sb}_x\text{Te}_{3-x-y}\text{Se}_x\text{S}_y$ . N1 -  $x = y = 0.15$ ; N2 -  $x = y = 0.3$ ; N3 -  $x = y = 0.45$ ; N4 -  $z = 0.4$ ,  $x = y = 0.3$ ; N5 -  $z = 0.6$ ,  $x = y = 0.45$ .

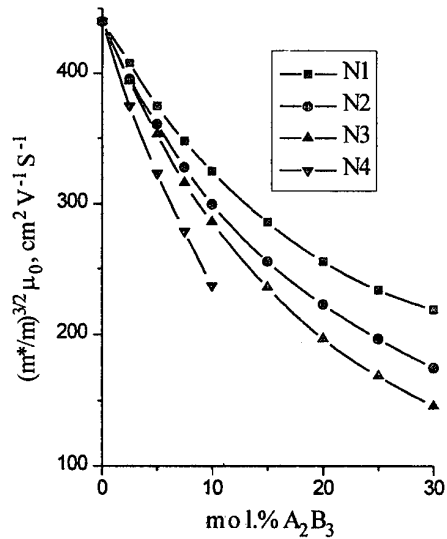


Fig.2 Dependence of  $(m^*/m)^{3/2}\mu_0$  parameter on composition of  $\text{Bi}_{2-x}\text{Sb}_x\text{Te}_{3-x-y}\text{Se}_x\text{S}_y$  solid solutions.  
N1 -  $(\text{Bi}_2\text{Te}_3)_{1-x} - (\text{Sb}_2\text{Se}_3)_x$ ; N2 -  $(\text{Bi}_2\text{Te}_3)_{1-x-y} - (\text{Sb}_2\text{Se}_3)_x - (\text{Sb}_2\text{S}_3)_y$ , for  $x = 2y$ ; N3 -  $(\text{Bi}_2\text{Te}_3)_{1-x-y} - (\text{Sb}_2\text{Se}_3)_x - (\text{Sb}_2\text{S}_3)_y$ , for  $x = y$ ; N4 -  $(\text{Bi}_2\text{Te}_3)_{1-y} - (\text{Sb}_2\text{S}_3)_y$ .

From analysis of the dependence  $(m^*/m)^{3/2}\mu_0$  parameter on concentration of the second component in the solid solution  $\text{Bi}_2\text{Te}_{3-x}\text{Se}_x$  it was shown, that a change of  $(m^*/m)^{3/2}\mu_0$  value is proportional to  $m^{*-1}$  in the range of a small concentration of  $x \leq 0.3$  [10]. This assumption is confirmed by data of Bergman [11] which calculated the value of the effective mass  $m^*$  in a single crystal of  $\text{Bi}_2\text{Te}_{3-x}\text{Se}_x$  from the measurements of galvanomagnetic coefficients. However for further increasing of  $x$  the value of  $m^*$  changes slightly (from 0.59 at  $x = 0.3$  to 0.61 at  $x = 0.9$ ). This result does not permit to explain decreasing of  $(m^*/m)^{3/2}\mu_0$  parameter with changing of  $m^*$  only. In this range of changing  $x$  value it is necessary to account the influence of a scattering charge carrier by atoms of the second components (Se atoms).

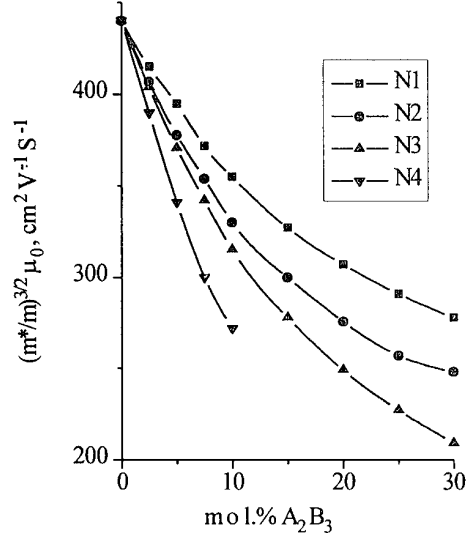


Fig.3 Dependence of  $(m^*/m)^{3/2}\mu_0$  parameter on composition of  $\text{Bi}_2\text{Te}_{3-x-y}\text{Se}_x\text{S}_y$  solid solutions.  
N1 -  $(\text{Bi}_2\text{Te}_3)_{1-x} - (\text{Bi}_2\text{Se}_3)_x$ ; N2 -  $(\text{Bi}_2\text{Te}_3)_{1-x-y} - (\text{Bi}_2\text{Se}_3)_x - (\text{Bi}_2\text{S}_3)_y$ , for  $x = 2y$ ; N3 -  $(\text{Bi}_2\text{Te}_3)_{1-x-y} - (\text{Bi}_2\text{Se}_3)_x - (\text{Bi}_2\text{S}_3)_y$ , for  $x = y$ ; N4 -  $(\text{Bi}_2\text{Te}_3)_{1-y} - (\text{Bi}_2\text{S}_3)_y$ .

Thus from data on  $\alpha(\sigma)$  dependence it is concluded that  $(m^*/m)^{3/2}\mu_0$  parameter is continuously decreased with growth of  $x,y,z$  for all considered n-type compositions of solid solutions based on  $\text{Bi}_2\text{Te}_3$ . For more values of  $x,y,z$  the change of  $(m^*/m)^{3/2}\mu_0$  are slightly in comparing with compositions nearby to bismuth telluride.

The solid solutions of  $\text{Bi}_{2-x}\text{Sb}_x\text{Te}_{3-y}\text{S}_y$  with solubility of  $\text{Bi}_2\text{S}_3$  (or  $\text{Sb}_2\text{S}_3$ ) no more than 10% mol. (i.e.  $x+y \leq 0.3$ ,  $z \leq 0.2$ ) have some important peculiarities. As seen from Fig.2 and 3 in these materials the values of  $(m^*/m)^{3/2}\mu_0$  are increased the most sharp in comparing with all another composition having as unlimited  $\text{Bi}_2\text{Se}_3$ , as limited solubility (70% mol.  $\text{Sb}_2\text{Se}_3$  [6], 30% mol.  $\text{Bi}_2\text{Se}_3 + \text{Bi}_2\text{S}_3$  [4]).

Investigation of thermoconductivity was made on the same compositions of solid solutions that the measurements of electroconductivity and thermoconductivity. An electron part of thermoconductivity  $\kappa_e$  was calculated with account of Wiedemann-Franz law for scattering parameter  $r = -0.5$ . The value of thermoconductivity of the crystal lattice  $\kappa_l$  in the

range of the impurity conductivity was calculated as a difference between a whole thermoconductivity  $\kappa$  and an electron part of thermoconductivity  $\kappa_e$ . The dependences of  $\kappa_i$  on composition of solid solution are shown in Fig.4,5 for equal charge carrier concentration.

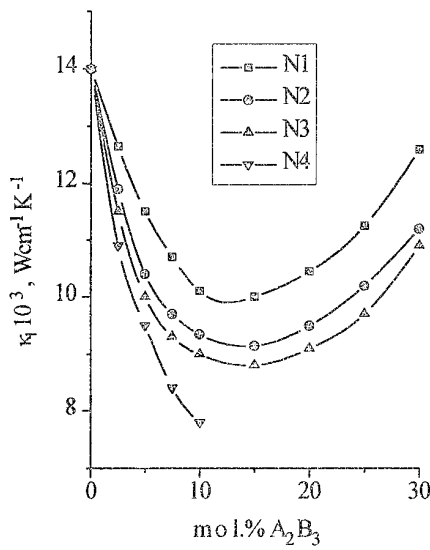


Fig.4 Dependence of the thermoconductivity of the crystal lattice ( $\kappa_i$ ) on composition of  $\text{Bi}_{2-x} \text{Te}_{3-x,y} \text{Se}_x \text{S}_y$  solid solutions.

N1 -  $(\text{Bi}_2\text{Te}_3)_{1-x} - (\text{Bi}_2\text{Se}_3)_x$ ; N2 -  $(\text{Bi}_2\text{Te}_3)_{1-x,y} - (\text{Bi}_2\text{Se}_3)_x - (\text{Bi}_2\text{S}_3)_y$  for  $x = 2y$ ; N3 -  $(\text{Bi}_2\text{Te}_3)_{1-x-y} - (\text{Bi}_2\text{Se}_3)_x - (\text{Bi}_2\text{S}_3)_y$  for  $x = y$ ; N4 -  $(\text{Bi}_2\text{Te}_3)_{1-y} - (\text{Bi}_2\text{S}_3)_y$ .

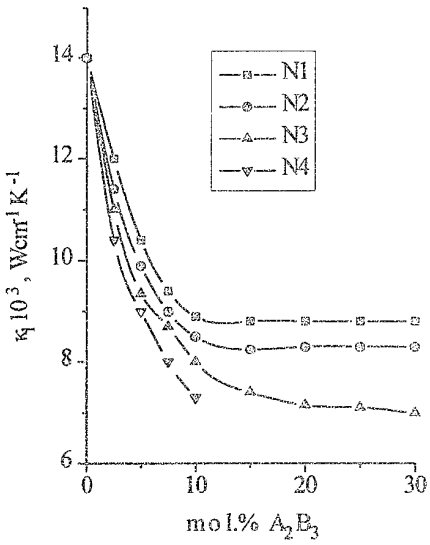


Fig.5 Dependence of the thermoconductivity of the crystal lattice ( $\kappa_i$ ) on composition of  $\text{Bi}_{2-x} \text{Sb}_x \text{Te}_{3-x,y} \text{Se}_x \text{S}_y$  solid solutions.

N1 -  $(\text{Bi}_2\text{Te}_3)_{1-x} - (\text{Sb}_2\text{Se}_3)_x$ ; N2 -  $(\text{Bi}_2\text{Te}_3)_{1-x-y} - (\text{Sb}_2\text{Se}_3)_x - (\text{Sb}_2\text{S}_3)_y$  for  $x = 2y$ ; N3 -  $(\text{Bi}_2\text{Te}_3)_{1-x-y} - (\text{Sb}_2\text{Se}_3)_x - (\text{Sb}_2\text{S}_3)_y$  for  $x = y$ ; N4 -  $(\text{Bi}_2\text{Te}_3)_{1-y} - (\text{Sb}_2\text{S}_3)_y$ .

As seen from Fig.4,5 for less values of  $x,y,z$  ( $x \leq 0.3$ ;  $x+y \leq 0.3$ ;  $x+y+z \leq 0.3$ ,  $z \leq 0.3$ )  $\kappa_i$  value is increased with

growth concentration of atoms participating in formation of solid solution. The value of  $\kappa_i$  have a minimum in the material which does not contain Sb atoms (Fig.4). The minimum of  $\kappa_i$  is explained by ordering a due to complete replacement of Te<sup>2</sup> to Se atoms in five-layer packet Te<sup>1</sup> - Bi - Te<sup>2</sup> - Bi - Te<sup>1</sup> in the solid solution  $\text{Bi}_2\text{Te}_{3-x} \text{Se}_x \text{S}_y$ . It is possible that in  $\text{Bi}_2\text{Te}_{3-x} \text{Se}_x \text{S}_y$  the solid solution the atoms of Se and S substitute Te<sup>2</sup> atoms.

Nevertheless appreciable differences in the concentration corresponding to minimum of the dependence  $\kappa_i$  on composition for  $x = 2y$  and  $x = y$  were not observed. The curve of  $\kappa_i$  for  $x = y$  places low then curve for  $x = 2y$  in all interval of changing Se and S concentrations (Fig.4, curves 3,4).

In  $\text{Bi}_{2-x} \text{Sb}_x \text{Te}_{3-x,y} \text{Se}_x \text{S}_y$  solid solutions not observed the whole ordering of the quintet for substitution of Sb to Bi atoms in two equivalent layers of the quintet. Therefore the minimum of  $\kappa_i$  dependence on composition of the solid solution was not observed (Fig.5). Thus the values of  $(m^*/m)^{3/2} \mu_0$  and  $\kappa_i$  are decreased nearby  $\text{Bi}_2\text{Te}_3$  with growth atom concentrations participating in formation of solid solution. However  $(m^*/m)^{3/2} \mu_0$  value changes less weakly than  $\kappa_i$  value. It is the main purpose of growth the figure of merit Z at 300 K in these materials.

In the range of low charge carrier concentration some contribution to Z value may be also connected the charge carrier of another sign which disappears with growth of the energy gap  $E_g$  in dependence on composition of the solid solution [12]. The value of Z have a maximum in  $\text{Bi}_2\text{Te}_{3-x} \text{Se}_x$  at  $x = 0.3$ , for further increasing of x the value of Z is decreased.

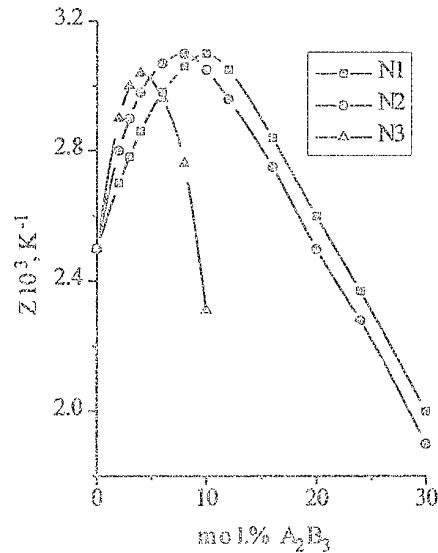


Fig.6 Dependence of the figure of merit (Z) on composition of  $\text{Bi}_{2-x} \text{Te}_{3-x,y} \text{Se}_x \text{S}_y$  solid solutions.  
N1 -  $\text{Bi}_2\text{Te}_{3-x} \text{Se}_x$ ; N2 -  $\text{Bi}_2\text{Te}_{3-x,y} \text{Se}_x \text{S}_y$ ; N3 -  $\text{Bi}_2\text{Te}_{3-y} \text{S}_y$ .

The dependence of Z value on composition in another n-type solid solutions based on  $\text{Bi}_2\text{Te}_1$  look like as  $\text{Bi}_2\text{Te}_{3-x} \text{Se}_x$ . The value of  $Z_{max} = (3 \div 3.1) 10^{-3} \text{ K}^{-1}$  at 300 K are achieved for different concentrations of the second

component: at  $y = 0.06 \div 0.1$  in  $\text{Bi}_2\text{Te}_{3-y}\text{S}_y$ , at  $x+y = 0.24$  in  $\text{Bi}_2\text{Te}_{3-x,y}\text{Se}_x\text{S}_y$  (Fig.6). Analogous dependence of the figure of merit  $Z$  on composition is observed in another solid solutions and also in  $\text{Bi}_{2-z}\text{Sb}_z\text{Te}_{3-x,y}\text{Se}_x\text{S}_y$ . From near arrangement of the curves  $Z(x,x+y,z)$  the dependences of  $Z$  on composition for these solid solutions were not given.

As it is mentioned, the solid solution of  $\text{Bi}_2\text{Te}_{3-x}\text{Se}_x$  is the most well-known material for manufacturing of the different cooling devices in the range of temperature near the room temperature. However for another temperatures (for low and also high temperatures) the thermoelectric properties of materials considered in this investigation may be more effective.

## References

- [1]. W.M. Yim, F.D. Rosi. Compound Tellurides and their Alloys for Peltier Cooling. Sol. St. Electr., 1972, v.15, No.9, p.p.1121-1140.
- [2]. H.J. Goldsmid. Electronic Refrigeration. London, Pion Limited, 1985, 227p.
- [3]. V.A. Semenyuk, L.D. Ivanova, T.E. Svechnikova. Peculiarity of Applications of Bismuth and Antimonide Chalcogenides of Solid Solution Monocrystals in Miniaturized Coolings. Izv. RAN, ser. Neorg. Mater., 1995, v.31, No.1, p.p.32-35.
- [4]. N.H. Abrikosov, M.L.Beglarian. Investigation of  $\text{Bi}_2\text{Se}_3$  -  $\text{Bi}_2\text{Te}_2\text{S}$  -  $\text{Bi}_2\text{Te}_3$  system. Izv. RAN, ser. Neorg. Mater., 1973, v.9, p.p. 1529-1536.
- [5]. E.A. Gurieva, A.I. Zaslavskii, V.A. Kutasov, I.A.Smirnov. Thermoconductivity of the Solid Solutions Based on Telluride. Fiz.Tverd.Tela (Leningrad), 1965, v.7, No.4, p.p.1221-1227.
- [6]. V.G. Kuznetsov, K.K. Palkina. Diagrams of Condition and Structures of Alloys in  $\text{Bi}_2\text{Se}_3$  -  $\text{Sb}_2\text{Te}_3$  -  $\text{Bi}_2\text{Te}_3$  -  $\text{Sb}_2\text{Te}_3$ . Zh. Neorg. Chim., 1963, v.8, No.5, p.p.1204-1217.
- [7]. W.A. Tiller. Growth and Perfection of Crystals. 1958, John Wiley and Sons. Inc., N.Y.,329 p.
- [8]. V.A. Kutasov, L.N. Luk'yanova. Carrier Density Dependence of the Effective Scattering Parameter of Solid Solutions Based on Bismuth Telluride. Fiz. Tverd. Tela (Leningrad), 1984, v.26, No.8, p.p.2501-2504.
- [9]. A.I. Anselm. Introduction to the Theory of Semiconductors. Moscow, 1978, 615p. (in Russian).
- [10]. B.M.Gol'tsman, G.N.Ikonnikova, V.A. Kutasov, Yu.I. Ravich. Scattering Mechanisms and Temperature Dependence of the Effective Mass of Electrons in Solid Solutions Based on Bismuth Telluride. Fiz. Tverd. Tela (Leningrad), 1985, v.27, No.2, p.p.542-545. (Sov. Phys. Sol. St., 1985, v.27, No.2, p.p.334-336).
- [11]. O. Beckman, P. Bergval, K. Tripathi. Doping Studies of  $\text{Bi}_2(\text{TeSe})_3$  Alloys. Ark. fur Fys., 1965, B28, Hf.3, p.p. 215-221.
- [12]. B.M. Gol'tsman, V.A.Kudinov, I.A.Smirnov. Semiconductor Thermoelectric Materials Based on  $\text{Bi}_2\text{Te}_3$ . Nauka, (Moscow), 1972, 320p.(in Russia).

# COMPOSITION DEPENDENCE ON THERMOELECTRIC PROPERTIES OF UNDOPED POLY-CRYSTAL $(Bi_2Te_3)_{1-y}(Sb_2Te_3)_y$ PREPARED BY PIES METHOD

T. Ohta<sup>1</sup>, A. Yamamoto<sup>1</sup>, T. Tanaka<sup>1</sup>, T. Fujimaki<sup>2</sup> and K. Kamisako<sup>2</sup>

<sup>1</sup>*Electrotechnical Laboratory, AIST, MITI, Tsukuba, 305, Japan*

<sup>2</sup>*Tokyo University of Agriculture and Technology, Tokyo, 184, Japan*

The PIES method (Pulverized and Intermixed Elements Sintering method) is a new preparation technique for bismuth telluride based materials and so on. It has a number of advantages over the melt technique. The room temperature figure of merit of PIES sample of undoped  $(Bi_2Te_3)_{0.2}(Sb_2Te_3)_{0.8}$  was similar to that of the best single crystal sample. As for the composition dependence on thermoelectric properties of undoped  $(Bi_2Te_3)_{1-y}(Sb_2Te_3)_y$  PIES materials, the room temperature properties and the temperature dependence of them changed systematically as y value changed. At a temperature from 300 to 440 K the power factor exhibited the maximum values when y=0.875. The oxygen in PIES materials which acted as donor affected the thermoelectric properties of the PIES materials.

## Introduction

Bismuth telluride based alloys are the most widely used thermoelectric materials, especially in commercial thermoelectric refrigeration. However, in previous studies bismuth telluride based alloys have been exclusively prepared by the conventional melt technique followed occasionally by the conventional sintering technique[1,2,3,4].

The PIES method (Pulverized and Intermixed Elements Sintering method) has been investigated as a new preparation technique not only for bismuth telluride based alloys[5,6,7] but for silicon-germanium based alloys[8], rare earth sulfides[9] and so on. It has a number of advantages over the conventional technique, for example, low energy inventory for preparation, low cost and short processing period, a potential for reducing grain size which favors a reduction in the thermal conductivity and an enhancement in the mechanical strength.

The thermoelectric figure of merit of bismuth telluride based PIES material was  $2.75 \times 10^{-3}K^{-1}$  which is near those of the best single crystal materials of up to  $2.9 \times 10^{-3}K^{-1}$ [10]. The properties of bismuth telluride based alloys prepared by the PIES method, however, are quite different from the conventional alloys prepared by the conventional method, detailed investigation of thermoelectric properties of the PIES materials are necessary in order to make sure the performance limit of the PIES materials. Hence the purpose of this study is to clarify the composition dependence of the thermoelectric properties of p-type  $(Bi_2Te_3)_{1-y}(Sb_2Te_3)_y$  PIES materials as a part of the detailed study of the PIES materials.

## Experimental

Sample specimens of undoped  $(Bi_2Te_3)_{1-y}(Sb_2Te_3)_y$  were prepared by PIES method which includes the pulverizing process of stoichiometric amount of elemental bismuth, antimony and

tellurium by high energy ball milling and the sintering process[5]. The high energy ball milling process was occasionally accomplished in an atmosphere of hydrogen. In this study hot pressing method were chosen as a sintering procedure. Hot pressing conditions were 753 K, 400 kgf/cm<sup>2</sup> for one hour. Typical size of the specimens was 10 mm φ x 1.5 mm thickness and the density values measured by the Archimedes' principle were more than 95 % of the ideal value. The preparation procedure and the conditions are shown in Figure 1.

Scanning Electron Microscopy-Electron Probe Micro Analyses and X-ray diffractometry were performed for examining morphology and composition of the specimens. Oxygen content was determined by the Non-Dispersive Infrared Spectrometry. The Seebeck coefficients were calculated from measurements of

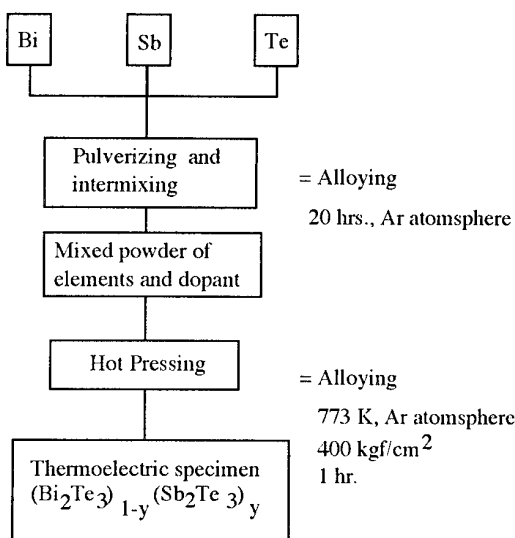


Figure 1. Preparation procedure and conditions of PIES method.

the electromotive forces with temperature difference of ten Kelvin. The electrical resistivity and the Hall effects measurements were performed by van der Pauw method. All measurements were performed from 300K to about 500K, except for the Hall effect measurement which was performed at 300K.

### Results and Discussion

**Thermoelectric Properties.** Figure 2 shows the composition dependence of carrier concentration for the various hot pressed samples at room temperature. The solid line indicates the composition dependence of carrier concentration of the single crystal samples[11]. The p-n transition was observed around  $y=0.7$ , while in the single crystal samples it was not observed whole composition range indicated in the figure. As composition  $y$  increased the p-type carrier increased monotonously.

Figure 3 shows the composition dependence of the Seebeck coefficient of the PIES samples at room temperature. At around  $y=0.7$  the bipolar conduction occurred because the electron concentration and the hole concentration were almost the same values. Thus the Seebeck coefficient values were small at this composition range. In the p-type conducting region the Seebeck coefficient values decreased with increasing composition of antimony telluride( $y$  value). On the other hand, in the n-type conducting region the absolute value of the Seebeck coefficient increased with increasing composition of antimony telluride. This is because the hole concentration increased with increasing  $y$  value in the p-type region, instead the electron concentration decreased with increasing  $y$  value in the n-type region according to the figure 2.

Figure 4 shows the composition dependence of the resistivity at room temperature. At around  $y=0.7$  the resistivity values were large because the total carrier concentration values (absolute electron concentration value + hole concentration value) were small. In the p-type conducting region the resistivity values

decreased with increasing  $y$  values (i.e. increasing hole concentration values), on the contrary, in the n-type conducting region the resistivity values increased with increasing  $y$  values (i.e. decreasing electron concentration).

Figures 5 and 6 shows the carrier concentration dependence of the Seebeck coefficient and the resistivity of the PIES samples respectively. These figures support the explanation of the figures 3 and 4. Thus the composition dependence of the electrical properties of PIES samples were explained in the same manner.

Figure 7 shows the temperature dependence of the Seebeck coefficient of the p-type PIES samples (i.e.  $y=0.775$ ). Y indicated the composition of the antimony telluride as described before. The composition dependence of the Seebeck coefficient values at room temperature had already explained by the figures 2, 3 and 5. The temperature dependence of it was also described in the same manner as follows. When  $y$  value was equal to 0.775 the hole concentration value was the smallest of the six samples at room temperature. The Seebeck coefficient values of the sample of

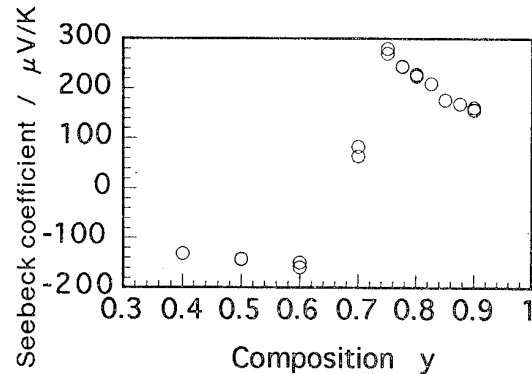


Figure 3. Composition dependence of Seebeck coefficient for PIES materials.

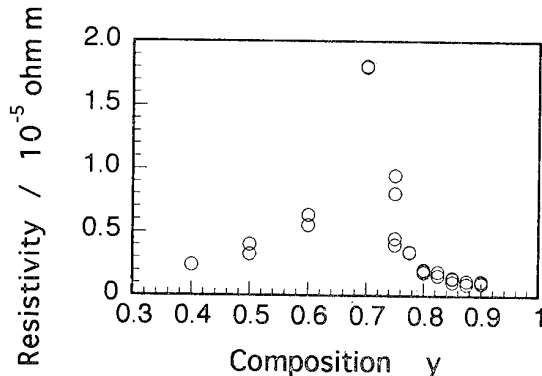


Figure 4. Composition dependence of electrical resistivity for PIES materials.

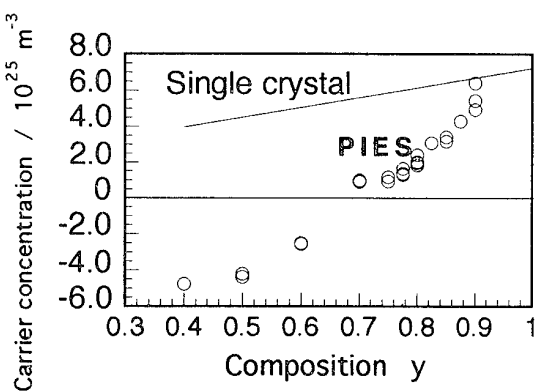


Figure 2. Composition dependence of carrier concentration for PIES materials.

$y=0.775$  were the largest and the bipolar conduction due to the thermal excitation of the valence band electrons began at the lowest temperature because of the lowest hole concentration value. Consequently the Seebeck coefficient of the sample of  $y=0.775$  exhibited the maximum value at the lowest temperature. The temperature at which the Seebeck coefficient exhibited the maximum value increased with increasing  $y$  values, i.e. with increasing the hole concentration values.

Figure 8 shows the temperature dependence of the resistivity of the p-type PIES samples and the characteristics were explained in the same manner. The magnitude of the resistivity values decreased with increasing  $y$  values, i.e. with increasing hole concentration values. The temperature at which the resistivity exhibited the maximum value increased with increasing  $y$  values. In this manner the temperature dependence of the electrical properties of p-type PIES samples were explained by considering the hole concentration values of the samples with various compositions.

Figure 9 shows the temperature dependence of the power

factor ( $\alpha^2/\rho$ ) of the p-type PIES samples. This factor is calculated by the Seebeck coefficient and the resistivity values, accordingly the curves were complicated a little. However some tendencies could be pointed out. When the  $y$  values were less than

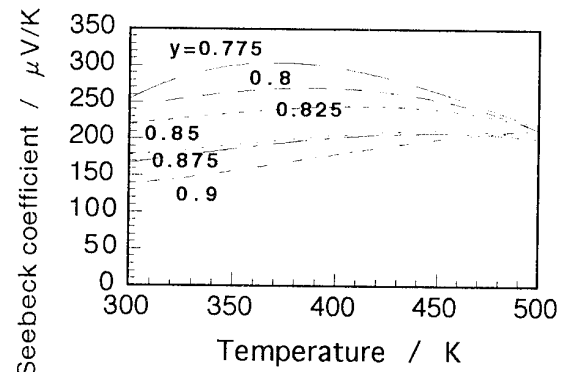


Figure 7. Temperature dependence of Seebeck coefficient of p-type PIES materials.

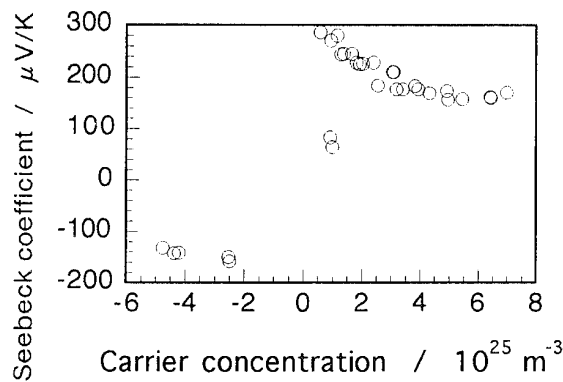


Figure 5. Carrier concentration dependence of Seebeck coefficient of PIES materials.

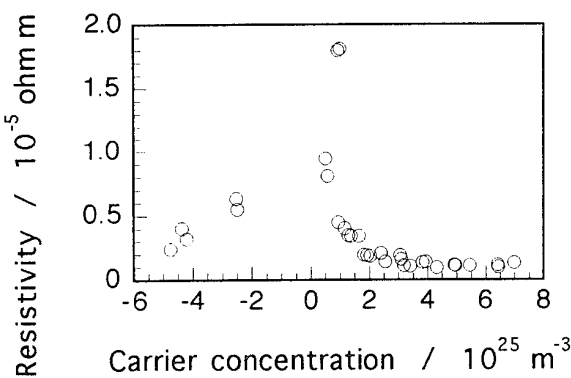


Figure 6. Carrier concentration dependence of electrical resistivity of PIES materials.

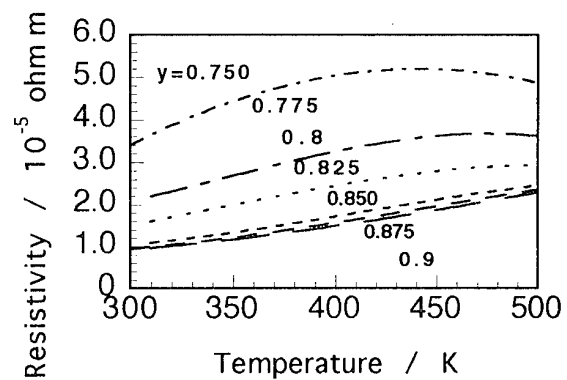


Figure 8. Temperature dependence of electrical resistivity of p-type PIES materials.

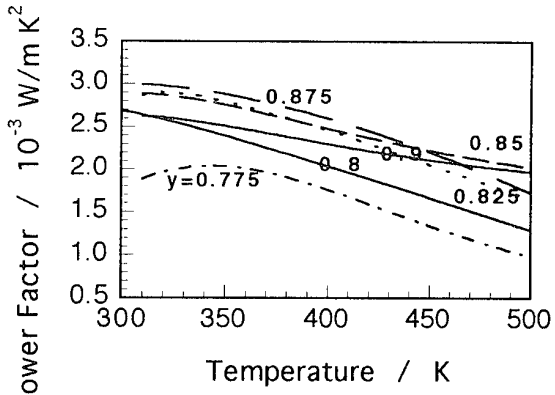


Figure 9. Temperature dependence of power factor of p-type PIES materials.

0.825, the power factor could be larger than other high  $y$  value samples in the temperature region below the room temperature. At around the room temperature, the samples which had  $y$  values from 0.825 to 0.875 exhibited the best power factor. At around the temperature close to 500K, The samples which had  $y$  values from 0.85 to 0.9 showed the best power factor. Hence the sample with  $y=0.875$  was the best sample in the undoped  $(\text{Bi}_2\text{Te}_3)_{1-y}(\text{Sb}_2\text{Te}_3)_y$  samples prepared by PIES method according to the power factor in the temperature range from 300K to 500K. Thus the electrical properties of the undoped  $(\text{Bi}_2\text{Te}_3)_{1-y}(\text{Sb}_2\text{Te}_3)_y$  PIES samples were obtained systematically.

**Affects of oxygen.** Figure 2 shows the composition dependence of the carrier concentration of the PIES samples and the single crystal ones. The PIES samples exhibited the p-n transition at around the composition value of 0.75, however, the single crystal exhibited p-type conduction in the whole composition range of  $y$  from 0.4 to 1.0. In other words the carrier concentration of the PIES samples were much more sensitive to the carrier concentration than that of

the single crystal samples. The difference between the electron concentration of the PIES samples and that of single crystal ones increased with decreasing the  $y$  value. There are several factors which yield the electrons in the PIES samples, for example the oxygen in the samples, the grain boundaries, the defects in the grains and so on.

In this discussion the influences on thermoelectric properties of oxygen content were examined experimentally. Figure 10 shows the oxygen content dependency of the room temperature resistivity of the undoped  $(\text{Bi}_2\text{Te}_3)_{0.15}(\text{Sb}_2\text{Te}_3)_{0.85}$  ( $y=0.15$ ) prepared by PIES method. The resistivity values increased with increasing the oxygen content, even though the error of the oxygen content measurement was taking into consideration (See error bar).

Figure 11 shows the oxygen content dependency of the room temperature carrier concentration of the same samples. The carrier concentration values decreased with increasing the oxygen content monotonously. This result suggest that the oxygen in the PIES samples yielded electrons, consequently the hole concentration decreased. The oxygen content of the PIES samples are much larger than those of the single crystal ones of less than 0.01 mass percent. According to the figure 2, the electron concentration values of the PIES samples were about  $3 \times 10^{25} \text{ m}^{-3}$  more than those of the single crystal. Assuming that the oxygen atoms yielded all of the excess electrons in the PIES samples, a oxygen atom yielded 0.0115 electron on the average. Further investigation on role of oxygen in the PIES materials should be necessary.

### Conclusions

The undoped  $(\text{Bi}_2\text{Te}_3)_{1-y}(\text{Sb}_2\text{Te}_3)_y$  prepared by PIES method had following characteristics:

- (1) The Seebeck coefficient, the resistivity, the Hall mobility and the carrier concentration values changed systematically as  $y$  value changed.
- (2) The p-type conduction was observed when the  $y$  value was more than 0.7.
- (3) The p-n transition was also observed at around  $y$  value of 0.7 which was different from the characteristics of the single crystal materials. The difference in oxygen content was a major factor of it.
- (4) The PIES materials had the oxygen concentration values of 0.3 to 0.8 mass percent which are much larger than those of single crystal values (less than 0.01 mass percent).
- (5) The oxygen in materials acted as donor because the hole concentration values increased with decreasing the oxygen concentration values. A oxygen atom yielded 0.0115 electron on the average.

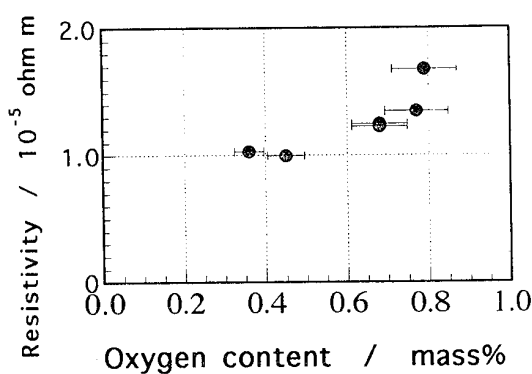


Figure 10. Oxygen content dependency of room temperature resistivity of undoped  $(\text{Bi}_2\text{Te}_3)_{0.15}(\text{Sb}_2\text{Te}_3)_{0.85}$ .

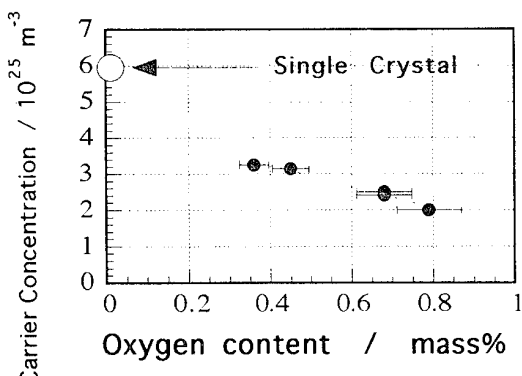


Figure 11. Oxygen content dependency of room temperature carrier concentration of undoped  $(\text{Bi}_2\text{Te}_3)_{0.15}(\text{Sb}_2\text{Te}_3)_{0.85}$ .

### Acknowledgement

Authors would like to express special thanks to Dr. A. Negishi for his help on microscopic analyses of morphology and composition.

### References

- [1]. W.M.Yim and F.D.Rosi, Solid-State Electronics, 1972, 15, pp.1121- 1140.
- [2]. T.Durst, H.J.Goldsmid and L.B.Harris, Solar Energy Materials, 1981, 5, pp.181-186.
- [3]. H.Kaibe, Y.Tanaka, M.Sakata and I.Nishida, J. Physics and Chemistry of Solids, 1989, 50, pp.945-950.
- [4]. T.Caillat, M.Carle, P.Pierrat, H.Scherrer and S.Scherrer, J. Phys. Chem. Solids, 1992, 53, PP.1121-1129.
- [5]. T.Ohta, T.Uesugi, T.Tokai, N.Nosaka and T.Kajikawa, "Pulverized and Intermixed Elements Sintering Method on  $(Bi,Sb)_2(Te,Se)_3$  Based N-type Thermoelectric Devices", in Proceedings of the Eighth International Conference on Thermoelectric Energy Conversion, 1988, pp. 7-11.
- [6]. T.Ohta, T.Uesugi, T.Tokai, N.Nosaka and T.Kajikawa, Trans. IEE of Japan, 1991, 111-B, pp.670-674, in Japanese.
- [7]. T.Tokai, T.Uesugi, K.Fukumoto, A.Hirayama, K.Ito, T.Ohta and T.Kajikawa, Thermoelectric characteristics of Bi-Te based PHEs materials after-sintering(II), in Proceedings of 1992 Spring Meeting of the Japan Institute of Metals, 1992, in Japanese.
- [8]. B.A.Cook, B.J.Beaudry, J.L.Harringa and W.J.Barnette, Modern Perspectives On Thermoelectrics and Related Materials, Pittsburgh: Material Research Society, 1991, pp. 111-116.
- [9]. S.H.Hann, K.A.Gschneidner Jr. and B.J.Beaudry, J. Alloys and Compounds, 1992, 181, pp.463.
- [10]. T.Ohta, A.Yamamoto and T.Tanaka, "Thermoelectric Properties of Undoped Polycrystal  $(Bi_2Te_3)_{0.2}(Sb_2Te_3)_{0.8}$  by PHEs Method", in Proceedings of the Thirteenth International Conference on Thermoelectrics, 1995, pp. 267-270.
- [11]. J-E Shim and D-B Hyun, Thermoelectric Properties of Bi-Sb-Te Ternary Single Crystals, in Proceedings of the IX International Conference on Thermoelectrics, 1990, pp. 27-35.

**(BiSb)<sub>2</sub>Te<sub>3</sub> AND Bi<sub>2</sub>(TeSe)<sub>3</sub> FILMS PREPARED BY VACUUM-ARC PLASMA METHOD:  
CHARACTERISATION AND APPLICATIONS**

I. V. Gasenkova<sup>1</sup>, E. I. Tochitsky<sup>2</sup>

<sup>1</sup>*Institute of Electronics, Belarus Academy of Sciences 22 Lagoiski Trakt, Minsk-90, 220841, Republic of Belarus*

<sup>2</sup>*Engineering Center "Plasmoteg", Belarus Academy of Sciences, 1/3 Zhodinskaya Str., Minsk 220141, Republic of Belarus*

The potentialities of a pulsed vacuum-arc plasma method are comprehensively disclosed as applied to formation of thermoelectric (BiSb)<sub>2</sub>Te<sub>3</sub> and Bi<sub>2</sub>(TeSe)<sub>3</sub> films. Characteristics of the films studied by XPS, SIMS, RBS, electron microscopy (TEM) and electron-diffraction techniques have demonstrated that this comparatively new method is suitable for making thermoelectric devices.

## Introduction

The need for thermoelectric materials with high thermoelectric efficiency stimulates both the search of new materials [1] and utilisation and modification of various technological means and methods of deposition of traditional materials [2-4]. The results of our previous studies have demonstrated the possibility of obtaining thermoelectric films based on bismuth telluride by pulsed vacuum-arc plasma (PVAP) method [5-6]. This method is chosen not only because of the possibility of reproducing the starting material composition in the films but also because the films obtained exhibit a good adhesion to substrate. Since bismuth telluride films have properties that are strongly dependent on their preparation method and on condensation conditions within a particular method [4], a detailed study is required of the films prepared by the PVAP method. This paper presents generalisation of the results of a comprehensive investigation of such films, including peculiarities incurred by the method. The advantages of using bismuth telluride-based films produced by PVAP method as thermobattery branches of thermoelectric transducers (TET) are briefly discussed

## Experimental

(BiSb)<sub>2</sub>Te<sub>3</sub> and Bi<sub>2</sub>(TeSe)<sub>3</sub> films were prepared in an oil-free vacuum of 10<sup>-5</sup> Pa on polyimide, NaCl and Al<sub>2</sub>O<sub>3</sub> substrates at 300 K, 425 K, 475 K and 575 K substrate temperatures. The corresponding energy characteristics of the plasma deposition unit and other process parameters are described in [7]. Phase composition and microstructure of the films 50 nm thick were studied by electron diffraction technique (ED) and electron microscopy. XPS method was employed to study physicochemical state of the film surface and that of the target material, chemical composition depth profile, and the effect of ion bombardment on the film phase composition. XPS spectra were taken by means of an ES-2401 spectrometer using Mg k<sub>α</sub> X-ray radiation and photon energy h ν = 1253.6 eV. Two measurement modes were used: full scanning and scanning of regions 20 eV wide in energy steps equal to 0.1 eV. 1s-line of carbon was used as a standard. Layerwise etching was conducted with 1 keV argon ions at 2.3 μA/cm<sup>2</sup> current density. Ar+ bombardment of specimen surface was performed at the incidence angle of 45 degrees. Spectra were measured for inner-shell C 1s, O 1s, Bi 4f, Sb 3d and Te 3d electrons. Elemental composition of the films, distribution of components over thickness and at the film-substrate interface were studied by SIMS method and Rutherford

back-scattering (RBS). SIMS data were obtained by means of an ion microanalyzer JMS-300 equipped with electrostatic energy filter. Registration of secondary ion signal was performed by using an electron multiplier in the ion counting mode. Oxygen ions with E = 5.5 keV and current densities j = 0.3, 0.1, 0.05 μA/cm<sup>2</sup> were used for bombarding films 2.5 μm, 78 nm and 35 nm thick, respectively. In order to increase the secondary ion yield, measurements were conducted with oxygen pressure increased up to 3·10<sup>-3</sup> Pa.

## Results

Analysis of the regularities of structural transformations in (BiSb)<sub>2</sub>Te<sub>3</sub> and Bi<sub>2</sub>(TeSe)<sub>3</sub> films prepared by PVAP method combined with investigation of 500 Å-film growth processes by electron microscopy and generalisation of experimental findings have shown that the basic condensation mechanism is of a "vapour-crystal"-type with coalescence in the substrate temperature range up to 573 K. Above this temperature, condensation of Bi<sub>2</sub>(TeSe)<sub>3</sub> films proceeds via "vapour-crystal" mechanism without coalescence, which is characteristic of substances with high vapour elasticity and high anisotropy of the surface tension coefficient. Condensation mechanism has a crucial effect on formation of continuous film structure and determines not only texturization behaviour and grain size in a continuous film but also formation of defects in the film structure.

The distinctive feature of the films deposited onto cold substrates is their high structural dispersivity, fine 2.0-3.0 nm grains being observed simultaneously with coarse 8.0-10.0 nm grains. The ratio of grains of the two size domains and their size itself are determined by the plasma accelerator unit operation regime and have been established by TEM using Fourier-transform of TEM structural pictures [6]. It should be noted that high kinetic energy of particles and degree of plasma flux ionisation typical of the PVAP method make it possible to prepare textured films on cold substrates, epitaxial growth of films being observed at substrate temperatures of 425-575 K (Fig. 1). In the Bi<sub>2</sub>(TeSe)<sub>3</sub> films, the {105} Bi<sub>2</sub>(TeSe)<sub>3</sub>//{001} NaCl orientation is predominant, the number of grains with the {105} Bi<sub>2</sub>(TeSe)<sub>3</sub>//{001} NaCl orientation is insignificant. In the (BiSb)<sub>2</sub>Te<sub>3</sub> films, grains are oriented with {105} and {005} planes parallel to {001} NaCl, both orientations being equally probable up to the condensation temperature of 475 K. At higher temperatures, the films have {001} (BiSb)<sub>2</sub>Te<sub>3</sub> //{001} NaCl orientation. In both films, two azimuthal orientations are observed: the directions [110] of {105}-oriented grains are mu-

tually perpendicular, and the directions [110] of {001}-oriented grains form an angle of 30 degrees.

The observed difference in textures can be explained by growth rate anisotropy and positions occupied by excess electronegative elements in the crystal lattice. Interstitial position of bismuth in  $\text{Bi}_2(\text{TeSe})_3$  results in a more chaotic distribution of atoms in the lattice, which justifies its description by a reduced pseudocubic cell. In accordance with the principle of parallelism of close-packed directions, a texture is formed where the cube faces of the reduced cell are parallel to {100} NaCl. In a true cell, the same cube faces correspond to {105} planes. The  $(\text{BiSb})_2\text{Te}_3$  structure can be described with better probability by a true cell, since in it excess elements are located in lattice sites. In accordance with the same parallelism principle, the {001}  $(\text{BiSb})_2\text{Te}_3 // \{001\}$  NaCl orientation is formed in this case.

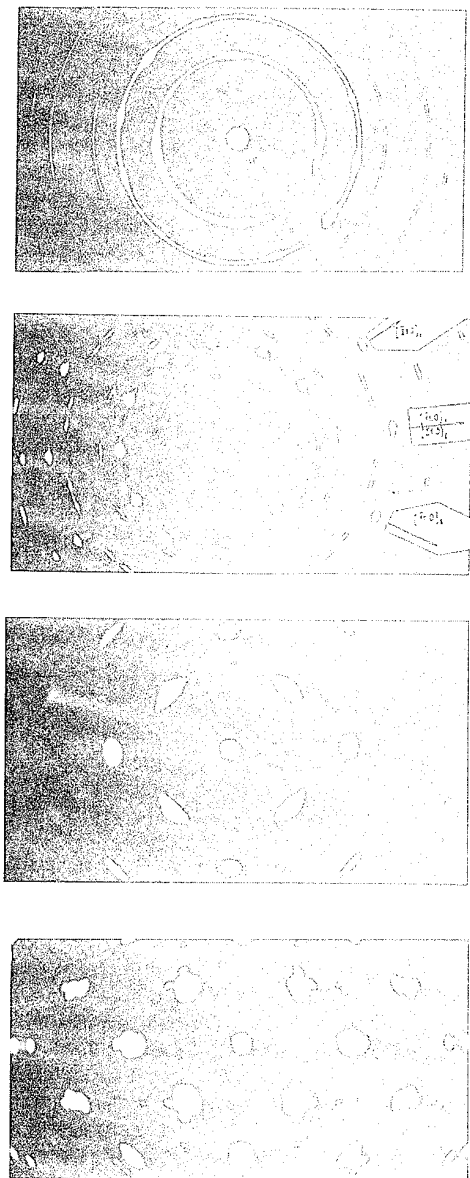


Fig.1. Electron diffraction patterns of  $(\text{BiSb})_2\text{Te}_3$  (I) and  $\text{Bi}_2(\text{TeSe})_3$  (II) films deposited on NaCl substrate at different substrate temperature: a, c-300K, b-575K, d-475K.

The appearance of electron-diffraction patterns changes in the case of films prepared at the condensation temperature of 475 K (Fig. 1). There emerge diffraction points caused by double reflection resulting from the presence of several grain orientations. Forbidden diffraction points arise from interaction of some allowed diffraction beams. The double diffraction is caused by formation and growth of grains on the grain already grown, which is evidenced by a moire pattern in the TEM image emerging owing to rotation of the grains with the same interplane distances by a small angle. The presence of stacking faults in the films gives rise to the streaks in the ED patterns. In addition to matrix reflections, the ED patterns from  $(\text{BiSb})_2\text{Te}_3$  and  $\text{Bi}_2(\text{TeSe})_3$  films exhibit weak reflections at the positions multiple to 1/3 (300) revealing the occurrence of ordering processes. Our studies have shown that changing of the condensation mechanism in the  $\text{Bi}_2(\text{TeSe})_3$  films gives rise to additional orientations which were not observed in films prepared by other methods. It is noted in [4] that microstructure also changes, featuring plate-like grains with twin boundaries.

XPS results indicate that the Bi, Sb, Te component ratio in the near-surface layer differs from those found in the film depth and in the target material. It should be noted that the component ratio across the near-surface layer is not constant, changing over its depth, which indicates a nonuniform distribution of Bi, Sb and Te. Comparison of the forms and energy positions of photoelectron lines  $\text{Te } 3d_{5/2}$ ,  $\text{Bi } 4f_{7/2}$  and  $\text{Sb } 3d_{5/2}$  in the course of layerwise analysis of specimens shows that the near surface and deeper layers of the film differ substantially in their phase compositions (Fig. 2)

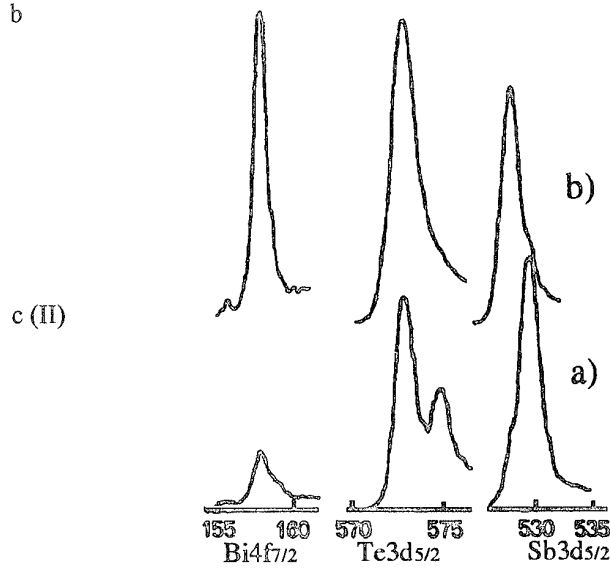


Fig. 2. XPS spectra from the surface of  $(\text{BiSb})_2\text{Te}_3$  films before (a) and after (b) etching with argon ion bombardment

Apart from the  $(\text{BiSb})_2\text{Te}_3$  phase, the near-surface layer contains oxides of Bi, Te and Sb. Argon ion bombardment of the film surface in the process of etching results in removal of oxidised layer and adsorbed carbon. Concentrations of Bi, Sb and Te in deeper layers tend to have constant values that correspond to their contents in the target material (sputtered target). Energy positions of photoelectron lines  $\text{Bi } 4f_{7/2}$ ,  $\text{Te } 3d_{5/2}$  and  $\text{Sb } 3d_{5/2}$  taken from the film surface cleaned by  $\text{Ar}^+$  bombardment testify that these elements are in chemically bound state in the form of

$(\text{BiSb})_2\text{Te}_3$  compound. Within the measurement error, the binding energies of the film components correspond exactly in value to those of the target material, namely, for Te 3ds/2 - Eb=572.2 eV, for Bi 4f7/2 - Eb=157.7 eV, for Sb 3ds/2 - Eb = 528.6 eV.

It has been found by SIMS that the elemental composition of the in-depth region of the films formed in optimised condensation regime corresponds to that of the target material and does not change from the near-surface to transition layer at the interface. Under the same experimental conditions, secondary ions yield values are identical for the target and the film and remain constant over the whole depth of the film, being equal to  $9.1 \cdot 10^5$ ,  $1.3 \cdot 10^5$  and  $1.6 \cdot 10^5$  counts for Bi, Te and Sb, respectively (Fig. 3). Consequently, concentration of components in the film corresponds to that of the target, and the component distribution over the film depth is uniform.

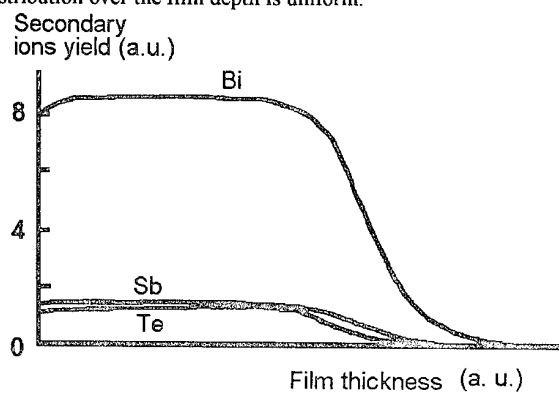


Fig.3. Distribution of secondary ions over the  $(\text{BiSb})_2\text{Te}_3$  film thickness

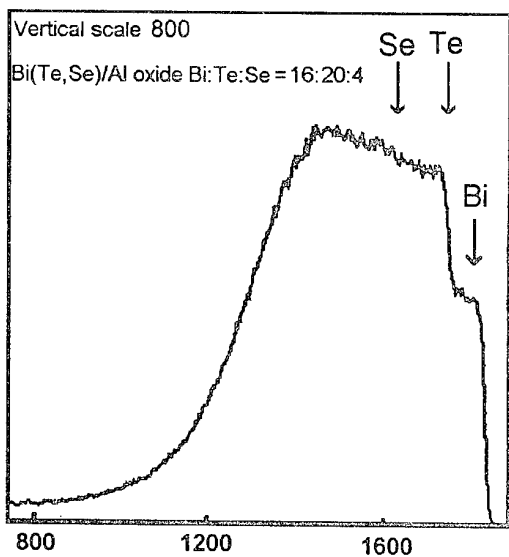


Fig.4. RBS spectrum taken from  $\text{Bi}_2(\text{TeSe})_3$  film used as n-type thermobattery branch of TET

Composition of the transition layer at the film-substrate interface is characterised by continuous lowering of concentration of the main film components down to zero and simultaneous rising of concentration of light substrate elements. The concentration profile at the interface and the width of transition region were calculated from spectra of He ions back-scattered from the films. The RBS spectrum from the  $\text{Bi}_2(\text{TeSe})_3$  film and the

corresponding component distribution profile at the film -  $\text{Al}_2\text{O}_3$  substrate interface are shown in Table and Fig. 4. Depth of diffusion into aluminium oxide was 870 nm for Bi and Te and 530 nm for Se. For the films condensed onto polyimide, the width of the transition region was about 200-300 nm. In the calculations, the atomic density value of  $9.18 \cdot 10^{-22} \text{ cm}^3$  was used that corresponded to polyimide density of  $1.42 \text{ g/cm}^3$ .

Based on a concrete design solution of the thermo-electrical transducer (TET) which had thermobattery branches made of  $(\text{BiSb})_2\text{Te}_3$  and  $\text{Bi}_2(\text{TeSe})_3$  films prepared by PVAP method, an advantage of such a transducer as compared with commercially produced devices has been demonstrated. It has been found experimentally that the new TET (see Fig. 5), described in detail in [8, 9], has the conversion coefficient of up to 12 V/W.

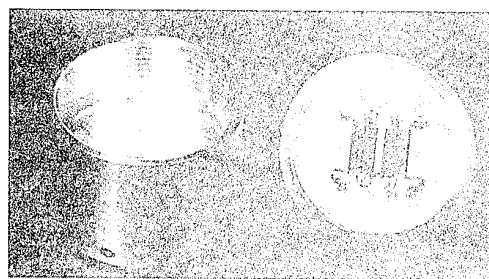


Fig.5. Appearance of a thin-film thermo-electrical transducer

Commercial TET with thermobattery branches made of GeTe and PbTe and a TET with  $(\text{BiSb})_2\text{Te}_3$  and  $\text{Bi}_2(\text{TeSe})_3$  branches formed by vacuum evaporation (discrete evaporation from a Knudsen cell at deposition rates of 0.0035 and 0.0060  $\mu\text{m/s}$ ) are characterised by the conversion coefficients not higher than 3 V/W. Another advantage of using  $(\text{BiSb})_2\text{Te}_3$  and  $\text{Bi}_2(\text{TeSe})_3$  films deposited by PVAP method instead of GeTe and PbTe for branches is that there is no need to apply a double SiO protection layer on the surface of thermobattery branches, thus making production process simpler. Further improvement of TET's characteristics is achieved by subsequent annealing in inert atmosphere. Thus, annealing for 30 minutes at 375 K increases the conversion coefficient up to 18 V/W. It should be noted that reduction of the sheet resistance after annealing makes it possible, firstly, to form thermosensitive elements with lower output resistance on the same substrate area, which reduces requirements to the input resistance of the secondary transducer, and, secondly, to reduce the substrate area used for the same nominal values of thermosensitive elements, which increases integration factor and decreases the device dimensions.

## Conclusion

The results of our investigations have demonstrated the possibility of forming  $(\text{BiSb})_2\text{Te}_3$  and  $\text{Bi}_2(\text{TeSe})_3$  films by PVAP method. By controlling condensation conditions, it is possible to obtain films with various grain sizes (from 2.0-7.0 nm to 50-60 nm) and degrees of texturing (from low-textured polycrystalline to epitaxial). Optimization of the deposition regime allows preparation of the films with composition corresponding to that of the target material and with uniform distribution of compo

TABLE  
The concentration profile at the interface  $\text{Bi}_2(\text{TeSe})_3 - \text{Al}_2\text{O}_3$

$\text{cm}^{-2}$	0, %	Bi, %	Te, %	Se, %
$3 \cdot 10^{18}$	60.00	16.00	20.00	4.00
$2 \cdot 10^{17}$	72.00	10.00	14.00	4.00
$3 \cdot 10^{17}$	79.00	7.00	11.00	3.00
$5 \cdot 10^{17}$	84.00	5.00	9.00	2.00
$1 \cdot 10^{18}$	88.00	4.00	7.00	1.00
$1 \cdot 10^{18}$	91.50	3.00	5.00	0.50
$1 \cdot 10^{18}$	95.00	2.00	3.00	0.00
$1 \cdot 10^{18}$	98.00	1.00	1.00	0.00
$2 \cdot 10^{18}$	99.00	0.50	0.50	0.00
	100.00	0.00	0.00	0.00

nents over the film thickness. The PVAP method is especially promising for making thermobattery branches of thin-filmthermoelectrical transducers, resulting in markedly higher conversion coefficient of the devices. There is no doubt that this method can be advantageously used for condensing other thermoelectric materials and for making various thermoelectrical devices.

#### References

- [1]. Proceedings XIII International Conference on Thermoelectrics. Kansas City, Missouri, USA, August 30-September 1, 1994.
- [2]. Film thermoelements: Physics and Application /Ed. by N. S. Lidorenko/, Moscow, Nauka, 1985, 232 p. (in Russian).
- [3]. A. Boyer, E. Charles, Synthese et propriétés thermoelectriques des semiconducteurs V2VI3, Vide, Couches, Minces, 1991, v. 47, No 25, pp. 99-105.
- [4]. B. B. Anisimov, M. G. Gopodze, I. Z. Dzhamagidze et al, Thermal deposition of multicomponent films of selectively evaporating alloys, *Pribory i Tekhnika Experimenta*, 1990, No 3, pp. 210-213, (in Russian).
- [5]. I. V. Gasenkova, Characterization of thermoelectric films prepared from pulsed flows of accelerated plasma, Proceedings CIP 93, June 6-11, 1993, Antibes-Juan-les-Pins, France, pp. 346-348.
- [6]. I. V. Gasenkova, E. I. Tochitsky, Investigation of AVBVI films by TEM, *Izvestiya of Rossiyskoi Akademii Nauk, seriya fizicheskaya*, 1995, v. 59, No. 2, pp 49-54. (in Russian).
- [7]. I. V. Gasenkova, A. M. Chaplanov, C. B. Dolzhikov et al, Formation of films with complex composition by electrcerosion plasma flows, *Voprosy atomnoi nauki i tekhniki, seriya: Yaderno-fizicheskie issledovaniya*, 1992, v. 1 (22), pp. 64-66. (in Russian).
- [8]. A. A. Archanov, D. R. Velder, Yu. I. Gorbachyov et al, Differenzial thin-films thermoelectric measuring transducer, *Tekhnika Sredstv Svyazi, seriya RIT*, 1983, v. 5 (51), pp. 30-37. (in Russian).
- [9]. I. V. Gasenkova, The AVBVI film application as functional elements of thermoelectric transducer, *Pribory i sistemy upravleniya*, 1993, No. 10, pp. 43-44. (in Russian).

## STRUCTURE AND PROPERTIES OF LARGE DIAMETER ZONE MELTING GROWN THERMOELECTRIC CRYSTALS

V.T. Bublik, V.V. Karataev, V.B. Osvensky, T.B. Sagalova, A.M. Frolov and O. Zhuravlev\*

*Institute of Chemical Problems of Microelectronics, 117571 Moscow, Russia*

\**Atrame Co., 11735 New York, USA*

The effect of growth conditions on the structure, texture type and chemical homogeneity of large diameter  $\text{Bi}_2\text{Te}_3$ -based crystals has been studied.

From the viewpoint of the cost-effectiveness of thermoelectric coolers fabrication, it would be a significant progress to increase the ingot diameter of thermoelectric materials (TEM) to at least 25 mm while retaining their high quality and desired properties. However, TEM crystals are still grown in up to 15-20 mm diameter ingots in the NIS countries. The major obstacles have been the poor reproducibility of alloying, deterioration of homogeneity, lack of the desired column structure orientation and, as a result, poor thermoelectric parameters.

Despite the above difficulties, it proves to be quite simple to grow high quality *p*-type TEM crystals of the  $\text{Sb}_2\text{Te}_3\text{-Bi}_2\text{Te}_3$  system with a diameter of more than 25 mm using zone melting with subsequent long-term annealing.

However, growth of *n*-type  $\text{Bi}_2\text{Te}_3\text{-Bi}_2\text{Se}_3$  TEM crystals with a diameter not less than 25 mm has a number of technical problems which originate from the dendrite liquation. In the ternary solid solution this effect shows itself in intra- and intergranular inhomogeneity and precipitation of nonequilibrium components. In other words, it is likely that the liquid phase stratifies into zones with different compositions from which TEM crystallize. Intragranular liquation is the stronger the larger is the concentration difference between the solidus and the liquidus in the phase diagram. Comparison of the T-X diagrams of the relevant binary systems showed that the above concentration difference of the  $\text{Bi}_2\text{Te}_3\text{-Bi}_2\text{Se}_3$  system is two times that of the  $\text{Sb}_2\text{Te}_3\text{-Bi}_2\text{Te}_3$  system. Hence, violation of particular conditions during the crystallization of Bi-Te-Se ternary solutions (e.g., low growth rate, large temperature gradient in the melt, stabilization of the melt temperature, etc.) may cause enhanced liquation which will produce pronounced dendrite structures.

Analysis of the crystallographic anisotropy and the related anisotropy of the physical properties of ternary TEM, such as the coefficients of thermo-emf ( $\alpha$ ), electrical conductivity ( $\sigma$ ) and heat conductivity ( $\kappa$ ), shows that  $\alpha$  is virtually isotropic, while  $\sigma$  and  $\kappa$  are the highest along the cleavage planes and the lowest in the perpendicular directions. In *n*-type TEM the anisotropy coefficients of  $\sigma$  are 4 to 6 and those of  $\kappa$  are 2 to 3 [1, 2]. The thermoelectric figure of merit  $Z$  is

$$Z = \alpha^2 \sigma / \kappa.$$

Figure 1 presents diagrams of  $\sigma$  and  $\kappa$  for a particular composition of the ternary solid solution, and Fig. 2 shows diagram of  $Z$ . The shape of the rotation ellipsoids which describe the anisotropy suggests that an orientation scatter of up to 5 arc deg has but a little effect on  $Z$ .

The cost-effectiveness of single crystal growth techniques is relatively low. A good alternative is the growth of large-diameter polycrystalline ingots with clearly pronounced ring texture which allows one to make use of the crystal anisotropy. For this texture the normal to the (00.1) planes is perpendicular to the growth axis and any normal to the planes of the [00.1]-zone may be parallel to this axis.

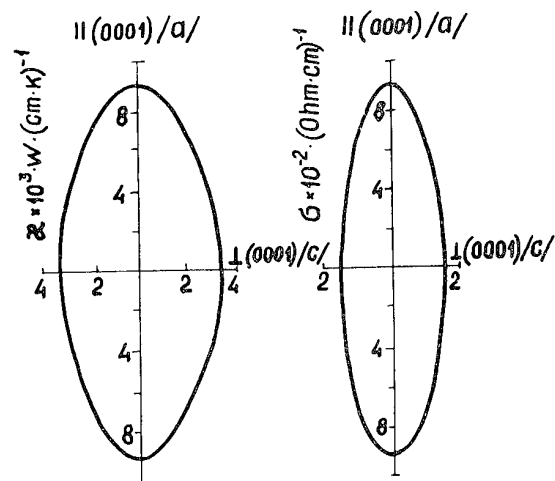


Fig. 1.  $\sigma$  and  $\kappa$  anisotropy rotation ellipsoids for conventional solid solutions of *n*-type TEM.

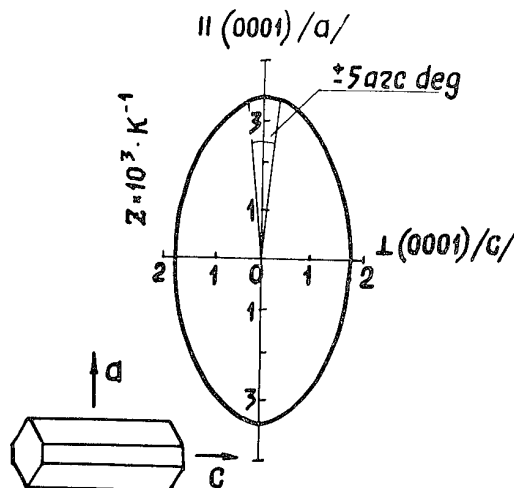


Fig. 2.  $Z$  anisotropy rotation ellipsoid for conventional solid solutions of *n*-type TEM.

$\text{Bi}_2\text{Te}_{2.7}\text{Se}_{0.3}$  and  $\text{Bi}_{0.5}\text{Sb}_{1.5}\text{Te}_3$  TEM ingots 25 mm in diameter were grown using vertical zone melting in sealed quartz ampoules by means of direct and 99.99 Sb, 99.999 Bi, 99.998 Te and 99.9992 Se. 99.99 Sb was shielded RF heating and resistive heating. The initial materials were obtained from 99.6 Sb by repeated vacuum-hydrogen distillation, and 99.998 Te was produced from 99.9 and 99.83 Te by distillation in the hydrogen

atmosphere of a quartz reactor. To obtain *n*-type TEM the polycrystals were doped with Cl.

X-ray diffractometry, Schultz topography and metallography (dark-field and in polarized light) were used to study the effect of TEM growth conditions (ingot diameter, heating mode, temperature and growth rate) on the phase composition, homogeneity of the ternary solid solution, microstructure and grain size. The results are summarized in Table I.

Table I. The effect of  $\text{Bi}_2\text{Te}_{2.7}\text{Se}_{0.3}+0.05\%\text{CdCl}_2$  TEM growth conditions on the structure, texture and thermoelectric properties at 300 K.

Nos.	Growth mode	Microstructure type and grain size	Main texture component and scatter	Thermoelectric properties
1	Resistive heating: $\Delta X = 3-5 \text{ mm}$ ; $V = 0.3-0.5 \text{ mm/min}$ ; $\varnothing = 12-20 \text{ mm}$ ; $\Delta T/\Delta X = 50 \text{ }^\circ\text{C/cm}$	Dendrites up to several cm in length; grains up to 1 mm in the interdendrite space	Lengthwise texture transition (13.5)-(11.0)-(10.23) with a scatter of up to several tens arc degrees	<i>n</i> -type; $\sigma = 800-1070 \text{ Ohm}^{-1}\text{cm}^{-1}$ ; $\alpha = 145-160 \mu\text{V/K}$ ; $\alpha^2\sigma = 27 \mu\text{W/m K}^2$
2	Direct RF heating: $\Delta X = 1-2 \text{ mm}$ ; $V = 0.1-0.25 \text{ mm/min}$ ; $\varnothing = 20-25 \text{ mm}$ ; $\Delta T/\Delta X = 150-200 \text{ }^\circ\text{C/cm}$	Column crystals sized more than 100 mm along the ingot axis and up to 50 mm perpendicular to it; subgrains sized $10 \times 1 \text{ mm}^2$	Clear ring [11.0] texture with a scatter of $\pm 15$ arc deg along the ingot axis and 1-3 arc deg perpendicular to it	<i>n</i> -type; $\sigma = 500-700 \text{ Ohm}^{-1}\text{cm}^{-1}$ ; $\alpha = 240-225 \mu\text{V/K}$ ; $\alpha^2\sigma = 29-35 \mu\text{W/m K}^2$
3	Shielded RF heating: $\Delta X = 1-2 \text{ mm}$ ; $V = 0.1-0.25 \text{ mm/min}$ ; $\varnothing = 20-25 \text{ mm}$ ; $\Delta T/\Delta X = 80-120 \text{ }^\circ\text{C/cm}$	Column crystals sized $100 \times 50 \text{ mm}^2$	Clear ring (10.0) texture; [00.1]-axis perpendicular to the ingot axis; a scatter of up to 3 arc deg	<i>n</i> -type; $\sigma = 700-950 \text{ Ohm}^{-1}\text{cm}^{-1}$ ; $\alpha = 231-210 \mu\text{V/K}$ ; $\alpha^2\sigma = 38-42 \mu\text{W/m K}^2$
4	Resistive heating: $\Delta X = 1 \text{ mm}$ ; $V = 0.1-0.15 \text{ mm/min}$ ; $\varnothing = 20-25 \text{ mm}$ ; $\Delta T/\Delta X = 80-120 \text{ }^\circ\text{C/cm}$	Column crystals sized $100 \times 50 \text{ mm}^2$	Ring texture; texture transition (21.5)-(11.0); a scatter of up to 5 arc deg	<i>n</i> -type; $\sigma = 950-980 \text{ Ohm}^{-1}\text{cm}^{-1}$ ; $\alpha = 210-215 \mu\text{V/K}$ ; $\alpha^2\sigma = 42-45 \mu\text{W/m K}^2$

Notes:  $\Delta X$  is the lash between the ampoule and the heater;  $V$  is the growth rate;  $\varnothing$  is the TEM ingot diameter;  $\Delta T/\Delta X$  is the axial temperature gradient near the crystallization front. The indices of the planes perpendicular to the growth axis are given.

The texture of the TEM ingots grown in mode 1 is multicomponent and axial both for *n*- and *p*-types. With increasing ingot diameter the number of strong reflections in the diffraction pattern increases to 14, and the main texture component becomes such that the C-axis directions are parallel to the growth axis. In this state the heat and electrical conductivities are the lowest, i.e., the thermoelectric parameters of the TEM are deteriorated. One may assume that the large number of the orientations originates from the nonplanar crystallization front and that the axial [00.1] texture forms because of the high radial component of the heat flow.

During dendrite crystallization (Fig. 3) chemical inhomogeneities, phase separation and grain refinement are observed. The interdendrite space is filled with small (sized from several microns to 1 mm) grains with a composition different from that of the dendrites.

The diffraction peaks of the samples grown in mode 1 are split and smeared due to the phase separation in the solid solution. The degree of the phase separation increases as one approaches the end of the ingot but changes insignificantly in the cross section.

The main technological objective of this work was to produce a column structure with such an orientation that the C-axis be perpendicular to the growth axis. This can be achieved by suppressing the radial heat flows at the crystallization front and enhancing the axial temperature gradient.

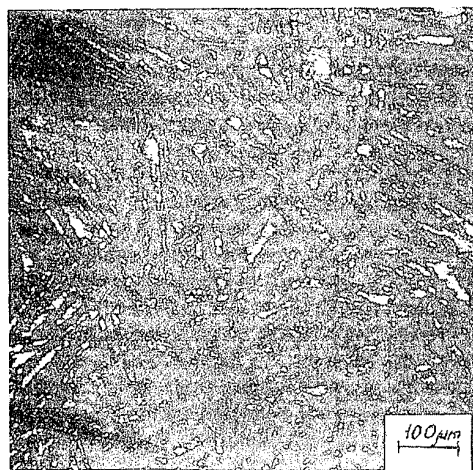


Fig. 3. Dendrite crystallization. The microstructure of the center of an *n*-type ingot (mode 1).

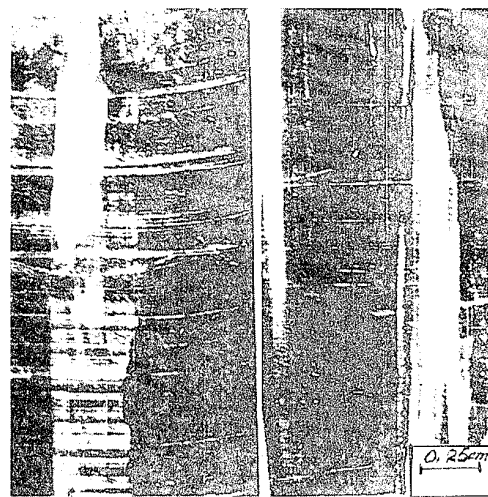


Fig. 4. Metallographic imaging of the lengthwise section of *n*-type ingots grown in modes (a) 4 and (b) 3.

The technical means elaborated in this work (Table 1) avoid dendrite crystallization thereby increasing the homogeneity both on micro- and macroscopic scale. The ingots grown in modes 3 or 4 contain stretched column crystals (100 mm) with a cross-section of 20-25 mm<sup>2</sup> (Fig. 4). However, these are not single crystals but consist of relatively large fiber-like subgrains (up to 0.1 mm<sup>2</sup> in section) stretched in the growth direction and oriented with a scatter of 1-3 deg relative to the growth axis and to one another.

The crystallization is likely to develop by the spiral-like growth of the (00.1) basis planes parallel to the growth axis and perpendicular to the radial heat removal direction. This assumption is confirmed by the hexagonal growth figures revealed by metallography in the longitudinal sections of samples grown in mode 3 (Fig. 5). The basis planes (11.0) or (10.0) appear to be perpendicular to the growth axis. The anisotropy of this ingot is favorable for the thermoelectric properties.

Suppression of the dendrite crystallization noticeably increases the chemical homogeneity of the solid solution both on micro- and macroscopic scale. It should be noted that there is a correlation in the radial composition inhomogeneity, the thermoelectric properties and the shape of the crystallization front (Fig. 6, a, b). For a flat crystallization front there was no radial composition inhomogeneity of the solid solution and the related thermoelectric properties were constant (mode 4). However, if the crystallization front shape was distorted by the radial heat flows, we observed a radial variation of the lattice parameter, indicating changes in the composition of the solid solution and, hence, in the thermoelectric properties.

TEM crystals grown without heat shields had even greater distortion of the crystallization front and greater thermal inhomogeneity in the transverse direction. The type of the texture remained the same, but the orientation scatter increased considerably (Table 1, mode 2).

TEM crystal grown with resistive heating retained an acceptable chemical homogeneity of the solid solution, but the texture orientation changed from (21.5) in the top of the ingot to (10.0) in its middle portion with but a moderate increase in the scatter (Table 1, mode 4).

Thus, study of preferred orientations in the lengthwise and transverse directions showed that:

(1) The type and scatter of the ring texture forming during crystallization can be changed by varying the growth mode;

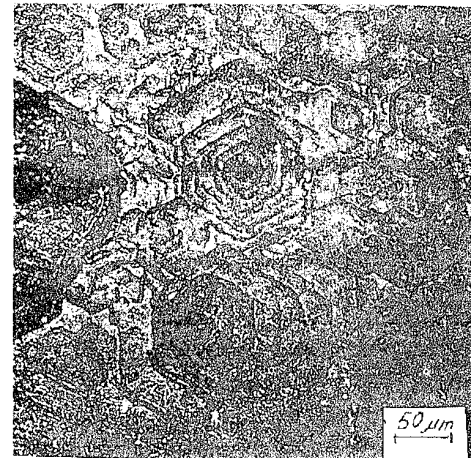


Fig. 5. Hexagonal growth figures revealed in a section along the growth axis of an *n*-type ingot grown in mode 3.

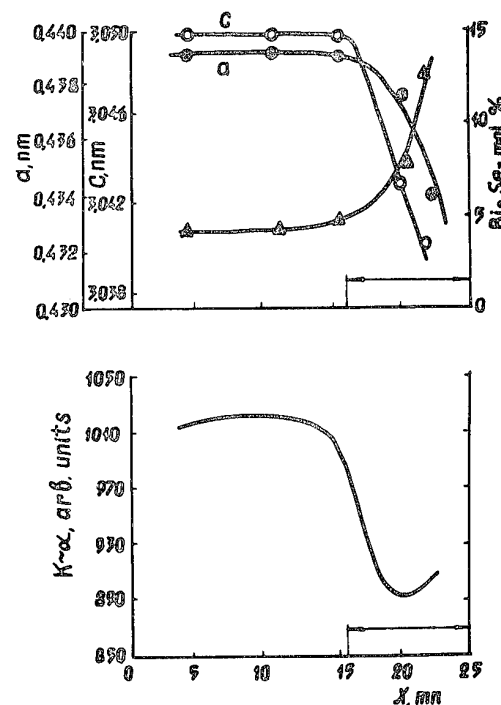


Fig. 6. Change in (a) lattice parameter and (b) thermo-emf along the diameter of an *n*-type ingot grown in mode 3. The arrow marks a distortion of the crystallization front.

(2) The crystallographic anisotropy of the test rhombohedral crystals with clearly pronounced textures determines the electrophysical and thermoelectric properties of the crystals. To obtain the best thermoelectric properties, one should provide for the growth of such a texture for which the (00.1) basis planes are parallel to the growth axis and the (11.0) and (10.0) planes of the (00.1)-zone are perpendicular to this axis.

The present results were used to develop the growth technique of *n*- and *p*-type TEM crystals up to 25 mm in diameter with good thermoelectric properties ( $Z = 3 \cdot 10^{-3} \text{ K}^{-1}$ ).

#### References

- [1]. B.M. Holtzman et al., Semiconductor Thermoelectric Materials Based on  $\text{Bi}_2\text{Te}_3$ , Moscow, Nauka, 1972.
- [2]. M.H. Francombe, *Brit. J. Appl. Phys.*, 1958, v. 9, No. 10, p. 415.

# MECHANICAL PROPERTIES OF Bi-Sb SINGLE CRYSTAL SOLID SOLUTIONS GROWN BY CZOCHRALSKI METHOD

A.D.Belava, S.A.Zavakin, V.S.Zemskov

Baikov Institute of Metallurgy, Moscow, 117911, Russia

Influence of size and surface quality of specimens on a results of mechanical tests of Bi-Sb single crystals was investigated. Strength properties of these materials were investigated at test temperatures 293K and 77K with the use of bending test method. Growth conditions of high strength Bi-Sb single crystals for highly efficient thermoelectric and thermomagnetic alloy compositions were obtained.

## INTRODUCTION

Single crystals of n-type Bi-Sb solid solutions containing 0-15 at.% Sb are unique in having the highest thermoelectric (TE), magneto-thermoelectric (MTE) and thermomagnetic (TM) figures of merit at temperatures lower than 200K [1]. In spite of this, the use of these materials in low temperature stages of solid state coolers is restrained because it is wide-spread opinion about low mechanical properties of these materials. At the same time there has been no detailed work done to determine strength properties of Bi-Sb single crystals and strength properties of wares manufactured from these materials (branches of thermocouples, for example).

In this connection we were engaged in research on mechanical properties of Bi-Sb single crystals with the main purpose to obtain data allowing to estimate a behavior of these materials in TE, MTE and TM coolers.

## EXPERIMENTAL METHODS

Investigation was carried out on Bi-Sb single crystals grown by Czochralski method. At present this method is best suited to growth of Bi-Sb single crystals for scientific and practical applications because makes it possible to produce homogeneous, highly perfect Bi-Sb single crystals with any crystallographic orientation at growth rate of no less than 0.05 mm/min. It is more than an order of magnitude higher than their growth rate by other known methods [2].

Content of Sb in crystals was inspected by the x-ray fluorescence method with an accuracy of 0.1%.

Specimens were cut from crystals by the electrospark method in the form

of rectangular plates with cross sections 3.10 and 20 square mm and the relation of width to thickness 2.5:1. Edges of plates were parallel to the bisectrix (C1), binary (C2) and trigonal (C3) axes of the crystal. Designated as No 1 and No2 orientations of specimens (Fig.1) are most interesting from the viewpoint of practical use of Bi-Sb single crystals as thermocouple branches. After cutting specimens were etched in nitric acid and polished. Using polishing method excluded of any mechanical actions on specimens during the process.

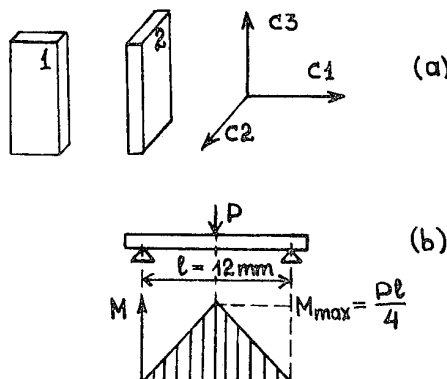


Fig.1  
Orientations of specimens (a) and scheme of the bending test method (b)

Mechanical properties of specimens were investigated on a "INSTRON" machine at the test temperatures 77K and 293K with the use of bending test method represented schematically in Fig. 1. The basis for choice of this method is that the material of a thermoelement is subjected when operating to action by bending thermal pressure. The velocity of loading accounted for 0.5 mm/min.

## RESULTS AND DISCUSSION

### Influence of cross section and surface quality of specimens on their mechanical properties

It is well known, that a results of investigation of mechanical properties of semiconductors depends upon quality of the surface of specimens: existence on a surface of the disrupted in cutting layer, scratches or cracks reduced their strength. In such cases the results of mechanical tests do not characterise the properties of material. Therefore the influence of surface quality is necessary to take into account and whenever possible to reduce to a minimum both at preparation and execution of mechanical tests and at manufacturing of wares [3]. Furthermore, for practical use of a results of investigation of mechanical properties the size of specimens and wares must be close or the influence of size of specimens on results of mechanical tests must be known.

In this connection first of all we investigated influence of surface quality of specimens on results of mechanical tests of Bi-Sb single crystals. This investigation was conducted for specimens containing 2 at.% Sb at the test temperature 293K. These results are shown in Fig.2a for specimens possessing orientation No1.

As illustrated in Fig.2a the mean value of bending strength of polished specimens is more than in two times higher than that for etched specimens, which possess relief surface. The area of cross section of etched specimens was  $(5.0 \times 2.5) = 10$  square mm. A polished specimens were prepared from etched specimens possessing such initial cross section. After polishing the sizes of specimens were  $(4.0-4.6)$  mm on width and  $(1.2-1.6)$  mm on thickness, that is essentially lower than initial sizes. In this connection it was necessary to evaluate following: is this increasing of strength a consequence of improvement of surface quality of specimens or is it stipulated by influence of size factor?

Influence of the size factor was investigated on three groups of etched specimens distinguished by area of cross sections. As shown in Fig.2b, at reduction of cross sections of specimens the tendency to increase of me-

an value of their bending strength is observed.

At the same time comparison of the data presented in Fig.2 permits to conclude that increase of strength of specimens during of polish is stipulated, basically, by improvement of quality of their surface whereas the influence of the size factor is essentially lower.

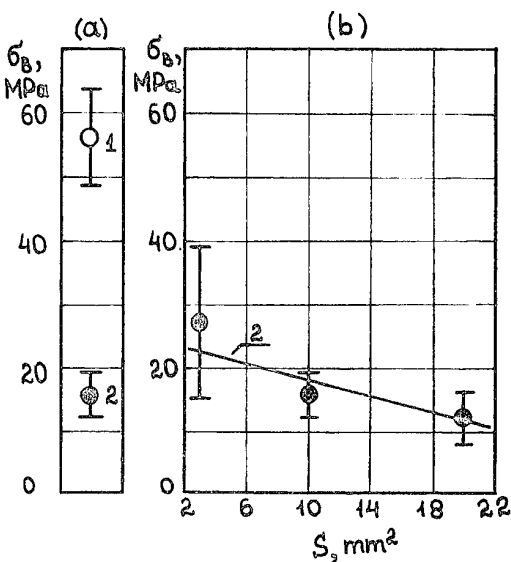


Fig.2  
Influence of surface quality (a) and cross section (b) of specimens possessing orientation No1 on their bending strength: 1. Polished specimens; 2. Etched specimens.

Influence of indicated factors on properties of specimens of orientation No2 has similar character. Subsequent submitted data were received on specimens with width of cross section  $(4.0-4.6)$  mm and thickness  $-(1.2-1.6)$  mm. The use of the data for estimation of strength properties of TE branches and other wares manufactured from Bi-Sb single crystals is apparently justified if the sizes of cross sections of wares do not exceed the appropriate sizes of cross sections of tested specimens. For wares, possessing square cross section, the party of a square should not exceed thickness of specimens.

Mechanical properties of Bi-Sb single crystals as function of alloy composition at 77K and 293K

The results of investigation of mechanical properties of Bi-Sb single crystals are submitted in Fig.3 and in the Table.

If to take into account dispersion of the results of tests, bending strength of these materials does not depend upon alloy composition at the test temperature 77K and makes 10-17 MPa. Mean value of the limiting relative strain (limiting strain) at this temperature decrease with increase of the content of Sb: that is possible to see in the Table for specimens, possessing orientation No2.

Increase of bending strength of specimens at 293K in comparison with that at 77K (Fig.3) is connected with the increase of their propensity to plastic deformation (the Table).

At room temperature mean values of bending strength and limiting strain depends upon alloy composition. Maximum of bending strength is reached for specimens containing 1.5 - 4 at.% Sb and makes approximately (50-55) MPa for specimens of orientation No1 and (40-45) MPa for specimens of orientation No2. Such increase of bending strength in comparison with that for Bi is connected with action of solid solution strengthening [4]. With a further increase of Sb content the tendency to reduction of bending strength of specimens connected with reduction of their propensity to be plastically deformed (the Table) is observed. This variation of these properties with Sb content increasing is conditioned by action of solid solution strengthening coincidentally with distortion of crystal lattice of these materials [5].

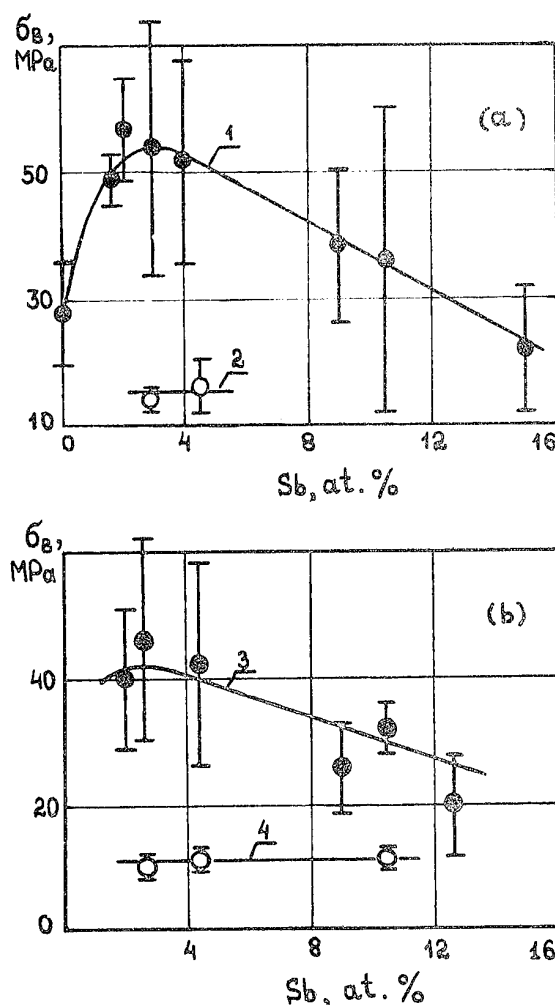


Fig.3  
Bending strength of Bi-Sb single crystals at the test temperatures 293K (1,3) and 77K (2,4): specimens possessing orientation No1 - (a) and No2 - (b).

Table

Mean values of the limiting strain (%) of Bi-Sb single crystals

T, K	Specimen orientation (Fig.1a)	Sb, at. %						
		0	2-3	4-4.6	9	10.5	12.5	14.5-15
293	1	5.7	6.2	4.3	1.6	0.3		0.1
	2		5.4	2.9	0.6	0.32	0.22	
77	1		0.07					
	2		0.062			0.046		

For practical use of above submitted data it should be taken into account that bending strength and limiting strain of specimens increase obviously with temperature increasing from 77K up to 293K. Therefore it is possible to think that the data obtained at 77K characterize approximately a bottom border of mechanical properties of Bi-Sb single crystals in their working range of temperatures.

It is necessary to take into account, that dependence of bending strength and limiting strain of these materials upon alloy composition established at 293K should be executed in some temperature range below this temperature. It permits to conclude that from the viewpoint of improvement of mechanical characteristics of TE, MTE and TM coolers it is best to apply for their manufacturing Bi-Sb alloys with the smaller contents of Sb.

The best mechanical properties are had by Bi-Sb alloys containing (2-4) at.% Sb being the most effective for TM cooling [1].

A comparison of the data for most effective TE and MTE alloy compositions, which in accordance with 1,6 are Bi-Sb alloys containing 8-9 and 15 at.% Sb, permit to conclude that the first alloy composition should be more reliable in service than the last.

#### Influence of growth conditions on mechanical properties of Bi-Sb single crystals

Mechanical properties of single crystals depend of these structure perfection, which, in turn, determined by choice of a method and conditions of crystal growth. Therefore alongside with reception the data about mechanical properties of Bi-Sb single crystals it is important to know dependence of these properties upon crystal growth conditions.

In this connection we investigated influence of growth conditions on mechanical properties of Bi-Sb single crystals containing 2 at.% Sb (effective TM alloy composition 1) and 9 at.% Sb (effective TE and MTE alloy composition [6]). Rate of pulling and angle of crystal growth were chosen as varied process parameters. Last parameter defines orientation of cleavage plane of crystal-(111)-relative growth direction.

Results of these researches received at 293K are shown in Fig.4.

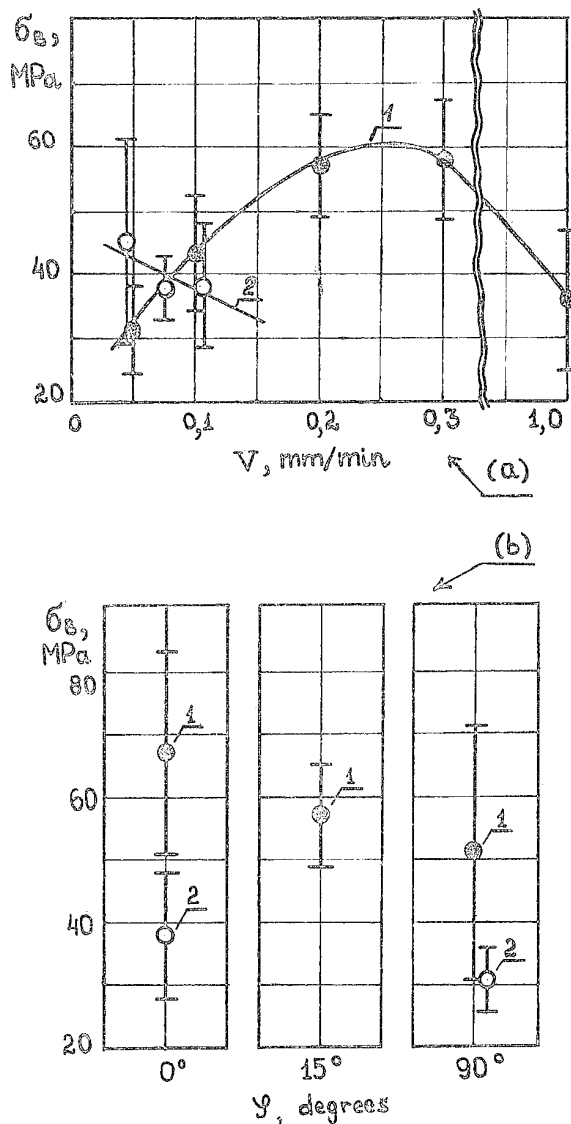


Fig.4  
Influence of the rate (a) and angle (b) of crystal growth on bending strength of Bi-Sb single crystals containing 2 at.% Sb (1) and 9 at.% Sb (2)

Maximum of mean value of strength of crystals, containing 2 at.% Sb, was reached at the range of rates 0.2 - 0.3 mm/min. Reduction of the pulling rate of crystals, containing 9 at.% Sb, to 0.05 mm/min was accompanied by increase of mean value of their strength (Fig.4a).

Change of an angle of growth of crystals, containing 2 at.% Sb and 9 at.% Sb, from 90 degrees (growth in direction perpendicular to the cleavage plane) up to 0 degrees (growth in direction along to the cleavage plane) is accompanied by increase of mean value of their strength (Fig. 4b). Established dependences have allowed to develop growth conditions of Bi-Sb single crystals having increased mechanical strength. These dependences are explained by change of structure perfection of Bi-Sb single crystals at changing of growth conditions. Appropriate structure researches were conducted in Ref. [7].

#### REFERENCES

- [1].W.M.Yim,A.Amith, Bi-Sb alloys for magneto-thermoelectric and thermomagnetic cooling, Solid State Electronics, 1972, v.15, pp.1141-1165.
- [2].V.S.Zemskov,A.D.Belaya,G.N.Kozhemyakin,et al, Growth of single crystals of bismuth-antimony alloys by Czochralski method,Journal of Crystal Growth,1985,v.71,pp.243-245.
- [3].Yu.A. Konzevoi, et al, Plasticity and strength of semiconducting materials and structures,Moscow,1983,239p.
- [4].R.W.K.Honeycombe,The plastic deformation of metals,Edward Arnold (Publishers) Ltd,1968.
- [5].V.Meisalo, Lattice parameters of Bi-Sb alloys at 4.2K, Journal Appl. Cryst.,1970,v.3,pp.224-226.
- [6].V.S.Zemskov,A.D.Belaya,P.G.Borodin,Thermoelectric and magnetothermoelectric figure of merit of bismuth and system of bismuth-antimony solid solutions,Izv.Akad.Nauk SSSR,Neorgan. Mater.,1982,v.18,No.7,pp.1154-1157.
- [7].V.S.Zemskov,A.D.Belaya,S.A.Zayakin,et al,Influence of growth conditions on structure perfection, strength and figure of merit of single crystals of Bi + 2 at.% Sb alloy, Metalli, 1994, No.1,pp.139-142.

ON THE DURABILITY OF DOPED  $\text{Bi}_2\text{Te}_3$  SINGLE CRYSTALS

M.A.Korzhuev, S.N.Chizhevskaya, T.E.Svechnikova,

N.M.Maksimova, and E.A.Kulakova

A.A.Baikov Institute of Metallurgy of Russian

Academy of Sciences, Moscow, 117911, Russia

Under the three point mechanical bend tests of doped, undoped and armed  $\text{Bi}_2\text{Te}_3$  single crystals and some  $\text{Bi}_2\text{Te}_3$  solid solutions the peculiar plastic deformation of samples of  $\Omega$  - type was studied.

## Introduction

Bismuth telluride  $\text{Bi}_2\text{Te}_3$  is known to be an effective material for thermoelectric energy converters [1]. The  $\text{Bi}_2\text{Te}_3$  crystals have a rhombohedral unit cell consisting of five atoms per cell ( two bismuth and three chalcogen ) and have the space symmetry group  $\bar{R}3m$ . The crystals are layered, the sequence of layers can be represented by -  $\text{Te}^1$  -  $\text{Bi}$  -  $\text{Te}^2$  -  $\text{Bi}$  -  $\text{Te}^1$  -. The superscripts ( 1, 2 ) refer to the two types of bonding, the  $\text{Te}^1$  atoms are bound by weak van der Waals forces to the  $\text{Te}^2$  atoms of the adjacent tellurium layer and by mixed covalent- ionic bonds to the  $\text{Bi}$  atoms, whereas the  $\text{Bi}$  -  $\text{Te}^2$  bond is less ionic. Because the bonding between tellurium atoms in different layers is much less than the bonding within the layers ( the spacing between the tellurium atoms is abnormally large ), one can easily cleave the crystals along the ( 0001 ) planes ( in the hexagonal set of axis ). Therefore the  $\text{Bi}_2\text{Te}_3$  structure may be treated as a "puff-pastry" [1].

Standard three point mechanical bend test of free samples usually results in plastic deformation of V - type due to bending the sample in the middle and corresponding elevation of its free ends ( see Fig.1, b ). To fix the ends of a sample on the top during tests one can get the peculiar plastic deformation of  $\Omega$  - type ( see Fig.1, a ) ( here V - or  $\Omega$  - are the symbols designated the sample's shape after plastic deformation ) [2-4].

Recently under the three point mechanical bend tests along trigonal axis the peculiar plastic

deformation of samples of  $\Omega$  - type was observed in free  $\text{Bi}_2\text{Te}_3$  single crystals for the first time [5]. It was surprising for solids because the ends of samples were not fixed on the top during tests. Nevertheless, the ends of the samples after tests remain horizontal with the accuracy of up from 1 to 5 corner degree. The phenomenon observed was presumably explained in [6] by easy bending of the layers and its easy sliding along the planes ( 0001 ) in crystals in question, but mechanism of the effect was not yet clear up in detail. The present paper aims at following investigating the nature of  $\Omega$  - type deformation observed in  $\text{Bi}_2\text{Te}_3$  single crystals. The more wide ranges of deformation rate  $v$  ( from 0.05 to 0.5 cm/min ) and bend hardnesses  $P$  of samples ( from 8 to 49 MPa ) were used in present paper, the last being obtained by  $\text{Bi}_2\text{Te}_3$  single crystals doping or armimg. The physical model was developed to clear up the nature of the effects observed.

## Experimental

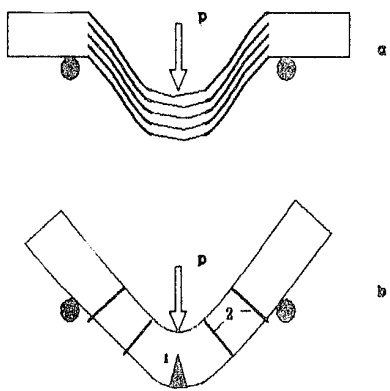
The  $\text{Bi}_2\text{Te}_3$  single crystals and some solid solutions  $\text{Bi}_{2,85}\text{Se}_{0,15}$ ,  $\text{Bi}_{1,98}\text{Sb}_{0,02}\text{Te}_{2,82}\text{Se}_{0,18}$ , and  $\text{Bi}_{1,96}\text{Sb}_{0,04}\text{Te}_{2,79}\text{Se}_{0,21}$  were prepared for investigations using high purity components ( Bi - Bi - 0000; Se, Te, Sb, Cu - OSCH ) by the Czochralsky technique [7]. Electrochemical technique [8] was applied to dope the samples with copper (  $\text{Cu}$  ) dopant concentration  $N_{\text{Cu}} = 1.10^{21} \text{ cm}^{-3}$  ). The samples were cut from the ingots by

Fig.1. The three point bend tests scheme.

a - unusual  $\Omega$ - type bend in  $\text{Bi}_2\text{Te}_3$ ;

b - usual V-type bend in solids.

1 - a crack; 2 - steel wires in armed  $\text{Bi}_2\text{Te}_3$  crystals.



the electro erosion technique. Dislocation densities observed on the cleavage planes of the samples varied from  $10^3$  to  $10^4 \text{ cm}^{-2}$ . The size of samples used was of  $3 \times 6 \times 25 \text{ mm}$ , the  $6 \times 25$  sides being parallel or perpendicular to  $(0001)$  planes ( $\sigma \perp \bar{3}$  and  $\sigma \parallel \bar{3}$  sets respectively, here  $\sigma$  is the mechanical strain, and  $\bar{3}$  is the trigonal axis). The samples were armed by the steel wires of  $0.3 \text{ mm}$  diameter (see Fig.1, b). Mechanical bend tests were carried out with an "Instron" tools using standard three point scheme (Fig.1), the rate of deformation was of  $v = 0.05$  to  $0.5 \text{ cm/min}$ , the diameter of support cylinders - of  $d=3 \text{ mm}$ , the distance between supports - of  $l=12 \text{ mm}$ .

#### Results and Discussion

The bend hardnesses  $P$  of some samples under tests corresponding to deformation rate of  $0.05 \text{ cm/min}$  are presented in Table 1. From Table 1 one can see, that doping of  $\text{Bi}_2\text{Te}_3$  single crystals with impurities used results into 5-6 time increase of bend hardnesses  $P$  of the material. The observed hardening the crystals when doping was due to strengthening of weak forces acting between the adjacent layers in  $\text{Bi}_2\text{Te}_3$  [6]. In addition, bend hardnesses  $P$  of samples was shown to be anisotropic, the

Fig.2. Physical model used for  $\text{Bi}_2\text{Te}_3$  peculiar plastic deformation of  $\Omega$ -type to explain.

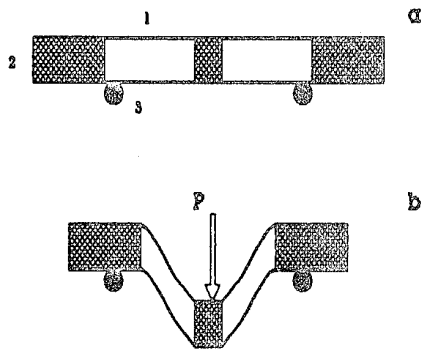
a - before the loading;

b - after the loading;

1 - plate springs;

2 - solid bodies;

3 - supports.



values measured in  $\sigma \perp \bar{3}$  set were from 10 to 20 per cent more than that for  $\sigma \parallel \bar{3}$  set (Table 1). The increased hardness of  $\text{Bi}_2\text{Te}_3$  single crystals in  $\sigma \perp \bar{3}$  set resulted from layered structure of samples was previously observed in micro hardness tests [6].

Anisotropy of crystal structure was shown to affect the deformation picture type too. For  $\sigma \perp \bar{3}$  set we obtained the usual V - type deformation picture for all the crystals and deformation rates used (see Fig.1). From the other hand, it was discovered that for  $\sigma \parallel \bar{3}$  set the peculiar  $\Omega$  - type deformation picture ( see Fig.1 ) may be observed only for low deformation rate  $v$ . It was shown for the first time, that even for  $\sigma \parallel \bar{3}$  set when the deformation rate being increased the  $\Omega$  - type deformation picture transformed to V - type one in a continuous manner. Such transformation depends significantly on the bend hardnesses  $P$  of samples. For the most hard doped samples ( Table.1 ) the from  $\Omega$ - to V- deformation type transformation may be observed for  $v > 0.2 \text{ cm/min}$ , but only for  $v > 1-3 \text{ cm/min}$  as deal with the soft undoped  $\text{Bi}_2\text{Te}_3$  single crystals.

To explain the peculiar V - type plastic deformation, observed in

Table 1  
Bend Hardness of samples tested under deformation rate of 0.05 cm/min

Samples	Bend Hardness P, MPa	Set
$\text{Bi}_2\text{Te}_3$	8	//
$\text{Bi}_2\text{Te}_3 < \text{Cu} >$	20	//
$\text{Bi}_2\text{Te}_{2,85}\text{Se}_{0,15}$	31	//
$\text{Bi}_2\text{Te}_{2,85}\text{Se}_{0,15} < \text{Cu} >$	36	//
$\text{Bi}_{1,98}\text{Sb}_{0,02}\text{Te}_{2,82}\text{Se}_{0,18}$	32	//
	41	±
$\text{Bi}_{1,96}\text{Sb}_{0,04}\text{Te}_{2,79}\text{Se}_{0,21}$	44	//
	49	±

\*) External strains  $\sigma$  were parallel (//) or perpendicular (±) to trigonal axes (3) of crystals.

$\text{Bi}_2\text{Te}_3$  single crystals in  $\sigma // \bar{3}$  set, the physical model (Fig.2) was used. The last consists of plate springs (1), solid bodies (2), and supports (3). It should be pointed out that the symmetry of proposed model was the same as the  $\text{Bi}_2\text{Te}_3$  single crystals one. The  $\text{Bi}_2\text{Te}_3$  samples used for tests contain up to  $3 \cdot 10^6$  -  $\text{Te}^1 - \text{Bi} - \text{Te}^2 - \text{Bi} - \text{Te}^1 -$  layers, bent hardness of a layer may be evaluated as no more than 10 Pa. Because the bonding between the layers in  $\text{Bi}_2\text{Te}_3$  is weak, any layer are able to slide relatively another along the planes (0001) under bend tests. To arm the crystals by steel wires (Fig.1, b), that prevent the planes from sliding, we have succeeded in 2 fold raise of crystal durability.

#### Conclusion

As a conclusion we should state the following. The peculiar V-type plastic deformation, observed in  $\text{Bi}_2\text{Te}_3$  single crystals in  $\sigma // \bar{3}$  set under three point bend tests can be attributed to layered structure of crystals and weak bonding between the layers. The hardening of bonding between the layers when doping as

well as arming or the deformation rate increase make sliding difficult and give rise the transition from Ω-type to V-type deformation.

#### References

- [1] D.R.Lovett, Semimetals & narrow-bandgap semiconductors, London, 1977, 276 p..
- [2] J.-P. Poirier, Plasticite a haute temperature des solides crystallins, Paris 1976, 382 p.
- [3] Design of tools for deformation processes. Ed. by T.Z.Blozinski, L.- N.Y. 1986, 565 p..
- [4] A.S. Ovchinskiy, Processes of destruction of composites, Moscow, 1988, 287 p.
- [5] V.N.Geminov, I.M.Kopiev, T.E.Svechnikova, N.K.Stark, S.N.Chizhevskaya, Fiz.. i Khim. obrabotki Mater., 1985, No.3, pp.132-138.
- [6] M.A.Korzhuev, S.N.Chizhevskaya, T.E.Svechnikova, O.G.Karpinskiy, A.V.Arakcheeva, G.U.Lubman, A.N.Milyich, Neorgan. Mater., 1992, v.28, 1383, No.7, pp.1383-1388.
- [7] N.Ch.Abrikosov, L.D.Ivanova, O.G.Karpinskiy, T.E.Svechnikova, Izv. AN SSSR. ser. Neorgan. Mater., 1977, v.13, No.3, pp.641-647.
- [8] M.A.Korzhuev, T.E.Svechnikova, S.N.Chizhevskaya, Fiz.. i Khim. obrabotki Mater., 1992, No.1, pp.132-138.

## INVERSION OF THE HALL COEFFICIENT IN $\text{Bi}_2\text{Te}_{3-x}\text{S}_x$ CRYSTALS

V.A.Kulbachinskii<sup>1</sup>, J.Horak<sup>2</sup>, P.Lostak<sup>2</sup>

<sup>1</sup> Low Temperature Physics Department, Moscow State University, 119899, Moscow,  
Russia

<sup>2</sup> University of Pardubice, Pardubice, Czech Republic

Galvanomagnetic effects and Shubnikov-de Haas effect have been investigated in  $\text{Bi}_2\text{Te}_{3-x}\text{S}_x$  single crystals with  $0 < x < 0.15$  in magnetic fields up to 7 T in the temperature range  $4.2 < T < 300$  K. We observed the inversion of conductivity type in p- $\text{Bi}_2\text{Te}_{3-x}\text{S}_x$  crystals when concentration x of S was more than 0.11.

### Introduction

Bismuth telluride belongs to the layer semiconductors with the  $D_{3d}^5$  symmetry group. Each layer of  $\text{Bi}_2\text{Te}_3$  consists of five atomic planes in sequence  $\text{Te}^{(1)}\text{-Bi-Te}^{(2)}\text{-Bi-Te}^{(1)}$ , where  $\text{Te}^{(1)}$  and Bi occupy the octahedral sites. Inside the layers there is a strong covalent binding, whereas the layers are held mainly by the van der Waals interaction.

The presence of antisite defects in  $\text{A}_2\text{VB}_3^{\text{VI}}$  narrow gap semiconductors was described in several papers [1,2]. In  $\text{Bi}_2\text{Te}_3$  crystals their existence was confirmed by a direct methods [1,2]. In spite of the intensive investigation of  $\text{A}_2\text{VB}_3^{\text{VI}}$  compounds in recent years, only a few papers were devoted to the  $\text{Bi}_2\text{Te}_{3-x}\text{S}_x$  compound. The effect of the polarisation of bonds in  $\text{Bi}_2\text{Te}_3$  crystals caused by the incorporation of isovalent S atoms into Te-sublattice was studied in [3]. The optical gap of  $\text{Bi}_2\text{Te}_{3-x}\text{S}_x$  crystals increases with increasing of S content [3,4]. With decreasing of the electronegativity difference between the atoms combined in a binary semiconductor, the bond polarity and ionicity decrease, but the probability of the formation of antisite defects increases.  $\text{Bi}_2\text{Te}_3$  stoichiometric crystals posses always p-type conductivity due to formation of antisite defects. The formation of antisite defects  $\text{Bi}'\text{Te}$  is accompanied by the creation of free holes and leads to the p-type conductivity.

We have prepared  $\text{Bi}_2\text{Te}_{3-x}\text{S}_x$  crystals with  $0 < x < 0.16$  and have measured temperature dependence of conductivity, Hall effect and Shubnikov de Haas effect at low temperatures

and dependence of the Hall coefficient on magnetic field and temperature to get information about changing of the energy spectrum of  $\text{Bi}_2\text{Te}_{3-x}\text{S}_x$ .

### Experimental

$\text{Bi}_2\text{Te}_{3-x}\text{S}_x$  single crystals were grown by a modified Bridgman method. Starting elements Bi, Te 5N purity, and 4.5N purity sulphur in the ratio corresponding to the given compositions were synthesised in evacuated conical-shaped silica ampoules at  $730^{\circ}\text{C}$  for 48 h. Then the ampoule with the melt was lowered at a rate of 1.2 mm/h through a sharp temperature gradient of  $80\text{K/cm}$ . After the growth, the single crystals were heat-treated at  $550^{\circ}\text{C}$  for 48 h. Samples for the transport measurements were cut by a spark erosion machine into a parallelepiped shape with typical dimensions  $1 \times 1 \times 6\text{mm}^3$ .

The conductivity was measured in the  $C_2$  direction, and the Hall coefficient  $R_H$  with the magnetic field  $\mathbf{B}$  parallel to the  $C$ -axis. Magnetic field up to 7 T was produced by a superconducting solenoid.

### Results

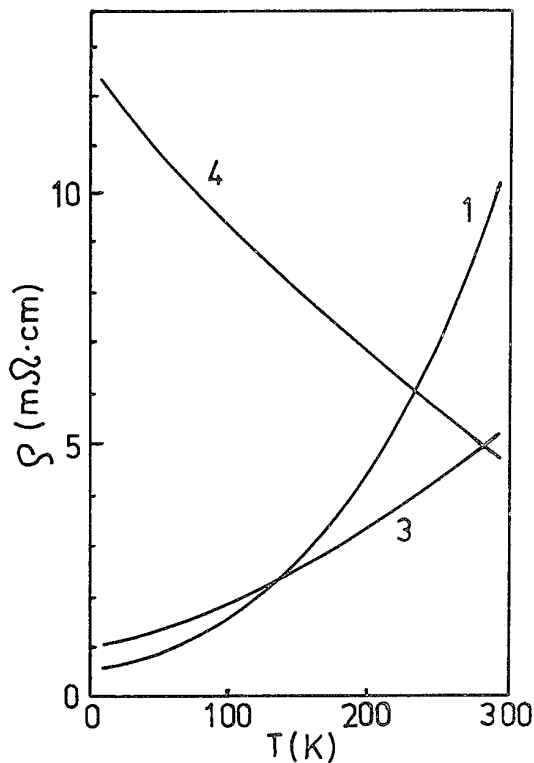
The results of the galvanomagnetic measurements show that with increasing of sulphur content in  $\text{Bi}_2\text{Te}_{3-x}\text{S}_x$  crystals up to  $x=0.10$  the electrical conductivity  $\sigma$  as well as the concentration of the free carriers decrease.

The temperature dependence of resistivity with decrease of hole concentration in samples changes from metallic behaviour to semiconductor one. The n-type of conductivity in  $\text{Bi}_2\text{Te}_{3-x}\text{S}_x$  crystals observed at high sulphur

Table 1 Parameters of samples at T=4.2K

N	composition x	$R_H$ , $\text{cm}^3/\text{C}$	$\mu$ , $\text{cm}^2/\text{Vs}$
1	0.075	2.7	4800
2	0.10	9.6	1600
3	0.12	-0.31	2700
4	0.15	-0.22	220
5	0.16	-0.21	2500

Fig.1 Temperature dependencies of resistivity for  $\text{Bi}_2\text{Te}_{3-x}\text{S}_x$  crystals. Numbers correspond to sample numbers in table 1.



concentrations. Some parameters of the samples are listed in the Table 1. The temperature dependencies of resistivity for some samples are shown in fig.1.

In p-type  $\text{Bi}_2\text{Te}_{3-x}\text{S}_x$  crystals the Hall coefficient depends on magnetic field at T=4.2K while in n-type samples the Hall coefficient is almost magnetic field independent. In fig.2 the magnetic field dependence of the Hall coefficient for two samples are shown.

The temperature dependence of the Hall coefficient is also different in p- and n-types  $\text{Bi}_2\text{Te}_{3-x}\text{S}_x$  crystals. In p-type samples the value of  $R_H$  decreases with temperature while in n-type sample the Hall coefficient is almost temperature independent. In fig. 3 we plotted the temperature dependence of the Hall coefficient  $R_H$  for two p- and n-types samples.

The Shubnikov-de Haas effect at B parallel to  $C_3$  axis was observed only in the sample N1. The concentration of carriers,

Fig.2 Magnetic field dependence of the Hall coefficient  $R_H$  at different temperatures for p-type sample 2  $\text{Bi}_2\text{Te}_{3-x}\text{S}_x$  and n-type sample N5  $\text{Bi}_2\text{Te}_{3-x}\text{S}_x$ .

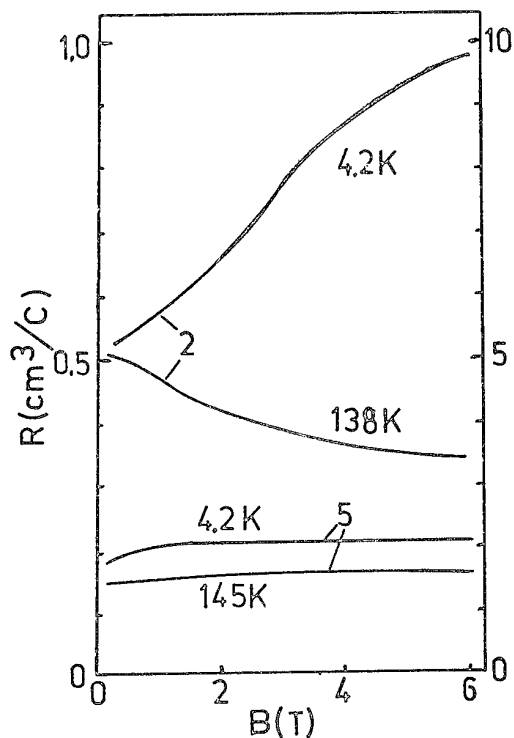
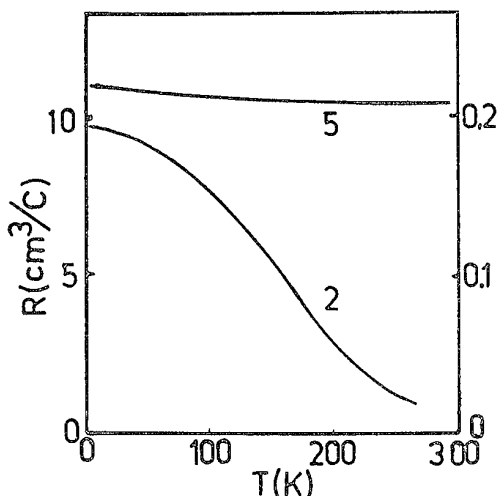


Fig.3 Temperature dependence of the Hall coefficient  $R_H$  for sample 2 p-type and sample 5 n-type  $\text{Bi}_2\text{Te}_{3-x}\text{S}_x$  crystals.



calculated from the Shubnikov de Haas effect coincided with the Hall effect data if we suggested the six-ellipsoidal Fermi surface with the same anisotropy as in  $\text{Bi}_2\text{Te}_3$  [5].

#### Discussion

A decrease in the electrical conductivity and an increase in the Hall coefficient with increasing of the sulphur content in  $\text{Bi}_2\text{Te}_{3-x}\text{S}_x$  crystals gives the evidence for a decrease in the free hole concentration. This conclusion is in agreement with the change of the absorption coefficient with composition of  $\text{Bi}_2\text{Te}_{3-x}\text{S}_x$  crystals [4]. The hole concentration may be decreased due to S doping by suppressing the cause of the formation of antistructural defects (that is Bi atoms in the anion sublattice), which are responsible for the high initial concentration of holes. The existence of p-type  $\text{Bi}_2\text{Te}_3$  is due to the overstoichiometric Bi content in the form of  $\text{BiTe}$  defects. In the undoped p- $\text{Bi}_2\text{Te}_3$  crystals prepared from melt with the stoichiometric composition, there about  $10^{18}\text{cm}^{-3}$  antisites defects  $\text{BiTe}$ . The increase in concentration of S-atoms incorporated in the crystal lattice particularly decrease the hole concentration. Near  $x=0.11$  a transition occurs to n-type

conductivity. These experimental results can be explained in the following way: with increasing content of S, the concentration of the anion vacancies increases. Beside this effect, the change in the antisite defect concentration must be taken into account. An increasing bond polarity in mixed crystals  $\text{Bi}_2\text{Te}_{3-x}\text{S}_x$  with the tetradyomite structure leads to a decrease in the probability of formation of antisite defects. Therefore it is possible to expect decrease in the antisite defect concentration and, hence, hole concentration caused by an increasing content of incorporated S atoms in the crystal lattice of the mixed crystals. Recently [7] it was supposed also that the increase of S concentration in the anion sublattice results in an increase of the probability of formation of positively charged anion vacancies. A faster increase in the anion vacancy concentration than antisite defect concentration with increasing content of S atoms may explain the change in the sign of the Hall coefficient.

In p-type  $\text{Bi}_2\text{Te}_{3-x}\text{S}_x$  crystals the Hall coefficient depends on magnetic field at  $T=4.2\text{K}$ . In a model of two degenerate hole gases the Hall coefficient  $R_H$  should always decrease with increasing magnetic field when the influences of geometrical factor in  $R_H$  for the second type of holes may be neglected. If we take into account the anisotropy factors for both types of hole,  $R_H$  may increase in the magnetic field. Quantitatively the effect of the increase of the Hall coefficient in magnetic field in this case was calculated in p- $\text{In}_x\text{Bi}_{2-x}\text{Te}_3$  [6]. In n- $\text{Bi}_2\text{Te}_{3-x}\text{S}_x$  crystals the Hall coefficient almost does not depend on magnetic field and temperature. The decrease of the Hall coefficient with temperature (fig.3) may be explained by thermoactivation of carriers. The p-type samples more sensitive to the generation of the electrons. When concentration  $x$  of S increases, the temperature dependence of resistivity of  $\text{Bi}_2\text{Te}_{3-x}\text{S}_x$  changes from metallic type to a semiconductor type (fig.2).

#### Conclusion

The incorporation of S atoms in the Te position in  $\text{Bi}_2\text{Te}_{3-x}\text{S}_x$  crystals causes the decrease in the free hole concentration and for  $x>0.11$  type of

conductivity changes to n-type. For small concentration of S atoms the and structure of  $\text{Bi}_2\text{Te}_{3-x}\text{S}_x$  crystals is the same as for the host  $\text{Bi}_2\text{Te}_3$  crystals.

#### References

- [1] G.R.Miller and C.-Y.Li, *J. Phys. Chem. Solids*, 1965, V.26, pp.173-182.  
[2] V.A.Kutasov and I.A.Smirnov, *Phys. Status Solidi*, 1966, V.18, pp.479-483.  
[3] J.Horak, P.Lostak, L.Kudelka and R.Novotny, *Sol. State Commun.*, 1985, V.55, N11, pp.1031-1034.  
[4] P.Lostak, J.Horak, and L.Koudelka, *Phys. Status Solidi (a)*, 1984, V.84, pp.k143-k147.  
[5] H.Koler, *Phys. Status Solidi (b)*, 1976, V.74, pp.591-599.  
[6] N.B.Brandt and V.A. Kulbachinskii, *Semicond. Sci. Technol.*, 1992, V.7, pp.907-911.  
[7] J. Horak, Z. Stary, and J. Votinsky, *Philosophical Magazin*, 1994, V.69, No.1, pp.31-38.

OBTAINING SEMICONDUCTOR SYSTEMS ALLOYS  
AT SUPER-RAPID RATES OF COOLING

V.M.GLAZOV, K.B.POYARKOV

Moscow Institute of Electronic Engineering ( Technical University ), Russia

The object of the present research program was to study the possibility of non-diffusion crystallization of semiconductor binary and pseudo-binary systems alloys. Supercooled alloys were obtained by solidification of a melt. The cooling rates of crystallization was  $10^6$  -  $10^8$  K/s. This paper describes the results of X - ray diffraction analysis.

Solid Bi-Sb, Ge-Si,  $\text{Bi}_2\text{Te}_3$ - $\text{Bi}_2\text{Se}_3$ ,  $\text{Bi}_2\text{Te}_3$ - $\text{Sb}_2\text{Te}_3$  systems solutions are of great interest as materials for thermoelectric energy transformers. The efficiency of thermoelectric devices for different applications is known to depend on the thermoelectric effectiveness of the material which tends to grow with the increase of its chemical homogeneity. Thus an important goal for thermal devices is to obtain chemically homogeneous solid solutions. But the task of obtaining a chemically homogeneous material is frequently complicated by using solid solutions with a strong tendency to liquation of any of the components. Homogeneous alloys are usually obtained by methods of zone recrystallization, powder metallurgy and prolonged annealing. These methods, however, are extremely arduous and they are not sufficient for coping the problem of obtaining a chemically homogeneous material.

Crystallization at cooling rates of  $10^6$  -  $10^8$  K/s is known to prevent segregational diffusion processes effectively, e.g. alloys of predetermined composition without a segregational process can be obtained by a method of non-diffusion crystallization [1].

The object of the present research program was to study the possibility of non-diffusion crystallization of the alloys above. Phase balances in these systems are characterized by diagrams for states with continuous solid and liquid solutions. For the preliminary assessment of the possible

crystallization of the alloy systems using non-diffusion pattern we have calculated the line  $T_0$  - equal values of Gibbs' energy of liquid and solid phases on the basis of the regular solution model. Calculations have shown that  $T_0$  line is located in a two-phase area between

the curves of liquidus and solidus, therefore overcooling of the melt necessary for non-diffusion crystallization is attainable in practice.

For the experimental solution of this problem samples of these systems with composition in the range of 10 to 80 at.% of the second component respectively, with the interval between them being not more than 10 at.%, have been subjected to the method of alloying the components in evacuated quartz ampoules. Alundum crucibles were used when necessary. The initial components were materials of high purity.

The supercooled alloys were obtained by two methods: 1 - clapping of a melt drop between two copper disks moving towards each other; 2 - solidification of a melt drop on the inside surface of a cylindrical crystallizer with two flat copper plates at the speed of 10.000 rpm [2]. The latter was of particular interest in view of its simplicity and possibility of obtaining films with strongly developed surfaces. In addition there was an opportunity to study surface (both contact and free) layers being cooled in different thermal conditions. The melting and crystallization camera was preliminarily evacuated up to 1.5 Pa. Experiments were carried out in the medium of spectrally pure argon at pressure of 0.4 Pa. The alloys were held for about 5 minutes at the temperature being 60 - 100 degrees higher than that of liquidus, then the melt with a mass of 5 - 10 mg was poured out onto the surface of the rotating crystallizer. The supercooled alloys were 5 - 15 mm long, 3 - 6 mm wide and 2 - 30  $\mu\text{m}$  thick film fragments.

Taking into consideration strong correlation of cooling rates with the thickness of the samples, we have determined the cooling rates as the function of time of various thickness melt films. The regimes of cooling were calculated applying the following equation of thermal conductivity

$$\frac{\partial T}{\partial \tau} = \chi^2 \frac{\partial^2 T}{\partial x^2}$$

where  $\chi$  - thermal conductivity coefficient. The boundary conditions selected correspond to the case of an ideal thermal contact

$$T|_{x=1} = 0, \quad \frac{\partial T}{\partial x}|_{x=0} = 0$$

where  $l$  - thickness of the melt film,  $x$  - the cross-section,  $x=0$  on the outer surface of the melt film. The analytical solution of this equation is given in the papers [2,3]. The results of the calculations, e.g. for melt composition 20 at. % Sb are presented in fig. 1a,b where one can see that for bulk layers of the melt there is some period of time beyond which the temperature maintains practically constant. The highest cooling rates are reached by the contact layers reach maximum rates some time later, the values of the cooling rates contact and bulk layers being several orders of value different. The presence of maxima on the dependence curve  $\lg V=f(\tau)$ , (Fig.2b) could be attributed to the gradient of the heat flow between the contact and outer layers of the melt film. Thus, during the process of cooling there appear sharp dramatic gradients of cooling rates significantly affecting the structure of alloys.

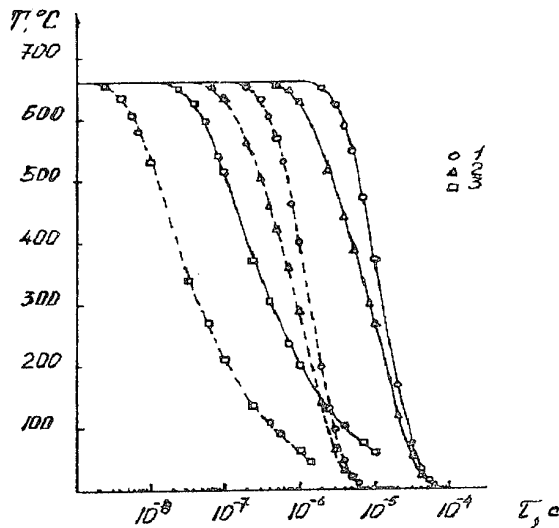


Fig.1a. The change of temperature  $T$  with the time  $\tau$  for melt 20 at.% Sb (continuous line -  $l=30\mu\text{m}$ , broken line -  $l=10\mu\text{m}$ , 1 -  $x=0.11$ , 2 -  $x=0.51$ , 3 -  $x=0.91$ ).

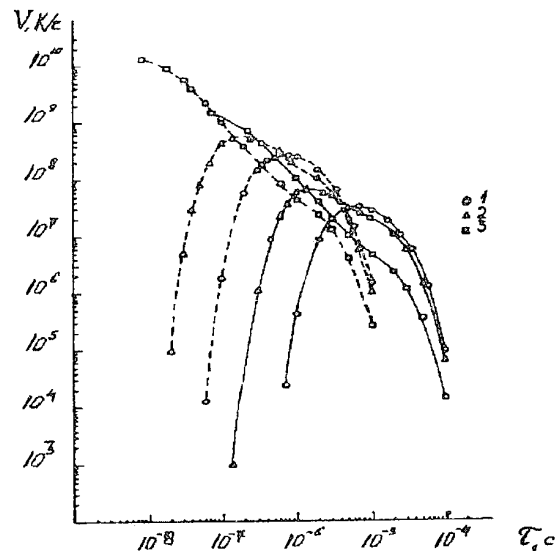


Fig.1b. The change of cooling rate with the time for melt 20 at.%Sb, (Bi-Sb).

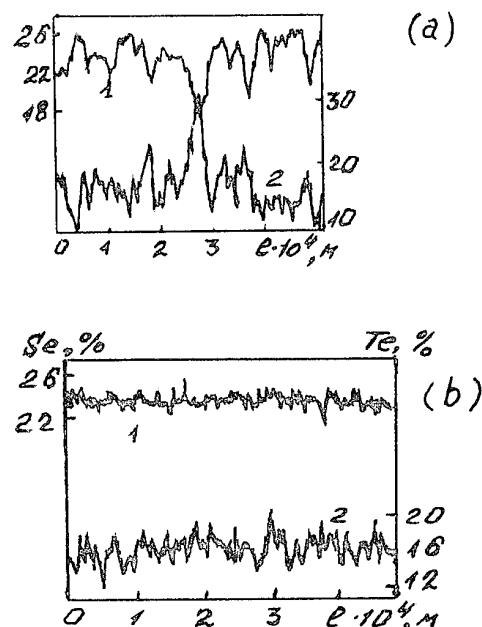


Fig.2a. Distribution curves of 1 - Se, 2 - Te along specimen before (a) and after supercooling (b), ( $\text{Bi}_2\text{Te}_{0.9}\text{Se}_{2.1}$ ).

To carry out the X-ray examination the melt films obtained were divided into two groups according to the calculated regimes of cooling: films 15 - 20  $\mu\text{m}$  thick and films not more than 5  $\mu\text{m}$

thick. This gave reason to believe that the heat exchange conditions of cooling the material were the same. The X-ray diffraction analysis was conducted on the D-501 Siemens diffractometer using Cu K<sub>α</sub> radiation. The preliminary analysis indicated that the initial alloys were not single-phase ones. The composition of supercooled alloys was determined according to the elementary cell parameter changes taking into account the linear character of its change with concentration. Line profiles with relative intensity not less than 10% were analysed. The overall picture for alloy systems Bi - Sb and Ge - Si obtained by the second method is as follows: the diffractograms of films 5 μm thick are characterized by the availability of a distinct symmetrical maxima corresponding to the initial composition of a liquid phase. The diffraction peak shape analysis demonstrates the absence of liquation microinhomogeneity. Thus we can state the formation of alloy structures according to a non-diffusion crystallization pattern at the cooling rate of 10<sup>6</sup>-10<sup>8</sup>K/s. The reproducibility of the experimental data has led to the conclusion that alloys enriched by a fusible component (up to 30 at % of the second component) have a greater tendency to non-diffusion crystallization. For Bi - Sb and Ge - Si films 25 μm thick there are two series of diffraction maxima, this being the evidence of two solid solutions enriched by the first and the second component respectively. Thorough examination of the composition of solid solutions being fixed in thick films enabled us to establish the effect of decomposition of the primarily solidifying solid solution to two constituents - the solid solution enriched by the first component and the solid solution close in its composition to the initial one, enriched by the second component.

To carry out the comparative analysis of the inhomogeneity level of synthesized and supercooled alloy systems Bi<sub>2</sub>Te<sub>3</sub> - Bi<sub>2</sub>Se<sub>3</sub> and Bi<sub>2</sub>Te<sub>3</sub> - Sb<sub>2</sub>Te<sub>3</sub> specimens were prepared in the form of columns made from powder by pressing were examined by means of the local X-ray spectral analysis using microprobe MC - 46 Kameca. The synthesized material was subjected to prolonged annealing (1420 hours). Distribution curves of Se and Te along the specimen cross-section are shown in Fig. 2a,b. The results obtained show that the level of homogeneous distribution of the initial components increases substantially with the solidification of the alloys at superrapid cooling rates. These results of great importance for the technology of manufacturing materials being used in thermoelectric energy transformers.

#### Reference

- [1]. V.M.Glazov, V.N.Vigdorovich, Reports Acad.Sc.,USSR, 1958, v.18, No.5,pp.924-927.
- [2]. V.M.Glazov, K.B.Poyarkov, O.A.Shamrov , Proc.Acad.Sc.,USSR, Inorganic mat, 1990, v.26, No.1, pp.28-33.
- [3]. V.M.Glazov, K.B.Poyarkov, Proc.Acad.Sc.USSR, Inorganic mat, 1991, v.12, pp. 2471-2475.

# Transport phenomena peculiarities caused of intervalley and interband scattering of charge carriers in bismuth type crystals

Grabov V.M.<sup>1</sup>, Bondarenko M.G.<sup>1</sup>, Uryupin O.N.<sup>2</sup>

<sup>1</sup>Herzen Russian State Pedagogical University, St. Petersburg, Russia

<sup>2</sup>A.F.Ioffe Physical-Technical Institute, St. Petersburg, Russia

There are produced systematic investigation of transport phenomena in bismuth, antimony and Bi-Sb alloys single crystals, including doped by donor and acceptor impurities, in wide temperatures interval. There is discovered general law in temperature dependence of specific electrical resistance of these crystals. There are found out peculiarities of specific resistance, Seebeck coefficient, including double change of Seebeck coefficient sign, and other transport phenomena at electontopological transitions in bismuth type semimetals, when at change of doping impurities concentration or temperature the Fermi level passes through energy extremum of energy bands. It is shown, that in bismuth type semimetals, having complex band structure, discovered general law in temperature dependence of specific electrical resistance and peculiarity of transport phenomena at electontopological transitions at  $T > 77$  K there are caused by predominance charge carriers scattering at their transitions between equivalent and non-equivalent extremum of energy bands with participation of phonons.

## Introduction

Temperature dependence of specific resistance of most of metals in wide temperatures range is determined by phonon mechanism and is described by universal Bloch-Grunaisen law [1]. The mobility of charge carriers of typical semiconductors at intravalley scattering by phonons depends on temperature as  $u \sim T^{-3/2}$  [1, 2]. It is might expect, that such temperature dependence of mobility for crystals semimetals will be performed at temperatures  $T/\Theta^* > 1$ , where  $\Theta^*$  - characteristic temperature, determining by dimensions of isoenergetical surface [2]:

$$k_B \cdot \Theta^* = \hbar \cdot k_F \cdot v_s.$$

$v_s$  is a sound velocity. For bismuth  $\Theta^* \approx 10K$ .

However, as it is followed from performed to present time investigations [3, 4, 5, 6, 7, 8, 9, 10, 18, 19] temperature dependence of specific resistance and mobility of charge carriers in bismuth type semimetals don't accommodate to above laws and it is not clears what mechanism determines relaxation processes of charge carriers in semimetals in wide range of temperatures [2].

In present work there are produced experimental investigation and analysis of temperature dependence of transport phenomena in crystals of Bi, Sb and Bi-Sb alloys undoped, Te-doped and Sn-doped at  $T > 77$  K. For completeness data of other authors [5, 6, 7, 8, 9, 10, 11, 18, 19], especially at  $T < 77$  K, are used also.

## Experimental procedures

Single crystals of Bi, Sb and alloys  $Bi_{1-x}Sb_x$  were grown method horizontal zone recrystallization at passage speeds of zone  $v \leq 0.5mm/h$  and temperatures gradient at front crystallization  $G \leq 20/m$ , that sufficient degree their homogeneity ensured [12]. Samples for measurements were cut from average part of crystal ingots by electrospark method. To remove destructed surface layer sample surface was etched. Sample dimensions were  $2.5 * 2.5 * 12mm^3$  with crystallographic axes parallel to ribs of samples and longitudinal axis of sample parallel or perpendicular axis  $C_3$ .

Stationary measurement of transport coefficients: specific resistance, Hall coefficient at weak magnetic field and Seebeck

coefficient had been performed in temperature interval 77-300 K, sometimes - in interval 77-500 K. The relative error does not exceed 5%.

## Results and discussion

Temperature ( $T/\Theta$ ) dependence of reduced specific resistance  $\rho/\rho_\Theta$  and specific resistance  $\rho$  undoped  $Bi, Sb, As$  crystals in wide temperature range there are presented on fig. 1,2. Values of Debye temperature  $\Theta$  for Bi, Sb and As are equal 121 K, 211 K and 281 K [13], respectively. For crystals  $Bi_{1-x}Sb_x$  (fig. 3,4) Debye temperature values there were calculated by linear interpolation method and were accepted independent from doping. Solid line on fig. 2 correspond values  $\rho_{11}$  for bismuth.

As indicated in fig. 1, universal law for temperature dependence specific resistance of bismuth type crystals is performed in wide temperature range. Agreement of reduced resistance data in dependence at reduced temperature  $T/\Theta$  strongly suggest on phonon charge carriers scattering mechanism. However, it have distinctive feature from Bloch-Grunaisen law.

In contrast to the most metals, universal dependence from reduced temperature  $T/\Theta$  is performed not only for  $\rho/\rho_\Theta$ , but also for absolute values of specific resistance Bi, Sb and As in wide temperature range  $T/\Theta > T/\Theta^*$  (fig. 2). Specific resistance of  $Bi_{1-x}Sb_x$  crystals for all (fig.3) including doped crystals (fig. 4) is approached to this law in range of reduced temperatures  $T/\Theta > 1$ . In addition, temperature dependence of bismuth and antimony specific resistance is inconsistent with  $\rho \sim T^5$  [2].

It is should bases believe, that found out law in behavior of specific resistance of Bi-type crystals are caused by complex band structure, at which charge carrier extrema, as conductivity band, and valent band there are located in k-space on distances order dimensions of Brillouin zone and prevalence of charge carriers scattering at their transitions between of band extrema with phonon participation [15].

On prevalence intervalley (recombination) phonon scattering in Bi-crystals at  $T > 15$  K ( $T > \Theta^*$ ) was indicated in electro-acoustic investigations [16].

Substantial role of charge carriers scattering at transitions between non-equivalent extrema with phonon participation

Fig. 1. Electrical resistivity  $\rho/\rho_0$  of Bi, Sb, As as a function of temperature  $T/\Theta$ .

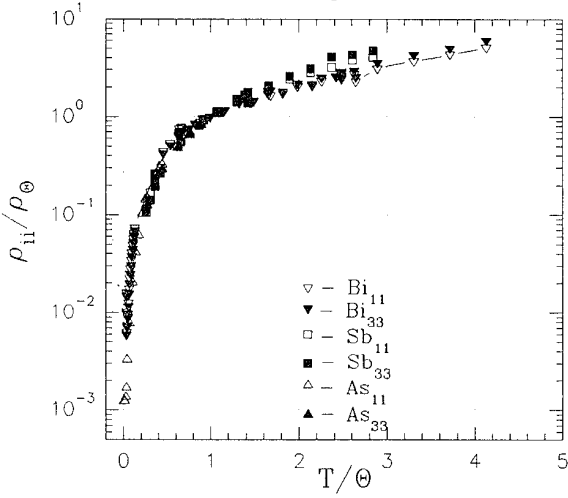


Fig. 2. Electrical resistivity of Bi, Sb, As as a function of temperature  $T/\Theta$ .

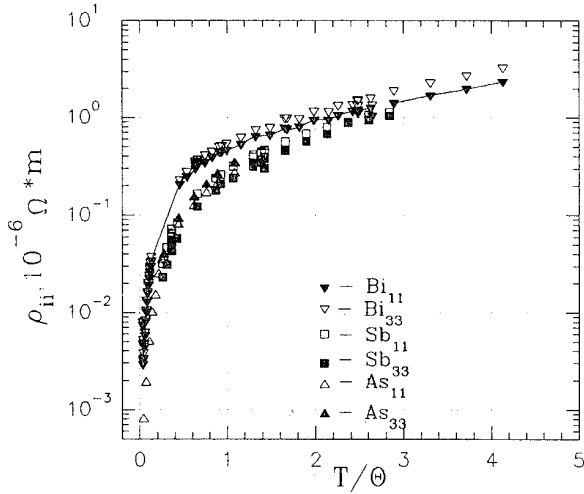
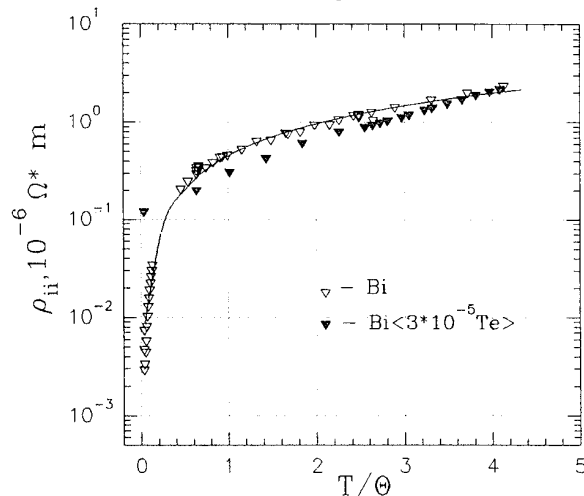


Fig. 3. Electrical resistivity of Bi and Bi<Te> as a function of temperature  $T/\Theta$ .



follow immediately from experimental data according to detection anomalous with double change-over of sign Seebeck coefficient and increase of specific resistance at switching on in transport phenomenon further extremum in temperature range  $T/\Theta \approx 1$  [17], i.e. at electron-topological transitions, that there is displayed especially clearly on dependence of specific resistance and Seebeck coefficient from contents of acceptor tin impurities in Bi-Sb crystals (fig. 5).

In temperature range  $T/\Theta^* > 1$  specific resistance of Bi-type crystals have close quantities at the same values  $T/\Theta$  (fig. 2-3). Thus distinction of charge carrier concentration  $n$  can reach 2-3 order. For  $T/\Theta = 1$  charge carrier concentration of for Bi, Sb, As to take equal to Te-doped up to 0.3 at.% bismuth fo tab.1.

Table 1: The charge carrier concentration

Materials	Concentration	Reference
Bi	$6.6 \cdot 10^{23} m^{-3}$	
Bi < 10⁻³ Te >	$4.8 \cdot 10^{25} m^{-3}$	[3, 4]
Sb	$4.0 \cdot 10^{25} m^{-3}$	
As	$2.0 \cdot 10^{26} m^{-3}$	[11]

So, in temperature range  $T/\Theta > 1$  universal law consists that temperature dependence of specific resistance described by linear law  $\rho \sim T^s$ ,  $s = 1$ , and practically does not depend on charge carriers concentration. Consequently, specific conduction

$$\sigma = e \cdot n \cdot u$$

depends on temperature according to law  $\sigma \sim T^{-1}$  and, if charge carrier concentration  $n \sim T^y$ , their mobility  $u \sim T^z$ ,  $z = -(y + 1)$ , i.e.

$$|\sigma| \sim (n \cdot T)^{-1}$$

It was found experimentally, that in the temperature range 80-300 K  $s=1$ ,  $y=3/2$ ,  $z=-5/2$  in bismuth crystals [3] and  $s=1$ ,  $y=0$ ,  $z=-1$  for Te-doped more 0.05 at.% bismuth crystals [4]. Relation  $z = -(y + 1)$  at various  $y(x)$  is performed well and for  $Bi_{1-x}Sb_x$  crystals [9].

Such dependence occur in condition of intervalley and interband scattering predominance. Possibly, it is caused by increase intervalley and interband phonon phase volume, owing to increase of isoenergetic surface area at increase of charge carriers concentration [15].

At  $T/\Theta < 1$ , universal law for temperature dependence of specific resistance Bi, Sb and As there is performed up to temperatures  $T/\Theta > 0.1$  or  $T/\Theta^* > 1$  (fig. 1-2). Specific resistance doped crystals of Bi-type and crystal alloys deflects from universal law owing to prevalence of scattering on defects of structure, fluctuations of alloy components and impurities, as well as transition some alloys to semiconductor state [14].

At high temperatures  $T/\Theta > 1$  intervalley scattering, as and intravalley, results in linear temperature dependence of resistance, however at low temperatures  $T/\Theta < 1$ , owing to location of valleys on distance of dimensions of Brillouin zone, should be observed exponential drop of resistance at temperature decrease. Some investigators allocated exponential part on temperature dependence of Bi specific resistance [6]. However, it is necessary to take into consideration participation in scattering acoustic phonons with  $\Theta = \Theta_a$  and optic phonons with  $\Theta = \Theta_o$ . For Bi-crystals  $\Theta_a = 43 K$ ,  $\Theta_o = 130 K$  [16], and in wide interval of temperatures  $T > \Theta^*$  specific resistance of Bi-crystals is described by function

Fig.4. Electrical resistivity of  $\text{Bi}_{1-x}\text{Sb}_x$  as a function of temperature  $T/\Theta$

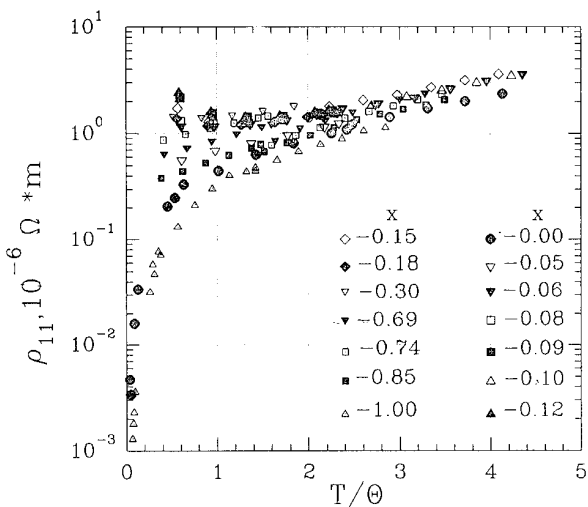
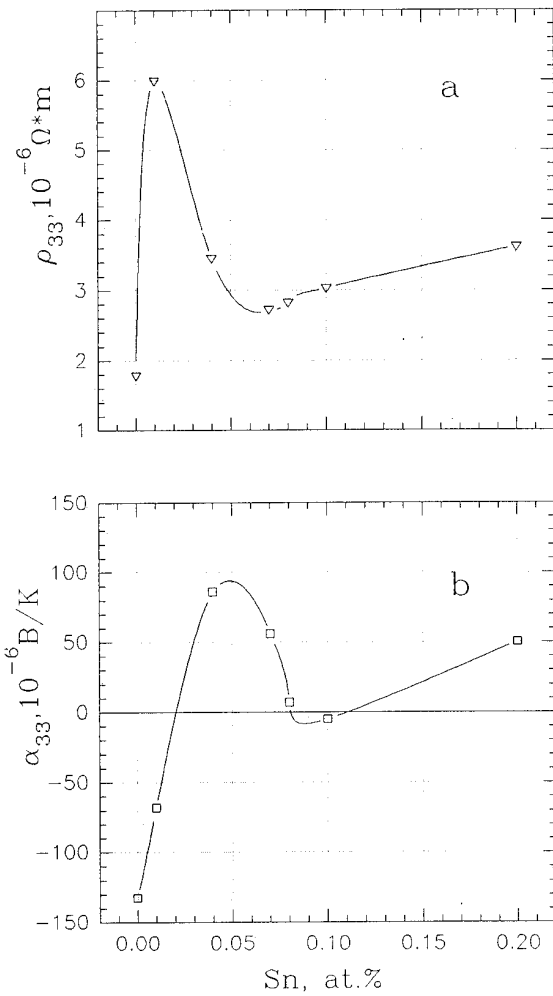


Fig.5. Electrical resistivity  $\rho_{33}$  (a) and Seebeck coefficient  $\alpha_{33}$  (b) as a function of Sn content in  $\text{Bi}_{0.95}\text{Sb}_{0.05}\langle\text{Sn}\rangle$ . T=80 K.



$$r = A \cdot T/\Theta + B \cdot f((T/\Theta) \cdot (\Theta/\Theta_a)) + C \cdot f((T/\Theta)(\Theta/\Theta_o)) \quad (1)$$

$f(x) = (\exp(x) - 1)^{-1}$  - the Boze-Einstein functions for acoustic and optic intervalley (interband) phonons,  $A = 1.7 \cdot 10^{-9} \Omega \cdot m$ ,  $B = 1 \cdot 10^{-7} \Omega \cdot m$ ,  $C = 2.25 \cdot 10^{-8} \Omega \cdot m$ .

The function (1) presented solid lines in fig. 3. The function (1) values is consistent with bismuth specific resistance experimental data at  $T > \Theta^*$  with less than 5% in error. It is good approximation for universal law of temperature dependence of specific resistance of bismuth type crystals in wide interval of temperatures.

It is necessary, however, to note, that in semimetal row Bi, Sb, As increase of charge carriers concentration and increase of Fermi surface closed section dimensions until their merge in arsenic [20] results in distinction reduction of intravalley and intervalley scattering laws, to smoothing of exponent sections in temperature dependence of specific resistance and reduction of its deviation from Bloch-Grunaisen function.

## Conclusions

So, from given experimental data it is necessary, that in wide interval of temperatures  $\Theta^* < T < T_{melt}$  for bismuth, antimony and arsenic,  $\Theta < T < T_{melt}$  for doped bismuth type crystals and  $T \gg \Theta$  for Bi-Sb alloy crystals specific resistance of bismuth type crystals is determined by number phonons and depend only slightly on the concentration of charge carriers. Then mobility is inversely proportional of charge carriers concentration.

Possibly, such dependence is caused by predominance of intervalley and interband charge carriers scattering by phonons and increase of intervalley and interband phonon phase volum, owing to increase of isoenergetic surface area at increase of charge carriers concentration.

In temperature range of prevalence intervalley and interband scattering by phonons additional nonequivalent band extremume in greater degree decrease of charge carriers mobility, than increase of charge carriers concentration. Therefore at electron-topological transitions possibly rise of specific resistance and occurrence of minimum on Seebeck coefficient concentration dependence with double change of Seebeck coefficient sign.

## References

- [1] Frank J. Blatt. Physics of electronic conduction in solids. McGraw-Hill Book Company, 1968.
- [2] Gandomer V.F., Levinson I.B. Current carriers dissipation in metals and semiconductors. Moscow.: Nauka, 1984. (in Russian).
- [3] Ivanov G.A. Fizika Tverdogo Tela. 1964, V.6, N.4, P.938-940. (in Russian)
- [4] Ivanov G.A. Fizika Tverdogo Tela. 1963, V.5, N.11, P.3173-3178. (in Russian).
- [5] Hartman R. Phys.Rev., 1969, V.181, N.3, p.1070-1086.
- [6] Chopra V., Ray R.K., Bhagat S.M. Phys.Stat.Sol.(a), 1971, V. 4, N. 1, P.205-214.
- [7] Issi J.P. Australian J. Phys., 1979, V. 32, N. 6, P. 585-628.

- [8] Tanaka K., Suri S.K., Jain A.L. Phys.Rew., 1968, V. 170, N. 3, P. 664-667.
- [9] Levitskii Y.T., Ivanov G.A. Fizika metallov i metallovedenie 1969, V.28, N.5, P.804-812. (in Rassian)
- [10] Jeavons A.P., Saunders G.A. Proc.Roy.Soc.A, 1969, V.310. P. 415-432.
- [11] Golban I.M. Dissipation anisotropic of charge carriers on the phonons acoustic in the bismuth, antimonium and arsenium. Kichinev. Preprint AN IPF MSSR 1987. 49 P. (in Russian).
- [12] Ivanov G.A., Krilov A.S., Kalugina I.K. Pribori i tehnika experimenta 1975, N.2, P.225-226. (in Russian).
- [13] Sobolev V.V. Energy structure of semiconductors. Kichinev. : Shtiitsa, 1983. 287p. (in Russian).
- [14] Grabov V.M., Ivanov G.A., Naletov V.L., Ponaryadov V.S., Yakovleva T.A. Fizika Tverdogo Tela. 1969. V.11, P.3653-3655. (in Russian).
- [15] Grabov V.M. Poluprovodniki s uzkoi zapreshennoi zonoi Materiali VIII Vsesoyuznogo symposiuma. Lvov, 1986. V.II, P.194-196. (in Russian).
- [16] Lopez A.A. Phys.Rev., 1968, V. 175, N. 3, P. 828-840.
- [17] Grabov V.M., Panarin A.F., Hudjakova I.I. Poluprovodniki s uzkoi zapreshennoi zonoi. Materiali VIII Vsesoyuznogo symposiuma. Lvov, 1980. V.II, P.217-219. (in Russian).
- [18] Red'ko N.A., Bresler M.S. Jurnal experimentalnoi i Teoretisheskoi Fiziki 1971, V. 61, N.1 (7), P. 287-300. (in Russian).
- [19] Heremans J., Issi J-P., Rashid A.A.M., Saunders G.A. J. Phys. C, 1977, V.10, N. 22, P. 4511-4522.
- [20] A.P.Cracknell, K.C.Wong. *The Fermi Surface*. Clarendon-Press, Oxford, 1973.

**THERMOELECTRICAL PROPERTIES AND ENERGY BAND SPECTRUM P-BI<sub>2</sub>TE<sub>3</sub>  
DOPED WITH ELEMENT OF III OR IV GROUP**

M.K.Zhitinskaya<sup>1</sup>, S.A.Nemov<sup>1</sup>, T.G.Abaidulina<sup>1</sup>, T.E.Sveshnicova<sup>2</sup>

<sup>1</sup> State Technical University, 29 Polytechnicheskaya, 195251 St.-Petersburg, Russia

<sup>2</sup> A.A.Baikov Institute of Metallurgy, Russia Acad.Sci., Moscow, Russia

The energy spectrum of p-Bi<sub>2</sub>Te<sub>3</sub> doped with In, Tl,Pb or Sn was studied by measuring of basic transport phenomena including Nermst-Ettingshausen (N-E) effect. The experimental data was used for determination the anisotropy of conductivity and Hall mobility, and for estimation the energy spectrum parameters. The effect of deviation from stoichiometric composition on the hole density of Bi<sub>2</sub>Te<sub>3</sub> doped by different impurities was investigated.

### Introduction

Bismuth telluride-base alloyes are doped by II, III and IV groups impurities in the small quantity for the benefit of thermoelectrical efficiency increasing<sup>[1-3]</sup>. In doing so electrical, thermal, mechanical and other physical properties are changed. The content of intrinsic defects and carrier concentration is changed too. The aim of this research is to study the physical reasons along with technology conditions. The investigation is concerned with Bi<sub>2</sub>Te<sub>3</sub>, material with the well known energy band spectrum among A<sup>V</sup>B<sup>VI</sup> compounds.

### Samples.

We investigated both single crystals and polycrystalline samples. The composition of the samples is described by the chemical formula (Bi<sub>1-x</sub>Me<sub>x</sub>)<sub>2</sub>Te<sub>3</sub>, where Me = In,Pb,Tl,Sn and x varies from 0 to 0,03 (x=0,01 corresponds to 6.10<sup>19</sup> cm<sup>-3</sup>). The amount of impurity dopant introduced was within the solubility limit. Single crystals were grown by the directional crystallization method or by the Chohralsky method with liquid phase adding. Polycrystalline samples were fabricated by the metal-ceramic method at a compression pressure P = 5 - 6 metric tons/cm<sup>2</sup>. The samples were annealed at a temperature of 380 C for 100h. For these samples the carrier density p and mobility are adjusted by the method described in paper [5]. We determined the

following independent components of the transport tensor: the Hall coefficients R<sub>123</sub> and R<sub>321</sub>, the thermoelectric powers S<sub>11</sub> and S<sub>33</sub>, the electrical conductivity σ<sub>11</sub> and the Nernst-Ettingshausen (N-E) coefficient Q<sub>123</sub> and Q<sub>321</sub>. In this notation the number 3 indicated the trigonal axis of a crystal. The indices (subscripts) of the coefficients represented the following, in the order they appeared: the first was used for the direction of the measured electric field, the second for the direction of the electric current or the temperature gradient, and the third for the direction of the magnetic field. The measurements were carried out mainly in the temperature range 77 - 420 K. The carrier density was determined from the expression

$$n,p = |eR_{321}(77 \text{ K})|^{-1} \quad (1)$$

The main parameters of the investigated samples are listed in Table 1. The temperature dependences of the electrical conductivity, thermoelectric power, Hall and N-E coefficients obtained under low impurity concentration (x<0,5 at.%), were similar to those of undoped p-Bi<sub>2</sub>Te<sub>3</sub> samples. We observed a deep minimum in dependences of the thermoelectric power and of the N-E coefficient on the hole density near p ~ (0,5 - 1)10<sup>19</sup> cm<sup>-3</sup> with increasing In density. It should be noted that Hall coefficients decrease in all temperature range for single crystal sample doped by Sn (x=0,05).

Table

Sample No	Impurity type	X	Structure of sample	$N_{\text{imp}}$ , $10^{19} \text{ cm}^{-3}$	$p^{77}, 10^{19} \text{ cm}^{-3}$	$\sigma_{11}/\sigma_{33}$ (100 K)	$m_d^*$ (120K)	$\epsilon_g$ eV
52	In	0.005	single	6.0	1.25	7.9	0.48	0.16
5-3	ditto	0.005	ditto	6.0	1.0	3.5	0.26	0.16
7-3	ditto	0.01	block	12.0	0.54		0.38	0.15
10-4	ditto	0.02	ditto	24.0	0.57	4.2	0.23	0.20
14-4	ditto	0.03	ditto	36.0	0.65	4.2	0.25	0.13
38-5	Tl	0.005	single	6.0	0.56	3.8	0.2	0.16
46-4	ditto	0.01	ditto	12.0	0.72	1.8	0.31	0.13
40-5	ditto	0.02	ditto	24.0	1.06	0.6	0.4	0.15
41-6	ditto	0.03	ditto	36.0	1.56			0.13
B-7	Pb	0.008	single	9.6	4.6	2.0	0.63	0.2
89(2)	Sn	0.01	single	6.0	0.85		0.55	0.21
90(4)	ditto	0.025	ditto	15.0	1.2		1.0	0.18
91(2)	ditto	0.05	ditto	30.0	0.65		0.76	0.21
81(1)	stech		single		0.95			

## Discussion

The obtained experimental results allowed to determine the doping action of In, Tl, Pb or Sn impurities in  $\text{Bi}_2\text{Te}_3$ . Dependence of the hole density calculated from the expression (1) on the density of impurity atoms in  $\text{Bi}_2\text{Te}_3$  is shown in Fig1.

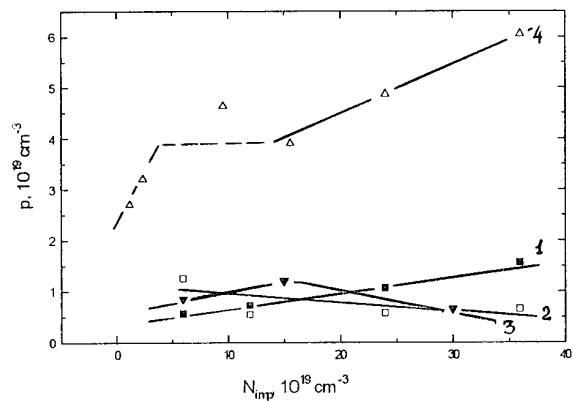


Fig.1 Hole density (p) in bismuth telluride doped with Tl (1), In (2), Sn (3), Pb (4) as a function of the impurity concentration  $N_{\text{imp}}$

As illustrated in Fig1, group III elements show weak electric activity : indium exhibits a donor action, gallium - acceptor (with efficiency  $\sim 0.1$  charge carrier/impurity atom). Group IV atoms differ in electrical activity. Data obtained for  $\text{Bi}_2\text{Te}_3$  doped by lead agree well with those observed in [5]. Lead activity depends on its site in lattice and could range

from 1.7 to 1.4. Sn at  $x < 0.025$ , like Tl, is weak acceptor but at  $x > 0.025$  it becomes weak donor. Energy band parameters were estimated for samples doped with Pb, Sn or Tl on hole density less than  $10^{19} \text{ cm}^{-3}$  and less than  $5 \times 10^{18} \text{ cm}^{-3}$  for  $\text{Bi}_2\text{Te}_3$  doped by In. At these hole densities we found that the one-band model could be used at temperatures below 160 K. A calculation of the density-of-states effective mass of holes in strongly degenerate samples was carried out using the expression

$$m_d^*/m_0 = (3/\pi)^{2/3} \hbar^2 / T_n^{2/3} e/k(S_{11} - Q_{123}/(R_{123}\sigma_{11})) \quad (2)$$

The results of a calculation of  $m_d^*$  are listed in Table 1. The density-of-states effective mass  $m_d^*$  was obtained for relatively low impurity concentration ( $< 1$  at %) and for hole densities arranged outside the limits of Seebeck and N-E effects peculiarities. This result is in agreement with the earlier data obtained for indium - free samples [6]. The band gap  $\epsilon_g$  was found by an analysis of the experimental data on the N-E effect in the region of mixed electron - hole conduction both from the temperature dependence of the coefficient  $Q_{123}$  and from the carrier-density dependence of the temperature at which the sign of the effect was reversed. The band gap determination was described in details in [6,7]. When indium and gallium concentrations were in the range  $x < 0.025$ , the value of  $\epsilon_g$  extrapolated to  $T=0$  K was  $\epsilon_g \approx 0.16$  eV, exactly as in the case of undoped  $\text{Bi}_2\text{Te}_3$  [6]. These values of  $m_d^*$  and  $\epsilon_g$  indicated that introduction of

group III and IV atoms in amounts up to 0.5 at % did not influence on the parameters of the energy band structure in any significant manner.  $\varepsilon_g$  is slowly increasing in the samples containing more than 0.5 at % impurity atoms. In lead-doping samples it increases up to 0.2 eV, and decreases up to 0.1 eV in the samples doped by In,Tl or Sn. It could be explained by solid solution production. It should be mentioned that the minimum in the hole density dependence of the thermoelectric power S is observed at the same hole densities at which the transport phenomena begin to manifest a contribution of the additional valence-band extrema [8]. Therefore, the appearance of the minimum can be explained by interband scattering of carriers [4] under In-impurity presence or it can be connected with resonant level existence in the vicinity of the additional valence-band extrema.

We used N-E coefficients for anisotropy electrical conductivity estimation. In the case when the hole gas is degenerate the following expression takes place:

$$Q_{123}/Q_{321} = (R_{123}\sigma_{11})/(R_{231}\sigma_{33}) \quad (3)$$

The ratio  $\sigma_{11}/\sigma_{33}$  defined from (3) shows that the electrical conductivity anisotropy is connected with hole density like in p-Bi<sub>2</sub>Te<sub>3</sub> [9]. It should be noted, that  $\sigma_{11}/\sigma_{33} = 7$  in samples doped by In which is higher than that for Bi<sub>2</sub>Te<sub>3</sub> doped by Tl ( $\sigma_{11}/\sigma_{33} = 2$ ). Probably this phenomenon explains thermoelectrical efficiency decreasing in Bi<sub>2</sub>Te<sub>3</sub>:In. This fact correlates with results obtained earlier which showed that increasing of anisotropy decreases the efficiency parameter.

Elements of group III demonstrated different electrical activity in Bi<sub>2</sub>Te<sub>3</sub>. This fact is closely connected with their electronegativity and ion radius. It could be proposed, that the effect of the impurities on the intrinsic defects composition will be different. We investigated the effect of deviation from stoichiometric composition on the Hall hole density of Bi<sub>2</sub>Te<sub>3</sub> doped by Pb, Sn or In coincident with Pb. Results are represented in Fig.2. These curves have common peculiarities. A deviation from stoichiometric composition toward an excess of Te and Bi causes a sharp decrease in the hole concentration which leads to stabilization. The slope changes on the curve, which corresponds to the transition to a stabilized current-carrier concentration. It can be explained in terms of the attainment of the

solubility limit of the components. In samples doped by In or Sn plots for the Hall concentration are alike, but in Bi<sub>2</sub>Te<sub>3</sub> doped by Pb it is higher. On the other hand, compound solubility region for samples with In and Pb is more wide than that for Sn-doped samples. J.Pancir et.al. suggested a model about the increasing of the bonds polarization in Bi<sub>2</sub>Te<sub>3</sub> on substitution of Bi by In. Theoretical outgrowth of this model allowed

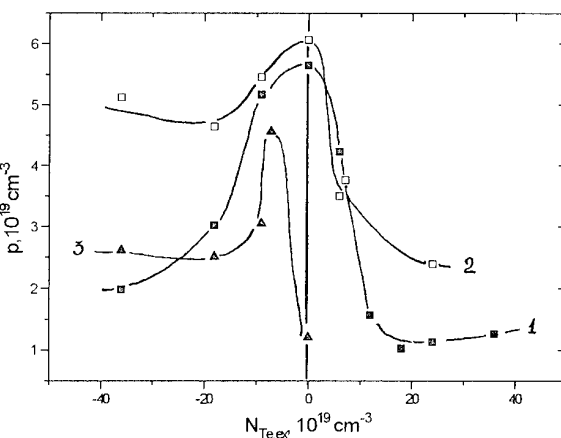


Fig.2 Hole density (p) versus the excess of tellurium N<sub>Te,ex</sub> in Bi<sub>2</sub>Te<sub>3</sub>:In :Pb (1), Bi<sub>2</sub>Te<sub>3</sub>: Pb (2), Bi<sub>2</sub>Te<sub>3</sub>: Sn (3).

us to explain experimental data obtained in [9]. Because of this increase in the polarization the probability of the antistructure Bi<sub>Te</sub> defects formation becomes suppressed and thus hole density decreases under increasing In concentration. N-type defects in indium-doped samples are formed upon introduction of excess Te and Bi. The difference in the number of defects (3/2 defects per excess Bi atom and 2/5 defect per excess Te atom) accounts for the asymmetric nature of the curve shown in Fig.2. The distinct level of the density stabilization for In (curve 1) and for Pb (curve 2) testifies that the In impurity presence accounts for significant increasing of atomic polarization and atomic bonds more than the Pb impurity presence. The data from the anisotropy of the electrical conductivity ( $\sigma_{11}/\sigma_{33}$ ) are higher in Bi<sub>2</sub>Te<sub>3</sub> doped by indium, which verifies the suggestion described above. Dependence of hole density from excess of Bi and Te in Bi<sub>2</sub>Te<sub>3</sub> doped by Sn has the same character as it has in Bi<sub>2</sub>Te<sub>3</sub>:In, but solubility limits of the components are narrowed down. Probably, Sn atoms increases the polarization of the atomic bonds too. Fig.3 demonstrates temperature dependence of specific power S<sup>2</sup> $\sigma$  for samples doped by variety impurities and made by

different technology methods. As it is seen from Fig.3, crystals with low defect concentration show the highest thermoelectric efficiency. These crystals were grown by IMET technology based on Chohralsky method.  $S^2\sigma$ , as a rule, is decreasing in the presence of defects and impurity atoms. Data obtained for single crystal  $\text{Bi}_2\text{Te}_3:\text{Sn}$  are exceptions to this rule. These crystals have the most  $S^2\sigma$ .

This work was supported by the Russia Higher Education State Committee (Grant No. 94-7.10-3050).

#### References

- [1]. T.E.Svechnikova, M.A.Korguev, Thermoelectric power of single cristal n- $\text{Bi}_2\text{Te}_3$  doped by Te, Neorg.Mat., 1994, v.30, No 9, pp.1123 -1128
- [2]. D.J.Ryden, A Comparision between the transport properties of single crystal, polycrystal and anisotropic semiconductors. J.Phys.C., 1971, v.4, No 10, pp.1193 - 1206
- [3]. V.V.Sologub, A.D.Poleckaya, I.G.Lans, S.T.Pavlov, Galvanomagnetic effect in p- $\text{Bi}_2\text{Te}_3$  and two-valence band model, Fiz.Tverd.Tela, 1973, v.15, No3, pp.850 - 855
- [4]. M.K.Zhitinskaya, S.A.Nemov, Yu.I.Ravich, T.G.Abaidulina, Electrophysical properties of indium-doped bismuth telluride, Fiz.Tekh.Poluprovodn., 1993, v.27, No10, pp.1724 - 1729
- [5]. H.Sussmann, A.Priemuth,U.Prohl, Doping properties of Pb and Ge in  $\text{Bi}_2\text{Te}_3$  and  $\text{Sb}_2\text{Te}_3$ , Phys.Stat.Sol.(a), 1984, v.82, pp.561 - 570
- [6]. M.K.Zhitinskaya, V.I.Kaidanov, S.A.Nemov, Investigating of Nernst-Ettingsgausen effect in single

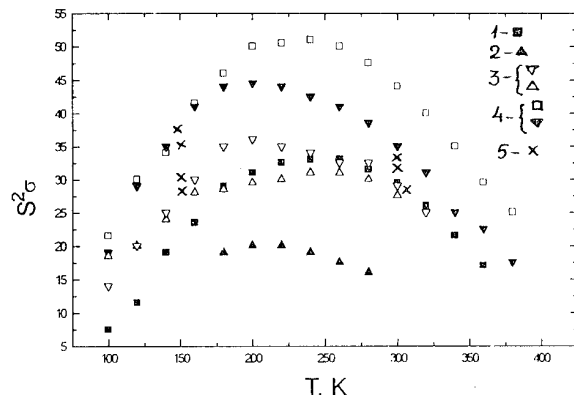


Fig.3 Specific power  $S^2\sigma$  against temperature T for  $\text{Bi}_2\text{Te}_3$ : 1) - undoped; doped by: 2) - In, 3) - Tl, 4) - Sn, 5) - I

- cristal  $\text{Bi}_2\text{Te}_3$ , Deposited Paper, 1976, No36278-76, 23p.
- [7]. Collection: Film Thermoclements - Physics and Applications, M., 1985, 230 p.
- [8]. B.M.Gol'tsman, V.A.Kudinov,I.A.Smirnov, Semiconductor thermoelectric materials based on  $\text{Bi}_2\text{Te}_3$ , M., 1972, 320 p.
- [9]. T.G.Abaidulina, M.K.Zhitinskaya, S.A.Nemov, Yu.I.Ravich. Experimental study of the intrinsic defects in doped bismuth telluride by electrical methods, Fiz.Tekh.Poluprovodn., 1994, v.28, No 9, pp.1613 - 1616
- [10]. J.Pancir, J.Horac, Z.Stary, Concentration of free carriers in  $\text{Bi}_{2-x}\text{In}_x\text{Te}_3$  mixed crystals. Phys.St.Sol.(a), 1987, v.103, pp.517 - 526

## Experimental investigation of Nernst-Ettingshausen effect in the Antimony Telluride

M. K. Zhitinskaya<sup>1</sup>, S. A. Nemov<sup>1</sup>, S. A. Rykov<sup>1</sup>, and L. D. Ivanova<sup>2</sup>

<sup>1</sup> State Technical University, 29 Polytechnicheskaya, 195251 St.Petersburg, Russia

<sup>2</sup> A.A. Baikov Institute of Metallurgy, Russian Academy of Science., Moscow, Russia

The Nernst-Ettingshausen (N-E) and other basic transport coefficients: conductivity, Hall, Seebeck and its anisotropy were investigated in single crystals of  $Sb_2Te_3$ , grown by Czochralsky method. The N-E effect was used for evaluation of the band structure parameters. The particularity in behavior of the kinetic coefficients can be explained on the basis of two valence band model.

### Introduction

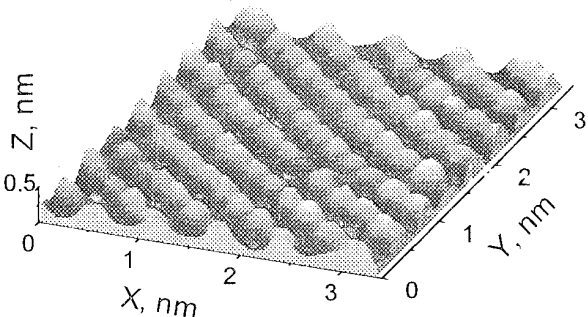
In recent years  $Sb_2Te_3$  is studied very actively [1-5]. The interest to this compound is explained by the fact that it is basic part of solid solutions  $(Sb_{1-x}Bi_x)_2Te_3$ . However it does not mean that energy spectrum of  $Sb_2Te_3$  is investigated reliably. The series of particularities of transport coefficients is not explained by six-ellipsoidal Drabble-Wolf's model [6] even when Kane's nonparabolicity and scattering anisotropy are taken into account. For explanation of dependence thermopower  $S$  on electroconductivity  $\sigma$  [7], anisotropy of thermopower at low temperature [8], particularities in behavior of thermoconductivity [9], a big effect of piezoresistivity [10] the authors of these works assumed that valence band consists from two subbands, the additional extremum with smaller effective mass is situated at the centre of Brillouin zone. The main difficulty lies in the fact that  $Sb_2Te_3$  has big hole concentration which is changed in the small interval. In this situation further investigations of basic transport coefficients of  $Sb_2Te_3$  are appropriate.

In our paper the results of experimental investigation of transverse isothermal Nernst-Ettingshausen (N-E) effect in the perfect single crystals of antimony telluride with heterovalent (Sn) and isovalent (Se, Bi) impurities are presented.

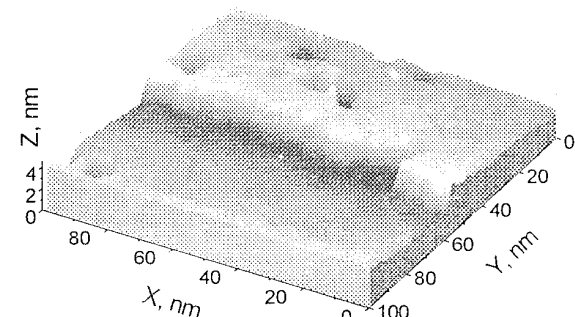
### Experimental procedure

The single crystals of  $Sb_2Te_3$  were grown by Czochralsky method with use of unique technology developed in the A.A.Baikov Institute of Metallurgy. These crystals have perfect structure with considerably small quantity of defects. The density of dislocation in these crystals is  $10^3$ - $10^4$  cm $^{-2}$ , i.e. two order below than density of dislocation in crystals grown by directional crystallization method. The microdistribution of hole concentration was estimated by testing of thermopower coefficient on surface of single crystals. The deviation in values thermopower  $\Delta S/S$  was less than 0.025. The

used method permits to get big crystals. Note that the size in direction trigonal axis is also big enough. We have begun the experiments with the scanning tunneling microscopy (STM) of these  $Sb_2Te_3$  single crystals. Our first results show that the quality of the crystal surface is very high and the STM technique can be useful for the study these objects. The STM images of the  $Sb_2Te_3$  surface are presented on the Fig. 1 (a - with atomical resolution, b - with monolayer steps).



a)



b)

Fig. 1. STM images of the  $Sb_2Te_3$  surface (a - atomical resolution; b - monolayer step) at 300 K.

Table

The electrophysical properties of the  $Sb_2Te_3$  samples

No. samples	Dopants	$N_D \cdot 10^{19}$ , cm <sup>-3</sup>	$p \cdot 10^{20}$ , cm <sup>-3</sup>	$m_d^*/m_0$	r	$\Delta$ , eV
29	-	-	1,21	0,83	0,3	0,1
100	-	-	0,89	0,88	0,22	0,12
128	Se	6,2	1,21	1,05	0,01	0,08
130	Bi	0,62	1,36	0,8	0,29	0,1
125	Sn	1,24	2,58	0,7	0,22	0,1
124	Sn	2,4	3,68	0,6	0,37	0,12

In this work we present the results of experimental investigation of transverse isothermal N-E and basic kinetic coefficients in  $Sb_2Te_3$ . Our experimental technique gives the opportunity to measure at every sample the following independent components of transport tensors: the Hall coefficients  $R_{123}$  and  $R_{321}$ , the thermoelectric powers  $S_{11}$  and  $S_{33}$ , the electrical conductivity  $\sigma_{11}$  and the N-E coefficients  $Q_{123}$  and  $Q_{132}$ . In this notation the number 3 indicated the trigonal axis of a crystal. The indices (subscripts) of the coefficients represented the following, in the order they appeared: the first was used for the direction of the measured electric field, the second for the direction of the electric current or the temperature gradient, and the third for the direction of the magnetic field. We used the special method adapted to the study of galvano- and thermomagnetic properties in thermoelectric materials. The measurements were carried out mainly in the temperature range 77-450 K. The carrier density was determined from the expression:  $p_{77K} = |qR_{321}|^{-1}$  [11]. The main parameters of the investigated samples are listed in Table.

### Results and discussion.

The results of the investigation of anisotropy and temperature dependencies of the electrical conductivity, thermoelectric power and Hall coefficient of undoped  $Sb_2Te_3$  are in a good agreement with those obtained earlier [12]. The temperature dependencies of the all kinetic coefficients are shown in Fig.2. It is evident from this figure that sign of coefficients  $Q_{123}$

and  $Q_{231}$  is negative, magnitude and its anisotropy increase with the rise of temperature. The isotropic thermopower at low temperature ( $T=100-140$  K) and anisotropy increasing for  $T = 140$  K are observed. The big increase of Hall coefficients is observed at the temperature above 200 K and up to 450 K. We explain these particularities of kinetic coefficients in a framework of two-valence band model. The temperature dependencies of  $Q(T)$  show transition to mixed electron-hole conductivity at the temperature above 500 K.

To observe the evolution of change of N-E coefficients with change of hole concentration we prepared the samples of  $Sb_2Te_3$  doped with heterovalent (Sn) and isovalent (Se; Bi) impurities. The hole concentration practically does not change when atoms Sb were replaced by atoms Bi, and atoms Te were replaced by atoms Se. When atoms Sb replaced by Sn we observed the increase of hole concentration similarly to work [3]. The change of magnitude  $Q_{123}$  with introduction of the different atoms are shown in Fig.3.

The basic particularities in behavior of kinetic coefficients with the temperature increasing in all doped samples were the same in common features:

1. the coefficients  $Q_{123}$  and  $Q_{231}$  are negative, magnitude and its anisotropy increases;
2. the anisotropy of thermopower increases;
3. the anisotropy of Hall coefficients is not very big and decreases.

If the charge carriers of one type take part in transport phenomena the anisotropy of N-E coefficients

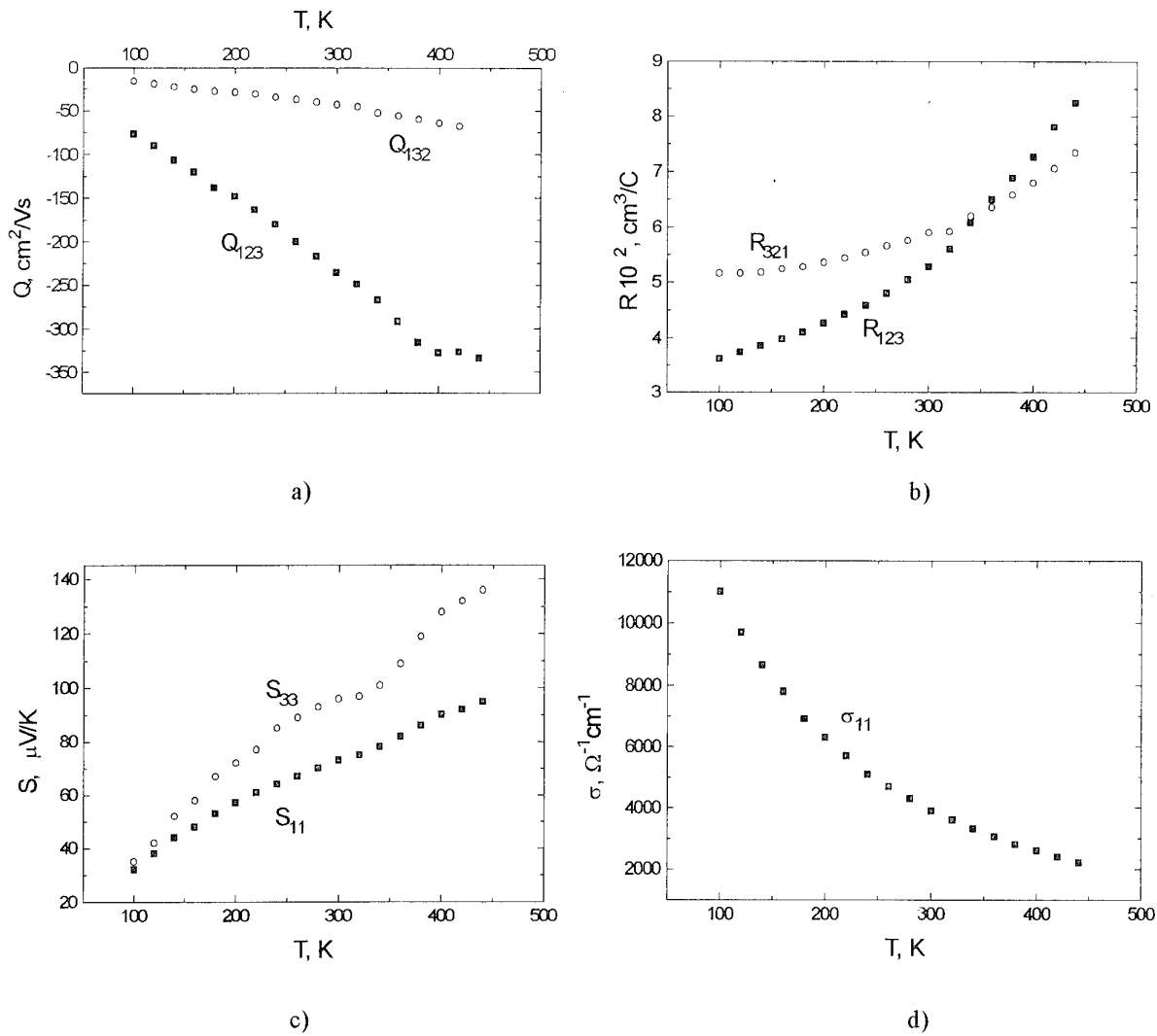


Fig.2. The temperature dependences of the kinetic coefficients of  $\text{Sb}_2\text{Te}_3$ , doped Bi : (a -  $Q$ , b -  $R$ ; c -  $S$ ; d -  $\sigma$ ).(sample No 130).

can be determined by anisotropy of Hall coefficients and anisotropy of electroconductivity under certain conditions  $Q_{ikl}=k/q \cdot B \cdot R_{ikl} \cdot \sigma_{kk}$ . The value of the ratio  $\sigma_{11}/\sigma_{33}$  calculated from our measurements at low temperature region for sample No. 29 is in agreement with date received in straight measurements. This fact taken together with thermopower isotropy at (100 - 140 K) gives us an opportunity to consider the value  $B$  as isotropic. In the case of many-ellipsoidal nonparabolicity model, for the elastic scattering of carriers and for criterion of strongly degenerate we used the following relation:  $S_{kk}-Q_{ikl}/(R_{ikl}\sigma_{kk})=S_\infty$  for evaluation density-of-states effective mass. The data  $m_d^*$  deduced from our calculations are presented in Table .

The formula for N-E coefficient can be written as  $Q=Q_1+Q_2+Q_{12}$ , where  $Q_{12} \sim \exp(-E_g/k_b T) \cdot (S_1-S_2) \times (R_1\sigma_1-R_2\sigma_2)$ , if charge carriers two types take part in transport phenomena. Here indexes 1 and 2 correspond to 1 and 2 bands or conductive and valence bands. This formula makes it clear that at the acoustic scattering (when partial coefficients  $Q_1, Q_2 < 0$ ) the increase of negative value of  $Q$  can occur in the case, when lightly energy band is located below than heavy energy one. At the temperature when minor carriers exert the strong influence on transport phenomena, the magnitude of  $Q$  sharply is decreased and the sign of  $Q$  reverses to positive. The procedure of extracting of term  $Q_{12}$  is discussed at [13] in more details.

The experimental results were used for estimation of the parameters of valence band of  $Sb_2Te_3$  (see the Table). The particularity in the temperature dependencies of kinetic coefficients: the increase of  $R$ , negative magnitude  $Q$ , anisotropy  $S$  with rising temperature are observed at the temperature range  $200 < T < 500$  K. For explanation of these dependencies we used the two subbands model. The estimation of energy gap between these bands gives the value 0.1 eV. We have to assume that the carriers in the second band have smaller effective mass and larger mobility to explain the increasing of negative magnitude  $Q$ . The decrease of the thermopower and the electroconductivity with the rise of hole concentration can be explained in the framework of the isotropic second subband.

#### Summary.

The N-E effect and other basic transport coefficients on perfect single crystals  $Sb_2Te_3$  were systematic investigated. The doping action of Bi, Se and Sn on  $Sb_2Te_3$  was investigated. The particularity on the temperature dependence of N-E effect is found. This particularity unambiguously indicates on the existence of additional extremum of the valence band with smaller effective mass and larger mobility. The energy gap  $\Delta \approx 0.1$  eV. The estimation of the fundamental energy gap in the temperature region with mixed electron-hole conductivity gave the value  $E_g = 0.27$  eV. At low temperature (100 K) the hole density-of-states effective mass and parameter of scattering were estimated.

This work was supported by the Russia Higher Education State Committee (Grant No. 94-7.10-3050),

#### References.

- [1] G.Simon and W.Eichler, Investigations on a Two-Vulence Band Model for  $Sb_2Te_3$ , *Physica Status Solidi(b)*, 1981, v.107, p.201.
- [2] J.Horak, P.Lostak, Point defects in  $Sb_2Te_{3-x}Se_x$  crystals, *Transport in verbindungshalbleitern*, Halle, 1990.
- [3] J.Horak, P.Lostak, M.Matyas, Point Defects in Sn-doped  $Sb_2Te_3$  Single Crystals, *Phisica Status Solidi (b)*, 1985, v.129, pp.381-386.
- [4] M.Stordeur, Investigation of the Weak-Field Charge Transport in Semiconducting V<sub>2</sub>-VI<sub>3</sub> Compounds with Trigonal Symmetry. 1.Expanded Model for the Transport Coefficients, *Physica Status Solidi(b)*, 1984,v.124,pp.439.2.Interpretation of the Weak-Field Charge Transport in  $Sb_2Te_3$  Single Crystals, 1984, v.124, pp.799-805.
- [5] V.A.Kulbachinskii, S.A.Azou, J.Horak, P.Lostak, Low temperature properties of  $Sb_2Te_3<Se,In>$ , *Transport in verbindungshalbleitern*, Martin-Luther-Universitat ,Halle, 1990.
- [6] B.M.Golzman, V.A.Kudinov, I.A.Smirnov, Semiconductor materials based on  $Bi_2Te_3$ , M, 320p.
- [7] B.Ronlund, O.Beckman, H.Levy, Dopind properties of  $Sb_2Te_3$  indicating a two valene band model *J.Phys.Chem.Sol.*, 1965, v.26, pp.1281-1286.
- [8] M.Stordeur, W.Heiliger, Anisotropy of the Thermopower of p- $Sb_2Te_3$ , *Physica Status solidi(b)*, 1976, v.78, K103.
- [9] I.A.Smirnov, A.A.Andreev, V.A.Kutasov, Influence of complex valence band on termal and electrical

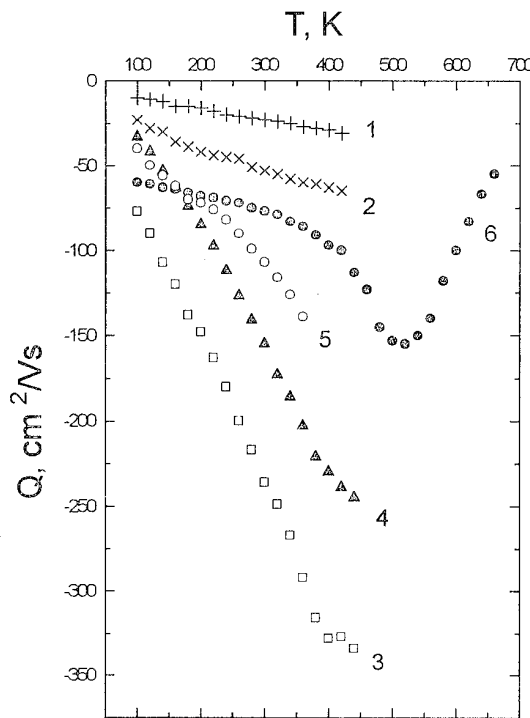


Fig.3. The temperature dependences  $Q_{123}$  of  $Sb_2Te_3$ , doped Sn ( No 124 -1, No 125 -2 ), Bi ( No 130- 3 ), Se ( No128 - 4 ), and undoped ( No 29 -5, No 100-6 ).

by Russian Foundation of Basic Research (Grant No. 93-02- 2041), by International Science Foundation (Grant No. NWK000), and by International Science Foundation and Russian Government (Grant No. NWK300).

- properties of  $Sb_2Te_3$ , Fizika Tverd Tela, 1968, v.10, No.6, pp.1782-1790.
- [10] D.M.Bercha, Z.V.Pankevich, A.V.Savizkii, K.D.Tovstuk, Piezoresistivity of  $Sb_2Te_3$ , Fiz.Tverd.Tela, 1965, v.7, No.8., pp.2437-2442.
- [11] W.Eichler, T.Krug, High Field Galvanomagnetic Transport Properties of  $Sb_2Te_3$  and p-type  $Bi_2Te_3$ , Physica Status Solidi(b), 1980, v.101,pp.K1-K6.
- [12] G.Simon, W.Eichler, Galvanomagnetische und thermoelectriche Transportuntersuchungen an  $Sb_2Te_3$ , Physica Status Solidi(b), 1981, v.103, pp.289.
- [13] M.K.Zhitinskaya, V.I.Kaidanov and S.A.Nemov, Transverse Nernst-Ettingshausen effect of bismuth telluride, Deposite Paper, 1976, No.3628-76, 23p.

STATISTICAL MICRO-INHOMOGENEITIES IN  $(Bi,Sb)_xTe_3$  SOLID  
SOLUTIONS GROWN FROM MELT WITH EXCESS CONTENT OF TELLURIUM

A.I.Anukhin 1, S.Ya.Skipidarov 2 and O.B.Sokolov 1

1. Telvis Co., Moscow, 109383, Russia.  
2. Nord Co., Moscow, 109383, Russia.

This paper presents a model of appearance the statistical inhomogeneities, that are defined by the phase diagram of equilibrium in  $Bi-Sb-Te$  system. The statistical deviation of charge carrier concentration from its average value is defined by  $dC_s/dT_s$  slope line, that is tangent to the solid curve at the crystallization temperature and depends on the solidus line form.

#### Introduction

The stable interest to the  $(Bi,Sb)_xTe_3$  solid solution is due to their high thermoelectric parameters. Of the entire variety of  $(Bi,Sb)_xTe_3$  solid solution compounds, the  $(Bi_{0.25}Sb_{0.75})_xTe_3$  compounds produced from charges containing approximately 2.5% excess tellurium have been considered for a longtime to be the fittest materials to use them in cooling devices. The lower figure of merit of materials differing in their chemical composition from the above mentioned alloys is attributed, above all, to the growth of the lattice related component of thermal conductivity, inherent in these compounds when their chemical composition deviates from this section.

Recent experiments on the basic of the zone melting technique, described in [1], showed that among solid solutions belonging to  $(Bi_{1-x}Sb_x)_xTe_3$ ,  $x > 0.5$ , sections there are no solutions with poor figure of merit, and there exists a temperature for each specific section, at which the figure of merit assumes its maximum value. The authors consider the creation of a structure of higher homogeneity to be one of the factors that allowed to produce materials of higher figure of merit.

The statistical inhomogeneities of concretraion in the  $(Bi,Sb)_xTe_3$  solid solutions considerably affect their thermoelectric properties, and the neglect of their role may result in significant errors in the interpretation of experimental results. This paper propose a model for the formation of statistical structural micro-inhomogeneities that emerge during the growth of solid solutions from a melt and are caused by the influence of liquidus surface shape on their value. This model can serve an explanation for the effect of an increaseing figure of merit that takes place in a narrow range of tellurium concentrations in the melt from which these solid solution have been produced.

#### Theory

The inhomogeneous distribution of a charge carrier concentration in semiconductors considerably modifies their effective parameters. In addition to the reduction of the effective energy gap, in an inhomogeneous medium the effective Seebeck

coefficient and electrical conductivity decrease, and the thermal conductivity increases [2], because of the emergence of vortex currents, bulk Peltier's effects, etc. These three parameters in total determine figure of merit which becomes in an inhomogeneous medium lower than in an homogeneous one. The effective values of thermoelectric parameters directly depend on the relative root-mean-square deviation of the carrier density of charge from the mean value  $\langle(\delta n)^2\rangle/\langle n^2\rangle$ , and they decrease as it grows [2]. The carrier density of charge in the  $(Bi,Sb)_xTe_3$  solid solutions is mainly defined by the antistructure defects that appear as a result of the deviation of the solid solution chemical composition from the stoichiometric one [3]. The deviation depends both on tellurium concentration in the melt from where it is crystallized and on the molar fraction of bismuth telluride and antimony in the solid solutions. In other words, the relationship

$$\langle(\delta n)^2\rangle/\langle n^2\rangle = \langle(\delta C_s)^2\rangle/\langle C_s^2\rangle \quad (1)$$

takes place, where  $\delta C_s$  is the deviation of the chemical composition of a solid solution from the stoichiometric one, expressed in percent of tellurium, and  $\langle(\delta C_s)^2\rangle$  is the root-mean-square deviation of tellurium concentration from the mean value of specimen volume.

The reduction of the effective energy gap in a inhomogeneous thermoelectric material also results to an increasing of the thermal conductivity component, due to an increased of bipolar diffusion of charge carrier.

The concentration inhomogeneities in  $(Bi,Sb)_xTe_3$  are mainly related with the chemical composition fluctuations of the melt, near a crystallization interface. It is advisable the emergence of concentration inhomogeneities in solid solutions to consider in depend on the analysis of the direct relationship between their size and the characteristic features of the  $Bi-Sb-Te$  phase diagram. It is difficult to use directly the phase equilibrium diagram to describe crystallisation process in such complex systems. Besides, the real crystallisation is essentially non equilibrium, whereas the diagram describes equilibrium process. We will, therefore, use phase equilibrium diagram for local re-

gions of the crystallisation interface, assuming that the equilibrium is locally achieved at any moment of time.

#### Isothermal concentration inhomogeneities

The component distribution along the crystallization interface in the process of crystallization in multi-component systems may have a fluctuating character. The local regions in which the component concentration differs from the mean value may be in an equilibrium with the solid phase under constant temperature when the component diffusion along the crystallization interface is hampered. Then one can use the isothermal section in the *Bi-Se-Te* system, to describe possible micro-inhomogeneities in the solid phase. Such sections corresponding to any temperature  $T_1$  and  $T_2$  are schematically shown in Fig.1. The  $CD$  solidus line for the  $(Bi,Sb)_2Te_3$  solid solutions, saturated to the great extent with tellurium at temperature  $T_1$  is conjugate with the  $EF$  liquidus line. The crystals, which are corresponded to the solidus of  $b$  and  $b'$  compositions (Fig.1) and are in the local equilibrium with the liquidus of  $a$  and  $a'$  compositions, are located in the different points of the correlations of bismuth and antimony. In addition, points  $b$  and  $b'$  are located at different distances from the stoichiometric section. These solid solution regions near the crystallization interface are, therefore, saturated with tellurium, which corresponds to different concentrations of electrically active antistructure defects in these regions. Thus, spatially inhomogeneous structures with a statistical distribution the carrier density of charge, and consequently with a statistical distribution of thermoelectric properties, can emerge near the crystallization of interface provided that the temperature is constant.

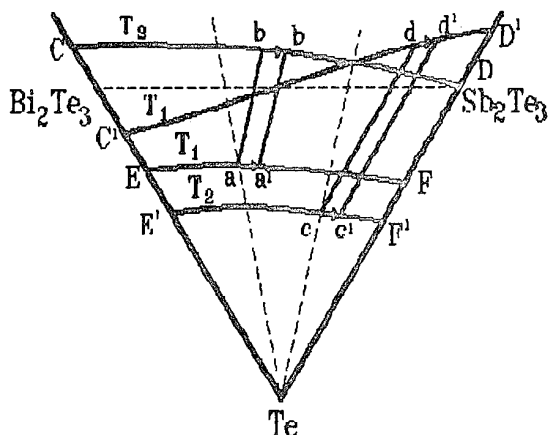


Fig.1. The schematic image of isothermal section part belonging to a equilibrium in *Bi-Sb-Te* system.

Figure 1 shows the location of solidus line for the case, when tellurium solubility at the constant temperature  $T_1$  rises with the increase in the molar proportion of antimony telluride, which is a characteristic of solid solutions, grown from the melt small deviated in its composition from the stoichiometry. The increase in the tellurium content in the melt lowers the crystallization temperature  $T_2$ , and the tellurium maximum solubility curve takes the position  $C'D'$  (Fig.1). Accordingly, points  $a$  and  $b$  change their positions for  $c$  and  $d$ , respectively, and also so do points  $a'$  and  $b'$  for  $c'$  and  $d'$ .

#### Polythermal concentration inhomogeneities

The component concentration fluctuations near the crystallization interface, may be also due to crystallization temperature variations. There can exist two types of tellurium solubility in the  $(Bi,Sb)_2Te_3$  solid solutions: the conventional one, inherent in solid solutions of a chemical composition close to bismuth telluride, and the retrograde one, inherent in solid solutions of chemical composition close to antimony telluride [3,4]. The intermediate case, which is a characteristic for solid solutions close to  $(Bi_{0.78}Sb_{0.22})_2Te_3$  in their chemical composition is also possible, when the tellurium solubility is of conventional type at high temperatures, and it transforms into a retrograde one at lower temperatures. The mechanism involved in the formation of chemically inhomogeneous structures in the solid solutions with conventional solubility does not differ from the one acting in the solid solutions with retrograde. Therefore confine ourselves to the consideration of the phase equilibrium diagram with conventional solubility only, and then go over to diagrams in which both types of solubility are available.

Figure 2 schematically shows a fragment of the polythermic section, typical to the  $Bi_2Te_3-Te$  quasi-binary system [3]. A  $\delta C_e$  fluctuation of tellurium concentration in the melt causes a  $\delta T_e$  variation in the crystallization temperature, which, in turn, results in tellurium concentration variations in the solid phase

$$\frac{\delta C_e}{\delta C_e} = \frac{dT_e}{dC_e} \quad (2)$$

where  $dC_e/dT_e$ ,  $dC_e/dT_e$  are angles between the temperature axis and the tangents to solidus and liquidus lines, respectively, at crystallization temperature. In this case,  $dT_e = dT_s$ .

The locality-inhomogeneity distribution of tellurium concentration along the crystallization interface will result in a inhomogeneity distribution of the crystallization temperature, and, therefore, in the interface nonsmoothness which, in turn, may be beginning of a concentration supercooling. The growth interface irregularly size (Fig.3) will be defined as

$$\delta_n = \delta T / \nabla T \quad (3)$$

where  $\nabla T$  is the temperature gradient near the growth interface.

The  $dC_s/dT_s$  derivative assumes maximum values near the maximum crystallization temperature on solidus curves. Temperature

fluctuation value  $\delta C_s$  for the tellurium solved in the solid solution. At this temperature, however,  $dT_s/dC_s$  reaches a minimum value, which will to some extent reduce the influence by exerted the fluctuations in the solid phase (equation 2).

The  $dC_s/dT_s$  derivative turns to zero at temperature  $T_0$  on a solidus curve, containing segments where the conventional solubility turns into a retrograde one (the solidus is schematically shown in Fig. 2b). The  $\delta C_s$  value also is equal to zero at this temperature. It means that the carrier density of charge distribution in the  $(Bi,Sb)_2Te_3$  solid solutions, produced from the melt of a chemical composition corresponding to the tellurium solubility transition point, will have no noticeable microinhomogeneities. The growth interface may be not smooth in this case.

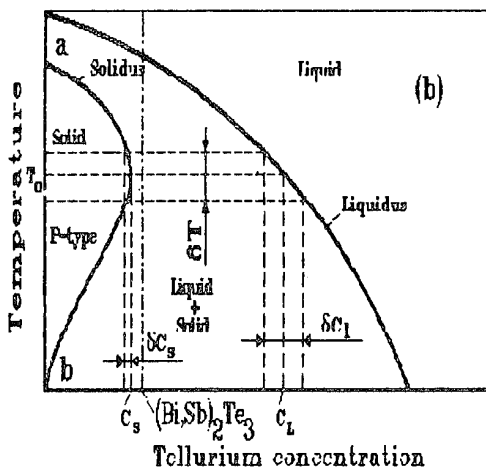
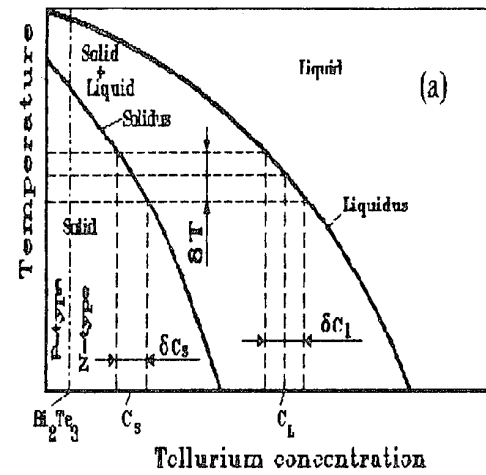


Fig.2. The schematic image of polythermic section belonging to  $(Bi,Sb)_2Te_3$  - Te system near the stoichiometric composition:  
a) for solidus with usual solubility of tellurium;  
b) for solidus with retrograde solubility of tellurium.

oscillations  $\delta T$  near the growth interface or fluctuations  $\delta C_s$  of tellurium concentration in the melt will result in a maximum

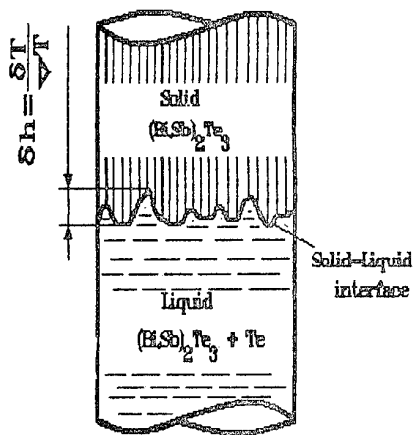


Fig.3. Schematic image of interface which explains a formation of dendrites.

Note too, that S-shaped liquidus [5] is usually conjugated with a retrograde solidus, and there exists a temperature region on this liquidus, where  $dT_s/dC_s=0$ , conjugated with the point on the solidus where  $dC_s/dT_s=0$ . Unfortunately, the experimental data available does not allow to infer the existence of an S-shaped liquidus in  $(Bi,Sb)_2Te_3$ , although its shape is of great interest as regards its influence on the formation of homogeneous structure. Further, the minimum microinhomogeneity of tellurium distribution may take place not only in the case of a retrograde solidus, but also when the tellurium solubility does not depend on temperature.

The tellurium solubility in  $(Bi,Sb)_2Te_3$  depends both on tellurium concentration in the melt and on the proportions of bismuth and antimony, and, therefore, it can be expressed as a function of the tellurium distribution coefficient  $k$  which depends on both variables. Then the spatial inhomoge-

neity amplitude of dissolved tellurium concentration is

$$\delta C_s = \frac{\partial k}{\partial C_{se}} \cdot \delta C_{se} + \frac{\partial k}{\partial C_e} \cdot \delta C_e \quad (4)$$

where  $\partial k / \partial C_{se}$  reflects the influence of the  $Sb_2Te_3$  ( $C_{se}$ ) concentration on tellurium solubility,  $\partial C_{se} / \partial C_e$  reflects the influence of tellurium concentration on the  $Sb_2Te_3$  concentration ( $Sb_2Te_3$  distribution coefficient) in the solid solution, and  $\partial k / \partial C_e$  reflects the influence of tellurium concentration on tellurium solubility in the solid phase.

The first item in equation (4) actually is the value of tellurium solubility inhomogeneity, that arises at constant crystallization temperatures, and the second item is the value of tellurium solubility, that arises when bismuth and antimony proportions in the melt are constant. It follows from equation (4) that these inhomogeneity formation mechanisms are independent of each other. The second item in equation (4) turn to zero at  $T=T_\sigma$  in solid solutions with a retrograde solidus. The experimental data available on the  $Bi-Sb-Te$  phase equilibrium does not allow to indicate specific compositions in which the antimony telluride distribution coefficient is independent of tellurium concentration. One cannot, therefore, assume the  $\delta C_s$  value turn to zero. It may, however, assume minimum values both since the second item turn to zero and since the first item reaches a minimum.

#### Experiment and discussion

The ingots under investigation were grown in evacuated quartz ampules of 9 to 12 mm inside diameter. The initial charge components purity were 99.99. The chemical composition of the loading was as follows:  $(Bi_{0.5}Sb_{0.5})_2Te+1.5\%Te$ ,  $(Bi_{0.5}Sb_{0.7})_2Te+2.5\%Te$ ,  $(Bi_{0.22}Sb_{0.78})_2Te+1.5\%Te$ . The length of zone-melted ingots was 9 to 12 cm. The electrical conductivity along ingot was measured at intervals of 1.0 cm at room temperature. In addition, figure of merit was measured using Harman technique in the 150 to 350 K temperature range on specimens of 3x3x5 mm size, cut out of each 5 mm long ingot. At the same time, electrical conductivity of these specimens was measured.

All ingots had cleaving planes preferably arranged parallel to the growth direction.

When the model with experimental data is compared, the distribution curve for figure of merit  $Z$  and electric conductivity  $C$  along ingots have been interpreted as functions of tellurium concentration in the melt. To do that, the coordinate value on ingot  $X$  was transformed into the excess tellurium concentration value using equation (5) [6]

$$C_L = C_o \cdot (1 + X/L) \quad (5)$$

where  $C_L$  is the excess tellurium concentration in the melt,  $C_o$  is the excess tellurium concentration in the charge,  $L$  is the

melted-zone length,  $X$  is the coordinate on the ingot. Then, the excess tellurium concentration value was recounted as an absolute proportion of tellurium in the melt.

It is well known the thermoelectric parameters of the  $(Bi_xSb_x)_2Te_3$  solid solutions depend on the temperature and, in addition, their figure of merit reaches a maximum in the temperature region in where thermoelectric properties were investigated. The maximum depends on a chemical composite of solid solutions. Therefore, in order to draw a plot of both figure of merit and electrical conductivity as function of tellurium concentration in the melt it is required to take into account this feature. In this paper these dependences were drawn for electrical conductivity  $(Bi_{0.5}Sb_{0.5})_2Te_3$  at temperature 180 K at where a contribution of ambipole diffusion of charge carriers may be neglected and for figure of merit at temperatures where its value is maximum.

Fig.4 shows these dependencies for the  $(Bi_{0.5}Sb_{0.5})_2Te_3$  solid solution. If  $C_{ro}=62.5\%$  in the melt, figure of merit of this solid solution turns to zero and to sinking of charge carrier, changes from positive to negative one. The dependence of conductivity upon tellurium concentration is linear one. The tangent angle of a straight line to the abscise axis in hole semiconducting area is more than that in electron.

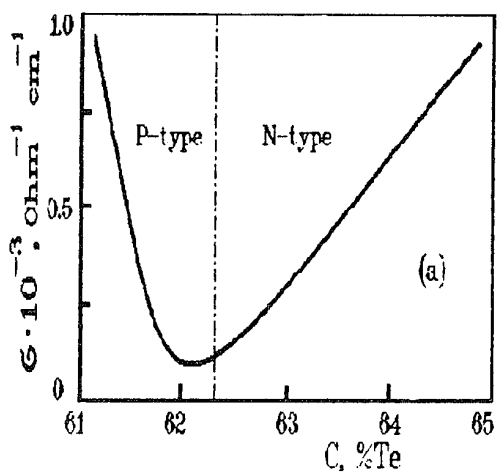
The dependencies of both the maximum of figure of merit and electrical conductivity at  $T=300$  K upon tellurium concentration in the melt for  $(Bi_{1-x}Sb_x)_2Te_3$  solid solution, where  $x=0.5$ , 0.7, and 0.78 are shown on Fig.5.

The maxima of figure of merit and minima on electrical conductivity appear on their curves, if tellurium concentration in the melt is equal 62.5%. Both figure of merit and electrical conductivity of  $(Bi_{0.5}Sb_{0.5})_2Te_3$  solid solution are not depend on tellurium concentration in the melt, if the  $C_{ro}$  concentration is more than 62%.

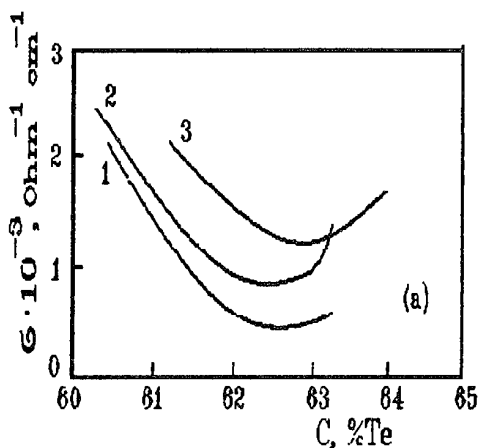
Within the frame of the generally adopted model of doping in  $Bi_2Te_3$  and in solid solutions produced on its basis, the dependence of electric conductivity upon tellurium concentration in the melt is interpreted as the dependence of tellurium solubility upon the crystallization temperature determined by chemical composition of the melt. I.e., the character of electric conductivity dependence upon tellurium concentration in the melt is defined by the solidus shape. It follows that when at  $C_e=62.5\%$  Te in  $(Bi_{0.5}Sb_{0.5})_2Te_3$  (Fig.4), the type of conductivity in solid solutions changes from the hole-type conductivity to the electron, it reflects the fact that the solidus intersects the stoichiometric flatness, and the solidus shape is similar to that shown in Fig.2a. The linear dependence of concentration of tellurium dissolved in the solid solution upon that in the melt practically makes the statistical inhomogeneity of concentration of dissolved tellurium constant in the whole of investigated range of component concentrations, if the

temperature fluctuation near the growth interface is constant value.

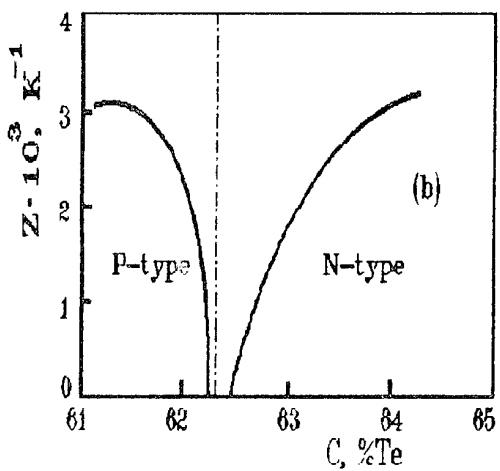
sing of charge carriers is changed from positive to negative [7].



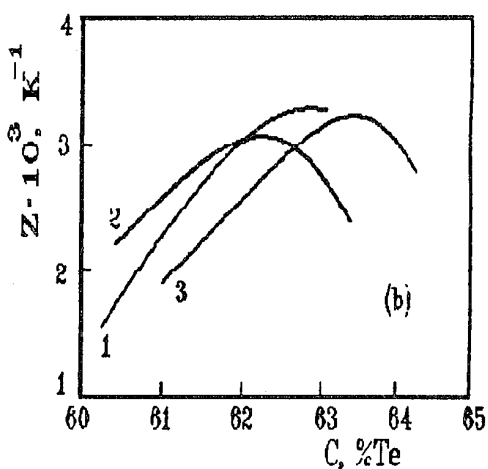
(a)



(a)



(b)



(b)

Fig.4. Specific electric conductivity (a) and figure of merit (b) measured at 180 K for  $(Bi_{0.8}Sb_{0.2})_2Te_3$  solid solution as functions of tellurium concentration in zone melt.

As it is well known, the maximum figure of merit in  $(Bi, Sb)_2Te_3$  should be observed when the electric conductivity is close to  $1000 \text{ ohm}^{-1}\text{cm}^{-1}$ . Therefore, it is difficult to explain its reducing at the same values of conductivity (Fig. 4) but that are reached at low temperature as a result the chemical composite approaching of the solid solution to the stoichiometry where the

Fig.5. Specific electric conductivity (a) and maximum figure of merit in 150-350 K temperature region (b) as function of tellurium concentration in zone melt:

- 1 -  $(Bi_{0.8}Sb_{0.2})_2Te_3$ ;
- 2 -  $(Bi_{0.9}Sb_{0.1})_2Te_3$ ;
- 3 -  $(Bi_{0.22}Sb_{0.78})_2Te_3$ ;

The parameters of solid solutions considerably are changed in a very narrow range of tellurium concentration variations in the melt from 61.5 to 63%. A 0.5% variation of tellurium concentration in the melt, equivalent, according to [ 8 ], to a 0.5 K

variation of the crystallization temperature, may be comparable with the amplitude of the tellurium concentration fluctuations near the crystallization interface (see equation (1)). The inhomogeneity of the component distribution in ingots suggests that the sharp reduction in figure of merit of the  $(Bi_{0.8}Sb_{0.2})_2Te_3$  solid solutions produced from melts containing 61.5 to 63.0% Te (Fig.4) may be due to presence of regions in which the inhomogeneity amplitude of the charge carrier concentration is comparable with the value of the concentration. Therefore, the regions may have different types of conductivity, and figure of merit decreases both because of compensation and because of the growth of the ambipolar diffusion of charge carriers in these regions are presented. As the chemical composition deviates of the solid solution from stoichiometric point, figure of merit increases.

The  $(Bi,Sb)_2Te_3$  solid solutions enriched with antimony telluride (Fig.5), are characterized by the hole type conductivity. If tellurium concentration in the melt increase, the electric conductivity of the  $(Bi_{0.8}Sb_{0.2})_2Te_3$  solid solutions first decrease, then its reduction decelerates, and it remains practically constant after the tellurium concentration in the melt reached 62.0%. It means that the charge carrier concentration in this solid solution becomes independent of the crystallization temperature, i.e., the tellurium solubility in these solid solutions reaches saturation. In this temperature range, or, equally, in the variation range of tellurium concentration in the melt, the tellurium concentration fluctuations near the growth interface exert practically no influence on the dissolved tellurium distribution in the bulk of the solid solution. In this variation range of tellurium concentration in the melt, the  $dC_e/dT_e$  derivative turns to zero (see equ. (8)), and figure of merit reaches its maximum (Fig.5).

Tellurium solubility in the solid solutions of a composition close to  $(Bi_{0.22}Sb_{0.78})_2Te_3$  changes from the conventional type in the solid solutions grown from the melt of near-stoichiometric composition to the retrograde type in melts containing over 62.8-63.0% Te. The transition region is rather broad, which can be seen in Fig.5 (curve 3) in which the dependencies of their electric conductivity and figure of merit on tellurium concentration in the melt are shown. Outside the transition region, figure of merit of the  $(Bi_{0.22}Sb_{0.78})_2Te_3$  and  $(Bi_{0.8}Sb_{0.2})_2Te_3$  solid solutions are lower than that in the transition region where the  $dC_e/dT_e$  derivative also turns to zero (Fig.5).

Thus, the proposed model for the influence of the solidus surface shape on the micro-inhomogeneous distribution of the charge carrier concentration finds its experimental confirmation.

Similar phenomena of the dependence of thermoelectric properties of the  $(Bi,Sb)_2Te_3$  solid solution on the chemical composition of the melt have also been observed in [8]. The increment of tellurium concentration in the melt was, however, ta-

ken to be too big in this investigation, and the sensitive effects of variation of thermoelectric properties remained unnoticed. In the experimental data given in this paper, the increment of tellurium concentration in the melt was determined by specimen length and by the zone melting process parameters. According to (4), the tellurium concentration variation per unit zone displacement length in zone melting equals

$$\frac{dC_e}{dx} = \frac{C_o}{L} \quad (6)$$

In the absolute values of tellurium concentration in the melt,

$$\frac{dC_e}{dx} = 0.4 \frac{C_o}{L} \quad (7)$$

When the length of specimen used to measure thermoelectric properties  $x=5$  mm, zone length  $L=20$  mm, and  $C_o=1.5\%$ , the increment of tellurium concentration in the melt is  $C_e=0.155\%$  in two adjacent parts of the ingot are one length of specimens apart to be grown. This is considerably lower value than that of tellurium concentration in the melt in the specimen produced by another authors, where it was equal to 5%.

#### Conclusion

1. A model is developed for the statistical inhomogeneity formation of the chemical composition in the  $(Bi,Sb)_2Te_3$  solid solutions grown from the melt in which component concentration fluctuations take place near the crystallization interface.

2. The greatest figure of merit is observed in the  $(Bi,Sb)_2Te_3$  solid solutions grown from the melt at the crystallization temperatures, at which the  $dC_e/dT_e$  derivative turns to zero on solidus, and accordingly, at which there take place a minimum sensibility to both chemical composition fluctuations of solid solutions and temperature fluctuations near the crystallization interface.

#### Acknowledgement

The authors would like to thank their assistance Boboshko N.A. and Mazin A.I. in the measurement process.

#### References

1. A.A.Aivazov, A.I.Anukhin, Thermoelectric properties of  $Bi_2Te_3-Sb_2Te_3$  low temperature materials with hole conductivity. Proceeding of the XII International Conference on Thermoelectrics. Yokohama, Japan, November, 9-11, 1993.
2. B.M.Goltzmann, B.A.Kudinov, I.A.Smirnov. Semiconducting thermoelectric materials based on  $Bi_2Te_3$ . Moscow, 1972, 320p. In Russian.
3. N.Kh.Abrikosov, V.F.Bankina, L.V.Poretskaya, L.E.Shelimova, and E.V.Skudnova.

Semiconducting II-IV, IV-VI, and V-VI compounds. Plenum press. New-York, 1969, 252p.

4. N.Kh.Abrikosov, L.V.Poretskaya. Physical and chemical equilibriums in ternary alloys of  $Sb_2Te_3$ - $Bi_2Te_3$ -Te system and quaternary alloys  $Sb_2Te_3$ - $Bi_2Te_3$ - $Bi_2Se_3$ -Te system. Izv. AN USSR. Inorganic materials. V.19, N3, 1983, pp.388-393. In Russian.

5. D.A.Petrov. Binary and ternary systems. Moscow, Metallurgiya, 1986, 256p. In Russian.

6. A.I.Anukhin, O.B.Sokolov, S.Ya.Skipidarov, K.V.Senin. Microstructure and thermoelectric properties of  $(Bi,Sb)_xTe_3$  solid solutions grown by zone melting technique. Proceeding of the XI International Conference on Thermoelectrics. Arlington. Texas, USA. October, 1992. pp.307-311.

7. A.I.Anukhin, O.B.Sokolov, S.Ya.Skipidarov. Thermoelectric and semiconducting properties of  $(Bi_{1-x}Sby)_xTe_3$  solid solutions grown by zone melting technique. Proceeding of the XII International Conference on Thermoelectrics. Yokohama,Japan, November, 9-11, 1993.

8. J.P.Fleurial, L.Gailliard, R.Triboulet, H.Scherrer, S.Scherrer. Thermal properties high quality single crystals of bismuth telluride. Part 1. Experimental characterization. J.Phis.Chem. Solidi. 1988, V.49, N10, pp.1237-1247.

**THERMOELECTRIC PROPERTIES OF n - Bi<sub>2</sub>Te<sub>3-x</sub>Se<sub>x</sub> (x < 0.4) SOLID SOLUTIONS IN THE RANGE OF TEMPERATURE FORM 80 TO 300 K**

G.T. Alekseeva, M.V. Vedernikov, P.P. Konstantinov, V.A. Kutasov, L.N. Luk'yanova

A.F.Ioffe Physical-Technical Institute of RAS, St.Petersburg, 194021, Russia

Thermoelectric properties of n - Bi<sub>2</sub>Te<sub>3-x</sub>Se<sub>x</sub> (x < 0.4) solid solution doped with superstoichiometric Te were studied in the range of temperature from 80 K to 300 K. A change of  $(m^*/m)^{3/2}\mu_0$  parameter ( $m^*$  is the density of states effective mass,  $\mu_0$  - the charge carrier mobility) from temperature is shown to decrease for growth of x value. It was established that the figure of merit Z increases in the n - Bi<sub>2</sub>Te<sub>3-x</sub>Se<sub>x</sub> (x < 0.4) solid solution at x=0.3 in comparing with x=0.12 for temperature below 200K.

Thermoelectric materials based on n - Bi<sub>2</sub>Te<sub>3-x</sub>Se<sub>x</sub> (x < 0.4) solid solutions have been widely used for thermoelectric cooling near the room temperature for a long time. Now the problem of cooling to low temperatures using with many cascade module was arisen. From published data [1] and our investigation [2,3] it was shown that  $\Delta T_{max}$  value may be reached to 140-150° in six-cascade module for temperature of the hot seal at 300 K. Therefore studying of the thermoelectric properties of n - Bi<sub>2</sub>Te<sub>3-x</sub>Se<sub>x</sub> (x < 0.4) solid solutions in the range of temperatures from 80 to 300 K is very important because the different composition of the solid solutions are widely used in many-cascade module.

In the present investigation electroconductivity ( $\sigma$ ), thermoconductivity ( $\kappa$ ) and thermoelectric power ( $\alpha$ ) of n - Bi<sub>2</sub>Te<sub>3-x</sub>Se<sub>x</sub> (x < 0.4) sample of solid solution grown by vertical directed crystallization method without concentration overcooling were studied [4]. The charge carrier concentration was changed by deviation of stoichiometric composition with excess of Te. The additional scattering are excluded at low temperatures due to doping of halogens ( CdCl<sub>2</sub>, BiBr<sub>3</sub>, etc.). For measurements of thermoelectric properties thermal flow and electric current were oriented along cleavage planes of the samples.

The thermoelectric parameters were determined in the range of temperature from 80 to 300 K [5]. Since thermoelectric materials were studied at low temperatures (<200 K) that the interval of carrier concentrations was limited to ( $1 \pm 10^{18} \text{ cm}^{-3}$ ) and almost all samples have a mixed conductivity at the room temperature.

Analysis of temperature dependences of  $\alpha$ ,  $\sigma$  and  $\kappa$  were carried out using acoustic scattering mechanism that is predominated in these materials (scattering parameter is equal to  $r = -0.5$ ). The value of the effective scattering parameter  $r_{ef}$  [6] in these solid solutions at low carrier concentration is changed from -0.4 to -0.6 in the temperature interval 80-300 K and therefore the scattering parameter  $r = -0.5$  may be used for qualitative evaluations.

Temperature dependences of experimental ( $\sigma$ ,  $\alpha$ ,  $\kappa$ ) data and the figure of merit Z in the solid solutions of n - Bi<sub>2</sub>Te<sub>3-x</sub>Se<sub>x</sub> (x=0.12, 0.3, 0.36) are shown in Fig. 1-4.

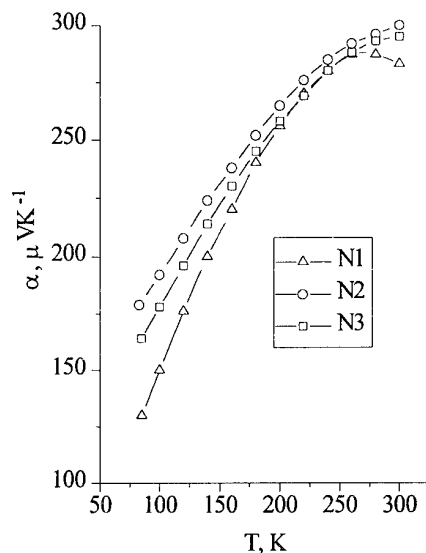


Fig.1. Temperature dependence of the thermoelectric power  $\alpha$  (N1-N3) in n - Bi<sub>2</sub>Te<sub>3-x</sub>Se<sub>x</sub> solid solutions. x: 1-0, 2-0.3, 3-0.36.

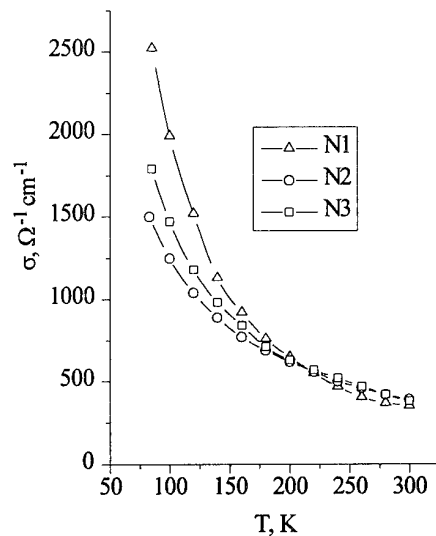


Fig.2. Temperature dependence of the conductivity  $\sigma$  (N1-N3) in n - Bi<sub>2</sub>Te<sub>3-x</sub>Se<sub>x</sub> solid solutions. x: 1-0, 2-0.3, 3-0.36.

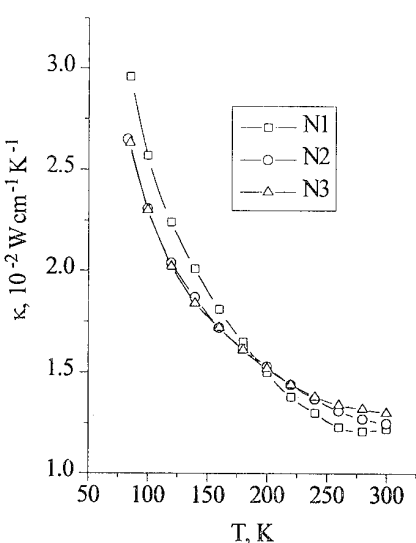


Fig.3. Temperature dependence of the thermoconductivity  $\kappa$  (N1-N3) in  $n - \text{Bi}_2\text{Te}_{3-x}\text{Se}_x$  solid solutions.  $x$ : 1-0, 2-0.3, 3-0.36.

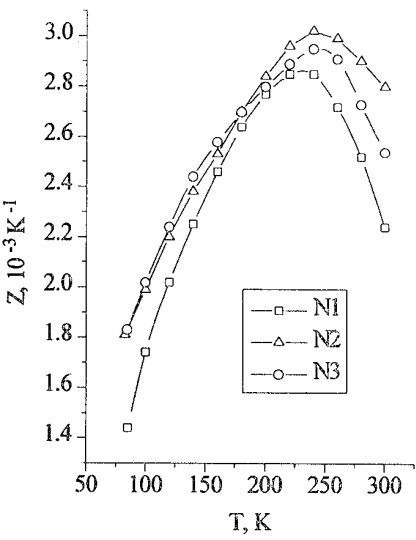


Fig.4. Temperature dependence of the figure of merit  $Z$  (N1-N3) in  $n - \text{Bi}_2\text{Te}_{3-x}\text{Se}_x$  solid solutions.  $x$ : 1-0, 2-0.3, 3-0.36.

Analysis of  $\alpha(T)$  dependences was performed in accordance with expressions from ref. [7]:

$$n = \frac{4(2\pi m^*/m_0 T)^{3/2}}{\sqrt{\pi} n^3} F_{1/2}(\eta) \quad (1)$$

where  $F_{1/2}(\eta)$  is the Fermi function:

$$F_S(\eta) = \int_0^\infty x^S [\exp(x - \eta) + 1]^{-1} dx$$

From the equation (1) the temperature dependence of the effective mass  $m^* \sim T^s$  may be defined for  $n=\text{const}$ . This

dependence of  $m^*/m$  on temperature explained by deviation of  $\alpha(T)$  from theoretical dependence (for  $r = -0.5$  and  $m=\text{const}$ ) in the different solid solutions based on bismuth telluride [8]. The value of  $s$  in the expression of  $m^* \sim T^s$  changed a sign with plus to minus in the solid solutions of  $n - \text{Bi}_{2-x}\text{Sb}_x\text{Te}_{3-y}\text{Se}_y$  [9]. For investigated solid solutions the value of  $s$  is equal to +0.1, -0.1, -0.12 for  $x=0.12, 0.3$  and 0.36, respectively.

Analysis of  $\sigma(T)$  dependences with account of the degeneracy was performed in accordance with relation:

$$\sigma_o = \frac{F_{1/2}(\eta, r)}{F_{1/2}(\eta, 0)} \cdot \frac{2}{\sqrt{\pi}} \sigma \quad (2)$$

The calculation of  $\sigma_o(T)$  was shown to decrease the index of a power in the expression of  $\sigma \sim T^{1/k}$ . This result is qualitatively agreed with changing of  $\sigma_o$  on temperature for constant carrier concentration and acoustic scattering mechanism as defined in [7]:

$$\sigma_o \sim T^{-3/2} m^{*(s-5/2)} \quad \frac{d \ln \sigma_o}{d \ln T} = -\frac{3}{2} - \frac{5}{2}s \quad (3)$$

Some difference of  $s$  determined from  $\alpha$  and  $\sigma$  temperature dependences may be explained by additional impurity scattering which arises due to excess superstoichiometric Te [10]. Thus the change of  $m^*$  dependence on temperature leads to weakening the dependences of  $\sigma(T)$  and  $\alpha(T)$  [9].

As known the figure of merit is given by:

$$Z \sim \frac{(m^*/m)^{3/2} \mu_o}{\kappa_l} \quad (4)$$

where  $\mu_o$  - the charge carrier mobility and  $\kappa_l$  - the thermoconductivity of the crystal lattice.

Temperature dependence of  $(m^*/m)^{3/2} \mu_o$  were calculated from experimental data on  $\alpha$  and  $\sigma$  with account of arbitrary degeneracy for acoustic scattering mechanism. The slope of  $\ln(m^*/m)^{3/2} \mu_o = f(\ln T)$  curves on temperature is shown to decrease, however in considered small interval of  $x$  the change of a slope is slight. The value of  $d \ln(m^*/m)^{3/2} \mu_o / d \ln T$  is equal to 1.4; 1.3 and 1.25 for  $x=0.12, 0.3$  and 0.36, respectively. At the room temperature for  $n - \text{Bi}_2\text{Te}_{3-x}\text{Se}_x$  samples the parameter of  $(m^*/m)^{3/2} \mu_o$  is continuously decreased with increase of  $x$  [10] in the range of the impurity conductivity. Analogous dependence but only at  $T=240-250$  K is observed for the samples, studied here. Thus the solid solutions with the same carrier concentration having the maximum value of parameter  $(m^*/m)^{3/2} \mu_o$  at indicated temperatures are kept its also at low temperatures.

A whole thermoconductivity in the range of impurity conductivity is determined as sum of electron and lattice thermoconductivity:

$$\kappa = \kappa_e + \kappa_l \quad (5)$$

The electron thermoconductivity  $\kappa_e$  was calculated on Weidemann-Franz law:

$$\kappa_l = L \sigma T \quad (6)$$

where L - Lorentz number.

The temperature dependence of  $\kappa_l$  is

$$\kappa_l \sim T \cdot T^{-3/2 - 5/2 s} = T^{-0.5 - 2.5 s} \quad (7)$$

The dependence of  $\kappa_l$  (T) in the solid solution of  $Bi_2Te_{3-x}Se_x$  is decreased and for  $s = -0.2$   $\kappa_l$  value does not change on temperature with increasing of Se concentration. It is shown that the part of  $\kappa_l$  in a whole of  $\kappa$  is decreased with reducing of temperature. In the studied material the ratio of  $\kappa_e/\kappa_l$  is equal to 0.15 in the range of temperature to 80-100 K, near the room temperature this ratio is increased to 0.25. Thus the main contribution to the whole thermoeconductivity of  $\kappa$  is determined by  $\kappa_l$ . The temperature dependence of  $\kappa_l$  in  $Bi_2Te_{3-x}Se_x$  ( $x \leq 1$ ) solid solutions is changed but to  $\kappa_l \sim T^1$  in undoped bismuth telluride to  $\kappa \sim T^{0.5}$  in  $Bi_2Te_2Se$  at higher Debye temperature( $T_D$ ). Specific dependence of  $\kappa_l(T)$  is a strong change of the index of a power k in the expression of  $\kappa_l \sim T^{-k}$  at low Se concentration. In the investigated of the solid solutions for  $x=0.12, 0.3, 0.36$  the  $|k|$  value were shown to change in the interval to 0.6-0.8. Thus with the increase of Se content in  $Bi_2Te_{3-x}Se_x$  solid solution the parameter of  $(m^*/m)^{3/2} \mu_0$  and  $\kappa_l$  have less strong dependence on temperature.

The value of ZT determining the thermoelectric converter parameters is given by relation [11]:

$$ZT \sim \beta \equiv \text{const} (m^*/m)^{3/2} \mu_0 \kappa^{-1} T^{5/2} \quad (8)$$

As follows from the expression (7,8) the value of  $\beta$  is proportional to  $T^2$  for the predominant acoustic scattering mechanism independent on temperature, effective mass and three-phonons scattering processes (for  $T \geq \theta_D$ ). Since in considered solid solution these assumptions do not carry out carefully, it is evidently that the change of  $\beta$  parameter is important in the interval to 80-200 K.

From calculation of  $\beta$  parameter it was shown that  $\beta(T)$  dependence more strong for  $x = 0.12$  ( $\beta \sim T^{1.9}$ ) than for  $x=0.3$  ( $\beta \sim T^{1.8}$ ). So as  $\beta$  has closed values for equal doped of the solid solution at temperatures 240-250 K for  $x=0.12$  and 0.3. It provides the essentially more figure of merit Z for  $x=0.3$  in the range of the temperature below 200 K (Fig.4).

With account of these results it is important to emphasize that the thermoconductivity of crystal lattice  $\kappa_l$  at 300 K is increased with growth of x [12]. However it is not compensated a weak reducing of  $d \ln \kappa_l / d \ln T$  value at low temperatures.

## References

- [1]. V.A. Kutasov, M.V. Vedernikov, P.P. Konstantinov, Yu. I. Ageev, G.T. Alekseeva, L.N. Luk'yanova, Yu.I. Ravich, M.I. Fedorov, Thermoelectric Materials for Temperatures below 150 K, Pis'ma Zh. Tekn. Fiz. 1992, v.18, No.16, pp. 79-82.
- [2]. V.A. Semenyuk, L.D. Ivanova, T.E. Svechnikova, Peculiarity of Applications of Bismuth and Antimonide Chalcogenides of Solid Solution Monocrystals in Miniaturized Coolings, Izv. RAN, ser. Neorg. mater., 1995, v.31, No.1, pp. 32-35.
- [3]. M.V. Vedernikov, V.A. Kutasov, V.L. Kuznetsov, L.N. Luk'yanova, P.P. Konstantinov, Yu.I. Ageev, G.T. Alekseeva, Yu.I. Ravich, M.I. Fedorov, E.A. Izupak, L.M. Gladikh, I.M. Bash, Thermoelectric Cooling to 130 K and Lower Temperature. XIII Intern. Confer. on Thermoelectrics, 1994, Kansas City, Missouri, USA, pp. B4-3.
- [4]. W.A. Tiller, Growth and Perfection of Crystals, 1958, John Wiley and Sons. Inc., N.Y., 329 p.
- [5]. M.V. Vedernikov, P.P. Konstantinov, A.T. Burkov, Development of Automated Techniques of Measuring the Temperature Dependences of Transport Properties of Thermoelectric Materials. VIII Intern. Conf. on Thermoelectric Energy Conversion, 1989, Nancy (France), pp.45-48.
- [6]. V.A. Kutasov, L.N. Luk'yanova, Carrier Density Dependence of the Effective Scattering Parameter of Solid Solutions Based on Bismuth Telluride, Fiz. Tverd. Tela (Leningrad), 1984, v.26, No.8, pp.2501-2504. (Sov. Phys. Sol. St., 1984, v.26, No.8, pp.1515-1516).
- [7]. A.I. Anselm, Introduction to the Theory of Semiconductors, Moscow, 1978, 615 p. (in Russian).
- [8]. B.M. Gol'tsman, V.A. Kudinov, I.A. Smirnov, Semiconductor Thermoelectric Materials Based on  $Bi_2Te_3$ , Nauka, Moscow, 1972, 320 p. (in Russian).
- [9]. B.M. Gol'tsman, G.N. Ikonnikova, V.A. Kutasov, Yu.I. Ravich, Scattering Mechanisms and Temperature Dependence of the Effective Mass of Electrons in Solid Solutions Based on Bismuth Telluride, Fiz. Tverd. Tela (Leningrad), 1985, v.27, No.2, pp. 542-545. (Sov. Phys. Sol. St., 1985, v.27, No.2, pp.334-336).
- [10]. A.I. Anukhin, A.I. Mazina, N.A. Boboshko, V.A. Kutasov, Thermoelectric Properties of  $Bi_{2-x}Sb_xTe_3$  Solid Solutions at Temperatures 300 K. The Abstracts of III Inter-State Meeting on Materials for Thermoelectric Converters, S-Petersburg, 1993, Phys. Tech. Ins. RAS, pp.14-15.
- [11]. R.P. Chasmar and R.J. Stratton, The Thermoelectric Figure of Merit and its Relation to Thermoelectric Generators, J.Electr. Contr., 1959, v.7, No 1, pp.52-72.
- [12]. H.J. Goldsmid, Resent Studies of Bismuth Telluride and its Alloys, J. Appl. Phys., 1961, suppl. to v.32, No. 10, pp. 2198-2202.

## HETEROVALENT REPLACEMENT IN $\text{Bi}_2\text{Te}_3$ : (Sn, Pb, In) SOLID SOLUTIONS

Alekseeva G.T., Vedernikov M.V., Konstantinov P.P., Kutasov V.A., Luk'yanova L.N., Ravich Yu.I.

*A.F. Ioffe Physical-Technical Institute, S-Petersburg, 194021, Russia.*

Electroconductivity, Hall coefficient and thermoelectric power temperature dependences were studied in  $\text{Bi}_2\text{Te}_3$  : (Sn, Pb, In) solid solutions. Anomalous reducing of electroconductivity temperature dependence may be explained by existence of the impurity levels. Stabilization of Fermi level and slow change of charge carrier concentration are shown to observe.

Influence of heterovalent replacement of atoms in cation and anion sublattice of bismuth telluride on transport properties is actively studied at present time and because these materials of p- and n-type conductivity can be used in different thermoelectric converters. Earlier researches of heterovalent substitutions in  $\text{A}^{\text{IV}}\text{B}^{\text{VI}}$  materials are shown to exist of impurity levels, stabilization of Fermi level, resonance scattering at doping different halogens and it is permitted to obtain a new information about energy spectrum and scattering mechanism of charge carriers in  $\text{A}^{\text{IV}}\text{B}^{\text{VI}}$  materials [1]. Heterovalent replacements in the cation sublattice of bismuth telluride doped with In, Pb, Sn, Ge were studied in ref.[2-5]. The influence of In and complicated doping by In+Cl on transport properties of  $\text{Bi}_2\text{Te}_3$  was studied in ref. [3]. Some peculiarities in the dependence of thermoelectric power  $\alpha$  on carrier concentration  $n$  may be explained by existence of heavy holes (by interband scattering). It was found in ref. [5] that the Fermi energy of holes in the high valence band increases with growth of  $x$  in  $\text{Bi}_{2-x}\text{Sn}_x\text{Te}_3$  solid solution, the impurity band being observed near the top of a low valence band.

Present investigation of electroconductivity, thermoelectric power and the components of Hall tensor ( $\rho_{123}$ ,  $\rho_{321}$ ) on temperature (77-300 K) in  $\text{Bi}_{2-x}\text{Sn}_x\text{Te}_3$  ( $x=0.005, 0.01, 0.02$ ) solid solutions doped by donor impurity of  $\text{CdCl}_2$  and also in  $\text{Bi}_{2-x-y}\text{Sn}_x\text{Pb}_y\text{Te}_3$  (for the same of  $x$  value,  $y=0.005, 0.01, 0.02, 0.03$ ) and in  $\text{Bi}_{2-x}\text{In}_x\text{Te}_3$  ( $x=0.005, 0.01, 0.02$ ) were considered. The samples for measurements were grown by directed crystallization method. Monocrystal samples for measurements of the Hall coefficients were cut from polycrystalline ingots. A thermal flow and electrical current are oriented along cleavage planes. Electroconductivity and thermoelectric power are measured by standard stationary method, but for Hall measurements alternative electric and magnetic fields are used [6].

The temperature dependences of  $\sigma$  and  $\alpha$  in  $\text{Bi}_{2-x}\text{Sn}_x\text{Te}_3$  samples doped by  $\text{CdCl}_2$  are shown in, Fig. 1-3. The dependence of  $\sigma(T)$  with growth of Sn concentration (undoped by  $\text{CdCl}_2$ ) is changed from metal to semiconductor like-dependence of conductivity Fig 1. The conductivity of p-type, Fig.1(2,4), is kept in the materials doped with  $\text{CdCl}_2$  at  $x=0.005, 0.01, 0.02$  (metallic dependence of conductivity) and then the conductivity changes to n-type with growth of donor impurity concentration, the value of  $d \ln \sigma / d T$  being strongly increased.

The temperature dependence of the thermoelectric power is also reduced in p-type materials however the change of

$\alpha(T)$  in a highdoped n-type material differs slightly in comparing with  $\text{Bi}_2\text{Te}_3$ , Fig. 3, (3, 5, 7). In  $\text{Bi}_{2-x-y}\text{Sn}_x\text{Pb}_y\text{Te}_3$  solid solution the increase of Pb concentration leads to change of specific temperature dependence of conductivity for constant Sn concentration and  $\sigma(T)$  for  $x=0.01, y=0.01$  and 0.03 have less slope in comparing with  $\text{Bi}_2\text{Te}_3$  : Pb, Fig.3(8,9).

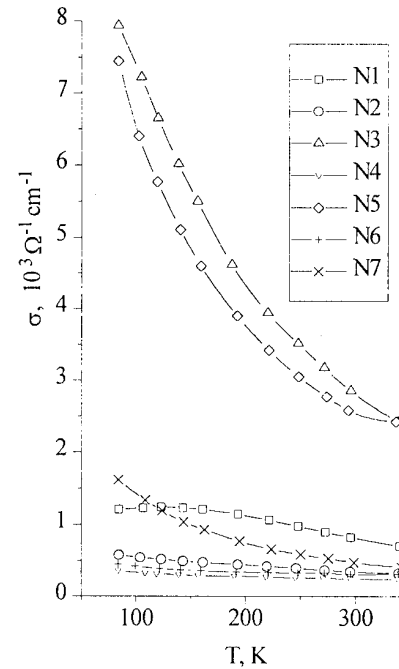


Fig.1. Temperature dependence of the electroconductivity  $\sigma$  in  $\text{Bi}_{2-x}\text{Sn}_x\text{Te}_3$  solid solution.  
x and  $\text{CdCl}_2$  (wt.%) : N1 -0.005 and 0, N2 -0.005 and 0.3, N3 -0.00, and 1, N4 -0.01 and 0.15, N5 -0.01 and 1, N6 -0.02 and 0.3, N7 -0.02 and 1.

The conductivity with account of degeneracy  $\sigma_o(T)$  were calculated from the experimental ( $\alpha, \sigma$ ) data in the solid solutions  $\text{Bi}_{2-x-y}\text{Sn}_x\text{Pb}_y\text{Te}_3$ . The value of  $|s|$  ( $\sigma_o - T^{-s}$ ) was close to 0 in the temperature range of 180-300 K. With increase of  $\text{CdCl}_2$  concentration s value changes from -0.5 to -1.4, close s values being also found for  $\text{Bi}_{2-x-y}\text{Sn}_x\text{Pb}_y\text{Te}_3$  solid solution. These s values were different from specific  $s = -2$  for p- $\text{Bi}_2\text{Te}_3$  and  $s =$

-1.7 for n-Bi<sub>2</sub>Te<sub>3</sub>. Analogous decrease of the thermoelectric power on temperature in the Bi<sub>2-x</sub>Sn<sub>x</sub>Te<sub>3</sub> samples doped by CdCl<sub>2</sub> was found into account of the expression  $\ln F_{1/2} = f \ln(T)$ , Fig.3.

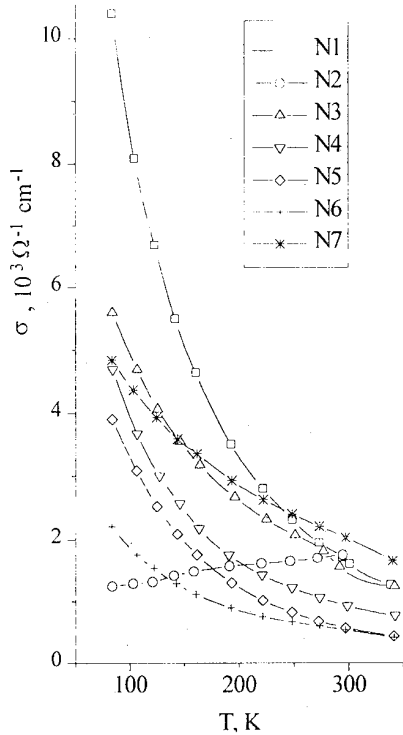


Fig.2. Temperature dependence of the electroconductivity  $\sigma$  in Bi<sub>2-x-y</sub>Sn<sub>x</sub>Pb<sub>y</sub>Te<sub>3</sub> and Bi<sub>2-x</sub>In<sub>x</sub>Te<sub>3</sub> solid solutions.  
Bi<sub>2-x-y</sub>Sn<sub>x</sub>Pb<sub>y</sub>Te<sub>3</sub> : x and y : N1 -0 and 0.01, N2 -0.01 and 0.01, N3 -0.01 and 0.03.  
Bi<sub>2-x</sub>In<sub>x</sub>Te<sub>3</sub> : x and CdCl<sub>2</sub> (wt.%) : N4 -0.005 and 0.15, N5 -0.02 and 0, N6 -0.01 and 0.15, N7 -0.02 and 0.6.

Some peculiarities of the thermoelectric properties of Bi<sub>2-x</sub>In<sub>x</sub>Te<sub>3</sub> system were observed for heterovalent replacement in cation sublattice (Fig.2,3). In spite of In like as Sn are a weak electroactive impurities for Bi<sub>2</sub>Te<sub>3</sub>, it was shown that  $\sigma_0 \sim T^{-s}$  dependence differs only by s value from ones for Bi<sub>2</sub>Te<sub>3</sub> ( $s = -1.5$ ) in the samples with close charge carrier concentrations. The thermoelectric power temperature dependences of  $\alpha(T)$  in the samples n- and p-type with low charge carrier concentrations are closed, and for highdoped samples of n-type the dependences of  $\alpha(T)$  are significantly reduced.

Strong decrease of mobility of charge carriers in n-Bi<sub>2-x</sub>In<sub>x</sub>Te<sub>2.85</sub>Se<sub>0.15</sub> solid solution for addition a small quantity of In [7] is supposed to induce additional charge carrier scattering, due to heterovalent replacement of In to Bi. Peculiarities of the Hall mobility and  $\alpha(T)$  dependences on carrier concentration in Bi<sub>2-x</sub>In<sub>x</sub>Te<sub>3</sub> [3] and  $\sigma(T)$  dependence in Bi<sub>2-x</sub>Sn<sub>x</sub>Te<sub>3</sub> solid solution [5] are explained by the existence of resonance levels, placed near a top of additional extremum of a valence band.

The temperature dependences of Hall tensor components  $\rho_{123}$  and  $\rho_{321}$  (Fig. 4) were measured in Bi<sub>2-x</sub>Sn<sub>x</sub>Te<sub>3</sub> and Bi<sub>2-x-y</sub>Sn<sub>x</sub>Pb<sub>y</sub>Te<sub>3</sub> solid solutions. For undoped samples of p-type solid solutions (Fig. 4, curves 1, 6)  $\rho_{123}$  and  $\rho_{312}$  values are weakly reduced with growth the temperature. The Hall coefficients were significantly reduced with growth the temperature with doping of solid solution by CdCl<sub>2</sub> (0.15 and 0.3 wt.%). Then the dependences of  $\rho_{123}(T)$  and  $\rho_{312}(T)$  were decreased with increase of CdCl<sub>2</sub> (1wt%) in n-type samples (Fig. 4, curve 4). These temperature dependences of  $\rho_{123}$  and  $\rho_{312}$  were qualitatively agreed with ref. [4] for Bi<sub>2-x</sub>Sn<sub>x</sub>Te<sub>3</sub> solid solutions. It is known that the Hall coefficients in p-Bi<sub>2</sub>Te<sub>3</sub> are increased on temperature. Thus the dependences of  $\rho_{123}(T)$  and  $\rho_{312}(T)$  in Bi<sub>2-x</sub>Sn<sub>x</sub>Te<sub>3</sub> solid solution were anomalous a due to increasing of the impurity scattering, the impurity levels of Sn being formed.

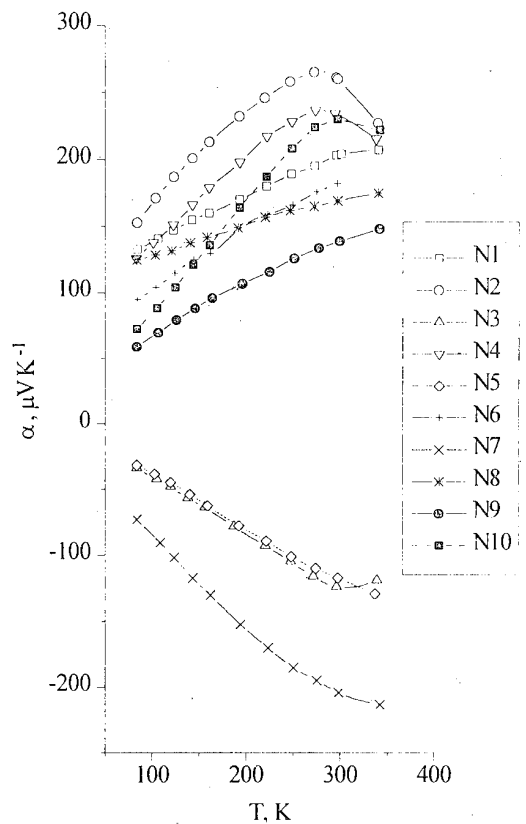


Fig.3. Temperature dependence of the thermoelectric power  $\alpha$  in Bi<sub>2-x-y</sub>Sn<sub>x</sub>Pb<sub>y</sub>Te<sub>3</sub>, Bi<sub>2-x-y</sub>Sn<sub>x</sub>Pb<sub>y</sub>Te<sub>3</sub> and Bi<sub>2-x</sub>In<sub>x</sub>Te<sub>3</sub> solid solutions.  
Bi<sub>2-x-y</sub>Sn<sub>x</sub>Pb<sub>y</sub>Te<sub>3</sub> : x and CdCl<sub>2</sub> (wt.%) : N1 -0.005 and 0, N2 -0.005 and 0.3, N3 -0.005 and 1, N4 -0.01 and 0.3, N5 -0.01 and 1, N6 -0.02 and 0, N7 -0.02 and 1.  
Bi<sub>2-x-y</sub>Sn<sub>x</sub>Pb<sub>y</sub>Te<sub>3</sub> : x and y : N8 -0.01 and 0.01, N9 -0.01 and 0.03.  
Bi<sub>2-x</sub>In<sub>x</sub>Te<sub>3</sub> : x : N10 -0.02

It is known that a Hall coefficient for Bi<sub>2</sub>Te<sub>3</sub>, measured in a weak magnetic field is related to charge carrier concentration in the form:

$$n = \frac{AB}{\rho_{123} e} \quad (1)$$

where  $\Lambda(r_{ef}, \eta)$  - Hall factor,  $B$  - anisotropy parameter, depending on scattering mechanism:

$$B_B = \left[ \left( \frac{\rho_{11} \rho_{1133}}{\rho_{123}^2} + 1 \right) \beta(r_{ef}, \eta) \right]^{-1} \quad (2)$$

$\beta(r_{ef}, \eta)$  - degeneracy parameter,  $\rho_{11}$ ,  $\rho_{1133}$  - the components of resistivity and magnetoresistivity tensors,  $\eta$  - a reduced Fermi level.

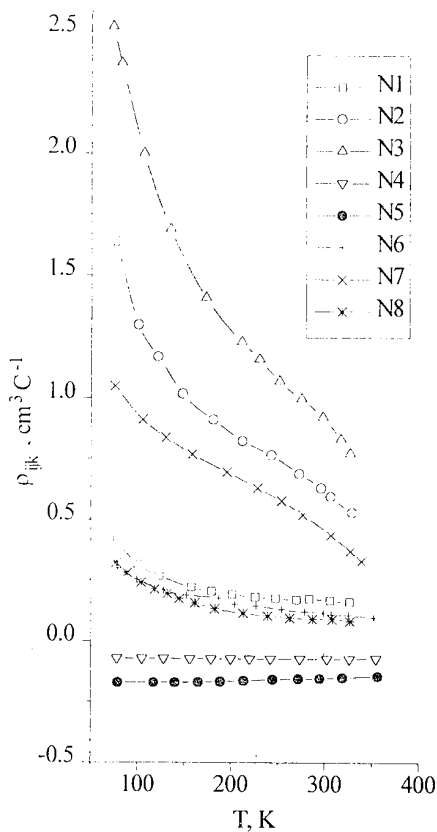


Fig. 4. Temperature dependence of the Hall tensor components  $\rho_{123}$  (N1, N2, N4, N6-N8) and  $\rho_{312}$  (N3, N5) in  $Bi_{2-x}Sn_xTe_3$  and  $Bi_{2-x}Sn_xPb_yTe_3$  solid solutions.

$Bi_{2-x}Sn_xTe_3$  : x and  $CdCl_2$  (wt.%) : N1 -0.005 and 0, N2 -0.005 and 0.3, N3 -0.005 and 0.3, N4 -0.005 and 1, N5 -0.005 and 1, N6 -0.02 and 0, N7 -0.01 and 0.15.

$Bi_{2-x}Sn_xPb_yTe_3$  : x and y : N8 -0.02 and 0.01

In accordance with the expression (1) a charge carrier concentration was evaluated in the samples of n-type solid solutions using  $\Lambda(r_{ef}, \eta)$  and B-parameters from ref. [8] for  $Bi_2Te_3$ . It was shown that in  $Bi_{2-x}Sn_xTe_3$  ( $x=0.005$ ) solid solution the charge carrier concentrations  $n$  were equal to  $1.3 \cdot 10^{19} \text{ cm}^{-3}$  for 0.6 wt.%  $CdCl_2$  and  $1.6 \cdot 10^{19} \text{ cm}^{-3}$  for 1 at.%  $CdCl_2$ , respectively. Whereas  $n$ -value in n-  $Bi_2Te_3 + 1$  wt. %  $CdCl_2$  is equal to  $9.2 \cdot 10^{19} \text{ cm}^{-3}$ . Thus a stabilization of the Fermi level and slow change of carrier concentration are shown to exist in the studied solid solutions.

## References

- [1]. V.I. Kaidanov, Yu.I. Ravich, S.A. Nemov. Electro-Active Impurity Selfcompensation by Intrinsic Defects in IV-VI Semiconductors. Fiz. i Tekn. Poluprovodnikov, 1994, v.28, No.3, p.369-393.
- [2]. H. Tamura. Preparation and Electrical Properties of  $Bi_2Te_3$ -Ge Alloys. Jap. J. Appl. Phys., 1966, v.5, No.7, p.p.593-602.
- [3]. M.K. Zhitinskaya, S.A. Nemov, Yu.I. Ravich, G.S. Bushmarina, I.A. Drabkin, V.V. Kompaneets. Electrophysical Properties of Bismuth Telluride Doped with In. The Abstracts of III Inter-State Meeting on Materials for Thermoelectric Converters, S-Petersburg, 1993, Phys. Tech. Ins. RAS, p.p.10-11, (in Russian).
- [4]. V.A. Kulbachinskii, N.E. Klokovala, J. Horak, P. Lostak, C.A. Azou, G.A. Mironova. Effect of Pressure on Energy Spectrum p- $Bi_2Te_3$ . Fiz. Tverd. Tela, 1989, v.31, No.1, p.p.205-208. (Sov. Phys. Sol. St., 1989, v.31, No.1, p.p.112-114).
- [5]. V.A. Kulbachinskii, M. Inoue, M. Sasaki, H. Negishi, W.X. Gao, K. Takase, Y. Gimai, P. Lostak, J. Horak. Valence-Band Energy Spectrum of Solid Solutions of Narrow-Gap Semiconductor  $Bi_{2-x}Sn_xTe_3$  Single Crystals. Phys. Rev., B, 1994, v.50, No.23, p.p.16921-16930.
- [6]. M.V. Vedernikov, P.P. Konstantinov, A.T. Burkov. Development of Automated Techniques of Measuring the Temperature Dependences of Transport Properties of Thermoelectric Materials. VIII Intern. Conf. on Thermoelectric Energy Conversion, 1989, Nancy, (France), p.p.45-48.
- [7]. G.T. Alekseeva, P.P. Konstantinov, V.A. Kutasov, L.N. Luk'yanova, T.E. Svechnikova, S.N. Chizhevskaya. Transport Phenomena in  $Bi_{2-x}In_xTe_{2.85}Se_{0.15}$  Solid Solutions. Fiz. Tverd. Tela, 1991, v.33, No.12, p.p.3539-3545. (Sov. Phys. Sol. St., 1991, v.33, No.12, p.p.1982-1984).
- [8]. V.A. Kutasov, L.N. Luk'yanova. Influence of Scattering Effective Parameter on State Density Mass and Mobility in Solid Solutions Based on Bismuth and Antimony Chalcogenides. Fiz. i Tech. Poluprovodnikov, 1989, v.23, No.4, p.p.652-656.

## PHONON THERMAL CONDUCTIVITY OF THE THERMOELECTRIC BI-SB ALLOYS

V.D.Kagan, N.A.Red'ko

*A.F.Ioffe Physical-Technical Institute, St.Petersburg, 194021, Russia*

The phonon thermal conductivity of Bi-Sb alloys is separated and its temperature, Sb atoms concentration, lateral dimensions of the samples dependences are analyzed. The electron-phonon interaction in these alloys is discussed. The experimental results for the thermal conductivity are compared with the theory of thermal conductivity for insulators.

### Introduction

The increase of the thermoelectric efficiency of materials can be obtained by the decrease of thermal conductivity ( $\kappa$ ) at nearly constant electrical properties - thermoelectric power and electric conductivity. The semiconducting Bi-Sb alloys have high values of thermoelectric power and electric conductivity, so it is important to investigate the ways to diminish their thermal conductivity.

The total thermal conductivity includes electron and phonon thermal conductivity. A classically high magnetic field allows to suppress the electron component and hence to separate the two components of thermal conductivity. At low temperatures the electron component of  $\kappa$  of the alloy is a negligibly small part of the total thermal conductivity, at high temperatures both components are of the same order of magnitude. We consider only the phonon thermal conductivity.

Bi consists of only one isotope and there is no isotopic phonon scattering which substantially reduces the value of thermal conductivity at low temperatures, so this element is a good model material for the phonon thermal conductivity investigation. Besides perfect Bi single crystals are available.

We use the term "clean" insulator for a material in which phonon scattering on different lattice defects, impurities and isotopes is substantially weaker than phonon-phonon scattering associated with the anharmonicity of lattice oscillations. As was pointed out by Paerls the final value of the thermal conductivity is determined not by the normal processes of the phonon-phonon scattering with the energy and momentum of the phonons being conserved, but by the umklapp-processes, in which phonons give their momentum to the lattice as a whole. The probability of these umklapp-processes is exponentially small at low temperatures, this results in exponential temperature dependence of thermal conductivity. This theory has been proved in experiments with Bi [1, 2].

### Phonon scattering in "dirty" insulator

Starting from pure Bi the binary alloys  $\text{Bi}_{1-x}\text{Sb}_x$  can be prepared, which allows to investigate the dependence of the value of thermal conductivity on the concentration of Sb atoms, which are point defects in these alloys [3]. We investigated alloys with the relative concentration of Sb  $0 \leq x \leq 0.16$  at temperatures  $2 \leq T \leq 300$  K. The monocrystalline samples with the dimensions  $4 \times 4 \times 40$  mm<sup>3</sup> were used for the measurements. These dimensions give rise to the maximum of thermal conductivity located at  $T_M \approx 4$  K.

The temperature dependences of  $\kappa$  for the alloys of different composition are presented on Fig.1. The increase of Sb concentration leads to the decrease of thermal

conductivity relative to its value for pure Bi. Temperature dependence of  $\kappa$  for Bi follows exponential law at  $T_M < T < 10$  K, and power-law for the Bi-Sb alloys. For  $0.08 < x < 0.16$  the thermal conductivity depends on  $T$  as  $T^{-4/3}$ . At temperatures higher than the Debye temperature ( $\Theta_D \approx 120$  K)  $\kappa \sim T^{-1}$  for pure Bi, whereas for the alloys  $\kappa \sim T^{-\alpha}$  where  $\alpha < 1$ . For the alloys with Sb concentration  $0.08 < x < 0.16$   $\alpha \approx 1/3$ .

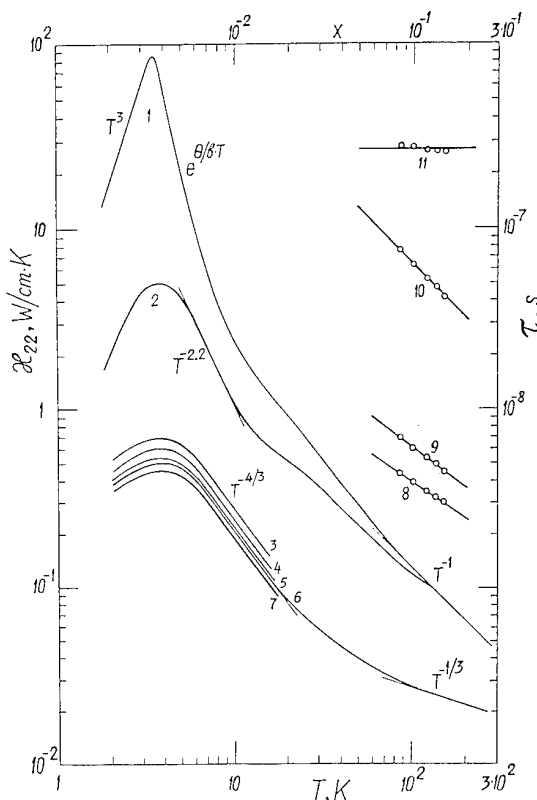


Fig.1 Temperature dependence of the phonon thermal conductivity  $\kappa_{22}(T)$  of single-crystal samples ( $\nabla T \parallel C_1$ ) of bismuth-based alloys (1-7). The figure includes also the following dependences on the concentration of Sb in  $\text{Bi}_{1-x}\text{Sb}_x$  ( $0.085 \leq x \leq 0.15$ ) alloys: 8 - thermal conductivity at  $T=7$  K ( $\kappa \sim x^{-2/3}$ ); 9 - at the maximum thermal conductivity for  $T=4$  K ( $\kappa_M \sim x^{3/4}$ ); 10 - phonon relaxation time  $\tau_{ph}(x)$ ; 11 -  $\tau_{ph}(x)=\text{const.}$  1 - pure bismuth [2]; 2-7 -  $\text{Bi}_{1-x}\text{Sb}_x$  alloys of the compositions  $x=0.001$  (2),  $0.085$  (3),  $0.1$  (4),  $0.12$  (5),  $0.135$  (6),  $0.15$  (7).

The dependence of the thermal conductivity on the concentration of Sb atoms is an important characteristic of the alloy as is the temperature dependence. The phonon scattering on Sb atoms depends on the following function of relative concentration

$$C = \frac{x(1-x)}{\left[1-x \frac{(m_{Bi}-m_{Sb})}{m_{Bi}}\right] \cdot \left[1-x \frac{(\rho_{Bi}-\rho_{Sb})}{\rho_{Bi}}\right]} . \quad (1)$$

For the values of atom masses ( $m$ ) and densities ( $\rho$ ) of Bi and Sb the values of function C are very close to the those of x for  $x \leq 0.16$ . As one can see from Fig.2 thermal conductivity depends on Sb concentration hyperbolically: at low concentrations ( $0.01 < x < 0.1$ )  $\kappa \sim C^{-1/2}$ , at higher concentrations ( $0.1 < x \leq 0.16$ )  $\kappa \sim C^{-3/4}$ .

At temperatures lower than  $T_D$  there is a maximum on the temperature dependence of  $\kappa$  both for "clean" and "dirty" insulators. The temperature dependences of  $\kappa$  mentioned above are characteristic for the temperatures higher than the temperature of the maximum and are caused by phonon scattering in the bulk of the insulator. At temperatures lower than the temperature of the maximum the phonon scattering on the boundary of the sample becomes an important factor. The dependence of the thermal conductivity on the lowest dimension of the sample is an additional characteristic in the investigation of the phonon scattering processes.

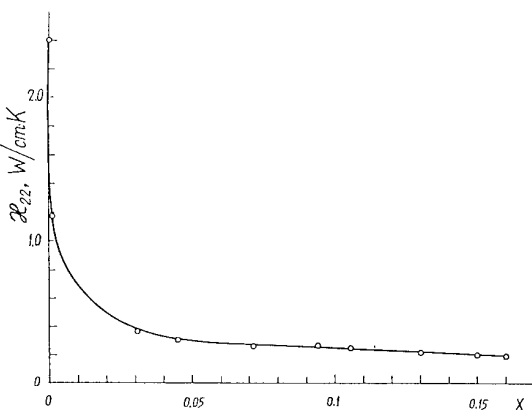


Fig.2 Phonon thermal conductivity  $\kappa_{22}(x)$  of  $\text{Bi}_{1-x}\text{Sb}_x$  ( $0 \leq x \leq 0.16$ ) alloys at  $T=10$  K as a function of the relative antimony concentration  $x$ .

The dependences of the thermal conductivity for the alloy  $\text{Bi}_{0.88}\text{Sb}_{0.12}$  on the temperature and the lowest dimension  $d$  are presented in Fig.3. The dependences of  $\kappa_M$  on  $d$  in pure Bi and in the alloy are differ from each other. In the alloy  $\kappa_M$  depends on Sb atoms concentration as  $\kappa_M \sim C^{-3/4}$ , as it is shown in Fig.1.

Let us consider the  $\kappa(T)$  dependence on Fig.3 at  $T > T_M$ .  $\kappa(T)$  does not depend on  $d$  in a certain temperature region only for  $d \geq 3$  mm. This observation allowed one to obtain the above mentioned power-law temperature dependence of  $\kappa$ , which is determined by bulk phonon scattering process only.

In the isotropic Debye model the thermal conductivity is

$$\kappa = \frac{1}{3(2\pi)^3} \sum_i \int_0^{\Theta/\hbar v_i} v_i^2 \cdot \tau_i(\omega_q) \cdot \hbar \omega_q^i \cdot \frac{\partial N_0}{\partial T} d^3 q , \quad (2)$$

where  $i$  - the phonon branch number, one of them longitudinal (l) and two of them transverse (t),  $v_i$  - the sound velocity,  $\omega_q^i = qv_i$  - the phonon frequency,  $N_0$  - the Plank distribution function,  $\tau(\omega_q)$  - the relaxation time, which includes both the phonon-impurity ( $\tau_{im}$ ) and the phonon-phonon ( $\tau_{ph}$ ) relaxation times

$$\tau^{-1}(\omega_q) = \tau_{im}^{-1}(\omega_q) + \tau_{ph}^{-1}(\omega_q) . \quad (3)$$

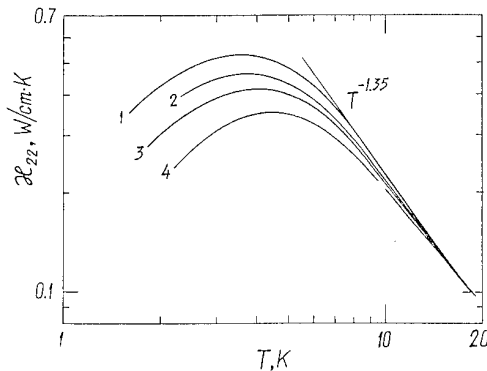


Fig.3 Temperature dependence of the phonon thermal conductivity  $\kappa_{22}$  of a  $\text{Bi}_{0.88}\text{Sb}_{0.12}$  alloy ( $V\Gamma \parallel C_1$ ) for samples with various transverse dimensions. 1 -  $d_1=3.18$  mm,  $d_2=3.3$  mm,  $d=(d_1 \times d_2)^{1/2}=3.2$  mm; 2 -  $d_1=2.3$  mm,  $d_2=2.0$  mm,  $d=2.2$  mm; 3 -  $d_1=1.33$  mm,  $d_2=1.15$  mm,  $d=1.24$  mm; 4 -  $d_1=0.99$  mm,  $d_2=0.8$  mm,  $d=0.88$  mm.

The scattering of phonons on impurities depends very sharply on the phonon frequency [4]

$$\tau_{im}^{-1}(\omega_q) = A \cdot C \cdot \omega_q^4 \quad (4)$$

In the "dirty" insulator the scattering of phonons on impurities dominates the phonon-phonon scattering. However we have to hold the term  $\tau_{ph}^{-1}(\omega_q)$  in the equation (3), because this time depends much weaker on the phonon frequency than  $\tau_{im}^{-1}(\omega_q)$  and allows one to avoid the divergence of the integral (2) on the lower limit. The main contribution to the integral (2) is due to those subthermal phonons, for which the intensity of the phonon-phonon scattering equals the intensity of the phonon-impurity scattering.

For the transverse low-frequency phonons the most important processes are the attachment of a subthermal transverse phonon (t) to a thermal longitudinal phonon (l), accompanied by the formation of a longitudinal thermal phonon (l) and the inverse decay process:

$$\tau_{ph}^{-1}(\omega_q) = B \cdot \omega_q \cdot T^4 \cdot [1 + (\gamma \frac{T}{\Theta})^3]^{-1} . \quad (5)$$

The calculation of the integral (2) leads to the result [3,5]

$$\kappa = \frac{n_t \cdot k \cdot [1 + (\gamma \frac{T}{\Theta})^3]^{1/3}}{3^{5/2} \cdot \pi \cdot v \cdot T^{4/3} \cdot (A \cdot C)^{2/3} \cdot B^{1/3}} , \quad (6)$$

where  $k$  - the Boltzman constant,  $n_t$  - the number of transverse branches ( $n_t=2$ ).

It is a more complex matter to determine  $\tau_{ph}$  because we have to take into account the Herring processes, which incorporate the symmetry of real crystals, where the degeneracy of two transverse branches is possible. In the Herring process a subthermal longitudinal phonon (l)

attaches to a transverse thermal phonon ( $t_1$ ) with the formation of a transverse thermal phonon of the other degenerate transverse branch ( $t_2$ ) [4]. However the consideration of these scattering processes leads to  $\kappa \sim T^{-2} \ln(T/T_0)$  [6], this temperature dependence differs very much from the experimentally obtained and we do not discuss this contribution, which value is presumably very small.

The power-law  $\kappa(T)$  dependences (6) coincide with the experimental ones for the alloys with  $x > 0.08$  at  $T \ll \Theta_D$  and at  $T \gg \Theta_D$  as well. For these alloys the  $\kappa(C)$  dependence (6) also coincides with the experimental one. The fractional power-law dependences of  $\kappa(T, C)$  have been first determined in [3].

In order to investigate the dependence of  $\kappa$  on transverse dimension we have found a solution of the kinetic equation for the phonons in the finite cylinder with radius  $d/2$ . The boundary phonon scattering have been supposed to be diffusive. Calculating the total energy flux and averaging it over the circular cross section of the sample, we can get the following expression for maximal thermal conductivity [3,5]

$$\kappa_M = 0.0562 \cdot \frac{k \cdot d^{1/4}}{v^{5/4} \cdot (A \cdot C)^{3/4}}. \quad (7)$$

The power-law dependences  $\kappa_M(d, C)$  in the equation (7) coincide with the experimental ones. So we can state that the thermal conductivity of  $\text{Bi}_{1-x}\text{Sb}_x$  alloys at  $0.08 < x \leq 0.16$  can be satisfactorily described by the theory of "dirty" insulators both at the maximum of temperature dependence and at  $T > T_M$ .

The comparison of the theoretical dependences (6,7) and the experimental ones allowed us to obtain relaxation times for the phonon-phonon and phonon-impurity scattering. The coefficients in the equations (4) and (5) are  $A=2.2 \times 10^{-40} \text{ s}^3$ ,  $B=1.7 \times 10^{-9} \text{ K}^{-4}$ ,  $\gamma=3.6$ . The obtained relaxation times can be used for the description of kinetic phenomena involving subthermal phonons.

#### The electron-phonon scattering

The alloys of Bi with Sb isovalent atoms have been doped by electrically active Te, Sn impurities leading to the creation of free charge carriers and to the additional source of scattering for phonons. Hence the thermal conductivity depends on the charge carriers characteristics - their effective mass and concentration [7]. Doping by Te atoms strongly increases the electron concentration, doping by Sn atoms - the hole concentration. As is shown on Fig. 4, 5 phonon scattering on these charge carriers substantially reduces the thermal conductivity at  $T < 10 \text{ K}$ .

The parabolic electron dispersion law leads to the following expression for the electron-phonon relaxation time in degenerated semiconductors and metals [8]

$$\tau_e^{-1} = \frac{U^2 \cdot m^2 \cdot q}{2\pi \cdot \hbar^3 \cdot \rho}, \quad (8)$$

where  $U$  - the constant of the deformation potential,  $m$  - electron effective mass,  $\hbar q$  - the phonon quasimomentum. When scattering of phonons by electron dominates, substitution of equation (8) in equation (2) leads to the quadratic temperature dependence of thermal conductivity. The observed maximum in the temperature dependence of phonon thermal conductivity of the semiconductor is determined exclusively by phonon scattering in the bulk of the sample, while in an insulator it is determined by phonon scattering by the boundaries of the sample.

In p-type alloy charge carriers are heavy  $\Sigma$ -holes with the effective mass  $0.9m_0$  and we can use parabolic equation (8) for the calculation of  $\kappa$ . In the region of quadratic dependence of  $\kappa$  on temperature the thermal

conductivity does not depend on the hole concentration. For n-type alloys we used a nonparabolic and anisotropic electron dispersion law of Kane's model

$$E = \left[ \left( \frac{E_g}{2} \right)^2 + \frac{E_g}{2} \left( \frac{p_1^2}{m_1} + \frac{p_2^2}{m_2} + \frac{p_3^2}{m_3} \right) \right]^{1/2} - \frac{E_g}{2}, \quad (9)$$

where  $E_g$  - the band gap,  $m_i$  - the electron effective masses along three mutually perpendicular axes. Then for the electron-phonon relaxation time we get [7]

$$\tau_e^{-1} = \frac{U^2 \cdot q \cdot N \cdot (m_1 m_2 m_3)^{2/3}}{2\pi \cdot \hbar^3 \cdot \rho} \left( 1 + \frac{2\mu}{E_g} \right)^2, \quad (10)$$

where  $\mu$  - the electron chemical potential,  $N$  - the number of ellipsoids with the electron dispersion law (9). Due to equation (10)  $\kappa$  depends on electron concentration even in the region of parabolic temperature dependence of  $\kappa$ .

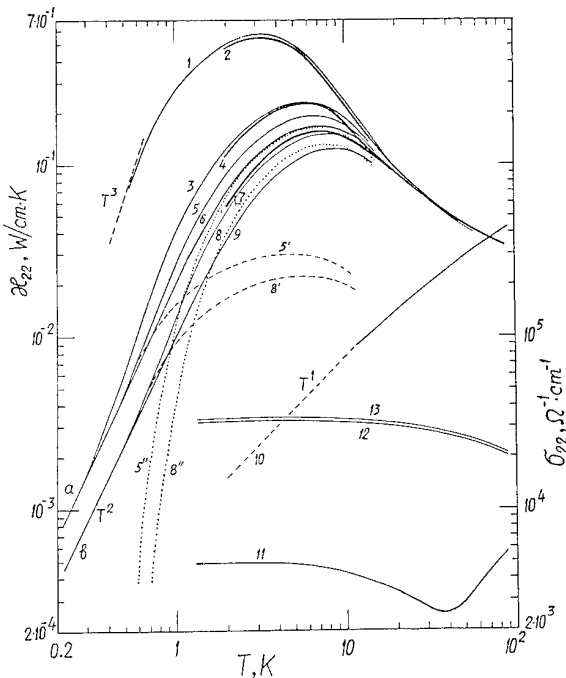


Fig.4 Experimental data on the temperature dependence of the phonon thermal conductivity  $\kappa_{22}$  (2, 4, 7) and of the conductivity  $\sigma_{22}$  (11-13) for  $\text{Bi}_{0.9}\text{Sb}_{0.1}$  samples Nos.1-3 (j,  $VT||C_1$ ). Values of the phonon thermal conductivity are computed taking into account scattering by electrons (3, 5, 6, 8, 9) and neglecting scattering of phonons by electrons (1). Curve 10 - electron component of the thermal conductivity for sample No.2. a - Calculation  $\kappa_{22}$  according to Eq.(21) [7] with  $D=4 \times 10^6 \text{ s}^{-1}\text{K}^{-1}$  and different characteristic temperatures:  $\Theta_e = 4 \text{ K}$  (3),  $5 \text{ K}$  (5) (curve 5' represents the contribution of the first integrals of Eq.(21) to  $\kappa_{22}$  and curve 6' represents the contribution of the second integral) and  $6 \text{ K}$  (6); b - Calculation of  $\kappa_{22}$  according to Eq.(21) [7] with  $D=8 \times 10^6 \text{ s}^{-1}\text{K}^{-1}$  and different characteristic temperatures:  $\Theta_e = 6 \text{ K}$  (8) (curve 8' represents the contribution of the first integrals of Eq.(21) to  $\kappa_{22}$  and curve 8'' represents the contribution of the second integral) and  $8 \text{ K}$  (9). Parameters of the samples: 1 -  $n_1 = 8.6 \times 10^{15} \text{ cm}^{-3}$ ,  $m_{d1}(E_F)/m_0 = 0.045$ ; 2 -  $n_2 = 1.4 \times 10^{19} \text{ cm}^{-3}$ ,  $m_{d2}(E_F)/m_0 = 0.42$ ; 3 -  $n_3 = 4.5 \times 10^{19} \text{ cm}^{-3}$ ,  $m_{d3}(E_F)/m_0 = 0.62$ .

According to the experimental data for  $\kappa$  (Figs. 4 and 5) the phonon thermal conductivity does not exhibit a parabolic dependence as the temperature decreases to 2 K, but only approaches it. For this reason in this temperature range one has to take into account the scattering of phonons not only by electrons but also by impurities, by the boundaries of the sample and by one another.

Consideration of the contribution to the thermal conductivity of all phonon scattering processes, which have comparable values, were performed by numerical calculations [7]. The Debye temperature  $\Theta_D=90\text{K}$  was used for the transverse branch and  $\Theta_D=135\text{K}$  for the longitudinal branch. The phonon-impurity relaxation time was taken from [4], the phonon-phonon collision time for the transverse branches - from [5]. For the longitudinal branch Herring's relaxation time was used, value of which was selected in the course of calculations. Proper choice of the parameters allowed us to adjust calculated and experimental data on thermal conductivity for the alloys with low carrier densities, the contribution of longitudinal branch was found to be negligibly small. At the consideration of electron-phonon relaxation it should be noted that only those phonons interact with the electrons whose quasimomentum is less or

equal to the twice the electron momentum. Hence the integrals on phonon frequencies can be divided into two integrals: the first takes into account phonons with the energy not exceeding  $\Theta_e^i = 2p_F \cdot v^i$ , which scatter on electrons, and the second one takes into account phonons with the energy higher than  $\Theta_e^i$ , which do not scatter on electrons.

Consideration of the contribution of electron-phonon scattering with the relaxation time (10) leads to the satisfactory agreement of calculated and experimental data in the temperature region near the thermal conductivity maximum. We continued the calculated curves of thermal conductivity towards temperatures lower than 2 K, where these curves showed quadratic temperature dependence due to predominance of electron-phonon scattering. As it can be expected at these low temperatures the thermal conductivity for p-type alloys does not depend on the hole concentration, but for n-type alloys it depends on the electron concentration.

### Conclusions

The phonon thermal conductivity in semiconducting  $\text{Bi}_{1-x}\text{Sb}_x$  alloys ( $0.08 < x \leq 0.16$ ) can be very well described by the theory of "dirty" insulators with the frequency of phonon-impurity scattering exceeding that of phonon-phonon scattering. In semiconducting alloys doped with electrically active impurities the characteristics of phonon scattering processes determined above were supplemented by taking into account the electron-phonon scattering process with nonparabolic dispersion law for the electron energy. Numerical calculations lead to the satisfactory description of thermal conductivity in the whole temperature range where the electron-phonon scattering exists.

### References

- [1]. V.N.Kopylov and L.P.Mezhov-Deglin, Investigation of the kinetic coefficients of bismuth at helium temperatures, *Sov. Phys. JETP* 1974, v.38, p.357; L.P.Mezhov-Deglin, V.N.Kopylov, E.S.Medvedev, Contribution of various phonon relaxation mechanisms to the thermal resistance of the crystal lattice of bismuth at temperatures below 2 K, *Sov. Phys. JETP*, 1975, v.40, p.557.
- [2]. J.-P.Issi, J.Hermanns. The thermal conductivity of the group V semimetals. *Proc. XV Int. Conf. on Thermal Conductivity*, Ottawa, 1977. pp.63-72.
- [3]. V.D.Kagan and N.A.Red'ko, Phonon thermal conductivity of bismuth alloys, *Sov. Phys. JETP*, 1991, v.73, No.4, pp.664- 671.
- [4]. V.L.Gurevich, *Transport in Phonon Systems*, Nauka, Moscow, 1980, p.400 (North-Holland, Amsterdam, 1986).
- [5]. V.D.Kagan and N.A.Red'ko, Phonon relaxation times in bismuth, *Sov. Phys. Solid State*, 1993, v.35, No.6, pp.849-854.
- [6]. R.N.Gyrzhii and A.O.Maksimov, Kinetic equation for thermal phonons with finite mean free time and thermal conductivity of dielectrics, *Sov. J. Low Temp. Phys.*, 1977, v.3, p.171.
- [7]. N.A.Red'ko and V.D.Kagan, Effect of the electron-phonon interaction on the phonon thermal conductivity of Bi-Sb semiconductor alloys, *Sov. Phys. Solid State*, 1994, v.36, No.7, pp.1081-1089.
- [8]. J.Ziman, *Electrons and Phonons*, Clarendon Press, Oxford, 1960.

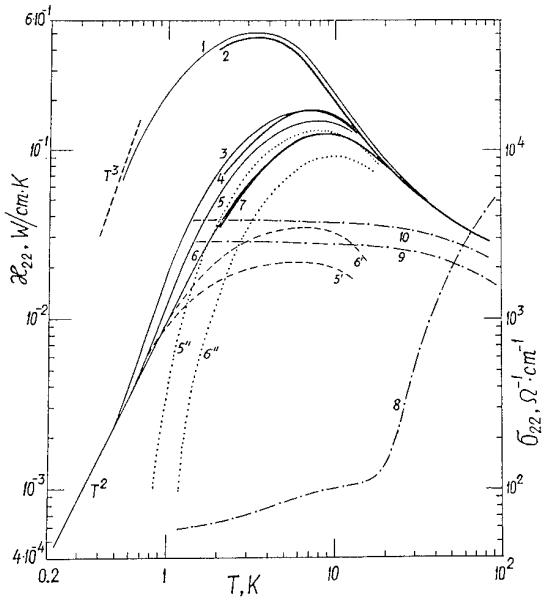


Fig.5 Experimental data on the temperature dependence of the phonon thermal conductivity  $\kappa_{22}$  (2, 4, 7) and the conductivity  $\sigma_{22}$  (8-10) for  $\text{Bi}_{0.88}\text{Sb}_{0.12}$  samples Nos.1-3 (j,  $\text{VT}||\text{C}_1$ ). The phonon thermal conductivity  $\kappa_{22}$  was calculated neglecting scattering of phonons by electrons (1) and taking into account scattering of phonons by electrons; the calculations were performed using Eq.(21) [7] with  $D=8 \times 10^6 \text{ s}^{-1}\text{K}^{-1}$  and different characteristic temperatures:  $\Theta_e = 5 \text{ K}$  (3),  $6 \text{ K}$  (5), and  $8 \text{ K}$  (6). The curves 5' and 6' represent the contribution to  $\kappa_{22}$  from the first integral of Eq.(21), and curves 5'' and 6'' represent the contribution from the second integral. Parameters of the samples: 1 -  $p_{L1} = 1.6 \times 10^{14} \text{ cm}^{-3}$  ( $m_{DL}(E_F)/m_0 = 0.033$ ); 2 -  $p_{L2} = 4 \times 10^{17} \text{ cm}^{-3}$  ( $m_{DL}(E_F)/m_0 = 0.13$ ),  $p_{T2} = 2.5 \times 10^{17} \text{ cm}^{-3}$  ( $m_{DT}(E_F)/m_0 = 0.14$ ),  $p_{S2} = 4.5 \times 10^{18} \text{ cm}^{-3}$  ( $m_2/m_0 = 0.9$ ); 3 -  $p_{L3} = 1 \times 10^{18} \text{ cm}^{-3}$  ( $m_{DL}(E_F)/m_0 = 0.17$ ),  $p_{T3} = 9 \times 10^{17} \text{ cm}^{-3}$  ( $m_{DT}(E_F)/m_0 = 0.16$ ),  $p_{S3} = 1.5 \times 10^{19} \text{ cm}^{-3}$  ( $m_2/m_0 = 0.9$ ).

## THERMOELECTRIC EFFICIENCY OF SEMICONDUCTING BI-SB ALLOYS

N.A.Red'ko

A.F.Ioffe Physical-Technical Institute, St.Petersburg, 194021, Russia

Physical reasons which lead to the difference of the thermoelectric efficiency of the n- and p-type branches of the thermoelements made of Bi-Sb semiconducting alloys are discussed.

The semiconducting Bi-Sb alloys have high thermoelectric efficiency ( $Z > 5 \times 10^{-3} \text{ K}^{-1}$ ) [1, 2, 3, 4] and are used as n-branches for low temperature thermoelements. Our experimental data for the temperature dependences of thermoelectric power ( $\alpha$ ), resistivity ( $\rho$ ), thermal conductivity ( $\kappa$ ) and thermoelectric efficiency for semiconducting n- and p-type  $\text{Bi}_{1-x}\text{Sb}_x$  ( $0.12 \leq x < 0.14$ ) alloys are presented on Figs. 1, 2. Our investigations of semiconducting Bi-Sb alloys elucidated the origin of high thermoelectric efficiency of n-branch and low thermoelectric efficiency of p-branch.

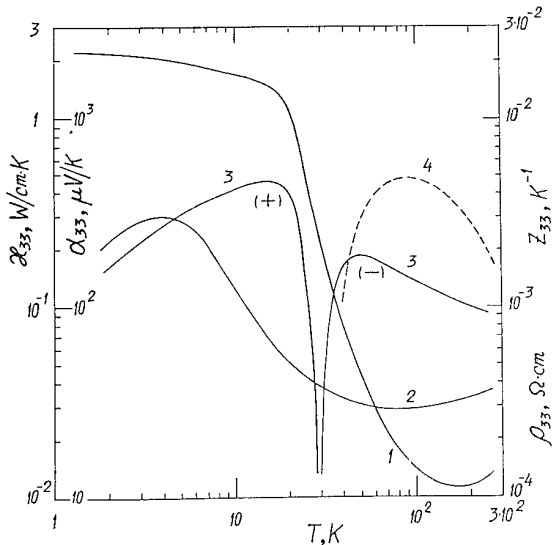


Fig.1 Temperature dependences of the resistivity  $\rho_{33}$  - (1), the thermal conductivity  $\kappa_{33}$  - (2), the thermoelectric power  $\alpha_{33}$  - (3) and the thermoelectric efficiency  $Z_{33}$  - (4) for p- $\text{Bi}_{0.88}\text{Sb}_{0.12}$  alloy ( $\nabla T, j \parallel C_3, p_L = 1.6 \times 10^{14} \text{ cm}^{-3}$  at  $T=4 \text{ K}$ ).

It was shown experimentally by many authors, that in the region of intrinsic conductivity the thermoelectric power of semiconducting alloys is always negative [1, 4-7], the sign of the thermoelectric power at low temperatures in the region of extrinsic conductivity can be either negative or positive according to the type of doping. The experimental data of the temperature dependence of the thermoelectric power for the n- and p-type semiconducting  $\text{Bi}_{1-x}\text{Sb}_x$  alloys ( $E_{gL}, E_T, E_\Sigma$ ) [8] presented on Fig. 3 clearly show the transition from extrinsic conductivity to intrinsic one at  $T > 30 \text{ K}$ .

Due to the narrow band gap ( $E_{gL} \leq 18 \text{ meV}$ ) of the semiconducting alloys this transition takes place at low temperatures. An increase of charge carrier concentration of these alloys leads to the shift of the transition temperature

to higher temperatures. An analysis of the temperature dependence of thermoelectric power in semiconducting alloys [8] showed that the negative sign of thermoelectric

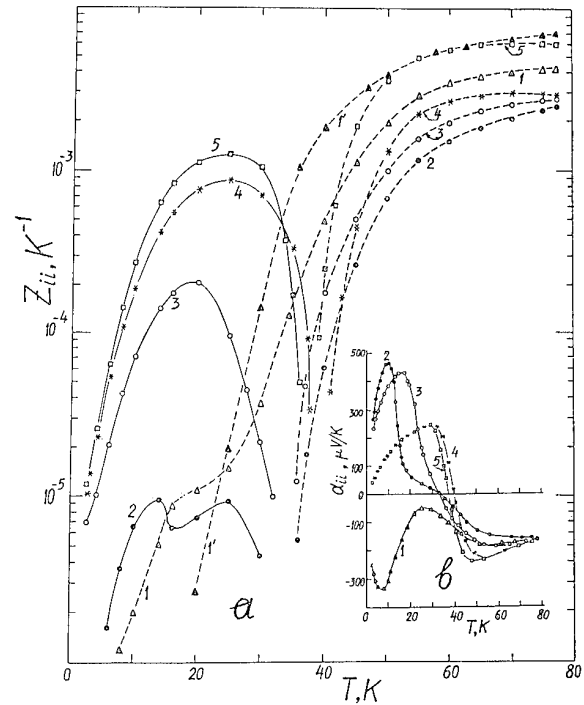


Fig.2 a) Temperature dependences of the thermoelectric efficiency  $Z_{ii}$  for specimens 1-5. The numbers on the curves correspond to the specimen number. The continuous  $Z_{ii}^p$  curves are for specimens with positive thermoelectric power. The dashed  $Z_{ii}^n$  curves are for specimens with negative thermoelectric power. b) - Temperature dependence of the magnetothermoelectric efficiency  $Z_{33,22}$  for specimen 1 in magnetic field  $H=0.8 \text{ kOe}$  at  $H \parallel C_1$ . b) Temperature dependence of thermoelectric power  $\alpha_{ii}$  for specimens 1-5. The numbers on the curves correspond to the specimen number. Basic parameters of specimens of the  $\text{Bi}_{1-x}\text{Sb}_x$  alloy ( $0.12 \leq x < 0.14$ ) are shown in the table.

Specimen number	Concentration $x \pm 0.005$	$\nabla T, j \parallel C_i$	$n, p_L, \text{cm}^{-3}$ ( $T=4 \text{ K}$ )
1	0.132	$C_3$	$n=4.1 \times 10^{13}$
2	0.125	$C_1$	$p=4.4 \times 10^{13}$
3	0.12	$C_1$	$p=2.1 \times 10^{14}$
4	0.135	$C_1$	$p=4.6 \times 10^{15}$
5	0.135	$C_3$	$p=4.6 \times 10^{15}$

power in the region of intrinsic conductivity is due to the peculiarities of the band structure of these alloys.

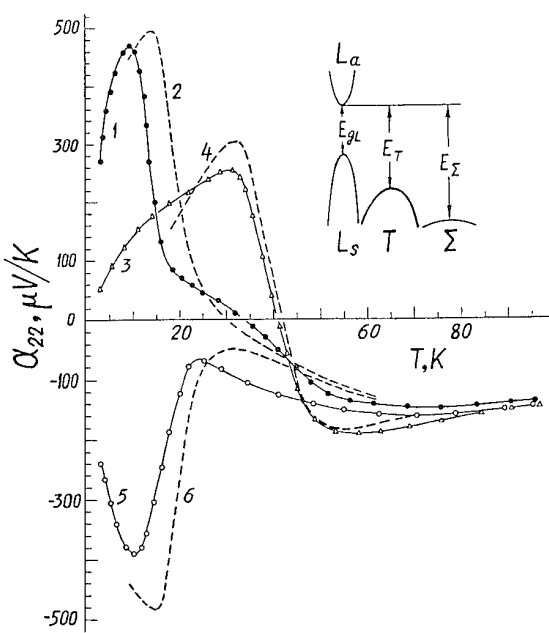


Fig.3 Temperature dependences of the thermoelectric power  $\alpha_{22}$  ( $VT \parallel C_1, H=0$ ) of  $Bi_{1-x}Sb_x$  alloys ( $E_{GL}, E_T, E_\Sigma$ ): 1, 3, 5 - experimental data for p-type  $Bi_{0.88}Sb_{0.115}$  ( $E_{GL}=16$  meV,  $E_T=30$  meV,  $E_\Sigma=37$  meV), p-type  $Bi_{0.86}Sb_{0.135}$  (20, 44, 33 meV), and n-type  $Bi_{0.88}Sb_{0.12}$  (17, 34, 36 meV) respectively; 2, 4, 6 - calculated curves taking into account the band structure shown in the insert obtained [8].

It is seen from the band structure of the alloys presented on Fig. 4 that the conductivity band remains a single one up to the electron energy  $E_{FL}=150$  meV. The valence band of the alloys is complex one and consists of a subband of light holes with the extremum in the point L of Brillouin band and closely spaced subband of heavy holes with the extrema in points T [9] and  $\Sigma$  [10]. So in the region of intrinsic conductivity of these alloys in addition to electrons  $L_a$  and light holes  $L_s$  heavy holes  $\Sigma$  and (or) T also take part in transport phenomena.

In the region of intrinsic conductivity in the valence band of these alloys a redistribution of charge carriers among bands  $L_s$  and  $\Sigma$ , T takes place according to their density of states. The state - density effective mass of holes at the top of  $L_s$  band depends on the alloy composition [11] and for  $Bi_{0.88}Sb_{0.12}$  alloy it is  $0.032m_0$ . Whereas at the top of T and  $\Sigma$  bands it amounts to  $0.14m_0$  and  $0.9m_0$  respectively and does not depend on the alloy composition ( $x < 0.17$ ). So eventually the contribution of light and heavy holes to the thermoelectric power appears small in comparison with that of the electrons in the region of intrinsic conductivity of the alloys, which follows from the analysis of the experimental data [8]. It can be interpreted qualitatively as:  $n_{La} \equiv p_{Ls} + p_\Sigma$  and  $p_\Sigma > p_{Ls}$ ,  $\sigma_{La} > \sigma_\Sigma, \sigma_{Ls}$  and one gets for the thermoelectric power:  $\alpha = (\alpha_{Ls} \times \sigma_{Ls} + \alpha_\Sigma \times \sigma_\Sigma - \alpha_{La} \times \sigma_{La}) / (\sigma_{Ls} + \sigma_\Sigma + \sigma_{La}) \approx -\alpha_{La} / (\sigma_{Ls} + \sigma_\Sigma + \sigma_{La})$ .

According to our investigation the peak thermoelectric efficiency for n-branch made of semiconducting alloys is  $Z=6 \times 10^{-3} K^{-1}$  [4]. This high value

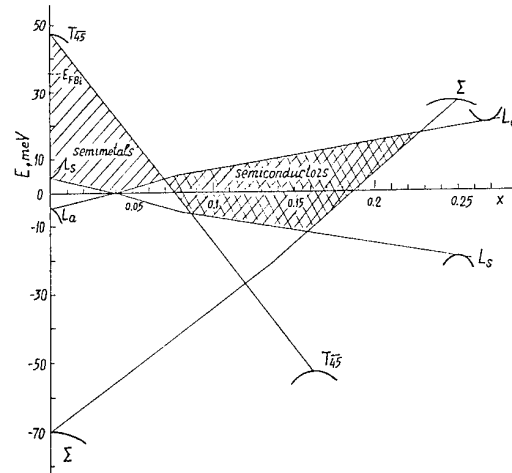


Fig.4 Rearrangement of the energy spectrum of  $Bi_{1-x}Sb_x$  alloys with variation in antimony concentration.

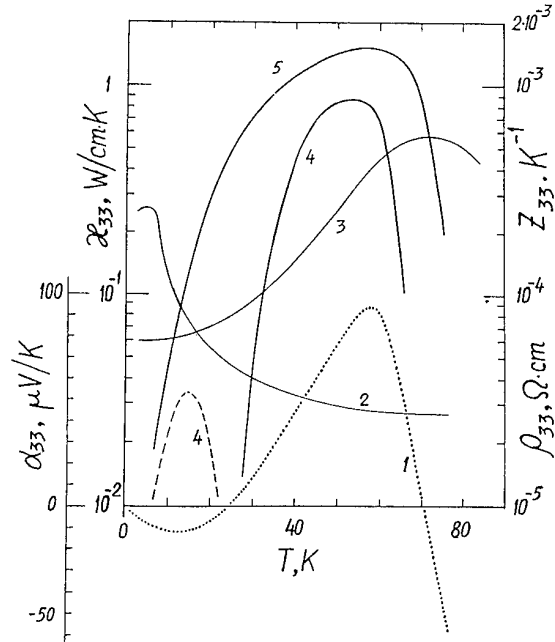


Fig.5 Temperature dependences of the thermoelectric power  $\alpha_{33}$  - (1), the thermal conductivity  $\kappa_{33}$  - (2), the resistivity  $\rho_{33}$  - (3), the thermoelectric efficiency:  $Z_{33} (H=0)$  - 4,  $Z_{33} (H=0.8 \text{ kOe at } H \parallel C_1)$  - (5) for  $Bi_{0.87}Sb_{0.13}$  alloy ( $VT, j \parallel C_3, \rho_L=1.5 \times 10^{17} \text{ cm}^{-3}, p_\Sigma=1.1 \times 10^{18} \text{ cm}^{-3}$  at  $T=4 \text{ K}$ ). The transition into the intrinsic conductivity range takes place at 70 K.

of  $Z$  is due to the high thermoelectric power for nondegenerate electronic gas and considerable electron

conductivity associated with the small effective masses of electrons and the small thermal conductivity of the alloys.

There are no such favourable conditions when Bi-Sb alloys are used as a p-branch. The strong doping of the alloy by acceptor impurity results in expansion of extrinsic hole conductivity temperature region to high temperatures. However for degenerated statistics the value of thermoelectric power is rather low ( $\alpha \sim kT/\zeta$ ). The increase of hole concentration leads to the negligibly small increase of the conductivity because of the high impurity concentration, which reduces the hole mobility via the hole-acceptor scattering. As a result the thermoelectric efficiency of alloy for p-branch ( $Z < 1 \cdot 10^{-3} \text{ K}^{-1}$ ) becomes lower than for n-branch [4].

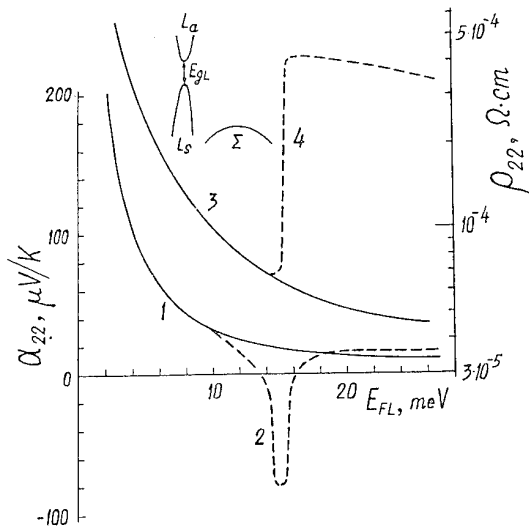


Fig.6 The thermoelectric power  $\alpha_{22}$  at  $T=12$  K and the resistivity  $\rho_{22}$  at  $T=4$  K for n-type and p-type  $\text{Bi}_{0.88}\text{Sb}_{0.12}$  ( $j, VT||C_1$ ) versus the Fermi energy  $E_{FL}$ . 1 - The absolute value of the thermoelectric power,  $|\alpha_{22}^n(E_{FL})|$  of the alloy n- $\text{Bi}_{0.88}\text{Sb}_{0.12}$  (solid line); 2 - the thermoelectric power  $\alpha_{22}^p(E_{FL})$  of the alloy p- $\text{Bi}_{0.88}\text{Sb}_{0.12}$  ( $\alpha_{22}^p(E_{FL}) \cong |\alpha_{22}^n(E_{FL})|$  at  $E_{FL} < 15$  meV); 3, 4 - the resistivity of the alloy n- $\text{Bi}_{0.88}\text{Sb}_{0.12}$  (solid line) and of the alloy p- $\text{Bi}_{0.88}\text{Sb}_{0.12}$  (dashed line,  $(\rho_{22}^p(E_{FL}) \cong \rho_{22}^n(E_{FL})$  at  $E_{FL} < 15$  meV). Shown at the top is an energy diagram of the  $L_a$ ,  $L_s$ ,  $\Sigma$  extrema for the semiconducting alloy  $\text{Bi}_{0.88}\text{Sb}_{0.12}$  with an energy gap  $E_{GL}=17.2$  meV.

Experimental data for the transport phenomena in p-type  $\text{Bi}_{0.87}\text{Sb}_{0.13}$  alloy are presented on Fig. 5. It is necessary to point out that at gradual doping of the semiconducting alloy by acceptor impurity Fermi level falls gradually in the valence band and at definite concentration of acceptors it enters the heavy hole band, that is a topological electron transition takes place. At the beginning of this transition when the concentration of heavy holes is much less than that of the light holes the temperature and concentration dependences of thermoelectric power show an anomalous behaviour. According to the experimental data shown on Figs. 5 and 6 the thermoelectric power changes its sign from positive to a negative one due to the interband scattering of the light

holes  $L_s$  to the heavy holes band  $\Sigma$  ( $L_s \Leftrightarrow \Sigma$ ). This conclusion was obtained by an analysis published in [12, 13]. Application of the magnetic field of 0.8 kOe to such a sample eliminates this anomaly and the working temperature range of p-branch expands and the thermoelectric efficiency increases up to the value  $Z \cong 1 \times 10^{-3} \text{ K}^{-1}$  [4]. This result is shown on Fig. 5.

## Conclusion

The peculiarities of the energy band structure of the semiconducting Bi-Sb alloys, associated with the presence in the valence band both light and heavy holes, lead to the difference of the thermoelectric efficiency of the n- and p-type branches of the thermocouples operated at temperatures near 100 K made of these alloys.

## References

- [1]. W.M.Yim, A.Amith, Bi-Sb alloys for magnetothermoelectric and thermomagnetic cooling, *Solid-State Electronics*, 1972, v.15, No.10, pp.1141-1165.
- [2]. G.A.Ivanov, V.A.Kulikov, V.L.Naletov, A.F.Panarin, A.R.Regel', Thermoelectric quality factor for pure and doped bismuth-antimony alloys in a magnetic field, *Sov. Phys. Semicond.*, 1972, v.6, p.1134.
- [3]. V.S.Zemskov, V.P.Gusakov, A.S.Roslov, A.D.Belya, V.V.Rozhdestvenskaya, Magnethotermoelectrical quality of the bismuth-antimony solid solutions alloyed by tellurium, *Sov. Phys. Dokl.*, 1975, v.20, p.339.
- [4]. N.A.Rodionov, G.A.Ivanov, N.A.Red'ko, Thermoelectric efficiency of  $\text{Bi}_{1-x}\text{Sb}_x$  ( $0.12 \leq x \leq 0.14$ ) p-type alloys at low temperatures, *Sov. Phys. Solid State*, 1982, v.24, No.6, pp.1074-1075.
- [5]. G.E.Smith, R.Wolfe, Thermoelectric properties of bismuth-antimony alloys, *J. Appl. Phys.*, 1962, v.33, No.3, pp.841-846.
- [6]. D.M.Brown, S.J.Silverman, Electrons in Bi-Sb alloys, *Phys. Rev.*, 1964, v.136A, No.1, pp.290-299.
- [7]. W.Lehnefinke, G.Schneider, Die elektrischen transportgrößen von dotiertem  $\text{Bi}_{0.88}\text{Sb}_{0.12}$  *Z.Naturforschung*, 1969, b.24a, h.10, pp.1594-1601.
- [8]. N.A.Red'ko, V.I.Belitskii, V.V.Kosarev, N.A.Rodionov, V.I.Pol'shin, Bands of heavy holes and sign of the thermoelectric power of Bi-Sb alloys, *Sov. Phys. Solid State*, 1986, v.28, No.12, pp.2111-2112.
- [9]. N.B.Brandt, R.Herrmann, G.I.Golysheva, L.I.Devyatova, D.Kusnik, V.Kraak, and Ya.G.Ponomaryov, Electron fermi surface in semimetal alloys  $\text{Bi}_{1-x}\text{Sb}_x$  ( $0.23 \leq x \leq 0.56$ ), *Sov. Phys. JETP*, 1982, v.56, p.1247.
- [10]. N.A.Red'ko, N.A.Rodionov, Topological phase transitions in  $\text{Bi}_{1-x}\text{Sb}_x$  alloys and composition dependence of the position of the heavy-hole band, *JETP Lett.*, 1985, v.42, No.6, pp.303-306.
- [11]. N.A.Red'ko, V.I.Pol'shin, V.V.Kosarev, G.A.Ivanov, Electronic density of states and its mass in the alloys  $\text{Bi}_{1-x}\text{Sb}_x$ , *Sov. Phys. Solid State*, 1983, v.25, No.10, pp.1807-1811.
- [12]. O.S.Gryaznov, G.A.Ivanov, B.Ya.Moizhes, V.N.Naumov, V.A.Nemchinskii, N.A.Rodionov, N.A.Red'ko, The effect of interband scattering on kinetic phenomena in p-type  $\text{Bi}_{1-x}\text{Sb}_x$ , *Sov. Phys. Solid State*, 1982, v.24, No.8, pp.1326-1330.
- [13]. N.A.Red'ko, Relaxation time of the interband scattering of  $L_s$  holes in the alloy p- $\text{Bi}_{0.88}\text{Sb}_{0.12}$ , *JETP Lett.*, 1992, v.55, No.5, pp.266-269.

# Transport Properties and Electronic Structure of Bismuth-Antimony Single Crystals doped by Tellurium at 80-530 K Temperature Range

V. Grabov<sup>1</sup>, D. Kolgunov<sup>2</sup>, O. Uryupin<sup>2</sup>

<sup>1</sup>Herzen Russian State Pedagogical University, St. Petersburg, Russia

<sup>2</sup>A.F.Ioffe Physical-Technical Institute, St.Petersburg, Russia

Thermopower and electrical resistivity of bismuth-antimony crystals with antimony content up to 12 at.%, doped by tellurium up to 0.3 at.% were measured in the wide temperature range 77÷530 K. The results are in accordance with reference. Anisotropy and observed maximum of the temperature dependence of thermopower at high temperature indicate on complicated nature of band electronic structure in these materials. The influences of the electronic band structure and scattering mechanisms of charge carriers on the temperature dependencies of transport properties are discussed.

## Introduction

Presently Bi-Sb based crystals are most effective materials for low temperature thermoelectric applications [1].

Transport properties investigation in dependence on doping by donor dopants of Bi-Sb crystals allows to carry out the study of band structure, energy spectrum of charge carriers as well as scattering mechanisms, which determines high thermoelectric efficiency of n-type crystals.

In work [2] the influence of dilute doping  $\text{Bi}_{1-y}\text{Sb}_y\langle\text{Te}_x\rangle$  crystals by Tellurium (donor dopant) on transport properties were studied in 77-300 K range. Single crystals with  $y=0.05$ , 0.08, 0.12, 0.20, and 0.30 doped by Tellurium in the range 0.01-0.3 at.% were measured. It was shown that at small doping minimum (maximum of absolute value) of temperature dependence of thermopower ( $S$ ) is observed. Dropping down of absolute value of  $S$  at temperatures above the maxima is connected with excitation of valent band carriers.

At high doping level the absolute value of  $S$  shows next features: it is monotonously increasing with temperature at the temperature range investigated; decreasing with doping (level increasing) and becomes anisotropic with  $S_{33} - S_{11} > 0$ . As we assumed the latter can be connected with extra n-type extremum contribution with anisotropy of the same type as that of T-heavy hole valent band.

These conclusions were supported by plasma reflection data [3]. These data indicate that an additional conducting band of  $\text{Bi}_{1-y}\text{Sb}_y$  should be taken into account and its extremum energy position decreases in comparison with L-extremum from about 250 meV at  $y=0.03$  to 100 meV at  $y=0.12$ . At high doping level above 1 at.% Te (these crystals were grown up at grown rate faster than equilibrium one because the equilibrium solubility of Te is less than 1 at.%) the extra band was also observed [4]. In the limits of quasi equilibrium doping S shows no anisotropy at  $T = 77 \div 300$  K and gives no evidence of 2.5-type Lifshich transition [5]. Which was observed in [4] for high level Te doping. Therefore it is of interest to study electronic transport temperature dependencies in  $\text{Bi}_{1-y}\text{Sb}_y$  ( $0 < y < 0.05$ ) crystals in a wider temperature range up to melting point in order to reveal the extra n-type band at smaller doping range. It is interesting as well to investigate the temperature dependencies of  $\rho_{33}$  and  $S_{33}$  of  $\text{Bi}_{0.88}\text{Sb}_{0.12} < 3 \cdot 10^{-3}\text{Te} >$ .

## Experiment

$\text{BiSb} < \text{Te} >$  homogeneous single crystals were grown up by horizontal zone melting method with growing rate

$V = 0.5\text{mm}/\text{h}$  and temperature gradient on the crystallization front  $G = 20\text{K}/\text{cm}$ . High purity Bi (Bi-000) and Sb (Sb-0000) were used. The samples were cut by spark erosion method from the middle of ingots.

The overage sample size was  $0.5 \times 2.5 \times 12 \text{ mm}^3$ . We prepared both sample orientations along to trigonal axis  $C_3$  (a-type) and perpendicular to one (B- and C-types). Destroyed layers of the samples were removed by etching in 50% $\text{HNO}_3 + 50\%\text{C}_2\text{H}_5\text{OH}$ .

Sb concentration was determined by X-ray microzond analysis on Comebax analizator with accurateness  $\pm 0.5\text{at.}\%$ . Deviation from homogenious distribution of Sb within samples not exceed the correctness of measurement.

It is well known that BiSb being doped by Te up to 0.3 at.% has the same lattice parameters and band structure as undoped one and that only Fermi level is shifted to the higher energy [3]. This fact gives us a possibility to check band structure in wide energy span (0-300 meV).

Thermopower was measured by differential method, electrical resistivity by usual 4-probes method on DC current. The measurements were done with  $2 \div 5 \text{ K/min}$  rate at every 2 grads on both cooling and heating. Temperature gradient along sample was about 5 K.

## Discussion

1. Electrical resistivity  $\text{Bi}_{1-y}\text{Sb}_y$  crystals at either of Te-doping investigated (see Fig.1-3) is increasing with temperature with enhancing Temperature Coefficient of Resistance (TCR) rate ( $d^2\rho/dT^2 > 0$ ).

Both temperature dependencies of electrical resistivity and its absolute value have weak non-monotonous dependence on Te doping (Fig.1-2) and Sb contain (Fig.3). For example for  $\text{Bi}_{0.97}\text{Sb}_{0.03} < \text{Te} >$  crystals at [11] orientation absolute value of electrical resistivity with charge carrier concentration (e.g. Te-doping) varies over 6 times has its absolute value within 30% (see Fig.1). This indicates on a general relationship for Bi-type crystals that first was observed in [9].

2. Thermopower of undoped and weak-doped  $\text{Bi}_{0.97}\text{Sb}_{0.03}(\text{Te})$  has anisotropy with  $S_{33} - S_{11} < 0$ . With doping thermopower first becomes isotropic and than again anisotropic, but with  $S_{33} - S_{11} > 0$ , see data for  $y=0.05$  - Fig.2 and data for  $x=0$ ,  $y \geq 0.05$  [2].

Taking into account an analogy with  $\text{Bi}_{1-y}\text{Sb}_y$  at  $y > 0.03$  [2] (where the same type of anisotropy was observed) we believe that that type of anisotropy ( $S_{33} - S_{11} > 0$ ) at least at

Figure 1: Temperature dependencies of Thermopower and electrical resistivity of  $\text{Bi}_{0.97}\text{Sb}_{0.03} < 10^{-2} \cdot \text{Te}_x$ , where  $\circ - x = 0.3$ ,  $\bullet - x = 0.2$ ,  $\nabla - x = 0.1$ ,  $\blacktriangledown - x = 0.005$

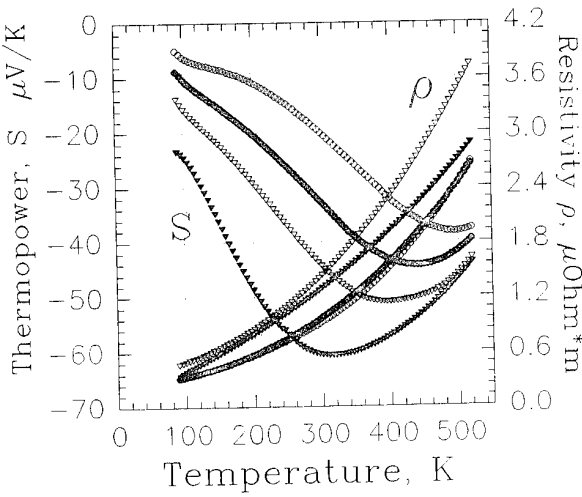


Figure 2: Temperature dependencies of Thermopower and electrical resistivity of  $\text{Bi}_{0.97}\text{Sb}_{0.03} < 10^{-2} \cdot \text{Te}_x$ , where  $x = 0.3 \circ - [33]$ ,  $\bullet - [11]$ ;  $x = 0.05 \nabla - [33]$ ,  $\blacktriangledown - [11]$

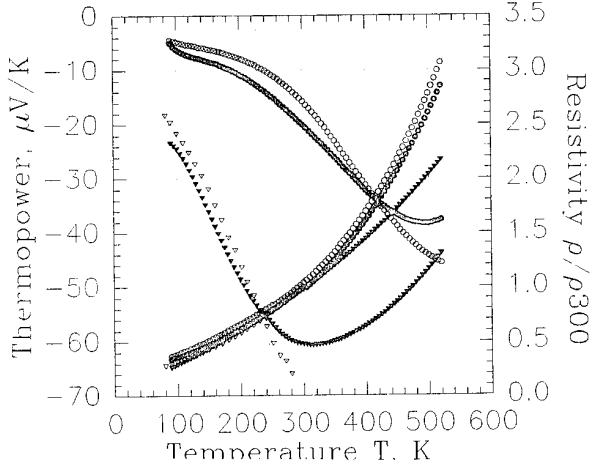
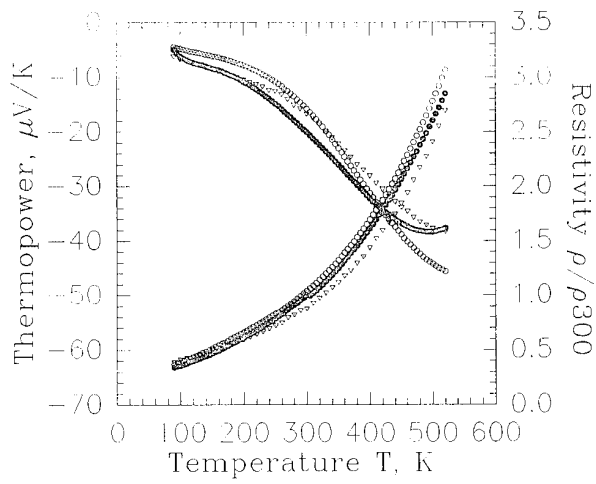


Figure 3: Temperature dependencies of Thermopower and electrical resistivity of  $\text{Bi}_{0.97}\text{Sb}_y < 10^{-2} \cdot \text{Te}_0.3$ , where  $y = 0.3 \circ - [33]$ ,  $\bullet - [11]$ ,  $y = 0.12 \nabla - [33]$



low temperature is directly connected with the extra C-band.

Therefore the additional C-band was observed at smaller doping for  $\text{Bi}_{0.97}\text{Sb}_{0.03} < \text{Te} >$  than for  $\text{Bi} < \text{Te} >$ .

It is also seen that the C-band shows its traces at lower Te-doping level in  $\text{Bi}_{1-y}\text{Sb}_y < \text{Te} >$  system than in  $\text{Bi} < \text{Te} >$ . The main feature of temperature dependence of S, which present data show is the pronounced maxima of absolute value S. Evidently it is connected with  $T^+$  band contribution. With temperature increasing absolute value of S first increases and then comes through the maximum decreases. It is necessary to mention that temperature dependencies of |S| in its increasing slope are unlinear function of temperature especially at high Te doping.

At temperatures 110-200 K ( $dS/dT > 0$ ) is much less than at both beneath and especially above to that temperature range. Exactly the same situation it is possible to see in  $\text{Bi} < \text{Te} >$  [5] and  $\text{Bi}_{1-y}\text{Sb}_y$  at  $x > 0.05$  [2] systems. It indicates on the beginning of Lifshich transition [4].

Moreover with capturing  $T^+$  band temperature dependences of S prone to be the same at most high temperatures investigated for all doping level. It is also connected with transition to the intrinsic conductivity at high temperatures. As a result of high anisotropy of  $T^+$  band the maximum temperature of S(T) is less for  $S_{11}$  direction than for  $S_{33}$  (see Fig.2). This anisotropy leads also to the anisotropy sign changing for S at temperatures above maximum.

### Conclusions

Study of transport property temperature dependencies and its anisotropy reveal transition to the intrinsic conductivity at high temperatures at either doping level investigated as well as to the additional C-band contribution which shows the same anisotropy as  $T^+$  band. The latter results to the anisotropy of S of ( $S_{33} - S_{11} > 0$ ) type at temperatures beneath maximum of S(T) for high Te doping level and to the small value of  $dS/dT$  at low temperatures.

Thus analysis of accepted band structure and the experimental data show that Fermi level rises above  $T^+$  band with Te doping and at high doping rate reaches n-type band.

## References

- [1] Ivanov G.A., Kulikov V.A., Naletov V.L., Panarin A.F., Regel A.R., Fizika i Tehnika Poluprovodnikov, 1972. V.6. N.7. P.1296-1299. (in Russian).
- [2] 2. Grabov V.M., Ivanov G.A., Ponaryadov V.S., Fiz.Tverd.Tela , 1970. V.12. N.1. P. 267-272. (in Russian).
- [3] 3. Grabov V.M., Kudashin V.V., Maltsev A.C., Poluprovodniki s uzkoi zapreshennoi zonoi i polumetalli. Materiali VII Vsesoyuznogo simpoziuma. Lvov,1986. V.2. P.167-169. (in Russian).
- [4] 4. Boyko M.P., Red'ko N.A., Rodionov N.A, Polchin V.I., Pisma v J.Exper. i Teor. Fiz. 1986. .43. N.1. .41-43.(in Russian).
- [5] 5. Grabov V.M., Ivanov G.A.,Fiz.Tverd.Tela 1966. .8. N.8. C.2460-2461.(in Russian).
- [6] 6. Kolpashtnikov G.N., Naletov V.L.,Utshenie zapiski Gercen LGPI. Leningrad. 1968. V.384. P.7-9.(in Russian).
- [7] 7. Ivanov K.G., Krilov A.C. Polumetalli i poluprovodniki, Gercen LGPI. Leningrad. 1975. P.24-29. (in Russian).
- [8] 8.Ivanov G.A., Krilov A.C., Naletov V.L., Polumetalli i poluprovodniki,Gercen LGPI. Leningrad. 1974. P.43- (in Russian).
- [9] 9. Grabov V.M. Materiali dlya Termoelektr. Preobrazatelyi. St.Petersburg, Ioffe Fiz.Techn. Institut., 1993.- P. 42-43. (in Russian).

## THE INFLUENCE OF THE TITANIUM DOPING ON THE THERMOELECTRIC PROPERTIES OF SB-RICHED BISMUTH-ANTIMONY TELLURIDES.

J. Navrátil <sup>1</sup>, Z. Starý <sup>1</sup>, P. Lošťák <sup>2</sup>, T. Plecháček <sup>1</sup>

<sup>1</sup> Joint Laboratory of Solid State Chemistry, Czech Academy of Sciences and University Pardubice,  
Studentská 84, 530 09 Pardubice, Czech Republic

<sup>2</sup> University Pardubice, nám. Legíí 565, 532 10 Pardubice, Czech Republic

The study of influence of titanium doping on thermoelectric properties of bismuth antimony tellurides  $\text{Bi}_{0.5-x/2}\text{Sb}_{2-x/2}\text{Ti}_x\text{Te}_3$ ,  $\text{Bi}_{1-x/2}\text{Sb}_{1-x/2}\text{Ti}_x\text{Te}_3$  and  $\text{Sb}_{2-x}\text{Ti}_x\text{Te}_3$  was carried out. There were measured temperature dependence of Seebeck coefficient on polycrystalline samples of these materials. The electrical conductivity and figure of merit at 293 K was also measured. A possible incorporation mechanism of titanium is proposed.

### Introduction

Sb-riched bismuth-antimony tellurides are generally used as a p-type thermoelectric materials. These materials, because of very high free carriers concentration have to be doped to achieve optimal concentration. Therefore, an investigation of the effect of various dopants on the physical properties of the above mentioned materials is interesting both for the basic and the applied research. Doping with iodium or overstoichiometric tellurium used to be very frequent. Up to this time there was not almost any systematic study of the doping effect such crystals by transition metals impurities. Only influence of the manganese doping on  $\text{Sb}_2\text{Te}_3$  properties [1] and vanadium and chromium doping on  $\text{Bi}_2\text{Te}_3$  properties [2,5] has been described.

In our previous works [3,4] we reported strong influence of titanium doping on thermoelectric and optical properties of  $\text{Sb}_2\text{Te}_3$  single crystals. In spite of limited solubility of this dopant in the studied crystals a very significant decrease of free carrier concentration resulting from both electrical (Hall coefficient) and optical (reflectivity) measurements occurs. Donor behaviour of titanium impurities is explained by occurring of 'multi-layered defects' in the studied materials.

This behaviour of titanium impurities in  $\text{Sb}_2\text{Te}_3$  lattice led us to study influence of such doping on thermoelectric properties of Sb-riched bismuth-antimony tellurides  $\text{Bi}_{x-y/2}\text{Sb}_{2-x-y/2}\text{Ti}_y\text{Te}_3$  and  $\text{Sb}_{2-y}\text{Ti}_y\text{Te}_3$ . The results of Seebeck coefficient, electrical conductivity and figure of merit measurements of the prepared polycrystalline materials in the following paper are presented with the aim to elucidate possible incorporation mechanism of the titanium atoms in the studied materials.

### Experimental

For the preparation of polycrystalline ingots were used antimony, bismuth and tellurium of 5N purity. Titanium in  $\text{TiTe}_2$  form was used as a dopant. The synthesis of the polycrystalline  $\text{TiTe}_2$  was carried out by heating a stoichiometric mixture of Ti and Te powder of 5N purity in an evacuated silica ampoule at 1400 K for 5 days. The X-ray diffractogram of the resulting product revealed only diffraction lines corresponding to the  $\text{TiTe}_2$  compound.

Titanium-doped polycrystalline materials were prepared from the mixture of above mentioned elements and  $\text{TiTe}_2$ , corresponding to atomic ratio  $(\text{Sb}+\text{Ti}):(\text{Te})=2:3$ ,  $(\text{Sb}+\text{Bi}+\text{Ti}):(\text{Te})=2:3$ , respectively. Series of samples corresponding to composition  $\text{Bi}_{x-y/2}\text{Sb}_{2-x-y/2}\text{Ti}_y\text{Te}_3$ , where  $x=0.5$ ; 1 and  $y=0-0.06$  and  $\text{Sb}_{2-y}\text{Ti}_y\text{Te}_3$  ( $y = 0-0.03$ ) were weighed. The synthesis was carried out in silica ampoules evacuated at the pressure of  $10^{-4}$  Pa at 1073 K for 48 hours. The rectangular samples of dimensions of  $2 \times 2 \times 4$  mm<sup>3</sup> for measurement of Seebeck coefficient, electrical conductivity and figure of merit were cut out from prepared compounds.

### Results and discussion

The temperature dependence of Seebeck coefficient  $S$  at 100-400 K temperature range of some  $\text{Sb}_2\text{Te}_3$  samples doped with titanium atoms is presented on the Fig. 1.

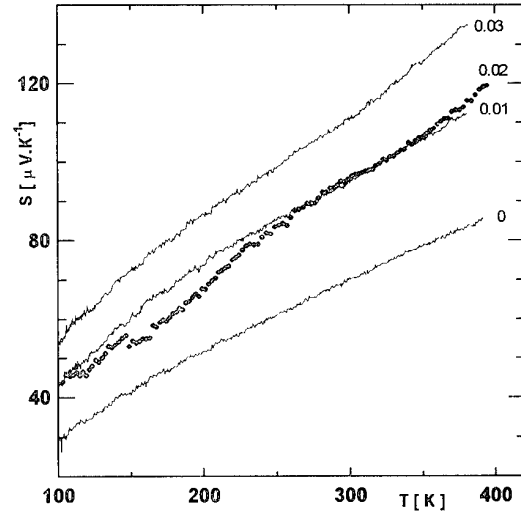


Fig 1: The temperature dependence of the Seebeck coefficient for some  $\text{Sb}_2\text{Ti}_x\text{Te}_3$  samples (curves are denoted with x).

It is evident that increasing titanium concentration in  $\text{Sb}_2\text{Te}_3$  does not influence character of  $S=f(T)$  dependence.

The changes of absolute value of Seebeck coefficient with increasing titanium content in the above mentioned samples shows Fig. 2. From Fig. 2 it is evident, that the introduction of Ti atoms into the structure of  $\text{Sb}_2\text{Te}_3$  results for low Ti concentrations in an increase of S-values.

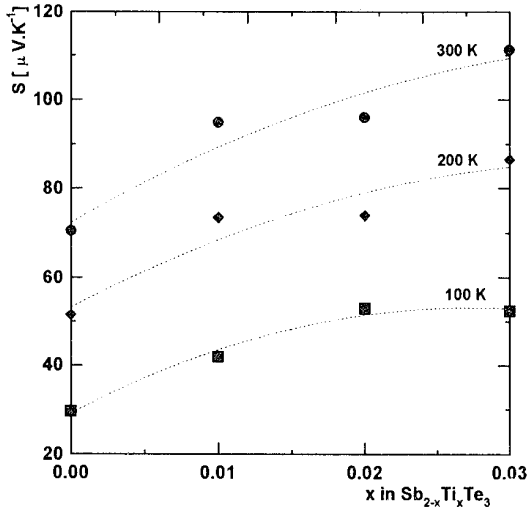


Fig. 2: The dependence of Seebeck coefficient on Ti-content in  $\text{Sb}_{2-x}\text{Tix}\text{Te}_3$  samples at 100, 200 and 300 K (curves are denoted with temperatures).

Fig. 3 shows concentration dependence of electrical conductivity  $\sigma$  at 293 K. It follows from the graph, that entering of Ti atoms results in a considerable decrease of  $\sigma$  values. All above presented measurements on polycrystalline  $\text{Sb}_{2-x}\text{Tix}\text{Te}_3$  samples are in accordance with these ones carried out on monocrystalline samples presented in [3].

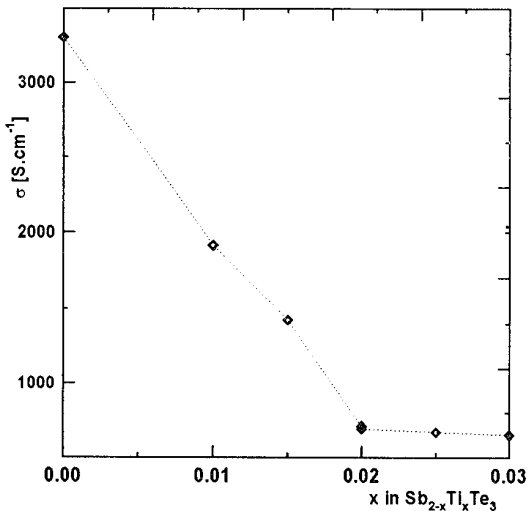


Fig. 3: The dependence of electrical conductivity on Ti-content in  $\text{Sb}_{2-x}\text{Tix}\text{Te}_3$  polycrystalline samples at 293 K.

In Fig. 4 are presented changes of  $\sigma$ ,  $S$  and *figure of merit*  $Z$  values with increasing titanium content in  $\text{Bi}_{0.5-x/2}\text{Sb}_{1.5-x/2}\text{Tix}\text{Te}_3$  polycrystals. It follows from this figure, that in the higher Ti content area ( $x \geq 0.02$ ), an incorporation of Ti atoms into  $\text{Bi}_{0.5}\text{Sb}_{1.5}\text{Te}_3$  solid solution lattice causes change of electrical conductivity type from p- to n-type. In keeping with the fact  $\sigma$  values of p-type samples with increasing  $x$  decrease; at n-type electrical conductivity area further increase of  $x$  causes also increase of  $\sigma$  values.

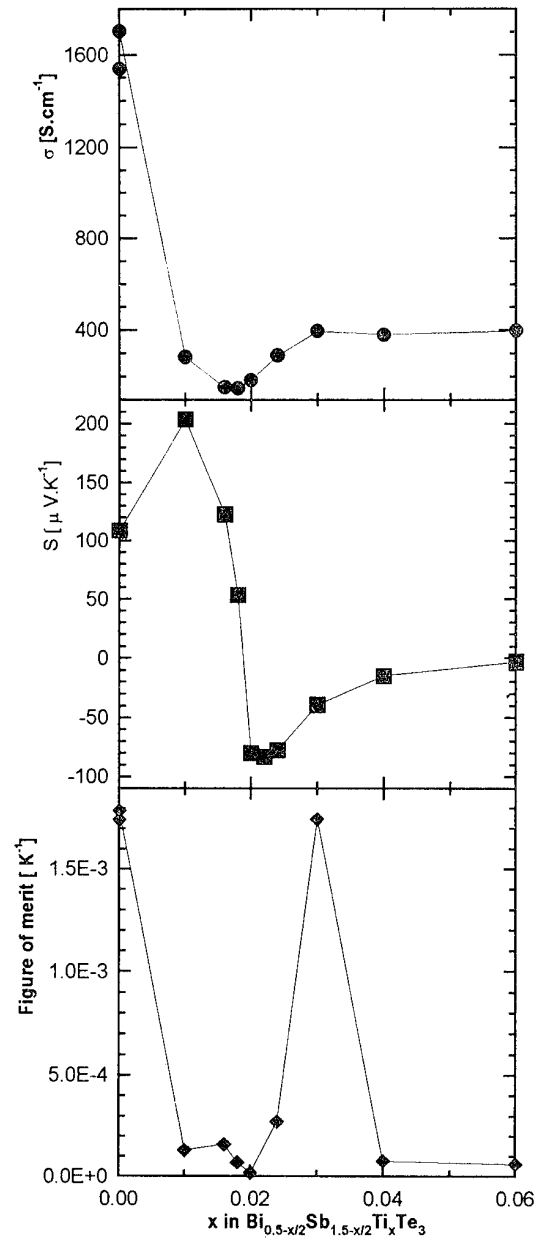


Fig. 4: The dependencies of electrical conductivity  $\sigma$ , Seebeck coefficient  $S$  and *figure of merit*  $Z$  on Ti content in  $\text{Bi}_{0.5-x/2}\text{Sb}_{1.5-x/2}\text{Tix}\text{Te}_3$  polycrystals at 293 K.

Fig. 4 shows also *figure of merit*  $Z$  values. We suppose observed increase of  $Z$  values of n-type samples indicate, that after optimization of titanium content (optimization of free carrier concentration) could be prepared n-type thermoelectric material on the  $\text{Bi}_{0.5}\text{Sb}_{1.5}\text{Te}_3$  basis of good thermoelectric properties.

Following Fig. 5 illustrate temperature dependence of Seebeck coefficient  $S$  of some samples from series of  $\text{Bi}_{0.5-x/2}\text{Sb}_{1.5-x/2}\text{Ti}_x\text{Te}_3$  polycrystals.

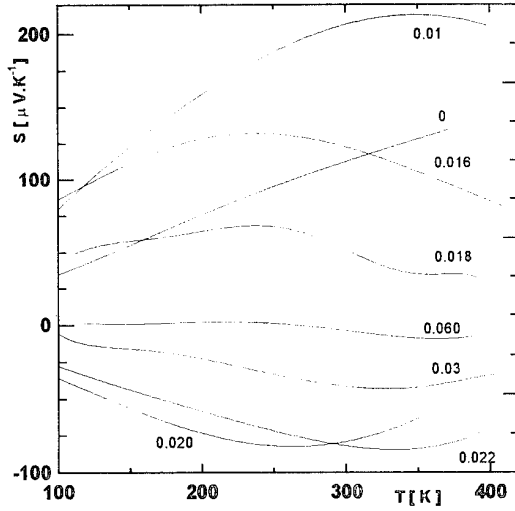


Fig. 5: The temperature dependence of Seebeck coefficient  $S$  of some  $\text{Bi}_{0.5-x/2}\text{Sb}_{1.5-x/2}\text{Ti}_x\text{Te}_3$  samples (curves are denoted with  $x$ ).

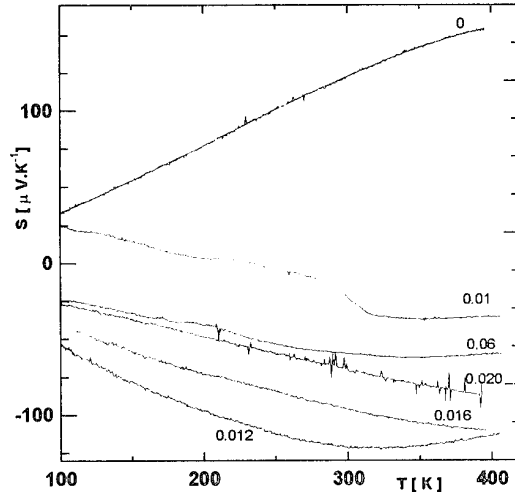


Fig. 6: The temperature dependence of Seebeck coefficient  $S$  of some  $\text{Bi}_{1-x/2}\text{Sb}_{1-x/2}\text{Ti}_x\text{Te}_3$  samples (curves are denoted with  $x$ ).

From Figs. 6 and 7, which show temperature dependence of Seebeck coefficient  $S$  and dependence  $S=f(x)$  for series of  $\text{Bi}_{1-x/2}\text{Sb}_{1-x/2}\text{Te}_3$  samples doped with Ti, there is apparently evident that similarly as at

$\text{Bi}_{0.5}\text{Sb}_{1.5}\text{Te}_3$  samples there is the change of electrical conductivity type from p- to n-type. However, this change occurs at lower concentrations of Ti in comparison with  $\text{Bi}_{0.5}\text{Sb}_{1.5}\text{Te}_3$  system ( $x \geq 0.01$ ). Electrical conductivity of n-type samples of  $\text{BiSbTe}_3$  (Ti) polycrystalline samples is presented at Fig. 8.

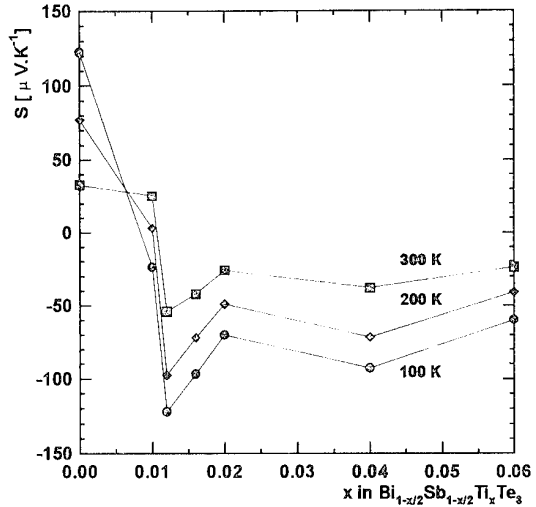


Fig. 7: The dependence of Seebeck coefficient on Ti-content in  $\text{Bi}_{1-x/2}\text{Sb}_{1-x/2}\text{Te}_3$  samples at 100, 200 and 300 K (curves are denoted with temperatures).

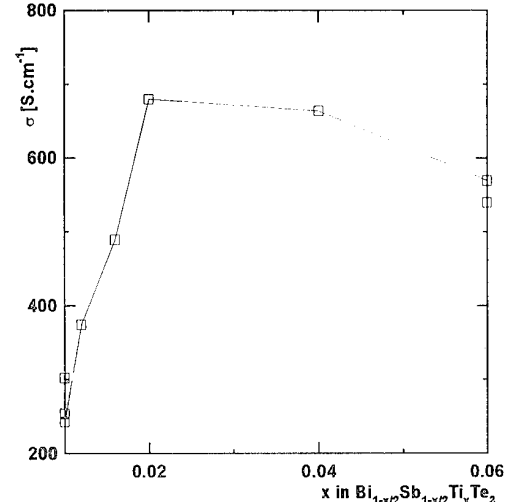


Fig. 8: The dependence of electrical conductivity on Ti-content in n-type  $\text{Bi}_{1-x/2}\text{Sb}_{1-x/2}\text{Ti}_x\text{Te}_3$  polycrystalline samples at 293 K.

From the above presented experimental results conclusion that titanium impurity in both  $\text{Sb}_2\text{Te}_3$  crystal lattice and  $\text{Bi}_x\text{Sb}_{2-x}\text{Te}_3$  solid solution crystal lattice ( $x=0.5, 1$ ) acts as donor follows. This conclusion is consistent with results on monocrystalline samples of  $\text{Sb}_2\text{Te}_3$  with Ti as dopant presented in [3, 4]. The donor-like behaviour of titanium is most likely connected

with way of incorporation of Ti atoms into the crystal lattice of the studied materials.

In accordance with the analysis of possible point defects (interstitial Ti atoms, substitutional defects in cation or anion sublattice or Ti atoms in the van der Waals gap), which is presented in [ 3 ], we suppose also in case of studied solid solutions one can accept following model of incorporation of Ti atoms into the crystal lattice of studied materials:

Ti atoms mostly in all probability are not incorporated into the crystal lattice as simple point defects, but forms three-layer lamellae Te-Ti-Te, which substitute present five-layer structure units Te-Me-Te-Me-Te ( Me=Bi, Sb ) of tetradymite type layer structure of these crystals. We suppose in this model that fragments Te-Ti-Te contain positively charged vacancies  $V_{Te}^+$  and  $V_{Te}^-$  respectively. Charges of these vacancies are compensated with free electrons. These electrons cause suppression of the hole concentration at p-type samples and increase of free carrier concentration at n-type samples.

### **Conclusion**

It has been shown that entering of titanium atoms into the structure of  $Sb_2Te_3$  crystals and  $Bi_xSb_{2-x}Te_3$  solid solutions (where  $x=0.5; 1$ ) has strong influence on the thermoelectric properties of these materials. The donor-like behaviour of this impurity can be explained by the forming of three-layer lamellae, which consist of Te-Ti-Te fragments. Positively charged tellurium vacancies contained in these fragments are compensated with free electrons. These electrons suppress the hole concentration of the studied materials. At Sb-riched bismuth antimony tellurides solid solutions can cause even change of electrical conductivity type. In our opinion some n-type materials of good thermoelectric properties could be prepared on the basis of the studied materials.

### **Acknowledgment**

The support of the Grant Agency of the Czech Republic via grant 106/93/2160 is acknowledged with thanks.

### **Literature**

- [1] J.Horák, M.Matyáš and L.Tichý, 'Lattice Point Defects in Manganese-Doped  $Sb_2Te_3$  Crystals', *Phys.Stat.Sol.(a)*, 1975, 27, 621-6
- [2] P.N. Sherov, K. Mukhiddinov, E.I. Shvednikov, 'Electrical Properties of  $Bi_2Te_3$  Single Crystals Doped with Vanadium and Thulium', *Inorg. Mater.*, 1992, 28, 391-3
- [3] P. Lošťák, Č. Drašar, J. Horák, R. Novotný, L. Beneš, 'Point Defects in Ti-Doped  $Sb_2Te_3$  Single Crystals', *Cryst. Res. Technol.*, to be published
- [4] Č. Drašar, P. Lošťák, J. Navrátil, T. Černohorský and V. Mach, 'Optical Properties of Titanium-doped  $Sb_2Te_3$  Single Crystals', *Phys. Stat. Sol. (a)*, to be published
- [5] P.N. Sherov, Electrophysical Properties of Bismuth Telluride Single Crystals Doped with Chromium, *Inorg. Mater.*, 1993, 29, 287-8

**INTERDIFFUSION AND SOME TRANSPORT PROPERTIES OF COLD PRESSED  
COMPOSITE MATERIALS ON THE BASIS OF  $\text{Bi}_2\text{Te}_3$ ,  $\text{Sb}_2\text{Te}_3$  AND  $\text{Bi}_2\text{Se}_3$   
WITH ADDITION OF INDIUM.**

Z. Starý, J. Navrátil, R. Novotný, T. Plecháček

Joint Laboratory of Solid State Chemistry, Czech Academy of Sciences and University Pardubice,  
Studentská 84, 530 09 Pardubice, Czech Republic

The tablets of the mixture of  $\text{Bi}_2\text{Te}_3$ ,  $\text{Bi}_2\text{Se}_3$ ,  $\text{Sb}_2\text{Te}_3$  and  $\text{In}_2\text{Te}_3$  powder were prepared in the result composition of  $\text{Bi}_{1.8}\text{Sb}_{0.19}\text{In}_{0.01}\text{Te}_{2.85}\text{Se}_{0.15}$ . On the samples the Seebeck coefficient, electrical conductivity and thermoelectric figure of merit were measured after sintering at 510°C. The heat conductivity was calculated. The interdiffusion profiles for  $\text{Bi}_2\text{Te}_3$  -  $\text{Bi}_2\text{Se}_3$  and  $\text{Bi}_2\text{Te}_3$ - $\text{Sb}_2\text{Te}_3$  systems were measured and interdiffusion coefficients were calculated. The figure of merit of this materials is smaller then that one of materials prepared directly from  $\text{Bi}_{1.8}\text{Sb}_{0.19}\text{In}_{0.01}\text{Te}_{2.85}\text{Se}_{0.15}$  powder.

### Introduction

The metallurgical technology of powders is often used to produce thermoelements. Although the single crystal technology yields materials of better thermoelectric quality, cold-pressed or hot-pressed powder materials have better mechanical properties and their production cost is lower. This technology gives us the possibility to produce composite materials or materials with variable composition across the length of tablet.

In our work we aim at an explanation of changes of thermoelectric properties in the course of sintering of tablets, which are pressed from  $\text{Bi}_2\text{Te}_3$ ,  $\text{Bi}_2\text{Se}_3$  and  $\text{Sb}_2\text{Te}_3$  powders. Some electrical properties and interdiffusion coefficients were measured. This paper follows our research of powder metallurgy of  $\text{Bi}_{1.8}\text{Sb}_{0.2-x}\text{In}_x\text{Te}_{2.85}\text{Se}_{0.15}$  materials, which are prospective for the production of N-type branches of thermoelectric generators. We point out the fact, that anti-site defects influence the free carrier concentration and the transport properties of these materials. Anti-site (AS) defects  $\text{Sb}_{\text{Te}}$  have been identified to exist in p-  $\text{Sb}_2\text{Te}_3$  crystals at concentration of about  $10^{20} \text{ cm}^{-3}$ , also the  $\text{Bi}_2\text{Te}_3$  crystals have been shown to contain AS defects of  $\text{Bi}_{\text{Te}}$  at concentration of about  $10^{18} \text{ cm}^{-3}$  [1,2]. Therefore, one can suppose that the AS defects also exist in mixed crystals and in powder materials too.

### Experimental

The bulks of  $\text{Bi}_2\text{Te}_3$ ,  $\text{Sb}_2\text{Te}_3$ ,  $\text{Bi}_2\text{Se}_3$  and  $\text{In}_2\text{Te}_3$  were prepared from elemental Bi, Sb, Se and Te of 5N purity. Samples were synthesized in quartz ampoules by heating at 730°C for 48 hrs (  $\text{Bi}_2\text{Te}_3$ ,  $\text{Sb}_2\text{Te}_3$ ,  $\text{Bi}_2\text{Se}_3$  ) and at 800°C (  $\text{In}_2\text{Te}_3$  ) for 48 hrs too. Then the samples were pulverized and separated by sieving. The size of particles was 50-80  $\mu\text{m}$ . The pulverized samples were mixed to achieve the composition of  $\text{Bi}_{1.8}\text{Sb}_{0.19}\text{In}_{0.01}\text{Te}_{2.85}\text{Se}_{0.15}$  and then compacted to tablets of size 2x2x4 mm<sup>3</sup> with the pressure 25 000 at and sintered by heating at 510°C for 5, 24, 48 and 100 hrs. On the tablets the temperature dependencies of electrical conductivity  $\sigma$ , Seebeck

coefficient  $S$  and thermoelectric figure of merit  $Z$  were measured. The figure of merit was measured by means of modified Harman method which went out from the equation for stable heat flow in the sample:

$$S.I.T = \lambda .. \Delta T \quad (1),$$

where  $S$  is the Seebeck coefficient,  $I$  is the electrical current,  $T$  is the temperature of cold junction of sample,  $\lambda$  is the thermal conductivity and  $\Delta T$  is the temperature difference on the sample. The equation (1) is valid for the case of the small electrical current and consequently small heat exchange with the surroundings. The computation of the figure of merit was carried out from the equation

$$Z = \frac{U_- - U_\sim}{U_\sim . T} \quad (2),$$

where  $U_- = R.I$ ,  $U_\sim = R.I + S.\Delta T$  and  $\Delta T$  is taken from the equation (1).

For the interdiffusion measurements the single crystals were used. The growth of the single crystals was carried out in the conical-shaped silica ampoules by means of a modified Bridgman method using a suitable temperature gradient and pulling rate of 1.2 mm/hr. The interdiffusion coefficient was calculated from the interdiffusion profile in the direction parallel to the trigonal c-axis. The single crystals were contacted together and heated for 96 hrs at 510°C. The concentration profiles were measured by means an energy-dispersive X-ray (EDX) microanalyser (KEVEX).

### Results and discussion

How it can be seen from the measurements of Seebeck coefficient  $S$  and electrical conductivity  $\sigma$ , all samples are N-type materials. Unlike of PIES method (Pulverized Intermixed Elements Sintering) [3] where powder contained the elements, we have pulverized compounds of  $\text{Bi}_2\text{Te}_3$ ,  $\text{Sb}_2\text{Te}_3$ ,  $\text{Bi}_2\text{Se}_3$  and  $\text{In}_2\text{Te}_3$  and mixed them in the

ratio, that corresponds to the composition which was meant in our last ICTEC contribution [4].

The figures 1- 4 show the Seebeck coefficient  $S$ , electrical conductivity  $\sigma$ , heat conductivity  $\lambda$  (calculated) and figure of merit  $Z$  as a function of temperature and sintering time. We can see, that the time of sintering influences the thermoelectrical properties of such materials.

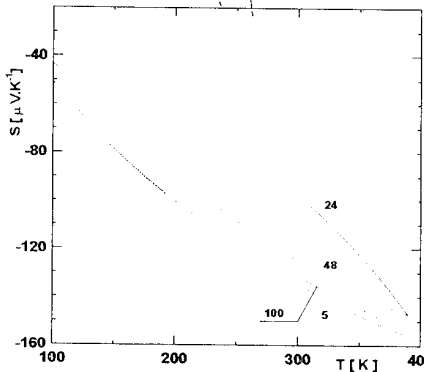


Fig. 1: The temperature dependence of Seebeck coefficient (curves are denoted with sintering time in hours).

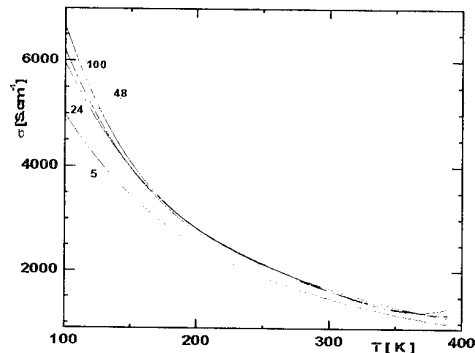


Fig. 2: The temperature dependence of the electrical conductivity (curves are denoted with sintering time in hours).

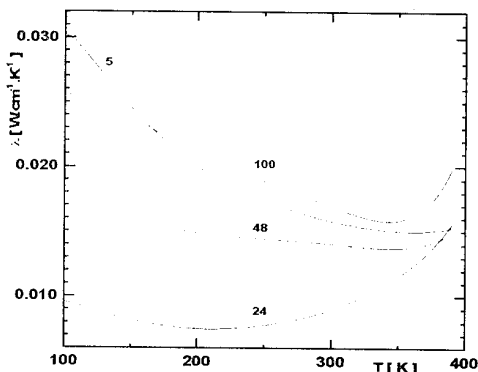


Fig. 3: The temperature dependence of the heat conductivity (calculated) (curves are denoted with sintering time in hours).

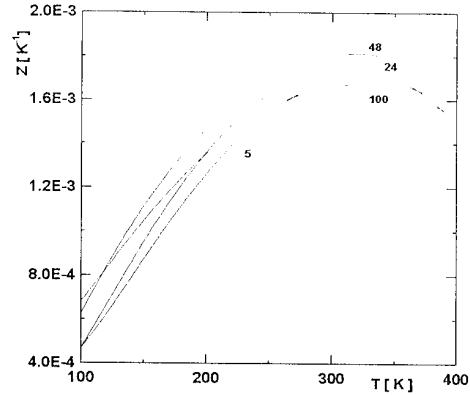


Fig. 4: The temperature dependence of the figure of merit (curves are denoted with sintering time in hours).

From the figure 5 - 8 we can see the Seebeck coefficient, electrical conductivity, heat conductivity and figure of merit at the room temperature (292° K) as the function of sintering time. We see, that all dependencies on the figures 5 - 8 have maximum or minimum after about 25-30 hrs of sintering. In our work [4] we show, that grinding of the  $\text{Bi}_{1.8}\text{Sb}_{0.2-x}\text{In}_x\text{Te}_{2.85}\text{Se}_{0.15}$  materials causes increasing of free electrons. The authors [5] propose following explanation: By mechanical treatment crossing dislocations, which give vacancies  $V_{\text{Bi}(\text{Sb})}$  and  $V_{\text{Te}}$  are produced. The ratio of cation vacancies vs. anion vacancies is about 2:3. Considering ones positively charged vacancies  $V^+_{\text{Te}}$  prevail. Smaller mobility of these vacancies, in comparison with the mobility of  $V_{\text{Bi}}$  vacancies, causes that they move more slowly during the sintering toward the grain surface.

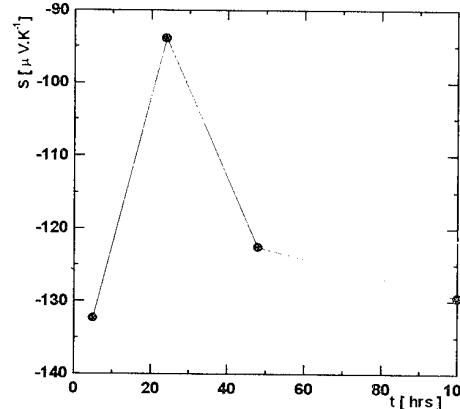


Fig. 5: The dependence Seebeck coefficient on the sintering time (292 K).

Our explanations is as follows: In connection with AS defects, which occurs in crystals in considerable concentration, the vacancies that really occur after the grinding at the ratio 2:3 do not diffuse to the grain surface but interact with AS defects according to following equation

$$2 V_{\text{Bi}} + 3 V^+_{\text{Te}} + \text{Bi}^+_{\text{Te}} = V_{\text{Bi}} + \text{Bi}_{\text{Bi}} + 4 V^+_{\text{Te}} + 3 e^- \quad (3)$$

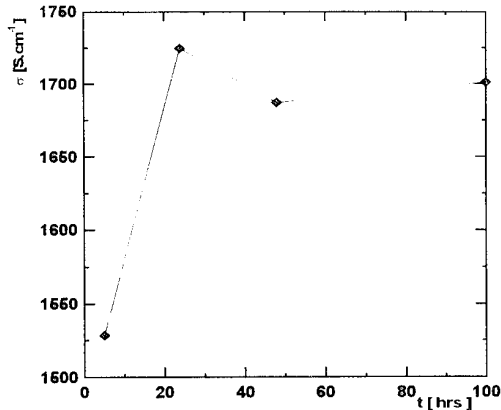


Fig. 6: The dependence of electrical conductivity at 292 K on the sintering time.

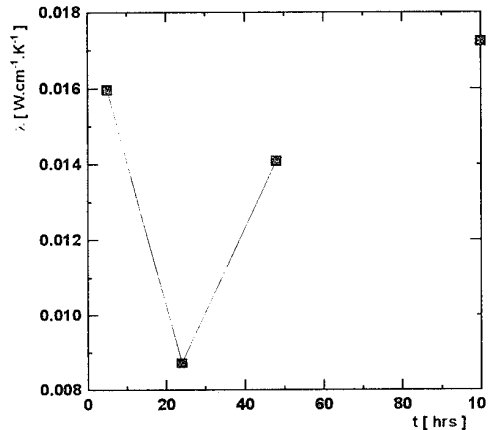


Fig. 7: The dependence of heat conductivity at 292 K on the sintering time.

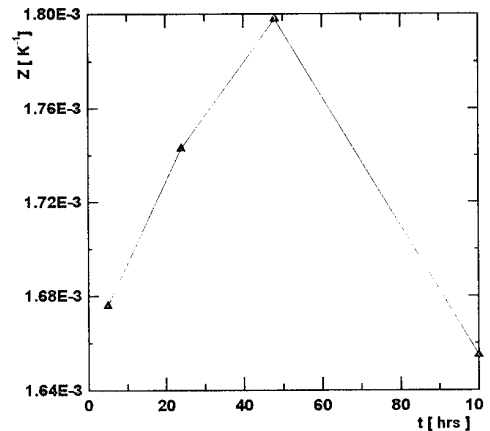


Fig. 8: The dependence of figure of merit at 292 K on the sintering time.

In other words the Bi-atom jumps from Te-sublattice to the vacancy in Bi-sublattice and Te-vacancy simultaneously comes into existence. We can see the result of this process in the figure 5 and 6 as maximum on the experimental dependencies of the Seebeck coefficient and electrical conductivity. The minimum of the heat

conductivity is probably caused by the rise of new phases on the intergrain region.

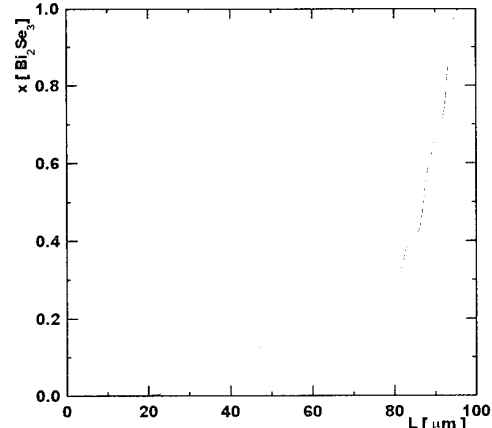


Fig. 9: The interdiffusion profile of  $\text{Bi}_2\text{Te}_3$  -  $\text{Bi}_2\text{Se}_3$  system after 96 hrs at 510°C.

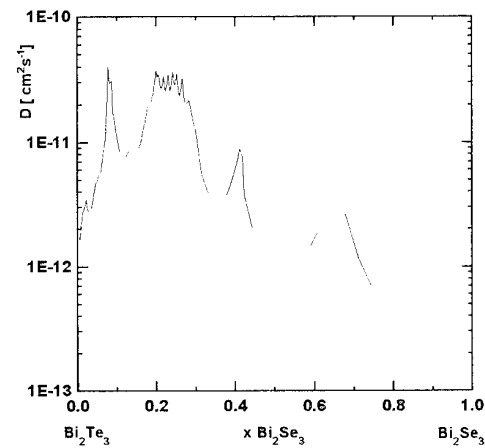


Fig. 10: The inter diffusion coefficients of the  $\text{Bi}_2\text{Te}_3$  -  $\text{Bi}_2\text{Se}_3$  system as a result of Boltzmann-Matano analysis.

We can imagine the speed of this process from the figure 9 - 12 where the interdiffusion profiles and interdiffusion coefficients are shown for the diffusion parallel to the trigonal c-axis. The interdiffusion coefficients are calculated from the profiles by using of Boltzmann-Matano analysis. We can see, that after 96 hrs at temperature 510 °C the width of the profile is about 80  $\mu\text{m}$ . If we consider that the shape of grains is flake-like then the diffusion of the direction parallel to the trigonal c-axis is the main diffusion direction. We can estimate that after 25 hrs approximately one third of material remains in the form of  $\text{Bi}_2\text{Te}_3$ ,  $\text{Sb}_2\text{Te}_3$ ,  $\text{Bi}_2\text{Se}_3$  compounds. As the sintering time increases the homogeneity of tablets increases too and the heat conduction increases from the minimum (see Fig. 7). From the figures 5,6 it is evident that after 30 hrs the concentration of free carriers decreases and after 60 hrs their mobility increases (see Fig.6). The first phenomenon could be caused by diffusion of antimony atoms into the rest of material (Sb-doping of

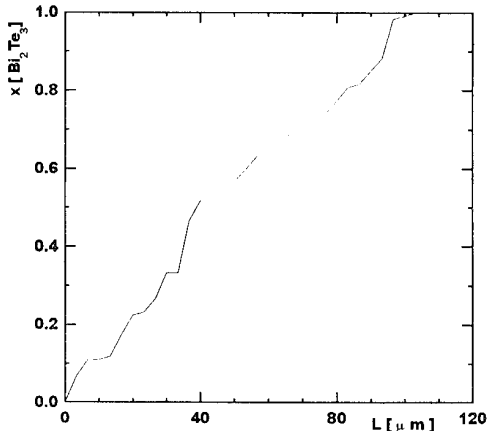


Fig. 11: The interdiffusion profile of  $\text{Bi}_2\text{Te}_3$  -  $\text{Sb}_2\text{Te}_3$  system after 96 hrs at 510°C.

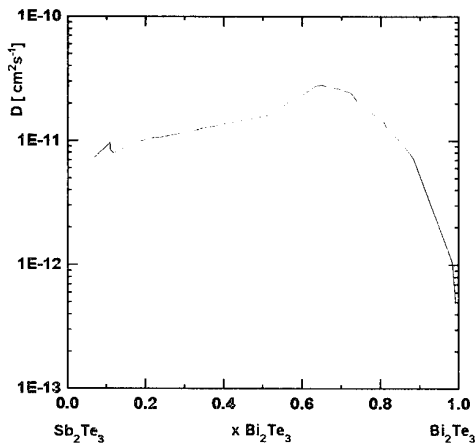


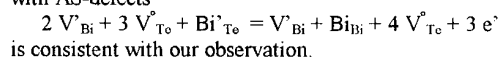
Fig. 12: The interdiffusion coefficients of the  $\text{Bi}_2\text{Te}_3$  -  $\text{Sb}_2\text{Te}_3$  system as a result of Boltzmann-Matano analysis.

$\text{Bi}_2\text{Te}_3$  causes decreasing of free electron concentration in the n-type  $\text{Bi}_2\text{Te}_3$  or increasing hole concentration in the p-type  $\text{Bi}_2\text{Te}_3$  [6]). The second one is caused by increasing of material homogeneity (see Fig. 6,7). Fig. 8 shows the figure of merit as a result of described processes. It is remarkable that even after short time of sintering from the diffusion point of view the figure of merit is set high enough. We can estimate from the diffusion measurement that after 5 hrs almost 90% of material remains unreacted.

### Conclusion

We tried to prepare the material for n-type thermoelectric branch of  $\text{Bi}_{1.8}\text{Sb}_{0.19}\text{In}_{0.01}\text{Te}_{2.85}\text{Se}_{0.15}$  by using the cold-pressed method from the powder of  $\text{Bi}_2\text{Te}_3$ ,  $\text{Sb}_2\text{Te}_3$ ,  $\text{Bi}_2\text{Se}_3$  and  $\text{In}_2\text{Te}_3$  compounds.

It is shown that our model of interaction of vacancies with AS-defects



We found out that the remarkable short time of sintering from the diffusion point of view is able to form the n-type branch of thermoelements. Its figure of merit however is smaller than that one of the material which is prepared directly from the  $\text{Bi}_{1.8}\text{Sb}_{0.19}\text{In}_{0.01}\text{Te}_{2.85}\text{Se}_{0.15}$  compound [4].

### Acknowledgment

The support of the Grant Agency of the Czech Republic via grant 106/93/2160 is acknowledged with thanks.

### Literature

- [1] J. Horák, L. Tichý, P. Lošťák and A. Vaško, *Crystal Lattice Defects*, 1976, v. 6, p. 223
- [2] R.F. Brebrick, *J.Phys.Chem.Solids*, 1969, v. 30, p. 719
- [3] T. Ohta, T. Uesugi, T. Tokai, N. Nosaka and T. Kajikawa, *8th ICTEC 1989*, p.7
- [4] Z. Starý, J. Navrátil and T. Plecháček, *13th ICTEC 1994*, p.286
- [5] R. Ionescu, J. Jaklovszky, N. Nistor and A. Chiculita, *Phys. Stat. Sol. (a)*, 1975, v. 27, p. 27
- [6] Z. Starý, J. Horák, M. Stordeur and M. Stoelzer, *J.Phys.Chem.Solids*, 1988, v.49, p.29

## HIGHEST FIGURE OF MERIT IN UNDOPED $\text{Bi}_{1-x}\text{Sb}_x$ ALLOYS

B. Lenoir<sup>1</sup>, M. Cassart<sup>2</sup>, A. Dauscher<sup>1</sup>, Yu. I. Ravich<sup>3</sup>, H. Scherrer<sup>1</sup>

<sup>1</sup>Laboratoire de Métallurgie Physique et Science des Matériaux, Ecole des Mines, Parc de Saurupt, F-54042 Nancy, France

<sup>2</sup>Unité de Physico-Chimie et de Physique des Matériaux, Louvain-la-Neuve, Belgique

<sup>3</sup>Ioffe Physico-Technical Institute, St Petersburg, Russia

The electrical resistivity, thermoelectric power, thermal conductivity and thermoelectric figure of merit have been measured between 4.2 and 300 K on three  $\text{Bi}_{1-x}\text{Sb}_x$  alloys of different composition ( $x = 0.144, 0.165$  and  $0.181$ ) prepared by the travelling heater method. The temperature dependences of these parameters follow the same general trends than semiconducting alloys having a lower Sb content. These complementary results, allowing to cover all the semiconducting range of Bi-Sb alloys, show that the figure of merit measured at 70 K is maximum for two Sb contents ( $x \approx 0.09$  and  $0.16$ ). These features have been qualitatively explained from the band structure and interband hole scattering mechanisms.

### Introduction

Bismuth-rich  $\text{Bi}_{1-x}\text{Sb}_x$  alloys are the best conventional materials for the n-type legs of thermocouples used in thermoelectric cooling devices operating at temperatures below 200 K [1].

The  $\text{Bi}_{1-x}\text{Sb}_x$  alloys constitute a continuous series of substitutional solid solutions for which drastic changes of their band structure are observed depending on the antimony content (Fig. 1). The semimetallic character of bismuth is determined by the overlap of the valence band maximum at the T point with the conduction band minimum at the L point of the Brillouin zone. When bismuth is alloyed with antimony, this overlap is reduced by increasing the Sb content. Moreover, the energy gap at the L point decreases with the increase of Sb content. After the inversion of the two L bands at  $x \approx 0.04$  [2,3], this energy gap again increases. For an Sb content of  $x \approx 0.07$  [4,5], there is no more overlap and the alloy becomes semiconducting. As the Sb concentration is further increased to about  $x \approx 0.22$  [6,7] the conduction band minimum at the L point overlaps an additional valence band extremum located at the H point inducing the alloy system to undergo from the semiconducting state to a semimetallic one. The semiconducting alloys present the peculiarity to possess thermal gaps that do not exceed 25-30 meV, so that they can be classified as narrow band-gap semiconductors. Besides, the very small direct energy gap at the L point is responsible for high carrier mobilities, small effective masses and non-parabolic energy momentum dispersion relation. Moreover, because this direct gap is small, the relative changes of this parameter with temperature is expected to be large as in pure bismuth [8,9] for temperatures higher than 90 K.

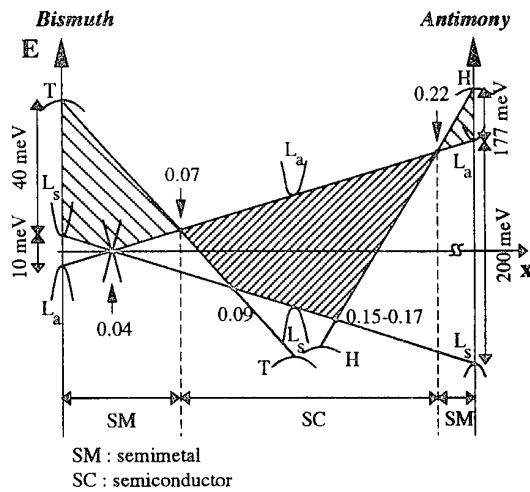


Figure 1. Schematic diagram of the band edge configuration of  $\text{Bi}_{1-x}\text{Sb}_x$  alloys as a function of  $x$  at  $T \approx 0$  K. In the semiconducting range, the band gap is maximum around  $x = 0.15-0.17$ .

So, there are many factors which change according to the band structure: the gap and other distances between bands, the effective masses, the non-parabolicity of the L bands, the densities of electrons and both light (L band) and heavy holes (T and H bands), the chemical potential, the scattering mechanisms including interband scattering.

All these factors affect the transport properties, particularly the thermopower ( $\alpha$ ), the electrical resistivity ( $\rho$ ) and the thermal conductivity ( $\lambda$ ). It results that the optimization, by the help of a calculation, of the figure of merit  $Z = \alpha^2/\rho\lambda$  in Bi-Sb alloys is difficult at present due to drastic changes of the band structure.

The temperature dependence of the figure of merit of  $\text{Bi}_{1-x}\text{Sb}_x$  alloys for  $x < 0.13$  has been previously described

in [10]. In this paper, we carry on with the investigation of some other compositions in order to cover a great part of the semiconducting range of the  $\text{Bi}_{1-x}\text{Sb}_x$  alloys.

After introducing the experimental part, we will discuss about electrical resistivity, thermoelectric power and thermal conductivity results obtained with three different alloys ( $x = 0.144, 0.165$  and  $0.181$ ). Then, we will report the evolution of the figure of merit against antimony content for a temperature of 70 K. Some qualitative explanations will be given to interpret the obtained features.

## Experimental

The Travelling Heater Method (THM) was used to grow  $\text{Bi}_{1-x}\text{Sb}_x$  crystals [11]. Special care was taken to reduce the detrimental effect of constitutional supercooling by using slow growth rates ( $4 \text{ mm day}^{-1}$ ). The temperature of the solvent zone heater was stabilized to within  $\pm 0.2 \text{ K}$ . Ingots of 15 mm in diameter and 90 mm in length were obtained. The antimony content was determined with a Cameca (CAMEBAX SX 50) microprobe analyser. The scatter of the antimony content along radial and longitudinal directions was about 3 and 5 at. % of the mean content, respectively.

Ingots grown by the THM method present large monocrystalline parts. Parallelepiped-shaped samples cut from large single crystals with a string saw were used in the investigation of the transport properties (typical dimension was  $2 \times 2 \times 12 \text{ mm}^3$ ). The largest dimension coincided with the trigonal axis.

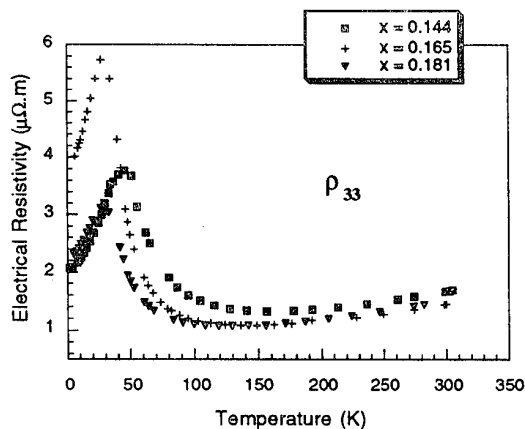


**Figure 2.** Temperature dependence of the electrical resistivity measured along a direction parallel to the trigonal axis of  $\text{Bi}_{1-x}\text{Sb}_x$  alloys.

Thermoelectric coefficients were measured on a thermal potentiometer [12,13] in the temperature range  $4.2 \leq T \leq 300 \text{ K}$ . The thermal conductivity and the thermoelectric power were measured by means of a heat and sink method, i.e by establishing a stationary temperature gradient by supplying heat at one end of the sample, while the other end is remained at a constant temperature. Special care was taken to avoid problems associated with thermal losses [13].

## Results and discussion

The temperature dependence between 4.2 and 300 K of the electrical resistivity measured along a direction parallel to the trigonal axis ( $\rho_{33}$ ) is shown in Fig. 2 for the three compositions studied. The resistivity first begins to increase sharply up to a temperature  $T_1$  located near 30-50 K. Then, it decreases down to a temperature  $T_2$  located around 100-130 K. Finally, it grows slowly until room temperature. The exact values of  $T_1$  and  $T_2$  depend on the antimony content. The same behaviour was already encountered in the semiconducting range of Bi-Sb alloys having lower antimony contents [10].

The features of these curves can be understood qualitatively as follows. Below  $T_1$ , the metallic behaviour of the electrical resistivity can be explained according to the hydrogenoid model in terms of an impurity band located in the conduction band [10]. When the intrinsic density of carriers becomes greater than the density of impurities, the classical temperature dependence of semiconductors is then obtained showing a decrease of the electrical resistivity as the temperature is increased. Supposing that the electrical resistivity varies in this temperature range as :

$$\rho = \rho_0 \exp\left(-\frac{\Delta E}{2kT}\right) \quad (1)$$

the values of the thermal gap  $\Delta E$  have been estimated (table 1). They are in good agreement with the results obtained by Alekseeva et al. [14].

When the thermal energy  $kT_2$  is nearly equal to  $\Delta E$ , the intrinsic density of carriers is weakly temperature dependent. The increase of the electrical resistivity for  $T > T_2$  reflects then the decrease of the mobility of the carriers.

**Table 1.** Estimation of the thermal gap deduced from relation (1).

x	0.144	0.165	0.181
$\Delta E$ (meV)	19.5	18.3	11.4

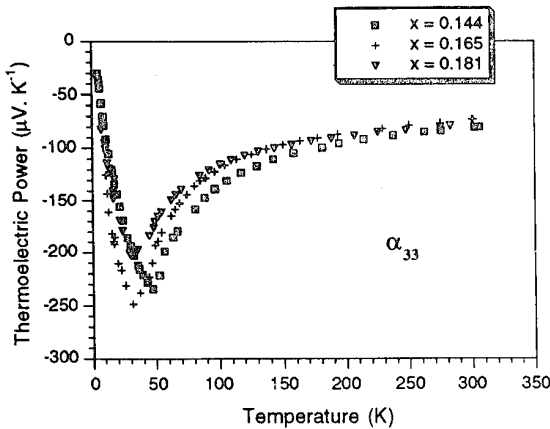


**Figure 3.** Temperature dependence of the thermoelectric power measured along a direction parallel to the trigonal axis of  $\text{Bi}_{1-x}\text{Sb}_x$  alloys.

The three temperature domains observed during the study of the electrical resistivity as a function of temperature are also encountered in the study of the thermoelectric power (Fig. 3). It can be mentioned that the temperature limits  $T_1$  and  $T_2$  of the domains are the same. High absolute numerical values are obtained for temperatures around  $T_1$  ( $\geq 200 \mu\text{V K}^{-1}$ ). Below  $T_1$ , the thermoelectric power varies linearly with temperature, in agreement with the proposal of the metallic behaviour observed for the electrical resistivity.

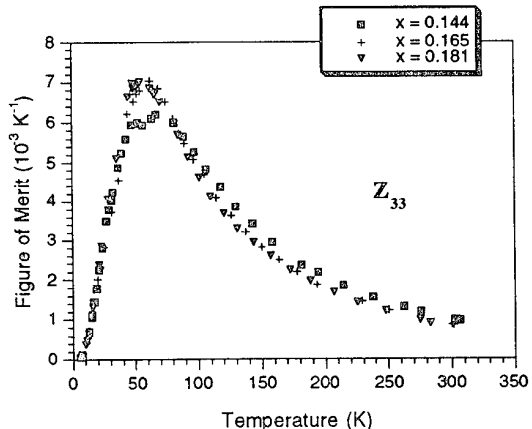


**Figure 5.** Temperature dependence of the thermoelectric figure of merit measured along a direction parallel to the trigonal axis of  $\text{Bi}_{1-x}\text{Sb}_x$  alloys.

The temperature dependence of the thermal conductivity is similar for the three studied alloys (Fig. 4). Contrary to previous results [10], the substitution of Bi by Sb atoms do not affect anymore the lattice thermal conductivity which is mainly responsible of the heat transport at low temperatures.

The figures of merit deduced from the previous transport coefficients are reported in Fig. 5 as a function of temperature. The curves present sharp maxima around 60 K. Values of roughly  $7.0 \cdot 10^{-3} \text{ K}^{-1}$  are obtained for  $x = 0.165$  and  $0.181$  alloys.

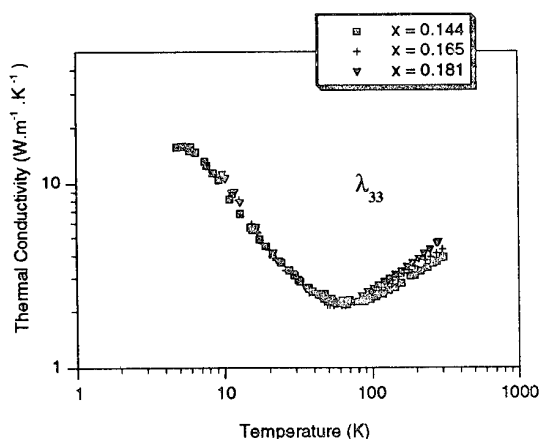


**Figure 4.** Temperature dependence of the thermal conductivity measured along a direction parallel to the trigonal axis of  $\text{Bi}_{1-x}\text{Sb}_x$  alloys.

The evolution with Sb content of the figure of merit obtained at 70 K for the  $\text{Bi}_{1-x}\text{Sb}_x$  alloys studied here and previously [10, the measurements were made in the same experimental conditions] are reported in Fig. 6. The curve presents two maxima : one for  $x \approx 0.16$  ( $Z = 6.8 \cdot 10^{-3} \text{ K}^{-1}$ ), corresponding to the value for which the thermal gap is the highest and another for  $x \approx 0.09$  ( $Z = 5.2 \cdot 10^{-3} \text{ K}^{-1}$ ), when tops of the valence bands at the L and T points are on the same level (like the situation for  $x \approx 0.16$  with L and H bands). At 70 K, in the composition range  $0.09 < x < 0.16$  of antimony, the top of the valence band consists in light mobile holes that influence the figure of merit in a negative way. The holes corresponding to additional band maxima are relatively heavy and immobile. The approach of one of this maximum up to the principal extremum decreases the density of the light holes and simultaneously increases the electron density. The lowering of the density of mobile

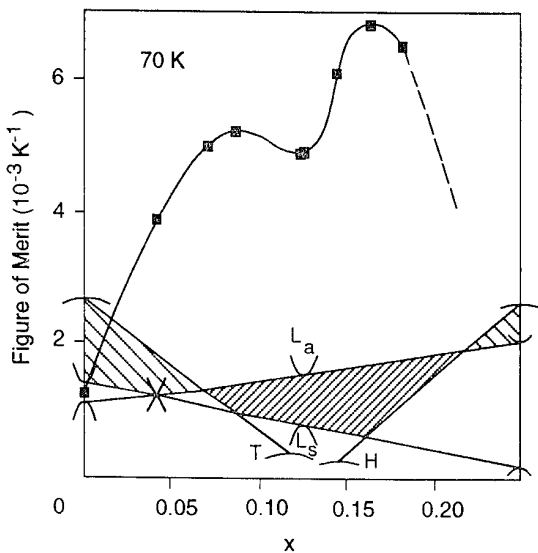


**Figure 6.** Antimony content dependence of the thermoelectric figure of merit at 70 K.

minority carriers always improves the figure of merit. The raise of both the electron density and the chemical potential may also be positive factors if the density is not optimal and the chemical potential is not near the bottom of the conduction band.

It is possible, however, that interband scattering occurring through transitions between the bands of light and heavy holes could be an important factor affecting the figure of merit. This mechanism of holes scattering may essentially lower the mobility of light holes and increase the figure of merit of n-type semiconductors. Within the composition range  $0.09 \leq x \leq 0.16$ , the interband scattering is maximal when the heavy hole extremum is on the same level than the light hole maximum. The figure of merit may be lowered outside this range because of the decrease of the thermal gap. Therefore, the interband hole scattering may explain the existence of the two maxima in the evolution of the figure of merit with Sb content at low temperatures. The same mechanism can certainly also explain why the bismuth-antimony alloys cannot be good p-type thermoelectric materials.

### Conclusion

The study of the transport properties within the temperature range [4.2-300] K of  $\text{Bi}_x\text{Sb}_{1-x}$  alloys ( $0.14 < x < 0.19$ ) completes the previous one performed on more Bi rich alloys. It allows an overview of the variation of

the thermoelectric figure of merit along a direction parallel to the trigonal axis for a wide range of compositions. The figure of merit obtained at 70 K is maximum for two values of  $x$  ( $x \approx 0.09$  and  $x \approx 0.16$ ) in the semiconducting range of the Bi-Sb alloys and reaches values as high as  $6.8 \cdot 10^{-3} \text{ K}^{-1}$ . The position of the two maxima can be qualitatively explained from the band structure and interband hole scattering mechanisms.

### Acknowledgment

The authors would like to thanks J.-P. Haussler for his technical assistance in microprobe analysis.

### References

- [1]. G. E. Smith, R. Wolfe, *J. Appl. Phys.*, **33**, 841 (1962)
- [2]. E. J. Tichovolsky, J. G. Mavroides, *Solid State Commun.* **7**, 927 (1969)
- [3]. G. Oelgart, R. Herrmann, *Phys. Stat. Sol. (b)* **75**, 189 (1976)
- [4]. P. W. Chao, H. T. Chu, Y. H. Kao, *Phys. Rev. B* **9**, 4030 (1974)
- [5]. S. M. Chudinov, B. A. Akimov, V. V. Moshchalkov, *Sov. Phys. Solid States* **17**, 1522 (1975)
- [6]. G. Oelgart, G. Schneider, W. Kraak, R. Herrmann, *Phys. Stat. Sol. (b)* **74**, K 75 (1976)
- [7]. N. B. Brandt, E. A. Svistova, M. V. Semenov, *Sov. Phys. JETP* **32**, 238 (1971)
- [8]. M. P. Vecchi, M. S. Dresselhaus, *Phys. Rev. B* **10**, 771 (1974)
- [9]. E. E. Mendez, Ph. D. Thesis, MIT (1979)
- [10]. B. Lenoir, M. Cassart, J.-P. Michenaud, S. Scherrer, H. Scherrer, *J. Phys. Chem. Solids*, in press
- [11]. B. Lenoir, A. Demouge, D. Perrin, H. Scherrer, S. Scherrer, M. Cassart, J.-P. Michenaud, *J. Phys. Chem. Solids* **56**, 99 (1995)
- [12]. L. Piraux, J.-P. Issi, P. Coopmans, *Measurement* **5**, 185 (1987)
- [13]. M. Cassart, E. Grivei, J.-P. Issi, E. Ben Salem, B. Chevalier, C. Brisson, A. Tressaud, *Physica C* **213**, 327 (1993)
- [14]. V. G. Alekseeva, N. F. Zaets, A. A. Kudryashov, A. B. Ormont, *Sov. Phys. Semicond.* **10**, 1332 (1976)

# THERMAL EXPANSION COEFFICIENT IN $\text{Bi}_{0.5}\text{Sb}_{1.5}\text{Te}_3$

N. Tamaki, A. Onodera, M. Ido, K. Fukuda<sup>1</sup>, H. Imaizumi<sup>1</sup> and T. Ishii<sup>1</sup>

*Department of Physics, Faculty of Science, Hokkaido University, Sapporo 060, Japan*

<sup>1</sup>*Advanced Research Laboratory, KOMATSU LTD, Hiratsuka 254, Japan*

Thermal expansion coefficient of bismuth telluride thermoelectric semiconductor,  $\text{Bi}_{0.5}\text{Sb}_{1.5}\text{Te}_3$ , was measured in the wide temperature range from 70 K to 410 K. A new anomaly was firstly found at 304 K, which corresponded to that observed in specific heat and elastic modulus. This evidence may be attributed to some changes in crystal structure and an existence of a structural phase transition.

## 1. INTRODUCTION

$\text{Bi}_2\text{Te}_3$ - $\text{Sb}_2\text{Te}_3$  alloys have been extensively studied as the most effective *p*-type thermoelectric material available for Peltier devices near room temperature [1, 2]. The crystal structures of  $\text{Bi}_2\text{Te}_3$  and  $\text{Sb}_2\text{Te}_3$  are both hexagonal (or rhombohedral) with  $a = 4.3835$ ,  $c = 30.487$  Å for  $\text{Bi}_2\text{Te}_3$  and  $a = 4.25$ ,  $c = 30.35$  Å for  $\text{Sb}_2\text{Te}_3$  at room temperature [3]. This crystal has an anisotropic layer structure and the layers alternate along the *c*-axis in the order of -Te-Bi-Te-Te-Bi-Te-Bi-Te-Te- ... . The -Te-Te-layers are bound weakly with the van der Waals force. Therefore these compounds have a characteristic easy plane of cleavage perpendicular to the hexagonal *c*-axis. Recently hot-pressed polycrystalline samples have been applied for Peltier devices, of which mechanical properties and figure of merit were drastically improved. However, due to the nature of crystal structure mentioned above, these compounds have some difficulty for mass production of small modules. To give enough strength for the elements, fine polycrystalline and sintered materials were extensively investigated. On the other hand, these processes affect sensitively thermoelectric properties.

Many studies have been reported on thermal properties of Bi-Te alloys such as thermal expansion, specific heat, thermal diffusivity and thermal conductivity. Previously we reported precise measurements of specific heat of  $\text{Bi}_{0.5}\text{Sb}_{1.5}\text{Te}_3$  in a wide temperature range from 70 K to 500 K by AC calorimetry [4]. A new anomaly was observed at 270 K in addition to the well known one at 370 K. According to Gruneisen formula, it is considered that a thermal expansion coefficient is proportional to the specific heat of lattice. Therefore the anomaly in thermal expansion coefficient should be expected at 270 K if this is related to some structural changes. However, previous X-ray experiments have shown that the linear expansion coefficients of  $\text{Bi}_2\text{Te}_3$  exhibit no anomalous temperature dependence from 4.2 K to 600 K [5].

In this paper, we investigated thermal expansion properties of hot-pressed  $\text{Bi}_{0.5}\text{Sb}_{1.5}\text{Te}_3$  *p*-type materials

to clarify whether the anomaly in thermal expansion can be detected or not. Temperature dependence of a linear thermal expansion coefficient  $\alpha$  was discussed in comparison with those in the specific heat ( $C_p$ ) in  $\text{Bi}_{0.5}\text{Sb}_{1.5}\text{Te}_3$ . An anomaly in  $\alpha$  was found firstly, which suggested an existence of a structural phase transition at 270 K.

## 2. EXPERIMENTAL

### (2.1) Preparation of Hot-Pressed Samples

Hot-pressed samples were synthesized from Bi, Sb and Te with purity of 99.999 % by melting. In preparation of  $(\text{Sb}_2\text{Te}_3)_{0.75}(\text{Bi}_2\text{Te}_3)_{0.25}$ , a stoichiometric amount of compounds and an additional excess of Te were encapsulated in glass tube with a few amount of inert gas. Excess Te is used to get adequate carrier concentrations. After melted solutions were shook for one hour, they were solidified rapidly by pulling out to the lower zone of the furnace. These ingots were ground into powders. After sieving powders, they were annealed at 620 K for ten hours in the atmosphere of hydrogen gas and pressed at about 770 K under the pressure of 400 kg/cm<sup>2</sup> in argon gas. Crystal structures of  $\text{Bi}_2\text{Te}_3$  and  $\text{Sb}_2\text{Te}_3$  are both hexagonal with space group of  $D_{3d}^5$ - $R\bar{3}m$  at room temperature. The lattice constants of the present hot-pressed sample are examined by X-ray diffraction (CuK $\alpha$ ) as  $a = 4.289(4)$  and  $c = 30.457(15)$  Å at room temperature. The value of  $a$  follows well with Vegard's law for alloys. However the *c* lattice constant shows a positive deviation, which is estimated as about 0.07 Å. The deviation of the hexagonal axis from Vegard's law was observed also in  $\text{Bi}_2\text{Se}_3$ - $\text{Bi}_2\text{Te}_3$  [6]. By X-ray diffraction, it was confirmed that these samples were highly oriented along the hexagonal *c*-axis [4].

### (2.2) Thermal Expansion Measurement

It is well known that V<sub>2</sub>-VI<sub>3</sub> compounds exhibit anisotropic thermoelectric properties. The linear thermal

expansion coefficient  $\alpha$  perpendicular to the hexagonal  $c$ -axis was measured by two strain gauge method with a reference sample Cu perpendicular to the pressing direction (almost the hexagonal  $c$ -axis) of hot-pressed samples. The dimension of samples used was  $4 \times 3.5 \text{ mm}^2$  in area and  $1 \sim 0.5 \text{ mm}$  along the hot-pressed hexagonal  $c$ -axis in thickness. Small strain gauges (Kyowa KFL-02) were attached by gauge cement (Kyowa PC-6) to the sample and the reference Cu sheet under the same condition.

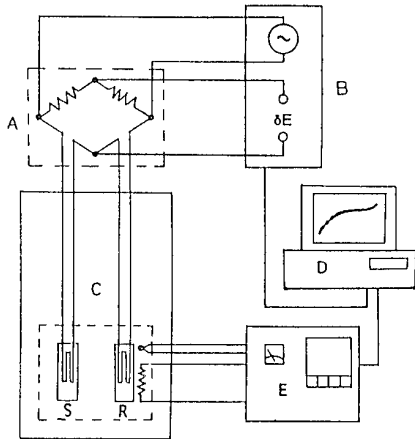


**FIGURE 1.** Schematic diagram of thermal expansion measurements. A : Wheatstone bridge, B : Gauge amplifier, C : Cryostat, D : Micro-computer, E : Temperature controller, S : Sample ( $\text{Bi}_{0.5}\text{Sb}_{1.5}\text{Te}_3$ ), R : Reference sample (Cu).

After annealing 1 hour at  $80^\circ\text{C}$ , 2 hours at  $130^\circ\text{C}$ , and 2 hours at  $150^\circ\text{C}$ , measurements were performed from liquid nitrogen temperature to  $410\text{ K}$ . Output signals of Wheatstone bridge amplified by a strain gauge amplifier (Kyowa DPM-611B) were monitored and analyzed by a personal computer. A schematic diagram of experimental setup was shown in Figure 1.

### 3. RESULTS AND DISCUSSION

#### (3.1) Thermal Expansion Coefficient

The volumetric and linear thermal expansion coefficients,  $\beta$  and  $\alpha$  are given as

$$\beta = (\delta \ln V / \delta T)_p,$$

$$\alpha = (\delta \ln l / \delta T)_p,$$

where  $V$  and  $l$  are volume and length of sample at temperature  $T$ . For isotropic solids, the relation  $\beta = 3\alpha$  hold.

Generally thermal expansion is considered to be induced by lattice vibrational, some electronic and magnetic contribution. At sufficient high temperature such as at room temperature for our samples, the lattice vibrational contribution is essential.

Temperature dependence of  $\alpha$  perpendicular to the hexagonal  $c$  axis of  $\text{Bi}_{0.5}\text{Sb}_{1.5}\text{Te}_3$  is shown in Figure 2. The value of  $\alpha$  at  $300\text{K}$  is  $16 \cdot 10^{-6} \text{ K}^{-1}$ , which is in good agreement with the values  $22 \cdot 10^{-6}$  for pure  $\text{Sb}_2\text{Te}_3$  [7] and  $14.4 \cdot 10^{-6} \text{ K}^{-1}$  for pure  $\text{Bi}_2\text{Te}_3$  [5]. Below room temperature,  $\alpha$  changes rather rapidly and shows a small but sharp peak at  $T_c = 304\text{ K}$ . In the high temperature region, it is almost constant but increase above  $400\text{ K}$ .

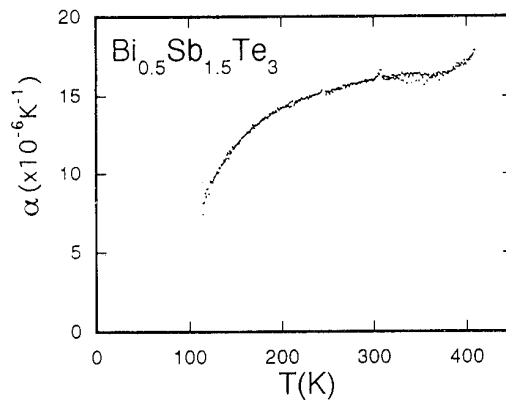


**FIGURE 2.** Temperature dependence of a linear coefficient of thermal expansion  $\alpha$  of  $\text{Bi}_{0.5}\text{Sb}_{1.5}\text{Te}_3$ . A new small peak was observed at  $304\text{ K}$ .

The small peak in  $\alpha$  is considered to be related to the anomaly in heat capacity as discussed in the following section. This evidence indicates that there are some structural changes at  $T_c$ , which may be expected to the occurrence of structural phase transition in  $\text{Bi}_{0.5}\text{Sb}_{1.5}\text{Te}_3$ . However the temperature of the anomaly in  $\alpha$  is about 20 K higher than that reported in the specific heat measurement [4]. Then it should be probable that the temperature  $T_c$  depends on the concentration of Bi and Sb in the samples. To see this possibility, we measured  $\alpha$  of  $\text{Bi}_2\text{Te}_3$  and  $\text{Sb}_2\text{Te}_3$ , of which results were shown in Figures 3 and 4. The general behaviour in  $\alpha$  shows similar temperature dependence each other. Around room temperature, the values of  $\alpha$  of  $\text{Bi}_{0.5}\text{Sb}_{1.5}\text{Te}_3$  are almost

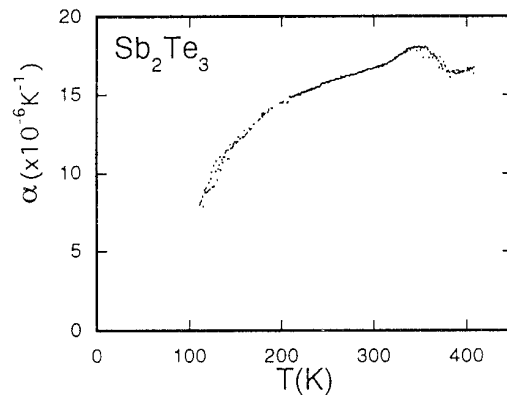


**FIGURE 3.** Temperature dependence of a linear coefficient of thermal expansion  $\alpha$  of  $\text{Sb}_2\text{Te}_3$ .

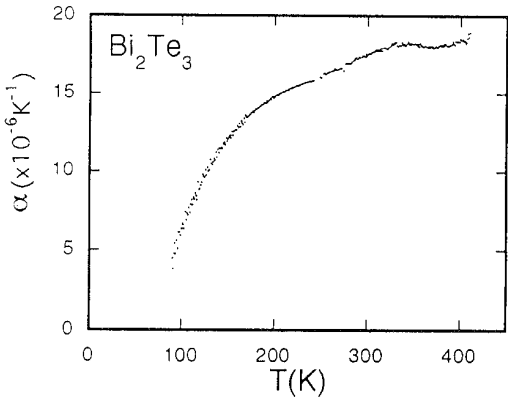


**FIGURE 4.** Temperature dependence of a linear coefficient of thermal expansion  $\alpha$  of  $\text{Bi}_2\text{Te}_3$ .

constant and are suppressed compared with those of  $\text{Sb}_2\text{Te}_3$  and  $\text{Bi}_2\text{Te}_3$ . The sharp peak of  $\alpha$  in  $\text{Bi}_{0.5}\text{Sb}_{1.5}\text{Te}_3$  changes a broad one around  $T_c = 346$  K in  $\text{Sb}_2\text{Te}_3$  and a vague one at  $T_c = 332$  K in  $\text{Bi}_2\text{Te}_3$ . The tendency of slight increase in  $\alpha$  was observed above 400 K in all three samples. Although it is not clear to confirm the explicit relation between  $T_c$  and the concentration ratio of Bi/Sb,  $T_c$  is influenced sensitively by the concentration or the hall concentration in these samples.

### (3.2) Comparison with Specific Heat

A change of volume  $\Delta V$  is known to follow the Gruneisen formula;

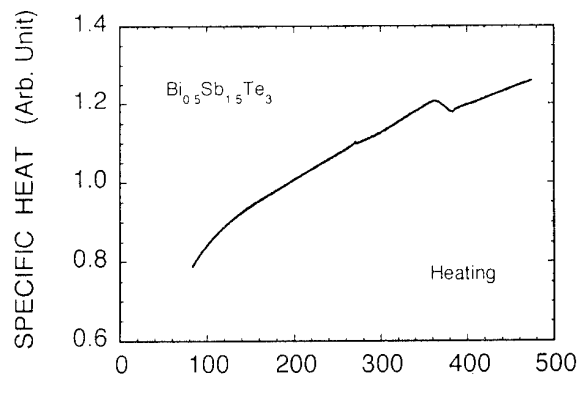
$$\frac{\Delta V}{V} = \kappa \gamma U(T)$$

where  $\kappa$ ,  $\gamma$  and  $U(T)$  are compressibility, Gruneisen constant and the energy in the lattice modes at  $T$ , respectively. Therefore the thermal expansion coefficient  $\beta$ , which is the derivative of the dilatation with  $T$ , is proportional to the phonon specific heat [8].

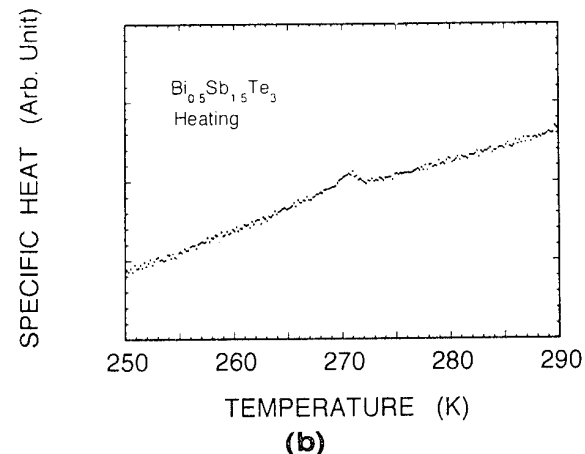
Figure 5 shows the temperature dependence of specific heat of hot-pressed sample of  $\text{Bi}_{0.5}\text{Sb}_{1.5}\text{Te}_3$  measured by an AC calorimeter [4], which shows two anomalies at 270 K and 370 K. Above room temperature, the anomalous part of  $C_p$  is relatively large compared with one at 270 K. The anomaly about 370 K is considered to correspond to the metal-insulator phase transition, which corresponds to the anomaly of resistivity of  $p$ -type  $\text{Bi}_2\text{Te}_{2.85}\text{Se}_{0.15}$  reported by Kaibe [9].

At 270 K, small and cusp-like anomaly was found. In single crystal of  $\text{Bi}_{0.5}\text{Sb}_{1.5}\text{Te}_3$ , the corresponding anomaly at 270 K was also detectable but it was rather broad which may be due to the inhomogeneity of the sample.

The behaviour of specific heat is very similar to those observed in linear coefficients of thermal expansion as expected from the Gruneisen formula, although our samples are not isotropic but axial crystals.



**(a)**



**(b)**

**FIGURE 5.** Temperature dependence of specific heat of hot-pressed  $\text{Bi}_{0.5}\text{Sb}_{1.5}\text{Te}_3$  measured by AC calorimetry. Two anomalies at 370 K and 270 K were found. (a) Overall dependence on temperature, and (b) an expanded plot of (a) around 270 K.

### (3.3) Comparison with Elastic Properties

The origin of this new anomaly in  $\alpha$  and  $C_p$  has not been well understood, but this suggests the possibility of structural phase transition at 270 K.

For axial crystals as our hexagonal samples, the linear coefficient  $\alpha$  is given as

$$\alpha = \{(s_{11} + s_{12}) \gamma_{\perp} + s_{13} \gamma_{\parallel}\} C_p / V$$

where  $s_{ij}$  are elastic compliances, and  $\gamma_{\perp}$  and  $\gamma_{\parallel}$  are principal Gruneisen functions perpendicular and parallel to the hexagonal axis [10]. Therefore similar anomalies should be expected in elastic properties of  $\text{Bi}_{0.5}\text{Sb}_{1.5}\text{Te}_3$ . Ultrasonic measurements of  $\text{Bi}_2\text{Te}_3$  [11] showed a small increase of elastic modulus  $c_{66}$  ( $= (c_{11} + c_{12})/2$ ) around 260

K, which might be regarded as the same origin of anomalies in thermal expansion and specific heat.

Recently, it is known that the IV-VI compounds such as GeTe, SnTe, Pb<sub>1-x</sub>Sn<sub>x</sub>Te, Pb<sub>1-x</sub>Ge<sub>x</sub>Te [12, 13, 14] and the II-VI compound Cd<sub>1-x</sub>Mn<sub>x</sub>Te [15], undergo structural phase transitions and represent a unique class of displacive ferroelectric semiconductors with a narrow energy gap.

#### 4. CONCLUSION

The thermal expansion properties of Bi<sub>0.5</sub>Sb<sub>1.5</sub>Te<sub>3</sub> were studied. It has been found that the new anomaly in thermal expansion coefficient was observed at 304 K as well as the anomalies in specific heat and elastic modulus. It may be explained well that this anomaly appears as a result of a new phase transition. Further structural studies of Bi<sub>0.5</sub>Sb<sub>1.5</sub>Te<sub>3</sub> crystals are necessary to confirm the existence of structural phase transition.

#### ACKNOWLEDGMENTS

Authors would like to express their sincere thanks to Professor M. Oda, Dr. J. Tuda and Professor H. Yamashita for kind suggestions and discussion.

- [3] R.W.G. Wyckoff, *Crystal Structures*, Vol. 2 (Interscience Publishers, New York, 1964) p.29.
- [4] K. Fukuda, A. Onodera and H. Haga, *Proc. of XII International Conference on Thermoelectrics* (Yokohama, 1993) p.274
- [5] J.O. Barnes, J.A. Rayne and R.W. Ure Jr, *Phys. Letters* **46A** (1974) 317.
- [6] G.R. Miller, Che-Yu Li and C.W. Spencer, *J. Appl. Phys.* **34** (1963) 1398.
- [7] A. Krost, Dissertation, RWTH Aachen (1981).
- [8] J. M. Ziman, *Principles of the Theory of Solids*, (Cambridge University Press, 1965, London) p.63.
- [9] H. Kaibe, *Study of Thermoelectric Properties of Bi<sub>2</sub>Te<sub>3</sub>- type Semiconductors* (Doctor thesis, Keio University, 1984).
- [10] T.H.K. Barron, J.G. Collins and G.K. White, *Advances in Physics* **29** (1980) 609.
- [11] J. O. Jenkins, J.A. Rayne and R.W. Ure Jr, *Phys. Rev. B5* (1972) 3171.
- [12] Q.T. Islam and B.A. Bunker, *Phys. Rev. Lett.* **59** (1987) 2701.
- [13] S. Katayama and K. Murase, *Solid State Commun.* **36** (1980) 707.
- [14] H. Yaraneri, A.D.C. Grassie, H. Yusheng and J.W. Loram, *J. Phys. C14* (1981) L441.
- [15] R. Weil, R. Nkum, E. Muranevich and L. Benguigui, *Phys. Rev. Lett.* **62** (1989) 2744.

#### References

- [1] C. Wood, *Rep. Prog. Phys.*, **51** (1988) 459.
- [2] M. Stordeur, *Phys. Stat. Sol. (b)*, **161** (1990) 831.

## Thermoelectric properties and segregation behaviors of n-type Bi<sub>2</sub>Te<sub>3</sub>-Bi<sub>2</sub>Se<sub>3</sub> solid solution

Heon Phil Ha, Dow Bin Hyun, Young Whan Cho and Jae Dong Shim

*Korea Institute of Science and Technology  
P.O. box 131, Cheongryang, Seoul, Korea*

### **Abstract**

The ingots of 90%Bi<sub>2</sub>Te<sub>3</sub>-10%Bi<sub>2</sub>Se<sub>3</sub> solid solution were grown by the zone melting method and their thermoelectric properties were measured. From the experimental study on the segregation behaviors of each component, it was found that the abrupt increase of the electrical resistivity and Seebeck coefficient near the top of the ingot originated mainly from the evaporation of Te and Se. The addition of 0.3 wt.% excess Te to the starting composition was found to be effective to have uniform carrier concentration and the thermoelectric properties vary little along the ingots.

### **Introduction**

In the previous study[1] on the thermoelectric properties of the Bi<sub>2</sub>Te<sub>3</sub>-Bi<sub>2</sub>Se<sub>3</sub> system, we confirmed that the maximum figure of merit higher than  $2.95 \times 10^{-3}$  K<sup>-1</sup> can be obtained at about 6–10 mol% Bi<sub>2</sub>Se<sub>3</sub> composition with CdCl<sub>2</sub> doping. When we examined the distributions of the thermoelectric properties along the ingots grown by the zone melting method, abrupt increases of the Seebeck coefficient and electrical resistivity were found near the top of the ingot which were caused by the segregation of the components. Because bismuth telluride ingots are usually grown by the zone melting method, it is important to have uniform thermoelectric properties for high yields. In the present study, several methods have been tried to alleviate the segregation problem and ingots having very uniform thermoelectric properties could be grown by the addition of excess Te or by using a dummy block in the ampoule.

### **Experimental**

High purity(>99.99%) Bi, Te and Se granules with CdCl<sub>2</sub> as dopants were weighed into a quartz tube 13

mm in internal diameter, the inside wall of which had been coated with carbon by acetone cracking. The weight of each ingot was 150g. The quartz tube was vacuum sealed under  $10^{-4}$  torr and the content melted and homogeneously mixed in a rocking furnace for 2 hours. The ingots were grown in the zone melting furnaces with narrow and normal zone lengths at 800°C and the growth speed was fixed at 0.1 mm/min. Rectangular samples of 5×5×10 mm were cut along the growth direction of the ingot by an electrodischarge cutting machine for the measurements of the thermoelectric properties parallel to the growth direction. The Seebeck coefficient  $\alpha$  was measured by the heat pulse method and the electrical resistivity and figure of merit by the Harman method at 300 K as described earlier[2]. The segregations of each component along the growth direction of the ingot were examined by the ICP analysis.

### **Results and Discussions**

#### *Thermoelectric properties along the ingot*

Fig. 1 shows the variations of the Seebeck coefficient and electrical resistivity along the ingot of 90%Bi<sub>2</sub>Te<sub>3</sub>-10%Bi<sub>2</sub>Se<sub>3</sub> solid solution with CdCl<sub>2</sub> dopant. The Seebeck coefficient and electrical resistivity react more sensitively to the variation of dopant than that of the composition. Thus uniform thermoelectric properties along the ingot except the top part means that the dopant segregation was little whereas there was considerable compositional segregation as shown in Fig. 2. Near the top of the ingot, however, they start to increase abruptly so that the power factor and the figure of merit decreased when Seebeck coefficient became higher than 250  $\mu\text{V/K}$ . When the molten zone length(i.e., the length of the furnace) was short, the Seebeck coefficient started to increase at the higher

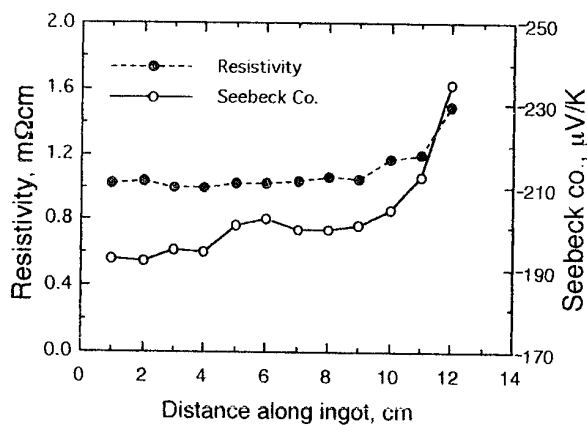


Fig. 1. Variation of electrical resistivity and Seebeck coefficient along ingots.

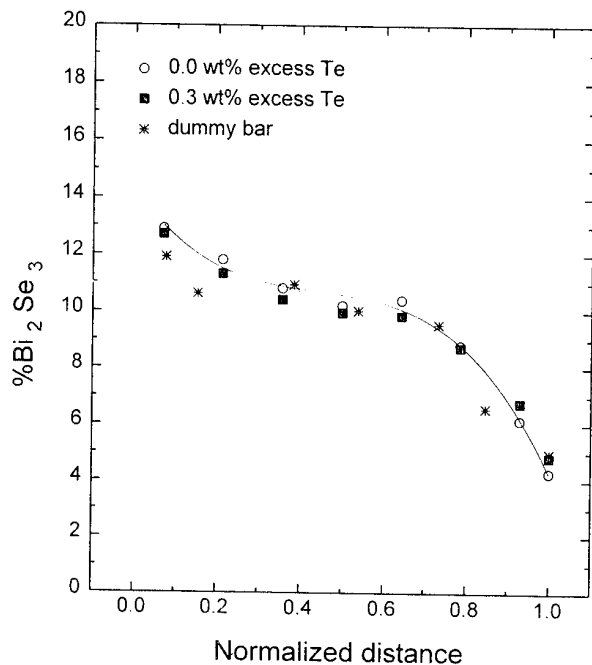
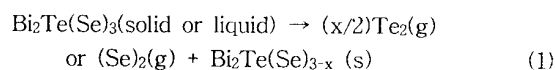


Fig. 2 Segregation of  $\text{Bi}_2\text{Se}_3$  along ingot.

part of the ingot. Because both the Seebeck coefficient and electrical resistivity increased simultaneously there must be decrease of carrier concentration near the top of the ingot. One can consider two possibilities of decrease in carrier concentration; one is the segregation of the halogen dopant and the other is that of the main

components because the evaporation of them may cause increase in Seebeck coefficient as well as in electrical resistivity. We assumed that the evaporation of Te and Se takes place by the following reaction.[3]



#### Effect of free space

Because Bi, Te and Se granules with  $\text{CdCl}_2$  dopants were weighed into a quartz tube and then melted and homogenized within a rocking furnace before growing by the zone melting method there was always free space at the upper part of the quartz tube. Thus near the end of the zone melting growth elements can be easily evaporated to the free space where pressure is lower than  $10^{-4}$  Torr. To check this a quartz rod as a dummy bar was inserted into the quartz tube after melting to reduce the free space as shown in Fig. 3. More uniform distribution of Seebeck coefficient as shown in Fig. 4 could be obtained whereas the compositional segregation along the ingot changed little as shown in Fig. 2. These results suggest that the increase in Seebeck coefficient near the top of the ingot was mainly due to the evaporation of Se or Te since the equilibrium partial pressures of Bi is much lower than those of chalcogenide Se and Te in the solid solution near the melting temperature. But the amount of evaporation was not high enough to bring discernible compositional change.

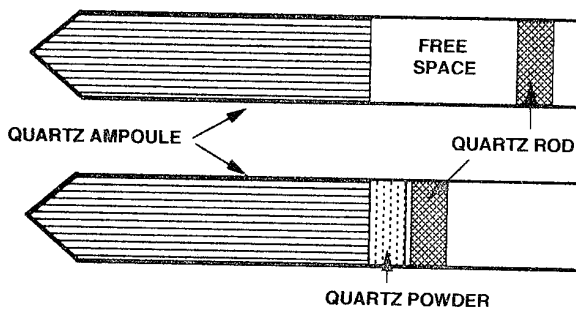


Fig. 3 Method of reducing free space

### *Effect of excess Te*

Although we can improve the yield of ingot by reducing the free space, this method needs additional time and quartz tube. To compensate the decrease of the carrier concentration by the evaporation of the components near the top of the ingot, excess Te was added to the starting composition. This idea came from the experimental results[4] on 22.5%Bi<sub>2</sub>Te<sub>3</sub>-77.5%Sb<sub>2</sub>Te<sub>3</sub> p-type solid solution where excess Te whose segregation coefficient is less than 1 goes to the top part of the ingot in the zone melting process and from the fact that Seebeck coefficient and electrical resistivity are much less sensitive to the excess Te than to the amount of dopant. Fig. 5 and Fig. 6 shows the effect of excess Te on Seebeck coefficient along the ingot. As can be seen in this figure, 0.3 wt% excess Te was enough to increase the uniformity of Seebeck coefficient considerably. It also confirms that the effect of dopant evaporation was small, if any. However too much excess Te slightly reduced Seebeck coefficient throughout the ingot. From these results, the decrease in carrier concentration according to the evaporation Te or Se can be explained as follows.

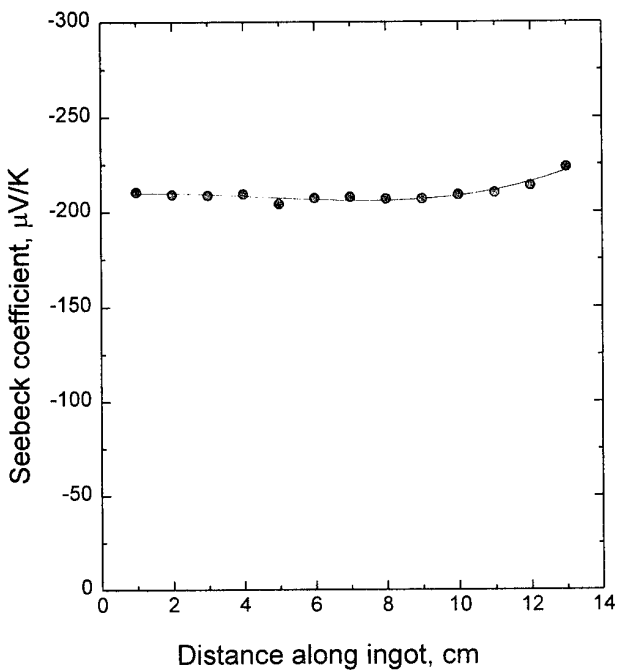


Fig. 4 Effect of dummy bar on Seebeck coefficient

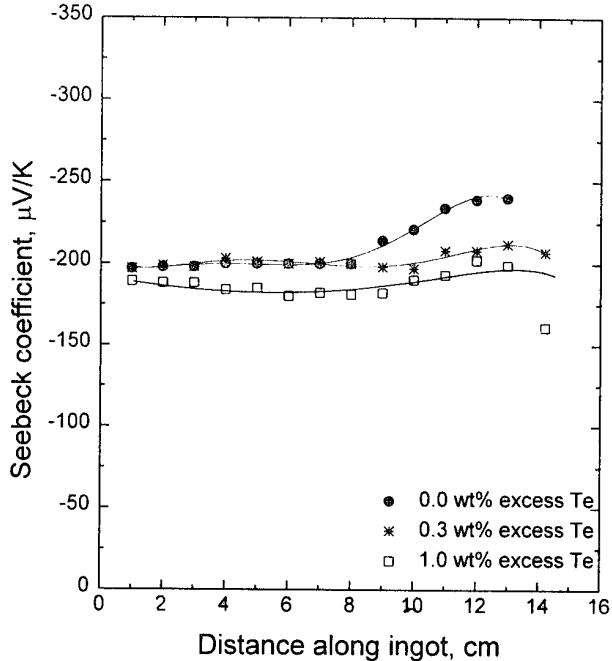


Fig. 5 Effect of excess Te on Seebeck coefficient

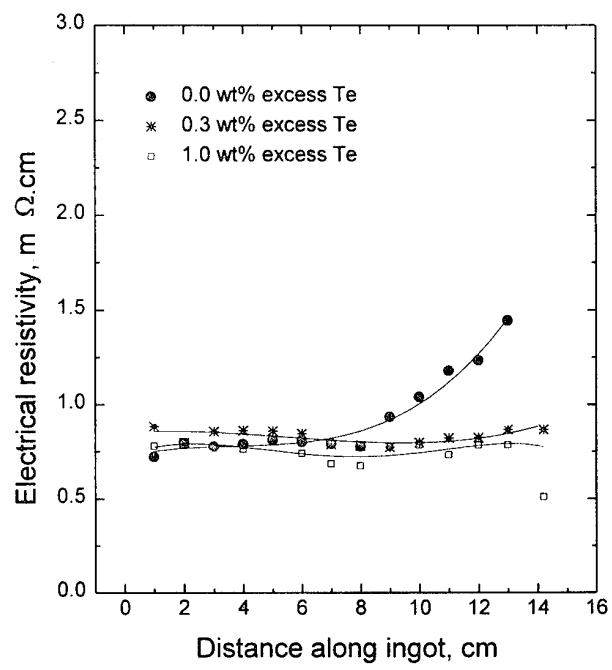


Fig. 6 Effect of excess Te on electrical resistivity.

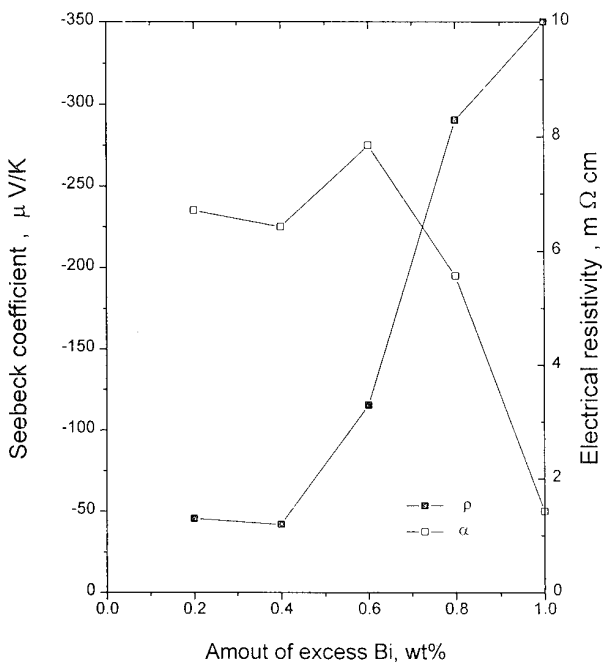


Fig. 7 Effect of excess Bi on Seebeck coefficient.

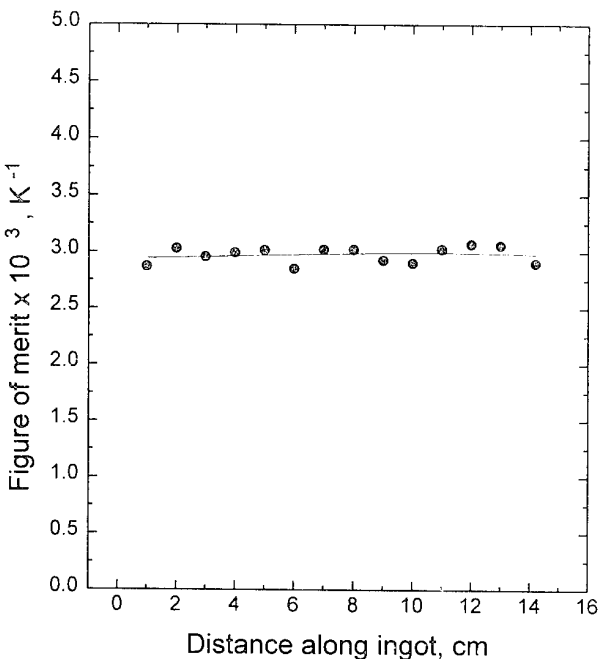


Fig. 8 Figure of merit along ingot.

When Te or Se is evaporated by the eqn. (1), the concentration of the melt becomes rich in Bi compared to the starting composition and the carrier concentration will be decreased near the top part of the ingot after solidification. On the other hand, Fig. 7 shows that the addition of excess Bi to the starting composition decreases carrier concentration whereas the effect of excess Te on the carrier concentration was small as shown in Fig. 5 and Fig. 6. With 0.3 wt% excess Te ingots having the figure of merit higher than  $3.0 \times 10^{-3} \text{ K}^{-1}$  throughout the ingot could be obtained as shown in Fig. 8.

### Conclusions

The abrupt increase in Seebeck coefficient along the ingot of  $90\% \text{Bi}_2\text{Te}_3 - 10\% \text{Bi}_2\text{Se}_3$  solid solution with  $\text{CdCl}_2$  dopant was caused by the evaporation of Se and Te. This can be prevented by reducing the free space in the quartz ampoule or by the addition of excess Te to the starting composition.

### References

1. Ha H. P., Cho Y. W., Hyun D. B. and Shim J. D. "Effects of Composition and Process Parameters on the Thermoelectric Properties of N-Type  $\text{Bi}_2\text{Te}_3-\text{Bi}_2\text{Se}_3$  Solid Solutions" in proceedings of the 13th International Conference on Thermoelectrics, Kansas Missouri USA August 30 - September 1, 1994.
2. Ha H. P., Cho Y. W., Byun J. Y. and Shim J. D. "Effects of Processing Parameters on the Thermoelectric Properties of P-Type  $\text{Bi}_2\text{Te}_3-\text{Sb}_2\text{Te}_3$  Solid Solution" in proceedings of the 12th International Conference on Thermoelectrics, Yokohama Japan, November 9-11, 1993.
3. Bardi G., Cafaro M. L., Gianfreda V. D. and Piacente V., High Temperature Science, Vol 16, pp 377-384 (1983).
4. Ha H. P., Cho Y. W., Byun J. Y. and Shim J. D. J. Phys. Chem. Solids Vol. 55 No 11 pp 1233-1238 (1994).

# THERMOELECTRIC PROPERTIES OF $\text{Sb}_2\text{Te}_3$ -SnTe AND $\text{Sb}_2\text{Te}_3$ -PbTe PSUDO-EUTECTIC ALLOYS

Kyung-Wook JANG<sup>\*</sup> and Dong-Hi LEE

*Department of Metallurgical Engineering, Yonsei University,  
134 Shinchon-dong, Seodaemun-gu, Seoul, 120-749, KOREA*

Thermoelectric properties of eutectic alloys in  $\text{Bi}_2\text{Te}_3$ -PbTe,  $\text{Sb}_2\text{Te}_3$ -PbTe and  $\text{Sb}_2\text{Te}_3$ -SnTe systems were investigated. Seebeck coefficients show little dependence on the content of PbTe or SnTe but electrical and thermal conductivities show different variations in each alloy system with PbTe or SnTe. The behaviors of electrical and thermal conductivities can be understood based on microstructural changes resulting from different cooling rates during solidification or by subsequent heat treatments. The relationship of thermoelectric properties and microstructures is discussed in light of scattering effects of dispersed phases on carriers and phonons.

## 1. INTRODUCTION

Efficiency of direct energy conversion with thermoelectric devices depends on figure of merit ( $Z=\alpha^2\sigma/k$ , where  $\alpha$  is Seebeck coefficient,  $\sigma$  electrical conductivity, and  $k$  thermal conductivity) of thermoelectric materials as well as devising techniques and operating conditions. High figure of merit can be achieved through increasing Seebeck coefficient and electrical conductivity and decreasing thermal conductivity[1].

But it is not possible to improve Seebeck coefficient and electrical conductivity together, because they vary in opposite way as a function of carrier concentration and mobility[2]. Thermal conductivity is closely related to the mobilities of carriers and phonons. Phonon contribution to thermal conductivity, namely lattice thermal conductivity, is made independent of carriers. A large amount of research on thermoelectric materials have been done to reduce lattice thermal conductivity by several methods such as solid solution alloying[3~5], fine powder sintering[6~12] and nonconducting powder dispersion[13~14]. Solid solution alloying proved its effectiveness to decrease the lattice thermal conductivity of  $\text{Bi}_2\text{Te}_3$  and  $\text{Sb}_2\text{Te}_3$  based thermoelectric materials. Despite the reduction of thermal conductivity by fine powder sintering and nonconducting powder dispersion, little improvement of figure of merit was achieved due to the accompanying reduction of electrical conductivity. On the other hand, fine particles with good electrical conductivity were used as dispersing phases to reduce lattice thermal conductivity without deteriorating electrical conductivity. We reported that the lattice thermal conductivity of  $\text{Bi}_2\text{Te}_3$ -19mol% PbTe alloy can be reduced by aligning rod type  $(\text{Bi}_2\text{Te}_3)_2(\text{PbTe})$  eutectic phases in the  $\text{Bi}_2\text{Te}_3$  matrix by unidirectional solidification[15].

In this study, uniform dispersion of PbTe or SnTe phase with good electrical conductivity in the corresponding matrix was attempted to reduce thermal conductivity. Thermoelectric properties of pseudo-eutectic alloys are examined with respect to the fraction of dispersed phase and their microstructures.

## 2. EXPERIMENTAL

$\text{Bi}_2\text{Te}_3$ ,  $\text{Sb}_2\text{Te}_3$ , PbTe, and SnTe were prepared by melting 99.99% pure Bi, Te, Sb, Pb, and Sn in each stoichiometric proportion at 800~1000°C in quartz tube of 13mm diameter vacuum sealed under  $10^{-5}$  torr. Microvibration during melting was applied to make sure compositional homogeneity.

$\text{Bi}_2\text{Te}_3$ -10~70mol% PbTe alloys of 6mm diameter were prepared —

by melting at 800°C and subsequent furnace cooling or water quenching.  $\text{Sb}_2\text{Te}_3$ -5~40mol% PbTe and  $\text{Sb}_2\text{Te}_3$ -5~40mol% SnTe alloys of the same size were water quenched from melts and part of these alloys were additionally heat treated at 300~500°C for 100 hrs.

Microstructures were examined by optical microscope after etching with  $\text{HNO}_3:\text{HCl}:\text{H}_2\text{O}=1:1:2$  and  $\text{HNO}_3:\text{H}_2\text{O}=1:1$  solution for  $\text{Bi}_2\text{Te}_3$ -based alloys and  $\text{Sb}_2\text{Te}_3$ -based alloys, respectively. The measurement method for Seebeck coefficient is described elsewhere[11,12]. AC 4 point probe method was employed for the measurement of electrical conductivity. Figures of merit were measured by Harman method[16], and thermal conductivities were evaluated from the figures of merit, Seebeck coefficients and electrical conductivities obtained.

## 3. RESULTS AND DISCUSSION

### 3.1. $\text{Bi}_2\text{Te}_3$ -PbTe alloys

In  $\text{Bi}_2\text{Te}_3$ -PbTe pseudo-binary system, eutectic alloy consisting of  $\text{Bi}_2\text{Te}_3$  and  $(\text{Bi}_2\text{Te}_3)_2(\text{PbTe})$  phases is formed at 19mol% PbTe[17,18]. The Seebeck coefficient and electrical conductivity of  $(\text{Bi}_2\text{Te}_3)_2(\text{PbTe})$  phase are  $87 \mu\text{V/K}^{-1}$  and  $950 \Omega^{-1}\text{cm}^{-1}$ , respectively.

Figure 1 shows the thermoelectric properties of  $\text{Bi}_2\text{Te}_3$ -PbTe pseudo-binary system as a function of PbTe mol%. Seebeck coefficient shows a slight increase with PbTe mol%. Different cooling methods in this system produced no difference in Seebeck coefficient within experimental error. Electrical conductivity decreases with the PbTe content. The electrical conductivities of furnace cooled alloys are slightly higher than those of water quenched ones. Thermal conductivities drastically decreases from  $4.5 \text{ Wm}^{-1}\text{K}^{-1}$  to  $0.8 \text{ Wm}^{-1}\text{K}^{-1}$  as the PbTe content increases from 10mol% to 20mol% regardless of cooling rate. However, cooling methods affected thermal conductivities in a different way. Above 20mol% PbTe, as shown in Fig. 1(c), the thermal conductivities of water quenched alloys decrease from  $4.5 \text{ Wm}^{-1}\text{K}^{-1}$  to  $1.1 \text{ Wm}^{-1}\text{K}^{-1}$ , but on the contrary those of furnace cooled ones increase from  $0.8 \text{ Wm}^{-1}\text{K}^{-1}$  to  $4.8 \text{ Wm}^{-1}\text{K}^{-1}$ , as the amount of PbTe increases.

Variation of thermoelectric properties with PbTe can be appreciated qualitatively from the mixture rule of composite materials[19] and their microstructural developments. We can explain the decrease in electrical conductivity with PbTe mol% with the following two aspects; one is the reduction of electron concentration due to alloying p-type PbTe in n-type  $\text{Bi}_2\text{Te}_3$  and the other is the increased electron scattering by dispersed  $(\text{Bi}_2\text{Te}_3)_2(\text{PbTe})$  phases.

The large difference in thermal conductivity above 20mol% PbTe

\* present address ; Dept. of Material Sci. and Eng., Hanseo Univ.  
360 Daegok-ri, Haemi, Seosan, Chung-Nam, 352-820, KOREA

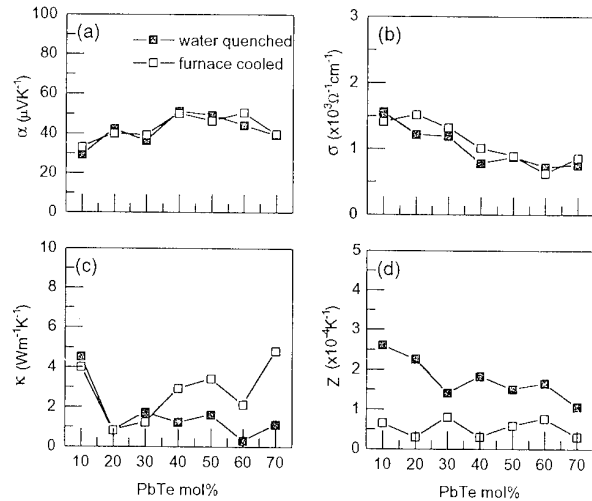


FIG. 1. Variation of thermoelectric properties with PbTe mol% in  $\text{Bi}_2\text{Te}_3$ -PbTe alloys ; (a) Seebeck coefficient, (b) electrical conductivity, (c) thermal conductivity and (d) figure of merit

between the furnace cooled and water quenched alloys can be understood from their microstructures. As shown in Photo. 1, fine dendrites of  $5\sim 7\text{ }\mu\text{m}$  diameter were formed in the matrix for water quenched alloys, but large dendrites of  $50\sim 70\text{ }\mu\text{m}$  diameter for furnace cooled ones. As the PbTe amount increases, dendrites of both types will increase phonons scattering in the matrix because the interdendritic spacing becomes smaller. However, in the case of furnace cooled alloys, the size of dendrite relative to the mean free path of long wavelength phonon will increase with PbTe. Therefore the thermal conductivity within dendrite will increase with PbTe due to the decreasing phonon scattering, resulting in the increase of overall thermal conductivity with PbTe.

### 3.2. $\text{Sb}_2\text{Te}_3$ -PbTe alloys

In  $\text{Sb}_2\text{Te}_3$ -PbTe system,  $(\text{Sb}_2\text{Te}_3)_3(\text{PbTe})_2$  phase which has  $53\text{ }\mu\text{V/K}$  of Seebeck coefficients and  $2.55\text{ Wm}^{-1}\text{K}^{-1}$  of thermal conductivity forms pseudo-eutectic alloy with  $\text{Sb}_2\text{Te}_3$ [19].

Figure 2 shows the trends of thermoelectric properties with PbTe in water quenched  $\text{Sb}_2\text{Te}_3$ -PbTe system. The Seebeck coefficient shows an abrupt drop around 15mol% PbTe and the electrical and thermal conductivities show somewhat weaker drops around 25mol% PbTe. This drop in electrical and thermal conductivity around 30mol% PbTe can be explained by a significant change in microstructure as shown in Photo. 2. Rod type of eutectic phases are observed up to 20mol% PbTe and lamellar type of microstructures appear from 30mol%. We believe that the significantly increased second phase fraction from 30mol% PbTe with the appearance of lamellar structure is responsible for such sudden decreases of electrical and thermal conductivities at the corresponding composition.

The variations of thermoelectric properties with microstructural changes were investigated for the 40mol% PbTe- $\text{Sb}_2\text{Te}_3$  alloy which showed the lowest thermal conductivity. The thermoelectric properties of the alloy as a function of cooling rates and heat treatments are summarized in Table 1. Similar to the results of  $\text{Bi}_2\text{Te}_3$ -PbTe system, the electrical and thermal conductivities of furnace cooled alloys are 1.8 and 1.6 times higher than those of water quenched ones, respectively. In water quenched samples, subsequent heat treatments increased electrical and thermal conductivities. Furthermore the higher temperature produced better electrical and thermal conductivities. As can be seen in Photo. 2(d) and Photo. 3(a) and (c), irregular shape of

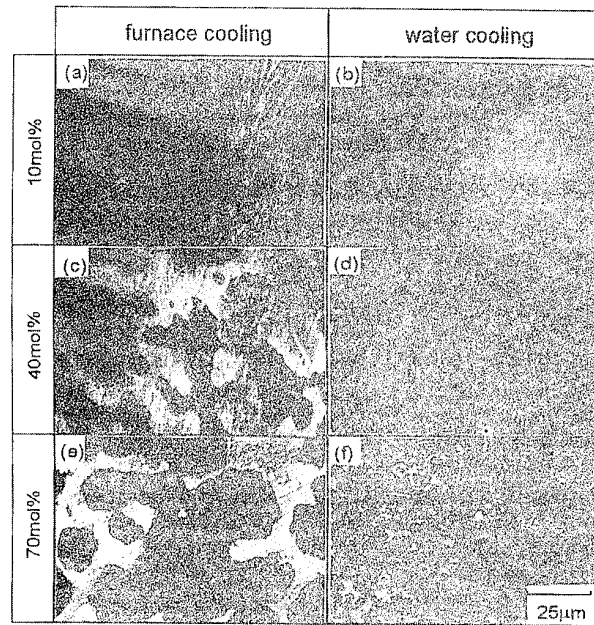


PHOTO. 1. Optical micrographs of  $\text{Bi}_2\text{Te}_3$ -PbTe alloys showing different dendritic morphologies due to cooling rate from melts; (a)-(b) 10mol% PbTe, (c)-(d) 40mol% PbTe and (e)-(f) 70mol% PbTe.

$(\text{Sb}_2\text{Te}_3)_3(\text{PbTe})_2$  phases in as-water-quenched state are changed to regular lamellar phases after heat treatments at  $300^\circ\text{C}$  and  $500^\circ\text{C}$ . Unstable microstructures of water quenched samples will have more solubility of PbTe and thus more lattice distortion in the matrix than stable lamellar structures in furnace cooled or subsequently heat treated samples. Therefore lamellar structure will have higher electrical and thermal conductivities.

### 3.3 $\text{Sb}_2\text{Te}_3$ -SnTe alloys

In the  $\text{Sb}_2\text{Te}_3$ -SnTe pseudo-binary system,  $(\text{Sb}_2\text{Te}_3)(\text{SnTe})$  phase has  $24\text{ }\mu\text{V/K}$  of Seebeck coefficient and  $3200\text{ }\Omega^{-1}\text{cm}^{-1}$  of electrical conductivity

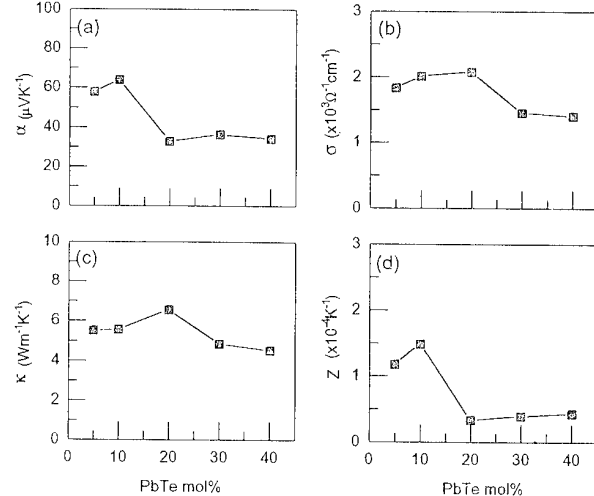


FIG. 2. Variation of thermoelectric properties with PbTe mol% in  $\text{Sb}_2\text{Te}_3$ -PbTe alloys; (a) Seebeck coefficient, (b) electrical conductivity, (c) thermal conductivity and (d) figure of merit

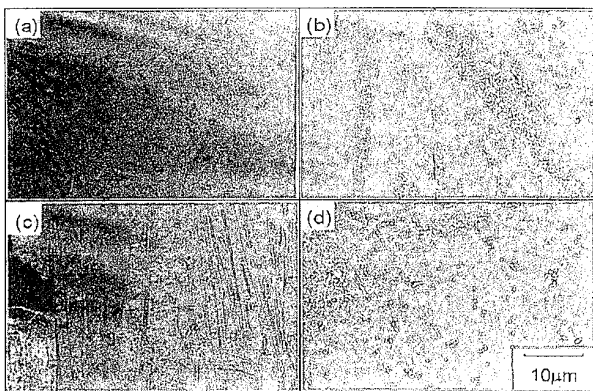


PHOTO. 2. Microstructural changes of water quenched  $\text{Sb}_2\text{Te}_3$ -PbTe alloys due to mole fraction of PbTe compounds; (a) 10mol% PbTe, (b) 20mol% PbTe, (c) 30mol% PbTe and (d) 40mol% PbTe.

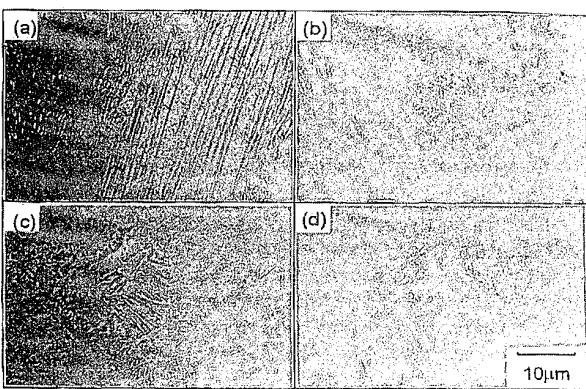


PHOTO. 3. Microstructural variation of  $\text{Sb}_2\text{Te}_3$ -PbTe and  $\text{Sb}_2\text{Te}_3$ -SnTe alloys with the heat treatment condition;  
 (a)  $\text{Sb}_2\text{Te}_3$  - 40mol% PbTe alloys at 300 C during 100 hours  
 (b)  $\text{Sb}_2\text{Te}_3$  - 30mol% SnTe alloys at 300 C during 100 hours  
 (c)  $\text{Sb}_2\text{Te}_3$  - 40mol% PbTe alloys at 500 C during 100 hours  
 (d)  $\text{Sb}_2\text{Te}_3$  - 30mol% SnTe alloys at 500 C during 100 hours

and forms eutectic alloy with  $\text{Sb}_2\text{Te}_3$  at 22mol % SnTe[18,21].

Fig. 3 shows the behaviors of thermoelectric properties with SnTe mol%. Seebeck coefficient decreases with SnTe, but electrical conductivity increases with SnTe. Thermal conductivity decreases with SnTe up to 30 mol% and then suddenly increases.

The behaviors of electrical and thermal conductivities with SnTe can be understood from the high electrical conductivity of  $(\text{Sn}_2\text{Te}_3)$  and the mixture rule for composite materials except at 30mol %.

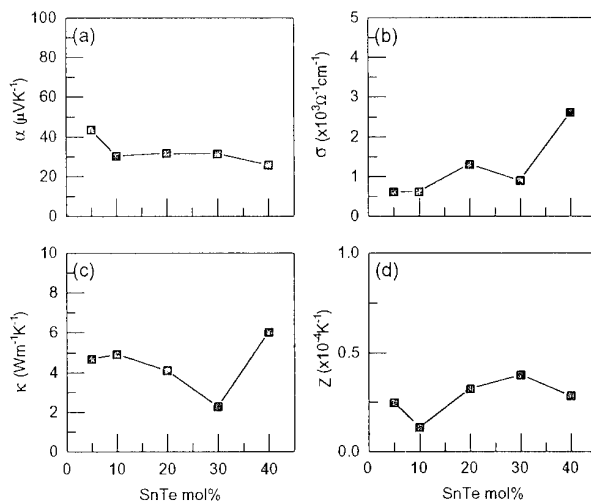


FIG. 3. Variation of thermoelectric properties with SnTe mol% in  $\text{Sb}_2\text{Te}_3$ -SnTe alloys ; (a) Seebeck coefficient, (b) electrical conductivity, (c) thermal conductivity and (d) figure of merit

Abnormal behaviors in some thermoelectric properties at 30mol % SnTe can be explained presumably by its unusual microstructure. As shown in Photo. 4(c), the 30mol% SnTe-Sb<sub>2</sub>Te<sub>3</sub> alloy which is located near the eutectic composition shows irregular needle-like phases of a few  $\mu\text{m}$  width. The boundaries of these phases are thought to act as scattering centers of carriers and phonons. This irregular needle-like structure changes to regular rod type and finally to spherical shape by heat treatments, as shown in Photo. 3(b) and (d).

As the treatment temperature increases from 300°C to 500°C, the electrical and thermal conductivities increase due to the improved regularity of microstructures as shown in Table 2.

#### 4. CONCLUSIONS

Eutectic alloys of  $\text{Bi}_2\text{Te}_3$ -PbTe,  $\text{Sb}_2\text{Te}_3$ -PbTe and  $\text{Sb}_2\text{Te}_3$ -SnTe systems were investigated with expectation that the dispersed phases such as  $(\text{Bi}_2\text{Te}_3)_2(\text{PbTe})$ ,  $(\text{Sb}_2\text{Te}_3)(\text{SnTe})$  and  $(\text{Sb}_2\text{Te}_3)_3(\text{PbTe})_2$  could reduce the lattice thermal conductivity without any significant reduction of electrical conductivity. Thermoelectric properties as a function of composition and microstructure were studied. The results are summarized as follows;

1) Seebeck coefficients show little variation but electrical and thermal conductivities show different variations in each alloy system as the content of PbTe or SnTe increases.

Table 1. Variations of thermoelectric properties of  $\text{Sb}_2\text{Te}_3$ -PbTe alloys with cooling rates from melts and heat treatment temperatures.

	$\alpha$ ( $\mu\text{V/K}^{-1}$ )	$\sigma$ ( $\Omega^{-1}\text{cm}^{-1}$ )	$\kappa$ ( $\text{Wm}^{-1}\text{K}^{-1}$ )	$Z(\times 10^{-4}\text{K}^{-1})$
furnace cooled from melts	37.9	2559	7.05	0.05
water quenched from melts	34	1396	4.51	0.36
water quenched from melts and heat-treated	300°C × 100hr	36.8	953	4.53
	400°C × 100hr	17.2	1653	6.12
	500°C × 100hr	22.3	1851	6.04

Table 2. Variations of thermoelectric properties of  $Sb_2Te_3-SnTe$  alloys with heat treatment temperatures.

	$\alpha (\mu V K^{-1})$	$\sigma (\Omega^{-1} cm^{-1})$	$\kappa (W m^{-1} K^{-1})$	$Z (\times 10^3 K^{-1})$
water quenched from melts	31.4	886	2.27	0.4
water quenched from melts and heat-treated	300°C × 100hr	40.5	1303	3.36
	400°C × 100hr	34.9	1737	3.62
	500°C × 100hr	34.3	1667	5.24
				0.43

2) Microstructural changes resulting from different cooling rates during solidification or by subsequent heat treatments have significant influences on the electrical and thermal conductivities. The dependence of thermoelectric properties on microstructure can be explained in terms of the scattering effects of dispersed phases on carriers and phonons.

## 5. REFERENCE

- [1] E.Altenkirch. Phys. Z., 1909, 10, p560
- [2] D.M.Rowe and C.M.Bhandari. "Modern thermoelectrics", Holt Rinehart and Winston, London, 1983
- [3] C.H.Champness, W.B.Muir and D.T.Chiang. Can. J. Phys., 1967, 45, pp3611-3626
- [4] W.M.Yim and F.D.Rosi. Solid State Electronics, 1972, 15, pp1121-1140
- [5] J.Jaklovszky, R.Ionescu, N.Nistor and A.Chiculita. Phys. Stat. Sol., (a), 1975, 27, pp329-332
- [6] D.M.Rowe, V.S.Shukla, and N.Savvides. Nature, 1981, 290, pp765-766
- [7] C.M.Bhandari and D.M.Rowe. J. Phys. C : Solid State Phys., 1978, 11, pp1787-1794
- [8] J.E.Parrot. J. Phys. C : Solid State Phys., 1969, 2, pp147
- [9] H.R.Meddins and J.E.Parrot. J. Phys. C : Solid State Phys., 1976, 9, pp1263-1275
- [10] R.G.Cope and A.W.Penn. J. Mater. Sci., 1968, 3, pp103-109
- [11] Chang-Mo Kim, Kyung-Wook Jang and Dong-Hi Lee. J. Korean Met., 1991, 29, pp1105-1110
- [12] Kyung-Wook Jang and Dong-Hi Lee. J. Korean Met, 1994, 32, 5, p609
- [13] J.P.Fleurial. Proc. of the 12th ICT, 1993, Yokohama, p1
- [14] Kyung-Wook Jang and Dong-Hi Lee. Proc. of the 12th ICT, 1993, Yokohama, p115
- [15] Chang-Guen Park, Byung-Gue Min and Dong-Hi Lee. Korea J. Mat. Res., 1995, 5, 2, p251
- [16] T.C.Harman, J.H.Cahn and M.J.Logan. J. Appl. Phys., 1959, 30, 9, pp1351-1359
- [17] N.Kh.Abrikosov et al. "Semiconductor II-VI, IV-VI, and V-VI compounds", Plenum Press, 1969, New York, Ch.3
- [18] E.I.Elagina et al. Zh.Neorg.Khim, 1959, 4, 7, p1638 (cited from Ref. 17)
- [19] N.Kh.Abrikosov et al. Izv.An SSSR, Neoorganich materialy, 1965, 1, 2, pp2151 (cited from Ref. 17)
- [20] D.K.Hale. J. Mat. Sci., 1976, 11, pp2105-2141
- [21] A.G.Talybov. Kristallografiya, 1961, 6, 1, p49 (cited from Ref. 17)

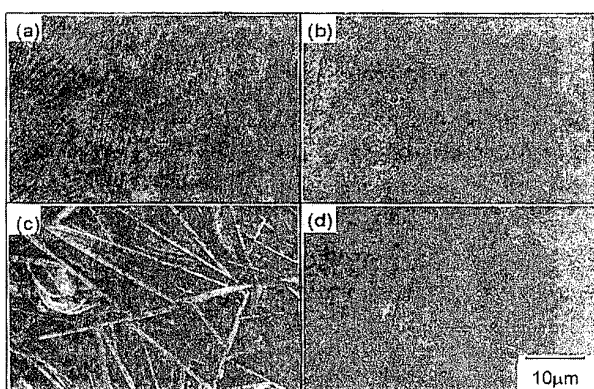


PHOTO. 4. Microstructural changes to water quenched  $Sb_2Te_3-SnTe$  alloys due to mole fraction of SnTe compounds; (a) 10mol% SnTe, (b) 20mol% SnTe, (c) 30mol% SnTe and (d) 40mol% SnTe.

# Influence of electric current flow during crystallization process on thermoelectric properties of materials

Liaschenok V.I., Strekopytova N.I.

*St. Petersburg State Academy of air-space Instrument Making, 190000, Russia*

An influence of electric current upon process of oriented crystallization of solid solutions based on bismuth telluride was studied.

Electric properties of grown ingots of solid solutions based on bismuth telluride can be influenced by various factors, such as misorientation of crystal grains due to an anisotropy of physical properties, heterogeneity of solid solution composition or dopant distribution and some circumstances of crystallization process which can affect the effective distribution coefficients of components and dopant.

Electric properties at room temperatures of grown crystals of solid solutions  $\text{Bi}_2\text{Te}_{2.4}\text{Se}_{0.6}$ ,  $\text{Bi}_{0.52}\text{Sb}_{1.43}\text{Te}_3$ , and  $\text{Bi}_{0.5}\text{Sb}_{0.5}\text{Se}_{0.6}$  were studied as a function of crystallization conditions, primarily to magnitude and direction of electric current flowing across crystallization area as well as to temperature gradient caused in the substance by heater, and to the rate of molten zone movement.

Changing the direction of electric current during the growth of solid solution  $\text{Bi}_2\text{Te}_{2.4}\text{Se}_{0.6}$  crystal effects the Zeebeck coefficient and electric conductivity. It is established that the sufficient brisk change of Zeebeck coefficient  $\Delta\alpha = |\alpha^+| - |\alpha^-|$  ( $\alpha^+$ ,  $\alpha^-$ -Zeebeck coefficients of those parts of crystal, which were grown when electric current created the release or absorption of the Peltier heat, correspondingly, provided that rate of growth and current density are the same) depends on the kind of dopant introduced into solid solution.

The highest values of Zeebeck coefficient jump  $\Delta\alpha$  was observed on materials doped with  $\text{Hg}_2\text{Cl}_2$  and  $\text{CdBr}_2$ . Fig. 1 shows typical distribution of local Zeebeck coefficient values along the ingot of solid solution  $\text{Bi}_2(\text{Te},\text{Se})_3$  doped with  $\text{Hg}_2\text{Cl}_2$ , the current direction being reversed during the growth process. The ingot was grown with a rate  $5 \cdot 10^{-7} \text{ m/s}$ , the temperature gradient being kept on the level  $1.45 \cdot 10^4 \text{ K/m}$  and current density  $1 \cdot 10^6 \text{ A/m}^2$ .

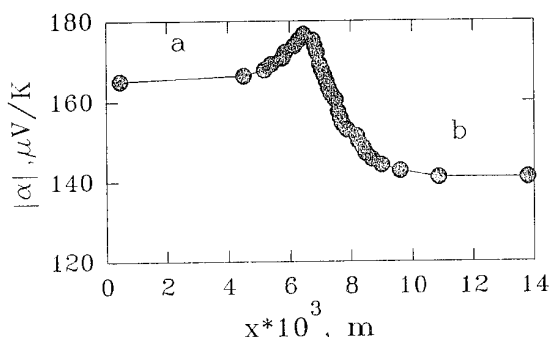


Figure 1: Distribution of Zeebeck coefficient values along the ingot of solid solution  $\text{Bi}_2(\text{Te},\text{Se})_3$  doped with  $\text{Hg}_2\text{Cl}_2$   
a - region corresponding to release of Peltier heat  
b - absorption of Peltier heat

Similar results were obtained on  $\text{Bi}_2(\text{Te},\text{Se})_3$  solid solution doped with  $\text{Hg}_2\text{Cl}_2$  for different values of the current density, temperature gradient, and growth rate. These results are presented in Fig.2, where the values of Zeebeck coefficient jump are shown versus current density  $j$  for different values of growth rate and temperature gradient. It can be seen that  $\Delta\alpha(j)$  functions display maxima; if temperature gradient remains constant, their magnitudes increase as the rate of growth diminishes, and they shift towards higher current densities. The growth rate being kept constant, the  $\Delta\alpha$  value decreases when temperature gradient rises.

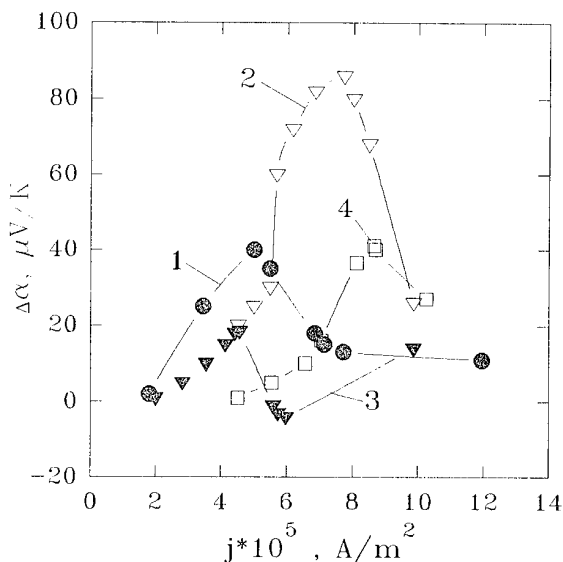


Figure 2: Distribution of Zeebeck coefficient jump created by inversion of electric current on the current density.  
Material:  $\text{Hg}_2\text{Cl}_2$ -doped solid solution  $\text{Bi}_2(\text{Te},\text{Se})_3$   
Temperature gradients  $G$  and growth rates  $v$ :  
Curve 1:  $G = 7 \cdot 10^3 \text{ K/m}$ ;  $v = 4.2 \cdot 10^{-6} \text{ m/s}$   
Curve 2:  $G = 7 \cdot 10^3 \text{ K/m}$ ;  $v = 1.4 \cdot 10^{-6} \text{ m/s}$   
Curve 3:  $G = 1.45 \cdot 10^4 \text{ K/m}$ ;  $v = 4.2 \cdot 10^{-6} \text{ m/s}$   
Curve 4:  $G = 1.45 \cdot 10^4 \text{ K/m}$ ;  $v = 5 \cdot 10^{-7} \text{ m/s}$

The appearance of maxima in  $\Delta\alpha(j)$  functions can be explained as follows. When the rate of growth is maintained at the level  $4.2 \cdot 10^{-6} \text{ m/s}$ , temperature gradient  $7 \cdot 10^3 \text{ K/m}$ , and no current is flowing (Fig.2, curve 1), the crystallization front will be rough because temperature gradient to growth rate ratio comprises  $1.7 \cdot 10^9 \text{ K} \cdot \text{s/m}^2$ , that is, less than the

critical value  $1 \cdot 10^{10} \text{ K}\cdot\text{s/m}^2$  for  $\text{Bi}_2\text{Te}_{2.4}\text{Se}_{0.6}$  solid solution [1]. If electric current flows so directed, that the Peltier heat is released, front roughness increases, and otherwise (Peltier heat is being absorbed) the boundary surface smoothes out. In accord with the degree of front roughness an effective distribution coefficient of dopant will change, and consequently so will the electric properties of material. As current density grows, the Joule heat becomes significant, and the difference of specific conductivities ( $6 \cdot 10^4 \Omega^{-1} \text{ m}^{-1}$  for solid  $\text{Bi}_2\text{Te}_{2.4}\text{Se}_{0.6}$  and  $3.5 \cdot 10^5 \Omega^{-1} \text{ m}^{-1}$  for liquid [2]) essentially brings the temperature gradient down. As a consequence, beginning from some value of current density up the crystallization front will be rough in no dependence on current direction. In this case a distribution coefficient will not change on current reversal, and  $\Delta\alpha$  will drop. It seems likely that for crystallization conditions corresponding to curve 1 this drop occurs at current density around  $5 \cdot 10^5 \text{ A/m}^2$ .

Curve 2 is built for samples grown under the same temperature gradient and lesser rate of growth, namely  $1.4 \cdot 10^{-6} \text{ m/s}$ . The position of maximum is shifted towards higher current density. Temperature gradient to growth rate ratio in this case equals to  $5 \cdot 10^9 \text{ K}\cdot\text{s/m}^2$ , that is closer to critical ratio, and therefore the Joule heat makes the smooth boundary rough at higher current density. Because of this, as Peltier effect turns more substantial, the maximum appears at higher current densities, and attains higher value. Similar considerations one can apply when comparing curves 3 and 4, which correspond to temperature gradient  $1.45 \cdot 10^4 \text{ K/m}$  and ratios of temperature gradient to growth rate  $3.5 \cdot 10^9 \text{ K}\cdot\text{s/m}^2$  and  $2.9 \cdot 10^{10} \text{ K}\cdot\text{s/m}^2$ , respectively. Diminishing of  $\Delta\alpha$  with a rise of temperature gradient when current density holds constant can be attributed to relative decrease of Peltier heat contribution into total heat flux at crystallization front (curve 3). Moderated diminishing of  $\Delta\alpha$  with current density increase on curve 1 as well as smooth rise of  $\Delta\alpha$  in high current density region ( $> 6 \cdot 10^5 \text{ A/m}^2$ ) for curve 3 can be obviously attributed to electromigration.

These investigations show that crystals with preset distribution of current carrier density along the ingot can be obtained by varying the direction and magnitude of electric current flowing across the crystallization front. This assumption was proved experimentally on the solid solution  $\text{Bi}_2(\text{Te},\text{Se})_3$  doped with  $\text{Hg}_2\text{Cl}_2$ ,  $\text{ZnCl}_2$  or  $\text{CdBr}_2$ . Micro-homogeneous crystals with predetermined distribution of current carrier density were grown through a gradual change of current value and its direction.

Fig. 3, curve 1 shows the distribution of Zeebeck coefficient values along the sample of solid solution  $\text{Bi}_2(\text{Te},\text{Se})_3$  doped with  $\text{Hg}_2\text{Cl}_2$ . The ingot was grown by the use of vertical zone melting setup with temperature gradient  $7 \cdot 10^3 \text{ K/m}$  and growth rate  $4.2 \cdot 10^{-6} \text{ m/s}$ . Electric current flowing across crystallization front varied in value and direction during the growth process. Variation of current density from  $+3 \cdot 10^5 \text{ A/m}^2$  down to  $-6 \cdot 10^5 \text{ A/m}^2$  (plus sign corresponds to Peltier heat absorption and vice versa) causes a smooth  $30 \mu\text{V/K}$  change of Zeebeck coefficient on the length of 6 mm.

Curve 2 shows the similar distributions of Zeebeck coefficient and electric conductivity along an ingot of solid solution doped with  $\text{Hg}_2\text{Cl}_2$ , obtained at the same growth rate and higher temperature gradient,  $1.45 \cdot 10^4 \text{ K/m}$ , when the current changed in sawtooth manner. In conductivity measurements the potential probes were separated by 1 mm. In identical conditions an ingot of  $\text{Bi}_2(\text{Te},\text{Se})_3$  doped with  $\text{Cd}_2\text{Br}_2$  was grown. Zeebeck coefficient distribution along the ingot is presented by

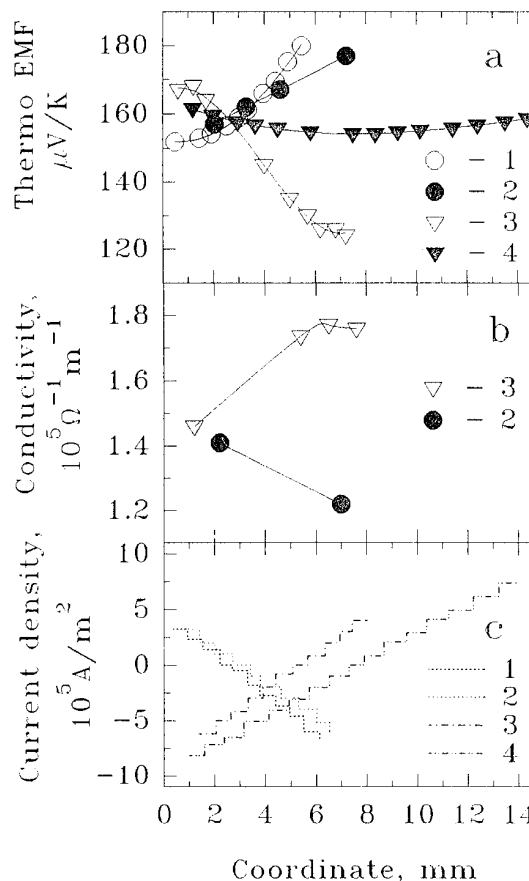


Figure 3: Distribution of Zeebeck coefficient (a) and conductivity (b) values along the sample of  $\text{Hg}_2\text{Cl}_2$ - (curves 1,2,4) or  $\text{CdCl}_2$ -doped (curve 3) solid solution  $\text{Bi}_2(\text{Te},\text{Se})_3$  caused by electric current flow of varying magnitude and direction across a crystallization front (c).

Temperature gradients  $G$  and growth rates  $v$ :

Curve 1:  $G = 7 \cdot 10^3 \text{ K/m}$ ;  $v = 4.2 \cdot 10^{-6} \text{ m/s}$

Curves 2,3:  $G = 1.45 \cdot 10^4 \text{ K/m}$ ;  $v = 4.2 \cdot 10^{-6} \text{ m/s}$

Curve 4:  $G = 7 \cdot 10^3 \text{ K/m}$ ;  $v = 1.4 \cdot 10^{-6} \text{ m/s}$

curve 3.

Unsuccessful was an attempt to obtain crystals with varying composition when rates of growth were lower, namely  $1.4 \cdot 10^{-6} \text{ m/s}$ . Curve 4 shows a Zeebeck coefficient distribution along the  $\text{Bi}_2(\text{Te},\text{Se})_3$  specimen doped with  $\text{Hg}_2\text{Cl}_2$  grown with a rate of  $1.4 \cdot 10^{-6} \text{ m/s}$  and temperature gradient  $7 \cdot 10^3 \text{ K/m}$ . Along the sample length 13mm the change of Zeebeck coefficient attains approximately  $10 \mu\text{V/K}$ . Such a low change can be attributed to composition levelling owing to solid phase diffusion. Because of low growth rate the material resides for a long time at high temperature, when intensive diffusion can occur. This influence of diffusion can be presumably diminished by further increase of temperature gradient.

It is known [3], that solid solution  $\text{Bi}_2(\text{Te},\text{Se})_3$  is the most effective thermoelectric material for temperature range 200–600K. Correlating data on temperature dependence of figure of merit  $Z = \frac{\sigma^2 \sigma}{k}$  for different carrier densities ([3], p.51) and those for 300K ([1], p.243) one can see that optimal carrier density offering maximum thermoelectric effectiveness in the in-

dicated range corresponds to values of Zeebeck coefficient at room temperature within the range 220...110  $\mu\text{V}/\text{K}$ .

Supposing a linear distribution of temperature along a thermoelement arm it is possible to achieve specimens of solid solutions  $\text{Bi}_2(\text{Te},\text{Se})_3$  with varying composition on each temperature level. Besides, the most significant changes of thermoelectric properties can be obtained on samples made out of solid solution doped with  $\text{Hg}_2\text{Cl}_2$  or  $\text{CdBr}_2$  when the rate of crystallization and temperature gradient are  $4.2 \cdot 10^{-6} \text{m/s}$  and  $1.45 \cdot 10^4 \text{K/m}$ , respectively (Fig.3, curves 2,3).

The thermoelectric efficiency of crystals with varied composition manufactured with the use of described technique will correspond in the operating temperature range to an envelope of curves presented in Fig.4.

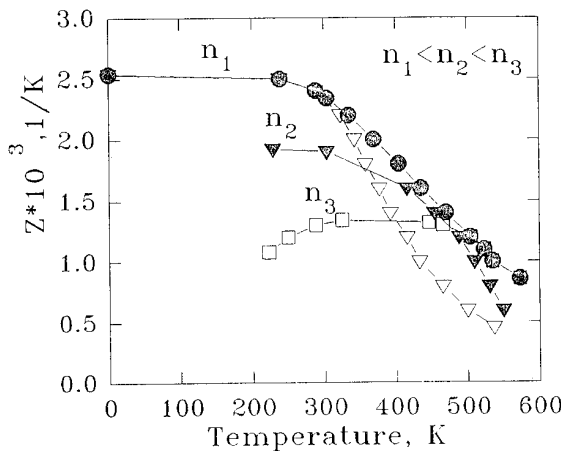


Figure 4: Family of curves representing temperature dependences of the thermoelectric figure of merit  $Z$  for different current carrier densities.

An averaged thermoelectric efficiency value  $Z$  will be 10...15 per cent higher than the efficiency of homogeneous material.

To check this assumption an averaged Zeebeck coefficient and electric conductivity were measured in temperature drop (310...525)K on a composition-varying specimen of  $\text{Hg}_2\text{Cl}_2$ -doped  $\text{Bi}_2(\text{Te},\text{Se})_3$ . At room temperature the figures varied smoothly along the specimen (8mm) and were as follows: Zeebeck coefficient changed between  $-185 \mu\text{V}/\text{K}$  and  $-150 \mu\text{V}/\text{K}$  and conductivity between  $6 \cdot 10^4 \Omega^{-1}\text{m}^{-1}$  and  $1.1 \cdot 10^5 \Omega^{-1}\text{m}^{-1}$ . Measurements were carried out with two different positions of sample in respect to temperature drop. First, this positioning corresponded to optimal distribution of carrier density values i.e. the part of specimen with Zeebeck coefficient  $\alpha = -185 \mu\text{V}/\text{K}$  was situated at 310K; otherwise, this part was situated at 525K while at temperature 310K was placed the part possessing  $\alpha = -150 \mu\text{V}/\text{K}$ . As it can be seen from Table 1, the values of Zeebeck coefficient  $\alpha$  and conductivity  $\sigma$  measured in temperature difference (310...525)K at the indicated positions differ in such a manner that relative divergence of power coefficient  $\alpha^2\sigma$  comprises 18.5 per cent.

Now we can make some suppositions concerning the way heat conductivity of varying-composition specimen diverges from that of homogeneous specimen. Simplifying, let us consider the heat conductivity of crystal lattice  $\kappa$  independent of current carrier density. An electron component of heat conductivity is determined by Wiedmann-Franz law :

$$\kappa_e = L/\sigma T, \quad (1)$$

Table 1: The values of measured thermoelectric figures for varying-composition specimen of solid solution  $\text{Bi}_2(\text{Te},\text{Se})_3$  in temperature drop (310...525)K.

Current carrier density distribution	$ \alpha , \mu\text{V}/\text{K}$	$\sigma \cdot 10^{-2}, \Omega^{-1}\text{m}^{-1}$	$\alpha^2\sigma \cdot 10^4, \text{W}/\text{K}^2\text{m}$	$\frac{\Delta(\alpha^2\sigma)}{\alpha^2\sigma}, \text{percent}$
Optimal	185	775	26.5	
Non-optimal	174	730	22.0	18.5

L- Lorentz number .

For solid solution  $\text{Bi}_2\text{Te}_3 - \text{Bi}_2\text{Se}_3$  the value of L can be estimated according to the method described in ([1],pp 80-81,105).

An analysis of functions  $\alpha(\xi^*)$  and  $L(\xi^*)$  ( $\xi^*$  – reduced chemical potential) shows that Lorentz number is almost independent on the degree of degeneracy when Zeebeck coefficient measures  $(150...190) \mu\text{V}/\text{K}$ . Thus, the electronic component of heat conductivity for invariant temperature will be proportional to electric conductivity.

Let us compare the values of heat conductivity in operating temperature range of varying-composition specimen with carrier density varying from  $n_1$  up to  $n_2$  with that of specimen possessing a uniform density  $n$  ( $n_1 < n < n_2$ ). If carrier density is distributed along varying-composition specimen in the optimal way, an effective measured value of heat conductivity in this specimen will be lower than in an uniform specimen. The reason is that in the first specimen the low-temperature part will possess thermal conductivity lowered because of less  $\kappa_e$  value; in high temperature region a thermal conductivity will reduce owing to diminished contribution of bipolar diffusion ,as in this part the current carrier density will be higher ([3],p.51) then in the second specimen. Conversely, varying-composition specimen turned into reverse ("unproper") position will display effective heat conductivity higher than homogeneous one.

On the basis of these considerations one can safely assume that relative difference of thermoelectric figures of merit  $Z = \frac{\alpha^2\sigma}{\kappa}$  for varying-composition specimen in "proper" and "unproper" positions will attain no less value than the difference of power coefficients  $\alpha^2\sigma$  (Table 1), which equals to 18 per cent. It means that in temperature range (310...525)K thermoelectric figure of merit for the varying-composition specimen with optimized distribution of carrier density will be higher then that for homogeneous ingot approximately by 9 per cent.

Thus, the possibility is demonstrated to manufacture crystals of solid solutions  $\text{Bi}_2(\text{Te},\text{Se})_3$  with optimized distribution of a current carrier density along the ingot by means of programmed variation of magnitude and direction of current flowing across the crystallization front during the process of crystal growth.

## References

- [1] B.M.Goltsman, V.A.Kudinov, I.A.Smirnov, Semiconducting thermoelectric materials based on  $\text{Bi}_2\text{Te}_3$  M., 1972, 320p (in Russian)
- [2] A.R.Regel, V.A.Ivoninsky, Thermoelectric properties of  $\text{Bi}_2\text{Te}_3 - \text{Bi}_2\text{S}_3$  system in liquid state. In: *The problems of crystallization and physics of solids*. L., 1965., pp 183-192. (in Russian)
- [3] E.K.Iordanishvili, Thermoelectric supply sources, M., 1968, 183p (in Russian).

# Thermoelectric figure of merit of horizontal zone-leveling prepared bismuth-antimony single crystals

Grabov V.M.<sup>1</sup>, Ivanov G.A.<sup>1</sup>, Naletov V.L.<sup>1</sup>, Bondarenko M.G.<sup>1</sup>, Uryupin O.N.<sup>2</sup>

<sup>1</sup>Herzen Russian State Pedagogical University, St. Petersburg, Russia

<sup>2</sup>A.F.Ioffe Physical-Technical Institute, St. Petersburg, Russia

Homogeneous single crystals of Bi-Sb alloys undoped and doped by Te and Sn were prepared by horizontal zone-leveling technique. High refined bismuth and antimony were used. The investigations of temperature dependences of Hall and Seebeck coefficients, electrical resistivity and heat conductivity were carried out on the prepared crystals. The thermoelectric figure of merit of Bi-Sb single crystals has been determined on the base of this experimental data. It was found, that when the refining degree of initial bismuth and homogeneity of the single crystals decreased, maximum of the thermoelectric figure of merit is shifted to alloys with antimony contents of 7-8 at.% in the temperature range 80 - 280 K. However, at  $T > 120K$  the increase of the refining degree of source materials and the crystals homogeneity practically does not influence on their thermoelectric properties. Results received are compared with those given in literature for the homogeneous and dendritic crystals of Bi-Sb alloys.

## Introduction

Bi-Sb crystals have a record value of thermoelectric figure of merit

$$Z = \frac{\alpha^2}{\rho \cdot \kappa}$$

in the low temperatures region  $T < 180K$  reaching in maximum the value  $Z = 5 - 6 \cdot 10^{-3} K^{-1}$  [1,2]. A practical interest to these materials increases in connection with a thermoelectric application of high-temperature superconductors [3].

The improvement of growing technique of  $Bi_{1-x}Sb_x$  single crystals [4-6] indicated that application of the low growth speed  $V \leq 0.5mm/h$  and the small temperatures gradient on crystallization front  $G \leq 20K/cm$  is required for preparation of the homogeneous crystals by zone recrystallization method.

First systematic investigations of thermoelectric figure of merit of  $Bi_{1-x}Sb_x$  single crystals [2] indicated that as distinct from the results [1] in the region of nitrogen temperatures it was observed an unmonotonous dependence of  $Z(x)$  with two maxima at  $x = 0.07-0.09$  and about  $x = 0.15$ , gradually transient to one at  $x = 0.07-0.12$  with the temperature increase. Such  $Z(x,T)$  dependence is caused by peculiarities of the band structure alteration and intervalley (interband) charge carriers scattering by phonons [7]. Investigation of the thermoelectric parameters of  $Bi_{1-x}Sb_x$  crystals grown at various speeds of a zone pass from 0.5 up to 20 mm/h [8] indicated that existence of the dendritic inhomogeneity in grown at large speeds  $Bi_{1-x}Sb_x$  crystals results in a reduction of  $Z$  value in the temperatures region  $T > 150K$ . The most interesting results [8] has been received in area of semiconductor state on  $x(T)$  diagram of  $Bi_{1-x}Sb_x$  crystals [9], where a dendritic liquation lowers appreciably the specific resistance so that the thermoelectric figure of merit of inhomogeneous crystals appears higher than that of homogeneous ones [9].

However,  $Z$  data in the article [10] devoted to the investigation of  $Bi_{1-x}Sb_x$  crystals grown by zone recrystallization method are different substantially from the results [1,2,7]. Besides the influence of the growth conditions on thermoelectric properties of  $Bi_{0.97}Sb_{0.03}$  crystals at  $V \leq 0.5mm/h$  and  $G \leq 40K/cm$  is not found out in this article.

The further investigations, directed to the more detailed study of thermoelectric figure of merit at the increase of accuracy of optimum composition determination [11-15], influence of a purity of source materials [16] and doping [17-18] on the thermoelectric figure of merit value, application of Czochralsky method [10-17], did not shed light to the understanding of the nature of observable distinctions  $Z$  but also caused to a greater spread of  $Z$  values.

The purpose of given article is to investigate the physical nature of observable distinctions of thermoelectric figure of merit of  $Bi_{1-x}Sb_x$  crystals grown by zone recrystallization method including the influence of growth conditions and the inhomogeneity on thermoelectric properties of these crystals as well as to make a comparative analysis of results of the thermoelectric parameters investigation.

## Experimental procedure

To receive the most reliable results of the thermoelectric parameters investigation and their comparison with other data the problem of the growing of  $Bi_{1-x}Sb_x$  single crystals using the most pure initial components has been realized. Initial antimony contained of residual impurities less than 0.0005 %. As the initial bismuth with 99.999% clearance had the residual impurities content a ten times as great as that of antimony, it has been subjected to an additional clearing by vacuum distillation with following zone clearing [18]. Such clearing according to data of spectral analysis ensures the reception of bismuth with 99.9999% clearance [19].  $Bi_{1-x}Sb_x$  single crystals has been grown by zone recrystallization method ( $V < 0.5mm/h$ ,  $G < 20K/cm$ ) [4-6,21-22]. In order to clear up the influence of growth conditions and connected with them crystals inhomogeneity [10-17] to their thermoelectric properties. The  $Bi_{0.85}Sb_{0.12}$  crystal having a clear-cut dendritic structure, was also grown at a speed of 10 mm/h.

Cut the rectangular parallelepiped samples for measurements with average dimensions of  $2.5 * 2.5 * 12mm^3$  and ribs, parallel to crystallographic axes was cut from the middle part of the grown single crystal by spark erosion method. Longitudinal samples axis were oriented parallel or perpendicularly to trigonal axis  $C_3$ . To remove a layer destroyed by spark erosion technique and to reject samples with units of other orientation,

samples were etched in 50%  $\text{HNO}_3$  + 50%  $\text{C}_2\text{H}_5\text{OH}$ .

An availability of a dendritic structure and an inhomogeneity in components distribution was determined by etching in 1%  $\text{HCl} + 99\% \text{H}_2\text{O}$  and as well as by X-ray diffraction analysis [8]. Antimony contents in  $\text{Bi}_{1-x}\text{Sb}_x$  single crystal samples was determined by X-ray method on X-ray diffractometer DRON-0.5 according to the change of crystal lattice parameters and by X-ray microprobe analysis on COMEBAX analyzer. The determination accuracy of antimony content in samples was  $\pm 0.5\text{at.\%}$  for both methods.

The quantitative evaluation of inhomogeneity degree of crystal  $\text{Bi}_{0.88}\text{Sb}_{0.12}$ , grown with speed of 10 mm/h, was made by the microhardness measurement with a load of 20 g. The antimony distribution in dendritic crystals was found according to single crystal microhardness dependence from antimony contents. As a dendritic inhomogeneity degree we considered the difference of values of antimony concentration determined by such a way in the dendritic and interdendritic space.

For revealing of structural inhomogeneity the volumes, occupied by dendritic and interdendritic areas has been determined by method of linear analysis in the assumption of uniform inhomogeneity distribution in the crystal volume (Tab.1).

Table 1: Antimony distribution in the inhomogeneous  $\text{Bi}_{0.88}\text{Sb}_{0.12}$  crystal

Type of inhomogeneity	Averaged microhardness	Antimony Concentration	Occupied volume
Dendrites ( centre )	$4.35 \cdot 10^8 \text{ H/m}^2$	14.3 at.%	80%
Interdendritic interlayer	$3.49 \cdot 10^8 \text{ H/m}^2$	8.8 at.%	20%

## Experimental results

The thermoelectric figure of merit value is calculated according to formula

$$Z_{33} = \frac{\alpha_{33}^2}{\rho_{33} \cdot \kappa_{33}} \quad (1)$$

with the use of experimental results of to Seebeck coefficient measurements, heat conductivity and specific resistivity (Fig.1).

Figure of merit of the investigated single crystals grows with a decrease of temperature, and does not reaches maximum in the temperature interval 80-300 K with the exception of crystal  $x = 0.15$ . It should be noted, that in the region 160 - 200 K the thermoelectric figure of merit values  $Z_{33}$  of the crystals with  $x = 0.05, 0.12, 0.15$  coincide practically among themselves. At the same time thermoelectric figure of merit  $Z_{33}$  of the crystal  $x = 0.07$  is higher  $Z_{33}$  values of other investigated crystals in the temperatures interval 80-300 K. So, maximum of thermoelectric figure of merit in temperature interval of 80-180 K for the homogeneous uniform  $\text{Bi}_{1-x}\text{Sb}_x$  crystals grown from refined bismuth corresponds to  $x = 0.07 - 0.08$ .

The experimental results of thermoelectric properties investigation of the dendritic  $\text{Bi}_{0.88}\text{Sb}_{0.12}$  crystal in comparison with the results, received on homogeneous single crystals are presented in Figs.2-3.

Fig. 2 shows, that Seebeck coefficient of  $\text{Bi}_{0.88}\text{Sb}_{0.12}$  crystals does not practically depend on the crystal inhomogeneity degree and a distinguish of heat conductivity of homogeneous

Fig.1. Temperature dependence of figure of merit  $Z_{33}$  of homogeneous  $\text{Bi}_{1-x}\text{Sb}_x$  crystals.

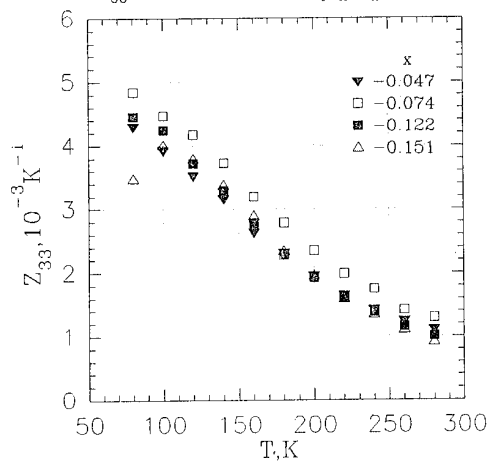


Fig.2. Temperature dependence of Seebeck coefficient and thermal conductivity of  $\text{Bi}_{0.88}\text{Sb}_{0.12}$

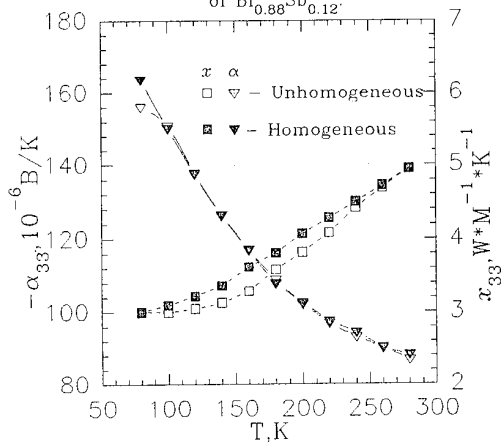
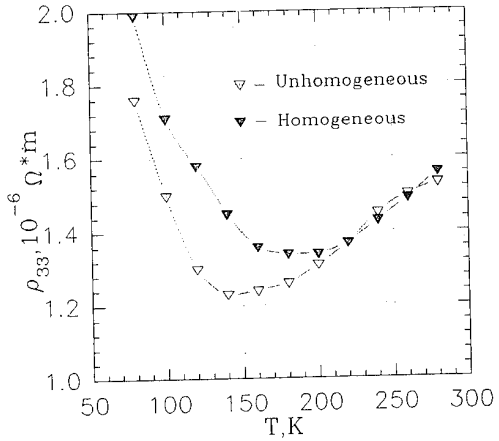


Fig.3. Electrical resistivity as a function of temperature for homogeneous and unhomogeneous  $\text{Bi}_{0.88}\text{Sb}_{0.12}$  crystals.



and dendritic crystals does not exceed the experimental error. The most distinctions are observed in the temperature dependence of specific resistance of homogeneous and dendritic crystals (Fig.3). At  $T < 200K$  the specific resistivity of dendritic crystal is substantial less, than one of homogeneous crystal but at  $T > 200K$  they practically coincide. Besides, for the dendritic crystal the temperature corresponding to the minimum of specific resistivity, decreases up to 145 K in comparison with 200 K for the homogeneous crystal. So, the greatest distinction of specific resistance of homogeneous and dendritic crystals, Fig.3, is observed in the area of semiconductor state of homogeneous crystals.

Such temperature dependence of the thermoelectric properties results in that in the area of semimetallic state the most homogeneous crystals have the greatest thermoelectric efficiency, while in area of semiconducting state thermoelectric figure of merit of dendritic crystals appears higher than in homogeneous crystals.

## Results discussion

The temperature dependences of specific resistance  $\rho_{33}$  of homogeneous  $\text{Bi}_{0.88}\text{Sb}_{0.12}$  crystal grown with use of addition ally refined bismuth and of dendritic crystal with the identical average composition in comparison with data of other authors [10,22] are presented in Fig.4.

As can be seen in Fig.4, the specific resistance values of homogeneous and dendritic crystals at temperatures  $T > 200K$  are close among themselves and are not differ from the results received by other authors. This conclusion can be made also with relation to thermoelectric figure of merit  $Z_{33}$  (Fig.5). Nevertheless, the greatest  $Z_{33}$  value corresponds to the most homogeneous crystal. It should be expected because of when temperature gradient occurs the inhomogeneity results in the appearance of the circular thermoelectric currents and in a energy transformation coefficient.

A different situation is observed in the area of semiconducting state of  $\text{Bi}_{1-x}\text{Sb}_x$  crystals, at  $T > 200K$  for  $x = 0.12$ . Specific resistivity of the homogeneous  $\text{Bi}_{1-x}\text{Sb}_x$  single crystals grown from additional refined bismuth proved to above in the all given in Fig.5 data. Results [23] in this temperatures area approximate to the specific resistivity values of dendritic crystals and data [10] proved to be even below. But, the lower the specific resistivity is the greater value has thermoelectric figure of merit Z (Fig.5).

In [9] the area of a semiconductor state of  $\text{Bi}_{1-x}\text{Sb}_x$  crystals in coordinates  $x(T)$ , has determined from the temperature dependence of specific resistivity and in particular from a position of a minimum in dependence  $\rho(T)$  (Fig.6).

As can be seen in Fig.6, temperature interval of semiconducting state increases for homogeneous crystals grown from the additionally refined bismuth and decreases in case of dendritic crystals (Fig.6).

The well expressed distinctions in the temperature dependence of specific resistivity at liquid nitrogen temperatures for our homogeneous single crystals  $\text{Bi}_{1-x}\text{Sb}_x$  with  $x = 0.12$  and  $x = 0.15$  and exhibited in other papers permit to use this parameter for determination of the growth conditions influence on the grown single crystals homogeneity.

Comparative analysis of the crystal growth conditions and the specific resistance values indicates, that at a high gradient at the crystallization front ( $G > 20\text{K/cm}$ ) a reduction of the growth speed less than 0.5 mm/h practically does not affect on the crystals quality and does not permit to receive homogeneous antimony distribution in  $\text{Bi}_{1-x}\text{Sb}_x$  crystals. However,

Fig.4. Temperature dependence of electrical resistivity for  $\text{Bi}_{0.88}\text{Sb}_{0.12}$  crystals.

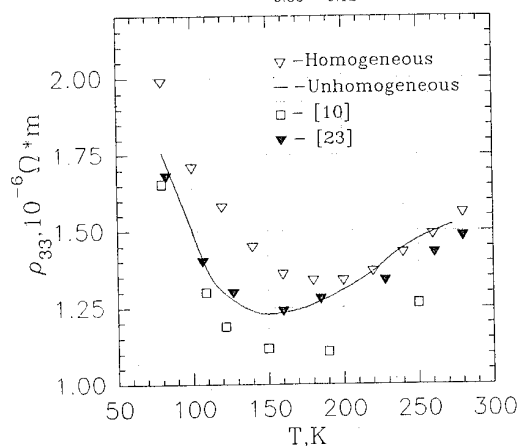


Fig.5. Temperature dependence of figure of merit for  $\text{Bi}_{0.88}\text{Sb}_{0.12}$  crystals.

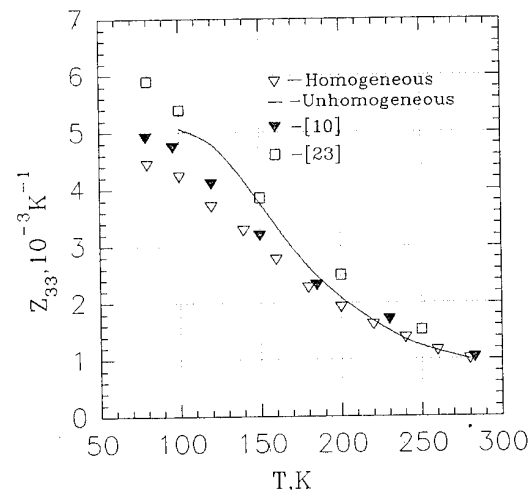
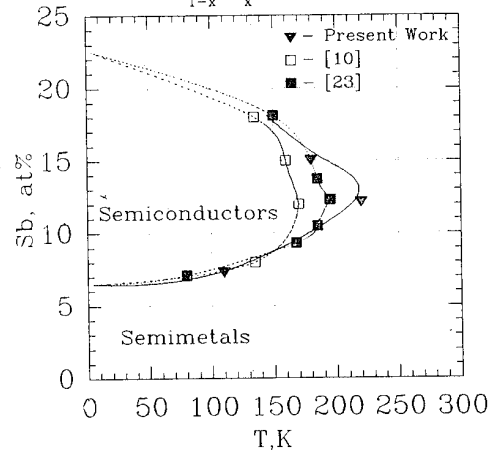


Fig.6. Semiconductor state diagram of  $\text{Bi}_{1-x}\text{Sb}_x$  crystals.



the increase of thermoelectric figure of merit of inhomogeneous crystals can be observed in comparison with homogeneous crystals in that case, when dendrites are in semiconductor state and interdendritic layers are in semimetallic state. This conclusion agrees well with results of theoretical investigations [24].

## Conclusions

As a result of experimental investigations of a correlation between  $\text{Bi}_{1-x}\text{Sb}_x$  crystals growth conditions, their homogeneity degree and thermoelectric properties it was established; that the increase of initial components purity degree and homogeneity degree of  $\text{Bi}_{1-x}\text{Sb}_x$  crystal results in expansion of a temperature area of semiconducting state.

The thermoelectric figure of merit of homogeneous single crystals  $\text{Bi}_{1-x}\text{Sb}_x$  in temperatures region 77-300 K has the greatest value  $x = 0.07\text{-}0.08$ .

In the semimetallic state area the homogeneous single crystals  $\text{Bi}_{1-x}\text{Sb}_x$  have the greatest values of figure of merit.

The thermoelectric figure of merit of dendritic crystals In the semiconducting state area surpasses the figure of merit of homogeneous  $\text{Bi}_{1-x}\text{Sb}_x$  crystals because of its low values of the specific resistivity.

Therefore, the dendritic  $\text{Bi}_{1-x}\text{Sb}_x$  crystals are proved to be preferable for the more practically important low-temperature applications at  $T < 200\text{K}$ . The absolute maximum position  $Z(x)$  is shifted to the values  $x = 0.15\text{-}0.17$ .

A distinction of thermoelectric figure of merit data of  $\text{Bi}_{1-x}\text{Sb}_x$  crystals with identical composition is observed in the literature. It is mainly caused by the distinction of growing conditions used.

## References

- [1] G.E.Smith and R.Wolfe // *J.Appl.Phys.* 1962. V.33. N.3. P.841-846.
- [2] Ivanov G.A., Kulikov B.A., Naletov V.L., Panarin A.F., Regel A.R. // *Fizika i tekhnika poluprovodnikov* 1972. V.6. P.1296-1299. (in Russian)
- [3] Kuznetsov V.L., Vedernikov M.V., Jandl P., Birkholz U. // *Proceedings of the 12th International Conference on Thermoelectrics*, 1993. November 9-11, Yohohama, Japan. P.423-428.
- [4] Ivanov G.A., Krilov A.S., Naletov V.L. // in: *Poluprovodniki i dielektriki*. Leningrad: LGPI im. A.I.Herzena 1974. P.43-46. (in Russian)
- [5] Ivanov G.A., Krilov A.S., Kalugina I.K. // *Pribori i tekhnika eksperimenta*. 1975. N.2. P.226-226. (in Russian)
- [6] Boshegov V.I., Ivanov G.A., Rodionov N.A., // *Pribori i tekhnika eksperimenta*. N.2. P.218-220. (in Russian)
- [7] Grabov V.M., Ivanov G.A., Naletov V.L., Panarin A.F. // in *Poluprovodnicovie materiali dla termoelektrisheskikh preobrazovatelei* Leningrad. Fiz. Teh. Inst. im. Ioffe. 1985. P. 30-31. (in Russian)
- [8] Naletov V.L., Ivanov G.A., Yakovleva T.A., Nikolaev V.I. // *Izvestiya AN SSSR. Neorganische materiali* 1971 V.7. N.8. P.1321-1324. (in Russian)
- [9] Grabov V.M., Ivanov G.A., Naletov V.L., Ponaryadov V.S., Yakovleva T.A. // *Fizika Tverdogo Tela*. 1969. V.11. N.12. P.3653-3655. (in Russian)
- [10] Yim W.M., Amith A. // *Solid State Electronics*. 1972. V.15. N.10. C.1141-1165.
- [11] Zemskov V.S., Gusakov V.P., Belya A.D., Roslov S.A. // *Izvestiya AN SSSR. Metali*. 1975. N.3. P.189-203. (in Russian)
- [12] Zemskov V.S., Belya A.D., Roslov S.A., Borodin P.G. // *Izvestiya AN SSSR. Metali*. 1978. N.1. P.73-77. (in Russian)
- [13] Zemskov V.S., Belya A.D., Kogemyakin G.N., // N 4305 - 80 Deponirovano v VINITI. Moskva. 1980. 52 p. (in Russian)
- [14] Zemskov V.S., Belya A.D., Borodin P.G. // *Izvestiya AN SSSR. Neorganisheskie materiali*. 1982. V.18. N.6. P.1154-1157. (in Russian)
- [15] Zemskov V.S., Lyutcau B.G., Belya A.D., Kogemyakin G.N., Kostyukova E.P., Kishkina O.A. in *Poluprovodniki s uzkoi zapreshennoi zonoi i polumetalli. Materiali V Vsesoyuznogo symposiuma*. Lvov, 1986. V.II, P.236-238. (in Russian).
- [16] Zemskov V.S., Belya A.D., Kogemyakin G.N., // *Izvestiya AN SSSR. Metali*. 1984. N.5. P.194-195. (in Russian)
- [17] Zemskov V.S., Gusakov V.P., Roslov S.A., Belya A.D., Rogdestvenskaya L.V. // *Dokladi AN SSSR*. 1975. V.222. N.2. P.316-318. (in Russian)
- [18] Gorobec A.E., Denisov A.K., Kulikov B.A., Tichenko A.P. // *Naushno-tehnisheskii otshet*. KGPI. Kurgan. 1980. N GR 79017516 33p. (in Russian)
- [19] Kulikov B.A., Gorobec A.E. etc.// *Naushno-tehnisheskii otshet*. KGPI. Kurgan. 1983. N GR 81069649 27p. (in Russian)
- [20] Zemskov V.S., Belya A.D., Zayakin S.A., Bulatova N.A. // *Izvestiya AN SSSR. Neorganisheskie materiali*. 1987. V.23. N.4. P.554-557. (in Russian)
- [21] Kolpashnikov G.N., Naletov B.L. in *Polumetalli*. Leningrad. LGPI imeni A.I.Herzena. 1968. P.3-6. (in Russian)
- [22] Naletov B.L. in *Polumetalli*. Leningrad. LGPI imeni A.I.Herzena. 1968. P.7-11. (in Russian)
- [23] Lenoir B. // *Docteur diss.* l'Ecole des Mines De Nansy, 1994.
- [24] Bergman D.J., Levy O. // *J.Appl.Phys.*, 1991. V.70. N.11. P.6821-6833.

## SERVICE PROPERTIES OF DOPED Bi-Sb SINGLE CRYSTALS

A.D.Belaya<sup>1</sup>, S.A.Zayakin<sup>1</sup>, V.S.Zemskov<sup>1</sup>, Y.G.Ponomarev<sup>2</sup>

<sup>1</sup>Baikov Institute of Metallurgy, Moscow, 117911, Russia

<sup>2</sup>Lomonosov Moscow State University, Moscow, 117234, Russia

Conditions of obtaining the optimum thermoelectric properties of Bi-Sb alloys and factors determining variation of these properties in doping with Te and Sn were considered. Possibility of producing of Bi-Sb single crystals with the optimum combination of thermoelectric, magnetothermoelectric, thermomagnetic and strength properties in doping was investigated.

### INTRODUCTION

The most promising application of Bi-Sb single crystals is to use them in low temperature stages of solid-state coolers, having important for practice working temperature range 77-200K. [1]. Service properties of cooling elements produced from these materials are determined by the values of thermoelectric (TE), magnetothermoelectric (MTE), thermomagnetic (TM) figure of merit and the strength properties of single crystals.

The well-known method of varying of TE,MTE,TM properties of Bi-Sb single crystals is to dope them with Te (donor) and Sn (acceptor). But effect of Te and Sn on these properties of single crystals of the most efficient alloy compositions does not studied carefully. Effect of Te and Sn on strength properties of these materials does not studied too.

In this work we investigated the possibility of producing of Bi-Sb single crystals having the optimum combination of TE,MTE,TM and strength properties in doping with Te and Sn. For this purpose: 1.- Analysis of the conditions of obtaining the optimum TE properties of these materials and factors determining their change in doping was carried out. 2.-Effect of Te and Sn on TE,MTE properties of single crystals of Bi with 9 at.% Sb and on TM properties of single crystals of Bi with 2 at.% Sb was studied. 3.- Strength properties of doped Bi-Sb single crystals with higher TE, MTE and TM figure of merit in comparison to strength properties of undoped crystals with the same content of Sb were investigated.

### EXPERIMENTAL METHODS

The following marks of initial mater-

ials were used in producing of crystals. Bi:Bi-0000 (99.999%), Sb: OSCh-18-4 (99.999%),Te:TV-4, Sn:VCh. Single crystals were grown by Czochralski method with feeding the melt by solid antimony [2]. The charge for pulling was calculated taking into account distribution coefficients of Sb,Te,Sn in Bi-Sb, Bi-Sb-Te, Bi-Sb-Sn alloy systems determined in Ref.[3,4] with the use of radioactive isotopes Sb-124,Te-125m,Sn-113. These coefficients allows to determine content of doping elements in crystals. Sb content in crystals was inspected by x-ray fluorescence method with an accuracy of 0.1 at.%.

Specimens were cut from crystals by the electrospark method with edge parallel to bisectrix (C1), binary (C2) and trigonal (C3) axes of the crystal. Corresponding dimensions of specimens intended for examining of TE,MTE,TM properties and for mechanical tests were respectively 3x4x(15-20)mm and 5x2x(15-20)mm. For removing the surface layer disrupted in cutting specimens were etched in nitric acid and the specimens for mechanical tests were also polishing. Their cross-section after polishing was (4.0-4.6)x(1.2-1.6) mm.

TE and MTE figure of merit Z(33) were examined with the use of separate measurements of resistivity ( $\rho$ ), thermal emf ( $\alpha$ ) and thermal conductivity ( $\kappa$ ). TM figure of merit Z(31) was measured by the Harman method [5]. Random errors of measurements of  $\rho$  at DC,  $\rho$  at AC,  $\alpha$  and  $\kappa$  did not exceed 3,4,1 and 4%, respectively. We measured  $\rho$  and  $\kappa$  on one and the same specimen and the errors of their determination formed in measuring of its length and cross-section were mutually eliminated when Z(33) was calculated. That is why the

random error of determining of  $Z(33)$  in this work was not higher than 5%. Random error of determining of  $Z(31)$  was no more than 7%.

The data on the concentration and mobility of the electrons in the examined crystals were obtained in The Institute of Semiconductor Physics of the Lithuanian Academy of Sciences by R.Pozhera with the use of magnetoplasma method [6].

Strength properties of crystals were investigated at 293K with the use of the three-point bending test method.

## RESULTS AND DISCUSSION

Conditions of obtaining the optimum thermoelectric properties of Bi-Sb alloys

According to principles of optimizing of TE properties, maximum of TE figure of merit ( $Z$ ) is obtained in material at same optimum, for this material, electron concentration  $N = N(\text{opt})$ . Deviation of  $N$  from  $N(\text{opt})$  with temperature reduces  $Z$ . At temperatures, at which  $N$  is not optimum,  $Z$  can increase by donor or acceptor doping if  $N$  is displaced to  $N(\text{opt})$  [7].

Temperature dependence of concentration of L-electrons  $N$ , L-holes  $P(L)$ , T-holes  $P(T)$  we calculated as an example for alloy of Bi with 9at.% Sb with use the data on its band structure at 4.2K[8], Fig.1. We used effective mass of T-holes in Bi, undepended of Sb content and temperature according to implication of [9], and established dependence of effective masses ( $m$ ) of electrons and L-holes on energy ( $\varepsilon$ ) from the data in [8]. In calculation of  $N$  or  $P(L)$  we "divided" corresponding energy band into narrow intervals in which individually energy dependence of  $m$  can be ignored. It permit to determine  $n(i)$  or  $p(i)$  in each  $i$ -th interval as for band with  $m$  undependent on  $\varepsilon$ . Summation of all  $n(i)$  or  $p(i)$  gives required concentration of carriers in the band. An example:

$$N = 4\pi \left[ \frac{2kT}{h^2} m_0 \right]^{\frac{3}{2}} \int_0^{\infty} \left[ \frac{m_d}{m_0} \right]^{\frac{3}{2}} \frac{1}{\varepsilon^2} \frac{d\varepsilon}{1 + e^{(\varepsilon - \eta)}}.$$

$m_0$  is the mass of free electron,  $m_d$  - effective mass of the density of sta-

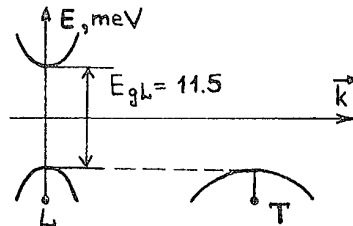


Fig.1  
Band structure of Bi+9at.%Sb alloy at 4.2K 8

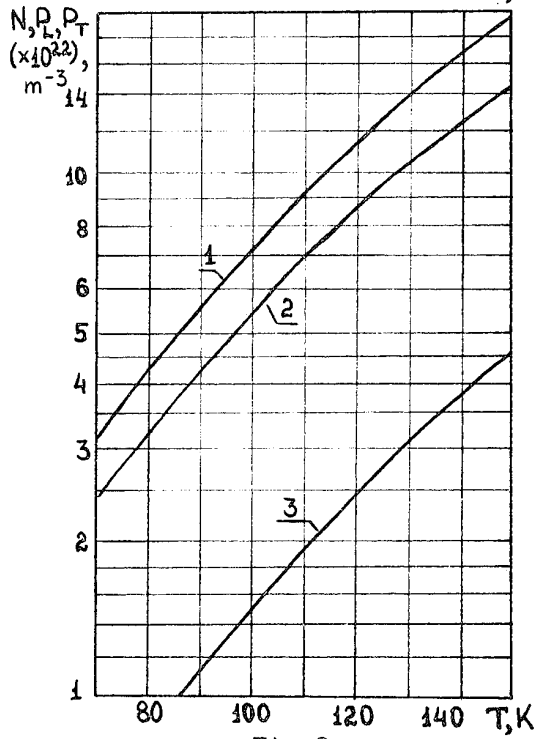
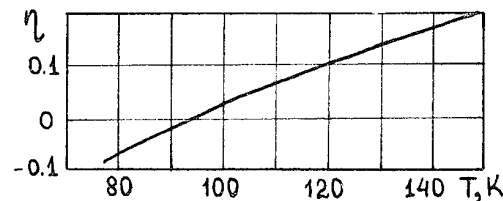


Fig.2  
Temperature dependencies of reduced Fermi energy (a) and carrier concentrations (b) in Bi+9at.%Sb alloy:  
(1)-electrons;(2)-T-holes;(3)-L-holes

tes of electrons,  $\varepsilon = E/(kT)$  - reduced energy,  $\eta$ -reduced Fermi energy.

With use the dependencies of  $N$ ,  $P(L)$ ,  $P(T)$  on  $\varepsilon$ , calculated at fixed temperatures, we obtained the values of  $\eta$ ,  $N$ ,  $P(L)$ ,  $P(T)$  from equation of electro-neutrality:  $N = P(L) + P(T)$ . The results of calculation are shown in Fig.2.

Influence of doping on TE, MTE and TM figure of merit of Bi-Sb single crystals

The effect of Te and Sn on the dimensionless thermoelectric, magnetothermoelectric figure of merit (TE f.m., MTE f.m.) of Bi-Sb single crystals, containing 9 at.% Sb, and thermomagnetic figure of merit (TM f.m.) of Bi-Sb single crystals, containing 2 at.% Sb, is shown in Fig.4. The doping of up to  $2 \times 10^{-4}$  at.% Te and to  $1 \times 10^{-3}$  at.% Sn have no marked effect on TE f.m. of Bi with 9 at.% Sb single crystals at temperatures above 200K. At lower temperatures Te reduces TE f.m. and Sn in an amount of up to  $1.5 \times 10^{-4}$  at.% appears to stabilize it on the level corresponding to the undoped alloy. The temperature range of stabilization of TE f.m. narrows with Sn content increasing. The change of TE f.m. of doped alloys at temperatures lower 120K makes it possible to assume that with further temperature decrease Te-doped alloys have TE f.m. higher than that of Sn-doped alloys. It should be mentioned that results obtained for TE f.m. are qualitatively explained by the variation of concentration and mobility of electrons in doping discussed above. Doping with Sn of the alloy may be useful at temperatures higher 120K for expanding the possibilities of selecting material having the optimum combination of  $\rho$ ,  $\alpha$  and  $\chi$  for matching the branches of thermocouples.

MTE f.m. was investigated in magnetic fields up to 1.15T. In Fig.4 are shown the maximum values of it obtained in this range of magnetic fields. As is seen, the effect of Sn on MTE f.m. retains basically the same form as in the absence of the magnetic field.

The effect of Te on MTE f.m. differs from that on TE f.m.: doping of  $1 \times 10^{-4}$  at.% Te increase MTE f.m. of the alloy by 10-15%. Addition of  $2 \times 10^{-4}$  at.% Te decrease MTE f.m. to the initial level of undoped alloy, therefore the doping the alloy with  $2 \times 10^{-4}$  at.% Te and greater to MTE f.m. increase is not efficient.

The data presented for TM f.m. were measured at the magnetic field 1.2T. Te reduces TM f.m. of Bi-Sb single crystals, containing 2 at.% Sb. Contrastingly, it was found that TM f.m. of crystals doping with  $1 \times 10^{-4}$  at.% Sn inclusive are close to that of undop-

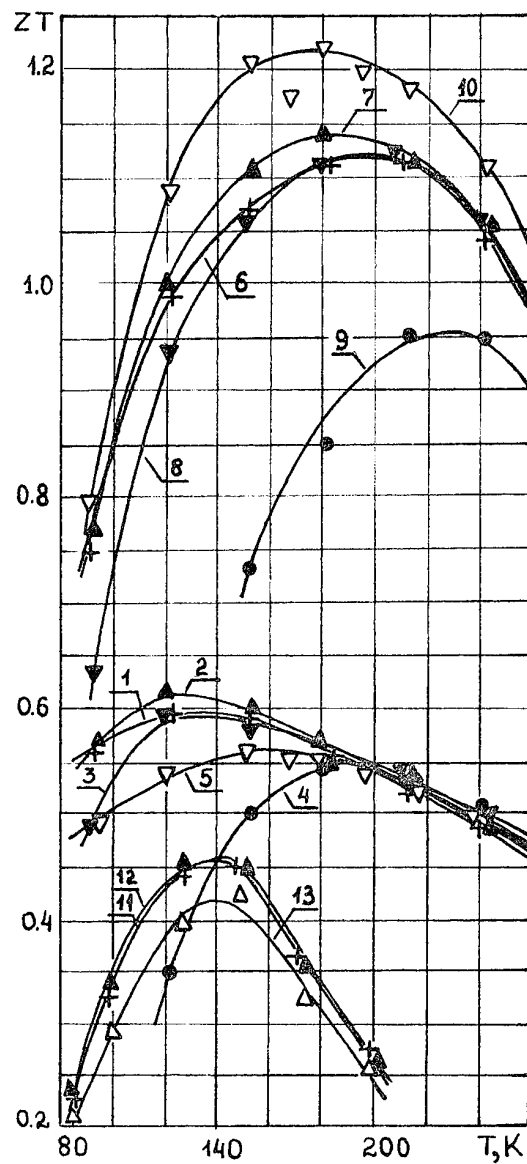


Fig.4  
Thermoelectric (1-5), magnetothermoelectric (6-10) figure of merit of single crystals of  $\text{Bi}+9\text{at.\%Sb}$  alloys and thermomagnetic figure of merit of single crystals of  $\text{Bi}+2\text{at.\%Sb}$  alloys (11-13). Undoped alloys - 1, 6, 11. Alloys doped with Sn:  $5 \times 10^{-5}$  at.% - 2, 7, 12;  $1 \times 10^{-4}$  at.% - 3, 8;  $1 \times 10^{-3}$  at.% - 4, 9; doped with Te:  $5 \times 10^{-5}$  at.% - 13;  $1 \times 10^{-4}$  at.% - 5, 10.  
For MTE f.m. are presented the maximum values measured in the range of magnetic fields 0-1.15T.  
For TM f.m. are presented the values measured in the magnetic field 1.2T.

Maximum values of Z of undoped alloy of Bi with 9 at.% Sb is obtained in the range 80 - 100K [10]. Taking into account the known yield coefficients of Te and Sn in Bi-Sb alloys [11], values of N calculated at 80K and 100K were used to determine the Te and Sn concentration at which Z may be increased at temperatures lower than 80K and higher than 100K, respectively. It was established, that the condition of obtaining N(opt) of this alloy cannot be fulfilled in doping with more than  $3 \times 10^{-4}$  at.% Te or with more than  $1 \times 10^{-3}$  at.% Sn.

So far as discussed above approach of optimization Z takes no account of Te and Sn influence on kinetic properties of carriers, we also examined the variation of effective mass and mobility of electrons in Bi-Sb alloys in doping.

#### Influence of doping on kinetic properties of electrons in Bi-Sb alloys

Using the data presented in Fig.2 in combination with the data about the anisotropy of the Fermi surface of the alloy [8], we calculated the dependence of mean value of effective mass ( $m$ ) of electrons in C3 direction, corresponding to the maximum of Z in these materials, upon N (Fig.3).

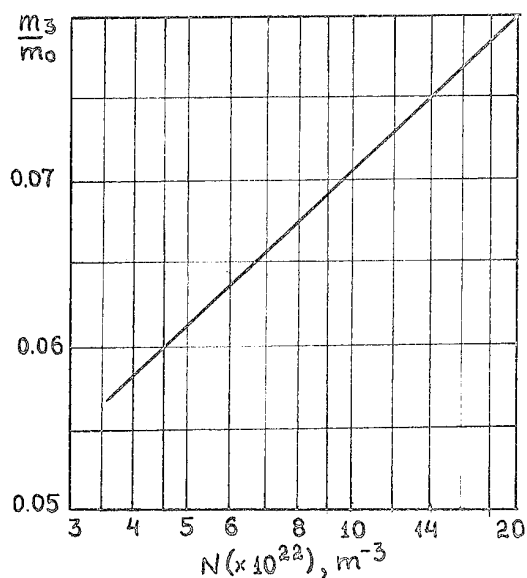


Fig.3

Dependence of the effective mass of electrons in C3 direction upon their concentration in the conduction band for Bi + 9 at.% Sb alloy

The dependence indicates that it is possible to change greatly the  $m$  and mobility ( $\mu$ ) of electrons (because  $\mu$  is proportional to  $1/m$ ) in doping of the alloy with Te or Sn.

In doping the alloy the change of  $m$  and  $\mu$  of L-holes occurs too, but in qualitative examination it may be disregarded since  $P(L)$  is low in comparison with  $P(T)$  and N (Fig.2b).

The results of measurements of  $\mu$  in C3 direction are shown in the Table:

Table

Mobility of electrons ( $\mu, m.m/(B.c)$ ) in C3 direction in Bi-Sb single crystals, containing 9 at.% Sb, at 77K

Undoped alloy	Doping (at.%)	
	Te, $1 \times 10^{-4}$	Sn, $1 \times 10^{-4}$
83.0	55.3	75.8

As is seen, at the same content of Te and Sn,  $\mu$  in the alloy doped with Te is lower than in the alloy doped with Sn. This is in agreement with the dependence of  $m$  upon N (fig.3). At the same time,  $\mu$  in doped single crystals is lower than in the undoped crystal. This may be caused by a reduction of structure perfection of single crystals in doping.

These results suggest that effect of doping on Z value of the alloy, being studied in this work, is determined by the action of two factors: variation of N causing an increase of Z when it approaches N(opt), and a reduction of  $\mu$  preventing this increase. The general features of the conduction band of Bi-Sb alloys [8] made it possible to use the results of this consideration for explanation experimental data obtained on other alloy compositions too. In this connection it is not improbable, that  $\mu$  may increase with small doping of Sn in alloys having initial lower  $\mu$  value than that in Bi with 9 at.% Sb alloy. Thus, such  $\mu$  increase from 52 to 58 (m.m)/(V.c) at 77K were detected in Bi with 15 at.% Sb alloy in doping with  $5 \times 10^{-5}$  at.% Sn. As the increase of  $\mu$  is one of the conditions of TM figure of merit increasing, we also examined the effect of Sn (in comparison with Te) on this parameter for Bi-Sb single crystals, containing 2 at.% Sb.

ed crystals. Further Sn content increasing reduces their TM f.m.

It may be assumed that effect of Sn on TM f.m. is associated with simultaneous variation of the electron mobility and the ratio of number of electrons and holes. When doping with Te effect of both these factors reduces TM f.m. of the alloy.

#### Strength properties of Bi-Sb single crystals doped with Te and Sn

We investigated the strength properties of doped Bi-Sb single crystals in comparison to that of undoped single crystals with the use of bending test method, because the stress state of specimen in bending is similar to distribution of stresses in thermocouple branches. Selected specimen orientation is the most important for making these wares from Bi-Sb crystals: the loading is proceeding in parallel to the cleavage plane (111) of the crystal, causing this plane becomes destructive one.

The results obtained for Bi-Sb single crystals containing 9 at.% Sb are shown in Fig.5, that for crystals containing 2 at.% Sb are shown in Fig.6.

As is clear from Fig.5, mean bending strength values of doped Bi-Sb crystals, containing 9 at.% Sb, are close to that of undoped one. Therefore it is possible to use doped with Te crystals, having the higher MTE f.m., or doped with Sn crystals, having different combination of  $\rho$ ,  $\alpha$ ,  $\chi$ , in producing of thermocouple branches like undoped crystals with the same content of Sb. Effect of Te and Sn on bending strength of Bi-Sb crystals, containing 2 at.% Sb, is positive (Fig.6). For crystals doping with Sn it is particularly remarkable that the increase of bending strength is attended with the dispersion of tests decreasing and, as noted above, TM f.m. of doped with Sn crystals, containing 2 at.% Sb, is close to that of undoped crystals with the same content of Sb.

Previous x-ray diffraction microscopy investigation suggests, that effect of Te and Sn on the bending strength of Bi with 2 at.% Sn single crystals is most likely conditioned by distinction between structure perfection of doped and undoped crystals. In turn, this distinction is consequence of change of crystallization conditions on crystal-melt interface with doping

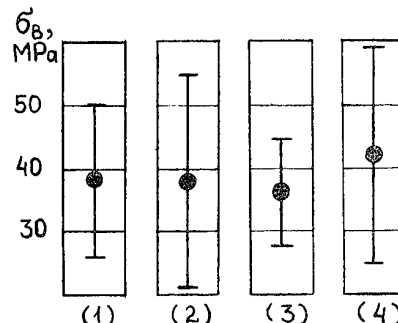


Fig.5

The bending strength of the Bi-Sb single crystals, containing 9 at.% Sb.  
Undoped alloy - 1. Alloys doped:  
with Te:  $1 \times 10^{-4}$  at.% - 2;  
with Sn:  $5 \times 10^{-5}$  at.% - 3,  
 $1.5 \times 10^{-4}$  at.% - 4.

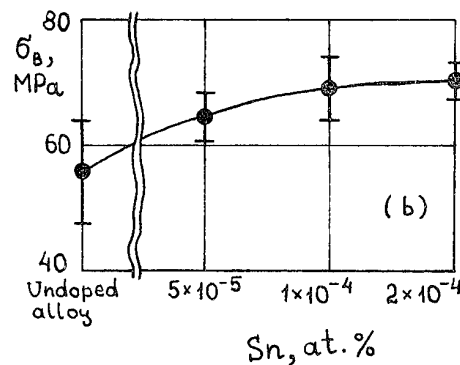
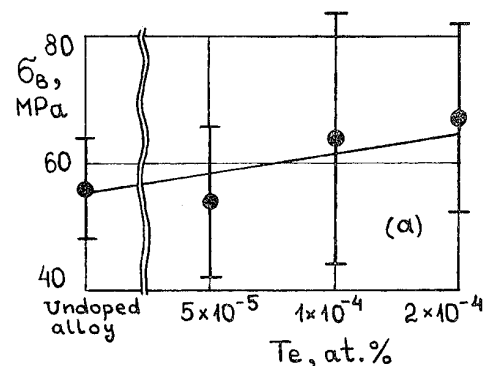


Fig.6

Influence of doping with Te (a) or Sn (b) on the bending strength of Bi-Sb single crystals, containing 2 at.% Sb

the melt. The low dispersion of the tests results for Sn doped crystals is directly related to homogeneous structure perfection.

#### CONCLUSION

At a result of investigation carried out on the doped Bi-Sb single crystals it may be concluded that at maximum thermoelectric, magnetothermoelectric and thermomagnetic figure of merit the strength properties of doped crystals at least are not lower than those of undoped crystals. The level of the strength properties of doped crystals makes it possible to carry out all tapes of treatment including brazing in producing branches and assembling thermoelements.

#### REFERENCES

- [1]. H.J.Goldsmid, Bismuth-antimony alloys, Phys.State Sol.(a), 1970, v. 1, No. 1, pp.7-28.
- [2]. N.Kh.Abrikosov, et al, Growth of single crystals of bismuth - antimony solid solution by pulling method, Fiz. Khim. Obrab. Mater., 1969, No.5, pp.47-51.
- [3]. V.S.Zemskov,et al, Distribution of tin and antimony between liquid and solid phases under crystallization of Bi-Sb-Sn alloys, Izv.Akad.Nauk SSSR,Neorgan.Mater.,1976, v.12, No.5, pp.805-809.
- [4]. V.S.Zemskov,et al,Growth of sing-  
le crystals of bismuth-antimony alloys by Czochralski method, J. Cryst. Growth, 1985, v.71, pp. 243-245.
- [5]. T.C.Harman,et al, Ettingshausen energy conversion figure of merit for Bi and Bi-4% Sb alloys, Solid-State Electronics, 1964, v.7, pp. 505-508.
- [6]. R.Pozera,et al, The influence of hydrostatic pressure on the effective concentration and cyclotron mobility of electrons in semiconducting Bi-Sb alloys,Phys.Stat.Sol.(b),1983, v.120, No.1, pp.165-171.
- [7]. A.F. Ioffe, et al, Thermoelectric cooling, Academy of Sciences of the USSR,Moscow and Leningrad,1956,110p.
- [8]. N.B.Brandt,et al, Electron Fermi surface of semimetal Bi-Sb alloys,Zh. Eksp.Teor.Fiz.,1982,v.83,No.6(12),pp. 2152-2169.
- [9]. N.B.Brandt, et al, Spin splitting and effective g-factor of T-holes in Bi-Sb alloys, Fiz.Nizkikh Temp.,1977, No.2,pp.152-160.
- [10]. V.S.Zemskov,et al, Thermoelectric and magnetothermoelectric figure of merit of bismuth and system of bismuth-antimony solid solutions, Izv. Akad. Nauk SSSR, Neorgan. Mater., 1982, v.18, No.7, pp.1154-1157.
- [11]. G.A.Ivanov,I.K.Kalugina, Materials for thermoelectric converters, Proc. of the 3rd Intergovernmental seminar, ST.Petersburg,1993,pp.46-47.

MICROSTRUCTURE  $Bi_2Te_3-Sb_2Te_3$  ALLOYS GROWN BY ZONE MELTING TECHNIQUE

A.I.Anukhin 1, S.Ya.Skipidarov 2, O.B.Sokolov 1, and A.A.Aivazov 3

1. Telvis Co., Moscow, 109383, Russia.
2. Nord Co., Moscow, 109383, Russia.
3. Moscow Institute of Electronic Engineering, Russia.

The new data about the microstructure of  $Bi_2Te_3-Sb_2Te_3$  alloys grown by zone melting technique is represented in this paper. The mathematical model of concentration supercooling is elaborated. The periodical micro- and macrodistribution of the components is explained.

## Introduction

The  $Bi_2Te_3$ ,  $Sb_2Te_3$ , and  $Bi_2Se_3$  based alloys are widely applied in thermoelectric cooling devices. The thermoelectric properties of these materials are determined by their structure. The structure of the grown  $Bi_2Te_3$ ,  $Sb_2Te_3$ , and  $Bi_2Se_3$  alloys is formed as a result of complicated heat and mass exchange processes near the growth interface. At present, there are publications dedicated to the problem of structure formation in the crystallization process of these alloys [1, 2], but they lack detailed investigations of microstructure properties and the reasons that generate structural features.

The object of this work is to investigations the influence of the chemical composition in charge and the growth rate of the microstructure of  $(Bi,Sb)_2Te_3$  and  $Bi_2(Te,Se)_3$  solid solutions grown by a zone melting technique and alloys produced.

## Experimental methodology

The  $(Bi_{1-x}Sbx)_2Te_3$ , where  $x=0.5$ ,  $0.6$ ,  $0.7$  and  $0.8$ , compositions were taken for investigation. The excess tellurium concentration in the charge was varied from  $0.5$  to  $2.5$  mass.%. A charge of  $(Bi_{0.8}Sb_{0.2})_2Te_3+8.0$  mass.% Te was also used. The elementary components were loaded in quartz ampoules coated with graphit by means of alcohol pyrolysis. The ampoules were evacuated and sealed.

The specimens under investigation were grown using vertical zone-melting technique. The growth rate was  $1.0$  to  $1.5$  cm/h. This ingots were  $9$  to  $12$  mm in diameter and up to  $100$  mm long. Then the obtained ingots were cut in the diametric cross section. The cross-section surface was ground, polished, and etched in a nitric acid solution of a  $18$  to  $20\%$  concentration. The observations were made using an optical metallographic microscope. To examine the dependence of microstructure variations on growth rate, which was sharply varied in the process of growth when the melted zone was located in the middle portion of the ingot.

## Experimental results

No fundamental distinctions between the microstructures of ingots with various



Fig.1. The microstructure of the initial (a) and (b) sections of the two-phase region in a  $(Bi_{0.8}Sb_{0.2})_2Te_3+1\% Te$  zone-melted ingot ( $\times 70$ ).

molar ratios of  $\text{Bi}_2\text{Te}_3$  and  $\text{Sb}_2\text{Te}_3$ , grown at the same rate have been observed. A microstructure characteristic of all the compositions, observed in specific cross sections will be discussed here.

All of the ingots grown at a constant rate from  $(\text{Bi}, \text{Sb})_2\text{Te} + \text{Te}$  loading were initially single-phase (Fig.1a). In the very end of the ingot (Fig.1b) the emergence of a second phase was observed. The two-phase region has a clear interface with the single-phase one. The two-phase region consists of almost regularly alternating bright and dark longitudinal layers oriented in the growing direction. In the very end of the two-phase region, another conditional interface is observed.

It divides the two-phase region into subregions with layers of various thickness. In the end of the subregion, the thickness of bright color layers is much greater and the layer thickness shows hopping changes.

The bright layers in the entire two-phase region are also inhomogeneous. Some part of a dark layer, neighboring a bright structural component, may be brighter than another.

It should be noted, that the two-phase region length depends on the excess tellurium concentration in the charge. Thus, the two-phase region length increases, if the excess tellurium concentration in the loading is increased too.

The thickness of the structural components in the two-phase region increases as the coordinate of the distance that is measured from the beginning of this region increases (see Table and Fig.2).

Table.

The average thickness of structural components in the two-phase region of a  $(\text{Bi}_{0.2}\text{Sb}_{0.78})_2\text{Te} + 1.0\% \text{ Te}$  ingot.

Distance from the beginning of the two-phase region, mm	0	1.0	2.0	4.0	5.0	7.0	9.0
Average thickness of dark layers, $d_1 \cdot 10^{-6} \text{ mm}$	0.74	0.82	1.0	1.2	1.4	1.6	0.5
Average thickness of bright layers, $d_2 \cdot 10^{-6} \text{ mm}$	0.06	0.1	0.15	0.18	0.25	0.3	0.5
Layer thickness ratio	12.3	8.2	6.7	6.7	5.6	4.6	0.6

The structural inhomogeneities invisible in the usual light. They are observed in the polarized light in the vicinity of the two-phase region. The dark color structural layers in the two-phase region are a continuation of the structural inhomogeneities born in the single-phase region (Fig.3).

The increase in the excess tellurium concentration in the charge to 8.0 mass % considerable changes in the microstructure the single phase region of the ingots grown under other conditions. The main difference is the emergence of a lamella transverse inhomogeneity with almost regular distribution along the ingot with a period of 5.5 s (Fig.4).

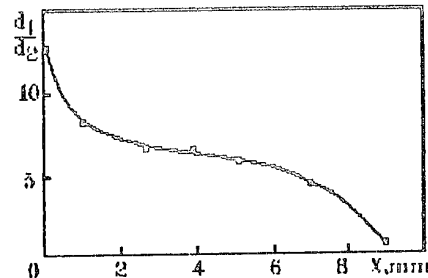


Fig.2. Thickness ratio dependence of dark and bright structural components of the two-phase region in a  $(\text{Bi}_{0.2}\text{Sb}_{0.78})_2\text{Te} + 1.0\% \text{ Te}$  ingot.

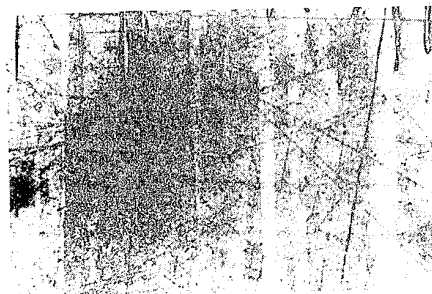


Fig.3. The microstructure of the initial portion of a two-phase region in  $(\text{Bi}_{0.2}\text{Sb}_{0.78})_2\text{Te} + 2.0\% \text{ Te}$  zone-melted ingots, observed in the polarized light ( $\times 120$ ).

Now, look what happens when the change of the rate in the process of growthing occurs. It affects both the character of micro- and macrostructure. At the moment of the abrupt increasing the growth rate, the second phase as a wide stripe emerges (Fig.5).

This stripe possesses a substructure and consists of the bright-color structural component spots against the background of the basic phase. The lamellea are located in an approximately periodical order along the ingot until they merge into a two-phase region in the end of the ingot portion.

A lamella-geometry transverse structure is also characteristic of the zone melted ingots of the  $\text{Bi}(\text{Te}, \text{Se})_2$  composition. Under low magnification (Fig.6) the distribution of lamellea along the ingot is almost periodic. Similar to the  $(\text{Bi}, \text{Sb})_2\text{Te}_3$  ingots, a change in the mutual location of lamellea including their merging is observed as chaotic one.

The macrostructure of the single-phase regions in the  $(\text{Bi}, \text{Sb})_2\text{Te}_3$  ingots grown from a charge containing up to 2.0% tellurium are observed in the form of diffuse transverse layers located strictly periodically along the ingot (Fig.7).

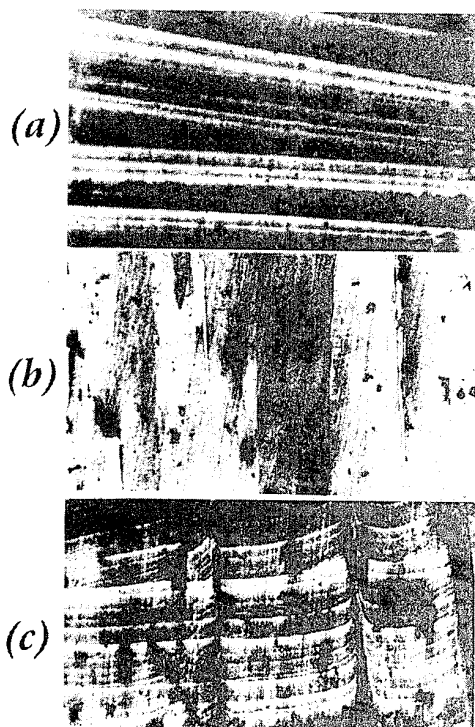


Fig.4. The microstructure of a  $(Bi_{0.9}Sb_{0.1})_3Te_3 + 2.0\% Te$  ingot ( $\times 120$ ):  
 a - single-phase region;  
 b - a region contiguous with the two-phase region;  
 c - two-phase region.

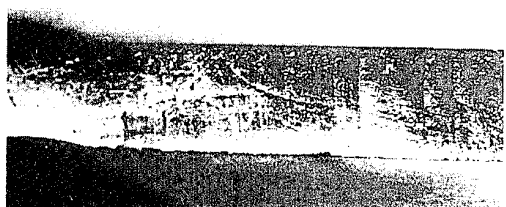


Fig.5. The macrostructure of the area on a  $(Bi_{0.9}Sb_{0.1})_3Te_3 + 2.0\% Te$  ingot, where the growth rate was increased from 1 cm/h to 2 cm/h ( $\times 2$ ).

(a)

(b)

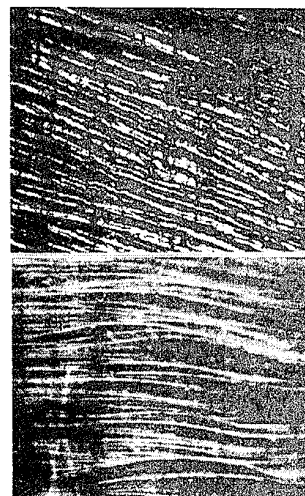


Fig.6. The microstructure of a  $Bi_2(Te_{0.9}Sb_{0.1})_3$  ingot ( $\times 7$ ):  
 a - longitudinal section;  
 b - transversal section.

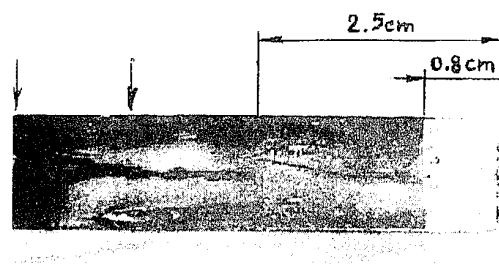


Fig.7. The macrostructure of a  $(Bi_{0.9}Sb_{0.1})_3Te_3 + 2.0\% Te$  zone-melted ingot ( $\times 1.8$ ).

It is not always possible to reveal such structures. However, on the specimen where it was noticed its periodicity was about 50 minutes (Fig.7). In the end of the same ingot one can observe macro-phenomena of a two-phase region formation, similar to that those shown in Fig.1. The two-phase crystallization begins at a distance of 2.5 cm from the beginning of the ingot.

#### Discussion

The complicated character of the microstructure observed in the thermoelectric materials under investigation reflects complicated process of component distribution

during the crystallization of the  $(Bi,Sb)_2Te_3$  solid solutions. The investigation of phase diagrams for the  $Bi-Sb-Te$  system [3] as well as the investigation of thermoelectric properties of the  $(Bi,Sb)_2Te_3$  solid solutions produced using zone melting technique [4, 5] allow to suggest that the free tellurium practically does not dissolve in the solid solution. If the  $(Bi,Sb)_2Te_3-Te$  system is considered, the free tellurium has a very small distribution coefficient there, and the growth interface pushes it, therefore, into the melt.

According to the phase equilibrium diagram in the  $Bi-Sb-Te$  system, the simultaneous crystallization both  $(Bi,Sb)_2Te_3$  solid solution and Te take place when the melt reaches eutectic composition. Something similar to the result of such crystallization may be seen in the microstructure represented in this work (Fig.1). The phase volume ratio varies, however, along the two-phase region (see Table 1 and Fig.2), and in addition, does not correspond to the relationship determined by the phase equilibrium diagram. The possible conclusion that the melt has reached the eutectic composition in the zone will not conform with the reality. The two-phase crystallization, on the contrary, can result from the fact that the melt has reached the eutectic composition in multiple local regions, which takes place when conditions arise for the concentration-induced supercooling well described in a two-component system by the Tiller condition

$$V_{er} = \frac{k_a \cdot D \cdot G}{(1-k_a) \cdot C_s} \cdot \frac{dC_L}{dT}, \quad (1)$$

where  $V_{er}$  is the critical growth rate to be exceeded given the temperature gradient  $G$  in the melt near the growth interface,  $D$  is the diffusing coefficient,  $C_s$  is the component concentration in the solid phase,  $dC_L/dT$  is the angle between the liquidus line and the temperature axis at the crystallization temperature, and  $k_a$  is the distribution coefficient.

Assuming the tellurium distribution coefficient in the  $(Bi,Sb)_2Te_3$  system is small ( $k_a \ll 1$ ), taking into account equation  $C_s = k_a \cdot C_L$  and the linear dependence of the free tellurium concentration  $C_L$  in the melt during zone-melting on the zone coordinate  $X$  on the ingot when zone length is  $L$  and the initial free tellurium concentration in the charge is  $C_0$  [4, 5]  $C_L = C_0(1+X/L)$ , we have

$$C_s = k_a \cdot C_0 \cdot (1+X/L) \quad (2)$$

and equation (1) looks as follows:

$$V_{er} = \frac{D \cdot G}{C_0 \cdot (1+X/L)} \cdot \frac{dC_L}{dT} \quad (3)$$

The zone coordinate on the ingot may be taken as the growth process variable instead of the growth rate. Then at a constant growth rate the increase in the zone coor-

dinate  $X$  on the ingot causes, according to (2), an increase in the tellurium concentration in the melt. Assuming the dependence of diffusion coefficient and temperature gradient  $G$  in the melt on concentration to be negligible, one can obtain a condition from the relationship (3), which determines the  $X_{er}$  coordinate on the ingot where the concentration-induced supercooling begins:

$$X_{er} = L \cdot \frac{D \cdot G}{V \cdot C_0} \cdot \frac{dC_L}{dT} \quad (4)$$

In stationary heat and mass exchange process during zone melting, the beginning of the concentration-induced supercooling appears simultaneously on the within ingot cross section that corresponds to the  $X_{er}$  coordinate. In general, the  $X_{er}$  value is determined not solely by the temperature gradient, and the interface line between single-phase and two-phase regions is the locus of points on which Tiller condition is met. The distortion of the surface where the concentration-induced supercooling begins, observed in Fig.1a, is obviously determined by the irregular temperature gradient and  $dC_L/dT$  fields as well as by the component concentration variation due to the convection in the bulk of the melt.

This approach also well provides for the phase volume ratio deviation from the one inherent in the eutectic crystallization. Indeed, the free tellurium is pushed already into the melt of the interdendrite region where heat and mass exchange with the zone melt are considerably hampered, and the dendrites additionally grow on the lateral surface. The essentially non equilibrium crystallization of the interdendrite melt ends at the eutectic temperature. However, during the crystallization of the interdendrite melt at the eutectic temperature, some part of it crystallizes on the lateral dendrite surface, which increases the phase volume ratio to the benefit of the dark structural component. When the melt reaches the eutectic composition in the zone due to a reduction of its length in the very end of the phase volume ratio (Table 1, last column), and can be easily seen in Fig.1b and 7.

The generation of dendrites starts already in the single-phase region (Fig.2), but nevertheless the growth of dendrites acquires a fundamentally new character when the second phase appears. The dendrites observed in the single-phase region are undoubtedly a consequence of the increase in the bismuth and antimony distribution coefficients, when the free tellurium concentration in the zone melt is risen. The dendrites in the single-phase region, that are a kind of forerunners of the two-phase crystallization, may be referred to first-order dendrites, and the dendrites in the two-phase region, to second order.

According to equation (4), a reduction of the  $X_{er}$  value, i.e., a displacement of the beginning of the two-phase crystallization to the beginning of the ingot, may be expected when the free tellurium concentration  $C_0$  in the charge increases. This

is exactly what is observed in Fig.3. Similar phenomena will be observed, too, when the growth rate increases.

The tellurium diffusion coefficient that is calculated using the results of measuring  $X_{cr}=7.5$  cm is approximately equal  $2.4 \cdot 10^{-7}$  m<sup>2</sup>/s., if the following data of  $dT/dX=140$  K/cm,  $V=1.5$  cm,  $C_a=2.0\%$  Te are accepted, and  $dC_L/dT=1.2$  1/K is calculated using liquidus line curve given in [6].

This figure is very close to the value of  $5.0 \cdot 10^{-7}$  m<sup>2</sup>/s. obtained in [7] for the same solid solution  $(Bi_{0.9}Sb_{0.1})_2Te_3$ , but grown by Czochralski technique.

The appearance of transverse growth strip in the single-phase region is hardly attributable to the periodicity of thermal processes in the melt, initiated by the functioning of a temperature regulator, or by the discreet increments of the drive that travels the ingot with respect to the heater. The average strip appearance period is close to 3.0 s. (Fig.4) while the temperature regulator time constant was close to 250 s., and the drive increment did not exceed +5 micrometers.

In our opinion, the most acceptable explanation for the factors that generate periodical transverse inhomogeneities may be the accumulation of sufficiently high free tellurium concentration in the melt, which entailed an increase in the antimony distribution coefficient, but did not yet result in a two-phase crystallization.

Such explanation seems there to be real since similar self-organization processes in system of melt-solid are also observed in the  $Bi_2Te_3$ - $Bi_2Se_3$  system (Fig.6) where the bismuth selenide distribution coefficient is close to 2.0.

The order in the growth strip location along the ingot is probably violated by the convection in the melt. In this case, the strip may have a complex distorted shape, they may merge and intersect depending on local temperature conditions.

It is difficult to refer the component distribution along the zone-crystallized ingots having a big location period of growth strip (up to 8.5 mm, see Fig.7) to the influence exerted on the strip by external factors.

The periodicity of the second-phase concentration distribution along the ingot, observed when the growth rate (Fig.5) or tellurium concentration in the end of the ingot (Fig.7, the end of the ingot, area a) increase, suggest a predominant role of periodical reproduction of conditions for the emergence of concentration-induced supercooling, due to the formation of a melt layer very rich in tellurium and contiguous with the crystallizing solid phase.

Thus, the investigations of the microstructure zone melted alloys produced from the  $(Bi,Sb)_2Te_3+Te$  charge, suggest a complex character of component distribution in the  $Bi-Sb-Te$  system. One of the basic processes leading to self-organization of various orders in melt-solid system is tellurium segregation and the influence exerted by tellurium concentration on bismuth and antimony distribution.

## Conclusions

1. The beginning of two-phase crystallization during zone melting of the  $(Bi,Sb)_2Te_3+Te$  alloys is preceded by the formation of the first-order dendrites.

2. The two-phase crystallization during zone melting of the  $(Bi,Sb)_2Te_3+Te$  alloy is consequence of the fact that a critical concentration of excess tellurium is reached, at which the formation of the second-order dendrites occurs.

3. Periodic inhomogeneity structure of various type, formed as a result of self-organization processes in the melt-solid system, are found during the crystallization of the  $(Bi,Sb)_2Te_3$ ,  $Bi_2(Te,Se)_3$  solid solution.

## References

1. W.M.Yim, F.D.Rosi. Compound tellurides and their alloys for Peltier cooling- a review. Solid state electronics. 1972, V.15, pp.1121-1140.
2. D.Tuomi. The challenges to development of thermoelectric and thermomagnetic cooling from ambient temperatures. Proceedings of the Intersociety Energy Conversion Engineering Conference. Boston, Massachusetts. August, 5-10, 1979, pp.1954-1960.
3. N.Kh.Abrikosov, L.V.Foretskaya. Physical and chemical equilibriums in ternary alloys of  $Sb_2Te_3$ - $Bi_2Te_3$ -Te system and quaternary alloys  $Sb_2Te_3$ - $Bi_2Te_3$ - $Bi_2Se_3$ -Te system. Izv. AN USSR. Inorganic materials. 1983, V.19, N3, pp.388-393. In Russian.
4. A.I.Anukhin, O.B.Sokolov, S.Ya.Skipidarov, K.V.Senin. Microstructure and thermoelectric properties of  $(Bi,Sb)_2Te_3$  solid solutions grown by zone melting technique. Proceeding of the XI International Conference on Thermoelectrics. Arlington, Texas, USA. October 7-9, 1992. pp.307-311.
5. A.A.Aivazov, A.I.Anukhin, Thermoelectric properties of  $Bi_2Te_3$ - $Sb_2Te_3$  low temperature materials with hole conductivity. Proceeding of the XII International Conference on Thermoelectrics. Yokohama, Japan, November 9-11, 1993.
6. J.P.Fleurial, L.Gailliard, R.Triboulet, H.Scherrer, S.Scherrer. Thermal properties high quality single crystals of bismuth telluride. Part 1. Experimental characterization. J.Phys.Chem. Solidi. 1988, V.49, N10, pp.1237-1247.
7. P.Reinshaus, H.Susman, U.Lampe. Investigation of macrosegregation in normalfrused  $(Bi)_2bTe_3$ - crystals. Proceedings of the XII-th International Conference on Thermoelectrics. Yokohama,Japan, November 9-11, 1993.

## MECHANICAL ALLOYING BEHAVIOR AND THERMOELECTRIC PROPERTIES OF $(\text{Bi},\text{Sb})_2\text{Te}_3$

B. Y. Jung<sup>1</sup>, J. S. Choi<sup>1</sup>, T. S. Oh<sup>1</sup>, D. B. Hyun<sup>2</sup>, H. P. Ha<sup>2</sup>, and J. D. Shim<sup>2</sup>

1) Dept. of Metallurgy and Materials Science, Hong Ik University, Seoul, Korea  
2) Metals Research Division, Korea Institute of Science and Technology, Seoul, Korea

### **Abstract**

Mechanical alloying behavior and thermoelectric properties of  $(\text{Bi},\text{Sb})_2\text{Te}_3$  have been investigated. Processing time for the complete formation of  $(\text{Bi}_{1-x}\text{Sb}_x)_2\text{Te}_3$  by mechanical alloying was increased with increasing Sb content, and was inversely proportional to the ball to powder weight ratio.

Figure of merit of  $\text{Bi}_{0.5}\text{Sb}_{1.5}\text{Te}_3$  at 300K, processed by mechanical alloying, was increased with hot pressing temperature, and was  $2.4 \times 10^{-3}/\text{K}$  when hot pressed at 575°C for 30 minutes.

### **Introduction**

Mechanical alloying is a technique in which intermetallic compound or alloy powders are fabricated from elemental powders through a sequence of collision events inside a high energy ball mill. This metallurgical process has been employed in industry since the early 1970's for production of oxide dispersion strengthened alloys and production of alloys with components which have widely different melting temperatures [1]. Recently, mechanical alloying has been applied to prepare thermoelectric materials, such as  $(\text{Bi},\text{Sb})_2\text{Te}_3$  and SiGe alloys [2,3,4].

Since the mechanical alloying process occurs near room temperature, this technique can be viewed as a cost-saving alternative for the production of polycrystalline thermoelectric materials to the conventional "vacuum melting/chill cooling/grinding" process where a long processing time, and high temperature and large scale facilities are required [3].

In this paper, mechanical alloying behavior of  $(\text{Bi},\text{Sb})_2\text{Te}_3$  was characterized, and thermoelectric properties of  $\text{Bi}_{0.5}\text{Sb}_{1.5}\text{Te}_3$ , hot pressed with mechanically alloyed powders and melt/ground powders, were compared.

### **Experimental procedure**

#### **1. Mechanical Alloying**

$(\text{Bi},\text{Sb})_2\text{Te}_3$  was fabricated with elemental Bi, Sb and Te powders of a particle size less than 44  $\mu\text{m}$  and purity higher than 99.999%. The appropriate amounts of Bi, Sb and Te powders were weighed and charged in a hardened tool steel vial with steel balls as milling media under Ar atmosphere. Ball to powder weight ratio was held 2 : 1, 4 : 1 and 10 : 1. Mechanical alloying was conducted by shaking the vial at approximately 1200 rpm using a Spex mixer/mill.

After the vibro-milling process, X-ray diffraction analysis was made to characterize the crystalline phases and to determine the lattice parameter of  $(\text{Bi},\text{Sb})_2\text{Te}_3$  formed by mechanical alloying.

Mechanical alloying behavior of  $(\text{Bi},\text{Sb})_2\text{Te}_3$  was characterized using the variation of the relative X-ray peak intensities of Bi, Sb, Te, and  $(\text{Bi},\text{Sb})_2\text{Te}_3$  with milling time. Since the diffraction angles of Bi (102), Sb (102), Te (101) and  $\text{Bi}_2\text{Te}_3$  (015) peaks are almost identical, the maximum intensities of Bi (110), Sb (110), Te (110) and  $\text{Bi}_2\text{Te}_3$  (110) peaks were compared relative to (220) peak intensity of Si powder which was mixed with the processed powders as internal standard after mechanical alloying. DTA was conducted at a scan rate of 5°C/min for the as-mixed and mechanically alloyed powders.

#### **2. Hot pressing and measurement of thermoelectric properties**

High purity (> 99.999%) Bi, Sb and Te powders were mechanical alloyed for 1 hour at ball to powder weight ratio of 10 : 1 to form  $\text{Bi}_{0.5}\text{Sb}_{1.5}\text{Te}_3$ .

To compare thermoelectric properties,  $\text{Bi}_{0.5}\text{Sb}_{1.5}\text{Te}_3$  powders were made by conventional melting and grinding process.  $\text{Bi}_{0.5}\text{Sb}_{1.5}\text{Te}_3$  powders were hot pressed in vacuum at temperatures ranged from 300 °C to 575 °C for 30 minutes.

Seebeck coefficient  $\alpha$  was characterized at 300K by the heat pulse method. The electrical resistivity  $\rho$  and thermal conductivity  $\kappa$  of the samples were characterized at 300K using Harman method in vacuum of  $10^{-5}$  torr to minimize thermal conduction through convection. Figure-of-merit  $Z$  was calculated using the equation  $Z = \alpha^2/\rho \cdot \kappa$ .

## Results and Discussion

### 1. Mechanical alloying behavior

Elemental Bi and Te powders were weighed for  $\text{Bi}_2\text{Te}_3$  composition and mechanically alloyed at ball to powder weight ratio of 2 : 1. X-ray diffraction patterns of the as-mixed and processed powders are shown in Fig. 1. Mechanical alloying behavior of  $\text{Bi}_2\text{Te}_3$ , characterized using the variation of the relative X-ray peak intensities of Bi, Te and  $\text{Bi}_2\text{Te}_3$  (Fig. 2), clearly illustrates complete formation of  $\text{Bi}_2\text{Te}_3$  by vibro-milling process for 1 hour.

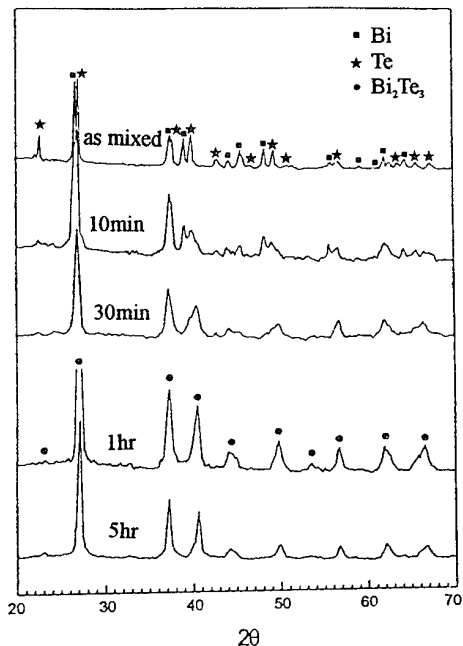


Fig. 1 XRD patterns of Bi and Te powders with different mechanical alloying time.  
(ball to powder weight ratio 2 : 1)

DTA curves of as-mixed and mechanically alloyed  $\text{Bi}_2\text{Te}_3$  powders are shown in Fig. 3. For the as-mixed powder, an endothermic peak at 272°C due to the melting of Bi and exothermic peaks, associated with successive reactions between Bi melt and solid Te to form  $\text{Bi}_2\text{Te}_3$ , were observed.

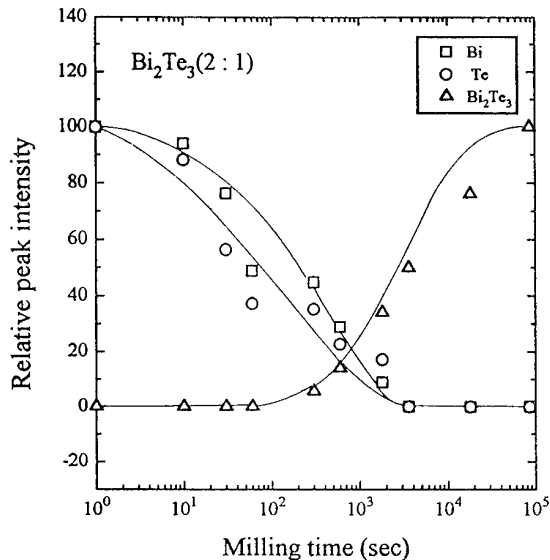


Fig. 2 Relative intensities of Bi (110), Te (110), and  $\text{Bi}_2\text{Te}_3$  (110) diffraction peaks with milling time. (ball to powder weight ratio 2 : 1)

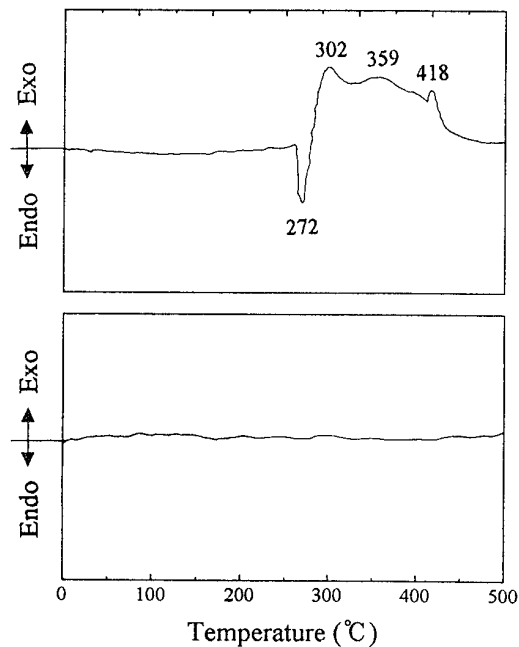


Fig. 3 DTA curves for  $\text{Bi}_2\text{Te}_3$  powders, a) as mixed and b) mechanically alloyed for 1 hour at ball to powder weight ratio of 2 : 1

However, such endothermic and exothermic peaks disappeared completely in the powder milled for 1 hour. With this result, it could be confirmed that the formation of  $\text{Bi}_2\text{Te}_3$  was completed by mechanical alloying of Bi and Te powders for 1 hour at ball to powder weight ratio of 2 : 1.

Processing time for the complete formation of  $(\text{Bi}_{1-x}\text{Sb}_x)_2\text{Te}_3$  by mechanical alloying at ball to powder weight ratio of 2 : 1 was 3 hours for  $x = 0.25$  and  $x = 0.5$  compositions, and 5 hours for  $x = 0.75$  and  $x = 1$ . Such retardation of the mechanical alloying process with increasing Sb content might be due to the bonding characteristics between  $\text{Bi}_2\text{Te}_3$  and  $\text{Sb}_2\text{Te}_3$ . Enthalpy of formation  $\Delta H_{\text{mix}}$  for  $\text{Bi}_2\text{Te}_3$  is negatively larger than  $\Delta H_{\text{mix}}$  for  $\text{Sb}_2\text{Te}_3$  [5], and Sb-Te bond is weaker than Bi-Te bond [6].

Processing time required for the complete formation of  $\text{Bi}_2\text{Te}_3$  and  $\text{Bi}_{0.25}\text{Sb}_{0.75}\text{Te}_3$  at various ball to powder weight ratio is illustrated in Fig. 4. Without depending on the composition, processing time for mechanical alloying of  $(\text{Bi}_{1-x}\text{Sb}_x)_2\text{Te}_3$  was inversely proportional to the ball to powder weight ratio.  $\text{Bi}_{0.5}\text{Sb}_{1.5}\text{Te}_3$  could be formed by mechanical alloying for 1 hour at ball to powder weight ratio of 10 : 1.

As shown in Fig. 5, lattice parameters of  $\text{Bi}_2\text{Te}_3$  fabricated by mechanical alloying,  $a = 0.4387 \text{ nm}$  and  $c = 3.0481 \text{ nm}$ , were in excellent agreement with values of  $a = 0.4385 \text{ nm}$  and  $c = 3.0483 \text{ nm}$ , reported for  $\text{Bi}_2\text{Te}_3$  powder made by melting and grinding [9]. Lattice parameters of mechanically alloyed  $\text{Bi}_2\text{Te}_3$  were not changed with ball to powder weight ratio and milling time.

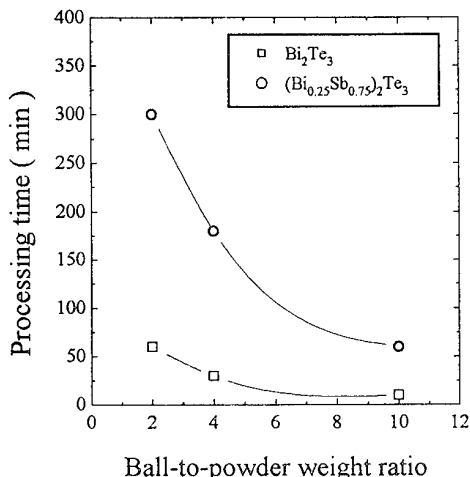


Fig. 4 Processing time for  $\text{Bi}_2\text{Te}_3$  and  $(\text{Bi}_{0.25}\text{Sb}_{0.75})_2\text{Te}_3$  formation with ball to powder weight ratio.

## 2. Thermoelectric properties

Seebeck coefficient, electrical resistivity and thermal conductivity of p-type  $\text{Bi}_{0.5}\text{Sb}_{1.5}\text{Te}_3$  alloys, measured at 300K, are illustrated in Fig. 6, Fig. 7 and Fig. 8, respectively.

Seebeck coefficients of cold pressed  $\text{Bi}_{0.5}\text{Sb}_{1.5}\text{Te}_3$  processed by mechanical alloying and conventionally ground powders were about  $150 \mu\text{V/K}$  before hot pressing, which is almost same as Seebeck coefficient of as-grown ingot of the same composition. Seebeck coefficient of the samples were increased by hot pressing, which indicates reduction of carrier concentration. In p-type  $(\text{Bi},\text{Sb})_2\text{Te}_3$  alloys, carriers are mainly generated by anti-structure defects. Thus, decrease of carrier concentration by hot pressing, shown in Fig. 6, is believed to be related to Te solubility in the matrix at hot pressing temperature. In  $\text{Sb}_2\text{Te}_3$ -rich compositions of  $\text{Bi}_2\text{Te}_3$ - $\text{Sb}_2\text{Te}_3$  pseudo binary system, it has been reported that equilibrium Te solubility decreases with increasing temperature [8]. Possibility of carrier concentration change due to mechanical point defects could be excluded as they could be annealed out at these hot pressing temperatures.

Seebeck coefficient of  $\text{Bi}_{0.5}\text{Sb}_{1.5}\text{Te}_3$  prepared with mechanically alloyed powders are higher than values of samples fabricated with melting and ground powders. It could be suggested that higher defects concentration in mechanically alloyed powders enhanced reduction of anti-structure defects.

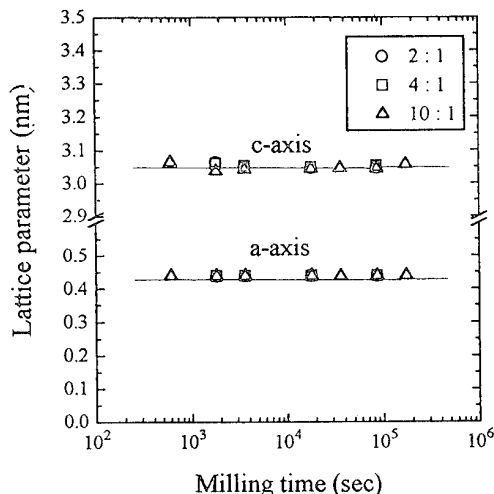


Fig. 5 Lattice parameters of mechanically alloyed  $\text{Bi}_2\text{Te}_3$

Variation of electrical resistivity with hot pressing temperature (Fig. 7) shows the same trend as that of Seebeck coefficient. In spite of high Seebeck coefficient,  $\text{Bi}_{0.5}\text{Sb}_{1.5}\text{Te}_3$  alloys fabricated with both powder processing methods still remain in extrinsic region at room temperature.

Lattice thermal conductivity  $\kappa_{ph}$  of the hot-pressed samples, which was obtained by subtracting  $\kappa_{el}$  from  $\kappa_{tot}$ , is lower than  $\kappa_{ph}$  (about 1 W/m·K)

of the as-grown ingot [9]. As shown in Fig. 10, figure of merit of  $\text{Bi}_{0.5}\text{Sb}_{1.5}\text{Te}_3$  processed with mechanically alloyed powders is a little lower than samples made with ground powders. As carrier concentration seems to be low in mechanically alloyed and hot pressed  $\text{Bi}_{0.5}\text{Sb}_{1.5}\text{Te}_3$  alloys, it is necessary to optimize carrier concentration by adding acceptor impurities to increase figure of merit.

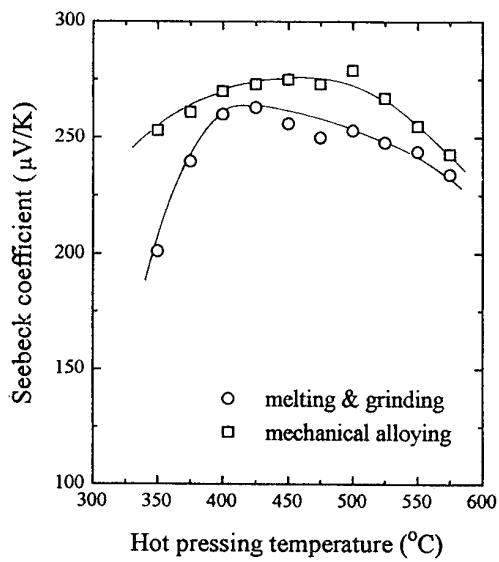


Fig. 6 Seebeck coefficient of  $\text{Bi}_{0.5}\text{Sb}_{1.5}\text{Te}_3$  with hot pressing temperature

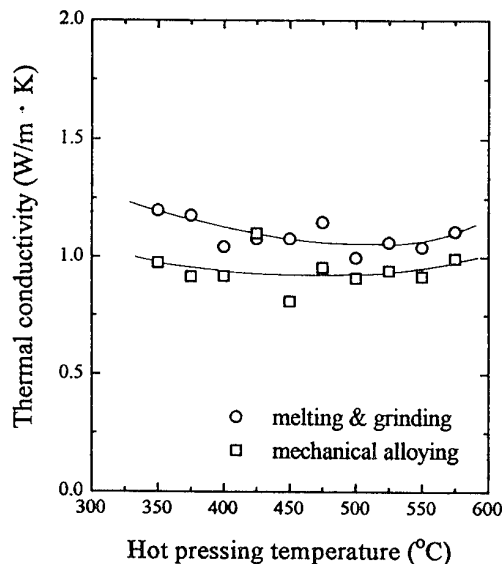


Fig. 8 Thermal conductivity of  $\text{Bi}_{0.5}\text{Sb}_{1.5}\text{Te}_3$  with hot pressing temperature

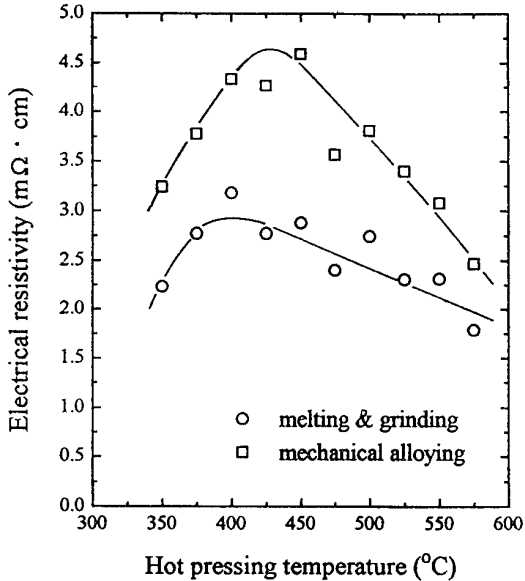


Fig. 7 Electrical resistivity of  $\text{Bi}_{0.5}\text{Sb}_{1.5}\text{Te}_3$  with hot pressing temperature

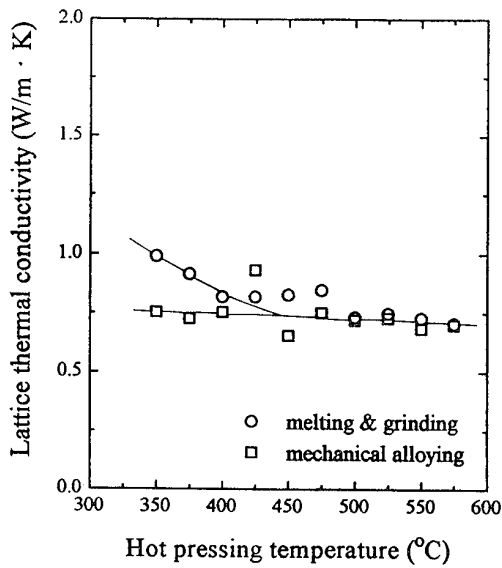


Fig. 9 Lattice thermal conductivity of  $\text{Bi}_{0.5}\text{Sb}_{1.5}\text{Te}_3$  with hot pressing temperature

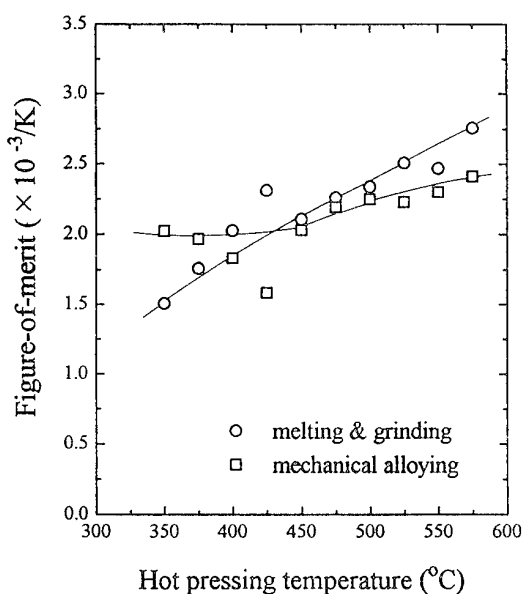


Fig. 10 Figure of merit of  $\text{Bi}_{0.5}\text{Sb}_{1.5}\text{Te}_3$  with hot pressing temperature

### Summary

Processing time for the complete formation of  $(\text{Bi}_{1-x}\text{Sb}_x)_2\text{Te}_3$  by mechanical alloying was increased with increasing Sb content, and was inversely proportional to the ball to powder weight ratio.  $\text{Bi}_2\text{Te}_3$  and  $\text{Bi}_{0.5}\text{Sb}_{1.5}\text{Te}_3$  could be formed by mechanical alloying at ball to powder weight ratio of 10 : 1 for 10 minutes and 1 hour, respectively.

Lattice parameters of  $\text{Bi}_2\text{Te}_3$  fabricated by mechanical alloying,  $a = 0.4387 \text{ nm}$  and  $c = 3.0481 \text{ nm}$ , were not changed with ball to powder weight ratio and milling time.

After cold pressing, Seebeck coefficient of about  $150 \mu\text{V}/\text{K}$  was obtained for both mechanically alloyed and conventionally ground  $\text{Bi}_{0.5}\text{Sb}_{1.5}\text{Te}_3$  powders. After hot pressing, Seebeck coefficient of  $\text{Bi}_{0.5}\text{Sb}_{1.5}\text{Te}_3$  prepared with mechanically alloyed powders are higher than values of  $\text{Bi}_{0.5}\text{Sb}_{1.5}\text{Te}_3$  fabricated with ground powders, due to the enhanced reduction of anti-structure defects in mechanical alloyed powders.

Figure of merit of  $\text{Bi}_{0.5}\text{Sb}_{1.5}\text{Te}_3$ , processed with mechanically alloyed powders, was increased with

increasing hot pressing temperature and was  $2.4 \times 10^{-3}/\text{K}$  when hot pressed at  $575^\circ\text{C}$  for 30 minutes. As carrier concentration seems to be low in mechanically alloyed and hot pressed  $\text{Bi}_{0.5}\text{Sb}_{1.5}\text{Te}_3$  alloys, it is necessary to optimize carrier concentration by adding acceptor impurities to increase figure of merit.

### References

- [1] R. Sundaresan and F. H. Froes, *J. of Metals*, 8, 22 (1987).
- [2] K. Hasezaki, M. Nishimura, M. Umata, H. Tsukuda, and M. Araoaka, Proc. 12th Int'l. Conf. on Thermoelectrics, 307 (1993).
- [3] B. A. Cook, B. J. Beaudry, J. L. Harringa, and W. J. Barnett, Proc. 24th Intersoc. Energy Conversion Eng. Conf., 693 (1989).
- [4] B. A. Cook, B. J. Beaudry, J. L. Harringa, and W. J. Barnett, Proc. 9th Int'l. Conf. on Thermoelectrics, 234 (1990).
- [5] I. Barin : *Thermochemical Data of Pure Substances*, VCH, New York (1989).
- [6] G. R. Miller and C. Y. Li, *J. Phys. Chem. Solids*, 26, 173 (1965).
- [7] JCPDS Card No. 15-863.
- [8] N. Kh. Abrikosov, V. F. Bankina, L. V. Poretskaya, L. E. Shelimova, and E. V. Skudnova, "Semiconducting II-VI, IV-VI, and V-VI Compounds" Plenum Press, New York, p.164 (1969).
- [9] H. P. Ha, Y. W. Cho, J. Y. Byun, and J. D. Shim, Proc. 12th Int'l. Conf. on Thermoelectrics, 105 (1993).

## ORIENTATIONAL DISTRIBUTION IN HOT PRESSED N-TYPE Bi<sub>2</sub>Te<sub>3</sub>

K. Fukuda<sup>1</sup>, H. Imaizumi<sup>1</sup>, T. Ishii<sup>1</sup>, F. Toyoda<sup>2</sup>, M. Yamanashi<sup>2</sup> and Y. Kibayashi<sup>2</sup>

<sup>1</sup>Research Center, KOMATSU Ltd., Hiratsuka 254, Japan

<sup>2</sup>Komatsu Electronics Inc., Hiratsuka 254, Japan

Two dimensional orientation distribution functions of n-type hot pressed (Bi<sub>2</sub>Te<sub>3</sub>)<sub>0.90</sub>(Bi<sub>2</sub>Se<sub>3</sub>)<sub>0.10</sub> were determined by X-ray diffraction. Based on the model for conductivity in uniaxial crystal and the orientation distribution function, the anisotropy of resistivity was calculated for three samples. The figures of merit of hot-pressed samples were successfully estimated.

### Introduction

Bi<sub>2</sub>Te<sub>3</sub> thermoelectric semiconductors show the highest figure of merit (Z) near room temperature. Then they are used as elements of the thermoelectric coolers. The Bi<sub>2</sub>Te<sub>3</sub> alloys were extensively studied. It is well known that the Sb<sub>2</sub>Te<sub>3</sub>-Bi<sub>2</sub>Te<sub>3</sub> and the Bi<sub>2</sub>Te<sub>3</sub>-Bi<sub>2</sub>Se<sub>3</sub> alloys are adequate as p-type and n-type materials respectively [1][2]. Their crystal structures are hexagonal (or rhombohedral) for all composition [3]. The lattice constants of Bi<sub>2</sub>Te<sub>3</sub> are a=4.3835, c=30.487Å at room temperature [4]. The crystal is composed of layers of atoms along the c-axis in a sequence: -Te(1)-Bi-Te(2)-Bi-Te(1)-Te(1)-. Drabble and Goodman [5] have proposed a model for the binding in Bi<sub>2</sub>Te<sub>3</sub>, covalent for the Te(2)-Bi bond, mixed covalent and ionic for the Te(1)-Bi bond and weak van der Waal's for the Te(1)-Te(1) (intermolecular band). Therefore, these compounds are cleaved perpendicular to the c-axis.

These single crystals show uniaxial anisotropy of thermal and electric properties [6][7]. The electrical and thermal conductivity in the direction perpendicular to the c-axis (parallel to the a-axis) are larger than that in the direction parallel to the c-axis. The Seebeck coefficient shows only slight difference in anisotropy [8]. Then the figure of merit in the plane perpendicular to the c-axis (Z<sub>a</sub>) is higher than that in the parallel c-axis (Z<sub>c</sub>). This difference is relatively small for p-type materials but the figure of merit Z<sub>a</sub> is about twice as large as Z<sub>c</sub> in n-type alloys [9]. Traditionally, Bi<sub>2</sub>Te<sub>3</sub> and its alloys for the thermoelectric coolers are produced by the zone melt method or Bridgeman method [10]. Using these methods, crystals are grown along the direction of the a-axis for which direction shows the highest Z (=Z<sub>a</sub>). The elements of thermoelectric coolers are cut in the direction of the current loading is along the growth direction to obtain the highest Z value. However, these melt grown materials tend to crack along their cleavage plane after being diced. For this reason sintered material has been studied.

Sintered Bi<sub>2</sub>Te<sub>3</sub> and its alloys also show anisotropy [11][12][13][14][15]. The resistivity in the pressed direction is greater than that in perpendicular to that direction. The powder's shape of Bi<sub>2</sub>Te<sub>3</sub> and its alloys are flaky because of their cleavage property. When the powder is pressed, its slips along the cleavage planes. Then each powder's c-axis tends to aligns to the pressed direction. Thus, the Z values of sintered materials depend on the distribution of powder orientation[16].

In this work, we estimated the orientational distribution in a hot pressed (Bi<sub>2</sub>Te<sub>3</sub>)<sub>0.90</sub>(Bi<sub>2</sub>Se<sub>3</sub>)<sub>0.10</sub> by X-Ray diffraction. Based on the two dimensional distribution function, we

calculated the anisotropic thermoelectric properties and compared them with observed ones.

### Model

At first, we consider electric and thermal conductivities in the direction with the angle  $\theta$  to the a-axis, in a uniaxial crystal like Bi<sub>2</sub>Te<sub>3</sub>[17]. There are two cases to measure electrical and thermal conductivities. In the first case, the electrical and thermal current density vectors are parallel to the axis of the sample and the electrical and thermal conductivities are measured parallel to the these vectors. This case as shown in Fig.1 would be realized in a long rod sample.

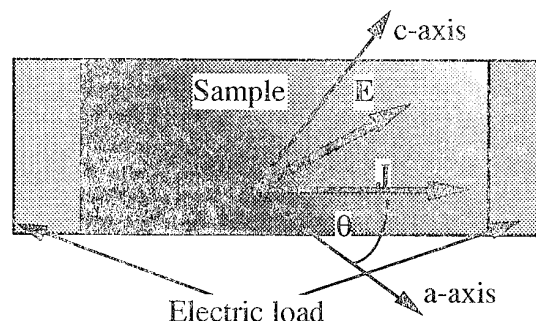


Fig. 1 Current density in a long rod. It makes the angle  $\theta$  with the a-axis of crystal

Fig.1 illustrates the electric current density vectors with the angle  $\theta$  to the a-axis. The electric current vector  $J$  is given by

$$\mathbf{J} = (J \cos \theta, J \sin \theta), \quad (1)$$

where  $J$  is the magnitude of the electric current density vector. The electric resistivity tensor is given by

$$\rho = \begin{pmatrix} \rho_a & 0 \\ 0 & \rho_c \end{pmatrix} \quad (2)$$

where  $\rho_a$  is the electric resistivity parallel to the a-axis and  $\rho_c$  is the resistivity parallel to the c-axis. The electric field vector  $E$  and electric resistivity  $\rho(\theta)$  with the angle  $\theta$  to the a-axis are given by

$$E = \rho \cdot J \quad (3)$$

and

$$\rho(\theta) = J \cdot E / J^2. \quad (4)$$

Then we obtain  $\rho(\theta)$  as follows;

$$\rho(\theta) = \rho_a \cos^2 \theta + \rho_c \sin^2 \theta \quad (5)$$

and the electrical conductivity is defined by

$$\sigma(\theta) = 1/\rho(\theta). \quad (6)$$

The thermal conductivity is obtained similarly.

In the second case, the electrical and thermal gradient vectors are parallel to the axis in the sample. The electrical and thermal conductivities are measured parallel to the these vectors. This case is shown in Fig. 2, and would be realized as a thin disk sample.

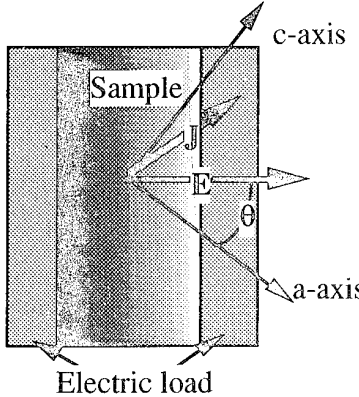


Fig. 2 Current density in a thin disk sample

When the electric field vector creates the angle  $\theta$  to the a-axis, the electric current vector  $E$  is given by

$$E = (E \cos \theta, E \sin \theta). \quad (7)$$

Using  $E$  and the electric conductivity tensor  $\sigma$  given by

$$\sigma = \begin{pmatrix} \sigma_a & 0 \\ 0 & \sigma_c \end{pmatrix}, \quad (8)$$

we obtained the electric conductivity as follows;

$$\sigma(\theta) = \sigma_a \cos^2 \theta + \sigma_c \sin^2 \theta. \quad (9)$$

In the present study, we prepared near the rod shape sample, so that we adopt the first case. There is sufficiently a large difference between two cases, when  $\theta$  is near  $\pi/4$  [17]. In the rod shape sample model the normalized electric resistivity  $\rho(\theta)$  and thermal resistivity  $r(\theta)$  are given respectively by

$$\rho(\theta)/\rho_a = \cos^2 \theta + \rho_c/\rho_a \sin^2 \theta \quad (10)$$

and

$$r(\theta)/r_a = \cos^2 \theta + r_c/r_a \sin^2 \theta \quad (11)$$

where  $r_c$  is thermal resistivity parallel to the c-axis and  $r_a$  is resistivity parallel to the a-axis.

In sintering materials, the crystal grains orient with the orientation distribution function including random distribution (constant). The two dimensional orientation distribution function  $\omega(\theta)$  is defined by how many crystal grains are oriented to the direction with angle  $\theta$  which is made by their cleavage plane in the hot pressed ingot and the plane perpendicular to the pressed direction. If the electric current is loaded in the direction perpendicular to the press direction, the

normalized electric resistivity of the  $\theta$ -orienting grain is shown as Eq.10. The electric resistance in a hot pressed material is regarded as a series of each grain's resistance, which are defined in each orientation angle  $\theta$ . Then using the orientation distribution function  $\omega(\theta)$  which is defined the probability of the existence of the  $\theta$ -oriented grain and considering symmetry, the electric resistivity in the direction perpendicular to the pressed direction  $\rho_A$  is normalized by  $\rho_a$  and given as

$$\begin{aligned} \rho_A / \rho_a &= \frac{1}{\rho_a} \int_0^{\pi/2} \rho(\theta) \omega(\theta) d\theta \\ &= \int_0^{\pi/2} (\cos^2 \theta + \rho_c / \rho_a \sin^2 \theta) \omega(\theta) d\theta \end{aligned} \quad (12)$$

and the normalized electric resistance in the direction parallel to the pressed direction  $\rho_C$  is given as

$$\begin{aligned} \rho_C / \rho_a &= \frac{1}{\rho_a} \int_0^{\pi/2} \rho(\theta) \omega(\pi/2 - \theta) d\theta \\ &= \int_0^{\pi/2} (\rho_c / \rho_a \cos^2 \theta + \sin^2 \theta) \omega(\theta) d\theta \end{aligned} \quad (13)$$

where  $\omega(\theta)$  is normalized for integration from 0 to  $\pi/2$ ;

$$1 = \int_0^{\pi/2} \omega(\theta) d\theta. \quad (14)$$

Notation A indicates the direction perpendicular to the pressed direction and notation C indicates the direction parallel to the pressed direction. With thermal resistivity, we can obtain this by changing a suffix from "ρ" to "r".

### Experimental Sample preparation

High purity components with grade of 99.999% were weighed with the ratio of stoichiometry of  $(\text{Bi}_2\text{Te}_3)_{0.90}(\text{Bi}_2\text{Se}_3)_{0.10}$  and encapsulated in an evacuated Pyrex tube with 0.3 atom argon gas. Before encapsulating,  $\text{HgCl}_2$  was added. The component elements and dopant in the Pyrex tube were heated to above the melting point. The melt in the tube was stirred sufficiently, rocking the furnace. By the vertical Briggeman method, the melt was solidified to the direction of thermal gradient. Using that method, the polycrystal's c-plane is almost oriented to the direction of thermal gradient. The solidified ingot was ground into a powder in a ceramic mortar and pestle into the grain size between 200 and 400 mesh (74 micron and 37 micron). This powder was annealed at 620K for 10 hours in reducing atmosphere of hydrogen gas. Hot pressing was accomplished at approximately 770K under the pressure of  $400\text{Kg/cm}^2$  argon atmosphere. The size of ingot size was  $40 \times 40 \times 20\text{mm}$ .

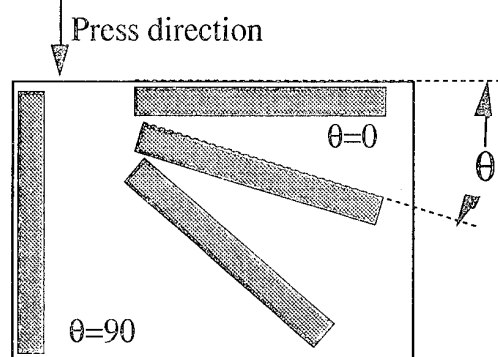


Fig. 3 Test pieces cut from hot pressed ingot

### X-ray Measurement

As for X-ray measurements, we referred to Ohsugi et.al[13]. Test pieces were cut from hot pressed ingots with tilting angle  $\theta$  as shown Fig. 3. Ohsugi cut the test piece tilting by 40 degrees, but we cut the test pieces with a dozen tilting angle from 0 to 90 degrees. The size of test piece size was 25 x 7.5 x 1 mm. Each test piece was set in the X-ray diffractometer holder ( CuK $\alpha$  radiation, 50KV and 150mA). Fig. 4 and 5 shows XRD patterns of the hot pressed sample cut with tilted 0 degree and 90 degrees (perpendicular press direction and parallel press direction) at room temperature. Reflections such as (0,0,3), (0,0,6) and (0,0,15) were observed in the 0-degree sample very well, but their intensities became very weak in the 90-degree sample. This means that c-axis of the grain in the hot pressed ingot oriented to the pressed direction more than perpendicular press direction. But reflections of the c-planes could be observed even in the 90-degree sample.

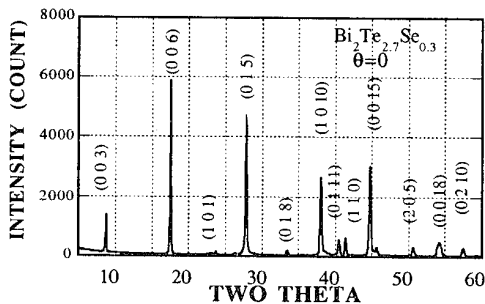


Fig 4 XRD pattern of the hot pressed sample tilted 0 degree

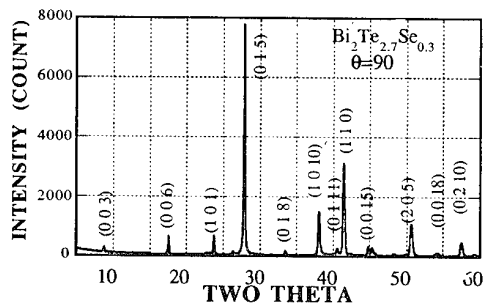


Fig. 5 XRD pattern of the hot pressed sample tilted 90 degree

We measured integral intensities of the Bragg reflection (0,0,6) of several pieces tilted angles from 0 to 90 degrees without intensity correction.

### Results and discussion

Fig 6 is the results of corrected normalized integral intensities of (0,0,6) and (0,0,3) Bragg reflections in a sample. Both results show cleavage planes tend to orient the perpendicular to the pressed direction. There is not a significant difference between two results. This means that integral intensities are calculated almost precisely. Slight difference in high  $\theta$  intensities between them is caused by weak intensities of (0,0,3) which can't be sufficiently counted by their intensities in the high  $\theta$ -degree test pieces. Although this difference is not significant, hot press ingot size was not enough to cut uniform test pieces for X-ray measurement , so measurement includes error related to the difference of in the orientational distribution in part of the ingot.

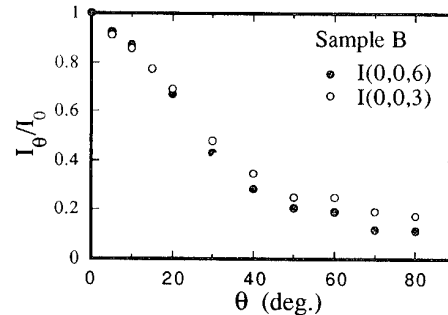


Fig 6 Relative integral intensity of (0,0,6) and (0,0,3) in the tilted test pieces of sample B

We measured the integral intensities of the (0,0,6) reflection of the tilting piece about three hot press ingot. These ingots were made of the same melts and the same batch of powder, and the hot pressed with the same condition. But samples B and C were annealed at 670 K and 830K respectively, and both of them were annealed for 40hours. Annealed ingots were made in order to measure different types of orientation distribution functions.

The samples: Seebeck coefficients, electrical resistivities, anisotropies of resistivities and density ratio are summarized in Table 1 . The Seebeck coefficient shows different values in each sample. The Seebeck coefficient is almost isotropic, but in sample A, the anisotropy arises slightly. The Seebeck coefficients in sample A show the highest value of the three samples. This means that the major carrier density in sample A is the smallest in the three samples , and thermally excited minority carriers influenced the Seebeck coefficients slightly at room temperature [8].

Table 1 Thermoelectric property of three hot pressed samples.

Sample	Anneal condition	$\alpha A(\mu V/\text{deg})$	$\alpha C(\mu V/\text{deg})$	$\rho A(\mu \Omega \text{cm})$	$\rho C(\mu \Omega \text{cm})$	$\rho C/\rho A$	Density ratio(%)
A	Non	199	197	1200	2040	1.70	99.9
B	670Kx48H	193	193	1100	2040	1.85	99.9
C	830Kx48H	198	198	1491	1716	1.15	91.3

Resistivity also shows a different value. This difference is caused by the difference in the carrier density of each samples as shown in the Seebeck coefficients. But the difference in the anisotropies  $\rho_C/\rho_A$  is not caused by the difference in the carrier density of each samples. The anisotropies of resistivity depend only on the orientation distribution function in the hot pressed ingot. This is because the anisotropy of resistivity in a single crystal doesn't depend on the carrier's density in the extrinsic range near the border of the intrinsic range [9].

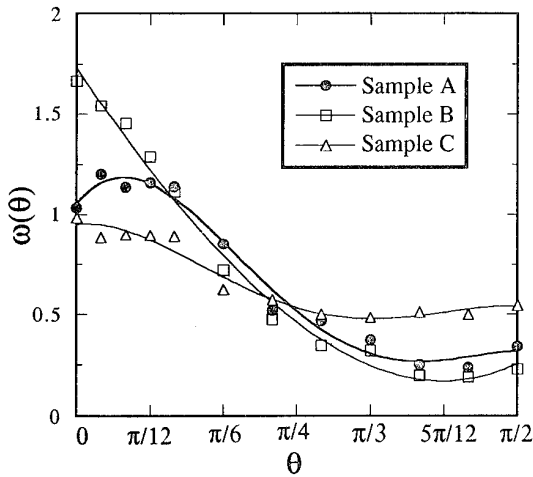


Fig. 7 Two dimensional orientation functions which were obtained by the X-ray measurement

Two dimensional distribution functions  $\omega(\theta)$  of three samples obtained by X-ray measurement are shown in Fig.7.. The results (plot in Fig.7) can't be fitted to adequate function like a Gaussian function [12][18]. Therefore, we fit them in polynomial functions and regard the functions as  $\omega(\theta)$  (line in Fig. 7). We assume that the ratio of anisotropy of electric resistivity  $\rho_C/\rho_A$  in the single crystal is 4 [9][17], and then calculate the normalized resistivities of both direction using Eq.12, 13 and the obtained  $\omega(\theta)$ . The anisotropy of electric resistivity  $\rho_A/\rho_C$  in each hot pressed sample is then obtained. The calculated results and measured results are shown in Table 2. The calculated results are good agreement with the observed ones. We could not confirm that sample B is more oriented than sample A by annealing. But it is sure that sample C was re-crystallized.

Table 2. Anisotropies of resistivity

Sample	Calculation	Measurement
A	1.59	1.70
B	1.85	1.85
C	1.22	1.15

By assuming that the anisotropy of thermal resistivity  $r_C/r_A$  in the single crystal is 2 [9][17] ,we can calculate the normalized thermal conductivity of all samples in order to estimate the figure of merit ZA along the A-direction of the hot pressed sample. The figure of merit Z is proportional to the ratio of  $r/\rho (= \sigma/\kappa)$  , if the Seebeck coefficient is constant.

Then the ratio of the normalized electrical resistivity  $\rho_A/\rho_A$  and thermal resistivity  $r_A/r_A$  give ZA/Za as shown in Table 3. The calculated result of a perfectly random sample is also shown and this doesn't have the same result as obtained by using three dimensional orientation distribution function [14][16][17]. Our results show the figure of merit is remarkably reduced by random orientation . Even in sample B, which marks the highest ZA/Za, the figure of merit is reduced by 29% compared with the single crystal. This discussion may be not practical. The phonon's thermal conductivity depends on the grain size [19] and it is reduced in a sintered material. We didn't take into account such effects in this discussion. But in the first approximation it could be stated that an orientational distribution of grains determines the performance of a sintered material.

Table 3 Calculation results of normalized Z-value

Sample	$\rho_A/\rho_A$	$r_A/r_A$	ZA/Za
A	1.93	1.31	0.67
B	1.75	1.25	0.71
C	2.25	1.41	0.62
Random	2.50	2.50	0.60

Finally, we assume that the two dimensional orientation distribution function is Gaussian.  $\omega(\theta)$  is given by

$$\omega(\theta)=N \exp(-\theta^2/d^2) \quad (15)$$

where N is the normalization factor and d is the distribution width. Fig.8 shows the distribution of sample B. The d-value of sample B is between 40 and 50 degrees. This results is almost the same in Ohsugi's work [13] .

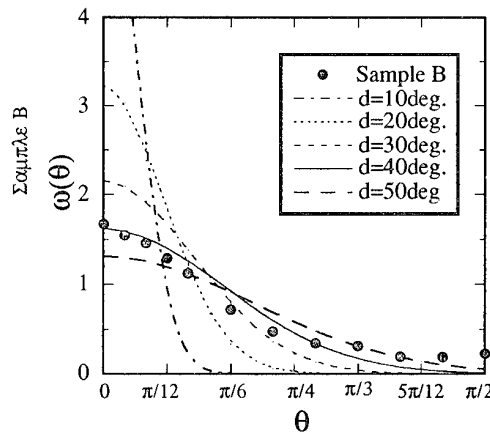


Fig.8 The Gaussian oriented distribution functions and d is the standard deviation.

We also calculated ZA/Za for these Gaussian orientation distribution functions (Fig.10). The narrow distribution width gives a high Z. And this result shows us how much we must improve the orientation to get a high Z. We believe that it can improve to d=30 degrees.

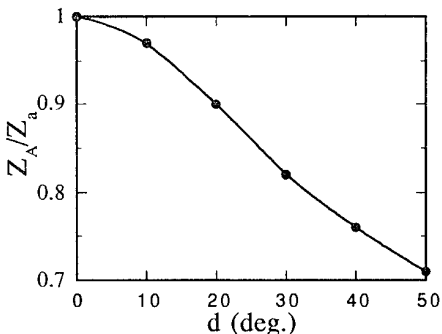


Fig. 9 The relation ship between the standard deviation d and the figure of merit Z in sintered  $\text{Bi}_2\text{Te}_3$

### Conclusion

Based on the two dimensional orientation distribution function, the calculated results of the anisotropy in the hot pressed  $(\text{Bi}_2\text{Te}_3)_{0.90}(\text{Bi}_2\text{Se}_3)_{0.10}$  alloy showed good agreement with the experimental results. In the first approximation, the orientation distribution determines the performance of the sintered materials. In our sample we discussed that the figure of merit decreased about 30% compared with those of the single crystal. Considering the relationship between Z and the distribution width, it seems to be possible to improve Z by 10%.

### Acknowledgments

We would like to express appreciation to Prof. A. Onodera and I. Ohsugi for many helpful discussions. We also would like to thank to N. Tamaki, T. Hironiwa, K. Hara, T. Nakajima , A .Karita and M .Hamada for measurement and preparation sample.

### References

- [1]. G.V.Kokosh and S.Sinani, Thermoelectric Properties of Alloys of The Pseudobainary System  $\text{Sb}_2\text{Te}_3\text{-}\text{Bi}_2\text{Te}_3$ , *Sov. Phys. Solid State*, 1960, v.13, No.8, pp.1012-1018.
- [2]. G.R.Miller, C.-Y. Li, and C.W.Spencer, Property of  $\text{Bi}_2\text{Te}_3\text{-}\text{Bi}_2\text{Se}_3$  Alloys, *J. Appl. Phys.*, 1963, v.34, No.5, pp.1398-1400.
- [3]. J.R.Wiese and L.Muldawer, Lattice Constants of  $\text{Bi}_2\text{Te}_3\text{-}\text{Bi}_2\text{Se}_3$  Solid Solution, *J. Phys. Chem. Solids*, 1960, v.15, pp.13-16.
- [4]. R.W.G.Wyckoff, *Crystal Structure*. Vol. 2. 1964, New York: Interscience Publisher.
- [5]. J.R.Drabble, Chemical Bonding in Bismuth Telluride, *J. Phys. Chem. Solids*, 1958, v.5, pp.142-144.
- [6]. J.R.Drabble, Galvanomagnetic Effects in p-Type Bismuth Telluride. *Proc. Phy. Soc. London*, London, 1958. pp. 380.
- [7]. J.R.Drabble, R.D.Groves, and R.Wolf. Galvanomagnetic Effects in n-Type Bismuth Telluride. *Proc. Phy. Soc. London*, London, 1958. pp. 430.
- [8]. Kaibe, et al. Anisotropy in the Galvanomagnetism and Thermoelectricity of P- and N-Type  $\text{Bi}_{2.85}\text{Se}_{0.15}$  Single Crystals. *Proc. 8th International Conference on Thermoelectric Energy Conversion*, Nancy France, 1989. pp. 195-199.
- [9]. H.J.Goldsmid, Recent Studies of Bismuth Telluride and its Alloys, *J. Appl. Phys.*, 1961, v.32, No.10, pp.2198-2202.
- [10]. C.B.Satterthwaite and J. R.W.Ure, Electrical and Thermal Properties of  $\text{Bi}_2\text{Te}_3$ , *Physical Review*, 1957, v.108, No.5, pp.1164-1170.
- [11]. H.Imaizumi, et al. Thermolectric Properties N-Type  $\text{Bi}_2(\text{Te},\text{Se})_3$  by Hot-Pressing. *Proc. 7th International Conference on Thermoelectric Energy Conversion*, Arington USA, 1988. pp. 141-145.
- [12]. I.J.Ohsugi, et al. Analysis of The Anisotropic Resistivites and Hall Coefficients of Sintered, N-type  $\text{Bi}_2\text{Te}_3$ . *Proc. 8th International Conference on Thermoelectric Energy Conversion*, Nancy France, 1989. pp. 32-34.
- [13]. I.J.Ohsugi, et al., Evaluation of Anisotropic Thermoelectricity of Sintered  $\text{Bi}_2\text{Te}_3$  on the Basis of the Orientation Distribution of Crystallites, *J. Appl. Phys.*, 1994, v.76, No.4, pp.2235-2239.
- [14]. H.J.Goldsmid and M.Situmorang. Sintered Bismuth Telluride Alloys-Problems of Orientation. *Proc. 8th International Conference on Thermoelectric Energy Conversion*, Nancy France, 1989. pp. 1-6.
- [15]. R.Griot, G.Brun, and J.C.Tednac. Orientation Effects in Sintered Thermoelectric Material. *Proc. 8th International Conference on Thermoelectric Energy Conversion*, Nancy , France, 1989. pp. 27-31.
- [16]. A.W.Penn, The Thermoelectric Propreties of N-Type Single Crystals of Bismuth Seleno-Telluride and thier Relationship those of Pressed Powder Compacts, *Advanced Energy Conversion*, 1968, v.7, pp.257-264.
- [17]. J.H.Madigan, Dependance of the Thermoelectric Figure of Merit on the Orientation in Uxial Crystals, *J. Appl. Phys.*, 1962, v.33, No.12, pp.3564-3567.
- [18]. I.J.Ohsugi, T.Kojima, and I.A.Nishida, Orientation Analysis of the Anisotropic Galvanomagnetism of Sintered  $\text{Bi}_2\text{Te}_3$ , *J. Appl. Phys.*, 1990, v.68, No.11, pp.5692-5695.
- [19]. D.M.Rowe and V.S.Shukla, The Effects of Grain Boundary of Phonon-Grain Boundary Phonon on the Latice Thermal Conductivity and Thermoelectric Conversion Efficiency of Heavily Doped Fine Grained Silicon-Germanium Alloys, *J. Appl. Phys.*, 1981, v.52, No.150, pp.7421-7426.

## A NEW-TYPE THERMOELECTRIC MODULE COMPOSED OF HAMBURGER-TYPE ELEMENTS

Y. Tanji,<sup>1</sup> Y. Nakagawa,<sup>2</sup> T. Kaneko,<sup>3</sup> H. Ido,<sup>4</sup>  
M. Kuboki,<sup>4</sup> M. Kogo,<sup>1</sup> T. Masumoto,<sup>3</sup> R. Sato,<sup>4</sup>

1. *R & D Division, Tohoku Technobrains Corporation, Sendai, Japan, 982.*
2. *Faculty of Engineering, Tohoku Institute of Technology, Sendai, Japan, 982.*
3. *Institute for Materials Research, Tohoku University, Sendai, Japan, 980.*
4. *Faculty of Engineering, Tohoku Gakuin University, Tagajo, Japan, 985.*

Three kinds of thermoelectric elements of hamburger-type are devised. Using the 'single-burger' element, a new-type thermoelectric module is designed. The module is assembled by screwing the elements with metal segments. Using the 8 modules, a laminated-type subunit for the thermo-electric generator is manufactured as a trial.

### INTRODUCTION

Studies on thermoelectric materials and generator/cooler systems have been carried out by many investigators from old times [1]-[3]. However, the fundamental structure of thermoelectric modules has scarcely been changed since Ioffe's work in 1950, and most studies are based on the conventional modules. The present work deals with the development of a new-type module. A role of the present work may be located in the field of technical research on the structure of module, as illustrated in Fig. 1.

Previously, we have pointed out that the conventional modules, composed of many thermocouples with  $\pi$ -type structure, have a serious defect with respect to thermal

shear stress [4, 5]. If this defect can be removed, the lifetime of the modules will be much more prolonged, so that the demand of the thermoelectric modules will be increased remarkably. And we have proposed two kinds of thermoelectric generators of laminated type which can well bear the thermal shear stress, although these generators have not yet been completed. Recently, we have designed three kinds of thermoelectric hamburger-type elements of the generator/cooler, which are named the 'single-burger', 'double-burger' and 'twin-burger' [8]. A new-type module composed of the 'single-burger' elements is reported in the present paper together with a subunit of the generator using this module. The 'double-burger' and 'twin-burger' elements can be applied in the fundamental design of the thermoelectric modules for the following purposes: the 'double-burger' may be used for increasing the efficiency of thermoelectric conversion covering a wide temperature range, and the 'twin-burger' elements for producing the modules of small size.

### THERMOELECTRIC MATERIALS

We use the single crystal-like materials for the 'single-burger' elements. The ingot with the large columnar grains of  $\text{Bi}_{1.8}\text{Sb}_{0.2}\text{Te}_{2.85}\text{Se}_{0.15} + 0.09$  wt%  $\text{HgBr}_2$  (p-type) or  $\text{Bi}_{0.5}\text{Sb}_{1.5}\text{Te}_{2.85}\text{Se}_{0.15} + 1.75$  wt% Se (n-type) was prepared by the Bridgman method using a crucible of special type reported previously [4]. The size of the ingot is about 1 cm in

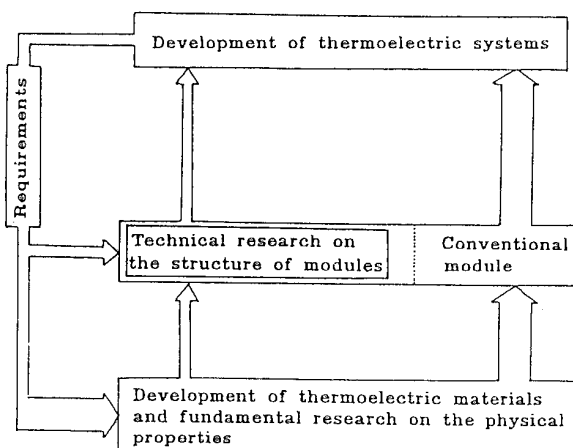


FIGURE 1. Role of the present work in the research on thermoelectricity.

diameter and 10 cm in length. The samples for chemical analysis were collected from upper and middle parts of the ingots of p- and n-type. The results of chemical analysis are shown in Table 1 together with the nominal concentration. The concentration of the upper part shows remarkable deviation from the nominal concentration. So, the upper and lower parts (1 cm in length) of the ingots were not used. From the middle part of 9 ingots of p- and n-type, 200 disks of 0.2 cm in thickness were obtained. The plane of the disk is nearly perpendicular to the cleavage plane (c-plane). Also from the middle part of the ingots of p- and n-type, small single crystal specimens for

the measurement of thermoelectric properties were cut out. The specimens are rectangular bars with planes perpendicular and parallel to the cleavage plane. The size of the specimens is listed in Table 2 together with the form factor  $A$  ( $=$  thickness  $L$  / cross sectional area  $S$ ) for the two modes of the measurement (perpendicular  $\parallel$  and parallel  $\perp$  to the cleavage plane). The thermoelectric properties were measured by a simple Peltier technique [5] based on the Harman method [6, 7]. Only the final results are shown in Table 3; the details will be reported elsewhere.

TABLE 1. Nominal concentration and chemical analysis of specimens.

Specimens	Elements		Bi	Sb	Te	Se	Hg	Br
	Nominal concentration (wt%)		15.50	27.09	53.94	3.48		
$\text{Bi}_{0.5}\text{Sb}_{1.5}\text{Te}_{2.85}\text{Se}_{0.05}$ + 0.75 wt% Se (p-type)	Chemical analysis (wt%)	upper part middle part	13.27 14.88	19.14 28.88	64.45 52.53	3.14 3.71		
	Nominal concentration (wt%)		48.43	3.14	46.81	1.53	0.05	0.05
$\text{Bi}_{1.8}\text{Sb}_{0.2}\text{Te}_{2.85}\text{Se}_{0.05}$ + 0.09 wt% $\text{HgBr}_2$ (n-type)	Chemical analysis (wt%)	upper part middle part	48.58 48.88	1.85 3.07	48.63 45.98	0.95 2.06	Non Non	Non Non

TABLE 2. Size of rectangular specimens and form factors  $A$  ( $= L/S$ ) ( $L$ : length,  $S$ : cross sectional area).  
 $\perp$ : perpendicular to the c axis;  $\parallel$ : parallel to the c axis.

Specimen	Size cm	Mode	$L$ cm	$S$ cm <sup>2</sup>	$A$ cm <sup>-1</sup>
$\text{Bi}_{0.5}\text{Sb}_{1.5}\text{Te}_{2.85}\text{Se}_{0.05}$ + 0.75 wt% Se (p-type)	0.5428 $\times$ 0.5118 $\times$ 0.2271	$\perp$ $\parallel$	0.2271 0.5428	0.2778 0.1162	0.817 4.671
$\text{Bi}_{1.8}\text{Sb}_{0.2}\text{Te}_{2.85}\text{Se}_{0.05}$ + 0.09 wt% $\text{HgBr}_2$ (n-type)	0.5444 $\times$ 0.2273 $\times$ 5154	$\perp$ $\parallel$	0.5154 0.5444	0.1237 0.1172	4.167 4.645

TABLE 3 Thermoelectric properties of single crystals of  $(\text{Bi}, \text{Sb})_2(\text{Te}, \text{Se})_3$  compounds of p- and n-type.

Specimens	Mode	$\rho \times 10^3$ $\Omega \text{cm}$	$\alpha$ $\mu \text{VK}^{-1}$	$\kappa \times 10^2$ $\text{Wcm}^{-1}\text{K}^{-1}$	$Z \times 10^3$ $\text{K}^{-1}$
$\text{Bi}_{0.5}\text{Sb}_{1.5}\text{Te}_{2.85}\text{Se}_{0.05}$ + 0.75 wt% Se (p-type)	$\perp$ $\parallel$	1.34 8.30	233 236	1.29 0.36	3.14 1.86
$\text{Bi}_{1.8}\text{Sb}_{0.2}\text{Te}_{2.85}\text{Se}_{0.05}$ + 0.09 wt% $\text{HgBr}_2$ (n-type)	$\perp$ $\parallel$	0.91 3.38	-241 -194	2.00 1.29	3.19 0.86

## SINGLE-BURGER ELEMENTS AND MODULE

Fig. 2(a) shows the 'single-burger' element, in which a disk of thermoelectric materials is sandwiched between two copper blocks having screw holes at the center. The element disk is soldered with the copper blocks. Fig. 2(b) shows the connection of the 'single-burger' elements and metal segments using screws. The p- and n-type elements were connected alternately. Fig. 2(c) shows a new-type module for thermoelectric generator of laminated type, which is composed of 25 'single-burger' elements of p- and n-type.

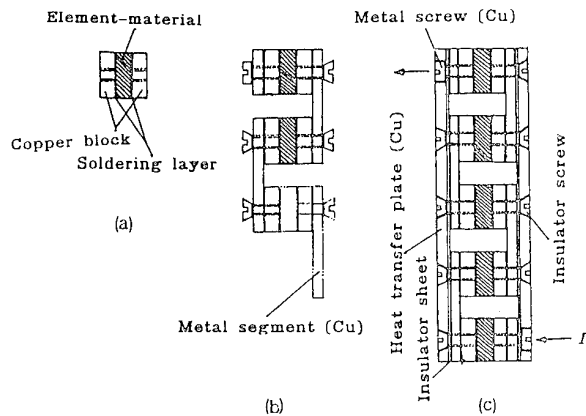


FIGURE 2. (a) 'Single-burger' element (thermoelectric disk sandwiched between two copper blocks with screw holes at the center). (b) Connection of the single-burger elements using screws. (c) Cross section of a module composed of the 25 single-burger elements.

Fig. 3 shows a photograph of the new-type module using the 'single-burger' elements. The elements are connected electrically in series and thermally in parallel. Although this module has the  $\pi$ -structure similar to the conventional modules, the connection method is different; the use of screws in the present module enables us to connect the elements quite easily. The 'single-burger' elements are screwed with the metal segments and the metal segments can be screwed with the heat transfer plates. In order to reduce the contact resistance, InGa-paste is spread between the 'single-burger' elements and the metal segments. Electric current flows across two terminal screws in the module. These screws are metallic and named the electrode screws. Other screws are made

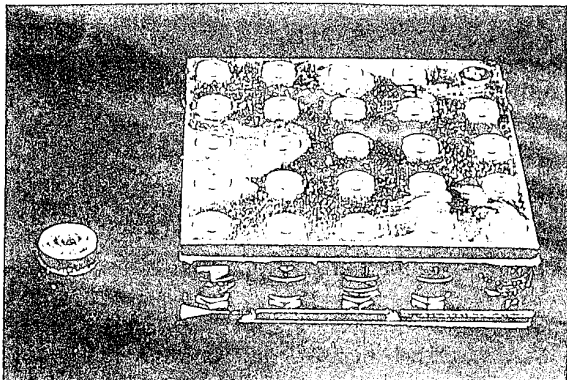


FIGURE 3. A photograph of single-burger element and new-type module composed of the element.

from acrylic resin in order to make electric insulation between the heat transfer plate and the metal segment. The element disks may be cleaved along the c-plane which is perpendicular to the disk plane. Even if the element disks are cleaved, however, the cleavage does not give a fatal failure for the thermoelectric properties of the modules, because the electric current is not disturbed by this cleavage. It should be also mentioned that the destroyed elements can easily be replaced because of the connection with the screws. And also, the assembly of the present modules is much easier than that of the conventional modules. This may be especially important for the mass production of thermoelectric generators/coolers.

## LAMINATED-TYPE SUBUNIT OF THERMOELECTRIC GENERATOR

Fig. 4 shows a laminated-type subunit of the thermoelectric generator, assembled by the 8 modules and 16 hot/cold heat transfer tubes. The design of this subunit is similar to that of the subunit using composite elements reported previously [4]. The hot/cold heat transfer tubes are connected in parallel through vinyl pipes to main pipes for hot/cold water flow. The heat transfer tubes and the modules are sandwiched between two electrode plates and pressed uniformly using screws. InGa-paste is spread for keeping electric and thermal connections between the heat transfer tubes and the heat transfer plates. The modules are connected electrically to the heat transfer tubes through the electrode screws.

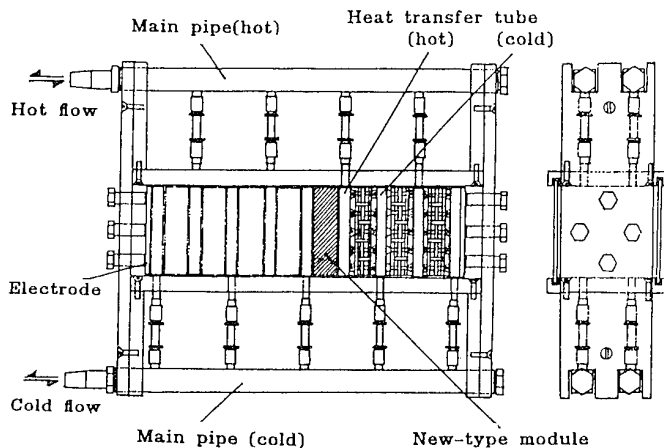


Fig. 4 A subunit of thermoelectric generator composed of the 8 modules.

#### CHARACTERISTICS OF SUBUNIT

When a load with resistance  $R_L$  is connected with the subunit with resistance  $R_{TEG}$ , we obtained the current  $I$ , the potential drop  $E_L$  and the power  $P$  consumed in the load as a function of the resistance ratio  $m$  ( $= R_L / R_{TEG}$ ). It is well known that  $P (= E_L I)$  is maximum at  $m = 1$ . The electromotive force in the circuit is expressed as  $n\alpha \Delta \theta_{TEG}$ , where  $n$  is the number of thermoelectric elements in the subunit,  $\alpha$  the Seebeck coefficient of element materials and  $\Delta \theta_{TEG}$  the temperature difference between hot and cold ends of the elements. The resistance  $R_{TEG}$  is given by  $n\rho L/S$ , where  $\rho$  is the resistivity of the element materials,  $L$  the length and  $S$  the cross sectional area of the elements, provided that the resistance of copper blocks, metal segments etc and all the contact resistance can be ignored. In the present subunit,  $n = 200$ ,  $L = 0.250$  cm and  $S = 0.785$   $\text{cm}^2$  (1 cm in diameter);  $\alpha$  and  $\rho$  are assumed to be given by average values for p- and n-type elements with the  $\perp$  mode listed in Table 3, i.e.  $\alpha = 237 \mu \text{V/K}$  and  $\rho = 1.13 \times 10^{-3} \Omega \text{cm}$ . Fig. 5 shows calculated values of  $P$  and  $E_L$  vs.  $m$  for  $\Delta \theta_{TEG} = 10, 30, 50$  and  $70$  K. As can be seen from the figure, the maximum power at  $\Delta \theta_{TEG} = 50$  K amounts to  $19.6$  W with  $I = 16.5$  A and  $E_L = 1.19$  V.

It is inevitable that the value of  $\Delta \theta_{TEG}$  is smaller than the temperature difference  $\Delta \theta (= \theta_H - \theta_C)$  between hot and cold water flows because of thermal resistance in the subunit. In order to

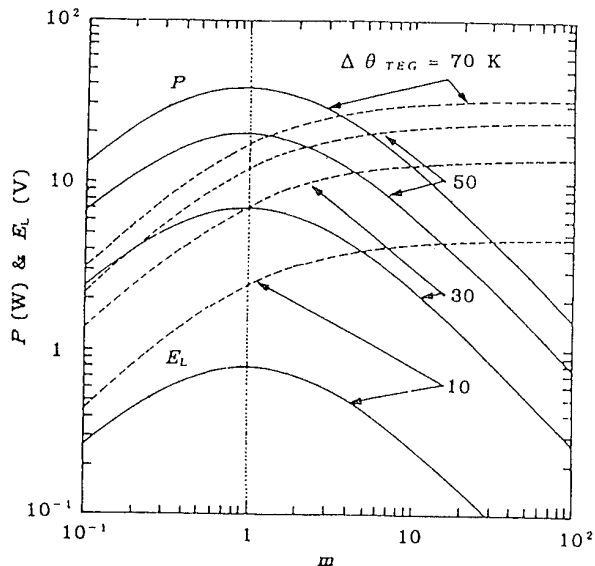


FIGURE 5. Calculated curves for the electric power  $P$  and load potential  $E_L$  vs. the resistance ratio  $m$  with temperature differences  $\Delta \theta_{TEG} = 10, 30, 50, 70$  K for the subunit of thermoelectric generator.

research this effect we measured the temperature distribution in the module; an example of the results is shown in Fig. 6. When the temperatures of hot and cold water flows were  $56^\circ\text{C}$  and  $2^\circ\text{C}$ , respectively, the experimental values of  $\Delta \theta_{TEG}$  amounted to only  $17$  K, which was less than half of  $\Delta \theta$ . For making a further improvement of the thermal conduction to obtain a larger value of  $\Delta \theta_{TEG}$ , we must develop a new-type of heat transfer structure, such as the heat transfer tube with inside fin.

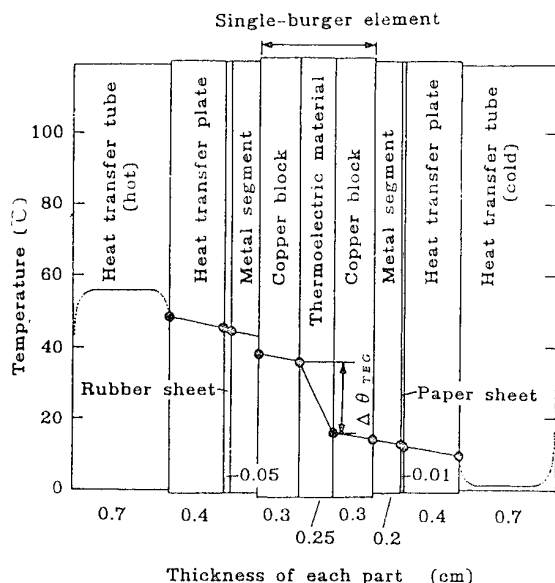


FIGURE 6. An example of temperature distribution in the thermoelectric module.

#### SUMMARY

We could solve the problem of thermal shear stress in thermoelectric elements by using the new-type module composed of the 'single-burger' elements, which are easily assembled by screwing.

A subunit of thermoelectric generator composed of the 8 modules is expected to generate the maximum electric power of 19.6 W with the current of 16.5 A and the voltage of 1.19 V at the temperature difference of 50 K.

Finally the present authors wish to thank Mr. A. Mori in R & D Division, Tokin Co., for assistance of experiments, and to Mr. T. Yoshida in Tohoku Mechanical Engineering Co., for manufacturing the thermoelectric modules and the subunit as a trial.

#### REFERENCES

- [1]. I. Φ . Ioffe: Thermoelement (translated into Japanese). (Nikkan Kogyo Newspaper Company, 1962).
- [2]. I. B. Cadof and E. Miller: Thermoelectric Materials and Devices (Reinhold Publishing Co., New York, 1960).

[3] K. Uemura and I. Nishida: Thermoelectric Semiconductor and Its Application (Nikkan Kogyo Newspaper Company, 1988).

[4] Y. Tanji, Y. Nakagawa, T. Kaneko, H. Ido, M. Kuboki, M. Kogo, T. Masumoto and R. Sato: Proceeding of 12th ICT, (1993), P. 452-457.

[5] Y. Tanji, Y. Nakagawa, T. Kaneko, H. Ido, M. Kuboki, M. Kogo, T. Masumoto and R. Sato: Proceeding of 13th ICT, (1994), P. 334-338.

[6] A. C. Harman, J. H. Cahn and M. J. Logan: *J. App. Phys.*, 30 (1959), 1351-1359.

[7] D. M. Rowe and C. M. Bhander: *Prog. Crystal Growth and Caract.*, 13 (1986), 251.

[8] Y. Tanji, Y. Nakagawa, T. Kaneko, H. Ido, M. Kuboki, M. Kogo, T. Masumoto and R. Sato: Application for a patent is pending.

## EFFECTS OF THICKNESS AND PROCESSING VARIABLES ON THE PERFORMANCE OF (Bi,Sb)<sub>2</sub>(Te,Se)<sub>3</sub>-BASED FILM TYPE THERMOELECTRIC MODULES

Il-Ho KIM, Byoung-Gue MIN and Dong-Hi LEE

*Department of Metallurgical Engineering, Yonsei University,  
134 Shinchon-dong, Seodaemun-gu, Seoul 120-749, Korea*

For the enhanced performance of thin film miniature modules of (Bi,Sb)<sub>2</sub>(Te,Se)<sub>3</sub>-based thermoelectrics, the variations in thickness and number of p/n couple of the modules were investigated. An attempt for the preparation of thick film modules was also carried out by employing thermal spray technique with the subsequent evaporation and annealing treatment.

### 1. INTRODUCTION

There have been various investigations[1 ~8] for the preparation and characterization of thin film thermoelectric modules of Bi-Sb-Te-Se system, in light of effective application to the cooling as well as the temperature sensing of localized small area. Increase in the number of p/n couple is expected to be necessary for the enhanced function of the thin film modules. This, however, causes the decrease of cross sectional area of each p- and n-legs because of the limited total area of module. As a consequence, high current density for effective cooling is inevitably accompanied by the unwanted side effect such as Joule heating. One solution to those problems is thought to make the film thicker without any significant changes in design variables of the modules.

In the present studies therefore the effect of film thickness and number of p/n couples on the thermoelectric cooling performance were investigated. Thin film modules were fabricated by flash evaporation technique described elsewhere[1, 2, 9 ~14]. P- and n-type materials used were Bi<sub>0.5</sub>Sb<sub>0.5</sub>Te<sub>3</sub> and Bi<sub>2</sub>Te<sub>2.4</sub>Se<sub>0.6</sub> respectively. The thickness varied from 2  $\mu\text{m}$  up to 8  $\mu\text{m}$ , and the number of p/n couples of the module ranged from 1 couple to 20 couples.

A rather unusual processing method for the preparation of thick film modules was attempted with the expectation of an easy thickening by adopting thermal spray coating together with subsequent selective evaporation and annealing. Developments in microstructures and changes in compositions were investigated and discussed in conjunction with the processing variables.

### 2. EXPERIMENTAL

The starting materials of proper compositions were prepared from elementary Bi, Sb, Te and Se of 99.999 % purity by vacuum-melting in a quartz tubes held at 1073 K for 24 hours with the assist of mechanical vibration to make complete alloying. To obtain the evaporants for the flash evaporation process, the ingot was crushed into powders of  $\approx$  250  $\mu\text{m}$  in mean particle size in the glove box of Ar atmosphere. Detailed procedures for the film deposition were described in the previous work[1, 2].

For the evaluation of the cooling performance of the modules, temperatures of hot ( $T_h$ ) and cold ( $T_c$ ) junction were measured by K-type thin ( $\phi = 0.1 \text{ mm}$ ) thermocouples using a vacuum jig which maintained the hot junction at 301 K. A paste of high thermal conductivity (YG-611 : Toshiba Silicon Co.) was applied between hot junction and heat sink of copper block to ensure good heat conduction.

Photo. 1 shows shape and dimension of thin film modules containing different numbers of p/n couples. It represents that the width of each p- or n-leg was reduced as the number of p/n couples per unit area of module increased. For example, the width of a leg

decreased from 10 mm for one couple module to 500  $\mu\text{m}$  for module of 20 couples. In addition to the variations in the number of p/n couples, film thickness was prepared to vary from 2 to 8  $\mu\text{m}$ . Therefore, it was possible to investigate the effects of the number of p/n couple as well as film thickness on the cooling performance of the modules.

Thermal spray coating with subsequent treatments, as a preliminary work of fast and easy method for the preparation of thick modules, was tried in order to overcome the limited thickness of  $\approx$  10  $\mu\text{m}$  by evaporation technique. A commercial type spray coater (Metco 5P-II) designed to use acetylene and oxygen gases was utilized for this purpose. Flow rates of operating gases were one of the many processing variables. Ratio of flow rates of oxygen to acetylene was controlled to vary from 1.0 to 1.5 by adjusting gas flow (acetylene : 0.55 ~ 0.72  $\text{m}^3/\text{hr}$  and oxygen : 0.55 ~ 1.3  $\text{m}^3/\text{hr}$ ). Finer powders were found to be desirable for the preparation of homogeneous films, but coalescence of fine powders made the powder feeding be difficult. Through the initial works, the optimal processing variables were chosen as follows ; powder size  $\approx$  75 ~ 125  $\mu\text{m}$ , powder feeding rate  $\approx$  4 g/min and spraying distance  $\approx$  20 cm. Films of about 300  $\mu\text{m}$  thick were possible to prepare under these conditions by spraying for about 5 minutes. Substrates used were Corning pyrex glass plates which were blast-treated prior to alumina grits for 5 seconds to give average surface roughness of  $R_a = 1.75 \mu\text{m}$  in order to improve adhesion of film on substrate. The coated film specimen was cooled by compressed air immediately after spraying. Surface morphologies and chemical compositions of the thick films prepared in this way were investigated by SEM and EDS respectively.

### 3. RESULTS AND DISCUSSION

#### 3.1. Quality of thin film modules

Photo. 2 shows the magnified view of p/n junction area of 20 couple module of 8  $\mu\text{m}$  thick. The width of each leg was  $\approx$  500  $\mu\text{m}$  and gap between legs was  $\approx$  300  $\mu\text{m}$ . Dimensions of these size are believed to be almost minimum possible values by the flash evaporation process utilizing masking plates. P/n junctions, in general, showed good appearance having a negligible dimensional distortion and surface roughness. Thickness and its variation (surface roughness) of legs were represented in Figure 1. Interleg spacings became narrowed as the thickness of film was increased. Surface roughness of film,  $R_a = 5 \sim 10 \text{ nm}$ , was only 1 % or less of total film thickness. SEM microphotograph (Photo. 3) showing the surface morphologies of legs before and after annealing indicated that there were no microcracks, but crystalline grains were grown up to 200 ~ 300 nm when annealed.

#### 3.2. Cooling performance of thin film modules

Cooling effectiveness ( $\Delta T = T_h - T_c$ ) of modules was varied with (1)

number of p/n couples, (2) film thickness and (3) current passed through junctions. The variations of  $\Delta T$  with the number of p/n couples and film thickness as a function of current were represented in Figure 2. This figure shows that  $\Delta T$ , in general, varied to reach a maximum point ( $\Delta T$ )<sub>max</sub> and then decreased as the input current increased further. This is believed being resulted from the competition between Peltier cooling and Joule heating ; i.e.  $\Delta T \approx \Delta T_{\text{Peltier}} + \Delta T_{\text{Joule}}$ . For the fixed number of p/n couples, the thicker the film, the larger was the maximum value of ( $\Delta T$ )<sub>max</sub>. And the position of optimal current ( $I_{\text{opt}}$ ) for ( $\Delta T$ )<sub>max</sub> was also shifted to higher input current. On the other hand, if the film thickness

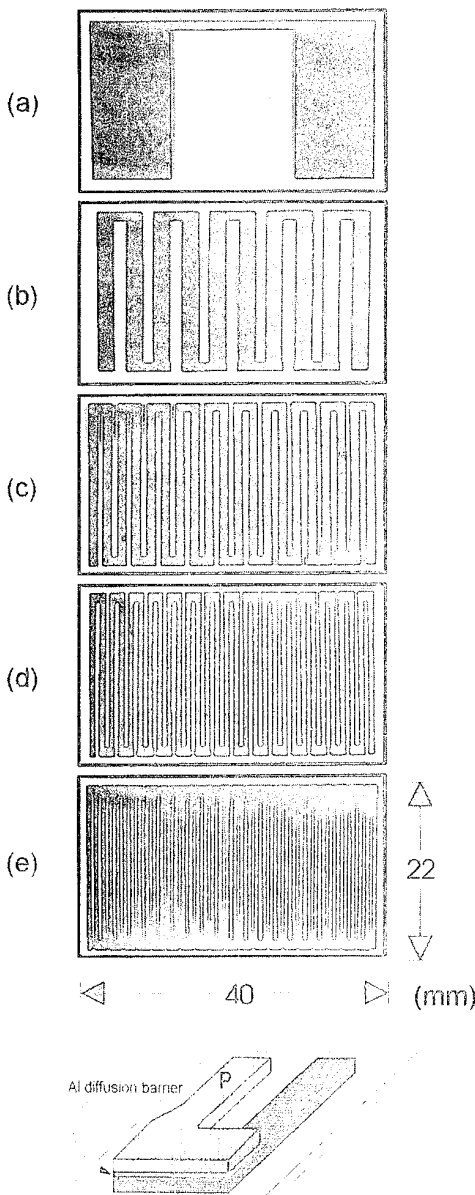


PHOTO. 1. Configurations of thermoelectric thin film modules.  
 (a) 1 couple      (b) 5 couples      (c) 10 couples  
 (d) 15 couples      (e) 20 couples

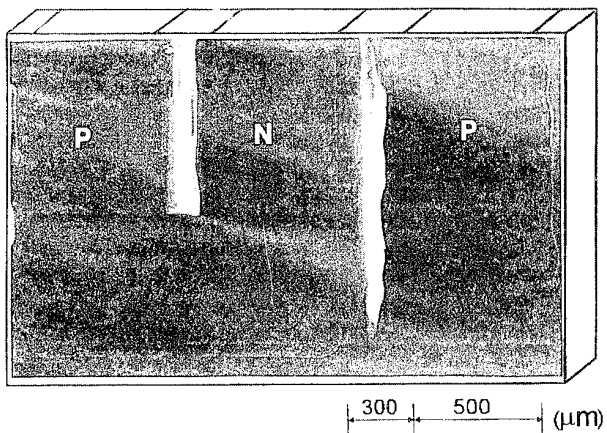


PHOTO. 2. Magnified view of p/n junction area of 8  $\mu\text{m}$ -20 couple module.

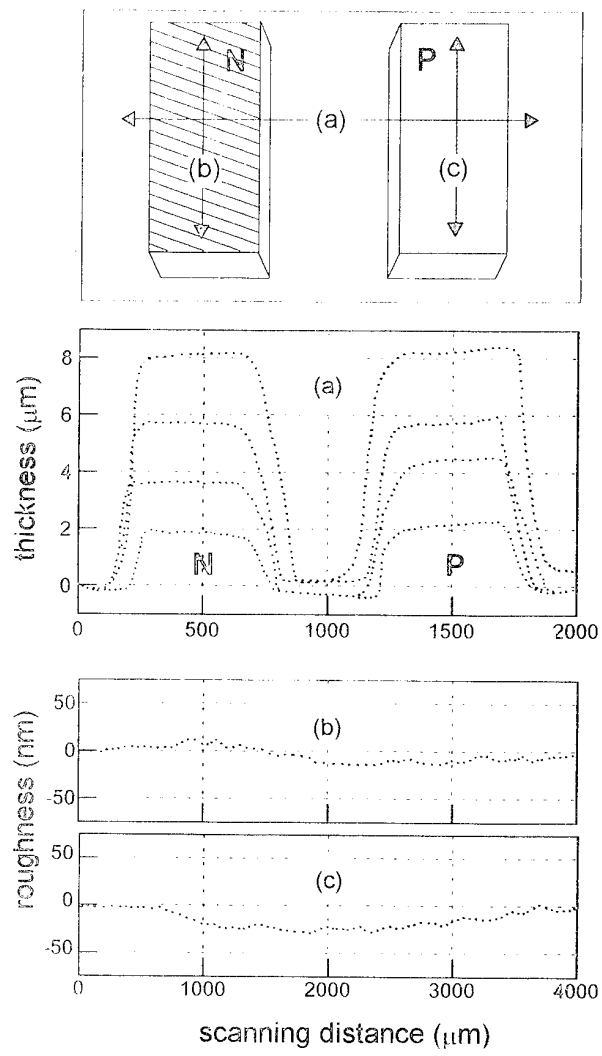


FIGURE 1. Variations in film thickness and surface roughness of p- and n-leg for 20 couple module.  
 (a) thickness( $2 \sim 8 \mu\text{m}$ )      (b) n-leg      (c) p-leg

was fixed, the values of  $(\Delta T)_{max}$  were not varied much with the number of couples except the  $I_{opt}$  which decreased with number of couples.

In order to figure it out the reasons for these variations, heating and cooling effects at junction were considered. Total absorption rate

of heat ( $Q$ ) at cold junction(s) of module can be expressed as follows ;

$$\begin{aligned} Q &= Q_P + Q_J + Q_E \\ &= [nI \alpha T] + [-\rho(nl)^2 \ell / wt] + Q_E \end{aligned} \quad (1)$$

where  $Q_P$  is heat absorption due to Peltier cooling,  $Q_J$  is heat evolution due to Joule heating (Joule heat produced through aluminium diffusion barrier layer was considered to be negligible), and  $Q_E$  is the extra heat absorbed, dissipated or evolved due to the complex effects such as thermal conduction occurring through substrate and along the p- and n-legs, and radiation at surface of junctions.  $n$  : number of p/n couples,  $\alpha$  : Seebeck coefficient of p/n couple,  $T$  : cold junction temperature,  $I$  : input current,  $\rho$  : average electrical resistivity of p/n couple,  $\ell$ ,  $w$  and  $t$  : length, width and thickness of a leg, respectively.

By this consideration, the results showed in Figure 2 could be divided into several individual effects contributed to the overall data. In Figure 3, variations of  $Q_P$ ,  $Q_J$  and  $(Q_P+Q_J)$  were illustrated on the theoretical basis. As shown in Eqn. (1),  $Q_P$  depends on number of couples only, whereas  $Q_J$  depends on both number of couples and film thickness. Therefore, for fixed number of couples (see Figure 3-a),  $Q_P$  increases with increasing input current, while  $Q_J$  is affected by both thickness and current. Consequently, the combined effect  $(Q_P+Q_J)$  has to increase. So it is necessary to thicken the films in order to raise  $(\Delta T)_{max}$  for the case of fixed number of couples. The maximum value of combined  $(Q_P+Q_J)_{max}$ , i.e.  $(\Delta T)_{max}$ , and the corresponding current  $I_{opt}$  increases with film thickness. That is the trend what was in general observed as in Figure 2. However, there are some discrepancy between the tendencies of theoretical and experimental thickness dependence on  $(Q_P+Q_J)_{max}$  or  $I_{opt}$ . The reasons for these can be analyzed by considering  $Q_E$ . Firstly, the decrease in thickness causes the increase of surface to volume ratio  $(\Delta S/\Delta V)$  of junction, which helps heat dissipation by

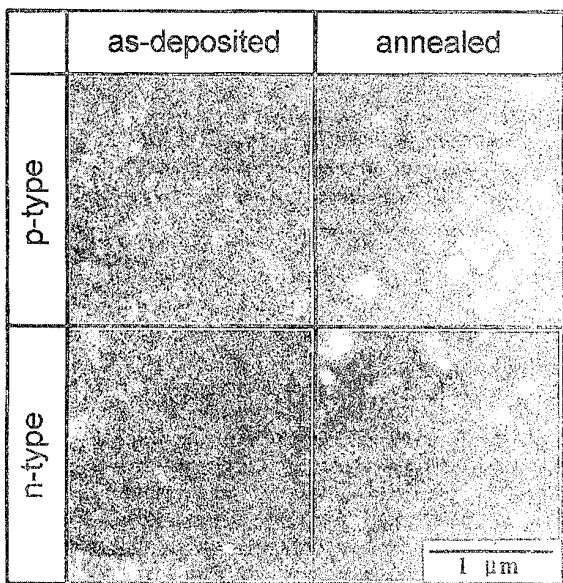


PHOTO. 3. Surface morphologies of p- and n-legs as-deposited and annealed (473 K, 1 hour).

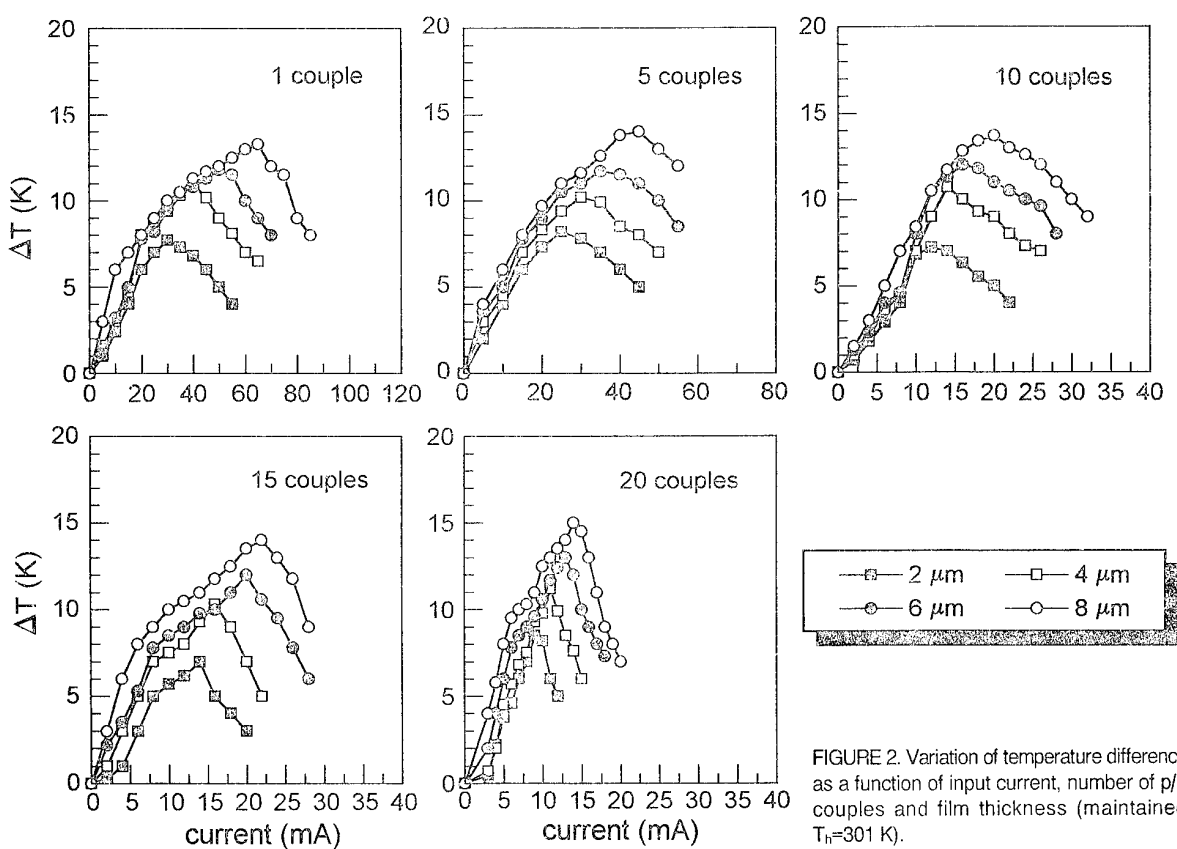


FIGURE 2. Variation of temperature difference as a function of input current, number of p/n couples and film thickness (maintained  $T_h=301$  K).

radiation. This, in turn, reduces heating effect of  $Q_J$ . So  $(Q_P+Q_J)_{\max}$  will shift to the right, that means increase of  $I_{opt}$ . Secondly, in Peltier cooling,  $Q_P$  has to be absorbed from outside through thermoelectric film at p/n junctions because p/n junctions were formed by overlapping two legs. This means that the effectiveness of heat absorption by Peltier effect decreases as film thickness increases. This affects  $I_{opt}$  being increased. Thirdly, thermal conduction along the legs due to temperature difference between hot and cold junctions increases with film thickness. That is, the thinner the film, the more effective cooling by Peltier may obtain. This also causes shift of  $I_{opt}$  to high value. Therefore,  $Q_E$  term in Eqn. (1) is becoming important when the thickness effect is considered.

In Figure 3-b, an analysis for the case of fixed film thickness, shows that  $(Q_P+Q_J)_{\max}$  retains almost constant value regardless of number of couples. As number of couples increases the ratio  $\Delta S/\Delta V$  increases, but its effect on  $\Delta T_{\max}$  and  $I_{opt}$  is negligible compared with the increase in  $Q_P$  and  $Q_J$ , because  $Q_P$  and  $Q_J$  vary with  $n$  and  $n^2$  respectively, whereas  $\Delta S/\Delta V$  depends on  $n$  by a fraction. Therefore, variation of  $(Q_P+Q_J)_{\max}$  has to remain almost same as that of  $(\Delta T)_{\max}$  because  $Q_E$  becomes negligible in this case.

From the data obtained,  $(\Delta T)_{\max}$  per electrical power input ( $P_{in}$ ) was calculated (Figure 4). The value of  $(\Delta T)_{\max}/P_{in}$  (an indication of cooling efficiency) was almost the same for the films of different thickness, provided number of couples was fixed. However, for a

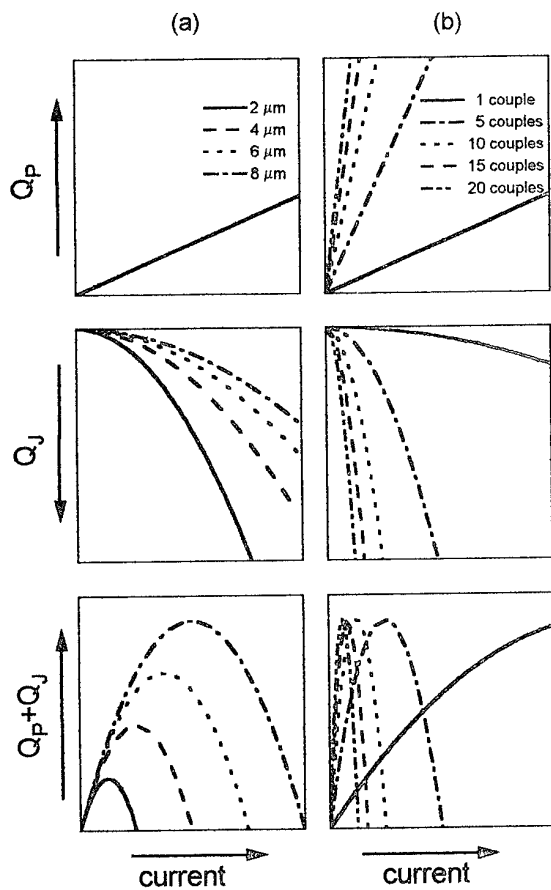


FIGURE 3. Illustration of separated heat effects.

(All units are shown arbitrarily.)

(a) for fixed number of couples

(b) for fixed film thickness

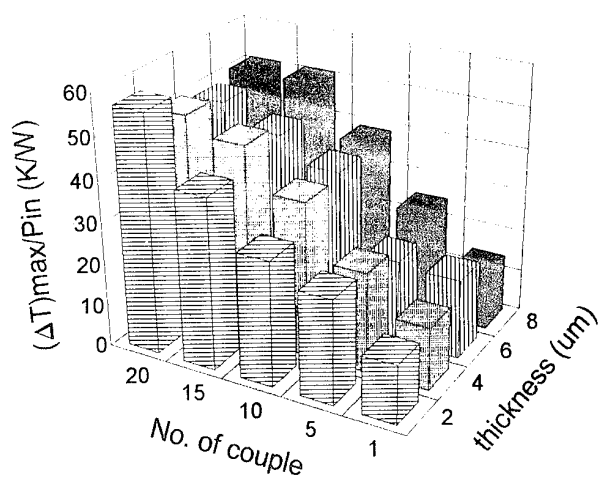


FIGURE 4. Variation of cooling efficiencies of modules with number of p/n couples and film thickness.

given thickness,  $(\Delta T)_{\max}/P_{in}$  increased as the number of couples was increased.

### 3.3. Thermal-sprayed thick films.

The intended chemical compositions of p- and n-type films were not able to obtain by thermal spray process when powders of same composition were used (Figure 5). The amounts of Te and Se of the spray-coated films were reduced while those of Sb and Bi were increased when compared with compositions of powders. As raising oxygen/acetylene ratio, there was a tendency of decrease in Sb and Bi contents, but it was opposite for the case of Te and Se. The reason for this was attributed to the higher vapor pressures of Te and Se than those of Bi and Sb.

Photo. 4 shows the surface morphology and cross-sections of coated films, together with oxygen/acetylene ratio. The lower the oxygen/acetylene ratio, the more dense the films obtained, because of the different heat input. But, in general, the films showed the typical spray-coated morphology with rough and porous surface. In the case of n-type films there were partially melted droplets together with spread layers. Particularly in Photo. 4-e, droplets were remained like a hemispherical shape. Quantitative metallographic analysis showed that as the ratio of oxygen/acetylene varied from 1.5 to 1.0, the density of coated films was increased up to  $\approx 95\%$  from 92%. However, chemical analysis showed that carbon was trapped  $\approx 2$  wt% in the coated films when the ratio decreased down to 1.0.

As the above results suggested, it was not possible to obtain the designed chemical compositions by thermal spray process alone. With the expectation to achieve stoichiometric compositions, the deficient amount of Te was carefully added (evaporated  $\approx 50 \mu\text{m}$  thick) by vacuum evaporation and then the film was heat-treated at  $300^\circ\text{C}$  for 10 hours in argon atmosphere hoping for sufficient diffusion. But it was found that the diffused depth of Te into the sprayed film was too small, compared with the total film thickness, to make complete compound of stoichiometric composition. The behavior of the other components was almost similar to that of Te. As a consequence, it was realized that there should be the other treatments needed to get the designed compositions of p- and n-type thick films. Perhaps, methods like zone heating or directional solidification may be utilized as a possible solution. It has not been tried yet, but one of those methods could be helpful to prepare thick films, which are structurally sound and compositionally homogeneous, when it is used as a second process together with thermal spraying.

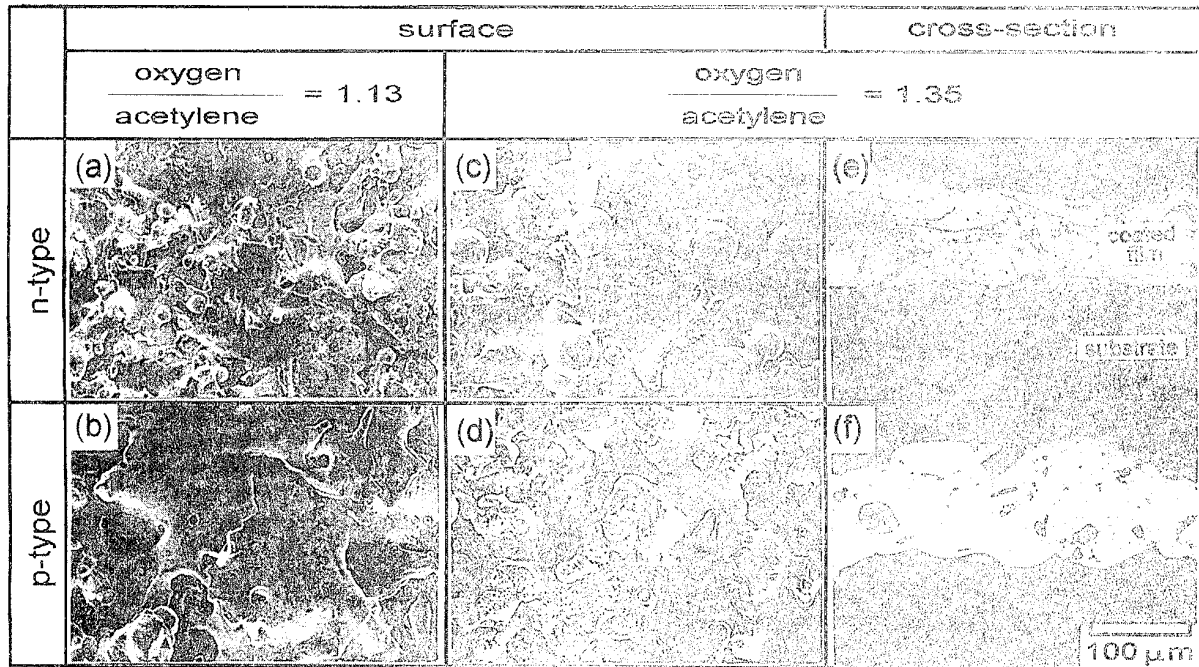


PHOTO. 4. Morphological variation of surface and cross-section of thermal-sprayed films with the ratio of oxygen to acetylene.

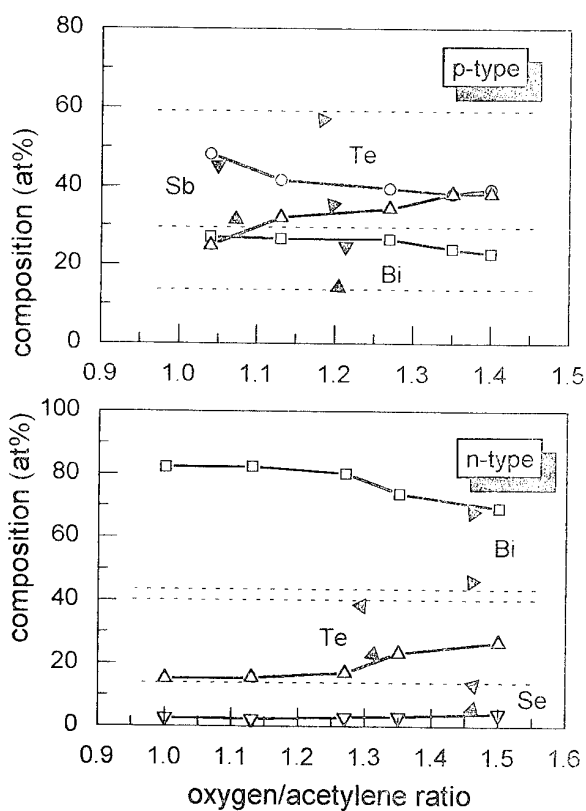


FIGURE 5. Compositional variations of sprayed films with oxygen/acetylene ratio (dotted lines : powder composition, solid lines : coated film composition).

#### 4. CONCLUSIONS

For the thin film modules of  $(\text{Bi}_2\text{Sb})_2(\text{Te}, \text{Se})_3$ , based thermoelectrics fabricated by the flash evaporation technique, the effects of film thickness and number of p/n couples on cooling performance of modules were investigated. The main results obtained in these studies are as follows;

1) P-type  $\text{Bi}_{0.5}\text{Sb}_{1.5}\text{Te}_3$  and n-type  $\text{Bi}_2\text{Te}_{2.4}\text{Se}_{0.6}$  films and the p/n junctions fabricated by the flash evaporation showed uniform thickness and homogeneous stoichiometric composition. P/n junctions retained good appearance and dimensional uniformity even after annealing (473K, 1 hour).

2) Interleg spacing was getting narrowed as the film thickness increased because evaporants were spreaded between mask and substrate. It was realized that the minimum possible interleg spacing was about 300 μm by this method. For the preparation of modules containing more than 20 couples in the size of 40 × 22 mm<sup>2</sup>, closer arrangement of distance between mask and substrate and more carefully controlled deposition will be necessary.

3) Maximum temperature difference generated by module was increased with the film thickness for a given number of p/n couples, but it was not changed much with the number of couples for the case of fixed thickness of film. The effect of film thickness and number of couples on the cooling performance of modules could be understood by taking account of complex effects on maximum temperature difference. It was found that the consideration of extra heat term was important for thin film modules, in addition to Peltier and Joule effects.

4) Maximum temperature difference achieved per electrical input power was almost the same for the films of different thickness when number of couples was fixed. However, it was increased with the number of couples for a given thickness.

5) Through the attempt for the preparation of thick films, it was found that some complementary process is required to solve compositional and structural inhomogeneity after thermal spraying.

**ACKNOWLEDGMENT:** Authors want to appreciate the financial supports from KOSEF through RETCAM.

## REFERENCES

- [1] Il-Ho Kim and Dong-Hi Lee, Preparation and Properties of  $(Bi,Sb)_2(Te,Se)_3$  Thin Film Thermoelectric Modules, *Proc. of the 12th ICT*, 1993, pp328-333
- [2] Il-Ho Kim and Dong-Hi Lee, Diffusion at p/n Junctions of Thin Film  $Bi_{0.5}Sb_{1.5}Te_3/Bi_2Te_{2.4}Se_{0.6}$  Thermoelectrics, *Proc. of the 13th ICT*, 1994, pp254-259
- [3] D.K.Benson and C.E.Tracy, Design and Fabrication of Thin Film Thermoelectric Generators, *Proc. of the 4th ICTEC*, 1982, pp.11-14
- [4] J.George and B.Pradeep, Preparation and Properties of Co-Evaporated Bismuth Telluride  $[Bi_2Te_3]$  Thin Films, *Solid State Commun.*, 1985, v.56, No.1, pp.117-120
- [5] J.Przyluski etal., Preparation of Thin Thermoelectric Films by the Method of the Solid State Reaction, *Proc. of the 3rd ICTEC*, 1980, pp.205-209
- [6] E.Charles etal., Structural and Electrical Properties of Bismuth Telluride Films Grown by the Molecular Beam Technique, *J. Mater. Sci. Lett.*, 1988, v.7, pp575-577
- [7] Yu.A.Boikov etal., Thin and Thick,  $(Bi,Sb)_2(Te,Se)_3$ -Based Thermoelectric Films, *Proc. of the 8th ICTEC*, 1989, pp.18-22
- [8] J.Przyluski and K.Borkowski, Thin Film Thermoelectric  $Bi_2Te_3$ -Based Module, *Proc. of the 6th ICTEC*, 1986, pp.100-104
- [9] M.G.Gu, S.Y.Lee and D.H.Lee, Thermoelectric Power of Mono-Junction Cu/Constantan Thin Film Couple, *Korean Appl. Phys.*, 1990, v.3, No.1, pp.73-80
- [10] J.M.Mycong, S.Y.Lee and D.H.Lee, Thermoelectric Power of Multi-Junction Cu/Constantan Thin Film Couple, *Korean Appl. Phys.*, 1990, v.3, pp.195-201
- [11] S.Y.Lee and D.H.Lee, Effects of Electron Transport Properties on the Thermoelectric Power of Cu/Constantan Thin Film Couples, *J. Korean Institute of Metals*, 1990, v.28, pp.627-633
- [12] S.Y.Lee, *Ph.D. thesis*, Yonsei University, Korca, 1990
- [13] F.Volklein etal., Transport Properties of Flash-Evaporated  $(Bi_{1-x}Sb_x)2Te_3$  Films I : Optimization of Film Properties, *Thin Solid Films*, 1990, v.187, pp.253-262
- [14] N.G.Patel and P.G.Patel, Thermoelectric Cooling Effect in a p-Sb<sub>x</sub>Te<sub>3</sub>-n-Bi<sub>2</sub>Te<sub>3</sub> Thin Film Thermocouple, *Solid State Electronics*, 1992, v.35, No.9, pp.1269-1272

TRANSIENT THERMOELECTRIC EFFECT IN  $Sb_{2-x}In_xTe_3$  AND  
 $Sb_2Te_{3-y}Se_y$  SOLID SOLUTIONS

V. A. Kulbachinskii<sup>1</sup>, M. Inoue<sup>2</sup>, M. Sacaki<sup>2</sup>, H. Negishi<sup>2</sup>, W. X. Gao<sup>2</sup>

<sup>1)</sup>Low Temperature Physics Department, Physics Faculty, Moscow State University, 119899, Moscow,  
 Russia

<sup>2)</sup>Department of Materials Science, Faculty of Science, Hiroshima University, Higashi-Hiroshima 739, Japan

Transient thermoelectric effect (TTE) and galvanomagnetic properties have been measured along the C<sub>2</sub> axis for two mixed crystals of p-type  $Sb_{2-x}In_xTe_3$  ( $0 < x < 0.4$ ) and  $Sb_2Te_{3-y}Se_y$  ( $0 < y < 1.8$ ). The observed TTE voltages decay exponentially with characteristic relaxation times  $\tau_i$  ( $i=1,2,\dots$ ) for thermal diffusions of photoinduced carriers, whose analyses give carrier mobilities and effective masses. New valence band contributing in the conductivity was found in  $Sb_2Te_{3-y}Se_y$  for  $y > 0.02$ .

### Introduction

Antimony telluride  $Sb_2Te_3$  belongs to a layered compound with the same tetradymite structure as  $Bi_2Te_3$ , in which a weak bond between Sb and Te layers exists. It usually involves antistructural defects (the occurrence of Sb atoms occupying Te lattice positions). Due to such native defects,  $Sb_2Te_3$  shows always a p-type conductivity with the hole concentration up to  $10^{20} \text{ cm}^{-3}$ . The upper valence band (UVB) of  $Sb_2Te_3$  consists of six ellipsoids tilted to the basal plane [1,2] and the lower valence band (LVB) which is known to be a multivalley, but the anisotropy of this valley is unknown. The value of the tilt angle  $\theta$  is not known exactly, but  $\theta \approx 50^\circ$  according to the extrapolation to  $x=1$  in  $(Bi_{1-x}Sbx)_2Te_3$  [2]. The energy separation between the tops of the UVB and LVB is reported to be of the order of 20-30 meV because that for  $(Bi_{1-x}Sbx)_2Te_3$  ( $0 < x < 1$ ) is about 30 meV [2]. In the present work we have carried out measurements of pulsed laser induced 'transient thermoelectric effect' (TTE) for  $Sb_{2-x}In_xTe_3$  ( $0 < x < 0.4$ ) and  $Sb_2Te_{3-y}Se_y$  ( $0 < y < 1.8$ ) single crystals along the C<sub>2</sub> axis at 300 K. Galvanomagnetic properties in the temperature range 4.2-300 K also have been measured. Our interest is concerned with the effect of In or Se substitution on the electronic properties of the host  $Sb_2Te_3$  and to get valuable information about changing of its energy spectrum, in particular, the valence bands.

### Experimental

$Sb_{2-x}In_xTe_3$  and  $Sb_2Te_{3-y}Se_y$  single crystals were grown by a modified Bridgman method from 5N purity elements [3,4]. The resistivity and Hall effect were measured by a potentiometric method with dc current along the C<sub>2</sub> direction in magnetic fields up to 7 T

applied along the C<sub>3</sub> axis (perpendicular to the layers) using a superconducting solenoid. The experimental setup and measuring principle of the TTE method have been described earlier [5]. In principle, a pulsed laser (laser power  $\sim 350$  mJ) produced by a Nd:YAG laser source with the wavelength of 1064 nm ( $\sim 1.17$  eV) and pulsewidth of 3 ns was irradiated normal to one end of a crystal. Photoinduced TTE voltages were detected over the wide time range 50 ns to 500 ms by a digital storage oscilloscope through a home-made preamplifier, whose output signal was fed to a computer for record and numerical analysis. The TTE method was applied recently for semiconductor  $Bi_{2-x}Sn_xTe_3$  [6].

TTE measurements were made only at 300 K, below which the TTE signals became too small to be detectable.

### Experimental results

#### A. Transient thermoelectric effect

Figure 1 shows typical photoinduced TTE signals along the C<sub>2</sub> direction for  $Sb_{2-x}In_xTe_3$  ( $x=0$  and  $0.2$ ) and  $Sb_2Te_{3-y}Se_y$  ( $y=0.2$ , and  $1.0$ ) at  $T=300$  K in the time intervals 0-20 ms, where the observed TTE signals are averaged out by 15-20 times because of extremely small magnitudes compared to those of the similar family of  $Bi_{2-x}Sn_xTe_3$  crystals [6]. For the host material  $Sb_2Te_3$ , immediately after the laser irradiation, the induced TTE voltage  $V(t)$  decreases drastically within 50 ns (minimum sampling time) and increases with time  $t$  up to about 25 mV in the short time range 0-20 ms. Similar TTE profiles are also observed for the solid solutions. As in the case for various solids [5,6], the TTE voltages  $V(t)$  at time  $t$  can be expressed in the exponential

Fig. 1. Typical photoinduced TTE voltages  $V(t)$  for  $Sb_2-xIn_xTe_3$  ( $x=0, 0.2$ ) and  $Sb_2Te_{3-y}Se_y$  ( $y=0.2$ , and  $1.0$ ) along the  $C_2$  axis at 300 K.

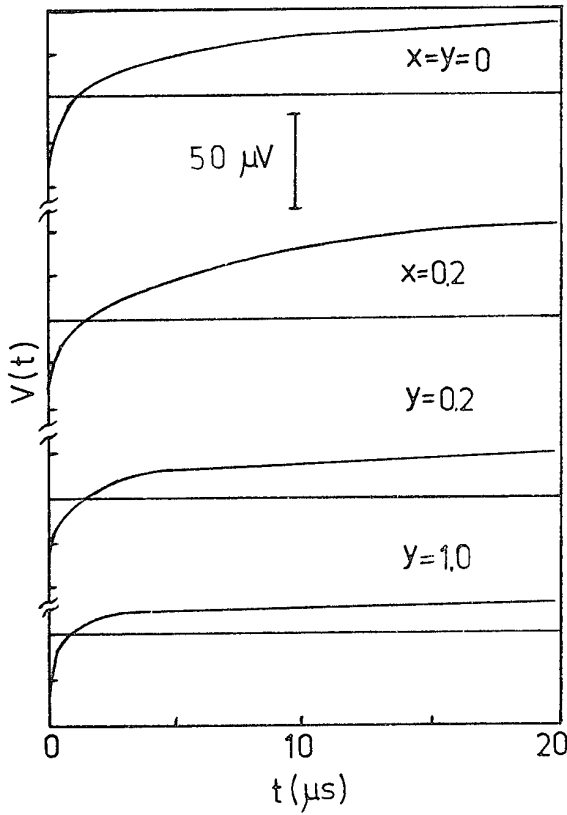
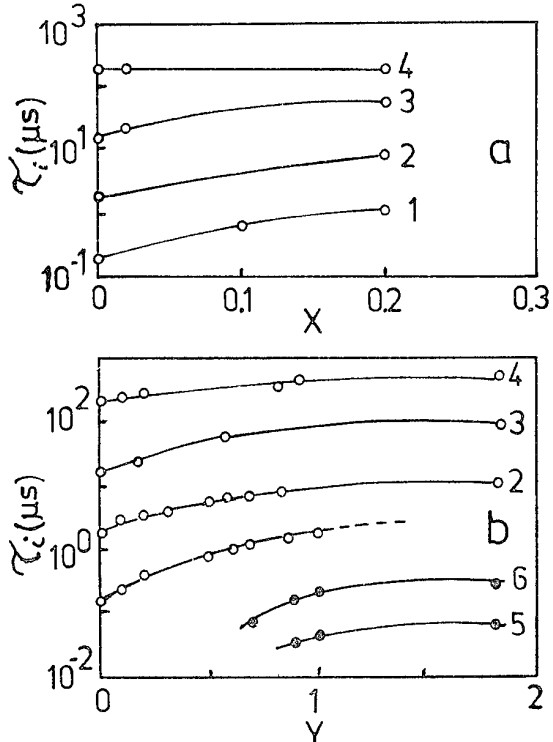


Fig. 2. (a) Observed relaxation times  $\tau_i$  ( $i=1-4$ ) for  $Sb_2-xIn_xTe_3$  ( $0 < x < 0.2$ ) plotted against In content  $x$  and (b) those of  $\tau_i$  ( $i=1-6$ ) for  $Sb_2Te_{3-y}Se_y$  ( $0 < y < 1.8$ ) plotted against Se content  $y$ .



#### B Galvanomagnetic effects

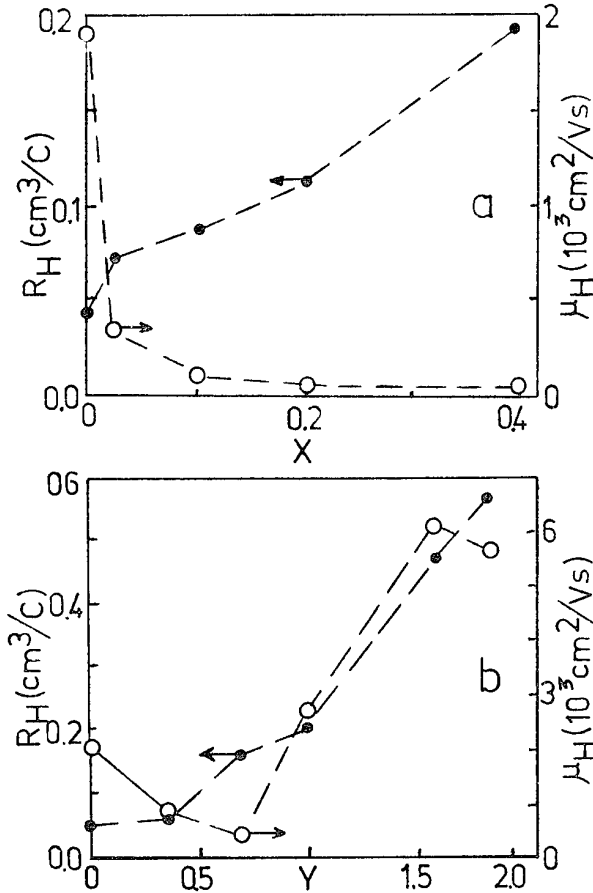
form,

$$V(t) = V_0 + \sum a_i \exp(-t/\tau_i), \quad (1)$$

where  $V_0$  is a constant value at  $t \rightarrow \infty$ ,  $a_i$  a relaxation amplitude, and  $\tau_i$  a relaxation time for the  $i$ th relaxation process or the type of carriers;  $a_i > 0$  or  $a_i < 0$  corresponds to a thermal diffusion of electrons or holes, respectively. From the analyses of the observed TTE signals we have obtained four kinds of relaxation times  $\tau_i$  ( $i=1-4$ ) due to 'holes' ( $a_i < 0$ ) for the host material and for In-substituted samples ( $x < 0.2$ ). For Se-substituted ones, we have also four relaxation times  $\tau_1-\tau_4$ , but the TTE signal corresponding to  $\tau_1$  becomes too weak for higher Se concentration  $y > 1.0$ . Moreover, two extra relaxation times  $\tau_i$  ( $i=5$  and  $6$ ;  $a_i < 0$ ) are observed for higher Se concentration  $y > 0.7$ . In Figs. 2(a) and 2(b) the values of  $\tau_i$  for  $Sb_{2-x}In_xTe_3$  and  $Sb_2Te_{3-y}Se_y$  are plotted against  $x$  and  $y$  in semilogarithmic scales, respectively, where we see that these values span a wide time range from  $10^{-2}$  to  $10^2$  ms, and that all relaxation times increase with  $x$  or  $y$ .

For all samples, the resistivity  $\rho$  decreases with decreasing temperature and then approaches a constant value at low temperatures. Residual resistivities increase with the substitution of In or Se atoms. In the temperature range 77-300 K, the  $\rho-T$  curves for  $Sb_2Te_{3-y}Se_y$  obey a power law of the form  $\rho=T^n$  with the exponent  $n \approx 1.3$  for all samples. The Hall coefficient  $R_H$  is positive for all samples and is almost independent of temperature in the whole temperature range 4.2-300 K and of magnetic field up to 7 T. The values of  $R_H$  and the Hall mobilities  $\mu_H$  at 4.2 K are plotted against the In or Se content in Figs. 3(a) and 3(b), respectively. The  $R_H$  increases monotonically with increasing the concentration of In or Se, which indicates that the apparent hole concentrations decrease with  $x$  or  $y$ . On the other hand, the Hall mobility  $\mu_H$  decreases drastically with increasing  $x$  for  $Sb_{2-x}In_xTe_3$ , while for  $Sb_2Te_{3-y}Se_y$  it falls at low Se concentration ( $y < 0.7$ ) and then increases up to  $y=1.8$ , followed by a decrease. One of the reasons for the drastic decrease in  $\mu_H$  with  $x$  for  $Sb_{2-x}In_xTe_3$  may be due to an appreciable increase of vacancies, as found for  $In_2Te_3$  [7].

Fig. 3. Hall coefficients  $R_H$  and Hall mobilities  $\mu_H = \sigma R_H$  at 4.2 K plotted against (a) In content  $x$  for  $Sb_{2-x}In_xTe_3$  and (b) Se content  $y$  for  $Sb_2Te_{3-y}Se_y$ .



For the  $Sb_2Te_{3-y}Se_y$  system, the increase in  $\mu_H$  for  $y > 0.7$  is due to the predominance of a new valence band (NVB) with a smaller effective mass compared to those of the main UVB and LVB, as described later.

The magnetoresistance of these crystals is proportional to the square of a magnetic field  $B$  at low magnetic fields, while it shows Shubnikov-de Haas (SdH) oscillations at high fields. In the present orientation of  $B$  parallel to the  $C_3$  axis, we have observed a single frequency, which indicates that the extremal cross-sections of the six ellipsoids of the UVB Fermi surfaces coincide. Due to a very sharp decrease in the Hall mobility with increasing In content of  $Sb_{2-x}In_xTe_3$ , the oscillation amplitude falls rapidly with  $x$ ; even for  $x=0.2$  it was impossible to detect the SdH effect in magnetic fields up to 35 T.

For  $Sb_2Te_{3-y}Se_y$  with Se concentrations  $y > 0.2$ , a new frequency appears in the SdH oscillations. This new frequency can be ascribable to a new valence band (NVB), as it will be discussed later. Thus the SdH data

confirmed the appearance of a NVB for  $y > 0.2$ , which is evident from the TTE data.

## Discussion

### A. $Sb_{2-x}In_xTe_3$

It is known that the UVB of the host  $Sb_2Te_3$  consists of six equivalent valleys, whose Fermi surfaces have ellipsoidal shape. Along the  $C_2$  direction there are two valleys with different effective masses, to which we attribute the observed relaxation times  $\tau_1$  and  $\tau_2$  of the TTE signals. On the other hand, much less is known about the Fermi surface of the LVB. However, in order to explain TTE experimental results reasonably, we propose a six-valley model for the LVB, as in the case for  $Bi_2Te_3$  [6] where we assign another two relaxation times  $\tau_3$  and  $\tau_4$  to two different valleys of the LVB along the  $C_2$  direction, similar to the case of the UVB.

Now according to the ellipsoidal nonparabolic model, [2,3] the energy spectrum of the holes in the UVB of  $Sb_2Te_3$  is represented in the form,

$$2m_0E=\hbar^2(a_{11}k_1^2+a_{22}k_2^2+a_{33}k_3^2+2a_{23}k_2k_3), \quad (2)$$

where the inverse mass tensor components  $a_{ij}$  depend on the energy. Here the momentum  $k_1$ ,  $k_2$ , and  $k_3$  form the Cartesian coordinates, which are parallel to one of the binary and bisectrix axes, and to the trigonal axis, respectively.

We have calculated the hole concentrations  $p_{SDH}$  at 4.2 K for  $Sb_{2-x}In_xTe_3$  using the parameters of the energy spectrum for  $Sb_2Te_3$ , where we have assumed that the anisotropy of the Fermi surface and tilt angle of the ellipsoids do not depend on the In concentration. We note that with increasing In content the hole concentration is decreased due to the suppression of antistructural defects formed in the host material. In addition,  $p_H$  is larger than  $p_{SDH}$  in each sample, which means that the holes in the UVB with  $p_{SDH}$  are responsible for the SdH effect, while those in the LVB do not due to very low mobility; thus  $p_{SDH}$  is regarded as the hole concentration  $p_U$  in the UVB. On the other hand, the theoretical analysis of the diffusion equation for photogenerated carriers gives the following relation between the relaxation time  $\tau_i$  and carrier mobility  $\mu_i$  of the  $i$ th carrier,

$$\tau_i = eL_i^2/(2k_B T\mu_i) \text{ or } \mu_i = eL_i^2/(2k_B T\tau_i), \quad (3)$$

where  $L_i$  is a diffusion length, which, we assume, is independent of the type of carriers ( $L_i = L$ ). Based on the above two-valence band model, we have evaluated the hole concentration  $p_U$  in the UVB,  $p_L$  in the LVB, and their mobility  $\mu_i$  along the  $C_2$  axis corresponding to  $\tau_i$  using Eq. (3), as in the following way. Here it is to be

noted that to the carrier transport along the C<sub>2</sub> direction, there contribute two equivalent hole pockets corresponding to  $\tau_1$  (or carrier mobility  $\mu_1$ ) and four ones corresponding to  $\tau_2$  (or  $\mu_2$ ) in the UVB. Similarly, for the LVB we propose two equivalent pockets corresponding to  $\tau_3$  (or  $\mu_3$ ) and four ones with  $\tau_4$  (or  $\mu_4$ ). Thus the total conductivity  $\sigma$ , Hall coefficient  $R_H$ , and Hall mobility  $\mu_H$  can be written for four different groups of carriers.

According to Eq. (3), the mobility ratio is expressed by the ratio for relaxation times of the UVB and LVB,  $\tau_1$ ,  $\tau_3$ , respectively, measured along the C<sub>2</sub> axis. The hole concentration  $p_U$  in the UVB is regarded as equal to the observed value  $p_{SDH}$  from the SdH effect with parameters which were determined for Sb<sub>2</sub>Te<sub>3</sub> [2]. With the values of  $p_U$  and mobility ratio we obtain the hole concentration  $p_L$  in the LVB. From the observed Hall mobility  $\mu_H$  we obtain the value of  $\mu_1$  and thus the carrier mobility  $\mu_3$  for the LVB. These evaluated parameters are:  $p_U = 0.2 \times 10^{20} \text{ cm}^{-3}$ ;  $p_L = 80 \times 10^{20} \text{ cm}^{-3}$ ;  $\mu_1 = 1400 \text{ cm}^2/\text{Vs}$ ;  $\mu_3 = 11 \text{ cm}^2/\text{Vs}$ . The hole concentrations  $p_U$  and  $p_L$  are decreased with increasing In content primarily due to the suppression of the antistructural defects by incorporating of In atoms in Sb sublattice, which in turn means that the Fermi energies of both UVB and LVB are decreased with increasing  $x$ . We should also note that the hole mobility  $\mu_1$  of the UVB is much larger than  $\mu_3$  of the LVB, and these values are drastically reduced with  $x$ , which indicates that ionized or neutral impurity scatterings by these crystal defects become predominant. Moreover, the substitution of In atoms into Sb sites in Sb<sub>2</sub>Te<sub>3</sub> may affect the anisotropy of the ellipsoidal Fermi surfaces of the UVB and LVB. To estimate the anisotropy in the effective mass, we use the following relation,

$$\frac{\tau_j}{\tau_i} = \mu_i / \mu_j = (m_j^*/m_i^*)^\gamma, \quad (4)$$

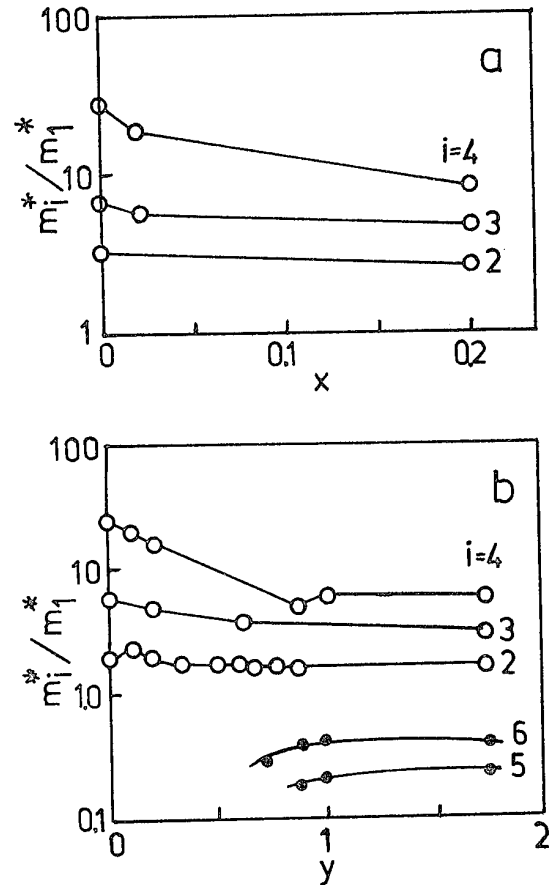
where  $\gamma$  is a parameter characterising a scattering mechanism. Assuming phonon scattering for all carriers in each pocket ( $\gamma=5/2$ ), with the observed relaxation times at 300 K (Fig. 2), we obtain the effective mass ratio with respect to  $m_1^*$  for the UVB,  $m_2^*/m_1^*$ , and that for the LVB with respect to  $m_3^*$ ,  $m_4^*/m_3^*$ , as shown in fig. 4.

We see that the anisotropy in the effective mass of the UVB is of the same order of magnitude as that of the LVB for the host material (about 3), and these values decrease with In alloying. In particular, the reduction is appreciable for the latter, which may arise from the increase in the tilt angle  $\theta$  with In alloying.

### B. Sb<sub>2</sub>Te<sub>3-y</sub>Se<sub>y</sub>

To our knowledge, there are no available information about the band parameters in Eq. (2) for the solid solution of Sb<sub>2</sub>Te<sub>3-y</sub>Se<sub>y</sub>. Hence in the present work, based on our band model we have attempted to evaluate the hole concentrations  $p_U$  and  $p_L$ , and hole mobilities  $\mu_1$ ,  $\mu_3$ , and  $\mu_5$  of the UVB, LVB, and NVB, respectively, using the

Fig. 4 Concentration dependencies of (a) the evaluated ratio of each effective masses to  $m_1^*$  for Sb<sub>2-x</sub>In<sub>x</sub>Te<sub>3</sub> (0 <  $x$  < 0.2) and (b) those for Sb<sub>2</sub>Te<sub>3-y</sub>Se<sub>y</sub> (0 <  $y$  < 1.8).



observed Hall data [Fig. 2(b)], TTE data  $\tau_i$  and the SdH frequencies. We should note that there are three different regions of Se concentration: In the first region  $0 < y < 0.2$ , there is only one frequency component in the SdH effect, but the Hall concentration is higher than SdH concentration, and we have observed four relaxation times. In the second region  $0.2 < y < 1.0$ , there are two frequency components in SdH effect at  $B \parallel C_3$ , and two additional relaxation times  $\tau_5$  and  $\tau_6$  are detected for  $y > 0.7$ , which we have attributed to a new valence band (NVB) with an anisotropic and small effective mass. The increase in the SdH frequency with  $y$  in the range

$0.2 < y < 1.0$  is due to the change of the positions of the UVB, LVB and NVB; NVB moves up and UVB moves down due to Se doping. For  $y > 1.0$  there are two extremes filled by holes, NVB and LVB, because UVB filled up to the top. The Fermi surfaces in the C<sub>1</sub>C<sub>2</sub> plane for the UVB consist of two types of hole valleys with the relaxation times  $\tau_1$  and  $\tau_2$ . We assume that the LVB is the same as that of the host that has a multivalley structure consisting of two types of hole valleys with the relaxation times  $\tau_3$  and  $\tau_4$  in C<sub>2</sub> direction in the whole region of Se concentration. With this model, we have evaluated the carrier concentration  $p_U = 1.7 \times 10^{19} \text{ cm}^{-3}$  for the UVB for  $y=0.2$  from the observed SdH frequency with the parameters of the energy spectrum which are extrapolated from those for Sb<sub>2</sub>Te<sub>3</sub> [2]. Then using four valley band model with the experimental values of mobility ratio and Hall effect data, the values of mobilities can be evaluated according to the procedure similar to that for Sb<sub>2-x</sub>In<sub>x</sub>Te<sub>3</sub>:  $\mu_I = 1810 \text{ cm}^2/\text{Vs}$  and  $\mu_3 = 29 \text{ cm}^2/\text{Vs}$ . However, this procedure is not acceptable for  $0.2 < y < 1.0$ , because in this region we have simultaneously three valence bands, UVB, LVB, and NVB, where the NVB is supposed to consist of six ellipsoids with the anisotropy less than that of the UVB. With such a three-valence-band model we calculated  $p_U = 0.3 \times 10^{19} \text{ cm}^{-3}$ ,  $p_N = 6.6 \times 10^{19} \text{ cm}^{-3}$ ,  $\mu_I = 12 \text{ cm}^2/\text{Vs}$ ,  $\mu_3 = 0.3 \text{ cm}^2/\text{Vs}$ ,  $\mu_5 = 540 \text{ cm}^2/\text{Vs}$  for  $y=0.7$ .

Moreover, for the region III with  $y \geq 1.0$ , we have evaluated the parameters using the two-valence-band model. According to the procedure as done in the region I, we have evaluated values the hole mobilities  $\mu_3 = 5.5 \text{ cm}^2/\text{Vs}$ ,  $\mu_5 = 7290 \text{ cm}^2/\text{Vs}$  and  $p_N = 3.2 \times 10^{19} \text{ cm}^{-3}$ ,  $p_L = 14 \times 10^{19} \text{ cm}^{-3}$  at 300 K. It is to be noted that the carrier mobility of the NVB  $\mu_5$  in the region III of the Se concentration is particularly large. However, for  $y=1.6$  and  $y=1.8$  it is difficult to fit all data under the assumption that the tilt angle and the shape of the ellipsoids of NVB are constant; if this is the case, we have to reduce  $p_N$  by 30%. Thus the anisotropy or tilt angle should change in the NVB ellipsoids by Se doping. The hole concentrations  $p_L$  in the LVB are of comparable magnitude with those found for Sb<sub>2-x</sub>In<sub>x</sub>Te<sub>3</sub> and decreases with increasing  $y$ , indicating the decrease in the Fermi energy of the LVB. We also note that all carrier mobilities decrease drastically in the region of the Se concentration  $0.2 < y < 1.0$ . In this case, three kinds of valence bands (UVB, LVB, and NVB) contribute to the dc transport. In this region, the carrier scattering between different valleys are very important and reduce the carrier mobilities. The most significant nature of the band structure for Sb<sub>2</sub>Te<sub>3-y</sub>Se<sub>y</sub> is the appearance of the NVB above  $y=0.2$ , as found from the SdH effect and TTE (for  $y>0.7$ ) experiments (Fig. 3). Here we have assumed that the NVB has also a six-

valley structure, since we have observed two relaxation times  $\tau_5$  and  $\tau_6$ . The NVB becomes predominant for  $y>1.0$ , which may originate from the valence bands of the constituent counterpart of Sb<sub>2</sub>Se<sub>3</sub>. But the total hole concentration decrease due to Se doping. Finally, using Eq. (8) we have estimated the effective mass ratio  $m_i^*/m_1^*$  ( $i=2-4$ ) for Sb<sub>2</sub>Te<sub>3-y</sub>Se<sub>y</sub> along the C<sub>2</sub> axis (fig.4). We see that these ratios are of the order of 2-20, which decrease by substituting Se atoms into the host Sb<sub>2</sub>Te<sub>3</sub>. The anisotropies in both UVB and LVB ( $m_2^*/m_1^*$  and  $m_4^*/m_3^*$ , respectively) are of the order of 2-3. These results indicate that both UVB and LVB have a multivalley structure with anisotropic band structure. In addition, the anisotropy for the NVB is similarly estimated to be  $m_6^*/m_5^* \approx 2$ . This NVB is expected to have an effective mass less than those in the UVB and LVB.

### Conclusion

From the static and dynamic transport measurements for solid solutions of p-type Sb<sub>2-x</sub>In<sub>x</sub>Te<sub>3</sub> ( $0 < x < 0.4$ ) and Sb<sub>2</sub>Te<sub>3-y</sub>Se<sub>y</sub> ( $0 < y < 1.8$ ) along the C<sub>2</sub> axis, we have found the systematic variations of the Hall coefficient and Hall mobility with In content  $x$  and Se content  $y$  below  $y<0.3$ . By heavily substitution of Se atoms into the host Sb<sub>2</sub>Te<sub>3</sub>, the Hall mobility increases drastically. The observed TTE voltages are characterised by a multiple relaxation process with different relaxation time  $\tau_i$  ( $i=1-6$ ) for thermal diffusions of photogenerated carriers, where  $\tau_1$  and  $\tau_2$  are due to holes in the UVB,  $\tau_3$  and  $\tau_4$  to LVB, and  $\tau_5$  and  $\tau_6$  (observable only for  $y>0.7$  in Se-substituted samples) due to the NVB with extremely large mobilities.

### References

- [1] A. von Middendorf, K. Dietrich, and G. Landwehr, *Solid State Communications*, 1973, V.13, pp.443-446.
- [2] H. Kohler and A. Freudberger, *Phys. Stat. Sol. (b)* 1977, V.84, pp.195-203.
- [3] J. Horak, P. Lostak, and L. Benes, *Phil. Mag.*, 1984, V.50, No6, pp.665-671.
- [4] P. Lostak, R. Novotny, L. Benes, S. Civis, *J. of Crystal Growth*, 1989, V.94, pp.656-662.
- [5] M. Sasaki, H. Negishi, and M. Inoue, *J. Appl. Phys.* 1986, V.59, No3, pp.796-802.
- [6] V. A. Kulbachinskii, M. Inoue, M. Sasaki, H. Negishi, W. X. Gao, K. Takase, Y. Gimai, P. Lostak, and J. Horak, *Phys. Rev. B*, 1994, V.50, pp.16921-16930.
- [7] V. M. Koshkin, L. P. Gal'chinetskii, V. N. Kulik, B.I. Minkov, and U. A. Ulmanis, *Sov. State Commun.*, 1973, V.13, No1, pp.1-4..

## SEEBECK COEFFICIENT AND ELECTRICAL CONDUCTIVITY OF $\text{Bi}_2\text{Te}_3\text{-Sb}_2\text{Te}_3$ ALLOYS PREPARED USING POWDER METALLURGY

D.M. Rowe and Gao Min

*School of Engineering, University of Wales Cardiff, Cardiff, UK.*

Grain size and compacting pressure are two important variables in materials preparation using powder metallurgy. The effects of both on the Seebeck coefficient and electrical conductivity in the preparation of  $\text{Bi}_2\text{Te}_3\text{-Sb}_2\text{Te}_3$  alloys using powder metallurgy were investigated. It was observed that the electrical resistivity decreases with an increase in the compacting pressure, while the Seebeck coefficient remains constant. The grain size had little effect on either the Seebeck coefficient or electrical resistivity for specimens with grain sizes larger than  $60 \mu\text{m}$ . The Seebeck coefficient and electrical conductivity were substantially lower in small grain size material, obtained using a vibratory mill. This reduction is due mainly to oxygen contamination rather than a grain boundary effect.

### Introduction

The thermoelectric figure-of-merit of materials prepared by powder metallurgy is usually smaller than that of their crystalline counterparts. This is especially true for materials with highly anisotropic transport properties, such as alloys based upon  $\text{Bi}_2\text{Te}_3$ . Nevertheless, there are considerable practical advantages in the use of the powder metallurgy process in the preparation of thermoelectric materials [1]. Furthermore, recent progress in the preparation of  $\text{Bi}_2\text{Te}_3$  using mechanical alloying [2] and in obtaining orientation aligned sintered material [3] has revived interest in the preparation of  $\text{Bi}_2\text{Te}_3$  alloys using powder metallurgy.

The powder metallurgy process usually involves a sequence of operations, these typically include: grinding, pressing and sintering. There are several factors in the powder metallurgy process which can affect the thermoelectric properties of the resulting materials. These include: density, orientation, grain size and contamination. The influence of these factors on the thermoelectric properties have previously been investigated by several authors [4-8]. However, previous investigations were mostly carried out on specimens after sintering process. The results obtained inevitably included the influence of the sintering. In order to avoid such ambiguous results, the effects of grain size and compacting pressure on the Seebeck coefficient and electrical resistivity of p-type  $\text{Bi}_2\text{Te}_3\text{-Sb}_2\text{Te}_3$  alloys were studied using cold-pressed specimens. The effect of sintering was also investigated using data obtained before and after the sintering process.

### Experimental

P-type polycrystalline  $\text{Bi}_2\text{Te}_3\text{-Sb}_2\text{Te}_3$  ingot grown from the melt using the Bridgmann method was chosen as a starting material. The ingot was crushed into powder using a mortar and pestle inside argon-filled a glove box and subsequently sieved into the following different grain-size ranges:  $500\text{-}1000 \mu\text{m}$ ,  $250\text{-}500 \mu\text{m}$ ,  $100\text{-}250 \mu\text{m}$ ,  $60\text{-}100 \mu\text{m}$ ,  $25\text{-}60 \mu\text{m}$ . A vibratory mill was also employed to produce fine-grain powder of  $<1 \mu\text{m}$ . The resulting powder was then charged into a die set of  $6 \text{ mm}$  in diameter for compaction. Several specimens were prepared using cold-pressing under a uni-axial pressure of  $200$ ,  $400$ ,  $600$ ,  $800$  and  $1000 \text{ MPa}$ . The Seebeck coefficient and electrical resistivity were

measured at room temperature using a hot-probe [9] and four probe apparatus [10], respectively. The density of the starting material was obtained using hydrostatic method to overcome difficulties due to irregular geometry, while the density of the specimens was obtained from measuring the volume and weight of the specimens. The sintering process was carried out at  $573 \text{ K}$  for 2 hours in an argon atmosphere.

### Results and discussion

In figure 1 is shown the density as a function of compacting pressure for specimens with different grain-sizes before sintering. The density increases with increase in both compacting pressure and grain size. The highest density is 97 % of corresponding crystal value, which was obtained from specimens compacted at  $1000 \text{ MPa}$  with grain size  $500\text{-}1000 \mu\text{m}$ . For specimens with grain size of  $<1 \mu\text{m}$ , only 85 % of corresponding crystalline density was obtained. This is probably due to the ratio of surface area to volume for grains increasing with a reduction in the grain size. Consequently, the specimens prepared with small grain size are likely to be more porous. The deviation in density due to different grain sizes is smaller for specimens prepared at higher pressure. This indicates

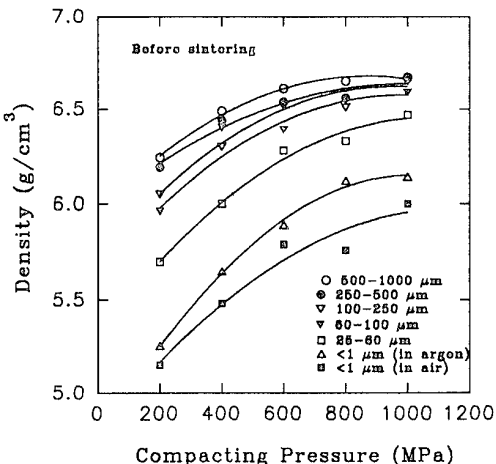


Figure 1 Density as a function of compacting pressure for different grain size.

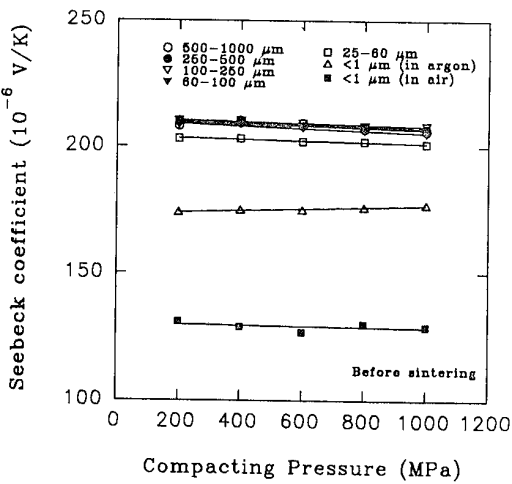


Figure 2 Seebeck coefficient as a function of compacting pressure for different grain sizes.

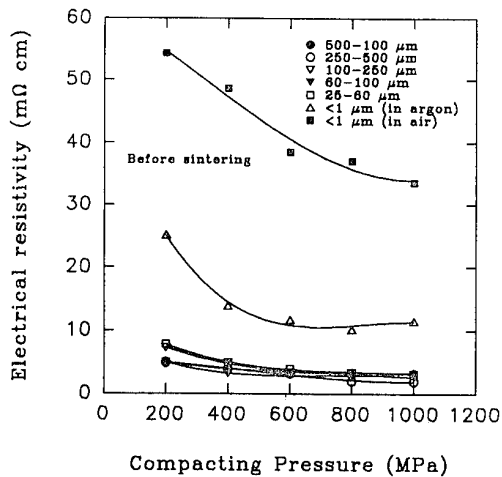


Figure 3 Electrical resistivity as a function of compacting pressure for different grain sizes.

that higher densities may be achieved in small grain size specimens if compacted at higher pressure. Unfortunately, in this investigation, it was observed that cracks appeared in the specimens prepared using small grain powder at high compacting pressure. Specimens prepared from the large grain powders ( $>100 \mu\text{m}$ ) showed no cracks at highest compacting pressure employed in this investigation (1000 MPa). However, specimens prepared from fine grain powders of less  $25 \mu\text{m}$  resulted in significant cracks even at a compacting pressure of 800 MPa.

The Seebeck coefficient and electrical resistivity as a function of compacting pressure for different grain sizes are shown in figure 2 and 3, respectively. The electrical resistivity decreases with an increase in the compacting pressure, while the Seebeck coefficient remains almost constant. From the data shown in figure 1, it can be seen that the specimens prepared at high compacting pressure possess higher density, or less porosity. It is expected that

porosity affects the charge carrier mobility due to carrier scattering by pores. Consequently, the electrical resistivity increased with an increase in porosity due to lower compacting pressure. Porosity appears to have no effect on the Seebeck coefficient. Usually, the Seebeck coefficient is also likely to be affected by different carrier scattering mechanisms. However, the results displayed in figure 3 indicate that the Seebeck coefficient may not be affected by certain mechanisms, though these mechanisms present significant scattering on charge carriers. Consequently, the electrical resistivity can be altered without affecting the Seebeck coefficient and a large electrical power factor ( $\alpha^2\sigma$ ) can be obtained.

Grain size presents no significant effect on both the Seebeck coefficient and electrical resistivity for specimens with grain size larger than  $25 \mu\text{m}$ . As shown in figure 3, the deviation in the electrical resistivity due to grain size is significantly less than that due to porosity for all the specimens except those prepared by the vibratory mill. For specimens with grain size larger than  $60 \mu\text{m}$ , no effect on the Seebeck coefficient was observed due to different grain sizes. However, a reduction in the Seebeck coefficient was evident for specimens with grain size between  $25-60 \mu\text{m}$ .

Substantial reduction in both the Seebeck coefficient and electrical conductivity occurs in fine grain ( $<1 \mu\text{m}$ ) specimens prepared using the vibratory mill. There are two mechanisms which may be responsible for this substantial reduction: 1) oxygen contamination; 2) grain-boundary scattering. The effect of oxygen contamination was investigated using a specimen prepared in air using the vibratory mill. It can be seen from figure 2 and 3 that both the Seebeck coefficient and electrical resistivity changed significantly due to different atmospheres. Evidently, oxygen contamination was responsible for the observed reduction. Reduction in grain size increases the surface area available for contamination. Consequently, the influence of oxygen contamination increases with a reduction grain size. The effect of pure grain-boundary scattering has to be investigated in a ultra high vacuum

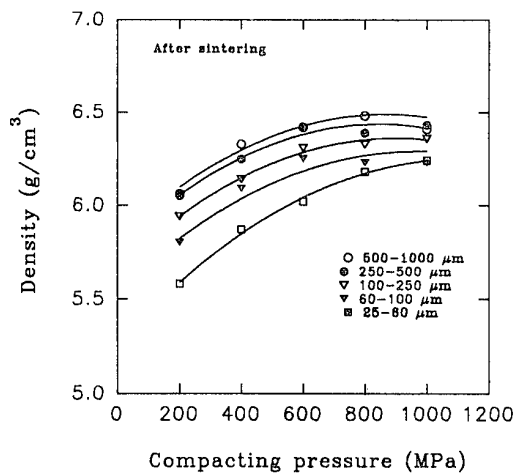


Figure 4 Density as a function of compacting pressure for different grain sizes after sintering.

which was not available for this investigation. However, it is expected that the effect of pure grain-boundary scattering is unlikely to be as significant as oxygen contamination for specimens prepared in an atmosphere available as used this investigation.

In figure 4-6 are shown the results of density, Seebeck coefficient and electrical resistivity respectively after sintering the specimens. Data analysis indicated that a reduction of about 3-5 % in density was observed after sintering for all specimens of different grain sizes and compacting pressures. The reduction appears to be more significant in specimens compacted at higher pressure, the Seebeck coefficient being more pressure dependent after sintering. A significant increase by about 20-30 % in the Seebeck coefficient is observed in all specimens except for those compacted at 200 MPa. The increase in the Seebeck coefficient is more significant for small-grain specimens compacted at higher pressure. The change in

the electrical resistivity is also affected by grain size. The electrical resistivity after sintering appears to decrease for specimens with grain size  $<250 \mu\text{m}$ , while it appears to increase for those with grain size  $>250 \mu\text{m}$ . It is apparent that the dependence of the thermoelectric properties on the grain size and compacting pressure can be significantly altered by the sintering process. Further investigation is needed to identify the mechanisms which are responsible for these changes during the sintering process.

### Conclusions

The Seebeck coefficient of  $\text{Bi}_2\text{Te}_3\text{-Sb}_2\text{Te}_3$  alloys prepared by cold-pressing is independent of compacting pressure (or porosity), while the electrical resistivity decreases with an increase in compacting pressure (or porosity). The Seebeck coefficient and electrical conductivity are also independent of the grain size for specimens with grain sizes between 60-1000  $\mu\text{m}$ . However, substantial reductions were observed in both the Seebeck coefficient and electrical conductivity for specimens with grain size less than 1  $\mu\text{m}$ . This significant reduction is mainly attributed to oxygen contamination rather than pure grain-boundary scattering. Oxygen contamination affects both the Seebeck coefficient and electrical conductivity, while the porosity appears to affect the electrical conductivity only. The density, electrical resistivity and the Seebeck coefficient were significantly altered after sintering. The density cannot be improved by sintering process. On the contrary, it decreased by about 5 %. The changes in the Seebeck coefficient and electrical resistivity appear to be quite complicated and further investigation is needed.

### Acknowledgements

This work is supported by the New Energy and Industrial Technology Development Organisation (NEDO), the Energy Conversion Centre, Japan.

### References

- [1] H.J. Goldsmid, *Electronic Refrigeration*, Pion Limited, London, 1986
- [2] T. Ohta, T. Uesugi, T. Tokai, N. Noaska, and T. Kajikawa, *Proc. of 8th Inter. Conf. on Thermoelectrics*, Nancy, France, 1989, p45
- [3] H. T. Kaibe, M. Sakata, Y. Isoda and I.A. Nishida, *J. Inst. Metals.*, 1989, **53**, p958
- [4] R.G. Cope, and A.W. Penn, *J. Mater. Sci.*, 1968, **3**, p103
- [5] R. Ionescu, J. Jaklovszky, N. Nistor, and A. Chiculita, *Phys. Status Solidi A*, 1975, **27**, p27
- [6] J. Jaklovszky, R. Ionescu, N. Nistor, and A. Chiculita, *Phys. Status Solidi A*, 1975, **27**, p329
- [7] R. A. Horne, *J. Appl. Phys.*, 1959, **30**, p393
- [8] H. J. Goldmid, and F.A. Underwood, *Adv. Energy Convers.*, 1968, **7**, p297
- [9] L.E. Cowles and L.A. Dauncey, *J. Sci. Instrum.*, 1962, **39** p16
- [10] L.B. Valdes, *Proc. IRE*, **42**, p420

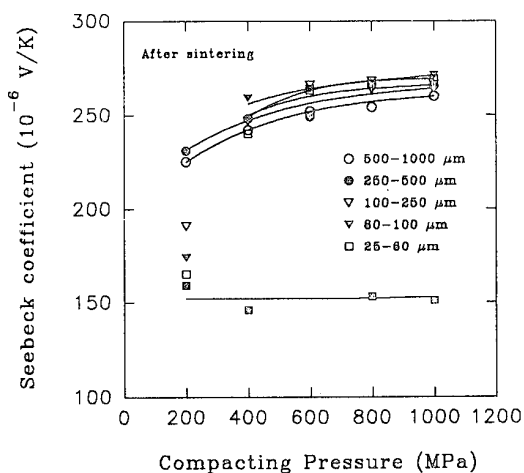


Figure 5 Seebeck coefficient as a function of compacting pressure for different grain size after sintering.

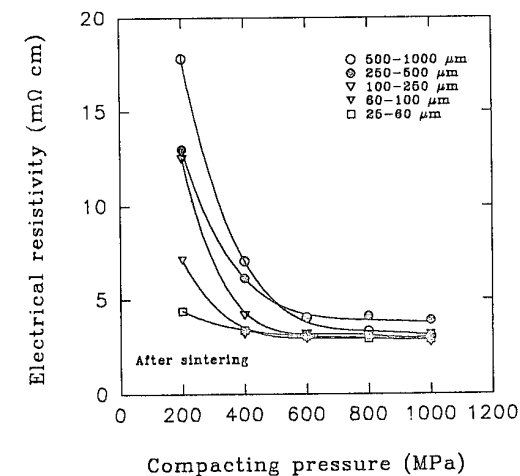


Figure 6 Electrical resistivity as a function of compacting pressure for different grain sizes after sintering.

## OPTIMIZATION OF BISMUTH TELLURIDE BASED ALLOYS FOR THERMOELECTRIC POWER GENERATION USING "WASTE" HEAT

D.M.Rowe, Gao Min and S.G.K. Williams

*School of Engineering, University of Wales, Cardiff, UK*

Conventionally  $\text{Bi}_2\text{Te}_3$  based alloys are used in Peltier modules operated around room temperature and below. In this paper, the thermoelectric properties of commercially available  $\text{Bi}_2\text{Te}_3$  based alloys were assessed over the temperature range 300-600 K for use in electrical power generation using "waste" heat. The results enabled the power output and conversion efficiency to be calculated taking into account the temperature dependence of these properties. The calculated data indicates that an improvement in both the power output and conversion efficiency is possible if the maximum values of the electrical power factor and thermoelectric figure-of-merit can be optimized over a higher temperature range.

### Introduction

Alloys based on bismuth telluride are the best existing thermoelectric materials for use in the temperature range around room temperature. The thermoelectric properties of these alloys below room temperature have previously been investigated to achieve the best performance for refrigeration [1-5]. However, there is less information available on the temperature dependence of the thermoelectric properties of  $\text{Bi}_2\text{Te}_3$  based alloys over the temperature range above room temperature. Accompanying the recent interest in the use of Peltier modules as generators for "waste" heat electrical power generation [6,7] is a requirement for information on the thermoelectric properties of bismuth telluride type alloys as a function of temperature above room temperature. This is necessary to enable realistic calculations to be made of the power output and conversion efficiency of these modules. The objective of the work reported in this paper is to provide up-to-date information on the temperature dependence of thermoelectric properties of  $\text{Bi}_2\text{Te}_3$  based alloys over the temperature range 300-600 K. The possibility of improving the thermoelectric performance of the modules by modifying the material is assessed by investigating the power output and conversion efficiency of a typical commercial available Peltier module.

### Thermoelectric properties over 300-600 K

Materials employed in this investigation were obtained from an established thermoelectric module manufacturer. The n and p-type materials are solid solutions of  $\text{Bi}_2\text{Te}_3\text{-Bi}_2\text{Se}_3$  and  $\text{Bi}_2\text{Te}_3\text{-Sb}_2\text{Te}_3$ , respectively. The Seebeck coefficient, electrical resistivity and thermal conductivity were measured using apparatus previously described [8, 9]. The transport properties of these alloys exhibit strong anisotropy. Consequently, the specimens were carefully prepared for the investigation along the "preferred" orientation (i.e., the direction perpendicular to c-axis). Specimens used for the Seebeck coefficient and electrical resistivity measurements were prepared in a rectangular shape (2 mm x 2 mm x 10 mm), while the disc-shaped specimens used for thermal

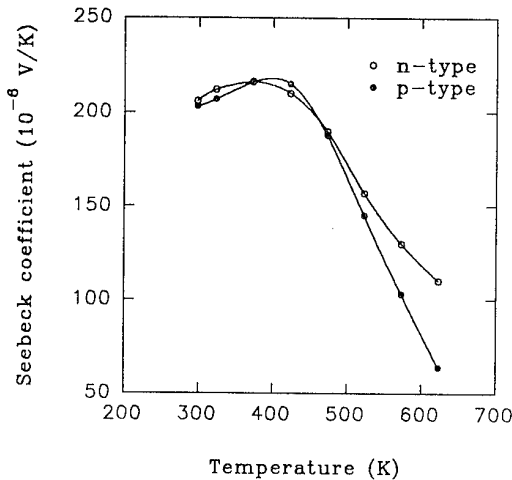


Figure 1 Seebeck coefficient versus temperature.

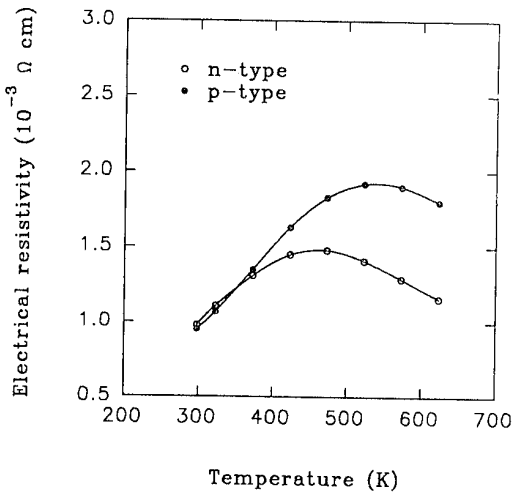


Figure 2 Electrical resistivity versus temperature.

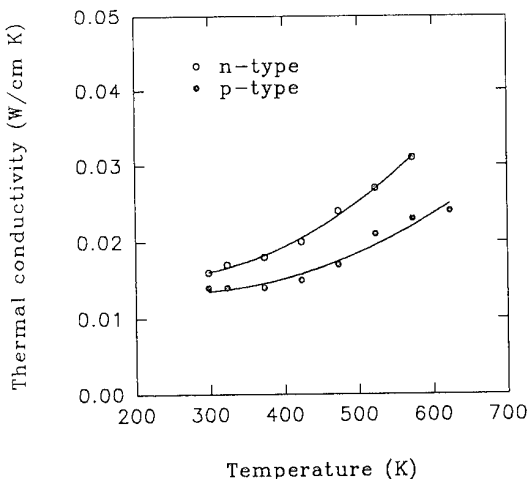


Figure 3 Thermal conductivity versus temperature.

conductivity measurement were 6.5 mm in diameter and about 1.5 mm thick. In figures 1-3 are shown the Seebeck coefficient, electrical resistivity and thermal conductivity as a function of temperature over the range 300-600 K for both n-type and p-type materials. It is apparent that the Seebeck coefficient and electrical resistivity initially increase with increasing temperature until they reach a maximum value, and then decrease with further increase in temperature. The maximum values for the Seebeck coefficient and electrical resistivity are achieved at about 400 and 500 K, respectively. The thermal conductivity increases monotonically with increasing temperature over the temperature range investigated.

The electrical power factor and thermoelectric figure-of-merit were also calculated using the data displayed in figures 1-3 and the results are presented as a function of temperature in figures 4 and 5. The electrical power factor and thermoelectric figure-of-merit decrease with an increase in temperature. Estimated reductions in electrical power factor and thermoelectric figure-of-merit are about 25 % and 30 % when the temperature increases from 300 to 400 K. It is apparent that a decrease in the thermoelectric performance of modules fabricated using  $\text{Bi}_2\text{Te}_3$  based alloys would accompany an increase in temperature. The dashed lines in figures 4 and 5 are the average values of n and p-type materials, while the general trend of low temperature behavior has been obtained from published data [1]. It can be seen that the optimum temperatures, which correspond to the maximum values of the electrical power factor and figure-of-merit, are around 300 K. The dotted lines shown in the figures are obtained by shifting the dashed lines along the T-axis to a position where the optimum temperatures are about 350 K.

#### Improving Power output and Conversion efficiency

The power output of a Peltier module when operated in generating mode can be calculated using [10],

$$P = \frac{1}{2} \frac{\alpha^2}{\rho} \frac{NA\Delta T^2}{(l+n)(1+2rl_c/l)^2} \quad (1)$$

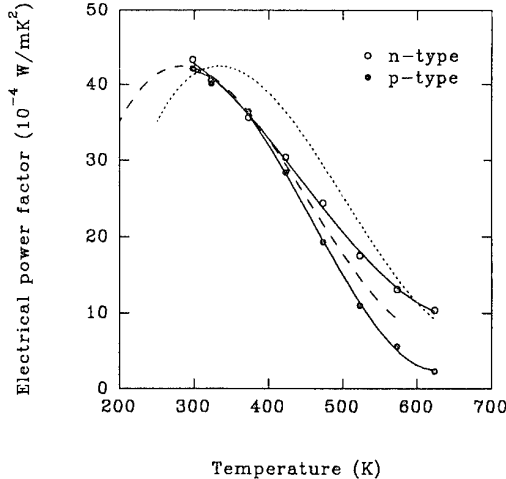


Figure 4 Electrical power factor versus temperature.

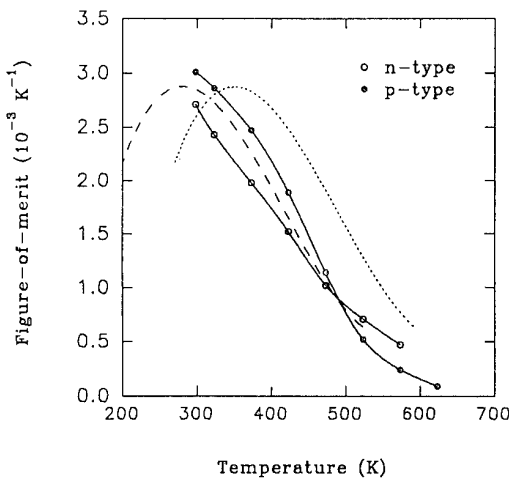


Figure 5 Figure-of-merit versus temperature.

where,  $\alpha$  and  $\rho$  are the Seebeck coefficient and electrical resistivity, respectively,  $N$  the number of the thermocouples in a module,  $A$  the cross-sectional area of the thermoelements,  $\Delta T$  the temperature difference across the module,  $l$  the length of thermoelements,  $l_c$  the thickness of the ceramic plate.  $n$  and  $r$  are the parameters related to the electrical and thermal contact resistances, respectively.

The power output is normally estimated using equation (1) by assuming that the electrical power factor ( $\alpha^2/\rho$ ) remains constant over  $\Delta T$ . However, as shown in figure 4, the electrical power factor is a function of temperature. Consequently, in a realistic calculation of the power output, the temperature dependence of the electrical power factor needs to be taken into consideration. In this case, the power output can be calculated by integrating equation (1) over the whole temperature range. The power output, based on a typical commercially available module

( $N=127$ ,  $A=1.4 \text{ mm} \times 1.4 \text{ mm}$ ,  $l=1.54 \text{ mm}$ ,  $l_c=1 \text{ mm}$ ,  $n=0.10 \text{ mm}$ ,  $r=0.20$ ,  $T_c=300 \text{ K}$ ), was calculated and the results are shown in figure 6. The solid line in the figure was obtained using room temperature ( $\alpha^2/\rho$ ) data and assuming that it remains constant over the whole temperature range. The dashed line was calculated using ( $\alpha^2/\rho$ ) values represented by the dashed line in figure 4. It can be seen that the power output is likely to be overestimated if the temperature dependence of ( $\alpha^2/\rho$ ) is not taken into consideration. Furthermore, assuming that the temperature dependence of the electrical power factor can be shifted to a position where the optimum temperature is around 350 K (i.e. represented by dotted lines in figure 4), the corresponding power output was calculated and the results are presented by a dotted line in figure 5. It is apparent that for applications over the temperature range 300-400 K, an increase of about 8 % can be obtained in principle.

The conversion efficiency of a Peltier module when operated in the generating mode is given by [10]

$$\phi = \left( \frac{T_h - T_c}{T_h} \right) \left( 1 + 2rl_c/l \right)^2 \left[ 2 - \frac{1}{2} \left( \frac{T_h - T_c}{T_h} \right) + \left( \frac{4}{zT_h} \right) \left( \frac{l+n}{l+2rl_c} \right) \right]^{-1} \quad (2)$$

where,  $z$  is the thermoelectric figure-of-merit of the thermoelectric material, and  $T_h$  and  $T_c$  are the temperatures on the hot and cold sides of the module. Employing the same assumption to that for calculating power output, the conversion efficiency was calculated and the results are displayed in figure 7 as a function of thermoelement length for several temperature differences. The solid lines and dotted lines were calculated using  $z$  values represented by the dashed line and dotted line in figure 5, respectively. It can be seen that for temperature difference  $>60 \text{ K}$ , an increase in conversion efficiency can be obtained by shifting  $z$  values from those represented by dashed lines to those by dotted line in figure 5.

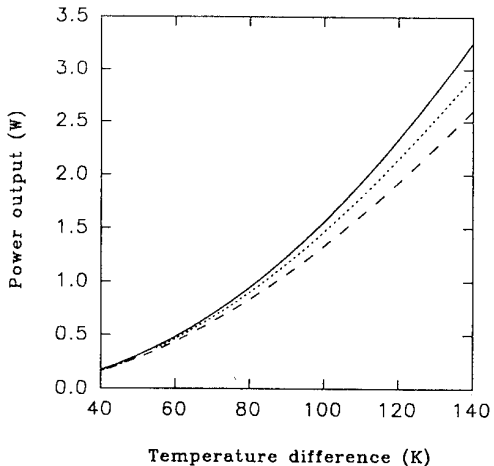


**Figure 6** The power output as a function of temperature difference. The solid line was calculated with  $(\alpha^2/\rho)$  remaining constant. The dashed line was calculated for  $(\alpha^2/\rho)$  optimized at 300 K. The dotted line for that optimized at 350 K.

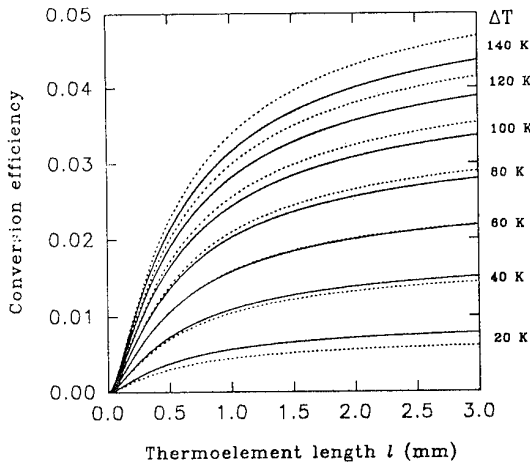


**Figure 7** Conversion efficiency as a function of thermoelement length for different temperatures. The solid lines were calculated for  $z$  optimized at 300 K and the dotted lines for that at 350 K.

#### Discussions and conclusions

The results of theoretical calculations show that an improvement up to 8 % in the electrical power factor and 6 % in the conversion efficiency can be obtained at a temperature difference of about 100 K. However, it is noted that the calculation was based upon the assumption that the maximum value of the electrical power factor or thermoelectric figure-of-merit, can be shifted to a higher temperature range without reduction. In practice, a shift of optimum temperature to higher temperature range may be accompanied by a decrease in the maximum value of the electrical power factor and thermoelectric figure-of-merit. As a result, the actual increase obtained is expected to be less than that calculated. In order to obtain the maximum possible improvement, it is essential that the optimum temperature can be shifted with a less significant decrease in the maximum value of the electrical power factor or thermoelectric figure-of-merit.

For  $\text{Bi}_2\text{Te}_3$  based alloys, it has been shown that the optimum temperature varies with carrier concentration and alloy composition without a significant reduction in the maximum value of the thermoelectric figure-of-merit [11]. It is known that the mechanism which affects the optimum temperature is the onset of intrinsic conduction [1]. Apparently, a possible approach to improve the thermoelectric performance of these alloys is to prevent the occurrence of intrinsic conduction over the temperature range where the module is operated. This could be achieved by increasing the carrier concentration or the energy band gap.

#### Acknowledgment

This work is supported by the New Energy and Industrial Technology Development Organization (NEDO) at the Energy Conversion Centre, Japan.

**References**

- [1] H. J. Goldsmid, *Proc. Phys. Soc.*, London, 1958, **72**, p17
- [2] F. D. Rosi, B. Abeles and R. V. Jensen, *J. Phys. Chem. Solids*, 1959, **10**, p191
- [3] W. M. Yim, E. V. Fitzke and F. D. Rosi, *J. Mat. Sci.*, 1966, **1**, p52
- [4] W.M. Yim and F.D.Rosi, *Solid-State Electron.* 1972, **15**, p1121
- [5] J. P. Fleurial, L. Gailliard, R. Triboulet, H. Scherrer, and S. Scherrer, *J.Phys. Chem. Solids.* 1988, **49**, p1237 and p1249
- [6] K.T. Matsuura, *IEE Japan*, 1987, 107-B (6), p307
- [7] Gao Min and D.M. Rowe, *J.Power Source*, 1992, **38**, p253
- [8] D.M. Rowe and Gao Min, *J. Phys. D: Appl. Phys.*, 1990, **23**, p258
- [9] S. G. K. Williams, Gao Min and D. M. Rowe, *Proc. 10th Int. Conf. Thermoelectrics*, Cardiff, UK, 1991, p74
- [10] Gao Min and D. M. Rowe, CRC Handbook of Thermoelectrics, Ed.Rowe, 1995, CRC Press Inc., Chapter 38
- [11] J. D. Shim and D. B. Hyun, *Proc. 9th Int. Conf. Thermoelectrics*, Pasadena, USA, 1990, p27

# Thermoelectric cooling modules based on bismuth telluride alloys: technique and use in the world patent documentation

B.Sh.Malkovitch

*Engineering & Production Firm "Cryotherm", St.Petersburg, 197348 Russia*

The results of the world patent documentation analysis in the field of the producing and use of the cooling thermoelectric modules are considered.

Thermoelectric cooling modules (TM) have found widespread application in various areas of human endeavour—in engineering, medicine, everyday life. In engineering they are used particularly for cooling of the optical radiation detectors and for controlling the temperature of an integrated circuite package, in medicine—for hypothermia treatment, for treatment of pain, for cooling the pharmaceutical preparations and biological objects, in everyday life—for air conditioning of indoors, for cooling the food-stuffs, etc. A variety of aspects of the practical use and manufacture of TM are embodied in the world patent documentation.

The problems of elaborating of the high efficiency thermoelectric materials, of the technique of their making, of the thermoelement design, of electrical and thermal joining of the adjacent legs of the thermoclements, of TM design, etc. are reflected in the patents related to the production of TM<sup>1</sup>.

The first patent document concerned the elaboration of the most effective n-type thermoelectric material was the Author's certificate of the USSR No. 107420, issued to the collaborators of the Institute of Semiconductors S.S.Sinani, G.V.Kokosh, G.N.Gordyakova, A.N.Shadrina and published in 1957, July (application priority 06.07.56). The authors of the invention elaborated for the negative leg of the thermoelement the composition  $\text{Bi}_2\text{Te}_3 - \text{Bi}_2\text{Se}_3$  with a dopant such as mercury or cadmium chlorides, copper or silver. In accordance with the object of the invention the optimum composition contained 90-70 at. % of bismuth telluride [1]. Unfortunately, no references to these author's certificate are present in the world patent file, while the reference to these authors article, published in the journal, is available [2]. As to the positive leg of the thermoclement, it was prepared from bismuth telluride based materials too, elaborated previously for the thermoelectric generator [3]. However, information about patenting such a material could not be found. But there are many references in the patent file to the patent of Radio Corporation of America [4], relating to similar p-type alloy, e.g.[5].

In the 50-60's there was a large body of research with the purpose to increase the performance of thermoelectric material [6-8] and to improve the technique of its fabricating [9,10]. Detailed description of the ingot preparing methods [6-9], including conditions of its making, sequence of manipulations, the shape and overall the dimensions of ingots, their properties, methods and arrangements for measuring the material parameters [11-14] one may find in patent documents.

Along with the thermoelectric material efficiency, a signifi-

cant aspect of the thermoelements fabricating is the quality of the junction between the legs of thermoclement and bridging members [15-19]. The junction quality must satisfy the special requirements to the technique of fabricating of the thermoelements and first of all to the soldering conditions and to the solders and fusing agents. According to available patent information this problem has attracted considerable interest of variety of companies.

At the same time with the individual thermoelement making, the technique of fabricating of TM was developed. Various methods of TM fabricating, described in a large number of patent documents, come under two groups: 1) fabricating TM with the legs of required length [20-25] and 2) fabricating TM of the sub-unit with the legs longer than required [26-28]. The patents of the first group are concerned with the dismountable matrix comprising the director plates. Furthermore, the bridging elements are solder bonded at both ends in matrix, and then director plates are extracted out. The patents of the second group are concerned with the depositing of legs in matrix and their sealing with the insulating material to obtain the monolithic block, following which this block is extracted from matrix and cut into sub-units of the required length.

The technique of fabricating TM is improved continuously, and companies—manufacturers of TM in a number of countries take a part in this process. An ever increasing number of technical decisions makes it possible, in particular, to mechanize the TM fabricating. Thus, the American company Varo, Inc. elaborated the conveyer assembly process of the TM with the automatic feed, stacking and alignment of TM members and their bonding [29]. The technique of industrial producing of a thermoelectric material [30] with the method of automatic assembly process of TM [31] are suggested in the patents of Japan Komatsu Ltd. The industrial process of TM fabricating was elaborated by French Compagnie Industrielle des Telecommunications CIT-ALCATEL [32].

The multistage TM designs are described in a number of patents. Thus, said Varo, Inc. has patented a mechanical assembly process of two-stage TM, completed by reflow soldering [33]. While the patents of Varo, Inc. are concerned with the mechanization of the TM assembly process [29,33], nevertheless any references to TM use of this company are lacking.

In a number of cases, instead of the traditional pyramid or parallelepiped configuration of the multistage TM, there occurs need to use the multistage thermobattery which configuration depends on the operating conditions of the cooling object. The four-stage thermobattery of the console type configuration [34] provides an example of such a non-standard multistage TM.

As early as 50-60's many companies of the leading countries

<sup>1</sup>Thermoelectric cooling module is an arrangement comprising a set of the thermoelements which junctions of the same type are located in the same plane. The free surfaces of the bridging members are joined in this case with the insulation plate of high thermal conductivity. One plate is in contact with cooling object, and another one with the heat sink.

have been deeply involved in the manufacture technique elaboration of the cooling thermoelements, and later TM. Such companies were Radio Corporation of America, Westinghouse Electric Company, General Motors Company. They possess now a lot of patents concerned TM fabricating technique aspects. Some companies have few such patents, but they are known now as manufacturers of commercially available TM (Marlow Ind., Inc., Borg-Warner Thermoelectrics). In European countries similar developments are involved in Germany (Licentia Patent-Verwaltung GmbH, Siemens AG, Siemens-Schuckert Aktiengesellschaft, etc.), in Great Britain (The General Electric Co., UK Atomic Energy Authority, etc.), in France (Compagnie Industrielle des Telecommunications CIT-ALCATEL, etc.), in USSR (Institute of Semiconductors of the Academy of Sciences of USSR, etc.).

Thermoelectric cooling modules started to use in the developments at the turn of the 60-70's, when they become commercially available. Nowadays, according to the world patent file, the USA companies only manufacture the commercially available TM. Here are these companies: Materials Electronic Products Corp., Trenton, N.Y. (Melcor); Marlow Industries, Inc., Dallas, Tex.; Cambridge Thermoionic Corp., Mass. (Cambion); Midland Ross of Cambridge, Mass.; Borg-Warner Corp., Chicago, Ill.; Thermo-Electric Cooling America Company, Chicago, Ill. The purchasers use the modules of these companies as completed members. It will be noted that some patent information about the use of commercially available TM is reported without any reference to the manufacturer.

Materials Electronic Products Corporation, founded in 1959, is the most important manufacturer of commercially available TM. The first report on utilization of Melcor commercially available TM has been found in the patent of Medical Electroscience Inc. [35]. Regular references to the utilization of the Melcor commercially available TM appeared from the middle 70's, but Melcor patents itself could be detected neither in the USA patent documentation nor in other countries one.

At least two companies-manufacturers mentioned above have their own developments of the arrangements with the utilization of TM. Thus, Marlow Industries, Inc. has patented noiseless refrigerator for hotels (Pat. No. 4644753) and transport self-containing refrigerating unit (Pat. N 4922721); Borg-Warner Corp. has patented downhole refrigerating system for cooling electronic components (Pat. No. 4375157).

There are several patenting directions in the field of thermoelectric cooling with the use of the solid solutions based on bismuth telluride alloys: (1) improvement in thermoelectric materials by impurity doping, (2) optimization of material fabrication conditions, (3) improvement in methods of thermoelement leg fabrication, (4) improvement in solders and fusing agents and optimization of the soldering conditions, (5) improvement in thermoelectric cooler construction, (6) use of TM as additional element in device construction, (7) modernization of device, in which the thermoelectric cooler is used.

The first four directions concerned the technological aspects are classified by the patent headings H01L 35/00-H01L 35/34 of the International Patent Classification (IPC). The fifth direction corresponds to the patent heading F25B 21/02 of IPC. The last two directions related to the improvement in operating characteristics of the arrangements correspond to those headings of IPC, in which the device is classified itself (e.g., a thermoelectric air conditioner used in vehicles is classified by the patent heading B60H 3/00), and in this case the heading F25B 21/02 may be written as the second or the third one.

Further the patents are listed in which companies-

manufacturers of commercially available modules are indicated. The following information is given: assignment of cooler, owner of patent, manufacturer of modules, patent number, International Patent Classification.

1. Apparatus for collecting and cooling blood. Medical Electroscience, Inc. - Melcor. 3 480 015. A61m 1/03; A61f 7/00.
2. Refrigerator boxes for use in mobile installation, such as in campers, trailers and boats. Mobile Metal Products, Inc. - Melcor. 3 821 881. F25B 21/02.
3. Cold slabs used by dentist and dental technicians for facilitate to mixing and storage of certain compounds. Syngnet Optical Co. - Melcor. 3 986 337. F25B 21/02.
4. Compact self-contained thermoelectric refrigerating unit for converting and existing insulated enclosure. L.L.Simms. - Melcor. 4 007 600. F25B 21/02; F25D 3/08.
5. Integrated circuit temperature gradient and moisture regulator. USA as represented by the Secretary of the Navy. - Marlow Ind., Inc. 4 253 515. F25B 29/00; F28F 27/00; H01L 23/02; H02B 1/00.
6. Double-walled vacuum insulated container having an actively refrigerated insulating system for product storage at cryogenic temperatures. Union Carbide Corp. - Melcor, Cambion, Borg-Warner Corp. 4 287 720. F17C 1/00.
7. Beverage heater and cooler. G.R.Keith. - Melcor. 4 384 512. A47f 31/053.
8. Hot/cold socket for package I.C.microprobing. NCR Corp. - Melcor. 4 402 185. F25B 21/02.
9. Cooled garment. K.Lehovec, R.Shuttleworth, Y.A.Bedri. - Borg-Warner Corp., Cambion. 4 470 263. F25B 21/02.
10. Apparatus for hypothermia treatment. Atlantic Richfield Co. - Cambion. 4 483 341. A61F 7/00.
11. Dehumidifier apparatus for disc drivers. Sperry Corp. - Cambion. 4 499 736. F25B 21/02.
12. Apparatus for treatment of pain by frequently alternating temperature stimulation. I.Kissin. - Melcor. 4 585 002. A61B 10/00.
13. Anesthetizing skin. R.F.Perler. - Borg-Warner Co. 4 614 191. A61F 7/00.
14. Noiseless refrigerator for use even in single room sleeping quarters. Marlow Ind., Inc. - Marlow Ind., Inc. 4 644 753. F25B 21/00.
15. Mounting enclosure for disc-drive computer memory device. Allen-Bradley Co., Inc. - Thermo-Electric Cooling America Co. 4 685 303. F25B 21/02; G11B 15/18.
16. Thermally controlled transmit/receive module test apparatus. USA as represented by the Secretary of the Air Force. - Midland Ross Corp. 4 704 872. F25B 21/02.
17. Thermal electric vapor trap arrangement. USA as represented by the US Department of Energy. - Melcor. 4 730 458. F25B 21/02.
18. Cooling and heating purified, filtered or tap water. J.M.Kerner, C.Palmer, P.Toffel. - Marlow Ind., Inc., Midland Ross Corp. 4 744 220; 4 833 888. F25B 21/02.
19. Kidney preservation. D.O.Bauer, N.W.Bauer. - Melcor, Borg-Warner Co. 4 745 759. F25B 21/02.
20. Frost collectors for freezers. Raytheon Co. - Melcor, Borg-Warner Co. 4 764 193. F25B 21/02.
21. Heat exchanger that provides high efficiency of operation. Allied Products Corp. - Melcor. 4 782 664. F25B 21/02
22. Thermoelectric cooling device with the spacer between cold surfaces of adjacent modules (and so as do not) arrange

in a stack. A fluid to be cooled is passed through those spacers separating the cold surfaces. Koslow Technology Corp. - Melcor. 4 829 771. F25B 21/02

23. Cooling optical radiation detector. Microluminetics. - Melcor. 4 833 889. F25B 21/02.

24. Apparatus for controlling the temperature of an integrated circuit package. Texas Instruments, Inc. - Marlow Ind., Inc. 4 848 090. F25B 21/02; H01L 23/28; F25B 29/00.

25. Liquid chiller or countertop cooler for the standard sized plastic water bottles with the capacity of 2.5 gallons. R.S.Bender, L.Pleet. - Melcor. 4 866 945. F25B 21/02.

26. Aquarium cooling to control a temperature. R.Tirano. - Melcor. 4 867 102. A01K 61/00; F25B 21/02.

27. Storing and dispensing of creamers. J.S.Caldarola. - Melcor. 4 891 949. F25B 21/02.

28. Heating and cooling a beverage. Q-Branch Technologies Inc. - Melcor. 4 914 920. F25B 21/02.

29. Transporter unit with communication media environmental storage modules. Marlow Ind., Inc. - Marlow Ind., Inc. 4 922 721. F25B 21/02.

30. Cooling system for wet process stations. R.W.Higgins. - Thermo-Electric Cooling America Co. 5 029 445. F25B 21/02.

31. Cooling of an integrated circuit package. Prime Computer, Inc. - Melcor. 5 040 381. F25B 21/02.

32. Storing and dispensing of food product which can be used in vehicles such as cars, trucks and boats. S.P.Sundhar. - Melcor, Marlow Ind., Inc. 5 042 258. F25B 21/02.

33. Microprocessor controlled fluid circulating system for medical uses. T.Quissenberry. - Melcor. 5 097 829. A61F 7/00; H05B 1/02.

## References

- [1] S. S. Sinani, G. V. Kokosh, G. N. Gordyakova, and A. N. Shadrina. SU Author's certificate No. 107420. July, 1957.
- [2] J. Rupprecht. US Patent No. 3310493. Mar. 21, 1967.
- [3] G. I. Shmelyov. Alloys based on three component compounds for thermoelements. Thesis abstr., 1949.
- [4] N. E. Lindenblad. US Patent No. 2762857. Sept. 11, 1956.
- [5] S. Poganski. US Patent No. 2993080. July 18, 1961. Prior. DE Feb. 3, 1958.
- [6] R. V. Jensen, F. D. Rosi. US Patent No. 2957937. Oct. 25, 1960.
- [7] H. J. Goldsmid, A. R. Sheard. US Patent No. 3017446. Jan. 16, 1962. Prior. GB Dec. 18, 1956.
- [8] F. F. Donahoe. US Patent No. 3208878. Sept. 28, 1965.
- [9] W. Hänlein, H. Schreiner. US Patent No. 3220199. Nov. 30, 1965. Prior. DE Feb. 23, 1961.
- [10] K. P. Stafeev et al. SU Author's certificate No. 534812. Nov. 5, 1976.
- [11] J. S. Lisker. SU Author's certificate No. 186538. Oct. 3, 1966.
- [12] J. C. Bagin, J. P. Sabo. SU Author's certificate No. 196143. May 16, 1967.
- [13] V. I. Tihonov et al. SU Author's certificate No. 716009. Feb. 15, 1980.
- [14] E. M. Lukishker, A. L. Vainer. SU Author's certificate No. 758317. Aug. 23, 1980.
- [15] V. Haba. US Patent No. 3017693. Jan. 23, 1962.
- [16] E. A. Kolenko et al. SU Author's certificate No. 123216. February, 1966.
- [17] E. A. Kolenko et al. SU Author's certificate No. 123395. Oct. 15, 1966.
- [18] V. Haba. US Patent No. 3079455. Feb. 26, 1963.
- [19] T. M. Elfving. US Patent No. 3200600. Aug. 17, 1965.
- [20] G. S. Bird. US Patent No. 3379577. Apr. 23, 1968.
- [21] B. M. Jaremus et al. US Patent No. 3247578. Apr. 26, 1966.
- [22] H. G. Traeger. US Patent No. 3223406. Dec. 14, 1965. Prior. DE May 12, 1962.
- [23] R. Claydon. US Patent No. 2980746. Apr. 18, 1961.
- [24] V. Haba. US Patent No. 3076051. Jan. 29, 1963.
- [25] D. V. Zuev et al. SU Author's certificate No. 546047. Feb. 5, 1977.
- [26] N. P. Danilov. SU Author's certificate No. 199223. July 13, 1967.
- [27] M. E. Alais et al. US Patent No. 3276105. Oct. 4, 1966. Prior. FR Apr. 18, 1961.
- [28] G. E. Hare et al. US Patent No. 3505728. Apr. 14, 1970.
- [29] T. A. Blaske et al. US Patent No. 4493939. Jan. 15, 1985.
- [30] T. Okumura. JP Patent specification No. 63-138789. June 10, 1988.
- [31] A. Okamoto. JP Patent specification No. 1-223781. Sept. 6, 1989.
- [32] M. Alais et al. FR Patent No. 2206034. May 31, 1974.
- [33] T. J. Hendricks. US Patent No. 4687879. Aug. 18, 1987.
- [34] G. F. Boesen. US Patent No. 4375157. Mar. 1, 1983.
- [35] F. A. Gonzalez. US Patent No. 3480015. Nov. 15, 1969.

# The Metallization of the Thermoelement Branches by Ionic Sputtering of the Nickel and Cobalt.

G.D. Kuznetsov, Y.G. Polystanskiy, V.A. Evseev  
State Institute of Steel and Alloys, Moscow, 117936, Russia

Making of effective thermoelectrical devices on the basis of chalcogenydes of tin, lead, bismuth, stibium in considerable degree is connected with elaboration of quality ohmic contacts of metal/semiconductor thermobranches. Obtaining of ohmic contacts on the marked materials of n-type conductivity does not evoke difficulties. Metals in that the work of exit is smaller than electronic affinity of semiconductor should be used for this. The most suitable materials of communication are nickel and cobalt [1].

For the materials of p-type it is not so clear. Nonetheless in both cases the preparation of surface of semiconductor thermoelement in combination with the process of coating of communication layer plays the determining role. As communication layer on the materials both n- and p-types conductivity it is worth while to use the mentioned above materials. Estimation calculations of junction resistance, for example the contact  $Ni - Bi_2Te_3$  p-type conductivity, give the value of  $(3.0 - 3.2) \cdot 10^{-6} \Omega cm^{-2}$  that is quite satisfactory. The predominant mechanism of transfer is thermofield emission.

In this work it is presented the results of metallization of the thermoelement branches on the basis of system  $Bi-Sb-Te-Se$  by nickel and cobalt with the use of combined in indivisible technological cycles of processes of ionic processing of surface of semiconductor and ionic coating of the layer of metal.

As the way of working up of surface and coating the layer it was used abnormal glow discharge on the direct current in environment of argon in the range of pressures  $50-100 Pa$ . The preliminary discharging in the work chamber on the level of  $10^{-3} Pa$  was reached. For the work of the regimes of commutation it was used the models of profile monocrystals, obtained by the directed crystallization. The thickness of branches was  $0.1-0.5 mm$ , the direction of planes of solderness - along the axis of growth. The models after cutting on the electrospark discharge machine were exposed to the polishing on the micropowders of oxide of aluminum (marks M-20 and M-10) with the following electrochemical processing. The structure characteristics of surface of thermobranches and metal layers were investigated with the help of optical and electron microscopy, and composition with methods of electronography and second ion-ionic emission (SIEE) with the magnetic division of secondary ion. The investigations were executed with the help of continuous measurement of intensity of corresponding ionic picks by ionic sputtering of the investigated surface. The electrophysical properties of contact were estimated by the results of measuring of transitional contacting resistance  $R_c$  which was accomplished by two-probing method on the alternating current. The threshold of sensibility was  $10^{-6} \Omega cm^{-2}$  by conductivity of thermoelectric material on the level of  $10^3 \Omega^{-1} cm^{-1}$ .

The mechanical characteristics of computational contacts were estimated by the results of adhesion data, received with the help of explosive machine with the speed of explosion  $50 \mu m / min$ .

For selection of conditions of processing and sputtering of metal layer at first the volt-ampere characteristics of glow discharge applied to used geometry of discharging chamber, materials and environment were taken. The investigations of kinetic of sputtering and precipitation of nickel and cobalt showed that the speed of precipitation was growing both with increase of discharge current ( $I$ ) or current density and tension of discharge combustion that is with increase of discharge specific capacity (Fig. 1).

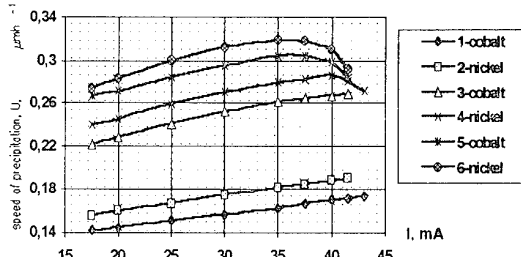


Fig.1 Dependence of speed of precipitation of nickel and cobalt from conditions of glow discharge

It was arranged the regimes in which the reduction of speed of precipitation happened (Fig. 1, curves 4, 5, 6). It can be connected that with increase of ion energy the part of knocked-on atoms increases which energy is sufficiently for the autodespersion of precipitating material that is the process of growing is accompanied by its partial sputtering [2, 3]. The calculation values of coefficient of precipitation are satisfactory conformed with experimental data. For the energy of ions  $600 eV$  the coefficient of sputtering is 1.52 and 1.36 for nickel and cobalt accordingly. The speed of ionic sputtering of semiconductor material changed in limits  $0.05-1.20 \mu m h^{-1}$  depending on composition of the model and parameters of discharge.

Structural and X-ray investigations of metallized thermobranches showed that by the tension of discharge combustion more than  $3 kV$  and density of discharge current more than  $0.7 mA cm^{-2}$  on the surface of metallization layer it is observed the surplus tellurium at the expense of transition of anode material (thermobranch) atoms part in gas phase and the following condensation on the surface of growing layer.

From the analysis of distribution spectrum of secondary ions of metallized thermobranches by the depth of branch with the help of the SIEE method it follows that for the cobalt it is observed more fluent distribution and for the nickel it is marked the sharp decrease of its concentration on the depth of  $400-500 nm$ . Mass-spectrometric analysis of composition and concentration distribution of metals showed the absence of component of thermoelements on the metallized surface. The concentration of tellurium on the distance of  $10-15 nm$  from the surface of thermobranch approximately is in

25-30 time smaller than in volume of thermobranch.

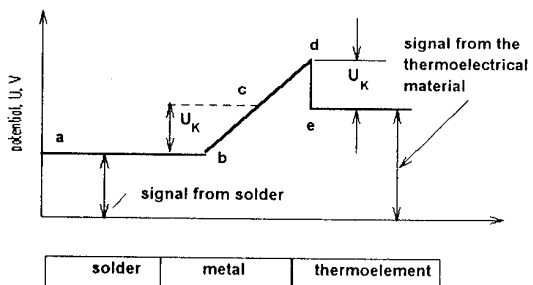


**Fig.2** The character of potential change along the specimen of metallized thermobranch

The character of potential change along the specimen of metallized thermobranch is shown on the fig.2. The section "bd" corresponds to the high-ohm transitional layer, arising in commutation zone, that can be identified with contact resistance. Prepared for the measurement specimen is presented as molding with area of diametrical section  $1 \times 1 \text{ mm}^2$  and length of 10 mm. To the specimen (semiconductor/metal) from both sides it was soldered contacts consisted of solder on the basis of bismuth. The thickness of metal layers was 0,8-1,0  $\mu\text{m}$ .

So the metallization of the thermoelement branches by ionic sputtering in glow discharge, combined with ionic-etching of thermoelement branches surface allow by far to decrease the value of transitional contact resistance. The use of new ionic processes for the receiving of commutational contact to the thermobranch allows to guarantee the value of adhesion on the level of  $50\text{-}80 \text{ kg cm}^{-2}$  for the different investigated semiconductor materials.

#### Literature.

- [1]. Jouravlev V.B., Kovalev A.N., Electric characteristics of contacts of metal-telluride lead, Electronic technic, 1979, ser.6, v.5(130), pp.21-24.
- [2]. Babad-Zachryapyn A.A., Kuznetsov G.D., Radiation-stimulated thermal processing, M., 1982, Energoizdat.
- [3]. Krapuchin V.V., Sokolov I.A., Kuznetsov G.D., Technology of materials of electronic technic, M., 1995, MISiS.

## The Film Structures on the $A^{IV}B^{VI}$ Compounds-base for Thermoelectric Transformers

Y.G. Polystanskiy, G.D. Kuznetsov, V.A. Evseev  
State Institute of Steel and Alloys, Moscow, 117936, Russia

In connection with diminution of electronic apparatus need in small-sized feed sources and measuring transformers of reverse tie feedback system has emerged. With their help it is possible to carry out the reequipment of the measuring apparatus of alternating current on the base of creation of digital apparatus of high accuracy and rapid. Analogous improvement can be reached in other apparatuses - thermosensors and sensitive elements for measurement of pressure, the gas expenditure, humidity and etc.

For the elaboration of the effective thin film thermoelements on the basis of perspective combination  $A^{IV}B^{VI}$  and technological methods of their obtaining with reproducing properties the physicochemical investigations are necessary with the aim of controlling the forming of compositions of assigned composition, doping, adhesion, macrodefects in films. The complex investigation of the properties of thin films  $PbTe$ ,  $PbTe-SnTe$ ,  $GeTe$ , obtained in the process of vacuum evaporation on the dielectric layers (mica-muscovite, sitall, polyamide,  $Al_2O_3$ ).

The method of evaporation of the preliminary doped material was used. The p- and n-type conductivity thin films with the thickness of (0,5-1,0)  $\mu m$  in the charge carriers' concentration range ( $1 \cdot 10^{18} - 1 \cdot 2 \cdot 10^{20}$ )  $cm^{-3}$  were obtained. The technological conditions of obtaining of thin films were worked out. The alloyed additions  $Na$ ,  $I$ ,  $In$ , ushered in initial material were used in obtaining of thin films on the basis of  $PbTe$ .

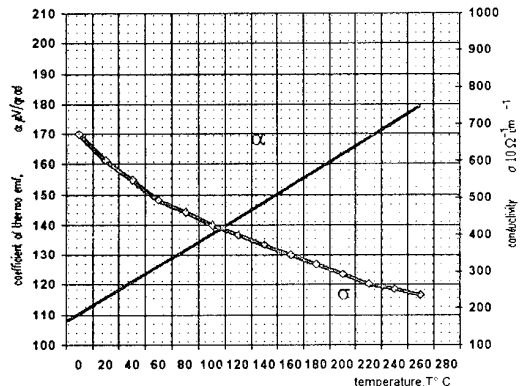


Fig.1 The temperature dependence of thermo emf coefficient and films conductivity of telluride of p-type conductivity lead

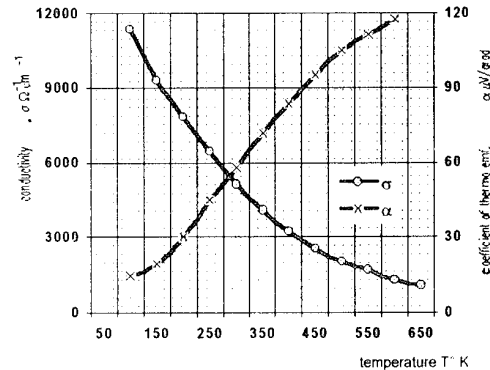


Fig.2 The temperature dependence of thermo emf and conductivity of films  $PbTe$  of n-type conductivity

On the fig. 1,2 it is presented the temperature dependence of the coefficient of thermo-electromotive force and conductivity of the films  $PbTe$  n- and p-type conductivity. From the brought dependencies, it is seen that temperature motion of shown value does not qualitatively differ from the similar dependence for the volume model. Extremely perspective material for use in branches of thermoclement is solid solution on the basis of telluride of lead and tin.

The significance of concentration of the charge carrier in alloys  $Pb_{1-x}Sn_xTe$  can be changed in broad limits by regulation of composition.

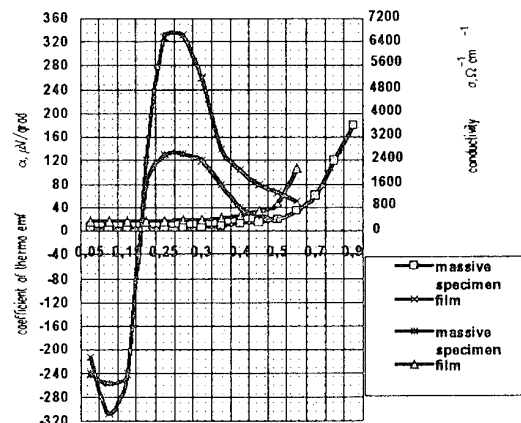


Fig.3 Electrophysical properties of films of solid solutions in dependence from their composition

On the fig.3 it is shown diagram composition-property of films of solid solution  $Pb_{1-x}Sn_xTe$ . As it can be seen from this diagram maximum significance of coefficient of thermo-electromotive force has films with following composition:  $Pb_{0.9}Sn_{0.1}Te$  (n-type conductivity). Inversion of sign of conductivity locates by  $x = 0.2-0.17$ . More

high extreme significance of coefficient of thermoelectromotive force in films shows that their composition is nearer to stoichiometric correlation of components than it is in volume crystal.

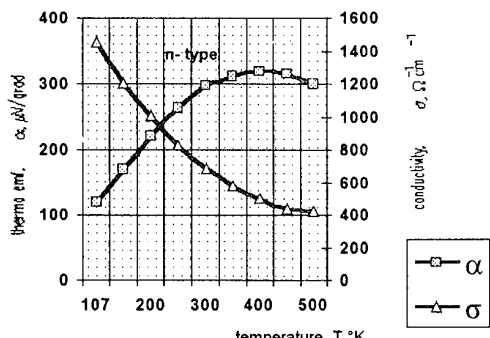
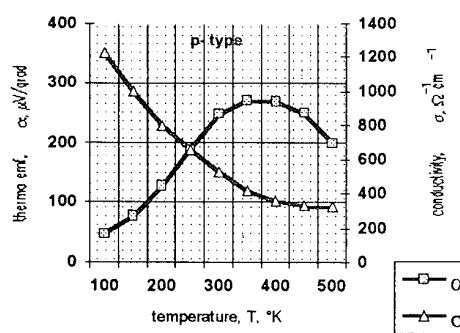


Fig.4 The temperature dependence of thermo emf coefficient and conductivity films of p- and n-type conductivity



On the fig.4 there is presented the temperature dependence of coefficient of thermo electromotive force and conductivity for the thin films of both types of conductivity. For chosen compositions the same regularities of temperature dependence could be observed.

As the effective material for p- branch of film thermoelement it can be taken GeTe, alloyed Bi or In.

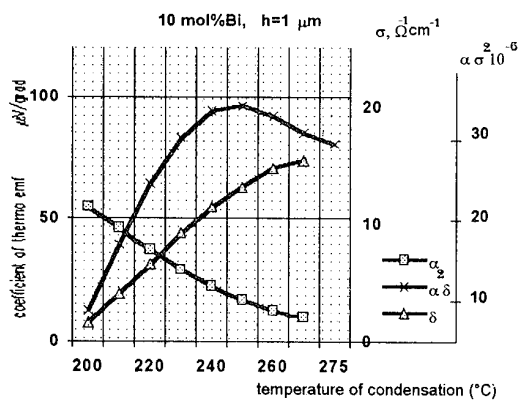


Fig.6 Dependence of thermoelectrical parameters of films from the quantity of bismuth additions

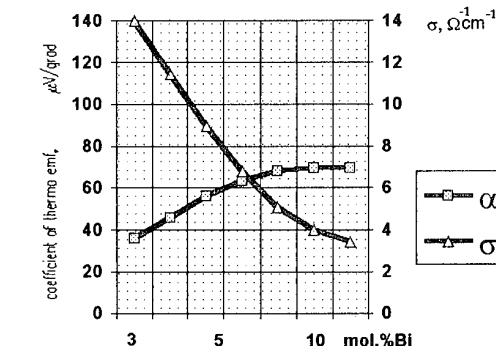


Fig.6 Dependence of thermoelectrical parameters of films from the quantity of bismuth additions

On the fig.5,6 it is shown the electrophysical properties of thin films GeTe in dependence from the contents of doping additions and conditions of their obtaining.

So sufficiently wide set of materials in the state of thin films with different thermoelectric properties and technological conditions of their obtaining can be offered that allows to select the branches of thermoelement for the concrete device.

*PbTe*, alloyed Na (p- type) and I (n- type) are recommended for the film transformer that works in range of temperatures (273-573) K. For the transformer that works in normal conditions, the solid solution  $Pb_{1-x}Sn_xTe$  n- and p- type conductivity of corresponding composition both without preliminary alloying and doped with In. As the positive branch of thermoelement *GeTe* (*Bi*, *In*) characterized by high significance of conductivity is highly prospective.

Elaborated materials in the form of thin films, technological regimes of synthesis of initial substances and processes of obtaining of film structures found practicable use. *PbTe*, doped with indium, (n- type conductivity) and *GeTe*, alloyed by bismuth (p- type conductivity) are used as the branches of thermoelectric differential transformer (TET).

TET is intended for transformation of alternating tension of arbitrary form into direct tension, proportional to midsquare significance of alternating current. Transformer is used in entrance device of digital voltammeter of alternating current. Exit parameters of TET: transformation coefficient is (6-8)  $m\text{ V} \cdot m\text{ W}^{-1}$ , exit resistance is not more than 5,0 kΩ.

The solid solutions of system  $Pb_{1-x}Sn_xTe$  and methods of their obtaining in the form of thin films were used in elaboration and making of film susceptible elements for the registration of thermal streams with intensiveness up to  $1,0 \text{ W/cm}^2$ . The main characteristics of apparatus practically do not depend on the body temperature that allows to use it without second transformation apparatus.

#### Literature

- [1] Pickalev A.P., Polystanskiy Y.G., Jemchugina E.A., The research of kinetic peculiarities of growing of tellurid of load., Electronic technic, Series Materials, 1973, v.4
- [2] Borde, Domimigal. This Doctingr, Fac.Sei., Univ Paris, Papp., CEA ., 1967, #3399, p.88.

[3] Polystanskiy Y.G., Alexandrova E.A., Andreev A.P., Structure and properties of thin films of system  $Pb_{1-x}Sn_xTe$  for the thermoelectrical devices., Electronic technic, Series Materials, 1984, v.2, pp.76-78.

[4] Komarov V.S., Andreev A.P., Polystanskiy Y.G., Turina G.N., Peculiarities of behavior of bismuth in thin films of telluride of germanium., Reports of A.S. BSSR, Minsk, 1988, v. XXXII, #1, pp. 39-42.

## INVESTIGATION OF ENERGY SPECTRUM AND PROPERTIES OF LEAD CHALCOGENIDES IMPLANTED BY OXYGEN

A.N.Veis , N.A.Suvorova

*St. Petersburg State Technical University, 195251, Russia*

In this paper the total number of optical properties of monocrystalline and polycrystalline (pressed) samples of PbSe implanted with oxygen ions and annealed in vacuum for an hour at  $T=300^\circ\text{C}$  has been investigated. It was shown that the oxygen forms the energy level which lays in valence band in all lead chalcogenides with the energy level position  $0.18 \pm 0.02\text{ eV}$ ;  $0.16 \pm 0.02\text{ eV}$  and  $0.145 \pm 0.02\text{ eV}$  at  $T=300\text{K}$  in PbTe, PbS and PbSe, respectively. The long-explored level connected with chalcogen vacancy was revealed in the valence band along with feature which can be connected with oxygen action. This result testifies that the oxygen in lead chalcogenid exhibits acceptor properties compensated by chalcogen vacancy.

### Introduction

Annealing of lead chalcogenides in oxygen or air atmosphere known as "activation" is being used for a long time to create photosensitive films on basis of lead chalcogenides [1-3]. That is why many attempts have been made to study the oxygen action features and the extent of oxygen influence on lead chalcogenides energy spectrum. In most causes, objects of such investigations were polycrystalline of lead sulphide. It was revealed that oxygen implanted in films occupied chalcogen vacancy ( $V_{ch}$ ). This fact made it possible to assume that hole conductivity type in activated films was caused by lead vacancies. Another model associates hole conductivity type with action of oxygen as acceptor

Different effect investigated (mainly photoelectrical ones) allowed to assume the existence of two deep levels in energy gap: recombination and adherence ones[1-3].

Assumption that these levels are associated with intercrystalline layers, along which the current flows in activated films, seems to be the most reasonable. Otherwise if the both levels associate with oxygen action , the appearance of two deep levels in narrow gap can not be explained.

Thus, numerous experimental investigations of activated polycrystalline PbS films did not allow to define exactly both mechanism of oxygen action and energy spectrum of impurity in lead chalcogenides . That is the reason of our decision to continue the study of this problem in the present paper. However, instead of annealing in air. or oxygen atmosphere we chose ion implantation as method of doping. The advantage of this method consist in possibility to introduce various impurities and intrinsic defects with high degree of layer homogeneity.

### Experimental

As object of investigation we used monocrystalline and polycrystalline films of lead chalcogenides with various composition and quantity of doping impurities in initial mixture. Doping of starting samples was used to control the chalcogenide vacancy concentration  $V_{ch}$  . The increase of vacancy concentration was obtained by adding acceptor impurities Tl and Na, superstoichiometry excess lead  $\text{Pb}_{ex}$  and tin in small quantities (less 2 atomic %) into the initial mixture. The decrease was achieved either by deviation of stoichiometry

up to the highest hole concentration available for this method of doping , or by introduction Tl and Na into initial mixture.

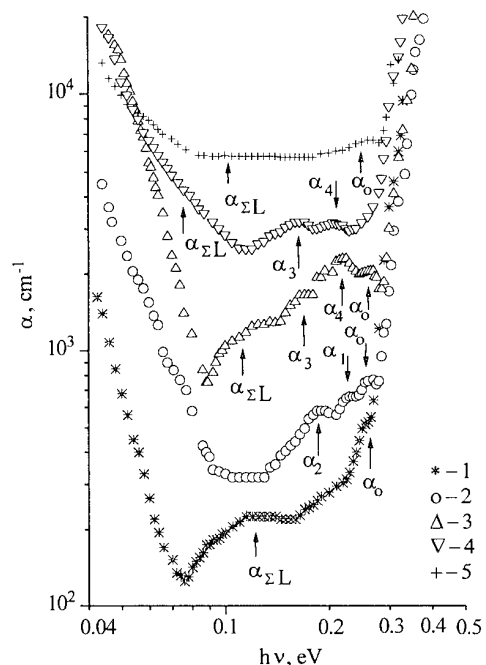


Fig.1 Spectral dependences  $\alpha(hv)$  in PbTe: Tl, Te<sub>ex</sub> (1-3,5) and p-PbTe, doping by deviation of stoichiometry (4) at  $T=300\text{K}$ .

1 - initial samples

2-4 - implanted O<sup>+</sup> samples

5 - implanted Zn<sup>+</sup> samples.

Post implantation annealing:

2 - without annealing

3-5 - with annealing.

$N_o \times 10^{16} \text{ cm}^{-2}$ : 1 - 0; 2 - 1.85; 3,4 - 3.7; 5 - 0.185.

$\alpha$  magnitudes were multiplied by 2, 3, 10 and 25 for curves 2, 3, 4 and 5, respectively.

The process of O<sup>+</sup> implantation was carried out into a previously prepared optical-grade surface. The implanted impurity doses  $N_o$  were varied in the range (  $1.25-3.70 \times 10^{16} \text{ cm}^{-2}$  ). Post-implantation annealing was performed in vacuum for an hour at  $T=300^\circ\text{C}$ . The thickness of implanted samples was reduced to  $d=3-6\text{mkm}$  by mechanical treatment of the opposite (unimplanted) side. Using thus prepared samples the

sign of thermoelectrical power coefficient  $S$ , and also optical absorption coefficient  $\alpha(hv)$  and reflection  $R(\lambda)$  spectra were measured. The optical spectra were investigated in all stages of doping and annealing.

### Results and discussion

Some experimental results obtained on PbTe, PbSe and PbS are shown in Fig.1,2. The spectra  $\alpha(hv)$  of the absorption coefficient of the initially p-type samples (Fig.1,2) are typical and have three singularities: a component  $\alpha_{\Sigma L}$  due to optical transitions of electrons between inequivalent extrema of a valence band ( $L_6^+$  and  $\Sigma_5$ ), a band  $\alpha_0$  associated with tellurium (in PbTe: Tl, Te<sub>ex</sub> samples) and a band  $\alpha_4$  associated with V<sub>ch</sub> (in lead chalcogenides, doped with Tl or Na and Pb<sub>ex</sub> or in Pb<sub>1-x</sub>Sn<sub>x</sub>Se(S)  $x \leq 0.05$ ). The absence of bands  $\alpha_4$  in PbTe: Tl, Te<sub>ex</sub> implies absence of strong self-compensation of tellurium acceptor action by chalcogen vacancies. The O<sup>+</sup> implantation was accompanied by inversion of conductivity type p-n. It is confirmed not only by change of sign  $S$  but by spectra  $\alpha(hv)$  as well. In these spectra (Fig.1, curve 2) the characteristic bell-shaped quasilocal bands of additional absorption associated with singlet  $\alpha_1$  and doublet  $\alpha_2$  terms of V<sub>ch</sub> [4] are clearly observed. The contribution of an unimplanted part of samples is presented by the tellurium bands  $\alpha_0$ .

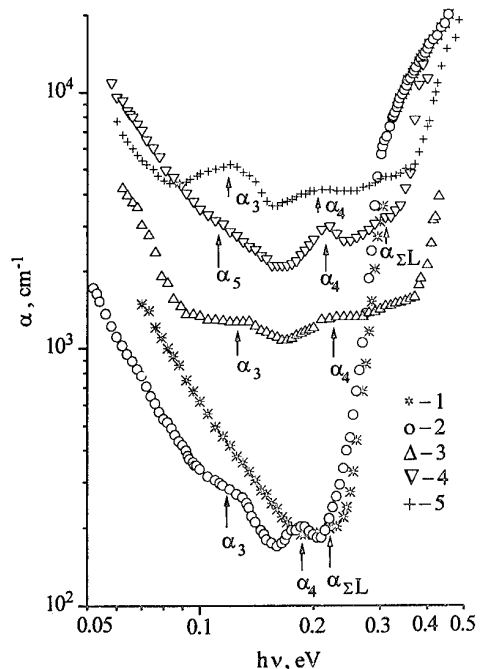


Fig.2 Spectral dependencies  $\alpha(hv)$  in PbSe (1, 2), PbS (3) and  $Pb_{0.95}Sn_{0.05}S$  (4, 5) at  $T=300K$ .

1, 4 - initial samples

2, 3, 5 - implanted O<sup>+</sup> samples ( $N_o = 1.25 \times 10^{16} \text{ cm}^{-2}$ ) and annealed in vacuum.

$\alpha$  magnitudes were multiplied by 2 for curve 3 and by 4 for curves 4 and 5.

It is interesting to note that the intensity of  $\alpha_1$  and  $\alpha_2$  bands associated with V<sub>ch</sub> in O<sup>+</sup> implanted but not annealed

samples of lead chalcogenides was found to be small, considerably less than that in PbTe(S): Zn<sup>+</sup> (Ar<sup>+</sup>) [4]. It means that the oxygen implantation does not allow to create considerable concentrations of intrinsic defects in lead chalcogenides, which considerably exceeds  $10^{19} \text{ cm}^{-3}$ .

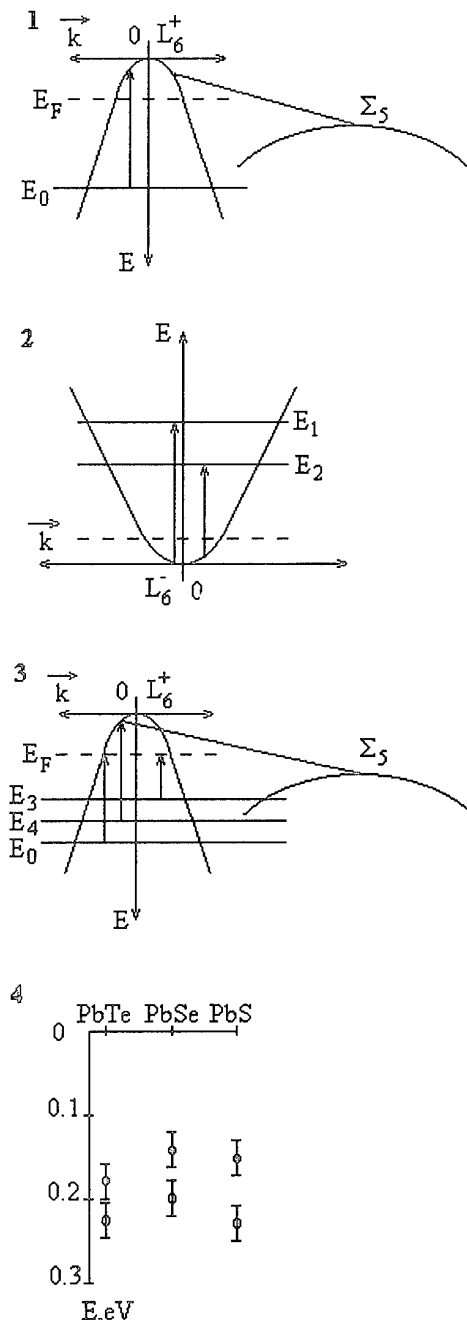


Fig.3 Energy scheme of PbTe: Tl, Te<sub>ex</sub> in initial state (1), after ion implantation before (2) and after annealing (3) in vacuum. The arrows identify the observed optical transitions due to appearance of additional absorption bands in optical spectra. The optical charge transfer energy of O<sup>+</sup> and V<sub>ch</sub> quasilocal centers in lead chalcogenides at  $T=300K$  (4).

The annealing of samples was accompanied by the inversion of conductivity type  $n \rightarrow p$ . In this case, such bands  $\alpha_4$  and new bell-shaped singularities  $\alpha_3$  appear in spectra  $\alpha(hv)$  of all samples. One of the bands studied above, namely  $\alpha_4$ , was observed in numerous experiments earlier (for example [5,6]), the other ( $\alpha_3$ ) has not analogues in literature. It points to that the new quasilocal levels  $E_3$  exist in implanted and annealed samples. These levels possibly correspond to oxygen. The increase of  $\alpha_3$  bands intensity depends on rise of implanted impurities dose and  $V_{ch}$  concentration in initial mixture (Fig.1,2) and this fact confirms proposed assumption. Such assumption is consistent with existing model in which oxygen occupies the chalcogen lattice sites. The only unusual feature can be noted in experimental data. All spectra  $\alpha(hv)$  have both components  $\alpha_3$  and components  $\alpha_4$ , associated with  $V_{ch}$ . The intensity of bands  $\alpha_4$  increases after implantation and annealing in samples with elevated  $V_{ch}$  concentration. As far as is known [7], the vacuum annealing with such regimes usually tends to eliminate the radiation point defects. This effect was observed in present work in investigation of p-PbTe implanted with  $Zn^+$  and annealed in vacuum for an hour at  $T=300^\circ C$  (Fig.1, curve 5). However annealing of  $O^+$  implanted samples of lead chalcogenides did not eliminate the intrinsic defects. This fact is the evidence that oxygen has acceptor action which is compensated by chalcogen vacancy.

The energy position of levels associated with bell shaped singularities was determined using the method given in Ref.4. The results were united in Fig.3. Notice that the energy  $E_4$  magnitudes in studied samples agree with literature data [6]. The energy  $E_4$  magnitude decreases with reduction of

temperature to 90K (the rate of reduction is close to  $dE_4/dT$  [6]).

#### References

- [1]. R.H.Bube, Photoconductivity of solids, N.Y.-London, 1960, 558p.
- [2]. L.N.Neustroev and V.V.Osipov, About the flow of current and photocurrent in polycrystals PbS, Fiz.Tech.Poluprovodn., 1984, v.18, No.2, pp.359-362.
- [3]. L.N.Neustroev and V.V.Osipov, About physical property theory of polycrystalline films like PbS. The model, conductivity and Hall effect , Fiz.Tech.Poluprovodn., 1986, v.20, No.1, pp.55-65.
- [4]. A.N. Veis, A.Yu. Rudanov and N.A.Suvorova, Energy spectrum of PbTe:Zn<sup>+</sup> deduced from optical absorption data, Fiz.Tech.Poluprovodn., 1993, v.27, No.4, pp.701-707.
- [5]. A.N. Veis and N.A. Suvorova, Energy spectrum of  $Pb_{0.995-y}Sn_{0.005}Na_ySe$  deduced from optical absorption data, Fiz.Tech.Poluprovodn., 1995, v.29, No.2, pp.278-285.
- [6]. A.N. Veis, V.I.Kaidanov and R.Yu.Krupitskaya, Resonance levels of strong compensation p-PbTe deduced from optical absorption data, Fiz.Tech.Poluprovodn., 1989, v.23, No.1, pp.185-186.
- [7]. L.Palmethofer, Ion implantation in IV-VI semiconductors, Appl.Phys. A, 1984, v.34, pp.139-153.

# THERMOELECTRIC PROPERTIES OF PbTe THIN FILMS:

## Dependence from surface layer conductance

Yu.A. Boikov, V.A. Danilov, O.S. Gribanova, I.M. Derjagina

*A.F. Ioffe Physical-Technical Institute, St.Petersburg, Russia.*

Lead telluride ( $PbTe$ ) thin films are attractive for applications in thermoelectric micro generators due to high values of the product of an electrical conductivity  $\sigma$  by thermoelectric power  $\alpha$ . Thin  $PbTe$  film were grown by conventional evaporation at the surface of mica substrate. Hall coefficient  $R_x$ , electrical conductivity  $\sigma$  and thermoelectric power  $\alpha$  of the films were measured immediately after film formation, during heat treatment, cooling and the pressure increase in the growth chamber. Structure and phase composition of the film were controlled by X-ray. The film morphology, density of a stable nucleuses and features of coalescence were studied be optical and electron microscopy.  $PbTe$  films were polycrystalline with well defined orientation of the grains - (100) or (111)  $PbTe \parallel (0001)$ mica, the second one was preferential. A carrier concatenation in the surface layer of the  $PbTe$  film was essentially dependent from preparation conditions.  $R_x$ ,  $\alpha$  and  $\sigma$  changed dramatically during increase of the pressure in the growth chamber due to oxygen molecules adsorption at the surface of the film. High anizotropy of the thermoelectric power was detected for the  $PbTe$  films when the surface layer had inverse conductance. The difference between  $\alpha$  measured in the plane of the substrate and along the normal to that was up to  $200\mu V/K$ .

Thin films n-  $PbTe$  have the high values of  $\alpha^2 \cdot \sigma$  at  $T=300K$ . This fact is promising in using these films in miniature thermoelectric generators and microcoolers.

The processes occurred on free surfaces have the substantial influence on the electrophysical properties on the films  $PbTe$ . The film properties depend on their internal structure also. The type of structure is defined by the type of a substrate (orienting or nonorienting) and the conditions of a deposition (the temperature of a substrate and crucible, etc.).

The films with a thickness of  $0.45\mu m$  were prepared using a method of the open crucible deposition in a vacuum  $1 \cdot 10^{-6}$  Torr. The fresh sample of mica "muskovit" was used as a substrate. The temperature during a condensation was equal to  $445 \pm 5K$ . After a deposition some films were subjected to a heat treatment at  $T=600 \pm 5K$  in vacuum during 30 minutes.

For nucleus forming at the initial stage of condensation of the  $PbTe$  layer two preferential orientations were substantial - (100) and (111)  $\parallel (0001)$  of mica such that the latter was the main one. While the mass of condensed substance increased the coalition of the separate nucleus occurred and their density decreased in 3-5 times. Fig.1 (a, b) shows the nucleus of  $PbTe$  before the coalition started (a) and during the coalition (b). Fig.1 (c) shows the surface morphology of the  $PbTe$  film. Fig.2 presents the diffraction image ( $\Theta - 2\Theta$ ) for the  $PbTe$  film on the (0001) mica. The parameter of a lattice is close to the corresponding parameters of the original material. The insert on the Fig.2 shows the (222) reflex of  $PbTe$ . This reflex is narrow,  $CuK \alpha_{1,2}$  is clearly distinguished, which implies the perfect structure of a film.

For studies of the electrophysical properties of films the same camera was used as for the deposition. These measurements were taken on the freshly made films, during the process of a heat treatment in vacuum and under increasing pressure in the camera up to 760 Torr. Fig.3 shows the obtained data for  $\alpha$  and  $\rho = \sigma^{-1}$ .

The obtained plots can interpreted in terms of two-layer model. A film is consisted of two layers. Each layer is characterized by its own set of electrophysical parameters. Fig.4 schematically shows such film:  $\sigma_s$ ,  $\alpha_s$ ,  $R_s$ ,  $n_s$  are electrical conductivity, thermopower, the Hall coefficient and the

concentration of carriers, correspondingly in the surface layer  $d_1 = L \ll d$ , and  $\sigma_v$ ,  $\alpha_v$ ,  $R_v$ ,  $n_v$  - are electrical conductivity, thermopower, the Hall coefficient and the concentration of carriers, correspondingly in the whole volume of the film  $d_2 = d - L$ . The total electrical conductivity and thermopower may be represented as follows:

$$\sigma = \rho^{-1} = \sigma_v + (\sigma_s - \sigma_v) \frac{L}{d} = \frac{\sigma_s L + \sigma_v(d - L)}{d} \quad (1)$$

$$\alpha = \alpha_v + (\alpha_s + \alpha_v) \frac{L \cdot \sigma_s}{d} \rho \quad (2)$$

where  $\sigma$  from (1).

Fig.3 shows the dependence of the thermopower coefficient for the freshly deposited n- $PbTe$  film when a pressure increased from  $10^{-6}$  to 750 Torr. The increasing of  $\alpha$  at the initial moment (the part AB) is due to the increasing of the absolute value of  $\alpha_s$  because of the decreasing of the concentration of electrons  $n_s$  in the surface layer. The decreasing of  $n_s$  is due to neutralization of the surface vacancies of  $Te$  by oxygen which has the donor properties in  $PbTe$  and to localization of electrons on the centers filled with an oxygen [1].

From the equation (2) follows that the changes in  $\alpha$  which are due to the decreasing of the concentration of electrons in the surface layer can be estimated by the following relationship:

$$\Delta\alpha = \alpha - \alpha_v \approx \frac{k}{e} \frac{\ln \frac{n_s}{n_v}}{[L + \frac{n_v}{n_c}(d - L)]L_{-1}} \quad (3)$$

This relationship is true in conditions of degenerative electron gas. A concentration of electrons in investigated freshly deposited films n- $PbTe$  was  $5 \cdot 10^{17} cm^3$  at the temperature  $T=300K$  which is follows from the data on the Hall coefficients. Figure shows calculated data for  $\alpha$  and  $\rho$  when the ratio  $n_v/n_s$  increased from 0.2 to 1.0 (curve 2) derived using relationships (2) and (3). From the comparisons of the experimental data

and calculated results it follows that the increasing of  $\alpha$  on  $50 - 60 \mu\text{V/K}$  is only possible if the ratio  $n_v/n_s$  had a value  $0.2 - 0.3$  before the pressure increasing in camera which means that the surface layer of the freshly deposited films  $PbTe$  formed on the heated substrates ( $T > 540\text{K}$ ) is enriched by electrons. The growth of  $\alpha_s$  is stopped when nonground carriers begin to substantial influence on the conductivity of the surface layer.  $\alpha_s$  is positive when near a surface of a film the layer with the inverse (p-type) conductivity is formed. The increasing of  $\sigma_s$  leads to the decreasing of  $\alpha$  and  $\rho$  according to (2) and (3) (the part CD on the plot).

The heat treatment of films in vacuum also leads to an enrichment by electrons of a surface layer of the films  $A^{IV}B^{VI}$ . This fact could be demonstrated by the data on a thermopower coefficient during the heat treatment in vacuum at the temperature  $540\text{ K}$  during  $120\text{ min}$ . During the heat treatment in vacuum the surface layer is enriched by a metal due to re-evaporation of  $Te$  which cause the increase of electron conductivity. At the beginning of  $\alpha$  measurements ( $\rho = 0.6\Omega \cdot cm$ , Fig.3) the surface layer had an electron conductivity, while the duration of heat treatment increased the product  $\sigma_s \cdot L$  increased monotonically. The decreasing of  $\alpha$  and increasing of  $\rho$  at the initial moment (part EP) indicates that in the course of heat treatment the increasing of a surface layer conductivity is accompanied by the decreasing of  $\sigma$  due to decreasing of a concentration and mobility of holes in the film volume. The decreasing of a concentration of holes in the film volume is caused by the increasing of a concentration of  $Te$  vacancies due to a diffusion towards a free surface.

The results obtained indicate the substantial dependence of the thermopower of films  $PbTe$  on a concentration and mobility of the charge carriers in the surface layer.

Creation and investigation of films having anisotropic thermopower is a matter of interest due to a development of rapid thermoelectric converters. n- and p- $PbTe$  films having nonuniform concentration of carriers could be used in the sensitive elements of anisotropic detectors of a heat flux. Longitudinal thermopower  $\epsilon$  appearing in a film thermoelectric system under conditions where temperature gradient is normal to a substrate plane could be represented by the following expression [2]

$$\epsilon \sim (\alpha_x \kappa_y - \alpha_y \kappa_x) \sin 2\varphi \quad (4)$$

where  $\alpha_x$ ,  $\alpha_y$ ,  $\kappa_x$ ,  $\kappa_y$  are components of thermopower and thermoconductivity tensors,  $\varphi$  is an angle between the substrate plane and the preferred cristallographic direction in a film. A necessary condition for anysotropic converters are being highly sensitive is a substantial anysotropy of thermoelectric parameters and an optimal angle  $\varphi$  as follows from (4). The anysotropy of a thermopower  $\Delta\alpha = \alpha_x - \alpha_y$  may be due to the characteristics of the initial material, the properties of a crystallic structure of formed layers, presence of concentrational inhomogeneities [3], etc.

One of the examples of inhomogeneous system is a film the surface layer of which has inverse conductivity. If the specific thermoconductivity is uniform over all film volume then  $\alpha$  measured along "x" and "y" could be represented by

$$\alpha_x = \frac{\alpha_s \sigma_s d_s - \alpha_v \sigma_v d_v}{\sigma_s d_s + \sigma_v d_v} \quad (5)$$

$$\alpha_y = \frac{\alpha_s d_s - \alpha_v d_v}{d_s + d_v} \quad (6)$$

If the thickness of a surface layer is significantly smaller than the thickness of a film ( $d_s \ll d_v$ ) then from (5) and (6) follows

$$\Delta\alpha = |(\alpha_v - \alpha_s) \cdot (\sigma_s - \sigma_v) \frac{d_s}{\sigma \cdot d}| \quad (7)$$

$$\text{where } d \cdot \sigma = \sigma_s d_s + \sigma_v d_v, d = d_s + d_v.$$

In the formed films due to a deviation from stoichiometry we changed a concentration of the charge carriers in a wide range varying the difference of temperatures of sublimation of a source material and condensation of vapor phase on a substrate. The freshly made condensates were subjected to a heat treatment in vacuum in order to form a  $PbTe$  layer on a film surface. In the course of heat treatment the surface layer and parts which were close to the crystallite borders were  $Te$  depleted due to its reevaporation [4]. Because of the surplus of  $Pb$  in  $PbTe$  possesing a donor activity, the conductivity of a surface layer becomes electronic after the heat treatment and the areas near the crystallite borders depleted the main carriers. In order to form a layer with the p-type conductivity in a surface layer of the  $PbTe$  films condensates were exposed to air during 10 days under room temperature.

As follows from the data on a Hall coefficient for the freshly made films a concentration of charge carriers  $n$  didn't exceed  $5 \cdot 10^{18} \text{ cm}^{-3}$  and their Hall mobility were less than 80 % from the corresponding values for monocrystals  $PbTe$ . As a lattice thermal conductivity of  $PbTe$  is isotropic and doesn't depend on a concentration of charge carriers for  $n < 5 \cdot 10^{18} \text{ cm}^{-3}$  and a contribution of charge carriers into heat transport is small we can assume that  $\kappa_s = \kappa_v$ . The changings of electrophysical parameters of the  $PbTe$  films during a process of formation of a layer with the inverse conductivity were studied by authors in [5,6]. In the films n- $PbTe$  under conditions of an absorption of the oxygen molecules on their free surface a thickness of the surface layer with the inverse conductivity is of the same order of magnitude as a Debay length of shielding which is much smaller than  $d$ . A type of temperatures dependencies of under conditions of impure conductivity also points to the small values of  $d_s$ .

Measured on the n- $PbTe$  films having a surface layer with a p-type conductivity,  $\Delta\alpha$  occurred to be close to 0. As follows from the data (see Fig.5) for the studied layers the electrical conductivity and a thermopower coefficient dependences on temperature were characteristic to n- $PbTe$  material. It means that electrophysical properties of these films under  $T < 300\text{K}$  were determined by parameters of a layer with the n-type conductivity. Under conditions  $\sigma_s d_s \ll \sigma_v d_v \approx \sigma d$  and  $(\sigma_s \sigma_v) d_s \ll \sigma d$ , the  $\Delta\alpha$  values should be close to 0 which is supported by the experimental data. The  $\Delta\alpha$  value measured on the p- $PbTe$  films having a surface layer with a n-type conductivity reached  $200 \mu\text{V/K}$ . Fig.6 shows the dependencies of  $\alpha$  and  $\sigma$  for the corresponding p- $PbTe$  film. The areas closed to the crystallite borders in the layer with p-type conductivity are lack of  $Te$  and present itself the potential barriers for the main carriers. That is why the increase of electrical conductivity with the increase of temperature is observed for  $T < 300\text{K}$ .

$$\sigma_v \approx \sigma_0 \cdot \exp \left( \frac{-e\varphi}{kT} \right) \quad (8)$$

where  $\varphi$  - the height of the potential barriers on the crystallite borders.

Scattering of holes on potential barriers decreases the conductivity of layer with the p-type conductivity which leads to the increasing of the relative contribution of a surface layer into film's electrical conductivity. While the temperature decreases this contribution increases. The areas contiguous to the borders of grains are enriched by  $Pb$  and don't have strong influence on the mobility of electrons. The increasing contribution of a surface layer having n-type conductivity in films p- $PbTe$  with a decreasing of temperature can explain the high relative values of the derivative  $d\alpha/d$  for  $T < 300K$  as well as the changing of the sign of  $\alpha$  and a type of temperatures dependence of  $\sigma$  for  $T \approx 240K$ .

Thus, due to the high values  $\sigma_s$  comparing to  $\sigma_v$ , the product  $(\sigma_s - \sigma_v) \cdot d$  is comparable to  $\sigma \cdot d$  already for  $T \approx 300 K$ . Because the difference  $(\alpha_v - \alpha_s)$  was in the range  $500 \div 700 \mu V/K$  the value reached several hundred microVolts/degree according to (5).

The results obtained imply a substantial dependence of electrophysical properties of thin films  $PbTe$  on the processes taking place on their free surface. Films  $PbTe$  having inhomogeneous concentration may possess a pronounced anisotropy of thermoelectric parameters.

As it was mentioned above, for a creation of the high sensitive anisotropic film converters an optimal orientation of axes "x" and "y" in a layer of a thermoelectrical material with a reference to the plane of thermal detector has the basic significance. Grains on the free surface have an orientation (100) and appeared as the tetrahedral peaks [7] (see Fig.1 a, b). This type of a surface of the growth of  $PbTe$  films enhance a formation of anisotropic film structures having necessary orientation. The main difficulty here is the creation of a different concentration of the charge carriers on the opposite sides of grains.

## References

- [1] Bykova T.G. In: Electronic processes on a surface and in the monocrystalline layers of semiconductors. Novosibirsk: 1967, P.181-187.
- [2] Pilat I.M., Belikov A.B., Kazanskaj L.L., Asheyllov A.A., Sov. Phys.T.S., 1976 ,V 10, N 5, P. 1019-1021.
- [3] Babin V.P., Gydkina T.S., Dashevskyi Z.M., Sov. Phys. T. S., 1974, V 8, N 4, P 748-753.
- [4] Boikov Yu.A., Kutasov V.A., Sov. Phys. S.S., 1987, V 29,N 5, P 1604-1606.
- [5] Boikov Yu.A., Danilov V.A., Kutasov V.A., Sov. Phys. S.S., 1985, V 27, N 11, P 3473-3476.
- [6] Boikov Yu.A., Danilov V.A., Kutasov V.A., Sov. Phys. S.S., 1987, V 29, N12, P 3688-3691.
- [7] Egerton R.F. ,Phil.Mag., 1969, v 20, N165, p 547-561.

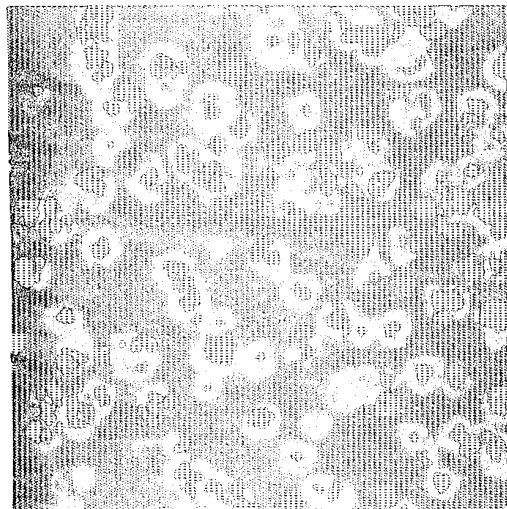


Figure 1: (a)  $PbTe$  grains before coalescence

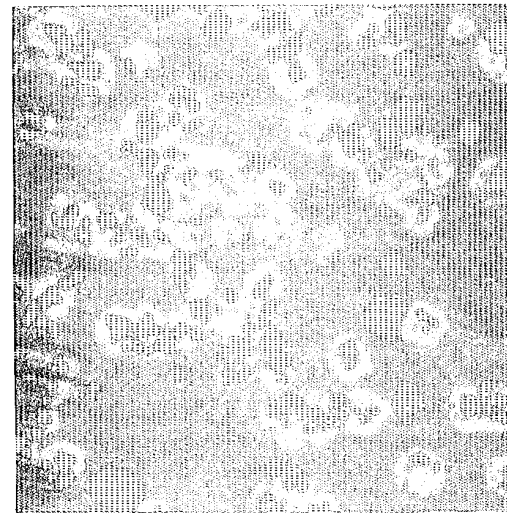


Figure 1: (b)  $PbTe$  grains during coalescence.

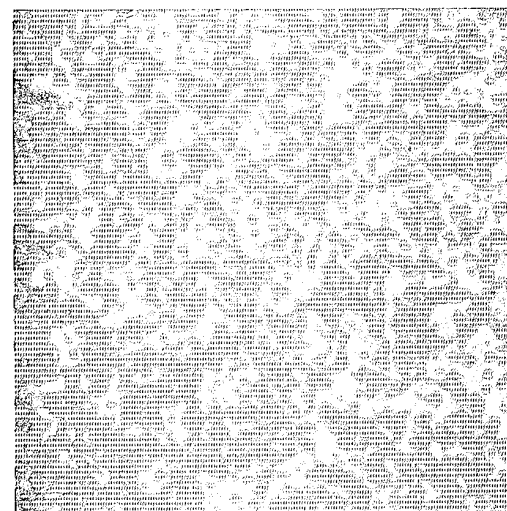


Figure 1: (c) Morphology of a surface of formed  $PbTe$  films.

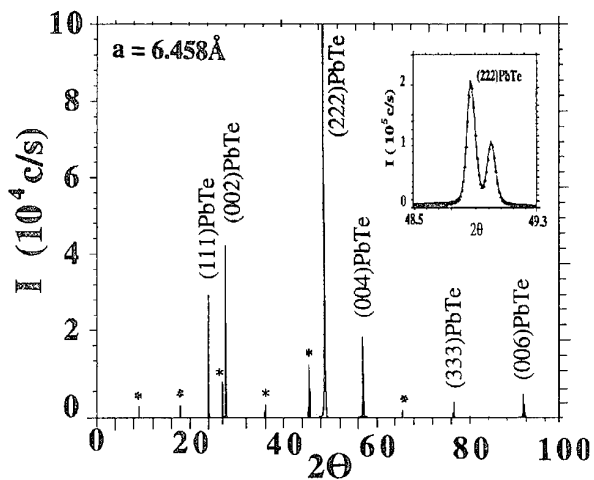


Figure 2: Diffractogramma ( $\Theta - 2\Theta$ ) for the  $PbTe$  film on the (0001) mica. On insert : (222) reflex  $PbTe$ .

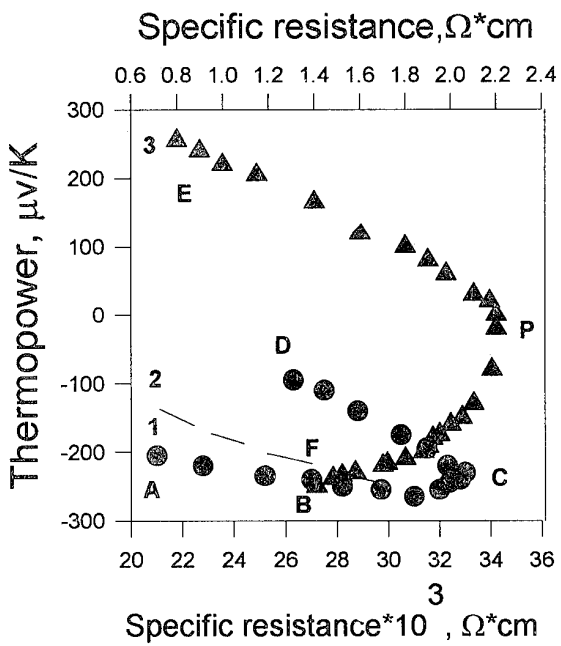


Figure 3: Experimental data for  $\alpha$  and  $\rho = \sigma^{-1}$ .

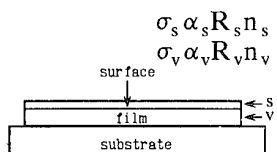
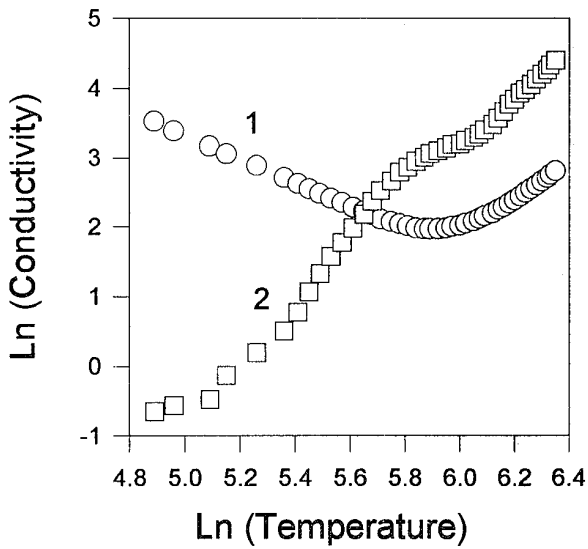
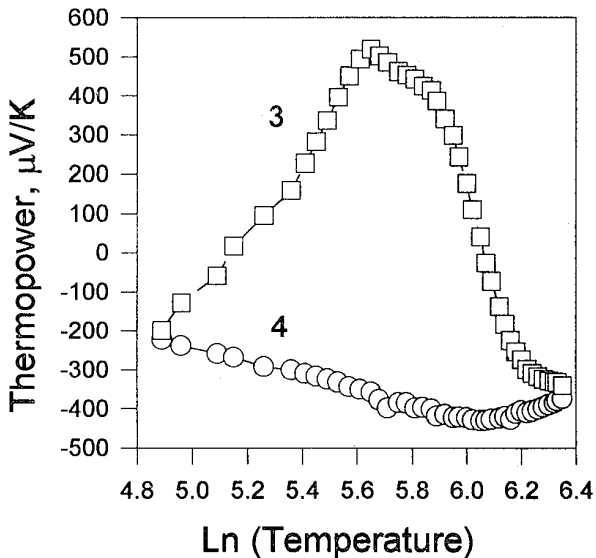


Figure 4: A film consisted of two layers. Each layer is characterised by its own set of electrical parameters.



a)



b)

Figure 5: The temperature dependence of an electric conductivity and a thermopower for  $PbTe$  films having n-type (1,4) and p-type (2,3) conductivity in the whole volume and surface layer with inverse conductivity.

## ELECTRICAL CONTACT FOR GALENA THERMOELEMENTS

Aloke Kumar Das<sup>1</sup>, H. N. Acharya<sup>1</sup>, R. N. P. Choudhary<sup>1</sup>, and Shuchitangshu Chatterjee<sup>2</sup>

<sup>1</sup>*Thermo-electric Lab, Dept. of Physics & Meteorology, Indian Institute of Technology,  
Kharagpur-721 302, India. Phone - 03222-2221-24/5917. Fax - 91-3222-2303.*

<sup>2</sup>*R&D Division, Mecan., (India) Ltd., Ranchi - 834 002, India.  
Phone - (0651) 501651, Fax. - 0651-502214/502189/501054.*

### Abstract

Thermoelectric generator (TEG) - a non - conventional source of energy today available in the market are generally made from high purity expensive materials such as PbTe, Bi<sub>2</sub>Te<sub>3</sub> etc. For wide industrial and socio-economic applications it is essential to have low cost TEG. In this attempt we have tried to fabricate TEG from galena ores(rich in PbS). Though its figure of merit is low ( $Z \sim 0.6 \times 10^3$  /deg.) its occurrence in nature prove that it can be used as a low cost TEG while has some unique applications. It has been realised that electrical contact is one of the main problems in achieving the desired results. This paper mainly reports the results of electrical contact on the thermo elements made from galena collected from various mines of India. We have studied various properties/parameters of electrical contacts made from a variety of metals on n & p type galena thermoelements. It has been found that Ni [work function  $W(Ni) = 5.15$  ev] and Sb [ $W(Sb) = 4.55$  ev] are promising materials for electrical (ohmic) contact. The electron affinity  $\chi = 4.6$  ev and band gap  $E_g = 0.41$  ev have been found for our galena sample which are very close to those of pure PbS. We have also found that work function  $W_{nn} \leq 4.6$  ev (for contact with n-type) and  $W_{pp} \geq 5.01$  ev (for contact with p-type galena) satisfy the general conditions for metal-semiconductor ohmic contact. Our further studies on the effect on environmental conditions (mechanical, thermal, humidity etc.) on contact show no significant degradation of the contacts/elements with time. Our detailed studies of contact mechanism on TEG module are discussed in our paper.

### Introduction

Themo-electric generator can be used to convert heat energy into electrical energy from industrial waste heat and sunrays. Thus it has some unique applications in industry, space vehicles and rural development. For wide industrial and socio-economic applications it is very essential to develop low cost TEGs specially for poorer countries. With this point of view we have selected Indian galena ores which is available in India. Realizing the potential benefits for India, R&D Division of MECON (I) Ltd., Ranchi and IIT, Kharagpur jointly conducted extensive studies to exploit the thermoelectric properties of Indian galena [1-8].

But the main problem is electrical contact. To make a TEG of 5W or more we have to interconnect the thermoelements electrically. So, we have to put metallic contact (ohmic) on both the sides of n & p-type thermoelements which are basically semiconductors (PbS). This paper reports the studies of Ni contact on p-type and Sb contact on n-type galena thermo-elements.

### Theory

There is no doubt that we must choose metals as contact material. But which metals for which type (n/p) of semiconductor. The general condition for metal-semiconductor ohmic contact is  $\phi_m \prec \phi_n$  for n-

type semiconductor and  $\phi_m \geq \phi_p$  for p-type semiconductor. Where  $\phi_m$  = work function of metal;  $\phi_n$  &  $\phi_p$  = work function of n & p-type semiconductors respectively. Now

$$\phi_n = \chi + (E_c - E_{F_n})$$

and

$$\phi_p = \chi + (E_c - E_{F_p})$$

where  $\chi$  = electron affinity of the semiconductor and  $E_{F_n}$  &  $E_{F_p}$  = Fermi levels of n & p type semiconductor. For heavily doped n-type semiconductor  $E_c - E_{F_n} \sim 0$  and for heavily doped p-type semiconductor  $E_c - E_{F_p} \sim E_g$  i.e. the band gap. Therefore,

$$\phi_n \approx \chi \text{ and } \phi_p \approx \chi + E_g.$$

For galena the measured  $\chi = 4.6$  ev and  $E_g = 0.41$  ev. So,  $\phi_n \approx 4.6$  ev and  $\phi_p = 4.6 + 0.41$  ev = 5.01 ev. So, the condition for metal galena ohmic contact is  $\phi_m \leq 4.60$  ev for contact with n-type and  $\phi_m \geq 5.01$  ev for contact with p-type galena.

From table of work functions of metals we find Antimony (Sb) has  $\phi_{Sb} = 4.55$  ev and Nickel (Ni) has  $\phi_{Ni} = 5.15$  ev. So we choose Sb for contact with n-type and Ni for contact with p-type galena thermoelements.

### Experimental Details

Galena chunk and concentrate were collected from Hindustan Zinc Ltd. , Udaypur (Rajasthan). Powder of different particle size was made from galena

chunk by mechanical grinding in the agate-mortar and sieving them by different sieves of different mesh size. Galena chunk is n-type in nature. So we took chunk powder of mesh size - 120 to + 150 B.S.S. (particle size  $-128 \times 10^{-3}$  to  $+102 \times 10^{-3}$  nm) to make thermoelements (n-type). We take galena concentrate powder of mesh size -240 to +300 B.S.S. (particle size  $-64 \times 10^{-3}$  to  $+51 \times 10^{-3}$  nm) to make p-type thermoelements. Our thermoelements are cylindrical pellets having length  $\sim 0.01$  m and diameter  $6.3 \times 10^{-3}$  m. The pellets are formed using cold press isostatic hydraulic press, applying a pressure upto  $2 \times 10^7$  N/m<sup>2</sup>. Nickel and Antimony powder was obtained, rubbing on small metal sheets by jeweller's file. The powder was put at the two ends of the pellets at the time of making pellets with the help of die-punch. Thus a thin layer of metallic contact was obtained at the two ends of the pellets. These pellets were sintered in an argon atmosphere for 4 hrs. at 584 °C for Sb contact and at 682 °C for Ni contact. The temperature was measured with the help of a Cromel-Alumel thermocouple kept inside a tubular quartz furnace and the constant temperature was maintained with the help of a temperature controller [ Aplab model no. - 9601]. The room temperature thermoelectric power (TEP) of p-type and n-type pellets were obtained by measuring the thermo emf with the help of a d.c. microvoltmeter with an input impedance of  $1 M\Omega$ . [ model MV - 022] and the sample holder designed and fabricated in laboratory. The resistance was measured by a microprocessor based LCR - Q meter ( Aplab - 4910 ). These electrical parameters were also measured for both p-type and n-type pellets and for both with and without contacts. The electron affinity  $\chi$  of galena pellets was obtained from standard table and the nature of  $E_g$  i.e. band gaps of galena was measured previously by the method of fundamental absorption edge at 300 K.

### Results and Discussion

a) Contacts with Sb on n-type pellets :  
Here two sets of data are being given. In the 1st set we put three pellets of type n without contact and four with contact on a fire brick and sintered at the same time for four hours at 589 °C. The result is as follows

Without contact

Dia.= $6.3 \times 10^{-3}$  m

V <sub>TH</sub> (mv)	T <sub>H</sub> (mv)	TEP ( $\mu$ V/K)	Resis-tance ( $\Omega$ )	Length (cm)	$\rho$ ( $\Omega$ -cm)
0.94	0.54	68	1.072	1.08	0.309
0.58	0.56	40	2.227	1.00	0.694
0.92	0.50	72	1.882	1.03	0.570
AVERAGE		60			0.168

With contact

Dia.= $6.3 \times 10^{-3}$  m

V <sub>TH</sub> (mv)	T <sub>H</sub> (mv)	TEP ( $\mu$ V/K)	Resis-tance ( $\Omega$ )	Length (cm)	$\rho$ ( $\Omega$ -cm)
1.00	0.58	67	0.391	1.07	0.114
0.82	0.54	60	0.320	1.05	0.096
1.40	0.56	97	0.639	0.94	0.212
0.22	0.54	16	0.832	1.04	0.250
AVERAGE		60			0.168

In the second set we took 5 pellets without contact and 5 pellets with contact. They were sintered at 605 °C for 4 hrs. The results are shown below:

N. B. : V<sub>TH</sub> = the thermo emf of each pellet when one end is kept at room temperature and the other end is held at higher temperature.

T<sub>H</sub> = the thermo emf in the thermocouple measured in the temparature of hot junction. It is converted to temperature in degrees using calibration table.

Without contact

Dia.= $6.3 \times 10^{-3}$  m

V <sub>TH</sub> (mv)	T <sub>H</sub> (mv)	TEP ( $\mu$ V/K)	Resis-tance ( $\Omega$ )	Length (cm)	$\rho$ ( $\Omega$ -cm)
1.3	0.50	102	0.605	1.12	0.168
2.0	0.48	163	0.530	1.01	1.164
1.4	0.40	136	0.565	1.12	0.157
1.5	0.52	113	0.615	1.05	0.183
2.6	0.64	160	0.460	1.11	0.129
AVERAGE		135			0.160

With contact

Dia.= $6.3 \times 10^{-3}$  m

$V_{TH}$ (mv)	$T_H$ (mv)	TEP ( $\mu V/K$ )	Resistance ( $\Omega$ )	Length (cm)	$\rho$ ( $\Omega$ - cm)
1.10	0.42	102	0.118	1.11	0.033
1.00	0.34	115	0.118	1.11	0.033
0.88	0.32	107	0.120	1.02	0.037
1.50	0.42	139	0.127	1.04	0.038
1.50	0.42	139	0.145	1.09	0.042
AVERAGE		120			0.037

Without contact

Dia.= $6.3 \times 10^{-3}$  m

$V_{TH}$ (mv)	$T_H$ (mv)	TEP ( $\mu V/K$ )	Resistance ( $\Omega$ )	Length (cm)	$\rho$ ( $\Omega$ - cm)
4.0	0.60	261	14.30	1.06	4.205
3.2	0.60	209	1370	1.06	4.029
3.5	0.58	236	16.36	1.14	4.474
AVERAGE		235			4236

With contact

Dia.= $6.3 \times 10^{-3}$  m

Without contact

Dia.= $6.3 \times 10^{-3}$  m

$V_{TH}$ (mv)	$T_H$ (mv)	TEP ( $\mu V/K$ )	Resistance ( $\Omega$ )	Length (cm)	$\rho$ ( $\Omega$ - cm)
2.8	0.50	218	21.0	1.12	5.84
3.0	0.56	209	12.75	1.07	3.71
3.0	0.60	196	18.37	1.08	5.30
AVERAGE		208			4.99

With contact

Dia.= $6.3 \times 10^{-3}$  m

$V_{TH}$ (mv)	$T_H$ (mv)	TEP ( $\mu V/K$ )	Resistance ( $\Omega$ )	Length (cm)	$\rho$ ( $\Omega$ - cm)
3.0	0.52	225	5.20	1.10	1.47
1.25	0.68	72	12.80	1.13	3.53
2.4	0.56	167	4.70	1.17	1.25
AVERAGE		155			2.08

In the 2nd set we took 3 p-type pellets without contact and 3 p-type pellets with contacts. They were sintered at 682 °C for 4 hrs. The results are shown below :

#### Discussion

So we see that in each cases for n-type as well as p-type the resistance of pellets with contact material is less by 2 to 4 time than the resistance of pellets without contact. This confirms that the contacts are ohmic in nature. So there will be no potential barrier if we make electrical connections between them.

#### Conclusion

As we said earlier the contact problem is one of the main hurdles to fabricate TEG from galena, we look this problem as a serious challenge and we have solved it. Now our TEG will have lesser internal resistance. So the power generation will be more using same no of pellets. We kept these pellets with contact for days. Even after that there is no significant change in resistivity and TEP. Another thing is to be noticed that as soon as resistance is lowered the TEP is also decreased. But TEP is not decreasing at the same rate of the decrement of resistance. As for example in the 1st set of (a) resistance is lowered by 3 times (app.) but TEP is same. In the 2nd set of (a) resistance is lowered by 4 times (app.) but TEP is lowered by 15  $\mu V/K$  only. On the contrary the decrement of TEP is more in the case of contact with Ni on p-type pellets [ see.(b) ].

### Acknowledgement

The cooperation received from the management of Hindustan Zinc Ltd., Rajasthan in supplying galena concentrate is greatly acknowledged. Authors are also thankful to our technical assistants Sri N. C. Roy and A. K. Singh for their kind experimental assistance. We are also thankful to our another research scholar S. R. Sanigrahi.

### References

- [1]. BEN. G. Streetmann, " Solid state Electron Devices ", Prentice Hall (India).
- [2]. S. Chatterjee, H. N. Acharya and V. V. Ratnam, " Effect of sintering temperature and time on the electrical properties of pellets made from beneficiated Galena ore. " J. Mater. Sci., 22, (1987) 2793.
- [3]. S. Chatterjee, H. N. Acharya and V. V. Ratnam, " Thermoelectric generator using natural galena aggregate and galena concentrate." - Seventh international conference on thermoelectric energy conservation, The university of Texas, at Arlington, U.S.A., March (1988) 14.
- [4]. S. Chatterjee, H. N. Acharya and V. V. Ratnam, " Effect of  $PbI_2$  on the properties of Galena concentrate for thermoelements. " - Second European Conference on Thermoelectrics, Naney, France, July (1989).
- [5]. S. Chatterjee, A. Dasgupta and H. N. Acharya, " Solar Thermoelectric generator using Indian Galena." - The National Solar Energy Convention, Calcutta, India (1990).
- [6]. S. Chatterjee, H. N. Acharya and V. V. Ratnam, " Grain size Effect on the polarity of Seebeck coefficient of natural Galena. " - J. Energy Convers. Mgmt. 31, 2(1991) 175.
- [7]. S. Chatterjee, T. K. Chaudhuri and H. N. Acharya, " Design parameters of 10 watt Thermoelectric Generator based on Indian Galena. " - Eleventh International Conference on Thermoelectrics, The university of Texas at Arlington, U.S.A., October (1992) 55.
- [8]. T. K. Chaudhuri and S. Chatterjee " Design of a thin film Solar Thermoelectric Generator ." - Eleventh International Conference on Thermoelectrics, The university of Texas at Arlington, U.S.A., October (1992) 40.

## RELIABILITY AND DEFECTS IN PbTe-BASED MATERIALS

V.Fano<sup>1</sup>, I.Ortalli<sup>1</sup>, K.Pozela<sup>2</sup>, G.Meletti<sup>3</sup>

<sup>1</sup> *Istituto Scienze Fisiche, Parma, Italy*

<sup>2</sup> *World Laboratory, Vilnius, Lithuania*

<sup>3</sup> *Maspec Institute, Parma, Italy*

The figure-of-merit of PbTe-based materials varies in a some range of values. The comparison of the electrical properties, related to single crystals, grown by vertical Bridgman technique at different growth rates and annealed, suggests that free convection can play a significant role in this phenomenology.

### **Introduction**

It is well known that the figure-of-merit  $Z$  is a function of the carrier concentration and temperature. For a chosen temperature range, the highest value of  $Z$  is obtained when the optimal carrier concentration is uniformly distributed in the thermoelement. In this case, the maximum reliability is reached, if the constituents are in thermal equilibrium. For a specific chemical composition of a single crystal growing from the melt, the crystal growth velocity ( $V$ ) and the thermal field of the growth apparatus are the parameters used for controlling the distribution of the components and, consequently, the physical properties of the solid phase. In fact these parameters control the heat transfer and mass transport at solid-melt interface. Further improvement of the reliability of the materials involves a better understanding of the transport phenomena in the melt.

Forced convection is absent in the vertical Bridgman method, characterized by the cooling of the melt from the bottom. In this case heat and mass transfer would take place via heat conduction and ionic diffusion only. However the presence of mixing by free convection can induce spontaneous temperature oscillations in the melt, which produce random compositional fluctuations.

Different types of fluid motion may be present, due to:

- concentrational convection,
- thermal convection,
- thermocapillary convection,
- capillary-concentrational convection,
- misalignment of ampoule axis and direction of gravity force
- not axis-symmetric heating.

On the other hand, only the flat shape of the solid-melt interface in the vertical Bridgman growth is compatible with a purely diffusive solute transport. In practice, a flat-shape rarely forms [1]. Other factors that affect the shape are not always obvious, but some are inherent to the same growth method. For instance, the interface shape is affected by the difference in the thermal conductivities of the melt and the solid and by the release of the latent heat at the solid-melt interface. When the thermal conductivity of the melt is greater than that of the solid, the charge is cooled by the crucible and therefore the interface shape is concave toward the melt [2]. Briefly, different convective motions are produced by departure from mechanical equilibrium and can

occur simultaneously, affecting thus one another and causing random variation of component distribution.

In this work we show that the figure-of-merit of PbTe single crystals, having the same nominal carrier concentration, varies in a some range of variability. The free convection may be the main cause of the variation of the electrical properties. The values of the concentration gradient at solid-melt interface of the  $\text{Pb}_{1-x}\text{Sn}_x\text{Te}$  system (LTT), the Rayleigh and Prandtl dimensionless parameters, the carrier concentration and mobility both of as grown and of annealed single crystals, are in agreement with the supposed free convection.

### **Figure-of-merit.**

Fig. 1 shows the figure-of-merit of some n-type and p-type single crystals of Na doped PbTe (p-type) and Cl doped PbTe (n-type). The single crystals have been grown using  $V = 8.33 \cdot 10^{-3} \text{ cm/min}$  and thermal gradient  $G = 20^\circ\text{C/cm}$ . Crystals having the same carrier concentration ( $3 \times 10^{19} \text{ cm}^{-3}$ ) have been selected.  $Z$  of each sample varies from that of the other samples in value and in temperature.

### **Free Convection**

There are the following criteria to evaluate the presence of the free convection in the melt during the growth. They give information about the onset of the instability.

- The Diffusional Boundary Layer. For all cases of solidification with convection present, one can consider the onset of a steady state concentration gradient of the element, which segregates at solid-melt interface. This gradient is assumed to form through diffusion in a layer of a limited thickness,  $\delta$ , ahead of the solidification front, apart from which mixing is taken to be complete. In the case of the growth by vertical Bridgman method, it is

$$\delta = 10 \alpha Pr^{0.25} Sc^{-0.5} (Gr + (Pr / Sc)^{0.5} Gr)^{-0.25} \cdot (a / l)^{-0.44} (\delta V / D)^{-0.26}$$

where  $a/l$  is the aspect ratio,  $D/V$  is the decay distance of the exponential concentration gradient ahead of the solid-melt interface,  $\text{Pr}$  is the Prandtl number,  $\text{Sc}$  is the Schmidt number,  $\text{Gr}$  is the Grashof number.

For the system  $\text{Pb}_{1-x}\text{Sn}_x\text{Te}$  ( $0.1 \leq x < 1$ ) grown at  $V = 8.33 \times 10^{-3} \text{ cm/min}$  and  $T = 20^\circ\text{C}$ , the calculated  $\delta$  values are in agreement with those of the partial melt mixing by free convection ( $1 \times 10^{-2} \text{ cm} < \delta < 2.5 \times 10^{-2}$ ).

Two other conditions, that indicate the onset of free convection induced by temperature oscillations, are

$$Ra = \frac{cg\Delta T l^3}{K} > 10^3$$

$$\text{Pr} = \frac{c\eta}{K} < 0.1$$

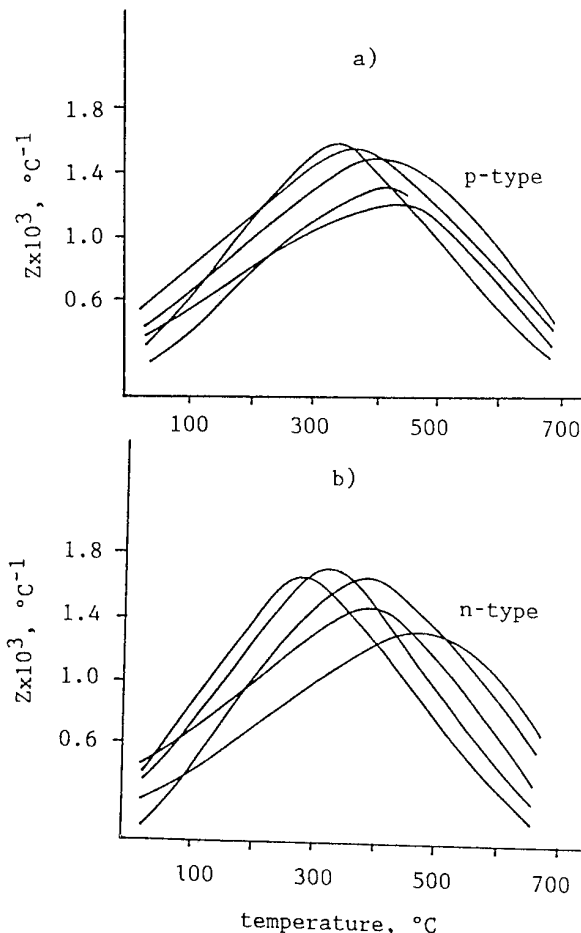


Fig. 1. Figures of merit of some PbTe single crystals. a) p-type PbTe; b) n-type PbTe. The carrier concentration of each sample (p- or n-type) is  $3 \times 10^{19} \text{ cm}^{-3}$  at room temperature. Growth velocity  $V = 8.33 \times 10^{-3} \text{ cm/min}$ , temperature gradient  $G = 20^\circ\text{C}/\text{cm}$ .

where  $Ra$  is the Rayleigh number,  $c$  is the specific heat,  $g$  is the gravity acceleration,  $K$  = thermal conductivity,  $\eta$  is the viscosity,  $\Delta T$  is the change in temperature between the interface and bulk liquid.

Both conditions are satisfied: for  $\text{Pb}_{0.83}\text{Sn}_{0.17}\text{Te}$ ,  $Ra = 4.5 \times 10^3$  and  $\text{Pr} = 5 \times 10^{-2}$ . For different stoichiometry, these values do not change significantly.

- The retrograde solubility. The precipitation of cations (in metal-saturated solid) or anions (in tellurium-saturated solid) on the dislocations occurs, when the temperature goes down to room temperature after crystallization. It is due to the decrease of the homogeneity range. In this way the precipitation of the majority component by annealing at lower temperatures ( $\sim 400^\circ\text{C}$ ) would result in the decrease of the majority carrier concentration.

To remove the contribution of these effects, the samples have been prepared by this method: single crystals have been grown from stoichiometric  $\text{PbTe}$  and  $\text{Pb}_{0.65}\text{Sn}_{0.35}\text{Te}$  melts, at very low velocity (1 mm/day). In this conditions, the criterion (1) is not satisfied and the constitutional supercooling is avoided, p-type samples ( $2 \times 3 \times 9 \text{ mm}^3$ , dislocation density  $\sim 10^5 \text{ cm}^{-2}$ ) were obtained from the ingot part corresponding to the solidification fraction  $x = 0.25$  (see Fig. 2) where the stoichiometric variation, due to the normal segregation, can be neglected [3]. The curves of Fig. 2 were calculated by the formula

$$g_i = \left\{ C_0 - C_i^L + 0.5(C_3 - C_1)g_2 + 0.5(C_4^S - C_2^S)g_3 + \dots + 0.5(C_i^S - C_{i-2}^S) \right\} \left[ 0.5(C_{i-1}^S - C_i^S) - C_i^L \right]^{-1}$$

following the method reported in [3].

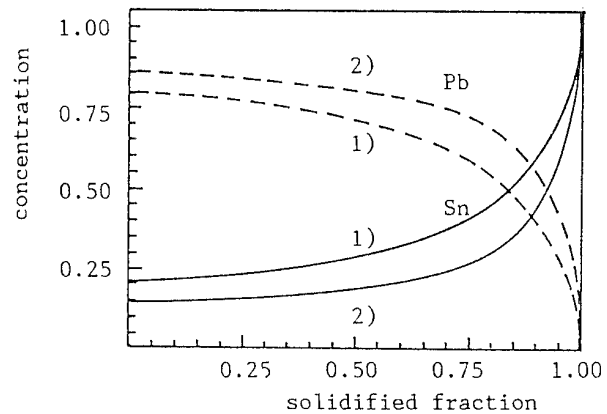


Fig. 2. Distribution of lead and tin in  $\text{Pb}_{1-x}\text{Sn}_x\text{Te}$  single crystals grown from a completely mixed melt. The curves 1) have been calculated for  $\text{Pb}_{0.65}\text{Sn}_{0.35}\text{Te}$  starting melt composition; the curves 2) have been calculated for  $\text{Pb}_{0.75}\text{Sn}_{0.25}\text{Te}$  starting melt composition.

Table 1

Materials	Annealing time, days	Annealing	p $10^{18} \text{ cm}^{-3}$	$\mu$ $\text{cm}^2 \text{V}^{-1} \text{sec}^{-1}$
PbTe (2.0 mm thick)	0		7.1	600
PbTe (1.5 mm thick)	0		2.2	820
PbTe (1.0 mm thick)	0		4.9	725
LTT (2.0 mm thick)	0		58.8	210
LTT (1.5 mm thick)	0		65.4	190
LTT (1.0 mm thick)	0		36.0	280
PbTe	20		1.8	870
LTT	20		70.0	180
PbTe	40		3.2	660
LTT	40		50.6	350
PbTe	60		3.0	760
LTT	60		59.0	300
PbTe	80		4.4	680
LTT	80		30.2	410
PbTe	100		2.0	820
LTT	100		64.0	220

SEM and microscopic analysis of the chemical etched samples do not show specific defects (grain boundaries, microphases). The carrier concentration and mobility of samples, submitted to repeated thinnings (2 mm, 1.5 mm, 1.0 mm) have been measured. After electrical measurements, the specimens have been submitted to the annealing in inert atmosphere at 400°C. The annealing was stopped by water quenching for periodic measurements of carrier concentration and mobility by the cross-modulation technique. The samples were analyzed every twenty days for five times (100 days annealing). According to thermoelectric power measurements, this time is by far long enough for precipitation process. Both the as grown samples and the annealed samples showed erratic variation of the electrical properties (see Table 1). Consequently, this behavior cannot be ascribed to the precipitation process. Conversely, these data support the hypothesis that the free convection plays an important role in the formation of unhomogeneity in solids.

## References

- [1] C.L.Jones, P.Capper, J.J.Gosney, Thermal modelling of Bridgman crystal growth, Journal of Crystal Growth, 1982, v. 52, pp. 581-590.
- [2] T.Jasinski, A.F.Witt, On control of the crystal-melt interface shape during growth in a vertical Bridgman configuration, Journal of Crystal Growth, 1995, v. 7, pp. 295-304.
- [3] R.Breschi, V.Fano, I.Ortalli, K.Pozela, Solid state recrystallization by unidirectional cooling of  $\text{Pb}_{1-x}\text{Sn}_x\text{Te}$ -type pseudobinary systems, Proceedings of 13th International Conference on Thermoelectrics, Kansas City, to be published.

## FROM ORE TO THERMOELECTRIC GENERATOR : A STUDY ON INDIAN GALENA

Shuchitangshu Chatterjee<sup>1</sup> and H.N. Acharya<sup>2</sup>

<sup>1</sup>R&D Division, MECON (India) Ltd, Ranchi-834002, India, Phone - (0651) 501865, Fax - 91-651-502214/502189

<sup>2</sup>Department of Physics, Indian Institute of Technology, Kharagpur-721302, India, Phone - (03222) 2221-2224/5917  
Fax - 91-3222-2303

The main thrust of our research is to undertake a critical study and to improve significantly the thermoelectric properties of Galena which is readily available in India. This R&D study will lead to development of cheap and reliable thermoelectric generators and other useful devices widely used in the industry, defence, cathodic protection in gas pipeline, communication, etc. The immediate thrust is directed to the development of industrial designs and fabrication of prototype products for various applications.

This project is a continuation of our earlier project on the development of Indian Galena. Galena is the principal lead mineral found in many countries including India and Australia. Thermoelectric studies on Indian Galena have established that elements made under various conditions have very encouraging properties needed to fabricate thermoelectric generators. The processing technology developed has been embodied in nine Indian Patents. This paper reports the results so far achieved for thermoelements from Indian Galena.

### Introduction

Galena is the principal lead mineral found in many countries including India and Australia. In India, proven reserves of galena is more than 100 million tonnes. Zawar and Rajpur-Dariba mines in Rajasthan and Bandalamottu in Andhra Pradesh as well as various other parts of the country have good quality galena in large quantities. These reserves can be gainfully exploited not only for the lead content of the ore but also for new materials that make use of the semiconducting and electrical properties of galena for diverse industrial uses.

In 1971, Bear and Barclay studied Australian galena [1-3]. Their studies were directed to the use of compact sulphide concentrates as electrodes in electro-winning of metals and for other electrochemical applications. Later, Landecker, trying to use galena as n-type arm of a thermoelectric generator [4,5] encountered many problems. It was also observed by Landecker that under some circumstances the substance was explosive, but we do not know which particular impurity was responsible for its explosive nature.

There are many semiconducting materials suitable for thermoelements at moderate temperatures. All these materials are, however, expensive and not readily available, although from performance considerations, some of these materials may be the most appropriate choices. On other hand, natural lead sulphide (galena ore) is available in India in large quantities. Galena is obtainable in various forms, and though it has thermoelectric power capacity of considerable magnitude, its electrical resistivity was too high for use as thermoelements.

Realizing potential benefits for India, R&D Division of MECON (I) Ltd, Ranchi and Indian Institute of Technology, Kharagpur took up a joint R&D project for developing 2w and 5w thermoelectric modules based on Indian galena. A drastic reduction, nine orders in magnitude, in the resistivity of doped samples was achieved - i.e. from Mega Ohm-cm to milli Ohm-cm and other parameters such as thermoelectric power ( $\alpha$ ) and thermal conductivity (K) were optimised. The avoidance of the necessity of using high purity starting material is thus another plus point. Apart from considerations of cost in purifying the starting material as in the case with the present material, another obvious advantage of these thermoelectric generators (TEGs) is that these cover a much wider range of the unutilised solar spectrum and waste heat. In view of the substantial cost difference between present by used materials and our material (galena), thermoelectric generator made from galena may turnout to be quite competitive. This paper reports the results so far achieved for thermoelements from Indian galena.

### Experimental Details

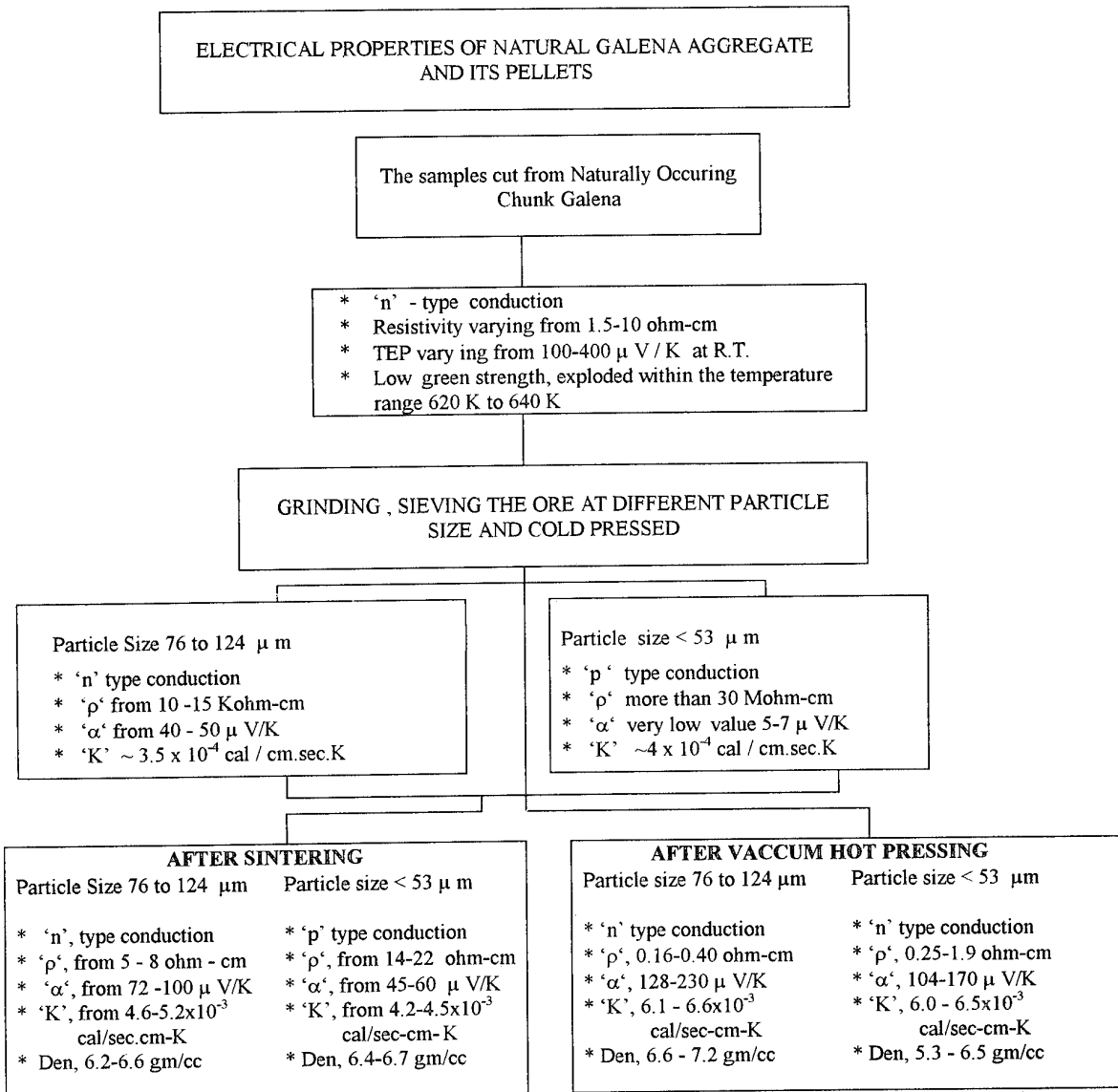
The details of the sample preparation, property measurements, sample analysis have been reported elsewhere [6-10].

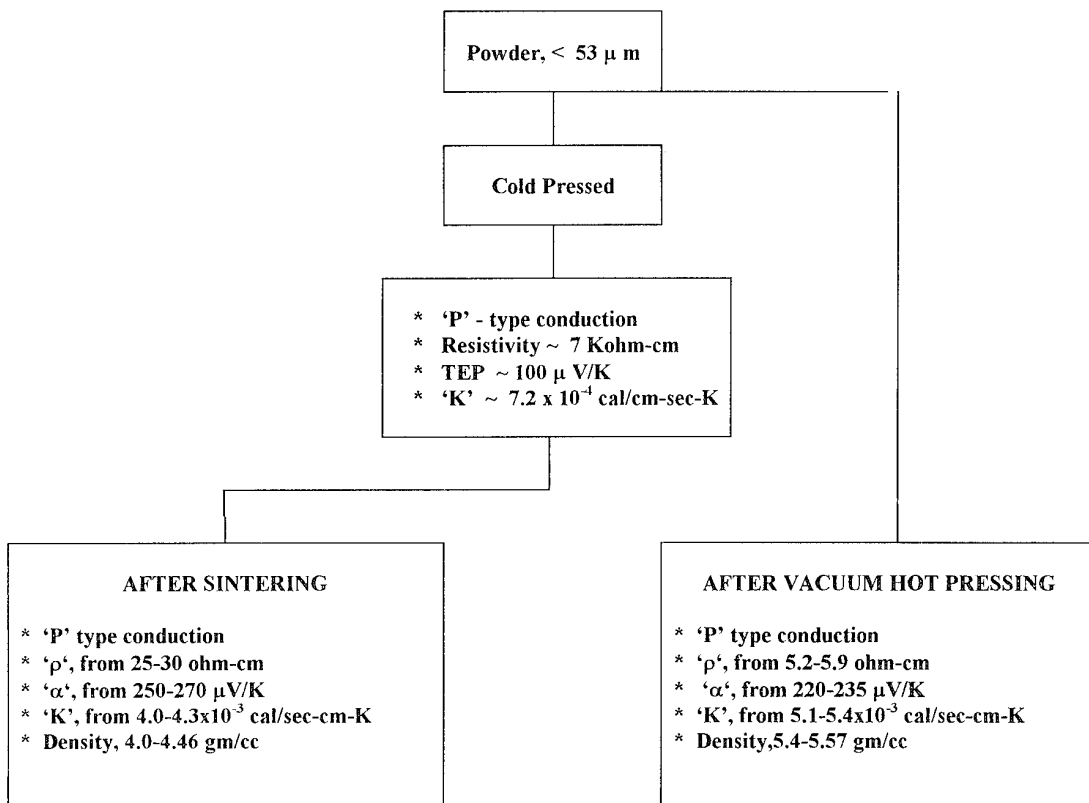
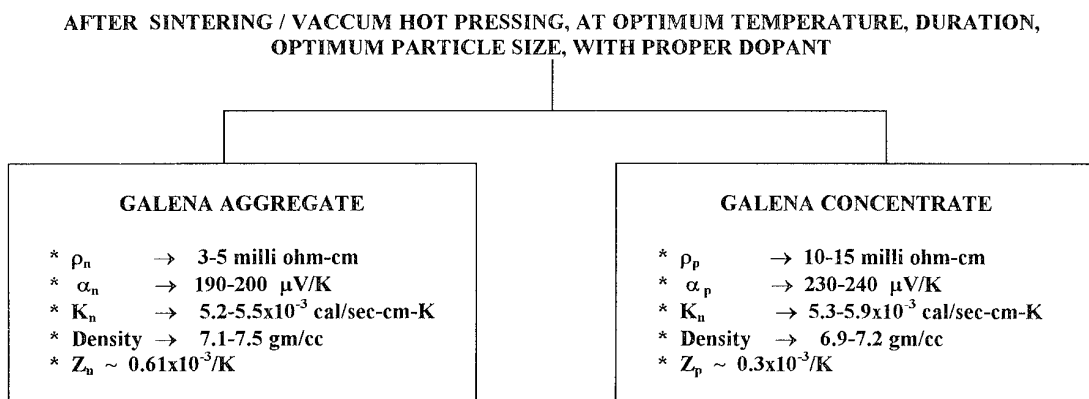
### Results and Discussion

For preparing the two arms of thermoelectric generators, two types of ore have been used which were collected from Zawar Mines, Rajasthan (India). One type of ore used was the crystalline galena (natural galena aggregate) available in some regions of the mines and the other was galena concentrate, which is normally used for manufacturing lead. This ore is beneficiated by separating galena by froth-floating technique.

The electrical properties of natural galena aggregate and some typical pellets at room temperature are shown in flow chart 1.

## FLOW CHART 1



**Flow Chart II****FLOW CHART III**

The room temperature electrical properties of some typical pellets made from Galena Concentrate are shown in flow chart II.

The room - temperature electrical properties of some typical pellets from Galena aggregate and galena concentrate with proper dopant, optimum particle size, after sintering / vaccum hot pressing at optimum temperature are shown in Flow Chart III.

**Conclusion**

The results obtained in this study indicate that now it would be possible to prepare low cost galena based thermoelectric generator, which might be of much use to specific civilian applications, urban as well as rural, and have strong defence use potential.

Crushing strength, Young's Modulus and Natural frequency of some typical sintered pellets made from galena aggregate and galena concentrate are shown in Table 1.

TABLE - 1

Type of Material	Crushing Strength (MPa)	Young's Modulus (GPa)	Natural Frequency (kHz) Longitudinal
Galena Aggregate, (n-type),	47.1-50.3 , 4.10-5.53	Fixed-Fixed ,	33.25-38.74 ,
Galena Concentrate, (p-type),	76.7-82.1 . 6.6-6.92 .	Fixed-Fixed ,	50.15-52.69 ,

The samples prepared from naturally occurring galena ore shows n-type conduction. This n-type conduction may be due to the excess of lead atoms or excess of donor impurities like Fe, Bi, Sb, etc. present in that composition as seen from the data of chemical analysis [8]. The resistivity of the ores varies from sample to sample. This variation can be explained on the basis of impurities present or deviations from the stoichiometry or the different grain size of the galena ore.

The pellets made by simple cold pressing have very high resistivity. This high value of resistivity has been explained on the basis of the resistance offered by grain boundaries

but on sintering or hot pressing a neck is formed between the grains by diffusion process which may be either surface diffusion or grain boundary diffusion or volume diffusion depending upon the temperature range. This might be one of the reasons for decreasing the resistance.

The sintered pellets made from larger grain sized particles of natural galena ore exhibit n-type conduction, whereas the pellets made from smaller grain sized natural galena show p-type conduction. This change in the nature of the dominant carrier has been explained on the basis of surface oxidation of smaller grains, converting the outer layers of the originally n-type particle to p-type layer and thus forming p-n-p junctions as proposed by J.C. Slater [11]. Such a p-n-p structure would show resultant p or n-type conduction depending upon the ratio of thickness of p and n layers.

The pellets made from galena concentrates always show p-type conduction. This p-type conduction may be due to the excess of sulphur or there seems to be an excess of p-type impurities (like Ag and Cu) present in this ore, which act as the acceptor. This excess of sulphur was confirmed from the data of chemical analysis [8].

## References

- [1] D.V. Barclay and I.J. Bear, "Relationship between semi-conducting properties and sintering conditions for hot pressed galena powder", Solid. State. Commun. 9(1971) 1567
- [2] I.J. Bear and D.V. Barclay, "Sintering Mechanisms in hot pressed PbS compacts via electrical measurements", Powd. Met. Int. 7(1975) 121
- [3] I.J. Bear, "Effect of Adsorbed atmospheric gases on electrical behaviour and sintering mechanism in hot-pressed PbS compacts", Powd. Met. Int. 9(1977) 72.
- [4] K. Landecker, "Conversion of Solar Energy into electrical power by means of the thermoelectric effect", Proc 1st Intn. Conf. on Thermoelectric Energy Conversion, Arlington, Texas (1976).1.
- [5] K. Landecker, "Power generating thermojunctions with radial flow of currents in coaxial disks", Proc. 1st Intn. Conf. on Thermoelectric Energy Conversion, Arlington, Texas, U.S.A (1976) 126
- [6] S. Chatterjee, H.N. Acharya and V.V. Ratnam, "Effect of sintering temperature and time on the electrical properties of pellets made from beneficiated galena ore", J. Mater. Sci. 22 (1987) 2793
- [7] S. Chatterjee, H.N. Acharya and V.V. Ratnam, "Grain size effect on the polarity of Seebeck Coefficient of natural Galena", J. Energy Convers Mgmt 31, 2(1991) 175
- [8] H.N. Acharya, S. Chatterjee and V.V. Ratnam, "On the properties of thermoelements made by hot pressing galena and beneficiated galena ore", Proc. 6th Intn. Conf. on Thermoelectric Energy Conversion, Arlington, Texas, USA (1986) 59
- [9] S. Chatterjee, H.N. Acharya and V.V. Ratnam, "An improved set-up for the simultaneous measurement of thermoelectric coefficient and electrical conductivity in vacuum/inert atmospheres at different ambient temperatures", J. Inst. Society of India, 17 (1987) 87
- [10] S. Chatterjee, H.N. Acharya and V.V. Ratnam, "On low cost approach for fabrication lead sulphide based TEG for terrestrial applications", Proc. 7th Intn. Conf. on Alternative Energy Source, Florida, U.S.A. (1985) 425
- [11] J.C. Slater, "Barrier theory of the photoconductivity of lead sulphide", Phys. Rev., 103 (1956) 1631

## DEVELOPMENT OF THERMOELEMENTS FROM DROSS GALENA

S. R. Shannigrahi<sup>1</sup>, H. N. Acharya<sup>1</sup>, R. N. P. Choudhary<sup>1</sup>, A. K. Singh<sup>1</sup> and Shuchitangshu Chatterjee<sup>2</sup>

<sup>1</sup>*Thermo-electric Lab, Dept. of Physics & Meteorology, Indian Institute of Technology,  
Kharagpur-721 302, India. Phone - 03222-2221-24/5917. Fax - 91-3222-2303.*

<sup>2</sup>*R&D Division, Mecon (India) Ltd., Ranchi - 834 002, India.  
Phone - (0651) 501651, Fax - 0651-502214/502189/501054.*

### Abstract

Dross -galena was collected from Chanderia Lead-Zinc Smelting Centre, Chitoregarh, Rajasthan, India. It is an intermediate stage of Lead-Zinc from galena concentrate. This paper reports some aspects of dross galena thermoelements for thermoelectric generator.

### Introduction

Thermoelectric generators (TEG) (a non-conventional source of energy ) of different output power, used in different industries, are usually fabricated from expensive semiconducting and conducting materials and hence are not widely used in developing countries. For wide industrial and socio-economic applications in these countries and elsewhere, low cost TEG is very much required. In order to achieve this goal, R & D Division of MECON(I) Ltd., Ranchi and I.I.T. Kharagpur jointly conducted extensive studies and fabricated thermoelement (TE) from galena (enrich PbS) which are abundantly available in India. Our previous work [1 - 7] on the efficiency of TEG prepared from chunk and concentrated galena showed encouraging performance TEG, we have worked on dross-galena namely, an intermediate stage of Lead-Zinc from galena concentrate.

In this paper we report our studies on composition, resistivity, density, thermoelectric power, microstructure, X-ray diffractogram and thermal expansion of thermoelements made from dross-galena.

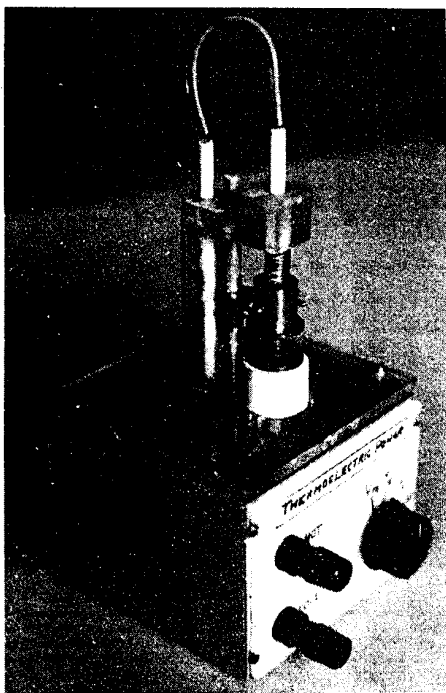
### Experimental Details

Dross galena was collected from Hindustan Zinc Ltd., Udaipur (Rajasthan). Homogeneous powder of dross galena was obtained by mechanical grinding in the agate-mortar. Powders of different mesh sizes were obtained from different sieves. In order to find elemental composition and the microstructure, energy dispersive analysis of X-ray (EDXA) was done by CAM-SCAN SERIES-II, along with the scanning microphotograph taken by the same instrument.

X-Ray diffractogram of the powder sample was recorded using X-Ray powder diffractometer (JXR - JAPAN) in wide  $2\theta$  range ( $20^\circ \leq 2\theta \leq 90^\circ$ ) with Cu  $K\alpha$  radiation for preliminary structural information. The cylindrical pellets samples of length 10 mm and diameter 6.3 mm were made from the

powder of the mesh size -200 to +240 BSS ( $-76 \times 10^{-3}$  to  $+64 \times 10^{-3}$  nm) using hydraulic press at a pressure upto  $2 \times 10^7$  N/m<sup>2</sup>. These samples were sintered in an argon atmosphere at 880 K temperature for 4 hrs. The sample temperature was measured with the help of Cromal-Alumel thermocouples kept inside a tubular quartz furnace and the constant temperature was maintained with the help of a temperature controller [Aplab model no. - 9601]. The room temperature thermoelectric power (TEP) of p-type dross galena pellets was obtained by measuring the thermo emf with the help of a d.c. microvoltmeter with an input impedance of 1 M $\Omega$  [model  $\mu$ V - 002]. The sample holder designed and fabricated in the laboratory. The photograph is shown in fig.1. The resistance was measured with the help of microprocessor based LCR-Q meter (Aplab-4910). These electrical parameters were also measured for the n-type samples made from dross - galena doped with Lead and Indium.

The density of all the undoped sintered pellets were determined to an accuracy of  $\pm 0.1\%$  with the help of the Archimedes' principle using distilled water as the buoyant liquid. The weight of the sample was accurately measured with the help of a sensitive balance (Dhona 100 DS) to an accuracy upto 0.1mg. The thermal expansion of the pellets was studied from room temperature to 350 °C with the help of dial gauge (Mitutoyo no 2109-10).



### Results and Discussions

The elemental composition of dross-galena as studied from (EDAX) was found to be:

S = 4.019% ; Ni = 0.718% ; Cu = 8.155% ; Zn = 23.895% ; Ag = 0.024% and Pb = 63.187%.

The profile of the EDAX is shown in fig.2.

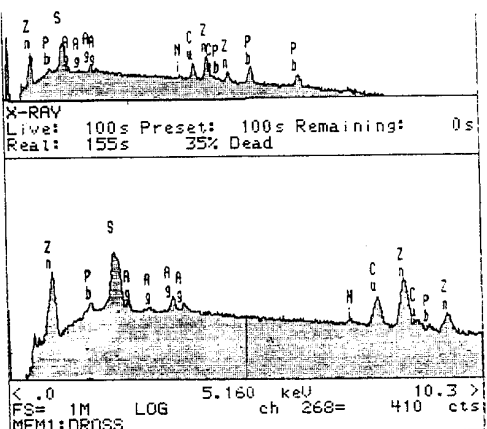


Fig.2

From the X-ray diffractograms, the d - values and the lattice parameters have been calculated for 27 reflections peak using a standard computer programme "powder".

Comparison of some d - values and cell parameters of PbS [powder diffraction file, card no- 5-0592] and dross-galena are shown in table 1.

Table 1

Comparison of d - values of PbS reported in [powder diffraction file, card no- 5-0592] and dross-galena.

PbS		dross-galena	
lattice parameter (mm)	d (mm)	lattice parameter (mm)	d (mm)
0.594	0.2969	0.5901	0.2968
	0.2099		0.2094
	0.1790		0.1765
	0.1714		0.1708
	0.1484		0.1494
	0.1362		0.1368

Comparison of some d - values and lattice parameter of PbS and dross-galena show good agreement between them. However there is also some disagreement of d- values, which suggests that dross-galena is not containing pure PbS. This is expected because of the presence of other elements. From SEM microphotograph, the grain size has been determined

Average value of grain size in horizontal direction = 2.53125  $\mu\text{m}$ .

Average value of grain size in vertical direction = 2.04843  $\mu\text{m}$ .

The SEM photograph is shown in fig 3.

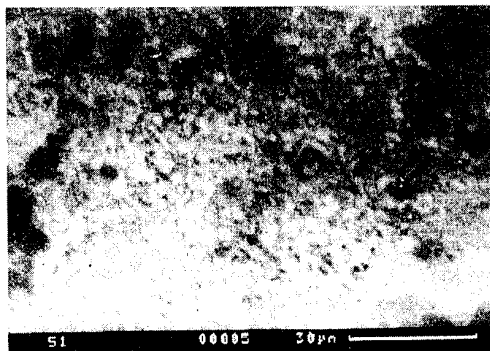


Fig.3

The room temperature resistance of undoped sintered pellets made from galena-dross, using same mesh size and different pellet lengths was found to be of the order of  $\sim 1.1 \text{ M}\Omega$ . The average calculated resistivity of the samples was also found to be of the order of  $0.41 \text{ M}\Omega\text{-cm}$  and the TEP is also very high

( ~ 20000  $\mu\text{V/K}$ ). All the pellets show p-type conduction. The results for some typical samples are given in table 2.

Table 2

Room temperature thermoelectric power, resistance, resistivity and density of some typical undoped sintered dross-galena pellets.

Sample no	Type	Resistance ( $M\Omega$ )	Resistivity ( $M\Omega\text{-cm}$ )	TEP ( $\mu\text{V/K}$ )	Density (g/cc)
1	p	0.75	0.243	21500	6.886
2	p	0.45	0.160	6.910	
3	p	0.74	0.228	21428	6.761
4	p	0.63	0.208	21000	6.903
5	p	1.50	0.482	25263	6.679
6	p	0.86	0.279	17894	6.399
7	p	1.10	0.411	24712	6.802
8	p	0.74	0.231	30487	6.836

The electrical properties of some typical pellets prepared from 0.48 mol% Pb doped dross-galena sintered at 880 K for 4 hrs in argon atmosphere have been shown in table 3.

Table 3

Room temperature thermoelectric power, resistance, resistivity and density of 0.48 mol% Pb doped dross-galena pellets.

Sample no	Type	Resistance ( $M\Omega$ )	Resistivity ( $M\Omega\text{-cm}$ )	TEP ( $\mu\text{V/K}$ )	Density (g/cc)
1	n	0.112	0.02872	198.88	6.680
2	n	0.080	0.01875	155.17	6.931
3	n	0.070	0.01723	80.64	6.731
4	n	0.032	0.00803	71.42	6.845
5	n	0.542	0.14347	107.69	6.729
6	n	0.012	0.00321	40.32	6.832

The electrical properties of some typical pellets prepared from 0.48 mol% of In doped dross-galena pellets, sintered at 880 K for 4 hrs in argon atmosphere have also been shown in table 4.

Table 4

Room temperature thermoelectric power, resistance, resistivity and density of 0.48 mol% In doped dross-galena pellets.

Sample no	Type	Resistance ( $M\Omega$ )	Resistivity ( $M\Omega\text{-cm}$ )	TEP ( $\mu\text{V/K}$ )	Density (g/cc)
1	n	0.236	0.071	3.00	6.768
2	n	0.376	0.139	2.33	6.830
3	n	0.432	0.129	2.61	6.833
4	n	0.055	0.015	3.12	6.716
5	n	1.68	0.447	2.39	6.725

The comparison of the above electrical properties (Table 2, 3 & 4) of undoped and doped samples show that undoped samples have p-type semiconducting property whereas samples doped with In and Pb have n-type properties. The resistivity of n-type dross-samples has dropped from mega - ohm to milli - ohm, which is very remarkable and desirable for our work. There was, however, a concomitant loss of thermoelectric power and this was not quite desirable.

From thermal expansion study, it is seen that the coefficient of linear thermal expansion ( $\sigma$ ) is quite independent of temperature and almost constant in the temperature range 100 - 350 °C. The value of  $\sigma$  for sintered undoped and Pb & In doped pellets are quite alike. The value is little larger than the predicted value of pure PbS. The variation of linear thermal expansion coefficient ( $\sigma$ ) with temperature is shown in fig 4.

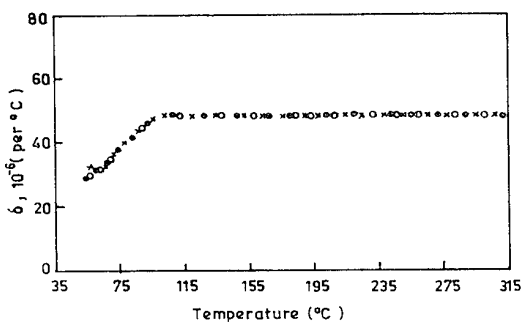


Fig. 4

### **Conclusion**

To optimise the device performance (i. e. figure of merit) we have to develop TE with low resistivity and high TEP. Our preliminary study on dross-galena and doped dross-galena samples shows that some more attempts have to be taken for making suitable TE, using different dopants. Further work is in progress.

### **Acknowledgement**

The cooperation received from the management of Hindustan Zinc Ltd., Rajasthan in supplying galena aggregate, galena concentrate and dross - galena is greatfully acknowledged. Authors are also thankful to Sri N. C. Roy, Mr. N. K. Mishra and Dr. S. Chakraborti dept. of Physics, III, Kharagpur for their kind assistance.

### **References**

- [7]. T. K. Chaudhuri and S. Chatterjee " Design of a thin film Solar Thermoelectric Generator " - Eleventh International Conference on Thermoelectrics, The university of Texas at Arlington, U.S A., October (1992) 40.
- [1]. S. Chatterjee, H. N. Acharya and V. V. Ratnam, " Effect of sintering temperature and time on the electrical properties of pellets made from benificiated Galena ore. " J. Mater. Sci., 22, (1987) 2793.
- [2]. S. Chatterjee, H. N. Acharya and V. V. Ratnam, " Thermoelectric generator using natural galena aggregate and galena concentrate." - Seventh international conference on thermoelectric energy conservation, The university of Texas, at Arlington, U.S.A., March (1988) 14.
- [3]. S. Chatterjee, H. N. Acharya and V. V. Ratnam, " Effect of  $PbI_2$  on the properties of Galena concentrate for thermoelements. " - Second European Conference on Thermoelectrics, Naney, France, July (1989).
- [4]. S. Chatterjee, A. Dasgupta and H. N. Acharya, " Solar Thermoelectric generator using Indian Galena." - The National Solar Energy Convention, Calcutta, India (1990).
- [5]. S. Chatterjee, H. N. Acharya and V. V. Ratnam, " Grain size Effect on the polarity of Seebeck coefficient of natural Galena. " - J. Energy Convers. Mgmt. 31, 2(1991) 175.
- [6]. S. Chatterjee, T. K. Chaudhuri and H. N. Acharya, " Design parameters of 10 watt Thermoelectric Generator based on Indian Galena. " - Eleventh International Conference on Thermoelectrics, The university of Texas at Arlington, U.S.A., October (1992) 55.

# Na-DOPING OF LEAD-TIN CHALCOGENIDES

G.T. Alekseeva, E.A. Gurieva, P.P. Konstantinov, L.V. Prokof'eva

*A.F. Ioffe Physico-Technical Institute, St.Petersburg, Russia.*

A study has been made of the impurity-concentration and temperature dependencies of the transport coefficients in Na-doped Pb(Sn)Te (LTT) and Pb(Sn)Se (LTS) mixed crystals. The Mössbauer method has been used to determine the charged states of the Sn atoms in these materials. The results obtained are interpreted taking into account the formation, interaction and influence the electron spectrum of the impurity and intrinsic defects.

## Introduction

In 80th years it was found that introduction of group IV elements in lead chalcogenides limited to a great extent the Na acceptor action and influenced the behavior of other effects [1, 2]. It meant that there was some common phenomenon which changed the electronic structure of the doped materials. The general manifestations of this phenomenon and its particular features being determined by the type of chalcogen are presented for consideration.

## Transport of charge carriers in dilute alloys

1. In both systems there is a region of the Fermi level pinning where the Na atoms don't display the acceptor properties and the Hall concentration no more follows the dopant content (fig. 1). In LTS the density of holes even falls in the localization range. In both cases the introduction of one Sn atom leads to the localization of 2 holes.

In LTT the range of the Hall coefficient saturation extends over no more than 1/2 of the total dopant concentration range and always adjoined the limit of this range. In the dilute LTS alloys the upper limit of the compensation range is inside the range of the Na solubility, so that at high dopant contents the Na atoms recover their activity giving rise to the second region of free-hole generation.

2. Only quantitative changes in temperature Hall coefficient behavior are typical of the doped LTT crystals (fig. 2) compared to the similar data of PbTe:Na. The fall of the Hall coefficient with temperature is not typical of this material. In LTS alloys the Hall curves are more complex (fig.3) The rate of the rise and the position of the maximum depend on the dopant amount. When the latter approaches double concentration of Sn it is observed only the falling branch of the curve.

3. In both systems an additional scattering mechanism appears at low T governing the decrease in the hole mobility and the changes in the thermopower (fig. 4 - 7). In LTS the changes in the mobility and thermopower have a resonance character, at low T the values of S may be both below and above the corresponding values |S| for the Cl-doped alloy of the same composition with the similar quantities of the band parameters.

All these results may be interpreted on the base of a resonance impurity state model. Using the data obtained one may draw an important conclusion, namely: the number of the localized holes in LTT alloys is never higher than the number of the free holes. It means that the filling of the impurity states always is not higher 1/2. There are no limitations of this parameter in LTS.

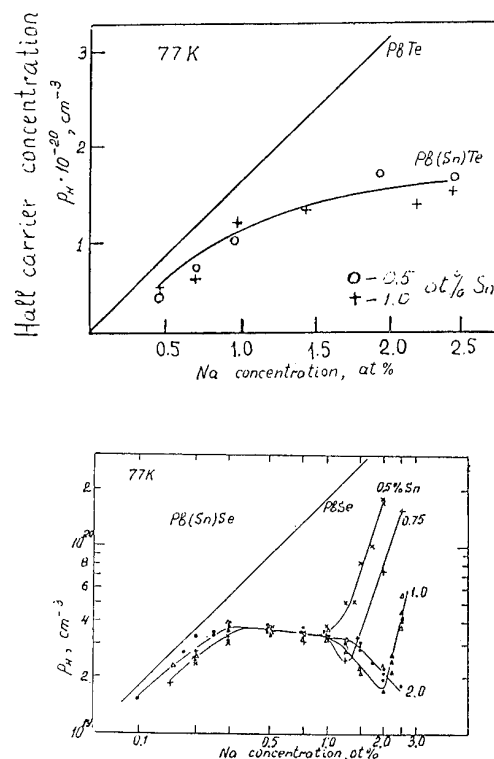


Figure 1: The dependence of the Hall density on the Na concentration in the binary compounds and solid solutions.

## The Mössbauer effect

The second important conclusion arises from the Mössbauer effect data [3]. The changes in the Mössbauer spectra due to replacement of Te with Se were determined (fig. 8). The Sn(2+) line which is the only one for a material containing only the Te atoms gradually weakens and disappears, the transformation of the Sn(4+) line is reversed. Therefore, in the Na-doped LTT solid solutions the Sn atoms are not directly the centers at which holes are localized. The Na atoms are not such centers, too, because in the opposite case the Na atoms should be attributed the charge 2+ which is unlikely. Therefore, we conclude there are the atoms of the main components, namely, the Te atoms to be responsible for the creation of the nonband

states. In the dilute LTS alloys the holes are localized at the Sn atoms.

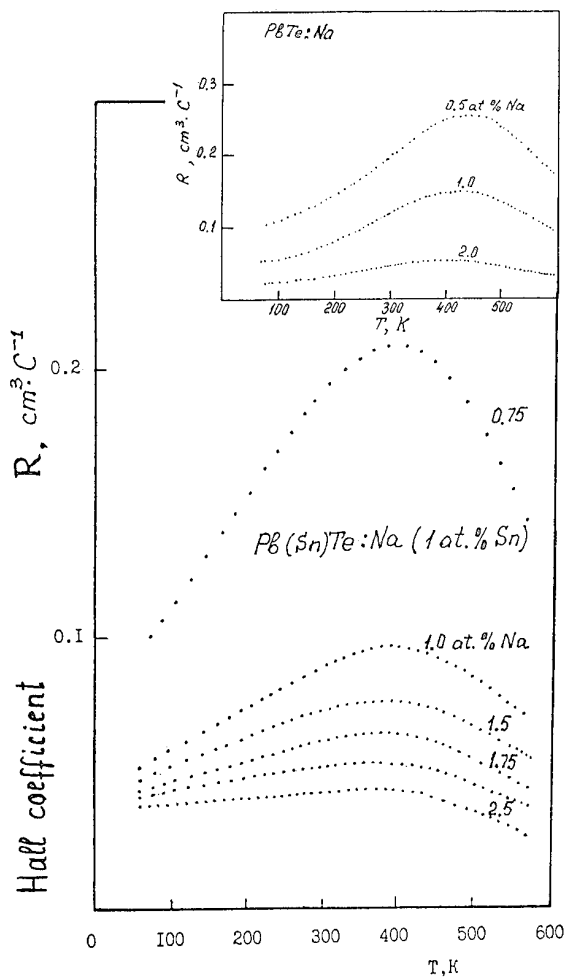


Figure 2: Temperature dependences of the Hall coefficient of  $PbTe$  and  $Pb(Sn)Te$  with various Na concentration.

### Transport effects in more concentrated LTS alloys

A study of the transport phenomena in more concentrated LTS solid solutions shows that the variation of the transport coefficients with both the dopant concentration and temperature are characterized by the same peculiarities (fig. 9 - 11).

The basic conclusions are following.

The impurity band position in energy is determined by the LTS alloy composition: the impurity states lower down deep into the valence band with increasing the Sn content.

In the concentrated LTS solid solutions there is no correlation between the number of the impurity states and the Sn content; as the latter increases, the number of the impurity states changes more less.

A number of the impurity states in the LTS alloys of different composition was evaluated using the low-temperature data on the thermopower (fig 11). A value of the Na concentration

has been determined where the absolute quantities

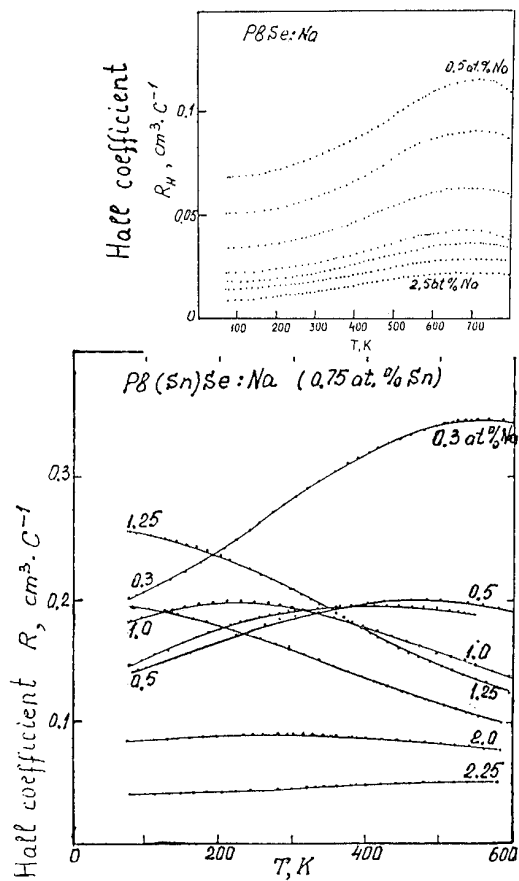


Figure 3: Temperature dependence of the Hall coefficient in  $PbSe$  and dilute  $Pb(Sn)Se$  solid solutions with various Na concentration.

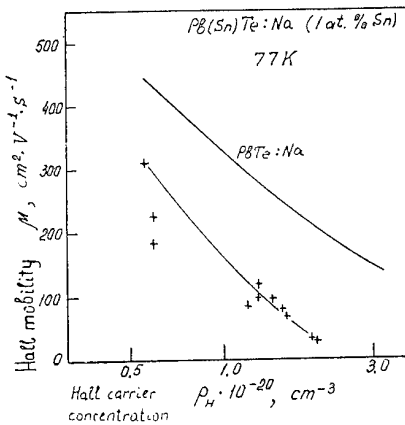


Figure 4: The hole mobility power vs. the Hall concentration in the Na-doped  $Pb(Sn)Te$  solid solutions.

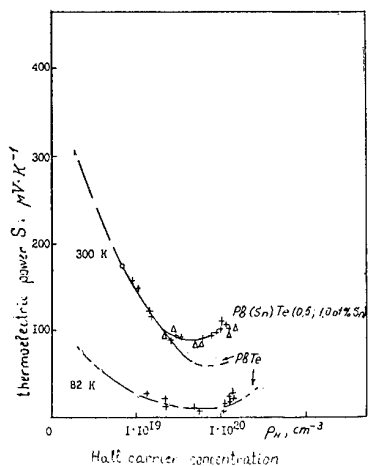


Figure 5: The thermoelectric power vs. the Hall concentration in the Na-doped Pb(Sn)Te solid solutions.

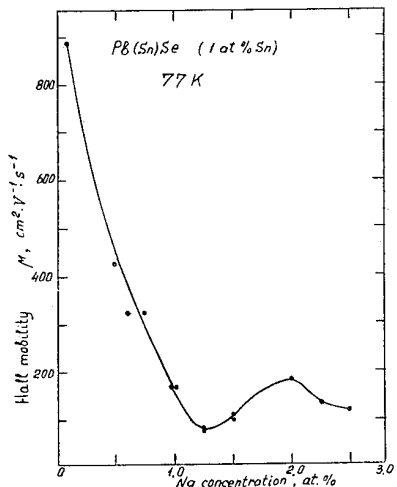


Figure 6: The hole mobility vs. the Na content in the Na-doped Pb(Sn)Se solid solutions.

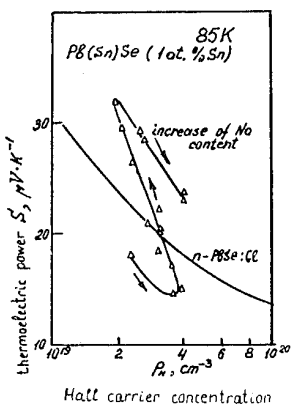


Figure 7: The thermoelectric power vs. the Hall concentration in the Na-doped Pb(Sn)Se solid solutions.

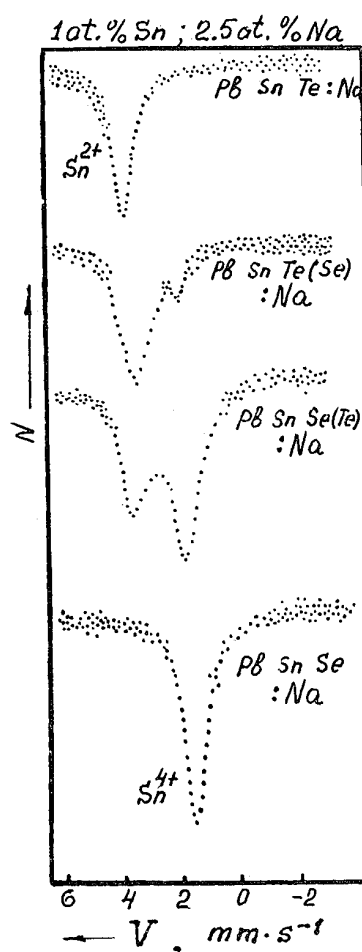


Figure 8: <sup>119</sup>Sn Mössbauer spectra recorded at 80 K for Pb-SnTe(Se) alloys doped with sodium.

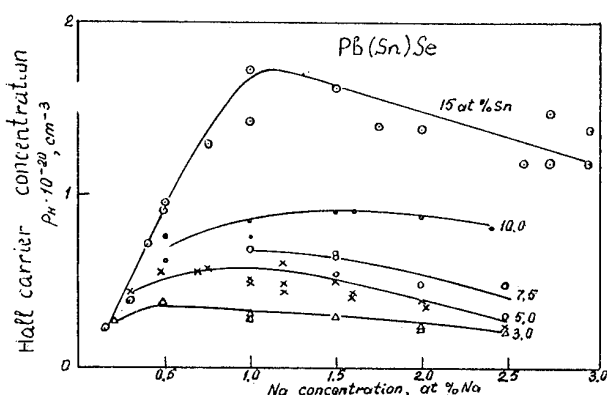


Figure 9: The Hall concentration vs. the Na content for more concentrated Pb(Sn)Se alloys.

concentration. Such a position for a Sn atom appears where the solid solution is formed and hence, it may be related to the peculiarities of the undoped alloy crystalline structure.

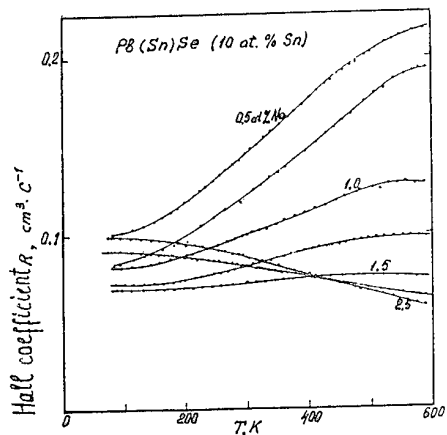


Figure 10: The the Hall coefficient vs. temperature for more concentrated Pb(Sn)Se alloys.

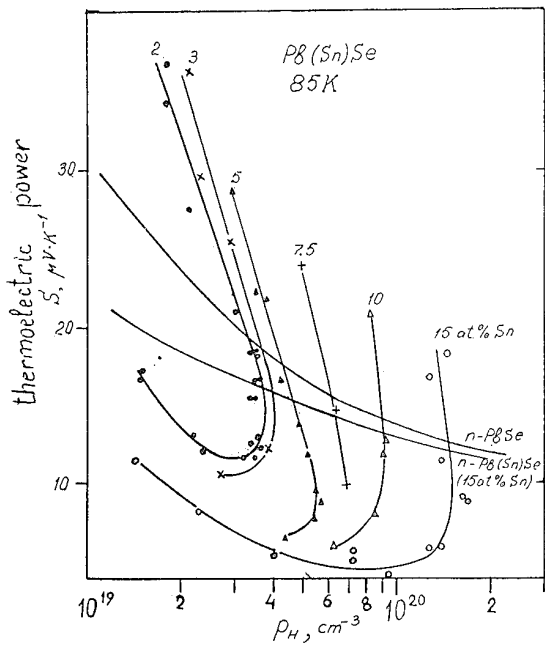


Figure 11: Concentration dependencies of the thermopower for Pb(Sn)Se alloys with the tin content of 3-15 at.-%.

of thermopower of p- and n-type samples are the same and, therefore, a contribution in thermopower due to the resonance hole scattering is equal to 0. In this case the Fermi level position is in the center of the impurity band and the filling of the impurity states is 1/2. In fig. 12 the values of  $N_A(1/2)$  vs. composition are given together with the Hall densities related to the same values of  $N_A$ . A difference of these quantities is a number of the localized holes, or 1/2 of a total number of states in the impurity band. One may see that at first the total number of the impurity states follows the Sn concentration, then its variation becomes much less.

Thus, only a small part of the Sn atoms occupy active positions in a lattice and are capable of affecting the free-hole

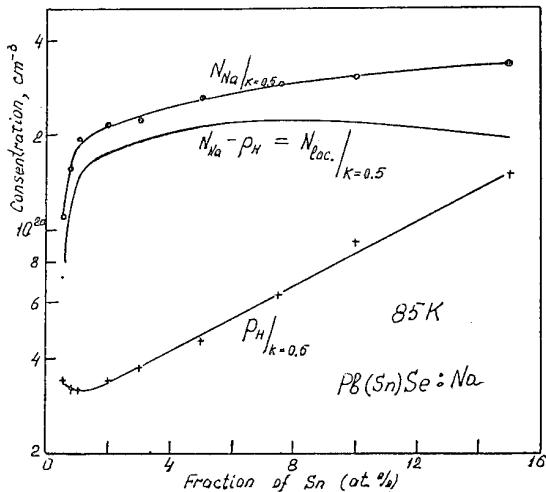


Figure 12: The dependences of  $N_A(1/2)$ ,  $p_H(1/2)$  and their difference on the Sn concentration in the Pb(Sn)Se alloys. Pb(Sn)Se : Na

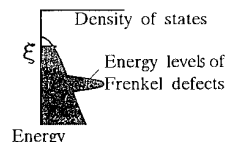
### Defects in the Na-doped lead-tin chalcogenides: formation, interaction, effect on the electron spectrum

#### 1. Formation of FRENKEL DEFECTS in UNDOPED lead-tin chalcogenides.

One may suppose that a part of the Sn atoms in the undoped solid solution occupy no regular sites in a lattice but interstitial positions forming the electroneutral Frenkel defects:

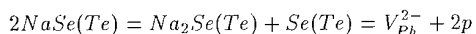
$$\underbrace{n(Sn_i^{2+} + V_{Pb}^{2-})}_{\text{FRENKEL DEFECT}} = 0$$

n - the Frenkel defect concentration. A local level with 2 electrons appears in the electron spectrum, a total number of states  $N_{\text{tot}} = 2n$ .



#### 2. ELECTROACTIVE DOPING of lead-tin chalcogenides with Na.

One may assume that appearance of free holes in the Na-doped crystals is associated with the presence of the metal vacancies, 2 holes per 1 vacancy which is equivalent to 1 hole per 1 atom of Na as follows from the experimental data:

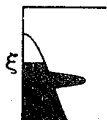


In such case Na-doping of the LTT and LTS alloys may be written:

$$n(Sn_i^{2+} + V_{Pb}^{2-}) + mSe(Te) =$$

$$n(Sn_i^{2+} + V_{Pb}^{2-}) + m(V_{Pb}^{2-} + 2p)$$

where  $m$  - the metal vacancy concentration,  $m = 1/2N_A$ . The Hall concentration  $p_H = 2m$ .



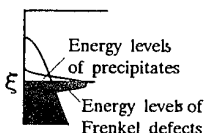
### 3. INTERACTION OF DEFECTS IN LTS ALLOYS. HOLE LOCALIZATION.

If the vacancy concentration exceeds a certain value determined by the Sn content the interaction between defects takes place. As a result of the interaction the precipitates are formed including an interstitial double charged impurity defect and a metal divacancy:

$$n(Sn_i^{2+} + V_{Pb}^{2-}) + m(V_{Pb}^{2-} + 2p) + kSe =$$

$$(n - k)(Sn_i^{2+} + V_{Pb}^{2-}) + m(V_{Pb}^{2-} + 2p) + k \underbrace{(Sn_i^{4+} + 2V_{Pb}^{2-})}_{\text{PRECIPITATE}}$$

$k$  - concentration of precipitates. No additional free holes appear,  $p_H = 2m = \text{Const}(k)$ . RANGE OF THE FERMI LEVEL PINNING, the holes fill the quasilocal states relating to the precipitates,  $N_{tot} = 2n$ .



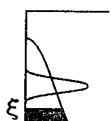
### 4. THE SECOND RANGE OF FREE-HOLE GENERATION in dilute LTS alloys.

After nearly all of the Frenkel defects have become bound up in precipitates can the additional metal vacancies again become capable of creating the free holes:

$$n(Sn_i^{4+} + 2V_{Pb}^{2-}) + m(V_{Pb}^{2-} + 2p) + sSe =$$

$$n(Sn_i^{4+} + 2V_{Pb}^{2-}) + (m + s)(V_{Pb}^{2-} + 2p)$$

$s$  - additional concentration of the metal vacancies. The Hall concentration  $p_H = 2(m + s)$ .

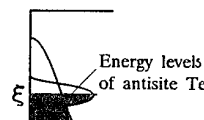


### 5. INTERACTION OF DEFECTS IN LTT ALLOYS. HOLE LOCALIZATION.

In other manner the defects interact in the doped LTT alloys. The Sn atom transfers to an usual regular site and creates the conditions for rearrangement of 2 metal vacancies in an antisite Te defect:

$$n(Sn_i^{2+} + V_{Pb}^{2-}) + m(V_{Pb}^{2-} + 2p) + kTe = (n - k)(Sn_i^{2+} + V_{Pb}^{2-}) + (m - k)V_{Pb}^{2-} + k \underbrace{Te_{Pb}^{2-}}_{\text{ANTISITE Te}} + 2mp + kSn_{Pb} + kTe_{Te}$$

$k$  - concentration of the antisite Te atoms. As follows from [3],  $m \geq n$ ,  $k \leq n$ . The Hall concentration remains constant,  $p_H = 2m = \text{Const}(k)$ . As, 4 quasilocal states which are half-filled with electrons are associated with one atom  $Te_{Pb}$ , a total number of the impurity states becomes a function of doping level,  $N_{tot} = 2(n - k) + 4k$ , it increases with increasing the antisite defect concentration, i.e. the Na content. In the case of  $n \cong k$  the antisite defect  $Te_{Pb}$  is the dominant type of defect,  $N_{tot} = 4k$ , the impurity band is half-filled with electrons (the heavily doped LTT alloys with the Sn content of 0.5:1.0 at.%,  $n \cong m \cong k = 0.5$  at.%) [3].



### References

- [1] L.V.Prokof'eva, M.N.Vinogradova, S.V.Zarubo, Doping effect of tin in  $Pb_{1-x}Sn_xSe$  and  $Pb_{1-y}Sn_yS$  solid solutions, *Fiz.Tekh.Poluprov.*, 1980,v.14,No.11,pp.2201-2204.
- [2] F.S.Nasredinov, L.V.Prokof'eva, P.P.Seregin, S.V.Zarubo, A.V.Ermolaev, A.N.Kurmantaev, Mössbauer study of two-electron exchange between neutral and ionized tin donor centers in solid solutions on the basis of PbS and PbSe, 1985, *Phys.stat.sol.(b)*,v.130,pp.727-735.
- [3] G.T.Alekseeva, B.G.Zemskov, P.P.Konstantinov, L.V.Prokof'eva, K.T.Urazbaeva, Role of defects in acceptor doping of PbTe-type semiconductors with group 1 elements, *Sov.Phys.Semicond.*, 1992,v.26,No.2,pp.202-207.

## PREPARATION AND INVESTIGATION OF THERMOELECTRICAL AND ELECTRICAL PROPERTIES OF CuInSe<sub>2</sub> BULK AND THIN FILMS CRYSTALS

M.A.Abdullaev ,R.M.Gagieva,I.Kh.Magomedova,P.P.Khochlachov, A.M.Khasbulatov  
*Institute of Physics,Daghestan Sc. Center RAS, Makhachkala,367003, RUSSIA*

Seebeck effect and electrical conductivity have been measured as function of temperature on samples of CuInSe<sub>2</sub> bulk and thin films crystals in which varying concentrations of donor and acceptor atoms have been incorporated. The behaviour above room temperature is found to be consistent with electrical conductivity dates. Small values of Seebeck voltage at the low temperatures believed to be caused by impurity band conduction.

### Introduction

Copper indium diselenide is a ternary-compound semiconductor with a chalcopyrite structure. CuInSe<sub>2</sub> films and bulk crystals are the very prospective materials to be used in solar power industry and thermoe.m.f. transformation[1]. This material it is advantageous is thermal and chemical stability and low cost. It has a direct energy band gap of about 1 eV and high absorption coefficient (about  $4 \times 10^5 \text{ cm}^{-1}$ ).

The holes of CuInSe<sub>2</sub> have a high effective mass  $0.76 m_0$ . Therefore it is expected that a rather large thermoelectric power originating from the holes is observed in CuInSe<sub>2</sub>. In the bulk crystals the observed thermoe.m.f. reached the large value of about  $650 \mu\text{VK}^{-1}$  [2]. CuInSe<sub>2</sub> physical properties and device constructions still have not been studied. The thermoe.m.f. of films dates is not published. In a previous paper [3] we reported on the electrical properties and carrier scattering mechanisms of CuInSe<sub>2</sub> bulk crystals. In this paper the results of study thermoelectrical and electrical properties of CuInSe<sub>2</sub> thin films, prepared by a flash evaporation are reported.

### Samples and measurements

Single - and polycrystalline CuInSe<sub>2</sub> samples are obtained by Bridgman vertical method under the temperature gradient conditions. The weights for synthesis are taken in stoichiometric proportions or with  $\pm 2 \text{ mol\%}$  deviations. Initial polycrystalline ingots are used as starting materials to grow the single crystals.

An ingot is crushed to powder and fused in a quartz ampoule under the pressure no more than  $10^{-3} \text{ Pa}$ . According to the thermoe.m.f. data, the stoichiometric weights give n - and p-type ingots were produced. At the same conditions the p-type ingots were prepared by cooling with rate not less than 3 grad/hour. X-ray microanalysis data give Cu<sub>1.0</sub>In<sub>0.98</sub>Se<sub>2.0</sub> composition in p-type ingots and Cu<sub>0.9</sub>In<sub>1.0</sub>Se<sub>2.0</sub> composition in n-type ingots, after fuse of the stoichiometric weights. Single crystal p- CuInSe<sub>2</sub> samples had charge carrier concentration  $4 - 5 \times 10^{17} \text{ cm}^{-3}$  and carriers mobility of  $10 - 15 \text{ cm}^2/\text{V}\cdot\text{s}$ . Fusing together with proportions of Cu:In:Se = 0.9:1.0:2.0 a single-phase n-type material has been prepared.

Single crystals were grown from near stoichiometric melt and then were pulverized into powder with particles size of about  $100 \mu\text{m}$ . The films were deposited by a flash evaporation in  $10^{-3} \text{ Pa}$  vacuum using spiral vibrating supplier with 2 gram per hour rate. The

films 2.5 - 3  $\mu\text{m}$  thick were deposited in quartz, crystal glass and optical glass substrates.

The perfectness and composition of the layers were controlled by XRMA-methods. Single phase stoichiometric films with chalcopyrite structure had  $2 \mu\text{m}$  grain size. To reduce a serial resistance the CuInSe<sub>2</sub> layers had excess of Cu atoms up to 1 at.percent.

Hole concentration and mobility at 300 K were  $1 - 6 \times 10^{17} \text{ cm}^{-3}$  and  $1.0 - 3.4 \text{ cm}^2/\text{V}\cdot\text{s}$  respectively. Electron concentration in n-type films had a value  $4 \times 10^{15} - 1 \times 10^{17} \text{ cm}^{-3}$  with  $12 - 70 \text{ cm}^2/\text{V}\cdot\text{s}$  mobility. Ohmic contacts of In and Au were evaporated in high vacuum. Substrate temperatures were 450 - 570 K, resistivity of n-CuInSe<sub>2</sub> films was  $10 - 15 \Omega\cdot\text{cm}$ , and p-type -  $1.5 - 5 \Omega\cdot\text{cm}$ . It was achieved by vacuum annealing of the film at 450 K during 15 min.

Electrical conductivity measurements were made at various temperatures in range 2.7 - 350 K and were in agreement with the published results at the 300 K [4].

Thermoe.m.f. obtained with helium gas in the container disagreed by several percent with the results obtained in high vacuum. This indicates a poorer thermal contact at the junctions in CuInSe<sub>2</sub> films than bulk samples where no such disagreement was found.

The thermocouples copper - constantan were secured in the central portion away from boundaries. The heater was constructed from manganin wire wrapped directly onto the films. Short length copper wire were wrapped and soldered around the sample at each thermocouple - CuInSe<sub>2</sub> junction and used to minimize temperature gradients along the thermocouple leads near the junction. The region between the thermocouples was electrically probed at room temperature and in the samples used was uniform to 20 percent.

The samples were mounted in a conventional apparatus consisting of a radiation shield inside an evacuated container. The lead wires were brought to the temperature of the radiation shield and were sufficiently long to insure a negligible heat. Lead along the wires and thus making measurements possible lead wires for electrical conductivity measurements were attached at the film ends and in some cases Hall leads were attached midway between the thermocouples.

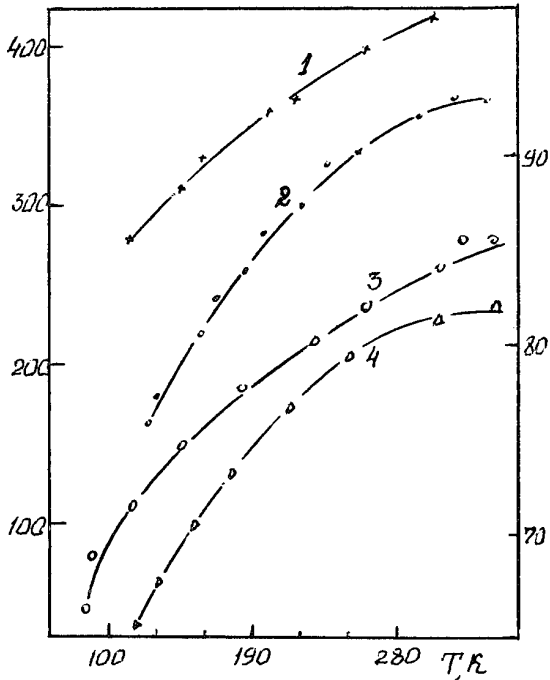
### Results

We shall consider the experimental data obtained for the 4 samples p - and n - CuInSe<sub>2</sub>. The thermoelectric power ( $\alpha$ ,

$\mu\text{V/K}$ ) is plotted as a function of the absolute temperature  $T$  in Fig.1. It can be seen that the samples with the highest value of  $\alpha$  around room temperature are those with the smallest concentration difference between the donor and acceptor atom, that is, those with the smallest density of mobile charge carriers. It is to be expected for any model in which the thermoelectric energy is transported by mobile charge carriers.

Calculations of the thermoelectric power in the impurity range, when lattice scattering and impurity range,

Fig.1. Temperature dependence of the thermoelectric power  $\alpha \mu\text{V}^{-1}$  in  $\text{CuInSe}_2$  films of p-type (curves 1,2 - left scale) and n-type (3,4 - right scale)



when lattice scattering are acting in parallel ( $0 \leq r \leq 2$ ), yields the following result:

$$\alpha = \frac{k}{l} \left[ r - \ln \frac{ph^3}{2(2\pi mkT)^{3/2}} \right] \quad (1)$$

Calculation of the effective mass of the holes at 300 - 350 K yields consistently the value  $m = 0.76m_0$ , that is agreement with results from microwave measurements [5].

The samples 1, 2 is not highly compensated, this means that below 160 K most of the holes are interacting to form the impurity band. If the impurity band is practically full, and if it does not overlap the valence band, it should rise to a positive thermoe.m.f. according to the equation:

$$\alpha = (\alpha_1 \sigma_1 + \alpha_2 \sigma_2) / \sigma \quad (2)$$

where the subscripts refer to valence (1) and impurity (2) bands.  $\alpha_2$  must be constant below 200 K, this is because the small percentage of compensation. Since  $\sigma_1$  values directly as  $p_1$ , while  $\alpha_1$  varies as  $\log p_1 + d\alpha_1/dT$ ,  $\sigma_1$  is probably the dominant term in Eq.(2), and value  $\alpha_2$

would enable one to estimate the energy difference between the valence band and the almost filled impurity band by a plot of  $\log(\alpha_1 - \alpha)$  against  $T$ .

From a sample 4, it is estimated that the concentration of donors is  $1 \times 10^{18} \text{ cm}^{-3}$ . The room temperature Hall - effect, gives the concentration of  $1.25 \times 10^{17}$  atoms greater than the vacancies concentration. Thus sample 4 is about 90 percent compensated and experimental points  $\alpha$  is very small at the low temperature. Because of the difficulty of measuring a small voltage over a high - impedance circuit, the low - temperature points scatter, however they appear to extrapolation to 0 at the  $T \leq 50 \text{ K}$ .

The electrical conductivity ( $\sigma, \Omega^{-1}\text{cm}^{-1}$ ) is plotted as a function of the absolute temperature  $T$  for p-type samples (1,2) and n-type samples (3,4) in Fig2. It can be seen from Figs 2 that the  $\log \sigma$  vs  $1/T$  plot gives a straight line above  $\sim 250 \text{ K}$ , but observed data below 160 K deviate upward from the straight line. So the hopping conduction is considered to be dominant below 160 K. The electrical conductivity can be expressed by

$$\sigma = \sigma_0 \exp(-E/kT) \quad (3)$$

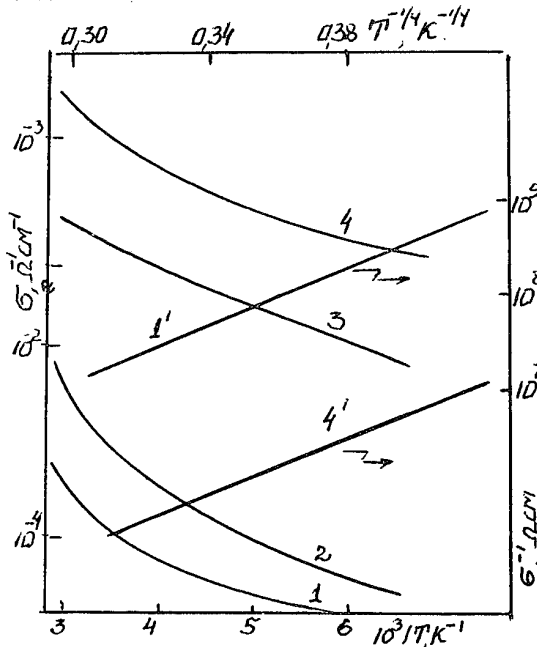
Here  $\sigma_0$  is the constant,  $E$  - the activation energy,  $k$  - the Boltzmann constant.

The variation of  $E$  with substrate temperature of p-type films was measured 0.18 - 0.20 eV and 0.01 - 0.008 eV for n-type films. The films with a larger thermoe.m.f has a larger activation energy. It may be accounted for the hopping conductivity following by the Mott law:

$$\sigma = \sigma_0 \exp(-T_0/T)^{1/4} \quad (4)$$

where  $\sigma_0 = \beta [kq(E_F)a^{-3}]^{-1}$ ,  $\beta = 21.2 \pm 1.2$ ;  $q(E_F)$  is density of states at Fermi level  $E_F$ ;  $a = \hbar(2mE_F)^{-1/2}$  - is the radius of localization.

Fig.2. Curve numerical corresponds to samples numbers. Samples: 1 - p =  $1 \times 10^{17} \text{ cm}^{-3}$ ; 2 - p =  $4 \times 10^{17} \text{ cm}^{-3}$ ; 3 - n =  $5 \times 10^{16} \text{ cm}^{-3}$ ; 4 - n =  $1 \times 10^{17} \text{ cm}^{-3}$ .



As can be see in Fig2,  $\sigma$  values experimentally obtained are straigntend by  $\lg\sigma$  vs  $(1/T)^{1/4}$  dependence. Value of  $T_0$  for sample 1, calculated by equation  $\lg\sigma = f(1/T)^{1/4}$ , allows us to estimate density of states at Fermi level as high as  $4 \times 10^{21} \text{eV}^{-1}\text{cm}^{-3}$ .

#### References

- [1]. A.Rockett, R.W.Birkmire. CuInSe<sub>2</sub> for photovoltaic Application. *J.Appl.Phys.(A)* , 1991,v.7,No.7, pp.R81 - R97.
- [2]. M.A.Abdullaev, I.Kh.Amirkhanova, R.M.Gadjieva, Annealing Effect on the Conductivity and Thermoe.m.f. of CuInSe<sub>2</sub> crystals p-type. *Neorgan.Mat.*,1993,v.29,No.6, pp.785 - 787.
- [3]. M.A.Abdullaev, I.Kh.Amirkhanova, R.M.Gadjieva et al. Preparation and investigation of CuInSe<sub>2</sub> bulk crystals and films. *Neorg.Mat.*,1992,v.28, No.5, pp.961 - 964.
- [4]. S.I.Kim, H.B.Im, Preparation and properties of selenized CuInSe<sub>2</sub> thin films. *Thin Solid Films*, 1992, v.214, No.2, pp.194 - 199.
- [5]. H.Neumann, H.Sobotta, W.Kissinger, R.Kuhn, Hole Effective Masses in CuInSe<sub>2</sub> , *Phys. Stat. Sol. B*, 1981, v.108, No.2, pp.483 - 486.

ON THE VALENCE BAND NON-PARABOLISITY IN  $\text{Cu}_{2-x}\text{Se}$   
SUPERIONIC CONDUCTOR

M.A.Korzhuev, and A.V.Laptev

*A.A.Baikov Institute of Metallurgy of Russian  
Academy of Sciences, Moscow, 117911, Russia*

The unusual negative non-parabolosity of conductivity effective mass  $m_c$  early declared by Gorbachev & Putilin (1973) for  $\text{Cu}_{2-x}\text{Se}$  was explained for the first time by taking into account the phase transformations  $\alpha \rightarrow \beta$ , observed in crystals at the room temperature.

#### Introduction

Copper Selenide  $\text{Cu}_{2-x}\text{Se}$  is known to be the non-stoichiometric compound ( $x = 0.0001$  to  $0.3$ ) of electronic (p-type) and ionic ( $\text{Cu}^{+1}$  ions) mixed conductivity  $\sigma = \sigma_e + \sigma_i$  ( $\sigma_e \gg \sigma_i$ ) [1]. Above the Curie temperature ( $T_c = 291$  to  $413$  K depending on the deviation from stoichiometry)  $\text{Cu}_{2-x}\text{Se}$  transforms from the low-temperature  $\alpha$ -phase (space group  $\text{Cm}$ ) to the high-temperature  $\beta$ -phase (space group  $\text{F}4\bar{3}\text{m}$ ), the last being superionic [2,3]. At the room temperature the  $\alpha \rightarrow \alpha+\beta \rightarrow \beta \rightarrow \beta + \text{Cu}_3\text{Se}_2$  phase transitions are observed in series in  $\text{Cu}_{2-x}\text{Se}$  when  $x$  increases ( $x_1 = 0.05$ ,  $x_2 = 0.20$ , and  $x_3 = 0.23$ ) [3]. In the  $\alpha$ - to  $\beta$ -transition, approximately half the copper ions in  $\text{Cu}_{2-x}\text{Se}$  are excited into interstitial sites and become mobile as in a liquid, the copper diffusion coefficient increases from about  $10^{-5}$   $\text{cm}^2/\text{s}$  in the  $\alpha$ -phase to about  $10^{-2}$   $\text{cm}^2/\text{s}$  in the  $\beta$ -phase [1,3]. Conductivity effective mass  $m_c$  and density of state one  $m_d$  in Copper Selenide  $\text{Cu}_{2-x}\text{Se}$  crystals were previously studied using the reflection spectra and electronic transport phenomena in [4] to [7], the Hall coefficient  $R = A/e$  (here  $A$  is Hall factor ( $A > 0$  for electrons,  $A < 0$  for holes) and  $e$  is the charge of an electron) was measured in [6-10]. The dependencies obtained were unusual

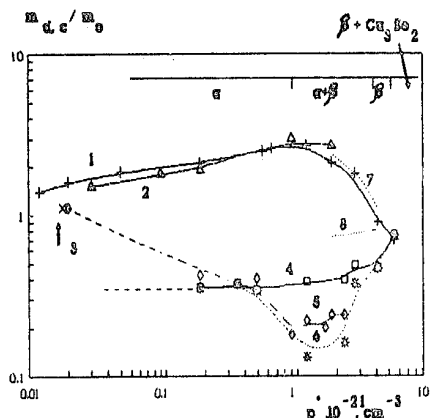
in some details. The \* Hall concentration of carriers  $p = 1/R$  was less than that calculated from the sample composition (i.e.  $/A/ < 1$ ) [6,7], the  $m_d$  versus  $p$  dependence was non-parabolic ( $d m_c / d p > 0$ ) [7,8], but the  $m_c$  versus  $p$  one was negative non-parabolic ( $d m_c / d p < 0$ ) [5] (curve 5, Fig.1), the last being hardly to explain in the framework of the standard band approach. So one proposed the complicated band structure as well as the narrow valence band for  $\text{Cu}_{2-x}\text{Se}$  [6,8]. From the other hand, due to superionic disorder the mobility of holes in  $\text{Cu}_{2-x}\text{Se}$  samples is too low ( $\mu \sim 10$   $\text{cm}^2/\text{V.s}$  at room temperature) [8], so the band approach validity for  $\text{Cu}_{2-x}\text{Se}$  may be in question at all [11,12]. According to [9], electronic transport phenomena in  $\text{Cu}_{2-x}\text{Se}$  samples may occur near-by the condition  $\lambda \rightarrow a$ , here  $\lambda$  is the mean free path of holes,  $a$  is the inter atomic space. Under the condition  $\lambda \rightarrow a$  Boltzmann kinetic equation becomes unsuitable as well as the classic band theory due to Heisenberg relation

$$\Delta E \sim \hbar / \langle \tau \rangle, \quad (1)$$

here  $\Delta E$  is the energy indeterminated region,  $\hbar = h/2\pi$  is the reduced Planck constant, and  $\langle \tau \rangle$  is the mean relaxation time of holes [11,12]. As the relation  $\Delta E/E_F \sim 1$  (here  $E_F$  is the Fermi energy) is equivalent to  $k_F \lambda \sim 1$  (here  $k_F = 0.11$  to  $0.48 \cdot 10^{-8}$

Fig.1. The dependencies of effective masses  $m_d/m_0$  (1-3, 7) and  $m_c/m_0$  (4-6,8) on Hall carrier concentration  $p^*$  in  $\text{Cu}_{2-x}\text{Se}$ . Curve 4 was calculated using the ultimate carrier density in ( $\alpha + \beta$ ) region.

T, K: 1-6 - 300; 7,8 - 450.



$\text{cm}^{-1}$  is the Fermi momentum of holes in  $\text{Cu}_{2-x}\text{Se}$  [10] and  $k_F \cdot \lambda = (k_F \cdot a) \cdot (\lambda/a)$ , the relations (1) for  $\text{Cu}_{2-x}\text{Se}$  samples is similar to the condition  $\lambda \sim a$ . From equation (1) one can see, that for  $\Delta E/E_F > 1$  the Fermi surface conception fails, for  $\Delta E/2W > 1$  (here  $2W$  is band width) the band conception fails in all [11,12].

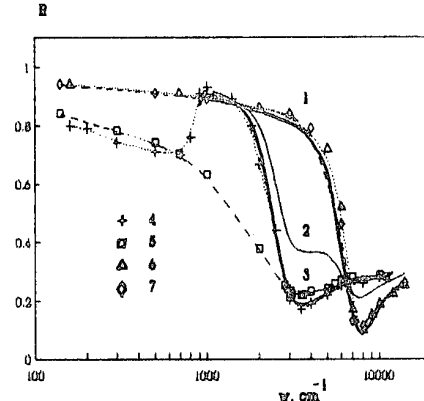
The present paper aims at reinvestigating the nature of hole conductivity and band approach validity in  $\text{Cu}_{2-x}\text{Se}$  within the temperature range from 300 to 500 K, which includes the superionic transition temperature ( $T_c$ ). The ununiform  $m_c$  versus  $p$  negative non-parabolic dependence, previously declared in [5], was showing to be the seeming effect, resulted from ignoring in [5] the phase transformations  $\alpha \rightarrow \alpha+\beta \rightarrow \beta \rightarrow \beta + \text{Cu}_3\text{Se}_2$ .

#### Experimental

Polycrystalline samples of  $\text{Cu}_{2-x}\text{Se}$  ( $x=0-0.3$ ) have been prepared from elements (of better than 99.9999% purity) by melting together the components at 1500 K for 3 h in evacuated and sealed quartz tubes. Cylindrical samples (10 mm in

Fig.2. Reflectivity spectra  $R(w)$  for two  $\text{Cu}_{2-x}\text{Se}$  samples. x: 1,6,7 - 0,05; 3-5 - 0.015; 1,3 - experimental, 2,4-7 - calculations. Curve 2 is the superposition of 1 and 3 ones with the weights of 0,3 and 0,7 respectively.

(T = 300 K)



diameter, 4-6 mm long) were used to get an optic spectra, ones (88 mm in diameter, 20 mm long) - for Seebeck coefficient study, and parallelepipeds of 1x3x15 mm in size - for Hall measurements [9]. The density of state effective masses  $m_d$  were calculated by

Seebeck coefficient technique using the values of  $\alpha$  and  $p = A/R \cdot e$  [8]. Conductivity (or optical) effective masses  $m_c$  were determined from the

position of plasma minima in reflectance spectra (Fig.2) [13]. Reflection factors  $R$  were measured using IFS 88 "Bruker" Fourier spectrophotometer within the wavelength range of  $\lambda = 0.5$  to  $10 \mu$  (wave number range of  $w = 1000$  to  $20000 \text{ cm}^{-1}$ ). The light beam used was of circular polarization, the incidence angle of light was of  $11^\circ$ . Before measurements the samples were optical polished by chromium oxide water paste. The position of plasma minima  $w_{\min}$  in the reflection spectra of samples in study was from  $2460$  to  $9000 \text{ cm}^{-1}$  ( $\lambda = 1$  to  $5 \mu$ ) (Table 1) in accordance with [5] and [14]. It should be pointed out, that within this range all the minima were locked or at  $w < 3800 \text{ cm}^{-1}$  (group I), or at  $w = 8000-9000 \text{ cm}^{-1}$  (group II) (Table 1). No minima were observed within  $w = 3800-8000 \text{ cm}^{-1}$  range as well as in [5]. The conductivity effective masses were

Table 1  
Some properties and plasma parameters of  $\text{Cu}_{2-x}\text{Se}$  samples

x	Phase composition	Hall/ calculated carrier density $p/p$ ( $10^{20} \text{ cm}^{-3}$ )	Hall mobility $\mu = R\sigma$ ( $\text{cm}^2/\text{V.s}$ )	Plasma frequency $w_{\min}$ ( $\text{cm}^{-1}$ )	Hole damping $\gamma$ ( $\text{cm}^{-1}$ )	Optical masses $m/m_o$
0.007	$\alpha$	2.1/ 1.4	12.0	2460	2210	0.35
0.015	$\alpha$	3.8/ 3.0	11.5	3500	2200	0.37
0.02	$\alpha$	5.4/ 4.0	11.6	3800	2380	0.34
.....	.....	.....	.....	.....	.....	.....
0.05	$\alpha+\beta$	13/ 10	11.0	8430	5320*	0.13*
					1930*	0.38*
0.10	$\alpha+\beta$	27/ 20	10.1	9000	5850*	0.16*
					2140*	0.39*
0.15	$\alpha+\beta$	31/ 30	10.0	8500	2530*	0.37*
					1630*	0.48
0.23	$\beta$	47/ 46	10.0	8700	2420	0.47
0.3	$\beta+\text{Cu}_3\text{Se}_2$	56/ 60	9.0	8100	1400	0.74

\*- calculations were carried out, using the ultimate carrier density in ( $\alpha+\beta$ ) region ( $p = 4.10^{21} \text{ cm}^{-3}$ ).

obtained from the comparison of experimental and calculated reflectivity spectra. The normal incident reflectivity is given by [13]

$$R = \frac{(n - 1)^2 + k^2}{(n + 1)^2 + k^2}, \quad (2)$$

where  $n$  is the refractive index,  $k$  is the extinction coefficient, both are calculated from the complex dielectric function

$$\begin{aligned} \epsilon &= (n + ik)^2 = \\ &= \epsilon_\infty \left( 1 - \frac{w_p^2}{w(w + i\gamma)} \right) + \\ &\quad + \frac{w_L^2 - w_T^2}{w_L^2 - w_T^2 - i\Gamma w}, \quad (3) \end{aligned}$$

by solving the equations:

$$\epsilon_1 = \text{Re } \epsilon = n^2 - k^2, \quad (4)$$

$$\epsilon_2 = \text{Im } \epsilon = 2nk, \quad (5)$$

here  $w$  is infrared frequency or wave number ( $w$  ( in rad/s )/  $2\pi c = w$  ( in  $\text{cm}^{-1}$  )) correspondingly,  $c$  is the velocity of light),  $\epsilon_\infty$  is the high-

frequency dielectric constant,  $w_L$  and  $w_T$  are the longitudinal and transverse optic-phonon frequencies, respectively,  $\Gamma$  is the phonon damping constant,

$$w_p^2 = 4\pi p e^2 / m_c \epsilon_\infty \quad (6)$$

defines the bulk plasma frequency due to free carriers of density  $p$  and effective mass  $m_c$ ,  $\gamma$  is the free-carriers damping constant. The  $\gamma = 1/\langle\tau\rangle = e/2\pi m_c \mu c$  values were determined from the carrier mobility  $\mu$  data ( Table 1 ). The high-frequency dielectric constant of the lattice  $\epsilon_\infty = 11,6$  was deduced from high frequency parts of experimental spectra ( Fig.2 ). The others parameters  $w_L = 2000 \text{ cm}^{-1}$ ,  $w_T = 1000 \text{ cm}^{-1}$  for all the samples have been obtained to get the best fit to measured spectra. The phonon damping constant  $\Gamma$  obtained was of  $50-100 \text{ cm}^{-1}$ , that seems to be unexpectedly small for soft lattice modes of superionics. The results of calculation for two samples from I and II groups ( see above ) are presented in Fig.2. Calculations were carried out in two ways: 1) by taking into account the hole as well as the two-

oscillator fit from TO and LO lattice modes; and 2) without the lattice contribution as in [5]. By comparison of experimental and calculated spectra the  $w_p < w_{min}$  values were obtained, then from expression (6)\* using the hole concentration  $p = A_p$  the values of  $m_c$  were calculated (Table 1). The accuracy of calculations was of  $\sim 10\%$  for  $m_c$ , and of  $\sim 5\%$  for  $m_d$ .

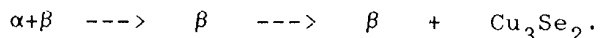
#### Experimental Results and Discussion

**Reflection spectra.** The reflection spectra obtained for  $Cu_{2-x}Se$  samples (Fig.2) were similar to those presented in [5] and [14]. But in addition to [5] and [14] it was shown, that for I group spectra the contribution of phonon-plasmon coupling to reflectivity  $R$  of  $Cu_{2-x}Se$  samples was considerable and so could not be neglected (points 3 and 5, Fig.2). Coupling ( $w_p/w_L = 1,25$  for curve 3) transformed spectra near-by  $w \sim w_L$  and made the plazmon dip near  $w_{min}$  more sharp (points 4 and 5, curve 3, Fig.2), but the values of  $m_c$  (Table 1) were practically the same as no coupling taking into account ones [5]. For II group spectra both calculations of  $R$  give rise practically the same results (points 6 and 7, curve 1, Fig.2) ( $w_p/w_L = 3,4$  for curve 1). This is in accordance with the theory of the phonon-plazmon resonance in solids, which predicts maximum coupling between the LO phonons and the plasmons at  $w_p/w_L \sim 1$  and no coupling at  $w_p/w_L \gg 1$  [13]. To explain the outstanding break of the spectra in two groups (Table 1) the phase composition of samples was taken into account. In fact, the boundary between this two groups (Table 1) is the phase boundary  $\alpha/(\alpha+\beta)$ . It is well known, that the reflectivity of two phase  $(\alpha+\beta)$  samples is a result of superposition of  $\alpha$ - and  $\beta$ -phase spectra [13,14]. Curve 3, Fig.2 was calculated using the phase diagram [3] for two phase  $(\alpha+\beta)$  sample ( $x=0,1$ ) as a superposition of experimental spectra of the boundary  $\alpha/(\alpha+\beta)$  ( $x=0,05$ ) and  $(\alpha+\beta)/\beta$  ( $x=0,20$ ) samples. But the experimental spectrum for  $Cu_{1.90}Se$  ( $w_{min} = 9000 \text{ cm}^{-1}$ , Table 1) differs fundamentally from calculated one. So as in [14] we have

concluded, that the surface states of all the samples within the two phase  $(\alpha+\beta)$  region ( $0,05 < x < 0,20$ ) is of the  $\beta$  ones ( $x_{surf} = 0,20$ ,  $p_{surf} = 4 \cdot 10^{21} \text{ cm}^{-3}$ ). Such a conclusion seems to be realistic because the surface of solids may be favorable for  $\beta$ -phase mobile ion excitation to occur.

**Effective masses.** From Fig.1 one can see that the density of state effective mass  $m_d$  (300 K) in

$Cu_{2-x}Se$  is slightly increased when  $p^*$  increased from  $0,01$  to  $1 \cdot 10^{21} \text{ cm}^{-3}$  and than drop in  $\beta$ -phase ( $p > 1 \cdot 10^{21} \text{ cm}^{-3}$ ) (curves 1 and 2). Such an extraordinary behavior of  $m_d$ , holding up to the high temperature (curve 7), may be due to  $Cu_{2-x}Se$  valence band being narrow (band width  $W < 1-2 \text{ eV}$ ) [8] as formed from 3d- and 4s-copper wave functions [17]. The  $m_c$  values calculated (Table 1) were  $\sim 4$  time less than  $m_d$  ones. For two phase  $(\alpha+\beta)$  region the  $m_c$  values were calculated by using: 1) volume hole concentration  $p = A_p$  as in [5]; or 2) ultimate hole concentration in  $(\alpha+\beta)$  region  $p_{surf} = 4 \cdot 10^{21} \text{ cm}^{-3}$  evaluated above. In so doing we have obtained the curves 5 and 4 of two different kind (Fig.1). The first looks like the mirror reflection of  $m_d$  versus  $p$  one (curve 5, Fig.1). For curve 5, Fig.1 the decrease of  $m$  with  $p$  increase at  $p = 0,2$  to  $2 \cdot 10^{21} \text{ cm}^{-3}$  was appeared in accordance with [5] (see curve 6), for  $p > 2 \cdot 10^{21} \text{ cm}^{-3}$  the increase of  $m_c$  with  $p$  increase was obtained (curve 5). Contrary to curve 5, the second curve 4 seems to be usual for high degenerated semiconductors. In [5], to extrapolate the curve 5 (Fig.1) into  $p < 0,2 \cdot 10^{21} \text{ cm}^{-3}$  region the value of  $m = 1,1 m_0$  at  $p = 2 \cdot 10^{21} \text{ cm}^{-3}$  from [4] was used (point 3, Fig.1). According to [4], the last being  $m_d$  but not  $m_c$ , so such an extrapolation seems to be wrong. So we have concluded, that curve 4, Fig.1 represents the real  $m_c$  versus  $p^*$  dependence in  $Cu_{2-x}Se$ , the  $m_c$  negative non-parabolism, declared in [5] (curves 5 and 6), is the seeming effect, resulted from ignoring of the phase transformations  $\alpha \rightarrow \beta$



*Multi valley band structure.* From curves 1 and 4, Fig.1 one can see that  $m_d > m_c$  in  $\text{Cu}_{2-x}\text{Se}$  for low hole concentrations, but  $m_d \rightarrow m_c$  for  $p^* \rightarrow 6 \cdot 10^{21} \text{ cm}^{-3}$  as well as when the temperature raised ( see curves 7 and 8 ). The equality  $m_d = m_c$  is known to be the characteristic of standard univalley band [15]. To explain the relation  $m_d > m_c$  previously observed for a number of multi valley semiconductors ( PbTe, GeTe,  $\text{Bi}_2\text{Te}_3$  and so on [16] ) one use the equation

$$m_d/m_c = 1/3 (N/K)^{2/3} (2K + 1), \quad (7)$$

( here  $N$  is the number of equivalent ellipsoids of rotation in a band,  $K = m_l/m_t$ ,  $m_l$  and  $m_t$  - the longitudinal and the transverse components of effective mass tensor of an ellipsoid) as well as the assumption for complicated Fermi surface, consisting of convex ( n-type ) and concave ( p-type ) parts [15,16]. According to band structure calculation made in [17], the valence band extremum in  $\text{Cu}_{2-x}\text{Se}$  locates near the  $\Gamma$  point (000) of Brillouin zone (  $N = 1$  ), so multi valley Fermi surface in  $\text{Cu}_{2-x}\text{Se}$  ( i.e.  $N > 1$  ) may arise due to change of the extremum from  $\Gamma$  point and its following multiplication by the symmetry demand. Using  $K = 1$  and the ratio of  $m_d/m_c \sim 4$  for the samples of the lowest hole concentration used (Fig.1) one can deduce from ( 7 ), that  $N$  is of 8. So we consider, that the hole extrema in  $\text{Cu}_{2-x}\text{Se}$  Brillouin zone may be changed along [111] directions (  $N=8$  ). The  $m_d/m_c$  ratio degerement observed for  $p^* \rightarrow 1 \cdot 10^{21} \text{ cm}^{-3}$  at the room temperature ( curve 1 and 4, Fig.1 ) may be due to following extrema consolidation in unique Fermi surface and Fermi surface rounding off while filling up a zone. At  $T > T_c$  the Fermi surface rounding off is increased by the temperature and the superionic phase disorder, so  $m_d/m_c$  ratio decrease was in progress ( curve 7 and 8, Fig.1 ).

*Band approximation.* The unequality  $m_d$

$> m_c$  observed ( Fig.1 ) may be the evidence for the wide band approach validity in superionic  $\text{Cu}_{2-x}\text{Se}$  within the temperature range used.

#### References

- [1] T.Ishikawa, S.Miatany, J. Phys. Soc. Japan, 1977, No.1, v.42, p.159.
- [2] O.Milat, Z. Vicic, and B.Ruscic, Solid State Ionics. 1987, v.23, p.37.
- [3] N.Ch.Abrikosov, V.F.Bankina, M.A.Korzhuev, G.K.Demenskiy, and O.A.Teplov, Fiz. Tverd. Tela, 1983, v.25, No.10, pp.2911-2916.
- [4] G.B.Abdullaev, Z.A. Aliyarova, and G.B.Asadov, phys. stat. solidi, 1967, v.21, No.2, pp.461- 464.
- [5] V.V.Gorbachev, and I.M.Putilin, phys.stat.solidi ( b ), 1973, v.16, No.2, pp.553-559.
- [6] A.A.Voskanyan, P.N.Inglizyan, Ya.M.Shevchenko, and T.B.Shmakova, Fiz. i Tech. Poluprovodnikov, 1980, v.14, No.4, pp.804- 805.
- [7] P.N.Inglizyan, Ya.M.Shevchenko, T.B.Shmakova, Izv. AN SSSR, ser.neorg. Mater., 1983, v.19, No.1, pp.155-156.
- [8] M.A.Korzhuev, and A.V.Laptev, Fiz. i Tech. Poluprovodnikov, 1986, v.20, No.20, pp.828- 833.
- [9] M.A.Korzhuev, V.F.Bankina, B.F.Gruzinov, and G.S.Bushmarina, Fiz. i Tech. Poluprovodnikov, 1989, v.23, No.9, pp.1545- 1552.
- [10] M.A.Korzhuev, V.F.Bankina, B.A.Efimova, and N.N.Filipovich, Fiz. i Tech. Poluprovodnikov, 1990, v.24, No.5, pp.805- 812.
- [11] C.Kao, and W.Hwang, Electrical Transport in Solids, Oxford, 1980, 350 p.
- [12] N.F.Mott, and F.A.Davis, Electron Processes in non-crystalline materials, Oxford, 1980, 633 p.
- [13] Handbook of Optical Constants of Solids, ed. by E.D.Palik, N.Y., 1985, 1200 p.
- [14] B.Vengalis, K.Valatska, N.Shiktorov, and V.Jasutis, Fiz. Tverd. Tela 1986, v.28, p.2675.
- [15] I.A.Drabkin, T.B.Zhukova, I.V.Nelson, and L.M.Sysoeva, Izv. AN SSSR, ser. neorgan. Mater., 1979, v.15, No. 7, pp.1194-1197.
- [16] O.S.Gryaznov, B.Ya.Moizhes, and A.N.Shmakov, Fiz. i Tech. Poluprovodnikov, 1981, v.15, No.7, pp.805-808.
- [17] E.J.D.Garba, and R.L.Jacobs, Physica, 1986, v.138 (B+C), No.3, pp.253-260.

# Structure and Transport Properties in Amorphous and Nano-Crystalline $Re_x - Si_{1-x}$ Thin Films at High Temperatures

A.T.Burkov\*, C.Gladun, A.Heinrich, W.Pitschke, J.Schumann  
 \*A.F.Ioffe Physico-Technical Institute Russian Academy of Sciences  
 Sankt-Petersburg 194021 Russia  
 Institute of Solid State and Materials Science Dresden e.V.  
 D-01171 Dresden, Germany

## Abstract

Experimental data on structure, electrical resistivity and thermoelectric power of  $Re - Si$  thin films are presented. The composition  $x$  varies around the value corresponding to the  $ReSi_2$  compound. The transport properties of the films were measured in the temperature range from 300 K up to 1300 K. The thermoelectric properties of the films can not be described on the bases of the effective media approximation.

## 1 Introduction

Among large variety of transition metal silicides which mainly show metallic type of conductivity a special place occupy those silicides which possess semiconducting properties. They have been considered as promising materials for Si-based optoelectronic, photovoltaic and thermoelectric applications [1, 2]. Within Re-Si system  $ReSi_2$  is a narrow-gap semiconductor. The forbidden gap was found to be in case of  $ReSi_2$  of 0.12 eV [3]. A great body of research has been devoted to the studies of bulk silicide materials, see for a review for example [4] and epitaxially grown silicide thin films on silicon [5, 6]. Much less has been done in studies of properties of the polycrystalline thin film of the semiconducting  $ReSi_2$  compounds, particularly of nano-crystalline materials [8].

Nano-crystalline materials (NC) are structurally characterized by ultrafine grains and a large volume fraction of interfaces. Many properties of such materials can be fundamentally different from conventional poly- or single crystalline materials [10]. Among variety of methods for synthesis of NC materials the crystallization from amorphous state possesses a number of unique advantages [11].

- In this method it is very simple and convenient to control the crystallization process. Conventional annealing can realize the nanocrystallization with different grain sizes in dependence on the heat treatment conditions.
- The nanocrystallization from an amorphous state provides an unique method to study interfacial phenomena in NC materials. Because in this method the crystalline phase is formed from the amorphous state

via solid state phase transformation the internal interfaces are clean.

- A combination of the heat treatment with in-situ transport property measurements or with in-situ X-ray investigations gives immediate and direct information about kinetics of nanocrystallization process and properties of the material.

Thin film silicides with compositions close to the stoichiometric composition of the semiconducting silicides form new interesting class of heterogeneous NC materials. In dependence of the initial film composition different types of the heterogeneous compounds could be formed in coarse of the heat treatment.

In this paper first systematic investigations of the crystallization processes in  $Re - Si$  thin films are presented. The structure of the thin film  $Re - Si$  compound was studied by means of in-situ and ex-situ X-ray measurements. Transport properties (electrical resistivity  $\rho$  and thermoelectric power  $S$ ) were measured during the heat treatment as functions of annealing time and temperature.

## 2 Experimental

The films were prepared by a magnetron co-sputtering from pure component targets onto unheated  $Si$  substrates with intermediate  $1\mu m$  thick  $SiO_2$  layer to prevent a reaction of the film with the  $Si$ -substrate. The film thickness was about 100-150 nm. The composition analysis of the films was carried out by Rutherford backscattering spectrometry (RBS) and Energy dispersive X-ray analysis (EDXS), the former with an accuracy of  $\pm 1$  at %. The structure of the compounds was determined by in-situ X-ray diffraction measurements during annealing at temperatures up to 1250 K and ex-situ at room temperature. From the X-ray line broadening analysis we estimated the size of the crystalline grains. Transport properties ( $\rho$  and  $S$ ) were measured during annealing of the films in high-purity helium atmosphere. This enable us to control phase formation in the films and gave immediate information on the transport properties of heterogenous compounds which form the film during the heat treatment. Electrical resistivity was measured by conventional DC four-probe

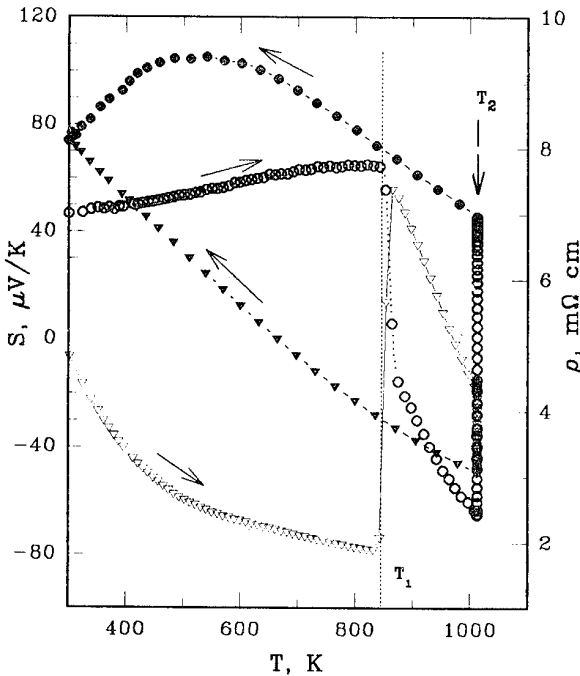


Figure 1: Electrical resistivity and thermopower of  $Re_{0.31}Si_{0.69}$  compound.

○ - S, on heating; ● - S, on cooling; ▽ -  $\rho$ , on heating; ▽ -  $\rho$ , on cooling.

method. In case of thermopower differential method was used. Both properties were measured simultaneously during the heat-treatment of a sample as functions of the temperature or of the time.

### 3 Results

Figure 1 presents thermopower and resistivity of a  $Re_{0.31}Si_{0.69}$  compound. The measurements were performed with constant temperature variation rate of 2 K/min on heating and 5 K/min - on cooling. At  $T_2 = 1012\text{ K}$  the sample was annealed during about 8 hours. Abrupt changes in both thermopower and resistivity at 850 K are connected according the X-ray data with the  $ReSi_2$  crystallization.

Within investigated range of the composition of the  $Re_xSi_{1-x}$  films ( $0.3 < x \leq 0.42$ ) this temperature is nearly independent on the Re/Si ratio.

From X-ray data it follows that in the films with Re excess the crystallization of Re starts at temperatures 950 K - 1000 K. The in-situ X-ray measurements and the X-ray-line broadening analysis yield information on the phase composition and crystalline grain sizes (d) in dependence on annealing temperature. These data are collected in Table 1.  $Re_{0.39}Si_{0.61}$  sample had been annealed at 900 K for 2 hours before the in-situ X-ray experiment.

Table 1: Crystalline grain sizes from in-situ X-ray data at different annealing temperatures  $T_a$

$T_a$ , K	$Re_{0.39}Si_{0.61}$		$Re_{0.34}Si_{0.66}$	
	d, nm $ReSi_2$	d, nm Re	d, nm $ReSi_2$	d, nm Re
750	52	-	-	-
800	51	-	-	-
850	58	-	-	-
900	69	-	24	-
950	50	22	17	-
1000	93	27	16	-
1050	83	24	18	-
1100	190	48	22	-
1150	-	-	23	-
1200	-	-	26	-
1250	-	-	37	-
1300	-	-	57	-

Figure 2 shows dependencies of the resistivity and thermopower on the annealing time at the constant temperature (1012 K). Note nonmonotonous variation of the resistivity and strong increase of the thermopower which change its sign in the coarse of annealing.

From X-Ray data it follows that on this stage of annealing the film consists of the nano-crystalline  $ReSi_2$  within amorphous Re-Si matrix (we will call such films partially crystallized (PC) films).

### 4 Discussion

From table 1 it is seen that in a broad range of the annealing temperatures of the Re-Si films the grain size of the crystalline phases remains constant. That means that the crystallization progresses not due to a growth of individual grains but due to increasing number of NC grains within amorphous matrix. This result is in agreement with the recent thermodynamic analysis of the crystallization from an amorphous state [11].

Structurally the PC silicide films are similar to the granular films. But there exists an essential difference between these NC systems. A classical granular film consists of NC metallic particles in an insulating matrix [13]. In contrast to that in the PC silicide films one or both components could be narrow-gap semiconductors. Moreover the conductivity of the components can depend on the film composition and its microstructure. To our knowledge no theoretical consideration of the transport properties have been made for such NC composites.

For PC Re-Si compounds with Si-excess we have observed in most cases that  $\rho \sim \exp(T^*/T)^t$  with t varying from  $\frac{1}{4}$  to 1 as it was found for granular metals [13]. However for some Si-rich films at the initial stage of annealing we have found that  $\rho \sim \exp(-T/T_0)$ .

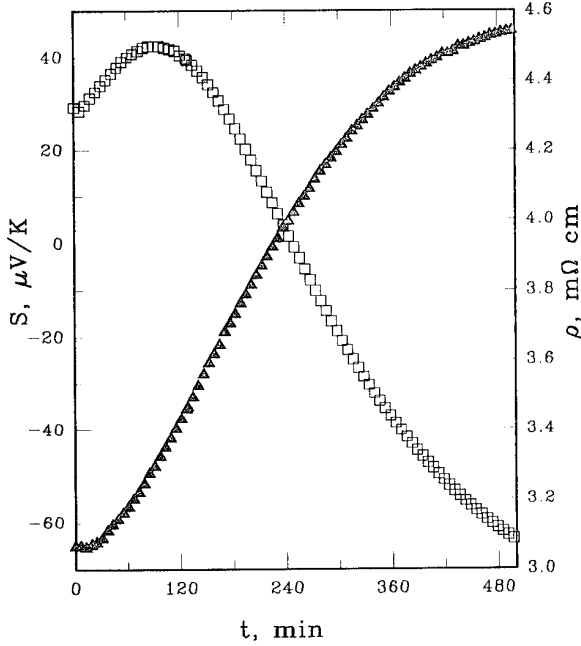


Figure 2: The variation of the electrical resistivity and thermopower of  $Re_{0.31}Si_{0.69}$  with annealing time  $t$  at  $T=1013\text{ K}$ .

$\square - \rho$ ;  $\triangle - S$ .

In a vicinity of the stoichiometric  $ReSi_2$  composition and on the Re-rich side our PC films reveal a different behavior. In the Re-rich PC compounds the electrical resistivity is a linear function of the temperature with a negative temperature coefficient:  $\rho(T) = a + b \cdot T$  ( $b \leq 0$ ). Close to the stoichiometric  $Re/Si$  ratio the resistivity of PC films follows to:  $\rho(T) \sim \exp(-\frac{T}{T^*})^{\frac{1}{2}}$ . There is no single conductivity mechanism which could account for the observed temperature dependent resistivity of the Re-rich and nearly-stoichiometric PC films.

Effective media approximation (EMA) is commonly employed to describe the composition dependence of composite system properties [14, 16]. Particularly the electrical resistivity  $\rho$  of a two-component composite system can be represented within EMA by the so called generalized effective media equation [14]:

$$\frac{f \cdot [\rho^{1/t} - \rho_1^{1/t}]}{\rho^{1/t} + \rho_1^{1/t} \cdot f_c / (1 - f_c)} + \frac{(1 - f) \cdot [\rho^{1/t} - \rho_2^{1/t}]}{\rho^{1/t} + \rho_2^{1/t} \cdot f_c / (1 - f_c)} = 0$$

where  $f$  is the volume fraction of the component "1" and  $f_c$  corresponds to percolation threshold. Whereas the thermopower is given by [15]

$$S = \frac{(S_1 \rho_2 \kappa_2 - S_2 \rho_1 \kappa_1) + \kappa \cdot \rho (S_2 - S_1)}{\kappa_2 \rho_2 - \kappa_1 \rho_1}$$

EMA predicts that both electrical resistivity and thermopower should be monotonous functions of the volume fraction  $f$  of one of the components as it is schematically shown in Figure 3.

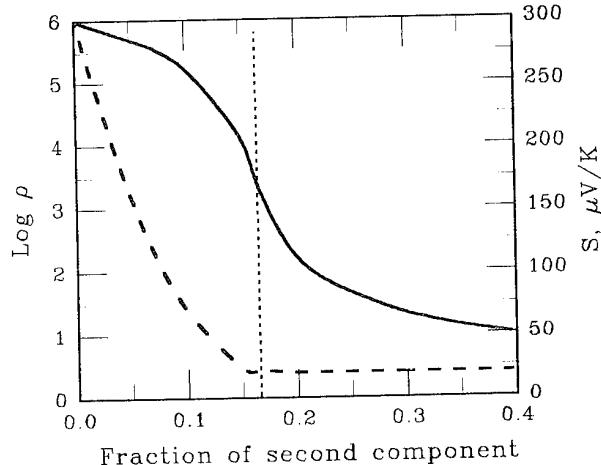


Figure 3: Variation of the electrical resistivity (solid line) and thermopower (broken line) of a binary mixture with the composition according to the EMA prediction.

Now the question arises, whether EMA is able to describe the properties of our NC and PC films. In general the NC silicides with a large deviation of the composition from that of the  $ReSi_2$  compound are composite systems with components whose properties are changing in the coarse of the heat-treatment. But in PC compounds close to the stoichiometric Si/Re(Cr) ratio the atomic composition of both the crystalline and amorphous phases remains the same during the annealing procedure, only the volume fractions of these phases are varying. The X-ray data confirm that no other phases appear in such compounds. Therefore we can assume that from structural point of view at least the stoichiometric films are the NC binary mixtures.

Starting from the single-phase amorphous film we can continuously transform by heat-treatment such films into crystalline single-phase state having for PC films a mixture of amorphous and NC phases.

Figure 4 presents the resistivity and thermopower variation of the film with composition  $Re_{0.34}Si_{0.66}$  close to the stoichiometric composition of  $ReSi_2$  with the annealing time.

The film was annealed at fixed temperatures from 785 K up to 1090 K in high-purity helium atmosphere. Each point at figure 4 represents the resistivity or thermopower measured (simultaneously) at 350 K after annealing during a given time. The most important conclusion which one can make from these dependencies is that neither the resistivity nor the thermopower follow the predictions of the EMA shown in figure 3. Both thermopower and resistivity of the PC film are considerably larger than those of single phase film (amorphous or poly-crystalline). This implies that in the PC films the interfaces between amorphous and NC phases play an important or even dominant role for the high-temperature transport properties.

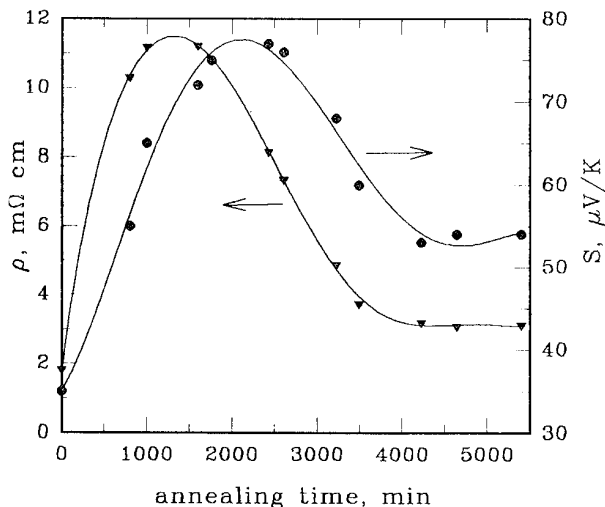


Figure 4: Electrical resistivity  $\rho(350)$  ( $\nabla$ ) and thermopower  $S(350)$  ( $\bullet$ ) of the  $Re_{0.34}Si_{0.66}$  film in dependence on the annealing time.

## 5 Conclusion

Structure and transport properties of amorphous and NC Re-Si thin films have been studied. The composition of the films varies in a vicinity of the stoichiometric  $Si/Re$  ratio of semiconducting  $ReSi_2$  compound. The NC films were obtained from the amorphous state by heat treatment procedures. X-ray and transport property data show that the activation temperature of the  $ReSi_2$  crystallization is about 850 K. This temperature is nearly composition independent. Above this temperature the compounds consist of the amorphous phase and NC  $ReSi_2$  phase.

In Re-Si films with Re-excess, pure Re crystallizes above about 950 K.

In a broad range of annealing temperatures the crystallization progresses due to increasing number of the NC grains with an average size of 20 - 50 nm. The analysis of composition dependencies of the electrical resistivity and thermopower reveals that they do not follow to the prediction of commonly used effective media approximation.

## Acknowledgments

The authors would like to thank M. Maeder and H. Thomas for performing the RBS and EDXS analysis. This work was supported in part by the Dr. Wilhelm Heinrich Heraeus and Else Heraeus-Stiftung (Germany). One of us (A.B.) would like to gratefully acknowledge the financial support of the Heraeus-Stiftung and kind hospitality of the Institute of Solid State and Materials Science Dresden e.V., Germany.

## References

- [1] Murarka, S.P., *Silicides for VLSI Applications*, Academic Press, Orlando 1983.
- [2] Vining, C.B., *Silicides as Promising Thermoelectric Materials*, Proceedings of the IXth International Conference on Thermoelectrics, ed. by C.B.Vining (Pasadena: California Institute of Technology), 1990, p.249.
- [3] Long, R.G., Bost, M.C., Mahan, Thin Film Solids **162** (1988) 29.
- [4] Samsonov, G.V., Vinitskii, I.M., *Handbook of Refractory Compounds*, IFI/Plenum, New York, 1980.
- [5] Chen, L.J., Tu, K.N., Materials Science Reports **6** (1991) 53.
- [6] Derrien, J., Chevrier, J., Le Thanh Vinh, Berbezier,I., Giannini, C., Lagomarsino,S., Grimaldi, M.G., Applied Surface Science **73** (1993) 90.
- [7] Nguyen Tan, T.A., Veuillen, J.Y., Muret, P., Kenou, S., Siokou, A., Ladas, S., Lahatra Razafindramisa, F., Brunei, M., J.Appl.Phys. **77** (1995) 2514.
- [8] Heinrich, A., Gladun, C., Burkow, A., Schumann, J., Elefant, D., *Thermoelectric Properties and Structure of  $Me_xSi_{1-x}$  ( $Me = Ir, Fe, Re$ ) Thin Films*, AIP Conference Proceedings 316, American Institute of Physics, New York, 1995, p.45.
- [9] Gladun, C., Heinrich, A., Schumann, J., Pitschke, W., Vinzelberg, H., Int.J.Electronics **77** (1994) 301.
- [10] Sigel, R.W., in: *Physics of New Materials*, ed. by F.E.Fujita, Springer Series in Material Sciences, v.**27**, Springer-Verlag, Berlin, 1994, p.65.
- [11] Lu, K., Phys.Rev.B, **51** (1995) 18.
- [12] Klug, H.P., Alexander, L.E., *X-ray Diffraction Procedures for Polycrystalline and Amorphous Materials*, Wiley, New York, 1974.
- [13] Abels, B., Ping Sheng, Coutts, M.D., Arie, Y., Adv.Phys. **24** (1975) 407.
- [14] McLachlan, D.S., J.Appl.Phys. **68** (1990) 195.
- [15] Halpern, V., J.Phys.C **16** (1983) L217.
- [16] Bergman, D.J., Levy, O., J.Appl.Phys. **70** (1991) 6821.

## Thermoelectric properties of small mobility materials in the hopping regime

Zaitsev V.K., Ktitorov S.A., Kalazin A.E., Fedorov M.I.

*A.F.Ioffe Physical-Technical Institute, RAS, St.Petersburg, Russia*

In the present work the results of the experimental study of the electrical conductivity, the thermopower and the thermoconductivity of some semiconductor materials with the polaronic transport.

The small polaron is formed in result of a strong interaction of electrons with longitudinal optical phonons. When a temperature gradient applied, the phonon subsystem is driven to an inequilibrium state. When the temperature is not too low, it concerns not only acoustical but optical phonons too: the corresponding branch population is determined by the parameter  $kT/\hbar\omega_0$  within the classical limit.

The heat flux maintained by this branch can be written as  $q_{lo} = CTv_{dlo}$ , where  $C$  is the longitudinal branch contribution to the heat capacitance,  $v_{dlo}$  is the drift velocity of these phonons. It can be expressed in terms of the group velocity  $v_{lo}$  and the

$$\text{thermoconductivity: } v_{dlo} = \frac{1}{3} \frac{v_{lo} l_{lo}}{T} \nabla T .$$

Here  $v_{lo}$  is the group velocity of the branch,  $l_{lo}$  is the mean path. The electric field induced by the drag effect creates the electron current in opposite direction with the drift velocity  $v_{ed}$ :  $\mu E = v_{ed}$ ,  $\mu$  - is the drift mobility of electrons.

At low temperatures  $T < \theta$  ( $\theta$  is Debye temperature) total quasimomentum carried by optical phonons increases with temperature giving rise to the exponential factor:

$$E = \frac{1}{3} \frac{v_{lo} l_{lo}}{\mu T} \nabla T \cdot e^{-\frac{\theta}{T}},$$

$$\alpha_{drag} = \frac{1}{3} \frac{v_{lo} l_{lo}}{\mu T} \cdot e^{-\frac{\theta}{T}} = \frac{k_B}{3} \frac{v_{lo}^2}{k_B T} \frac{\tau_{ph}}{\mu} \cdot e^{-\frac{\theta}{T}}$$

or,

$$= \frac{1}{3} \frac{k_B}{e} \frac{v_{lo}^2 \tau_{ph}}{D_{pol}} \cdot e^{-\frac{\theta}{T}}$$
(1)

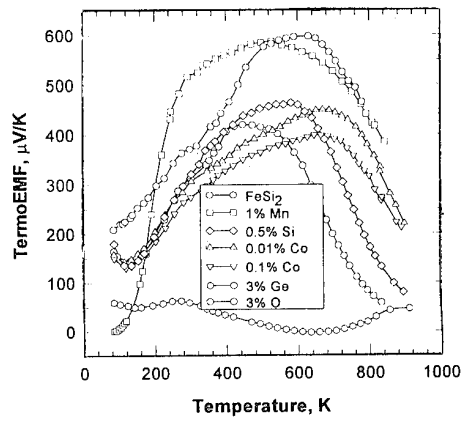
where  $\tau_{ph}$  stands for the phonon transport time,  $D_{pol} = \frac{\mu k_B T}{e}$

is the polaron diffusion coefficient.

Small value of the polaron diffusion coefficient enables a sound contribution of the drag effect into the thermopower in the polaronic semiconductor notwithstanding the deviation of the phonon distribution function from the equilibrium state is rather small for an optical branch.

In result we get the temperature dependence qualitatively fitting fast thermopower increase at low temperatures  $<\theta \sim \hbar\omega_0/k_B$ , observed in experiments. (Fig.1)

**Fig. 1. Measured thermoEMF of bulk samples  $\beta\text{-FeSi}_2$  with different impurities.**



Notice, that this mechanism gives rise to the essential anisotropy of the thermopower. In opposite to the isotropic contribution given by the Morin formula:

$$\alpha = \frac{1}{e} \frac{\zeta}{T} = \frac{k_B}{e} \ln \left( \frac{n}{N-n} \right), \quad (2)$$

where  $\zeta$  is the chemical potential,  $n$  is the carrier concentration: formula (1) provides a pronounced anisotropy.

At high temperatures ( $T > \theta$ ) the drug effect can be considered as saturated: drift velocities of phonons and polarons are approximately equal.

The following dimensionless parameters are introduced in the small polaron theory [1]

$$\eta_1 = \frac{J}{E_a}, \quad \eta_2 = \frac{J^2}{\hbar\omega_0 \sqrt{E_a k_B T}}, \quad \eta_3 = \frac{J^2}{E_a k_B T}. \quad (3)$$

where  $J$  is the intersite tunneling parameter and  $\omega_0$  is the characteristic phonon frequency.  $E_a$  is the activation energy.

At  $\eta_1 \ll 1$ ,  $\eta_3 \ll 1$  the problem is significantly simplified and can be reduced to the Holstein two-site problem [2]. In the case of the non-adiabatic polaron  $\eta_2 > 1$  we have

$$D = \frac{Z}{4\pi} a^2 \omega_0 e^{-E_a/k_B T}, \quad (4)$$

where  $Z$  is the nearest neighbor's number.

Now we can estimate the polaron contribution to drag effect for not too high temperatures, when phonon-phonon scattering can be neglected:

$$\alpha = \frac{1}{3} \frac{k_B}{e} \frac{(\Delta\omega)^2 \tau_{ph}}{(Z 4\pi) \omega_o} e^{E_a / k_B T}, \quad (5)$$

$$\approx \frac{4\pi}{3Z} \frac{k_B}{e} \left( \frac{\Delta\omega}{\omega_o} \right) (\Delta\omega \tau_{ph}) e^{E_a / k_B T}$$

where  $\Delta\omega$  is the phonon band width characterizing the dispersion of the mode. We take for an estimate  $\Delta\omega/\omega_o \sim 0.1$ ,  $\Delta\omega \tau_{ph} \sim 1$ . Thus, the effect is not small but decreases with the temperature increase. On the other hand, a decrease of the temperature freezes optic phonons decreasing the optical phonon contribution to the thermoconductivity.

At higher temperatures phonon-phonon scattering due to the enharmonic interaction makes the drag effect ineffective, resulting in a power-law decrease of the thermopower.

### **Our estimations allow us to make the following conclusions:**

1. The suggested mechanism of the *optical phonon polaron drag effect* qualitatively correctly describes the observed thermopower temperature dependence with the characteristic maximum at high temperatures.
2. Our calculations overestimate the contribution as the drag effect was supposed to be perfect that can be true only if longitudinal phonons control the polaron mobility so that an influence of other branches is negligible.
3. The drag effect on polarons considered above can manifest itself not only in the thermoelectric power but in thermoconductivity too. It follows from an interference between electronic and phonon energy fluxes in the Kubo formula. At low temperature (band transport regime) electronic contribution enhances the thermoconductivity. When the temperature increases, polaron mobility very fast decreases and polarons can be considered as a sort of short-range scatterers for phonons making the thermoconductivity to decrease. Nontrivial behavior can be waited in the intermediate temperature range that can be seen on the Fig. 3

**Fig. 2. Conductivity vs T. (Labels see Fig. 1.)**

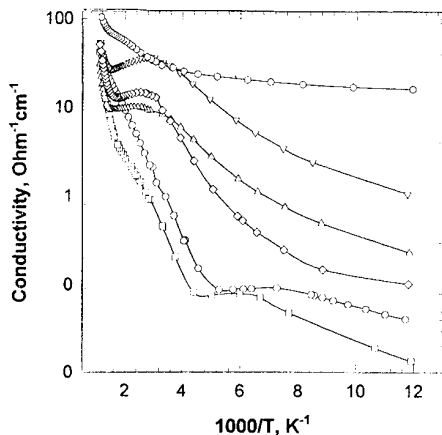
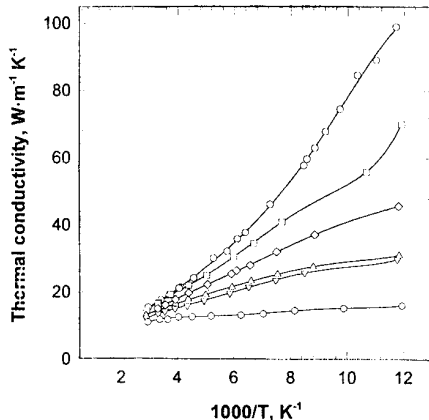


**Fig. 3. Thermal conductivity vs T. (Labels see Fig. 1.)**



### **Acknowledgments**

The work is supported by the Russian Foundation for basic research, grant № 95-02-04103-a

### **References**

1. Polaron. ed. by Yu.A.Firsov. M.: "Nauka", 1975, 423 p.
2. Kudinov E.K., Firsov Yu.A. Stochastic aspects of small polaron theory of low mobility. *Zh. Exp. and Tech. Phys.* 1965, v.49, 3, p.867-884
3. H. Fritzsche. A general expression for the thermoelectric power. *Solid State Comm.*, 1971, v.9, 21, p.1813

# Thermoelectric waves in anisotropic crystal of Higher Manganese Silicide (HMS)

Stanislav V. Ordin

*A.F.Ioffe Physical-Technical Institute, RAS, St.Petersburg, Russia*

Formation of a thermodynamically equilibrium heterostructure in the crystal of HMS [1] (Fig.1) is determined by incommensurate manganese and silicon sublattices along tetragonal  $C$  axis (Fig.2,3). Peculiarities of HMS crystal structure show themselves in strong anisotropy of kinetic properties: thermoelectric power  $170 - 100 \mu V/K$ , electrical conductivity  $100 - 700 \Omega m^{-1} \cdot cm^{-1}$ , at room temperature parallel and perpendicular axis  $C$ , accordingly [2], and what especially significant in anisotropy of optical properties [3].

Study of reflection spectra HMS in a wide spectral range 0.5 to  $500 \mu m$  manifest strong polarization dependence of lattice oscillator numbers upon the orientation of electrical vector in relation to axis  $C$  (Fig.4). At perpendicular orientation,  $E \perp C$ , rich set of oscillators in the range  $20 - 500 \mu m$  is observed. At the same time at parallel orientation,  $E \parallel C$ , only one oscillator about  $20 \mu m$  is observed. Besides, at perpendicular orientation anomalous for classical crystals dependence of plasma-reflection from orientation of wave vector  $k$  relative axis  $C$  is found.

HMS quasicrystals can be used in a wide field of new highly effective optoelectronic devices. On the basis of HMS quasicrystals highly sensitive IR detectors devices have been created and tested already [4]. The high-speed thermoelectric detectors of radiation (HSTD) based on HMS single crystals has higher detectivity  $D^*$  than thermodetectors based on piezoelectric effect [5]. The response times of HSTD are up to  $1 \mu s$  in a harmonic regime and up to  $10-1 \mu s$  in differential one, that is much lower than the response time of the usual thermoelectric detectors which is not more than  $5 \mu s$  as a rule. The HSTD can be used for producing devices for absolute measurements of any kind of radiation. Using a HSTD matrix one can obtain high sensitive visualiser of radiation pattern, for example, a new type of IR thermovisor could be designed.

In the present work an investigation of spatial and frequency dependence of potential difference  $U(x, f)$  observed in HMS sample was carried out (Fig.5). At the measurement quasiharmonic modulation of heat flow  $q$  was applied:  $q = q(1 + \sin 2\pi f)$ , where  $f$  - modulation frequency. The angle between spreading heat flow  $q$  and axis  $C$  was about  $10^\circ$ . Local heated area (diameter  $1 \text{ mm}$ ) of upper sample face was steadily moved from the first contact ( $x = 1.5 \text{ mm}$ ) to the other one ( $x = 7.3 \text{ mm}$ ). It is seen from  $U(x, f)$  dependencies (Fig.6) that amplitude of output voltage of unmodulated heat flow ( $f = 0 \text{ Hz}$ ) is defined by longitudinal amplitude components  $U(1.5 \text{ mm}, 0 \text{ Hz})$  and  $U(7.3 \text{ mm}, 0 \text{ Hz})$ , transverse amplitude component  $U(4.4 \text{ mm}, 0 \text{ Hz})$ , and their sign. At non-zero modulation frequency curve strongly depends on phase difference of components indicated. Resonance character of phase dependence  $U(x, f)$ :

$$U(3 \text{ mm}, 0 \text{ Hz}) = 0 \Rightarrow \phi_{U(4.4 \text{ mm}, 0 \text{ Hz})} = \phi_{U(7.3 \text{ mm}, 0 \text{ Hz})}$$

$$U(6.7 \text{ mm}, 30 \text{ Hz}) = 0 \Rightarrow \phi_{U(6.7 \text{ mm}, 30 \text{ Hz})} = \phi_{U(6.7 \text{ mm}, 30 \text{ Hz})} + \pi$$

indicates that weakly damping wave exists.

By a definition, a wave is excitation, which transfers energy without mass transmission - transferring of thermoelectric part of energy of heat flow into the input of registered channel devices is observed as amplitude of signal. One of the main harmonic wave characteristic is phase  $\phi = 2\pi ft + \phi_0$  - crossing  $\Delta\phi$  of output signal over  $\pi$ , which is natural for a resonance, is observed.  $U(x, f)$  dependence shape is essentially changed with decreasing thickness of sample plate (Fig.7). Observed at small thickness set of extrema  $U(x, f)$  can be connected with crossing of phase differences of components next values:  $\Delta\phi = n\pi$ , where  $n = 1, 2, 3, \dots$ . Observed effects can not be described by slow temperature waves [6]:

$$T = \exp(-Z/\lambda) \exp[i(wt - Z/\lambda)] \quad (1)$$

where  $\lambda = 2a/\omega$ ,  $a$  - temperature conductivity. The reason is that according to formula (1), temperature waves damping is so significant, that really only heat frontier is observed, i.e.  $\Delta\phi < \pi/4$ . Because  $\Delta\phi = n\pi$ , where  $n \geq 1$  is observed in experiment, it is possible to admit that dynamic vertex current contribution into the process of heat flow spreading leads to appearance of weakly damping thermoelectric wave, which spreading gives local decreasing and increasing of temperature into the crystal volume.

## Acknowledgments

The work was supported by Russian Foundation for Basic Research, grant No 95-02-04096-a.

## References

- [1] Ordin S.V., Zaitsev V.K., Engalychev A.E., Soloviev V.A. Electron microscopic study of materials based on higher manganese silicide. in *Materials for thermoelectric converters*, 1987, Leningrad, p.99-100.
- [2] Zaitsev V.K. Thermoelectric properties of anisotropic  $MnSi_{1.75}$ . *CRC Handbook of Thermoelectrics*, ed. by D.M.Rowe, CRC Press, 1995, p.299-310.
- [3] Ordin S.V., Zaitsev V.K., Engalychev A.E. Anisotropy of IR reflection spectra of higher manganese silicide single crystals. in *Semiconductor materials for thermoelectric converters*. 1985, Leningrad, p.85-86.
- [4] S.V.Ordin. Detector of radiation. Accepted application for Russian patent No.93036965/25 (037129) of 21th July 1993.
- [5] *IR-detectoren und zuberhör*. München, 1993, 147 p.
- [6] Domenicalli C.A. Irreversible thermodynamics of thermoelectricity *Rev. Mod. Phys.*, 1954, v.26, p.237-275.

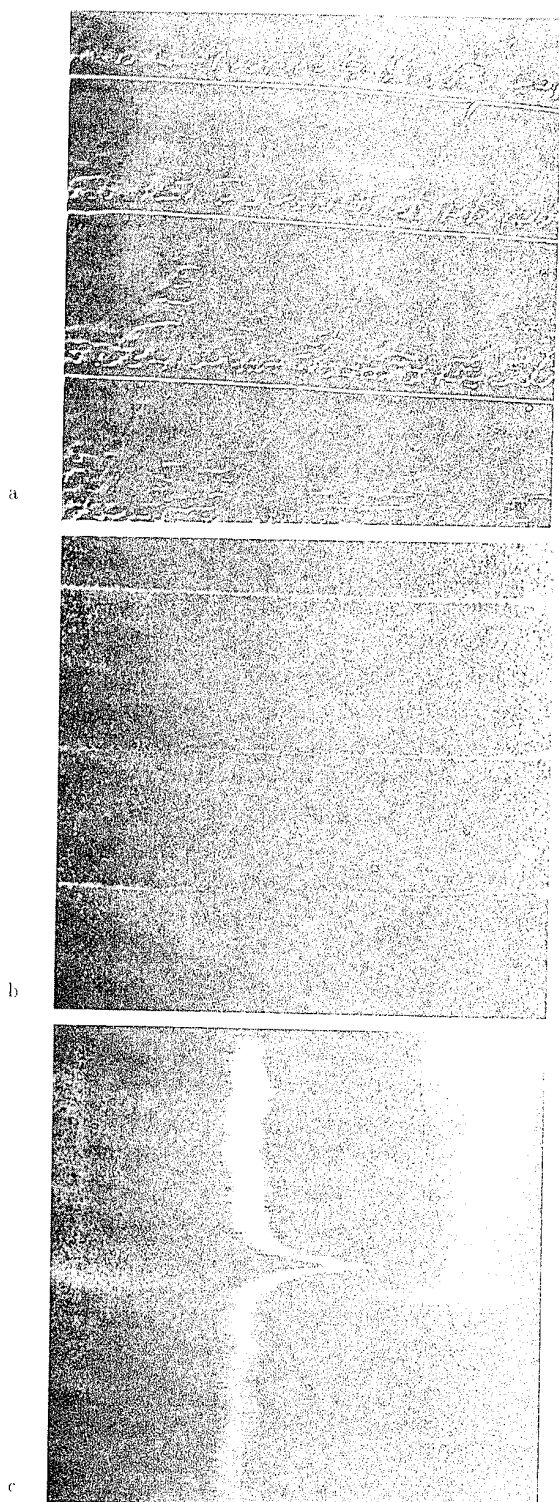


Figure 1: Scanning electron-microscopic photographs of HMS crystal.

a) Etched surface, contrast shows relief of the surface. (Scale  $3.5\mu\text{m}$  in 1 cm).

b) Polished surface, contrast shows variation of Mn to Si concentrations ratio along the surface. (Scale  $3.5\mu\text{m}$  in 1 cm).

c) Polished surface, the dependence of Mn to Si concentrations ratio on sample length is shown either.



Figure 2: Transmission electron-microscopic photograph of HMS crystal surface between stripes shown on Fig. 1. (Scale  $250 \text{\AA}$  in 1 cm).

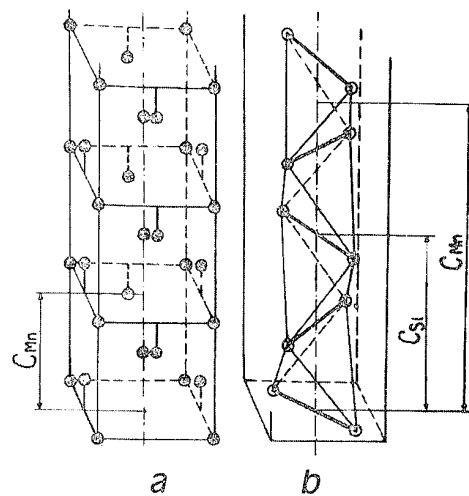


Figure 3: Crystal structure of HMS.

a - manganese sublattice

b - silicon sublattice

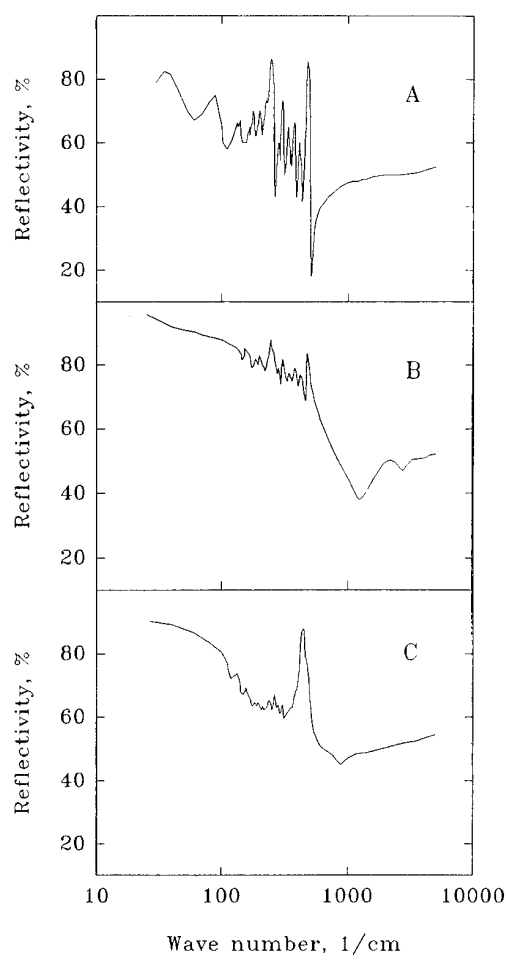


Figure 4: Reflection spectra of HMS.

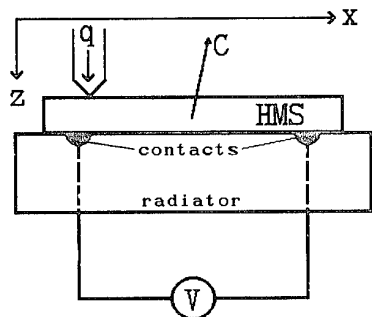
a -  $\vec{k} \parallel \text{C-axis}, \vec{E} \perp \text{C-axis}$ b -  $\vec{k} \perp \text{C-axis}, \vec{E} \perp \text{C-axis}$ c -  $\vec{k} \perp \text{C-axis}, \vec{E} \parallel \text{C-axis}$ 

Figure 5: Scheme of the experiment on observation of thermo-electric waves

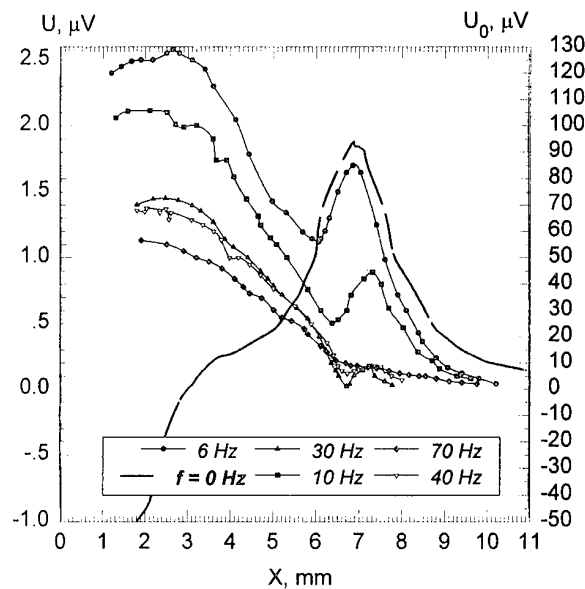
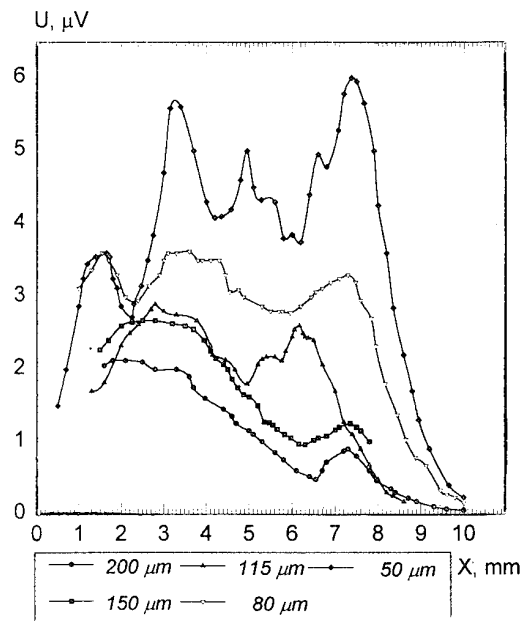
Figure 6: Space dependence of potential difference on HMS plate at thickness  $\approx 200\mu\text{m}$  for various modulation frequency.

Figure 7: Space dependence of potential difference on HMS plate at modulation frequency 10 Hz for various thickness.

# Electrochemical deposition of metal layers on the transition metal silicides

F.Yu.Solomkin, M.I.Fedorov, V.K.Zaitsev

*A.F. Ioffe Physical-Technical Institute, St.Petersburg, Russia.*

A method of electrochemical deposition of metal layers on silicide substrate and electrolyte composing is suggested. The method allows to produce metal layers of reliable connection with substrate material and of low transition resistance.

## Introduction

The deposition of metallic layers with low electric resistivity on a boundary between metal and semiconductor material ( $R_0$ ) is important problem in the technology of thermoelectric devices production. To be used in thermoelectric generators the layers must not lose electrical properties at high temperature and when thermocycling.

We suppose to use electrochemical deposition method to solve this problem. It is found out experimentally that transition metal films on some transition metal silicides with properties mentioned above can be obtained only if electrolyte combines properties of polishing dissolver (PD) and solution for electrochemical deposition (ED) of metallic films.

So the main aims of our work were:

- 1.to find simple method which let us to compose solutions combining PD- and ED-properties : "PD,ED-electrolytes".
- 2.to find different "PD,ED-electrolyte" compositions for deposition metal films on different semiconductors.

## Some questions of electrochemical polishing and deposition

It is known [1] that there is a liquid layer (LL) in solution near the surface of sample or a solid layer (SL) on the surface which consists of products of reaction between surface and solution for both chemical (CH) and electrochemical (ECH) polishing process. LL and SL form a structure for transmission of free charge along surface and between surface and solution. Such a structure usually has high electrical resistivity. We suppose, a polishing regime can exist only when SL-LL structure provides higher rate of charge exchange between various points of solid surface than between the surface and solution. The disadvantage of such a process is low rate of polishing because of LL-SL structure high resistivity. To increase the polishing rate it is necessary to reduce the resistivity of interface structure.

We supposed that such an interface structure can be formed by metal ions and an acid (for silicon based materials HF can be used).

In solution of a metal salt the concentration of metal ions of certain valence is much higher than concentration of metal ions of other valence. Such a state is an equilibrium one. Acid addition can result in forming almost inequilibrium state with higher concentration of metal ions of other valence in comparison with concentration without acid (so called resonance structure [2]).

So, there are ions of various valence in the structure and hence a lot of energy states takes place. The occupation of the structure with free current carriers takes place when anodic activating the substrate. The free carriers are generated either when negative ions discharging on anode. These processes

result in production of a layer enriched in free carriers.

Such an electrolyte can be used as a polishing dissolver only at first stage of the deposition process when a current direction allows only polishing. At the second stage at opposite current direction both processes (polishing and deposition) take place but the deposition rate is much higher than that of polishing. The use of the first stage enable us to apply unpolished substrates cut with a diamond disk.

## Metal layer deposition and electrolyte composing

PD-ED electrolyte can be composed using optical transparency spectrum of solutions in visible light. To find the composition of electrolyte we applied the next rules:

1. Spectrum of metal ions solution was considered as a base one.
2. Others components were added in a maximum concentration which changes the base spectrum not more than 5%.

Metal ion concentration can vary in very wide range - from 2 g/l up to solving limit. The concentration increase results in deposition rate increase.

We used these rules to compose electrolytes for Ni, Co, Cr deposition on higher manganese and iron silicides and cobalt monosilicide. Such electrolytes allow to deposit metal films with thickness up to 200  $\mu m$ . Fig.1 shows the section of nickel layer deposited at higher manganese silicide substrate. The rate of deposition is not higher than 20  $\mu m/min$  and depends on metal ion concentration and current density. Fig.2 shows dependence of deposition rate on current density at cobalt ions concentration 400 g/l.

## Properties of deposited layers

Transition resistance  $R_0$  of deposited layers of transition metals on silicide substrate was measured by microprobe method. All layers had transition resistance less than  $1 \cdot 10^{-5} \Omega \cdot cm^2$ . Some layers were ruptured to check connection quality. More than 90 % layers were ruptured with substrate material covering all layer.

Layers of nickel and chromium deposited on higher manganese silicide were used for thermoelement production [3]. The thermoelements worked in air at 800 K during 700 hours. Transition resistance increase was less than 10% during first 100 hours and less than 2% during other 600 hours. The thermoelements underwent by thermocycling from room temperature to 800 K and vice versa. There was no noticeable change in transition resistance after 100 cycles.

### Conclusion

The method proposed for electrolyte composing and electrochemical deposition of metal layers on silicide substrate allows to produce layers which can be used in thermoelement production. Due to their low transition resistance and high connection reliability such layers can increase working time of thermoelectric generators and decrease the volume of thermoelectric used in such a generator.

### References

- [1] P.A.Jacquet. On the anodic behaviour of copper in aqueous solutions of orthophosphoric acid. *Trans. Electrochem. Soc.*, **69**, 629 (1936); *Compt. rend.*, **201**, 1473 (1935); **202**, 403 (1936)  
T.P.Hoar, T.W.Farthing. Solid films on electropolishing anodes. *Nature*, **169**, 324-325 (1952)  
R.Pinner. Theory and practice of chemical polishing. Part 1. Chemical process for copper-base alloys. *Electroplating and Metal Spraying*, **6**, No 10, 360-367 (1953)
- [2] I.S.Dmitriev. *An electron from chemist view*. Leningrad, Chemistry, 1983, pp.177, 184.
- [3] M.I.Fedorov, A.E.Engalychev, V.K.Zaitsev, A.E.Kaliazin, F.Yu.Solomkin. Universal thermoelectric unit, *AIP Conference Proceedings 316, Thirteen International Conference on Thermoelectrics N.-Y.*, 1995, p.324-327

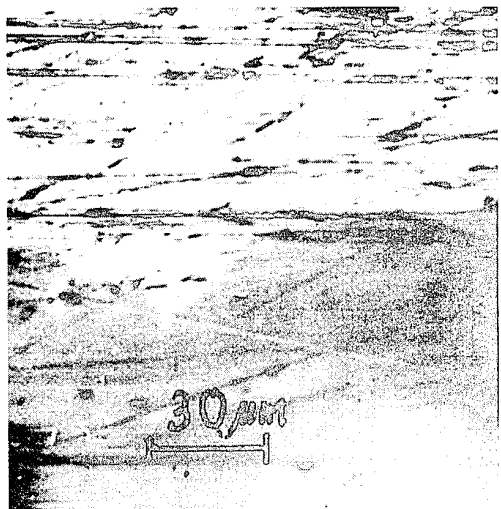


Figure 1: Section of nickel layer deposited at higher manganese silicide (HMS) substrate. It is possible to see a HMS cavern filled by nickel

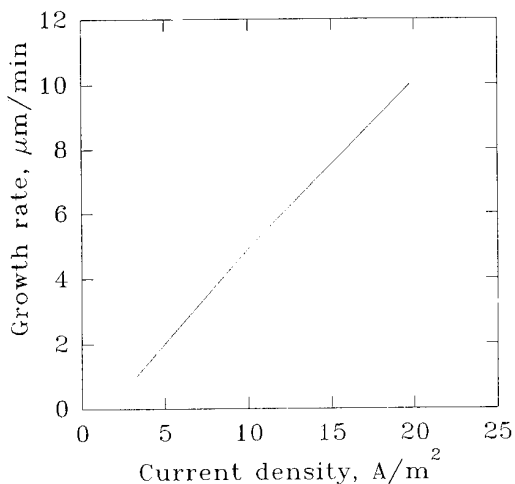


Figure 2: Dependence of cobalt deposition rate on current density at cobalt ions concentration 400 g/l.

## THERMOELECTRIC PROPERTIES OF NEW INTERMETALLIC COMPOUNDS $M^I M^{II} Sn$

N.D.Marchuk<sup>1</sup>, R.V.Skolozdra<sup>2</sup> and Y.V.Stadnyk<sup>2</sup>

<sup>1</sup> Institute for Nuclear Research, National Ukrainian Academy of Sciences, Kiev, 252022, 47, pr.Nauki, Ukraine

<sup>2</sup> Lviv State University, Lviv, Ukraine

Usually compounds are characterized metallic properties. Some ternary compounds being formed by metals evince non-ordinary electrophysical characteristics. In first order this has to do with so-called Gaisler's phases of  $M^I M^{II} Sn$  equiatomic structure, where  $M^I$  - transition elements of IV group of Periodic System,  $M^{II}$  - metals of Fe or Pt family. They possess a MgAgAs type cubic structure and some from them are semiconductors with narrow forbidden zone of energy. By our investigation the perspectivity of  $M^I M^{II} Sn$  as middle-and high-temperature thermoelectric materials was shown due to their high melting temperatures (about 2000°C), simple method of synthesis and fine thermoelectric characteristics. The new results of properties of intermetallic compounds n-, p-NiZnSn, TiNiSn, GfNiSn and others are presented.

### I. Introduction.

The intermetallic compounds (intermetallids) are compounds, formed between metals or metals and semimetals (or even with some non-metals, for example: Boron, Carbon, Nitrogen) are characterized usually by electrokinetic properties, poorly distinguished from properties of metals. Though the properties of intermetallids of transitive metals with Tin (especially ternary) are investigated insufficiently, however the being available data testify to them non-ordinar electrophysical characteristics [1]. First of all it concerns to so-called Gaisler's phases of  $M^I M^{II} Sn$  equiatomic structures, there:

$M^I$  - transition elements of IV group of Periodical system.  
 $M^{II}$ - metals of Ferrum's and Platinum's family.

They possess a MgAgAs-type cubic structure, and some from its are semiconductors with narrow forbidden zone of energy, in spite of the fact that they are formed by typical metals.

It is known, that some of narrow-zone semiconductors, for example,  $FeSi_2$  [2], or solid solutions Si-Ge [3], are good thermoelectrical materials.

Researches carried out by us have shown a perspectivity of  $M^I M^{II} Sn$  phases as high-temperature thermoelectric materials. Crystal chemical analysis and review of properties of Gaisler's phases in  $M^I M^{II} Sn$  and some new results are presented in this work.

### 2. Composition and Crystal Structure.

$M^I M^{II} Sn$  stannides of MgAgAs structure type and their parameter of crystal lattice  $a$  are shown in Table I [4-6]. Structure type of gAgAs is a superstructure to type of  $CaF_2$  [7.8]. As atoms occupy positions of Ca atoms, which are form the most dense cubic packing (4(a) 0 0 0), Ag and Mg atoms- positions of F or atoms allocated in tetrahedral emptinesses. In connection with well-ordered distribution of atoms Ag (4(c) 1/4 1/4 1/4) and Mg (4(d) 3/4 3/4 3/4) type MgAgAs belongs to another space group (F43m), than type  $CaF_2$ (Fm3m). The structure of MgAgAs is showed on Fig.1.

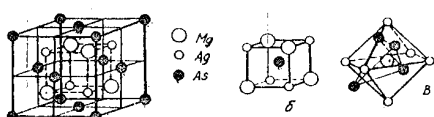


Fig.1. Elementary cell of MgAgAs structure (a) and coordinate polygrams of As (b) and Mg(Ag) (c) atoms.

Coordinate polygram [CP] of As atoms is a cube. Mg and Ag atoms- a tetrahedr formed by As atoms. If we admit that CP of this atoms was formed also by atoms situated by a distance of 1/2a ( $\sim 0.3$  nm), which form regular octahedron, then CP Ag and Mg is a combination of cube and octahedron (Fig.1).

Table I.  
Parameter of lattice of stannides structural type MgAgAs.

Compound	$a$ , nm	Compound	$a$ , nm
TiCoSn	0.6003	ZrPtSn	0.6336
TiNiSn	0.5941	HfNiSn	0.6083
TiRhSn	0.62	HfPdSn	0.6229
TiIrSn	0.61890	NbCoSn	0.5947
TiPtSn	0.6168	NbRhSn	0.6132
ZrNiSn	0.6113	MnIrSn	0.6182
ZrPdSn	0.6321	MnPTSn	0.6263

With the same atomic coordinates it is possible another distribution, which was observed for MgCuSb compound. In this case atoms of smallest size (Cu) occupy positions 4(a), atoms Mg- 4(c), atoms Sb - 4(d). If the origin of coordinate basis will be displaced to an atom Sb position, than Cu atom position will be correspond to tetrahedral emptiness, positions of Mg atoms-octahedral emptinesses of the densest packing. Like that, structure type MgAgAs is vacancial, a half of tetrahedral emptinesses are unoccupied there. Filling of these emptinesses results in Gaisler's phases  $M^I M^{II} Sn$  and to a structural type  $MnCu_2Al$ . The correlation between structures MgAgAs and MgCuSb is in details considered in [9]. Authors [9] proceed from the assumption that As and Sb are anions. If the type of coupling is like to ionical, that anion (As) is surrounded by 8 cations (Ag, Mg), every cation - by 4 anions, and in this case MgAgAs type is realized. If type of coupling is closer to metal, as it take place for MgCuSb, anion (Sb) is surrounded by 4 cations (Cu), one of cations - by 4 cations and 4 anions, another cation - by 4 cations, and MgCuSb type is formed. Now in the literature there is one designation - structural type MgAgAs [6].

The analysis of literature data shows, that if  $M^I$  and  $M^{II}$  are transitive metals, or one of metals is transitive, than 4(a) 000 position, as a rule, occupy atoms with small size. Manganese may occupy position 4(a) or 4(c) 1/4 1/4 1/4 in compounds with Platinum metals, which have a radii exceed a Mn radius. Gaisler's phases of equiatomic composition may be formed by s- and p-metals also in compounds with N, P, As, Bi. In these compounds 4(a) positions occupy p-element atoms of the V-group periodical system. If the state of atom in compound corresponds to metallic

one, then it conforms with the tendency to occupy 4(a) position by atoms which have a small size. However, as is shown in [8], compounds which possess such atomic distribution, have a semiconducting character and, apparently, covalent-ion bond have been displayed, and it lead to changing of radii in comparison with metallic state. The correlation between atomic radii  $Mel$  and  $Me^{II}$  (or opposite) don't exceed 1.24, and more than 2/3 of compounds have the radii correlation lies inside range from 1.00 to 1.10. It indicates that the influence of sizing factor to MgAgAs phase type formation exist. However, by a fact, the main role for such compounds formation belongs to factor of electronic concentration (EC).

It must be noticed that equiatomic compounds ZrCoSn and HfCoSn have a structure different from ZrNiSn and HfNiSn ones, they have ZrNiAl-type structure [10,11]. Compound NbNiSn in general will not be formed [12]. The difference among phase structures ZrNiSn and ZrCoNi, and absence of NbNiSn-stannide can't be explained by the structure factor only.

It must be noticed, that compounds of MgAgAs-type, containing metals with filled d-sublevel, have 8 valent s- and p-electrons per each of formulae units. Compounds of transitive metals have analogic electronic concentration, if it is supposed, that elements of 3b - 6b subgroups give to EC its valent s- and d-electrons, while metals of 8b-subgroup, because of filling of 3d-band by the expense of valent electrons of other atoms, decrease EC (Fe, Co) or haven't influence on it (Ni, Pd, Pt). For instance, ZrNiSn has EC equal 8 electrons per formulae unit (el/f.u) under condition of filling 3d-band of Nickel; NbCoSn-8 too, if Cobalt 3d-band is filled. In compound ZrCoSn filling of Cobalts 3d-band decreases EC to value considerably smaller than 8 and structure of MgAgAs type become unstable (data of magnetic susceptibility measurements give evidence about filling of 3d band of Ni and Co), moreover, the more closely packed structure ZrNiAl-type is formed (it is a superstructure to  $Fe_2P$ -type).

The breaking of EC 8 el/f.u rule for compounds MgAgAs-type may be compensated by filling of all tetrahedral vacancies by means of insertion of smaller size atoms with formation of  $MnCu_2Al$  type structure. Apparently, the absence of phases MgAgAs type with 3a-subgroup elements and transitive metals 4b-5b subgroups (except TiRhGa) [6] and existence of large amount of Gaisler's phases  $Me^I Me^{II} \{Al, Ga, In\}$  may be explained by such considerations.

### 3. Properties of $Me^I Me^{II} Sn$ compounds.

The properties of  $Me^I Me^{II} Sn$  stannides (for ones from Table I) is better investigated for ZrNiSn, TiNiSn, and HfNiSn. The thermal dependences of resistivity ( $\rho$ ) and differential thermo-e.m.f. ( $\alpha$ ) were measured for these materials (Fig.2). The  $\rho$  and  $\alpha$  values of these compounds are differ from  $\rho$  and  $\alpha$  of metals and intermetalls and exceed them on 2-4 order. Dependencies of  $\rho(T)$  have an abnormal character in comparison with intermetallids - the resistivity decreases with increasing of temperature. The dependencies of  $\rho(T)$  and  $\alpha(T)$  for compounds TiNiSn, ZrNiSn and HfNiSn in temperature range 78-900 K are showed in Fig.2. Thermo-e.m.f. has a negative value and growing absolutely with temperature increasing. Maximum values are achieved with ~450K, ~600K, ~700K for compounds TiNiSn, ZrNiSn and HfNiSn respectively. In high-temperature range the  $\rho(T)$  dependence for stannides TiNiSn, ZrNiSn and HfNiSn follows to an exponential dependence  $\rho = \rho_0 \exp(E_A/kT)$  with an activation energy  $E_A \sim 0.1-0.2$  eV. In low-temperature region, as a rule, it is impossible to determine a form of temperature dependence  $\rho(T)$  [13,14]. But for some samples of ZrNiSn in low-temperature

region (less than 20K) Mott's law  $\rho = \rho_0 \exp(T_0/T)^{1/4}$  is fulfilled [15].

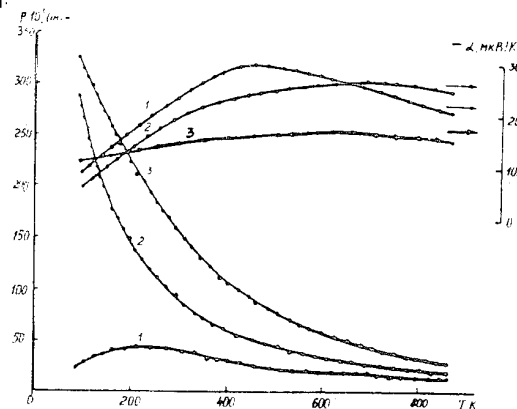


Fig 2. Resistivity  $\rho(T)$  and thermal-e.m.f.  $\alpha(T)$  dependencies for TiNiSn (1), ZrNiSn (2) and HfNiSn (3) compounds.

It was determined, that the annealing duration have cause influence on the dependences of  $\rho(T)$  and  $\alpha(T)$  for ZrNiSn compound, but the difference in dependences  $\rho(T)$ , caused by annealing, for these alloys almost don't observed in the temperature region ~250 K or higher.

Monocrystals of compound TiNiSn were obtained by us, the size of crystals was nearly 2x2x4 mm. Monocrystals have a high value of thermo-e.m.f. (~ -380  $\mu$ V/K with the temperature equals 290K), resistivity at 290K is nearly  $200 \times 10^{-6} \Omega \cdot m$ .

The results of calculations of thermo-e.m.f. with using of simple parabolic zone model for phases  $MeNiSn$  ( $Me = Ti, Zr, Hf$ ), were quoted in [16]. As calculations showed, experimental data for differential thermo-e.m.f. in temperature range  $100K < T < 300K$  are well described under effective mass value  $m^* \sim (2 \div 4) m_0$  and carrier concentration  $n_N \sim 10^{20}$ . Activative processes at temperatures higher than 300K have control thermoelectric properties and at more higher temperatures  $\alpha$  become decreasing. Optical properties of compounds TiNiSn, ZrNiSn and HfNiSn were investigated too. Results of optical investigations gives confirmation for existence of gap in the density of states in the neighbourhood of Fermi energy and about extraordinarity of kinetic properties of  $Me^I NiSn$  compounds among intermetallic materials [14].

Specimens of ZrNiSn have enough large value of thermal conductivity  $\kappa$ , which equals  $8 \div 10$  W/m·K under room temperature. The thermoelectric figure of merit  $Z$  is not exceed value of  $0.5 \cdot 10^{-3} K^{-1}$  in the temperature range  $900 \div 1100K$ , because  $\kappa$  have a high value. Now we have carry out investigations for influence of donor doping on the thermal conductivity with the aim to decrease it.

We had examine a solubility of Co in the ZrNiSn stannide. Properties of monophase alloys were investigated. Compound  $ZrNi_{0.45}Co_{0.55}Sn$  belongs to the solid solution region, but alloy  $ZrNi_{0.30}Co_{0.70}Sn$  already is two-phase. For  $ZrNi_{1-x}Co_xSn$  alloys it was observed, that resistivity  $\rho(T)$  decreases with the increasing of  $x$ ; the dependence of  $\rho$  from temperature decreases with growing  $x$ . The sign of thermo-e.m.f. change to positive (in comparison with  $\alpha$  of ZrNiSn) and its value achieves  $140 \mu V/K$  under temperature 600K.

On the ground of compound HfNiSn have been synthesized a substituted solid solutions  $HfNi_{1-x}Co_xSn$  [17]. The temperature dependences of resistivity and differential thermo-e.m.f. were measured in the temperature range  $300 \div 1300K$  (Fig.3). The  $\rho(T)$

dependence have a form, which is characteristic for semiconductors. The doping of compound by cobalt leads to an abrupt change of  $\alpha$  to positive values ( $\alpha$  for not doped ZrNiSn is negative), and positive values of  $\alpha$  are kept in the whole region of solid solution existence.

In the article [17.a] branches for thermomodule, manufactured from HfNiSn (n) and HfNi<sub>0.6</sub>Co<sub>0.4</sub>Sn, have been proposed. Figure of merit for these branches equals respectively  $0.87 \cdot 10^{-3} K^{-1}$  and  $0.33 \cdot 10^{-3} K^{-1}$ . The perspectivity of these branches for long time autonomous operation have been noticed.

We have examined an electrophysical properties of compounds TiRhSn, ZrPdSn, HfPdSn, NbRhSn, MnIrSn, TiIrSn, TiPtSn, ZrPtSn, HfPtSn and MnRhSn in the temperature range 78-400K (Fig.4-7). Most of the investigated compounds, which contain a platinum-like metals, possess an anomaly in its electrophysical properties. The highest resistivity is characteristic for TiPtSn, ZrPdSn and HfPdSn. With the increasing of temperature resistivity of ZrPdSn and HfPdSn is decreasing, for TiPtSn the function  $\rho(T)$  have a wide maximum. The thermo-e.m.f. all of that compounds is positive and have a high value, and it is not characteristic for metallic alloys. Less values of  $\rho$  are characteristic for stannides ZrPtSn and HfPtSn. The function  $\alpha(T)$  is almost linear in the low T region and it is characterized by negative curvature in the high T region, the sign of  $\alpha$  is positive. Among other compounds, which have a structure of MgAgAs type, stannides NbRhSn, MnIrSn and MnRhSn have a likely metallic properties, two of the rest stannides - TiRhSn and TiIrSn have an intermediate values of  $\rho$ . Thermo-e.m.f. of TiRhSn is negative.

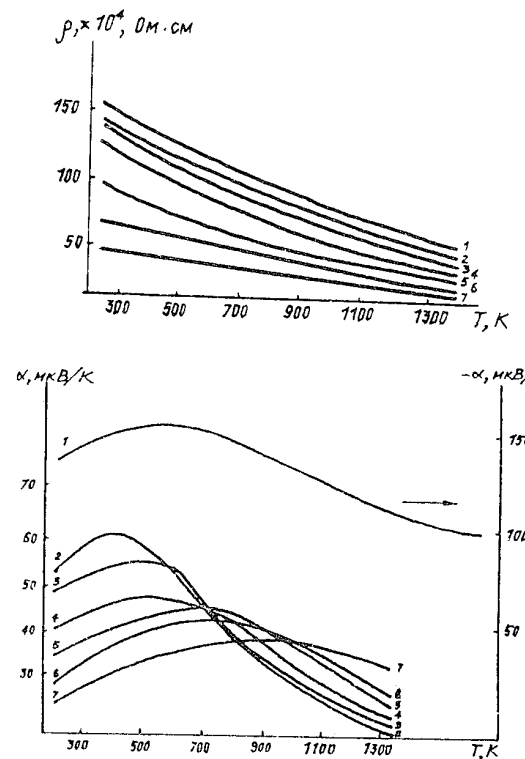


Fig 3.  $\rho(T)$ -(a) and  $\alpha(T)$ -(b) dependencies for alloys HfNiSn - (1). HfNi<sub>0.95</sub>Co<sub>0.05</sub>Sn - (2), HfNi<sub>0.90</sub>Co<sub>0.10</sub>Sn - (3). HfNi<sub>0.85</sub>Co<sub>0.15</sub>Sn - (4), HfNi<sub>0.80</sub>Co<sub>0.20</sub>Sn - (5). HfNi<sub>0.75</sub>Co<sub>0.25</sub>Sn - (6), HfNi<sub>0.60</sub>Co<sub>0.40</sub>Sn - (7).

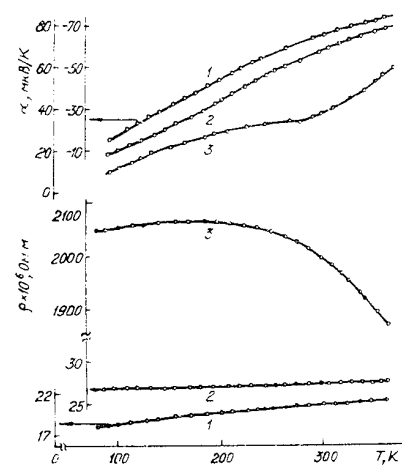


Fig 4.  $\alpha(T)$  and  $\rho(T)$  dependencies for compounds TiRhSn - (1), TiIrSn - (2). TiPtSn - (3).

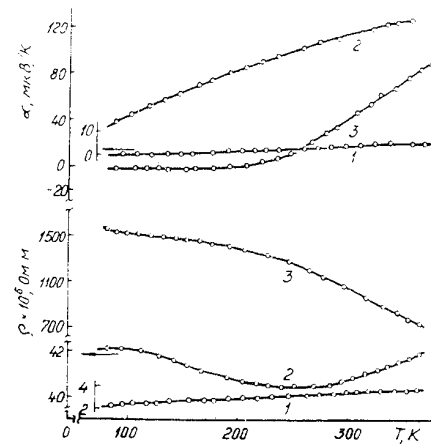


Fig 5.  $\alpha(T)$  and  $\rho(T)$  dependencies for compounds ZrIrSn - (1). ZrPtSn - (2). ZrPdSn - (3).

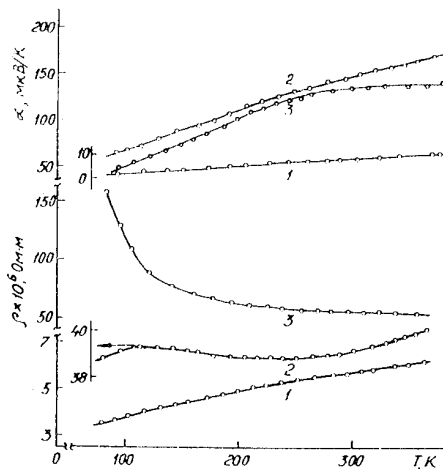


Fig 6.  $\alpha(T)$  and  $\rho(T)$  dependencies for compounds HfIrSn - (1). HfPtSn - (2). HfPdSn - (3).

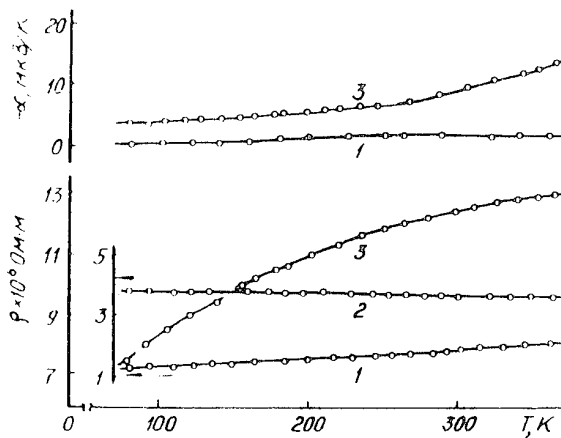


Fig 7.  $\alpha(T)$  and  $\rho(T)$  dependencies for compounds MnPtSn - (1), MnIrSn - (2), NbRhSn - (3).

The received data show that stannides of 4b-subgroup metals with Pt and Pd are characterized by properties similar ones of MeNiSn-phases, and it give evidence about a formation of dielectric gap in the electron energy spectrum. However, in distinction from compounds Me<sup>I</sup>NiSn, there take place p-type conductivity, and observed dependence  $\rho(T)$ , apparently, is tied with peculiarities of impurity zone structure and possible electron localization. P-type conductivity may be caused by formation of additional vacancies  $l(Me^{I}Pt_{1-x}Sn)$ , which arise as consequence of increasing of atomic radii Pt and Pd in comparison with Ni.

It is interesting, that compounds UNiSn, URhSb, UPtSn, ThNiSn, ThPtSn, which are characterized by structure type MgAgAs too, have an abnormally high resistivity and a complicated temperature dependence of  $\rho$  [18]. First three of them are submitted to a magnetic ordering in low temperature region. The compounds URhSb ( $680 \cdot 10^{-6} \Omega \cdot m$  under 300K) and UPtSn ( $360 \cdot 10^{-6} \Omega \cdot m$  under 300K) have the highest resistivity, and their temperature dependences  $\rho(T)$  obeys a maximum value near temperature 200K. Under high temperature the dependence  $\rho(T)$  is nearly exponential with activation energy 0.12eV for UNiSn, 0.44eV for URhSb and 0.34eV for UPtSn. In the article [19] the same authors in addition have cite properties of ThRhSn, HfRnSb, HfPtSn and TiPtSn. First two ones are characterized by growing of  $\rho$  with increasing T from 4.2K to 300K ( $(26.4 \pm 30) \cdot 10^{-6} \Omega \cdot m$  and  $(3.85 \pm 8.50) \cdot 10^{-6} \Omega \cdot m$ , respectively). For TiPtSn and HfPtSn  $\rho$  decreased with increasing of temperature from value  $6300 \cdot 10^{-6} \Omega \cdot m$  to  $5100 \cdot 10^{-6} \Omega \cdot m$  for TiPtSn and from  $280 \cdot 10^{-6} \Omega \cdot m$  to  $145 \cdot 10^{-6} \Omega \cdot m$  for HfPtSn.

Authors noted, that the structure (type MgAgAs) have a decisive role in forming properties of such phases, but interpretation of properties is absent, except a conclusion about presence of energy gap in electron energy spectra in such compounds.

#### 4. Models of electron structure for phases Me<sup>I</sup>Me<sup>II</sup>Sn.

Properties of investigated phases Me<sup>I</sup>Me<sup>II</sup>Sn indicate to a dielectrization of electron energy spectra and a semiconducting character most of such compounds. It may be ensured by simultaneous action of two factors - by peculiarities of crystallic structure MgAgAs-type and by atomic orbitals structure of atoms, which have form compounds.

X-ray spectra parameters  $K_{\alpha 1,2}$  and  $K_{\beta 1}$  of Nickel lines were investigated for compounds TiNiSn, ZrNiSn and HfNiSn. It was observed a considerable low-energy displacement of Nickel  $K_{\beta 1}$  line. This displacement give evidence about increasing of s-electron density in the radiating atom volume. High energy displacement for  $K_{\alpha 1,2}$  lines of Nickel was observed. It can give evidence about slight increasing of d-electron density in the atomic volume of Nickel. Thus, the formation of Me<sup>I</sup>NiSn compounds is accompanied by transfer of electron density to Nickel's atom sphere. Observed shifts were too large and can't be explained by metallic type bond only. It give an evidence about presence of ionic type bond in Me<sup>I</sup>NiSn compounds.

In the crystal lattice Ni-atoms form thetaedric environment for atoms of Sn and Me<sup>I</sup>, and atoms of Sn and Me<sup>I</sup> may form thetaedrical hybridized orbitals  $sp^3$  and  $sd^3$  accordingly, like elements of IV group of periodic system. These orbitals are oriented to Ni atoms, placed in the center of a cube, which is formed by Sn and Me<sup>I</sup> atoms. In the process of chemical bond formation it have place a displacement of electron density centre to Ni-atoms positions and with a less degree - to Me<sup>I</sup>-atoms positions. Thus, atoms of Sn possess a surplus positive electric charge. Consequently, in compounds Me<sup>I</sup>NiSn exists a system of ionic-covalent bonds. If it take place a substitution of atoms Ti, Zr and Hf by atoms of another kind, and this substitution results in variation of EC from value equals eight, then the breaking of ionic-covalent bonds system occurs and compound acquire properties of metal. From this point of view properties some of compounds Me<sup>I</sup>Me<sup>II</sup>Sn can be explained. For compounds TiRhSn and TiIrSn the decreasing of EC to value equals 7 occurs. This leads to violation of ionic-covalent bonds system, but, as it may be concluded from observed values  $\rho$  and  $\alpha$ , the share of ionic-covalent bonds remains significant. For MnIrSn and MnPtSn-stannides the excess of EC (10 and 11 el/f.u. accordingly, if we suppose, that Mn atom possess 7 valent electrons), leads to metallic bond formation. But from this point of view it is hardly understand a low value of  $\rho$  for NbRhSn and NbCoSn, which possess a metallic properties. The filling of second half of structure vacancies by Ni atoms leads to the same effect, so long as Gaisler's phases MeNi<sub>2</sub>Sn have values of  $\rho$  and  $\alpha$  close to ones of metals.

Somewhat different scheme for valent bonds formation in compounds of MgAgAs-type was proposed in the [20-22]. It is convenient to assume, that in the compound TiNiSn atomic valency is twice less than a coordination number: it equals 4 for Ni atom, 2 - for atoms of Ti and Sn. The coordination number, which corresponds to crystal lattice, is provided with a bond delocalization between two possible positions. It is assumed, that in the TiNiSn compound atoms of Ni form hibridized  $4s$   $3d_{xy}d_{xz}d_{yz}$ -bonds, which have a  $T_d$ -symmetry, and atoms of Ti and Ni, accordingly, form hibridized bonds  $4s$   $3d_{xz}$  and  $5p_{x,z}$  possessing  $C_{2v}$ -symmetry. The sum of valent electrons in the compound must be equal to 18 (we have take into account d-electrons of Ni). The main destabilizing factor for that group of compounds is a deviation of valent electrons sum from value equals 18.

Models for electron energy bands structure for MeNiSn phases have been proposed in [16]. In the first case (Fig.8a.), valent band have been fully filled by electrons and its energy edge arranges by 0.2eV below from mobility edge  $E_c$  of conductivity band ( $E_g = E_c - E_v$ ). In the other case ( Fig.8.b.), the valent band is overlapping with the conduction band ( $E_g = E_c - E_v$ ). From the analysis of experimental data authors make conclusion about most probable electron band structure for stannides MeNiSn. From their point of view, it is structure pictured on Fig.8.b.

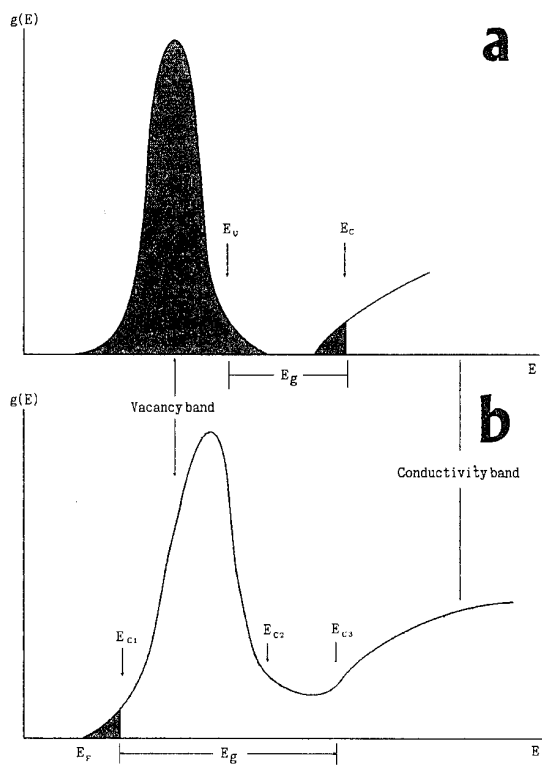


Fig 8. Proposed energy band structure of MeNiSn compounds [16].

#### Conclusion.

Particularities of the crystal structure and an atom electronic structure leads to an extraordinary properties of stannides  $\text{Me}^{\text{I}}\text{Me}^{\text{II}}\text{Sn}$ , which have MgAgAs structure type. The condition for dielectric gap forming are fulfilled when an electron concentration have a distinct value, namely 8 el/f.u. If it take place a deviation of EC from its value equals 8, or in the compound  $\text{Me}^{\text{I}}\text{NiSn}$  all tetrahedral vacancies are have been filled, (that is  $\text{MeNi}_2\text{Sn}$ -phases are have been formed), than a system of ionic-covalent bonds breaks and compound acquire metallic properties. These peculiarities allow modification of compound properties by changing dielectric gap width by means of atom substitution, which leads to increasing or decreasing of EC. The  $\text{Me}^{\text{I}}\text{Me}^{\text{II}}\text{Sn}$  alloys have a good thermal and electric properties and are stable under high temperatures. These alloys can be easily synthesized and are a perspective high and medium-temperature thermoelectric materials.

#### References.

1. Skolozdra R.V. Lviv, "Svit", 194 (1993).
2. T.Kojima. Phys.Stat.Sol. (a) 111, 223 (1989).
3. G.A.Slack, M.A.Hussain. J.Appl.Phys. 70 (5), 2694 (1991).
4. Skolozdra R.V. Tezisi dokl. Wsesojuzn. konf. po kristallogimii intermetal. soedinenij. Lvov, 14-21 october 1971., Lvov: Lvov un-t, 1971, p. 16-17.
5. W.Jeitschko. Metallurg. Trans. 1, 3159 (1970).
6. Villars P., Calvert L.D. American Society for Metals, I-3, 3258 (1985)
7. Kripjakevich P.I. M.: Nauka, 288 (1977).
8. Pirson Y. M.: I.2. 890 (1977).
9. Gladishevski E.I., Kripjakevich P.I. Dokl. AN SSSR. 102, 743 (1955).
10. Massara R., Ferro R., Rambaldi G. J. Less-Common Metals., 39, 341 (1975).
11. Skolozdra R.V., Stadnjik Ju.V., Starodjinova O.E. Ukr. Fiz. Jurn., 31, 1258 (1986).
12. Skolozdra R.V., Ohrimovich H.O. Izv. AN SSSR, Metallji, N6, 190 (1971).
13. Aliev F.G., Brandt N.B., Kozirkov V.V., Moschalkov V.V., Skolozdra R.V., Stadnjik Ju.V. Fiz. niz. temperat., 12, 498 (1987).
14. Aliev F.G., Belgororohov F.I., Brandt N.B., Kozirkov V.V., Skolozdra R.V., Stadnjik Ju.V. Pisma w JETP. 47, 151 (1988).
15. Aliev F.G., Brandt N.B., Kozirkov V.V., Moschalkov V.V., Skolozdra R.V., Stadnjik Ju.V., Pecharski V.K. Pisma w JETP, 45, 325 (1987).
16. Aliev F.G., Kozyrkov V.V., Moshchalkov V.V., Skolozdra R.V., Durchewski K.Z. Phys. B, 80, 353 (1990).
17. Avetisjan A.O., Gorjachev Ju.M., Kalchenko S.V., Skolozdra R.V., Stadnjik Ju.V. Ukr. Fiz. J., 36, 773 (1990).
18. Palstra T.T.M., Nieuwehny G.J., Mydoch Y.A., Buschow K.H.J. J.Magn. and Magn. Mater. 54-57, 549 (1986).
19. Palstra T.T.M., Nieuwehny G.J., Vlastuin et al. J.Magn. and Magn. Mater. 67, 331 (1987).
20. Dutkin L.D., Dashevskij E.M., Skolozdra R.V. Neorgan. mater., 29, 313 (1993).
21. Dutkin L.D., Dashevskij E.M., Skolozdra R.V. Neorgan. mater., 29, 319 (1993).
22. Lidorenko N.S., Dashevskij E.M., Dutkin L.D., Skolozdra R.V. Dokl. Akad. Nauk, 324, 567 (1992).

## EFFECTIVE MEIDIUM ANALYSIS AND EQUI-Z-CONTOUR MAP IN POROSITY CONTROLLED SiC:B<sub>4</sub>C SYSTEM

Y.Okamoto, T.Miyakawa, J.Morimoto, A.Aruga and S.Fujimoto

*Department of Materials Science and Engineering, National Defense Academy,  
Yokosuka, Kanagawa 239, Japan*

Experimental data on thermoelectric properties of pressure sintered SiC:B<sub>4</sub>C:PSS system are fitted to approximate expressions in cubic mosaic model. Using parameters found in this fitting equi-Z-maps are constructed to predict prospective region of B<sub>4</sub>C and PSS concentrations for the improved Z. The effects of pores on  $\sigma$  and  $\kappa$  tends to cancel in the expression for Z. Temperature dependence of Z is discussed.

### 1. Introduction

Recent development in the effective medium theory [1,2] has reached a stage to give bounds on the expected parameter values of a composite. "Exact" theories are given even for multi-field cases, and bounds for the thermoelectric figure of merit Z are also discussed [3,4]. Results of model calculations are used to analyze the properties of sedimentary rocks [5]. On the other hand, no serious efforts seem to have been reported to apply this kind of analysis in the area of materials design.

In this paper we report on the preliminary application of a simpler version of the effective medium theory i.e. the mosaic model [6] and the layered shell model [7] to study the effect of pores on Z, and extrapolate temperature dependent thermoelectric parameters of sintered SiC:B<sub>4</sub>C:PSS (polysilastren) system [8]. Equi-Z-contour maps [9] are constructed on the plane of B<sub>4</sub>C, PSS concentrations to show prospective region of these concentrations.

### 2. Model and Expressions for the Effective Parameters

In our simplified model the system is supposed to be a composite in which cubic (crystalline) grains 1 are embedded in a background substance 2 forming boundary layers between crystallites. Pores are assumed to be formed either in the effective medium consisting of material 1 and 2 or in the boundary layers. Figure 1. a) and b) show schematically these models. In Fig.2, we show the layered shell model in which the central sphere 1 represents the pore while the shell 2 is the effective medium consisting of material 1 and 2 above.

#### 2.1. Effect of Porosity on the Thermoelectric Parameters

When the enhancement of cross sectional area beyond the pores of both electric and thermal flow is neglected the effect of pores can be replaced by the decrease in the effective cross section of flow. Under the same

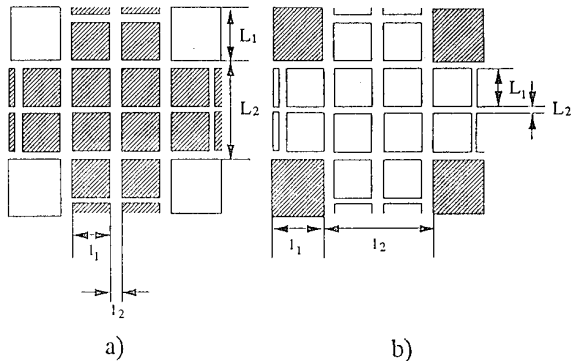


Fig.1. Cubic mosaic model for SiC:B<sub>4</sub>C:PSS system. a) pores of edge L<sub>1</sub> in an effective medium  
b) pores of edge L<sub>1</sub> in boundary layers. Shaded cubes represent grains.

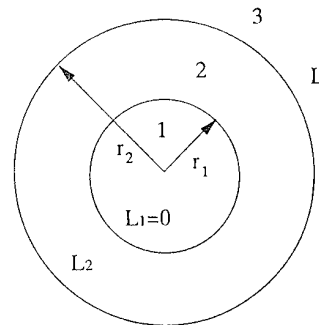


Fig.2. Spherical shell model for a medium 2 with a spherical pore 1 of radius  $r_1$  with  $L_1=0$ .  $L_1$  and  $L_2$  are transport coefficient matrix of effective and shell medium.

approximation Seebeck coefficient  $\alpha$  will suffer no change by the presence of pores. Thus both electrical and thermal conductivities  $\sigma$  and  $\kappa$  will be reduced by a factor  $1-\phi^{2/3}$  where  $\phi$  is the porosity defined as the

volume ratio  $\Delta V/V_0$  with  $\Delta V$ , and  $V_0$  denoting the volumes of pores and the original material, respectively. If the thermal conduction of gases in the pores is taken into account  $\kappa$  will increase slightly above the value predicted by the factor  $1-\phi^{2/3}$ .

In the layered shell model one can show that although  $\phi$ -dependence changes to  $(1-\phi)/(1+\phi/2)$ , this factor is common to both  $\sigma$  and  $\kappa$ . Thus even if the enhancement of effective  $\phi$  by the ratio of total to boundary layer volume is taken into account the effect of pores on  $\sigma$  and  $\kappa$  almost cancel in the expression for the figure of merit  $Z=\sigma\alpha^2/\kappa$ .

## 2.2. Expressions for the Effective Transport Coefficients

Using the notation  $z=l/l_1$  for the ratio of the thickness of the boundary layer to the edge of the cube,  $u=\sigma_1/\sigma_2$ ,  $v=\kappa_1/\kappa_2$ , and  $w=\alpha_1/\alpha_2$  for ratios of grain to boundary parameters the effective parameters  $\sigma_e$ ,  $\kappa_e$  and  $\alpha_e$  can be expressed in the following form [6];

$$\sigma_e/\sigma_1 = [u(1+z)+z(2+z)(1+uz)]/[u(1+z)^2(1+uz)] = f[u, z] \quad (2.1)$$

$$\kappa_e/\kappa_1 = f[v, z] \quad (2.2)$$

$$\alpha_e/\alpha_1 = [wu+z(2+z)+vz(u+z(2+z))]/[w(1+vz)(u+z(2+z))] = g[z, u, v, w] \quad (2.3)$$

These expressions give forms consistent with the  $\phi$ -dependence of the last subsection in the limit  $\sigma_1 \rightarrow 0$ ,  $\kappa_1 \rightarrow 0$ ,  $\alpha_1 \rightarrow 0$ .  $f[u, z]$  is a monotonously decreasing function of  $z$  with  $f[1, z]=1$  and changes by a factor of two or so over the range  $u=1 \sim 10$  for a reasonably small value of  $z$ .  $g[z, u, v, 1]=1$  and  $g$  is also a monotonously decreasing function of  $w$ . It increases with increase in  $u$  or  $v$  but stays between 1 and 1/2 for  $1 \leq u, v \leq 10$ . Thus the measured values of effective parameters are determined in a first approximation by those of grains if  $z$  is small and are rather insensitive to the characteristics of boundaries.

This situation allows us to first estimate thermoelectric parameters of grains and then infer characteristics of the boundaries.

## 2.3. Models for the Porosity Controlled SiC:B<sub>4</sub>C:PSS System

### 2.3.1. Model of Figure 1.a)

In this model pores (open squares) are embedded in the effective medium consisting of grains 1 (shaded squares) and boundary medium 2. The final form for

the effective parameters  $\sigma_e$ ,  $\kappa_e$  and  $\alpha_e$  as functions of temperature  $t$  and of concentrations  $x$  and  $y$  of B<sub>4</sub>C and PSS, respectively, are;

$$\begin{aligned} \sigma_e[x, y, t] &= \sigma_e[x, y, t][1-\phi^{2/3}(y)] \\ \kappa_e[x, y, t] &= \kappa_e[x, y, t][1-\phi^{2/3}(y)+v'\phi^{1/3}(y)] \\ \alpha_e[x, y, t] &= \alpha_e[x, y, t] \end{aligned} \quad (2.4)$$

with  $v' = \kappa_g/\kappa_e$ ;  $\kappa_g$  being the thermal conductivity of gases in the pore.

Here,  $\sigma_e$ ,  $\kappa_e$ , and  $\alpha_e$  are defined in (2.1) to (2.3) through functions  $f$  and  $g$  which depend on  $x$ ,  $y$  and  $t$  through arguments  $u$ ,  $v$ , and  $w$  defined by;

$$\begin{aligned} u &= \sigma_1[x, t]/\sigma_2[y, t] = u_0 f s_1[x, t]/f s_2[y, t] \\ v &= \kappa_1[x, t]/\kappa_2[y, t] = v_0 f k_1[x, t]/f k_2[y, t] \\ w &= \alpha_1[x, t]/\alpha_2[y, t] = w_0 f z_1[x, t]/f z_2[y, t] \end{aligned} \quad (2.5)$$

The thermoelectric figure of merit  $Z_t$  can be expressed relative to  $Z_1 = \sigma_1 \alpha_1^2 / \kappa_1$ .  $Z_1$  is the figure of merit of an imaginary "crystal" which has the same thermoelectric parameters as our "crystalline" grains. If we exclude the physically unrealistic case of boundary layers having the superior characteristics compared to grains i.e.  $uw^2/v<1$ , we will be looking after the region of  $x$  and  $y$  which gives  $Z_t$  closest to  $Z_1$ .

$$\begin{aligned} Z_t/Z_1 &= q[y, v'] G[z, u, v, w, t] \\ q[y, v'] &= [1-\phi^{2/3}(y)] / [1-\phi^{2/3}(y)+v'\phi^{1/3}(y)] \\ G[z, u, v, w, t] &= f[u, z] g^2[z, u, v, w] / f[v, z] \end{aligned} \quad (2.6)$$

As  $q[y, v']$  is very close to unity,  $Z_t/Z_1$  is determined by the function  $G$ .

### 2.3.2. Model of Figure 1.b)

In this model pores (open squares) are assumed to localize exclusively in the boundary layer. The final effective parameters  $\sigma_e$ ,  $\kappa_e$  and  $\alpha_e$  are formally equal to  $\sigma_e$ ,  $\kappa_e$  and  $\alpha_e$  in equations (2.1) to (2.3) with arguments  $u''$  and  $v''$  now being functions of the effective porosity  $\phi_e$  through their dependence on  $\sigma_2[y, t]$  and  $\kappa_2[y, t]$ ;

$$\begin{aligned} u'' &= u / [1-\phi_e^{2/3}(y)] \\ v'' &= v / [1-\phi_e^{2/3}(y)+v'\phi^{1/3}] \\ \phi_e &= \phi(1+z)^3 / [(1+z)^3 - 1] \end{aligned} \quad (2.7)$$

In this model the effect of pores appear only through

parameters  $u''$  and  $v''$ . As the value of  $u_0$  may differ from  $v_0$  the complete cancellation of pore effect will not be expected in  $Z_f$ . This is due to the situation that although both  $\sigma_2$  and  $\kappa_2$  are affected by the same factor due to the porosity, they may have different effect on the final effective parameters because of the different ratio of grain parameters  $\sigma_1$  and  $\kappa_1$  to  $\sigma_2$  and  $\kappa_2$ . Though the effective porosity  $\phi_e$  is enhanced by a factor  $[1-(1+z)^{-3}]^{-1}$  its effect is reduced by the weak dependence of  $f[u'', z]$ 's on  $u''$ .

#### 2.4. Fitting to Experimental Temperature and Concentration Dependencies of Parameters

We have assumed the following functional forms to simulate the temperature and concentration dependencies of measured effective conductivity and Seebeck coefficient:  $\sigma_e[x, 0, t]$ ,  $\sigma_e[x_1, y, t]$ ,  $\kappa_e[x, 0, t]$ ,  $\kappa_e[x_1, y, t]$ ,  $\alpha_e[x, 0, t]$ , and  $\alpha_e[x_1, y, t]$

$$fs_1[x, t] = 1 + a_1 \cdot x \cdot \exp[-\theta_1/t]$$

$$fs_2[y, t] = 1 + a_2 \cdot y \cdot \exp[-\theta_2/t]$$

$$a_1 = 10^6, \theta_1 = 3000 \text{ K}, a_2 = 10^6, \theta_2 = \theta_1$$

$$fk_1[x, t] = h[x, d_1] [1 + b_1 \cdot (\theta_2/t)^2]$$

$$h[x, d] = [1 + d \cdot (1-x)^2]/(1+d)$$

$$fk_2[y, t] = h[y, d_2] [1 + b_2 \cdot (\theta_4/t)^2]$$

$$b_1 = 2, b_2 = 1, d_1 = 100, d_2 = 50, \theta_2 = 500 \text{ K}, \theta_4 = 400 \text{ K}$$

$$fz_1[x, t] = 1 + c_1 \cdot \ln[fs_1(x, t)]$$

$$fz_2[y, t] = 1 + c_2 \cdot \ln[fs_2(y, t)]$$

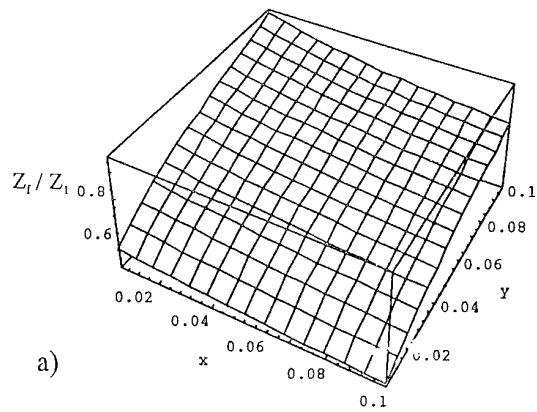
$$c_1 = 1, c_2 = 1 \quad (2.8)$$

One also find from y-dependence of relative density  $d/d_0$ ;  $\phi(y) = s \cdot y \quad s = 0.617$

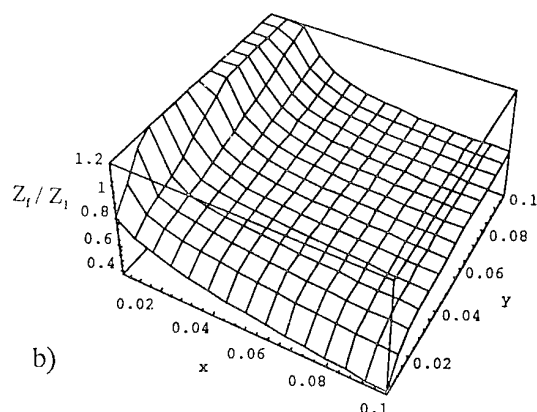
#### 3. Equi-Z-Contour Map

With parameters in the expressions (2.8) for the x, t and y, t dependence of the grain and boundary layer thermoelectric parameters determined to simulate experimental data, the only parameters left at our disposals are the ratios; z of grain size to boundary layer thickness,  $u_0$  of grain to boundary ratio in conductivity,  $v_0$  ratio in thermal conductivity, and  $w_0$  that in Seebeck coefficients. When we rather arbitrarily set these values as  $z=0.1$ ,  $u_0=5$ ,  $v_0=4$ , and  $w_0=5$  we can construct 3D- $Z_f$ -surface on the x-y plane at various temperatures.

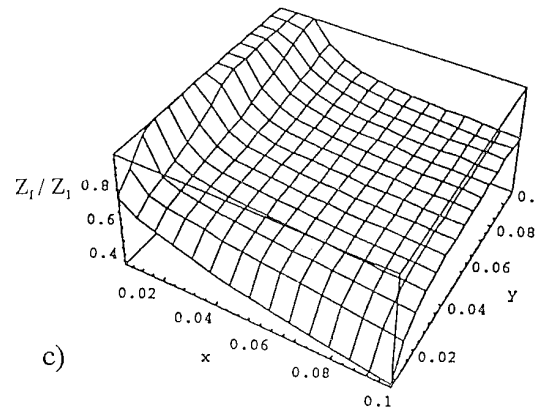
Figure 3. a~c show such 3D-plots at  $t=300, 600$  and  $900 \text{ K}$ .  $Z_f$  normalized to  $\sigma_1 \alpha_1^2 / \kappa_1$  increases monotonously



a)



b)



c)

Fig.3. 3D  $Z_f$ -map on x-y plane. a)  $T=300 \text{ K}$ .  
b)  $T=600 \text{ K}$ . c)  $T=900 \text{ K}$ .  $u_0=5, v_0=4$  and  $w_0=5$ .

as a function of y but show a slight tendency to saturate because of  $q[y, v']$  factor (we assume  $v'=0.1$ ). The increase in  $Z_f$  as a function of y becomes more pronounced at a smaller values of x. At higher

temperatures  $Z_f$  exhibits a weak maximum at a small value of  $x$ . This suggests that there is a rather narrow region of  $B_4C$  concentration  $x$  where  $Z_f$  can assume an optimum value.

Figure 4.a and b show a similar 3D-plot and equi-Z-contour map for  $z=0.1$ ,  $u_0=10$ ,  $v_0=4$ , and  $w_0=5$ .

One can also see that although numerical details may differ, the overall behavior of  $Z_f$ -x-y 3D-plots in model 2 is qualitatively the same.

#### 4. Discussion

We have implicitly assumed that possible effects of processing e.g. pressure and temperature schedule and resultant changes in microstructure of the composite may be represented through the values of parameters  $z$ ,  $u$ ,  $v$ , and  $w$ . As the functions  $f$  and  $g$  depend rather weakly on these parameters  $\sigma_e$ ,  $\kappa_e$  and  $\alpha_e$  reflects, in the first approximation, characteristics of grains. Properties of boundary layers manifest themselves through parameters  $u$ ,  $v$ , and  $w$ .

We have shown that although pores are expected to have strong effect on  $\sigma$  and  $\kappa$  separately, their effect on  $Z$  will be rather weak if not completely cancel each other.

Determination of parameters values in the model is a difficult task. In the case of pressure-sintered  $Bi_2Te_2$  system one could take advantage of the anisotropy. Thus the use of correlation between thermoelectric characteristics and orientation factor, as well as the microscopic observation of grain sizes helped us to identify the possible values of parameters [9]. On the contrary, thermoelectric properties of our present system depend on so many model parameters. So we adopted a simple minded approach in which parameters of grains are determined mainly by  $B_4C$  concentration  $x$  while those of boundary layers are determined by PSS concentration  $y$ , and estimated model parameters to reproduce both the temperature and concentration dependence of thermoelectric coefficients.

Of course such simulations are based on the extrapolation of measured parameters and one must be careful not to place too much weight on it. Thus we have limited our region of extrapolation to a lower values of  $x$  because one may expect possible structural changes at higher  $B_4C$  concentrations. Also we have to note not to include the unrealistic region of parameters which imply that thermoelectric properties of boundaries are superior to those of grains.

The results of our simulations show that in spite of the simplicity of the model one can recognize a prospective

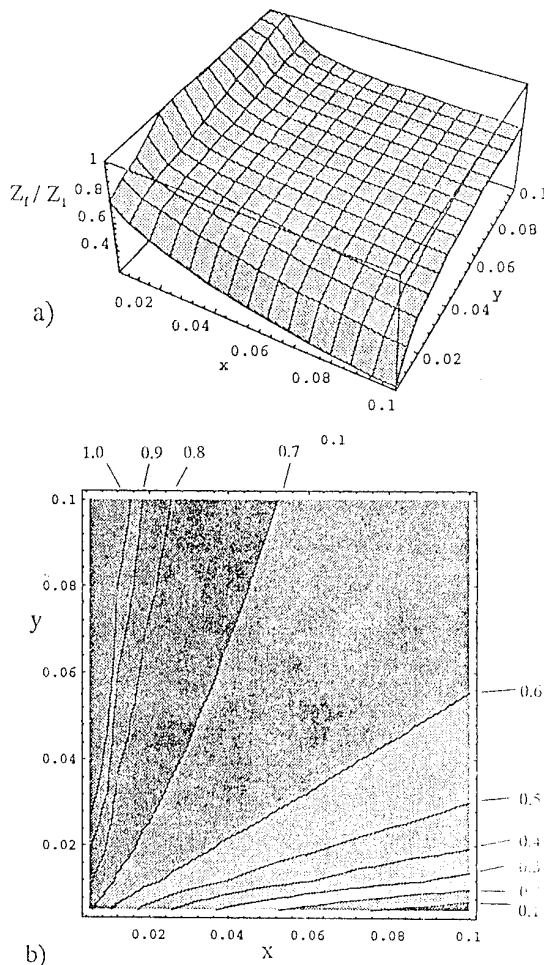


Fig.4. a) 3D  $Z_f$ -map on x-y plane and b) Equi Z contour map for  $T=900$  K and  $u_0=10$ ,  $v_0=4$  and  $w_0=5$ .

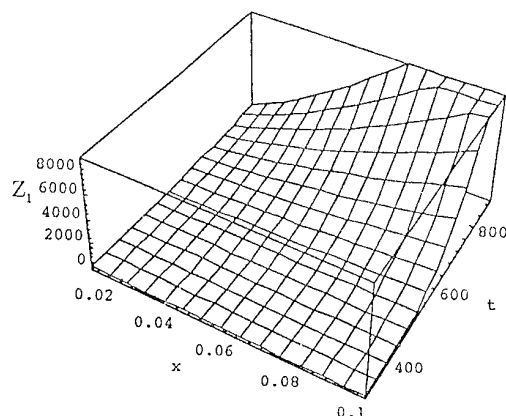


Fig.5. Figure of merit  $Z_1(x,t)$  of "crystallites".

region of  $x$  and  $y$  values where we may expect an improvement in the value of  $Z_f/Z_i$ . Moreover, the overall behavior of such 3D-plots or equi-Z-contours seems to be rather insensitive to the fine details of the model.

This result is a reflection of the experimental fact that both  $x$  and  $y$  increases  $\sigma$  and  $\alpha$  but decreases  $\kappa$  combined with the basic assumption of the model that  $x$  and  $y$  separately governs the grain and boundary characteristics. Increase in  $x$  increases  $u$  and  $w$  but decreases  $v$ , while increase in  $y$  have the opposite tendency. Because both  $f$  and  $g$  are monotonously decreasing functions of its arguments increase in  $y$  increases while increase in  $x$  decreases the value of  $Z_f$ .

So to make  $Z_f/Z_i$  as close to unity one has to choose a small values of  $x$  consistent with the condition not to make  $uw^2 < v$ . But one has also to note that  $Z_f$  of an imaginary "crystal" increase with increase in both  $x$  and temperature as shown in Fig.5. Taking into account of saturation of  $Z_i$  with  $x$ , one will finally find region of  $x$  for an optimum  $Z_f$ . Thus one may expect such

simulations to give a reasonable clue in the design of composites.

#### References

- [1]. J.L.Erickson et al.: *Homogenization and Effective Moduli of Materials and Media*, (Springer, New York, 1986).
- [2]. R.C.McPhedran and G.W.Milton: *Appl.Phys.* **A26**, 207 (1981).
- [3]. M.Milgrom: *Phys.Rev.* **B41**, 12494 (1990).
- [4]. D.J.Bergman and O.Levy: *J.Appl.Phys.* **70**, 6821 (1991).
- [5]. K.S.Mendelson, M.H.Cohen: *Geophysics* **47**, 257 (1982).
- [6]. R.H.Bube: *Appl.Phys.Lett.* **13**, 136 (1968).
- [7]. M.Milgrom and S.Shtrikman: *J.Appl.Phys.* **66**, 3429 (1989).
- [8]. Y.Okamoto et al.: *Proc. of ICT'94* (AIP, 1995).
- [9]. H.Wada et al. : *J.Matr.Sci.* **27**, 881 (1992).

# Effect of Intergrain Defects on Thermoelectric Properties of $\beta$ -FeSi<sub>2</sub>

## – Electron Spin Resonance Study –

T. Miki<sup>1</sup>, Y. Teraoka<sup>1</sup>, K. Kishimoto<sup>1</sup> and K. Matsubara<sup>2</sup>

<sup>1</sup>Department of Electrical and Electronic Engineering, Yamaguchi University,  
Ube, Yamaguchi 755, Japan

<sup>2</sup>Yamaguchi College, Tokyo Science University,  
Onoda, Yamaguchi 756, Japan

**ABSTRACT** Thermoelectric properties of  $\beta$ -FeSi<sub>2</sub> are improved by SiH<sub>4</sub> or O<sub>2</sub> rf-plasma processing of FeSi<sub>2</sub> grains before sintering. The plasma processing modifies the microstructure of ceramics especially at grain boundaries. Electron spin resonance studies have shown that the improved thermoelectric properties are associated with the annihilation of defects associated with Fe<sup>3+</sup> ions at intergrain regions. The results suggest that controlling grain boundary defects is effective for improving the electrical conductivity of thermoelectric ceramics.

## INTRODUCTION

Electrical properties of ceramic materials are often influenced by the presence of point defects or localized electronic levels at grain boundaries. Such defects or localized levels are easily introduced in ceramics in the course of sample preparation. Therefore suitable microstructure modification, especially at grain boundary, may improve the thermoelectric properties of ceramic materials. In fact, several papers have shown the improvement of thermoelectric properties by microstructure modification [1-4].

This study was undertaken to investigate the role of grain boundary defects on the electric properties of  $\beta$ -FeSi<sub>2</sub> ceramics. Iron disilicide exhibits relatively low figure-of-merit, but this material is still attractive for wide applications because of its low cost. In the present investigation, we used three types of  $\beta$ -FeSi<sub>2</sub> ceramics: One was prepared by the ordinary procedure of cold pressing and subsequent sintering and annealing, and the other two were processed in rf-plasma of silane or oxygen before sintering. In this paper, we confine ourselves to the role of point defects on the improved electrical conductivity in plasma-processed  $\beta$ -FeSi<sub>2</sub>.

## EXPERIMENTAL

The  $\beta$ -FeSi<sub>2</sub> samples used in this work were prepared by the procedures shown in Fig. 1. Detailed conditions in the

sample preparation was described in the previous articles [1-4].

The crystal structure of the samples were examined by x-ray diffraction (XRD) before measuring the thermoelectric properties. The electrical conductivity of the samples was measured by the four-point probe method at 290 – 800 K, and the Seebeck was obtained from the thermoelectric e.m.f acquired while applying a temperature difference of about 5 K to the both ends of a rectangular prism of ceramic chips. The point defects in the samples were detected with an X-band electron spin resonance (ESR) spectrometer (JEOL, FE-1X). The ESR spectrum was taken at 77 K to prevent the microwave loss due to conduction electrons and/or holes.

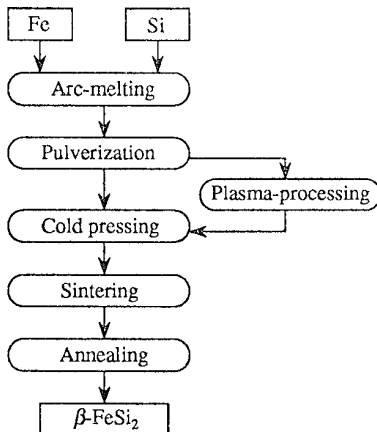


Fig. 1. Sample preparation procedure.

## RESULTS

### (A) Thermoelectric properties

XRD measurements indicated that all samples prepared are  $\beta$ -FeSi<sub>2</sub>, and no other phases, such as iron monosilicide and silicon phases, were detected. All samples obtained are *p*-type. As reported previously [1,3], plasma processing of FeSi<sub>2</sub> grains prior to sintering increases the electrical conductivity and Seebeck, as shown in Figs. 2 and 3.

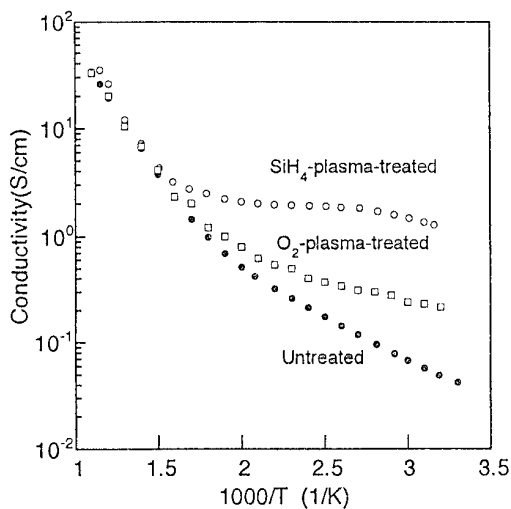


Fig. 2. Electrical conductivities of  $\beta$ -FeSi<sub>2</sub> samples.

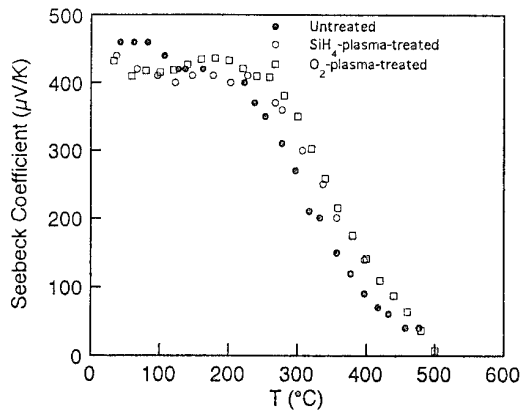


Fig. 3. The Seebeck coefficients of  $\beta$ -FeSi<sub>2</sub> samples.

Upon processing in SiH<sub>4</sub> or O<sub>2</sub> plasma, the electrical conductivity increases at temperatures below 350 K. It should be noted that the conductivity increases more remarkably by SiH<sub>4</sub>-plasma processing than O<sub>2</sub>-plasma-processing.

Despite the indicative change in electrical conductivity, plasma processing causes no significant change in the Seebeck coefficient, as shown in Fig. 3.

#### (B) ESR analysis

Figure 4 shows the ESR spectra of  $\beta$ -FeSi<sub>2</sub> ceramic samples of no plasma processing, SiH<sub>4</sub>-plasma processing and O<sub>2</sub>-plasma processing. The spectrum of no processed sample (see trace A) consists of a multiplet signal [2] and several singlet signals around 330 mT. The most remarkable change by plasma-processing is the decrease of the multiplet signal

intensity. It should be noted that SiH<sub>4</sub>-plasma processing more strongly decreases the multiplet signal than O<sub>2</sub>-plasma processing.

The multiplet signal was already ascribed to a closed pair of a high spin Fe<sup>3+</sup> ion ( $S = 5/2$ ) and an unidentified  $S = 1/2$  center [2,3]. Because plasma-processing only modifies the surface of  $\alpha$ -FeSi<sub>2</sub> fine particles, it is reasonably considered that the center responsible for the multiplet signal exists at the intergrain region of  $\beta$ -FeSi<sub>2</sub> ceramics. This consideration is consistent with the fact that the multiplet signal intensity becomes weak in the ceramics sintered using larger FeSi<sub>2</sub> grains. In GeH<sub>4</sub>-plasma-processed FeSi<sub>2</sub> [4], which shows larger electrical conductivity than no processed one, no appreciable multiplet signal was detected.

These results indicate that the grain surface modification by plasma-processing before sintering decreases the density of Fe<sup>3+</sup> ion-associated defects at grain boundaries in sintered  $\beta$ -FeSi<sub>2</sub> ceramics.

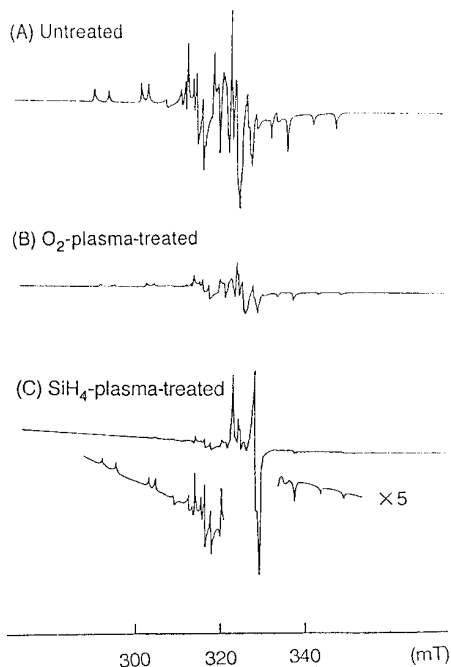


Fig. 4. ESR spectra of  $\beta$ -FeSi<sub>2</sub> samples.

## DISCUSSION

In a previous paper [3], we have proposed that the increase of electrical conductivity by SiH<sub>4</sub>-plasma processing is caused by the annihilation of the multiplet centers at grain boundaries. The present study using different processing gases has shown a clear correlation between the conductivity increase

and multiplet signal intensity decrease.

In Fig. 5 are shown the band schemes for explaining the conductivity increase by grain boundary modification due to plasma processing. In ordinary  $\beta$ -FeSi<sub>2</sub> ceramics, there would be intergrain defects associated with Fe<sup>3+</sup> ions as described in the previous section. Such defects probably form deep levels, and give rise to a potential barrier at grain boundaries (see Fig. 5a). Plasma processing results in the decrease of the intergrain defects, which was confirmed by ESR, therefore lowers the barrier height (see Fig. 5b). Thus, the increase of conductivity by plasma processing may be associated with the increase of carrier mobility caused by the barrier height reduction. In fact, we observed increased mobility in GeH<sub>4</sub>-plasma-treated  $\beta$ -FeSi<sub>2</sub> [4]. So the model described above reasonably explains the increased conductivity.

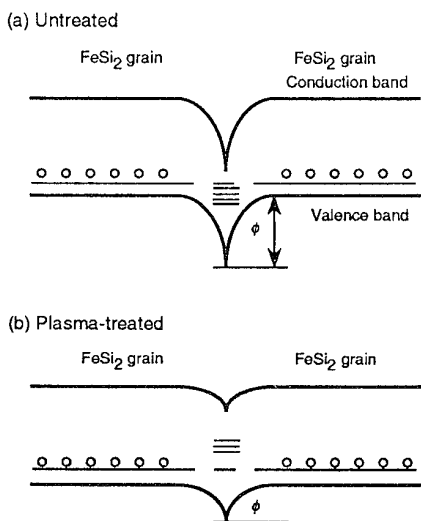


Fig. 5. Band schemes of unprocessed and plasma-processed  $\beta$ -FeSi<sub>2</sub> ceramics (replotted from ref. [3]).

Our remaining question is how the deep levels or Fe<sup>3+</sup>-associated defects are annihilated by plasma processing. The formation of Fe<sup>3+</sup>-associated defects in untreated FeSi<sub>2</sub> probably needs a selective oxidation of iron at grain boundaries. Such oxidation might take place if silicon is deficient and if there are reactive oxygen at grain boundaries. The native oxide on the FeSi<sub>2</sub> grain surface may be a good source of the reactive oxygen.

It is well known that plasma processing modifies the surface structure of the micrograins. In the case of SiH<sub>4</sub>-plasma-processing, a thin silicon layer is formed by the deposition of amorphous-silicon on the grain surface. The excess Silicon in the layer may be mobile to react with iron, and may suppress the formation of Fe<sup>3+</sup>-associated intergrain defects by preventing the oxidation of iron. Thus the amorphous-silicon layer may glue the grains forming a good electrical contact. In the case of GeH<sub>4</sub>-plasma processing, the

story would be same as the case of SiH<sub>4</sub>-plasma processing, because GeH<sub>4</sub>-plasma processing also forms a thin amorphous-Ge layer on the grain surface.

On the other hand, O<sub>2</sub>-plasma processing forms neither silicon nor germanium layers on the grain surface, but only disorders the FeSi<sub>2</sub> crystalline lattice. Such disordered lattice was recognized by transmission electron microscope measurements. By the bombardment of energetic ions, the native oxide layer may be also removed. In the case of O<sub>2</sub>-plasma-processed FeSi<sub>2</sub>, such disordered lattice may be rather important for suppressing the formation of Fe<sup>3+</sup>-associated intergrain defects, although detailed mechanism on the suppression of Fe<sup>3+</sup>-associated intergrain defects has not been understood well.

It is of special interest to note that the grain boundary modification is effective for improving the electrical conductivity in other thermoelectric ceramics. Kishimoto *et al.* [5] have observed a preferential increase in electrical conductivity of plasma-processed SiGe ceramics, in which they found the increase in the Hall mobility. Thus, plasma processing seems to fade out unidentified electronic levels at grain boundaries of SiGe ceramics.

## CONCLUSION

The electron spin resonance study of iron disilicide ceramics has revealed that the annihilation of intergrain defects is important for improving the thermoelectric properties, especially for electrical conductivity increase, of plasma-processed  $\beta$ -FeSi<sub>2</sub> ceramics. The increase of electrical conductivity by plasma processing is reasonably explained in terms of the potential barrier decrease caused by the annihilation of intergrain defects.

The obtained results suggest that controlling grain boundary defects is effective for improving the electrical conductivity of not only  $\beta$ -FeSi<sub>2</sub> ceramics but also other thermoelectric materials such as SiGe alloys.

## ACKNOWLEDGEMENT

We thank Mr. Y. Matsui for help with the ESR measurements. This work was partly supported by a Grant-in-Aid for Scientific Research (No. 07680534) from the Ministry of Education, Science and Culture, Japan.

## REFERENCES

- [1] K. Matsubara, K. Kishimoto, K. Nagao, O. Ueda, T. Miki, T. Koyanagi and I. Fujii, Iron disilicide: the possibility of improving thermoelectric figure of merit values by rf-plasma processing, *Proc. 12th Int. Conf. Thermoelectrics*, 1991, pp. 223-230.

- [2] T. Miki, Y. Matsui, K. Matsubara and K. Kishimoto, Electron paramagnetic resonance of defects in  $\beta$ -iron disilicide ceramics, *J. Appl. Phys.*, 1994, **75**, 1693–1698.
- [3] T. Miki, Y. Matsui, Y. Teraoka, Y. Ebina., K. Matsubara and K. Kishimoto, Point defects and thermoelectric properties of iron disilicide ceramics sintered with SiH<sub>4</sub>-plasma-processed micrograins, *J. Appl. Phys.*, 1994, **76**, 2097–2103.
- [4] K. Kishimoto, Y. Nagamoto, K. Nagao, T. Miki, T. Koyanagi and K. Matsubara, Microstructure control of  $\beta$ -FeSi<sub>2</sub> ceramics by rf-plasma processing in SiH<sub>4</sub> and GeH<sub>4</sub> gases, *Proc. 13th Int. Conf. Thermoelectrics*, AIP Press, 1994, pp. 123–126.
- [5] K. Kishimoto, Y. Nagamoto, T. Miki, T. Koyanagi and K. Matsubara, Thermoelectric properties of SiGe ceramics sintered with germane or silane plasma processed micrograins, *Proc. 14th Int. Conf. Thermoelectrics*, 1995 (to be published).

## THERMOELECTRIC MATERIALS WITH THE SKUTTERUDITE STRUCTURE: NEW RESULTS

Jean-Pierre Fleurial, Thierry Caillat and Alex Borshchevsky

Jet Propulsion Laboratory/California Institute of Technology  
4800, Oak Grove Drive, MS 277-212, Pasadena, CA 91109, USA

Skutterudite semiconductors possess attractive transport properties and have a good potential for achieving high ZT values. A large number of isostructural compounds, solid solutions and related phases are investigated. These skutterudite compositions offer many possibilities for substantially reducing the lattice thermal conductivity and for optimizing the electrical properties to a specific temperature range of thermoelectric applications. An overview of recent results is provided and current approaches to experimentally achieving high ZT in skutterudite materials are discussed.

### Introduction

A systematic search for new thermoelectric materials was started at JPL several years ago. A family of compounds with the skutterudite crystal structure was identified as a good candidate for high performance conversion efficiency [1]. In skutterudites, the bonding is predominantly covalent [2], which accounts for the high carrier mobilities experimentally obtained on several compounds such as  $\text{CoAs}_3$  [3],  $\text{CoSb}_3$  [4, 5],  $\text{IrSb}_3$  [6],  $\text{RhSb}_3$  [5, 7],  $\text{RhAs}_3$  [3] and  $\text{RhP}_3$  [8]. Also, the relatively large unit cell indicates that a low lattice thermal conductivity might be achieved. The skutterudite structure, illustrated in Figure 1, was originally attributed to a mineral from Skutterud (Norway) with a general formula  $(\text{Fe}, \text{Co}, \text{Ni})\text{As}_3$  [9].

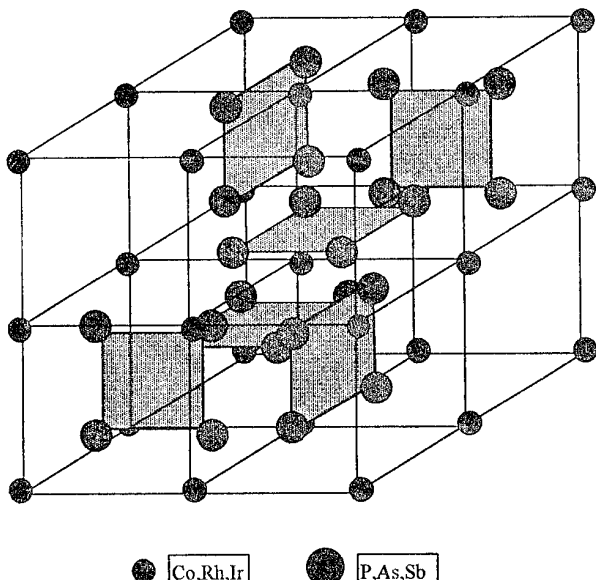


Figure 1: The skutterudite unit cell of formula  $\text{TPn}_3$  ( $\text{T}$  = transition metal,  $\text{Pn}$  = pnictogen).

The unit cell of the skutterudite contains square radicals  $[\text{As}_4]^{4-}$ . This anion located in the center of the smaller cube is surrounded by 8  $\text{Co}^{3+}$  cations. The unit cell was found to consist of 8 smaller cubes (octants) described above but two of them do not have the anions  $[\text{As}_4]^{4-}$  in the center. This is necessary to keep the ratio  $\text{Co}^{3+} : [\text{As}_4]^{4-} = 4:3$ . Thus, a typical coordination

structure results with  $\text{Co}_8[\text{As}_4]_6 = 2\text{Co}_4[\text{As}_4]_3$  composition and 32 atoms per cell with 8  $\text{AB}_3$  groups.

For the state of the art thermoelectric materials such as  $\text{PbTe}$  and  $\text{Bi}_2\text{Te}_3$  alloys, the number of isostructural compounds is limited and the possibilities to optimize their properties for maximum performance in different temperature ranges of operation are also very limited. This is not the case for skutterudites which show a variety of decomposition temperatures, band gaps and compositions which offers the possibility to optimize composition and doping level for a specific temperature range. Skutterudite compounds, solid solutions and related phases are briefly reviewed in the following sections.

### Existence and composition of skutterudites

Binary compounds. Binary skutterudite compounds are formed with all nine possible combinations of the elements Co, Rh, Ir with P, As, Sb. In this structure each metal atom has six bonds to a pnictogen and each of three pnictogens has two bonds to another pnictogen. Thus, each bond has two electrons which is consistent with the fact that they are diamagnetic semiconductors [10].

Table 1. Lattice parameter  $a$ , decomposition temperature  $T_m$ , band gap  $E_g$ , Hall mobility  $\mu_H$  and thermal conductivity  $\lambda$  of binary skutterudite compounds

Compound	$a$ (Å)	$T_m$ (°C)	$E_g$ (eV)	reference
$\text{CoP}_3$	7.7073	>1000	0.43*	11
$\text{CoAs}_3$	8.2043	960	0.69*	3
$\text{CoSb}_3$	9.0385	850	0.63*	5
$\text{RhP}_3$	7.9951	>1200	-	8
$\text{RhAs}_3$	8.4427	>1000	>0.85*	3
$\text{RhSb}_3$	9.2322	900	0.80*	5
$\text{IrP}_3$	8.0151	>1200	-	11
$\text{IrAs}_3$	8.4673	>1200	-	12
$\text{IrSb}_3$	9.2533	1141*	1.18*	6
$\text{NiP}_3$	7.819	>850	metallic	13
$\text{PdP}_3$	7.705	>650	metallic	13

\* JPL findings

Known values for the lattice parameter, peritectic decomposition temperature and band gap of these nine binary compounds are reported in Table 1. Decomposition temperatures for  $\text{CoP}_3$ ,  $\text{RhP}_3$ ,  $\text{RhAs}_3$ ,  $\text{IrP}_3$  and  $\text{IrAs}_3$  are only lower limit estimates. We have calculated the band gap values of

$\text{IrSb}_3$ ,  $\text{KhSb}_3$ ,  $\text{CoSb}_3$ ,  $\text{RhAs}_3$ ,  $\text{CoAs}_3$ , and  $\text{CoP}_3$  from high temperature Hall effect measurements. The p-type  $\text{RhAs}_3$  sample was still not fully intrinsic at the highest temperature of measurement, thus the value of 0.85 should only be considered a lower limit. Less heavily doped samples must be obtained to accurately determine the band gap of  $\text{RhAs}_3$ . The value obtained for  $\text{CoP}_3$  is only preliminary because the sample used for measurement contained  $\text{CoP}_2$  inclusions. The only other binary skutterudites known are  $\text{NiP}_3$  and  $\text{PdP}_3$  which have one more electron valence per formula unit and consequently show metallic conduction [13]. For the arsenides and antimonides, the band gap increases in sequence from the Co- to the Ir-based compounds as well as from the antimonides to the arsenides.

Ternary compositions. Skutterudite related phases can be formed by substitution by neighboring atoms for the anion or the cation in binary skutterudite compounds, the condition being that the valence-electron count remains constant. This is similar to the diamond-like family of semiconductors. The substitution can occur on the anion site ( $\text{CoAs}_3 \rightarrow \text{CoGe}_{1.5}\text{Se}_{1.5}$ ) or on the cation site ( $\text{CoSb}_3 \rightarrow \text{Fe}_{0.5}\text{Ni}_{0.5}\text{Sb}_3$ ). Structurally related skutterudite phases can also be formed by partial substitution of the cation and the anion ( $\text{RhSb}_3 \rightarrow \text{RuSb}_2\text{Te}$ ).

Table 2: Skutterudite related phases

Compound	a (Å)	$T_m$ (°C)	$E_g$ (eV)	Reference
$\text{CoGe}_{1.5}\text{S}_{1.5}$	8.017	1000	-	[14]
$\text{CoGe}_{1.5}\text{Se}_{1.5}^*$	8.299	800	-	[14]
$\text{CoSn}_{1.5}\text{Te}_{1.5}^*$	-	-	-	
$\text{RhGe}_{1.5}\text{S}_{1.5}$	8.2746	> 800	-	[15]
$\text{IrGe}_{1.5}\text{S}_{1.5}$	8.297	> 800	-	[15]
$\text{IrGe}_{1.5}\text{Se}_{1.5}^*$	8.5591	> 800	-	[15]
$\text{IrSn}_{1.5}\text{S}_{1.5}$	8.7059	> 800	-	[15]
$\text{IrSn}_{1.5}\text{Te}_{1.5}^*$	-	-	-	
$\text{Fe}_{0.5}\text{Ni}_{0.5}\text{Sb}_3^*$	9.0904	729 *	~0.16*	[16]
$\text{Fe}_{0.5}\text{Pd}_{0.5}\text{Sb}_3^*$	9.2060*	-	-	
$\text{Fe}_{0.5}\text{Pt}_{0.5}\text{Sb}_3^*$	9.1950*	-	-	
$\text{Ru}_{0.5}\text{Ni}_{0.5}\text{Sb}_3^*$	9.1780*	-	-	
$\text{Ru}_{0.5}\text{Pd}_{0.5}\text{Sb}_3^*$	9.2960*	647 *	~0.60*	[17]
$\text{Ru}_{0.5}\text{Pt}_{0.5}\text{Sb}_3^*$	-	-	-	
$\text{Fe}_{0.5}\text{Ni}_{0.5}\text{As}_3$	8.256	-	-	[18]
$\text{FeSb}_2\text{Se}^*$	-	-	-	
$\text{FeSb}_2\text{Te}^*$	9.112*	556*	~0.27*	
$\text{RuSb}_2\text{Se}^*$	9.257*	-	-	
$\text{RuSb}_2\text{Te}^*$	9.268*	810*	1.20*	
$\text{PtSn}_{1.2}\text{Sb}_{1.8}$	9.390	-	-	[19]

\* JPL findings

Nine ternary skutterudite related phases have been reported in literature [14-19]. Based on X-ray diffraction analyses, eleven new compositions were discovered at JPL. A number of isostructural quaternary and more complex compositions have also been identified. Values for the lattice parameter  $a$ , decomposition temperature  $T_m$  and band gap  $E_g$  are reported in Table 2.

Solid solutions. The only solid solutions between binary skutterudite compounds reported in the literature show that  $\text{CoP}_3$  and  $\text{CoAs}_3$  form a complete range of solid solutions which obey the Vegard's rule and that the system  $\text{CoAs}_{3-x}\text{Sb}_x$  has a miscibility gap in the region of  $x = 0.4$  to  $2.8$  [20]. Work at JPL on  $\text{CoSb}_3\text{-IrSb}_3$  compositions also demonstrated that a partial range of solid solutions exists in this system [21]. Our more recent experimental results, summarized in Table 3, have shown that there is an extensive number of skutterudite compounds and related phases form solid solutions, at least in some limited range of composition.

Table 3. Existence of skutterudite solid solutions

Solid Solutions	Partial Range of Compositions	Full Range of Compositions
$\text{CoP}_3$		$\text{CoAs}_3^*$
$\text{CoAs}_3$	$\text{CoSb}_3^*, \text{IrAs}_3$	
$\text{CoSb}_3$	$\text{CoAs}_3^*, \text{IrSb}_3,$ $\text{Fe}_{0.5}\text{Ni}_{0.5}\text{Sb}_3, \text{FeSb}_2\text{Te}$	
$\text{RhSb}_3$		$\text{IrSb}_3$
$\text{IrAs}_3$	$\text{CoAs}_3, \text{IrSb}_3$	
$\text{IrSb}_3$	$\text{CoSb}_3, \text{IrAs}_3$	$\text{RhSb}_3, \text{RuSb}_2\text{Te}$
$\text{Fe}_{0.5}\text{Ni}_{0.5}\text{Sb}_3$	$\text{CoSb}_3, \text{IrSb}_3, \text{Ru}_{0.5}\text{Pd}_{0.5}\text{Sb}_3$	$\text{Ru}_{0.5}\text{Pd}_{0.5}\text{Sb}_3$
$\text{Ru}_{0.5}\text{Pd}_{0.5}\text{Sb}_3$	$\text{CoSb}_3, \text{IrSb}_3$	$\text{Fe}_{0.5}\text{Ni}_{0.5}\text{Sb}_3$
$\text{FeSb}_2\text{Te}$	$\text{CoSb}_3, \text{RuSb}_2\text{Te}$	
$\text{RuSb}_2\text{Te}$	$\text{FeSb}_2\text{Te}$	$\text{IrSb}_3$

\*literature results

Filled skutterudites. A large number of these materials have already been synthesized (see for example [22-25]). The composition of these types of compounds can be represented by the formula  $\text{LnT}_4\text{Pn}_{12}$  ( $\text{Ln}$  = rare earth, Th; T = Fe, Ru, Os; Pn = P, As, Sb). In these compounds, the empty octants of the skutterudite structure (see Figure 1) which are formed in the  $\text{TPn}_3$  ( $\sim \text{T}_4\text{Pn}_{12}$ ) framework are filled with a rare earth element. Because the  $\text{T}_4\text{Pn}_{12}$  groups using Fe, Ru or Os are electron-deficient relative (by 4 e<sup>-</sup>) to the skutterudite electronic structure (using Co, Rh or Ir), the introduction of the rare earth atom compensates this deficiency by adding free electrons. However, the number of valence electrons given up by the rare earth atoms is generally insufficient: for example, La has a 3+ oxidation state, Ce can be 3+ or 4+. This means that most of these compounds behave as metals, or very heavily doped p-type semi-metals. However, it has been shown that some of them such as  $\text{UFe}_4\text{P}_{12}$  and  $\text{CeF}_4\text{P}_{12}$  are semiconductors [22]. The addition of a new ion(s) in the voids could be an efficient phonon scattering center and could result in substantially lower lattice thermal conductivity values. The properties of such skutterudite compounds remain to be fully characterized

### Thermoelectric properties of skutterudites

Skutterudite compounds have exceptionally high hole mobilities, substantially higher than state-of-the-art semiconductors for a given carrier concentration. We have measured a Hall mobility value close to  $8000 \text{ cm}^2 \cdot \text{V}^{-1} \text{s}^{-1}$  on a p-type  $\text{RhSb}_3$  single crystal

with a Hall carrier concentration of about  $3.5 \times 10^{18} \text{ cm}^{-3}$ . This is the highest p-type mobility ever measured at this doping level. All p-type skutterudites (binary and ternary compounds) investigated so far have high hole mobilities which make them very promising materials for thermoelectric applications.

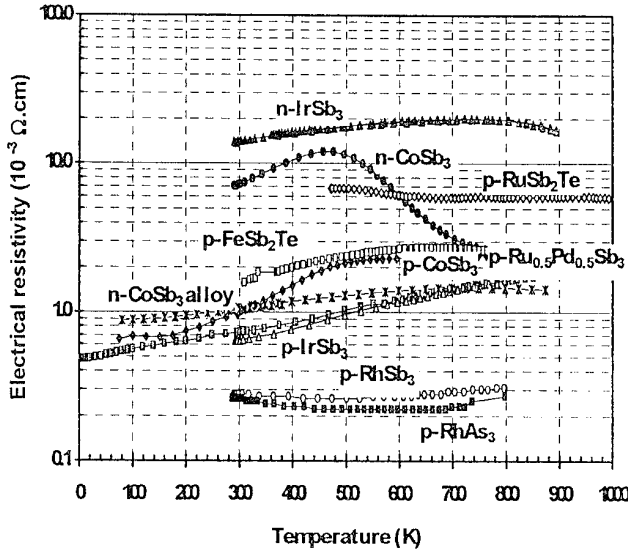


Fig. 2: Electrical resistivity as a function of temperature for several n-type and p-type skutterudite compounds.

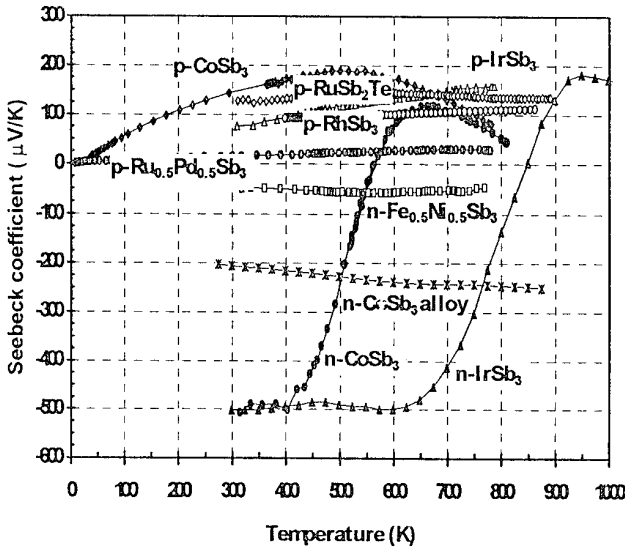


Fig. 3: Seebeck coefficient as a function of temperature for several n-type and p-type skutterudite compounds.

N-type samples have been obtained for CoSb<sub>3</sub> and IrSb<sub>3</sub> by doping with elements such as Ni, Pd, Pt and Te [26, 27]. The Hall mobility of n-type samples was found to be much lower than for p-type materials, resulting in higher electrical resistivity values. However, the large electron effective mass translated into high Seebeck coefficient, up to  $600 \mu\text{V.K}^{-1}$  for n-type samples compared to only up to  $200 \mu\text{V.K}^{-1}$  for p-type samples. As a consequence, optimum doping levels for n-type binary

compounds are roughly one order of magnitude higher than for p-type skutterudites.

The experimental temperature variations of the electrical resistivity and the Seebeck coefficient of some binary skutterudites are shown in Figures 2 and 3, respectively. Minority carrier concentration effects (high mobility holes) are responsible for the change in Seebeck coefficient from positive to negative at high temperatures for n-type CoSb<sub>3</sub> and IrSb<sub>3</sub> samples (Figure 3). Because of a smaller band gap, this compensation occurs at lower temperatures in CoSb<sub>3</sub>. The contribution from the minority carriers is much more limited in n-type CoSb<sub>3</sub>-based compositions prepared with high doping levels. This results in the Seebeck coefficient remaining n-type throughout the whole temperature range and a strong decrease in the electrical resistivity.

Almost no information about the thermal and electrical properties of ternary skutterudite related phases is available in the literature. Some results obtained at JPL on four ternary phases, FeSb<sub>2</sub>Te, RuSb<sub>2</sub>Tc, Fe<sub>0.5</sub>Ni<sub>0.5</sub>Sb<sub>3</sub> and Ru<sub>0.5</sub>Pd<sub>0.5</sub>Sb<sub>3</sub> are reported in Figures 2 and 3. Fe<sub>0.5</sub>Ni<sub>0.5</sub>Sb<sub>3</sub> and FeSb<sub>2</sub>Te are two ternary phases derived from CoSb<sub>3</sub>, and the calculated band gap values, 0.16 and 0.27 eV respectively, are much smaller than the 0.63 eV value for CoSb<sub>3</sub>. Similar results are obtained for Ru<sub>0.5</sub>Pd<sub>0.5</sub>Sb<sub>3</sub> (0.6 eV), which is derived from RhSb<sub>3</sub> (0.8 eV). The lower band gap values are consistent with the lower decomposition temperatures. This is not the case of RuSb<sub>2</sub>Te however, which has a band gap of 1.20 eV.

The electrical properties of the ternary skutterudites also vary substantially from the results obtained on the binary compounds. It ranges from very heavily doped (Ru<sub>0.5</sub>Pd<sub>0.5</sub>Sb<sub>3</sub>) to more lightly doped (RuSb<sub>2</sub>Te), and from extrinsic p-type behavior (FeSb<sub>2</sub>Te) to mixed conduction n-type behavior (Fe<sub>0.5</sub>Ni<sub>0.5</sub>Sb<sub>3</sub>). These findings indicate that significant changes in band structure and doping behavior were brought by changes in the atomic and electronic structure. In particular, fluctuations in the valence of the transition metal atoms could be imposed by the need to conserve the skutterudite crystal structure. Understanding and controlling these changes is a key step in designing a skutterudite composition with superior thermoelectric properties.

#### Thermal conductivity

The thermal conductivity of p-type CoSb<sub>3</sub>, RhSb<sub>3</sub> and IrSb<sub>3</sub> samples was measured from 10 to 800K [4, 26-27]. The results plotted in Figure 4 are compared to typical values obtained for state of the art thermoelectric alloys. Room temperature values of these three compounds range from 110 to 130 mW.cm<sup>-1</sup>.K<sup>-1</sup> depending on the carrier concentration level. These values are quite reasonable considering the relatively high decomposition temperature and bandgap of skutterudites (see Table 1). Additional measurements conducted on p-type CoAs<sub>3</sub> and RhAs<sub>3</sub> [3] indicated that the room temperature thermal conductivity values increase slightly from antimonides to arsenides, and also from Co-based compounds to Ir-based compounds. The Wiedemann-Franz law can be used to calculate the lattice thermal conductivity of p-type CoSb<sub>3</sub>, RhSb<sub>3</sub> and IrSb<sub>3</sub> samples. For a carrier concentration of  $1 \times 10^{19} \text{ cm}^{-3}$ , calculations show that about 90% of the total thermal conductivity is due to the lattice contribution. Though we have not yet measured heavily doped n-type samples, the thermal conductivity of binary skutterudites appears to be too high to result in high ZT values. Experimental and theoretical results on p-type IrSb<sub>3</sub> showed that

a maximum ZT value of 0.4 can be obtained at 900K [28]. Reductions in the lattice thermal conductivity must be obtained to achieve values comparable to those of state of the art thermoelectric materials ( $10\text{-}40 \text{ mW.cm}^{-1}\text{K}^{-1}$ ).

Solid solutions possess a much lower lattice thermal conductivity due to atomic mass and volume fluctuations. However, a higher phonon scattering rate always has some negative impact on the carrier mobility, but because the drop in thermal conductivity is usually larger than the degradation of the electrical properties, ZT values are overall substantially improved. This process has been used for all the state of the art thermoelectric materials, and is of interest for skutterudite compounds. Thermal conductivity measurements of several  $\text{CoSb}_3$ - $\text{IrSb}_3$  alloyed samples showed that the thermal conductivity dropped to about  $30\text{-}35 \text{ mW.cm}^{-1}\text{K}^{-1}$  at room temperature, a value 3 to 4 times smaller than for the individual compounds [21]. These results are also reported in Figure 4.

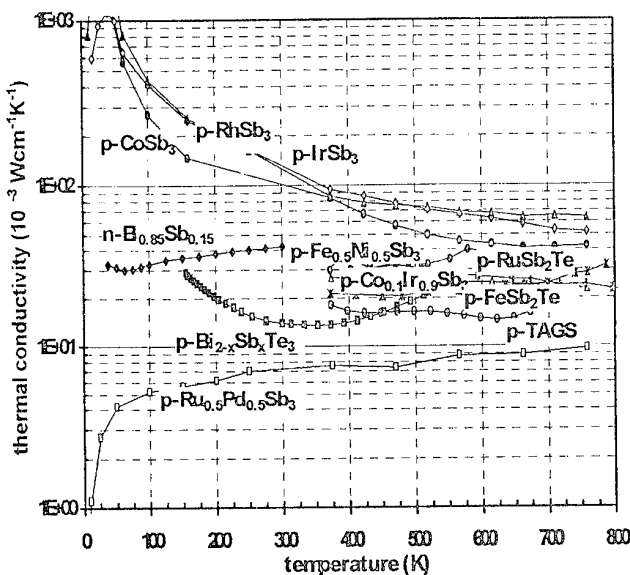


Fig. 4: Thermal conductivity as a function of temperature for several n-type and p-type skutterudite compounds, solid solutions and related phases.

As well as for solid solutions, the lattice thermal conductivity of ternary skutterudite phases was expected to be lower than for binary compounds. Our first results on six such ternary phases (five of them are new compositions) confirmed these predictions. JPL experimental data on four ternary phases,  $\text{FeSb}_2\text{Te}$ ,  $\text{RuSb}_2\text{Te}$ ,  $\text{Fe}_{0.5}\text{Ni}_{0.5}\text{Sb}_3$  and  $\text{Ru}_{0.5}\text{Pd}_{0.5}\text{Sb}_3$  are plotted in Figure 4. The thermal conductivity is greatly reduced in these materials, with room temperature values ranging from 7 to 30  $\text{mW.cm}^{-1}\text{K}^{-1}$ . The low thermal conductivity values of these compounds, while very encouraging, are nevertheless a bit surprising considering that the atomic mass and volume differences introduced by the substituting anion/cation are fairly small. This indicates that additional mechanisms must be involved such as electron exchange scattering of phonons [29]. Of particular interest is the glassy behavior of  $\text{Ru}_{0.5}\text{Pd}_{0.5}\text{Sb}_3$  where the thermal conductivity decreases with decreasing temperatures. At room temperature, the thermal conductivity value is  $7 \text{ mW.cm}^{-1}\text{K}^{-1}$ , about 15 times lower than for  $\text{RhSb}_3$ ,

(or  $\text{IrSb}_3$ ). This is also lower than the values obtained for the state of the art thermoelectric materials. The lattice contribution was estimated at  $2.5\text{-}3.0 \text{ mW.cm}^{-1}\text{K}^{-1}$ , which is an extremely low value. However, this unoptimized material is still too heavily doped and the carrier concentration must be reduced to achieve larger Seebeck coefficient values.

Moreover, the possibility of forming solid solutions between these ternary compounds and the high mobility binary compounds (as described in Table 3) offers an excellent opportunity of finding a very low thermal conductivity material with good electrical properties. These results demonstrate the great potential of skutterudites for high ZT values as very high mobilities, large Seebeck coefficients and very low lattice thermal conductivities can be obtained with materials of the same crystal structure.

## Conclusion

A new family of promising thermoelectric materials with the skutterudite crystal structure has been presented. A number of binary compounds, solid solutions and ternary related phases have been briefly reviewed. Initial results obtained on some of their representatives demonstrated the great potential of skutterudites for high ZT values. Both p-type and n-type materials appear promising, though in a different range of carrier concentrations. If the good electrical properties of the binary skutterudite compounds can be somewhat preserved, there are several approaches for large reductions in thermal conductivity that could lead to ZT values substantially larger than 1.

## Acknowledgments

The work described in this paper was carried out by the Jet Propulsion Laboratory/ California Institute of Technology, under a contract with the National Aeronautics and Space Administration. The authors would like to thank Roger Williams for preparing the  $\text{CoP}_3$  sample.

## References

- [1] T. Caillat, A. Borshchevsky, and J.-P. Fleurial, "Search for New High Temperature Thermoelectric Materials" in *Proc. 27<sup>th</sup> Intersoc. Ener. Conv. Engin. Conf.*, San Diego, California, August 3-7,(3) 499-503 (1992).
- [2] A. D. Kjekshus, G. Nicholson, T. Rakke, *Acta Chem. Scand.* 27, 4 (1973).
- [3] T. Caillat, J.-P. Fleurial, and A. Borshchevsky, "Progress in the Search for Advanced Thermoelectric Materials For Terrestrial Applications at the Jet Propulsion Laboratory" in *Proc. 30<sup>th</sup> Intersoc. Ener. Conv. Engin. Conf.*, Orlando, Florida, August 3-7, (1995).
- [4] D.T. Morelli, T. Caillat, J.-P. Fleurial, A. Borshchevsky, J. Vandersande, B. Chen and C. Uher, "Low temperature transport properties of p-type  $\text{CoSb}_3$ ", *Phys. Rev. B*, (51), 15, 9622-9628 (1995).
- [5] T. Caillat, J.-P. Fleurial, and A. Borshchevsky, "Bridgman-solution crystal growth and characterization of the skutterudite compounds  $\text{CoSb}_3$  and  $\text{RhSb}_3$ ", to be published in *J. Cryst. Growth* (1995).
- [6] T. Caillat, A. Borshchevsky, and J.-P. Fleurial, in *Proc. XI<sup>th</sup> Int. Conf. on Thermoelectrics*, p. 98, 1993, (Arlington, TX, 1992).

- [7] G. Kliche, W. Bauhofer, Mat. Res. Bull., 22, 551 (1987).
- [8] J. P. Odile, S. Soled, C. A. Castro, A. Wold, Inorganic Chemistry, 17, 2, 283 (1978).
- [9] I. Oftedal, Z. Kristallogr., 66, 517 (1928).
- [10] F. Hulliger, Helv. Phys. Acta, 34, 782 (1961).
- [11] S. Rundqvist and N.O. Ersson, "Structure and bonding in skutterudite-type phosphides", Arkiv For Kemi, (30), 10, 103-114 (1968)
- [12] A. Kjekshus and G. Pedersen, "The Crystal Structure of IrAs<sub>3</sub> and IrSb<sub>3</sub>", Acta Cryst., 14, 1065-1070 (1961).
- [13] W. Jeitschko, D. Braun, Acta Cryst., B33, 3401 (1977).
- [14] R. Korenstein, S. Soled, A. Wold, G. Collin, Inorganic Chemistry, 16, 9, 2344 (1977).
- [15] A. Lyons, R. P. Gruska, C. Case, S. N. Subbarao, A. Wold, Mat. Res. Bul., 125 (1978).
- [16] A. Kjekshus, T. Rakke, Acta Chemica Scandinavica, A28, 99 (1974).
- [17] T. Caillat, A. Borshchevsky, and J.-P. Fleurial, "Existence and Some Properties of New Ternary Skutterudite Phases", Proc. XIII Intl. Conf. on Thermoelectrics, AIP Press No. 316, 209-211, Kansas City, MO (1994).
- [18] H. D. Lutz, G. Kliche, J. Solid State Chemistry, 40, 64 (1981).
- [19] S. Bahn, T. Gödecke, , K. Schubert, J. of Less-Common Metals, 19, 121 (1969).
- [20] N. Mandel, J. Donohue, Acta Cryst., B27, 2288 (1971).
- [21] A. Borshchevsky, J.-P. Fleurial, C.E. Allevato, and T. Caillat, "CoSb<sub>3</sub>-IrSb<sub>3</sub> Solid Solutions: Preparation and Characterization", Proc. XIII Intl. Conf. on Thermoelectrics, AIP Press No. 316, 3-6, Kansas City, MO
- [22] (J.994) Meisner, M. S. Torikachvili, K. N. Yang, M. B. Maple, R. P. Guertin, J. Appl. Phys., 57, 1, 3073 (1985).
- [23] D. Jung, M. H. Whangbo, S. Alvarez, Inorganic Chemistry, 29, 2252 (1990).
- [24] F. Grandjean, A. Gérard, D. J. Braun, W. Jeitschko, J. Phys. Chem. Solids, 45, 8/9, 877 (1984).
- [25] N. T. Stetson, S. M. Kauzlarich, H. Hope, Journal of Solid State Chemistry, 91, 140 (1991).
- [26] T. Caillat, A. Borshchevsky, and J.-P. Fleurial, J.-P., "Preparation and Thermoelectric Properties of p and n-Type CoSb<sub>3</sub>", Proc. XIII Intl. Conf. on Thermoelectrics, AIP Press No. 316, 58-61, Kansas City, MO (1994).
- [27] T. Caillat, A. Borshchevsky, and J.-P. Fleurial, J.-P., "Preparation and Thermoelectric Properties of p and n-Type IrSb<sub>3</sub>", Proc. XIII Intl. Conf. on Thermoelectrics, AIP Press No. 316, 31-34, Kansas City, MO (1994).
- [28] J.-P. Fleurial, "Modeling of the Thermoelectric Properties of p-Type IrSb<sub>3</sub>", Proc. XIII Intl. Conf. on Thermoelectrics, AIP Press No. 316, 86-91, Kansas City, MO (1994).
- [29] G. Slack, Private communication.

NEW MATERIALS FOR THERMOELECTRIC COOLING BASED ON IrSb<sub>3</sub>George S. Nolas<sup>1</sup>, Glen A. Slack<sup>1</sup>, Terry M. Tritt<sup>2</sup>, and Donald T. Morelli<sup>3</sup><sup>1</sup>*Department of Physics, Rensselaer Polytechnic Institute  
Troy, New York 12180*<sup>2</sup>*Material Science Branch, U. S. Naval Research Laboratory  
Washington, D.C. 20375-5000*<sup>3</sup>*Physics Department, General Motors Research and Development Center  
Warren, Michigan 48090-9055*

## ABSTRACT

Polycrystalline samples of Ir<sub>4</sub>LaGe<sub>3</sub>Sb<sub>9</sub> and Ir<sub>4</sub>NdGe<sub>3</sub>Sb<sub>9</sub> have been made by hot isostatic pressing of powders. The lattice thermal conductivity of these filled skutterudites is markedly smaller than that of IrSb<sub>3</sub> and thus this filling shows promise as a method for improving the thermoelectric properties of these materials. We present the lattice thermal conductivity,  $\kappa_g$ , of these filled skutterudites from 300K to 10K. It is observed that the decrease in  $\kappa_g$  is greater in the Nd-filled sample than in the La-filled sample. The smaller atoms "rattle" more readily in the voids of the structure and therefore interact with a larger spectrum of phonons. Electrical resistivity, Seebeck coefficient, and carrier mobility are also presented.

## INTRODUCTION

The semiconducting compound iridium triantimonide, IrSb<sub>3</sub>, is one of a number of compounds with the skutterudite or CoAs<sub>3</sub> structure[1,2,3,4,5,6]. Compounds of this kind have shown good potential for thermoelectric applications[1,7]. Lowering the thermal conductivity of these skutterudite materials, however, is a key goal in increasing the figure of merit[8]. Different approaches have been attempted toward this end[9,10]. In the present study we have undertaken the task of reducing the thermal conductivity of IrSb<sub>3</sub> by employing a totally new and unique approach from that of previous studies, see Slack and Tsoukala[1].

The binary skutterudites have the cubic Im<sup>3</sup> ( $T_h^5$ ) structure and are of the form AB<sub>3</sub> where A represents a metal atom and B represents a pnictogen atom. There are eight formula units in the cubic unit cell. In addition there are two voids per unit cell in the structure. Skutterudites form covalent structures with low coordination numbers for the constituent atoms and so can incorporate atoms in the voids. We have calculated the void radii of the nine binary semiconducting skutterudites[1,4,11,12] compounds from x-ray crystallographic data[2,3,4,11,12]. The radius, r(B), of the B atom is taken to be one half of the average B-B separation. The void radius is taken as the distance, d, from the center of the void to any one of the twelve surrounding B atoms minus r(B):

$$r(\text{void}) = d - r(B). \quad (1)$$

These are listed in Table 1.

Table 1. Lattice parameters[1,4,11,12],  $a_0$ , and void radii,  $r$ , in Å, of the nine normal semiconducting skutterudites.

CoP <sub>3</sub>	CoAs <sub>3</sub>	CoSb <sub>3</sub>
$a_0=7.7073$	$a_0=8.205$	$a_0=9.0385$
$r=1.763$	$r=1.825$	$r=1.892$
RhP <sub>3</sub>	RhAs <sub>3</sub>	RhSb <sub>3</sub>
$a_0=7.9951$	$a_0=8.4507$	$a_0=9.2322$
$r=1.909$	$r=1.934$	$r=1.2024$
IrP <sub>3</sub>	IrAs <sub>3</sub>	IrSb <sub>3</sub>
$a_0=8.0151$	$a_0=8.4673$	$a_0=9.2503$
$r=1.906$	$r=1.931$	$r=2.040$

As seen from the table, the void radii range from 1.763 Å in CoP<sub>3</sub> to 2.040 Å in IrSb<sub>3</sub>. In the present study we have succeeded in putting rare earth ions into the voids of IrSb<sub>3</sub>, chosen because it has the largest size voids as well as having good thermoelectric properties, in an attempt to study their effect on the lattice thermal conductivity,  $\kappa_g$ . The reduction of  $\kappa_g$  of a crystalline compound by introducing "guest" atoms, or molecules, into "openings" in the crystal structure has been studied in clathrate hydrates[13] and channel compounds[13,14,15,16]. Due to the weak bonding of the guest atom or molecule within the host lattice in these studies, these guests are able to "rattle" in their "cages" and thereby interact with low frequency phonons. The guest atoms or molecules interact with a larger spectrum of phonons than they would if mass fluctuation scattering alone were present, thereby having a larger influence on  $\kappa_g$ .

## SAMPLE PREPARATION

Single phase polycrystalline samples of Ir<sub>4</sub>LaGe<sub>3</sub>Sb<sub>9</sub> and Ir<sub>4</sub>NdGe<sub>3</sub>Sb<sub>9</sub> were similarly prepared as follows.

First the lanthanum (La) or neodymium (Nd) rare earth (RE, 99.99% pure), in lump form, was reacted with Germanium (Ge, 99.9999% pure) powder, in the stoichiometric ratio 1:3 at 960°C for 4 days, in order to obtain an intimate mixture of the RE with Ge ( $\text{REGe}_2 + \text{Ge}$ ). All RE elements and RE compounds were handled in an argon atmosphere since high purity RE elements are very reactive in air. The resulting mixture was ground to fine powder with a boron carbide ( $\text{B}_4\text{C}$ ) mortar and pestle. It was then mixed and reacted with the proper stoichiometric amounts of iridium (Ir, 99.99% pure) and antimony (Sb, 99.9999% pure) powders at 960°C for 2 days. In both cases the powder was held in a chemically vapor deposited 2.67-cm-diameter, 6.5-cm-tall pyrolytic boron nitride (BN) crucible which itself was sealed inside an evacuated, fused quartz ampule. This ampule was heated in an external atmosphere of flowing argon in order to prevent the inward diffusion of air and water vapor during the run. The product was removed from the ampule, ground in the  $\text{B}_4\text{C}$  mortar and pestle, reloaded into a BN crucible, and re-reacted for another 2 days at 960°C as described above. After removal, the resulting powders were cold pressed into cylindrical pellets and then sealed inside of an evacuated pyrex ampule. This ampule was then placed in a hot isostatic press where the pellets were consolidated at 925°C for 2 hours at 29,500 lb/in<sup>2</sup> of argon pressure. The Ge randomly substitutes for Sb in the structure and is used for charge compensation of the RE. The three Ge atoms act as "acceptors" for the three "donated" electrons from each RE atom. The resulting polycrystalline La and Nd-filled skutterudite samples were 82% and 72% of theoretical density, respectively. The density measurements were performed by weighing a precisely cut cube of each material. The density measurements were verified using an Olympus System Microscope model BHT, with camera, interfaced to a Macintosh computer. Images of polished surfaces of the samples were digitized and the porosity was calculated automatically. In addition, images of the  $\text{Ir}_4\text{NdGe}_3\text{Sb}_9$  sample etched with aqua regia were also used to measure the average grain size[17]. The average grain size of this sample was measured to be 7  $\mu\text{m}$ . An 82% dense  $\text{IrSb}_3$  polycrystalline sample was also prepared in order to experimentally compare it to the filled skutterudite samples.

Metallographic and electron-beam microprobe (JOEL 733 superprobe) examination of the polished surface of each sample verified the stoichiometry of the samples. The annealed samples were ground and analysed by x-ray diffractometry using Cu K $\alpha$  radiation with a powdered silicon (Standard Reference Material 640b) internal standard. Both a graphite-monochromatized Philips model 5520 diffractometer with a scintillation detector and a Scintag XDS 2000 diffractometer which utilizes a solid state detector were used. The results from these measurements showed that the samples were single phase. The intensity of the x-ray reflections were compared with intensities calculated for different concentrations of RE in the voids using

POWD7 software[18]. The calculated powder pattern intensities verified that the RE occupy the voids in the structure at the 100% filling level, in agreement with the microprobe results.

## EXPERIMENTAL RESULTS

We have measured the cubic x-ray lattice parameter at room-temperature of powdered  $\text{Ir}_4\text{LaGe}_3\text{Sb}_9$  and  $\text{Ir}_4\text{NdGe}_3\text{Sb}_9$  using the silicon internal standard. The results are  $9.104 \pm 0.001$  Å and  $9.112 \pm 0.002$  Å, respectively. These results show lattice parameters that are smaller than for  $\text{IrSb}_3$ ,  $a_0 = 9.2503 \pm 0.0003$  Å[1]. A lattice parameter model calculation for "unfilled"  $\text{Ir}_4\text{Ge}_3\text{Sb}_9$  gives  $a_0 = 9.0021$  Å using  $r(\text{Sb})=1.452$  Å,  $r(\text{Ir})=1.161$  Å, and  $r(\text{Ge})=1.2249$  Å. The Ir and Sb radii were calculated from the Sb–Sb and Ir–Sb bonds in  $\text{IrSb}_3$  as described above and the Ge radius is from the elemental Ge crystal structure[19]. The reduction in the lattice parameter of these RE-filled skutterudites compared to  $\text{IrSb}_3$  is therefore presumably due to the smaller Ge atom introduced into the structure. The RE elements in the voids expand the lattice compared to the zero filling lattice parameter.

Figure 1. Lattice thermal conductivity,  $\kappa_g$ , vs. temperature for the La and Nd-filled as well as the "unfilled" skutterudite samples. The calculated minimum thermal conductivity[20],  $\kappa_{\min}$ , for  $\text{IrSb}_3$  is also included in the Figure. In addition, a plot of  $\kappa_g$  calculated for grain-boundary scattering for 7- $\mu\text{m}$  grains is indicated by an arrow.

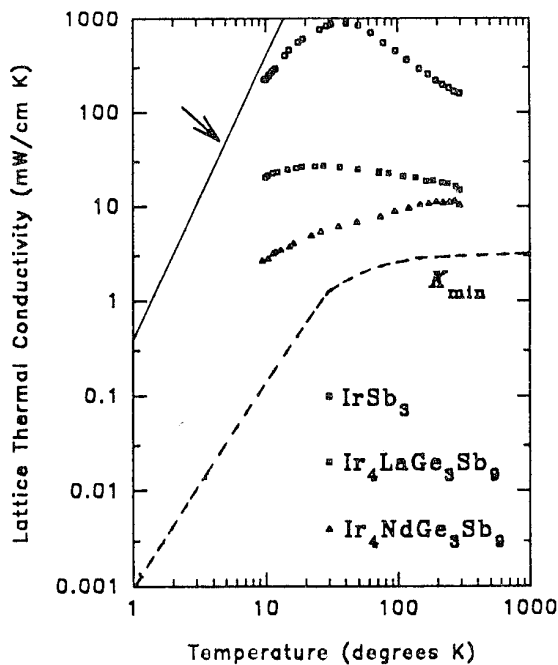


Figure 1 shows  $\kappa_g$  as a function of temperature for the La and Nd-filled skutterudite samples as well as for the "unfilled" skutterudite sample. Thermal transport measurements were carried out by the two thermocouple, steady state heat-flow technique which has been described in detail elsewhere[21,22]. Samples were cut with a high speed diamond saw in the shape of parallelepipeds with the heat flow measured along the longest axis. Since the skutterudite structure is cubic,  $\kappa_g$  is essentially isotropic. Due to the low thermal conductivity,  $\kappa$ , of these samples, the radiation loss, measured to be 1.2 mW/K at room temperature, was corrected for. We estimate the absolute error below 200 K to be 5%, which arises primarily from the error in measuring the geometric factor of these samples. From the measured value of the electrical resistivity and the Wiedmann-Franz law, we have estimated and subtracted the electronic contribution to  $\kappa$  in the figure. A detailed analysis of the resistivity of these samples as a function of temperature is presented in reference 23. We have assumed the Wiedmann-Franz-Lorenz coefficient to be  $2.44 \times 10^{-8} \text{ V}^2/\text{deg}^2$ , a value experimentally verified for doped Si-Ge mixed crystals at low temperatures[24]. In addition,  $\kappa_g$  was corrected for porosity[25,26].

Table 2. Measured Parameters:  $\rho$ = resistivity (milliohm-cm); n=hole(+) or electron(−) concentration ( $\text{cm}^{-3}$ );  $\mu$ =mobility( $\text{cm}^2/\text{V}\cdot\text{sec}$ ); S=Absolute Seebeck coefficient ( $\mu\text{V}/\text{K}$ ); Temp=temperature (K).

\*\* — Magnetic effects due to  $\text{Nd}^{3+}$

Sample	Temp	$\rho$	n	$\mu$	S
$\text{IrSb}_3$	300	0.468	$+1.2 \times 10^{19}$	1149	+77
	77	0.318	---	---	+34
$\text{Ir}_4\text{LaGe}_3\text{Sb}_9$	300	0.927	$+8.8 \times 10^{20}$	7.64	+6.4
	77	0.637	$-2.0 \times 10^{23}$	.047	-3.7
$\text{Ir}_4\text{NdGe}_3\text{Sb}_9$	300	1.49	**	**	+0.89
	77	1.10	**	**	-7.9

Room and liquid-nitrogen temperature electrical resistivity, Seebeck coefficient, carrier concentration, and mobility measurements are summarized in Table 2. The electrical resistivity, carrier concentration, and mobility data were measured on flat, square pieces of material using the van der Pauw technique. Care was taken to insure that no heating of the samples occurred during the course of a measurement. These data are in good agreement with data taken at the U. S. Naval Research Laboratory[23]. From Table 2 it is clear that the thermoelectric properties of these "filled" skutterudites were not optimized. Further work on charge compensation for the donated electrons by the RE ions is currently underway.

## DISCUSSION

The mass fluctuation scattering of phonons in  $\text{Ir}_{0.5}\text{Rh}_{0.5}\text{Sb}_3$  mixed crystals has been studied by Slack and Tsoukala[1] from 720 K to 300 K. At 300 K the mixed crystal had a  $\kappa_g$  56% of that of  $\text{IrSb}_3$ . The La and Nd-filled samples have a  $\kappa_g$  9.4% and 6.5%, respectively, of that of  $\text{IrSb}_3$ . The Ge substitution for Sb in  $\text{IrSb}_3$  can be estimated to produce a relatively small decrease in  $\kappa_g$ . If it behaves similarly to the rhodium, Rh, substitution for Ir, i.e. only mass fluctuation scattering is produced, we calculate  $\kappa_g$  at 300 K to be 58% of that of pure  $\text{IrSb}_3$ [27,28,29]. An additional strain field correction[30] due to the difference in the Ge and Sb radii gives an estimated  $\kappa_g$  at 300 K to be 30% of that of pure  $\text{IrSb}_3$ . Low values for  $\kappa_g$  have also been reported for  $\text{CeFe}_4\text{Sb}_{12}$ , also a filled-skutterudite, in which no substitution on the Sb site occurs[31]. Thus the Ge is not the main cause of the reduced  $\kappa_g$  in the RE-filled samples. In order to verify that the low  $\kappa_g$  of the Nd-filled skutterudite sample is not due to grain-boundary scattering, we have calculated  $\kappa_g$  for a sample with 7  $\mu\text{m}$  grains. This plot is indicated by an arrow in Figure 1. It is evident that the cause for the low  $\kappa_g$  is the RE ions, not grain boundary scattering.

From Figure 1 we see there is more than an order-of-magnitude decrease in  $\kappa_g$  over the temperature range of interest for the RE-filled skutterudite samples as compared to that for  $\text{IrSb}_3$ . The  $\text{Nd}^{3+}$  ion, which is more massive than the  $\text{La}^{3+}$  ion, has a smaller radius than  $\text{La}^{3+}$ . This is known as lanthanide contraction. The off-center positions of the RE ions in the voids of the skutterudite structure have been estimated to be 0.32 Å and 0.43 Å, respectively, for  $\text{La}^{3+}$  and  $\text{Nd}^{3+}$ . The RE radii in  $\text{LaSb}$ [19] and  $\text{NdSb}$ [19] have been used in this estimate. The  $\text{Nd}^{3+}$  ions are therefore more free to rattle inside the voids of the skutterudite structure, and are thereby able to interact with lower frequency phonons than in the case of the  $\text{La}^{3+}$  ions. The result is a larger decrease in  $\kappa_g$ . This (guest atom) – (phonon) coupling is an effective phonon scattering mechanism, and one that shows promise for improved thermoelectric materials based on the skutterudite structure. In addition, the low-lying 4f electronic energy levels in the  $\text{Nd}^{3+}$  ion also produce phonon scattering, further reducing  $\kappa_g$ . This additional phonon scattering is magnified at lower temperatures[32], as seen in Figure 1.

## CONCLUSION

We have prepared samples with the skutterudite structure with  $\text{La}^{3+}$  and  $\text{Nd}^{3+}$  ions in the voids in order to study their effect on  $\kappa_g$ . The rattling motion of the RE elements have a substantial influence on the phonon propagation in this structure as seen in Figure 1. We believe this method of reducing  $\kappa_g$  is most promising in improving the thermoelectric figure of merit of the skutterudite compounds.

## ACKNOWLEDGMENT

This work was supported, in part, by the U. S. Office of Naval Research, Grant Number N00014 - 94 - 1 - 0341.

## REFERENCES

- [1] G. A. Slack and V. G. Tsoukala, *J. Appl. Phys.*, 1994, vol. 76, p. 1665.
- [2] A. Kjekshus and G. Pederson, *Acta Cryst.* 1961, vol. 14, p. 1065.
- [3] N. N. Zhuravlev and G. S. Zhdanov, *Kristallogr.* 1956, vol. 1, p. 509 [*Sov. Phys. Cryst.*, 1956, vol. 1 p. 404].
- [4] A. Kjekshus and T. Rakke, *Acta Chem. Scand.*, 1974, vol. A28, p. 99.
- [5] A. Kjekshus, *Acta Chem. Scand.*, 1961, vol. 15, p. 678.
- [6] F. Hulliger, *Helv. Phys. Acta*, 1961, vol. 34, p. 782.
- [7] J. -P. Fleurial, T. Caillat, and A. Borshchevsky, "Skutterudites: a New Class of Promising Thermoelectric Materials" in *Proceedings of the Thirteenth International Conference on Thermoelectrics*, Kansas City, MO, USA, American Institute of Physics, edited by B. Mathiprakasam and P. Heenan, 1995.
- [8] G. A. Slack, in *Thermoelectric Handbook*, Chemical Rubber, Boca Raton, FL, edited by M. Rowe, to be published in 1995.
- [9] T. Caillat, A. Borshchevsky, and J. -P. Fleurial, "CoSb<sub>3</sub>-IrSb<sub>3</sub> Solid Solutions: Preparation and Characterization" in *Proceedings of the Thirteenth International Conference on Thermoelectrics*, Kansas City, MO, USA, American Institute of Physics, edited by B. Mathiprakasam and P. Heenan, 1995.
- [10] A. Borshchevsky, J. -P. Fleurial, E. Allevato, and T. Caillat, "Existence and Some Properties of New Ternary Skutterudite Phases", *ibid.*
- [11] S. Rundquist and N. O. Ersson, *Arkiv fur Kemi* (Stockholm), 1968, vol. 30, p. 103.
- [12] T. Schmidt, G. Klische, and H. D. Lutz, *Acta Cryst.*, 1987, vol. 43C, p. 1678.
- [13] R. G. Ross, *Phys. Chem. Liq.*, 1991, vol. 23, p. 189, and references therein.
- [14] G. A. Slack, D. W. Oliver, and F. H. Horn, *Phys. Rev. B*, 1971, vol. 4, p. 1714.
- [15] D. G. Cahill, H. E. Fischer, S. K. Watson, R. O. Pohl, and G. A. Slack, *Phys. Rev. B*, 1989, vol. 40, p. 3254.
- [16] P. A. Medwick, R. O. Pohl, and T. Tanaka, in *Proceedings of the Eleventh International Symposium on Boron, Borides and Related Compounds: J. Appl. Phys., Series 10*, Tsukuba, Japan, edited by Ryosei Uno and Iwami Higashi, 1994, p. 106.
- [17] Metals Handbook, 9th edition, Vol. 9: Metallography and Microstructure, American Society of Metals, 1985, pp. 122 - 134 and references therein.
- [18] Reports of the University of California, Lawrence Radiation Laboratory (Smith (1963) UCRL - 7176 and (1976) UCRL - 50264); Clark, Smith, and Johnson, Bulletins of the College of Earth and Mineral Sciences, The Pennsylvania State University, 1973
- [19] R. W. G. Wyckoff, *Crystal Structures*, 2nd edition, Interscience, New York, 1963.
- [20] G. A. Slack, in *Solid State Physics*, Vol. 34, Academic Press, New York, edited by H Ehrenreich, F. Seitz, and D. Turnbull, 1979.
- [21] D. T. Morelli and C. Uher, *Phys. Rev. B*, 1983, vol. 28, p. 4242.
- [22] D. T. Morelli, *Phys. Rev. B*, 1991, vol. 44, p. 5453.
- [23] T. M. Tritt, D. J. Gillespie, A. C. Ehrlich, G. S. Nolas, G. A. Slack, and J. L. Cohen, "Low Temperature Transport Properties of IrSb<sub>3</sub>", this conference.
- [24] G. S. Kumar, J. W. Vandersande, T. Klistner, R. O. Pohl, and G. A. Slack, *Phys. Rev. B*, 1985, vol. 31, p. 2157.
- [25] S. L. Loeb, *J. Am. Ceram. Soc.*, 1954, vol. 37, p. 96.
- [26] J. Franc and W. D. Kingery, *ibid.*, p. 99.
- [27] G. A. Slack, *Phys. Rev.*, 1957, vol. 105, p. 829.
- [28] G. A. Slack, *Phys. Rev.*, 1961, vol. 122, p. 1451.
- [29] M. G. Holland, *Phys. Rev.*, 1964, vol. 134, p. A471.
- [30] B. Abeles, *Phys. Rev.*, 1963, vol. 131, p. 1906.
- [31] D. T. Morelli and G. P. Meisner, *J. Appl. Phys.*, 1995, vol. 77, p. 3777.
- [32] G. A. Slack and D. W. Oliver, *Phys. Rev. B*, 1971, vol. 4, p. 592.

## LOW TEMPERATURE TRANSPORT PROPERTIES OF IrSb<sub>3</sub>

Terry M. Tritt<sup>1</sup>, D. J. Gillespie<sup>1</sup>, A. C. Ehrlich<sup>1</sup>, George Nolas<sup>2</sup>, Glen Slack<sup>2</sup> and  
Josh L. Cohn,<sup>3</sup>

<sup>1</sup> Materials Physics Branch, Naval Research Laboratory,  
Washington DC 20375, USA

<sup>2</sup> Department of Physics, Rensselaer Polytechnic Institute,  
Troy, New York 12180

<sup>3</sup> Department of Physics, University of Miami,  
Coral Gables, FL 33124

### ABSTRACT

We have measured the electrical resistivity,  $\rho$ , thermoelectric power,  $\alpha$ , and thermal conductivity,  $\lambda$ , of IrSb<sub>3</sub> in a temperature range from 300K down to 4K. It is found that the electrical resistivity and thermopower decrease monotonically as the temperature is reduced to 50 - 60K. Below approximately 60K the resistivity rises in a semiconducting manner and the thermopower also starts to rise at a slightly lower temperature. It appears the thermopower exhibits a large phonon drag peak at around 20K and then falls towards zero. We will compare these results to higher temperature data from Slack and Tsoukala.<sup>(1)</sup> There also appears to be some unusual temperature dependence of the thermal conductivity with a maximum corresponding to the peak in the thermopower which we will also discuss. We have also measured two of the so called "filled skutterudites", Ir<sub>4</sub>LaGe<sub>3</sub>Sb<sub>9</sub>, and Ir<sub>4</sub>NdGe<sub>3</sub>Sb<sub>9</sub>, and the thermoelectric properties will be presented. We will compare the results for the filled and unfilled skutterudite samples in relation to the thermoelectric figure of merit.

### INTRODUCTION

Approximately 30 years ago the field of thermoelectrics was at the height of its study and research. There was great promise of utilizing thermoelectric materials to perform a variety of solid state refrigeration needs. In the late 50's and 60's materials were extensively studied and optimized for their thermoelectric application. Most of the research effort since that time has been involved in optimizing the properties of those materials; alloys based on the Bi<sub>2</sub>Te<sub>3</sub> system, the BiSb system, the Si<sub>1-x</sub>Ge<sub>x</sub> system or the PbTe system, to improve their thermoelectric capabilities. Thermoelectric energy conversion utilizes the Peltier heat generated when an electric current is passed through a thermoelectric material to provide a temperature difference between the heat sink and the object being cooled or heated. The advantages of thermoelectric solid state energy conversion are compactness, quietness (no moving parts) and localized heating or cooling. It provides long term stability with lifetimes on the order of 20 years or more. Some applications of thermoelectrics include cooling of CCD's, infrared detectors and low noise amplifiers and computer chips. They also are very stable and can be used for temperature stabilization of laser diodes and/or electronic components.

The essence of defining a good thermoelectric material lies in determining the material's figure of merit,

$$Z = \frac{\alpha^2 \sigma}{\lambda} \quad (1)$$

where  $\alpha$  is the Seebeck coefficient,  $\sigma$  the electrical conductivity and  $\lambda$  the total thermal conductivity ( $\lambda = \lambda_L + \lambda_C$ , the lattice and electronic contributions respectively).

The Seebeck coefficient is related to the Peltier effect by

$$\Pi = \alpha T = \frac{Q_P}{I} \quad (2)$$

where  $\Pi$  is the Peltier coefficient,  $Q_P$  is the rate of heating or cooling and  $I$  is the electrical current. Excellent reviews of thermoelectric properties of materials and thermoelectric refrigeration is given in references 2-4. In summary, the efficiency and coefficient of performance of a device is directly related to the figure of merit of the material. Semiconductors have long been proven to be the material of choice for thermoelectric applications. It is found that the most promising materials have a carrier concentration of approximately 10<sup>19</sup> carriers/cm<sup>3</sup>. The power factor,  $\alpha^2 \sigma$ , is typically optimized through doping by adjusting the electron concentration to give the largest  $Z$ . Also, attempts are made to lower the lattice thermal conductivity without decreasing the power factor proportionally and thus further maximizing the figure of merit. The standard industrial material for operation near room temperature is the (Bi,Sb)<sub>2</sub>(Te,Se)<sub>3</sub> system. (2-5) For this material,  $Z \approx 3.4 \times 10^{-3}$  K<sup>-1</sup> and thus the dimensionless figure of merit  $ZT \approx 1$  at  $T = 300$ K. This  $ZT = 1$  has been an upper limit for more than 20 years but with no theoretical or thermodynamic reason why it can not be larger if an appropriate material can be found. For example, if a material with  $ZT \approx 2$  could be found, feasible applications would possibly increase by an order of magnitude.

Recently there has been substantial renewed interest in the field of thermoelectrics as new materials become available and

new needs become evident. One of these groups of new materials is the promising skutterudite system which includes IrSb<sub>3</sub> and CoSb<sub>3</sub>. (6-8) Initial studies by various groups have indicated that this material shows some promise as a potential thermoelectric material. The carriers have high mobilities and there are large vacancies in the structure of this material which can be interstitially doped and filled in attempts to manipulate the thermal conductivity.

The skutterudite structure, AB<sub>3</sub> (where A is the transition metal element Ir, Co, Pd and Rh, and B is the pnictogen element such as P, As and Sb). The prototype is the CoAs<sub>3</sub> system. The structure is cubic (with space group Im3) and the unit cell contains 8 AB<sub>3</sub> groups with 32 atoms per unit cell. Also there exist two voids in the unit cell. A good example of the structure is shown in references 6 and 9. A recent paper by Morelli gives an excellent summary of the known transport properties of some of these materials and concludes that our knowledge of them is inadequate at best, especially regarding their low temperature behavior.(9) Very recently there has been research on the low temperature properties of CoSb<sub>3</sub> by Morelli et.al. (9) and Mandrus et.al.(10) Both of these workers compare their results to recent band structure calculations of Singh and Pickett (S&P)(11) who predict a semiconducting behavior for these materials and also predict them to exhibit a highly non parabolic valence band. Mandrus et. al. find a semiconducting energy gap of E<sub>G</sub> ≈ 580 K (50 meV) in CoSb<sub>3</sub> in agreement with S&P. Morelli et. al. find that the CoSb<sub>3</sub> material exhibits large hole mobilities, a large lattice contribution to the thermal conductivity to low temperatures and large phonon drag effects evident in the thermoelectric power.

These skutterudite materials exhibit relatively low thermal conductivity on the order of 20 W/mK with approximately 90% of that due to the lattice. These materials have large unit cells with lots of atoms and thus present possibilities of being able to manipulate the thermal conductivity through the lattice thermal conductivity. From Slack's minimum thermal conductivity theory (12) it is estimated that the thermal conductivity in these skutterudite materials could be lowered by a factor of 40 thus greatly enhancing the figure of merit for these materials.(1) In a companion paper to this one we present results on the properties of IrSb<sub>3</sub> and also the so called "filled skutterudites" where the voids have now been filled with various atoms in an effort to manipulate the thermal conductivity of these materials.(13)

The focus of this paper will be primarily on the low temperature transport properties of IrSb<sub>3</sub>. We will also present data on the impact of filling of these voids with La and Nd in relation to the electrical properties, resistivity and thermoelectric power, and the thermal conductivity. The temperature dependence of the properties of the La filled system will be presented and the room temperature properties of the Nd filled system will be discussed.

## EXPERIMENTAL PROCEDURE

The description of the preparation of these materials is given in detail in another publication. (13) Our samples have been made by hot isostatic pressing (Hipping) of powders. As

such, they do not always achieve their full theoretical density. These samples are polycrystalline with typical sizes of 12mm x 5mm x 3 mm and were cut into these sizes with a high speed diamond saw. We have performed standard four-probe resistance measurements on all our samples. We used 0.005" Au-Fe (0.07at%) vs. Cr thermocouples attached to the samples with GE 7031 varnish to make the ΔT measurements. The sample voltage (V<sub>S</sub>) as well as the thermocouple voltage (V<sub>TC</sub>) were measured with a Keithley 182 nanovoltmeter. The Au-Fe vs. Cr thermocouples provide adequate sensitivity even to the lower temperatures (T≈4K). The temperature of the sample is determined using a Lake Shore calibrated Cernox sensor. The resistance of the sample was taken by reversing the current at each temperature and measuring the sample voltage and then taking an average. Typical sample currents were 5-50 mA. The thermopower was measured in two ways. First a standard V<sub>S</sub> vs. ΔT curve was taken at several temperatures with the gradient on the sample being swept from -ΔT to +ΔT with ΔT ≈ 2-5% of T. The slope was calculated and the Au lead contribution subtracted thus giving the absolute thermopower of the material. We used this method to check our more typical method. In this method a ΔT of 2-5% T was established across the sample. Then under computer control the sample current was cycled in the following sequence: (1.) +I, (2) I = 0, (3) -I, (4) I = 0, (5) +I, with sample current and voltage, absolute temperature and thermocouple voltage being read and recorded at each step. The sample resistance was calculated from averaging steps 1, 3, and 5 and the thermopower was calculated from an average of steps 2 and 4. Excellent agreement was found with the two methods. In regards to the temperature dependence of these properties, the temperature of the sample was slowly lowered in a variable temperature dewar from T = 300K to T = 4K over a period of 12 - 14 hours and the resistance and thermopower monitored as a function of temperature.

The thermal conductivity λ is the most difficult parameter to measure accurately in the determination of a material's figure of merit. There are many corrections for problems such as heat loss by conduction and radiation effects and they can vary considerably in importance with sample geometry. Good thermoelectric materials (high Z) have a very low λ, on the order of 2-10 W/m-K, further complicating the measurement. The samples in this work are somewhat large for thermal conductivity measurements. The thermal conductivity of smaller pieces of these samples were measured using a standard steady state technique and is essentially the same technique as described elsewhere by Morelli. (14,15) We also measured the α and ρ of some of these smaller samples and we will discuss these results.

## RESULTS AND DISCUSSION

We have measured the temperature dependence of α, ρ of three types of these samples; IrSb<sub>3</sub>, Ir<sub>4</sub>LaGe<sub>3</sub>Sb<sub>9</sub>, and Ir<sub>4</sub>NdGe<sub>3</sub>Sb<sub>9</sub>, and also λ of two types IrSb<sub>3</sub> and Ir<sub>4</sub>LaGe<sub>3</sub>Sb<sub>9</sub>. The thermal conductivity of the Ir<sub>4</sub>NdGe<sub>3</sub>Sb<sub>9</sub> sample was measured by Morelli and the data is presented in reference 13. In Figure 1 is shown the temperature dependence of standard unfilled IrSb<sub>3</sub> with a density of 82% of the theoretical density. The resistance is monotonically decreasing with decreasing temperature down to T≈ 60 K where there is a broad minimum and then a change in sign of dR/dT below this. The

thermopower also monotonically decreases with temperature typical of linear diffusion thermopower down to  $T \approx 40$  K with a strong peak at  $T \approx 25$  K and then decreases toward zero as  $T$  goes to zero. This is typical of a strong phonon drag thermopower.

We compare our room temperature measurements on the 82% dense sample to measurements made on a 98% dense sample reported by Slack and Tsoukala (S&T).<sup>(1)</sup> They are as follows with our results given first: thermopower (+76.7, +73)  $\mu\text{V/K}$ , resistivity ( $4.23, 4.4$ )  $\times 10^{-4}$  ohm-cm, and thermal conductivity (20, 17.5) Watt/m-K. Thus, there is very good agreement between the results on this sample and that in reference 1, suggesting that the results are relatively insensitive to the density.

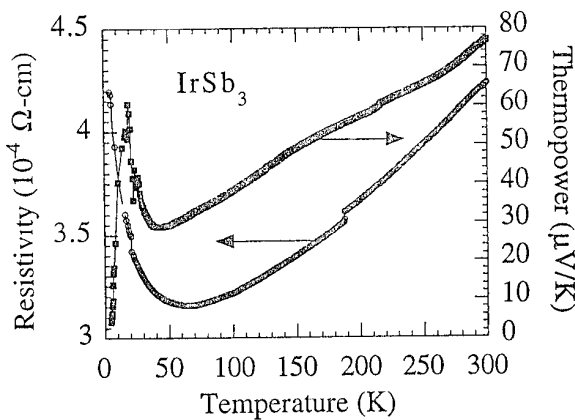


Fig. 1. The resistance ( $\rho$ ) and thermopower ( $\alpha$ ) of polycrystalline  $\text{IrSb}_3$  (82% dense) as a function of temperature.

In Figure 2 is the same data blown up to show the low temperature region ( $T < 150$  K). It became more difficult to establish a temperature gradient on this sample around the region of the peak, as if the thermal conductivity was becoming much larger. We measured  $\rho$ ,  $\alpha$  and  $\lambda$  of a small sliver from the outside edge of this sample. The thermal conductivity results are shown in Figure 3. There is a large peak in the thermal conductivity at approximately the same temperature as the "phonon drag" peak in the thermopower thus confirming a large phonon contribution to both parameters at these low temperatures. The thermal conductivity of  $\text{IrSb}_3$  has a strong temperature dependence and is very similar to that measured by Morelli et. al for the  $\text{CoSb}_3$ . The  $\text{CoSb}_3$  material also shows a phonon drag peak in the thermopower close to the peak in the thermal conductivity. There was very good agreement with the resistivity measurements for the primary sample and the small sliver, however the thermopower measurements showed some differences. In the small sliver sample the large phonon drag peak was not evident and the room temperature thermopower was less, 62  $\mu\text{V/K}$  as compared to 76  $\mu\text{V/K}$ , than those in Figure 1. It may be that the sample was nonuniform since the sliver would have been in contact with the sides of the press. We are presently performing experiments to check this explanation.

Note the large upturn in resistance at  $T \approx 60$  K where the resistance now shows a semiconducting type behavior which would correspond to a narrow band gap of  $E_G \approx 10$  meV. Singh and Pickett<sup>(11)</sup> actually predict that  $\text{IrSb}_3$  would be essentially a zero gap semiconductor. Our results on the  $\text{IrSb}_3$  are consistent with a very small gap. It is difficult to get Iridium very pure and thus some of the impurities in the Iridium could be affecting our results. Mandrus et. al<sup>(10)</sup> performed measurements on the low temperature properties of  $\text{CoSb}_3$  and found excellent agreement with the predicted band gap of 50 meV by S&P.

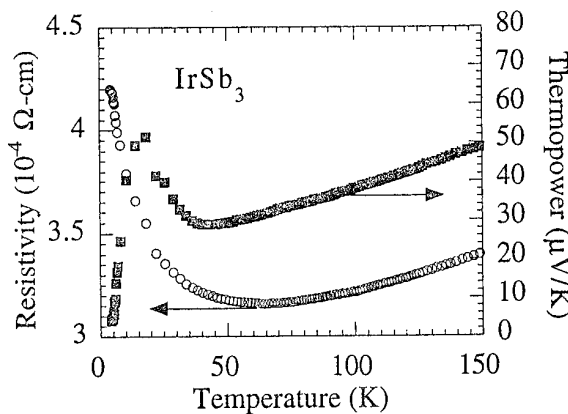


Fig. 2. The resistance ( $\rho$ ) and thermopower ( $\alpha$ ) of polycrystalline  $\text{IrSb}_3$  (82% dense) as a function of temperature for  $T < 150$  K.

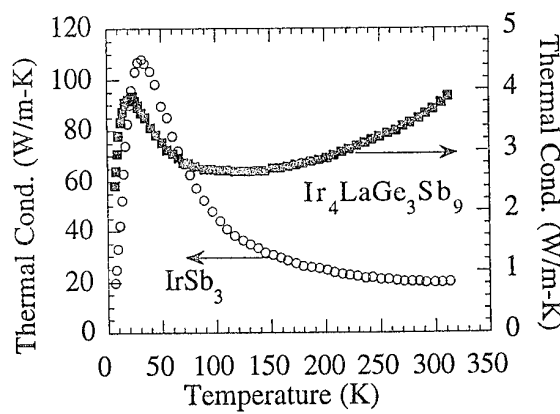


Fig. 3. The total thermal conductivity  $\lambda_T$  of polycrystalline  $\text{IrSb}_3$  (82% dense) and  $\text{Ir}_4\text{LaGe}_3\text{Sb}_9$  as a function of temperature.

In Figure 4 we show  $\alpha$  and  $\rho$  of one of the filled skutterudites,  $\text{Ir}_4\text{LaGe}_3\text{Sb}_9$ , where La was put into the voids of the  $\text{IrSb}_3$  structure. The Ge was added in an attempt at charge compensation for the La. It is apparent from the values of  $\alpha$  and  $\rho$  that these properties of the filled skutterudite were not optimized. As stated in our companion paper (13) much more work needs to be done in regards to the charge compensation for the donated electrons by the rare earth ions and this is underway. Notice that the resistivity has a more metallic temperature dependence even to 4K and the room temperature resistivity is approximately three times that of the unfilled sample. Also the room temperature thermopower is approximately a factor of 10-12 smaller than the unfilled sample. There still exists a low temperature peak in the thermopower at about the same temperature as the  $\text{IrSb}_3$ . This peak in the thermopower corresponds to the peak in the thermal conductivity shown in Figure 3. In addition the thermopower undergoes a change in sign at  $T \approx 180$  K indicating a change in dominant carrier from p-type to n-type suggesting multi-band conduction. This suggests simultaneous electron and hole transport and itself could account for the reduced value of  $\alpha$  compared to  $\text{IrSb}_3$ . We hope to confirm this with Hall measurements that are planned for the future. We also measured  $\alpha$  and  $\rho$  of a sliver of the  $\text{Ir}_4\text{LaGe}_3\text{Sb}_9$  sample and there was excellent agreement of this data and the data on the primary sample, thus making the  $\text{IrSb}_3$  difference more likely to be nonuniformity and not a difference in measurements of the two pieces

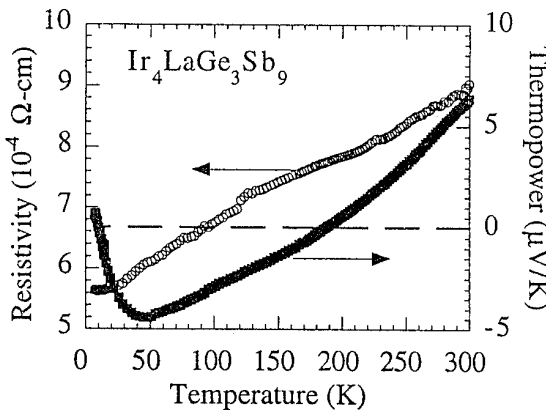


Fig. 4. The resistance ( $\rho$ ) and thermopower ( $\alpha$ ) of a filled skutterudite  $\text{Ir}_4\text{LaGe}_3\text{Sb}_9$  (also 82% dense) as a function of temperature.

The thermal conductivity of the La filled skutterudite is reduced by approximately an order of magnitude in comparison to the unfilled material,  $\text{IrSb}_3$  with respective values of 20 W/m-K for  $\text{IrSb}_3$  and 3.7 W/m-K for the La filled system. This shows that the thermal conductivity can be substantially altered by this filling of the voids, but that much more work needs to be done to optimize the electrical properties through charge compensation.

We have also measured the room temperature resistivity and thermopower of a Nd filled sample,  $\text{Ir}_4\text{NdGe}_3\text{Sb}_9$ . This sample has a room temperature thermopower of +1  $\mu\text{V}/\text{K}$  and a resistivity of  $15 \times 10^{-4} \Omega\text{-cm}$ . The thermal conductivity has been measured by Morelli and is presented in reference 13. The thermal conductivity is even lower than that for the La filled sample. All of the results for these three samples is summarized in Table 1 below. We have also estimated the lattice thermal conductivity by calculating the electronic part of the thermal conductivity  $\lambda_E$  from the Wiedemann-Franz law  $\lambda_E = L_0\sigma T$  where  $L_0$  is the Lorentz number ( $2.45 \times 10^{-8}$  Watt- $\Omega / \text{K}^2$ ),  $\sigma$  is the electrical conductivity ( $\sigma = 1/\rho$ ) and  $T$  is the temperature and in Table 1,  $T = 300\text{K}$ . The dimensionless figure of merit  $ZT$  ( $T=300\text{K}$ ) is also listed and as is obvious, even though we are greatly reducing the thermal conductivity the  $ZT$  is also being severely reduced. Thus as stated previously charge compensation is an essential part of this problem. We need to keep the large thermopower and high conductivity while reducing the thermal conductivity.

**TABLE 1. Summary of Properties.**

	IrSb <sub>3</sub>	w/La	w/Nd
$\alpha$ (300K) ( $\mu\text{V}/\text{K}$ )	+76.7	+6.4	+0.9
$\rho$ (300K) $10^{-4} \Omega\text{-cm}$	4.23	9.04	16.9
$\lambda_T$ (300K) (W/m-K)	20	3.7	1.0
$\lambda_L$ (300K) (W/m-K)	18.2	2.9	0.57
$ZT$ (300K)	$2.1 \times 10^{-2}$	$3.7 \times 10^{-4}$	$1.4 \times 10^{-5}$

Table 1. Summary of the properties that are used in the figure of merit,  $Z$ , in relation to the filling of the voids.

## CONCLUSION AND SUMMARY

We have measured resistivity, thermopower and the thermal conductivity of a series of three materials; the unfilled  $\text{IrSb}_3$  and two filled skutterudites,  $\text{Ir}_4\text{LaGe}_3\text{Sb}_9$  and  $\text{Ir}_4\text{NdGe}_3\text{Sb}_9$ . We have found that the thermal conductivity can be greatly effected by this filling and reduced as expected by the increased number of scattering centers. We have found that these materials exhibit interesting temperature dependence of these properties at low temperatures,  $T < 300\text{K}$ . Much more work needs to be done to optimize the electrical properties of these materials through charge compensation for filling with the rare earth atoms. Also, more research needs to be done to establish this material as a viable material for thermoelectric applications but a lot of progress is being made especially in the area of minimizing the thermal conductivity.

### ACKNOWLEDGMENTS

We would like to acknowledge Hylan B. Lyon Jr. of Marlowe Industries for general and interesting discussions on thermoelectrics and on the skutterudite materials. We would like to also acknowledge the U. S. Office of Naval Research for partial support of this work.

### REFERENCES

- [1]. Glen A. Slack and V. G. Tsoukala, Jour. Appl. Phys. **76**, 1635 (1994)
- [2]. H. J. Goldsmid, *Electronic Refrigeration*, Pion Limited Publishing, London 1986
- [3]. D. M. Rowe and C. M. Bhandari, *Modern Thermoelectrics*, Reston Publishing (Prentice Hall) , Reston VA 1983
- [4]. C. Wood, Rep. Prog. Phys. **51**, 459-539 (1988)
- [5]. W. M. Kim and F. D. Rosi, Solid State Electronics, **15**, 1121 (1972)
- [6]. J. P. Fleurial, T. Caillet and A. Borshchevsky, "Skutterudites, a New Class of Promising Thermoelectric Materials" in, *Proceedings of the XIII International Conference on Thermoelectrics* Kansas City, MO, USA, American Institute of Physics, edited by B. Mathiprakasaru and P. Heenan, 1995, pp 40-44
- [7]. T. Caillet, A. Borshchevsky and J. P. Fleurial, "Preparation and Thermoelectric Properties of p- and n-type IrSb<sub>3</sub>" ibid ref 6 pp 31-34.
- [8]. T. Caillet, A. Borshchevsky and J. P. Fleurial, "Preparation and Thermoelectric Properties of p- and n-type CoSb<sub>3</sub>" ibid ref 6 pp 58-61.
- [9]. D. T. Morelli et. al., Phys. Rev B, **51**, 9622 (1995)
- [10]. D. Mandrus et. al., submitted to Phys. Rev. B, (1995)
- [11]. David J. Singh and Warren E. Pickett, Phys. Rev. B, **50**, 11235, (1995)
- [12]. Glen A. Slack, in Solid State Physics, edited by H. Ehrenreich, F. Seitz and D. Turnbull (Academic, New York, (1979), Vol. 34, p. 1
- [13]. George S. Nolas, Glen A. Slack, Terry M. Tritt and Donald T. Morelli, *Proceedings of the XIV International Conference on Thermo-electrics* (this conference), New Thermoelectric Material based on IrSb<sub>3</sub>.
- [14]. D. T. Morelli and C. Uher, Phys. Rev B, **28**, 4242 (1983)
- [15]. D. T. Morelli Phys. Rev. B, **44**, 5453 (1991)

## THERMOELECTRIC PERFORMANCE OF ZnO-BASED MIXED OXIDES AS A PROMISING HIGH-TEMPERATURE MATERIAL

M. Ohtaki, T. Tsubota, K. Eguchi, and H. Arai

*Department of Materials Science and Technology, Graduate School of Engineering Sciences, Kyushu University,  
Kasuga, Fukuoka 816 JAPAN*

Investigation on thermoelectric properties of ZnO-based mixed oxides reveals exceedingly promising performance of  $(\text{Zn}_{1-x}\text{Al}_x)\text{O}$  among oxide materials so far reported. Addition of even a small amount of Al as  $x = 0.01$  causes marked increase in the electrical conductivity, whereas the Seebeck coefficient of the oxide retains moderate negative values. Consequently, the power factor of  $(\text{Zn}_{1-x}\text{Al}_x)\text{O}$  up to  $x = 0.05$  reaches  $8 - 15 \times 10^{-4} \text{ W/m K}^2$  over a range from room temperature to  $1000^\circ\text{C}$ . Although the thermal conductivity of the oxide is substantially high at present, the oxide at  $x = 0.02$  achieves the figure of merit of  $0.24 \times 10^{-3} \text{ K}^{-1}$  and the  $ZT$  value of 0.30 at  $1000^\circ\text{C}$ .

### Introduction

Rapidly increasing importance of thermoelectric energy conversion has intensively stimulated search for new thermoelectric materials [1-4], because improvement in thermoelectric performance of conventional materials appears to be almost levelling off. In particular, materials suitable for high-temperature operation are of great interest in terms of thermoelectric power generation, since the energy conversion efficiency improves with increasing temperature difference over which a thermoelectric device operates [5]. This means that, even if the thermoelectric figure of merit  $Z$  of a new material would not be so eminent, the dimensionless figure of merit  $ZT$ , which directly reflects the conversion efficiency, could become sufficient if the material has preferable properties at higher temperatures.

One of the most popular refractory materials is oxide, since metal oxides at their common oxidation states are generally very stable at elevated temperature in air. Electrical conduction in oxide materials has also been extensively studied, and there is a wide variety in their electrical properties from insulating to superconducting. Nevertheless, research on oxide materials have scarcely been reported in thermoelectrics. Although excellent durability of metal oxides at high temperature in air should apparently be advantageous, oxide materials have been left out of consideration presumably owing to poor thermoelectric performance predicted by the conventional broad-band semiconductor theories [6] for the low carrier mobility as often found in oxides.

Conventional thermoelectric materials in practical use have all been semiconducting compounds and alloys in which the interatomic bonds are highly covalent, e.g.,  $\text{Bi}_2\text{Te}_3$ ,  $\text{PbTe}$ , and Si-Ge alloys, because a large overlap of the bonding orbitals in these materials yields the high carrier mobilities, and based on the broad-band theories, this leads to both large thermoelectric power and high electrical conductivity. In this context, oxides, which are considered to be substantially ionic materials, are of no much interest. The highly ionic character of oxides more or less localizes conduction electrons, and would result in poor carrier mobilities. A few high- $T_c$  superconducting cuprates having perovskite-related structures were once proposed to be a low temperature material for thermoelectric cooling [7], but the proposal was concluded to be hopeless because of their very low carrier mobility as *ca.*  $0.1 \text{ cm}^2 / \text{V s}$  due to a highly localized nature of these cuprates [8,9]. Some metal oxides, however, exhibit rather high carrier mobility, such as high as  $240 \text{ cm}^2 / \text{V s}$  reported for  $\text{SnO}_2$  [10], which value is similar to that of the drift mobility of metal Cu. Moreover, even though the mobility of somewhat localized electrons such as small polarons in oxides should apparently be low, the upper limit of thermoelectric performance predicted by the broad-band theories might no longer hold for such materials deviating from the collective free-electron model. For example, boron carbides with small polaron hopping conduction mechanism are known to show

excellent thermoelectric performance at high temperatures [11-13].

Recently, we have been investigating the thermoelectric properties of several highly conductive oxides as a trial to open up a novel field of materials in thermoelectrics. We first reported that  $\text{In}_2\text{O}_3$ -based mixed metal oxides show fairly good thermoelectric performance at high temperatures, and that they might be hopeful in high-temperature thermoelectrics [14,15]. Subsequently, We have also pointed out that partially substituted  $\text{CaMnO}_3$  perovskite-type oxides are rather promising as a new candidate material [16]. These oxide materials are fit well to conventional ceramic processing techniques for their preparation, and apparently stable in air at least up to  $1300^\circ\text{C}$  without any surface protection. The performance of these oxides, however, has not yet been overwhelming compared to other high-temperature candidate materials.

Here we report the thermoelectric properties of Al-doped ZnO which exhibits outstandingly promising performance for the first time as oxide, and is surpassing other non-oxide candidates. The Al doping markedly increases the electrical conductivity of the oxide maintaining the moderate thermoelectric power, and attains in this first report one-third of the ability of the practical state-of-the-art materials. A Jonker-type analysis reveals inherent advantages of the oxide in its electrical properties, even with the high thermal conductivity found at present.

### Experimental

Samples of  $(\text{Zn}_{1-x}\text{Al}_x)\text{O}$  ( $x = 0.0 - 0.1$ ) were prepared from fine powders of  $\text{ZnO}$  and  $\text{Al}_2\text{O}_3$  by solid state reaction. Properly weighed powders were mixed in a nylon-lined ball mill for 24 h, and then isostatically pressed into pellet at a pressure of 116 MPa at room temperature. The pellet was sintered at  $1400^\circ\text{C}$  for 10 h in air.

Crystal phases in the samples were examined by a powder X-ray diffraction (XRD) study. The relative density of the sintered samples was determined by the Archimedes' method. The electrical measurements were carried out on the samples cut out from the sintered pellets as parallelepiped bars of *ca.*  $4 \text{ mm} \times 3 \text{ mm} \times 15 \text{ mm}$  in size. The electrical conductivity  $\sigma$  and the Seebeck coefficient  $S$  were measured simultaneously at the steady-state temperature. The measurement procedures and an experimental setup have been described elsewhere in detail [15]. Briefly, two Pt/Rh-Pt thermocouples were attached on both end surfaces of the sample bar, and another two Pt paste electrodes were placed between them in the standard 4-wire arrangement. First, after an even and steady temperature was attained,  $\sigma$  was measured by the d.c. 4-wire technique using Pt legs of each Pt/Rh-Pt thermocouple as current leads. Subsequently, varying extent of small ( $< 5 \text{ K}$ ) and steady-state temperature gradients were applied by a heater located near by one end of the sample, and  $S$  was obtained from the slope of the least-square regressions for the thermoelectromotive force as a function of the temperature differ-

ence. The measurements were carried out from room temperature up to 1000 °C. The thermal conductivity  $\kappa$  was determined from the thermal diffusivity and the specific heat capacity measured by the laser flash technique on an ULVAC TC-7000 thermal constant measurement system. The temperature dependence of  $\kappa$  was measured up to 1000 °C *in vacuo*, and all the  $\kappa$  measurements were calibrated with a standard sample of sapphire single crystal.

## Results and Discussion

All the samples of  $(\text{Zn}_{1-x}\text{Al}_x)\text{O}$  obtained as above were completely dense sintered bodies with the relative density of more than 99%, and consisted of  $\text{ZnO}$  single phase confirmed by an XRD study, except samples at  $x \geq 0.02$  those also contained only a slight amount of  $\text{ZnAl}_2\text{O}_4$  spinel phase. Undoped sample of  $\text{ZnO}$  was a semiconductor with rather low electrical conductivity at least at room temperature as shown in Fig. 1. Although the phase diagrams so far reported on the system Zn-Al-O have indicated no solid solu-

tion regime near the  $\text{ZnO}$  end member, addition of even a small amount of Al as  $x = 0.01$  causes marked increase in  $\sigma$  of more than 3 orders of magnitude at room temperature, and changes its behavior from semiconducting to metallic as seen in Fig. 1. Since the  $\text{ZnAl}_2\text{O}_4$  single phase also examined was electrically almost insulating, aluminum, at least with a smaller fraction than nominal compositions, should hence dissolve into  $\text{ZnO}$  to act as a donor. However, the  $\sigma$  values for the samples at  $x > 0.02$  begin to decrease again, presumably owing to incorporation of substantial amount of the highly resistant  $\text{ZnAl}_2\text{O}_4$  phase.

The Seebeck coefficient  $S$  of the undoped sample was large and negative, indicating the n-type conduction. The doping with Al caused a decrease in the absolute values of  $S$  as seen in Fig. 2, in qualitative accordance with the increase in  $\sigma$  stated above. Nevertheless,  $|S|$  remain moderate as 100 - 150  $\mu\text{V} / \text{K}$  at room temperature, and show a slight increase with increasing temperature up to ca. 180  $\mu\text{V} / \text{K}$  at 1000 °C.

Consequently, the power factors  $S^2\sigma$  of the Al-doped samples up to  $x = 0.05$  attained the markedly large values of  $8 - 15 \times 10^{-4} \text{ W} / \text{m K}^2$  over a wide temperature range from room temperature to 1000 °C, as exemplified in Fig. 5 for  $x = 0.02$ . These values of the power factor infer that the oxide  $(\text{Zn}_{1-x}\text{Al}_x)\text{O}$  is highly promising for thermoelectric applications, and imply that the electrical properties of the oxide have an inherent advantage among oxide materials. We have hence conducted further analysis on the electrical transport properties of the present oxide.

The three physical parameters in the thermoelectric figure of merit,  $Z = S^2\sigma/\kappa$ , are all related to the carrier concentration. Assuming a simple two-band model for extrinsic n-type semiconductors with negligible hole conduction, the following equations can be derived [17,18],

$$\sigma = ne\mu, \quad (1)$$

$$S = -(k/e)[\ln(N_v/n) + A], \quad (2)$$

where  $n$  is the electron concentration,  $e$  is the electric charge of the carrier,  $\mu$  is the mobility,  $k$  is the Boltzmann constant,  $N_v$  is the density of states (DOS), and  $A$  is a transport constant typically  $0 \leq A \leq 2$ . From eqs. (1) and (2), one can obtain

$$S = -(k/e)\ln\sigma - (k/e)\ln[N_v e\mu \exp(A)]. \quad (3)$$

Assuming the constant DOS and mobility, a plot of  $S$  versus  $\ln\sigma$  will thereby give a straight line with a slope of  $+k/e$  or  $+86.17 \mu\text{V} / \text{K}$  and an intercept governed by a product of DOS and the mobility [18]. We have carried out this Jonker-type analysis [17] on  $(\text{Zn}_{1-x}\text{Al}_x)\text{O}$  ( $0.0 \leq x \leq 0.1$ ), and plotted the results in Fig. 3. A solid line in the figure stands for the least-square regressions with a fixed slope of  $+86.17 \mu\text{V} / \text{K}$  for the data at 900 and 1000 °C. The good linearity of the plots confirms the validity of the analysis, and allows to obtain  $\ln\sigma_0$  as an intercept on the x-axis at  $S = 0$  in Fig. 3, which reflects the DOS-mobility product. From the value of  $\ln\sigma_0$  obtained as 12.4 in the unit of  $\text{S/m}$ ,  $|S|$  can be calculated with eq. (3) as  $k/e(\ln\sigma - \ln\sigma_0)$  as a function of the conductivity  $\sigma$ . The power factor  $S^2\sigma$  or  $Z\kappa$  thereby becomes also a function of  $\sigma$ , and gives its predicted maximum as  $9.8 \times 10^{-4} \text{ W} / \text{m K}^2$  at which  $\sigma = 3.30 \times 10^4 \text{ S/m}$  and  $S = 172 \mu\text{V} / \text{K}$ . Actually, somewhat larger maximum of  $16.6 \times 10^{-4} \text{ W} / \text{m K}^2$  was achieved for  $x = 0.02$  at 600 °C, where  $\sigma = 6.14 \times 10^4 \text{ S/m}$  and  $S = 164 \mu\text{V} / \text{K}$ , in fundamentally good accordance with the calculation based on the simple assumption.

The values of the power factor observed for  $(\text{Zn}_{1-x}\text{Al}_x)\text{O}$  are well comparable to those of the conventional thermoelectric materials in practical use, and are several times superior to those of  $\text{In}_2\text{O}_3$ .

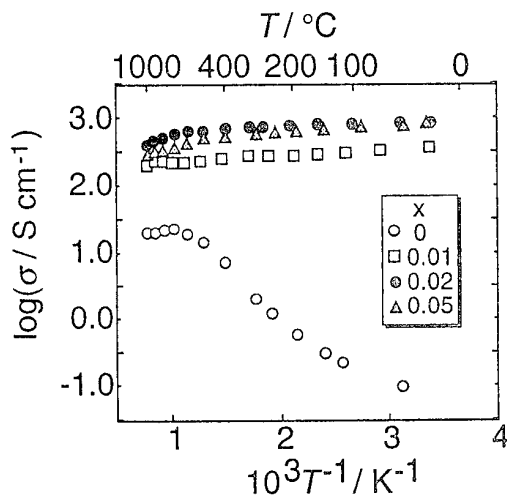


Fig. 1 Temperature dependence of the electrical conductivities for  $(\text{Zn}_{1-x}\text{Al}_x)\text{O}$ .

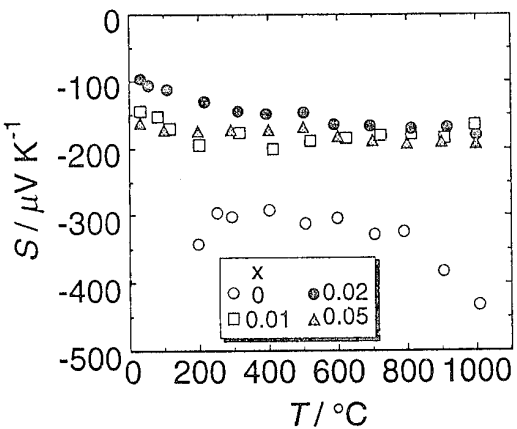
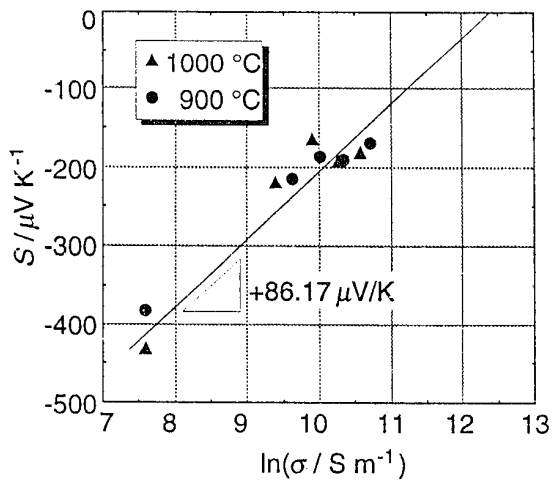
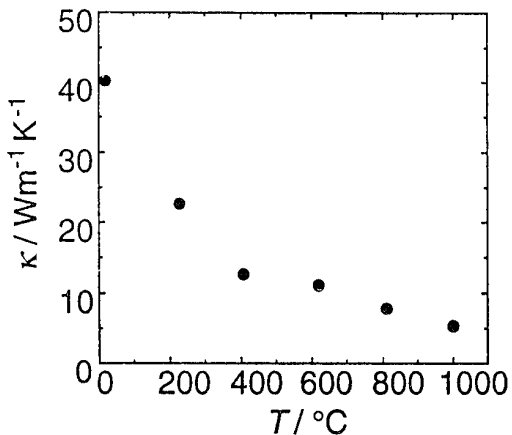
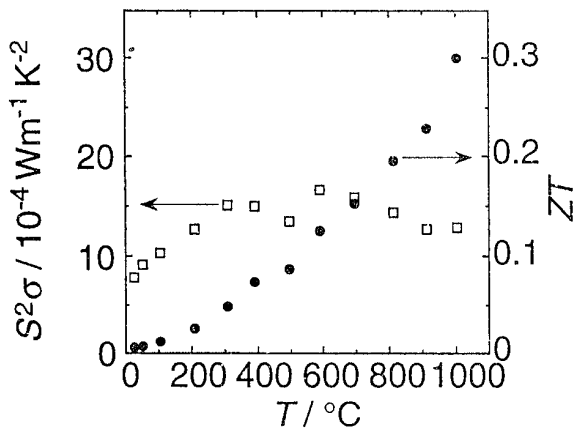


Fig. 2 Temperature dependence of the Seebeck coefficients for  $(\text{Zn}_{1-x}\text{Al}_x)\text{O}$ .

Fig. 3 The Jonker plots for  $(\text{Zn}_{1-x}\text{Al}_x)\text{O}$ .

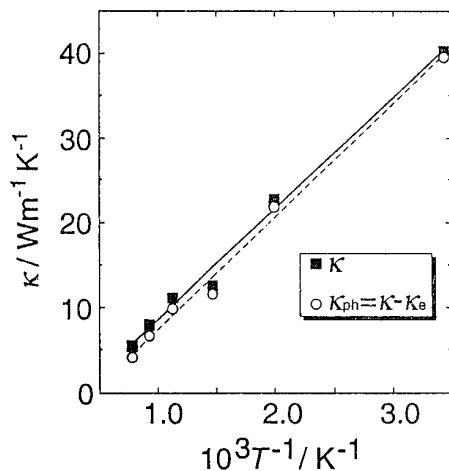
based mixed oxides [14,15] and partially substituted  $\text{CaMnO}_3$  perovskite-type oxides [16] we have already reported. It should also be noted that the maxima of  $S^2\sigma$  of  $(\text{Zn}_{1-x}\text{Al}_x)\text{O}$  locate at temperatures higher than those of such as  $\text{Bi}_2\text{Te}_3$  and  $\text{PbTe}$ , and can lead to larger  $ZT$  values. The  $\ln\sigma_0$  value obtained for  $(\text{Zn}_{1-x}\text{Al}_x)\text{O}$  is much greater than the value estimated for a series of high- $T_c$  superconducting cuprates as  $\ln\sigma_0 = 10.1$ , for which possibility of thermoelectric applications has been concluded to be unlikely due to their very low mobilities [8]. The large DOS-mobility product of the present oxide revealed here means inherent advantages in the electrical transport properties of the oxide in contrast to other oxides such as the superconducting cuprates, and endorses expected applicability of the  $\text{ZnO}$ -based oxides to high-temperature thermoelectric conversion.

The thermal conductivity  $\kappa$  is another fundamental parameter in  $Z$ . At present, unfortunately,  $\kappa$  of the Al-doped  $\text{ZnO}$  is found to be substantially high. As shown in Fig. 4,  $\kappa$  of  $(\text{Zn}_{0.98}\text{Al}_{0.02})\text{O}$  at room temperature was determined as markedly high as  $40.2 \text{ W/mK}$ , and found to decrease down to  $5.4 \text{ W/mK}$  at  $1000^\circ\text{C}$  with increasing

Fig. 4 Temperature dependence of the thermal conductivity for  $(\text{Zn}_{0.98}\text{Al}_{0.02})\text{O}$ .Fig. 5 Temperature dependence of the power factor and the  $ZT$  value of  $(\text{Zn}_{0.98}\text{Al}_{0.02})\text{O}$ .

temperature. Nevertheless, even with such high values of the thermal conductivity, the oxide achieved the figure of merit  $Z = S^2\sigma/\kappa$  of  $0.24 \times 10^{-3} \text{ K}^{-1}$  and hence the  $ZT$  value of  $0.30$  at  $1000^\circ\text{C}$  as presented in Fig. 6. This value is about one-third of the ability of the practical state-of-the-art materials even in this first report, and is of course outstandingly the largest for oxide materials ever reported.

A substantial suppression of the thermal conductivity is expected to result in further improvement in the thermoelectric performance of the present oxide. The plots of  $\kappa$  versus  $1/T$  depicted in Fig. 6 shows a good linearity which concludes the dominant contribution of the lattice vibration or phonons to heat transport in the oxide. This is further confirmed by an analysis on components of the overall thermal conductivity  $\kappa$ . The electronic thermal conductivity,  $\kappa_e$ , can be estimated from the electrical conductivity  $\sigma$  by the Wiedemann-Franz relation  $\kappa_e = L\sigma T$  ( $L$  is the Lorenz number) for which validity on several electronic-conducting oxides has also been

Fig. 6 The thermal conductivities of  $(\text{Zn}_{0.98}\text{Al}_{0.02})\text{O}$  as a function of  $1/T$ . The contribution of phonons,  $\kappa_{\text{ph}}$ , is calculated from the overall  $\kappa$  by subtracting the contribution of electrons,  $\kappa_e$ , estimated by the Wiedemann-Franz relation.

confirmed [19]. Figure 6 also presents that the thermal conductivity of the oxide consists of a predominant proportion of the phonon thermal conductivity,  $\kappa_{ph}$ , which is calculated by subtracting  $\kappa_e$  from the overall  $\kappa$ . These results strongly suggest that a significant reduction of the overall  $\kappa$  without seriously affecting the electrical properties by selective scattering of lattice phonons should be possible [20,21]. The promising electrical transport properties and the expected improvement in the thermal transport properties of  $(Zn_{1-x}Al_x)O$  presented here would make it possible to propose ZnO-based oxides as a novel high-temperature thermoelectric material competitive well to the conventional non-oxide materials, besides the oxides are also highly durable to high-temperature operation in air at least up to 1300 °C without any surface protection and can lead to higher  $ZT$  values.

### Conclusions

A metal oxide which can exhibit the thermoelectric performance well comparable to the conventional materials was first reported. The oxide,  $(Zn_{1-x}Al_x)O$  ( $0 < x \leq 0.1$ ), showed marked increase in the electrical conductivity with incorporation of a small amount of  $Al_2O_3$ , implying the  $Al$ -doping. On the other hand, the Seebeck coefficient remained moderate in its absolute values, and resulted in significantly large values of the power factor as  $8 - 15 \times 10^{-4} W / m K^2$ . The Jonker-type analysis revealed an inherent advantage in the electrical properties of the present oxide due to a large value of the product of the density-of-state and the mobility, in contrast to other oxide materials such as superconducting cuprates. Even though the thermal conductivity of the present oxide is currently substantially high, the oxide at  $x = 0.02$  achieved the figure of merit of  $0.24 \times 10^{-3} K^{-1}$  and the  $ZT$  value of 0.30 at 1000°C. Estimation of the phonon thermal conductivity clarified the predominant contribution of phonons to the overall thermal conductivity, and strongly suggested possibility of a significant reduction of the thermal conductivity without seriously affecting its electrical properties, which leads to a considerable improvement in its thermoelectric performance.

### Acknowledgment

The authors thank to Mr. Yasuhiro Yamada of Government Industrial Research Institute, Kyushu, for his kind cooperation on the laser flash measurement of  $\kappa$ .

### References

- [1] C. Wood, Materials for thermoelectric energy conversion, *Rep. Prog. Phys.*, **51**, 459-539 (1988).
- [2] C. B. Vining, Thermoelectric materials of the future, *Proc. 12th Int. Conf. Thermoelectrics*, pp. 126-131, Inst. Electrical Engineers Jpn., Tokyo, 1994.
- [3] T. Caillat, A. Borshchevsky, and J.-P. Fleurial, Novel transition metal compounds with promising thermoelectric properties, *Proc. 12th Int. Conf. Thermoelectrics*, pp. 132-136, Inst. Electrical Engineers Jpn., Tokyo, 1994.
- [4] J.-P. Fleurial, T. Caillat, and A. Borshchevsky, Skutterudites: a new class of promising thermoelectric materials, *Proc. 13th Int. Conf. Thermoelectrics*, pp. 40-44, American Institute of Physics., New York, 1995.
- [5] A. F. Ioffe, Semiconductor thermoelements and thermoelectric cooling, Infosearch, London, 1957.
- [6] R. Simon, Thermoelectric figure of merit of two-band semiconductors, *J. Appl. Phys.*, **33**, 1830-1841 (1962).
- [7] W. J. Macklin and P. T. Moseley, On the use of oxides for thermoelectric refrigeration, *Mater. Sci. Eng.*, **B7**, 111-117 (1990).
- [8] T. O. Mason, Comment on "On the use of oxides for thermoelectric refrigeration," *Mater. Sci. Eng.*, **B10**, 257-259 (1991).
- [9] W. J. Macklin and P. T. Moseley, Reply to comment on "On the use of oxides for thermoelectric refrigeration," *Mater. Sci. Eng.*, **B10**, 260 (1991).
- [10] C. G. Fonstad and R. H. Rediker, Electrical properties of high-quality stannic oxide crystal, *J. Appl. Phys.*, **42**, 2911-2918 (1971).
- [11] C. Wood and D. Emin, Conduction mechanism in boron carbide, *Phys. Rev. B*, **29**, 4582-4587 (1984).
- [12] M. Bouchacourt and F. Thevenot, The correlation between the thermoelectric properties and stoichiometry in the boron carbide phase  $B_4C-B_{10.5}C$ , *J. Mater. Sci.*, **20**, 1237-1247 (1985).
- [13] I. A. Howard, C. L. Beckel, and D. Emin, Bipolarons in boron-rich icosahedra: Effects of carbon substitution, *Phys. Rev. B*, **35**, 9265-9270 (1984).
- [14] M. Ohtaki, D. Ogura, K. Eguchi, and H. Arai, Thermoelectric properties and applicability of  $In_2O_3$ -based mixed metal oxides for thermoelectric conversion at high temperature, *Proc. 12th Int. Conf. Thermoelectrics*, pp. 212-217, Inst. Electrical Engineers Jpn., Tokyo, 1994.
- [15] M. Ohtaki, D. Ogura, K. Eguchi, and H. Arai, High-temperature thermoelectric properties of  $In_2O_3$ -based mixed oxides and their applicability to thermoelectric power generation, *J. Mater. Chem.*, **4**, 653-656 (1994).
- [16] M. Ohtaki, H. Koga, K. Eguchi, and H. Arai, Thermoelectric properties of  $(Ca_{1-x}Bi_x)MnO_3$  perovskite-type oxides as a new material for high temperature thermoelectric conversion, *Proc. 13th Int. Conf. Thermoelectrics*, pp. 115-118, American Institute of Physics, New York, 1995.
- [17] G. H. Jonker, The application of combined conductivity and Seebeck-effect plots for the analysis of semiconductor properties, *Phillips Res. Rep.*, **23**, 131-138 (1968).
- [18] M.-Y. Su, C. E. Elsbernd, and T. O. Mason, Jonker "pear" analysis of oxide superconductors, *J. Am. Ceram. Soc.*, **73**, 415-419 (1990).
- [19] M. E. Fine and N. Hsieh, Wiedemann-Franz-Lorenz relation in highly electronic-conducting oxides, *J. Am. Ceram. Soc.*, **57**, 502-503 (1974).
- [20] C. B. Vining, A model for the high-temperature transport properties of heavily doped n-type silicon-germanium alloys, *J. Appl. Phys.*, **69**, 331-341 (1991).
- [21] G. A. Slack and M. A. Hussain, The maximum possible conversion efficiency of silicon-germanium thermoelectric generators, *J. Appl. Phys.*, **70**, 2694-2718 (1991).

## Microstructure Analysis of Thermoelectric TiNiSn Alloy

Z. S. Tan, W. A. Jesser

*Department of Materials Science and Engineering,  
University of Virginia, Charlottesville, VA 22903*

### Abstract

Three phases have been identified from the powder X-ray diffraction pattern: two f.c.c. cubic phases with respective lattice parameters  $a_1 = 0.5941\text{nm}$  and  $a_2 = 0.6062\text{nm}$ , and an intermetallic compound  $\text{Ti}_5\text{Sn}_5$  with a hexagonal crystal structure. Transmission electron microscopy observations revealed two typical microstructures in the arc melted alloy: one showing a mottled contrast and the other a basket weave contrast. The annealing experiments have demonstrated that the minor phase and the cubic phase of larger lattice parameter are thermally unstable, and that the basket weave spinodal structure changes to a two phase segregation structure after just a few hours of annealing at  $800^\circ\text{C}$ . It is also found that over annealing causes the loss of low melting point component Sn.

### 1 Introduction

A well annealed ternary TiNiSn alloy was studied recently by Aliev and his colleagues[1,2]. It was reported that the alloy exhibited a variety of interesting properties characteristic of a narrow gap semiconductor. These properties include a negative temperature coefficient of electrical resistivity and a high Seebeck coefficient which is about  $300\text{ }\mu\text{V/K}$  at room temperature. According to the thermoelectric theories, which was briefly summarized by Rosi [3], the Seebeck coefficient ( $\alpha$ ) is a crucial parameter for the engineering application of the thermoelectric materials; and efficiency of thermoelectric energy conversion is determined by the figure of merit  $Z=\alpha^2/\rho\kappa$ , where  $\rho$  is electrical resistivity and  $\kappa$  is thermal conductivity of the materials. The figure of merit was measured at the University of Virginia and found to be about  $0.1 \times 10^{-3}\text{ }1/\text{K}$  in the annealed TiNiSn alloy. This value is much smaller than that of such thermoelectric alloys in use as Bi-Te alloys for cooling device and Si-Ge alloys for power generation; however, among the metallic alloys, it is no doubt that TiNiSn has the highest Seebeck coefficient so far.

With regard to the crystal structure of the well annealed TiNiSn intermetallic compound, the X-ray diffraction experiment of Jeitschko [4] demonstrated it has the MgAgAs type structure. This structure can be described as three interpenetrating f.c.c. sublattices occupied respectively by Ti, Ni, Sn atoms at coordinates (000), (1/4 1/4 1/4) and (3/4 3/4 3/4). As to the microstructure study on the arc-melted TiNiSn alloy, no report has been found so far. Because of the significance to a comprehensive understanding of the properties of the alloy, and because of the scarcity of detailed microstructural information about the ternary TiNiSn alloy system, a TEM analysis of the microstructure and microchemistry of the TiNiSn alloy is presented in this paper.

### 2. Experiment Procedure

Titanium, nickel and tin of purity 99.99% were arc melted in the argon atmosphere to make alloys. The elemental material was placed in a copper receptacle which is cold. The electrode, which is tungsten, was cleaned just before using by directing the arc to a high melting point metal for a suitable time. Then the arc was moved to the elemental material to be melted. The alloy ingot was turned over or crushed, and reloaded for the second melting. This

process was repeated a few times to achieve homogeneity of the alloy concentration. At the last melting, a long ingot of semi-cylindrical shape was obtained. A resistivity profile along the ingot length was measured to determine uniformity of the composition.

A piece of the final alloy was crushed to a fine powder in an alumina mortar by a pestle in order to collect X-ray diffraction spectra. The X-ray wavelength is  $\text{CuK}_{\alpha}$ ,  $0.15406\text{ nm}$ . A continuous scanning rate of 3 degree per minute was used.

Additional characterization of the microstructure was accomplished by transmission electron microscopy. A conventional method was used to prepare samples for TEM observation. A disc of diameter 3 mm was cut ultrasonically from a slice of thickness about  $500\text{ }\mu\text{m}$ . The disc was mechanically polished on sic paper to thickness around  $150\text{ }\mu\text{m}$ . A dimpler machine was used to thin the central area of the disc to the thickness of about  $15\text{--}20\mu\text{m}$ . Then the disc was finally thinned to electron transparency by using a Gatan ion milling apparatus.

The arc melted TiNiSn alloy was encapsulated in an evacuated quartz ampoule. Because of the chemical reactivity of Ti with the quartz wall at high temperature, an alumina container was used for isolating samples. Then the alloy was annealed at  $800\pm10^\circ\text{C}$  for various periods of time. Due to the brittleness of the alloys, quenching was avoided after annealing to reduce cracking from thermal shock. The annealed sample was cooled slowly from the annealing temperature inside the furnace by shutting off the power and self cooling the system in its ambient temperature. The X-ray diffraction patterns of quenched samples and slowly cooled samples were compared. No obvious differences were found. This indicates that the final phases present in the alloy do not significantly change during the slow cooling process.

### 3. Experimental Results and Analysis

#### 3.1. X-ray diffraction analysis of the arc-melted alloy.

Fig. 1 shows an X-ray diffraction result of the arc-melted alloy in powder form. Three phases have been identified in this alloy, and the diffraction peaks from these phases can be indexed consistently. The experimental d-spacings and corresponding indices are labeled on the X-ray diffraction peaks also. Among the identified phases, the first phase, whose indices are labeled as  $(hkl)_1$ , has an f.c.c. structure with lattice parameter  $a_1 = 0.5941 \pm 0.0002\text{ nm}$ , which is consistent with the data of the well annealed stoichiometric

compound TiNiSn as reported by Jeitschko[4]; The second phase, whose indices are labeled as  $(hkl)_{II}$ , has the same type of crystal structure as the first phase, but with a slightly different lattice parameter. The similarity of the crystal structure between these two phases is clearly demonstrated by two sets of strong side-by-side peaks on the pattern. The lattice parameter of the second phase has been determined to be  $a_{II} = 0.6062 \pm 0.0002$  nm, which is slightly smaller than that of the stoichiometric compound  $TiNi_2Sn$  reported as  $0.6091 \pm 0.0001$  nm by Kripyakevich and Markiv[5]. The third phase is a minor phase which was not observed by Aliev et al. [1,2], and can be identified as the intermetallic compound  $Ti_6Sn_5$ . The crystal structure of  $Ti_6Sn_5$  was studied by Piatrokowsky and Frink [6] in 1957, as well as Van Vucht et al.[7] in 1964, employing the

method of X-ray diffraction. It has a hexagonal structure, space group  $P\bar{6}3/mmc$  (No194), with lattice parameter  $a=0.922$  nm and  $c=0.569$  nm. The X-ray diffraction peaks of this phase are labeled in Fig. 1 by the indices unique to the hexagonal system.

However, there still exist some weak diffraction peaks indicated by arrows on the X-ray peaks of Fig.1, whose phase structure could not be identified because of its complexity and limited completeness of the Ti-Ni-Sn phase diagram database. It should be pointed out here that these unknown peaks disappear after about 20 hours of annealing at  $800^{\circ}C$ , but the peaks belonging to the phase  $Ti_6Sn_5$  still have a large intensity after this annealing. Further studies in this alloy system are required to determine the crystal structure of the arrowed peaks.

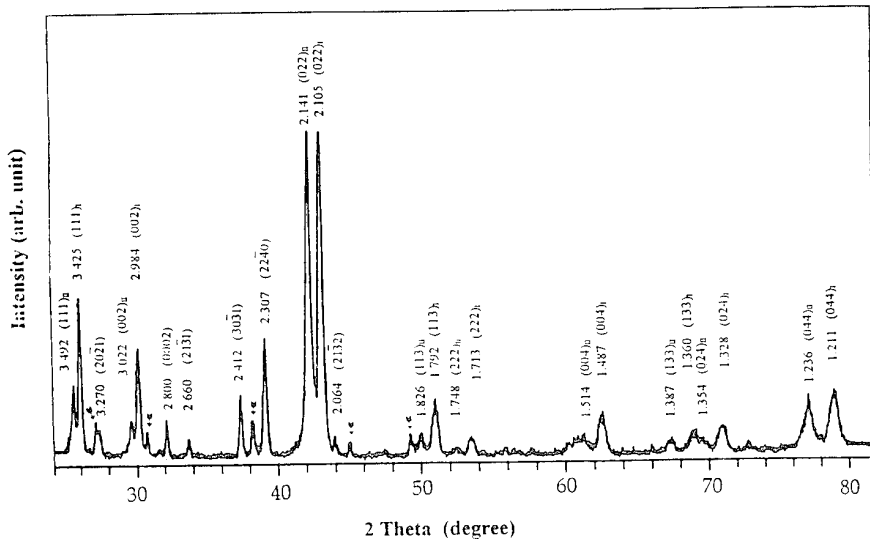


Fig.1, X-ray diffraction from a powder sample of arc melted TiNiSn alloy, performed on a Scintag diffractometer apparatus using  $CuK_{\alpha}$  radiation

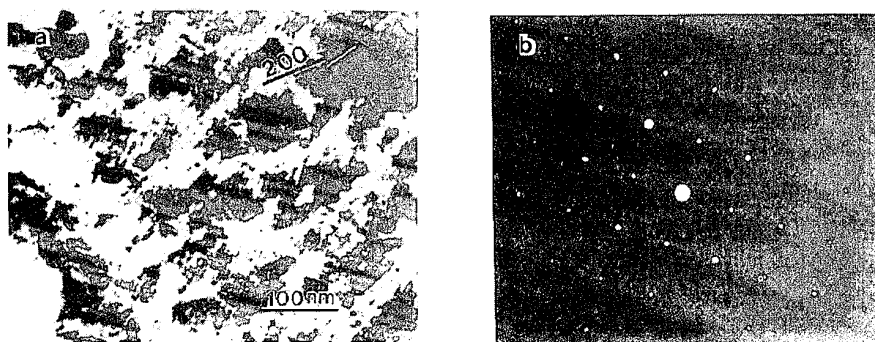


Fig.2, (a) Bright field electron micrograph of the mottled structure observed in arc melted TiNiSn alloy. The orientation of the foil is  $B \sim [011]$  in a two beam condition  $g = [200]$ . (b) [001] zone axis selected area diffraction (SAD) pattern from the mottled structure shown in (a). Note the microsegregation results in two f.c.c. cubic phases (i.e. doubling of the diffraction spots)

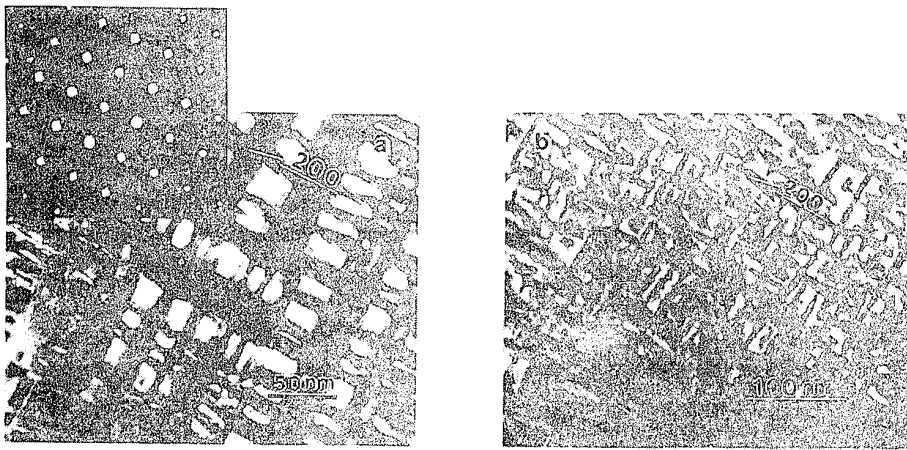


Fig.3, Bright field electron micrographs of the basket weave structures observed in arc melting TiNiSn alloy,  $g = [200]$  and  $B \sim [001]$ , and a [001] zone axis SAD pattern from this structure

### 3.2. Microstructure analysis of the arc-melted alloy by TEM.

Although the microstructure of the alloy after arc-melting has been found to be microscopically non uniform and varies in morphology from one location to another depending on the kinetics of solidification, nevertheless, basically two morphologies can be classified. One is a mottled domain structure with a typical electron micrograph shown in Fig. 2 (a). The other is a so-called basket weave structure, representatively shown in Fig. 3, where two types of basket weave morphologies are exhibited. A similar striated basket weave structure had been also reported in Ni-Al-Ti alloy by Yang et al.[8] and in beta brass by Kubo and Wayman[9]. The basket weave contrast is typical of a two phase structure resulting from spinodal decomposition. It is worth pointing out that no large differences in overall concentration have been found between the two areas exhibiting the two types of basket weave structure. The composition analysis was performed by TEM/EDS (X-ray energy dispersive spectroscopy) and a quantitative processing program for thin films.

### 3.3. Selected area diffraction analysis of the mottled structure.

The mottled structure and the basket weave structure yield different selected area diffraction (SAD) patterns. The [001] zone axis SAD pattern from the area exhibiting a mottled structure is shown in Fig. 2 (b). Careful examination of this pattern reveals two superimposed diffraction patterns with the low index spots almost overlapped, but the high index spots discriminated as double. The SAD pattern from the area containing mottled contrast can be readily explained by the two major f.c.c. phases identified by X-ray diffraction in the previous section. These two phases have lattice parameters which differ by only about 1.7%. The characteristics of the image and the SAD pattern tell us that in this region these two f.c.c. phases have a microsegregation structure so that one of the phases has a different composition from the other phase consistent with the light and dark contrast.

### 3.4. Selected area diffraction analysis of the basket weave structure

The basket weave structure gives rise to much more complicated SAD pattern shown in Fig3 (a). It is interesting and worth noting that there exist cross, well defined streaks associated

with the strong spots, and continuous diffuse streaks connecting the weak spots to the strong spots. Also it has been found that the intensity of the weak spots depends on the delicate variation of the basket weave structure. One finds that the lenticular basket weave structure gives the strongest intensity to the weak spots. The crystal structure corresponding to the set of strong spots is an f.c.c. structure with lattice parameter close to that of either TiNiSn or the intermetallic compound  $TiNi_2Sn$ . The periodicity analysis makes out that the weak reflections consist of fundamental spots and double diffraction spots by the strong reflection beams of the matrix. With respect to the X-ray spectra of the arc melted alloy, it is reasonable to consider that a minor phase  $Ti_6Sn_5$  gives rise to the reflections of weak spots.

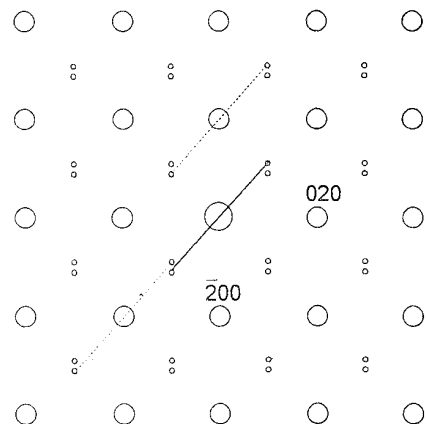


Fig.4, Schematic illustrations of the crystal structure analysis of a [001] SAD patterns, the small open circles denote weak diffraction from the minor phase  $Ti_6Sn_5$

Analysis of the [001] zone axis pattern of the cubic matrix is illustrated in Fig.4, where the big open circles stand for the strong diffraction spots of the matrix and the small open circles for the weak spots of the minor phase. The spots connected by a solid straight line through the transmitted beam are corresponding to the fundamental diffraction spots of a minor phase; and the spots attached to the dashed straight line passing through the diffraction beams apparently arise by double diffraction. As the weak spots, presumed to arise from the minor phase  $T_6Sn_5$ , are only present as  $\pm$  a single g-vector, it is difficult to add further analysis to the SAD pattern.

### 3.5. Discussion on the streaks and the morphology of the minor phase.

Now let us take a look at the streaks exhibited on both <001> directions of the matrix and weak spots presumed to arise from the minor phase. The streaks on the matrix spots are attributed to the spinodal structure, i.e., the modulation of the concentration and lattice parameter in the {001} direction of the f.c.c. matrix. Based on the structural similarity of the TiNi<sub>2</sub>Sn compound

(MnCu<sub>2</sub>Al type structure) to the TiNiSn compound (MgAgAs type structure), the composition modulation of the matrix is thought to be caused by the varied occupation percentage of nickel atoms at position coordinate (1/2, 1/2, 1/2). Regarding the diffuse continuous streaks on the weak spots, no satisfactory explanation has been made yet. As to the morphology of the minor phase, the contrast inside the dark thick striations, demonstrated in Fig.3 (a), suggests that the presence of the small particles of the minor phase is associated with a relatively large nickel-rich region. The striations with dark contrast is thought to be the nickel-rich region, because the small vacancy occupancy to the MnCu<sub>2</sub>Al lattice position gives rise to a large structure factor of scattering to the incident electron beam, and therefore, the bright field image should show dark contrast for that region.

### 3.6. Annealing effect on the microstructure of arc melted alloy

#### (1) Alloy annealed at 800°C for 5 hours

Fig.5 shows a typical morphology of the arc-melted TiNiSn alloy annealed at temperature 800°C for 5 hours. It is clearly a two phase structure with a metastable phase in the matrix. The

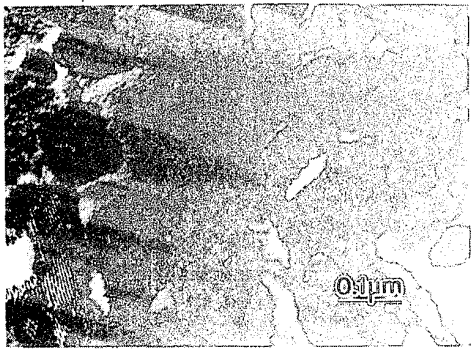


Fig.5, Bright field electron micrograph of TiNiSn alloy annealed for 5 hours at 800 °C

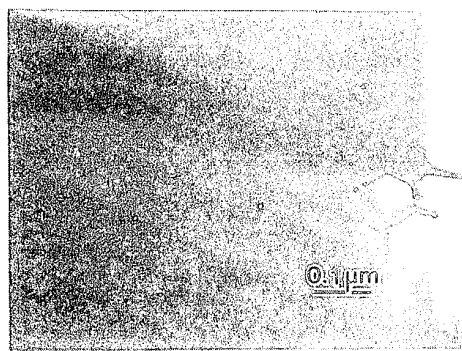


Fig.7. Bright field electron micrograph of TiNiSn alloy annealed for 4 weeks at 800 °C,  $g=[200]$   $B-[012]$

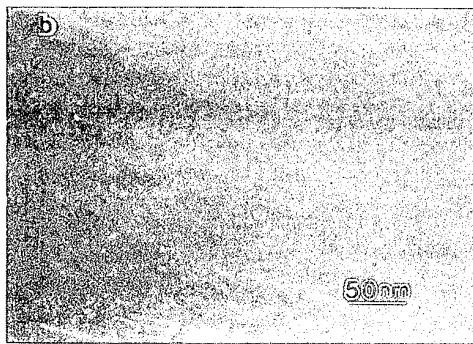
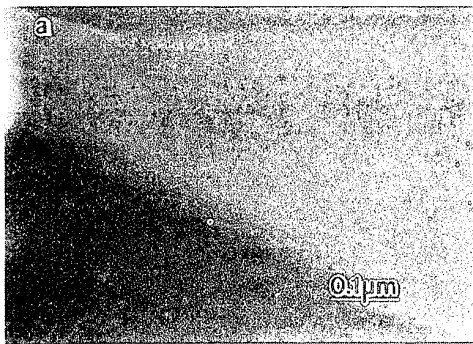


Fig.6, (a) Bright field electron micrograph of TiNiSn alloy annealed for 24 hours at 800 °C, (b) Magnified bright field electron micrograph showing the structure of the minor nanophase in the matrix,  $g=[220]$   $B-[001]$

metastable phase has its composition and crystal structure close to  $TiNi_2Sn$ . The matrix corresponds to the structure of stoichiometric intermetallic compound  $TiNiSn$ . Although the metastable phase and matrix have related crystal structures, lattice mismatch and a difference of atomic ordering sequence exist at the phase boundary. Interface defects could include misfit dislocation (MD), interfacial step (IS) and antiphase stacking. Depending on the foil orientation and diffraction contrast conditions, the corresponding features of the electron micrograph might consist of misfit dislocation lines, IS images (very similar to the image of dislocations), thickness fringes, moire fringes caused by slight differences of lattice parameter, and antiphase boundary (APB) contrast. A detail analysis of these defects requires film tilting experiments and also image simulation. Because of its complexity, no further discussion will be made here.

#### (2) Alloy annealed at 800°C for 24 hours

Fig. 6 (a) shows an electron micrograph of the arc melting  $TiNiSn$  alloy annealed at 800°C for 24 hours. The metastable cubic phase of round shape can still be readily found. But the volume fraction of this phase is much smaller than that in the alloy annealed for 5 hours. A high magnified image of the fine structure of the matrix is shown in Fig. 6 (b). A high density of nanoscale particles is observed. The SAD pattern from this area exhibits a set of weak spots whose positions and features are similar to the illustration of the weak spots of Fig.4. Presumably, this nanoscale phase is  $Ti_6Sn_5$  compound. X-ray diffraction analysis of the annealed alloy gives evidence supporting this result. The fact that the  $Ti_6Sn_5$  phase remains in the area where the metallic cubic phase  $TiNi_2Sn$  disappears indicates that the minor phase  $Ti_6Sn_5$  in the arc melted alloy is more thermally stable than the major cubic phase  $TiNi_2Sn$  which transformed to the stable cubic phase  $TiNiSn$ .

#### (3) Alloy annealed at 800°C for 4 weeks

Fig.7 shows an electron micrograph of the arc melted alloy annealed for 4 weeks. A uniform  $TiNiSn$  phase is exhibited in this alloy. Near grain boundaries, dislocation networks can be readily found. The SAD pattern of this alloy shows a single diffraction pattern of the f. c. c. cubic structure. As the annealing time increases, the dislocation network eventually disappears, while low angle grain boundaries accommodated by dislocations are readily observed. Finally, it is worth pointing out that long time annealing causes loss of low melting point component Sn. The loss of Sn causes the average concentration of the alloy to deviate from the stoichiometric ratio. Also seen in Fig. 7 is a fine distribution of nanoscale precipitate particles which occupy a very small volume fraction of the sample. These precipitates formed after a loss of Sn from the sample and upon further annealing coarsened to a cubic phase with a lattice parameter close to that of the  $TiNi_2Sn$  structure. It is also found that over-annealing causes a degradation of thermoelectric properties partially due to the loss of Sn from the alloys.

## 4. Conclusions

- Three phases are identified in arc melted  $TiNiSn$  thermoelectric alloy. Two of them have f.c.c. structure. One cubic phase is intermetallic compound  $TiNiSn$ ; while another cubic phase has lattice constant slightly smaller than that of equilibrium intermetallic compound  $TiNi_2Sn$ . A third and minor phase is  $Ti_6Sn_5$ , which is observed to be associated with the Ni-rich cubic phase,  $TiNi_2Sn$ .
- Two typical microstructure morphologies of arc melted alloy are revealed: one is a mottled structure; another is the basket weave spinodal structure. The latter is thermally unstable during annealing and changes to a two phase segregation structure. It is also found that particles of the minor phase  $Ti_6Sn_5$  still remain in the matrix after the metastable cubic phase  $TiNi_2Sn$  has transformed during annealing to  $TiNiSn$ .
- A uniform structure of intermetallic compound  $TiNiSn$  can be achieved by suitable annealing at a temperature of 800 °C. However, over annealing may cause the loss of low melting point component Sn.

## Acknowledgments

We thank Vadim V. Kozyrkov and Conrad A. B. Ball, Department of Physics at the University of Port Elizabeth for discussions regarding the  $TiNiSn$  alloy. Also acknowledged are general discussions with F. D. Rosi, who has been very helpful.

## References

- [1]. F. G. Aliev V.V. Kozyrkov, V.V. Moshchalkov, R. V. Scolozdra, and K. Durczewski, Z. Phys. B, Condensed Matter, 80, 353 (1990)
- [2]. F.G. Aliev, N.B.Brandt, V.V. Moshchalkov, V.V. Kozyrkov, R. V. Scolozdra, and A. C. Belogozokhov, Z. Phys. B, Condensed Matter, 75, 167 (1989)
- [3]. F. D. Rosi, Solid State Electronics, Pergamon Press, 11, 833 (1968)
- [4]. W. Jeitschko, Metal. Trans. 1, 3159 (1970)
- [5]. P. I. Kripyakevich and V. Ja. Markiv, Dopov. Akad. Nauk Ukr. PSR., no. 12, 1606 (1963)
- [6]. P. Pietrokowsky and E. P. Frink, Trans. of the Amer. Soc. of Metals, 49, 339 (1957)
- [7]. J. H. N. Van Vucht, H. A. C. M. Bruning, H. C. Donkersloot and A. H. Gomes de Mesquita, Philips Res. Rep., 19, 407 (1964)
- [8]. R. Yang, J. A. Leake, R. W. Cahn, and C. Small, Scripta Metall. & Mater. 26, 1169 (1992)
- [9]. H. Kubo and C. M. Wayman, Metall. Trans. A, 10A, 633 (1979)

# Prospects of various thermoelectric use in thermoelectric generators

M.I.Fedorov, E.A.Gurieva, L.V.Prokof'eva, V.K.Zaitsev

*A.F. Ioffe Physical-Technical Institute, St.Petersburg, Russia.*

The results of study of temperature dependencies of thermoelectric parameters of some thermoelectrics based on lead sulphide and lead selenide and some silicon based thermoelectrics are presented. The results of calculation of a number thermoelectric batteries are presented either. The conclusions of various thermoelectrics use prospects are discussed on the base of presented results.

## Introduction

There are a few perspective areas of thermoelectric generator use. These are far space missions, electric energy supply units for remote regions, waste heat use and some others. If discuss only earth problems a number of thermoelectrics can be used in such generators. These are materials based on bismuth and antimony chalcogenides solid solutions, lead, tin and germanium chalcogenides, transition metal silicides, magnesium compounds with IV group elements and some other.

There are two groups among these materials: materials working at temperature below 600K and below 1000 K. Solid solutions based on bismuth and antimony chalcogenides compose the first group. Other mentioned materials compose another group. In the second group germanium compounds take special place because of germanium high cost. We shall not discuss them here. This report is a short review of results of a few thermoelectrics study fulfilled in the laboratory of physics of thermoelements of Ioffe Physical-technical Institute.

When there is a problem of thermoelectric generator designing first of all it is necessary to choice best couple of thermoelectrics. If one wants to calculate thermoelectric battery he should know temperature dependencies of three thermoelectric parameters: electrical conductivity, thermopower and thermal conductivity. Usually even in a handbook (see for example [1]) it is possible to find out only temperature dependence of figure of merit of some material and probably there is a temperature dependence of one of thermoelectric parameters measured on other sample in other laboratory.

## Thermoelectric parameters of lead chalcogenides

Since "ancient" times lead telluride has been the most efficient thermoelectric among the thermoelectrics working at temperature below 1000K [2]. Its properties are studied well, there are many thermoelectric devices using lead telluride. Figures 1 and 2 show temperature dependencies of lead telluride thermoelectric parameters at various carrier concentration for n- and p-type material.

There was no consequent study of other lead chalcogenides - PbSe and PbS before because of their low figure of merit. But these materials have higher melting point [2] and can be used at higher temperatures. Figure 3 and 4 show temperature dependencies of lead selenide thermoelectric parameters and figure 5 and 6 those of lead sulphide.

Samples for measurements were made by hot pressing. VII and I group elements were used as dopants for n- and p-type materials production. Thermoelectric parameters were measured by stationary absolute method. The authors paid much

attention to thermal conductivity measurements because of great variety of different author's data. The data described are the results of comparison of measurements of many groups of similar materials. The comparison of figures 1 and 3 and then 2 and 4 shows that in lead selenide intrinsic conductivity influence begins at temperature 50-100 K higher than in telluride sample of the same carrier concentration. Lead sulphide has the largest energy gap in the row of lead chalcogenides and that results in increase of optimal carrier concentration.

## Thermoelectric parameters of some silicides

There is another group of materials for temperature region below 1000 K. Higher manganese silicide (HMS - MnSi<sub>1.71-1.75</sub> - p-type, and solid solutions based on Mg<sub>2</sub>B<sup>IV</sup>(B<sup>IV</sup> = Si, Ge, Sn) - n-type) compounds. These materials are the most effective ones among the non-chalcogenide materials [3, 4]. The temperature dependencies of parameters of two thermoelectrics based on HMS and solid solution Mg<sub>2</sub>Si<sub>0.7</sub>Sn<sub>0.3</sub> are shown on the figures 8 - 9. Temperature dependencies of CoSi (n-type) thermoelectric parameters are shown on these figures either.

The samples for measurement were prepared mostly by vacuum casting method and some of them by directed crystallization (Bridgeman method). Thermoelectric parameters were measured by the same method as for lead chalcogenide materials.

## Calculation of parameters of thermoelectric modules

On the base of the measured data we calculated coefficient of performance of thermoelectric modules from different thermoelectrics. A module of 4 mm in height and 2 mm in width was used as a base for calculation. P-leg thickness was 2 mm and that of n-leg was calculated using the formula:

$$\frac{S_n}{S_p} = \sqrt{\frac{\sigma_p \kappa_p}{\sigma_n \kappa_n}}$$

The obtained thickness was rounded to tenth of millimeter.

Parameters of modules were calculated using the following formulas:

$$\eta = \frac{W}{Q}$$

$$W = I^2 R_t$$

$$Q = \bar{\kappa}_t \cdot (T_h - T_c) - 0.5I^2 R_t + I\alpha_t T_h$$

$$I = \frac{\bar{\alpha}_t \cdot (T_h - T_c)}{2R_t}$$

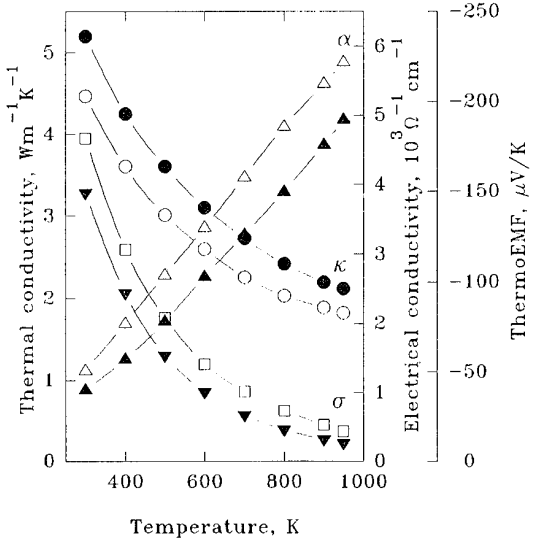


Figure 5: Thermoelectric parameters of n-type PbS.  
 $n(cm^{-3}) = 1 - 7.3 \cdot 10^{19}; 2 - 1.1 \cdot 10^{20}$

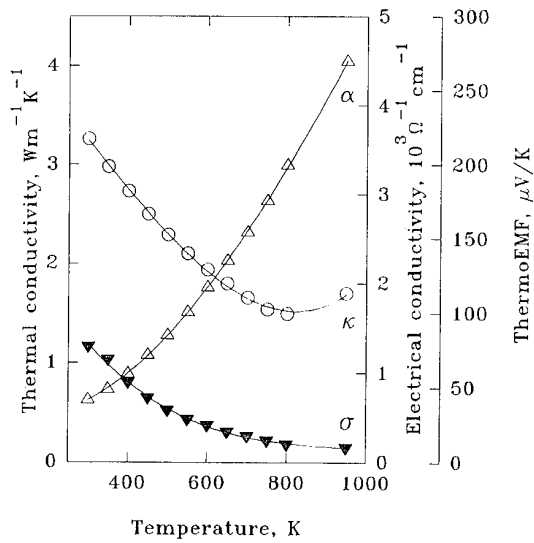


Figure 6: Thermoelectric parameters of p-type PbS.  
 $p = 7.3 \cdot 10^{19} cm^{-3}$

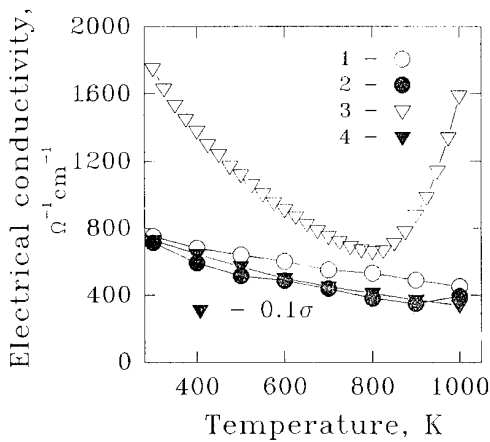


Figure 7: Temperature dependencies of electrical conductivity for some silicon based materials.  
1 - HMS (optimized); 2 - HMS < Ge >; 3 -  $Mg_2Si_{0.7}Sn_{0.3}$ ; 4 - CoSi

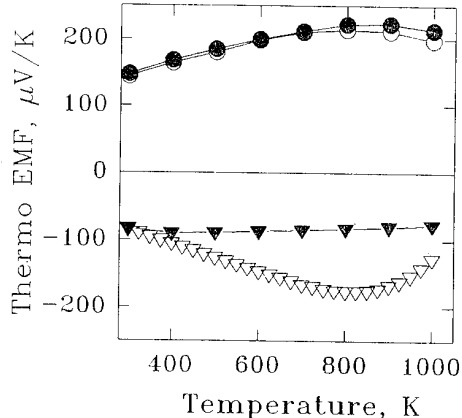


Figure 8: Temperature dependencies of thermopower for some silicon based materials. The symbols are the same as at fig.7

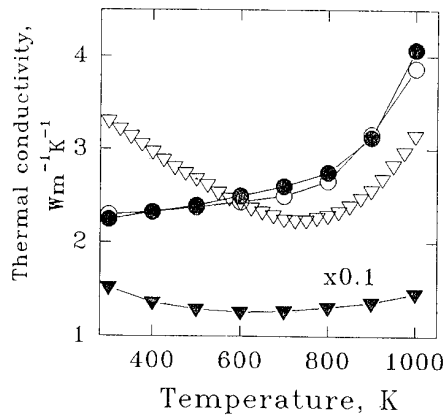


Figure 9: Temperature dependencies of thermal conductivity for some silicon based materials. The symbols are the same as at fig. 7.

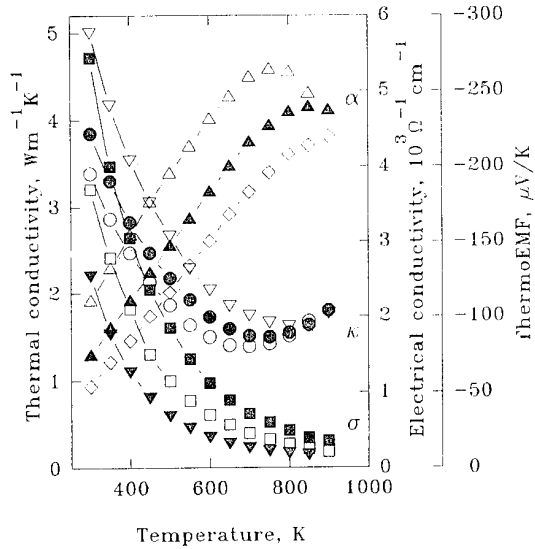


Figure 1: Thermoelectric parameters of n-type PbTe.  
 $n(cm^{-3}) = 1 - 1 \cdot 10^{19}; 2 - 2 \cdot 10^{19}; 3 - 3.5 \cdot 10^{19}$

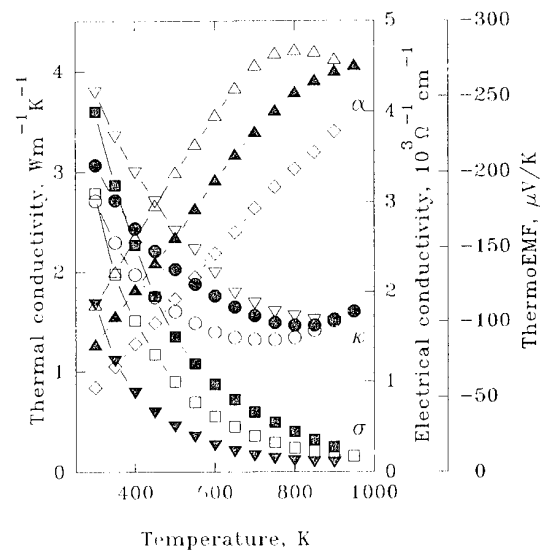


Figure 3: Thermoelectric parameters of n-type PbSe.  
 $n(cm^{-3}) = 1 - 1 \cdot 10^{19}; 2 - 2 \cdot 10^{19}; 3 - 3.5 \cdot 10^{19}$

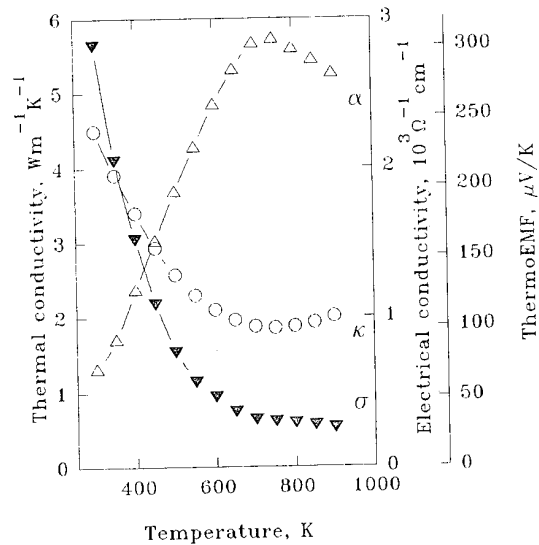


Figure 2: Thermoelectric parameters of p-type PbTe.  
 $p = 2 \cdot 10^{20} cm^{-3}$

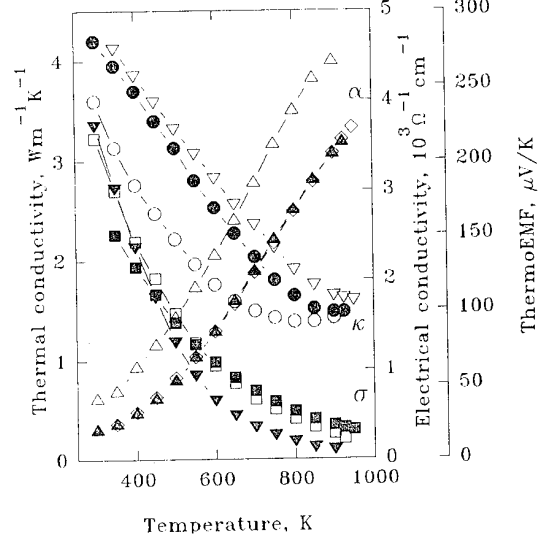


Figure 4: Thermoelectric parameters of p-type PbSe.  
 $p(cm^{-3}) = 1 - 7 \cdot 10^{19}; 2 - 2.8 \cdot 10^{20}; 3 - 4.5 \cdot 10^{20}$

Table 1: Parameters of various thermoelectric modules

$$\begin{aligned}
 R_t = & (1/d_n \bar{\sigma}_n + 1/d_p \bar{\sigma}_p)l/h + 2 \frac{r_l}{h(d_n + d_p)} + \\
 & + \frac{(\rho_{mh} + \rho_{mc})((d_n + d_p) * 0.6 + d_i)}{hd_m} \\
 \alpha_t = & \alpha_p - \alpha_n \\
 \kappa_t = & (\kappa_n d_n + \kappa_p d_p + \kappa_i d_i)h/l
 \end{aligned}$$

where  $\eta$  - coefficient of performance (CoP)

$W$  - electrical power

$Q$  - current of heat through thermocouple

$I$  - electrical current through thermocouple

$R$  - electrical resistance of thermocouple

$T$  - junction temperature

$\alpha$  - thermopower

$\kappa$  - thermal conductivity

$\sigma$  - electrical conductivity

$l$  - height of thermocouple

$h$  - width of thermocouple

$d$  - thickness of legs, contact metal plate insulating layer

$r_l$  - resistivity of transition layer between metal and semiconductor

$\rho_m$  - specific resistance of contact metal plate

$\bar{a}$  means average value of  $a$  in the range  $T_h - T_c$

indexes mean t - thermocouple;

n - n-leg;

p - p-leg;

i - insulator;

m - contact (metal) plate;

l - transition layer;

h - hot junction;

c - cold junction.

The coefficient of performance of such a module was calculated for temperature range 350-600 K to compare a possibility of using such materials instead of materials based on bismuth telluride and at highest hot junction temperature for this couple of materials. The coefficient of performance of module using  $\text{Bi}_2(\text{TeSe})_3$  and  $(\text{BiSb})_2\text{Te}_3$  was calculated either. The data for calculation were kindly presented by V.A.Kutasov.

Figure 10 shows dependencies of CoP of such modules on cold junction temperature when that of hot junction is 900K for lead telluride and lead selenide and 1000 K for other materials. CoP for maximum temperature range and for temperature range 350 - 600 K are shown in the table. The values of electrical power and leg cross-sections ratio for each module are presented either. In the last column parameter of specific electrical power is presented. It shows electrical power that can be produced by 1 gram of thermoelectric materials.

## Discussion

As the table shows in the temperature range 350 - 600 K the only material which has CoP close to that of bismuth telluride based material is lead telluride but it has no advantages in comparison with bismuth telluride. The pair  $\text{Mg}_2(\text{SiSn})$  and HMS has better mechanical properties and much cheaper. Thus it can be used instead of bismuth telluride based material in some devices.

n-leg	material	W, mW	$\eta$ , %	$S_n/S_p$	$\dot{W}/m, \text{W/g}$
working range 350 - 600 K					
$\text{Bi}_2(\text{TeSe})_3$	$(\text{BiSb})_2\text{Te}_3$	75.6	7.6	1	0.24
$\text{PbTe}^1$ <sup>a</sup>	PbTe	71.1	5.9	1	0.21
$\text{PbSe}^1$	PbSe <sup>1</sup>	40.1	4.0	1	0.12
$\text{PbS}^1$	PbS	14.5	1.5	0.5	0.07
$\text{Mg}_2(\text{SiSn})$	HMS	45.1	4.2	0.7	0.32
CoSi	HMS	34.3	3.1	0.15	0.23
Kopel	HMS	30.2	3.1	0.06	0.30
working range 350 - 900 K					
$\text{PbTe}^2$	PbTe	293	12.4	1	0.86
$\text{PbSe}^2$	PbSe <sup>1</sup>	176	8.7	1	0.52
$\text{PbSe}^2$	PbTe	295	13.1	1	0.87
$\text{PbS}^1$	PbTe	227	10.3	0.65	1.03
working range 350 - 1000 K					
$\text{PbS}^1$	PbS	126	6.2	0.5	0.63
$\text{Mg}_2(\text{SiSn})$	HMS	329	11.3	0.7	2.36
CoSi	HMS	232	7.6	0.15	1.55
Kopel	HMS	226	7.4	0.06	2.26

<sup>a</sup>A number near chemical formula means the number of curve from the corresponding figure

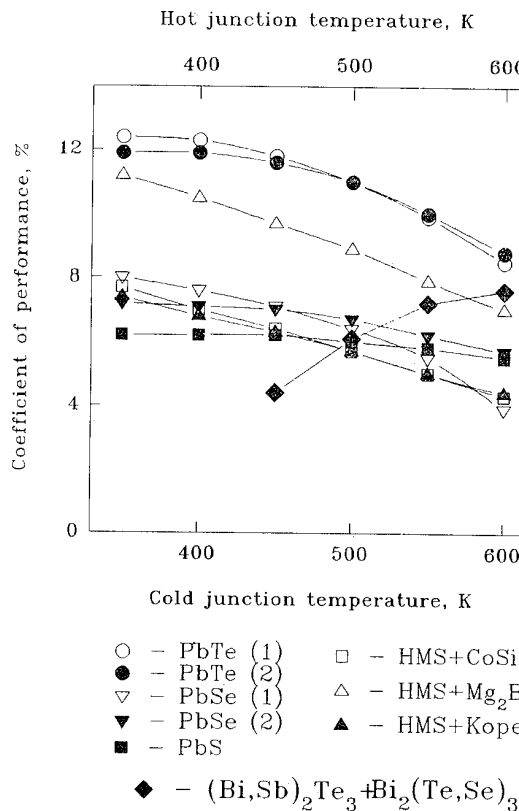


Figure 10: CoP dependencies of reviewed materials on cold junction temperature and CoP dependence of  $\text{Bi}_2(\text{TeSe})_3 - (\text{BiSb})_2\text{Te}_3$  couple on hot junction temperature

When full temperature interval of thermoelectric is used the

pair lead telluride - lead selenide allows to obtain maximum coefficient of performance and the lead telluride pair is a little bit worse. The substitution of n-type lead selenide or lead telluride by lead sulphide results in decrease of CoP but in increase of specific electric power.

The silicide pair ( $Mg_2(SiSn)$  - HMS) has a lower CoP than lead telluride pair, however, one should take into account that thermoelectrics based on lead chalcogenides must be protected against oxidization and sublimation. This factor can diminish difference between lead chalcogenide couples and the HMS

$Mg_2(SiSn)$  couple. Our forecasting calculation shows that thermoelectric parameters of  $Mg_2(SiSn)$  can be drastically improved by addition of small quantity of germanium. Thermocouples HMS-Kopel and in particular HMS -  $Mg_2(SiSn)$  have the highest values of specific electric power and can be used preferably when mass of thermoelectric should be diminished.

Other couples have close values of CoP and in this case other factors, for example, price, mass of module, mechanical and chemical strength, thermal expansion coefficient and some other should be taken into account when generator designing.

The item of interest is creation of two-stage generator with low temperature stage made from material based on  $Bi_2Te_3$  solid solutions. The figure 10 shows that CoP of such a generator can achieve 18% when high temperature stage is made of lead chalcogenides and 16% with silicide high temperature stage. The hot junction temperature of low temperature stage can be lowered without CoP decrease. This lowering can improve the reliability of such a generator and increase its lifetime.

#### References

- [1] Anatychuk L.I. *Thermoelements and thermoelectric devices (Handbook)* Kiev, 1979, 766 p. (in Russian)
- [2] Ravich Yu.I., Efimova B.A., Smirnov I.A. *Semiconducting lead chalcogenides* N.-Y., L. 1970, 377 c.
- [3] M.V. Vedernikov, A.E. Engalychev, V.K. Zaitsev, S.V. Ordin, M.I. Fedorov. Thermoelectric properties of material based on higher silicide of manganese and cobalt monosilicide. *Proc. of the Seventh International Conference on Thermoelectric Energy Conversion* 1988, Arlington, pp.150-155.
- [4] N.D. Marchuk, V.K. Zaitsev, M.I. Fedorov, A.E. Kalyazin. Thermoelectric properties of some cheap n-type materials *Proc. of the VIIth Int. Conf. on Thermoelectric Energy Conversion* 1989, Nancy, pp.152-155.

**THERMOPOWER AND ELECTRICAL RESISTIVITY OF  $\beta$ -FeSi<sub>2</sub> SINGLE CRYSTALS  
DOPED WITH Cr, Co AND Mn**

A.Heinrich<sup>1</sup>, C.Gladun<sup>1</sup>, A.Burkov<sup>2</sup>, Y.Tomm<sup>3</sup>, S.Brehme<sup>3</sup> and H.Lange<sup>3</sup>

<sup>1</sup> *Institut für Festkörper- und Werkstoffforschung Dresden e.V., D-01171 Dresden, Germany*

<sup>2</sup> *A.F.Ioffe Physico-Technical Institute, St. Petersburg, 194021 Russia*

<sup>3</sup> *Hahn-Meitner-Institut Berlin GmbH, D-12489 Berlin, Germany*

Single crystals of  $\beta$ -FeSi<sub>2</sub> were grown by chemical transport reaction using iodine as transport agent. As doping elements Cr, Co and Mn were used. Resistivity, Hall effect and thermopower of the samples have been investigated in a wide temperature range between 20K and 1050K. The thermopower measurements have shown that Cr and Mn yield p-type crystals, Co n-type crystals. All investigated transport parameters show characteristic changes of their temperature dependence in the same temperature ranges. It was concluded that at low temperatures conduction takes place mainly within an impurity band and at higher temperatures mainly in the conduction (valence) band. The change between these two regimes is rather sharp and seems to be a general feature of doped  $\beta$ -FeSi<sub>2</sub>. An additional impurity state was found below the impurity band.

### **Introduction**

Within the group of semiconducting silicides the compound  $\beta$ -FeSi<sub>2</sub> is one of the most promising thermoelectric material for high temperature application [1-3]. By appropriate doping both n-type and p-type compounds were obtained and many efforts have been made to get a high thermoelectric figure of merit  $Z=S^2/(\rho \times \kappa)$  in a broad temperature range ( $S$ ,  $\rho$  and  $\kappa$  are thermopower, electrical resistivity and thermal conductivity, respectively). The common way to achieve high values of  $Z$  is the variation of kind and degree of doping [1-7] and the optimization of the preparation technology, see e.g. [5,8]. Both bulk material [1-5] and thin films [6-9] have been investigated. It is now well established that doping with transition metals from the right side of Fe in the periodic table like Co and Ni yield n-type  $\beta$ -FeSi<sub>2</sub> and doping by transition metals from the left like Cr and Mn p-type material. But also other doping elements have been used, e.g. Al for p-type [1,10] and B for n-type material [11]. In [12] it was shown that also oxygen can give a strong increase of the thermoelectric efficiency Z.

In many cases the influence of doping on the thermoelectric properties of  $\beta$ -FeSi<sub>2</sub> depends strongly on the preparation technology. This is especially valid for ceramic material. Often it is not possible to separate the influence of technology and of doping. Also deviations from stoichiometry can occur which can

have an additional doping effect or can lead to precipitations of a second phase. Therefore, the microscopic understanding of the doping and transport mechanisms is far from complete and the possible improvement of  $Z$  by optimal doping is not yet known.

The aim of this paper is to contribute to the understanding of the doping of  $\beta$ -FeSi<sub>2</sub> with transition metals by investigating single crystals. The chosen doping elements are Cr, Mn, Co and Ni. In this paper first results are presented about the thermopower and resistivity in a wide temperature range. Comparison will be made with non-intentionally doped single crystals.

### **Experimental**

#### *Sample preparation:*

The  $\beta$ -FeSi<sub>2</sub> single crystals were grown in closed ampoules by chemical vapour transport using iodine as a transporting agent. As starting materials FeSi<sub>2</sub> powder of 99.98% purity and iodine contents of 4 and 7mg I<sub>2</sub>/cm<sup>3</sup> were used. The ampoule was placed in a temperature gradient between 950 and 680°C. The growth times were in between 1 and 2 weeks. Needle-like crystals were obtained which are about 10-15mm long and have a diameter of 1-2mm. Not in all cases the habitus was really prismatic. The crystallographic parameters of the grown crystals were determined by X-ray diffraction using CuK $\alpha$ -radiation. The measured peaks were correlated only to the orthorhombic  $\beta$ -FeSi<sub>2</sub> phase, no traces of  $\alpha$ -FeSi<sub>2</sub> were found.

The doping elements Co, Mn, Cr and Ni were added to the starting powder in a concentration of 2wt%, for Co also of 5wt%. Doping was found to have an influence on the crystal size, the doped crystals were larger and much more crystals were grown. From electron paramagnetic spin resonance [13,14] and EDX measurements the doping concentrations in the single crystals were found to be about  $10^{19}\text{cm}^{-3}$ , i.e. <0.1at% (for the higher concentration of Co 0.5at%). From the EPR measurements it was concluded that all doping elements occupy Fe sites, Mn and Cr both inequivalent Fe sites of the  $\beta\text{-FeSi}_2$  lattice, but Co and Ni only one.

#### *Transport Measurements:*

The thermopower and resistivity of the doped and undoped single crystals have been measured in the temperature range from below 20K to 1000K. The thermopower was measured with a static temperature gradient, the resistivity by conventional four probe technique. The high temperature measurements were carried out in pure He atmosphere. By repeated heating and cooling the stability of the samples and contacts was tested. Due to limitations in sample size and stability of contacts high temperature results are shown in this paper only for Cr and Co doped samples. Hall measurements were carried out from 300K to below 20K. The magnetic field strength was in the range 0.1 to 0.8T, a standard value was 0.495T. Bridge and van der Pauw configurations were used.

## Results and discussion

#### *Carrier concentration:*

The carrier concentration was determined from the Hall coefficient  $R_H$  setting the Hall factor  $r=1$ . At 300K the determination of the Hall coefficient for most crystals was difficult because of the low mobility. For Cr-doped samples carrier concentrations of some  $10^{18}\text{cm}^{-3}$  were found and mobilities of  $10\text{cm}^2/\text{Vs}$ . In Fig.1 the carrier concentration is shown of p-type  $\beta\text{-FeSi}_2$  below room temperature, of one undoped crystal and two crystals doped with Mn and Cr, respectively. The common features of  $p(T)$  of all samples are the strong decrease below 300K and a saturation below about 75K. This behaviour can not be explained by carrier statistics using a simple one acceptor one band model. There is up to now no explanation for this behaviour. But in the following it will be shown that also the transport properties show special characteristics in the transition range from the strong slope of  $p(T)$  to saturation.

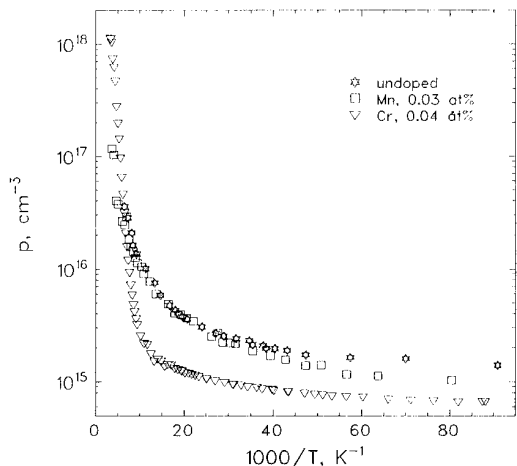


Fig.1 Carrier concentration of p-type  $\beta\text{-FeSi}_2$  single crystals below 300K

From the strong slope of  $p(T)$  between 100K and 300K an activation energy of about 75meV was determined for the Cr-doped sample, and of about 40meV for the Mn-doped sample. The undoped sample of Fig.1 shows a very similar behaviour as the Mn-doped crystal. This is in agreement with results of the analysis. Mn was found to be a main impurity in most of the undoped crystals.

#### *Electrical Resistivity:*

In Fig.2 the resistivity  $\rho(T)$  is shown of a Cr-doped crystal in the whole considered temperature range from 10K to 1050K. One can distinguish four temperature ranges with different characteristics of the temperature dependence  $\rho(T)$ : (i) Below about 100K the temperature dependence is much weaker than  $1/T$  and corresponds below 50K to Mott's law  $\ln \rho \propto T^{-1/4}$  of variable range hopping, see Fig.2a. (ii) Between 100K and room temperature  $\rho(T)$  shows a large slope which yields a decrease by two order of magnitudes. (iii) Above 300K the resistivity increases slightly with an approximately linear temperature dependence. (iv) Above 600K there is again an exponential decrease.

Taking into account the results of Hall measurements (see Fig.1) the behaviour of  $\rho(T)$  can be qualitatively described. The temperature range of nearly constant carrier concentration obviously agrees with the temperature range of hopping conduction. In this range there is almost no activation of carriers into the valence

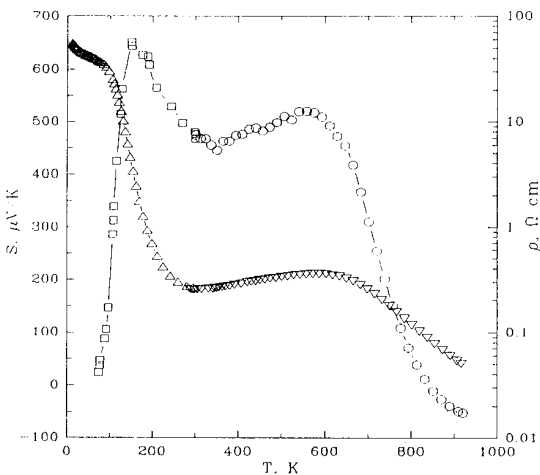


Fig.2 Electrical resistivity and thermopower of Cr-doped  $\beta$ -FeSi<sub>2</sub> with Cr content 0.1at%

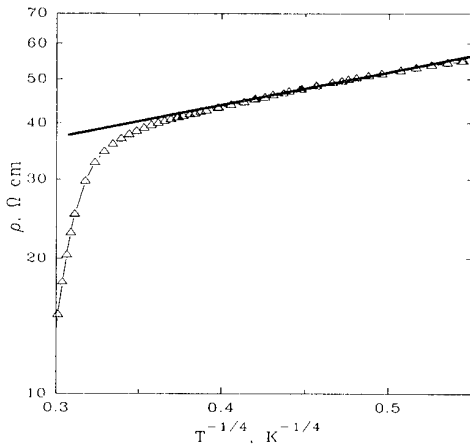


Fig.2a Electrical resistivity of Cr-doped  $\beta$ -FeSi<sub>2</sub> in the plot  $\lg \rho$  vs.  $T^{-1/4}$

band (p-type samples), the conduction takes place within the impurity band. Above 100K the activation of carriers into the valence band gives rise to the observed decrease of  $\rho(T)$ . The activation energy of resistivity is with  $\approx 50$ meV in the same order of magnitude as that of the carrier concentration. The increase of  $\rho(T)$  between 300K and 600K means that the increase of electron-phonon scattering in the valence band exceeds the further increase of carrier concentration. The opposite should be responsible for the decrease of  $\rho(T)$  above 600K. The resistivity does not follow a simple  $1/T$ -dependence. The estimation of an averaged activation energy gives some tenths eV which is much larger than the activation energy between 100K and 300K.

In Fig.3 the resistivity of a non-intentionally doped crystal is shown above 250K, which has in contrast to the undoped sample of Fig.1a much higher resistivity. The resistivity of this undoped sample decreases in the whole temperature range without the drastic changes shown in Fig.2. Especially there is no activation of a shallow impurity. But the averaged activation energy at high temperatures is in agreement with that of the Cr-doped sample above 600K. This high activation energy is obviously not connected with the intentional doping. With regard to the results on the thermopower the decrease of  $\rho(T)$  above 600K reflects in both the doped and undoped samples the onset of intrinsic conduction [17,19].

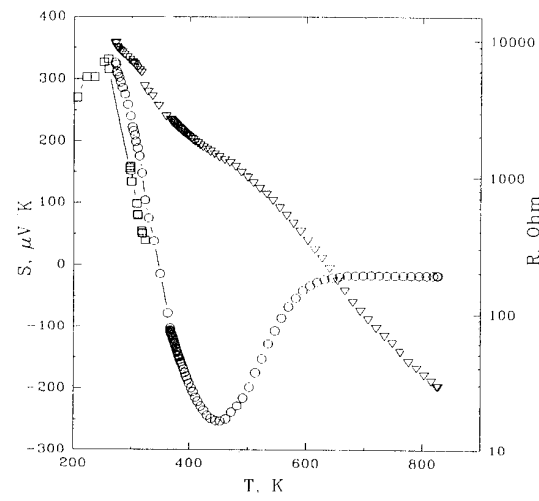


Fig.3 Electrical resistivity and thermopower of non-intentionally doped high ohmic  $\beta$ -FeSi<sub>2</sub>

From Hall measurements it was already concluded in [20] that at low temperatures conduction takes place within an impurity band and that additional impurity states exist below this band. The activation energies determined in [20] are in the same order of magnitude as found in our measurements.

#### *Thermopower:*

The temperature dependence of the thermopower  $S(T)$  of the doped  $\beta$ -FeSi<sub>2</sub> crystals corresponds to the behaviour of the resistivity. There are also four temperature ranges with different temperature dependences. In Fig.2 the results are shown for the Cr-doped sample in the range from 60K to 1050K. The thermopower shows an oscillating behaviour with two maxima at about 150K and 580K. Below the first

maximum  $S(T)$  shows a very strong increase with increasing temperature. The decrease above 150K follows up to about 350K a  $1/T$ -law. The following increase of  $S(T)$  up to 600K and the decrease for  $T > 600$ K completely correspond to the temperature dependence of the resistivity. The decrease of  $S(T)$  leads at  $T \approx 850$ K to a change in sign.

This behaviour of the thermopower can be qualitatively explained in agreement with the results of the resistivity and carrier concentration. The sharp increase of  $S(T)$  above 70K from small values of about  $10\mu\text{V/K}$  to more than  $600\mu\text{V/K}$  at 150K is connected with the transition from conduction in the impurity band to conduction in the valence band. If the conduction occurs mainly within the valence band  $S(T)$  shows the usual  $E_A/T$ -behaviour of a semiconductor with conduction in one band. The corresponding activation energy is in Cr-doped samples between 30meV and 50meV in agreement with the Hall data. The increase of  $S(T)$  between 350K and about 600K corresponds also to the behaviour of the resistivity. The thermopower increases linear with  $T$  as in metallic systems. The decrease above 600K reflects the onset of intrinsic conduction. This interpretation is supported by the change in sign at the highest temperatures. Also the behaviour of  $/S(T)$  at  $T > 600$ K of the undoped sample (Fig.3) is consistent with the assumption of the onset of intrinsic conduction.

There is an alternative explanation of the strong increase of  $S(T)$  at low temperatures and of the first maximum. At low temperatures ( $T \approx T_{\text{Debye}}/5$ ) in addition to the electronic contribution also the phonon system can contribute to the thermopower [15,16]. This phonon drag effect can lead to a low temperature maximum of  $S(T)$  with an increase  $S(T) \propto T^\alpha$  with  $\alpha=3$  in metals [15] and  $3/2 \leq \alpha \leq 5$  in semiconductors [16]. Experimentally the increase of  $S(T)$  can be fitted in corresponding temperature ranges with an exponent  $2 < \alpha < 4$ . Assuming the occurrence of this effect one has to explain the decrease of  $S(T)$  above the first maximum by a combination of the decrease of the phonon drag effect and of the electronic part of the thermopower. From the experimental point of view further investigations are necessary to decide between the two interpretations.

In Fig.4 the thermopower is shown of a Co-doped  $\beta$ - $\text{FeSi}_2$  crystal. This n-type sample exhibits the same

temperature dependence  $S(T)$  as the p-type Cr-doped sample. Again there are four ranges of different behaviour at similar temperatures and with similar activation energies. The only small difference is the slope in the temperature range between 300K and 550K. In Cr-doped samples the slope is positive, in Co-doped samples negative.

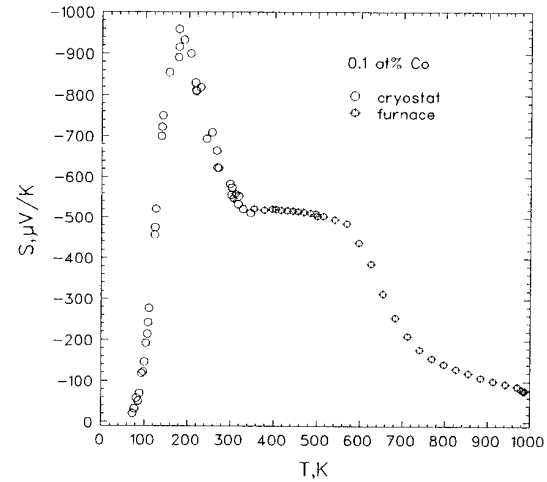


Fig.4 Thermopower of Co-doped  $\beta$ - $\text{FeSi}_2$  with Co content 0.1at%

The explanation of the decrease of thermopower and resistivity above 600K with the onset of intrinsic conduction requires the comparison of the corresponding activation energy with the energy gap. From optical measurements the direct gap was determined to be  $E_g = 0.80 \dots 0.85\text{eV}$  [17]. An indirect gap was found about 0.01eV below this direct one. These results are in agreement with the bandstructure calculations in [18]. From this it follows  $E_A = E_g/2 = 0.4\text{eV}$  for the activation energy of intrinsic conduction in good agreement with the resistivity data.

Similar results for thermopower and resistivity as shown in Figs.2-4 were found in sintered  $\beta$ - $\text{FeSi}_2$  doped with Al and Co [1]. Several samples exhibit also the four characteristic temperature ranges discussed above. In [1] the data were explained including polaron effects due to strong electron phonon coupling in  $\beta$ - $\text{FeSi}_2$ . Only further investigations including high temperature Hall measurements and with that a more quantitative description should give insight in the strength of this coupling and the role of polaron effects.

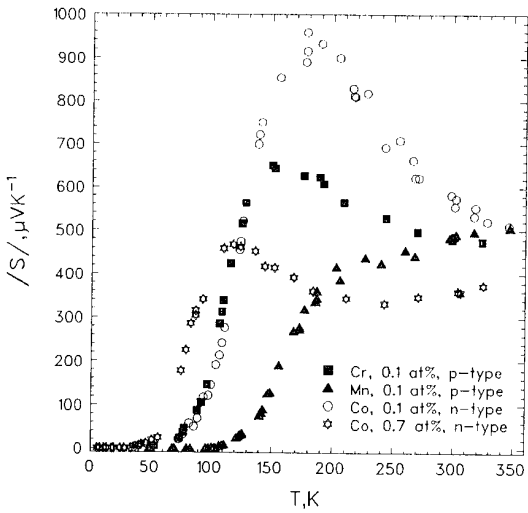


Fig.5 Thermopower of n-type and p-type  $\beta$ -FeSi<sub>2</sub> below 300K

In Fig.5 the low temperature thermopower is shown in more detail. The results of n-type and p-type samples are compared. The main features of S(T) are the same for all samples: small values  $< 10 \mu\text{V}/\text{K}$  below 50...80K, a strong increase at 75...125K up to 500...1000  $\mu\text{V}/\text{K}$  and above the maximum a decrease according to band conduction. Only in the Mn-doped crystal the increase of S(T) is more slowly and does not result in a maximum.

## Conclusions

The effect of doping on the transport properties of  $\beta$ -FeSi<sub>2</sub> single crystals has been investigated. Thermopower, resistivity and the Hall constant were measured and qualitatively discussed. It was found that there exist four temperature ranges with different temperature dependences of the transport parameters.

It was concluded that at low temperatures conduction takes place mainly within an impurity band and at higher temperatures mainly in the conduction (valence) band. The change between these two regimes is rather sharp which seems to be a general feature of doped  $\beta$ -FeSi<sub>2</sub> but is not yet understood. From the activated behaviour of thermopower and resistivity the existence has been deduced of impurity states below the impurity bands. These additional impurity states are probably not connected with the intentional doping.

Further investigations will be done to get a more quantitative insight into the transport mechanisms and to find the dependence on impurity concentration. Then it should also be possible to clarify the role of phonon drag effects and of polaron conduction.

## Acknowledgments

One of us (A.B.) is very grateful for financial support to the Dr.Wilhelm Heinrich Heraeus und Else Heraeus-Stiftung (Hanau).

## References

- [1] U.Birkholz, J.Schelm, phys.stat.sol. 27 (1968) 413.
- [2] I.Nishida, J.Mat.Sci.Soc.(Japan) 15 (1978) 15.
- [3] C.B.Vining, Proc. IX. Intern. Conf. Thermoel., Pasadena, Calif. Inst. Techn. (1990) p.249.
- [4] Y.Isoda, T.Ohkoshi, I.Nishida and H.Kaibe, J. Mater. Science Soc. Jap. 25 (1989) 311.
- [5] U.Stöhrer, R.Voggesberger, G.Wagner and U. Birkholz, Energy Convers. Mgmt. 20 (1990) 143.
- [6] M.Kombayashi and S.Ido, Jap.J.Appl.Phys. 30 (1991) 2883; J.Cer.Soc.Jap.Int.Ed. 100 (1992) 21.
- [7] M.Kombayashi, K.Hijikata and S.Ino, Jap.J. Appl.Phys. 30 (1991) 331.
- [8] K.Matsubara, K.Kishimoto, K.Nagao, O.Ueda, T.Miki, T.Koyanagi and I.Fujii, Proc. XII. ICT, 1993, eds. K.Matsuura, Tokyo 1994, p.223.
- [9] A.Heinrich, C.Gladun, A.Burkov, J.Schumann and D.Elefant, AIP Conf.Proc. 316 (1995) p.45.
- [10] S.Tokita, T.Amato, M.Okabayashi and I.A.Nishida, see[8] p.197.
- [11] Y.Isoda, M.A.Okamoto, T.Ohkoshi and I.A.Nishida, see [8] p.192.
- [12] K.Matsubara, T.Koyanagi and T.Tagaki, Proc. 6th IC Thermoel Energy Conv., Arlington (1986) p.1.
- [13] K.Irmscher, W.Gehlhoff, Y.Tomm and H.Lange, Proc. GADEST'95, Berlin, to be published.
- [14] Y.Tomm, L.Ivanenko, K.Irmscher, S.Brehme, W.Henrion, I.Sieber and H.Lange, E-MRS 1995, Symposium G, paper G-IV/P44, to be published.
- [15] R.D.Barnard, „Thermoelectricity in Metals and Alloys“, Taylor&Francis, London (1972).
- [16] S.M.Puri and T.H.Geballe, in „Semiconductors and Semimetals“ vol.1, Academic.Press, New York 1966, p.203.
- [17] C.A.Dimitriades, J.H.Werner, S.Logothetidis, M.Stutzmann, J.Weber and R.Nesper, J.Appl.Phys. 68 (1990)1726.
- [18] N.E.Christensen, Phys.Rev. B 42 (1990) 7148.
- [19] M.C.Bost, J.Mahan, J.Appl.Phys. 58 (1985) 2696.
- [20] E.Arushanov, Ch.Kloc and E.Bucher, Phys.Rev. B 50 (1994) 2653.

## INVESTIGATION OF DOPANTS FOR RUTHENIUM SILICIDE

A. Yamamoto, T. Ohta, \*Y. Sawade, T. Tanaka and \*K. Kamisako

*Electrotechnical Laboratory, AIST, MITI  
Umezono 1-1-4 Tsukuba-city Ibaraki 305, JAPAN*  
*\*Tokyo University of Agriculture and Technology*

An attempt was made to find proper dopant elements for ruthenium silicide ( $\text{Ru}_2\text{Si}_3$ ). Samples were prepared by the arc-melting/hot-pressing method. While undoped samples thus obtained exhibited p-type conduction and had carrier concentrations on the orders of  $10^{24} \text{ m}^{-3}$ , the phosphorous- and gallium-doped sample exhibited n-type conduction with high carrier concentration on the order of  $10^{26} \text{ m}^{-3}$ . It was found that phosphorous and gallium can be used as an n-type dopant and phosphorous is a candidate of dopant that enables carrier concentration over  $10^{26} \text{ m}^{-3}$ .

## Introduction

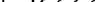
It is well known that many transition metal silicide groups exhibit semiconductive properties. Moreover they usually have high melting points, low electrical resistivities and quite large Seebeck coefficients that are favorable for high temperature thermoelectric material. From these reasons, energetic researches on the transition metal silicides such as IrSi<sub>2</sub>, Ru<sub>2</sub>Si<sub>3</sub>, OsSi<sub>2</sub>, CrSi<sub>2</sub>, FeSi<sub>2</sub>, MnSi<sub>2</sub> have been done[1-4] and several candidates for thermoelectric materials were selected. Ruthenium silicide, which has a crystal structure of the orthorhombic symmetry group[5] and a lower thermal conductivity compared with currently used SiGe, was chosen as one of the candidates based on experimental data on transport properties and semi-quantitative prediction[6].

Measured intrinsic properties of polycrystal[7] and single crystal[8] Ru<sub>2</sub>Si<sub>3</sub> confirmed the potential for high temperature applications. The thermal conductivity, around 2 W/mK at 1000K, was much lower than that of SiGe alloys[9]. The measured Seebeck coefficients, varying from -400 to 300  $\mu$ V/K

in polycrystal and -200 to 450  $\mu$ V/K in single crystal Ru<sub>2</sub>Si<sub>3</sub>, were large enough to proceed to further investigations. The temperature dependence of the electrical resistivity showed ordinary semiconducting properties which had an intrinsic region above 700K. Although the resistivity in the extrinsic region was rather high, on the order of  $10^2 \Omega m$ , this value seemed to be decreased by proper doping. These measured data on undoped Ru<sub>2</sub>Si<sub>3</sub> were enough to prove its potential.

The only problem was how to optimize its thermoelectric properties, actually, its carrier concentration. In order to maximize the figure of merit, carrier concentrations on the order of  $10^{26} \text{ m}^{-3}$  must be achieved without reducing the carrier mobility seriously.

For this problem, a number of efforts toward finding proper dopants have been made in Jet Propulsion Laboratory as shown in Figure 1 and several favorable doping elements such as manganese for p-type and iridium for n-type have been identified. However, fundamental progress on figure of merit has not been realized yet.

Fig.1 Candidate dopants examined experimentally up to this point. (+) and (-) indicate sign of the Hall coefficient at room temperature  indicate experiment in JPL[10], and  this study.

In this study, attempts were made to find a proper dopant by using the arc-melting/hot-pressing method. An adoption of this processing technique to ruthenium silicide was performed successfully and reported earlier[11]. Undoped sample thus obtained showed self-doped p-type properties and had much lower resistivity than that of single crystal ones. Supposing substitution for silicon atoms, dopant elements were selected from untested groups seen in Figure 1. By using following methods, the investigation was carried out.

### Experimenal details

The aim of this investigation is to identify the proper dopant element for ruthenium silicides. Initial ingots were prepared by arc-melting on a water cooled copper hearth. These ingots were prepared from 99.99% purity ruthenium, silicon and dopant element powder. Each dopant element was added to be 1 at% of total amount (10 grams) of the ingot. Only a small weight loss was observed after arc-melting. Examination was carried out by using atomic absorption spectroscopy(AAS) in order to determine the very dissolved amount of dopant. After the arc-melting, an ingot thus obtained was pulverized into powder again and classified under 100 mesh. Testing specimens, having dimensions of 10 mm in diameter and approximately 1 mm in thickness, were prepared by hot-pressing the powder at 1450–1610 °C and 69 MPa for 4 hours in argon atmosphere.

All hot-pressed samples were fully dense (>98%) and had good mechanical strength. These samples were polished with aluminum oxide ( $\text{Al}_2\text{O}_3$ ) powder to avoid any effects of surface conditions.

Examinations under optical and electron microscope were done in order to observe textures seen in samples. Although it was a very small amount, there were secondary phases in  $\text{Ru}_2\text{Si}_3$  main phase. By using EPMA, Shimadu EPM-810, the phase were identified as ruthenium rich phase such as  $\text{RuSi}$  and  $\text{Ru}_2\text{Si}$ . Tests under X-ray diffraction were also done and diffraction patterns obtained from  $\theta - 2\theta$  observation indicated that  $\text{Ru}_2\text{Si}_3$  was successfully synthesized while some samples had very weak peaks corresponding to ruthenium rich phase. Lattice constants of each sample were identified from the peak shift of XRD patterns.

Hall mobility and resistivity measurements were performed simultaneously between room temperature and 900K using the van der Pauw method. The Seebeck coefficient was estimated from the electromotive force at a temperature difference of 50K in a range from room temperature to 1300K. The thermal conductivity was calculated using the measured density, the thermal diffusivity and the heat capacity. The thermal diffusivity was measured by laser flash method with an estimated error of  $\pm 2\%$ . Densities and heat capacities were estimated by the Archimedes method and a differential scanning calorimetry, respectively.

### Results

Table 1 summarizes results of doping test measured at room temperature. The net amount of dissolved dopant was measured by using atomic absorption spectroscopy. Every dopant element was added to be 1 at% of total amount before arc-melting, however, there were wide variations in measured values. By microscopic observation very few cracks and pores were seen in hot-pressed samples and the grain size were determined to be up to  $50 \mu\text{m}$  and isotropic. Except of gallium-doped and zinc-doped samples, small dispersed ruthenium rich phases were observed. The sintering qualities of doped samples were better than that of undoped ones.

In XRD pattern of hot-pressed samples each peaks observed were corresponding to standard peak with slight peak shifts. All doped samples had peaks at decreased  $2\theta$ , which means the dissolution of the dopant into the matrix expands the crystal structure of  $\text{Ru}_2\text{Si}_3$ . Lattice constants of  $\text{Ru}_2\text{Si}_3$  unit cells were calculated from XRD peaks corresponding to (102); (200), (240) planes also shown in Table 1. The expansion of the lattice reaches 2-3%.

The results of Hall measurements at room temperature are also shown in Table 1. The carrier concentration was calculated by usual manner of  $n = 1/R_H/e$  and Hall mobility was calculated from the electrical resistivity and the Hall coefficient with the relation of  $\mu = R_H/\rho$ . While the carrier concentration of the undoped sample was  $6 \times 10^{25} \text{ m}^{-3}$ , that of doped samples varied in a wide range from  $9.8 \times 10^{25} \text{ m}^{-3}$  of n-type to  $3.5 \times 10^{25} \text{ m}^{-3}$  of p-type. Substantial changes were observed in manganese-,

Table 1. Results of doping test

	Ag	Au	Bi	Cu	Ga	In	Mn	Nb	P	Sb	Zn	Undoped
Dissolved %	0.47	0.76	0.66	0.64	0.58	0.02		0.49	0	0.28	0.65	
Lattice const	a	5.530	5.547	5.567	5.613	5.530	5.599	--	5.618	5.663	5.599	5.562
	b	11.06	11.24	11.09	10.94	11.06	11.11	--	11.11	11.14	11.11	11.08
	c	8.951	8.979	9.030	9.144	8.938	9.109	--	9.144	9.256	9.100	9.028
Carrier conc. n	0.6	0.7	0.6	1.2	-1.9	1.0	3.5	2.0	-9.8	0.4	0.06	0.6
Mobility	15.8	5.9	21.2	2.8	0.5	14.1	4.8	9.8	3.8	4.5	11.4	6.8

Units : lattice constants in  $10^{-10}\text{m}$ , Carrier concentration in  $10^{25}\text{ m}^{-3}$  mobility in  $10^{-4}\text{ m}^2/\text{Vs}$ .  
(-) sign in Carrier concentration denotes n-type conduction.

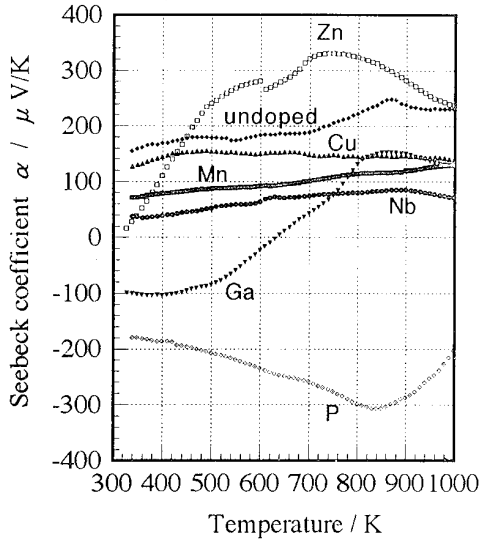


Fig. 2 Seebeck coefficients of hot-pressed samples. Dopants plotted here exhibited apparent changes in Seebeck coefficients Ag, Au, Bi, In, Sb doped samples had the same values as undoped ones.

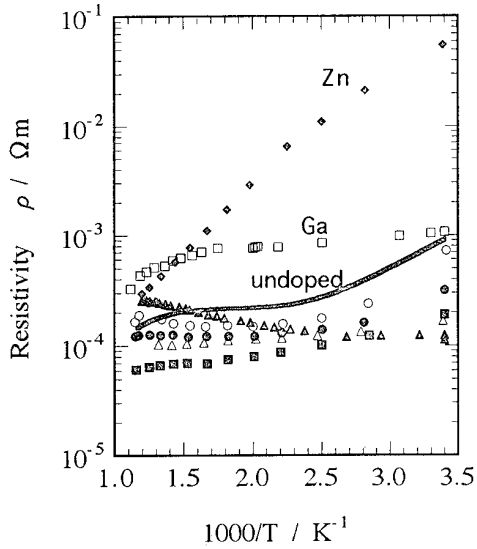


Fig. 3 Temperature dependence of resistivity. The line indicates the undoped sample and mark  $\circ$ ,  $\otimes$ ,  $\triangle$ ,  $\square$ ,  $\blacksquare$  indicate Bi, In, Mn, P, Nb, respectively. Elements not shown here did not exhibit changes from the undoped sample.

niobium- and phosphorous-doped samples. The Hall mobility at room temperature was higher than that of single crystal ones [8].

The temperature dependence of the Seebeck coefficient and the electrical resistivity are shown in Figures 2 and 3. The Seebeck coefficient of the undoped sample exhibited p-type. While manganese and niobium acted as p-type dopant and gallium and phosphorous acted as an n-type dopant, other dopants such as indium, copper, silver, gold, bismuth and antimony had only small effects on the Seebeck coefficients.

The resistivity of undoped and doped samples, except phosphorous-doped one, decreased with increasing temperature

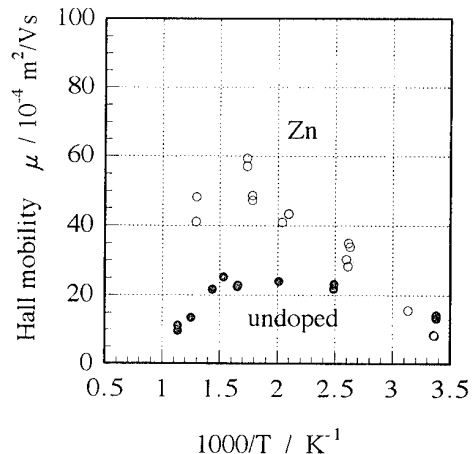


Fig. 4 Temperature dependence of the Hall mobilities

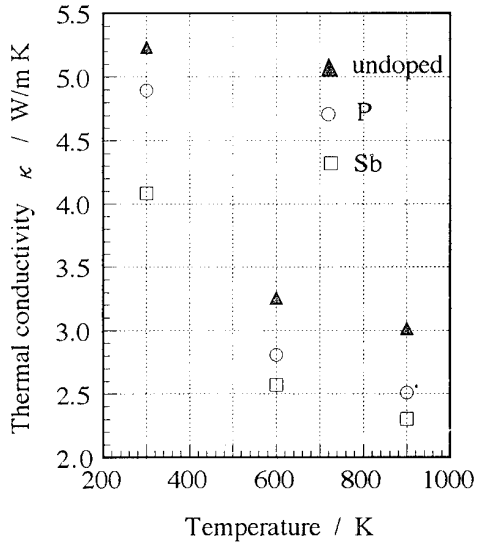


Fig. 5 Temperature dependence of the thermal conductivity

over the entire temperature range. Although a pure intrinsic semiconductor has a transition temperature from extrinsic to intrinsic region, hot-pressed samples exhibit rather weak dependence on temperature. The niobium-doped sample has a resistivity of  $2 \times 10^{-4} \Omega \text{m}$  at room temperature, that is two orders lower than that of single crystal ones.

Figure 4 shows results of Hall measurements on undoped and zinc-doped samples. The Hall mobility of both samples had maxima of  $6 \times 10^{-3} \text{ m}^2/\text{Vs}$  and  $25 \times 10^{-3} \text{ m}^2/\text{Vs}$  around 600 K and they were on the same level as polycrystal ones[7]. The carrier concentrations of these two samples increased with increasing temperature. These temperature dependences are quite usual for a semiconductor. The zinc-doped sample had a low carrier concentration on the order of  $10^{23} \text{ m}^{-3}$ , the same order as measured in single crystal ones[8].

Figure 5 shows the thermal conductivity of undoped, antimony-doped and phosphorous-doped samples. The thermal conductivity decreases with increasing temperature and phosphorous- and antimony-doped samples have lower values than undoped ones over the entire temperature. This appears to be due to the effects of the dissolution of dopant atoms into the Ru<sub>2</sub>Si<sub>3</sub> matrix in the same way as reported in the investigation of SiGe system[12].

### Discussion

In order to achieve a high carrier concentration, it is necessary for a dopant to have two features, a high solubility into the matrix and a high electrical activity as a source of carriers. Though the dissolution into matrix was confirmed by checking the peak shifts of XRD pattern, the measured amount of very dissolved dopant revealed that the aimed 1at% of the total amount was not achieved. There are many factors such as arc-melting temperature, melting point of a dopant influencing this deficiency of dissolved dopant. Here we took notice of the ionic radii of each dopant. Ruthenium and silicon have ionic radii of 1.34 Å and 1.32 Å, respectively. As shown in Figure 6, while the estimated dissolution amount would have some errors, those amount and the ratio of ionic radii seems to have some correlations nevertheless. A large difference between the radii of ruthenium and the dopants results in a deficiency of dopant and it is difficult to achieve a high carrier concentration.

The electrical activity, the other important feature for a dopant, was calculated from the carrier concentration and the dissolved amount of dopants. Figure 7 shows the carrier concentration change per dissolved net amount of dopant. Because of the very small net amount of doped phosphorous and uncertainty in the measurement, it is not plotted in the figure. However, phosphorous is the most active dopant as seen in Table 1. As shown in Figure 7, it is evident that indium- and phosphorous-doped samples are much more effective as sources of carriers than zinc- manganese- and niobium-doped samples. While indium and phosphorous atoms are likely to substitute for silicon atoms considering the periodic table, manganese and niobium atoms are likely to substitute for ruthenium atoms. It appears that there is a correlation between the substitution site of the doped atoms and attainable carrier concentrations. This results would be understandable by taking its crystal structure into account, however, there is no consistent interpretation of this result yet.

In the undoped sample, the microscopic observation revealed that there are small amounts of ruthenium rich phases and silicon deficiency around those phases. An vacancy production of silicon atom sites means a creation of holes, because ruthenium atoms seemed to attract electrons from silicon

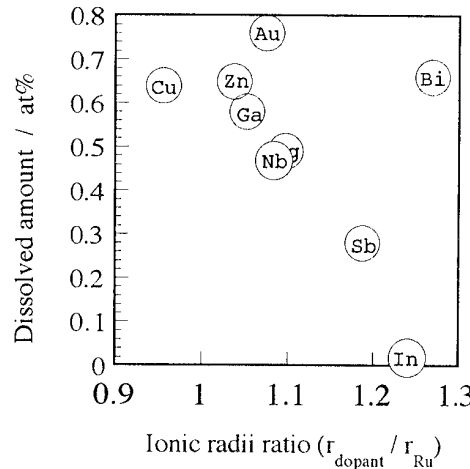


Fig.6 Ionic radii ratio vs dissolved amount of dopants

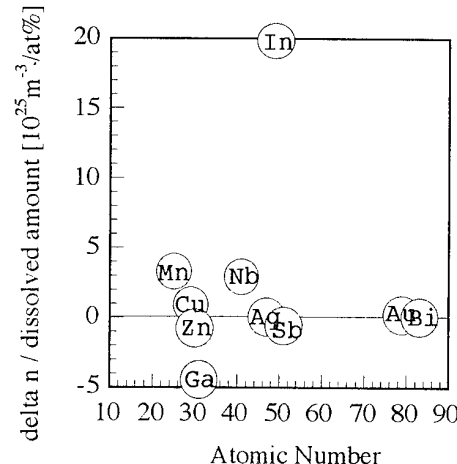


Fig. 7 Electrical activity of dopants

atom in order to stabilize its  $\beta$ -Sn structure[13]. The undoped hot-pressed sample exhibited a p-type conduction as shown in Figure 2, and such a deficiency of silicon atoms seems to be the main reason of the p-type properties of the undoped sample. In doped samples, on the other hand, it is confirmed that a dopant also act as a sintering agent. Only a few pores were observed in the sample, that means a lower level of ruthenium deficiency. As shown in Figure 3, zinc- and gallium-doped samples have higher resistivities, and this seems to be due to a depletion of holes which were created by lack of silicon atoms. Moreover, the zinc-doped sample had a higher Hall mobility compared with the polycrystalline sample made by using the Bridgman method[7]. This means that the addition of dopants decreases the scattering of carriers in some cases.

### **Conclusions**

The results of examinations on the Ru<sub>2</sub>Si<sub>3</sub> doped sample prepared by arc-melting/hot-pressing method revealed the following points;

- (1) The ionic radii ratio is a good index to estimate the solubility of the dopant into the matrix material.
- (2) Dopant elements near to silicon in the periodic table are more effective than transition metal elements.
- (3) Both indium and phosphorous are electrical active dopants, even though phosphorous is the candidate which makes it possible to achieve high carrier concentration.

### **Acknowledgment**

The authors wish to express their special thanks to Dr. A.Negishi for his help on XRD, SEM and EDX , Dr. S.Yoshida for Hall effect measurements and Dr. T.Baba for thermal conductivity measurements.

### **References**

- [1] Vining, C. B., Proc. of the 9th Int.Conference on Thermoelectrics, pp. 249-259 (1990)
- [2] J.Hesse, Phys. Rev. 5, p.272 (1970)
- [3] I.Nishida, J.Mater.Sci., 7, p.1119 (1972)
- [4] I.Nishida, J.Mater.Sci., 7, p.435 (1972)
- [5] D.J.Poutcharovsky, Acta Cryst., B30, p.2692 (1974)
- [6] Vining, C. B., Proc. of the 9th Symposium on Space Nuclear Power Systems 1, pp. 338-342. (1992)
- [7] Ohta, T., Vining, C. B. and Allevato, Proc. of the 26th IECEC 3, pp. 196-201. (1991)
- [8] Vining, C. B. and Allevato, C. E., Proc. of 10th Int. Conference on Thermoelectrics, pp. 167-173 (1991)
- [9] J.S.Beaty et al., Proc. of 27th IECEC 3, pp.471-475 (1992)
- [10] Vining, C. B. and Allevato, C. E., Proc. of 27th IECEC 3, pp.489-492 (1992)
- [11] Y.Sawade et al., Proc. of 13th Int. Conference on Thermoelectrics, pp. 99-104 (1994)
- [12] F.D.Rosi,Solid State Electronics, 11, p.833 (1968)
- [13] W.Jeitschko, Acta Crystallogr., 22, p.417 (1967)

## Temperature dependence of thermoelectric properties of SiC/Al

Y. Okamoto, A. Aruga, H. Tashiro, J. Morimoto, T. Miyakawa and S. Fujimoto

*Department of Materials Science and Engineering National Defense Academy*

*Hashirimizu, Yokosuka, Kanagawa, 239 Japan*

The thermoelectric properties of the p-type SiC/Al system has been studied over the temperature ranging from room temperature to 700°C as a function of both Al concentration ( $x = 0.5 \text{ wt.\%} \sim 4 \text{ wt.\%}$ ) and sintering temperature ( $T_s = 1950^\circ\text{C} \sim 2250^\circ\text{C}$ ). Drastic decrease of electrical resistivity is observed at higher temperature. Though, thermal conductivity shows its low value about 10W/K, electrical resistivity has a minimum value  $10^{-3} \Omega \text{ m}$  at 700°C for  $x = 4.0 \text{ wt.\%}$ ,  $T_s = 2250^\circ\text{C}$ . The figure of merit Z approaches to the  $4 \times 10^{-4} \text{ K}^{-1}$  around 700°C. We conclude that the SiC/Al system is a promising candidate for thermoelectric devices at high temperature region.

### 1 Introduction

Recently, strong effort has been directed towards the development of sintered thermoelectric materials with improved characteristics at comparatively higher temperatures. We have reported on room temperature performance of sintered  $\text{Bi}_2\text{Te}_3$ [1, 2] system and temperature dependence of thermoelectric properties of p-type SiC/ $\text{B}_4\text{C}$  system[3,4] over the range  $RT \sim 600^\circ\text{C}$ .

While  $\text{Bi}_2\text{Te}_3$  system is promising at room temperature, SiC based system is expected to be useful at higher temperature region because of pyrolytic property of SiC. Measurements of electrical resistivity, thermoelectric power and thermal conductivity on SiC as a function of both  $\text{B}_4\text{C}$  concentration, temperature and sample porosity revealed that the figure of merit of this system reaches up to  $10^{-6} \text{ K}^{-1}$  at around 600°C. And also, we have reported about control of thermal conductivity through sample porosity[5].

Here we report on the results of study on the temperature dependence of thermoelectric properties of SiC/Al system over the temperature range  $RT \sim 700^\circ\text{C}$ . We found that electrical conductivity and figure of merit of the SiC/Al system can be improved drastically compared to SiC/ $\text{B}_4\text{C}$  system.

### 2 Experiment

#### 2.1 Sample preparation

$\beta$ -SiC (average particle size  $0.15 \mu\text{m}$  and BET surface area  $19.5 \text{ m}^2/\text{g}$ , Mitsui Toatsu Co., Ltd. MSC-20) and Al (average particle size  $3 \mu\text{m}$ , Rare Metallic Co., Ltd.) were used as starting materials.

Slurries were made from mixed SiC and  $0.5 \sim 20.0 \text{ wt.\%}$  Al powders in polyethylene jars with nylon coated iron balls as the grinding media and xylene solution as the mixing agent. After mixing for 20 hours and passing through  $75 \mu\text{m}$  mesh sieve, these slurries were dried. The dried mixture were granulated using  $500 \mu\text{m}$  mesh sieve and pressed into  $20 \text{ mm} \phi \times 6 \text{ mm}$  pellet at  $2 \times 10^{17} \text{ N/m}^2 (\sim 0.2 \text{ ton/m}^2)$ . Then the pellets were sealed into an evacuated rubber tube and then pressed isostatically at  $2 \times 10^{18} \text{ N/m}^2 (\sim 2 \text{ ton/m}^2)$ .

Each pellet covered with the same compositional powder was placed into a carbon crucible. Sintering procedure was carried out heated by RF induction. First, the furnace was heated up to  $1100^\circ\text{C}$  at a rate of  $20^\circ\text{C}/\text{min}$ . in vacuum, and Ar gas was introduced up to normal pressure. Then the temperature was raised to sintering temperature ( $1950^\circ\text{C}$ ,  $2100^\circ\text{C}$ ,  $2250^\circ\text{C}$ ) at a rate of  $10^\circ\text{C}/\text{min}$ ., the sample is kept at this temperature for 2 hours and cooled naturally down to room temperature. Sintered materials were cut into rectangular shaped specimens of  $3 \times 4 \times 8 \sim 10 \text{ mm}^3$  in dimensions.

#### 2.2 Thermal and electrical measurement

The crystal properties and constituent of prepared samples are studied by using powder X-ray diffraction and ICP (Inductively Coupled Plasma). Measurements of thermoelectric power and DC electrical resistivity were made over the temperature range from room temperature to  $700^\circ\text{C}$ , while those on thermal conductivity is made on the temperature range from room temperature to  $300^\circ\text{C}$ . Conventional four probes method was employed in

DC electrical resistivity measurement. Thermoelectric power is measured by the standard DC method.

Thermal conductivity measurement was made by a differential phase analysis of PPE(Photo Pyro Electric) signal ( $\Delta L - \Delta \theta$  analysis) reported in our previous paper[6,7].

In the PPE method one can measure thermal diffusivity  $\alpha$ . Thermal conductivity is given by

$$\kappa = \alpha \cdot d \cdot C \quad \dots \dots \dots (1)$$

here,  $\kappa$ ,  $\alpha$ ,  $d$  and  $C$  are thermal conductivity, thermal diffusivity, density and specific heat, respectively. We calculate specific heat of SiC/Al system from that of SiC and Al. The values of  $d$  and  $\alpha$  were measured. At room temperature, we use PVF<sub>2</sub> (Poly Vinylidene diFloride) films as heat sensor in the PPE measurement, because of high sensitivity. In the higher temperature region, we use thermocouple as in previous reports.

### 3 Results and Discussion

#### 3.1 Crystal property

The crystal properties and composition of prepared samples are studied by using powder X-ray diffraction and ICP. A number of large diffraction peaks can be assigned to SiC. Additional small peaks can not be identified to the compound materials of Si, Al and/or C. From the results of powder X-ray diffraction, it is found that crystal structure of SiC/Al sintered materials changes into  $\alpha$ -SiC after sintering at 2250°C. After sintering at 2100°C and 1950°C, crystal structure remains  $\beta$ -SiC same as starting SiC powder. No dominant impurities were found from ICP analysis.

#### 3.2 Al concentration dependence at RT

Figure 1 shows Al concentration  $x$  and sintering temperature  $T_s$  dependence of sample density. Sample density increases with Al concentration, but not influenced by sintering temperature. The samples with Al concentration higher than 4 wt.% became deformed hardly. Therefore, we could not measure their thermoelectric properties exactly. This deformation may be responsible to low melting point of Al.

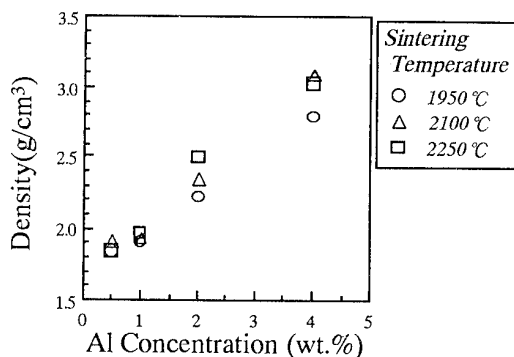


Figure 1 The Al doping concentration and sintering temperature dependence of sample density.

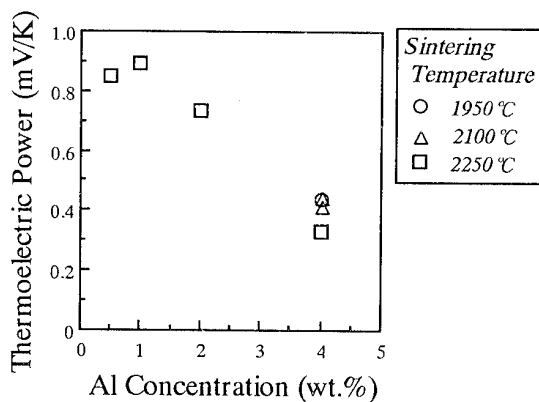


Figure 2 The Al doping concentration and sintering temperature dependence of thermoelectric power measured at room temperature.

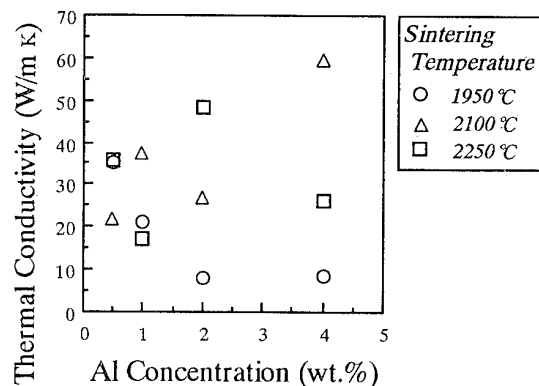


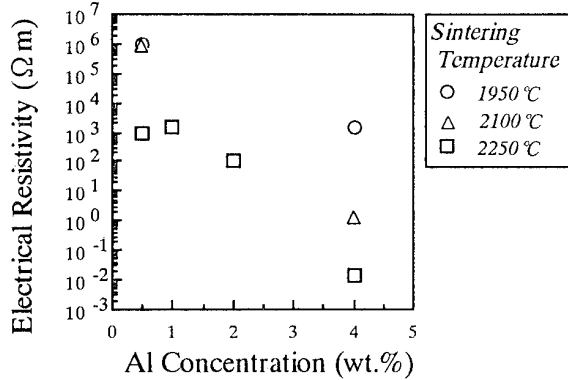
Figure 3 The Al doping concentration and sintering temperature dependence of thermal conductivity measured at room temperature.

Figure 2 shows electrical resistivity at room temperature as a function of  $x$  and  $T_s$ . Nonlinearity in current voltage characteristics could not be observed. Electrical resistivity decreases drastically, with increase in  $x$  and  $T_s$ . The electrical resistivity of samples with lower  $x$  and lower  $T_s$  was too high ( $> 10^9 \Omega$ ) to be measured accurately with our experimental apparatus.

Figure 3 shows thermoelectric power at room temperature as a function of  $x$  and  $T_s$ . Thermoelectric power decreases with  $x$ , but sintering temperature dependence is not well defined.

Figure 4 shows thermal conductivity at room temperature as a function of  $x$ . From this figure, we could not find definite dependence on Al concentration and/or sintering temperature.

Figure 5 shows figure of merit at room temperature as a function of Al concentration. The figure of merit Z is evaluated from electrical resistivity, thermal conductivity and thermoelectric power. The figure of merit Z increases about 4 decades with the increase in  $x$  range from 0.5% to 4%.



**Figure 4** The Al doping concentration and sintering temperature dependence of electrical resistivity measured at room temperature.

### 3.3 Temperature dependence

Figure 6 shows temperature dependence of electrical resistivity. The resistivity of these samples exhibit typical semiconductor-like temperature dependence and decreases from 5 to over 20 decades with increase in temperature from 20 ~ 700°C. The decrease of the resistivity becomes weaker for samples with higher concentration of Al.

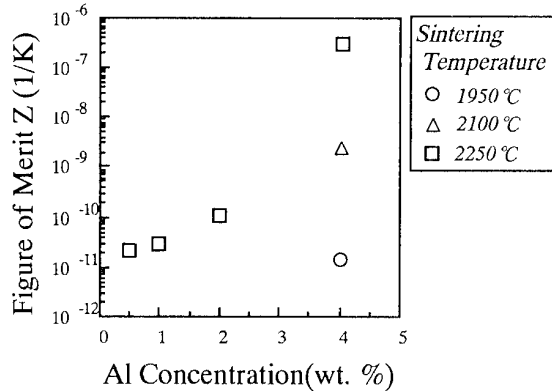


**Figure 5** The Al doping concentration and sintering temperature dependence of figure of merit Z measured at room temperature.

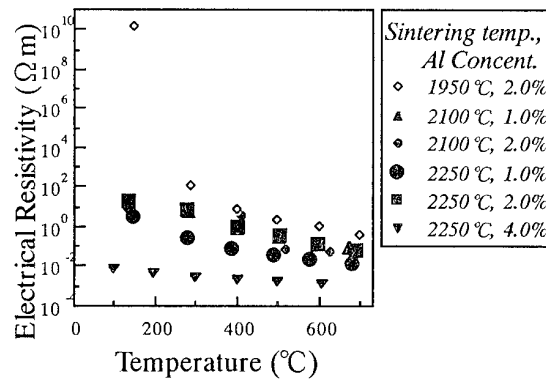


**Figure 6** The temperature dependence of electrical resistivity.

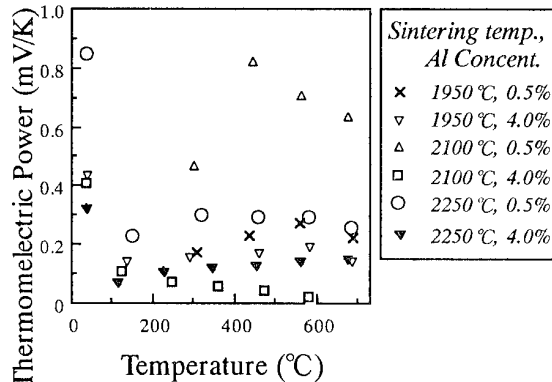


**Figure 7** Temperature dependence of thermoelectric power.

Figure 7 shows the temperature dependence of thermoelectric power. Almost all the samples have

thermoelectric power which stays almost constant within factor of 2, over this temperature range.

Figure 8 shows temperature dependence of thermal conductivity measured from temperature 20 up to 300 °C. In the temperature range 20 ~ 100 °C, thermal conductivity decreases with temperature, and over 100 °C, thermal conductivity tends to saturate.

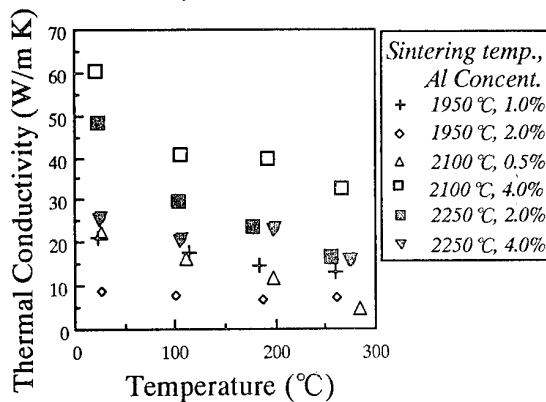


**Figure 8** The temperature dependence of thermal conductivity with varying the Al doping concentration and sintering temperature.

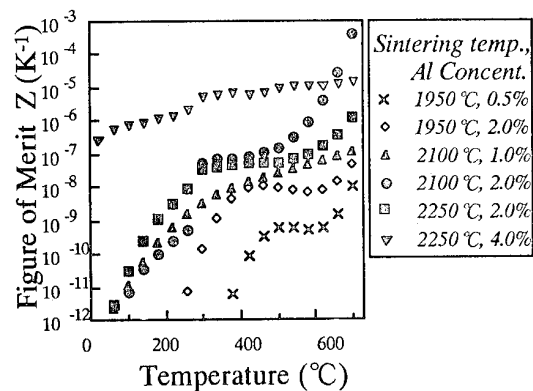


**Figure 9** The temperature dependence of figure of merit Z calculated from measured values of electrical resistivity, thermal conductivity and thermoelectric power.

Figure 9 shows the figure of merit Z of the samples as a function of temperature. The figure of merit Z is estimated using least squares fitting of electrical resistivity, thermoelectric power and thermal conductivity by polynomial functions of temperature. In this procedure, we have made an assumption that thermal conductivity stays constant over 300 °C. The figure of merit Z increases with temperature over the range studied

in this report. The samples with 4 % Al concentration and 2100°C and 2250°C sintering temperature show a very weak increase (< 1.5 decade/700 degree) in figure of merit. Another sample shows an increase in Z over 7 decades over a temperature range RT ~ 700°C

Compared with practical materials, Z value of our present SiC/Al system is still smaller about 1 or 2 decades. We found that the sample with  $T_s = 2250^\circ\text{C}$  and  $x = 2\%$  takes the maximum value of figure of merit  $Z(5 \times 10^{-6} \text{ K}^{-1})$  at around 700 °C. At that temperature, sintering temperature  $T_s$  and concentration  $x$  the thermoelectric power also reaches about  $800 \mu\text{V/K}$  and thermal conductivity takes the minimum value  $10\text{W/m} \cdot \text{K}$  while electrical resistivity also takes a minimum value of  $10^3 \Omega \text{m}$ . The values of thermoelectric power and thermal conductivity are comparable to those of the  $\text{Bi}_2\text{Te}_3$  system at the room temperature. Therefore high electrical resistivity in spite of the Al inclusions is responsible for the small value of Z. One may expect to improve Z values by improvement of the sintering process, which results in specimen with a higher Al concentration. In such a sample one may further reduce electrical resistivity at higher temperatures resulting in an improved Z.

#### 4 CONCLUSION

The figure of merit Z of SiC/Al thermoelectric semiconductors strongly depends both on temperature and Al concentration. Especially, electrical resistivity decreases drastically with temperature. We found that the figure of merit Z takes a maximum value of  $4 \times 10^{-4} \text{ K}^{-1}$  at 700 °C with Al concentration of 2 %. The thermoelectric power ( $800 \mu\text{V/K}$ ) and thermal conductivity ( $10\text{W/m-K}$ ) are almost comparable or better than those of the practical materials. The additions of Al results in remarkable improvement of figure of merit Z compared with  $\text{B}_4\text{C}$  in previous paper. Further reduction in electrical resistivity and thermal conductivity, is expected to improve the performance of SiC/Al system.

#### Acknowledgment

The authors expresses their thanks to Mr. K. Kato and

Mr. K. Asai of The National Defense Academy for their assistance.

#### References

- [1]. H. Wada, T. Sato, K. Takahashi and N. Nakatsukasa, J. Mater. Res. 5 (1990) 1052.
- [2]. H. Wada, Y. Okamoto, T. Miyakawa and T. Irie, J. Mater. Sci. 27 (1992) 881.
- [3]. Y. Okamoto, A. Aruga, K. Shioi, J. Morimoto, T. Miyakawa and S. Fujimoto, Proc. 12th Int. Conf. Thermoelectric, (1993 Yokohama) 184.
- [4]. Y. Okamoto, A. Aruga, H. Kasai, J. Morimoto, T. Miyakawa and S. Fujimoto, Proc. 13th Int. Conf. Thermoelectric, (1994 Kansas) 92.
- [5]. Y. Okamoto, K. Tanaka, A. Aruga, M. Furuta, J. Morimoto, T. Miyakawa and S. Fujimoto, Proc. 13th Int. Conf. Thermoelectric, (1994 Kansas) 62.
- [6]. H. Wada, M. Watabnabe, J. Morimoto and T. Miyakawa, J. Mater. Res. 6 (1991) 1711.
- [7]. J. Morimoto, Y. Okamoto and T. Miyakawa, Jpn. J. Appl. Phys. 31 Suppl. 31-1 (1992) 38

# THERMOELECTRIC PROPERTIES OF SiGe CERAMICS SINTERED WITH GeH<sub>4</sub>-PLASMA-PROCESSED MICROGRAINS

K. Kishimoto, Y. Nagamoto, T. Miki, T. Koyanagi, and K. Matsubara  
*Yamaguchi University, Ube, Yamaguchi 755, Japan*

The microstructure control by the plasma processing has been investigated to improve the thermoelectric figure-of-merit of SiGe ceramics. SiGe ceramics were prepared by sintering micrograins, which were exposed to a GeH<sub>4</sub>-plasma to be coated with Ge layers. The sintered ceramics have a higher electrical conductivity than non-processed one. By the treatment the figure-of-merit of SiGe ceramics was increased about three times at room temperature.

## Introduction

For last several years, we have attempted the microstructure control of FeSi<sub>2</sub> ceramics to improve the thermoelectric figure-of-merit Z using the plasma processing[1-5]. The micrograins of FeSi<sub>2</sub> were treated in plasmas of reactive gases, such as O<sub>2</sub>, SiH<sub>4</sub>, or GeH<sub>4</sub>, and subsequently were sintered into ceramics. The resulting ceramics had higher electrical conductivities than non-processed ceramics. As a result, the plasma-processed FeSi<sub>2</sub> ceramics showed the higher figure-of-merit as compared with the non-processed ceramics. This plasma treatment effect is currently interpreted as the results of changes in the microstructure around the grain boundary.

SiGe is one of the most well-known thermoelectric materials[6-10], and has a simpler crystal structure and conduction mechanism than FeSi<sub>2</sub>[11,12]. So, SiGe seems to be a suitable material for investigation of the plasma effect. In this paper, we examine GeH<sub>4</sub>-plasma treatment effects on the thermoelectric properties and the structure of SiGe ceramics. The relation between the ceramics structure and the thermoelectric properties is discussed.

## Experimental

Figure 1 shows the sample preparation procedure. The Si<sub>80</sub>Ge<sub>20</sub> micrograins of 1 to 10  $\mu\text{m}$  size were obtained by milling arc-melted SiGe ingots. The micrograins were exposed to an rf-plasma. The processing apparatus was same as described previously[2]. The treatment was made under the following conditions: processing gas 5 % GeH<sub>4</sub> diluted with Ar; rf-power 100 W; total pressure 0.2 Torr; process interval 1 h; micrograin amount 15 g. The treated micrograins were hot-pressed under the following conditions: vacuum of 10<sup>-3</sup> Torr; sintering temperature 1473 K; pressing pressure 32 MPa. For comparison, Si<sub>80</sub>Ge<sub>20</sub> ceramics were prepared without treating the micrograins in an rf-plasma. The sintering conditions were same as those of the plasma-processed ceramics.

The crystal structure was examined by the x-ray diffraction (XRD) measurement. The ceramics composition was measured by the electron probe microanalysis (EPMA). The electrical conductivity was measured by the four-point probe method. The electrical conductivity and Seebeck coefficient were obtained from 300 to 1000 K. The thermal conductivity was measured by the

laser-flash method at room temperature. The Hall measurement was also made at room temperature.

## Results and discussion

**Microstructure.** By GeH<sub>4</sub>-plasma treatment, Ge layers were successfully deposited on the SiGe micrograins. The Ge layers modified the structure of sintered SiGe ceramics samples. EPMA analysis revealed that Si/Ge composition ratio of the treated sample was 77/23, while that of the untreated one was 80/20. The increase in Ge content by the plasma treatment is due to Ge layers coated on the micrograins.

In XRD patterns of the GeH<sub>4</sub>-plasma-treated ceramics, Ge crystalline peaks were hardly observed, indicating that a part of coated Ge might diffuse into the grains while sintering. Figure 2 shows XRD peaks of SiGe(111) of the ceramics. The peak position is shifted to a lower angle by the plasma treatment. This shift is considered to be due to an increase in the Ge content of SiGe grains by diffusion of Ge coating layers into the grains. However, the peak position should be shifted to a further lower angle if the Ge layers coated on the micrograins diffused homogeneously. The expected peak position of Si<sub>77</sub>Ge<sub>23</sub> alloy is indicated by the dashed curve in Fig.2. Therefore, it seems that some of the coated Ge is still left at the grain boundary even after sintering.

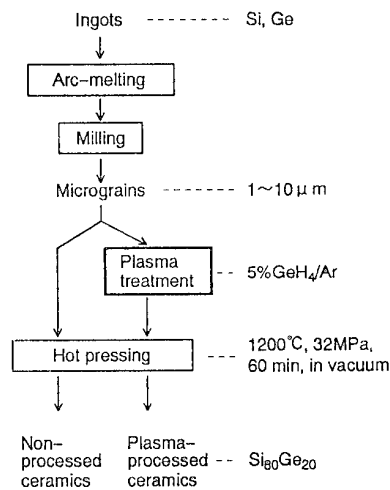


Fig.1. Schematic diagram of sample preparation procedure.

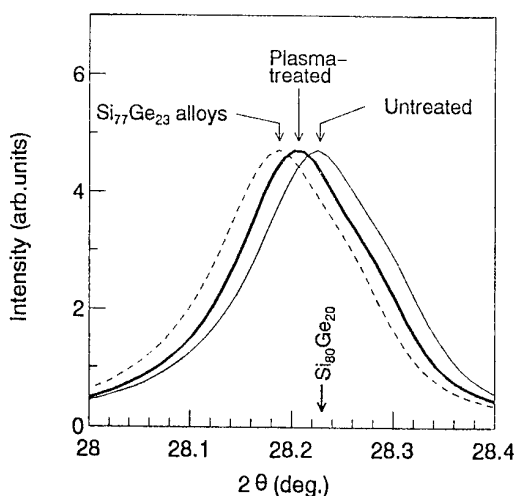


Fig.2. XRD peaks of SiGe(111) of the ceramics samples. Thick, thin, and dashed curves indicate data for the GeH<sub>4</sub>-plasma-treated ceramics sample, the untreated one, and a homogeneous Si<sub>77</sub>Ge<sub>23</sub> alloy, respectively.

From these analysis and consideration on the ceramics structure, it seems that the processed ceramics were composed of SiGe grains with Ge-rich grain boundary.

**Thermoelectric properties.** Figure 3 shows the temperature dependence of the electrical conductivity for GeH<sub>4</sub>-plasma-treated and untreated SiGe ceramics. The plasma-treated ceramics have larger conductivities than the untreated one from 300 to 800 K. At room temperature, the conductivity increases about twice. Above 800 K, in the intrinsic region, the conductivities are almost same.

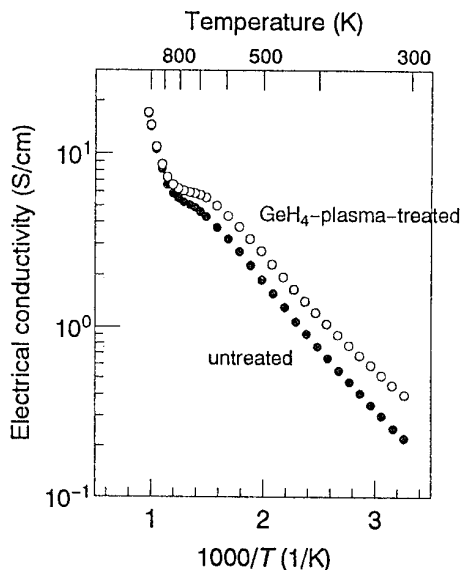


Fig.3. The temperature dependence of the electrical conductivities. Open and closed circles indicate data for the plasma-treated and untreated samples, respectively.

The electrical conductivity usually increases with increasing ceramics density, which is known as the porosity effect[7]. In this experiment, the density of ceramics treated in the GeH<sub>4</sub>-plasma is slightly lower than that of the untreated ceramics, and the electrical conductivities above 800 K are equal to those of the untreated ceramics. From these results, it is concluded that the increase in the electrical conductivities by the plasma treatment are not related to the porosity effect.

To obtain more detailed information on the increased conductivity, we made Hall measurements at room temperature. The results of the Hall measurement are summarized in Table 1. The carrier concentration does not change significantly, while the Hall mobility increases about twice by the treatment, in spite of an increase in the alloy scattering caused by the decrease in Si/Ge ratio[10]. The increase of the Hall mobility leads to the increase in the electrical conductivity.

Table 1. Results of the Hall measurement at room temperature.

	$\sigma$ (S/cm)	$n$ ( $10^{17}/\text{cm}^3$ )	$\mu_H$ ( $\text{cm}^2/\text{V}\cdot\text{s}$ )
Plasma-treated	0.40	1.5	17
Untreated	0.22	1.4	10

The increases in the electrical conductivity and the mobility by the plasma treatment have been observed in the FeSi<sub>2</sub> ceramics[1-5]. In the case of FeSi<sub>2</sub> ceramics, the plasma treatment reduces some of defects at the grain boundary[2,4]. Usually some of defects at the grain boundary form a potential barrier, so that the carrier mobility is lowered. Therefore, it is considered that the reduction of the defects by the plasma treatment is related to the increase in the carrier mobility.

SiGe ceramics have been studied well, and are expected to have such a potential barrier at the grain boundary[9,10]. In this experiment, the GeH<sub>4</sub>-plasma treatment modified the microstructure, especially around the grain boundary. At this stage, unfortunately, we have not obtained any evidences on such defects at the grain boundary. We, however, expect that the plasma treatment reduces the defects at the grain boundary for the SiGe ceramics and that the carrier mobility increases because of the reduction of the potential barrier.

The change in the microstructure of ceramics seems to depend on the plasma processing and sintering conditions strongly. For example, when the sintering time and/or the sintering temperature increase, the diffusion of the coated Ge may proceed further. The study on effects of those conditions on the thermoelectric properties and microstructure will give us more detailed information on the plasma treatment effect.

Figure 4 shows the temperature dependence of the Seebeck coefficient for the samples as shown in Fig.3. The plasma treatment slightly increases the Seebeck coefficient below 700 K. Above 700 K, in the intrinsic re-

gion, the plasma effect is not observed significantly. In general, the Seebeck coefficient increases with decreasing the carrier concentration. The results in this experiment do not, however, agree with the relationship between the Seebeck coefficient and the carrier concentration (see Table 1). We can not explain the change of the Seebeck coefficient now.

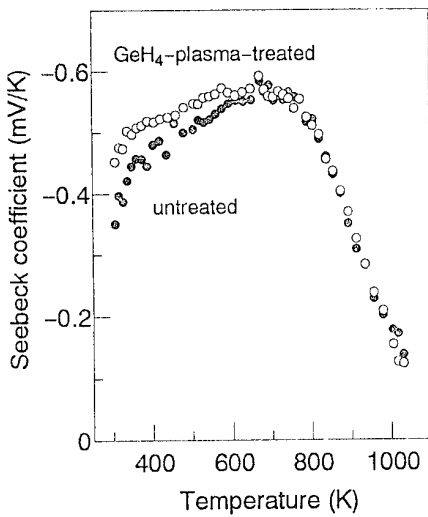


Fig.4. The temperature dependence of the Seebeck coefficients for the sample as shown in Fig.3.

To examine the effect of the plasma treatment on the figure-of-merit, the thermal conductivities were measured at room temperature. Table 2 summarizes the thermoelectric properties at room temperature. The thermal conductivity was decreased by about 20 percent by the treatment. As a result, the figure-of-merit for SiGe ceramics was increased about three times by the GeH<sub>4</sub>-plasma treatment.

Table 2. Thermoelectric properties of the plasma-treated and untreated SiGe samples at room temperature.

	$\kappa$ (W/cm/K)	$\sigma$ (S/cm)	S (mV/K)	Z ( $10^{-6}/\text{K}$ )
Plasma-processed	0.023	0.40	-0.48	4.0
Non-processed	0.030	0.22	-0.42	1.3

### Conclusions

We investigated the effects of the GeH<sub>4</sub>-plasma treatment on the thermoelectric properties and the microstructure of Si<sub>80</sub>Ge<sub>20</sub> ceramics to improve the figure-of-merit.

The plasma treatment modified the microstructure of the ceramics. The GeH<sub>4</sub>-plasma-treated ceramics seem to be composed of SiGe grains with Ge-rich grain boundary. The treatment increased the carrier mobility, and decreased the thermal conductivity. As a result, the

figure-of-merit was increased about three times at room temperature.

It is found that the plasma treatment is effective for improving the figure-of-merit of SiGe ceramics as well as that of FeSi<sub>2</sub> ceramics. Probably, it is considered that the improvement of the thermoelectric properties is due to the microstructure modification, especially around the grain boundary. At the next stage, we would like to make clear the plasma treatment effect by controlling the plasma processing and sintering conditions.

### References

- [1]. K. Matsubara, N. Minemura, J. Miyata, K. Kishimoto, K. Kawamura, T. Koyanagi, and T. Miki, Thermoelectric properties of FeSi<sub>2</sub> ceramics developed by plasma ion processing, *Proc. 10th Int. Conf. Thermolectrics*, Cardiff, UK, 1991, pp.40-43.
- [2]. K. Matsubara, T. Miki, K. Nagao, K. Kishimoto, O. Nakanishi, O. Ueda, and K. Fujii, Characterization and thermoelectric properties of new  $\beta$ -FeSi<sub>2</sub> ceramics developed by an rf-plasma processing in O<sub>2</sub> and SiH<sub>4</sub> gases, *Proc. 11th Int. Conf. Thermolectrics*, Arlington, USA, 1992, pp.24-27.
- [3]. K. Matsubara, K. Kishimoto, K. Nagao, O. Ueda, T. Miki, T. Koyanagi, and I. Fujii, Iron disilicides: the possibility of improving thermoelectric figure-of-merit values by rf-plasma processing, *Proc. 12th Int. Conf. Thermolectrics*, Yokohama, Japan, 1994, pp.223-230.
- [4]. T. Miki, Y. Matsui, Y. Teraoka, Y. Ebina, K. Matsubara, and K. Kishimoto, Point defects and thermoelectric properties of iron disilicide ceramics sintered with SiH<sub>4</sub>-plasma-processed micrograins, *J. Appl. Phys.*, 1994, vol.76, No.4, pp.2097-2103.
- [5]. K. Kishimoto, Y. Nagamoto, K. Nagao, T. Miki, T. Koyanagi, and K. Matsubara, Microstructure control of  $\beta$ -FeSi<sub>2</sub> ceramics by rf-plasma processing in SiH<sub>4</sub> and GeH<sub>4</sub> gases, *Proc. 13th Int. Conf. Thermolectrics*, Kansas, USA, 1995, pp.123-126.
- [6]. J. P. Dismukes, L. Ekstrom, E. F. Steigmeier, I. Kudman, and D. S. Beers, Thermal and electrical properties of heavily doped Ge-Si alloys up to 1300 K, *J. Appl. Phys.*, 1964, vol.35, No.10, pp.2899-2907.
- [7]. N. Savvides and H. J. Goldsmid, Boundary scattering of phonons in fine-grained hot-pressed Ge-Si alloys: I. The dependence of lattice thermal conductivity on grain size and porosity, *J. Phys. C: Solid St. Phys.*, 1980, vol.13, No.25, pp.4657-4670.
- [8]. D. M. Rowe, V. S. Shukla, and N. Savvides, Phonon scattering at grain boundaries in heavily doped fine-grained silicon-germanium alloys, *Nature*, 1981, vol.290, No.5809, pp.765-766.
- [9]. C. B. Vining, W. Laskow, J. O. Hanson, R. R. Van der Beck, and P. D. Gorsuch, Thermoelectric properties of pressure-sintered Si<sub>0.8</sub>Ge<sub>0.2</sub> thermoelectric alloys, *J. Appl. Phys.*, 1991, vol.69, No.8, pp.4333-4340.
- [10]. G. A. Slack and M. A. Hussain, The maximum possible conversion efficiency of silicon-germanium thermoelectric generators, *J. Appl. Phys.*, 1991, vol.70, No.5, pp.2694-2718.
- [11]. Y. Dusausoy, J. Prota, R. Wandji, and B. Roques, Structure cristalline du disilicium de fer, FeSi<sub>2</sub> $\beta$ , *Acta Cryst.*, 1971, vol.B27, pp.1209-1218.
- [12]. U. Birkholz and J. Schelm, Mechanism of electrical conduction in  $\beta$ -FeSi<sub>2</sub>, *phys. stat. sol.*, 1968, vol.27, No.1, pp.413-425.

## EFFECTIVE THERMAL CONDUCTIVITY OF POROUS OXIDES AT TEMPERATURES $T \geq 1000K$

E.M.Sher

A.F.Ioffe Physical Technical Institute RAS, St.Petersburg, 194021, Russia

Successful study and thermoelectric application of the porous oxides layers (o.l.) of alkaline-earth metals (a-e.m.) depends largely on reliable determination of their effective thermal conductivity  $\chi_{eff}$ . The experimental data about

$\chi_{eff}$  and its parts are given and discussed.

### Introduction

The specific properties of porous a-e.m.-oxides gave A.F.Ioffe and B.Ja.Moizhes reasons to propose a possibility of high thermoelectric efficiency in such materials [1,2]. This proposal find its corroboration in some experiments [2,3]. The oxide layers of a-e.m.,(Ba,Sr)O, (Ba,Sr,Ca)O have high porosity-up to 70-80%,fine-dispersed structure-grain dimensions 1-3mcm and small electron work function- 1,7ev at 1000K. These oxides are semiconductors with wide forbidden energy band about 4,5ev and this provides a high transparency for thermal radiation. The dispersion of thermal radiation in oxide crystals by free electrons is small because of their small concentration. High porosity, fine-dispersed structure and slight contacts between crystal grains must conditioned high thermal resistivity through crystal frame (o.l. grains+contacts between them ).The small work function provides appreciable electron gas concentration in pores by electron emission from grains at high temperatures. It leads to some heat transfer through o.l. by electron gas in pores. In such a manner, there are three component of heat flow through the o.l. :

1. Heat flow through porous oxide from small crystals of transparent semiconductor with wide forbidden energy band.
2. Heat flow through crystal frame of porous oxide (small grains +contacts between them).
3. Heat flow which transferred through o.l. by gas of free electrons in pores.

Each of these flows make a contribution to total value of effective thermal conductivity  $\chi_{eff}$  of porous o.l. at high temperatures.

### Thermal conductivity of o.l. crystal frame $\chi_{cf}$

The conventional methods for measuring thermal conductivity are based on measurements of the temperature difference at a fixed amount of heat going through the sample. But they are not suitable for determining  $\chi_{cf}$  at high temperatures because of high o.l. transparency. Calculation formulas for  $\chi_{cf}$  from the known values of porosity, dispersion and a-e.m.-oxides crystal thermal conductivity can't give correct quantity. It is explained by small size of the contact area between grains. The thermal resistivity completely determines by these contacts and strong depends from o.l. density. The  $\chi_{cf}$  value was determined with the help of especially developed method [3,4], which represents a modification of Kohlraush method. As it is known, this method is suitable for measuring thermal conductivity of thin metallic wires with their diameter far less then their length. The developed method of measuring  $\chi_{cf}$  at high temperatures ( $>1000K$ ) can be used:

1. for thin o.l. in the disk form located between two metallic electrodes when its diameter well above its length (thickness).

2. for o.l. with nonlinear resistance .

3. when the o.l. electrical conductivity is mainly provided by grains emission. The developed method was consisted in the following. Thin layer (with thickness 100-300mcm) of a-e.m.-oxides was located between two cylindrical Ni-electrodes with diameter 8mm. Each electrode had its own heater from isolated W-wire. The heater power supply was carried out from electronic stabilizer. All measurements was made in vacuum  $10^{-7}$  Torr. The o.l. warming up was carried out from a sonic generator with current freqency about 40-60 hertz. The o.l. initial resistance  $R_0$  and its variation  $\Delta R$  at warming up was measured with alternating current bridge on the frequency 4,5khz. The resistance changing  $\Delta R$  was recalculated in the appropriate increasing  $\Delta T$  of the o.l. average temperature. The value  $\Delta T$  is determined by the crystal frame thermal conductivity .The o.l. is a nonlinear resistance. Because of that, the alternating current bridge compensation was made at the moment when the warming voltage was passing through zero. The following relationship for calculation thermal conductivity  $\chi_{eff}$  of crystal frame from the measurements  $\Delta R$  of o.l. during its warming up was received by B.Ja.Moizhes [4]:

$$\chi_{eff} = \frac{P \cdot d}{12\Delta R / R_0} \cdot \frac{d \ln R_0}{dT} \left( 1 - \frac{4}{5} \frac{\Delta R}{R_0} \right) \quad (1)$$

here P-the power of alternating current warming up the o.l., d-o.l. thickness. The value  $d \ln R / dT$  was determined from measurements the dependence  $R(T)$ . The high transparency and small o.l. absorption of radiation ( $a \sim 1cm^{-1}$ ) was assumed. The valuation of the radiation heat removal from the o.l. crystal frame warmed up by current was made . It was shown that radiation didn't played essential role ( $d=100-300mcm$ , thus  $ad \ll 1$ ).

The measurements by developed method gave for  $\chi_{cf} = 1,5-5,0 \cdot 10^{-6} W \cdot cm^{-1} \cdot K^{-1}$ . These results was compared with  $\chi_{cf}$  measurements at low temperatures (near room temperatures) on the same samples. The received values for  $\chi_{cf}$  at low temperatures are in good agreement with high temperatures data. Small values of  $\chi_{cf}$  at high temperatures can be connected only with high thermal resistance on the contacts between oxide grains. In connection with this result, the value of  $\chi_{cf}$  must be very sensitive to the structure of oxides with high porosity. This result is also in good agreement with electrical conductivity probe measurements of o.l. at  $T \geq 1000K$  [5,6]. The developed method can be useful for lattice thermal conductivity measurements of semiconductor materials with high transparency for thermal radiation.

### Thermal conductivity of free electron gas in o.l. pores.

The small value of electron work function is provided free electron concentration  $n$  in pores about  $n \sim 10^{12} cm^{-3}$  (at 1000K)

and, respectively, electrical conductivity about  $\sigma = 3 \cdot 10^{-3}$   $\text{Om}^{-1} \cdot \text{cm}^{-1}$ . For electronic thermal conductivity in the case of nondegenerate electron gas in pores the Viedeman-Franz law gives[7]:

$$\chi_e = (r+2) \left( \frac{k}{e} \right)^2 \sigma T \quad (2)$$

where  $r$  - index of the power in the electron free path length dependence from energy,  $k$  - Boltzman constant,  $e$  - charge of electron,  $T$  - absolute temperature. The value of  $\chi_e$  isn't exceeded  $1 \cdot 2 \cdot 10^{-7} \text{ W} \cdot \text{cm}^{-1} \cdot \text{K}^{-1}$  - it can be seen from the maximum values received for  $\sigma_{el}$  at high temperatures [3,5] and from equation (2). Thus the value of  $\chi_e$  on 1,0 - 1,5 degrees less then value of  $\chi_{eff}$  at  $T > 1000\text{K}$ .

#### Effective thermal conductivity of o.l.

As mentioned above, the heat transfer at temperatures  $> 1000\text{K}$  will take place mainly by heat radiation through o.l. The experimental data are confirmed this suggestion. On the fig.1 the experimental dependencies of effective thermal conductivity  $\chi_{eff}$  are shown in coordinates  $\lg \chi_{eff}$  ( $\lg T$ ). The dependencies are straight lines with the slope near 4. I.e.,  $\chi_{eff} \sim T^4$  as must be when heat flow transferred mainly by radiation.

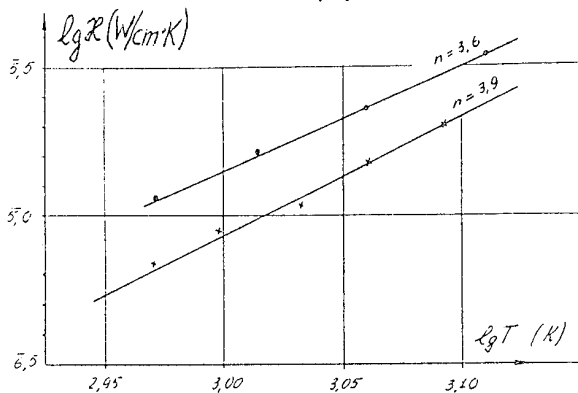


Fig 1. Experimental dependences  $\lg \chi_{eff}$  ( $\lg T$ ) for two samples of o.l.

The total, effective value of o.l. thermal conductivity was measured [3,4] with the help of three-electrode device in vacuum  $\sim 10^{-7}$  Torr (fig.2).

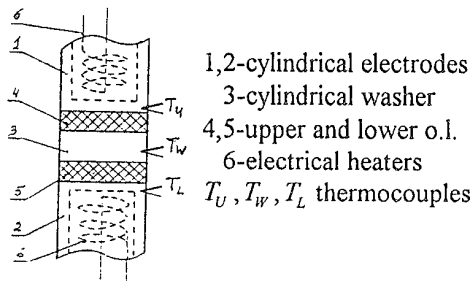


Fig 2. Construction scheme of the device for measurements  $\chi$  and  $\epsilon$  and their dependence from  $T$  for two o.l.

For measurement  $\chi_{eff}$  of lower o.l. (4, fig.2) the temperature distribution:  $T_u = T_w < T_l$  was supported.

The equation  $T_u = T_w$  can be maintained with high accuracy by adjustment to zero the value of upper o.l. thermoemf. In this case the heat  $Q_x$  which passed through lower o.l. will be equal:

$$Q_x = \chi_{eff} \cdot \frac{\pi \cdot r^2}{l} \Delta T \quad (3)$$

where  $r$ -washers (3,fig1) radius,  $l$  - o.l. thickness,  $\Delta T = T_l - T_w$ . The heat  $Q_x$  is completely radiated from lateral surface of the washer:

$$Q_x = \epsilon_w \sigma_0 \cdot T_w^4 \delta 2\pi r \quad (4)$$

where  $\epsilon_w$  - radiation emissivity of the washer,  $T_w$  - temperature of the washer,  $\delta$  - washer thickness.

From (3)=(4) :

$$\chi_{eff} = \epsilon_w \sigma_0 \frac{2\delta \cdot l}{r} \frac{T_w^4}{\Delta T} \quad (5)$$

The  $\chi_{eff}$  value for upper o.l. can be calculated similar by adjusting the following temperature distribution:  $T_l = T_w < T_u$ . Thus for the effective thermal conductivity determination we must know the value of  $\epsilon_w$  - radiation emissivity of the lateral surface of the washer. The value of  $\epsilon_w$  can be strongly dependent from the washer surface state. For reliable determination the radiation emissivity  $\epsilon_w$ , the following method was developed [8]. The washer from investigated material (Cu) was suspended on its Pt-PtRh-thermo-couple in the glass tube with vacuum  $\sim 10^{-7}$  Torr. As the thermocouple can't be directly welded to copper, small cylindrical Ni-pins was inserted into the Cu-sample and the thermocouple was welded to that pins. Then the sample was heated from inductor of high frequency generator to necessary temperature, the inductor was removed and the recording of temperature decreasing of the sample was made. For calculation of the sample radiation emissivity was enough to know the rate of the sample cooling in dependence from its temperature. The heat removal through thermocouple and the radiation from Ni-pins was taken into account. Several measurements with each sample and results was averaged. The radiation emissivity of the sample was determined from the heat balance equation:

$$\epsilon_w = \frac{C_m \left| \frac{\partial T}{\partial t} \right| - \epsilon_p \sigma_0 S_p (T^4 - T_0^4) - \sum q_i}{\sigma_0 S (T^4 - T_0^4)} \quad (6)$$

where  $c$  and  $m$  - specific thermal capacity and mass of the sample,  $S_p$  and  $\epsilon_p$  - area of the Ni - pins surface and their radiation emissivity,  $S$  - area of sample surface (minus area of pins),  $\sum q_i$  - heat flow summary outgoing from the sample through thermocouple wires,  $t$  - time.

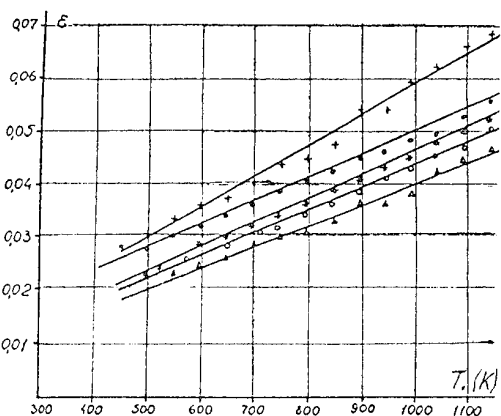


Fig 3. The experimental dependences of the radiation emissivity  $\varepsilon_w$  from temperature for five Cu-samples.

Evaluations and repeated  $\varepsilon_w$  measurements on the same samples with developed method was shown that accuracy of such measurements not worse then  $\pm 5\%$ . For different samples, as it is seen from fig.3, the meanings of  $\varepsilon_w$  differs more noticeably because of variations in properties of original material and technology of their treatment. The results of measurements of the radiation emissivity  $\varepsilon_w$  by this method received for 5 samples from oxygenless copper (from which the "cold" electrodes - washers was made) are shown on the fig.3. The measurements of effective thermal conductivity carried out by two developed methods gives for  $\chi_{eff}$  meanings in the limits  $\chi_{eff} \sim 10^{-4} - 10^{-5} \text{ W.cm}^{-1}. \text{K}^{-1}$  for different o.l. at  $\sim 1000\text{K}$ .

#### Conclusions

Thus the thermal conductivity of porous o.l. at high temperatures have three components: 1. through crystal frame, 2. by free electron gas in pores, and 3. for account of radiation through o.l. The last component, in fact, is determining the effective value of thermal conductivity of o.l., because it is on 2-3 degrees higher then two else. Therefore one can improve, for example, electrical conductivity even on 1 or 2 degrees without increasing the value of  $\chi_{eff}$ . On the other side, because  $\chi_{eff}$  is determined by radiation exchange between "hot" Ni - cylinder and "cold" - washer, the value of  $\chi_{eff}$  can be decreased in several times by the way of decreasing the value of effective radiation emissivity of this system  $\varepsilon_{eff}$ . Preparing one electrode in this system from material with minimum  $\varepsilon$  (from copper or gold) we will decrease the  $\chi_{eff}$  in 2 - 3 times [3].

#### Acknowledgments

Author would like to thank B.Ja.Moizhes for advises and discussion results during performance of this and [3] works.

#### References

- [1].A.F.Ioffe.Semiconductor Thermoclements(in.Russian) M - L, AS USSR, 1960, 188p
- [2]B.Ja.Moizhes. Physical Processes in Oxide Cathode (in Russian).M.,"Science", 1968,479p.
- [3]. E.M.Sher. Proceed. of XII ICT, Yokohama, 1993, pp.54 - 59.
- [4].B.Ja.Moizhes,I.N.Petrov,E.M.Sher, O. V.Sorokin. "Radiotekhnika e Elektronika" (in Russian, "Radio Enginnering and Electronics"),1966,11,pp.1674-1681
- [5].E.M.Sher.Radiotekhnika e Electronika (in Russian,"Radio Engineering and Electronics"),1966,10,pp.1721 - 1723.
- [6].B.Ja.Moizhes,E.M.Sher."Electronnosc priborostroenie" (in Russian, "Electronic Instrument Engineering"), Issue 3, L., "Energy",1967, pp.89 - 108
- [7].L.Stilbans Phisics of Semiconductors (in Russian) M., "Sov. Radio", 1967, p451
- [8].E.M.Sher O. V.Sorokin"Elecctronnaja Technika", (in Russian) "Electronics",1973, s.4,is.5, pp.43-48.

# CLUSTER SUPERLATTICE AS 3D-ARRAY OF THERMIONIC ENERGY CONVERTERS

V.N. Bogomolov<sup>1</sup>, D.A. Kurdyukov<sup>1</sup>, A.V. Prokofiev<sup>1</sup>, Yu.I. Ravich<sup>1</sup>, L.A. Samoilovich<sup>2</sup>, S.M. Samoilovich<sup>3</sup>

<sup>1</sup> *Ioffe Physical Technical Institute, 194021, St. Petersburg, Russia*

<sup>2</sup> *Almaztechnocrystal company, 601600, Aleksandrov, Russia*

<sup>3</sup> *Moscow State University, Russia*

The metal or semiconductor clusters were impregnated into cavities of the opal crystal. The thermionic emission arises through small gaps between the clusters. The nanolattice of thermionic energy converters is considered as a Seebeck media. The measured Seebeck coefficient for GaAs cluster lattice is in agreement with the calculated one. The thermoelectric figure of merit is analysed.

Opal crystal is a package of touching silica spheres [1]. All these spheres are of the same diameter about 2500 Å. These spheres form a face-centered cubic lattice. Two type of empty cavities (voids) exist between the touching spheres. The cavities with "octahedron" configuration have a diameter ~ 1000 Å, ones with "tetrahedron" configuration are of size ~ 500 Å [2,3]. The voids are connected each with other through bottleneck-like channels. A width of the channels is of order 100 Å. The cavities form the superlattice also with a cubic symmetry, as the silica spheres do. The system of the cavities is represented in Fig. 1 in the form of cubes and tetrahedrons inserted into the cavities.

The nanosize metal or semiconductor clusters can be impregnated into the cavities of opal matrix as into porous glass [4] in molten form under high hydrostatic pressure. Thus, a 3D-replica of the opal matrix is formed [2,3]. The clusters can be either separated, or coupled, or separated with small gaps of size from 20 to 50 Å. The last case is the most interesting from a thermoelectric point of view because a thermionic emission is possible through gaps. Therefore, this superlattice may be considered as a 3D-array of thermionic energy converters of a superhigh density ~10<sup>14</sup> cm<sup>-3</sup> with extremely low cathode-anode gaps.

The composite material in question may be called as a Seebeck media, like Josephson media prepared of the superconducting weakly coupled clusters [3].

When calculating the thermionic current  $j$  and a heat flow  $q$  between two clusters, we should consider the work

functions of two clusters to be equal to the same value  $\varphi$ . The calculated quantities are

$$j = I_1 - I_2, \quad (1)$$

$$q = j(\varphi + V) + \frac{2k}{e}(I_1 T_1 - I_2 T_2), \quad (2)$$

$$I_1 = AT_1^2 \exp\left(-\frac{e(\varphi + V)}{kT_1}\right), \quad (3)$$

$$I_2 = AT_2^2 \exp\left(-\frac{e\varphi}{kT_2}\right), \quad (4)$$

$V$  being the difference of potentials between the clusters,  $\Delta T = T_1 - T_2$  being temperature difference,  $A$  being the usual thermionic constant ~ 100 A/cm<sup>2</sup>K<sup>2</sup>.

Because of high electrical and thermal resistance of intercluster channels, the differences of potentials and temperatures on a sample are concentrated mainly on the channels. The differences on each element are however small,  $V \ll \frac{kT}{e}$ ,  $\Delta T \ll T$  because of large number of elements. Therefore, the charge and heat flows may be calculated in a linear approximation, and the flows through a media are linear functions of the generalized forces:

$$V = \rho j + S\Delta T \quad (5)$$

$$q = \Pi j - \alpha\Delta T \quad (6)$$

The effective electric conductivity  $\sigma = \rho^{-1}$ , thermal conductivity  $\alpha$  and Seebeck coefficient  $S$  were calculated with a linearization of the expressions (1) - (4), the Peltier coefficient  $\Pi$  was given by the Thomson relation  $\Pi = ST$ . These thermoelectric parameters of the cluster lattice due to thermionic emission were obtained in a following form:

$$S = \frac{k}{e} (2 + \varphi^*) \quad (7)$$

$$\sigma = \frac{e}{k} A T e^{-\varphi^*} \delta \quad (8)$$

$$\alpha = L \sigma T, \quad L = 2 \left( \frac{k}{e} \right)^2 \quad (9)$$

where  $\varphi^*$  is a work function in  $kT$ -units,  $L$  is a Lorenz number,  $\delta$  is a factor describing a density of the elements and their relative cross section.

At a usual work function and a temperature above room one, the system has a high thermopower, low electric and thermal conductivity. It is very like a weakly doped semiconductor, although any semiconducting ingredients may be absent at all. When decreasing gaps between clusters, tunnel current arises and the composite material turns into a metal or semiconductor in dependence on the material of clusters.

Really, some contributions of other than thermionic origin must be added to the above expressions at small thermionic electric and thermal conductivities. Due to these additions, the total conductivities and Seebeck coefficient are equal:

$$\sigma_t = \sigma_0 + \sigma, \quad (10)$$

$$\alpha_t = \alpha_0 + \alpha, \quad (11)$$

$$S_t = \frac{S + s S_0 e^{\varphi^*}}{1 + s e^{\varphi^*}} \quad (12)$$

where  $\sigma_0$ ,  $\alpha_0$ ,  $S_0$  are values without the thermionic current and a parameter  $s$  characterizes additional contribution into the total electric conductivity:

$$s = \frac{\sigma_0}{\sigma e^{\varphi^*}} = \frac{k}{e} \frac{\sigma_0}{A T \delta} \quad (13)$$

The contribution of thermionic current increases exponentially with temperature. The strong exponential dependence is excluded of the parameter  $s$ , however this parameter may weakly depend on temperature. The Seebeck coefficient may be as usual in the temperature range where the thermionic current is small in comparison with additional one. It arises quickly when the current becomes mainly thermionic. The Seebeck coefficient calculated when using (7) and (12) is represented on Fig.2 as a function of  $\varphi^*$  at various values of the parameter  $s$ . Since  $\varphi^*$  is proportional  $T^{-1}$ , these curves show also the dependence of thermopower on  $T^{-1}$ . The curves have high non-symmetric maxima just when thermionic contribution becomes large.

The samples with GaAs semiconductor clusters in the opal matrix were prepared and the thermopower was measured. This nanocomposite material was created by means of the physico-chemical methods [3,4] and controlled by X-Ray analysis.

The unannealed samples showed the thermopower as in usual p-type GaAs. After thermal annealing, the Seebeck

Fig.1 Thermoelectric power of GaAs-cluster lattice after annealing. Insertion: schematical draft of the cluster lattice in opal matrix.

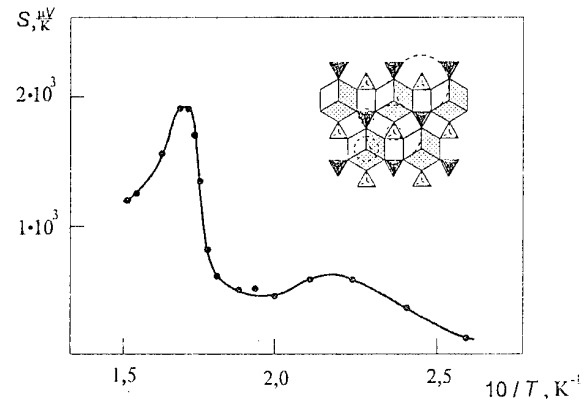
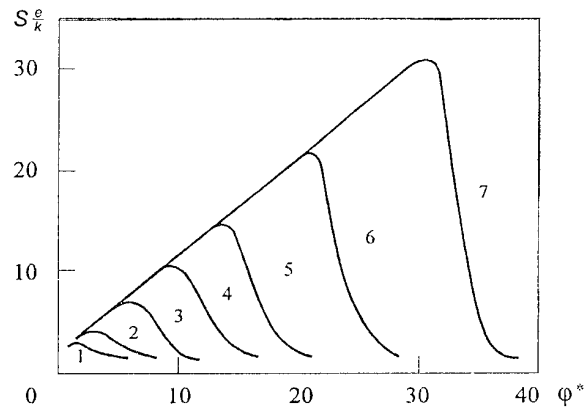


Fig.2 The calculated dimensionless Seebeck coefficient  $\frac{Se}{k}$  versus  $\varphi^*$  according (7) and (12).  $s : 1 - 10^{-1}, 2 - 10^{-2}, 3 - 10^{-3}, 4 - 10^{-5}, 5 - 10^{-7}, 6 - 10^{-10}, 7 - 10^{-14}$ .



coefficient strongly increased up to  $2000 \mu V/K$  and non-symmetric maximum arose like the theoretical one (Fig.1). We supposed that gaps and the thermionic emission through them were formed due to the annealing. After further thermal treatment, the maximum disappeared again what might be explained with increasing the gaps. Therefore, theoretical and experimental results are in a qualitative agreement each with other. However, a sign of the thermopower turned out to be positive what pointed out that the current over barriers was created by holes. It was possible if holes went between clusters through a dielectric, obviously, through silica.

Further, a thermoelectric figure of merit of the cluster superlattice was considered. The Ioffe criterion  $ZT$  does not exceed unity in the best usual semiconducting thermoelectrics.

The optimal reduced work function  $\varphi^*$  and the maximal Ioffe criterion  $ZT$  were found. The procedure can be fulfilled in an analytical form as for non-degenerated semiconductors. The Ioffe criterion

$$ZT = \frac{(2 + \varphi^*)^2}{2(1 + B e^{\varphi^*})} \quad (14)$$

depends on a dimensionless parameter

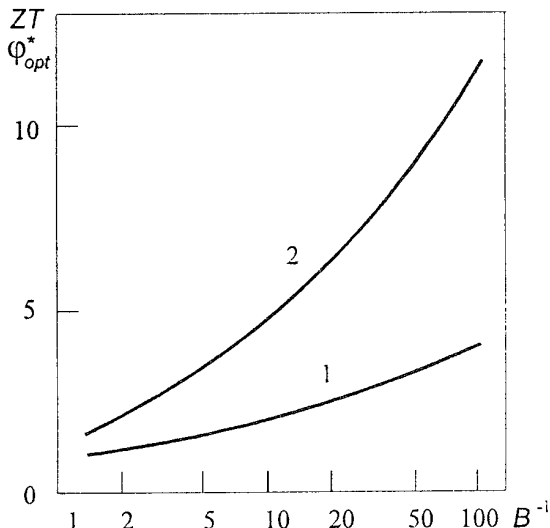
$$B = \frac{e\alpha_o}{2 k T^2 A \delta} \quad (15)$$

$\alpha_o$  being additional (phonon and radiation) thermal conductivity. The quantity (14) is maximal if the optimal work function  $\varphi^* = \varphi_{opt}$  and the parameter  $B$  are connected each with other by the formula:

$$B = \frac{2}{\varphi_{opt}^* e^{\varphi_{opt}^*}}, \quad (16)$$

The results of the calculation of  $\varphi_{opt}^*$  and  $ZT$  at  $\varphi = \varphi_{opt}$  are represented on Fig. 3 in the form of universal dependencies on the  $B$ . At  $B < 1$ , the maximal Ioffe criterion  $ZT$  is more than unity. Therefore, the cluster lattice can represent a new perspective class of thermoelectric materials.

Fig.3 The calculated optimal reduced work function  $\varphi^*$  (1) and the maximal Ioffe criterion  $ZT$  (2) versus the parameter  $B^{-1}$ .



Some polycrystalline thermoelectrics including iron disilicide exhibit thermopower like observed in the opal with GaAs clusters. The high maximum in the temperature dependence of the thermopower in  $\text{FeSi}_2$  is without any definite explanation at present moment. It seems to be probable that the reasons of the maxima in the opal and the iron disilicide are like. The energy barriers may arise in  $\text{FeSi}_2$  between crystal

grains. Therefore, the discussed system may be considered as an artificial model of the  $\text{FeSi}_2$ -type materials.

### References

- [1] J.B. Jones, J.V. Sanders., E.R. Segnit, Structure of opal, *Nature*, 1964 , v.204, No 4962, pp. 990-991.
- [2] V.G. Balakirev, V.N. Bogomolov, Yu.A. Kumzerov, V.P. Petranovsky, S.G. Romanov, L.A. Samoilovich, Three-dimensional superlattices in opal matrices, *Kristallografiya*, 1993, v.38, No 3, pp.111-120 (in Russian).
- [3] V.N. Bogomolov, Yu.A. Kumserov, S.G. Romanov, V.V. Zhuravlev, Josephson properties of the three-dimensional regular lattice of the weakly coupled nanoparticles, *Physica C*, 1993, v.208, No 4, pp. 371-384 .
- [4] J.H.P. Watson, Transition temperature of superconducting Indium, Thallium and Lead grains, *Phys. Rev. B*, 1970, v.2, No 5, pp. 1282-1286 .

## MULTILAYER THIN FILM THERMOELECTRICS PRODUCED BY SPUTTERING.

Andrew V. Wagner, Ronald J. Foreman, Leslie J. Summers,  
Troy W. Barbee, Jr., and Joseph C. Farmer

*Chemistry and Materials Science Department  
Lawrence Livermore National Laboratory  
7000 East Avenue Livermore, CA 94550 USA*

### Introduction

Thermoelectric materials are currently used in applications where it is advantageous to have no moving parts which provides an increase in reliability, the elimination of vibration, and ease of miniaturization. While thermoelectrics are used in countless temperature sensing applications, their use for electrical power generation or cooling is limited by their relatively low efficiency. However, they have found a niche generating power in nuclear-fueled power sources for space exploration and in silent power sources for the military. Thermoelectric cooling devices are also currently being used to cool infrared detectors, CCD cameras, and portable food and beverage coolers.

Over the last 30 years increases in the efficiency of thermoelectric materials for power generation or cooling have been small. However the development of the ability to manipulate materials on a nanometer length scale, thus tailoring their electrical properties, has renewed interest in the field. Theoretical predictions by Hicks and Dresselhaus suggest that using 2D quantum confinement of the charge carriers in multilayer thermoelectric materials may lead to an increase in the figure of merit [1-2]. In order to pursue this possible enhancement in the electronic properties of multilayer materials, it is imperative to grow high quality thin film thermoelectric materials. Although thin films of thermoelectric materials have been deposited by various means for over 30 years, a new emphasis must be placed on the film quality to build nanometer length scale multilayers. The growth surface, for example, must be flat at the length scale of the multilayer. Also, to reduce interdiffusion in these layered structures, it is important to develop a technique for depositing them at the lowest possible temperatures at which quality growth can be maintained. The high quality films which are essential for building quantum confined layer structures are also of interest for building miniature devices. The ability to build miniature cooling devices which can produce useful temperature differences will depend on the ability to make high quality thermoelectric films.

A number of issues have arisen while trying to grow multilayer thermoelectrics [3,4]. Both the conductivity and the Seebeck coefficient for multilayer films were found to be lower than published values for bulk material of the conduction layer.

Thick single layer films were also deposited for comparison with the multilayer films. For the case of Bi and  $\text{Bi}_{0.86}\text{Sb}_{0.14}$  these showed a resistivity consistent with that being observed in the multilayer films, which is about 5 times that of bulk Bi or  $\text{Bi}_{0.86}\text{Sb}_{0.14}$ . This is in agreement with results from the literature which suggest that grain boundary and impurity scattering may be the cause of the high resistivity. Volklein et al. have modeled grain boundary scattering and shown it to be consistent with experimental observations [5]. To achieve a high value for the coefficient of performance from thin film materials, it is important that this grain boundary scattering problem be overcome.

In this work we explore the possibility of achieving bulk electrical properties in single layer sputter deposited films grown epitaxially on (111) oriented  $\text{BaF}_2$  substrates. There are a number of sputter deposition parameters that can be varied in order to optimize the film quality. It is important to understand the effect of varying the deposition temperature, Ar sputtering gas pressure, and the substrate bias. We will consider only Bi and  $\text{Bi}_{0.86}\text{Sb}_{0.14}$  films in this paper. These materials were chosen since they have the same simple structure, two different band gaps and do not change significantly either in physical or electrical properties with small amounts of cross contamination.

We will also present our work on multilayer thermoelectrics made of Bi and  $\text{Bi}_{0.86}\text{Sb}_{0.14}$  layers. There has been considerable interest in this multilayer structure in the literature. Theoretical calculations of the band structure and interface states of these multilayer structures have been made by Mustafaev and Agassi et al. respectively [6,7]. Experimentally Yoshida et al. have examined similar multilayer structures grown by MBE as well as Bi/Sb multilayer samples in which they report an anomalous thermoelectric power [8].

### Experimental procedures

#### Sputtering Deposition

Sputter deposition has been chosen to deposit these thermoelectric multilayers for several reasons. First, sputtering gives a steady deposition rate which allows uniform thickness layers for the multilayer samples. Second, it allows multicomponent materials to be deposited from a single source without many of the compositional shifts associated with

thermal evaporation techniques. Third, by biasing the substrates the argon ions from the sputtering gas can be used to bombard the growing film at low energies. This ion bombardment can change the growth morphology by imparting extra energy to the growth surface. Finally, the technology for large scale deposition has already been developed, and it has been shown that the large quantities of material needed to make multilayer thermoelectrics commercially viable can be produced relatively economically.

The films discussed here were all synthesized in a system originally designed to fabricate multilayer X-ray optics. The system is pumped with a cryogenic pump and usually achieves base pressures of approximately  $1 \times 10^{-7}$  torr prior to sputtering. Substrates are mounted on either a heated or water cooled region of a carousel which rotates below the two magnetron sputtering guns. The 2.5-inch diameter sputter sources are usually operated at an argon pressure around 0.01 torr and a power of 15 watts to give deposition rates directly under the gun of about 5 Å/s. To deposit multilayer samples the substrates are alternately swung under the two magnetron sputtering sources, one depositing a conduction layer and the other depositing a barrier layer. Single layer films can be made by running only a single sputtering source and either sweeping under the sputtering gun, or sitting the substrate directly below the gun.

#### Physical characterization

SEM has been used to characterize the morphology of the samples, as well as to measure the thickness of single layer films. X-ray diffraction has been used to determine the crystallographic orientation of the films. A Cu rotating anode Rigaku diffractometer, equipped with a single crystal monochromator has been used for observing the degree of texturing (by observing relative peak intensities as well as the intensity of the diffraction peaks as the sample is rocked in

theta). Multilayer side bands on the diffraction peaks give an accurate measure of the bilayer thickness  $d$ , which can be determined from the equation:

$$d = \frac{\lambda}{2(\sin \theta_b \pm \sin \theta_{ml})} \quad (1)$$

as well as demonstrating that the structure has not interdiffused during deposition. A Read thin film camera was also used to observe the degree of texturing or epitaxy. It has the advantage of capturing a large portion of reciprocal space on film in a single exposure.

#### Electrical characterization

The Seebeck coefficient was determined as a function of temperature for these films at temperatures ranging from near the melting point of Bi down to liquid nitrogen temperature [4]. The measurements were made in vacuum by bridging the samples between two stages that can be cooled with liquid nitrogen and then heated with a boron nitride resistive heater element. The films were deposited on an insulating substrate to insure that the electrical properties of the substrate do not effect the values measured and to keep the film isolated from the grounded stages. Fine (0.003") K type thermocouples were secured with silver paint to each end of the sample and used for both temperature and voltage measurement. The thermal EMF in each lead is well known with respect to platinum so the graphs shown are plotted as the Seebeck coefficient relative to platinum. The absolute Seebeck coefficient of platinum is also shown on the graph so that the absolute value of the Seebeck coefficient can be easily read as the difference between the two curves.

The resistivity of the samples has been measured in vacuum over the temperature range from liquid nitrogen temperatures to near the melting temperature of the films. A four point probe technique was used with an alternating current and a pair of lock-in amplifiers [4].

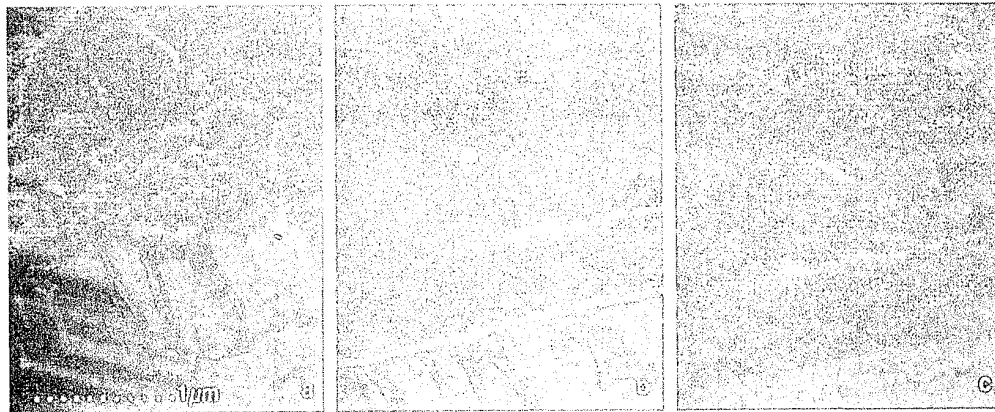


Figure 1: SEM micrographs of a series of Bi films deposited at 8 mtorr Ar -10v bias. a) Deposited at 100°C on polished BaF<sub>2</sub>. Columnar growth is evident. b) Epitaxial film deposited at 100°C on cleaved BaF<sub>2</sub>. c) Epitaxial film deposited at 200°C on cleaved BaF<sub>2</sub>.

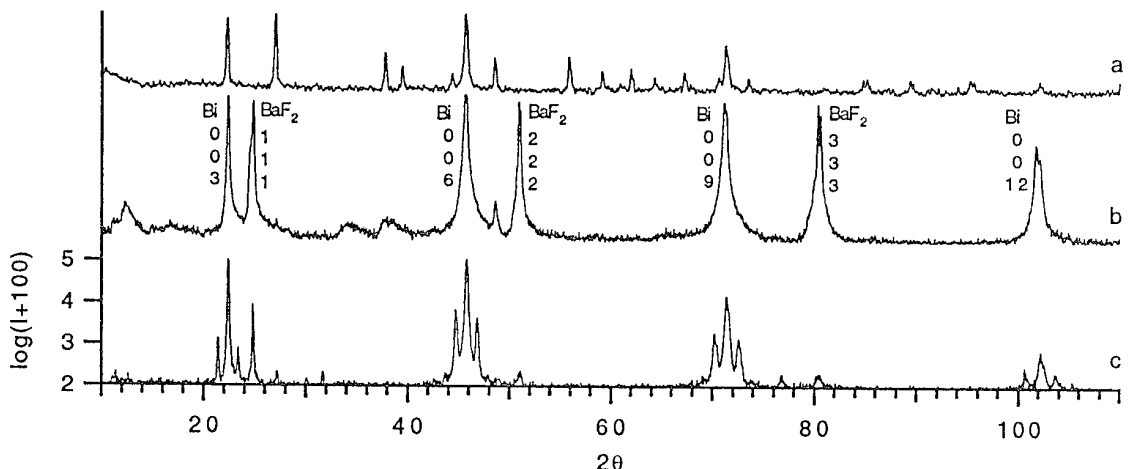


Figure 2: X-ray diffraction scans of a) Bi sample on glass showing texture, b) epitaxial Bi film on cleaved BaF<sub>2</sub>, and c) Bi/Bi<sub>0.86</sub>Sb<sub>0.14</sub> multilayer film showing satellite peaks.

## Results and Discussion

## Single layer Bi films

A series of experiments have been performed in order to optimize the quality of single layer Bi and  $\text{Bi}_{0.86}\text{Sb}_{0.14}$  films. The effect of different substrates, deposition temperatures, Ar sputtering gas pressure, and sample bias were investigated and are presented below.

Samples deposited on glass, silicon (with a native oxide) and (1102) sapphire and were all found to have a rough surface (data not shown). This is caused by Bi crystallites nucleating in random orientation on the substrate surface. As the film grows, those grains with favorable conditions appear to grow preferentially relative to their neighbors, resulting in a non-epitaxial (003) textured film with the average crystallite size increasing with film thickness.

In order to grow films without the rough columnar structure, a substrate was chosen on which a Bi film could grow epitaxially. The (111) face of BaF<sub>2</sub> (cubic) is such a substrate having an atomic spacing only 3.6% smaller than the 003 planes of Bi (rhombohedral). Bi<sub>1-x</sub>Sb<sub>x</sub> also has the Bi structure where the addition of Sb reduces the lattice dimensions, thus decreasing the mismatch with BaF<sub>2</sub>. Depositing on a polished BaF<sub>2</sub> surface (figure 1a) gave results similar to that found for glass, silicon, and sapphire. Presumably this is a result of surface damage caused by polishing. On freshly cleaved BaF<sub>2</sub>, however, epitaxial growth has been achieved (figure 1b, 1c). A difference in the quality of the films can be observed visually. Those on freshly cleaved BaF<sub>2</sub> are shiny, while on the other substrates the rough film surface appears dull.

While the non-epitaxial films show numerous faceted crystallites, the epitaxial films show only minimal surface topography in the SEM. The film surface also shows a well aligned triangular surface structure. The length scale of this structure does not change appreciably when the films are grown to a thickness of 3 $\mu$ m. For the non-epitaxial films, the fracture

surface is rough with the films breaking along grain boundaries. For the epitaxial films, however, the fracture surface is smooth with no evidence of grain boundaries.

A series of x-ray measurements have been made to examine the crystallographic orientation of the films. For the non-epitaxial films, growth is textured with the (003) axis perpendicular to the substrate. This can be seen from the Read thin film x-ray camera pictures which show the polycrystalline Cu K $\alpha$  diffraction rings broken into arcs (data not shown). The 0-20 scan shown in figure 2a also shows evidence of texturing with a much higher relative intensity for the (003) family of peaks than would be expected for a randomly oriented film. 0-20 scans on films deposited on cleaved BaF<sub>2</sub> show that the degree of orientation is very good. The 003, 006, 009, 0012 peaks from the film dominate the spectra (figure 2b). The BaF<sub>2</sub> 111, 222, and 333 peaks can also be seen. The position of

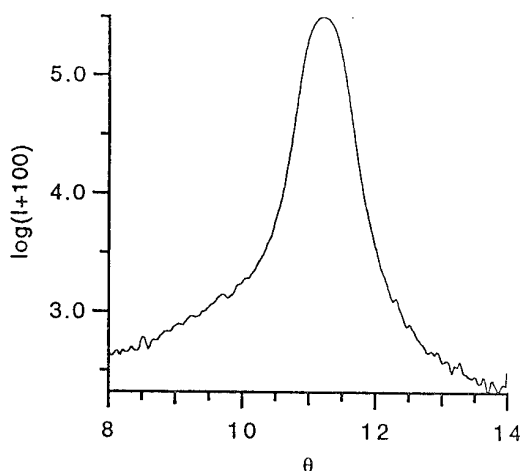


Figure 3 X-ray diffraction scan taken with the detector fixed on the 003 peak at  $22.4^\circ$  of the sample shown in figure 2b and the sample rocked in theta.

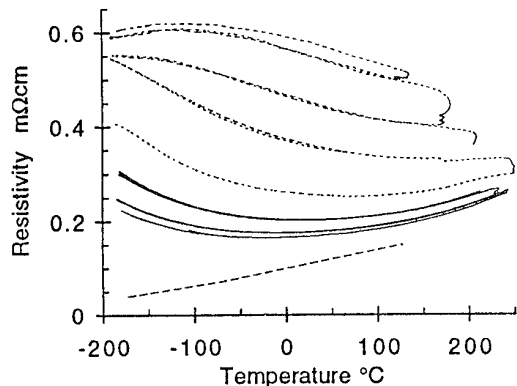


Figure 4: Resistivity of Bi. Top curve (small dash) shows a sample deposited at 100°C, -25v bias, and 16 mtorr Ar. The sample was temperature cycled from liquid nitrogen temperature to progressively higher temperatures. Annealing that occurs during each temperature cycle lowers the resistivity. Center curve (solid line) shows a sample deposited at 200°C, -10v bias, and 8 mtorr Ar. Bottom curve (long dashes) is literature value for bulk Bi.

these peaks can be calibrated with the BaF<sub>2</sub> 111 lines from the substrate. The angles for the film peaks are lower in angle than one would expect showing that the unit cell is elongated out of the plane of the film as a result of compressive stress in the plane of the film. With the detector positioned on the (003) peak, the sample can be rocked in theta to show the degree of orientation of the crystallites (figure 3). This shows that the orientation of the crystallites with the substrate is good to within about 1/2°.

Increasing the deposition temperature gives the depositing atoms increased mobility on the growth surface and allows the growth of higher quality films. Increased temperature may also help reduce the incorporation of foreign atoms, such as Ar in the growing film, since they are more likely to be desorbed at higher temperature. Depositing Bi films at 200°C gives a larger surface structure as shown in figure 1c. The resistivity of this film is also quite low and above room temperature there is metallic behavior (increasing resistance with increasing temperature) as is found in the bulk. Further annealing to nearly the melting point reduces the resistivity slightly further. This behavior can be compared with the resistivity of films deposited at 100°C. In these films the resistivity is considerably higher. With annealing (in the measurement chamber) the resistivity of these films also drops but the films never become as metallic as the films deposited at higher temperature (figure 4).

For multilayer growth it is important to be able to deposit films at the lowest possible temperature in order to avoid interdiffusion. Surface mobility can be increased during sputtering by providing energy by low energy ion bombardment. This can be achieved by negatively biasing the sample holder and substrates.

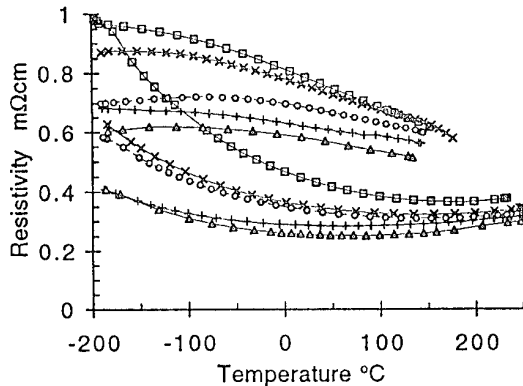


Figure 5: Resistivity of Bi films deposited at 100°C under different conditions. Both the as deposited resistivity is shown (convex) as well as resistivity after a 250°C anneal. In all cases the resistance has decreased with annealing. A film deposited at 8 mtorr Ar and 10v bias on polished BaF<sub>2</sub> (□), or on cleaved BaF<sub>2</sub> (X). A film deposited on cleaved BaF<sub>2</sub> at -25v bias, and 8 mtorr Ar (○), or on cleaved BaF<sub>2</sub> at -10v bias and 16 mtorr Ar (+), or on cleaved BaF<sub>2</sub> at -25v bias and 16 mtorr Ar (Δ). Small uncertainties in sample dimensions made it necessary to adjust the vertical scale for individual samples based on the annealed high temperature behavior to make trends more clear.

Increasing the Ar pressure or increasing the bias of the substrate holder both have an effect on the sample resistivity as can be seen in figure 5. In both cases the resistance is reduced in the as deposited film. There is also a decrease in the slope of the resistance curve. Both high bias and Ar pressure lead to the deposition of the lowest resistance films at 100°C.

In summary it has been shown that single layer epitaxial films can be grown on freshly cleaved BaF<sub>2</sub> substrates. Films grown at higher temperatures have a lower resistivity than those deposited at lower temperature. Deposition with a substrate bias and a higher Ar pressure improved the conductivity of the films deposited at low temperature. However in all cases the resistivity is still higher than that of bulk material.

#### Bi/Bi<sub>0.86</sub>Sb<sub>0.14</sub> multilayer sample

Multilayer samples composed of Bi and Bi<sub>0.86</sub>Sb<sub>0.14</sub> layers have been deposited on cleaved BaF<sub>2</sub> both at room temperature and 100°C. The existence of a multilayer structure has been verified by x-ray diffraction (figure 2c). The satellite peaks clearly show that a layered structure has been achieved with a layer pair repeat distance of 91 Å.

The Seebeck coefficients of the Bi and Bi/Bi<sub>0.86</sub>Sb<sub>0.14</sub> multilayer films are shown in figure 6. The Seebeck coefficient for both films is found to be approximately the same.

Our work agrees the work of Yoshida et. al. in which they found that samples grown on BaF<sub>2</sub> had no evidence of an anomalously high Seebeck coefficient. This is in contrast to their reports of an anomalous thermoelectric power in Bi/Sb multilayer samples deposited on Si.

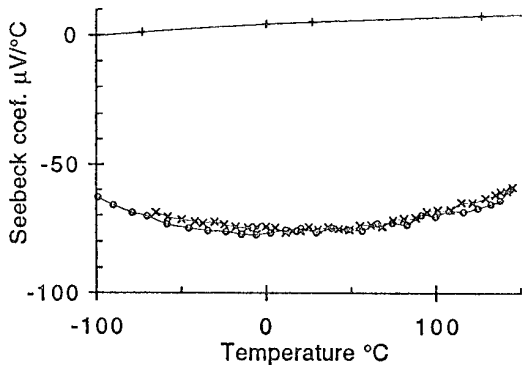


Figure 6: Seebeck coefficient of a Bi film (o) and a Bi/Bi<sub>0.86</sub>Sb<sub>0.14</sub> multilayer film (x) relative to platinum. The top curve (+) is the absolute Seebeck coefficient relative to platinum and forms the zero for the absolute Seebeck coefficient scale.

The resistivity of these films can be compared with that of Bi and Bi<sub>0.86</sub>Sb<sub>0.14</sub> single layer films. The resistivity of the Bi<sub>0.86</sub>Sb<sub>0.14</sub> film is higher than that of the Bi film, as is found for bulk material (figure 7). The resistivity for the multilayer is higher than either the Bi or Bi<sub>0.86</sub>Sb<sub>0.14</sub> single layer films. The multilayer films show no evidence of enhancement in the electrical conductivity from confinement of the conduction electrons in the multilayer structure. It is likely that the observed small increase in resistance is from scattering at the multilayer interfaces.

In conclusion we have demonstrated that multilayers of Bi and Bi<sub>0.86</sub>Sb<sub>0.14</sub> can be deposited at high enough temperature to achieve epitaxy, and yet not get complete interdiffusion of the layers. This is the first time that high quality epitaxial multilayers of these materials have been produced at a length scale where quantum confinement effects may become apparent. The small modulation in the bandgap in this multilayer structure, however, is found not enhance the electrical conductivity.

#### Directions

We have demonstrated that it is possible to deposit multilayer films at high enough temperature to achieve epitaxial growth in the Bi, Bi<sub>0.86</sub>Sb<sub>0.14</sub> system, and presented many of the important parameters for sputter deposition. This work is now being extended to the Bi<sub>2-x</sub>Sb<sub>x</sub>Te<sub>3-y</sub>Se<sub>y</sub> compound thermoelectric materials. This family of materials includes some of the best thermoelectric materials known, as well as allowing a wide range of possible bandgaps. The similarity of crystal structure of these materials to Bi and Bi<sub>0.86</sub>Sb<sub>0.14</sub> suggests that many of the parameters defined above can be applied to these more complicated materials. These high quality multilayers will allow us to explore the possibility of theoretically predicted enhancements in thermoelectric materials caused by quantum confinement in layered structures.

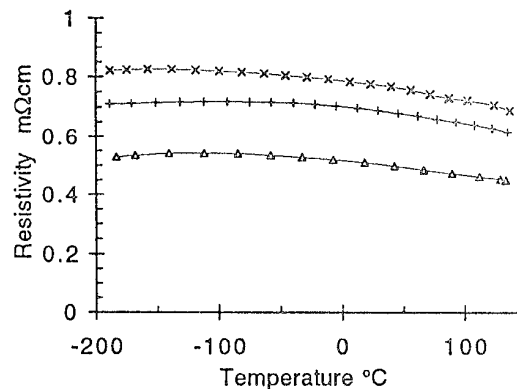


Figure 7: Resistivity for films of: Bi (Δ), Bi<sub>0.86</sub>Sb<sub>0.14</sub> (+), and Bi/Bi<sub>0.86</sub>Sb<sub>0.14</sub> multilayer (x).

#### Acknowledgments

Funding for this project was provided by W. Polansky and D. Barney of the United States Department of Energy (U.S. DOE) Office of Basic Energy Sciences (OBES). We would like to acknowledge D. Makowiecki for use of the sputtering chamber, and J. Yoshiyama for doing the SEM. This work was done under the auspices of the U.S. DOE by Lawrence Livermore National Laboratory under Contract No. W-7405-Eng-48.

#### Reference

- [1] L.D. Hicks, M.S. Dresselhaus, "Effect of Quantum-Well Structures on the Thermoelectric Figure of Merit," *Phys. Rev. B* 1993, v.47, No.19, pp.12727-12731.
- [2] L.D. Hicks, M.S. Dresselhaus, "BiSb/PbTeSe Superlattices as a New Thermoelectric Cooling Material: Optimization of the Figure of Merit," unpublished report, March 15, 1993.
- [3] J.C. Farmer, T.W. Barbee Jr., G.C. Chapline Jr., R.J. Foreman, L.J. Summers, M.S. Dresselhaus, and L.D. Hicks, "Sputter Deposition of Multilayer Thermoelectric Films: An Approach to the Fabrication of Two-Dimensional Quantum Wells," Proc. of the XIII International Conference on Thermoelectrics, 1994, pp.217-225.
- [4] A.V. Wagner, R.J. Foreman, L.J. Summers, T.W. Barbee, Jr., and J.C. Farmer, "Multilayer Thermoelectric Films: A Strategy For The Enhancement of ZT", to be published in, *Proceedings of the 30th Intersociety Energy Conversion Engineering Conference*, 1995.
- [5] F. Volklein and E. Kessler, "Temperature and Thickness Dependence of Electrical and Thermal Transport Coefficients of Bi<sub>1-x</sub>Sb<sub>x</sub> Films in an Anisotropic, Non-Degenerate Two-Band Model," *Phys. Stat. Sol. (b)* 1986, v.134, pp.351-362.
- [6] N.B. Mustafaev, "Energy Band Structure of Bi-Bi<sub>1-x</sub>Sb<sub>x</sub> Compositional Superlattices," *J. Phys.: Condens. Matter.* 1994, v.6, pp.2039-2046.
- [7] D. Agassi and T.K. Chu, "Interface States in Bi/Bi<sub>1-x</sub>Sb<sub>x</sub> Heterojunctions," *Appl. Phys. Lett.*, 1987, v.51, pp.2227-2229.
- [8] I. Yoshida, S. Tanuma, and J. Takahashi, "Anomalous Thermoelectric Power of Bi/Sb Multilayer Films and Related Transport Phenomena," *J. of Magnetism and Magnetic Materials*, 1993, v.126, pp.608-611.

## ESTIMATION OF THE MAXIMUM ELECTRICAL POWER FACTOR OF THERMOELECTRIC MATERIALS USING $\alpha\text{-}ln\sigma$ PLOT

D.M.Rowe, Gao Min and S.G.K. Williams

*School of Engineering, University of Wales Cardiff, UK.*

In thermoelectric semiconductors, the electrical power factor  $\alpha^2\sigma$  (where  $\alpha$  is the Seebeck coefficient and  $\sigma$  is the electrical conductivity) is strongly dependent upon the carrier concentration. This dependence creates some difficulty when experimentally evaluating potential thermoelectric materials which are non-optimally doped at the temperature of measurement, or if the doping levels are unknown. In this paper, a relationship between the electrical power factor and  $\alpha\text{-}ln\sigma$  plots is investigated. The results indicate that  $\alpha\text{-}ln\sigma$  plots can be used to estimate the maximum electrical power factor of semiconductors using the Seebeck coefficient and electrical conductivity as measured on non-optimized specimens. The use of an  $\alpha\text{-}ln\sigma$  plot provides a better estimate of the electrical power factor than the so-called materials parameter.

### Introduction

During the past five years or so the unique properties of a thermoelectric energy conversion system has attracted increased attention for commercial applications when operated in both the Peltier mode (refrigeration) and in the Seebeck mode (generation). The major factor restricting the wide-spread commercial application of thermoelectric devices is the low values of the dimensionless figure-of-merit (currently around 1). Supported by the Japanese New Energy and Industrial Development Organization (NEDO), the thermoelectric group at Cardiff has embarked upon a programme of research aimed at developing material with improved thermoelectric performance.

Central to any programme of material development is the availability of facilities/procedures to rapidly assess the thermoelectric properties of the prepared materials. In this paper a procedure is described which enables an initial screening to be carried out and facilitates the identification of potentially good thermoelectric materials.

### Conventional material parameter

Conventionally the material parameter,  $\beta$ , is employed in the search for potential thermoelectric materials and is related to the dimensionless thermoelectric figure-of-merit,  $ZT$ , by [1]

$$ZT = \frac{\alpha^2\sigma T}{\lambda} = \frac{((s+5/2)-\xi)^2}{(s+5/2)+(\beta \exp(\xi))^{-1}} \quad (1)$$

where,  $\alpha$  is the Seebeck coefficient and  $\sigma$  the electrical conductivity,  $\lambda$  the thermal conductivity,  $T$  is the absolute temperature,  $s$  the scattering parameter,  $\xi$  the reduced Fermi energy and

$$\beta = 5.74 \times 10^{-6} T^{3/2} (m^*/m_0)^{3/2} \mu / \lambda_l \quad (2)$$

here,  $m^*$  the effective mass,  $m_0$  the free electron mass,  $\mu$  the carrier mobility and  $\lambda_l$  the lattice component of thermal conductivity.

In principle,  $ZT$  provides guidelines in identifying potentially good thermoelectric materials (i.e., materials

with a high Seebeck coefficient, high electrical conductivity and low thermal conductivity). However, usually  $\alpha$ ,  $\sigma$  and  $\lambda$  change significantly with both temperature and carrier concentration. Consequently, in practice, it is not convenient to use  $ZT$  as a performance indicator because of the prohibitive amount of work associated with the preparation of specimens at various doping levels and the subsequent measurements of  $\alpha$ ,  $\sigma$  and  $\lambda$  over a wide temperature range.

The parameters  $m^*$ ,  $\mu$  and  $\lambda_l$  in equation (2) depend weakly on the carrier concentration and the values of  $\beta$  obtained for non-optimized specimens does not differ significantly from that of optimized specimens. Consequently,  $\beta$  has been employed as an indicator in searching for a potentially high  $ZT$  materials [2-5]. In the expression for  $\beta$ , the thermal conductivity and electrical power factor ( $\alpha^2\sigma$ ) are incorporated in  $\lambda_l$  and the quantity  $(m^*/m_0)^{3/2}\mu$ , respectively. Since the determination of  $m^*$  and  $\mu$  requires sophisticated measurement techniques, the practical use of  $\beta$  has been limited.

### $\alpha\text{-}ln\sigma$ plot

Based on a simple theoretical model using Boltzmann statistics, the Seebeck coefficient, carrier concentration and electrical conductivity of semiconductors are respectively given by

$$\alpha = \frac{k}{e} ((s+5/2)-\xi) \quad (3)$$

$$n = N_c \exp(\xi) \approx 4.83 \times 10^{21} T^{3/2} (m^*/m_0)^{3/2} \exp(\xi) \quad (4)$$

$$\sigma = en\mu \quad (5)$$

where,  $k$  is the Boltzmann constant and  $e$  the electronic charge. A relationship between the Seebeck coefficient and electrical conductivity can be obtained

\*The work reported here is based upon a paper submitted to Journal of Material Science Letters.

$$\alpha = m(b - \ln \sigma) \quad (6)$$

where

$$m = k/e \approx 86.14 \text{ } \mu\text{V/K} \quad (7)$$

$$b = 5/2 + s + \ln N_c \mu e \\ \approx s + \ln[T^{3/2}(m^*/m_0)^{3/2} \mu] - 4.66 \quad (8)$$

It can be seen from equation (6) that the plot of  $\alpha$  versus  $\ln \sigma$  is a straight line, whose slope is  $m$  ( $=k/e$ ) with an intercept  $b$  on the  $\ln \sigma$  axis. This indicates that the quantity  $T^{3/2}(m^*/m_0)^{3/2} \mu$  may be obtained indirectly from measurements of  $\alpha$  and  $\sigma$ , which in practice are much easier to measure than  $\mu$  and  $m^*$ .

The optimum electrical conductivity  $\sigma_{opt}$  and the maximum electrical power factor  $(\alpha^2 \sigma)_{max}$  are given by

$$\sigma_{opt} = \exp(b-2) \quad (9)$$

$$(\alpha^2 \sigma)_{max} = 4m^2 \exp(b-2) \quad (10)$$

It can be seen that the maximum electrical power factor is dependent upon both  $m$  and  $b$  of the  $\alpha$ - $\ln \sigma$  plot. Since an increase in  $T^{3/2}(m^*/m_0)^{3/2} \mu$  results in an increase in  $b$ , a large value of  $T^{3/2}(m^*/m_0)^{3/2} \mu$  indicates a potentially large electrical power factor. However, it should be noted that the maximum electrical power factor can also be affected by  $m$  and  $s$ . Evidently, the use of  $\beta$  as a thermoelectric performance indicator neglects the influence of  $m$  and  $s$ .

#### Discussion and conclusion

In figure 1 are shown room temperature  $\alpha$ - $\ln \sigma$  plots obtained from published data for several thermoelectric materials [6-10]. A linear relationship between  $\alpha$  and  $\ln \sigma$  is evident for all the materials investigated. However, the slope of these straight lines,  $m$ , is not exactly equal to  $k/e$ , but varies with different materials. The values of  $b$  are around 9.5 for  $\text{Bi}_2\text{Te}_3$ ,  $\text{PbTe}$  and  $\text{SiGe}$ , but are significantly less for materials such as  $\text{LaS}$ ,  $\text{LaTe}$  and  $\text{AgSbTe}$ . The corresponding electrical power factors can be calculated using figure 1 and the results are displayed as a function of electrical conductivity as shown in figure 2.

As is evident from equation 1, the influence of  $s$  on the thermoelectric figure-of-merit is neglected when  $\beta$  is used as a thermoelectric performance indicator. However, the influence of  $m$  is unexpected as the theoretical model employed in deriving  $\beta$  indicates that  $m$  is a constant for all extrinsic semiconductors at any temperatures. The experimental data presented in figure 1 show that  $m$  varies for different materials and also changes with temperature as shown in figure 3. Although only  $\text{SiGe-GaP}$  alloy data is shown in figure 3, other materials such as  $\text{Bi}_2\text{Te}_3$  and  $\text{PbTe}$  exhibited similar features, i.e.,  $m$  changes with temperature but  $b$  remains almost constant over the temperature ranges investigated. However, in the case of

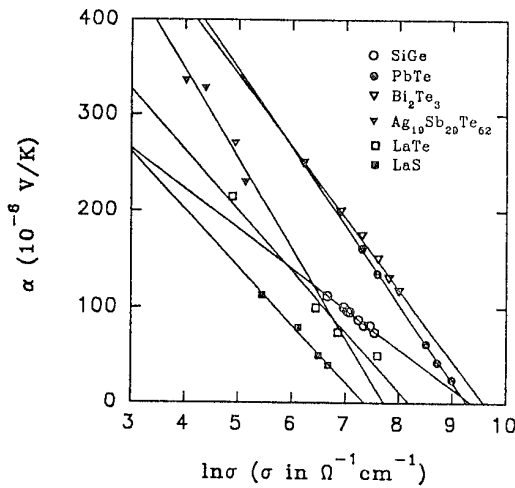


Figure 1.  $\alpha$ - $\ln \sigma$  plots for  $\text{SiGe}$ ,  $\text{PbTe}$ ,  $\text{Bi}_2\text{Te}_3$ ,  $\text{LaTe}$ ,  $\text{LaS}$  and  $\text{Ag}_{19}\text{Sb}_{29}\text{Te}_{52}$ .

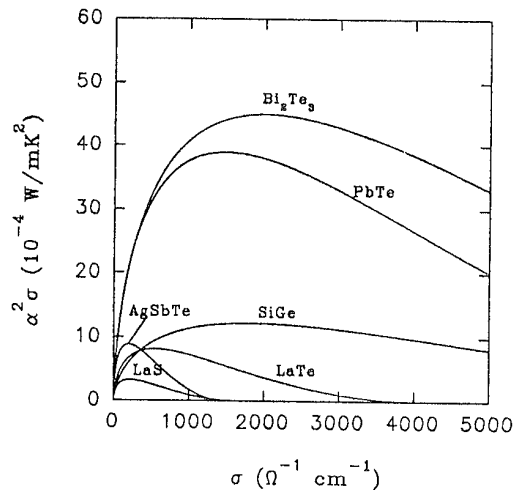


Figure 2. The electrical power factor  $(\alpha^2 \sigma)$  as a function of the electrical conductivity ( $\sigma$ ).

$\text{Bi}_2\text{Te}_3$  and  $\text{PbTe}$ ,  $m$  decreases with increasing temperature over the temperature range 300-600 K. The temperature independence of  $b$  may be explained by the fact that an increase in  $T^{3/2}(m^*/m_0)^{3/2} \mu$  with increasing temperature is compensated by a decrease in  $\mu$ , while the density-of-states effective mass is almost independent of temperature [11]. Although the authors cannot explain the variation of  $m$  with materials and temperature, its influence on the electrical power factor is evident. Furthermore, this result shows a failure of the simplified theoretical model in describing the detailed relationship between  $\alpha$  and  $\sigma$ . It is apparent that a deeper knowledge of this relationship and

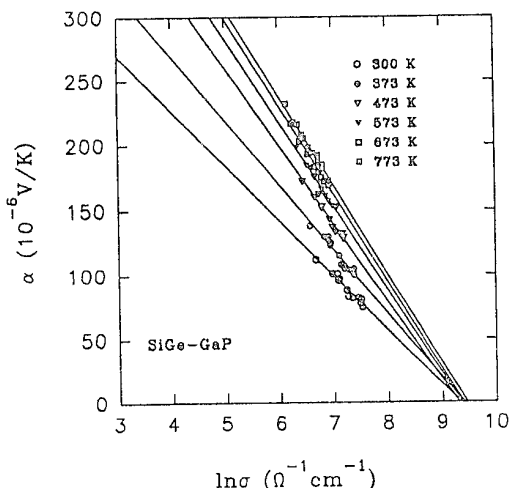


Figure 3.  $\alpha$ -ln $\sigma$  plots for SiGe-GaP alloys at different temperatures.

the factors influencing "m" will provide helpful theoretical guidelines for improving the electrical power factor.

In conclusion, an  $\alpha$ -ln $\sigma$  plot provides a better estimate of the electrical power factor than  $T^{3/2}(m^*/m_0)^{3/2}\mu$ . The use of  $\alpha$ -ln $\sigma$  plot only requires data from relative simple measurements, and also provides a better indication of thermoelectric performance as it takes into account the influence of both  $m$  and  $s$ . Furthermore,  $\alpha$ -ln $\sigma$  plot can readily be used to estimate the optimum electrical conductivity of the thermoelectric materials.

#### Acknowledgment

This work is supported by the New Energy and Industrial Technology Development Organization (NEDO), the Energy Conversion Centre, Japan.

#### References

- [1] H. J. Goldsmid, *Electronic Refrigeration*, Pion, London, 1986, p58
- [2] A. F. Ioffe, *Semiconductor Thermoelements and Thermoelectric cooling*, Infosearch, London, 1957, p53
- [3] D. M. Rowe and C. M. Bhandri, *Modern thermoelectrics* Holt, Rinehart and Winston, London, 1981, p29
- [4] C. B. Vining, *Proceedings of 12th International Conference on Thermoelectric*, Yokohama, Japan, November 9-11, 1993, edited by K. Matsuura, p126
- [5] G. A. Slack, *CRC Handbook of Thermoelectrics*, edited by D.M.Rowe, to be published in 1995.
- [6] H. J. Goldsmid, *Electronic Refrigeration*, Pion, London, 1986, p95
- [7] R. W. Fritts, private communication.
- [8] L. R. Danielson, S. Marsuda and V. Raag, *Proceedings of 5th International Conference on Thermoelectric*, Texas, USA, 1984, p41
- [9] L. R. Danielson, M. N. Alexander, C. Vining, R. A. Lockwood and C. Wood, *Proceedings of 7th International Conference on Thermoelectric*, Texas, USA, 1988, p71
- [10] R. M. Ayrat-Marin, G. Brun and J. C. Tedenac, *Proceedings of 13th International Conference on Thermoelectric*, Nancy, France, 1989, p117
- [11] D. M. Rowe and Gao Min, *Proceedings of 13th International Conference on Thermoelectric*, Kansas, USA, 1994, p250

## IMPROVING THE POWER OUTPUT AND CONVERSION EFFICIENCY OF PELTIER MODULES WHEN USED AS GENERATORS

D.M. Rowe, Gao Min and S.G.K. Williams

*School of Engineering, University of Wales Cardiff, UK*

A realistic model which takes into consideration thermal and electrical contact resistances is used to investigate the factors which influence the power output and conversion efficiency of thermoelectric modules. The analysis indicates that these contact resistances are competitive factors which affect both power output and conversion efficiency. Although improvements in power output and conversion efficiency can be achieved by reducing either of these resistances, a reduction in thermal contact resistance has a more significant effect.

### Introduction

Recent interest in "low temperature" waste heat energy conversion have encouraged investigation into the use of Peltier modules as generators [1-3]. Results of previous investigations [4,5] showed that the power output and conversion efficiency of a Peltier module are dependent upon several factors, among them are thermocouple length, and electrical and thermal contact resistances. The conversion efficiency decreases with a decrease in thermocouple length, while the power output reaches a maximum at an optimum length. It was shown that the dependence of the power output and conversion efficiency on the thermocouple length are significantly affected by the electrical and thermal contact resistances. Improvement in either of these resistances can also result in an increase in the power output and conversion efficiency. The objective of the work reported in this paper is to identify dominant factors contributing to these contact resistances which limit the thermoelectric performance of a Peltier module when operated in the generating mode.

### Contact effect on power output

The basic structure of a Peltier module is shown schematically in figure 1. It consists of n-type and p-type semiconductor thermoelements which are connected in series by highly conducting copper strips and sandwiched between two plates of high thermally conducting but electrically insulating ceramics. The electrical contact comprises the copper strips / thermoelement interfaces as indicated by 3 and 4 in the figure. The thermal contact includes ceramic layers, copper strips together with the interfaces shown in the figure. Based upon a model previously reported [5] which took into account the influence of these contact resistances, the power output per unit area of the thermocouple in a Peltier module can be expressed as,

$$P = \frac{P}{NA} = \frac{\alpha^2}{2\rho(l+n)(1+2rl_c/l)^2} \Delta T^2 \quad (1)$$

where,  $\alpha$  and  $\rho$  are the Seebeck coefficient and electrical resistivity of the thermoelectric material, respectively.  $N$  is

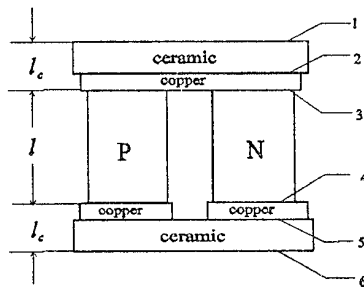


**Figure 1** Simplified structure of Peltier module. Interfaces 1-6 contribute to the thermal contact resistance; interfaces 3 and 4 contribute to the electrical contact resistance.

the number of thermocouples in a module,  $A$  the cross-sectional area of thermoelements,  $\Delta T$  the temperature difference across the module,  $l$  the length of the thermocouples,  $l_c$  the thickness of the ceramic plates, and  $n=2\rho/\rho$  is the ratio of contact to bulk electrical resistivity,  $r=\lambda/\lambda_c$  is the ratio of bulk to contact thermal conductivity.

Using equation (1) and assuming  $\alpha=200 \mu V/K$ ,  $\rho=10^{-3} \Omega cm$ ,  $\Delta T=100 K$ ,  $l=1 mm$  and  $l_c=1 mm$ , the power output per unit area was calculated and the results are shown as a function of contact parameters  $n$  and  $r$  in figure 2. It can be seen that the power output increases with a decrease in  $n$  or  $r$ . However, an increase in power output which accompanies a reduction in  $r$  is much more significant than that due to reducing  $n$ . A reduction in  $r$  from 0.2 to 0.02 can result in more than a doubling of the power output. However, an increase of less than 10 % can be obtained by a similar reduction in  $n$ . For commercially available Peltier modules, values of 0.1 mm and 0.2 for  $n$  and  $r$  respectively have been obtained [6]. It is apparent that a more substantial increase in power output can be achieved by improving the thermal contact resistance rather than the electrical contact resistance.

For a given thermoelectric material, the reduction in  $r$  can be achieved by increasing  $\lambda_c$ , which is an equivalent thermal conductivity comprised of a combined effect of the copper strips, ceramic plates and all the interfaces

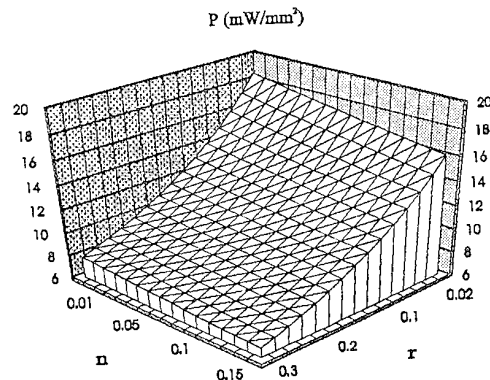


Figure 2 Power output per unit area as a function of thermal and electrical contact parameters  $r$  and  $n$ .

shown in figure 1. Usually, the influence of the copper strips on  $\lambda_c$  can be neglected due to their very high thermal conductivity and a very large ratio of cross-sectional area to length. In this case,  $\lambda_c$  can be expressed as

$$\lambda_c = \frac{\lambda_1 \lambda_2 l_c}{\lambda_1 + \lambda_2 l_c} \quad (2)$$

where,  $\lambda_1$  is the thermal conductivity of the ceramic layer, and  $\lambda_2$  the equivalent thermal conductivity of all interfaces. In order to identify the dominant factors among  $\lambda_c$ , the power output per unit area was calculated and is shown as a function of thermocouple length for different  $\lambda_1$ ,  $\lambda_2$  and  $l_c$  in figures 3-5, respectively. For commercially available Peltier modules, the value of  $l_c$  is about 0.7-1 mm,  $\lambda_1$  is about 34 W/mK for  $\text{Al}_2\text{O}_3$  ceramic plates and  $\lambda_2$  is around  $10^4$  W/m<sup>2</sup>K [7]. It can be seen that a very limited increase in the power output can be obtained by increasing the thermal conductivity or by reducing the thickness of the ceramic insulating plates. However, a significant

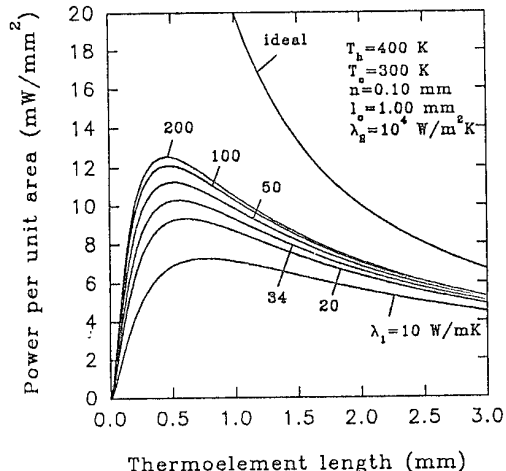


Figure 3 Power output per unit area as a function of thermocouple length for different  $\lambda_1$ .

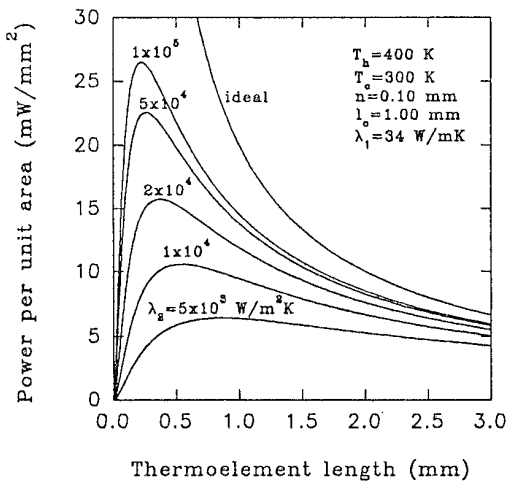


Figure 4 Power output per unit area as a function of thermocouple length for different  $\lambda_2$ .

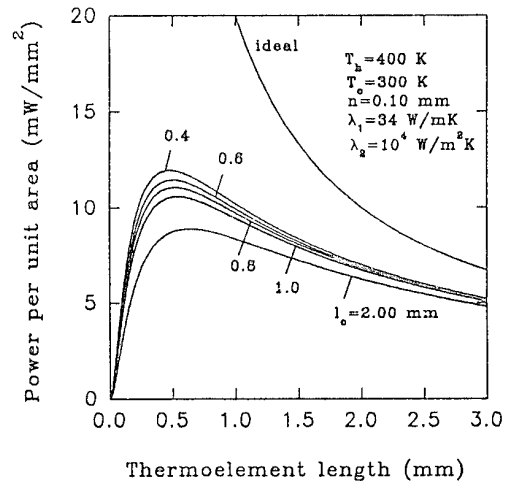


Figure 5 Power output per unit area as a function of thermocouple length for different  $l_c$ .

increase in the power output can be obtained by reducing the thermal conductivity of the interfaces. Evidently, the thermal contact resistance due to the interfaces is the dominant factor which limits the power output of the modules.

#### Contact effect on conversion efficiency

The conversion efficiency of a Peltier module when operated as a generator can be expressed as [5],

$$\phi = \left( \frac{T_h - T_c}{T_h} \right) \left[ \left( 1 + 2r_c/l \right)^2 \left[ 2 - \frac{1}{2} \left( \frac{T_h - T_c}{T_h} \right) + \left( \frac{4}{zT_h} \right) \left( \frac{l+n}{l+2r_c} \right) \right] \right]^{-1} \quad (3)$$

where,  $z$  is the thermoelectric figure-of-merit of the thermocouple material,  $T_h$  and  $T_c$  are temperatures on the hot and cold sides of the module.

Using equation (3) and making similar assumptions to those employed in the previous section, the conversion efficiency of Peltier modules when used in the generating mode was calculated and is shown as a function of  $n$  and  $r$  in figure 6. It can be seen that the electrical and thermal contact resistances affect the conversion efficiency in a similar manner to power output. Furthermore, it is noted that the percentage increase in the power output due to a reduction in  $r$  (or  $n$ ) is independent of the value of  $n$  (or  $r$ ). However, the percentage increase in the conversion efficiency by reducing  $r$  (or  $n$ ) is dependent upon the value of  $n$  (or  $r$ ) and is more significant for a given  $n$  (or  $r$ ) with a smaller value than a larger value. This result indicates that  $n$  and  $r$  are competitive factors whose effect on the conversion efficiency depends on their relative values. For

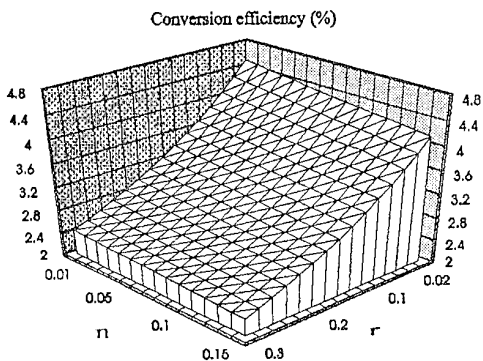


Figure 6 Conversion efficiency as a function of thermal and electrical contact parameters  $r$  and  $n$ .

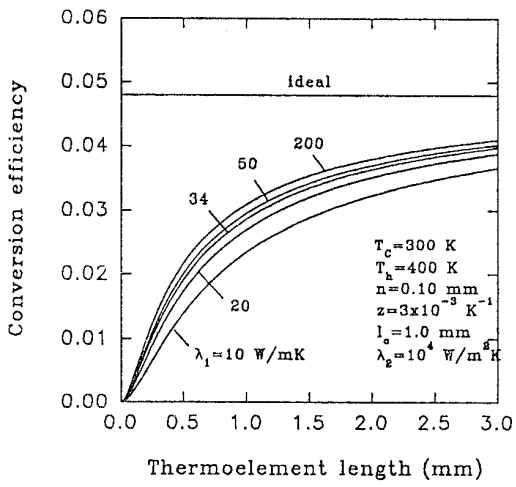


Figure 7 Conversion efficiency as a function of thermocouple length for different  $\lambda_1$ .

commercially available Peltier modules ( $r=0.20$  and  $n=0.10$  mm), it can be seen from figure 6 that reducing the thermal contact resistance plays a more important role in increasing the conversion efficiency than reducing the electrical contact resistance.

In figures 7-9 are shown the conversion efficiency as a function of the thermocouple length for different  $\lambda_1$ ,  $\lambda_2$  and  $l_c$ , respectively. The conversion efficiency decreases monotonically with reducing thermocouple length due to contact effects. For a given thermocouple length, the conversion efficiency is affected by  $\lambda_1$ ,  $\lambda_2$  and  $l_c$ . In practice, a very limited increase in the conversion efficiency can be obtained by increasing the thermal conductivity or reducing the thickness of ceramic plates. However, a significant increase in conversion efficiency

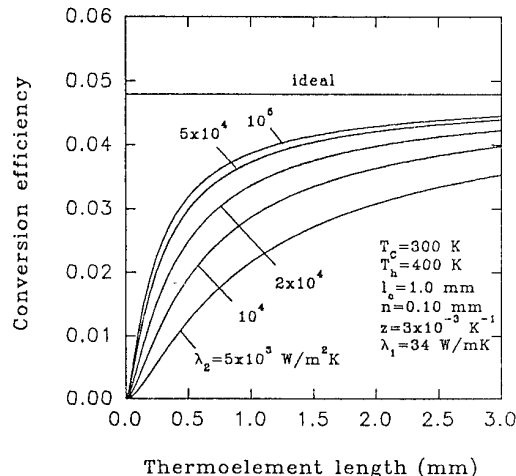


Figure 8 Conversion efficiency as a function of thermocouple length for different  $\lambda_2$ .

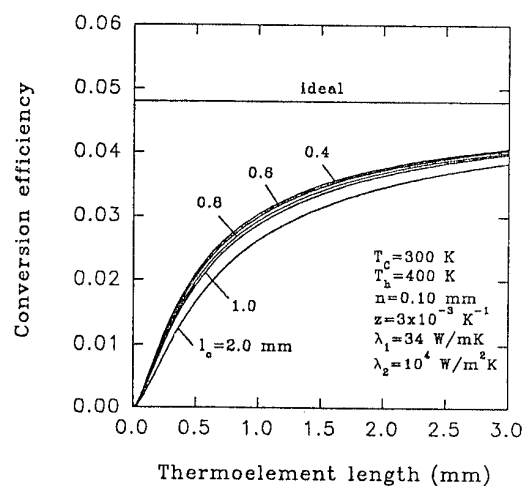


Figure 9 Conversion efficiency as a function of thermocouple length for different  $l_c$ .

may be possible by reducing the thermal conductivity of the interfaces. Consequently, the efforts to improve the thermoelectric performance of Peltier modules when used as generators should concentrated on reducing the thermal conductivity at the interfaces.

### Conclusions

The electrical and thermal contact resistance affect the length dependence of power output and conversion efficiency of Peltier modules when used in the generating mode. A decrease in the electrical or thermal contact resistance is beneficial both in improving the power output and conversion efficiency and in reducing the thermocouple length (i.e., a reduction in thermoelectric material). However, the results obtained from this investigation show that significant improvement in power output and conversion efficiency can only be obtained by reducing the thermal contact resistance. Furthermore, it has been identified that the thermal contact resistance at the interfaces is the dominant factor which contributes to the thermal contact resistance of the modules.

### Acknowledgment

This work is supported by the New Energy and Industrial Technology Development Organization, Japan.

### References

- [1] E.J. Burke and R.J. Buist, *Proc. 5th Int. Conf. Thermoelectric Energy*, Arlington, Texas, March 14-16, 1984, p91
- [2] K.T. Matsuura, *IEE. Japan*, 107-B (6), 1987, p307
- [3] G. Min and D. M. Rowe, *J. Power Sources*, 38, 1992, p253
- [4] A.F.Ioffe, *Semiconductor Thermoelements and Thermoelectric Cooling*, Infosearch Ltd., London, 1957.
- [5] G. Min and D.M. Rowe, *CRC Handbook of Thermoelectrics*, Ed. Rowe, 1995, CRC press, inc. Chapter 38
- [6] G. Min and D.M. Rowe, *Proc. 1st Young Scientists Conf., Yunnan Province*, China, 1992, p130
- [7] G. Min, D.M.Rowe, O. Assis and S.G.K. Williams, *Proc. 11th Int. Conf. Thermoelectrics*, Arlington, Texas, 1992, p210

## PROBLEMS AND PERSPECTIVES FOR THERMOELECTRICS

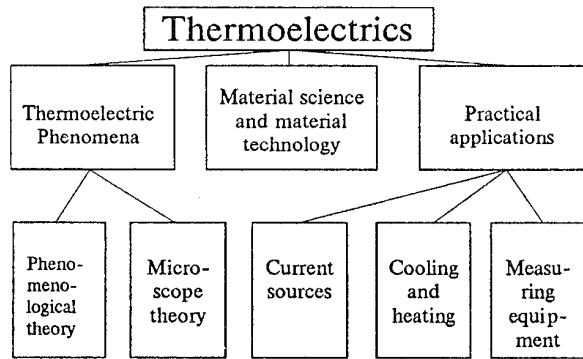
Anatychuk L.I.

*Institute of Thermoelectricity, Chernovtsy, 274000, General Post Office, box 86, Ukraine*

The results of main thermoelectrics development directions analysis are given. The priority directions of investigations in physics, technology and thermoelectricity using are formulated.

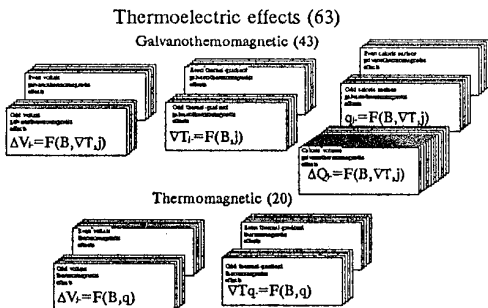
By now there are several priority directions for thermoelectrics development [fig.1]. These are theory for thermoelectric phenomena - phenomenological and microscopic; thermoelectric material science and materials technology; three main practical applications for thermoelectricity - energy sources, thermoelectric cooling and heating, measuring equipment.

*Fig.1. Main directions of thermoelectric development.*



Phenomenological investigations have led us to creating the full classification for all thermoelectric phenomena [fig.2] and finding the new 21 effects, which are of practical interest [1,2]. We want to emphasize that classification is only for linear approximations over the field influencing the substance. Studying the new linear effects and creating the classification for non-linear effects is the first important direction of thermoelectric study.

*Fig.2. Classification of the linear thermoelectric effects.*  
V - thermal e.m.f., B - magnetic field, j - current density,  
q - heat flow,  $\Delta Q$  - heat production.  
Effects number is shown in parenthesis.



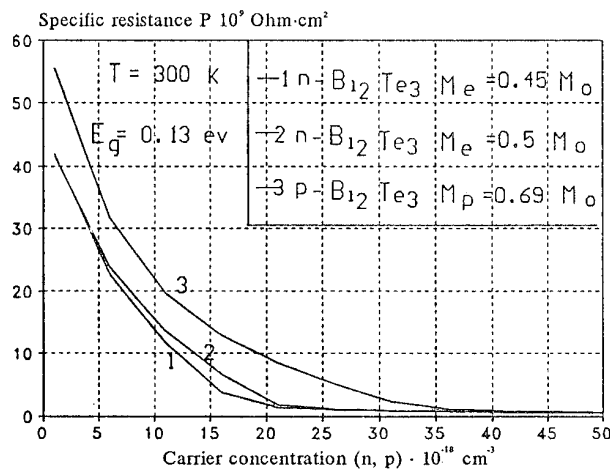
Phenomenological theory also allowed us to classify all versions of thermoelectric energy conversions. It was already mentioned that from this view thermoelectrics is in the initial stage of its development - of 124 versions only 15 are studied. Their study is the second important direction.

Therewith the given classification does not deal with variety of thermoelectric possibilities in different dynamic modes when heat fluxes, electric currents, magnetic fields, force affections and the substance qualities are the functions of time. Studies of dynamic cooling modes show the possibility to improve  $\Delta T$  and COP [3,4]. In general, dynamic modes investigations are the new step for thermoelectrics and the creation of absolutely new devices on combination of electric equipment and thermoelectrics is becoming possible. This is the third thermoelectric study direction.

Microscopic theory of thermoelectricity is created on the background of solid state physics and semiconductor physics advantages. Their use allows to solve the most of thermoelectric problems. But thermoelectric phenomena in the extremal conditions are not studied well, namely when the temperature gradient is big. Even the first investigations of this show the beautiful perspectives for conversion efficiency increase [5]. This is the fourth important direction for thermoelectric study.

The microscope theory of contact phenomena in the boundary thermoelectric material - metal requires the further development. Studies [6] have determined the approximate limits of possibly minimum values of contact resistances [fig.3]. This is extremely important information both for minimizing the thermoelectric converters and to effective study of dynamic modes. But the real physical models of contacts are not studied yet and they are fifth direction for thermoelectric study.

*Fig.3. Minimal specific contact resistance.*



## New Effects

N	Effect name	Expression for effect description
	<b>Caloric volume effects:</b>	
1	Divergent Peltier effect	$-T j \text{Div}_T \alpha^{s+}$
2	Odd eddy Peltier effect	$-T j \text{rot} N^+$
3	Even eddy Peltier effect	$-T j \text{Div}_T \alpha^{s-}$
4	Even Thomson effect	$-T j \frac{\partial}{\partial T} \alpha^{s+} \tau - \frac{\partial}{\partial T} N^+ [\tau \times j]$
5	Deviator Bridgman effect	$-T j \text{Dev}(\alpha^{s+}) : \text{Def } j$
6	Eddy Bridgman effect	$-T N^+ \text{rot} j$
	<b>Thermal gradient effects:</b>	
7	Even transverse Maggi-Righi-LeDuc effect in longitudinal field	$\Delta \tau_q^+ C \perp$
8	Odd transverse Maggi-Righi-LeDuc effect in longitudinal field	$\Delta \tau_q^- C \perp$
9	Even thermomagnetic analog of Grabner effect	$\Delta \tau_q^+ P \perp G$
10	Odd thermomagnetic analog of Grabner effect	$\Delta \tau_q^- P \perp G$
11	Even thermomagnetic analog of Hall effect	$\Delta \tau_q^+ P \perp G$
12	Galvanothermomagnetic thermal	$\Delta \tau_j^+ P \perp H$
13	gradient	$\Delta \tau_j^+ P \parallel G$
14	effects	$\Delta \tau_j^+ C \perp$
15	(effects have no names yet)	$\Delta \tau_j^- P \parallel$
16		$\Delta \tau_j^- P \parallel G$
17	Caloric	$\Delta K P \parallel$
18	surface	$\Delta K_j P \parallel G$
19	Galvanothermomagnetic	$\Delta K_j C \parallel$
20	effects	$\Delta K_j C \perp$
21	(effects have no names yet)	$\Delta K_j P \perp H$

Symbol list:  
 T - temperature, j - current density,  $\alpha$  - Seebeck coefficient, N - Nernst vector,  $\tau$  - temperature gradient, q - heat flow density, II - longitudinal,  $\perp$  - transversal (to magnetic field), c - colinear, p - transversal (to initial flow), G - analog of Grabner effect, H - analog of Grabner effect, K - surface heat production density

Problems of material science and material technology are still the main ones. First of all these are problems of increasing the figure of merit  $ZT \approx 1$ . Now the value of it is about 1. This means that in generation mode thermoelectrics is competitive by efficiency at capacities less than 1 kW [fig.4] [7], and in the cooling mode [fig.5] at coefficients of performance less than 20 - 30 W [8]. Making it more competitive in classical manner is supposed to be due to  $Z$  increase. But it is known that at  $Z$  increase the conversion efficiency increases much less [fig.6]. Thus, at  $ZT$  increase at 10 times the conversion efficiency increases no more than 2-3 times [fig.7]. That's why it is important to know what maximum values for  $ZT$  can one expect in the future. This is the sixth direction for the study.

*Fig.4. The dependence of the energy heat engine-operated electric generators efficiency on the electric power. 1-carburator engine; 2-diesel; 3-gas and steam turbine; 4-TE konvertors efficiency limit. The quadrates correspond to the well-known Stirling engines using*

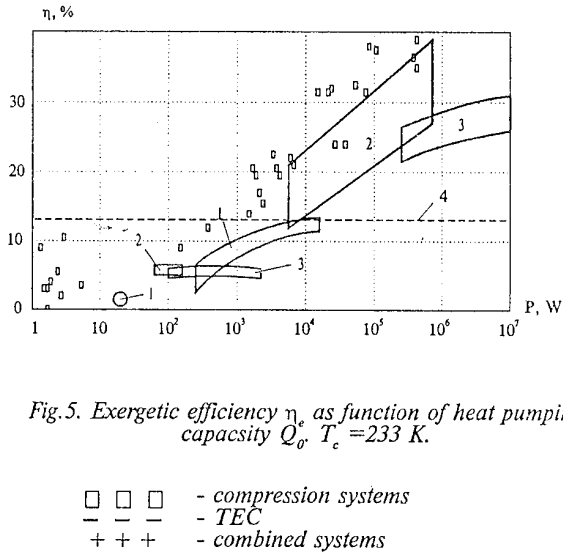
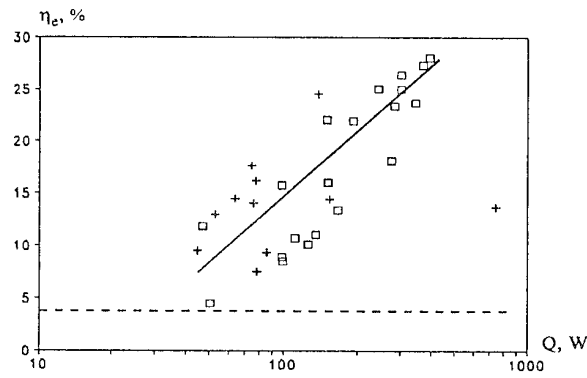


*Fig.5. Exergetic efficiency  $\eta_e$  as function of heat pumping capacity  $Q_o$ ,  $T_c = 233$  K.*



Investigations done in the Institute of Thermoelectricity, Ukraine [fig.8] for the known models of electron and phonon spectra and for the best combinations of microscopic substance parameters, have shown that in the best case value of  $ZT$  can reach 3 [9]. Really this value will be much less, that's why we should not expect the big changes in thermoelectric energy conversion due to figure of merit increase in usual thermoelectric materials. In this connection we must look for the materials with high  $ZT$  value beyond the usual thermoelectric structures. It is necessary to create structures and technologies for artificial

thermoelectric materials where we can create the conditions for the best  $Z$  values. This is direction number seven.

*Fig.6. Dependence of the thermoelectric conversion efficiency by Carnot cycle one on the thermoelectric figure of merit*

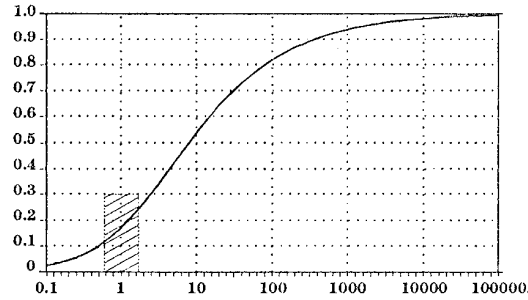


*Fig.7. Dependence of thermoelectric conversion efficiency on figure of merit for different maximum operation temperature.*

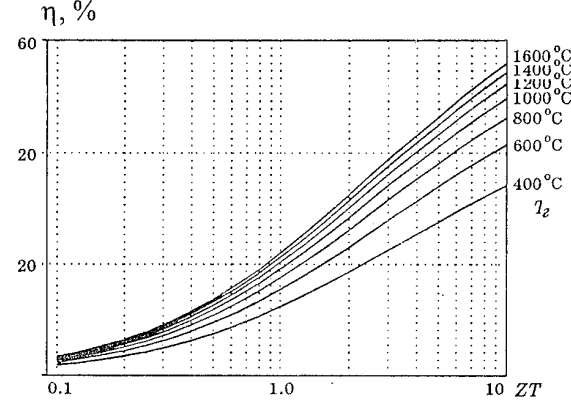
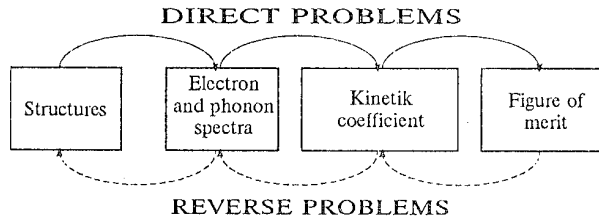


*Fig.8. Scheme for providing the computer modelling of artificial thermoelectric structure*

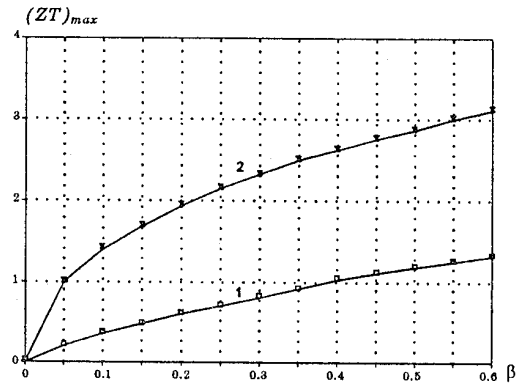


One of the methods for these materials search is computer modelling the artificial structures [10]. This is eighth direction in thermoelectric study. For its realization we must work on the reliable methods for description the connections between substance structure, phonon and electron spectra, kinetic coefficients and figure of merit [fig.9]. Such methods are developed for solving the direct problems of solid state physics, where from the prescribed substance structure the material figure of merit is defined. Computer modelling supposes the material structure finding for the prescribed limiting values of figure of merit [11].

*Fig. 11. Classification of optimal control problems in thermoelectricity*

Fig.9. Dependence thermoelectric figure og merit on parameter  $\beta$

- 1 - for the carrier-acoustic phonon scattering
- 2 - for the carrier-ionized impurity scattering



The other important direction of thermoelectric material science is the transfer from optimization by numbers to the same by functions for reaching the maximum figure of merit. This is ninth direction of thermoelectric study. Let's deal with it more precisely.

After discovering the Seebeck and Peltier effects thermoelectric material and thermoelement size optimization were done by the best numbers

$$n = n_0; p = p_0;$$

$$\frac{S_n}{l_n} = \left( \frac{S_n}{l_n} \right)_0;$$

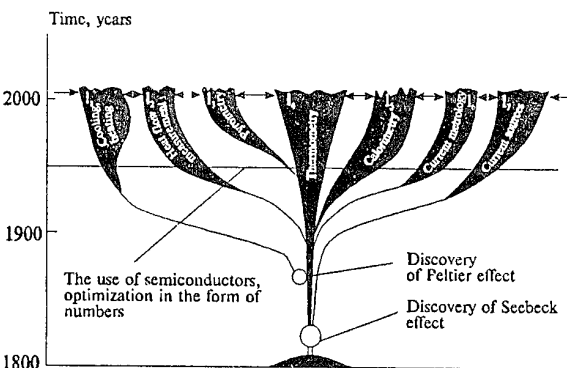
$$\frac{S_p}{l_p} = \left( \frac{S_p}{l_p} \right)_0;$$

$$I = I_0$$

where  $n, p$  are electrons and holes concentrations,  $S, l$  are legs dimensions,  $I$  is current.

This was the main method for thermoelectric conversion efficiency increase. This approach has led to the fast development of all the practical thermoelectricity applications [fig.10].

Fig.10. The tree of thermoelectricity evolution.



Now the reaching of maximum conversion efficiency by using optimal functions, material inhomogeneity, thermoelements dimensions and the current dependence on time, are studied more and more:

$$n = n(x); p = p(x);$$

$$\frac{S_n}{l_n} = \frac{S_n(x)}{l_n};$$

$$\frac{S_p}{l_p} = \frac{S_p(x)}{l_p};$$

$$I = I(t)$$

Search for such functions is being made by optimal control theory methods. The classification of all the thermoelectricity problems connected with optimal functions search, was made [fig.11] [12]. During this time several of these problems marked in the table, were solved.

Fig.12 shows the results of using optimal control for increasing the thermogenerators efficiency compared to the electric stations with internal combustion engines efficiency. It is seen that the efficiency reached makes thermogenerators competitive at capacities under 1 kW. Using cascade batteries of  $Bi-Te$ ,  $Pb-Te$ ,  $Ge-Si$  allows to increase the efficiency to about 15%. Making these batteries of optimal inhomogeneous materials will allow to increase thermogenerators efficiency up to 25%. Using optimal control when creating combined emission and thermoelectric generators will give the value of 40 - 45%. These efficiencies are big prospective to use the direct energy conversion methods.

Optimal control allows to increase materially also the characteristics for thermoelectric cooling. Thus, Using optimal functions of magnetic field in cascade low-temperature coolers of  $Bi-Te$  allows to increase the COP for 200 - 300 % [13]. So, using optimal functions makes thermoelectricity applications much more spread [Fig. 13].

Fig.12. Results of STEG optimal control.  
 1 - efficiency of internal combustion engine; 2 - attained TEG level; 3 -  $Bi-Te + Pb-Te + Ge-Si$  stage battery ( 15.7 %); 4 - stage battery with optimal control ( 16.9 %); 5-  $Bi-Te + PbTe$  (  $Ge-Te$  ) +  $Ge-Si$  functional gradient material stage battery ( 25 %); 6- combined emission + functional gradient material TEG ( 40 - 45%).

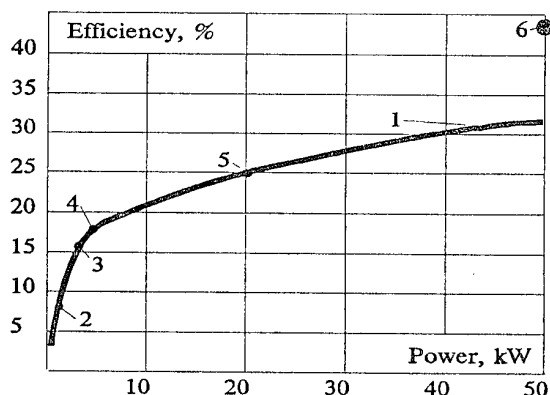
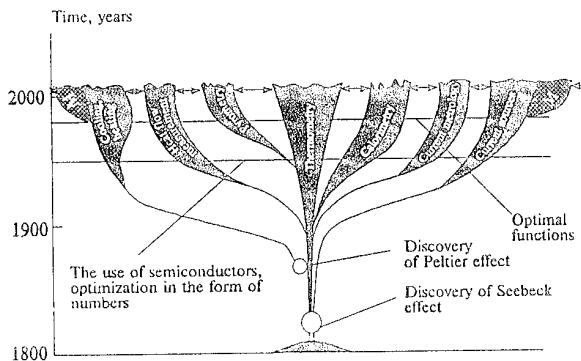


Fig.13. The tree of thermoelectricity evolution including the use of optimal functions.



The aforesaid nine directions for thermoelectric study do not include all the problems. But they are the base for creating the program for thermoelectric investigations in Ukraine. In this program several scientific centers of NAS and universities are involved.

This study range is far out of one country interests. For example, they are the matter of interest of Japan, where the society for functional-gradient materials is created.

Volume and complexity of thermoelectric studies is far out of separate scientists or separate laboratories possibilities. That's why the desire of scientists to cooperate is natural. That's why in September, 1994, the International Thermoelectric Academy was created. In the Academy the leading scientists of the USA, Japan, France, Russia, Belarus, Moldova, Kazakhstan and Ukraine are working together.

The aim of the Academy is to promote the growth of scientific research and students training in thermoelectrics.

The Journal of Thermoelectricity contains information of ITA activity and for publishing the results of scientific research.

#### References

1. O.J. Luste. Prognosis and classification of thermoelectric effects. Proc. XI International Conference on Thermoelectrics, Arlington, Texas, Okt. 7-9, 1992, pp. 125-135.
2. L.I. Anatychuk, O.J. Luste, Generalized criterions of Thermoelectric materials figure of merit. Proc XI International Conference on Thermoelectrics, Arlington, Texas, Okt. 7-9, 1992, pp. 87-91.
3. E.K. Iordanishvili, V.P. Babin. Non-stationary processes in thermoelectric and thermomagnetic systems of energy conversion. Moskva, Nauka, 1983, p. 216.
- 4 L.I. Anatychuk, A.V. Mikhailenko. To optimal controlling the dynamic processes in thermoelectric devices. Visnyk NAN Ukrayini, 1981, N 3,  
p. 14-20.
- 5 L.P. Bulat. On the nonlinear and nonlocal theory of thermoelectricity. Proceeding in IX International Conference on Thermoelectrics, 1990,  
p. 296-302.
6. L.I. Anatychuk, V.I. Litvinov, V.K. Dugaev, V.L. Volkov. On a possibility of determination of minimal contact resistance between metall and thermoelectric material. Journal of Thermoelectricity, 1993, No1,  
p. 70-77.
7. L.I. Anatychuk, L.N. Vikhor, L.Ja. Kushneryk, L.P. Lubarchuk. Rational field application for combined thermoelectric cooling devices. Journal of Thermoelectricity, 1994, No1, p. 16-26.
8. V.I. Mikhailovsky, V.V. Konopelnyuk. Rational usage of thermoelectric generators with a catalytic heat source. Journal of Thermoelectricity , 1994, No 2, p. 76-89.
9. L.P. Bulat, V.S. Zakordonets. Thermoelectric figure of merit limit. Journal of Thermoelectricity, 1994, No 2, p. 21-28.
10. L.I. Anatychuk, S.V. Kosyachenko, S.V. Melnichuk, V.M. Chernov. Theory for optimization of thermoelectric powder materials, in Proceedings of the XII International Conference on Thermoelectrics, Kanzas, USA, Aug., 1994.
11. O.N. Manik. Comprehensive approach to calculating thermoelectric material parameters. Journal of Thermoelectricity, 1994, No 1, p. 63-72.
12. L.I. Anatychuk, V.A. Semenyuk. Optimal control of thermoelectric material and devices properties, - Chernovtsy, Prut, 1992, p. 264.
13. L.I. Anatychuk, L.N. Vikhor. Optimal functions of magnetic field for the Peltier coolers, in Proceedings of XIV International Conference on Thermoelectrics, St. Peterburg, June, 1995.

## THE EXTRINSIC THOMSON EFFECT (ETE)

Richard J. Buist

TE Technology, Inc.

1590 Keane Drive

Traverse City, Michigan 49686

There are two well-known thermodynamic effects (with no magnetic field present) that give rise to or enhance the cooling effect in thermoelectric (TE) materials: The Peltier effect and the Thomson effect. The Thomson effect is produced by a Seebeck coefficient gradient induced by the temperature gradient in an operating TE pellet. This paper introduces a third TE cooling effect which is similar to the Thomson effect. It is similar in that it is an "extra" cooling effect brought on by an artificially or extrinsically produced Seebeck gradient. This effect, therefore, shall be referred to as the Extrinsic Thomson Effect (ETE).

### Introduction

The principle of the ETE was discovered at the Borg-Warner Research Center, Des Plaines, Illinois, in the early 1960's. It was later patented by Reich [1] in 1971. Technical papers were published on this subject by Reich [2] and Buist [3] in 1972. This effect was experimentally verified over 20 years ago at the Borg-Warner Research Center but was strategically not promoted and went essentially unnoticed in the thermoelectric (TE) industry. Thus, this paper is a re-introduction of the ETE in an effort to advance the future potentials for thermoelectric cooling applications.

### Derivation of the ETE

The discovery of the ETE was mathematically based as opposed to laboratory experimentation. It was first derived "on paper" and subsequently verified by experiment. It emerged via analysis of the fundamental one-dimensional thermodynamic equation derived by Domenicali [4]. This equation expressed the thermal equilibrium of a material under an applied electric field.

$$\nabla \cdot (\kappa \nabla T) - T (J_e \cdot \nabla S) = -J_e^2 \rho \quad (1)$$

Where:

$\kappa$  = thermal conductivity,  
 $T$  = absolute temperature,  
 $J_e$  = current density,  
 $S$  = Seebeck coefficient, and  
 $\rho$  = electrical resistivity.

The one-dimensional form reduces to:

$$d/dx (\kappa A dT/dx) - I T dS/dx = -I^2 \rho \quad (2)$$

Where:

$x$  = dimension in the direction of current flow,  
 $A$  = cross-sectional area, and  
 $I$  = current.

The second term of this equation can be expanded as follows:

$$I T dS/dx = I T \delta S/\delta T dT/dx + I T \delta S/\delta x \quad (3)$$

The first term on the right hand side of equation (3) is the well-known Thomson term:

$$I T \delta S/\delta T dT/dx = \text{Thomson Effect} \quad (4)$$

The second term in this expression is the ETE term:

$$I T \delta S/\delta x = \text{Extrinsic Thomson Effect} \quad (5)$$

If the Thomson term is of the proper algebraic sign, it will enhance cooling. Because of the similarity of these terms, if the ETE term is non-zero and of the proper algebraic sign it, too, will enhance cooling. That is, the only difference between these two terms is that in one case the Seebeck coefficient varies intrinsically along the length of the material, while in the other case, the Seebeck coefficient variance is extrinsic.

### Model Description

Although rigorous, the equations above are very complicated to solve, given the temperature-dependent nature of TE materials. Therefore, the simple but equally rigorous and accurate TE cooling calculation method presented by Buist [5] was used to carefully examine the nature of the ETE. This modeling process is a numerical method suitable for today's high-speed computational technology available in personal computers. It had been developed to accurately quantify the TE cooling performance in the presence of temperature-produced TE parameter variances in an operating TE pellet. In this case, however, it provided the means for separating the intrinsic versus extrinsic effects produced by parameter variance. As such, it has been employed to clearly and definitively establish the nature and some general principles of the ETE.

An example of the numerical calculation model for a given TE pellet is illustrated in Figure 1. This particular example illustrates how the TE pellet is mathematically dissected into 20 equal-sized segments. Actually, 80 such segments were used in the calculations described herein in order to provide a very high level of resolution and accuracy. The purpose of using multiple segments is to allow the use of "constant-parameter" theory which is simple to use and easy to understand.

The calculations proceeded upward from the base, or hot-side, of the TE pellet where the temperature was known. The detailed application of the constant-parameter equations is illustrated in the expanded segment #7, given in Figure 2. Details of this calculation process was given in the paper on this subject by Buist [5]. It had been shown in this paper that this calculation method precisely captures and accounts for the "temperature-induced" Thomson cooling effect and, therefore, would also model the impact of extrinsically induced property gradients. One has only to artificially assign constant values of  $S$ ,  $\rho$ ,  $\kappa$  (and, therefore,  $Z$ ) for each segment and proceed with the calculations as described in the above-referenced paper.

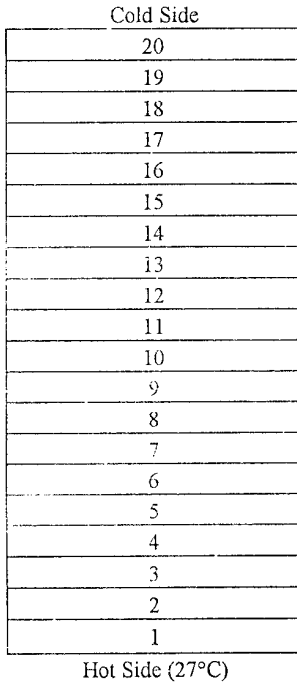


Figure 1: TE Pellet Thermal Model (20 Segments).

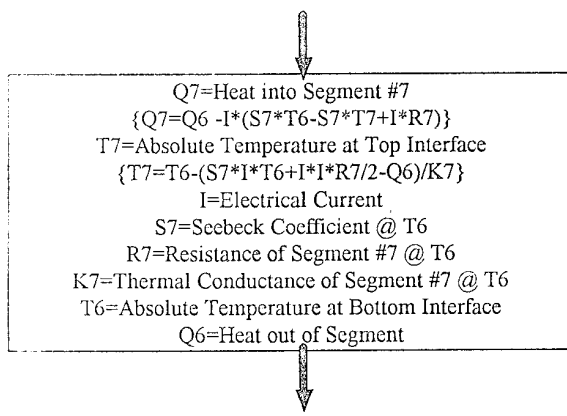


Figure 2: Example Segment #7 description and equations.

#### Calculations

In order to isolate and illustrate extrinsic effects of TE material parameter variance, each segment of the model was assigned a constant, temperature-independent set of  $S$ ,  $\rho$ , and  $\kappa$  parameters. These data were selected from the set given in table 1. These data were generated subject to the following criteria:

1. All segments of all cases had the same, exact  $Z$ .
2. All pellets had approximately the same average  $S$ ,  $\rho$ , and  $\kappa$ .
3. Case 1 was generated by holding  $S$  to the average, constant value for all segments and significantly varying  $\rho$  and  $\kappa$  from one-half of the pellet to the other. This was done keeping each parameter of each segment within a given half-pellet the same constant value.
4. Case 2 was simply the reverse of case 1.
5. Cases 3, 4, 5 and 6 were similarly generated but sequentially holding  $\rho$  or  $\kappa$  constant and significantly changing  $S$  from one-half of the TE pellet to the other.

6. Case 7 was generated by holding  $\kappa$  constant, but linearly varying Seebeck for each segment of the pellet.
7. Case 8 was similar to case 7 but with the Seebeck variance in the reverse direction.

**Table 1**  
TE Material Parameters  
Used in Calculation Demonstration  
 $(Z=2.7 \times 10^{-3} \text{ }^{\circ}\text{K}^{-1}$  for all Segments for all cases)

	Description	Seg- ments	Seebeck $\mu\text{V}/^{\circ}\text{C}$	Rho $\Omega\cdot\text{m}$	Kappa $\text{W}/\text{m}/^{\circ}\text{C}$
1	Const.S/F	1-40	200	10	1.482
		41-80	200	20	0.741
2	Const.S/R	1-40	200	20	0.741
		41-80	200	10	1.482
3	Const. $\kappa$ /F	1-40	250	23.15	1.0
		41-80	150	8.33	1.0
4	Const. $\kappa$ /R	1-40	150	8.33	1.0
		41-80	250	23.15	1.0
5	Const. $\rho$ /F	1-40	250	15	1.543
		41-80	150	15	0.556
6	Const. $\rho$ /R	1-40	150	15	0.556
		41-80	250	15	1.543
7	Special/F	1-80	250-150	15	1.543-0.556
8	Special/R	1-80	150-250	15	0.556-1.543

Mathematical models were constructed for each of the cases indicated in Table 1 and calculations were performed in accordance with the procedures and processes as described above for sequentially selected values of applied current. The results for Cases 1-4 are given in Figure 3. The calculated performance curve for Cases 1 and 2 were totally and exactly the same. In fact, additional calculations performed with various scenarios of changing  $\rho$  and  $\kappa$  throughout the pellet had no effect whatsoever on the maximum  $\Delta T$  as long as  $S$  was constant. For these cases, the maximum  $\Delta T$  was equal to the well-known, constant-parameter expression,  $\Delta T_{\max} = 1/2 Z T c^2$ . This is very much what one would expect for constant properties.

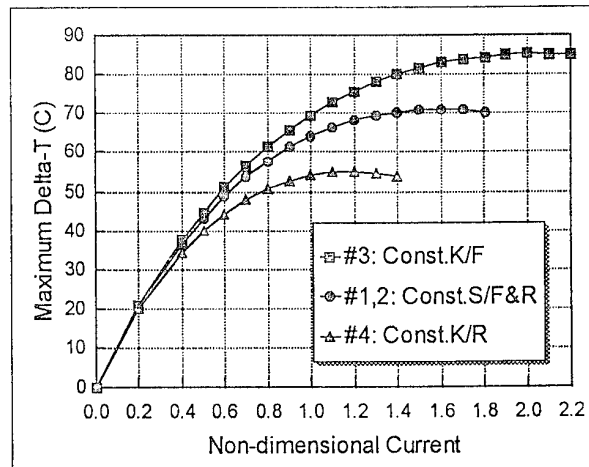


Figure 3: Cooling Performance Calculation for Cases 1-4.

In sharp contrast, the cooling performance curves for variable  $S$  were greatly affected as concluded from the equations and analysis given above. Furthermore, the lower  $\Delta T_{\max}$  for the reverse case was, indeed, consistent with the algebraic sign of

extrinsic Thomson term, equation [5]. These set of curves also illustrate the fact that the forward direction (Case 3) produces its  $\Delta T_{\text{max}}$  at a current which is higher than what would be predicted from the average properties, while the reverse is true for Case 4.

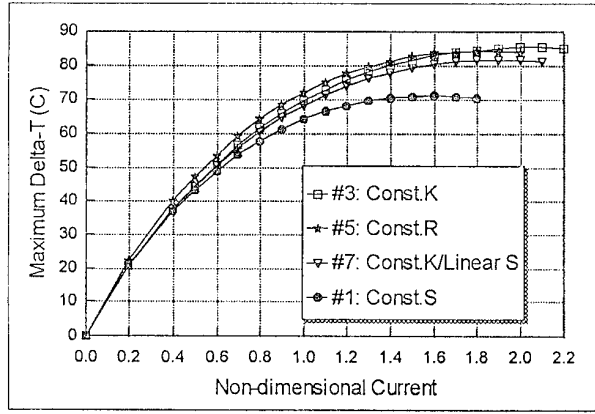


Figure 4: Forward mode performance calculations, cases 1, 3, 5, and 7.

Figure 4 is a similar plot, but for all forward cases studied. There are several interesting effects illustrated in these four cases. One is that there is some observable difference in  $\Delta T_{\text{max}}$  for when  $\kappa$  is held constant versus holding  $\rho$  constant even with exactly the same  $S$  variance. Thus, there appears to be some secondary interactive, but minor impact of  $\rho$  and  $\kappa$  variance, not at all evident whenever  $S$  is held constant. The more dramatic observation is the lower  $\Delta T_{\text{max}}$  for the case where  $S$  is varied linearly versus the step-function mid-way along the pellet.

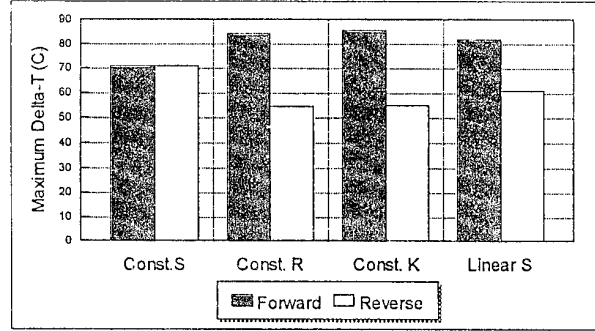


Figure 5:  $\Delta T_{\text{max}}$  calculations for all cases studied.

The  $\Delta T_{\text{max}}$  results for all 8 cases studied are summarized in Figure 5. Clearly, this is dramatic evidence of the ETE, ruling out the possibility that the observed enhancements may have been caused by the naturally less Joule heat produced in the cold half of the TE pellet where  $\rho$  is low when  $S$  is low.

#### Test Data

There was one very convenient result observed from these study cases: There was no apparent penalty, and perhaps it was even desirable, to produce ETE enhancement with an abrupt, step-functional variance in Seebeck coefficient. This allowed for the fabrication of simple, but effective, ETE devices by soldering TE pellet segments together as shown in Figure 6. Alternatively, powder metallurgy can totally eliminate the extra solder interface.

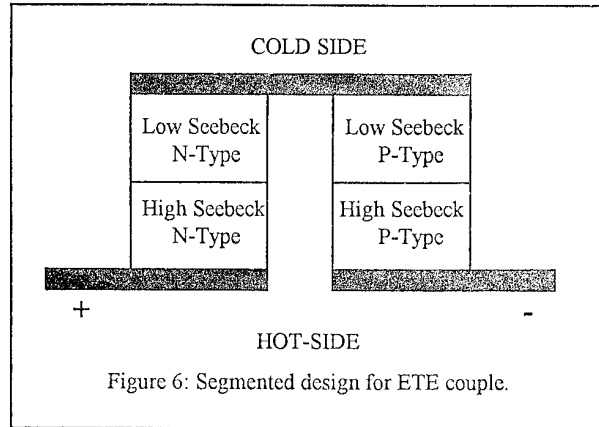


Figure 6: Segmented design for ETE couple.

Single test couples such as that illustrated in Figure 6 were fabricated by simply soldering high and low Seebeck, N and P-type segments together. This work was performed during the late 1960's by the author at the facilities at the Borg-Warner Research Center in Des Plaines, Illinois. Also, High-S and Low-S control couples were fabricated from homogeneous pellets extracted from the same TE material wafers as those used to form the segments of the ETE couple. All couples were then instrumented with thermocouples and all mounted together on the same, temperature controlled base plate within a vacuum system. The base plate was held to 27°C for all test points. The vacuum was held to approximately  $5 \times 10^{-5}$  Torr. The test configuration was a large bell jar with no radiation shielding employed whatsoever. The applied current was stepped sequentially and held constant to allow for steady-state testing. The results are shown in Figure 7. Clearly, these tests validated the existence of the ETE as a new, additive TE cooling effect with performance enhancement far above that produced via intrinsic means.

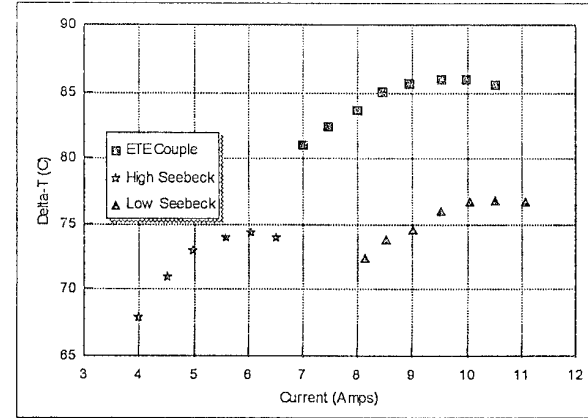


Figure 7: Test data on a 2-segment ETE couple versus homogeneous couples fabricated from low and high  $S$  TE materials from which the ETE couple was produced.

As one might surmise, the ETE is increased for larger and larger Seebeck gradients. However, the penalty for that is lower and lower average  $Z$ . That is, there will be some Seebeck value for TE cooling material for which  $Z$  is maximized. As Seebeck is varied left and right of this maximum,  $Z$  falls off, thereby sacrificing the primary cooling effect. It is nevertheless true that

the ETE is so large that it produces significant overall cooling enhancement even though the average Z is sacrificed.

In order to further enhance cooling performance, a three-segment TE pellet was produced and tested at Borg-Warner Research Center by inserting a medium Seebeck, high Z segment in the middle, as shown schematically in Figure 8. The measured values of Seebeck and Z for each segment were as shown.

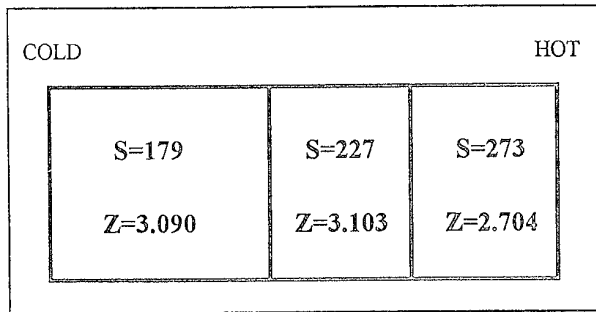


Figure 8: Schematic for 3-segment ETE test pellet.

This was a single, N-type TE pellet and was tested as such in a vacuum system using a special test fixture. It provided a pre-cooled electrical connection at a temperature always slightly above the cold junction of the test pellet. As such, the cold electrode was assured to always apply a slight heat load to the test pellet in order to preclude the possibility for external cooling of the test pellet.

The test results of this 3-segment TE pellet are given in Figure 9. This produced a dramatic maximum  $\Delta T$  of  $92.5^{\circ}\text{C}$  from a  $27^{\circ}\text{C}$  hot side temperature and set the standard for a whole new state-of-the-art in single-stage TE cooling devices.

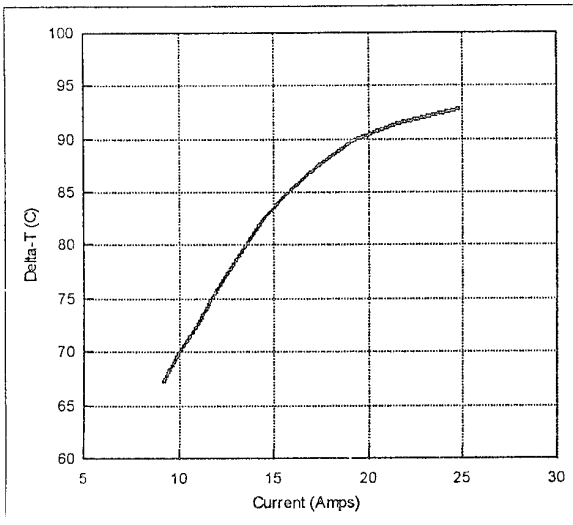


Figure 9: Test data on 3-segment ETE pellet.

### Conclusions

The Extrinsic Thomson Effect was initially discovered on paper by simply not ignoring one of the terms that resulted from the fundamental heat balance equation. Like many good discoveries, it seems simple and obvious once disclosed. Nevertheless, it has gone unnoticed and un-exploited since its discovery more than 35 years ago.

The Thomson effect was known to enhance TE cooling because of the positive  $dS/dT$  slope of typical TE cooling materials near room temperature. Thus, it was surmised that if a TE pellet were produced with an artificially produced extrinsic Seebeck variance in the same direction, it also would enhance TE cooling.

Initial experiments proved this to be the case and inhomogeneous TE pellets and couples were produced which significantly out-performed any homogeneous TE couple even today, 35 years later.

Now, with the precision of numerical models and high-speed computers, demonstrations have clearly re-established the nature of the ETE phenomenon and have provided the means for practical device design optimization. It is hoped that the ETE can be exploited by all thermoelectricians to set new standards for thermoelectric cooling for the challenging years that face our industry.

### References

- [1] A.D. Reich, M. Stanley and K. Kountz, U.S. Patent Number 3,564,860 (1971).
- [2] A.D. Reich, Infrared Information Symposium (IRIS) meeting proceedings (1972).
- [3] R.J. Buist, Infrared Information Symposium (IRIS) meeting proceedings (1972).
- [4] C.A. Domenicali, "Irreversible Thermodynamics of Thermoelectricity", Reviews of Modern Physics, vol. 26, pp.237-275, (1954).
- [5] R.J. Buist, "Design and Engineering of Thermoelectric Cooling Devices", 10th International Conference on Thermoelectrics, Cardiff, Wales, September 10-12, (1991).

## THE DISTRIBUTED PELTIER EFFECT AND ITS INFLUENCE ON COOLING DEVICES

C A B Ball<sup>1</sup>, W A Jesser and J R Maddux

*Department of Materials Science and Engineering, University of Virginia, Charlottesville, Va 22903, USA.*

<sup>1</sup> on leave from the Department of Physics, University of Port Elizabeth, P O Box 1600, Port Elizabeth 6000, South Africa

The Distributed Peltier Effect has been suggested to enhance performance of cooling devices. In these devices the n- and/or p-type thermoelements are segmented so that the absolute value of the Seebeck coefficient increases from the cold to the hot junctions. Calculations are presented to quantify this effect and it is shown that for the case of the best known materials an improvement of 10% is obtained if temperature independent materials constants are used. This is reduced to about 4% for temperature dependent parameters.

### Introduction

Peltier cooling devices offer refrigeration with no moving parts and no pollution after manufacture, and consequently have been the subject of considerable research effort over several decades. The goal has been to achieve high coefficients of performance or large temperature differences which compare favourably with conventional refrigeration systems. However these have not yet been realised and Peltier cooling is used only in niche applications.

Of primary importance is the development of new semiconductor materials of both n- and p- types with the highest possible figures of merit

$$Z = \frac{\alpha^2}{\kappa\rho} \quad (1)$$

where  $\alpha$  is the Seebeck coefficient,  $\kappa$  the thermal conductivity and  $\rho$  the electrical resistivity. Ideally the figure of merit should be close to its maximum value over the temperature range of the element of that material in the device. At present the highest values of  $Z$  are approaching  $3.9 \times 10^3 \text{ K}^{-1}$  for p-type materials and about 20% less for n-type materials.

With given materials it is important to configure devices to achieve optimum performance. Considerations would include the shape and size of individual elements and variation of materials properties, either in a discrete or continuous manner within the elements.

It does not appear that the shape and size of a thermoelement will affect its performance in the ideal case of zero heat absorption from the environment (apart from the ends). This conclusion may be drawn from the results of Kawai, Yoshida and Imai[1]. The quantity of heat pumped is of course size and current dependent.

Variation of the composition of a thermoelement from the hot to the cold end has been suggested for at least two distinct reasons. Firstly the values of the materials parameters  $\alpha$ ,  $\kappa$  and  $\rho$  are temperature dependent and consequently the value of the figure of merit  $Z$  will vary. Grading the composition to maximise  $Z$  at the working temperature at each point along the element should improve its performance [2]. Secondly, the variation of composition along the length of thermoelements in such a way that the absolute value of the Seebeck coefficient decreases from the hot to the cold end will cause cooling, not only at the cold p-n junction, but also at intermediate junctions, or, in the case of continuous grading, along

the entire length[3,4]. This can serve to reduce the heat transferred to the cold junction from hotter parts. The heat pumping at a junction is given by

$$H = I\alpha_{12} T \quad (2)$$

where  $I$  is the current,  $\alpha_{12}$  the difference in Seebeck coefficients on either side of the junction and  $T$  the absolute temperature. For a given current the heat pumping is greater at higher temperatures. This could be used to improve the performance of devices. This strategy has appropriately been called the distributed Peltier effect or the external Thompson effect by Reich, Stanley and Kountz [5]. The case of continuous grading is analogous to the Thompson effect, but with a variation in  $\alpha$  due to composition rather than temperature. We prefer "the distributed Peltier effect" because the Thompson effect is essentially due to temperature variation and the Peltier effect is due to variation of the Seebeck coefficient at a junction where there is a composition change.

In this paper we examine the usefulness of the distributed Peltier effect on cooling devices. In order to separate this effect from temperature dependent effects, it is first assumed that the materials constants of the thermoelements are temperature independent. Temperature dependent effects have been considered and these are also presented.

### Physical configuration and governing equations

A conventional Peltier cooling device consists of a p-type thermoelement and an n-type thermoelement in the configuration shown in figure 1(a). One end of each thermoelement is in thermal contact with a heat reservoir at the constant hotter temperature  $T_h$  and the other ends form the cold junction where the materials are in thermal contact at a colder temperature  $T_c$ . The electric current  $I$  is passed through the device in the direction shown so that heat is pumped from the cold junction by the Peltier effect. In order to use the distributed Peltier effect a similar device is used but each of the n- and p-type thermoelements is of varying composition along its length. The composition change may be continuous or at abrupt intermediate junctions. The Seebeck constant,  $\alpha$ , is varied around the circuit so that it decreases from the hot p-type end to the cold p-type end. It then becomes negative at the cold n-type end and the absolute value of  $\alpha$  is increased towards the hot n-type end. In figure 1(b) a segmented device is shown. The case of continuous grading is not considered further here.

It is assumed that heat only enters or leaves the device by one of the following processes: (1) Joule heating, (2) transfer of heat to or from the hot or cold reservoirs at  $T_h$  or  $T_c$  respectively and (3)

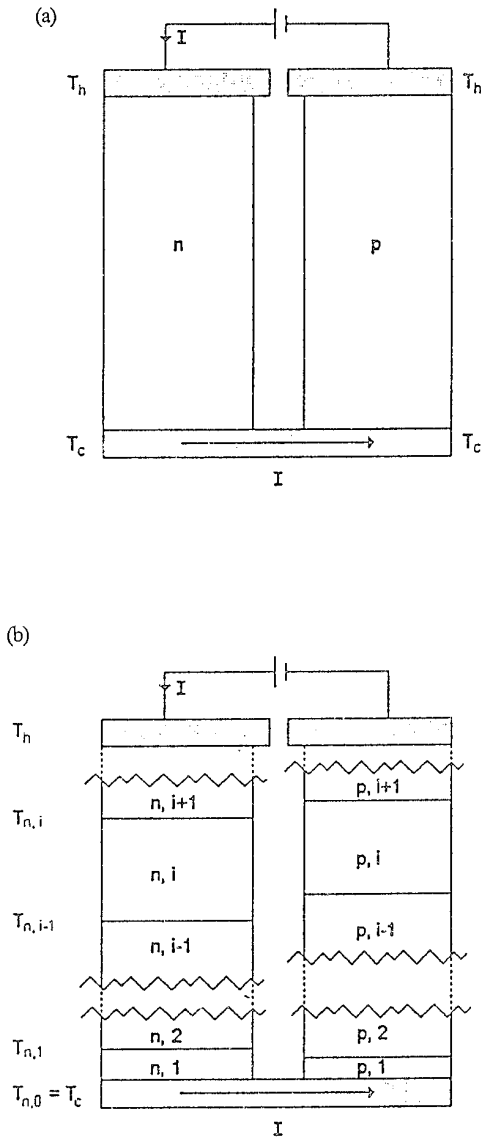


Figure 1 (a) Simple and (b) multiple segment Peltier cooling devices.

Peltier cooling at the junctions (including the intermediate ones in the n- and p-type thermoelements). Heat losses/gains to the environment by radiation etc along the length of the thermoelements is assumed to be negligible.

The coefficient of performance

$$\eta = \frac{\text{Heat pumped from cold junction}}{\text{Electrical energy supplied to system}} \quad (3)$$

may be calculated for any fixed  $T_h$  and  $T_c$ . The maximum obtainable temperature difference for given materials,  $T_h$  and  $I$  namely

$$\Delta T_{\max} = T_h - T_c \quad (4)$$

is calculated on the assumption that under these conditions zero the heat being pumped from the cold junction is reduced to zero.

The governing equations are obtained by considering the conservation of heat at each junction. The heat pumped at the cold junction is

$$H_0 = \alpha_{p,1} IT_c - K_{p,1}(T_{p,1} - T_c) - \frac{1}{2} I^2 R_{p,1} \quad (5)$$

$$- \alpha_{n,1} IT_c - K_{n,1}(T_{n,1} - T_c) - \frac{1}{2} I^2 R_{n,1}$$

and the conservation of heat at any intermediate junction requires that

$$\begin{aligned} & |\alpha_{q,i+1} - \alpha_{q,i}| IT_{q,i} + K_{q,i}(T_{q,i} - T_{q,i-1}) - \frac{1}{2} I^2 R_{q,i} \\ & = K_{q,i+1}(T_{q,i+1} - T_{q,i}) + \frac{1}{2} I^2 R_{q,i+1}, \quad q=n,p. \end{aligned} \quad (6)$$

Here the first subscript refers to the n- or p-type thermoelement and the second to the segment in the thermoelement numbered from the cold end. Hence

$$R_{q,i} = \frac{\rho_{q,i} l_{q,i}}{S_{q,i}}, \quad q=n,p. \quad (7)$$

is the resistance of the  $i$ 'th segment of the n- or p-type thermoelement with resistivity  $\rho_{q,i}$ , length  $l_{q,i}$  and cross-sectional area (considered constant) of  $S_{q,i}$ . Similarly the heat conductance of the same segment is

$$K_{q,i} = \frac{k_{q,i} S_{q,i}}{l_{q,i}}, \quad q=n,p. \quad (8)$$

The temperatures similarly are referred to the n- and p-type thermoelements and the junctions are numbered from the cold junction which is junction 0. Hence  $T_{n,0} = T_{p,0} = T_c$  and  $T_{q,i}$  is the temperature of the  $i$ 'th junction from the cold end in the n- or p-type thermoelement etc. In the case of three segment thermoelements  $T_{n,3} = T_{p,3} = T_h$ .

The principle of equipartition of Joule heat [1] has been applied, in which the Joule heat generated in a segment is assumed to be conducted equally to both ends of that segment.

It will be seen that if  $T_h$ ,  $T_c$  and  $I$  are specified as well as the Seebeck coefficient, the resistance and heat conductance of each segment, then there are as many equations like equation (6) as there are unknown intermediate temperatures  $T_{q,i}$ . This set of equations can then be solved and the values of the intermediate temperatures determined. The coefficient of performance given by equation (3) becomes

$$\eta = \frac{H_0}{\sum_{q=n,p} \sum_i [I^2 R_{q,i} + I | \alpha_{q,i} | (T_{q,i} - T_{q,i-1})]} \quad (9)$$

which may then also be calculated using equation (5).

On the other hand if the theoretical maximum temperature difference  $\Delta T$  for given  $T_h$ ,  $I$  and device configuration is required then equation (5) with  $H_0$  equal to zero gives an additional equation and with the

set of equations (6) may be used to calculate the unknown intermediate temperatures and  $T_c$ .

### Determination of the ideal device configuration

The ideal device will consist of the most suitable available material for each segment and the size of each segment in turn will be such that the resistance and heat conductance, as well as the electric current, optimise performance in a desired temperature range.

It can be shown that both the maximum coefficient of performance and the  $\Delta T_{\max}$  for given materials (ie the device is optimised with respect to current, segment resistances and heat conductances) is dependent only on the values of  $\alpha$  and  $Z$  of each segment. By combining equations (5) and (9) one obtains for the coefficient of performance

$$\eta = \frac{\sum_{q=n,p} [|\alpha_{q,i}|T_c V - \frac{\alpha_{q,i}^2(T_{q,i} - T_c)}{Z_{q,i} F_{q,i}} - \frac{1}{2} V^2 F_{q,i}]}{V^2 + V \sum_{q=n,p} \sum_i |\alpha_{q,i}|(T_i - T_{i-1})} \quad (10)$$

where  $V=IR$  and  $R$  is the sum of the resistances of the individual segments. Further

$$F_{q,i} = \frac{R_{q,i}}{R} \quad q=n,p \quad (11)$$

are the ratios of the individual segment resistances to the total device resistance. It follows that

$$\sum_{q=n,p} \sum_i F_{q,i} = 1 \quad (12)$$

The equations used to derive the intermediate temperatures (equations (6)) may be rewritten in terms of the same parameters to obtain

$$\begin{aligned} & |\alpha_{q,i+1} - \alpha_{q,i}| V T_{q,i} + \frac{\alpha_{q,i}^2 (T_{q,i} - T_{q,i-1})}{Z_{q,i} F_{q,i}} - \frac{1}{2} F_{q,i} V^2 \\ & = \frac{\alpha_{q,i+1}^2 (T_{q,n+1} - T_{q,i})}{Z_{q,i+1} F_{q,i+1}} + \frac{1}{2} F_{q,i+1} V^2, \quad q=n,p. \end{aligned} \quad (13)$$

The quantities  $V$  and all but one of  $F_{q,i}$  (because of equation (12)) are then considered as parameters which are varied to obtain the maximum coefficient of performance  $\eta_{\max}$  or the maximum  $\Delta T_{\max}$ . It follows that  $\eta_{\max}$  and  $\Delta T_{\max}$  are dependent only on  $T_h$ ,  $\alpha_{q,i}$  and  $Z_{q,i}$  and also, in the case of  $\eta_{\max}$ , on  $T_c$ . The device is then manufactured with the appropriate segment lengths as determined by the optimising parameters  $F_{q,i}$  and operated with the current that optimises the performance.

The problem remains as to which material is to be used in each segment. It is clear that

$$|\alpha_{q,i+1}| > |\alpha_{q,i}| \quad q=n,p \quad (14)$$

in order for heat to be pumped from the system at each junction. From numerical solutions it has always been found that for any one given  $\alpha_{q,i}$  the performance is always improved when  $Z_{q,i}$  increases. It is also evident from numerical calculations that a large variation

in  $\alpha$  in the n- or p-type thermoelement is advantageous. There must then be a compromise between large  $Z$  for each segment and large variation in  $\alpha$  over each of the thermoelements.

If the strategy of using the distributed Peltier effect in cooling devices is to be successful, a range of materials must be found with the highest possible  $Z$  and a large variation of  $\alpha$ .

### Results for double segment thermoelements

In order to show that in principle the distributed Peltier effect can lead to higher coefficients of performance and  $\Delta T_{\max}$  values than with simple Peltier cooling devices two segment p-type thermoelements will be considered with "neutral" return n-type thermoelements, i.e. with no heat pumping, electrical resistance or thermal conduction in the n-type material.

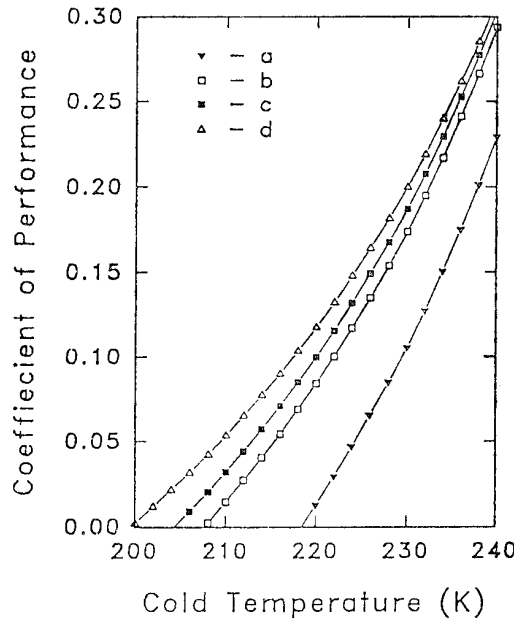


Figure 2 Coefficient of performance against  $T_c$ ,  $Z=0.00342\text{K}^{-1}$  in each case and  $\alpha_1, \alpha_2 =$  (a) 240, 240 (b) 205, 280, (c) 195, 295 and (d) 180, 320  $\mu\text{V K}^{-1}$ .

In figure 2, the effect of variation of  $\Delta\alpha = \alpha_2 - \alpha_1$  at constant  $Z=0.00342\text{K}^{-1}$  is shown. In all cases  $T_h = 300\text{ K}$ . As  $T_c$  approaches  $T_h$  all the curves coincide with the curve (a). The intercept on the temperature axis gives the maximum theoretical  $\Delta T$ . It will be seen that both the coefficient of performance and  $\Delta T_{\max}$  are improved as  $\Delta\alpha$  increases. However, figure 2 shows a highly idealised situation where it is assumed that high  $Z$  can be achieved over a wide range of  $\alpha$ . In practice, of course, a maximum  $Z$  will be obtained for a specific  $\alpha$  and one needs to find a compromise between high  $Z$  and high  $\Delta\alpha$ .

The system of  $\text{Bi}_2\text{Te}_3\text{-Sb}_2\text{Te}_3\text{-Sb}_2\text{Se}_3$  pseudo-ternary alloys provides materials with the highest known  $Z$  values for cooling devices operating around room temperature and is used for illustrative purposes. A curve of experimentally obtained values of maximum  $Z$  obtained as a function of  $\alpha$  is shown in figure 3 [7].

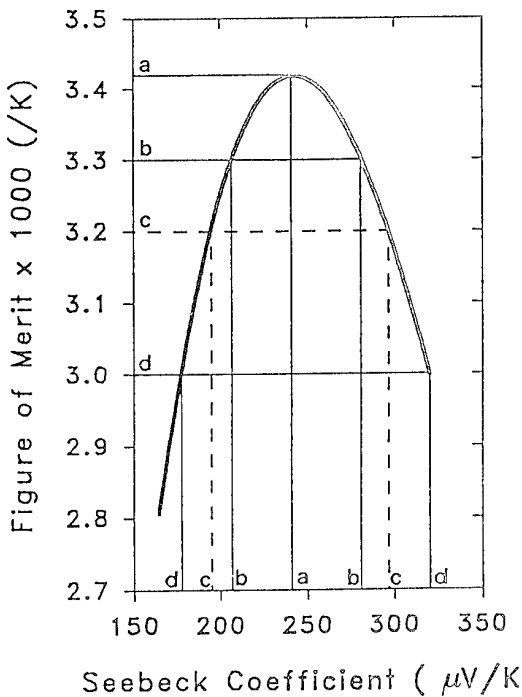


Figure 3 Dependence of maximum Figure of Merit  $Z$  on Seebeck coefficient  $\alpha$  [7]. For the values  $Z =$  (a) 3.42, (b) 3.3, (c) 3.2 and (d)  $3.0 \mu\text{V/K}$ , increasing values of  $\Delta\alpha$  are obtained.

Figure 4 was obtained in the same way as figure 2 but using  $Z$  and  $\alpha$  values from figure 3. There is hence a compromise between high  $Z$  and large  $\Delta\alpha$ . Thus for curve (a) in figure 4,  $Z$  is at the maximum value of  $0.00342 \text{ K}^{-1}$  but  $\alpha_1 = \alpha_2 = 240 \mu\text{V K}^{-1}$  as indicated by the line marked (a) in figure 3. This corresponds to a single segment thermoelement. Curves (b), (c) and (d) correspond double segment thermoelements with increasing  $\Delta\alpha$  but decreasing  $Z$ . In each case  $T_b$  was taken as 300 K. The minimum obtainable  $T_c$  is again given by the intercept on the  $T_c$  axis.

It will be seen that for small temperature differences less than 60K ( $T_c = 240\text{K}$ ) there is nothing to be gained by the additional complexity of producing segmented devices. However, for large temperature differences, coefficients of performance can be substantially improved by using even two segment thermoelements. It is further apparent that when the criterion is maximum  $\Delta T$ , then p-type two segment thermoelements offer an improvement of up to some 12 K. The improvement using three segment thermoelements is approximately a further 3 K. These values are somewhat reduced when the n-type thermoelement is included because of the lower  $Z$  values of n-type materials in this system of alloys. However the calculations lead to  $\Delta T_{\max}$  values of 80.5, 86.5 and 88.0 K for one, two and three segments respectively in both the p- and n-type thermoelements.

#### Effect of temperature dependent properties

In the above analysis the properties of the thermoelements have been taken as their room temperature values in order to isolate the effect of the distributed Peltier effect. In general, however, the properties of thermoelectric materials are temperature dependent. In order to more accurately model the performance of a device based on the

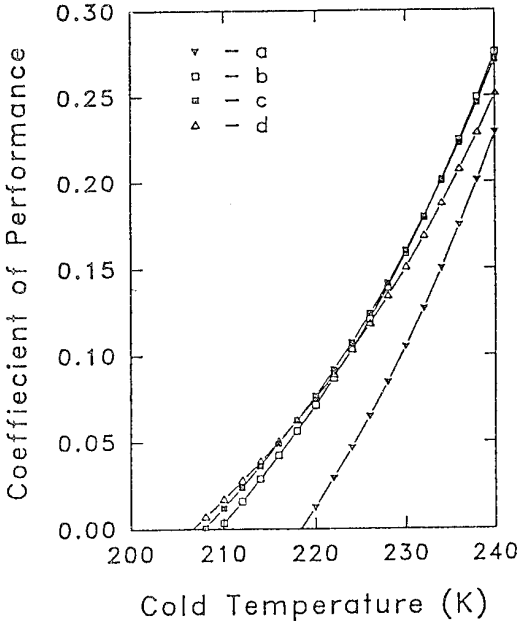


Figure 4 Coefficient of performance against  $T_c$ . (a), (b), (c) and (d) refer to the  $Z$  and  $\alpha$  values given in figure 3.

distributed Peltier effect, the temperature dependence of the properties should be considered. To perform calculations for thermoelectric coolers in which the properties vary with temperature, a numerical method was used which was based on a finite difference technique[8] which was adapted for use with Peltier couples [9] to calculate  $\Delta T_{\max}$ . This technique makes it possible to perform calculations for devices in which the properties of the thermoelements vary with both position and temperature. For the sake of brevity, only the results of these calculations are shown here.

Before performing  $\Delta T_{\max}$  calculations, models for the variation of thermoelectric properties with temperature were developed. Two different forms for the relationships of these properties were investigated.

For the first approach, a semi-empirical modelling technique was used. The appropriate functional forms for temperature dependence of the thermoelectric properties have been established based on physical principles. These relationships contain a number of essentially adjustable parameters which were subsequently determined by curve fitting to experimental data[9]. In this approach, Fermi-Dirac statistics were used to describe the electronic component of the properties. This model has been referred to as the "exact model".

In the second model, simplified linear relationships for the dependence of the thermoelectric properties with temperature were assumed. These relationships were obtained for the desired doping level by interpolating from linear curve fits to experimental data over the temperature range 200 - 300 K. This model has been referred to as the "linear model". The linear model was investigated to determine if it was adequate to model the thermoelectric properties of these alloys over the limited range of temperature in which a single-stage Peltier cooler typically operates.

Three different devices were considered in this analysis. The first

was a conventional Peltier couple, in which each thermoelement consisted of a single segment. Additionally, calculations were performed for two segmented Peltier couples, in which each thermoelement consisted of either two or three segments. These devices do not represent the ultimate optimised  $\Delta T_{\max}$  which may be obtained by utilising the distributed Peltier effect, but they serve as a comparison between the calculation methods. The room temperature properties of the segments have been given in table 1.

**Table 1** Room temperature thermoelectric properties of segments in the Peltier coolers.

	$\rho$ mΩ cm	$\alpha$ μV/K	$\kappa$ mW/cm K
<b>n-type</b>			
1-segment	1.11	-216	13.7
2-segment (hot) (cold)	2.54	-272	13.5
	1.11	-216	13.7
3-segment (hot) (mid) (cold)	2.73	-277	13.7
	1.12	-217	13.7
	0.60	-167	16.8
<b>p-type</b>			
1-segment	1.17	223	13.5
2-segment (hot) (cold)	2.61	285	13.4
	1.17	223	13.5
3-segment (hot) (mid) (cold)	2.60	285	13.4
	1.39	238	13.1
	0.70	180	16.0

The results of the calculations for these devices using both models, along with the results for the temperature independent case have been presented in Table 2. As shown, the agreement between the exact and linear models was quite good in all three cases. The difference between the two increased as the number of segments in the device increased, but the disagreement was still less than 1 % for the three segment device.

**Table 2** Calculated  $\Delta T_{\max}$  (in K) for temperature dependent (exact and linear models) and temperature independent (room temperature) materials properties.

	Exact Model	Linear Model	Temperature Independent
1-segment	78.9	78.9	80.5
2-segment	81.7	81.5	86.5
3-segment	83.1	82.3	88.0

The results indicate good agreement between the two temperature dependent calculations, indicating that the linear model was adequate for this analysis, at least over the range of temperature studied.

While the agreement between the two temperature dependent calculations was reasonable, comparison of these results with the

temperature independent calculations indicates significant differences when the thermoelements are composed of multiple segments.  $\Delta T_{\max}$  for the case of two and three segment devices is considerably less using the temperature dependent calculations. Nevertheless even with the decreased  $\Delta T_{\max}$  as a result of the temperature dependence of the parameters an improvement of 3.2 degrees can be expected for a three segment device which is equivalent to an improvement of approximately 4% in Z. In the case of optimised materials and geometry this improvement is expected to be considerably enhanced.

For this system of materials the reason for this decrease in  $\Delta T_{\max}$  for multiple segment devices appears to be the result of the trade off between an improvement in  $\Delta\alpha$  when temperature dependence is taken into account and a decrease in Z from room temperature to lower temperatures [10]. For the single segment configuration with constant  $\alpha$  there is no benefit from pumping heat from intermediate positions on the thermoelement. The temperature dependence of  $\alpha$  (i.e. the Thompson effect) causes an improvement in  $\Delta T_{\max}$  but this is more or less cancelled by the decrease in Z. In the case of multiple segments the changes in  $\alpha$  are not significant compared to the built in variation of  $\alpha$  of the distributed Peltier effect, but the reduction of Z due to temperature dependence is still the same.

If the Distributed Peltier Effect is to be useful, there needs to be very particular attention paid to the variation of Z and  $\alpha$  over the range of temperature of the device. It would appear that it would be beneficial if Z peaks at some median temperature.

#### Acknowledgements

One of the authors (CABB) wishes to thank the University of Port Elizabeth, the South African Foundation for Research Development and the University of Virginia for financial assistance that made this work possible.

#### References

- [1] T. Kawai, I. Yoshida and I. Imai, J. Phys. Soc. Japan, 1994, v. 63, No 3, p. 948.
- [2] J.C. Bass and N. B. Elsner, in *Proceedings of the Third International Conference on Thermoelectric Energy Conversion*, Arlington, TX, edited by K. R. Rao (IEEE, New York, 1980), p.8.
- [3] N. B. Elsner, J. Chin and G. H. Reynolds, in *Proceedings of the Third International Conference on Thermoelectric Energy Conversion*, Arlington, TX, edited by K. R. Rao (IEEE, New York, 1980), p.105.
- [4] G. D. Mahan, J. Appl. Phys., 1991, v. 70 No 8, p. 4551-4554.
- [5] A.D.Reich, M. L. Stanley and K. Kountz, U. S. Patent 3,564,860 Feb 3, 1971.
- [6] D. Tuomi, Mat. Res. Soc. Symp. Proc., 1991, v. 234, p. 179.
- [7] W. A. Jesser and M. Ettenburg, Private communication, 1994.
- [8] R. J. Buist, in *Proceedings of the Tenth International Conference on Thermoelectric Energy Conversion*, Cardiff, Wales, 1991.
- [9] J. R. Maddux, PhD Thesis, University of Virginia, 1995.
- [10] W. M. Yim, E. V. Fitzke and F. D. Rosi, J. Materials Science, 1966, v. 1, p 52.

# *grad T = const, IS IT CORRECT?*

Lev P. Bulat

*St.Petersburg State Academy of Refrigeration,  
Lomonosova St. 9, St.Petersburg, 191002, Russia*

An assumption  $\text{grad } T = \text{const}$  is discussed. It is shown, that generally this assumption leads to a physical absurd results, i.e. to unlimited increasing of electrons energy. It was found that only consistent taking into account of non-local and non-linear terms in solving of the kinetic equation gives a possibility to eliminate the kinetic integrals diverges. Thus, the non-locality is a new limitation mechanism of electrons running effect.

## 1 Introduction

In a traditional thermoelectric theory it is always considered that a temperature gradient sets in an every sample's point. But in fact, a temperature field sets in a sample only in consequence of heat boundary conditions. It is also necessary to take in consideration that a semiconductor thermoelectric material consists of a number of quasi-particles subsystems: electrons, holes, phonons, etc. Moreover, we have to speak about different temperatures distribution of every kind of quasi-particles in a sample [1]. In addition, heat boundary conditions may be formed separately for different kinds of quasi-particles [1]. It is pointed in [1] that an assumption  $\text{grad } T = \text{const}$  is no correct, at least, near sample's boundaries and this assumption must be proved in every concrete condition for specific type of quasi-particles.

So, we can see that in limited samples an assumption  $\text{grad } T = \text{const}$  can give a gross error in connection with boundary effects. It seems that the assumption  $\text{grad } T = \text{const}$  proved to be correct in massive samples if it is possible to neglect boundary effects. We shall demonstrate now that this assumption is no correct in any case.

Let's take into consideration a simple phenomenological formulas. We shall consider a sample with only one type of quasi-particles. We can use a linear equation

$$\text{div } \vec{q} = \vec{j} \cdot \vec{E} \quad (1)$$

for determine a temperature distribution.

Here  $\vec{q}$  and  $\vec{j}$  are a heat flow density and a current density,  $\vec{E}$  - a gradient of an electro-chemical potential with a reverse sign,

$$\vec{j} = \sigma \vec{E} - \sigma \alpha \text{grad } T \quad (2)$$

$$\vec{q} = -\kappa \text{grad } T + \Pi \vec{j} \quad (3)$$

Kinetic coefficients  $\sigma(T)$ ,  $\alpha(T)$ ,  $\Pi(T)$  are functions of temperature; this fact follows as a consequence from a microscopic theory of a transport phenomena in solids. Moreover, if it is found that the thermoelectric coefficient  $\alpha$  (the Peltier coefficient  $\Pi$ ) does not depend on a temperature, than the Peltier coefficient  $\Pi$  (the thermoelectric coefficient  $\alpha$ ) must depend on temperature in accordance with the formulae

$$\Pi = \alpha T. \quad (4)$$

So, we can point that no one from connected with thermoelectricity kinetic coefficients may be independent on temperature in any case. As it follows from (1)-(3), it is two reasons of non-linear dependence of temperature from coordinates: 1) presence of electric current in a sample; 2) dependence of kinetic coefficients from a temperature. We can see from (1)-(3), that  $\text{grad } T$  can be constant only if  $\vec{j} = 0$  and  $\kappa = \text{const}$ . So, in the whole lot the assumption  $\text{grad } T = \text{const}$  is not correct in thermoelectric problem.

We shall show here that this assumption is not only uncorrected, this assumption leads to physically absurd results: to an unlimited increasing of electrons velocities (an electrons running).

## 2 Theory

Let's take into consideration a homogeneous isotropic non-degenerated semiconductor with a standard band structure. An electrons concentration is not so great, it means that it exists control in electronic subsystem [1] (we can not introduce an electrons temperature). The problem is one-dimensional, i.e. a phonons temperature and electric field changes only in  $x$ -direction. Let's use the stationary Boltzmann kinetic equation for electrons

$$\frac{1}{m} p_x \frac{\partial f}{\partial x} + E \frac{\partial f}{\partial p_x} = \hat{S}_e f \quad (5)$$

where  $m$  and  $\vec{p}$  — electrons effective mass and their quasi-momentum,  $\hat{S}_e f$  — a collisions term (we use the units system with the electrons charge  $e = 1$  and the Boltzmann's constant  $k_B = 1$ ).

Let's expand the unknown distribution function of electrons by the Legendre polynomes [2]

$$f(\vec{p}) = \sum_{l=0}^{\infty} f_l(\epsilon) P_l(\cos \theta), \quad (6)$$

where  $\epsilon$  is electrons energy,  $\theta$  — an angle between electrons quasi-momentum  $\vec{p}$  and  $x$ -axis.

After expending the all terms of equation (5) in the series of the Legendre polynomes, we shall have unlimited series of differential equations for determining  $f_l(\epsilon)$ . Than we shall tear these series and neglect the  $f_l(\epsilon)$  with  $l \geq 2$ . Such assumption is called "the diffusion assumption" in a theory of hot electrons [2]. This assumption is correct if

$$\frac{4}{15} \frac{L_p^2}{L_T^2} \ll 1, \quad (7)$$

$$\frac{1}{15} \frac{L_p^2}{L_E^2} \ll 1, \quad (8)$$

$L_E = \frac{\bar{\epsilon}}{E}$  — the non-local length [2],  $L_p$  — the momentum's average mean free path of electrons,  $L_T = \frac{T}{|grad T|}$  — a characteristic length of the temperature change [3-5].

In the assumption (7), (8) we have the two equations for symmetric and anti-symmetric parts of electrons distribution function

$$\frac{1}{3} \left[ \frac{p}{m} \frac{\partial f_1}{\partial x} + \frac{E}{p^2} \frac{\partial}{\partial p} (p^2 f_1) \right] = \hat{L} f_0, \quad (9)$$

$$f_1 = -\nu_p^{-1} \left( \frac{p}{m} \frac{\partial f_0}{\partial x} + E \frac{\partial f_0}{\partial p} \right). \quad (10)$$

The equations (9), (10) can be united in an elliptical equation for determining the  $f_0(\epsilon)$ . This equation was solved by using the perturbation theory with small parameters [2-5]

$$g_r = \frac{1}{3} \frac{L_e^2}{L_T^2}, \quad (11)$$

$$g_E = \frac{1}{12} \frac{L_e^2}{L_E^2}, \quad (12)$$

$L_e$  — the average cooling length of electrons [1].

Let's suppose that electrons energy scattering is realized with acoustic phonons and electrons momentum scattering is realized with acoustic phonons or with ionized impurities.

The solution in a zero order is the Maxwell function

$$f_0^{(0)} = a_0 e^{-w}. \quad (13)$$

where  $w = \frac{\epsilon}{T}$ , and the solution in a first order

$$\begin{aligned} f_0^{(1)} = f_0^{(0)} & \left\{ 1 + \xi \tau_r \left[ A_1 \left( \beta(w) - \frac{1}{12} w^2 - \right. \right. \right. \\ & \left. \left. \left. - \frac{1}{2} w - \beta_{1/2} + \frac{17}{16} \right) + \right. \right. \\ & \left. \left. \left. + (1-r) \left( A_2 \left( \frac{1}{12} w^2 - \frac{5}{16} \right) + A_3 \left( \frac{1}{3} w - \frac{3}{4} \right) + \right. \right. \right. \right. \\ & \left. \left. \left. \left. + A_4 (\ln w - 2 + 2 \ln 2 + C) \right) - \right. \right. \\ & \left. \left. \left. \left. - r \left( A_5 \left( \frac{1}{4} w^4 - \frac{945}{64} \right) + A_6 \left( \frac{1}{3} w^3 - \frac{35}{8} \right) - \right. \right. \right. \right. \\ & \left. \left. \left. \left. - A_4 \left( \frac{1}{6} w^2 - \frac{5}{8} \right) \right) \right) \right] \right\}, \end{aligned} \quad (14)$$

where  $C$  — the Euler constant,

$$\begin{aligned} \beta(w) &= \sum_{n=1}^{\infty} \frac{w^n}{n(n+1)!} - 1, \\ \beta_{1/2} &= \frac{1}{\sqrt{p}} \sum_{n=1}^{\infty} \frac{\Gamma(1 + \frac{1}{2})}{nn!} = 1.31375, \end{aligned} \quad (15)$$

$\Gamma(1 + \frac{1}{2})$  —  $\Gamma$ -functions,

$$\begin{aligned} A_1 &= \frac{(2r+1)}{T^2} \left[ 2(Z + (Z-6)r) \left( \frac{dT}{dx} \right)^2 + \right. \\ &\quad \left. + (3r-Z)F \frac{dT}{dx} + T \frac{dF}{dx} - 2(1+r)T \frac{d^2T}{dx^2} \right], \end{aligned}$$

$$\begin{aligned} A_2 &= \frac{1}{T^2} \left[ 2(Z+3) \left( \frac{dT}{dx} \right)^2 - ZF \frac{dT}{dx} + \right. \\ &\quad \left. + T \frac{dF}{dx} - 2T \frac{d^2T}{dx^2} \right], \end{aligned} \quad (16)$$

$$\begin{aligned} A_3 &= \frac{1}{T^2} \left[ 2Z \left( \frac{dT}{dx} \right)^2 - (Z+4)F \frac{dT}{dx} + T \frac{dF}{dx} \right], \\ A_4 &= \frac{1+2r}{T^2} F \left( F - Z \frac{dT}{dx} \right), \\ A_5 &= -\frac{1}{T^2} \left( \frac{dT}{dx} \right)^2, \\ A_6 &= \frac{1}{T^2} \left[ -3 \left( \frac{dT}{dx} \right)^2 + 2F \frac{dT}{dx} - T \frac{d^2T}{dx^2} \right], \end{aligned}$$

where

$$F = E - \frac{d\zeta}{dx} + \frac{\zeta}{T} \frac{dT}{dx}, \quad (17)$$

$$Z = \frac{\zeta}{T} - \frac{d\zeta}{dT}. \quad (18)$$

$\zeta$  — a chemical potential,

$$\xi = \frac{l T^{3/2}}{3(2m^3)^{1/2} s^2}, \quad (19)$$

$l$  — the average mean free path of the electrons momentum scattering with acoustic phonons,  $s$  — a sound velocity,  $r$  connects with the electrons momentum scattering: in scattering with acoustic phonons  $r = 0$ , in scattering with ionized impurities  $r = 1$ ,

$$\tau_r = \nu_{pr}^{-1} w^{(1-4r)/2}$$

— an averaged electrons momentum relaxation time,  $\nu_{pr}$  — an electrons momentum relaxation frequency.

### 3 Discussion

We shall point out that the electrons distribution function (14) depends on a square of temperature's gradient and a square of electro-chemical potential's gradient. It means that the electrons distribution function has a non-linear character. Besides, the distribution function depends on a second order derivative from a temperature and from an electro-chemical potential. It signifies that the distribution function is non-local one. It means that the electrons distribution function are determined not only by properties of a sample at a given point, but by adjacent points as well.

The energy dependence of the electrons distribution function (14) connects with the type of  $\beta(w)$  function. We can have from (15) that

$$\lim_{w \rightarrow \infty} \beta(w) = \frac{e^w}{w^2} \quad (10)$$

and

$$\lim_{w \rightarrow \infty} f_0^{(1)} \sim \frac{1}{w^2} \quad (21)$$

Thus, the distribution function of electrons with large energies is enough deformed when  $\epsilon \rightarrow \infty$ . This phenomena is well known in theories of a solid state [6] and a gas plasma [7]. Such effect called in this theories as the electrons running effect [6,7]. The electrons running effect can be proved in kinetic integrals divergence [6,7]. In our case these integrals have a form:

$$\beta_i = \int_0^\infty w^i \beta(w) e^{-w} dw \quad (22)$$

But successive taking into account of all non-linear and non-local terms in expressions (13), (16) leads to the elimination of the kinetic integrals divergence.

The distribution function (14) was obtain in the first order on the parameters (11), (12). It is precisely this fact that explain the non-linear and non-local terms. We can see now that it is an error to take into consideration only the non-linear terms in (14)-(16) and to neglect the non-local terms. On the contrary, it is incorrect to take into consideration only the non-local terms and to neglect the non-linear terms. In this both cases we have a physically absurd results as unlimited increasing of electrons energy. We shall point that the conditions giving a possibility to neglecting of the first order terms are discussed in [9].

In the assumption when non-local terms are not taken into account, i.e. in assumption  $\text{grad } T = \text{const}$  and  $E = \text{const}$ , and  $\text{grad } \zeta = \text{const}$ , the divergence remains. Such electrons distribution function was received in [9] and this function leads to kinetic integrals diverges. The direct way to elimination of diverges is taking into account non-local terms.

The transport theory of hot electrons in semiconductors come more than once across the problem of the electrons running effect [7]. It is known that there are few running limitation mechanisms [7].

It was found that only consistent taking into account of non-local terms in solving the kinetic equation leads to eliminate of the integrals divergence. Thus, we can say that the non-locality is a new limitation mechanism of the electrons running.

## 4 References

- [1]. Buss F.G., Bochkov V.S., Gurevich Y.G. Electrons and phonons in limited semiconductors. Moscow, Nauka, 1984, 289 p.
- [2]. Bulat L.P., Tomchuk P.M. Solving of kinetic equation under strong unhomogeneity. Kiev, 1987, 12 p.
- [3]. Anatychuk L.I., Bulat L.P. Influence of temperature gradient on the kinetic coefficients in semiconductors. Mobility, diffusion coefficient, thermoelectric power. *Fiz. Tekn. Polupr.*, 1981, v.15, No.8, p.1664.
- [4]. Anatychuk L.I., Bulat L.P. Influence of temperature gradient on the kinetic coefficients in semiconductors. The Benedicks, Peltier and Thomson effects, thermal conductivity. *Fiz. Tekn. Polupr.*, 1981, v.15, No.8, p.1666.
- [5]. Anatychuk L.I., Bulat L.P. The properties of thermoelectric materials under large heat flux (Revue). *Visnik AN USSR*, 1987, No.3, pp.5-15.
- [6]. Pojela Ju.K. Plasma and current untenabilities in semiconductors. Moscow, Nauka, 1977, 368 p.
- [7]. Lifshits E.M., Pitajevsky L.P. Physical Kinetics. Moscow, Nauka, 1979, 528 p.
- [8]. Bulat L.P. Influence of temperature gradient on changing electron distribution in semiconductors// *Fiz. Tekn. Polupr.* - 1977.- V.11.- No 11.- P.2181-2187.
- [9]. Bulat L.P., Stefansky V.A. Thermoelectric properties of high electron concentration materials under large temperature gradients. Proc. XIII Int. Conf. on Thermoelectrics. Kansas City, 1994.

# EXPERIMENTAL TESTING OF THE DEFORMATION OF THERMOELECTRICAL FIELD IN ANISOTROPIC INHOMOGENEOUS SEMICONDUCTORS

V.I. Bochegov

*Kurgan State Pedagogical Institute, 640000, Russia, Sovetskaya st., 63*

A theoretical calculation of this problem was offered in the paper [1]. The expression for the calculation of the electric potential in a rectangular sample was obtained, and the formulae of the difference of the potentials of the points  $x=0$  and  $x=1$  on each of the two opposite facets were worked out on its basis.

$$U_{(y=0)}^{\parallel} = \Delta T \cdot \alpha_{11}(l) - \frac{a \cdot l}{2} \cdot \delta_2 - a \cdot l^2 \cdot \gamma_2 \quad (1)$$

$$U_{(y=c)}^{\parallel} = \Delta T \cdot \alpha_{11}(l) + \frac{a \cdot l}{2} \cdot \delta_2 \quad (2)$$

where  $\Delta T$  is the difference of temperature of points  $X = 0$  and  $X = l$  (gradient of temperature is directed along the coordinate  $X$ ),  $a$  – is the width of the sample,  $\gamma_2$  and  $\delta_2$  – the coefficients in the quadratic dependence of the transversal component of the tensor of Zeebeck coefficient from the coordinate  $X$ :

$$\alpha_{12}(X) = \gamma_2 \cdot X^2 + \delta_2 \cdot X + \beta_2 \quad (3)$$

the sign  $\parallel$  means the transversal difference of the potentials.

On the basis of the same conclusions [1] it is possible to get the expression for the difference of the potentials between the points situated on the opposite facets of the sample with the

same coordinate  $X$ , i.e. for the transversal difference of the potentials (sign  $\perp$ ).

$$U_{\perp} = \gamma_2 \cdot X^2 + \delta_2 \cdot X + \beta_2 + \frac{1}{6} \cdot \frac{\sigma_{11}}{\sigma_{22}} \cdot \gamma_2 \cdot a^2 \quad (4)$$

where  $\sigma_{11}$  and  $\sigma_{22}$  are the components of the tensor of conductivity of the material.

The measurement of the transversal difference of the potentials for three different coordinates  $X = 0$ ,  $X = l_1$  and  $X = l_2$  will make it possible to calculate the parameters of heterogeneity  $\gamma_2$  and  $\delta_2$ , entering also formulas (1), (2). In particular, having put the obtained parameters of heterogeneity in the expressions (1), (2) or in their linear combination it is possible to estimate the degree of correspondence of the calculated and measured values. The experiment, conducted by the author brought satisfactory results in comparison with the theory.

## References

- [1]. V.I. Bochegov, The Calculation of the Deformity of the Field of the Potential of Termoelectric Effect in a Heterogeneous Anisotropic Sample in a Quadratic Approximation, Materials for Thermoelectric Transformators, S-Petersburg, 1994.

# PROGRAMMING OF THE DISTRIBUTION OF IMPURITY IN THE CONTINUUM OF SEMICONDUCTOR BY THE METHOD OF CRYSTALLIZATION

S.A.Podgorbunskikh, V.I.Bochegov, V.M.Ovsjanov

*Kurgan State Pedagogical Institute, 640000, Russia, Kurgan, Sovetskaya st., 63*

The necessity in materials with various properties arose with the development of semiconductor physics and with the enlargement of semiconductor electronics application. The semiconductor properties mainly are conditioned by its structure and degree of heterogeneity; consequently, we can get necessary properties when the structure of material is conditioned.

We suggest one of the ways of setting the necessary distribution of impurity in the continuum of semiconductor. It is based on two crystallization methods: normal and zone. It consists in the following: at first a model is crystallized normally and then it is recrystallized with the zone directed towards or parallel to normal.

Let us consider the codirected recrystallization on the basis of [1]. It is possible to describe this process mathematically with the differential equation

$$dC(x) = \frac{k}{l} \cdot \left\{ C_0 \cdot k \cdot \left( 1 - \frac{x+l}{L} \right)^{(k-1)} - C(x) \right\} \cdot dx \quad (1)$$

where  $l$  – the width of the zone,  $L$  – the length of the sample,  $k$  – impurity distribution equilibrium coefficient,  $C$  – initial impurity concentration. This equation is correct on the segment  $x \leq L-l$ . On the rest of the segment the impurity distribution is described by the equation

$$C(x) = C(L-l) \cdot \left( \frac{L-x}{l} \right)^{(k-1)} \quad (2)$$

It is impossible to solve the equation (1) analytically in the final form that is why it is easy to solve it numerically on the computer.

Below you can see the algorithm of solving this equation:

1.  $C_0, l, L, k, dx$ ;
2.  $C(0) = \frac{k \cdot L \cdot C_0}{l} \cdot \left( 1 - \left( 1 - \frac{l}{L} \right)^k \right)$  is calculated;  $x=0$ ;
3.  $dC(x)$  is calculated by use formula (1);
4.  $C(x+dx) = C(x) + dC(x)$ ;
5.  $x = x + dx$ ;
6.  $C(x) = C(x+dx)$ ;
7. if  $x \leq L-l$  return to point 3.

We substituted the result  $C(L-l)$  in the formula (2) and counted the concentration of the remaining segment. The solving of this problem is illustrated by fig. 1. Calculation and the succession of solving of this problem for the contrary recrystallization is the same. The results of this solving are illustrated by fig. 2.

The present method allows to get the materials of three components in which the concentration of one component is practically constant and of another is visibly changed (fig. 1,2).

Conducted experiment proves theoretical calculations which were made.

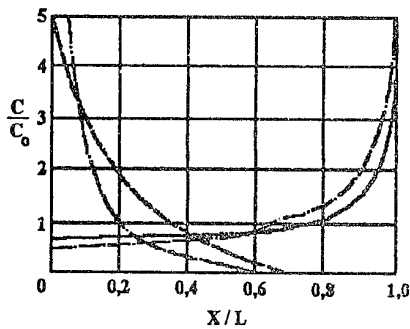


Fig. 1. Distribution of impurity along the ingot length at codirected recrystallization. ( $l = L/3$ , normal crystallization: —  $k=0.6$ , - - -  $k=5$ , recrystallization with the zone: - · -  $k=0.6, \dots k=5$ .)

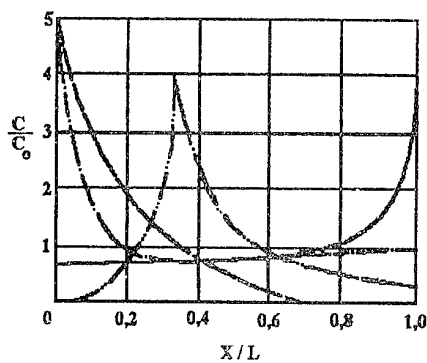


Fig. 2. Distribution of impurity along the ingot length at contrary recrystallization. ( $l = L/3$ , normal crystallization: —  $k=0.6$ , - - -  $k=5$ , recrystallization with the zone: - · -  $k=0.6, \dots k=5$ .)

## References

- [1]. W.G.Pfann, Zone melting, Moscow, 1970, 320 p.

THERMOELECTRIC FIGURE OF MERIT  
OF NONDEGENERATE SEMICONDUCTOR  
SUBMICRON LAYERS

Yu. G. Gurevich<sup>1</sup>, G.N. Logvinov<sup>2</sup> and O.Yu.Titov<sup>1</sup>  
<sup>1</sup>Centro de Investigación y de Estudios Avanzados del  
 Instituto Politécnico Nacional, Apartado Postal 14-740,  
 07000 Mexico D.F. Mexico  
<sup>2</sup>Institute of Thermoelectricity, Chernivtsi, P.O.274000.  
 P.B. 86, Ukraine.

Thermoelectric figure of merit of nondegenerate semiconductor submicron films is obtained in twotemperature approximation. It is shown that it value can be much more than in the bulk samples.

It is well known that bulk nondegenerate semiconductor have highly small value of thermoelectric figure of merit  $Z_e = \alpha^2 \sigma / (\kappa_p + \kappa_e)$ , where  $\alpha$  is the coefficient of thermoelectric power,  $\sigma$  is electrical conductivity,  $\kappa_p$  ( $\kappa_e$ ) is the phonon (electron) thermal conductivity. Mainly it is based on the large value  $\kappa_p$  in comparison with  $\kappa_e$ . It leads to that the phonon heat flux is excess of electron heat flux essentially so only trifling part of heat transforms to the useful work.

The situation can be changed in the semiconductor layers with the thickness  $2a < l$ , where  $l$  is the scale of the electron-phonon energy interaction length, referred to as the cooling length (the typical magnitude of the cooling length are  $10^{-2} \pm 10^{-3}$  sm in semiconductors).

Really, using the correct procedure of formulating separately boundary conditions for both subsystems of quasiparticles (electrons and phonons) [1], we obtain that in submicron layers ( $2a < l$ ) electron's and phonon's temperatures are different in any point of semiconductor sample [2]. It gives the possibility to vary heat fluxes by variation of boundary conditions and thus to reduce the phonon flux.

Let an isotropic semiconductor of finite dimensions, has the shape of a parallelepiped with end faces at  $x = \pm a$  in contact with constant-temperature chambers kept at different temperatures  $T_1$  and  $T_2$  ( $T_1 > T_2$ ):

the side faces are assumed to be adiabatically isolated for all the quasiparticle subsystems. The sample is closed by an external metal resistance  $R_m$  of length  $2b$ , so that a thermoelectric current  $j$  flows in the circuit. It is assumed that boundary conditions for the electron and phonon subsystems satisfy the most general heat-conduction conditions of this kind [3] (known as the boundary conditions of the second kind):

$$\tilde{\Pi} - \chi_e \frac{dT_e}{dx} \Big|_{x=\pm a} = \eta_e (T_e - T_{2,1}) \Big|_{x=\pm a}, \quad (1)$$

$$-\chi_p \frac{dT_p}{dx} \Big|_{x=\pm a} = \eta_p (T_p - T_{2,1}) \Big|_{x=\pm a} \quad (2)$$

Here  $\chi_e$  and  $\chi_p$  are the electron and phonon thermal conductivities;  $\tilde{\Pi} = \Pi - \Pi_s$ , where  $\Pi$  and  $\Pi_s$  are the bulk and Peltier coefficients;  $\eta_e$  and  $\eta_p$  are the coefficients describing the efficiency of heat transfer between the electron and phonon subsystems, on the one hand, and the constant-temperature chambers, on the other;  $T_p$  is the phonon temperature.

The temperatures  $T_{e,p}$  can be found by solving the energy balance equations for electrons and phonons [3], which allow for the possibility of heating of quasiparticles by the thermoelectric current flowing in a closed circuit:

$$\frac{dq_e}{dx} + P(T_e - T_p) = -j \frac{d\phi}{dx}, \quad (3)$$

$$\frac{dq_e}{dx} - P(T_e - T_p) = 0, \quad (4)$$

where

$$q_e = -\chi_e \frac{dT_e}{dx} + \left[ \Pi(T_e) + \frac{1}{e} \mu(T_e) \right] J, \quad (5)$$

$$q_e = -\chi_p \frac{dT_p}{dx} \quad (6)$$

and  $P$  is a parameter representing the strength of the electron-phonon interaction.

The solution of the system (1) obtained in an approximation which is linear in terms of  $t = (T_1 - T_2)/T^*$  [ $T^* = (T_1 + T_2)/2$ ] is as follows:

$$T_{e,p} = T^* - \frac{\Delta T}{2} - \left\{ \frac{x}{a} Z^{-1} \left[ (1 + \xi_e \text{th } ak) + \delta(1 + \xi_p \text{th } ak) \right] \frac{x}{a} - \gamma_{e,p} (\xi_e - \xi_p) x \times \frac{\sin kx}{\sin ak} \right\} + \frac{q\tilde{\alpha}}{\chi_e} Z^{-1} \left[ \delta(1 + \xi_p \text{th } ak) \frac{x}{a} + \gamma_{e,p} (1 + \xi_p \text{th } ak) \frac{\sin kx}{ak \sin ak} \right]. \quad (7)$$

Here

$$Z = (1 + \xi_e \text{th } ak)(1 + \xi_p \text{th } ak) +$$

$$+ \delta(1 + \xi_p \text{th } ak)(1 + \xi_e \text{th } ak);$$

$$\Delta T = T_1 - T_2; \xi_{e,p} = \eta_{e,p}/(\chi_{e,p} k);$$

$$k = l^{-1} = \sqrt{k_e^2 + k_p^2}; k_{e,p} = P/\chi_{e,p};$$

$$\delta = (k_p/k_e)^2 = \chi_e/\chi_p; \gamma_e = 1, \gamma_p = -\delta. \quad (8)$$

In spite of the fact that in the approximation linear in  $t$  we can ignore the term  $J(d\psi/dx)$  in Eq. (3), the solution given by Eq. (7) for  $J \neq 0$  (closed circuit) is not identical with the corresponding expression given in Ref. 4.

We shall define the current  $J$  using the Kichhoff law [3]. If we ignore the value of  $\alpha$  in the metal part of the circuit, we find that integration over the closed

circuit, including the contacts, reduces to

$$\begin{aligned} JR = \oint \frac{J}{\sigma} dl &= - \left[ \lim_{\Delta \rightarrow 0} \int_{-a-\Delta}^{-a+\Delta} \alpha \frac{dT_e}{dx} dx + \right. \\ &+ \left. \int_{-a}^a \alpha \frac{dT_p}{dx} dx + \lim_{\Delta \rightarrow 0} \int_{a-\Delta}^{a+\Delta} \alpha \frac{dT_e}{dx} dx \right] = \\ &= -[\alpha_s (T_e|_{x=-a} - T_1) + \right. \\ &\left. + \alpha_s (T_2 - T_e|_{x=a}) + \alpha_s (T_2 - T_1)], \quad (9) \end{aligned}$$

where  $\alpha_s = \lim_{\Delta \rightarrow 0} \bar{\alpha}_k$  is the thermoelectric power,  $\bar{\alpha}_k$  is the average value of the thermoelectric power at the contact between the semiconductor and the metal,  $R = R_O + R_m$ ;  $R_O = 2a/\sigma + 2/\sigma_s$  is the resistance of the semiconductor sample,  $\sigma$  is the electrical conductivity of this sample,  $\sigma_s$  is the surface conductance of the sample,  $R_m = 2b/\sigma_m$ , and  $\sigma_m$  is the conductivity of the metal part of the circuit.

Combining Eqs. (7) and (9), we obtain the expression for the current density

$$J = \frac{(1-\beta)\alpha_s + \beta\alpha}{R + R_H} \Delta T, \quad (10)$$

and it is natural to call  $R_H = 2\alpha\gamma(d\psi/dx + \alpha_s)/\chi_e$  the Peltier resistance,

$$\beta = 1 - Z^{-1} [1 + \xi_e \text{th } ak + \delta(1 + \xi_p \text{th } ak) - (\xi_e - \xi_p) \text{ th } ak] \quad (11)$$

$$\gamma = Z^{-1} [\delta(1 + \xi_p \text{th } ak) + (1 + \xi_p \text{th } ak) \text{ th } ak/ak]. \quad (12)$$

Going back to Eq. (7) for temperature and substituting in it the expression (10), we obtain the following final expression for the temperatures  $T_{e,p}$ :

$$T_{e,p} = T^* - \frac{\Delta T}{2} \left\{ \frac{x}{a} Z^{-1} \left[ (1 + \xi_e \text{th } ak) + \right. \right.$$

$$+ \delta(1+\lambda)(1+\xi_p \text{th } \alpha k) \frac{x}{\alpha} \\ - \gamma_{e,p} (\xi_e^* - \xi_p) \frac{\text{sh } kx}{\text{ch } \alpha k} \Big\}. \quad (13)$$

Here

$$\lambda = \frac{2\alpha \tilde{\eta}}{\chi_e} \frac{(1-\beta)\alpha_s + \beta \alpha}{R+R_H}; \\ \xi_e^* = \xi_e - \lambda(\alpha k)^{-1} x \\ x (1+\xi_p \alpha k) = \eta_e^*/(\chi_e k); \\ \eta_e^* = \eta_e - 2\tilde{\eta}\lambda(1+\xi_p \alpha k) \quad (14)$$

The quantity  $\eta_e^*$  governs the effective value of the coefficient that determines the rate of heat transfer between electrons and the constant-temperature chambers. It should be noted that it depends parametrically on the resistance of the external load.

Let us go to the limit of submicron film, e.i. let us assume that  $RQ \ll 1$ . In this case the expressions (13) tends to the follow system:

$$T_e = T - \left(1 + \frac{1+\lambda}{1+\alpha_{es}/\alpha_e} \frac{\Delta T}{2\alpha}\right) x, \quad (15)$$

$$T_p = T - \left(1 - \frac{1+\lambda}{1+\alpha_{ps}/\alpha_p} \frac{\Delta T}{2\alpha}\right) x, \quad (16)$$

where  $\alpha_{es} = \alpha \eta_e$  ( $\alpha_{ps} = \alpha \eta_p$ ) is electron (phonon) surface heat conductivity.

We can see that electron and phonon temperatures are independent in submicron films and don't coincide anywhere generally. It is clear that  $T_p \approx T$  if

$$\alpha_{ps} \ll \alpha_p \quad (17)$$

This is mean that heat exchange of phonon gas is slightly effective with the thermostats, the large value of bulk heat conductivity equalizes the temperature  $T_p$  along the sample at the same time.

If the condition (17) takes

place the  $\nabla T_p \ll \nabla T_e$ . At the same time, since  $\alpha_p \gg \alpha_e$  the correlation between both electron and phonon fluxes is determined by parameter  $\alpha_{ps}/\alpha_e$  (if the both conditions as (18) so  $\alpha_{es}/\alpha_e \gg 1$  take place).  $\eta_p \ll \eta_e$  if  $\alpha_{ps} \ll \alpha_e$ , and heat flux will flow along electron gas mainly.

Supposing the phonon boundary conditions as adiabatical we can to get the efficiency of submicron thermogenerating laer as [5]

$$\eta = \frac{2\Delta T}{T_1(1+p) + T_2(1-p)} \times \\ \times p \left\{ \left[ 1 + \alpha_{es} p^2 \left\{ \alpha \left[ T_1(1+\delta) + T_2(1-\delta) \right] \times \right. \right. \right. \\ \left. \left. \left. \times \left[ \frac{(1-\beta)\alpha_s + \beta \alpha}{R+R_H} \right]^2 R_H \right] \right\}^{-1} \right\} \quad (18)$$

where  $p = (\alpha_{es}/\alpha_e - \lambda)/(\alpha_{es}/\alpha_e + 1)$

In the isotermic limit ( $\alpha_{es} \gg \alpha_e$ ) the expression (20) tends to

$$\eta = \eta_e [1 + (4Z_s T)^{-1}]^{-1} \quad (19)$$

Here  $\eta_e$  is Carno efficiency.

$Z_s = \frac{\alpha^2 \theta_e}{\alpha_e}$  is thermoelectric figure of merit of submicron film.

Term  $Z_s$  doesn't content the phonon heat conductivity so the ratio  $Z_s/Z_e \gg 1$ .

This inequality demonstrates submicron films as a perspective materials for thermoelectricity.

#### References

- [1]. Granovski M.Ja., Gurevich Yu.G., Fiz. Tekn. Poluprovodn., 1975, v.9, N.8, p.p. 1552-1554.
- [2]. Logvinov G.N., Fiz. Tekn. Poluprovodn., 1991, v. 25, N10, p.p. 1815-1818.
- [3]. Gurevich Yu.G., Logvinov G.N., Fiz. Tekn. Poluprovodn., 1992 v.26, N11, p.p.1945-1951.
- [4]. F.G. Bass, V.S. Bochkov and Yu.G. Gurevich, Electrons and phonons in Bounded Semiconductors, Moscow, 1984.
- [5]. Logvinov G.N., Izvestija vuzov. Fizika, 1993, N9, p.p. 68-72.

## COMPUTER MODELLING OF THERMOELECTRIC MATERIAL ANISOTROPIC POWDER STRUCTURES.

L.I.Anatychuk, S.V.Melnichuk, S.V.Kosyachenko

*Institute of Thermoelectricity, Chernovtsy, 274000, General Post Office, box 86, Ukraine*

The computer simulation method was used for investigation of anisotropic materials, consisting of pressed powder layers. The influence of porosity, texture and number of layers on effective thermoelectrical characteristics was studied. It was found the possibility to control the anisotropy of such samples properties.

When we consider pressed semiconductor samples it is often necessary that their texture to be taken into account. The properties of pressed powders are anisotropic because of the texture. Such samples can be treated as a heterogeneous media.

In order to estimate heterogeneous media permissible limits from applied problems point of view it is necessary to know the effective kinetic coefficients which macroscopically, take into account real distortions of fields and flows in a sample due to space inhomogeneity. In this work we determine effective kinetic coefficients for heterogeneous layered media that represent a set of two material alternating layers being in ideal thermal and electrical contact. Each layer is a pressed powder made of anisotropic crystallites with crystallographic axes primarily along macrolayer planes.

It is assumed that thickness of a layer is much greater than the corresponding free path but much less than thickness of the sample. This assumption allows us to neglect the boundary conditions.

We also assume that anisotropy of the constituent materials is described by tensors of the form

$$\hat{a} = \begin{pmatrix} a_{xx} & a_{xy} & 0 \\ a_{yx} & a_{yy} & 0 \\ 0 & 0 & a_{zz} \end{pmatrix} \quad (1)$$

where z-axis is perpendicular to layer plane.

### 1. Simulation of Bi<sub>2</sub>Te<sub>3</sub> type powder and calculation of its effective characteristics.

Bi<sub>2</sub>Te<sub>3</sub> type materials are characterized by existence of cleavage planes along which crushing occurs. This is the cause of appearance of texture in pressed samples (mainly in the region of contact with a base) This is why for the simulation method proposed in [1] it is more convenient to use rectangles (Fig.1., Fig.2.)

*Fig.1.*

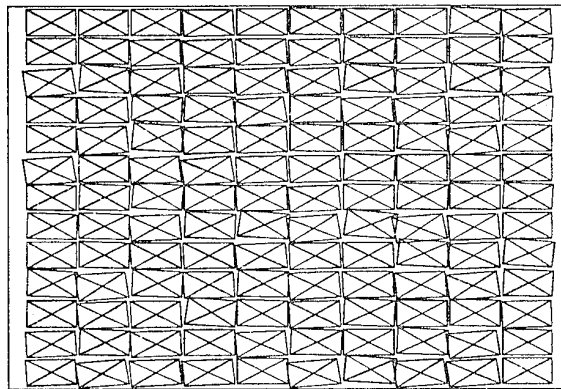
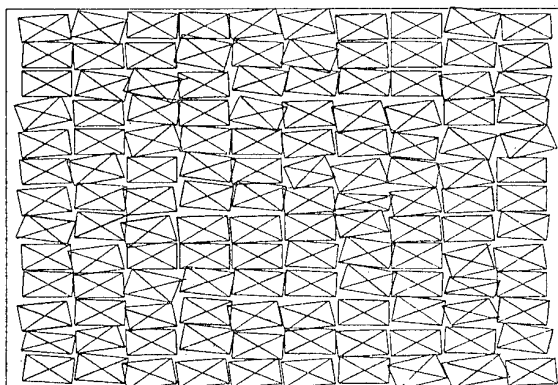


*Fig.2.*



Calculation of effective kinetic coefficients was carried out by the "random walks" method. The calculation is based upon relationship:

$$\langle R^2 \rangle = \langle X^2 \rangle + \langle Y^2 \rangle \approx 2dN(D_x + D_y), N \rightarrow \infty \quad (2)$$

$\langle R^2 \rangle$  is meansquared displacement of a particle;  $D_i$  is diffusion coefficient along i-axis; d is space dimension.

Relationship (2) relates meansquared displacement of a particle to its diffusion coefficients. Conductivity was determined with the help of the Einstein relation

$$\sigma_i = k(1 - \Phi)D_i \quad (3)$$

where  $\Phi$  is medium porosity,  $k$  is a proportionality factor.

The calculations were carried out for a large number of random points ( $10^5$ ). Each point started its motion from randomly chosen medium points. Every step of the particle has a fixed value along crystallographic axis. And it varies with orientation of the axis. (the orientation is specified for each crystallite when the structure is formed). The only steps that are allowed are those between the points belonging to a semiconductor. Motion in pores and jumping through pores are forbidden. Cyclic boundary conditions were applied. Diffusion coefficient was averaged over a number of random points.

Calculations of thermal conductivity coefficients for such media were also done by formulae (2)-(3). In doing this we took into account that:

1. The step of a moving particle was increased proportionally to a phonon free path.

2. Motion in pores in smaller "isotropic" steps, proportional to thermal conductivity of pores filler.

Fig.3-4 show the results of calculations of Bi<sub>2</sub>Te<sub>3</sub> pressed powder electrical and thermal conductivity with its texture being taken into account. For this semiconductor thermal and electrical conductivity are anisotropic whereas thermo-power coefficient is isotropic.

Fig.3.

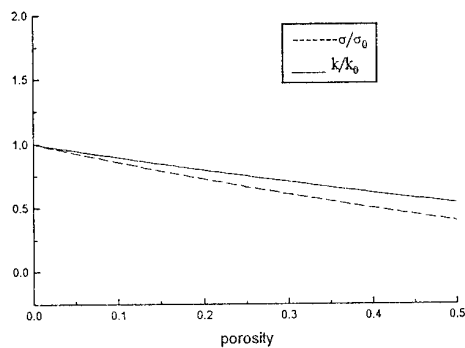


Fig.4.

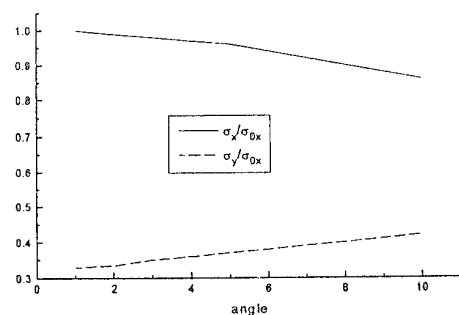


Fig.3 shows the dependence of relative values of thermal and electrical conductivity on powder porosity for samples with the same texture. In this case the behaviour of relative conductivities along both principal crystallographic axes will be the same. Fig.4 show the graphs for  $\sigma_x$  and  $\sigma_y$  for the case of the same porosity samples but the different texture (different value of particular crystalite axis displacement from the axis of principal direction).

## 2. Calculation of effective kinetic characteristics of layered powder structures.

Calculations of effective values of kinetic coefficients was carried out by two methods. For heterogeneous media the method [2] was used, whereas for composite structure calculations were done by the described above method of computer simulation.

Heterogeneous material represents a set of alternating layers of two different materials. We considered two possibilities:

1. Semiconductor material with different porosity was the materials for layers

2. Two different semiconductors were used.

The calculation formula are:

$$\begin{aligned} \rho_{xx}^{af} &= \langle \rho_{xx} \rangle + d1 \cdot d2 \cdot [F1(\rho_{xy}^{(1)} - \rho_{xy}^{(2)}) + P1(\alpha_{xx}^{(1)} - \alpha_{xx}^{(2)})], \\ \rho_{yx}^{af} &= \langle \rho_{yx} \rangle + d1 \cdot d2 \cdot [F1(\rho_{yy}^{(1)} - \rho_{yy}^{(2)}) + P1(\alpha_{yx}^{(1)} - \alpha_{yx}^{(2)})], \end{aligned} \quad (4)$$

$$\begin{aligned} F1 &= (c1(-\tilde{\kappa}_{xx}) - f1 \cdot \tilde{\alpha}_{yx}) / \Delta, \\ \Delta &= \bar{\rho}_{yy}(-\tilde{\kappa}_{xx}) - \bar{\alpha}_{yx} \cdot \tilde{\Pi}_{xy}, \\ \text{where } \bar{\alpha} &= d2 \cdot \alpha^{(1)} + d1 \cdot \alpha^{(2)}, \\ c &= \rho_{yx}^{(1)} - \rho_{yx}^{(2)}, f1 = \Pi_{xx}^{(2)} - \Pi_{xx}^{(1)}, \end{aligned} \quad (5)$$

$d_1, d_2$  are partial volumes of particular components;

$\Pi$  is the Peltier coefficient tensor

$$\begin{aligned} \alpha_{xy}^{af} &= \langle \alpha_{xy} \rangle + d1 \cdot d2 \cdot [F2(\rho_{xy}^{(1)} - \rho_{xy}^{(2)}) + P2(\alpha_{xy}^{(1)} - \alpha_{xy}^{(2)})], \\ \alpha_{yy}^{af} &= \langle \alpha_{yy} \rangle + d1 \cdot d2 \cdot [F2(\rho_{yy}^{(1)} - \rho_{yy}^{(2)}) + P2(\alpha_{yy}^{(1)} - \alpha_{yy}^{(2)})], \end{aligned} \quad (6)$$

$$\begin{aligned} \kappa_{xy}^{af} &= \langle \kappa_{xy} \rangle + d1 \cdot d2 \cdot [-F2(\Pi_{xy}^{(1)} - \Pi_{xy}^{(2)}) + P2(\kappa_{xx}^{(1)} - \kappa_{xx}^{(2)})], \\ \kappa_{yy}^{af} &= \langle \kappa_{yy} \rangle + d1 \cdot d2 \cdot [-F2(\Pi_{yy}^{(1)} - \Pi_{yy}^{(2)}) + P2(\kappa_{yy}^{(1)} - \kappa_{yy}^{(2)})], \end{aligned} \quad (7)$$

$$\alpha_{xx}^{af} = \alpha_{xx}^{(2)} + d1 \cdot d2 \cdot [F4(\rho_{xy}^{(1)} - \rho_{xy}^{(2)}) + P4(\alpha_{xx}^{(1)} - \alpha_{xx}^{(2)})], \quad (8)$$

$$\alpha_{yx}^{af} = \alpha_{yx}^{(2)} + d1 \cdot d2 \cdot [F4(\rho_{yy}^{(1)} - \rho_{yy}^{(2)}) + P4(\alpha_{yx}^{(1)} - \alpha_{yx}^{(2)})], \quad (8)$$

$$\kappa_{xx}^{af} = \kappa_{xx}^{(2)} + d1 \cdot d2 \cdot [-F4(\Pi_{xy}^{(1)} - \Pi_{xy}^{(2)}) + P4(\kappa_{xx}^{(1)} - \kappa_{xx}^{(2)})], \quad (9)$$

$$\kappa_{yx}^{af} = \kappa_{yx}^{(2)} + d1 \cdot d2 \cdot [-F4(\Pi_{yy}^{(1)} - \Pi_{yy}^{(2)}) + P4(\kappa_{yx}^{(1)} - \kappa_{yx}^{(2)})], \quad (9)$$

$$\rho_{xy}^{af} = \rho_{xy}^{(2)} + d1 \cdot d2 \cdot [F3(\rho_{xy}^{(1)} - \rho_{xy}^{(2)}) + P3(\alpha_{xx}^{(1)} - \alpha_{xx}^{(2)})], \quad (10)$$

$$\rho_{yy}^{af} = \rho_{yy}^{(2)} + d1 \cdot d2 \cdot [F3(\rho_{yy}^{(1)} - \rho_{yy}^{(2)}) + P3(\alpha_{yx}^{(1)} - \alpha_{yx}^{(2)})], \quad (10)$$

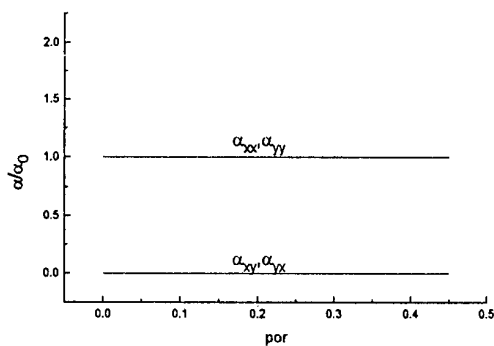
$$F2 = (c2(-\bar{\kappa}_{xx}) - f2 \cdot \bar{\alpha}_{yx}) / \Delta, \quad (11)$$

$$c2 = \alpha_{yx}^{(1)} - \alpha_{yx}^{(2)}, \quad f2 = \kappa_{xx}^{(2)} - \kappa_{xx}^{(1)},$$

These relationships were used to set up a computer program for calculation of layered structures containing arbitrary number of arbitrary thickness layers of two different materials. Algorithm of n-layered system calculation consists in replacement of n-1-layered system with one layer for one-layered one, with effective averaged parameters and total thickness with added a new homogeneous layer.

We considered the case of  $\text{Bi}_2\text{Te}_3$  for monocrystals with isotropic thermo-e.m.f. and anisotropic thermal and electrical conductivities. Results of calculations of  $\alpha$ ,  $\kappa$ ,  $\rho$  for 2-layered system are shown in Fig. 5-7. The second layer is a monocrystal (porosity = 0).

Fig. 5 Dependence of thermo-e.m.f. on 2-layered composite (porosity of the 2-nd layer is 0).



Similar calculations were carried out for various cases when porosities of alternating layers vary in the interval from 0 to 0.5 and number of layers can be arbitrary. The results show that thermo-e.m.f. tensor coefficients are not depend of the number of layers and porosity values. Q qualities  $Z_{xx}$  and  $Z_{yy}$  decrease gradually with porosity growth.

Fig. 6 Dependence of thermal conductivity on porosity

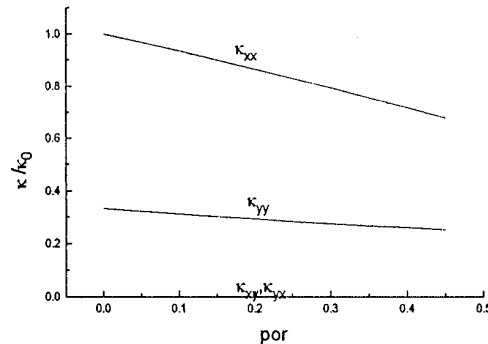
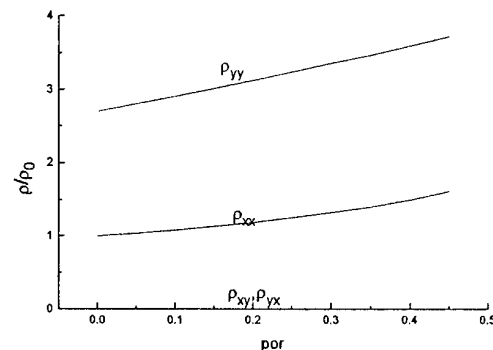


Fig. 7 Dependence of resistance on porosity for 2-layered system (porosity of the second layer 0)



Let us consider the case of alternating layers of two different porous materials that differ in conductivity type and consequently in the sign of thermo-e.m.f.. Fig. 8-11 show dependences of thermoelectrical characteristics and Qqualities on odd number layer porosities, even number layer porosities being fixed.

Diagonal components  $\sigma$ ,  $\kappa$ ,  $\alpha$ , have monotonous dependence on porosity.  $\kappa_{xx}$ ,  $\alpha_{xx}$  and  $\rho_{yy}$  are not changed with a number of layers increase whereas  $\kappa_{yy}$ ,  $\alpha_{yy}$  and  $\rho_{xx}$  are greatly depend on the number of layers. Thermoelectrical Q-quality is monotonously dependent on porosity as the number of layers increases. Difference  $Z_{xx} - Z_{yy}$  is greatly depend on number of layers (Fig. 11).

Fig.8

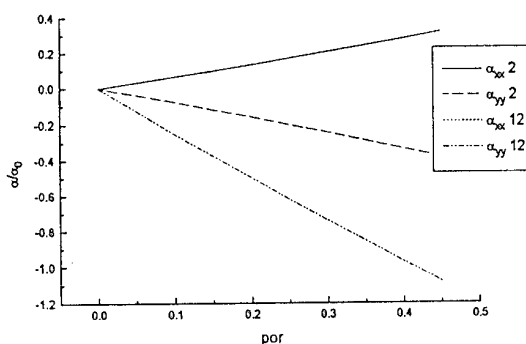


Fig.9

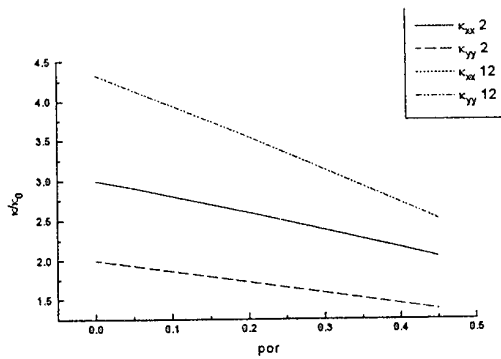


Fig.10

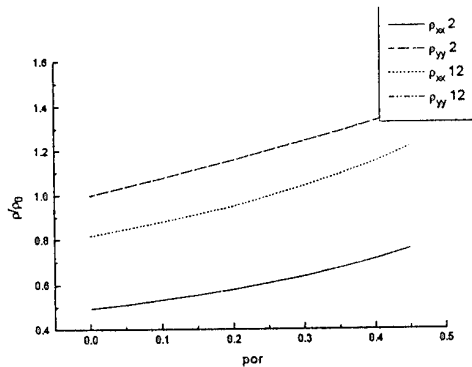
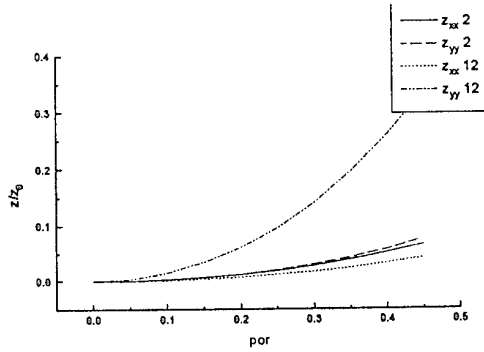


Fig.11



Finally, we consider the case of orientation of laboratory frame reference axes being different from that of crystal symmetry axes. In this case the kinetic coefficients tensor has a form (1). After averaging by formulae(4-9) we find the effective values of tensor components depending on porosity of materials, number of layers and dip angles of semiconductor material texture axes. The results of calculations for nondiagonal components[3]

$$Z_{xy} = \alpha_{xy}^2 / (\rho_{xx} \cdot \kappa_{yy}), \quad (12)$$

are shown in Fig.12-14

Fig. 12.

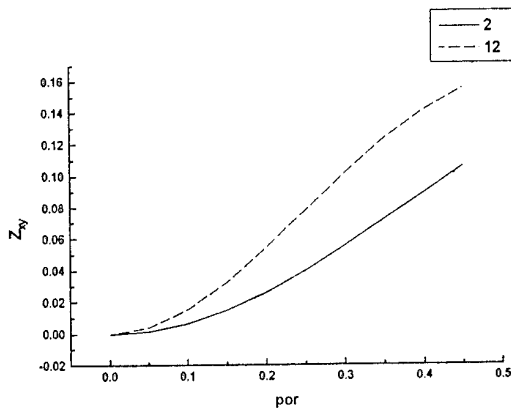


Fig. 13

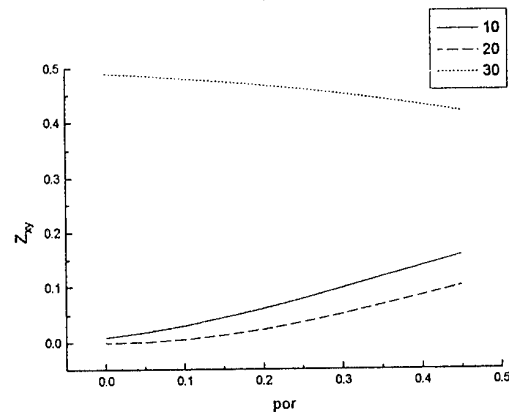
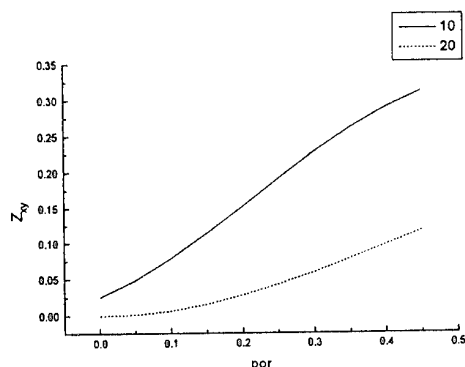


Fig. 14



We assumed, as before, that adjacent layers have different conductivity type. In the case of identical conductivity of layers  $Z_{xy} = 0$  for arbitrary porosity.

Therefore we are able to alter material effective thermoelectrical characteristics in quite wide range by altering the texture axis slope, porosity of material and layer thickness.

#### References:

[1]. L.I.Anatychuk , S.V.Kosyachenko, S.V.Melnychuk, V.M.Chernov, Theory for optimization of thermoelectric powder materials. Thesis on 13 International conference on thermoelectrics. Kansas City, USA, August 30-September 1, 1994.

[2]. Г.С.Гудкин , Е.К.Иорданишвили , В.А.Кудинов , Е.Э.Фискинд, Термоэлектрические, гальваномагнитные и термомагнитные свойства гетерогенных слоистых сред. I, *ФТП*, 1982, т.16, №9, с.1620-1624.

[3]. Г.С.Гудкин, Е.Э.Фискинд, Термоэлектрические, гальваномагнитные и термомагнитные свойства гетерогенных слоистых сред. II, *ФТП*, 1984, т.18, №2, с.234-237.

## THERMOMAGNETIC PHENOMENA IN RANDOMLY INHOMOGENEOUS SOLID STATE SYSTEMS

I.I.Fishchuk and N.D.Marchuk

*Institute for Nuclear Research, National Ukrainian Academy of Sciences  
Kiev, 252022, 47, pr.Nauki, Ukraine*

The theory of the thermomagnetic phenomena in randomly inhomogeneous solid-state media, within of a method of effective medium in a square-law on a magnetic field approximation, is developed. General system of equations for calculation of effective thermopower tensor components changes, caused by a magnetic field, is obtained. Calculations are carried out for systems, consisting from random high- and low-conducting components. Are found dependences of antisymmetric part and changes, caused by a magnetic field, of symmetric part of effective thermopower tensor from share of volume which occupy a high-conducting component of system.

### Introduction

During last years a great attention has been given to investigations of the thermoelectric and thermomagnetic phenomena in non-uniform systems. For research of thermopower in three-dimensional non-uniform systems were used a theory of effective medium (EMT) and computer calculations [1,2]. In work [3] the EMT was used for investigations of the changes of thermopower caused by magnetic field and the Nernst effect in three-dimensional systems with randomly distributed dielectric inclusions.

In present work we develop in the frameworks of EMT the general theory for thermomagnetic phenomena in inhomogeneous systems in presence of a weak magnetic field. Calculations are performed for systems, which consist from random high- and low-conducting components with any ratio of partial volumes of high- and low-conducting regions.

### The theory

We consider a solid-state system with randomly distributed inhomogeneities when a local values of kinetic coefficients may be introduced. Let us write the local electric current  $\vec{j}$  and flow of heat  $\vec{q}$  densities in the form

$$\vec{j} = \hat{\sigma} \vec{E} + \hat{\beta} \vec{G}, \quad (1)$$

$$\vec{q} = \hat{\gamma} \vec{E} + \hat{\kappa} \vec{G}, \quad (2)$$

where  $\vec{E}$  and  $\vec{G}$  are intensities of electric and temperature fields. The effective values  $\hat{\sigma}_e$ ,  $\hat{\beta}_e$ ,  $\hat{\gamma}_e$ ,  $\hat{\kappa}_e$ ,  $\vec{j}_e$  and  $\vec{q}_e$  are connected by

$$\vec{j}_e = \hat{\sigma}_e \vec{E}_e + \hat{\beta}_e \vec{G}_e, \quad (3)$$

$$\vec{q}_e = \hat{\gamma}_e \vec{E}_e + \hat{\kappa}_e \vec{G}_e, \quad (4)$$

where  $\vec{F}_e = \langle \vec{F} \rangle_e$  ( $\vec{F}_e = \vec{j}_e, \vec{q}_e, \vec{E}_e, \vec{G}_e$ ). The angular brackets means the configuration (space) averaging.

The local thermopower  $\hat{\alpha}$  and effective thermopower  $\hat{\alpha}_e$  may be found from conditions  $\vec{j} = 0$  and  $\vec{j}_e = 0$  in (1) and (3). From last condition we have

$$\hat{\alpha}_e = \hat{\sigma}_e^{-1} \hat{\beta}_e \quad (5)$$

Tensors  $\hat{\gamma}$  and  $\hat{\beta}$  are connected by  $\hat{\gamma} = T \hat{\beta}^T$ , where  $\hat{\beta}^T$  is transpose of  $\hat{\beta}$ . We suppose that  $\hat{\gamma}_e = T \hat{\beta}_e^T$ . This connection allows to replace calculation of electric currents (1) and (3) at presence of external temperature field by calculation of energy currents (2) and (4) at presence of external electric field. Thus, for calculation of  $\hat{\alpha}_e$  we can use expressions

$$\vec{j} = \hat{\sigma} \vec{E}, \quad \vec{j}_e = \hat{\sigma}_e \vec{E}_e. \quad (6)$$

$$\vec{q} = T \hat{\beta}^T \vec{E}, \quad \vec{q}_e = T \hat{\beta}_e^T \vec{E}_e. \quad (7)$$

From (6) and (7), using the EMT, we can find values  $\hat{\sigma}_e$  and  $\hat{\beta}_e^T$  independently. Such calculation for  $\hat{\sigma}_e$  in general form was made in [4]. Let us consider the weak magnetic field, directed along the OZ-axis. Then for calculations of values  $\sigma_e^0$ ,  $\sigma_e^{yx}$ ,  $\Delta\sigma_e^{yy} = \Delta\sigma_e^{yy} = \sigma_e^{yy} - \sigma_e^0$  and  $\Delta\sigma_e^{zz} = \sigma_e^{zz} - \sigma_e^0$  using results of [4] up to the H<sup>2</sup> approximation it is easy to obtain following system of equations

$$\left\langle \frac{\sigma - \sigma_e^0}{\sigma + 2\sigma_e^0} \right\rangle_c = 0, \quad \left\langle \frac{\sigma_{yx} - \sigma_e^{yx}}{(\sigma + 2\sigma_e^0)^2} \right\rangle_c = 0 \quad (8)$$

$$\left\langle \frac{\Delta\sigma_{yy} - \Delta\sigma_e^{yy}}{(\sigma + 2\sigma_e^0)^2} \right\rangle_c + \Delta\Gamma_1 \left\langle \frac{(\sigma - \sigma_e^0)^2}{(\sigma + 2\sigma_e^0)^2} \right\rangle_c + \left\langle \frac{(\sigma_{yx} - \sigma_e^{yx})^2}{(\sigma + 2\sigma_e^0)^2} \right\rangle_c = 0 \quad (9)$$

$$\Delta\sigma_e^{zz} \left\langle \frac{1}{(\sigma + 2\sigma_e^0)^2} \right\rangle_c - \Delta\Gamma_2 \left\langle \frac{(\sigma - \sigma_e^0)^2}{(\sigma + 2\sigma_e^0)^2} \right\rangle_c = 0 \quad (10)$$

where

$$\Delta\Gamma_1 = \frac{1}{15} \cdot \frac{1}{(\sigma_e^0)^2} [4\Delta\sigma_e^{xx} + \Delta\sigma_e^{zz}], \quad \Delta\Gamma_2 = \frac{1}{15} \cdot \frac{1}{(\sigma_e^0)^2} [2\Delta\sigma_e^{xx} + 3\Delta\sigma_e^{zz}] \quad (11)$$

Similar system of equations can be obtained for calculations of values  $\beta_e^0$ ,  $\beta_e^{yx}$ ,  $\Delta\beta_e^{xx} = \Delta\beta_e^{yy} = \beta_e^{xx} - \beta_e^0$  and

$\Delta\beta_e^{zz} = \beta_e^{zz} - \beta_e^0$ . In these systems of equations local values of calculated coefficients have such form

$$\sigma = en\mu, \quad \sigma_{yx} = \sigma \frac{\langle \tau^2 \rangle}{\langle \tau \rangle^2} \cdot \frac{\mu H}{c}, \quad \Delta\sigma_{xx} = -\sigma \frac{\langle \tau^3 \rangle}{\langle \tau \rangle^3} \cdot \left( \frac{\mu H}{c} \right)^2 \quad (12)$$

$$\beta = \alpha\sigma, \quad \beta_{yx} = \alpha \frac{\langle \tau^2 \chi \rangle - \xi}{\langle \tau \chi \rangle - \xi} \sigma_{yx}, \quad \Delta\beta_{xx} = \alpha \frac{\langle \tau^3 \chi \rangle - \xi}{\langle \tau \chi \rangle - \xi} \sigma_{xx} \quad (13)$$

Here  $\mu = \frac{e}{m} \langle \tau \rangle$ ,  $\alpha = \frac{k}{e} \left( \frac{\langle \tau \chi \rangle}{\langle \tau \rangle} - \frac{\xi}{kT} \right)$ ,  $\chi = \frac{\varepsilon}{kT}$ ,  $\xi$  is a chemical potential. The angular brackets denote energy averaging. Note, that  $\Delta\sigma_{zz} = 0$ , but  $\Delta\sigma_e^{zz} \neq 0$  due to inhomogeneities. We believe that only an electron concentration  $n$  have inhomogeneities. From expressions for  $\sigma$  and  $\alpha$  we may see, that  $\alpha$  changes weakly if  $\sigma$  changes strongly. Thus, in present paper we neglect fluctuations of  $\alpha$ . We consider a two-component system, which consist of random high- and low-conducting regions.

We choose the distribution function on  $\sigma$  in the form

$$P(\sigma) = p\delta(\sigma - \sigma_0) + (1-p)\delta(\sigma - \sigma_1), \quad (14)$$

where  $p$  is the high-conducting part of the system volume, i.e. we suppose that  $\sigma_0 \gg \sigma_1$ .

For components of the effective thermopower tensor  $\hat{\alpha}_e$  we obtain from (5) expressions

$$\alpha_e^{yx} = \frac{\beta_e^0}{\sigma_e^0} \left\{ \frac{\beta_e^{yx}}{\beta_e^0} - \frac{\sigma_e^{yx}}{\sigma_e^0} \right\}, \quad \Delta\alpha_e^{zz} = \frac{\beta_e^0}{\sigma_e^0} \left\{ \frac{\Delta\beta_e^{zz}}{\beta_e^0} - \frac{\Delta\sigma_e^{zz}}{\sigma_e^0} \right\} \quad (15)$$

$$\Delta\alpha_e^{xx} = \frac{\beta_e^0}{\sigma_e^0} \left\{ \frac{\Delta\beta_e^{xx}}{\beta_e^0} - \frac{\Delta\sigma_e^{xx}}{\sigma_e^0} + \frac{\beta_e^{yx}}{\beta_e^0} \cdot \frac{\sigma_e^{yx}}{\sigma_e^0} - \left( \frac{\sigma_e^{yx}}{\sigma_e^0} \right)^2 \right\} \quad (16)$$

Carrying out in (8)-(10) configuration averaging with use of (14), calculating components of effective values  $\hat{\sigma}_e$  and  $\hat{\beta}_e$  and substituting them into (15) and (16), we find components of effective thermopower tensor  $\hat{\alpha}_e$ .

In fig.1 functions  $\alpha_e^{yx}/\alpha_0^{yx}$ ,  $\Delta\alpha_e^{xx}/\Delta\alpha_0$ ,  $\Delta\alpha_e^{zz}/\Delta\alpha_0$  and  $\Delta\alpha_e^{zz}/\Delta\alpha_e^{xx}$  versus  $p$  for value  $\sigma_1/\sigma_0 = 0.01$  in non-degenerate system are shown. Values  $\alpha_0^{yx}$  and  $\Delta\alpha_0$  corresponds to homogeneous system.

Forms of curves are very weakly dependent on the type of an electron scattering.

### Discussion

Let us discuss main results.

The antisymmetric component  $\alpha_e^{yx}$ , which determines the Nernst effect, has the minimum value in the vicinity of percolation threshold  $P_c = 1/3$  (Fig.1(1)).

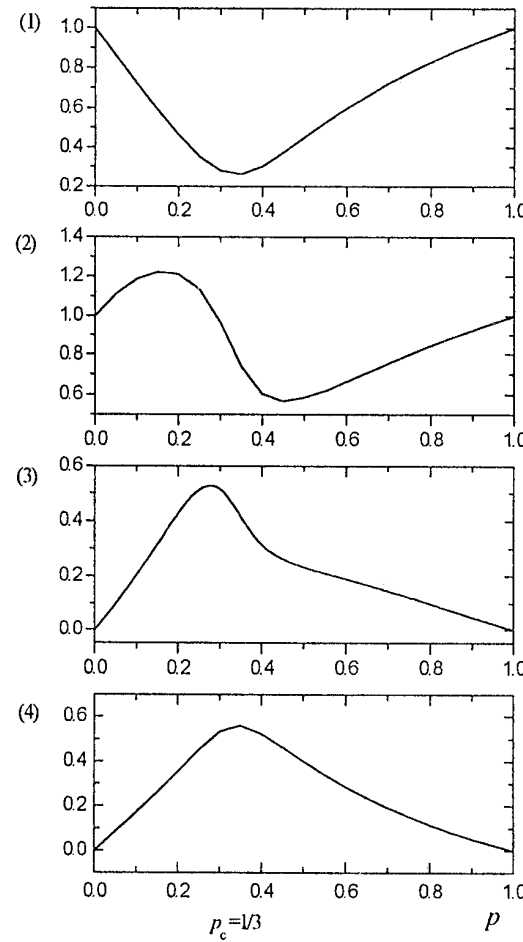


Fig.1. Dependencies of (1)  $\alpha_e^{yx}/\alpha_0^{yx}$ , (2)  $\Delta\alpha_e^{xx}/\Delta\alpha_0$ , (3)  $\Delta\alpha_e^{zz}/\Delta\alpha_0$  and (4)  $\Delta\alpha_e^{zz}/\Delta\alpha_e^{xx}$  on  $p$  for  $\sigma_1/\sigma_0 = 0.01$ .

The transverse changes of the thermopower tensor in magnetic field  $\Delta\alpha_e^{xx}$  increases if we include high-conducting components and decreases if we include low-conducting components. (Fig.1(2)). In homogeneous non-degenerate medium changes of the thermopower tensor in magnetic field does not depend on conductivity. We obtained, that due to inhomogeneity we have the longitudinal changes of the effective thermopower tensor in magnetic field  $\Delta\alpha_e^{zz}$ , which are absent in homogeneous system (Fig.1(3)). These changes have a maximum at the percolation threshold  $P_c$ . The ratio  $\Delta\alpha_e^{zz}/\Delta\alpha_e^{xx}$  have the maximum value at percolation threshold too (Fig.1(4)).

#### References

1. Webman I., Jortner I. and Cohen M., Phys. Rev., 1977, v.16, N9, p.2959-2964.
2. Xia T.K. and Zend X.C., J. Phys. Chem., 1987, V.20, N32, p.L907-L910.
3. Fishchuk I.I., Fiz. tverd. tela, 1990, v.32, N12, p.3540-3544.
4. Stroud D., Phys. Rev. B, 1975, v.12, N8, p. 3368-3373.

## ENHANCED THERMOELECTRIC EFFICIENCY OF SUBMICRON-THICK STRUCTURES

V. B. Yurchenko

*Institute of Radiophysics and Electronics, National Academy of Sciences of Ukraine,  
12 Proskura St., Kharkov, 310085, Ukraine*

Computer simulation of the nonlinear thermoelectric effect in submicron-thick structures has been carried out. Both a uniform layer and structures of different doping profiles have been studied. Current-voltage characteristics and thermoelectric efficiency of the structures evaluated.

### Introduction

Increasing the efficiency of thermoelectric devices is the main goal in thermoelectric activity [1]. The efficiency is primarily determined by thermoelectric material quality estimated by the figure of merit  $Z = \alpha^2\sigma/\kappa$  where  $\alpha$  is the Seebeck coefficient,  $\sigma$  is the electrical conductivity, and  $\kappa$  is the total heat conductivity including both phonon and electron specific heat conductivities. In view of this relation, the ordinary way for improving thermoelectric devices is to prepare materials with the increased value of  $Z$  by means of resolving the conflict between the growth (drop) of  $\sigma$  and simultaneous drop (growth) of  $\alpha^2/\kappa$  when electrical parameters of a material changed.

But, from the more general point of view, the efficiency of a whole device is something different from the efficiency of a mere material. The difference is especially important in the case of thin-film thermoelectric devices operating under the very large heat fluxes. In this case, both nonlinear and nonlocal heat and charge transfer processes appear in a semiconductor structure when the structure size is compared to the main characteristic lengths associated with the electron-phonon transport phenomena. Due to these processes, the effective non-equilibrium relation between the averaged values of  $\sigma$  and  $\alpha^2/\kappa$  for the whole structure could differ essentially from the equilibrium one for the given material. It is a circumstance that opens potentially new ways for thermoelectric devices improvement.

For to-day, the advances in modern technology made it possible to produce high-quality semiconductor structures of a submicron scale. It is a scale of the electron-phonon and the electron-electron energy relaxation lengths in semiconductors that is the case needed for the effects mentioned above to appear. It means that the finest features of the electron-phonon transport in thin-film structures could now be controlled and optimized in accordance with the most rigid requirements of a theory. On the other hand, it means also that the kinetic processes could be optimized on the very detailed level of analysis which opens new possibilities for thermoelectric devices optimization. Clearly, it is one of those technological achievements which according to C. B. Vining [2] could potentially crack the well-known  $ZT$  barrier in thermoelectricity.

The aim of the present work was, therefore, to study the effects of the nonlinear and nonlocal heat and

charge transfer processes across submicron-thick semiconductor structures in order to determine the main conditions for thermoelectric devices improvement.

### Thermo-e.m.f. arising due to non-Maxwell's carrier energy distribution

The common theoretical treatment of thermoelectric phenomena is conventionally carried out in terms of the temperature  $T$  and the electrochemical potential  $\tilde{\varphi}$  ascribed to the electron-phonon system of a semiconductor [1]. An approach of this kind is valid for the 'thick' structures, with the typical thickness  $d$  exceeding any characteristic length of the electron-phonon interaction [3]. In this case, both the electrons and the phonons are described by the quasi-equilibrium energy distributions with a unique temperature  $T = T(x)$ ,  $x$  being the coordinate along the temperature gradient.

In the case of the very thin structures, such an approach is, however, unacceptable. A specific form of the correct formulation depends on the relation between the structure thickness  $d$  and the main characteristic lengths of a semiconductor  $l_i$ ,  $l_{ee}$ , and  $l_e$  which are the average lengths of the electron momentum relaxation, the electron-electron collisions, and the electron energy relaxation due to electron-phonon scattering, respectively. While any 'thick' structure corresponds to the relation

$$l_i, l_{ee}, l_e \ll d, \quad (1)$$

the cases of a 'thin' sample could be of different kind. Since the condition

$$l_i \ll l_{ee} \ll l_e \quad (2)$$

is very common for semiconductors [3], one has primary to consider the cases

$$l_i, l_{ee} \ll d \ll l_e, \quad (3)$$

and

$$l_i \ll d \ll l_{ee}, l_e. \quad (4)$$

Under the conditions (3), the electrons and phonons are described by the quasi-equilibrium energy distributions as well, but with the different temperatures  $T_e(x)$  and  $T(x)$ , respectively, which are determined by the different energy balance equations for the electrons and the phonons separately. It means that the electrons

are independent to some extent of the phonons, and the resulting thermoelectric effects would differ from the ordinary ones taking place in 'thick' structures.

The conditions (4) provide even more possibilities for the electrons to become non-equilibrium so that their energy distribution alters when the heat flux appeared in the structure. Indeed, because of the relation  $d \ll l_{ee}, l_\epsilon$ , the electrons have no chance to dissipate their energy inside of the structure. Therefore, the energy distribution of the electrons (i.e. the symmetrical part  $f_S = f_S(\epsilon, x)$  of the total distribution function  $f = f(\vec{p}, x)$  where  $\epsilon$  and  $\vec{p}$  are the electron energy and momentum, respectively) differs drastically from the Maxwell-like (or Fermi-like) distribution which would take place under the conditions (1) or (3).

Under the conditions (4), the very concepts of both the electron temperature and the electrochemical potential are unacceptable for analyzing kinetic processes in semiconductor structures [4]. Instead, the Boltzmann's kinetic equation must be solved to calculate transport phenomena in the structures of this kind. It is the case that happens usually in the structures of submicron thickness [3] which are of the main interest in this paper.

Clearly, non-conventional thermoelectric effects would appear in semiconductor structures under the conditions (4). Yu. G. Gurevich and V. B. Yurchenko have shown previously [5] that the distortion of the distribution function  $f_S(\epsilon, x)$  as compared to the Maxwell's form  $f_T(\epsilon, x)$  with the local temperature  $T(x) = 2/3 < \epsilon >$ ,

$$\delta f(\epsilon, x) = f_S(\epsilon, x) - f_T(\epsilon, x), \quad (5)$$

gives rise to a special e.m.f. because of disbalance of the partial currents of the charge carriers of different energies. The e.m.f. of this kind could even appear in a uniform unipolar sample under the conditions of  $< \epsilon > = const$  and  $n = const$ ,  $< \epsilon >$  and  $n$  being the mean carrier energy and the carrier density, respectively.

In the case of an arbitrary carrier excitation and inhomogeneous samples, the effect looks like an additional thermo-e.m.f. generation as compared to the common e.m.f. arising due to the gradients of  $T = T(x)$  and  $n = n(x)$  while  $f_S(\epsilon, x) = f_T(\epsilon, x)$ . An example of such an effect has been studied by the author of this paper [6] who calculated the voltage arising in submicron-thick structures due to the charge carrier heating under the microwave illumination.

Under the heat flux across a very thin structure satisfying the conditions (4), the distortion of the function  $f_S$  appears as a result of the partial fluxes of the 'hot' and the 'cold' electrons flowing into the structure from the opposite surfaces  $x = 0$  and  $x = d$  kept at the different temperatures  $T_1 = T(0)$  and  $T_2 = T(d)$  ( $0 < x < d$ ). Since there are no energy dissipation processes within the structure except the full relaxation at the surfaces where different Maxwell's functions  $f_1 = f_S(\epsilon, 0)$  and  $f_2 = f_S(\epsilon, d)$  being formed, the resulting function  $f_S(\epsilon, x)$  inside of the structure becomes a

kind of some 'mixture' of  $f_1$  and  $f_2$ , but not a single Maxwell's function at the mean temperature  $T_e(x)$ .

To get an exact solution of the problem, one should also take into account an additional increase or decrease of the electron energy because of thermoelectric and external electric fields, or any built-in-field in the inhomogeneous structures. Thus, the problem as a whole is nonlinear and, in fact, rather complicated.

The analytical treatment of thermoelectric effects of this kind has been undertaken by Yu. G. Gurevich, G. N. Logvinov, and O. Yu. Titov [4] for the case of a uniform layer under the assumption of the small temperature drop  $\Delta T = T_2 - T_1$ . Unfortunately, all the effects of the non-Maxwell's carrier distribution disappear in a uniform layer under the linear approximation used in [4].

In this paper, other cases of the thermo-e.m.f. generation in submicron-thick structures are investigated. Both the uniform layers and the gradually doped structures of different doping profiles are considered. The nonlinear processes of the thermo-e.m.f. generation due to the large heat fluxes across the structure have been studied.

### Models of submicron-thick structures and basic equations

Let us consider a uniform layer ('a') and the two kinds ('b' and 'c') of the gradually doped structures with the following carrier density profiles:

$$n(x) = A_1 + B_1 \exp(x/L) \quad (6)$$

and

$$n(x) = A_2 + B_2 \cos(\pi x/d), \quad (7)$$

respectively. The ratio  $n(d)/n(0) = 10$  and the value  $n(d) = 0.1N_c$  are assumed where  $N_c$  is the effective density of states in the conductive band at the mean temperature  $T_0 = (T_1 + T_2)/2$ . The conditions (4) are supposed, with the Debye radius being small as compared to the structure thickness  $d$ .

Under the conditions described, the symmetrical part of the carrier distribution function is determined by the steady-state Boltzmann's equation which does not account for the electron-electron and the electron-phonon energy relaxation processes in the bulk of the structure. The energy relaxation occurs at the surfaces  $x = 0$  and  $x = d$  where the metal leads are supposed and the equilibrium carrier distribution functions at the temperatures  $T_1$  and  $T_2$  assumed as the boundary conditions. In the case considered, the original Boltzmann's equation could be reduced to the nonlinear partial differential equation for the symmetrical part of the carrier distribution function  $f_S(\epsilon, x)$  only. Following the well-known approach [4], an explicit form of the nonlinear equation in  $f_S$  under the varied phonon temperature  $T(x)$  has been obtained:

$$\frac{\partial^2 f_S}{\partial x^2} + \epsilon^2 E^2 \frac{\partial^2 f_S}{\partial \epsilon^2} + 2eE \frac{\partial^2 f_S}{\partial x \partial \epsilon} +$$

$$+ \left( (q + 3/2) \frac{eE}{\epsilon} + \frac{s}{T} \frac{dT}{dx} \right) \left( eE \frac{\partial f_S}{\partial \epsilon} + \frac{\partial f_S}{\partial x} \right) + \\ + e \frac{dE}{dx} \frac{\partial f_S}{\partial \epsilon} = 0 \quad (8)$$

where  $e$  is the electron charge and  $E = E(x)$  is the total electric field in the structure. The electron momentum relaxation time  $\tau$  was assumed to depend on both the phonon temperature  $T$  and the electron energy  $\epsilon$  as follows:

$$\tau(\epsilon, T) = \tau_0 (T/T_0)^S (\epsilon/T_0)^q . \quad (9)$$

The total field  $E(x)$  includes the thermoelectric field arising due to thermoelectric effect in the structure, the external field if the total current  $J$  is non-zero, and the built-in-field existing in the gradually doped structures. The field  $E(x)$  depends on the function  $f_S(\epsilon, x)$  and is found self-consistently according to the relation

$$E(x) = (j + e \nabla_x (D n)) / \sigma \quad (10)$$

where  $j$  is the current density across the structure,  $D$  and  $\sigma$  are the non-equilibrium diffusion coefficient and the electrical conductivity, respectively, which differ from the equilibrium ones because of the non-Maxwell's form of the carrier distribution function  $f_S$ :

$$D = C_1 \int_0^\infty f_S \epsilon^{q+3/2} d\epsilon , \quad (11)$$

$$\sigma = C_2 \int_0^\infty f_S \epsilon^{q+1/2} d\epsilon , \quad (12)$$

$C_1$  and  $C_2$  being the normalizing coefficients.

The deformation acoustic (DA) carrier scattering mechanism is supposed ( $q = -1/2$ ,  $s = -1$ ) which corresponds to the following boundary condition for the function  $f_S(\epsilon, x)$  at the small energies:

$$\frac{\partial f_S(\epsilon, x)}{\partial \epsilon} = 0 , \quad \epsilon \rightarrow 0 , \quad (13)$$

with the common condition  $f_S(\epsilon, x) = 0$  at the energies  $\epsilon \rightarrow \infty$ .

When the function  $f_S(\epsilon, x)$  obtained, the problem of the correct procedure for the e.m.f. calculation appears. As it was mentioned above, in the case of the non-Maxwell's function  $f_S$ , the concepts of the electron temperature and the electrochemical potential within a non-equilibrium medium are invalid. So, the definition of the e.m.f. in terms of  $T_e$  and  $\tilde{\varphi}$  is improper, and the demand arises for a new method of the thermo-e.m.f. calculation taking into account the electromotive force caused by the carrier distribution function distortion. Analysis based on the ideas [7] has, however, shown that, in the most general case, the e.m.f. could be calculated from the ordinary expression for the total voltage  $V$  across the structure if the latter written in a special form taking

into account the total electric field  $E$  within the structure and the temperatures  $T_1$  and  $T_2$  at the surfaces only:

$$V = - \int_0^d E dx + \frac{T_2}{e} \ln \frac{n(d)}{N_c(T_2)} - \frac{T_1}{e} \ln \frac{n(0)}{N_c(T_1)} \quad (14)$$

Under the open-circuit conditions,  $V$  is the value of the thermo-e.m.f. generated in the structure.

#### Thermo-voltage and the efficiency of submicron-thick structures

The equation (8) was solved numerically by means of a specially developed method based on the Stone's strongly implicit procedure [8] which was completed with the self-consistent calculation of the electric field  $E(x)$ . Solutions have been used to calculate the voltage  $V$  for different structures [9]. The results were compared with the values of the voltage  $V_T$  calculated for the same structures under the conditions (1) when the Maxwell's function  $f_T(\epsilon, x)$  with the temperature  $T(x) = T_1 + \Delta T x/d$  takes place. The relative voltages  $eV/T_0$  and  $eV_T/T_0$  obtained for the structures 'a', 'b' and 'c' at the temperature drop  $|\Delta T| =$

$= 0.4T_0$  are given in the Table 1. The indexes 1 and 2 denote the cases of  $T_1 < T_2$  and  $T_1 > T_2$ , respectively.

Table 1. Open-circuit thermo-voltage for different structures

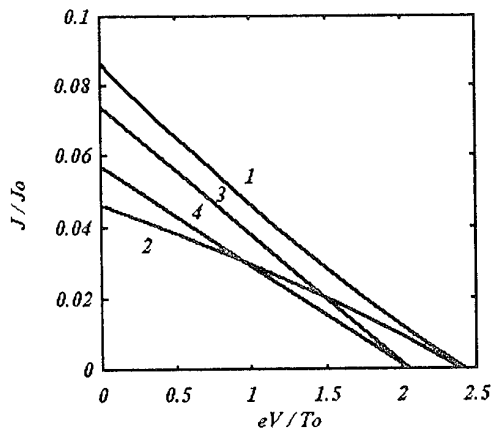
Structure	$eV/T_0$	$eV_T/T_0$
'a'	1.72	1.72
'b'_1	2.44	2.18
'b'_2	2.41	2.18
'c'_1	2.51	2.05
'c'_2	2.41	2.05

The results have shown that non-Maxwell's carrier energy distribution formation increases thermo-e.m.f. generated in submicron-thick structures. In a uniform layer, the increase of the thermo-e.m.f. is, however, negligible (it is less than a percent of a common e.m.f.). On the contrary, the increase of the thermo-e.m.f. in the gradually doped structures is essential being from ten to twenty percents under the conditions considered. The thermo-e.m.f. appears to be higher in the case of the structures with a built-in-field localized inside of the sample (the case 'c'). When the built-in-field is almost uniform (the case 'b'), the observed effect is not so significant. Change of the sign of the electron density gradient in the gradually doped structures at a given temperature drop  $\Delta T$  does not result in change of the sign of additional thermo-e.m.f. and promotes only a minor variation in its value. Nevertheless, the total thermo-e.m.f. is a little greater in the case of both the phonon temperature and the electron density gradients being parallel.

In order to estimate variations in the efficiency of the structures, the current-voltage characteristics have

been calculated for the structure 'c' at the different sign of the temperature drop  $\Delta T$  under both the conditions (1) and (4) (Fig.1).

Figure 1: Current-voltage characteristics of the structure 'c' under the conditions (4) ( 1-  $\Delta T > 0$  ; 2-  $\Delta T < 0$  ) and (1) ( 3 -  $\Delta T > 0$  ; 4 -  $\Delta T < 0$  )



The results have shown that the sign of  $\Delta T$  has a profound effect on the thermoelectric current generated in the structure. At any voltage applied, the current is greater under the conditions (4) as compared to (1) when both the temperature and the carrier density drops,  $\Delta T$  and  $\Delta n$  respectively, are of the same sign (curve 1). On the contrary, the current tends to decrease in the case of the opposite signs of  $\Delta T$  and  $\Delta n$ , so that the short-circuit current under the conditions (4) is even less than the similar current under (1) (curves 2 and 4, respectively).

The estimate shows that, due to non-equilibrium carrier energy distribution formation, the total thermoelectric efficiency of the gradually doped submicron-thick structure 'c' is greater by 25% of its initial value when the conditions (4) instead of (1) satisfied and both  $\Delta T$  and  $\Delta n$  are of the same sign.

### Conclusions

The computer simulation of the nonlinear thermoelectric effects arising in submicron-thick semiconductor structures under the large heat fluxes has shown a possibility to increase the efficiency of thermoelectric devices. It is a result of the non-equilibrium carrier energy distribution forming because of diminishing the electron-phonon and the electron-electron energy relaxation in the structures. The effect grows in the gradually doped structures with the built-in-field being localized in the middle of the structure.

The calculations revealed an increase of the open-circuit voltage for all the structures considered, as compared to the case of the Maxwell's carrier distribution function. The gain of the efficiency depends, however,

on the sign of the temperature drop across the gradually doped structure. The efficiency increases in the case of both the lattice temperature and the carrier density gradients being of the same sign, and decreases in the opposite case.

The results obtained could be also applied to the classical superlattices. Various homo- and heterostructures of a saw-like doping profile, with the carrier energy relaxation decreased in the lightly doped regions and increased in the heavily doped ones, are promising for the given effect to appear. The effect is supposed to be increased by means of the doping profile optimization, special heterostructures implementation, or another scattering mechanism utilization, that is the subject for the future research.

### References

- [1] L.I.Anatychuk, Thermoelectric cells and thermoelectric devices, Kiev, 1979, 766 p. (in Russian).
- [2] C.B.Vining, Thermoelectric materials of the future, *12th Int. Conf. on Thermoelectrics. Program and Abstracts*, Yokohama, 1993, p.35.
- [3] F.G.Bass, V.S.Bochkov and Y.G.Gurevich, Electrons and phonons in bounded semiconductors, Moscow, 1984, 288 p. (in Russian).
- [4] Yu.G.Gurevich, G.N.Logvinov and O.Yu.Titov, Theory of thermoelectric effects under violation of temperature approximation, *Sov. Phys. Semicond.*, 1994, v.28, No.1, pp.113-119 (in Russian).
- [5] Yu.G.Gurevich and V.B.Yurchenko, Generation of photovoltage in homogeneous unipolar conductive media, *Solid State Commun.*, 1989, v.72, No.10, pp. 1057-1058.
- [6] V.B.Yurchenko, New hot-carrier effects in submicron structures for infrared and millimeter wave receivers, *18th Int. Conf. on Infrared and Millimeter Waves*, James R. Birch, Terence J. Parker, Editors, Proc. SPIE, 1993, v.2104, pp.46-47.
- [7] Yu.G.Gurevich and V.B.Yurchenko, Problem of EMF formation in semiconductors and its supply to external circuit, *Sov. Phys. Semicond.*, 1991, v.25, No.12, pp.1268-1272.
- [8] R. Hockney and J. Eastwood, Computer simulation using particles, Moscow, 1987, 638 p. (in Russian).
- [9] A.S.Anopchenko and V.B.Yurchenko, Numerical simulation of nonlinear thermo-e.m.f. in submicron-thick semiconductor structures, *12th Int. Conf. on Thermoelectrics. Program and Abstracts*. Yokohama, 1993, p.24.

## THE THERMOELECTRICAL AND ELECTRICAL PROPERTIES OF THE SYSTEM Au/p-CdTe/Au

Svetla Vackova<sup>1</sup>, Juraj Racko<sup>2</sup>, Daniel Donoval<sup>2</sup>, Yuri G. Gurevich<sup>3</sup>

<sup>1</sup> Department of Semiconductors, Charles University, Ke Karlovu 5, 121 16 Prague 2, Czech  
Republik

<sup>2</sup> Microelectronics Department, Slovak Technical University, Bratislava, Slovakia

<sup>3</sup> Depto. de Fisica, CIVESTAV I. P. N., Mexico

The thermoelectrical and electrical properties of the system Au/p-CdTe/Au were measured. Non equilibrium holes are redistributed in the sample in agreement with Gurevich et al. theory [1]. The aim of our work is to verify it experimentally in our system Au/p-CdTe/Au. For this reason the extended thermoemission and thermoemission-diffusion theories of charge carrier transport through a Schottky diode structure were applied on measured I-U characteristics. The influence of Richardson constant was also considered for the carriers passing from the metal into the semiconductor.

### Introduction

Thirty years ago Plavita [2] has published interesting theoretical work (in accordance with the work L. Georgescu [3]) about the role of the optical phonons (optical phonon drag effect) in Seebeck effect and in related transport phenomena. While the acoustical phonon drag contribution can enlarge significantly the value of thermopower, on the contrary the optical phonon drag effect can reduce it. This was shown for the first time in 1972 [4] (measured on CdTe n and p types and even in CdSe). Later was this observation also verified by other authors [5].

### Experiment

Single-crystals of p-CdTe wafers were prepared in the laboratory of prof. O. Panchuk (State Chernivtsi University, Ukraine). Bulk resistivity measured at room temperature by four point method was about 100 ohm.cm, Hall mobility 80 cm<sup>2</sup>/V.s (from Hall measurements).

The contacts were prepared by electroless deposition of gold on fresh surface (cut immediately before the deposition) in air. The gold belts (1x4) mm<sup>2</sup> were deposited on fresh splitted orientated surface of p-CdTe. The sample was pressed between two copper blocks with electrical heaters inside.

The contacts indicated rectifying properties. The I-U characteristics of the system Au/p-CdTe/Au were measured. Simple three point method was used for measurements of current - voltage (I-U) characteristics - which presents an easy control of contact properties. The temperature difference applied on the sample significantly shifts I-U characteristics.

### The description of the observed effect

In our last work [6] we described the following experiment: Keeping the temperature of one contact Au/p-CdTe constant and increasing the temperature of second one, one can control the current flowing through the contact kept at constant temperature. The temperature gradient  $\Delta T$  on the system Au/p-CdTe/Au significantly controls the electrical current through the sample, it can enlarge or diminish it in the dependence of the gradient direction.

Nonohmic contacts registered the changes near the Au/p-CdTe interfaces. The I-U characteristics were measured and the significant shift with temperature gradient is observed. The greater is the thermovoltage  $\alpha \Delta T$ , the greater is the current change

$$\log I_1 - \log I_0 \sim \alpha \Delta T \quad \text{for } U = \text{const.},$$

where  $I_1$  is the current at a given temperature difference  $\Delta T$  and  $I_0$  stays for  $\Delta T=0$ .

In this contribution our experiment was changed with respect to the suggestions in the last theoretical paper [1]: the temperature on constant value  $T^* = (T_1 + T_2)/2$ ,  $\Delta T = T_2 - T_1$  and the temperature gradient along the sample, see Fig. 3. To eliminate the influence and changes on two Schottky barriers, we analysed the reverse I-U characteristics of the system Au/p-CdTe/Au.

### The simulations of reverse I-U characteristics ( $\Delta T = 0$ )

The thermionic emission current density of free charge carriers through a Schottky barrier can be described by the formula derived by Bethe [7]

$$J_{te} = A_s T^2 \exp\left(-\frac{\Phi_b}{kT}\right) \left[ \exp\left(\frac{qV_a + \Delta\phi_b}{kT}\right) - 1 \right]. \quad (1)$$

Here  $A_s$  is the Richardson constant for electrons in semiconductor,  $\Phi_b$  is the Schottky barrier height,  $\Delta\phi_b$  is its change due to the external applied voltage  $V_a$ . Other symbols have their usual meanings.

It has been found that for some structures Eqn. (1) does not allow to reach reasonable agreement of simulated reverse I-U characteristics with experimentally obtained data. These discrepancies become particularly significant in the case of Schottky diodes prepared on p-CdTe substrates. We propose to employ the extended thermoionic emission theory [8] in which the transport through the Schottky barrier is expressed as

$$J_{te} = T^2 \exp\left(-\frac{\Phi_b}{kT}\right) \left\{ A_s \left[ \exp\left(\frac{qV_a + \Delta\phi_b}{kT}\right) - 1 \right] - A_M \left[ \exp\left(\frac{\Delta\phi_b}{kT}\right) - 1 \right] \right\}. \quad (2)$$

By comparing Eqns. (1) and (2) one can see that the extended thermoionic emission theory considers the Richardson constant not only for free charge carriers in the semiconductor but also in the metal.

In our simulations of reverse I-U characteristic of Au/p-CdTe/Au system the change of the Schottky barrier height was expressed as

$$\Delta\phi_b = \sqrt{\frac{q^3}{4\pi\epsilon}} (\sqrt{E_{max0}} - \sqrt{E_{max}}) + q\alpha(E_{max0} \cdot \kappa_{max}), \quad (3)$$

where

$$E_{max} = \sqrt{\frac{2qN_D^+}{\epsilon}(V_k - V_a)} \quad (4)$$

is the maximum strength of internal electric field on the metal-semiconductor interface,

$$E_{max0} = \sqrt{\frac{2qN_D^+}{\epsilon}V_k} \quad (5)$$

is the maximum strength of internal electric field at the interface under thermodynamic equilibrium ( $V_a = 0$ ) and  $\alpha$  is a parameter characterizing the the interface quality. Its magnitude ranges from 0,5 to 2,0 nm.

The modified Richardson constants for electrons and holes in the metal and in the semiconductor are defined by the expression

$$A_{S,M} = \frac{4\pi q m_0 k^2}{h^3} \frac{m_{S,M}}{m_0}. \quad (6)$$

The attempt is done to calculate note masses in CdTe semiconductor and in the metal Au. (See tab. 1.)

$\phi_b$ [eV]	T [K]	$\alpha$ [nm]	$m_{\text{metal}}$ [ $m_0$ ]	$m_{\text{sem}}$ [ $m_0$ ]	$N_A$ [ $m^{-3}$ ]
0.56	295	1.0	25.0	0.60	$1 \times 10^{21}$

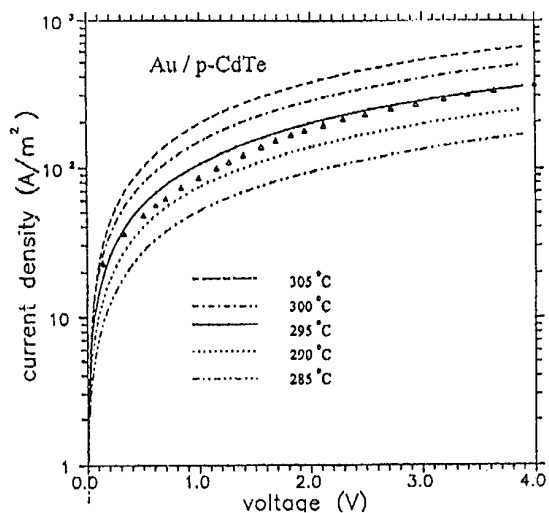


Fig. 2. The influence of temperature change on I-U characteristic of system Au/p-CdTe/Au (C 4) ( $\Delta T = 0$ )

#### From new ideas of Gurevich (et al.) theory

Under the temperature gradient two processes can be mathematically described in the sample in agreement with Anselm [9], which in fact act mutually against them and give the rise of internal electric field. In this case the following equation

$F_n^\circ = -E_g - F_p^\circ$ , ( $F_n^\circ, F_p^\circ$  represent the electrochemical potential of electrons and holes,  $E_g$  is the energy gap) is valid.

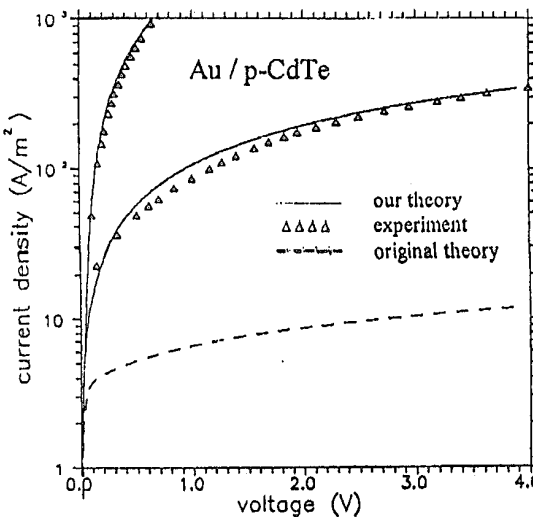


Fig. 1. Fitted I-U characteristics of system Au/p-CdTe/Au (C 4) after extended thermoionic emission theory. The characteristic for forward direction was obtained from three point method ( $\Delta T = 0$ )

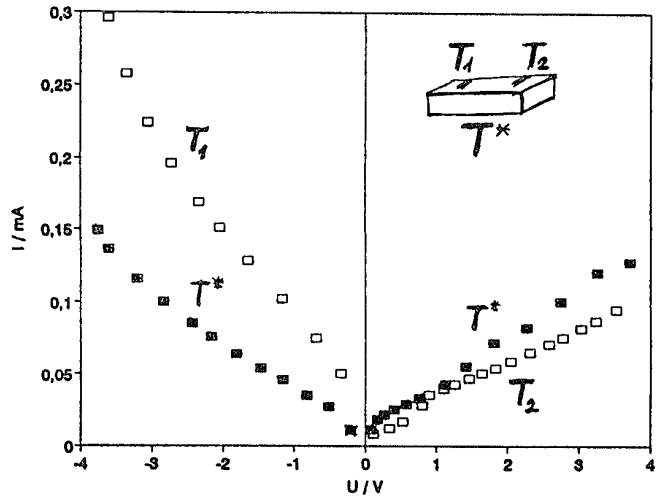


Fig. 3. The influence of temperature gradient on I-U characteristic system Au/p-CdTe/Au (C 10/5).  $T^* = 296$  K (■),  $T_1 = 307.8$  K,  $T_2 = 285$  K,  $\Delta T = 22.8$  K (□)

When phonon drag effect is included, this equation begins to be limited; carriers redistribution appears and still more we obtain two quasi Fermi levels. The two types of carriers move through the sample independently. In this case there is no difference, if we take in our consideration the electrons and holes or two sorts of holes (as in p-CdTe). We calculated then also carrier redistribution in the sample. For our sample with hole concentration  $p = 7,8 \cdot 10^{15} \text{ cm}^{-3}$  by  $T^* = 300 \text{ K}$  we calculated two quasi Fermi levels (in eV) in three steps by [1]

	$x = -a$	$x = +a$
$T^* = 300 \text{ K}$		
$\Delta T = 0 \text{ K}$	-0,20049	-0,20049
$\Delta T = 10 \text{ K}$		
without phonon drag	-0,20799	-0,19299
$\Delta T = 10 \text{ K}$		
after diffusion	-0,20799	-0,19299
without phonon drag	$-1,8 \cdot 10^{-8}$	$+1,8 \cdot 10^{-8}$
phonon drag, $\Delta T = 10 \text{ K}$	-0,20799	-0,19299
for light holes	$+2,18 \cdot 10^{-4}$	$+2,18 \cdot 10^{-4}$
for heavy holes	$+4,78 \cdot 10^{-3}$	$4,78 \cdot 10^{-3}$

The temperature  $T_1$  for  $x = -a$ ,  $T_2$  for  $x = +a$

### Conclusions

1. Modified Bethe theory - the extended thermoionic emission theory [8] comparatively well describes the experimental curves (Fig. 1). It records the influence of temperature change of the sample (Fig. 2).

2. Further measurements are required for the quantitative evidence of hole redistribution in the system Au/p-CdTe/Au under the influence of phonon drag. Nevertheless the experimental change of I-U characteristic for  $\Delta T \neq 0$  is greater than the changes calculated above.

### References

- [1] Yu. G. Gurevich, O. Yu. Titov, G. N. Longvinov, O. I. Lyubimov, Phys. Rev. B, vol.51, No. 11, 1995, 6999 - 7004
- [2] C. N. Plăviču, phys. stat. sol. 12, 1965, 265
- [3] L. Georgescu, Physica 35, 1967, 107
- [4] S. Kubálková (Vacková), phys. stat. sol. (b), 50, 1972, 111 - 123
- [5] J. Rosenzweig, U. Birkholz, phys.stat.sol. 71, 1982, K 41-45
- [6] S. Vacková, Seebeck effect in p-CdTe. The control of electrical properties of Au/p-CdTe/Au system by temperature gradient, Proceedings of 13th International Conference of Thermoelectrics, Kansas City, American Institute of Physics (AIP), Kansas City, Missouri, USA, Aug.30 - Sept.1, 1994
- [7] H. A. Bethe, MIT Rad. Lab. Rep., 1942, 43-12
- [8] J. Racko et al., EDS'95 Brno, 1992
- [9] A. I. Anselm, Introduction to Semiconductor Theory, MIR, Moscow/Prentice-Hall, Englewood Cliffs, NY, 1981

## THERMOELECTROMOTIVE FORCE OF HOT CARRIERS IN METAL-p-Ge AND -GaAs CONTACTS

*S. Ašmontas, A. Sužiedėlis*

*Semiconductor Physics Institute, A. Goštauto 11, 2600 Vilnius, Lithuania*

### 2. Samples and technique

#### 1. Introduction

Semiconductor devices, which performance is based on the thermoelectromotive force (thermoemf) of hot carriers, are widely used for detection, mixing and power measurements of microwave (MW) signals [1]. The carriers are heated by the nonuniform MW field, and the lattice temperature remains relatively unchanged. Such devices are usually constructed as small area diodes [2] with so-called l-h junction, i.e. junction of two parts of semiconductor with the same type of conductivity, but with a quite different doping level [3]. These devices are attractive both due their high upper frequency limit of operation, which is set by the momentum relaxation time of hot carriers [4], and due their high burn-out power. A great advantage is also high electrical stability over long periods of use [5].

While the first MW power detectors were made from Ge, appreciable advance in investigation of thermoemf of hot carriers was achieved in the case of silicon [6] because the technology of small area l-h junction formation is well developed for this material. However, due the low electrical mobility of electrons and holes in Si, resulting in low value of voltage-power sensitivity (the ratio of detected signal and applied MW power) of those diodes, it is of interest to investigate the diodes made on the base of n-GaAs. Two more properties of gallium arsenide is important for its application as a MW power measurement element. Namely, the nonmonotonical field dependence of energy relaxation time [7] and diffusion coefficient [8] of electrons in n-GaAs at room temperature. These dependences let us hope to have the more wide region of MW power, where the dependence of detected signal on applied power is linear. Therefore, the first aim of this work was to investigate the properties of GaAs diodes with n-n<sup>+</sup> junction in wide range of dc and MW applied power.

Point contacts of Au to p-type Ge are widely used for measurement and detection of MW power [9]. Usually such contacts are produced by evaporation of Au on a Ge surface and following formation of a contact by dc electric current. The latter process is far from perfection from the technological point of view - moreover, Au is amphoteric impurity in Ge. It also complicates the studies of such contacts. That is why the second aim of this work was to investigate the diodes of p-Ge with narrow-long shape ohmic contacts, which have been made using as a metals to contacts not only Au but also In and Al, which are well-known shallow acceptors in germanium.

The point contact GaAs diode were prepared from n<sup>+</sup>-n-n<sup>+</sup> epitaxial structures. The thickness of n epitaxy layer and density of impurities there were 29 μm and 1.1·10<sup>15</sup> cm<sup>-3</sup>, respectively. The thickness of the contact layer was 1 μm. The impurity density in the contact layer and in the substrate was 2·10<sup>18</sup> cm<sup>-3</sup>. Electron mobility in n-layer at room temperature was  $\mu = 7000$  cm<sup>2</sup>/V·s. The ohmic contacts of the diode were made by thermal evaporation of separate Ge/Ni/Au layers through the windows created in photoresist by photolithography method and by following annealing in inert gas atmosphere. The small area n-n<sup>+</sup> junctions of point contact diode were formed by chemical etching of GaAs.

The p-Ge diodes were prepared from semiconductor wafers with surface orientation (100). Specific resistances of monocrystals were 15 and 30 Ω·cm. Both surfaces of the wafer were polished mechanically and one of them chemically. Indium and aluminum were evaporated thermally in vacuum onto semiconductor surfaces after their refreshing in hydrogen peroxide solution. Photolithography technique was used to make small area metal contacts. The Au contacts to p-Ge were made by the electrochemical plating of gold onto semiconductor surface through the windows created in photoresist. The metal contacts were annealed in hydrogen atmosphere at different temperatures (300÷600°C) during 10 minutes.

In order to avoid the crystal-lattice heating, the short pulses of electric current and microwave signal with duration of a few microseconds and the repetition rate (40÷50) Hz were used. The circuit of balanced bridge was used to investigate the diode in dc electric field. As a source of MW electric field, the clystron generating high-frequency signals in frequency range f=(26÷37.5) GHz was used. The diodes were placed in rectangular waveguide.

### 3. Experimental results and discussion

On the basis of the set of equations including energy conservation, density of electric current, current continuity and Poisson, we obtained the analytical formula for the difference of point contact resistance when contact was based in reverse and forward direction

$$\Delta R = R_2 - R_1 = \frac{8U\rho\mu_0[\tau_z(1+s) + \tau_M]}{3\pi^2 r_k^3}, \quad (1)$$

where  $U$  is applied voltage;  $\rho$  and  $\mu_0$  denote specific resistivity and electron mobility, respectively;  $s$  stands for the index of power dependence of electron momentum relaxation time;  $\tau_z$  and  $\tau_M$  are electron energy and Maxwell relaxation time, respectively;  $r_k$  is

point contact radius.

The expression (1) is valid for slight electron heating (warm electron region approximation), when  $\mathcal{E}/\mathcal{E}_0 \ll \mathcal{E}_0$ , where  $\mathcal{E}_0$  is equilibrium value of electron energy. In the case of sufficiently low frequencies when  $(\omega r_s)^2 \ll 1$  ( $\omega$  is angular frequency of MW field) and conductivity current exceeds displacement one, the voltage sensitivity of the detector with n-n<sup>+</sup> junction is related to the current-voltage (I-V) characteristics asymmetry [10]

$$S = U_d/P = \Delta R/2U, \quad (2)$$

where  $U_d$  is the detected signal,  $P$  is the MW power which the detector have absorbed. Thus, from I-V characteristics measurement in dc regime the expected value of potential different arising in I-h junction under MW signal effect can be established.

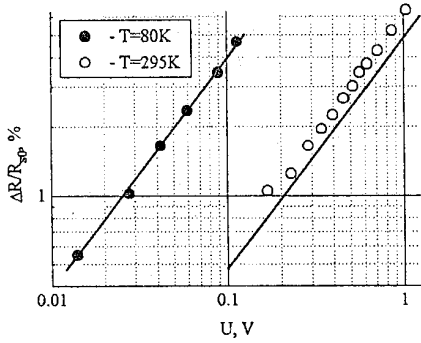


Fig. 1. The dependence of the relative resistance difference on the applied voltage of n-GaAs point contact diode

The dc measurements of I-V characteristics of the point contact n-GaAs diodes at room (T=295 K) and liquid nitrogen (T=80 K) temperatures have shown that the quality of investigated n-n<sup>+</sup> structures was good enough to verify the theoretical results presented above. Fig. 1 depicts the experimental dependences of the relative resistances difference on applied voltage of point contact diode at room (light dots) and liquid nitrogen (dark dots) temperatures. In the figure the theoretical dependences obtained from (1) are presented also. The values of electron energy relaxation time at T=295 K and T=80 K were taken from [11]. At liquid nitrogen temperature the relative resistances difference of the diode is greater than that at the room temperature for the same value of applied voltage. It is connected with the higher value of electron mobility and energy relaxation time in n-GaAs at T=80 K in comparison with those at room temperature.

Using the MW electric field, the dependence of the detected signal on the applied MW power was measured at room and liquid nitrogen temperatures. When the MW power is small (the electrons are slightly heated by the electric field) the value of the detected signal is directly proportional to the microwave power. Therefore, those semiconductor structures may be used as the measurement element of MW power. The volt-power characteristic at room temperature is linear in wider range of MW power than that at liquid nitrogen temperature. This is associated with the fact that at T=295 K  $r_s$  depends slightly on the instantaneous value of

the MW electric field strength  $E_m$ , whereas at liquid nitrogen

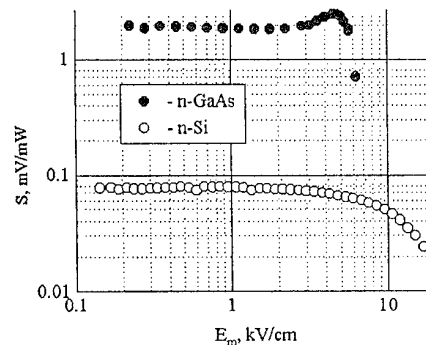


Fig. 2. The field dependence of sensitivity of n-GaAs and n-Si point contact diodes

temperature the electron energy relaxation time decreases rapidly with  $E_m$  increase.

The measurement of the detected signal of diode at room temperature in stronger MW electric fields have shown that the volt-power characteristic becomes superlinear in contrast to the diodes fabricated on the base of Si. The dependences of the voltage sensitivity  $S$  on  $E_m$  of point contact diodes based on n-GaAs and n-Si are shown in Fig. 2. The voltage sensitivity of GaAs diodes increases with the absorbed MW power, reaches a maximum and then starts to decrease. The field dependence of voltage sensitivity follows that one of diffusion coefficient in n-GaAs at room temperature determined from noise temperature measurements [8]. The slight trend to decrease of  $S$  before its increase is noteworthy. Such a peculiarity also observed in [12] for the spectral density of the current fluctuation, which was attributed to the decrease of electron diffusivity in short n<sup>+</sup>-n-n<sup>+</sup> structures of GaAs. Thus, it may be concluded, that the increase of the voltage sensitivity of the diode based on the small area GaAs n-n<sup>+</sup> junction accounts for by electron energy relaxation time and the diffusion coefficient increase in strong electric field. It is interesting to note, that the voltage sensitivity of n-GaAs diode is more than one order greater than that of silicon one, though the value of resistance of the diodes is the same ( $R_s=490 \Omega$ ). The electric field strength in the n-n<sup>+</sup> region near the flat n-n<sup>+</sup> junction may be expressed as

$$E_m = \frac{4U}{\pi r_k} = \frac{4\sqrt{2R_s P}}{\pi r_k}. \quad (3)$$

where  $R_s$  is resistance of point contact and  $P$  denotes absorbed MW power.

The I-V characteristics measurements of Au-p-pGe non-heated point contact diodes in dc regime have shown the presence of considerable value of contact resistance of the diodes. Nevertheless, the sign of detected signal in MW electric field at room temperature corresponds to the thermoelectric of hot carriers when MW power is low. With the increase of MW power the detected signal changes its polarity. At liquid nitrogen temperature specific resistance of the Au-p-Ge point contact diodes has different value and the sign of detected signal was opposite to that at room

temperature.

The influence of contact resistance on diode operation can be decreased by using the l-h contacts of large crossection. In order to maintain the high value of voltage sensitivity of such a diode, the narrow-long shape contacts were made [13]. The asymmetry of I-V characteristic of these diodes at room temperature corresponds to that one of l-h junction, while at liquid nitrogen temperature it takes place only for low value of applied voltage. For higher voltages the sign of asymmetry was opposite. The sign of detected signal of such the diodes follows the sign of I-V characteristics asymmetry. The experimental value of asymmetry at room temperature exceeds calculated one for a diode with l-h junction of narrow-long shape

$$\Delta R = \frac{\pi[(1+s)\tau_g + \tau_M^n]U}{12Lr_k^2ep_0\ln(4L/r_k)} \quad (4)$$

where  $2L$  is the length of contact, and  $2r_k$  is the width of contact.

The experimental and theoretical values of asymmetry at  $T=80K$  are in close agreement. Nevertheless, it could not say that we deal with l-h junction of good quality, because the nonmonotonical dependence of resistance change on applied voltage was not observed at  $T=80K$  for forward current. The barrierless structure of Au-p-Ge is taken to explain the above experimental

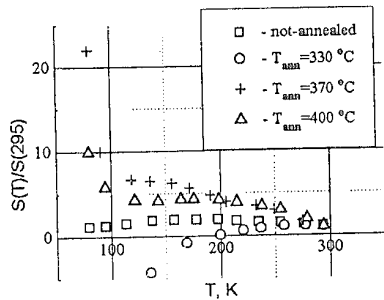


Fig. 3. Temperature dependence of voltage sensitivity of Au-p-Ge contacts diode annealed at different temperatures in hydrogen atmosphere

facts at liquid nitrogen temperature.

The thermal annealing of Au-p-Ge contacts in hydrogen atmosphere changes strongly their electrical properties. The resistance of the diode decreases with lattice cooling for not-annealed contact and for that annealed at  $400\text{ }^{\circ}\text{C}$ . However, the temperature dependence of the resistance of the diodes did not follow the temperature dependence of specific resistance of p-Ge. The temperature dependence of voltage sensitivity of Au-p-Ge contacts diodes depends strongly on annealing temperature  $T_{\text{ann}}$  of those (Fig. 3). The slight temperature dependence of non-annealed contact should be noted. This feature of the diode determined the wide use of it in MW power measurement devices. The annealing of Au-p-Ge contacts made the temperature dependence of voltage sensitivity of the diode more pronounced. If the  $T_{\text{ann}}$  is less than eutectic temperature of Au-Ge ( $T_{\text{Au-Ge}}=356\text{ }^{\circ}\text{C}$ ),  $S$  decreases and changes its sign with lattice cooling. When  $T_{\text{ann}} > T_{\text{Au-Ge}}$  the voltage sensitivity increases slightly with lattice temperature decrease up to

$100\text{K}$ . The further cooling causes a considerable increase of  $S$ .

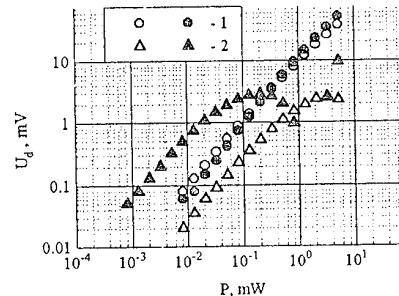


Fig. 4. The dependence of the Au-p-Ge contacts diode detected signal on applied MW power. 1 - not-annealed contact; 2 - annealed at  $370\text{ }^{\circ}\text{C}$ . Dark dots corresponds  $T=80\text{K}$ , the light dots stand for  $T=295\text{K}$ .

It is interesting to analyze the voltage-power characteristics of such diodes at liquid nitrogen temperature. Fig. 4 depicts these characteristics of not-annealed diodes and diodes annealed at  $370\text{ }^{\circ}\text{C}$  in hydrogen atmosphere. While the voltage-power characteristics of not-annealed diodes are linear both at  $T=295\text{K}$  and  $T=80\text{K}$ , then those for the annealed diodes are nonmonotonical at liquid nitrogen temperature. Firstly, the dependence of  $U_d$  on applied MW power follows square law, reaches a maximum, decreases rapidly and, finally, negative region of detection signal appears (negative values of  $U_d$  are not shown). We have found this dependence very similar to that in highly compensated InSb<Cr> and, consequently, attributed the existence of region with negative detection signal to the electron-gas cooling effect. The essence of this phenomenon is electron localization in the random potential valleys after optical phonon emission [14].

The I-V characteristics of In-p-Ge diodes at room temperature are similar to those of l-h junction, although the experimental value of their asymmetry exceeds one order of theoretical one. The sign of asymmetry at  $T=80\text{K}$  corresponds to that one of l-h junction for low value of applied voltage, while for higher voltage the asymmetry changes its sign. The field dependence of detected signal of such a diode placed in MW electric field follows the field dependence of I-V characteristics asymmetry. Measurements of temperature dependences of voltage sensitivity have shown their weak dependence on annealing temperature. The value of voltage sensitivity does not change when lattice temperature exceeds  $T=250\text{K}$ , then at lower temperatures voltage sensitivity changes its sign.

The quality of l-h junction diodes depends on doping level of heavily doped region. Doping, in our case, is produced by melting process. Consequently, Al is preferable as doping material, since it has better solubility in germanium in comparison to that of Au and In. We observed that really the diodes based on Al-p-Ge contacts has much better temperature dependence of voltage sensitivity than in the case of Au and In contacts diodes. High value of specific contact resistance is characteristic to Al-p-Ge contacts annealed at temperature below the eutectic one ( $T_{\text{Al-Ge}}=424\text{ }^{\circ}\text{C}$ ). The voltage sensitivity of Al-p-Ge diodes annealed at temperature, which exceeds  $T_{\text{Al-Ge}}$ , increases with lattice cooling. However, the

temperature dependence of  $S$  does not correspond the temperature dependence of electron energy relaxation time and mobility in germanium [15]. That is why either in the case of Al contact to germanium we deal with quasi-ohmic contact.

#### 4. Conclusions

1. The voltage sensitivity of the diode based on small area GaAs n-n<sup>\*</sup> junction increases with electric field strength due to the increase of both the electron energy relaxation time and the diffusion coefficient.

2. Investigated contacts of different metals (Au, In, Al) to p-type germanium manifest itself as quasi-ohmic contacts. The thermoelectromotive force of hot holes in such contacts is found to increase with the decreasing lattice temperature. We associate it to the increase in hole mobility and phenomenological energy relaxation time.

3. The nonmonotonical dependence of thermoelectromotive force, arising in Au-p-Ge annealed contacts on applied microwave power, can be explained by hole cooling effect in germanium.

#### References

- [1]. V. Dienys, J. Požela, Hot electrons, "Mintis", Vilnius, 1971 (in Russian).
- [2]. R.I. Harrison, J. Zucker. Microwave detection and mixing using the thermoelectric effect of hot carriers in semiconductors. - J. Appl. Phys. Lett., 1963, v. 3, No. 2, pp.153-154.
- [3]. J.B. Arthur, A.F. Gibson, J.B. Gunn. Carrier accumulation in Ge. -Proc. Phys. Soc., 1956, v. 69B, pt. 7, pp.697-704.
- [4]. A.M. Cowley, H.O. Sorensen. Quantitative comparison of solid state microwave detectors. - IEEE Trans. on Microwave Theor. and Techn., 1966, v. MTT-14, No. 12, pp. 588-602.
- [5]. R.I. Harrison, J. Zucker. Hot-carrier microwave detector. - Proc. IEEE, 1966, v. 54, No. 4, pp.588-595.
- [6]. S. Ašmontas, Electrogradient phenomena in semiconductors, "Mokslas", Vilnius, 1984, 183 p. (in Russian).
- [7]. K. Ashida, M. Inoue, J. Shirafuji, Y. Inuishi. Energy relaxation effect of hot electrons in GaAs. - J. Phys. Soc. Jap., 1974, v. 37, No. 2. pp. 408-414.
- [8]. D. Gasquet, M. de Murcia, J.P. Nougier, C. Gontrand. Transport parameters of hot electron in GaAs at 300 K. - Physica B+C, 1985, v. 134 B+C, No. 1/3, pp. 264-268.
- [9]. M.I. Bilko, A.K. Tomashevsky, Measurements of microwave power, "Radio i svjaz", Moscow, 1986 (in Russian).
- [10]. S. Ašmontas, L. Vingelis, V. Guoga, A. Olekas and A. Sužiedėlis. Relationship between voltage sensitivity and I-V characteristics asymmetry of detector with point contact n-n<sup>\*</sup> junction - Fiz. Tekh. Poluprovodn., 1982, v. 16, No. 2, pp.367-369.
- [11]. V. Dienys, S. Dedulevič, Ž. Kancleris, Z. Martūnas, A. Šetkus. Warm electron conductivity of GaAs in dc and ac electric fields. - Lithuanian Journal of Physics, 1989, v. 29, No. 1, pp.46-52.
- [12]. V. Bareikis, K. Kibickas, J. Liberis, A. Matulionis, R. Miliušyté, J. Paršeliūnas, J. Požela, and P. Sakalas. Velocity overshoot and suppression of diffusivity and microwave noise in short n<sup>+</sup>-n-n<sup>\*</sup> structures of GaAs. - In High-Speed Electronics, Ed. by B. Kallback, H. Beneking, Springer-Verlag, Berlin, 1986, pp. 28-31.
- [13]. S. Ašmontas and A. Sužiedėlis. Electric properties of small area nn<sup>\*</sup> junctions in silicon. - Lithuanian Journal of Physics, 1987, v. 27, No. 3, pp.297-303.
- [14]. S. Ašmontas, L. Subačius, G. Valušis. Hot-electron effects in high-resistivity InSb. - Acta Phys. Polonica, 1993, v. 84, No. 4, pp. 717-720.
- [15]. A. Dargys and J. Kundrotas. Handbook on physical properties of Ge, Si, GaAs and InP. Vilnius: Science and Encyclopedia Publishers, 1994, 264 p.

# THERMOELECTRIC MODULES QUALITY TESTING BY A MANUFACTURER.

V.P.Babin, S.M.Gorodetskiy

*EPF "CRYOTHERM", St.Petersburg, Russia.*

## Introduction

A thermoelectric module (TM) is a thermoelectric battery, consisted of thermocouples and sandwiched between two ceramic plates (heat exchangers). Each thermocouple involves two elements n-type and p-type conductivity, respectively. TM thermocouples are placed in series to the electric current and in parallel to the heat flow.

If TM are manufactured in considerable amount, direct determination of their consumer parameters (maximum temperature differential  $\Delta T_m$ , maximum heat pumping capacity  $Q_m$ , current and voltage to reach  $\Delta T_m$  or  $Q_m$ ) takes a lot of time. That is why we obtain such data from random tests. To determine the quality of all produced TM they are tested by computer-aided system (CAS), that is intended to measure TM parameters (figure of merit Z and resistance R) in air at room temperature in passive thermostats by modified Harman method<sup>1</sup>. By analogy with [1] the TM figure of merit in air is taken equal to:

$$Z = \frac{S_m^2}{R(K + K_a)} \quad (1)$$

where TM Seebeck coefficient  $S_m = N(|S_n| + |S_p|)$  ( $|S_n|$  and  $|S_p|$  are absolute values of n-type and p-type element Seebeck coefficients, respectively, and  $N$  denotes the thermocouple quantity in a TM),  $R$  and  $K$  are TM resistance and thermal conductance, respectively, and  $K_a$  designates thermal conductance of air, sandwiched between TM heat exchangers.

When a weak direct current  $I$  flows through a TM, a small temperature difference between TM heat exchangers reaches  $\Delta T = T_h - T_c$  ( $T_h$  and  $T_c$  denote hot and cold exchanger temperatures, respectively) in steady state conditions. Then TM terminal voltage will be:

$$U_i = IR + U_s \quad (2)$$

where TM terminal voltage due to temperature difference  $\Delta T$  is equal to:

$$U_s = S_m \Delta T \quad (3)$$

## Measurement of TM parameters

The CAS consists of a managing personal computer PC with a display D, measurement means (digital voltmeter DV and a instantaneous sampling unit ISU), commutator C and a stabilized direct current source CS. TM are enclosed in passive thermostats PT1 and PT2. A conceptual sketch of CAS is shown in fig.1, where double and single lines display pathways of digital and analog values, respectively.

Enclosed in a passive thermostat TM is connected to measurement means by four-wired circuit - two wires for current and two - for voltage. In the initial stage of the test a current does not flow through a TM and TM terminal voltage  $U_0$  is

measured so long as  $U_0$  absolute value remains bigger than the predetermined one.

When the initial stage is completed, a depending on the TM type stabilized current is switched on and TM terminal voltage  $U_i$  is measured so long as the voltage remains a variable. In the second stage a TM heat equilibrium with environment has been reached, when the voltage becomes constant or can vary with a rate, that is less than the predetermined value.

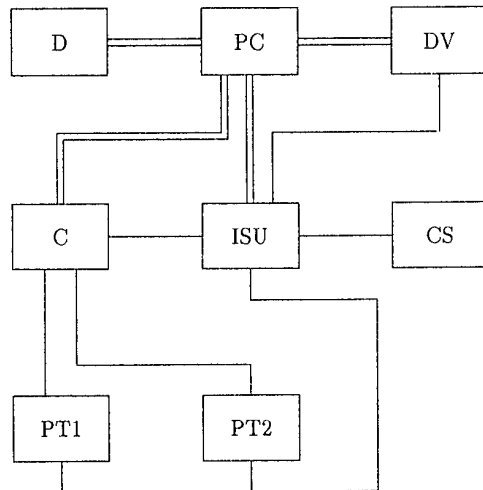


Figure 1: A schematic sketch of computer-aided system

When the second stage is completed, CAS measures  $U_s$ . It is done by the same measurement means, but now the current is interrupted for a short measurement time at a frequency of 10 Hz. When the current is interrupted for a short time, the TM terminal voltage is equal to  $U_s$ . To a first approximation, the TM parameters can be calculated by following expressions:

$$R = \frac{U_i - U_s}{I} \quad (4)$$

$$Z = \frac{1}{T} \cdot \frac{U_s}{U_i - U_s} \quad (5)$$

where  $T$  is equal to  $(T_h + T_c)/2$  - mean TM temperature, that is approximately equal to  $T_a$  - passive thermostat temperature (Harman expression [2, 3]). The temperature  $T_a$  is measured by a resistance thermometer before the initial stage.

During the second stage the current  $I$  is measured by terminal voltage across a reference resistance  $R_r$  connected in series with TM under test. If the current differs from the fixed depending on TM type value by a predetermined part of it, some message appears on display and a short melody sounds.

We have the same reaction, if something is wrong with the test. For example, if the initial or the second stage takes too

<sup>1</sup>The note added in proof: Similar problems are discussed in [5].

values, that are the corresponding parameters of the measured TM, if it were without the fault.

In the (A) type fault case the damaged TM part (or two adjacent parts) has a low resistance and thermoEMF as compared to intact analogous TM parts. There is a method for estimation of the shunted thermocouples quantity and the shunt resistance. If the last is significantly below the shunted thermocouples resistance, it can be obtained from Ohm's law and expression (1), that :

$$\frac{R}{R_0} = \frac{N - N_F}{N} \quad (13)$$

$$\frac{Z}{Z_0} = \frac{N - N_F}{N + N_F Z_0 T} \quad (14)$$

where  $N_F$  - shunted thermocouples quantity, and a product  $Z_0 T$  here may be considered to be equal to 0.73. It is interesting, that, if shunted thermocouples line has an open circuit, the expression (13) is valid but the expression (14) has to be replaced by :

$$\frac{Z}{Z_0} = \frac{N - N_F}{N} \quad (15)$$

If a heat exchange of the shunted thermocouples with intact TM parts is hampered by some causes, an influence of the shunting on the TM figure of merit is become weaker, and if such heat exchange is absent, the same is true for the influence. There are expressions for more general cases, when a shunt resistance and a local extra resistance in the shunted thermocouples line may have arbitrary values, or when the ceramic plates have an arbitrary conductance in the base plane direction, but these expressions are too cumbersome.

In the (B) type fault case, that affects on any TM element to one or another extent, there is a detectable dispersion of the TM part resistances and thermoEMFs, when a TM part thermocouple quantity is constant. It may be shown under some assumptions, that the (B) type fault scarcely affects on the damaged element heat conductance and lowers the element thermoEMF and its resistance so, that the first is proportional to the second. So, the ratio between a thermoEMF and resistance is approximately equal to a constant for any TM part. The highest resistance  $R_m$ , that a undamaged comprising of  $M$  thermocouples TM part can have, is equal to :

$$R_m = M(\rho_n + \rho_p) \frac{L}{S} \quad (16)$$

where  $\rho_n$  and  $\rho_p$  are the highest resistivities of suitable materials with a n-type and p-type conductivity, respectively, and the  $L$  and  $S$  are the length and cross section area of a TM element. If the TM part resistance is equal to or less than  $R_m$ , and if a TM part has the highest resistance in comparison with resistances of other parts of TM under test, such TM part may be considered to be undamaged. Thus, the required expressions will be the following :

$$R_0 = R_h \frac{N}{N_h} \quad (17)$$

$$\frac{Z}{Z_0} = \frac{R}{R_0} \quad (18)$$

where  $R_h$  and  $N_h$  are sums of resistances and thermocouple quantitatives, respectively, of undamaged TM parts in the sense of (B) type fault.

If the TM under test has a part with resistance, that is higher, than the  $R_m$  obtained from the expression (16), such part is decided to have a (C) type fault. A (C) type fault may often be detected and/or confirmed by a TM resistance

dependence on a local pressure. In such a case, the expressions will be :

$$R_0 = R_a \frac{N}{N_a} \quad (19)$$

$$\frac{Z}{Z_0} = \frac{R_0}{R} \quad (20)$$

where  $R_a$  and  $N_a$  are sums of resistances and thermocouple quantitatives, respectively, of undamaged TM parts in the sense of (C) type fault.

If all TM parts have resistances with nearly the same values and some of them have reduced thermoEMFs as compared to another parts, it can be assumed, that (D) type faults exist in the TM. If the TM under test contains  $N_p$  of (D) type faults, the expressions will be the followig :

$$\frac{R}{R_0} = 1 \quad (21)$$

$$\frac{Z}{Z_0} = (1 - \frac{N_p}{N})^2 \quad (22)$$

If in the assembly of a TM a ceramic plate (or plates) with a pattern of commutation was improperly oriented in relation to the matrix of elements, the (E) type fault exists in the TM. The TM parameters are reduced and the reduction depends on thermocouple commutation circuit.

If we have to suppose several fault types in one TM, the calculations are performed step by step. The order of such calculations to "repair" the TM is as follows: type (C) and type (A) and then types (B) and (D). To obtain  $R_0$  value by expression (19), type (C) and type (A) have to be taken into account simultaneously. If a (E) type fault takes place in the TM under test, it has to be "repaired" first of all.

Use of these expressions makes a search for faults quantitative and more certain. When such faults could be removed, a sufficient accuracy of these expressions was confirmed.

There are some faults, that influence on TM performance but can not be detected because they do not directly affect on the TM figure of merit and TM resistance. This is an improper polarity of a TM as a whole, or a bad heat contact of a thermocouple with a heat exchanger, that is particularly dangerous on the hot side of a TM. The elaboration of methods and means for detecting such faults is in our long-term plans.

## References

- [1] A.F.Ioffe. *Semiconductor thermoelements*. Moscow - Leningrad, 1960. (in Russian)
- [2] T.C.Harman, Special Techniques for Measurement of Thermoelectric Properties, *J. of Appl. Phys.*, 1958, v.29, No.9, pp.1373-1374.
- [3] T.C.Harman, J.H.Cahn, M.J.Logan, Measurement of Thermal Conductivity by Utilization of the Peltier Effect, *J. of Appl. Phys.*, 1959, v.30, No.9, pp.1351-1359.
- [4] G.N.Dulnev, E.M.Semyashkin, *Heat exchange in radio-electronic devices "Energiya"*, Leningrad, 1968 (in Russian)
- [5] R.J.Buist. A new method for testing thermoelectric materials and devices. *XI International conference on thermoelectrics*, Arlington, Texas, USA, 1992.

much time, or some voltage is more than a predetermined value, or TM parameters are out of fixed interval, and so on. Thus, CAS can automatically reject the flawed TMs. When the occasion requires, an operator has to choose between several options, what to do.

Six TMs are measured at once in one passive thermostat to lower testing time. All these TMs are connected in series to electric current provided by the current source CS. To measure a voltage across each TM or a reference resistance, their terminals are connected to measurement means by a commutator C. While these six TMs are being measured, an operator have a possibility to replace the metered TMs in the other passive thermostat by new six ones.

A serial No and parameters of metered TM is associated with the place, where it have been measured, and this information is stored in PC memory. Such data serves to reject the flawed TMs. Also such data is available for statistical treatment, printing, transmitting to another computer and so on.

CAS provides high reproducibility of the TM parameters measurements ( $\pm 0.25\%$  for a TM with more than 70 thermocouples).

### Corrections to Harman expression estimation

Corrections to Harman expression were calculated by TM energy balance analysis. TM Joule heating, thermal conductance of air, heat flow through wires, and heat exchange with environment by radiation and convection were taken into account in TM energy balance analysis. For this purpose a simultaneous solution of two ceramic plate heat balance equations must be obtained. The equations are as follows:

$$-S_m IT_c + \frac{1}{2} I^2 R + (K + K_a) \Delta T + H_v(T_a - T_c) = 0 \quad (6)$$

$$S_m IT_h + \frac{1}{2} I^2 R - (K + K_a) \Delta T - H_n(T_h - T_a) = 0 \quad (7)$$

where (6) and (7) are related to cold and hot ceramic plates, respectively.  $H_v$  and  $H_n$  are effective heat conductances of heat exchange processes between a corresponding plate and environment. Effective heat exchange coefficients due to convective and radiative processes between the plate and environment are included in  $H_v$  and  $H_n$  as summands. An effective heat exchange coefficient due to heat contact between the plate and lead wires is also included in  $H_n$  as a summand. It is considered, that lead wires have a heat exchange with environment due to convective and radiative processes and current wires Joule heating could be neglected. If a current is altered, one have to interchange the position of  $H_v$  and  $H_n$  in (6) and (7).  $H_v$  and  $H_n$  can be estimated approximately by methods described in [4], if all dimensions of the plate and distances between its outer surface and thermostat inner walls are known. Let us denote the difference  $T_h - T_a$  by  $\Delta T_h$  and point out, that the difference  $T_a - T_c$  is equal to  $\Delta T - \Delta T_h$ . Subtracting (6) from (7) one can obtain :

$$\begin{aligned} Z &= \frac{T_a}{T_a + \Delta T_h - \Delta T/2} \cdot \\ &\left( 1 + \frac{H_v(\Delta T - \Delta T_h) + H_n \Delta T_h}{2(K + K_a) \Delta T} \right) \cdot \frac{1}{T_a} \cdot \frac{U_s}{U_i - U_s} \end{aligned} \quad (8)$$

The equation (8) differs from (5) by two correction factors, that by first approximation may be taken as 1. The first of them is a ratio of environment temperature  $T_a$  to TM mean temperature, that is equal to  $T_a + \Delta T_h - \Delta T/2$ , and the second one takes properly into account the influence of heat exchange

between the TM and environment on TM figure of merit. A following equation can be obtained from the sum of (6) and (7) :

$$\Delta T_h = \frac{H_v \Delta T + IU_i}{H_v + H_n} \quad (9)$$

A TM resistance  $R$ , that was measured at mean TM temperature, is to be related to a temperature of 295 K by temperature coefficient of TM resistance, that is equal to  $0.4\%/\text{K}$ :

$$R = \frac{U_i - U_s}{I} (1 + 0.004(295 - T_a - \Delta T_h + \Delta T/2)) \quad (10)$$

By the first approximation, the values  $\Delta T$  and  $\Delta T_h$  in (10) may be taken as zero.

By successive approximation, the Seebeck coefficient  $S_m$  can be calculated from expression (1) :

$$S_m = \sqrt{ZR(K + K_a)} \quad (11)$$

if the heat conductivities of TM elements and air, and dimensions of all TM parts are known. Thus, the temperature difference  $\Delta T$  can be calculated from expression (3) :

$$\Delta T = U_s / S_m \quad (12)$$

By successive approximation, the  $\Delta T_h$ ,  $Z$  and  $R$  values can be calculated from expressions (9), (7) and (10), respectively. The iterative scheme converges to unique solution rapidly for a TM.

The corrected values of  $R$  and  $Z$  allow to calculate the consumer parameters each of produced TM with sufficient accuracy. In these calculations, it has to be taken into account, that the vacuum value of the TM figure of merit can be obtained, if the corrected value of  $Z$  is multiplied by a factor  $1 + K_a/K$ . The averaged over a performance temperature interval vacuum value of the TM figure of merit is reduced by 4 % as compared to the room temperature one.

### TM rejection causes analysis

In order to affect on the production process, the TM rejection causes analysis is performed. If the TM parameters are out of predetermined interval, the TM is tested to find faults responsible for decrease its figure of merit and for variation its resistance. This test is performed by a facility, that is intended to measure resistance and thermoEMF of separate TM parts. An analysis of such data allows to suppose some TM faults.

Let us list the commonly occurring faults in the rejected TMs.

(A) - there is some resistance in parallel with a part of the TM thermocouples circuit (for instance, a short circuit);

(B) - there is a shunting of an element side surface part adjacent to the junction by solder;

(C) - there is a local heightened resistance due to the junction low-quality soldering;

(D) - there is an improper conductivity type element (there is an element misalignment in relation to the TM process drawing);

(E) - there is an improper commutation of the TM thermocouples circuit;

(F) - there are arbitrary combinations of the above-listed faults in a TM.

We shall describe major indications allowing to suppose one or other fault type. New expressions describing the effect of typical faults on TM  $R$  and  $Z$  values have been derived. These expressions provide a possibility of estimating the  $R_0$  and  $Z_0$

## HIGH-PRECISE THERMOELECTRIC A.C. CONVERTERS

L.I.Anatychuk, V.I.Bodnaruk, L.A.Shcherbina

*Institute of Thermoelectricity, Chernovtsy, 274000, General Post Office, box 86, Ukraine*

Thermoelectric A.C. converters (TEC) are used in measuring technique and metrology. High-precise measuring devices and equipment, standards, reference measures of current, voltage and power operating in wide frequency range have been developed on the base of TECs.

TEC is a device consists of a thermocouple or a thermobattery having thermal contact with a resistance heater and enclosed into an evacuated case [1]. Fig.1,2 shows the electric circuit and TEC structure. The input circuit made by the heater is in the most cases insulated from output circuit made by a thermocouple.

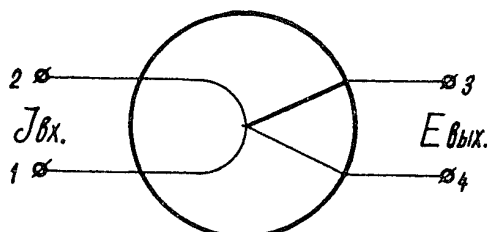


Fig.1. TEC electrical circuit. 1,2 - input, 3,4 - output.

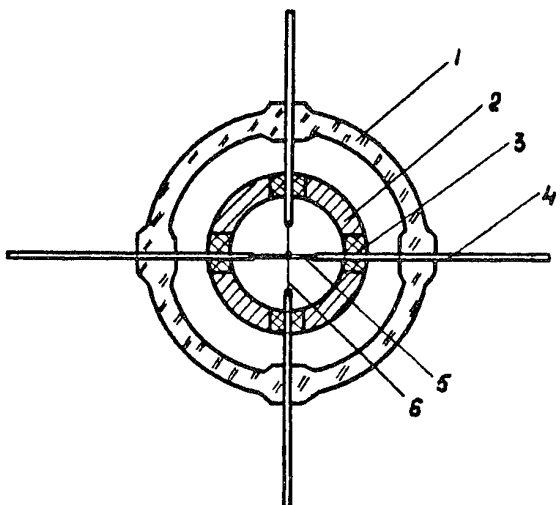


Fig.2. TEC's structure

1 - case, 2 - thermostatting bus, 3 - thermal conductive electrical insulation, 4 - mounting leads, 5 - thermocouple, 6 - heater.

Previously thermoelectric converters were made, as a rule, on the base metal thermocouples (chromel-copel,

chromel-alimel, copper-constantan and the like). Increased requirements for A.C. measurements precision and reliability showed that TEC base on metal thermocouples have been exhausted and cannot provide further development of high-precise A.C. measuring means in full measure.

Next step that permitted sufficiently increase TECs parameters and characteristics was the use of thermocouples made of semiconductor thermoelectric materials combined high thermoelectric figure of merit with time and temperature stability of their parameters. As the investigations showed [2], semiconductor thermoelectric materials based on CdSb and Bi<sub>2</sub>Te<sub>3</sub> solid alloys optimized in response to measuring engineering and metrology requirements were the best.

Developed procedure of microminiature semiconductor thermocouples production enable in traditional structure solutions to realize the best sensitivity values (more tan 100 V/W) that is an order of magnitude higher of the best TECs with metal thermocouples sensitivity.

Development semiconductor TECs with one thermocouple operating in inert gases medium with reduced thermal conductance predetermined the possibility of structure materials wider choice and as a consequence, sufficient reduction of a frequency error.

Squareness of TEC volt-ampere characteristics is along with sensitivity and frequency error the basic characteristic in the devices for power and A.C. power coefficient measurements. Squareness improvement in TECs with metal thermocouples is achieved basically by the use of thermobatteries with 30-50 thermocouples that as a rule, sharply limits the frequency range of these TECs use.

As a result of complex investigations we have established that use of high-efficient semiconductor thermocouples will enable to solve the problem of TECs parameters and characteristics control. The basis for control is the TECs parameters dependence on heat exchange with ambient conditions. The deviation of a semiconductor TEC volt-ampere characteristic from the squareness law can be essentially reduced by the choice of special heat exchange conditions [3]. It should be noted that the required deviations from squareness (0.02%) in semiconductor TECs are realized in structures with one thermocouple that greatly extends operating frequency range. Change of heat exchange conditions is achieved by choice and the TEC operation volume filling with a composition of inert gases mixture both as at reduced and elevated pressure. Gas-filled TECs possess relatively high sensitivity (5-10 V/W), wide operating frequency range of application (10Hz-150MHz) at

squareness of volt-ampere characteristic no worth than 0.02% (see Table 1, TPV, TPG types).

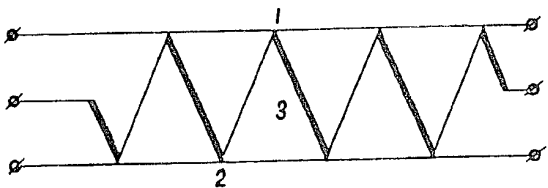


Fig.3. DTEC electrical circuit

1,2 - heaters, 3 - differential thermobattery.

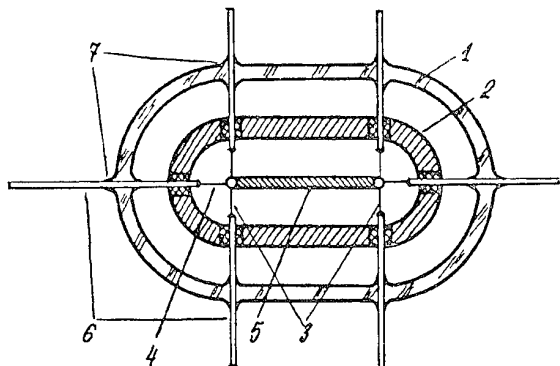


Fig.4. DTEC's structure

1 - case, 2 - thermostatting bus,  
3 - identical heaters, 4 - a thermocouple electrical leads,  
5 - thermocouple (thermobattery), 6 - mounting leads,  
7 - sealing leads.

Development of digital A.C. measuring devices caused production and wide spread of differential TECs (DTECs that have two identical inputs and a differential thermocouple or a battery of thermocouples (see fig.3,4). The method of simultaneous comparison, that is, A.C. measured value is judged by the difference of A.C. and D.C. signal thermal effects, is realized in measuring devices by such DTECs. Identity of volt-ampere characteristics on the both inputs that directly effects on conversion precision is of special importance for such TECs. It was made semiconductor DTECs the characteristic slope control of which is carried out by heat exchange intensity change between thermoelements and thermostat-case. Volt-ampere characteristics identity of corrected DTECs is no worth than 0.02% (DTEC type, Table 1). It should be pointed out that DTECs characteristics correction can be done during operation. This ensures the possibility of DTECs metrological properties recovery in their worsening due to peak overload effects or other reasons.

For automatic measuring complexes it was developed DTECs supplied with additional correcting heaters, not connected galvanically with working heaters and thermocouples. Such DTECs enable to correct a number of errors (nonidentity, temperature, frequency) with the help of program devices.

Fast response TECs were developed on the base of semiconductor thermocouples, period of stationary state setting is not exceeded 0.1 s. These TECs have high sensitivity and increased reliability (TPB type, Table 1).

The developed semiconductor TECs and DTECs by conversion precision, measured values dynamic range, fast response, conversion frequency range, reliability and other parameters compared favourably with the known converters with metal thermocouples. They made a good showing in devices of welding processes control and automatization [4], in development of reference means of metrological purposes [5] (T480 type), and can be further used in design of reference digital converters of metrological purpose.

#### REFERENCES

1. L.I.Anatychuk. Thermoelements and thermoelectric devices. Reference book. - Kiev.: Naukova dumka, 1979, -766.
2. L.I.Anatychuk, V.I.Bodnaruk. Physical principles and methods of thermoconverter parameters improvement. In book. "precise measurement of energy values: A.C., voltage, power, phase shift energy and angle". Tez.dokl. - Lenungrad, 1982, pp. 13-14.
3. L.I.Anatychuk, V.I.Bodnaruk, A.V.Mikhailenko. Semiconductor thermoelectric converters squareness control. In book. "Physical basis of primary measuring converters development". Tez.dokl. Vinnitsa, 1977, p. 104.
4. B.I.Bodnaruk, V.A.Ivanitsky, L.A.Shcherbina. Measuring converter with frequency error automatic correction. In col."Control system and welding process technological control detectors". - Kiev: IES, 1991, pp.90-94.
5. S.A.Andrusyak, A.V.Berezovsky, V.I.Bodnaruk, O.P.Galakhova and others. Methodics of experimental determination of voltage differential thermoelectric comparators. Izmeritel'naya tekhnika, 1987, N2, pp.66-67.

## PRECISE DETERMINING OF METAL-THERMOELECTRIC MATERIAL CONTACT RESISTANCE

L.I.Anatychuk, O.J.Luste, S.V.Pervozvansky

*Institute of Thermoelectricity, Chernovtsy, 274000, General Post Office, box 86, Ukraine*

It was developed and described the mathematical model and on its basis it was determined an instrumental error of the contact resistance measurement pulse method. Contact resistance measurement error dependence on different parameters (pulse duration, contact resistance value) was analyzed.

Contact resistance value is one of the most important parameters of thermoelements significantly effecting on their quality and especially on the miniature thermoelements maximum temperature difference and coefficient of performance.

The known methods [1,2,3] permit to calculate contact resistance value in steady-state and pulse conditions.

The work [1] proposes the method of metal-semiconductor contact resistance determination by indication of thermo-e.m.f. zero equality developed by the contact when direct current pulses passed through the contact. In accordance with [1] the contact resistance equals to

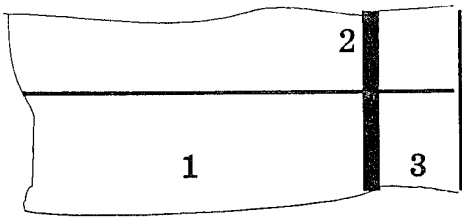
$$R_k = (\alpha_1 - \alpha_2)T / I_0,$$

where  $(\alpha_1 - \alpha_2)$  is the difference of semiconductor and metal coefficients of thermo-e.m.f.,  $T$  is the contact temperature,  $I_0$  is the pulse current corresponding to the thermo-e.m.f. zero signal.

The paper [1] unfortunately did not take into account the Joule heat entered to the contact of a semiconductor, metal and semiconductor thermal capacity, error of the used zero-indicator, and it did not give the precise assessment of the proposed method. The present paper gives the temperature dynamics temperature of thermoelectric material with metal plate contact when direct current rectangular pulses passed through the contact; compensation current corresponding to the contact zero temperature at the end of pulse action and the error of contact resistance determination by the compensation current.

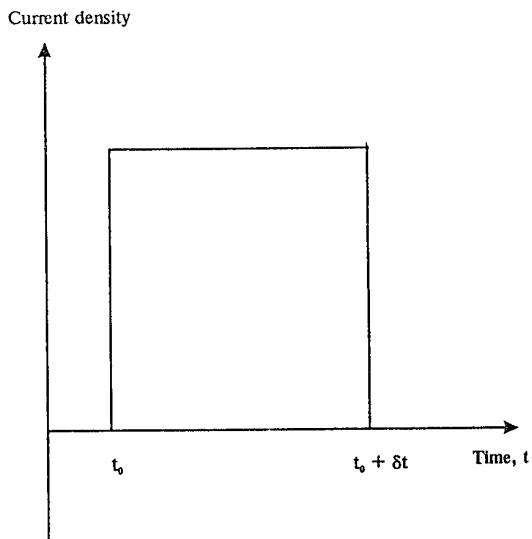
Diagram of the contact is given in Fig.1.

*Fig.1. Diagram of a metal-thermoelectric material contact.*



Model for calculation is given in Fig.1. It has a leg of thermoelectric material 1 which is in thermal and electric contact 2 with a commutation plate 3. Direct current pulse of  $j$  density is passed through the contact (Fig.2).

*Fig.2 Rectangular current pulse passed through the contact metal-thermoelectric material.*



The contact overheating temperature can be represented as the sum (Fig.3)

$$\Delta T(t) = \Delta T_{Joule.contact} + \Delta T_{Joule.branch} + \Delta T_{Peltier},$$

$\Delta T$  is the contact temperature change due to current passing at the end of a pulse,

$\Delta T_{Joule.contact}$  is the contact temperature change due to the Joule heat release on the contact at the end of a pulse,

$\Delta T_{Joule.branch}$  is the contact temperature change due to the Joule heat release in a leg at the end of a pulse,

$\Delta T_{Peltier}$  is the contact temperature change due to the Peltier heat release in the contact at the end of a pulse,

$$\Delta T_{Joule.contact} = \frac{\delta t \cdot \gamma \cdot j^2}{c},$$

Table I.

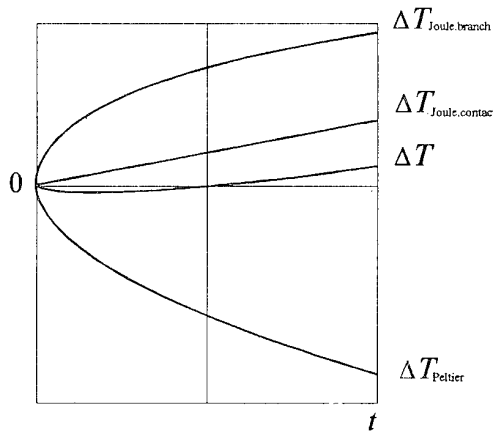
Parameter	Type of TE converter	DTP 480/1	DTP 480/3	DTP 480/5	DTP 480/10	TPB 3	TPB 5	TPV 3	TPV 5	TPG 1	TPG 3	TPG 5	T480/1	T480/3	T480/5	T480/10
1. Rated current, mA	1	3	5	10	3	5	3	5	1	3	5	1	3	5	10	
2. Resistance of heater, ohm	750	500	300	100	40	3000	110	50	200	50	2.5	750	500	300	100	
3. Resistance of the TE converter, ohm	500	400	400	50	500	300	300	500	500	500	500	500	400	400	50	
4. Rated thermo-emf, mV	10	20	30	50	10	20	10	10	10	20	30	10	20	30	80	
5. Sensitivity, V/W	13.3	4.4	4	5	30	30	10	10	50	50	50	13.4	4.4	4.0	8.0	
6. Frequency range, Hz	$20 \cdot 2 \cdot 10^5$	$20 \cdot 10^6$	$1 \cdot 10^6$	$20 \cdot 10^6$	$1 \cdot 10^6$	$20 \cdot 10^8$	$20 \cdot 10^8$	$20 \cdot 10^8$	$20 \cdot 10^5$	$20 \cdot 10^5$	$20 \cdot 10^5$	$20 \cdot 10^5$				
7. Instability after 5 min operation, %	0.01-0.02	0.01-0.02	0.01-0.02	0.01-0.02	0.05-0.1	0.05-0.1	0.02-0.05	0.02-0.05	0.05-0.1	0.05-0.1	0.05-0.1	0.01-0.02	0.01-0.02	0.01-0.02	0.01-0.02	
8. Frequency error, %	0.01-0.02	0.01-0.02	0.01-0.02	0.01-0.02	0.05-0.1	0.05-0.1	0.02-0.05	0.02-0.05	0.05-0.1	0.05-0.1	0.05-0.1	0.005-0.05	0.005-0.05	0.005-0.05	0.005-0.05	
9. Response time, s	5	5	3	3	0.1	0.07	3-4	3-4	2	2	2	2	3-4	3-4	3-4	3-4
10. Error on d.c. direction change, %	0.02-0.05	0.02-0.05	0.02-0.05	0.02-0.05	0.05-0.1	0.05-0.1	0.01-0.05	0.01-0.05	0.01-0.05	0.01-0.05	0.01-0.05	0.02-0.05	0.02-0.05	0.02-0.05	0.02-0.05	
11. Non-root-mean-square ness or nonidentity, %	0.01-0.05	0.01-0.05	0.01-0.05	0.01-0.05	0.005-0.05	0.005-0.05	0.005-0.05	0.005-0.05	0.05-0.1	0.05-0.1	0.05-0.1	0.05-0.1	0.05-0.1	0.05-0.1	0.05-0.1	
12. Temperature error, %/ $10K$	0.001-0.05	0.001-0.05	0.001-0.05	0.001-0.05	0.05-0.1	0.05-0.1	0.05-0.1	0.05-0.1	0.05-0.1	0.05-0.1	0.05-0.1	0.001-0.05	0.001-0.05	0.001-0.05	0.001-0.05	
13. Instability of time constant, %	0.1-0.5	0.1-0.5	0.1-0.5	0.1-0.5	0.1-0.5	0.1-0.5	0.1-0.5	0.1-0.5	0.1-0.5	0.1-0.5	0.1-0.5	0.1-0.5	0.1-0.5	0.1-0.5	0.1-0.5	
14. Dynamic range, mA	0.1-1	0.3-3	0.5-5	1-10	0.3-3	0.5-5	0.3-3	0.5-5	0.1-1	0.3-3	0.5-5	0.1-1	0.3-3	0.5-5	1-10	
15. Overload capacity, %	600	400	250	200	200	400	400	250	250	250	250	600	400	250	250	
16. Capacitance between input and output, pF																
17. Overall dimension Ø, mm	18	18	18	22x22	22x22	11	11	20	20	20	18	18	18	18	18	
h, mm	28	28	28	15	15	4	4	16	16	16	28	28	28	28	28	
18. Mass, g	34	34	34	34	22.5	22.5	0.9	0.9	4.4	4.4	4.4	34	34	34	34	

$$\Delta T_{Joule, branch} = \frac{4 \cdot \delta t \cdot \rho \cdot j^2 \cdot \sqrt{a \cdot \delta t}}{3 \cdot \sqrt{\pi} \cdot c},$$

$$\Delta T_{Peltier} = -\frac{\delta t \cdot \alpha \cdot j \cdot T_0}{c},$$

where  $\delta t$  is pulse duration,  $T_0$  is the initial contact temperature,  $\alpha$  is the leg coefficient of thermo-e.m.f.,  $\rho$  is the leg specific resistance,  $\kappa$  is the leg specific heat conductivity,  $a$  is the thermal conduction,  $h_{Cu}$  the commutation plate thickness,  $\gamma$  is specific contact resistance,  $c\delta_{Cu}$  is the commutation plate cube thermal capacity,  $c$  is the commutation plate thermal capacity per a unit of the contact area.

Fig.3. Dynamics of the contact overheating  $T$  and its components during a pulse of current.



If the registered equipment sensitivity is  $\Delta V$  then the balance current

$$j_0 = \frac{\alpha T_0}{\Gamma},$$

$$\text{where } \Gamma = \gamma + \frac{4 \cdot \rho \cdot \sqrt{a \cdot \delta t}}{3\sqrt{\pi}}$$

is registered with some error  $\Delta j$ .

The contact overheating therewith is

$$\Delta T = \frac{\Delta V}{\alpha} = \frac{\delta t \cdot \alpha \cdot T_0 \cdot \Delta j + \delta t \cdot \Delta j^2 \cdot \Gamma}{c(\delta t)}, \quad (*)$$

where

$$c(\delta t) = c\delta_{Cu} \cdot \sqrt{a_{Cu} \cdot \delta t} = \sqrt{\kappa_{Cu} \cdot c\delta_{Cu} \cdot \delta t},$$

From (\*) we have the equation for  $\Delta j$  determination

$$\Delta j^2 + \frac{\alpha T_0}{\Gamma} \cdot \Delta j - \frac{\Delta V}{\alpha} \cdot \frac{c(\delta t)}{\Gamma \cdot \delta t} = 0$$

$$\Delta j^2 + j_0 \cdot \Delta j - \frac{\Delta V}{\alpha^2 \cdot T_0} \cdot \frac{c(\delta t) \cdot j_0}{\delta t} = 0$$

$$\Delta j = \frac{j_0}{2} (D - 1),$$

$$\text{where } D = \sqrt{1 + \frac{4 \Delta V \cdot c(\delta t) \cdot j_0}{\alpha^2 T_0 \cdot \delta t}}.$$

Erroneous result of the contact resistance measurement

$$\gamma^* = \frac{\alpha \cdot T_0}{j^*} - \frac{4 \cdot \rho \cdot \sqrt{a \cdot \delta t}}{3\sqrt{\pi}},$$

where  $j^* = j_0 + \Delta j$  corresponds to this current determination error.

Thus, the absolute measurement error  $\Delta \gamma$  is

$$\Delta \gamma = \frac{\alpha T_0}{j_0} \left( \frac{1-D}{1+D} \right)$$

and relative error is

$$\varepsilon = \frac{\Delta \gamma}{\gamma} = \frac{\alpha T_0}{\gamma \cdot j_0} \left( \frac{1-D}{1+D} \right). \quad (1)$$

As the formula (1) shows  $\varepsilon$  is the function of three variable we are interested in: the contact resistance value  $\gamma$ , pulse duration  $\delta t$  and zero error measurement of the thermo-e.m.f. register  $\Delta V$ .

Different combinations of these dependences sets are given in Fig.4-6 for standard set of parameters

$\kappa_{Cu} = 3.9 \text{ W/(cm}\cdot\text{K)}$ ,  $C\delta_{Cu} = 3.393 \text{ J/(cm}^3\cdot\text{K)}$ ,  $\alpha = 0.0002 \text{ V/K}$ ,  $T_0 = 300 \text{ K}$ ,  $\rho = 0.001 \text{ Ohm}\cdot\text{cm}$ ,  $a = 0.005 \text{ cm}^2/\text{s}$

It is evident from figures that the measurement error of the contact resistance in the range of  $10^{-8}$  -  $10^{-7}$  Ohm $\cdot$ cm $^2$  can be reduced to several percents if the registered equipment sensitivity is no less than 1 meV in the wide current pulse duration range ( $10^{-6}$  -  $10^{-3}$  s)

Error dependence on the pulse duration has different character at different contact resistance and registered equipment sensitivity values but such dependence is rather weak. This can be used for optimal choice of a pulse duration in particular conditions of measurements.

The obtained results testify about reality of precise measurement of metal - thermoelectric material contact resistance of  $10^{-8}$  -  $10^{-7}$  Ohm $\cdot$ cm $^2$  by the pulse method under proper choice of the registered equipment.

Fig.4. Contact resistance  $\varepsilon$  error measurement dependence on the contact resistance value  $\gamma$  at different pulse  $\delta t$  duration and registered equipment sensitivity  $\Delta V$ .

a)  $\delta t = 10^{-3}$  s, b)  $\delta t = 10^{-6}$  s, c)  $\Delta V = 10^{-5}$  V, d)  $\Delta V = 10^{-7}$  V;  
 1:  $\Delta V = 10^{-5}$  V, 2:  $\Delta V = 3 \cdot 10^{-6}$  V, 3:  $\Delta V = 10^{-6}$  V,  
 4:  $\Delta V = 7 \cdot 10^{-7}$  V, 5:  $\Delta V = 3 \cdot 10^{-6}$  V, 6:  $\Delta V = 10^{-7}$  V,  
 7:  $\delta t = 5 \cdot 10^{-4}$  s, 8:  $\delta t = 10^{-4}$  s, 9:  $\delta t = 5 \cdot 10^{-5}$  s,  
 10:  $\delta t = 10^{-5}$  s, 11:  $\delta t = 5 \cdot 10^{-6}$  s, 12:  $\delta t = 10^{-6}$  s.

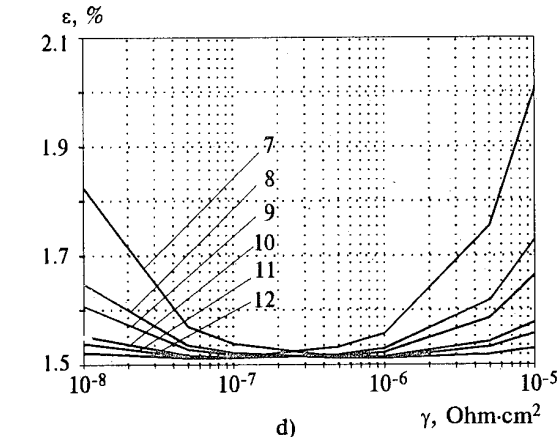
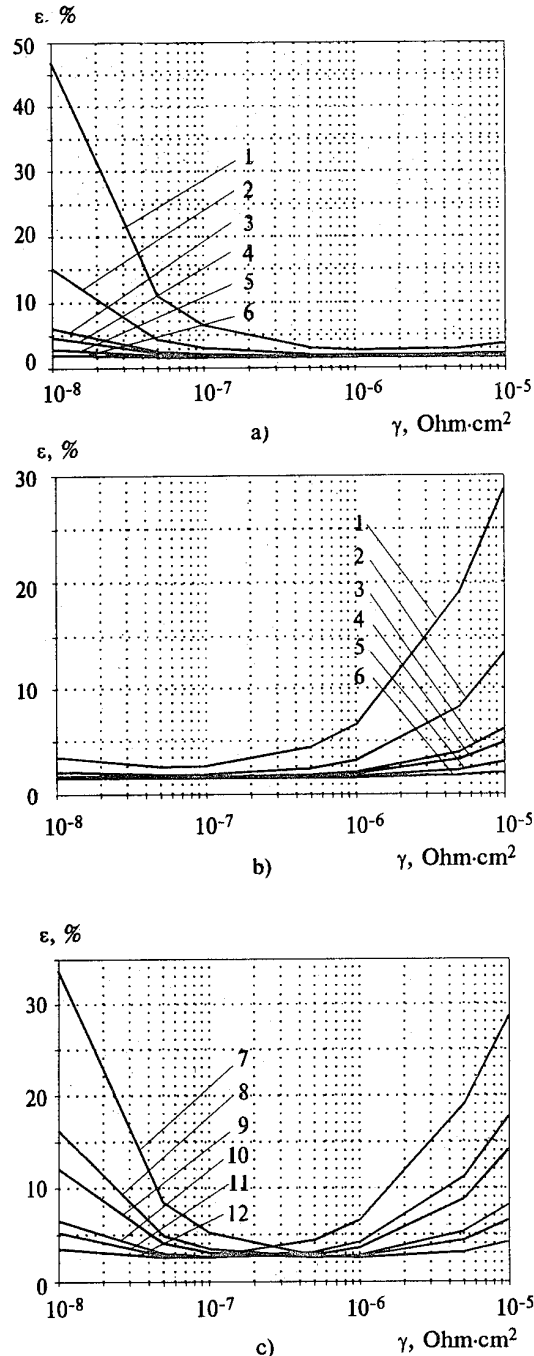
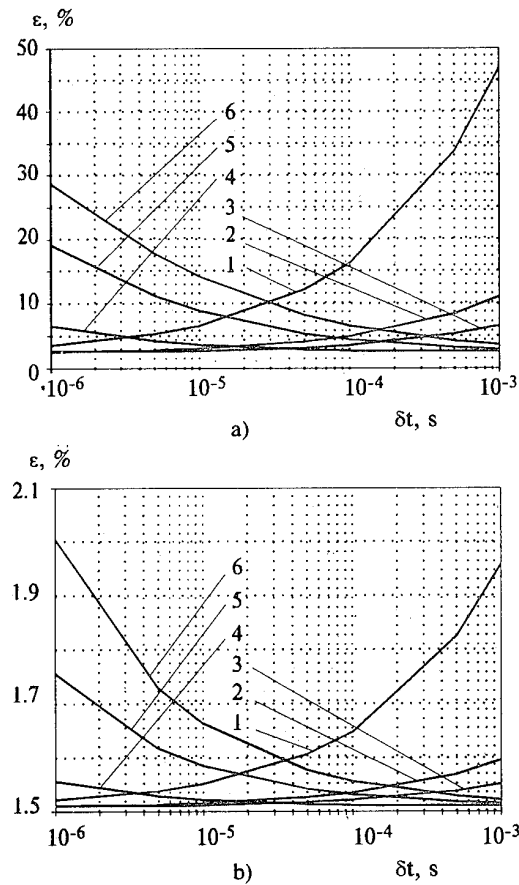


Fig.5. Contact resistance  $\varepsilon$  error measurement dependence on the pulse  $\delta t$  duration at different contact resistance value  $\gamma$  and registered equipment sensitivity  $\Delta V$ .

a)  $\Delta V = 10^{-5}$  V, b)  $\Delta V = 10^{-7}$  V, c)  $\gamma = 10^{-5}$  Ohm·cm<sup>2</sup>,  
 d)  $\gamma = 10^{-7}$  Ohm·cm<sup>2</sup>, e)  $\gamma = 10^{-8}$  Ohm·cm<sup>2</sup>;  
 1:  $\gamma = 10^{-8}$  Ohm·cm<sup>2</sup>, 2:  $\gamma = 5 \cdot 10^{-8}$  Ohm·cm<sup>2</sup>,  
 3:  $\gamma = 10^{-7}$  Ohm·cm<sup>2</sup>, 4:  $\gamma = 10^{-6}$  Ohm·cm<sup>2</sup>,  
 5:  $\gamma = 5 \cdot 10^{-6}$  Ohm·cm<sup>2</sup>, 6:  $\gamma = 10^{-5}$  Ohm·cm<sup>2</sup>,  
 7:  $\Delta V = 10^{-5}$  V, 8:  $\Delta V = 3 \cdot 10^{-6}$  V, 9:  $\Delta V = 10^{-6}$  V,  
 10:  $\Delta V = 7 \cdot 10^{-7}$  V, 11:  $\Delta V = 3 \cdot 10^{-6}$  V, 12:  $\Delta V = 10^{-7}$  V.



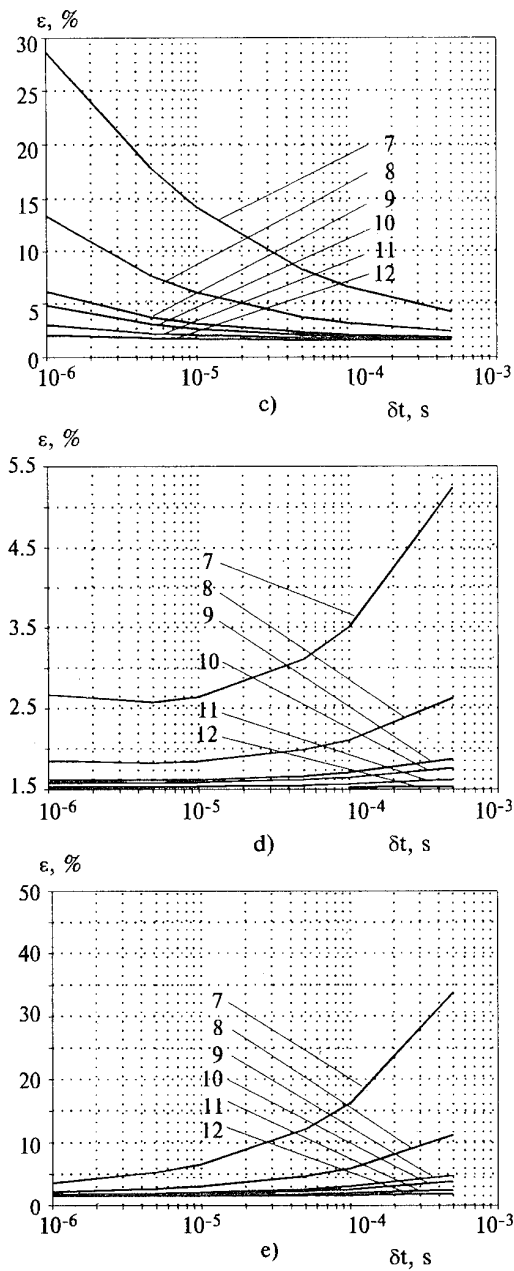


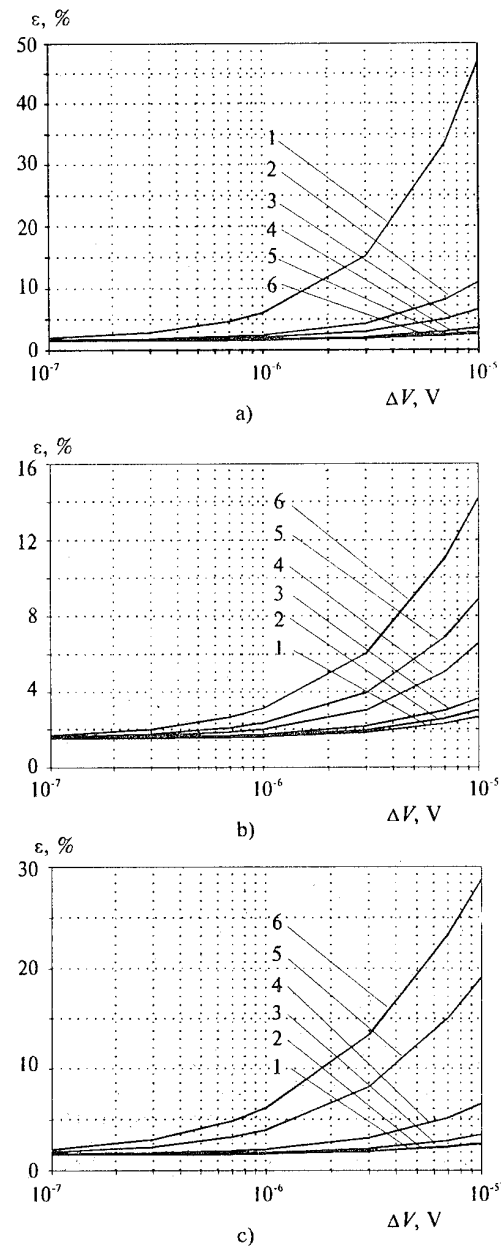
Fig.6. Contact resistance  $\gamma$  and error measurement dependence on the registered equipment sensitivity  $\Delta V$  at different pulse  $\delta t$  duration and contact resistance value  $\gamma$ .

a)  $\delta t=10^{-3} s$ , b)  $\delta t=10^{-5} s$ , c)  $\delta t=10^{-6} s$ ,

1:  $\gamma=10^{-8} \text{ Ohm}\cdot\text{cm}^2$ , 2:  $\gamma=5\cdot10^{-8} \text{ Ohm}\cdot\text{cm}^2$ ,

3:  $\gamma=10^{-7} \text{ Ohm}\cdot\text{cm}^2$ , 4:  $\gamma=10^{-6} \text{ Ohm}\cdot\text{cm}^2$ ,

5:  $\gamma=5\cdot10^{-6} \text{ Ohm}\cdot\text{cm}^2$ , 6:  $\gamma=10^{-5} \text{ Ohm}\cdot\text{cm}^2$ ,



## References

- [1]. Yu.I.Ageev, I.A. Sagaidachny, L.S.Stilbans."Method of the contact resistance measurements". *Pribory i technika eksperimenta*, N 4, 1979, p.253-255.
- [2]. G.Min, D.M.Rowe, D.Assis and S.R.G.Williams. Determining the Electrical and Thermal Contact

Resistance of a Thermoelectric Module. 11-th Int.Conf. on Thermoelectrics, Arlington, Oct.7-9, 1992, p.210-212.

[3]. J. Nagao, H. Unuma, F. Kiya, T. Tamaka, N. Sasa. Seebeck Coefficient and Contact Conductance of *PbTe*-metal junctions. XII International Thermoelectric Conference in Yokohama, Japan, 1993, p. 358.

# THE DEVICE FOR PRECISE THERMOELECTRIC MATERIAL PARAMETERS MEASUREMENT IN THE RANGE OF 100-400 K

V.V.Razinkov, A.A.Khabrenko, Ya.A.Shevchukovich

*Institute of Thermoelectricity, Chernovtsy, 274000, General Post Office, Box 86, Ukraine*

## Introduction

The aspiration to develop precise methods of the thermoelectric material parameters determination is motivated both by the necessity of thermoelectric material improvement and precise and effective thermoelectric devices (coolers, current sources, devices for metrological purposes) design [1]. Thermoelectric material metrology runs in parallel with thermoelectric material science and at present evolves into independent approaches of thermoelectricity development.

Absolute measurement method in stationary conditions is the promising method for precise thermoelectric material parameters measurements. The work [2] presents a measuring cell thermal model for the absolute method of TEM parameters and the errors analysis.

## Structure of the measuring device

Block-diagram of the measuring device is shown in fig.1. Structurally the measuring device consists of a measuring cell with installed sample to be measured, a measuring pillar with apparatus and a vacuum system.

*Fig.1. Block diagram of measuring device for TEM parameters measurement*

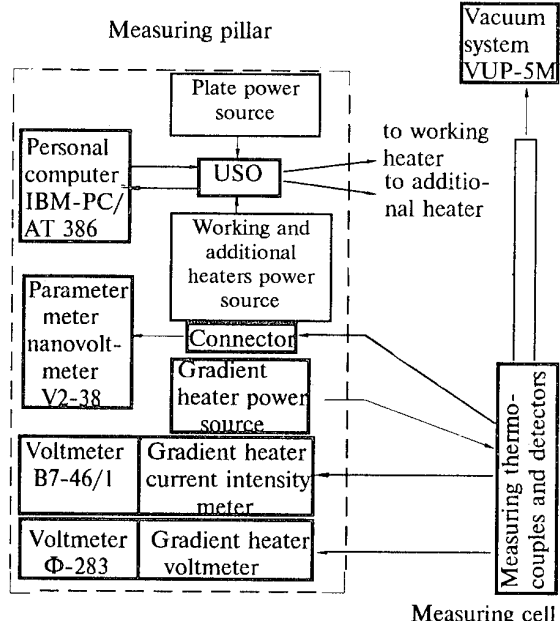
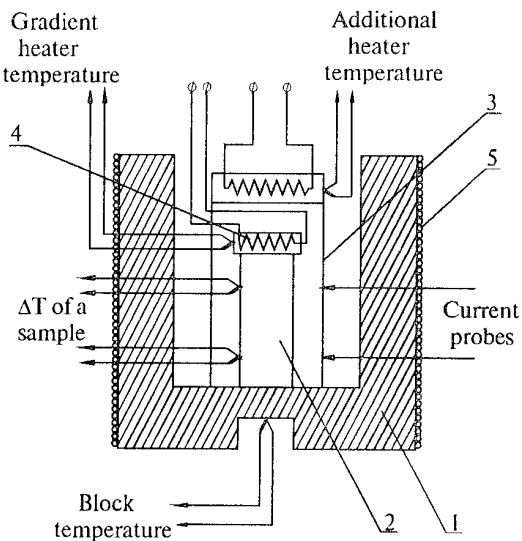


Diagram of the measuring cell is shown in fig.2. The measuring cell is a cylinder structure consist of mass thermal conductive block 1 where the measured sample 2 is placed, and shield 3. Gradient heater 4 being in thermal contact with the sample is mounted on one of the sample ends. The additional heater is placed on the shield. The second end of the sample has reliable thermal contact with the block mass. Thermocouple are mounted here in the block to measure temperature difference on the sample, temperature of the gradient and additional heaters as well as current supplying probes for the sample electrical conduction measurement. The block 1 has a working furnace 5 producing the necessary for measurements temperature. Copper resistance thermometer serves as temperature detector of the working furnace. The block with the working furnace has outside thin-walled copper housing that is sold to the extended part of the block that ensures tightness of the cell working volume.

*Fig.2. Diagram of a measuring cell for TEM parameters measurement*



General-purpose vacuum post *VUP-5M* is used as the vacuum system. Equipment part of the measuring device is arranged on the independent measuring pillar (Fig.1). The main element of the measuring device is the system of the cell volume working temperature control and additional compensated heater that is realized by personal computer *IBM PC/AT*. The necessary temperature and its maintenance precision are set via the computer terminal and the whole process of the system output to the stationary condition at the real time is displayed on the monitor screen. Maintenance precision of the working temperature is no worse than 0.05 °C at

each temperature point. As analogue-digital converter of thermocouple measuring circuits were used standard digital devices of *SH 300* type. The basic measuring data (thermocouple and detector indications) are recorded by *V2-38* nanovoltmeter. Switching unit switches measurement modes.

Low temperetures are achieved by the cell emmersion into condensed nitrogen.

The measuring cell is calibrated in the temperature range of 100-400 K.

The obtained data are processed on the computer. The absolute values of the coefficient of performance, electrical conductance, thermal conductance and thermoefficiency are determined in the process. Output data are printed as tables of thermoelectric parameters local values and temperature dependence graphs in the indicated temperature range.

The investigations of the measuring device show that measurement errors are 0.3-1% for coefficient of performance and electrical conductance, and up to 2-2.5% for thermal conductance.

#### References

- [1]. A.S.Okhotin, A.S.Pushkarskaya, R.P.Borovikova, V.A.Simonov. Methods for thermoelectric material and converter characteristics measurement. M.: Nauka,1974.
- [2]. L.I.Anatychuk, S.V.Pervozvansky, V.V.Razinkov. Precise measurement of cooling thermoelectric material parameters: methods, arrangements and procedures. Proc. 12th.Int.Conf. on Thermoelectrics. Yokohama, 1993, pp.112-124.

## INFORMATION SYSTEM FOR THERMOELECTRIC MATERIAL PARAMETERS EXACT DETERMINATION

V.V.Razinkov, S.V.Pervozvansky, A.A.Shchedrin

*Institute of Thermoelectricity, Chernovtsy, 274000, General Post Office, box 86, Ukraine*

The present paper studies the question of the information system development based on the modern methods of gathering, processing and transmission of measuring information that permits to determine thermoelectric material parameters in a wide temperature range of -100 °C to +100 °C with high precision and low cost.

### Introduction

In thermoelectric products development the basic thermoelectric material parameters determination in a wide temperature range is of paramount importance. Construction of multi-stage thermoelectric cooling modules, thermoelectric generators and the like, requires sufficiently exact knowledge of such parameters.

At present the use of information technologies in thermoelectric production became a norm. One of such use of modern computer technology is construction of flexible measuring information system that permits to determine the basic parameters of thermoelectric materials with sufficient exactness.

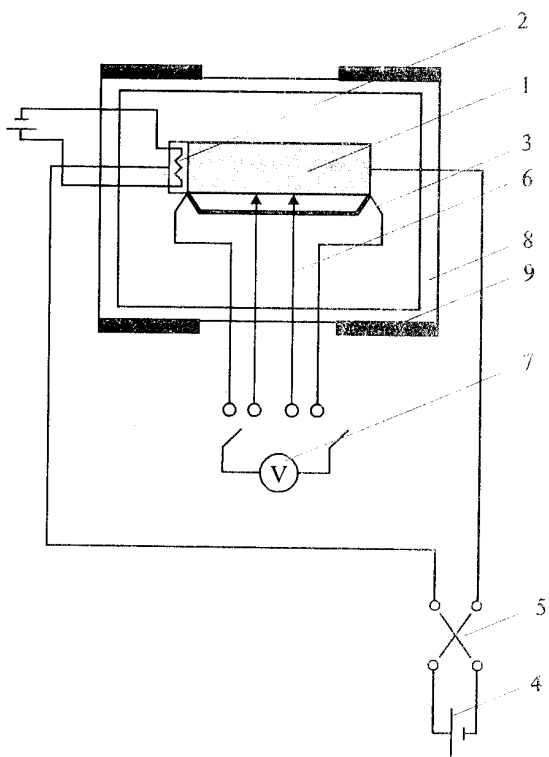
The present paper is dedicated to such measuring information system construction.

Methods of thermoelectric material parameters determination and the calculation of measurement errors.

In the measuring system coefficient of thermo-e.m.f. ( $\alpha$ ) and thermal conduction ( $\kappa$ ) and coefficient of electrical conduction ( $\sigma$ ) are measured by the methods described in details in [1,2].

Diagram of such parameter measurements is given in fig.1. Temperature difference  $\Delta T$  measured by the differential thermocouple 3 along a specimen of regular geometric shape (a cylindrical bar, for example) is maintained by the heater 2. With the help of current source 4 and a switcher 5 the electric current  $I'$  is passed through the specimen in two directions. The potential difference  $U$  is measured by voltmeter 7 on the measuring probe 6 and a thermocouple. The specimen and the heater 2 are placed into a measuring cell 8 on the side walls of which eight three-stage thermoelectric coolers are located symmetrically as to central section and which set the cell's temperature measured by a resistance platinum thermometer 10. The cell with coolers are placed in vacuum. The heater 2, current source 4, voltmeter 7, and coolers 9 operating conditions are set by a computer.

*Fig.1. Measurement scheme.*



The calculation formula for the coefficient of thermo-e.m.f. is

$$\alpha = \frac{E}{\Delta T}. \quad (1)$$

The calculation formula for the coefficient of electrical conductivity is

$$\sigma = \frac{I' \cdot l}{U \cdot S}. \quad (2)$$

The calculation formula for the coefficient of thermal conductivity is

$$\kappa = \left( I^2 \cdot R - \sum_i p_i \right) \frac{I}{\Delta T \cdot S}, \quad (3)$$

where  $R$  is the heater 2 resistance,  $I$  is current across the heater 2,  $S$  are the specimen length and cross-section, respectively,  $\sum_i p_i$  is sum of thermal power losses.

To calculate the instrumental errors it was assumed that the instrumental error of each direct measurements is described by a standard law. The error of an indirect measurement is calculated based on the law of special errors storage. Then the relative instrumental error in  $\alpha$  measurement is equal to 1.1%,  $\sigma$  is 0.8%,  $\kappa$  is 2.1% with confident probability 0.98.

#### Description of the measuring system block-diagram

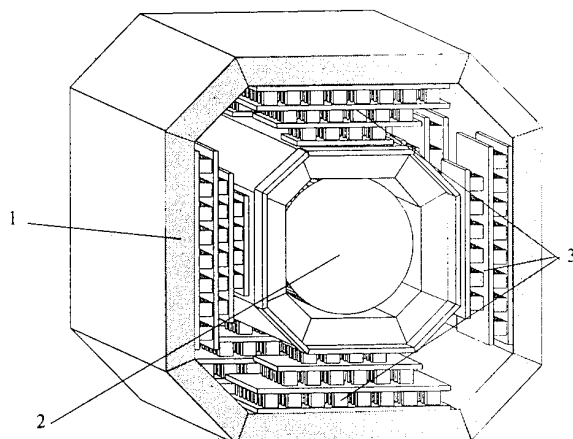
The block-diagram of the information measuring system may be arbitrary divided into two large parts, instrumental and program.

Instrumental part of the measuring system includes the next components: 1)measuring cell itself, 2) D.C precision amplifier block on which inputs signals from differential thermocouples, resistance thermometers are delivered, 3) multiplexer-commutator, 4) digital voltmeters supplied with interface in standard IEEE-488, 5) personal computer of IBM PC type that is the controller in the system, 6) current sources controlled by digital code for operation conditions specification of three-stage thermoelectric cooling modules, 7) a vacuum unit. 8) a compression refrigerator.

Fig.2 gives the diagram of three-stage thermoelectric modules arrangement relative to the sample studied and the arrangement of these modules relative to external heat sink.

*Fig.2. The diagram of thermoelectric modules arrangement relative to the studied sample and external heat sink.*

1 - the external heat sink, 2 - the chamber with studied sample, 3 - three-stage thermoelectric cooling modules.



The program part of the measuring system performs the next functions:

1) it is the controller in information gathering system from the measuring equipment;

2) it generates signals for the control by current sources feeding thermoelectric modules;

3) it commutes signals from the differential thermocouples, resistance thermometers and the like,

4) it performs the thermoregulator algorithm by proportion-integral law in three canal regime;

5) it sets temperature points and measures  $\alpha$ ,  $\sigma$ ,  $\kappa$ ;

6) it permits an operator to intervene both as to the process of a temperature point setting and directly to measurements;

7) it controls  $\alpha$ ,  $\sigma$ ,  $\kappa$  functions on temperature at the computer monitor display;

8) it prints results and so on.

#### Description of the measuring unit operation algorithm

Programmly and instrumentally the measuring unit is made in such way that each of blocks generates the information that is the "event". In this connection the algorithm of the measuring unit operation is based on the information/event mechanism transmitted to the basic module of the program called the information/event supervisor. All information/events result in one or other relations of the main program that passes the control to the corresponding procedures.

At the beginning of the whole program operation the testing and equipment serviceability control takes place, to do this there are built-in corresponding functions into the apparatus part. After this the program learn the value of the first temperature point from an operator and initializes the mechanism of information.

Exit to the given temperature point is ensured by the three-canal program thermoregulator. Two canals of the thermoregulator output the sample itself at the given temperature regime. The third canal of the thermoregulator acts as a gradient heater, for  $\alpha$ ,  $\kappa$  measurements. As the thermoregulator system sets the required temperature with required precision it informs the "event supervisor" about it. The measurement command is formed after that the system passes to the next temperature point. The use of parallel and independent operation of three thermoregulators enables sufficiently to reduce time of output at the required temperature.

At the intervals between measurements the operator can actively control the process of output at the regimes, for that the monitor display can give the output curves at these regimes.

Besides the main tasks the program do measurement statistics and calibrated "zeroes" of equipment and so on.

#### Conclusion

Use of the above described system permits to determine  $\alpha$  with an accuracy no worse than 1.3%,  $\sigma$  - 1%.  $\kappa$  - 2.5%.

The information system of main thermoelectric material parameters measurement is a good equipment for precise and quick investigations conduction. Use of such systems enable to increase the capacity of highly precise measurements in a wide temperature range.

#### References

- [1]. L.I.Anatychuk. Thermoelements and Thermoelectric Devices. Kiev: Naukova dumka, 1979, 767 p.
- [2]. L.I.Anatychuk, S.V.Pervozvansky, V.V.Razinkov. Precise Measurements of Cooling Thermoelectric Material Parameters: Methods, Arrangements and Procedures. Materials of the XII Int, Conf. on Thermoelectrics, Yokohama, Japan. - 1993, - pp. 553-564.

# A new kind of gradient heating for thermopower measurements at low temperatures and high magnetic fields

R.Resel, E.Bauer, T.Nakama<sup>1</sup>, M.Higa<sup>1</sup>,  
K.Yagasaki<sup>1</sup>, A.T.Burkov<sup>2</sup>

*Institute for Experimental Physics, Technical University Vienna, Austria*

<sup>1</sup> *College of Science, University of the Ryukyus, Okinawa, Japan*

<sup>2</sup> *A.F. Ioffe Physical - Technical Institute, St. Petersburg, Russia*

A measurement system was built up for thermopower measurements of small metallic samples in the low temperature range of 3K up to 320K and at magnetic fields up to 15 Tesla. Two gradient heaters on either end of the sample are used for generating temperature gradients along the sample; during the measurement always one of both heater is on. We obtain by a special heating method the subtraction of the spurious voltages, excellent thermal stability of the sample and good measurement accuracy. We adapted the system with the calibration of the Chromel - Constantan thermocouples for thermopower measurements at high magnetic fields. The cryogenic design of the sample holder allows small temperature gradients ( $\Delta T \approx 0.2\text{K}$ ) by a small heating power. Experimental results on pure In at zero field and at 4.8T are presented and compared with literature data.

## Introduction

The thermopower of small metallic samples at low temperatures are measured with the differential method. A small temperature difference  $\Delta T$  ( $< 1\text{K}$ ) is applied along the sample by a gradient heater. A small thermal voltage is generated and spurious voltages are source of error. Special techniques are required for the subtraction of the spurious voltages, they are connected mostly by changing the state of the gradient heater. However, at low temperatures a change (i.e. switch off) of the gradient heating power is connected with destabilizing of the middle sample temperature and additional errors arises. Our method of gradient heating, we call it "Seesaw Heating", overcomes these problems.

With the use of Chromel - Constantan thermocouples which show small magnetic field dependence [1,2] and due to two separate calibration procedures, one for the relative thermopower of the Chromel - Constantan thermocouple  $S_{ChCo}$  and the other for the absolute thermopower of our reference material Chromel  $S_{Ch}$ , we adapted the system for measurements at high magnetic fields. However, the use of Chromel - Constantan thermocouples makes the application only above 3K possible. With this system we can perform measurements in the temperature range 3 ... 320K and in magnetic fields up to 15 Tesla.

## The Experimental Setup

Seesaw Heating is alternating heating on either end of the sample as suggested in the upper part of fig.1; the two heaters are indicated besides the sample X. The state *heater 1 on* and *heater 2 off* heats the left side of the sample and a temperature difference  $\Delta T_1$  is set up. After the accommodation time the state of the heater system is changed to *heater 1 off* and *heater 2 on* and a temperature difference  $\Delta T_2$  on the other side of the sample is generated. During the measurement the heater system is always switched between these two states. The sample is provided at all the time by the same amount of heat, therefore, we get good thermal stability.

The thermal voltages are taken by thermocouples as depicted in fig. 1. The Chromel - Constantan wires are spot welded to each other, the junctions are touching the surface of the sample. The other end of the thermocouple legs are connected

with Cu, this junction is immersed in an ice bath. The Cu wires are lead to the voltage measurement equipments. The voltages  $V_{Chx}^{(1)}$  and  $V_{Chx}^{(2)}$  are generated in the Chromel circuit ( $\text{Cu} - \text{Chromel 1} - \text{Sample X} - \text{Chromel 2} - \text{Cu}$ ),  $V_{Cox}^{(1)}$  and  $V_{Cox}^{(2)}$  are the voltages in the Constantan circuit ( $\text{Cu} - \text{Constantan 1} - \text{Sample X} - \text{Constantan 2} - \text{Cu}$ ), the extensions denote the temperature difference  $\Delta T_1$  or  $\Delta T_2$ , respectively.

These four voltages are used for the thermopower measurement of the sample. The thermal voltage  $V_{ChCo1}$  arises from a conventional thermocouple circuit ( $\text{Cu} - \text{Chromel 1} - \text{Constantan 1} - \text{Cu}$ ),  $V_{ChCo2}$  is the thermal voltage in the second thermocouple circuit ( $\text{Cu} - \text{Chromel 2} - \text{Constantan 2} - \text{Cu}$ ); these two voltages are used for calibration. The voltage of the Chromel circuit is measured by a Keithley 2001 Multimeter with a Keithley 1801 Preamplifier; the voltages of the Constantan circuit,  $V_{ChCo1}$  and  $V_{ChCo2}$  are measured via a Keithley 7001 Switch System, 7168 Nanovolt Card with a Keithley 182 Nanovoltmeter.

With the assumption that the spurious voltage  $V_{Chw}$  in the Chromel circuit does not change during the accommodation time we obtain

$$V_{Chx}^{(1)} = S_{Chx} \Delta T_1 + V_{Chw} \quad V_{Chx}^{(2)} = -S_{Chx} \Delta T_2 + V_{Chw} \quad (1)$$

$S_{Chx}$  designate the relative thermopower between Chromel and the sample X:  $S_{Chx} = S_{Ch} - S_x$ ,  $S_{Ch}$  and  $S_x$  denotes the absolute thermopower of Chromel and of the sample X, respectively. A subtraction of these two voltages eliminates the wrong voltage of the Chromel circuit:

$$V_{Ch} = V_{Chx}^{(1)} - V_{Chx}^{(2)} = S_{Chx} (\Delta T_1 + \Delta T_2). \quad (2)$$

Similar equations are valid for the Constantan circuit and we obtain the measurement formula [3]:

$$S_x(T, B) = S_{Ch}(T, B) - \frac{V_{Ch}}{V_{Ch} - V_{Co}} S_{ChCo} \quad (3)$$

$S_{ChCo}$  as well as  $S_{Ch}$  are temperature and field dependent quantities, they are determined by calibration while  $V_{Chx}^{(1)}$ ,  $V_{Chx}^{(2)}$ ,  $V_{Cox}^{(1)}$  and  $V_{Cox}^{(2)}$  are obtained by voltage measurements.

An integral method is used to get  $S_{ChCo}(T, B)$ . Within our experimental setup (fig.1) we measure  $V_{ChCo1}$  and  $V_{ChCo2}$ , the thermal derivation of these voltages represent  $S_{ChCo1}$  and

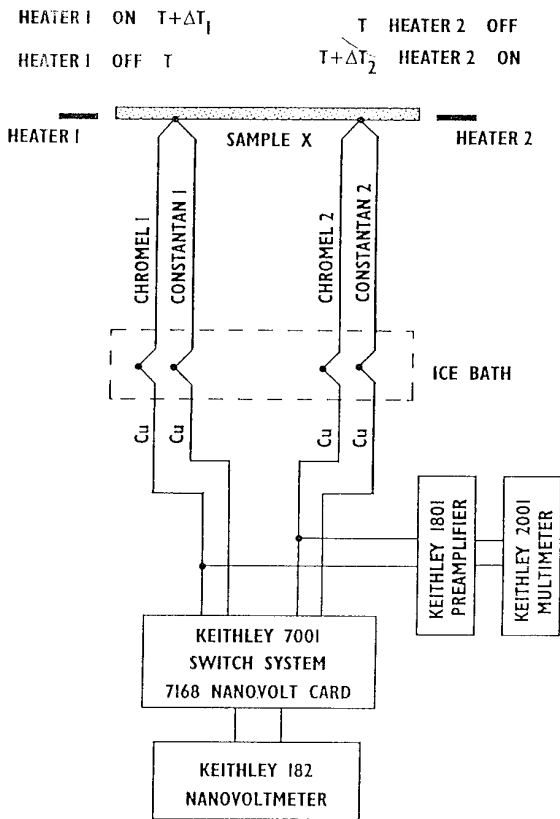


Figure 1: Setup for voltage measurement using a scanner and two voltmeters. The used circuits along the Cu wires and thermocouple legs are described in the text. The function of Seesaw Heating is suggested above, both heaters are drawn besides the sample.

$S_{ChCo_2}$ , respectively. This calibration was performed at zero field and at 15 Tesla. No significant difference could be detected between  $S_{ChCo_1}$  and  $S_{ChCo_2}$ , small field dependence could be detected only at very low temperatures ( $T < 6K$ ). However, the small values of  $S_{ChCo}$  makes a calibration below 3K impossible. From the second calibration procedure we got the temperature and field dependence of  $S_{Ch}$ . Pure Pb was used as sample to obtain the temperature and field dependence at high temperatures ( $T > 80K$ ); a strong influence of a magnetic field was detected for Pb at low temperatures [4]. A piece of  $YBa_2Cu_3O_7$  was used as sample to get  $S_{Ch}(T, B)$  at low temperatures ( $T < 80K$ ) and high magnetic fields. This calibration measurements was performed at zero field and at 3, 6, 9, 12 and 15 Tesla. A magnetic field change  $S_{Ch}$  slightly; the biggest change is  $0.8\mu V/K$ , it was observed in a magnetic field of 15T at the temperature of 60K. The results agree well with literature data [5,6].

The construction of the inner part of the sample holder is depicted in fig.2. The thermocouples are enclosed to cylindrical  $Al_2O_3$  ceramics (denoted as 8), their junctions are pressed with springs (9) to the surface of the sample. Of course, the thermocouples are thermally anchored to the heat sink (6). The temperature of the heat sink is measured with a  $RuO_2$  based thick film resistor (7) which obeys nearly no influence of a magnetic field and has a good reproducibility. The sample (crosshatched) is fixed between two electrical isolating materials, on one side glass epoxyd material (1) and on the other side

two AlN plates (2). The sample can be replaced by removing (1).

Two strain gauges are used as heater (4). They are glued to a thin layer of Cu (3) obtained from an electrical print plate (5+3). The thermal contact between sample and heater is good, because Cu as well as AlN provides good thermal conductivity even at low temperatures [7]. The part of the sample holder which obeys good thermal conductivity (2+3+4) is separated from the heat sink by glass epoxyd material (5) of low thermal conductivity which makes an upset of a temperature difference along the sample possible. The cryogenic characteristic of the sample holder is strongly dependent on the thickness of (5) and also on the thermal conductivity along the sample. Thin metallic samples of a minimum length of 9mm are necessary.

The inner part of the sample holder is constructed symmetrically, to obtain  $\Delta T_1 \approx \Delta T_2$ . A temperature difference of approximately 0.2K is generated with the heating power of 1mW at 3K and of 20mW at 300K. An accommodation time of 20s is used at low temperatures, at room temperatures 40s is required.

## Results

We chose pure In as test material for our measurement system. The temperature dependent behaviour of the thermopower  $S(T)$  shows a peak at about 20K, however different absolute values are reported [8,9].

The measurement of In at zero field and at 4.8T in the temperature range up to 100K is given in fig.3. The positive peak as well as the value of the absolute thermopower of In could be confirmed. A suppression of the peak by a magnetic field is detected similar to literature data [9]. So we can give the absolute accuracy of our system within  $1\mu V/K$  at all temperatures. The relative accuracy is within  $0.1\mu V/K$ .

## References

- [1] A.von Middendorff, *Cryogenics*, **11**, 318 (1971)
- [2] H.H.Sample, L.J.Neuringer, L.G.Rubin, *Rev.Sci.Instrum.*, **45**, 64 (1974)
- [3] E.Nagy, J.Toth, *J.Phys.Chem.Solids*, **24**, 1043 (1963)
- [4] A.D.Caplin, C.K.Chiang, P.A.Schroeder, *Phil.Mag.*, **30**, 1177 (1974)
- [5] C.K.Chiang, *Rev.Sci.Instrum.*, **45**, 985 (1974)
- [6] G.S.Abilov, B.I.Alshin, V.M.Belin, L.A.Medvedeva, N.G.Flerov, *Instrum.Exp.Tech.*, **26**, 239 (1983)
- [7] R.B.Dinwiddie, A.J.Whittaker, D.G.Onn, *Int.J.Thermophys.*, **10**, 1075 (1989)
- [8] B.Bosacchi, R.P.Huebener, *J.Phys.F*, **1**, L27 (1971)
- [9] A.D.Caplin, C.K.Chiang, J.Tracy, P.A.Schroeder, *phys.stat.sol.(a)*, **26**, 497, (1974)

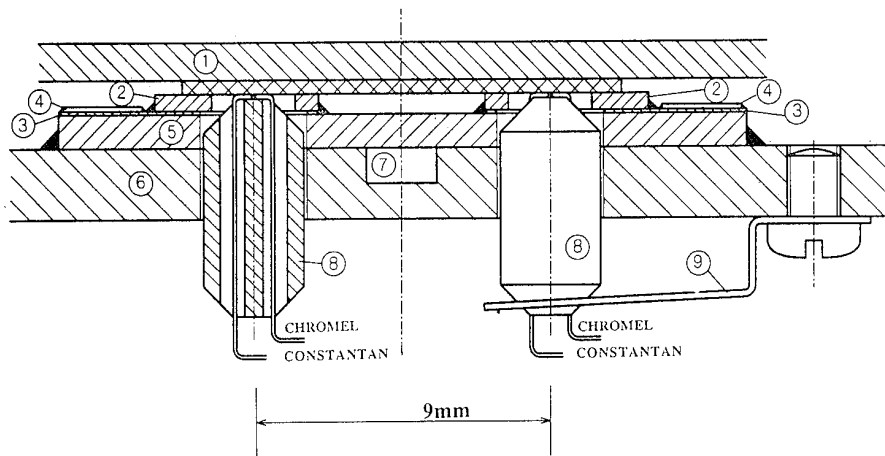


Figure 2: Cryogenic design of the sample holder: (1) glass epoxyd material, (2) AlN plates; (3) Cu layers, (4) heaters, (5) glass epoxyd material, (6) heat sink, (7) temperature sensor, (8)  $\text{Al}_2\text{O}_3$  ceramics, (9) spring

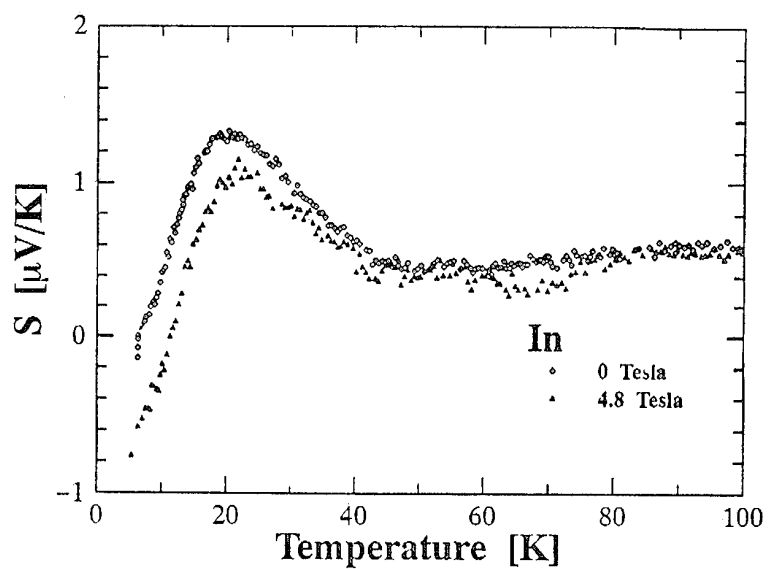


Figure 3: The thermopower of In as a function of temperature at zero and 4.8T.

## Evaluation of commercially available Peltier modules for use in hot-water driven thermoelectric generator

**D.M. Rowe, S.G.K. Williams and G.Min**

*NEDO Centre for Electronic Energy Conversion,  
School of Engineering, University of Wales Cardiff,  
Cardiff, CF2 1XH, United Kingdom.*

A method is described for accurately measuring the maximum electrical power output of low resistance thermoelectric modules ( $<<1\Omega$ ). The method eliminates problems associated with the temperature dependence of the module resistance. The normalised power outputs of commercially available Peltier modules when operated in the generating mode are obtained over the temperature range 20-90 deg C. The results indicate that the normalised power outputs serve as a "quality indicator" of the technology employed in the module manufacture.

### Introduction

Commercially available Peltier modules employ Bismuth Telluride materials, usually optimised below room temperature for thermoelectric cooling applications. Furthermore the geometry of these devices, including thermoelement dimensions, are designed for best performance in thermoelectric cooling [1].

Supported by the New Energy and Industrial Technology Development Organisation (NEDO), Japan, the thermoelectric group at Cardiff has embarked upon a programme of research into the large scale thermoelectric production of electricity from waste hot-water. Conventional Peltier cooler modules are used in the generating mode at an average hot-side temperature of around 95 deg C, with a temperature difference of upto 80 deg C. Of considerable relevance to the project is the generating performance of currently available modules when operated over this temperature range.

In this paper sixteen different thermoelectric modules, from eight manufacturers, have been compared for the electrical power output when operated with a temperature difference between 10-80K. A description of the method used to obtain a reasonably accurate estimation of the maximum power output from low resistance thermoelectric modules is given. A comparison is drawn of the power output, power output per

unit area, and cost per Watt, the manufacturer names and device numbers have been ommitted and are referred to by letters (A, B, C etc.) and the respective modules identified by roman numerals.

### Method

A temperature gradient was established across each module and the open circuit voltage,  $V_{oc}$  and short circuit current,  $I_{sc}$  measured. The maximum electrical output power of the module is given by [2] (see figure 1):

$$P_{max} = \frac{V_{oc} I_{sc}}{4} \quad (1)$$

$V_{oc}$ , can be measured accurately and without difficulties using a high impedance voltmeter. However to obtain  $I_{sc}$  accurately is very difficult, especially for very low resistance modules. When current measurements are made using an ammeter, with the internal resistance of the ammeter comparable to the module, a relationship between measured current,  $I_m$  and true short circuit,  $I_{sc}$  can be derived as follows.

$$V_{ab} = I_m R_m = E - I_m r = V_{oc} - I_m r \quad (2)$$

$$I_{sc} = E/r = V_{oc}/r \quad (3)$$

so  $r = V_{oc}/I_m - R_m$

$$\begin{aligned} I_{sc} &= I_m \left( 1 + \frac{R_m}{r} \right) \\ &= I_m \left( \frac{V_{oc}}{V_{oc} - I_m R_m} \right) \end{aligned} \quad (4)$$

Consequently,

$$P_{\max} = \frac{I_m V_{oc}^2}{4(V_{oc} - I_m R_m)} \quad (5)$$

The accuracy of this technique relies on the measurement of  $R_m$ , the internal resistance of the ammeter. A very low value of  $R_m$  is required for a high current flow, however this increases the error in the measurement of the resistance. In practice this method is suitable for higher resistance modules, although it gives large uncertainties ( $> 20\%$ ) for modules with resistance  $< 0.5 \Omega$ .

Another approach is to use a high impedance voltmeter to measure the voltage drop across an accurately known resistance. The resistance value should be low enough to achieve a large voltage drop, thus reducing errors in its measurement. However, very small resistance values become increasingly difficult to measure accurately, and it is important to take into account the resistance of the wiring and connections.

A high quality digital ohmmeter or bridge can be used to make resistance measurements to a resolution of greater than  $1 \mu\Omega$ . Experimentally, problems with reproducibility of connections to a circuit and effects of temperature change mean that a resolution of  $1 m\Omega$  is a realistic practical limit. Therefore the total load resistance including wiring should not be smaller than  $0.1 \Omega$ , to achieve a measurement accuracy of around 1%.

The temperature stability of this resistance is also important and high wattage wirewound resistors are used to reduce the effects of Joule heating.

In figure 2 is shown the arrangement used to determine the maximum electrical power output of Peltier modules when used in the generating mode. The circuit comprises a  $0.1\Omega$  100W wirewound resistor (5% tolerance, temperature

coefficient 100ppm) and heavy duty microswitch. All interconnections are clamped tightly and made using high quality oxygen-free copper (OFC) cable. Prior to each measurement, the total resistance of the circuit is measured using a Keithley 197 digital meter, and is  $0.115 \pm 0.001 \Omega$  at 20 deg C. The module is connected to the circuit using 13A screw-connectors. Open circuit voltage across the module is measured using a Keithley 197 digital microvoltmeter, this reads the voltage drop across the total load resistance when the switch is closed.

A single-module thermoelectric generator, designated WATT-1 (Waste-heat Alternative Thermoelectric Technology) was used for the module evaluation, shown schematically in figure 3. The generator block is comprised of two identical water channels fitted with flat copper heat-exchanger plates as a lid to each channel. The thermoelectric module tested is sandwiched between the two heat-exchanger plates, thermal contact between the module and plates was improved using a high thermal conductivity paste.

A Haake B3 circulator with 2kW heater (DC1-B3) provided a variable/constant temperature hot water source to one of the channels. The circulator was modified so that its temperature control sensor could be fitted near the inlet to the water channel, thus providing a stable input temperature independent of water flow. The second channel was supplied with variable/constant temperature cold water using a NESLAB GP200DP circulator and immersion cooler (NESLAB CC6511FV). The flow rates of the hot and cold supplies were variable and measured using electronic rotary flow sensors. Water and copper plate temperatures for both hot and cold water channels were measured using calibrated K-type thermocouples. Thermocouple outputs were connected to a scanner/microvoltmeter system (Keithley 199) using a reference junction oil-bath.

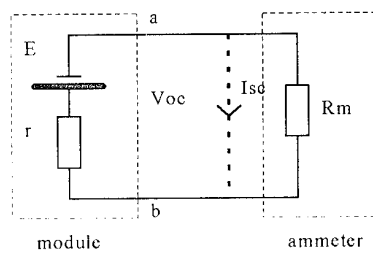


Figure 1. Relationship between measured current and short circuit current for low resistance thermoelectric modules.

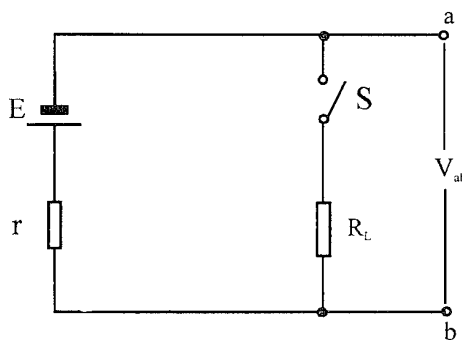


Figure 2. Measurement of maximum power output of a module operating in the generating mode.

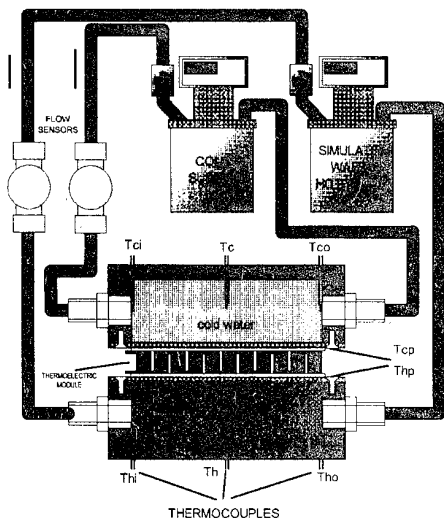


Figure 3. Schematic diagram of single module thermoelectric generator

## Results

In figures 4 and 5 are shown the maximum power output of each module plotted against temperature difference across the device, for 127-element and 31/50 element modules respectively. In figure 6-8 are shown a comparison of the maximum output power values for different manufacturers and devices, for a temperature difference of 40K, 60K and 80K respectively. Figure 9-11 shows how the output power per unit area (per 1000mm<sup>2</sup> or approximately 3cm x 3cm) compares between

devices and manufacturers for temperature differences of 40K, 60K and 80K respectively. This normalisation does not take into account the total element area of the device, since there are usually spaces between the thermocouples. In figure 12-14 the average cost per Watt for each device operating at temperature differences of 40K, 60K and 80K respectively are compared. These values are based on current prices (1994-95) and do not reflect any discount possibly available on larger quantity purchases.

## Discussion and Conclusions

As can be seen from figure 4 and 5, there is a significant variation in the output powers of 127-element modules, compared to the higher current devices comprising 31 or 50 thermocouples. There is a general trend in variation of maximum power output with thermocouple length, with the shorter thermocouples producing higher output. Only 2 of the devices show significantly higher output powers of around 1.5W, an indication of possibly higher device quality, with most devices having similar outputs of around 1W for a temperature difference of 75K. One of the devices, F(ii), has a very low output of only 0.7W at a temperature difference of 75K. Thus an almost doubling of output power ( $\Delta T=75K$ ) can be expected by changing from between small devices F(ii) to E(iii). Device D(i) is also comparable with E(iii), and has a slightly longer thermocouple length of 23%. A shorter element device from this manufacturer would be worth studying.

There is less variation in output power levels for the 31/50 thermocouple devices studied, see figure 5. This can be explained by the similarities in thermocouple length. Output powers range from 1.45W to around 2W for a temperature difference of 75K.

A maximum output power of over 0.5W can be achieved for an operating temperature difference of 40K, as shown in figure 6.

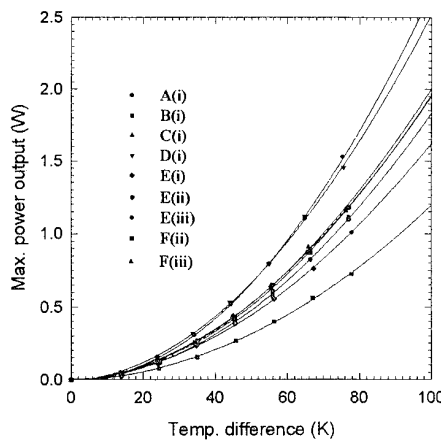


Figure 4. Maximum power output as a function of temperature difference for Peltier modules comprising 127 thermoelements.

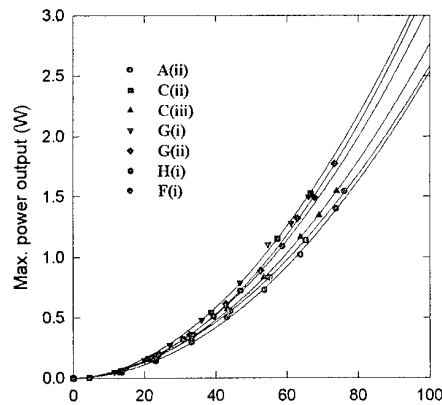


Figure 5. Maximum power output as a function of temperature difference for Peltier modules comprising 31 or 50 thermoelements.

using four of the modules investigated. Average output power is 0.41W for the sixteen devices studied, with a low of 0.21W produced by device F(ii). For higher temperature differences of 60K and 80K (as shown in figures 7 and 8) the average power output increases to 0.90W and 1.56W respectively. At  $\Delta T=80K$ , a maximum output power of 2.18W is achievable using devices C(ii) or G(i).

In figures 9-11 are shown output power normalised to a device surface area of  $1000\text{mm}^2$ , about 3cm by 3cm. It should be noted that the variation in power output values is smaller than shown in figures 6-8. For a temperature difference of 40K there is a difference of 0.17W when normalised, compared to 0.38W in figure 6. The data shown in figures 9-11 provides a "quality indicator" for the technology employed in the modules, that is thermoelement geometry, semiconductor materials, contacts and packaging. Thus for a temperature difference of 80K, three of the sixteen modules investigated can offer power outputs of greater than 1 Watt per  $1000\text{mm}^2$ .

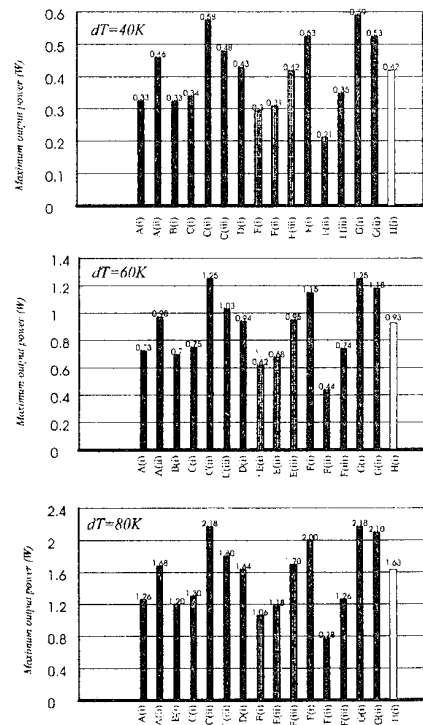


Figure 6-8. Comparison of maximum power outputs of Peltier modules when operated in the generation mode , for temperature differences of 40, 60 and 80K respectively.

In considering the choice of device, cost is of importance. Figures 12-14 provide an indication of the raise in cost per Watt, of the devices studied for different temperature differences. Clearly the cost per Watt is reduced dramatically when employing higher temperature differences, typically by four times when  $\Delta T$  is increased from 40 to 80K. At

$\Delta T=40K$ , costs vary from as little as £12.62 per Watt to £246 per Watt. At  $\Delta T=80K$ , the minimum cost per Watt is £3.12 for manufacturer E, with the average cost per Watt being £18.

Finally in figure 15 is shown how the cost per Watt varies with temperature difference of operation and type of device. The reduction in cost for an increase in operating temperature difference is consistent for all devices studied, the most significant reduction in cost can be achieved between selecting suitable devices. From this graph it is possible to estimate the cost per Watt for a specific temperature difference and device.

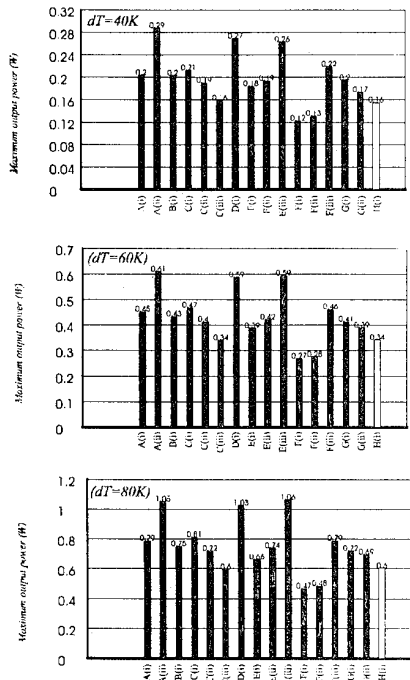


Figure 9-11. Comparison of maximum power output per unit area ( $1000\text{mm}^2 \approx 3 \times 3 \text{ cm}$ ) of Peltier modules when operated in the generation mode , for temperature differences of 40, 60 and 80K respectively.

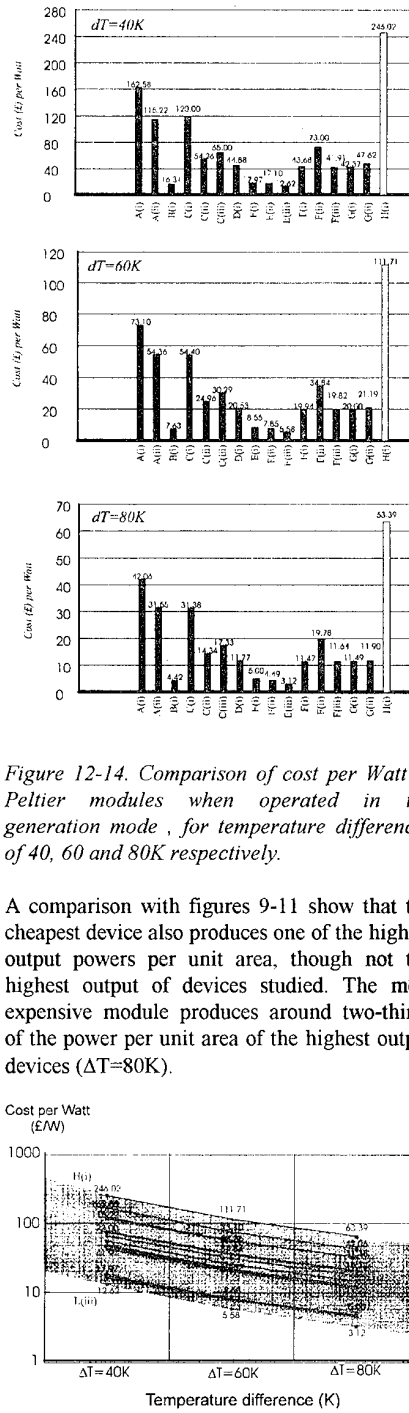


Figure 12-14. Comparison of cost per Watt of Peltier modules when operated in the generation mode , for temperature differences of 40, 60 and 80K respectively.

A comparison with figures 9-11 show that the cheapest device also produces one of the highest output powers per unit area, though not the highest output of devices studied. The most expensive module produces around two-thirds of the power per unit area of the highest output devices ( $\Delta T=80\text{K}$ ).

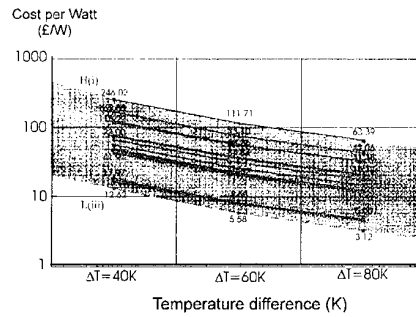


Figure 15. Variation of cost per Watt for different manufacturers and modules with temperature difference across device.

Another important factor in the choice of devices for generating applications is reliability. Reliability studies are presently being undertaken, the results will be published in a future paper. However preliminary studies indicate that although the cheapest modules investigated produce a high output power, they are not necessarily the most reliable of devices when operated above the temperatures intended for cooling.

### Acknowledgements

This work is supported by the New Energy and Industrial Technology Development Organisation (NEDO), Japan.

### References

1. K. Uemura, Proc. 10th International conference on thermoelectrics, Cardiff, UK, pp.69-73, 1991.
2. H.J. Goldsmid, Applications of thermoelectricity, Methuen & Co., London, 1960.

# APPLICATION OF LASER DOPPLER ANEMOMETRY FOR EXPERIMENTAL INVESTIGATION OF THERMOELECTRIC ELEMENTS DYNAMIC DEFORMATION

N.A. Sidorenko and V.N. Soutorshin

*Institute for Problems in Mechanics,  
prospect Vernadskogo 101, PO 117526, Moscow, Russia*

Laser method of distant measurements of ultra low velocities and displacements based on the principle of Laser Doppler Anemometry is presented in the report. This method provides accurate direct observations of thermoelectric elements (Peltier or Seebeck) dynamic deformations. The validity of presented method is illustrated on the examples of investigation of dynamic deformation of Peltier cooling element.

## 1. Introduction

In solving the problem of reliability improvement of thermo electric (TE) elements (Peltier or Seebeck), it is very important to ensure direct measurements of deformation and the rate of deformation of TE branches and the whole TE elements in actual time of deformation process after electric current or heat begins to flow through TE elements.

It seems to be incorrect to use film or wire tensometers to measure small deformations of tested elements in the conditions of temperature variation during deformation process, because of considerable temperature dependence of tensometers resistance and uncertainty of tensor thermal conditions. Besides it is difficult to get reliable attachment of tensometers to a small rough surface of TE branch for example.

Methods of optic and electron microscopy are also hardly applicable for observations of dynamic deformation of TE branches and elements, especially if TE elements are mounted in operating device.

Commonly used laser interferometers allow to measure displacement of specimen surface with high accuracy but are sensitive to adjustment of their optics and give the best results only for displacements normal to investigated surface.

Recent development of multi exposure laser holographic interferometry methods allow to reconstruct the whole picture of tested specimen deformation in sequence of exposure time moments. But these methods also need very accurate adjustment of the whole setup and besides are very expensive in realization.

To facilitate initial adjustment of the laser set up of deformation measurements and improve accuracy of dynamic deformation measurements, it is preferably to pick out and measure only deformation altering in time. Such principle is realized in Laser Doppler Anemometry (LDA) methods, where Doppler signal of alternating phase reflected from moving tested specimen surface is an informative signal, which is picked out and undergone electronic treatment and measurement [1].

The characteristic values of velocities and displacements that need to measure during deformation process of TE elements are in the ranges of  $(0.01-10)\mu\text{m/s}$  and  $(0.1-100)\mu\text{m}$  correspondingly. So the corresponding Doppler frequency

shift for visible laser radiation is in the range of  $(0.01-10)\text{s}^{-1}$  and cannot be detect by ordinary LDA methods. The possibility of LDA method improvement to measure ultra low velocities and displacements was clearly shown in [2].

The object of the present report consists in:

- to give principles of ultra low velocities and displacements measurements by LDA methods,
- to give an example of LDA set up realization to investigate dynamic deformation of TE elements,
- to illustrate the benefit of LDA method on the examples of investigation of dynamic deformation of some Peltier cooling element like MELCOR's CP1.4-127-06L.

## 2. Principles of ultra low velocities and displacements measurements by LDA-method

It is well known, that frequency of coherent laser radiation scattered by moving (relatively the laser) sample surface reveals Doppler frequency shift  $\omega_D$ , which can be expressed in laboratory coordinate system and flat radiation front as:

$$\omega_D = (\mathbf{k}_s - \mathbf{k}_o) \cdot \mathbf{v}, \quad (1)$$

where  $\mathbf{k}_s$  and  $\mathbf{k}_o$  are wave vectors of scattered and original radiation correspondingly,  $\mathbf{v}$  is a velocity vector of scattering surface.

To separate low frequency Doppler deviation of original laser radiation frequency the differential scheme is used: original laser beam is splitting into two coherent beams, which are being focused then on tested surface area. The scattered laser beams are superimposed and received by photo receiver.

Doppler modulation frequency  $\omega_m$  of superposition amplitude of two scattered laser beams is:

$$\omega_m = \omega_{D1} - \omega_{D2} = (\mathbf{k}_{s1} - \mathbf{k}_{o1}) \cdot \mathbf{v} - (\mathbf{k}_{s2} - \mathbf{k}_{o2}) \cdot \mathbf{v}, \quad (2)$$

or approximately

$$\omega_m = k \cdot v \cdot \cos\phi \cdot \alpha, \quad (3)$$

where  $\omega_{D1}$  and  $\omega_{D2}$  are the Doppler frequency shifts of the first and second coherent laser beams,  $\alpha$  is an angle between wave vectors of two laser beams falling on tested surface (ordinary  $\alpha \ll 1$ ),  $k = 2\pi/\lambda$  and  $\lambda$  is a wavelength of laser radiation,  $V$  is a value of scattering surface velocity,  $\phi$  is an angle between  $V$  and scattering vector ( $k_s - k_o$ ).

In the case of fixed wave vectors difference ( $k_{o2} - k_{o1}$ ) of original probing laser beams, the variation  $\delta\omega_m$  of Doppler modulation frequency depends on variation  $\delta V$  of velocity vector of scattering surface and variation  $\delta(k_{s1} - k_{s2})$  of wave vectors difference of scattered laser beams:

$$\delta\omega_m = [(k_{o2} - k_{o1}) - (k_{s1} - k_{s2})] \cdot \delta V + \delta(k_{s1} - k_{s2}) \cdot V . \quad (4)$$

The variation  $\delta(k_{s1} - k_{s2})$  is determined by change of reflection properties of tested surface area, which are not depended on surface movement directly.

Output voltage  $U(t)$  of photo receiver which detects scattered laser radiation is in general:

$$U(t) = U_b(t) + U_D(t) \cdot \sin(\omega_m t) , \quad (5)$$

where  $U_b(t)$  is background signal,  $U_D(t)$  is an amplitude of Doppler signal.

During measurement of ultra low values of  $V$  underground and Doppler signals has similar low frequency spectra, so special modulation of the probe laser beams should be used to separate Doppler signal [2]. Let phase of one of the probe beams undergoes pulse modulation by the value  $\pm\pi/2$  with period  $T$ , where  $2\pi/T > \omega_m$ ,  $\delta\omega_m$ . Modulation phase shift is described in Fig.1.

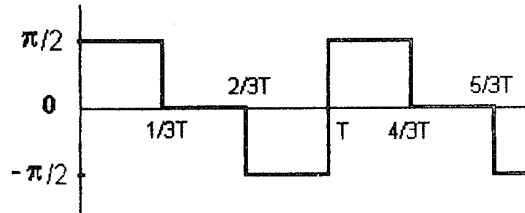


Fig. 1. Additional shift of probe beam phase due to phase pulse modulation.

As a result of such pulse phase modulation three two-beam interference lattices are arising on scattered surface. Two of these lattices are shifted in space relative central lattice by the distance  $\pm\lambda/4$ , due to phase shift  $\pm\pi/2$  of modulated probe beam. These three lattices exist in different time intervals and there is no interaction among them.

In a motion of tested surface area through interference lattices the variation of scattered laser radiation intensity arises. The laser radiation receiver output voltage  $U(t)$  during

every period of modulation can be expressed as a sequence of three scattered Doppler signals:

$$U_i(t) = U_b(t) + U_D(t) \cdot \sin[(\omega_m t + (2-i)\pi/2)] , \quad (6)$$

where  $i=1, 2, 3$  during first, second and third parts of modulation period correspondingly (see Fig.1).

The receiver output signal  $U(t)$  should be splitted up into three separated Doppler signals in accordance with their modulation phase shift. The splitting procedure is carried out with the help of electronic commutator, which switch signal  $U(t)$  between three partial signal lines every  $T/3$  part of modulation period.

After smoothing procedure of separated signals there are three separated low frequency Doppler signals  $U_i(t)$  shifted relative each other by the phase value  $\pm\pi/2$ . To eliminate background signal  $U_b(t)$ , smoothed Doppler signals  $U_i(t)$  are sent to arithmetic processor to carry out the following procedure:

$$U_2(t) = [U_1(t) + U_3(t)]/2 . \quad (7)$$

So the output arithmetic processor voltage  $U_{out}(t)$  is free of background component:

$$U_{out}(t) = U_D(t) \cdot \sin(\omega_m t) . \quad (8)$$

The general requirements of equation (8) fulfillment are: flat laser radiation front and sufficiently high frequency of laser phase modulation in comparison with Doppler modulation frequency  $\omega_m$  and its variation  $\delta\omega_m$ .

Signal  $U_{out}(t)$  is send to the input of electronic block of low frequency measurement. The output voltage  $U(\omega_m)$  of this block is proportional to  $\omega_m$  and after digital integration serves to control deflection of both laser beams so that spot of laser radiation on tested surface area moves together with this area and illuminates always the same part of tested surface. As a result of such control signal is minimized and the output signal of integrator  $U(\delta x)$  is proportional to displacement  $\delta x$  of illuminating part of tested surface.

Sign of velocity of scattering surface motion is determined by determination the sign of difference between values of phase of  $U_1(t)$  and  $U_2(t)$  signals:

-the difference  $+\pi/2$  corresponds to positive sign of  $\omega_m$  and  $V$ ,

-the difference  $\pi/2$  corresponds to negative sign of  $\omega_m$  and  $V$ .

So the presented method is the LDA method of velocities and displacements measurements with compensation of Doppler signal. The output information signals are: velocity and displacement of scattered tested surface and sign of velocity.

### 3. LDA set-up and experiment

The structural scheme of experimental LDA set-up realizing the above mentioned LDA principles are depicted in the Fig.2. The set-up consists of single mode He-Ne laser 1 of  $\lambda=632.8\text{nm}$  and power 3mW, focusing lens 2, laser beam splitter 3, modulator of probe laser beam phase 4, deflector of the probe laser beams 5, focusing lens 6, receiver optics 7, photo receiver 8, synchronizer 9, 10-12 - synchronized switches of electronic commutator, 13-15 -low frequency smoothers, arithmetic processor 16, selector of velocity sign 17, frequency measurement scheme 18, integrator of the Doppler signal 19, tested TE element 20, plotter 21 to record time dependence of displacement of tested surface area. Arrows in the Fig.3 indicate directions of laser beams wave vectors.

The output voltage of integrator 19 is send to deflector 5 of the probe beams and to the "Y" input of plotter 21. Synchronized total signal controlling modulator 4 and partial signals controlling switches of electronic commutator are shown in Fig.2 also.

In order to demonstrate some facilities of the LDA method in experimental investigation of TE batteries dynamic deformation some experiments were performed to register dependence on time of TE branch displacements, after moment when electric current begins to flow through TE battery. The tested TE battery ( $40\times40\times3\text{mm}^3$  of dimensions) consisted of 127 thermocouples is produced by NORD Co. (Moscow, RUSSIA). The USA equivalent of tested battery is MELCOR's CP 1.4-127-06L.

The general scheme of experiment is presented in Fig.3. The probe laser beams 1 and 2 is focusing on surface of outlying branch near cold side of TE battery 3. The area of irradiated spot on the branch surface is approximately  $0.1\text{mm}^2$ . The tested TE battery is mounted inside vacuum chamber 4 on massive copper base 5 with the help of needle press (6) and BeO paste. This ensures good thermal contact of TE battery and copper base 5 and approximately constant temperature of battery hot side during experiments. The hot side temperature is measured by thermocouple 7.

Temperature difference  $\Delta T$  between hot and cold sides of TE battery during experiments is measured by thermocouple 8. The signal of thermocouple 8 is send to "Y" input of plotter and time dependence of  $\Delta T$  is recorded by coordinate plotter during experiments. Simultaneously time dependence of displacement signal  $U(\delta x)$  is recorded by another coordinate plotter.

Some experimental results of observation of TE branch dynamic deformation by LDA method are presented in Fig.4. Here curves 1 and 2 show time dependence of displacement  $\delta x$  of chosen surface area (where both of probe laser beams are focused) of tested TE branch. Points  $x_{01}$  ( $x_{02}$ ) and  $x_{f1}$  ( $x_{f2}$ ) indicate original (before DC electric current turn on) and final (after electric current being turned on for a long time) coordinates of chosen surface area of tested TE branch. Number 1 corresponds to electric current  $I=1.6\text{A}$  and maximum of temperature difference (at this value of I)  $\Delta T_{\max}=30^\circ\text{C}$ , number 2 corresponds to  $I=2.2\text{A}$  and  $\Delta T_{\max}=36^\circ\text{C}$ . Values  $x_{f1}$  and  $x_{f2}$  corresponds to the

time when  $\Delta T_{\max}$  is achieved. In the Fig.4 the "on" indices indicate time moment when electric current begins to flow through TE battery. Curve 3 indicates time dependence of TE battery relative temperature difference  $\Delta T/\Delta T_{\max}$ . Comparison of 1-3 curves allows to connect TE branch deformation and regime of  $\Delta T$  alteration.

Presented experimental results show that deformations of TE branch are sufficiently sharper in the first part of deformation process caused by  $\Delta T$  increase. Perhaps such behavior of  $\delta x$  is the evidence of solder plastic deformation when the rates  $d(\delta x)/dt$  and  $d(\Delta T)/dt$  are sufficiently lower than in the first part of TE branch deformation.

Obtained results could be useful to formulate correct regime of TE battery operation to increase its life-time.

Of course, one should consider the obtained results as the first pilot results, which show the validity and prospects of presented LDA method in investigation of TE elements dynamic deformation.

### 4. Conclusions

Presented LDA method of time dependent deformation measurements allows:

- 1) to carry out distant measurements of deformation and rate of deformation of TE elements in wide range of alteration of these parameters independently on environmental conditions at the place of TE elements (temperature, nuclear radiation, vacuum, liquid or gaseous surroundings etc.).
- 2) to determine requirements on "on-off" regime of TE batteries or another kinds of TE elements to increase their reliability and life-time,
- 3) to build up portable and inexpensive highly accurate device for distant measurements of small deformations and ultra low velocities of deformation; minimum surface area of object under investigation can be less than  $0.1\text{mm}^2$ .

### 5. References

- [1]. Yu. Dubnishev and B.S. Rinkevichus, *Methods of Laser Doppler Anemometry*, Moscow, 1982, 304 p. (in Russian).
- [2]. E.V. Cherstov, A.N. Mokhel, R.L. Salganik and V.N. Sutorshin, Investigation and prediction of creep and creep-like behavior of solids by laser methods, *Journal of Electronic Packaging*, 1992, v.114, No.9, pp.310-313.

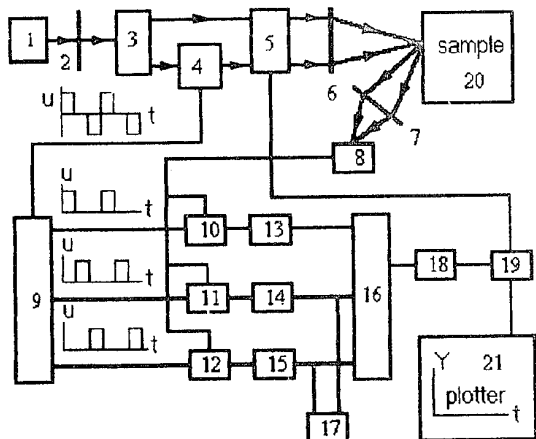


**Fig.2.** Structural scheme of experimental LDA set-up: (1) - single mode He-Ne laser of  $\lambda=632.8\text{nm}$  and power 3mW, (2) -lens, (3) -laser beam splitter, (4) -probe laser beam phase modulator, (5) -deflectors of the probe beams, (6) -focusing lens, (7) -receiver optics, (8) -photo receiver, (9) -synchronizer, (10)-(12) -synchronized switches of electronic commutator, (13)-(15) -low frequency smoothers, (16) -arithmetic processor, (17) -selector of velocity sign, (18) -frequency measurement scheme, (19) -integrator, (20) -tested sample of TE element, (21) -plotter to record time dependence of displacement of tested surface area. Arrows indicate directions of laser beams wave vectors.

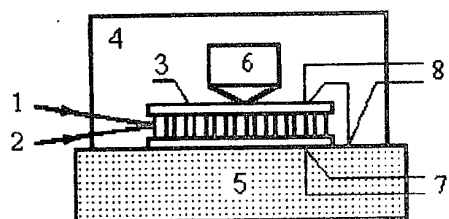


**Fig.3.** General scheme of experiment: (1) and (2) -the probe laser beams , (3) -TE battery, (4) -vacuum chamber, (5) -massive copper base, (6) -needle press , (7) -hot base thermo couple, (8) -temperature difference thermocouple.

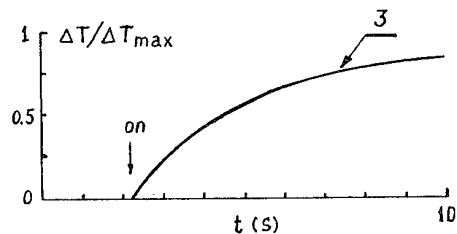
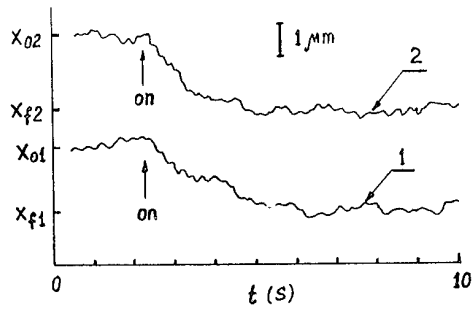


**Fig.4.** Experimental time dependence of measured by LDA method surface area coordinate of tested TE branch: curve 1 corresponds to DC electric current  $I=1.6\text{A}$  and  $\Delta T_{\max}=30^{\circ}\text{C}$ , curve 2 corresponds to  $I=2.2\text{A}$  and  $\Delta T_{\max}=36^{\circ}\text{C}$ , curve 3 indicates time dependence of TE battery relative temperature difference  $\Delta T/\Delta T_{\max}$ . The "on" indices indicate time moment when electric current begins to flow through TE battery.

#### Acknowledgments

The authors would like to thank Dr. E.V. Cherstov for help and useful discussions.

# THERMOELECTRIC LINEAR MOTOR

Lev P. Bulat

*St.Petersburg State Academy of Refrigeration,  
Lomonosova St. 9, St.Petersburg, 191002, Russia*

The new type of linear electric motor — "Thermoelectric Linear Motor" is suggested. The motor used two effects: 1) the Peltier effect and 2) the form memory effect. The theoretical and experimental analysis shows that the Thermoelectric Linear Motor has some important advantages over traditional linear motors. This advantages gives a possibility to use the Motor for designing of effective and reliable manipulators for creation different automatic control systems.

In our report we suggest the new type of linear electric motor, we call it "Thermoelectric Linear Motor" (TELM) [1]. The TELM used two effects: 1) the Peltier effect; 2) the form memory effect.

There are known a lot of materials holding the form memory [2]. Let's consider a content of the form memory effect [2].

At first, let's give a new form (at a temperature  $T_g$ ) to a sample holding the form memory. Then we cool the sample to a temperature  $T_c$  which is lower than the special temperature  $T_m$  for this sample ( $T_m$  is the temperature of phase transition). The next step is a positive imparting of its original form to the sample and a liquidation of the deformation. After these manipulations we have to heat our sample to a certain temperature, which is upper than  $T_m$ . In this condition a sample with the form memory will reduce its form, which it got at the temperature  $T_g$ .

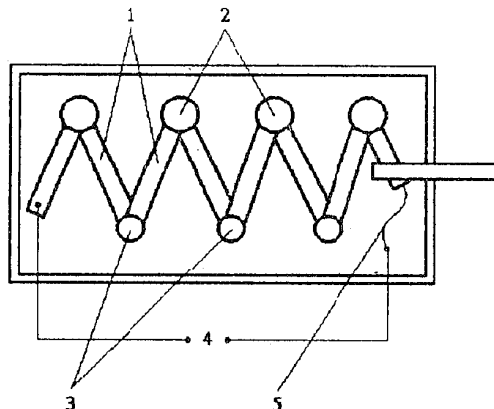
Recently there appears more than 500 papers, which suggested an application of materials with the form memory in energetic devices and machines for different purposes [2]. These materials used in designing and manufacturing of 1) linear and rotors motors; 2) sensors for temperature measuring, for heat protection and regulation; 3) connecting devices, e.g. couplings, commutators; 4) technical transforming blocks; 5) medical orthopedic devices etc.[2].

An efficiency and a reliability of energetic devices and machines with the form memory effect strongly depends on ways of energy admission and remission. We are sure that the thermoelectric method is the

best one of energy guaranteeing for the devices with the form memory effect. Really, this method gives a possibility to cool or to heat a battery junctions by reversing an electric current.

We suggest the Thermoelectric Linear Motor [1], which is a new type of linear electric motor with the thermoelectric method of cooling and heating material with the form memory effect. The main idea of this motor is shown on Fig.1.

Figure 1: The Thermoelectric Linear Motor



1 — semiconductor's branches (bars); 2 — electrical junctions under the branches from a material with the form memory; 3 — electrical junctions under the branches from a fixable wire; 4 — current source; 5 — conducting wire.

The TELM consists from a number of semiconductor branches *p*- and *n*-types (bars) 1, united in a thermoelectric battery. The upper electrical junctions between the branches carry out by the bridges from a material with the form memory 2. On the other side of the battery are the electrical junctions which are manufactured from a fixable wire 3.

When passing a direct electric current through the contact of *p*- and *n*-branches the temperature of the bridges is decreasing (or increasing) in accordance with the Peltier effect. Than the bridges are changing their form because of the form memory. Thus, the angle under *p*- and *n*-branches is changing and the thermoelectric battery also is changing as a whole its form as like as an accordion. The thermoelectric battery's branches are fixed kinematically on hinges (do not shown on Fig.1). So, an electric current leads to moving of the battery. The commutation of the current leads to reversion of moving (a tension changes to a pressing).

We designed an experimental device of TELM for investigation of its energetic characteristics. It is used  $\text{Bi}_2\text{Tc}_3$  of *p*- and *n*-types as a material for thermoelectric battery. Also it is used NiTi-55 as a materials with the form memory. We bridge to TELM an electric current with a known drain power (about 7W) to determine its efficiency. Mechanical power was measured with using a force measurer. A typical temperature of the hot junctions was

$T_0 \approx 260K$ , the temperature of the cold junctions was  $T_1 \approx 340K$ . The mechanical force  $F \approx (15.5 - 18.5)N$ , the time of movement reversing  $\tau \approx (8 - 10)s$ , the travel  $l \approx 0.8\text{cm}$ . The resulting efficiency was  $\eta \approx (0.2 - 0.3)$  per cent.

It was suggested a simple physical model for theoretical analysis of TELM's efficiency. In conditions of the experiment the formulae gives  $\eta \approx 12 - 15$  per cent.

An analysis shows that the TELM has several important advantages over traditional linear motors. Really, it is possible 1) to create with the TELM lower velocities of motor's working part, 2) to fix a working part in a necessary point, 3) to use a standard source of current; moreover, 4) the TELM is noiseless and 5) the TELM has small size. This advantages gives a possibility to use the TELM for designing of effective and reliable manipulators for creation different automatic control systems.

## References

- [1]. Bulat L.P., Gutsal D.D. The Electric Motor of Linear Motion. Patent No. SU 1394348 (USSR). Priority by 23.07.85. Publ.07.05.88.
- [2]. Proceeding of XXVI Int. Workshop for Materials with Form Memory Effect and its Application. St.Petersburg, ADVELA, 1992.

## STAGE THERMIONIC AND THERMOELECTRIC ENERGY CONVERTER

L.I.Anatychuk<sup>1</sup>, L.N.Vikhor<sup>1</sup>, Yu.V.Nikolaev<sup>2</sup>

<sup>1</sup>Institute of Thermoelectricity, Chernovtsy, 274000, General Post Office, box 86, Ukraine

<sup>2</sup>SIA-Lutch, Podolsk, Moscow Region, 142100, Zheleznodorozhnaya Str.,24, Russia

Optimal control methods are used for the best characteristics of complex electric energy generation combined system calculation. High-temperature stage of this system has a thermionic converter, low-temperature has a stage thermoelectric generator. Examples demonstrating such designing efficiency for stage energy conversion systems have been given.

### Introduction

Development of new nontraditional high effective schemes of direct thermal energy conversion into the electric energy is the important and actual problem. Thermoelectric and thermionic generators made a good showing as stationary thermal energy converters.

Thermoelectric method of conversion is the most developed one. This enables to design power sources with conversion efficiency up to 18%.

Such efficiency value can be provided with thermoelectric generator stage schemes, each stage must be made of semiconductor materials with best figure of merit for a stage operating temperature range. This is connected with thermoelectric material figure of merit heavy dependence on temperature [1] and their dependences maximum position for different materials at different temperatures.

Today there is no thermoelectric materials of *p*- and *n*-types with sufficiently high figure of merit in the temperature range higher 1300 K. This fact and technological problems connected with production of high-temperature batteries (with hot junction temperature up to 2000 K) limit the temperature range of energy conversion thermoelectric method use.

On the other hand, in the temperature range of 1300-2000 K thermionic converters are effective [2]. Theoretically thermionic generators can provide the efficiency up to 30% at high operating temperatures of electrodes: an emitter temperature of about 2000 K, a collector temperature of about 1000 K. It is naturally lead to the idea of a combined thermionic-thermoelectric system of electric energy generation development, the operating range of which may be wide temperature range: from 300 K to 2000 K. Arranging thermoelectric generator hot junctions in thermal contact with collector of thermionic one we additionally convert a part of emitted from the collector energy into the electric one increasing thereby the conversion efficiency. This idea is not new. It was studied, for instance, in the Japanese papers [3,4]

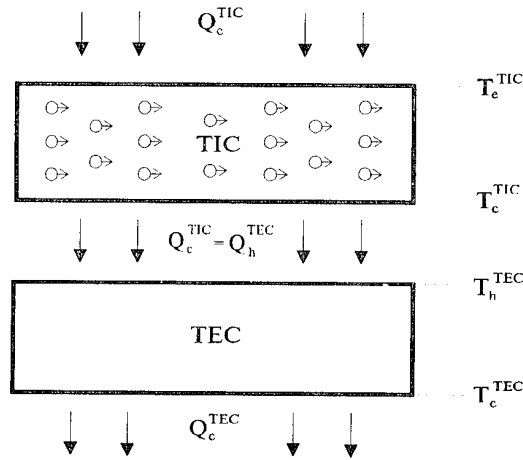
devoted to designing of Super-HYDECS - high effective hybrid direct energy conversion system.

The present paper proposes the method of such system optimization based on the optimal control theory methods. This method showed itself as an effective tool for combined cooling systems [5] and cascade thermoelectric energy converters design.

### Statement of the problem

Let us examine the possibilities for the optimal control method spreading on the combined thermionic-thermoelectric system of electric energy generation. Such device scheme is given in Fig.1. Optimization basic data

Fig.1 Thermionic-thermoelectric generator model.



include the emitter temperature of a thermionic generator (TIC)  $T_e^{TIC}$ , heat release surface temperature of a thermoelectric generator (TEC)  $T_c^{TEC}$ , as well as the experimental dependence of thermionic converter

efficiency on emitter temperature  $T_e^{TIC}$  and collector temperature  $T_c^{TIC}$  in the form

$$\eta_{TIC} = f(T_e^{TIC}, T_c^{TIC}) \quad (1)$$

Semiconductor material properties used in each cascade must be known for thermoelectric stage:

$$\begin{aligned} \alpha_{n,p} &= \alpha_{n,p}(T), \quad \sigma_{n,p} = \sigma_{n,p}(T), \\ \kappa_{n,p} &= \kappa_{n,p}(T) \end{aligned} \quad (2)$$

The problem of the generation combined system maximum efficiency achievement determined as

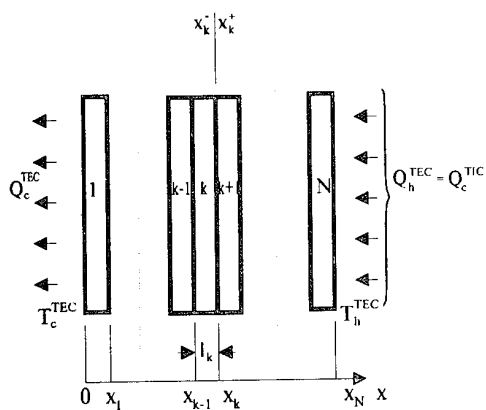
$$\eta = 1 - \prod_{i=1}^2 (1 - \eta_i), \quad (3)$$

is of the most practical interest. Here  $\eta_i$  - is the efficiency of the generator  $i$ -stage. Instead of (3) it is convenient to insert the functional

$$J = \ln(1 - \eta) = \ln(1 - \eta_{TIC}) + J_{TEC}, \quad (4)$$

where  $J_{TEC}$  is the functional of  $N$ -cascade thermoelectric stage scheme of which is given in Fig.2.  $J_{TEC}$  is defined by the expression

Fig.2.  $N$ -cascade thermoelectric generator model.



$$J_{TEC} = \sum_{k=1}^N (\ln q_0^k - \ln q_1^k), \quad (5)$$

with specific (referred to current intensity) heat fluxes on thermocouple junctions calculated as

$$\begin{aligned} q_1^k &= \sum_{n,p} [q(x_k^-) + i_k r_0] \\ q_0^k &= \sum_{n,p} [q(x_{k-1}^+) - i_k r_0] \end{aligned} \quad (6)$$

where  $r_0$  is electric resistance of a contact surface unit.

Specific fluxes involved into (6) depend on generated current densities  $i_k$  and legs size which can be varied. It is necessary to find such parameters values which deliver minimum to the functional  $J$  (4). Calculations of boundary heat fluxes are carried out similarly as in the problem of optimal control by a stage generator. Difference is in the form of boundary conditions for nonequilibrium thermodynamics differential equation system

$$\left. \begin{aligned} \frac{dT}{dx} &= -\frac{\alpha_k i_k}{\kappa_k} T - \frac{i_k}{\kappa_k} q \\ \frac{dq}{dx} &= \frac{\alpha_k^2 i_k}{\kappa_k} T + \frac{\alpha_k i_k}{\kappa_k} q + \frac{i_k}{\sigma_k} \end{aligned} \right\}_{n,p} \quad k = 1, \dots, N. \quad (7)$$

In this case heat absorbing surface temperature of thermoelectric stage is not fixed but is agreed with the collector temperature of the thermionic stage  $T_c^{TIC}$  and is the optimization parameter. The boundary conditions therewith have the form

$$\left. \begin{aligned} T_n(0^+) &= T_p(0^+) = T_c^{TEC}; \\ T_n(x_k^-) &= T_p(x_k^-) \\ T_n(x_k^+) &= T_p(x_k^+); \\ T_n(x_N^-) &= T_p(x_N^-) \\ T_n(x_k^-) &= T_n(x_k^+) + \delta T \end{aligned} \right\}_{n,p} \quad k = 1, \dots, N-1 \quad (8)$$

where  $\delta T$  is the temperature difference at the TEC cascades joint.

TIC efficiency value incorporated into (4) is determined by the experimental dependence (1). It is necessary to take into account that at the boundary between TEC and TIC temperature difference  $\Delta T$  arises, so

$$T_c^{TIC} = T_h^{TEC} + \Delta T \quad (9)$$

On the optimal control language the problem is stated as follows. There is an object in the form of the generation combined system that described by the differential equations system (7). The equations contain phase coordinates  $T$ ,  $q$  and  $2N$ -dimensional vector parameter  $i$ . The system mobility is limited by multi-point edge conditions (8), point location  $x_k$  is not fixed. It is necessary to find such values of  $i$ -parameter, coordinate  $x_k$  and phase trajectories  $T$ ,  $q$  which deliver minimum to the functional  $J$  (4) under (1), (8), (9) limitations. The fulfilment of these conditions defines thermoelectric stage optimal structure which is in agreement with the thermionic generator. The problem solution is effected on the base of the Pontryagin maximum principle [6] from which the functional extremum conditions in the optimal control problems are determined.

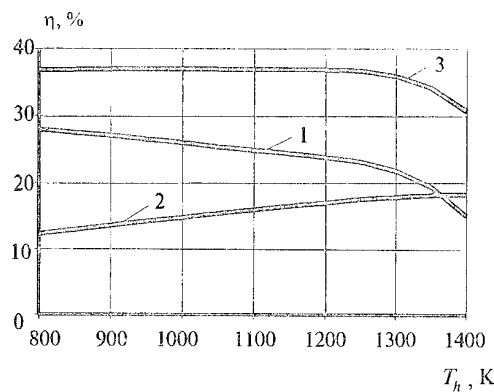
The computer program for optimal combined thermionic - thermoelectric systems of energy generation has been worked out.

## Results of calculation

The calculation of the combined generation system optimal efficiency operated at temperature difference 300-2000 K has been given as an example illustrated the outlined method possibilities. Thermoelectric stage of this system is a three-cascade generator. Low-temperature cascade was made of materials based on *Bi-Te*, average-temperature cascade - on the base of *Pb-Te*, high-temperature - on the base of *Si-Ge*. A generator used in Japanese project Super-HYDECS [4] was taken for the thermionic stage. The required for calculation its efficiency dependence on the collector temperature at the emitter temperature of 2000 K is given in Fig.3. The efficiency dependence of thermoelectric stage on heat absorbing junctions temperature and the total efficiency of the generation combined system as a function of interstage temperature are given in the same figure. It is seen that with temperature change between stages from 800 to 1200 K the efficiency of such combined system is practically unchanged. The obtained during calculation the efficiency maximum value was at the TIC and TEC boundary temperature of 950 K and is 37%. This value testifies about the efficiency of such electric power generation combined system.

*Fig.3. Efficiency dependence on temperature  $T_h$  between TIC and TEC. 1 - efficiency of thermionic stage,  $T_h^{TIC} = 2000K$ ,*

$$\begin{aligned} T_c^{TIC} &= T_h; \quad 2 - \text{efficiency of thermoelectric stage,} \\ T_h^{TEC} &= T_h, \quad T_c^{TEC} = 300K; \quad 3 - \text{efficiency of combined} \\ &\text{system, } T_h^{TIC} = 2000K, \quad T_c^{TEC} = 300K. \end{aligned}$$



[3]. Niiono Masauyki, Chen Lidong. Projected Research on High-efficiency Hybrid Direct Energy Conversion System. In Proc. of 12th International Conf. on Thermoelectrics, Japan, Nov., 1992, pp.527-531.

[4]. K.Eguchi, T.Hoshino. A Design Approach to Super HYDECS for Space Power Applications, in Proc. of Japan-Russia-Ukraine International Workshop on Energy Conversion Materials, Japan, January, 1995, p.165-176.

[5]. L.I.Anatychuk, V.V.Razinkov, L.N.Vikhor. Combined Cooler Design by Optimal Control Theory Method. in Proc. of the 13th Int.Conf. on Thermoelectrics. Kansas, Aug. 1994.

[6]. L.S.Pontryagin, V.G.Boltyansky, R.V.Gamkrelidze, E.F.Mischenko. Mathematical Theory of Optimal Processes. M., Nauka, 1976, p.392.

## References

- [1]. A.S.Okhotin, A.A.Efremov, A.S.Pushkarsky et al. Thermoelectric materials. M. Atomizdat, 1971.
- [2]. Yu.V.Lazarenko, A.A.Pustovalov, V.P.Shapovalov. Portable nuclear electric power sources. M., Energoizdat, 1992.

## OPTIMAL CONTROL IN STAGE THERMOELECTRIC GENERATORS DESIGN

L.I.Anatychuk, L.N.Vikhor

*Institute of Thermoelectricity, Chernovtsy, 274000, General Post Office, box 86, Ukraine*

The present paper examines the possibilities of optimal control use for stage generators design. The computer program enables to solve best the problem of interstage matching considering temperature dependences of the material properties and all types of electric and thermal losses has been developed.

### Introduction

Advances in thermoelectricity practical application for electric energy generation are connected with maximum efficiency attainment which in the simplest case is determined by the expression [1]

$$\eta = \frac{T_1 - T_2}{T_1} \cdot \frac{M - 1}{M + \frac{T_2}{T_1}}, \quad (1)$$

$$M = \sqrt{1 + Z(T_1 + T_2) / 2}.$$

The formula includes thermodynamic component that is the Carnot cycle efficiency. The second term depends on thermoelectric material figure of merit  $Z$ . It follows from (1) that there are two possibilities for large values of the efficiency obtaining. The first is connected with temperature difference increase. The second consists in figure of merit increase. Both possibilities ultimately depend on thermoelectric material properties. On the one hand, the Carnot efficiency increase is limited by the thermoelement material melting temperature. On the other hand, the material quality defines its figure of merit and preservation of this parameter large value in the wide temperature range. All thermoelectric materials are characterized by temperature dependence of figure of merit in the form of the function with maximum. Hence there is optimal  $Z$  for each material only in the definite temperature range. Temperature ranges with rather large figure of merit values are not very wide and usually are in the range of 200 - 500 degrees. Thus it is appeared the conventional material separation on low, medium and high-temperature ones. The most effective ones stand out of the multitude of materials and are at present conventional for thermoelectricity [2].

Relatively narrow temperature intervals of materials brought the thermoelectric converters designers to the idea of stage generators development [3,4,5]. Each stage is made of material with the best figure of merit for the stage operating temperature interval.

It is necessary to note that stage generator optimization for maximum efficiency achievement is a

very complicated problem. The problem is in the necessity to consider starting material temperature dependences, commutation and contact resistances, interstage losses, heat exchange with surroundings. To calculate stage device characteristics as a whole, it is necessary to take into account the interaction of all stage regimes. Mathematical model of a thermoelectric generator is a system of heat-electric exchange equations connected by integration conditions [6]. Temperature dependences of material properties define nonlinearity of such model. Thus the problem of determination of thermoelectric energy converter characteristics reduces to the differential equations solution of the nonlinear system. It is necessary to use numerical methods to get the exact solution. This imposes difficulties in generation stage device optimization. To our mind sufficiently exact method of stage thermoelectric batteries design has not been developed up to now.

Institute of Thermoelectricity (Ukraine) conducts researches directed at such methods search. It gives the possibility for additional increase of thermoelectric energy generators efficiency.

The present paper proposes the method of stage thermoelectric generators optimization based on the optimal control theory methods. Just these methods were successfully used for stage coolers optimization [7]. It enables to solve best the interstage matching problem and to enhance electric parameters of stage coolers even without figure of merit improvement by 30-50%.

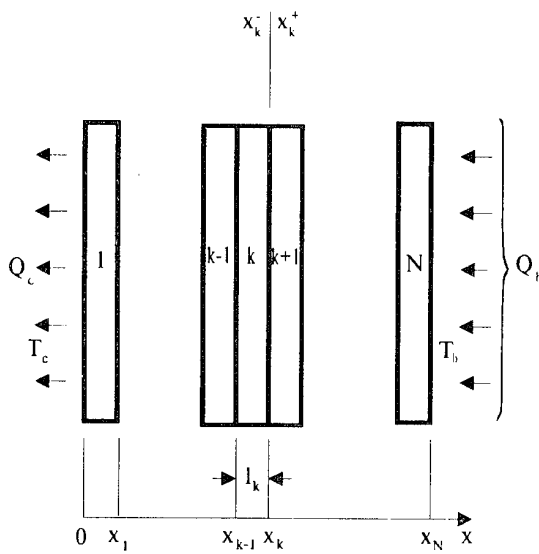
### Statement of the problem

Let us consider possibilities of optimal control use for stage generators efficiency optimization. Fig.1 shows the model of  $N$ -stage thermoelectric generator. Stage numbering is from cold to hot stage. Axis  $x$  giving a thermoelement length marking out is pointed to the same direction.

Starting data for optimization include the temperature of a heat absorbing surface  $T_h$  and the heat releasing temperature  $T_c$ . Temperature dependences of semiconductor material parameters such as Seebeck coefficient  $\alpha$ , electric conductivity  $\sigma$  and thermal

conductivity  $\kappa$ , must be also specified with its own material

Fig. 1.  $N$ -stage thermoelectric generator model.



used in each stage. It is also necessary to take into account losses connected with imperfection of thermal and electric contacts. Therefore contact resistance  $r_c$  and interstage temperature difference  $\delta T$  values should be added to the starting data.

The problem of a generator maximum efficiency is of considerable practical interest. It can be written as

$$\eta = \frac{Q_h - Q_c}{Q_h} = 1 - \varphi \quad (2)$$

where  $Q_c$ ,  $Q_h$  are external heat fluxes on cold and hot surfaces of a generator, respectively. Function  $\varphi = \frac{Q_c}{Q_h}$

may be considered as minimized functional. It may be conveniently represented as

$$\varphi = \prod_{k=1}^N \varphi_k, \quad (3)$$

where

$$\varphi_k = \frac{Q_0^k}{Q_1^k}, \quad k = 1, \dots, N, \quad (4)$$

$Q_0^k$ ,  $Q_1^k$  are  $k$ -stage heat on cold and hot surfaces. In (3) conclusion we used the equalities of the stage thermal matching

$$\begin{aligned} Q_0^{k+1} &= Q_0^k, \quad k = 1, \dots, N-1, \\ Q_0^1 &= -Q_c, \quad Q_1^N = -Q_h. \end{aligned} \quad (5)$$

For convenience let us pass on to the equivalent logarithmic functional  $J = \ln \varphi$ , which in view of (3) and (4) is brought to the form

$$J = \sum_{k=1}^N (\ln q_1^k - \ln q_0^k), \quad (6)$$

where

$$q_1^k = \frac{Q_1^k}{I}, \quad q_0^k = \frac{Q_0^k}{I}, \quad (7)$$

are specific (referred to current intensity) heat fluxes on the thermocouple junctions correspondingly. Expressions for these heat fluxes have the form

$$\left. \begin{aligned} q_1^k &= \sum_{n,p} [q(x_{k-}) + i_k r_c] \\ q_0^k &= \sum_{n,p} [q(x_{k-1}) - i_k r_c] \end{aligned} \right\}, \quad k = 1, \dots, N \quad (8)$$

They depend on the controlled parameters: generated current density in stages  $i_k$ . It is necessary to find such values of these parameters that deliver minimum to the functional  $J$ .

To calculate boundary heat fluxes  $q$  included into (8), it is necessary to use the system of  $4N$  differential equations of nonequilibrium thermodynamics

$$\left. \begin{aligned} \frac{dT}{dx} &= -\frac{\alpha_k i_k}{\kappa_k} T - \frac{i_k}{\kappa_k} q \\ \frac{dq}{dx} &= \frac{\alpha_k^2 i_k}{\kappa_k} T + \frac{\alpha_k i_k}{\kappa_k} q + \frac{i_k}{\sigma_k} \end{aligned} \right\}_{n,p}, \quad (9)$$

with temperature-dependent kinetic coefficients and boundary conditions

$$\begin{aligned} T_n(0^+) &= T_p(0^+) = T_c, \\ T_n(x_N^-) &= T_p(x_N^-) = T_h, \\ T_n(x_k^+) &= T_p(x_k^+), \\ T_n(x_k^-) &= T_p(x_k^-), \\ T_n(x_k^-) &= T(x_k^+) + \delta T \end{aligned} \quad (10)$$

the location of  $x_k$ ,  $k=1, \dots, N-1$  points is not fixed.

On the optimal process theory language the problem is formulated as follows. There is an object ( $N$ -stage generator) the behaviour of which is described by  $4N$ -dimensional system of differential equations (9) including phase variables  $T_{n,p}(x)$ ,  $q_{n,p}(x)$  and  $2N$ -dimensional vector-parameter  $i = (i_1, \dots, i_N)_{n,p}$ . The system mobility is limited by multi-point boundary conditions (10), the location of  $x_k$ ,  $k=1, \dots, N$  points is not fixed. The functional (6) can be specified as a phase coordinate function at the ends of interval and at the internal points. It is necessary to find the controlled vector-parameter  $i$ ,

coordinate  $x_k$  values and the corresponding phase trajectory  $T(x)$ ,  $q(x)$  for both types of thermoelements which deliver minimum to the functional (6).

The solution of the stated optimal problem is given by the Pontryagin maximum principle according to which the following conditions must be fulfilled for maximum  $J$ :

1. Current densities in stages must satisfy the equalities

$$-\frac{\partial J}{\partial i_{n,p}^k} + \int_{x_{k-1}}^{x_k} \frac{\partial H^k(\psi, T, q, i_n^k, i_p^k)}{\partial i_{n,p}^k} dx = 0, \quad (11)$$

$$k = 1, \dots, N,$$

where the Hamilton function  $H^k$  has the form

$$H^k = \sum_{n,p} (\psi_1 f_1^k + \psi_2 f_2^k), \quad (12)$$

$(f_1^k, f_2^k)_{n,p}$  - are the right parts of (9),  $\psi = (\psi_1, \psi_2)_{n,p}$  is pulses vector conjugated to phase variable vector  $y = (T, q)_{n,p}$ .

2. Coordinates of joint points  $x_k$  satisfy the conditions

$$H^k(x_k^-) = H^{k+1}(x_k^+), \quad k = 1, \dots, N-1. \quad (13)$$

3. Temperatures of joint points must satisfy the system

$$\sum_{n,p} \psi_1(x_k^+) = \sum_{n,p} \psi_1(x_k^-), \quad k = 1, \dots, N-1. \quad (14)$$

The solution of this problem was realized by the numerical method of successive approximations. It was developed the computer program for optimal control which permits to calculate optimal density distribution of generated current in stages and optimal sequence of interstage temperatures for thermoelectric generator maximum efficiency.

### Discussion of the results

To illustrate the proposed method of stage generator optimization calculations of 3-stage thermoelectric module efficiency has been carried out for different temperature differences between cold and hot surfaces. Temperature dependences of standard thermoelectric material characteristics figure of merit of which is shown in Fig.2 were used for calculations.  $Bi-Tc$  based materials obtained in the Institute of Thermoelectricity were used for a low-temperature stage,  $n$ - and  $p$ -type  $Pb-Tc$  based material characteristics for mean-temperature stage were borrowed from [8], and  $Si-Ge$  based material ones for high-temperature region - from [9]. Fig.3 gives the results of the efficiency calculations.

Fig.2. Thermoelectric material figure of merit as a function of temperature.

—  $n$ -type materials, - - -  $p$ -type materials.  
1 -  $Bi-Tc$  based materials, 2 -  $Pb-Tc$  based materials [8].  
3 -  $Si-Ge$  based materials [9].

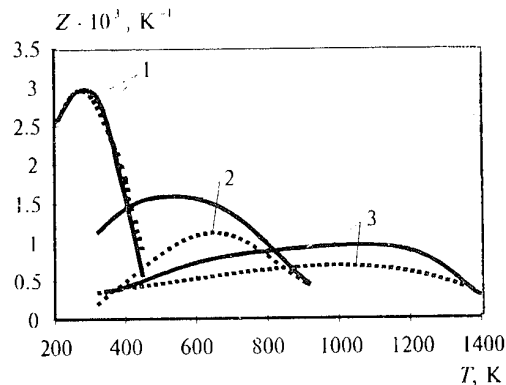
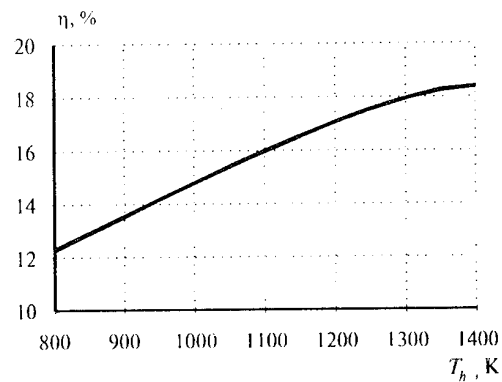


Fig.3. Efficiency calculation results of three-stage generator at different temperatures of heat absorbing junctions  $T_h$ .  $T_c = 300K$ .



The obtained results were compared with the similar device calculation results given in one of the Japanese papers [10]. Calculations in that paper were carried out according to standard formulas not taking into account electric and heat losses between stages by corresponding material figure of merit averages in the operation temperature ranges of individual stages. These temperature intervals were chosen from the equality condition of the material figure of merit of the adjacent stages. The efficiency values in the calculations made by the optimal control method was higher despite of additional interstage losses. Proper determination of interstage temperature optimal function results in the efficiency improvement. This confirms the prospects of

optimal control theory use for design of stage thermoelectric energy generator optimal structures.

### References

- [1]. A.F.Ioffe. Semiconductor thermoelements. M.-L.: Izd-vo AN SSSR, 1960.
- [2]. D.M.Rowe. Low Powed Thermoelectric Generators and Devices, in Proc. of 12th Int.Conf. on Thermolectrics, Japan, Nov., 1992, pp.429-431.
- [3]. A.I.Burshtein. On stage generators economy, *FTT*, v.11, No.10, 1960.
- [4]. E.K.Iordanishvili. Thermoelectric power sources. M., "Sov.radio", 1968.
- [5]. A.S.Okhotin, A.A.Efremov, V.S.Okhotin, A.S.Pushkarsky. Thermoelectric Generators. M., Atomizdat, 1971.
- [6]. Yu.N.Lobunets. Thermoelectric Energy Converters Calculation and Design Methods, K., Naukova Dumka, 1989.
- [7]. L.I.Anatychuk, V.A.Semenyuk. Optimal Control for the Thermoelectric Material and Device Properties. Chernovtsy, Prut, 1992, p.264.
- [8]. J.D.Richards. Procedure for the Simultaneous Determination of Thermoelectric Properties. *Energy Conversion*. v.9, pp.73-82, 1969.
- [9]. J.P.Dismukes, L.Ekstrom, E.F.Steigmeier, I.Kudman, D.S.Beers. Thermal and Electrical Properties of Heavi Doped *Ge-Si* Alloys up to 1300K. *J.of Appl.Physics*, v.35, N 10, pp.2899-2907, 1964.
- [10]. K.Eguchi, T.Hoshino. A Design Approach to Super HYDECS for Space Power Applications, in Proc. of Japan-Russia-Ukraine International Workshop on Energy Conversion Materials, Japan, January, 1995, p.165-176.

## PECULIARITIES OF FUEL COMBUSTION PROCESS CONTROL IN CATALYTIC HEAT SOURCES FOR TECS

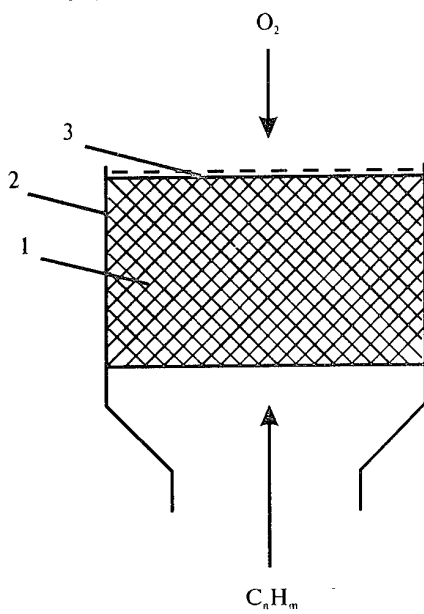
V.Ya.Mikhailovsky, L.T.Strutinskaya

*Institute of Thermoelectricity, 274000, General Post Office, box 86, Ukraine*

The peculiarities and some methods of fuel catalytic combustion control in counterflow heat sources have been investigated. Valuation of factors effect caused by catalyst properties and heat source peculiarities on fuel oxidation process stability has been done. It was shown that the behaviour of catalytic reaction initial period defined the possibility of the burner stable operation later on.

One of the most important step of TEG development and improvement is design of efficient heat sources for them. At present sources with fuel catalytic combustion are widely used for this purpose. In principle they may be of two types: 1 - with combined fuel and air supply to the catalyst, (that is fuel-air mixture is prepared); 2 - with separate supply of these components, that is the fuel is forcedly entered the catalyst layer, the air diffuses towards it spontaneously. Each type of fuel combustion has its advantages and disadvantages but we do not discuss them here. The object of the present paper is study of burners with separate reagent supply (counterflow burners). The simplest diagram of such burner is shown in fig.1.

*Fig.1. Principal diagram of the counter flow catalytic burner.  
1 - catalyst; 2 - housing; 3 - armouring screen.*



The counterflow burner received small attention in literature. It may be because the fuel combustion in them is poorly meet the standard concept about catalyst reactor operation. First, it is unclear how the air enters the catalyst layer towards to emerging reaction products. Generally it is attributed to diffusion [1]. However the

calculation of diffusion rate to the catalyst layer surface shows that it is approximately comparable to the rate of the leaving gases contrary motion. At the same time for reaction it is necessary that the air enters into the layer's depth between the catalyst grains where the counterflow rate is few tens as much. Nevertheless such air access to the catalyst layer is observed. It is probable that there is more complicated turbulent eddy phenomena take place. We have no answer this question for now.

Counterflow burners may be designed either for liquid fuel operation (benzine, kerosene, spirit and others) or for gas fuel (propan, butan, metan and others). Peculiarity of such burners operation control is in some additional degree of freedom caused by impossibility to determine oxygen supply to the catalyst layer. The ability of the burner for self-control resulted from it, external intervention into its operation must be within the self-control conservation limits.

The object of self-control in the counterflow burner is the oxidation process stability depended on temperature stability in the combustion zone. Temperature stability condition is to be the equation

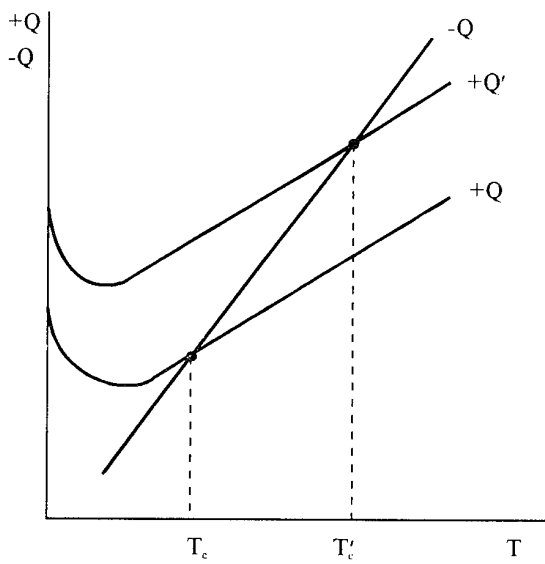
$$\frac{d(-Q)}{dT} > \frac{d(+Q)}{dT}$$

where  $(+Q)$  and  $(-Q)$  are heat income and consumption, respectively,  $T$  is temperature.

For burners of various structures this principle follows by different ways.

In the burner with liquid fuel its evaporation is due the reaction heat, that is, the amount of vapor supplied to the catalyst depends on temperature in the catalyst layer. In order to examine the stabilization scheme of such heat source it is necessary to define the character of the reaction speed function on temperature. In the given case the reaction is gone in the diffusion region because it is limited by the fuel evaporation speed. This means that speed function on temperature is linear. Heat consumption is also linearly dependent on temperature. Based on this fact it was built the diagram showing the temperature stabilization conditions in a heat source working on the liquid fuel (fig.2).

Fig.2. Temperature stability conditions in the catalytic burner on the liquid fuel, ( $+Q$ ) and ( $-Q$ ) heat input and consumption,  $T$  - temperature.



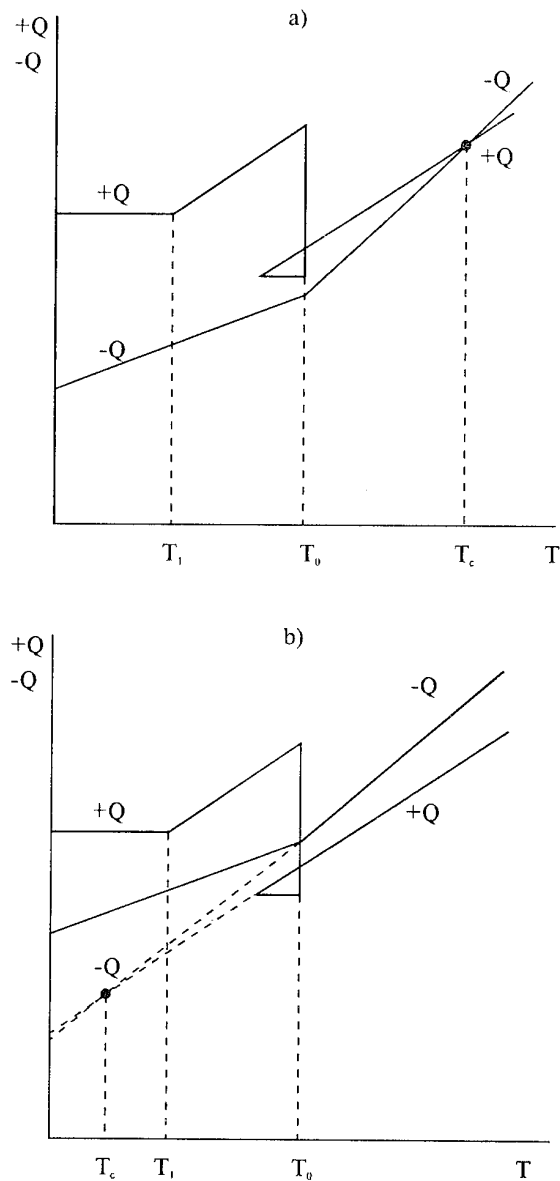
In the given figure the catalyst starting into working is accomplished by the flame way [1]. During burning out of starting fuel the catalyst temperature grows and reaches the level when in addition to noncatalytic heating flameless oxidation on the catalyst is added. So, smooth transition from flame burning to the catalytic one happens. This transition is reflected on the curve  $+Q$  as minimum.

The stability condition is achieved in the point of intersection of the heat income and consumption, the stable temperature marked as  $T_c$ . To show the effect of feedback on the stable temperature value the diagram shows two cases of the catalyst starting heating that differ in the heat quantity inserted in heating. As one can see from the figure the higher temperature of stable running burning process ( $T_c' > T_c$ ) will be at  $+Q' > +Q$ .

In a heat source on gaseous fuel it supply is effected under excess pressure then there is no feedback between temperature and fuel quantity. Fig.3 shows the diagram of temperature stabilization in such burner. In the given case the catalyst heat source starting is effected by an electric heater. Combustible gas is supplied continuously and after the catalyst temperature  $T_1$  the oxidation reaction is initiated. The initiation of the reaction can be determined by spontaneous temperature increase. The moment of the heating switch off is denoted as  $T_0$  in scheme. Heat income  $+Q$  and temperature decrease happens then. On the contrary, heat consumption increases because of losses due to electric heating switch off.

Contrary to a liquid fuel burner temperature  $T_0$  plays here an important role. If it sufficiently high (Fig.3a) then the stable temperature  $T_c$  will be sufficiently high for prolong stable condition conservation of heat source operation. If it is low (Fig.3b) then stabilization is on lower level and the burner stops its operation.

Fig.3. Diagram for the burner stability operation on the gas fuel in the starting period.



Thus, the duration and stability of the burner operation is greatly define by catalytic oxidation starting period and the way of fuel and air deliver to the reaction zone. The air access to the catalyst layer depth is controlled by the gas deliver speed the increase of which reduces the depth of air penetration and by temperature the increase of which gives reverse effect. Mutual effect of these factors defines the combustion zone location, that is, the most heating catalyst interlayer where the reaction speed is maximum under optimum ratio of reacting components. It should be noted that heat radiation at the TEG generating elements is effected through the external surface of the catalyst layer.

The typical method of stable temperature maintenance by self-controlling system may be observed at gas supply speed flow down and respectively heat input. As gas supply speed slows down the combustion

zone moves into the catalyst layer depth removing from its outside surface. By this heat emission intensity by the surface decreases. The decrease of heat input is compensated by its consumption decrease. If the gas supply increases than occurs the reverse phenomenon. As this takes place the combustion zone moves upward following the displaced air. However, its movement speed is limited by the constant temperature preservation condition. This takes place for as long as heat losses at the given temperature exceed heat input. This offends autothermalization and the burner stops its operation.

Investigation of the catalyst upper layer revealed the carrier structure and nature effect at the autothermalization process preservation.

Active aluminum  $\gamma$ -oxide in the form of grains and silicon oxide made in the form of fibre porous tab were used as carriers. *Co-Cr*, *Co-Cr-Mn* and *Cu-Cr* active phases were tested on each of the carriers. Oxidation stability on the porous fibre catalyst was higher than that of the grain one. The main cause of heat losses even at the initial period is the catalyst upper surface. Its insulation stabilizes the process.

If the oxidation process is in the diffusion region then the autothermalization condition is heat loss limitation through the layer upper surface. This function performs best fibre carrier.

The combustion zone movement along the catalyst height in the starting components counterflow conditions can promote proceeding of side reactions. If the combustion zone moves to the catalyst surface then there is an interlayer below it which air cannot access to. Thus the temperature here is sufficiently high to cause cracking and dehydrogenation. These reaction products olefines primarily are burned incompletely and can adsorbed on the active centers of the catalyst poisoning it. This circumstance is dramatized by the fact that the oxidation catalysts are usually good dehydration catalysts [2].

From literature data [3] follows that the poisoning process is reversible and at the constant temperature the catalyst activeness reduces tending to some constant value for the given temperature. At the temperature decrease olefine sorption increases and the catalyst activeness decreases. These regularities were obtained under thermostatted oxidation. In our conditions the heat source operates autothermally so the catalyst partial poisoning results in temperature decrease that in its turn leads to the poisoning amplification and so on.

Thus, with olefines appearance the catalyst quick interruption of work is to be expected, however this does not occur in practical situations. The temperature decrease is suppressed by the combustion zone movement deep into the layer that simultaneously decreases olefines output.

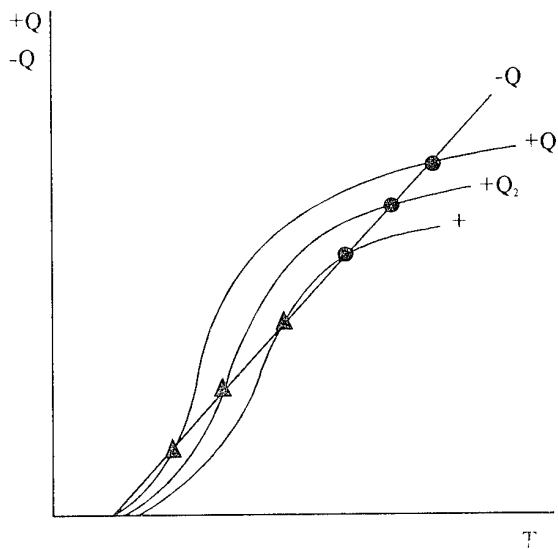
Nevertheless, at the catalyst long operation it continuously loses its activeness and this results in temperature decrease. It is probable that the cause of activity decrease is not only olefines adsorption but irreversible changes in the catalyst structure itself.

We developed the conditions for olefines continued formation during the process of the oxidation catalyst

prolong service tests. The burner initial temperature was 500 °C, the final temperature when its operation was discontinued was less than 200 °C. The burning process was more than 700 hours. The temperature was gradually decreased, combustible gas conversion state was dropped but burning stability did not disrupted. It is hardly can be explained only by the combustion zone movement. It is likely that the burner has other mechanisms of burning stabilization.

In theory this phenomenon of simultaneous temperature decrease and its stability conditions preservation may be conceived on the following basis. Temperature decrease due to reversible poisoning by olefines results in change of reaction zone from a diffusion to a kinetic one. Its speed dependence (and consequently heat release) on temperature is represented by S-shaped curve (Fig.4). The top bend of this curve is caused by maximum conversion degree that is achievable at the given catalyst activeness and temperature. As on the reaction progress the progressive catalyst activeness decrease takes place it is represented in fig. by three curves of heat input  $+Q_1 > +Q_2 > +Q_3$ . Points at the intersection of these curves with heat consumption line  $-Q$  show the region where temperature stability condition is preserved, triangles show the region where that condition does not preserved.

Fig.4. Regions of the gas oxidation process stability at catalyst activeness change from  $+Q_1$  to  $+Q_3$ .



It is not difficult to see that in a specific temperature range its decrease does not cause to stability condition violation. Only when this decrease passes the intersection point with  $+Q_3$  curve the system come out of the stability zone and the burner stops its operation. This is the scheme of these phenomena though their mechanism is not yet throughout clear.

#### References

- [1]. B.M.Cadenatsy, V.I.Sakeev, B.S.Korobskoi. Flameless catalytic heat sources. In "Deep catalytic

hydrocarbons oxidation" ser. Problemy kinetiki i kataliza.  
- M., Nayka, 1981, v.18.

[2]. S.K.Ogorodnikov, G.S.Idlis. Isoprene production -  
L.: Khimiya, 1973, 205 p.

[3]. T.G.Alkhazov, L.Ya.Margolis. Deep catalytic  
oxidation of organic substances. - M.: Khimiya, 19985.  
192 p.

## MULTICHANNEL THERMOELECTRIC FLAME DETECTOR.

Razinkov V.V., Gritsai V.V., Opyr L.A., Gromko E.D.

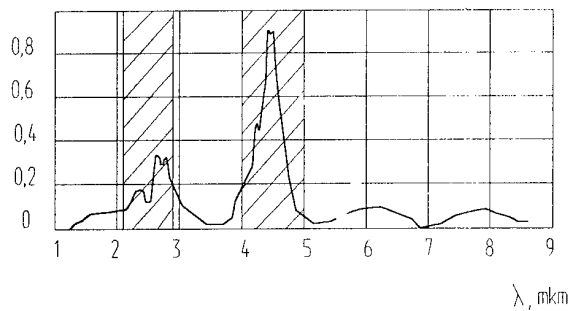
*Institute of Thermoelectricity, Chernovtsi, 274000, General Post Office, box 86, Ukraine*

Spectral sensitivity of thermoelectric radiation detectors is dictated by optical characteristics of input window. Therefore, it is possible to use various optical filters for the analyses of radiation sources according to spectral composition. In view of high performance characteristics obtained recently [1-2], the thin-film thermoelectric detectors have become most preferable to be used in conservative devices: spectrophotometers, radiometers, pyrometers, as well as in new developments, specifically, in flame detectors.

The characteristic property of a flame detector lies in its false operation protection. It is obtained due to the analysis of two typical sections of hydrocarbon combustion spectrum.

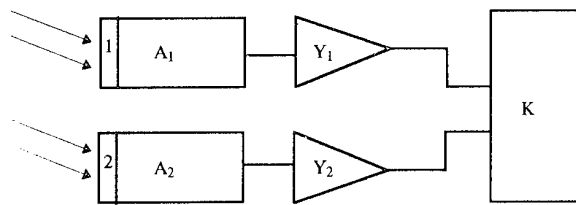
The hydrocarbon combustion spectrum is shown in Fig.1.

*Fig.1. Radiation spectrum of hydrocarbon combustion flame.*



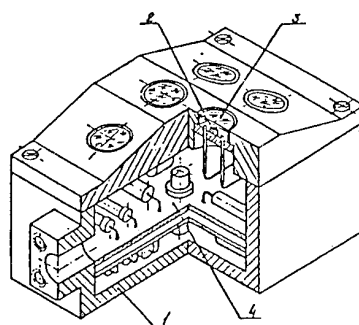
The interference filters help to single out spectrum sections of 2.2-2.8 and 4-5 mcm. Signal processing is realized according to block-diagram in Fig.2.

*Fig.2.1 - interference filter with the transmission area of 2.2- 2.8 mcm; 2 - interference filter with the transmission area of 4-5 mcm; A<sub>1</sub> - A<sub>2</sub> - thermoelectric detectors, Y<sub>1</sub> - Y<sub>2</sub> - amplifiers, K - comparator*



The energy rebased in the combustion of hydrocarbons in the above two characteristic ranges comes through the interference filters 1 and 2 to the thermoelectric detectors. When amplified by the amplifiers A<sub>1</sub> and A<sub>2</sub>, the energy signals from the detectors come to the comparator which compares the signals. It should be noted that signal ratio in two channels for various kinds of fuel (benzene, kerosene, etc.) is different. According to the problem being solved, the detector can be designed for combustion of any type of hydrocarbon or specific fuel type. The detector can be used as a fire alarm which optimally corresponds to the modern concept of fire protection, providing high resolution when finding the place of combustion and low probability of false operation. The fire alarm is installed in a strong metal casing 1 (Fig.3).

*Fig. 3.*



Specially designed high - sensitive, high - speed film thermoelectric detectors (2) have been used as the sensors of IR- radiation. The interference filters 3 serve as the input windows of detectors. The electrical scheme of signal processing is mounted on a two - sided board 4.

Specifications of the fire alarm:

- 1) Minimum area of open flame, providing reliable operation of the alarm at the distance of 10 m - 0.2m<sup>2</sup>.
- 2) Time of generation of command signal about the existence of combustion since the moment of the flame coming to the detecting elements of the alarm- 10 ms.
- 3) Field of view angl - 120°C, not less.
- 4) Power requirement - 0.01 W.
- 5) The device preserves its serviceability at the ambient temperature from -60°C to +60°C, relative humidity to 80% AT 25°C ± 10°C, acoustic noises to 120dB.

**References**

[1]. Institut fur physikalische hochtechnologie e.V.  
Miniaturisierter thermischer strahlungssensor TS-100.  
IPHT JENA.

[2]. Razinkov V.V., Tsypko N.K., Gritsai V.V. High  
responsive thermoelectric radiation receivers. Journal of  
Thermoelectricity, No.1, Oct.1993. p.p.62-66.

# Optimum Design of a Thermoelectric Generating Module for Use of a Waste Heat Thermoelectric Generator

A.Tsuyoshi<sup>1</sup>, S.Kagawa<sup>2</sup>, I.Endo<sup>2</sup>, M.Hino<sup>2</sup>, K.Matsuura<sup>3</sup>

<sup>1</sup>Kobe City College of Technology, JAPAN

<sup>2</sup>KUBOTA Corporation, JAPAN

<sup>3</sup>Osaka University, JAPAN

A thermoelectric module cost should be reduced so that a waste heat thermoelectric generator can compete in generating cost with conventional method. Because the modules will be the most costly item in any large scale generating system. The currently cost of a thermoelectric module used in the 300 K - 500 K range may be \$10 per 1W(e). In the case when a generator will be continually operated for 10 years, a module cost is 11 cents per kWh. Thus generating cost by thermoelectric generator is higher than the price of electricity generated by conventional method. At least a module cost should be reduced to around \$1 per W(e). One of the way to reduce a module cost is an improvement of a module construction. In this paper the optimum design of a thermoelectric generating module for use in a commercially available thermoelectric generator was discussed.

## 1. Introduction

As a conceptual design of a large scale t.e.(thermoelectric) generator OTEC(Ocean Thermal Energy Conversion)<sup>(1)</sup>, generating system using waste heat of a fuel cell plant<sup>(2)</sup> and generating system utilizing heat of combustible solid waste<sup>(3)</sup> were investigated in Japan. But a t.e. generating module which is the most costly item in a t.e. generator is not produced in Japan. Concerning to a world market a t.e. generating module is produced mainly for a use of a special application, like a generator in a space probe or a generator used in an isolated district. Thus the price of a t.e. generating module is guessed to be very high as well as t.e. generating system. But if the price of a t.e. generating module becomes lower and waste heat is employed as a heat source there is a possibility that a t.e. generation is applied for commercial electricity generation. This paper analyzed dependency of dimensions of a t.e. generating module on performance and economics of electricity generation by use of waste heat.

At first relation between dimensions of a t.e. element and property of a t.e. generator was studied. Influence of thickness and cross section area of an element on generating performance was investigated.

In the second place an influence of a layer of a insulator on generating performance was investigated. An electrode of which surface is insulator formed by FGM (Functionally Gradient Material) is proposed.

Finally a shape of an electrode and a t.e. element was discussed. Relation of length of an electrode along current direction and a Joule loss in an electrode was calculated. In this paper an electrode which has gradually changed thickness is proposed to reduce Joule loss in an electrode.

## 2. Relation between a dimension of a t.e. element and property of a t.e. generator

### <2.1>Measurement of a contact thermal resistance

To investigate contact thermal resistance an experimental t.e. generator was prepared as shown Fig.2-1.

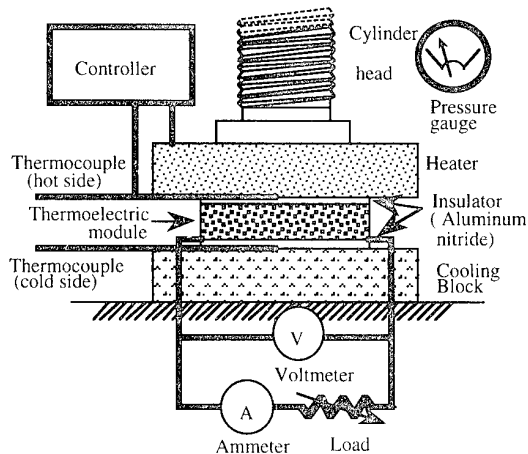


Fig.2-1 Experimental t.e. generator

In the generator HiZ 13.5W module which has 48 couples of elements and 53mm\*53mm cross sectional area was employed. Aluminum nitride of which electrical resistivity is  $10^{14}[\Omega \text{ m}]$  was used as an insulator. Temperatures at surface of the heater and surface of the cooling block were measured as well as thermal voltage. These measured values gave the total contact thermal resistance shown in Fig.2-2. If the contact thermal resistances in 4 contact layer are equal each contact thermal resistance is 0.095[K/W]. This value is equivalent to  $2.7 \times 10^4[m^2\text{K/W}]$ .

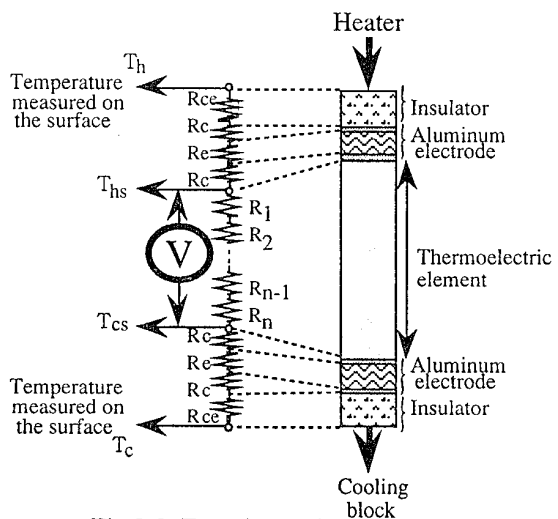


Fig.2-2 Experimental t.e. generator

## &lt;2.2&gt;Influence of thickness of a t.e. element

Figure2-3 shows electrical output calculated as a function of thickness of a t.e. element in the condition expressed in Table1. As a result electrical output is maximized at thickness of 2-3mm, which is optimum thickness.

Table 1. Condition of calculation shown Fig.2-3.

Temperature on the surface of heater	175°C
Temperature on the surface of cooling block	50°C
Thermoelectric module	HiZ13.5W
Total contact thermal resistance	0.38K/W

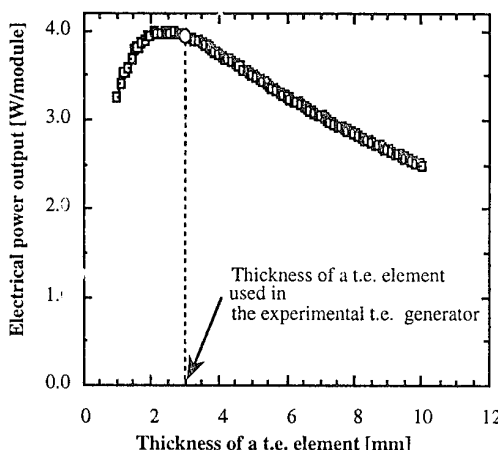


Fig.2-3 Electrical output as a function of thickness of a t.e. element

Figure2-4 shows optimum thickness of a t.e. element and electrical output as a function of temperature at the surface of a heater.

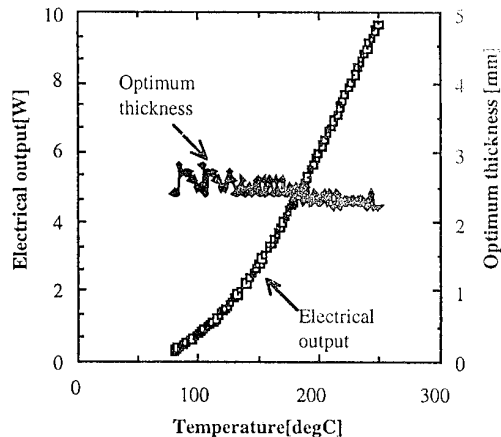


Fig.2-4 Optimum thickness of t.e. elements and electrical output as a function of a temperature at the surface of a heater(Temperature at the surface of the cooling block is assumed to be 50°C).

## 3. Insulator of a generating module

## &lt;3.1&gt;Construction of generating module

A typical t.e. module, which consists of p and n type of t.e. elements, electrodes and insulators, is attached to heat source and cooling block as shown in Fig.3-1(a). In this case a contact thermal resistance contains 4 layers of contact thermal resistances which should not be negligible.

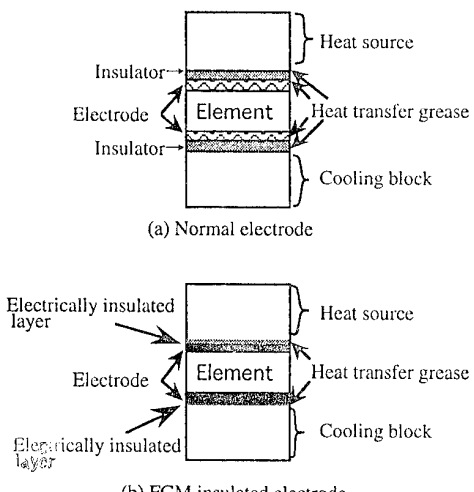


Fig.3-1 Model of a t.e. module.

In this paper it is proposed that the surface of an electrode is treated to form electrically insulated layer as shown Fig.3-1(b). As contact layer no longer exist between a t.e. element and an insulator, a contact thermal resistance can be reduced. This layer which has been treated by Ionized Beam is structured as FGM. FGM is a concept of material which has gradually changed structure. By using FGM a

generator can resist repetitive stress.

But a FGM insulator layer is not perfect insulator. Thus small leak current flows through FGM insulator layer and causes loss of electricity generation.

<3.2>Comparison of a normal insulator with FGM  
FGM insulator has the advantage of reduction of contact thermal resistance. In Fig.3-2 FGM insulator is compared with a normal insulator on the viewpoint of electrical output and optimum thickness of t.e. element.

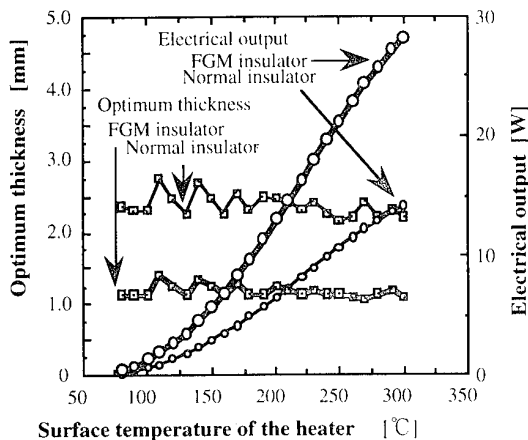


Fig.3-2 Electrical output and optimum thickness of a t.e. element as a function of a temperature of a heater.

#### 4. A shape of electrodes and t.e. element

Figure4-1 shows a calculation model of a t.e. element and electrodes on both sides. Current density in a electrode is big near the connection to the next element. When thickness of a t.e. element is quite small current is so big that Joule loss in electrodes should not be negligible.

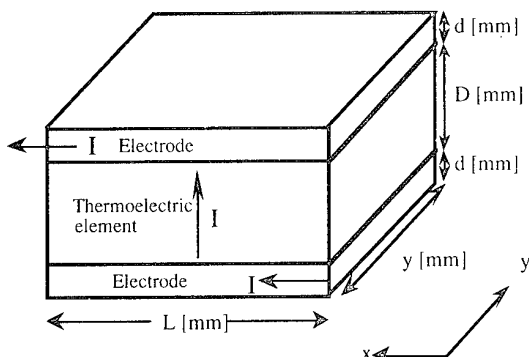


Fig.4-1 A calculation model of a t.e. element and electrodes.

#### <4.1>Thickness of t.e. elements and electrodes

To investigate Joule loss in electrodes an equivalent circuit of t.e. element and electrodes shown in Fig.4-2 is used. Figure4-3 shows generator performance considered Joule loss as a function of a thickness of t.e. elements D[mm] and a thickness of electrodes d[mm].

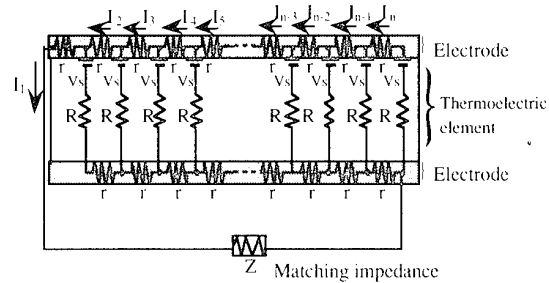


Fig.4-2 Equivalent circuit of a t.e. element and electrodes

- D=3mm/d=4mm
- D=3mm/d=1mm
- D=2mm/d=4mm
- D=2mm/d=1mm
- D=1mm/d=4mm
- D=1mm/d=1mm

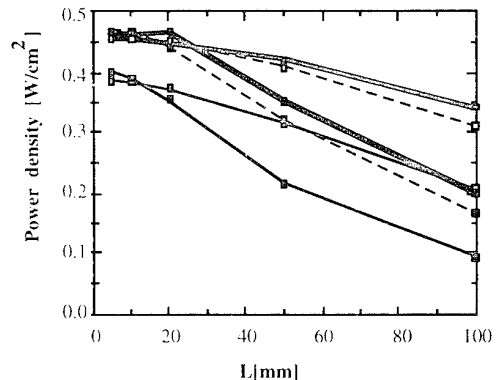


Fig.4-3 Generator performance as a function of dimensions of a t.e. element and electrodes.

#### <4.2>Improved electrode

To reduce Joule loss an improved electrode shown as Fig.4-4 was proposed. The improved electrode has a wedge-shape so that current density in electrodes is impartial. Figure4-5 shows an equivalent circuits of t.e. material and improved electrodes. Figure4-6 shows a comparison of improved electrodes with normal electrodes on the view point of generating performance in variation of dimensions of a t.e. element and electrodes.

## 5. Conclusions

To optimize t.e. module thickness of an element should be decided considering a contact thermal resistance. In this paper contact thermal resistance was estimated by using experimental t.e. generator. Concluding remarks are summarized as follows.

1. When normal insulators are employed optimum thickness is about 2mm to 3mm.
2. When FGM insulator is employed, optimum thickness of a t.e. element is estimated to be 1mm to 1.5mm and it is expected that generating performance will be improved.
3. As temperature at the hot side becomes higher, a decreasing tendency of optimum thickness of a t.e. element is seen.
4. When a t.e. element which has big cross sectional area is employed, improved electrodes is effective to reduce Joule loss.

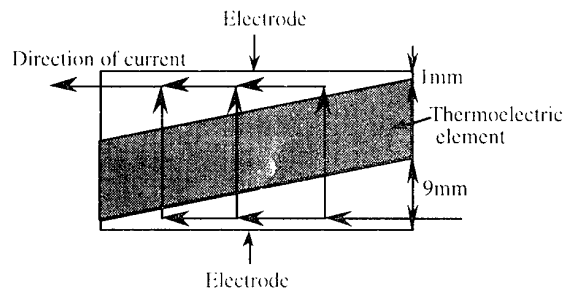


Fig.4-4 Improved electrode.

## References

- (1) T.Kajikawa et al. Proc.of the 8th Ocean Energy Conference, Washington,DC,253-257(1981)
- (2) Y.Hori et al."The case study thermoelectric generating system using the waste heat of the phosphoric acid fuel cells",497-500,12th ITC(1993)
- (3) T.Kajikawa et al."Conceptual design of thermoelectric power generation system utilizing heat of combustible solid waste" 491-496 12th ITC(1993)

## Acknowledgement

A.Tsuyoshi, one of authors, acknowledge Dr.D.M.Rowe (UWCC) and researchers in his laboratory for collaborating to prepare the experimental t.e. generator.

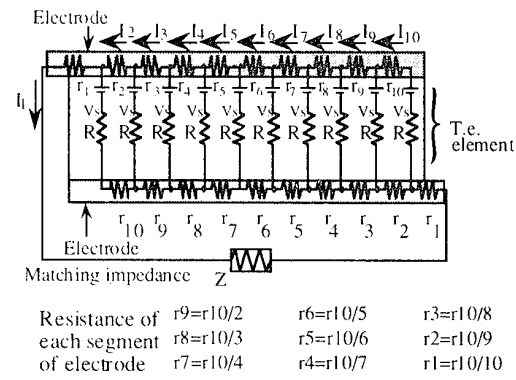


Fig.4-5 Equivalent circuit of t.e. element with improved electrodes

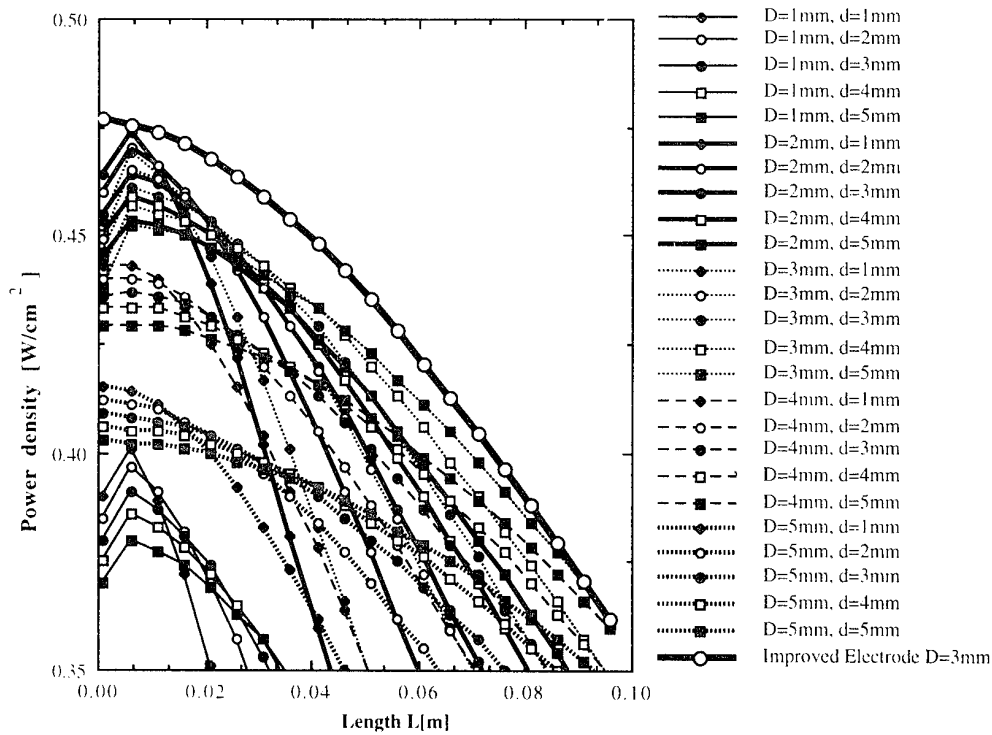


Fig.4-6 Comparison of improved electrodes with normal electrodes.

## LARGE SCALE THERMOELECTRIC CONVERSION OF WASTE HEAT AND ITS USE IN THE PRODUCTION OF HYDROGEN

K. Matsuura<sup>1</sup> and D.M. Rowe<sup>2</sup>

*1. Osaka University, Suita-shi, Osaka 565, Japan*

*2. University of Wales, Cardiff, PO Box 917, Cardiff, CF2 1XH, U.K.*

Hydrogen gas can readily be produced by the electrolysis of water and the low voltage, high d.c. current output of a thermoelectric generator provides an ideal source of electric power. These considerations have resulted in the construction of a prototype laboratory scale solid polymer electrolyte (SPE) electrolysis plant combined with a 150 W(e) thermoelectric generator powered by low grade waste heat. The system is currently being evaluated and preliminary results are reported in this paper.

### **Abstract**

Hydrogen gas is a good future clean fuel candidate. It can readily be produced by the electrolysis of water, and the low voltage, high d.c. current output of a thermoelectric generator provides an ideal source of electric power. It is estimated that in an advanced electrolysis process employing a solid polymer electrolyte (SPE), an electrolysis efficiency of 90% would be obtained at a current density of 1A/cm<sup>2</sup>. This current density is five times higher than present commercial electrolysis processes using aqueous electrolytes. These considerations have resulted in the construction of a prototype laboratory scale SPE electrolysis plant combined with 150W(e) thermoelectric generator powered by low grade "waste" heat. The total system is currently being evaluated and preliminary results are reported in this paper. The research collaboration between the Department of Electrical Engineering, Osaka University and the School of Engineering, University of Wales, Cardiff, is being supported by the British Council via a LINK programme.

### **1. Introduction**

A considerable stimulus to research into the utilisation of electrical power produced by the thermoelectric conversion of low-grade heat is being afforded by the need for energy saving and environmentally friendly energy resources. Hydrogen is a good future clean fuel candidate which is produced by electrolysis using low voltages and high currents. This power requirement is readily met by the output of a thermoelectric generator. The system is relatively simple and will make a useful contribution to the energy saving programme.

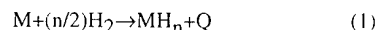
Large scale commercial electrolysis processes which employ aqueous electrolytes, operate at an average temperature of 80°C, and the corresponding cell voltage and current density are 1.8-2.1 V and 0.2 A/cm<sup>2</sup> respectively. Hydrogen gas is produced at a rate of about 1Nm<sup>3</sup>/4.8kWh. As an example, a 10 MW(e) plant for the electrolysis of water (25-30% KOH solution) can produce hydrogen gas at the rate of 2000 Nm/h. The process has the efficiency of 60-70%. In the advanced SPE<sup>(1)</sup> process, the cell voltage is expected to be 1.65 V at 90°C and an efficiency of 70-90% achieved at a current density of 1A/cm<sup>2</sup> which is 5 times larger than that of a commercial process using aqueous electrolytes. Thus, in the advanced process, the low voltage, high d.c. current electric power produced by thermoelectric generation using low-grade heat

will be used more effectively in the production of hydrogen gas. The hydrogen produced can be transported in the form of MH<sub>n</sub> (ex LaNi<sub>5</sub>H<sub>6</sub>, CaNi<sub>5</sub>H<sub>4</sub> etc.) which has a hydrogen density about 1000 times that of hydrogen gas at normal pressure and temperature.

It has already been successfully demonstrated that electricity can be thermoelectrically generated using low grade waste heat as a fuel. The use of this source of electrical power to produce hydrogen, in an easily transportable form, is a very environmentally friendly future energy resource. These considerations lead to the programme of research embodied in this paper.

### **2. Proposed System**

In the advanced process which employs a solid polymer electrolyte (SPE) in the electrolysis of water as indicated in figure 1, the cell voltage at the surface of electrode decreases with increasing temperature at a certain current density. This desirable behaviour is introduced into the proposed system displayed in figure 2. The generated hydrogen gas is absorbed into hydrogen absorbing alloys such as CaNi<sub>5</sub>, LaNi<sub>5</sub> and TiFe, and at the same time the heat, Q, is generated by the following reaction.



where M denotes a hydrogen-absorbing alloy. The generated heat, Q, (20-70 kJ/mol) is positively fed back to the SPE cell whose temperature increases and is accompanied by an increase in the electrolysis efficiency.

The conversion efficiency from electricity to hydrogen energy is estimate with reference to figure 3 as follows. In the system P<sub>T</sub> is defined as the electric power output of the thermoelectric generator, P<sub>C</sub> the required power for operating the compressor connected to the hydrogen absorbing alloy reaction vessel, N, the generation rate of hydrogen gas and Q<sub>M</sub> the reaction heat of the hydrogen absorbing ally per mol of H<sub>2</sub>. Then N is given by

$$N = (P_T - P_C)/(2V_C F) \quad (2)$$

where  $V_C$  and  $F$  are cell voltage and Faraday constant (96485.3[C]), respectively. At the final stage, when generated hydrogen gas is used,  $\eta_U$  the conversion efficiency from electricity to hydrogen energy is expressed by

$$\eta_U = (N\Delta H - NQ_M)/P_T = (1 - Q_M \Delta H)\eta_F \quad (3)$$

where  $\Delta H$  is the chemical energy of 1mol of  $H_2$ [J/mol] and  $\eta_F$  is the conversion efficiency from electricity to hydrogen gas storage in hydrogen absorbing alloy.

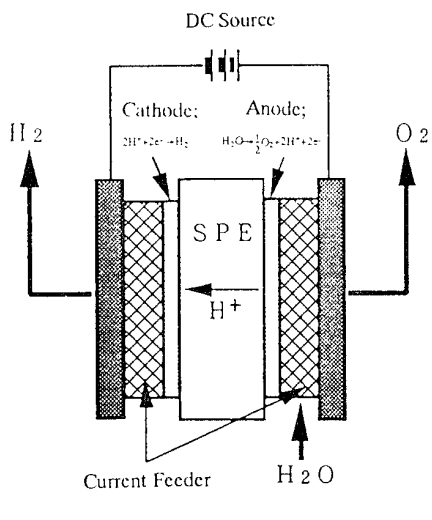


Fig. 1 Electrolysis of water using solid polymer electrolyte.

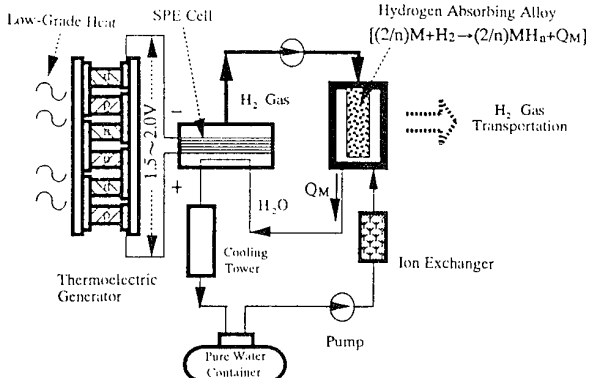


Fig. 2 Proposed system of SPE with positive feed back loop of reaction heat powered by thermoelectric generator.

Considering a situation when  $P_T = 10\text{kW}(e)$ , current density in the SPE cell is  $1\text{A/cm}^2$ , compression ratio of hydrogen gas at the compressor is 10, pure water flow rate in the SPE cell at  $90^\circ\text{C}$  is  $3.6\text{l/min}$ , and heat exchange rate at the hydrogen absorbing alloy reaction chamber is 80%,  $\eta_U$  and  $\eta_F$  are estimated to be 79% and 89% respectively. In the above estimation the following reaction is applied to hydrogen.



If the generated heat  $Q(=67[\text{kJ/mol.H}_2])$  is not fed back to the SPE cell  $\eta_U$  and  $\eta_F$  are 66% and 75% respectively. The salient points of the above discussion are summarised in Table 1.

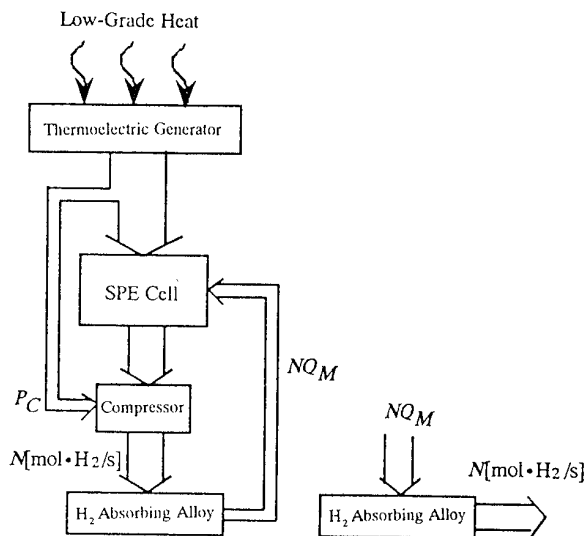


Fig. 3 Energy flow diagram of the proposed system for SPE water electrolysis.

Table 1 Design specification of  $10\text{kW}(e)$  thermoelectric generator-SPE cell hydrogen gas generating process

#### System specifications

Thermoelectric generator	$10\text{kW}(e)$
Compressor power	$255\text{W}(e)$
Hydrogen absorbing alloy	$\text{CaNi}_5$
Total area of SPE	$0.6\text{m}^2$
Hydrogen gas generation rate	$2.5\text{Nm}^3/\text{h}$
Heat exchange rate at reaction vessel	80 %
Conversion efficiency	79 %

#### Operating conditions

Electrolysis temperature	$90^\circ\text{C}$
Current density in SPE	$1\text{A/cm}^2$
Total current through SPE	$6\text{kA}$
SPE cell voltage	$1.65\text{V}$
Feed water rate in SPE	$3.6\text{l/min.}$
Compression ratio of hydrogen gas	10

### 3. Prototype Plant

A laboratory scale prototype thermoelectric generator combined with an advanced process for SPE and a hydrogen absorbing alloy reaction chamber for returning its reaction heat to the SPE cell (positive heat feedback) has been designed and constructed as Osaka University. The plant lay-out of the prototype system capable of producing hydrogen gas at a rate of 0.02 Nm<sup>3</sup>/h is shown in figure 4. The electric power required for the electrolysis of water is supplied by a 150 W(e) thermoelectric generator (2). In the generator an array of 20 thermoelectric modules is located between the hot and cold heat transfer tubes. Each heat transfer tube is 1.5 m in length and of rectangular

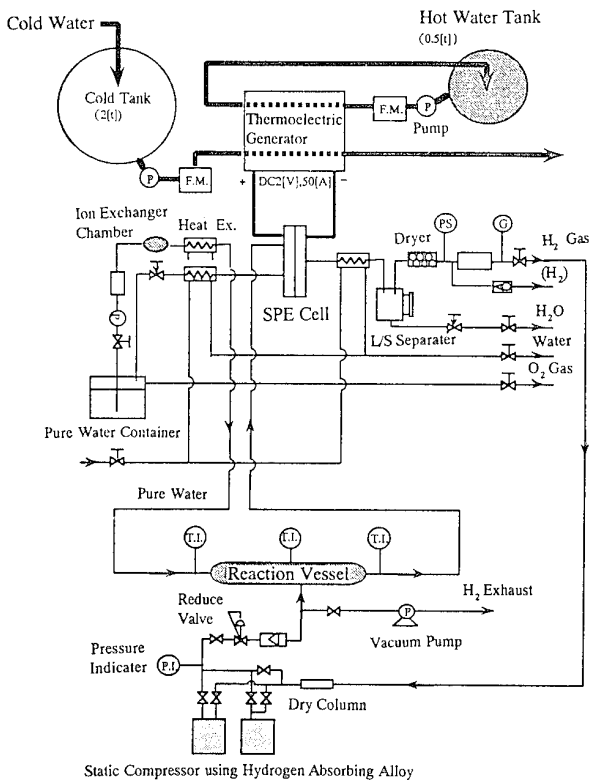


Fig. 4 Plant diagram of prototype process for TEG/SPE water electrolysis installed at Osaka University.

cross-section (80 mm x 40 mm). The thermoelectric modules (Melcor, CP5-31-10L used in two units of the generator and CP5-31-6L for the other two units) each consist of 31 couples based on bismuth telluride, solid state cooling technology. One unit of the generator is composed of 4 heat transfer tubes with the 150W(e) generator consisting of 4 units in total.

The SPE cell is constructed as shown in figure 5. The cell consists of a thin film of Nafion<sup>R</sup>117 (0.2 mm in thickness

and 80mm in diameter) with platinum plated electrode having a surface of 50cm<sup>2</sup>. It can be operated at a maximum temperature of 90°C with a maximum current of 50 A and under hydrogen gas at a pressure in the range 0.3 kgf/cm<sup>2</sup>G. The hydrogen reaction vessel contains 320 gram of hydrogen absorbing alloy (LaNi<sub>4.5</sub>Al<sub>0.5</sub>). The heat generated by the reaction between the hydrogen and the hydrogen absorbing alloy (Eq.1) is 9.3 kcal/mo1.H<sub>2</sub>. The inner construction is illustrated in figure 6. The reaction vessel is connected to a static thermal compressor in which hydrogen gas is pressurised up to 16 kg/cm<sup>2</sup> (abs.) by heating LaNi<sub>4.78</sub> Al<sub>0.22</sub> alloy at 75°C.

The prototype system shown in figure 4 incorporates a pure water (ion exchange) generating plant. The electrical resistivity of the generated pure water is more than  $5 \times 10^6 \Omega \text{ cm}$ . The pure water is fed to the SPE cell at a flow rate of 30 cm<sup>3</sup>/min and is electrolysed in the cell by the following reactions.

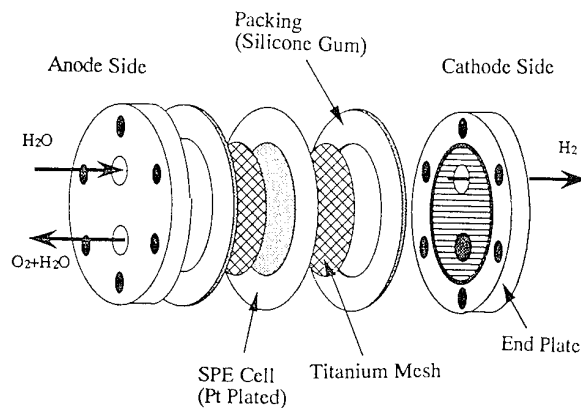


Fig. 5 Construction of SPE cell.

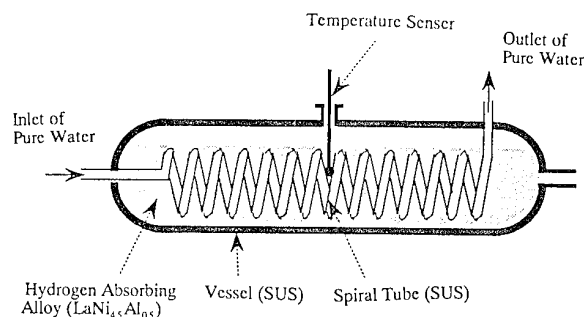
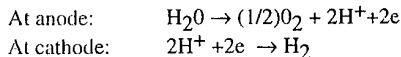


Fig. 6 Hydrogen/hydrogen absorbing alloy reaction vessel.



The generated hydrogen gas in the SPE cell contains moisture and is dried through the gas/liquid separator and the moisture removing chamber. Finally, high purity hydrogen gas (99.99%) is obtained.

The total project concept is of a mobile, easily transportable system and a parallel programme of research, to the use of a solid polymer electrolyte in the production of hydrogen electrolysis of water, is being undertaken to increase the conversion efficiency of the thermoelectric generator and increase its specific power (electrical power to mass ratio). Improved water flow channels with more effective heat-to-module transfer characteristics have been designed and are being evaluated. Modules currently employed in the 150W(e) thermoelectric generator housed at Osaka University are designed specifically for Peltier applications and modifications in both the geometry of construction and thermoelement material composition are being made to meet thermoelectric generation requirements.

#### 4. Results and Discussions

The temperature dependence of the SPE cell voltage was measured as a function of current density. The results are shown in figure 7 together with the behaviour of an advanced SPE cell as a reference. The SPE cell employed in the prototype system (platinum as anode and cathode) is commercially available for high temperature use and its cell voltage is larger than the cell voltage of the advanced SPE cell (P-Ir as anode and Pt as cathode). If the advanced SPE cell were adopted, the cell voltage will decrease to 1.65 V under the current density of 1 A/cm<sup>2</sup> and temperature at 90°C<sup>(1)</sup>. However, in both cases it is found that the cell voltage decreases with increasing temperature - this was as expected.

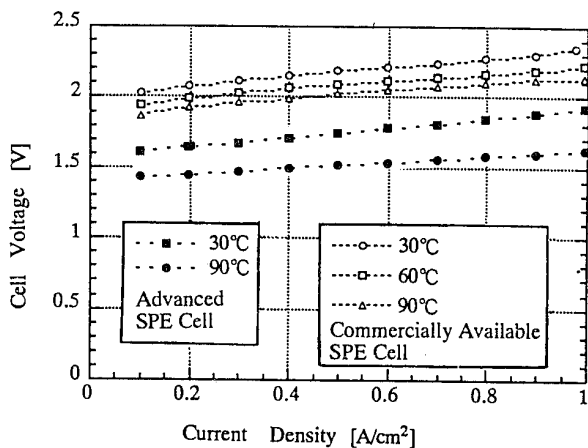


Fig. 7 Cell voltage-current density relations with temperature.

In figure 8 is shown one example of operating point. The operating point is determined by the point where the voltage vs current curve of the thermoelectric generator and the SPE cell voltage vs current curve intersects. As is apparent from the figure, the former has a large negative slope and the latter a slight positive slope. This makes the operating point very stable.

The performance of the heat exchangers in the hydrogen/hydrogen absorbing alloy reaction vessel was investigated. One of the experimental results is shown in figure 9 in which the variations of feed water temperature at the entrance and the exit of the reaction vessel, and of hydrogen absorbing alloy are plotted under the conditions of the feed water flow rate of 30 cm<sup>3</sup>/min and the feed hydrogen gas flow rate of 2 Nl/min. It is

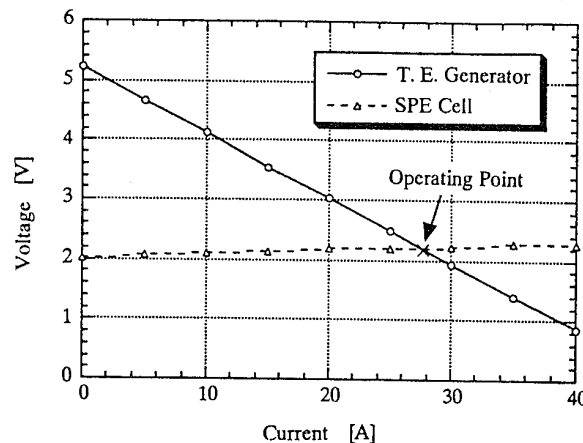


Fig. 8 One example of operating point in the prototype system.

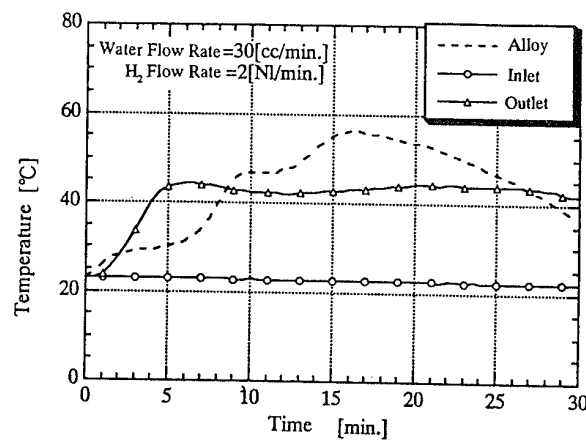


Fig. 9 Heat exchange performance in the hydrogen/hydrogen absorbing alloy reaction vessel.

found from the figure that temperature of the feed water increased about 20°C. This figure corresponds to heat exchange rate of 75.2% with the remaining 24.8% heat being dissipated through thermal conduction in the piping systems. When this system was designed as explained in Chapter 2, it was assumed that the heat exchange rate would be 80%. The actually observed value is 75.2% as mentioned above and it is slightly less than the target value. A small improvement in the design of the reaction vessel will solve the problem. The hydrogen gas generation rate observed in the prototype system was 0.02 Nm<sup>3</sup>/h at an electrolysis current efficiency of 93%, operating temperature of 90°C and at the cell current density of 1A/cm<sup>2</sup> which is 5 times as large as that of the commercial process for aqueous electrolytes. The increase in the conversion efficiency of 12% was due to the effect of positive feed back of the reaction heat under the operational conditions mentioned above.

Improvements in performance of the thermoelectric generator result from a number of modifications. In addition to channel water flow characteristics, heat transfer from the warm water to the modules depends upon channel/module interface material and channel section design. Significant improvements in heat transfer have been achieved using a copper channel/module interface plate along whose length has been attached off-set copper fins. Optimisation of thermoelement geometry for power generation has been reported previously (3). Implementation of the recommendations at the module manufacturing stage coupled with a decrease in the inter-element spacing will result in a significant improvement in module power output per unit area. Materials employed in Peltier devices are based on bismuth telluride technology with the alloy composition and doping level chosen to optimise the materials' figure of merit at or below room temperature. Optimisation of the materials transport properties for operation at an average temperature of 50°C will result in an increase in conversion efficiency of more than 5%. Preliminary theoretical analysis combined with experimental results indicate that a combination of the modifications discussed above will result in a doubling of the present thermoelectric generator's specific power.

### 5. Conclusions

A thermoelectric generator powered by low temperature "waste" heat provided the required low voltage, high current power source for a SPE electrolysis cell. Hydrogen gas produced during the electrolysis was absorbed in hydrogen absorbing alloy and the reaction heat positively fed back to the SPE cell in order to increase the conversion efficiency. Through the operation of the prototype system it was observed that the hydrogen generating conversion efficiency increased by 12% due to the effect of the positive feed back of the reaction heat and the system operates stably. Significant progress has also been made towards increasing the power density of the thermoelectric generator. Modifications to the water-flow channels coupled with improvements in thermoelement design and optimisation of the thermoelement alloys will result in a

doubling of the specific power. In conclusion, the work described in this paper is a small step forward in the development of an environmentally friendly hydrogen energy system.

### Acknowledgements

The authors would like to express grateful appreciation to Messrs. Akira Tsuyoshi of Kobe City College of Technology; Hideo Tsumura, Hiroyuki Todaka and Zyun Takemura of Osaka University for their contributions to this work. The valuable suggestions for designing the prototype thermoelectric generator-SPE electrolysis process given by Dr. K. Oguro of Osaka National Research Institute are gratefully acknowledged. Financial support for a part of this work by the Kansai Electric Power Company and the British Council are also appreciated.

### References

- (1) P. Millet and M. Pineri, "New Solid Polymer Electrolyte Composites for Water Electrolysis", Journal of Applied Electrochemistry, Vol 19, pp. 162-166, 1989.
- (2) K. Matsuura, "Large Scale Thermoelectric Generation of Low-Grade Heat, the Future", Proc. of the XII International Conference on Thermoelectrics, V1-2, pp. 439-446, Yokohama, Japan, November 1993.
- (3) D.M. Rowe and Gao Min, "Optimisation of Thermoelectric module Geometry for Waste Heat Electric Power Generation" International Journal of Power Sources 38, 3, pp. 253-259, 1992.

# Catalytic thermoelectric generators (CATEG) for systems of cathode protection and telemechanic devices of gas mains

A.A.Pustovalov<sup>1</sup>, N.N.Rybkin<sup>1</sup>, V.V.Gusev<sup>1</sup>, L.P.Nebera<sup>1</sup>, I.I.Gubanok<sup>2</sup>, V.K.Lavrukhin<sup>2</sup>

<sup>1</sup> BIAPOS Scientific-Production Enterprise 38 Leninsky Prospekt, build.6, 117334 Moscow, Russia  
<sup>2</sup> SEVERGAZPROM Production Association 39/2 Prospekt Lenina, 169400 Uchta, Komi Republic, Russia

This report treats the results of developing the injection-type catalytic thermoelectric generators (CATEG) operated with natural gas or propane-butane mixtures. Technical data are presented for the CATEG prototypes developed to operate within a 15-90 W electric power range.

A wide class of equipment used by consumers of electric power is impossible or economically inefficient to energize directly by laying power lines to the equipment operation sites. This type of equipment is energized from an autonomous power supply, namely, electric cell battery, electrochemical generator, Diesel-operated generator, wind-electric plant, thermoelectric generator, etc. The merits and demerits of these units define the applicability scope of each of the power sources.

The injection-type catalytic thermoelectric generators (CATEGs) operated with natural gas or propane-butane mixtures are particularly distinguished among the above devices.

CATEGs belong to the class of autonomous power sources that can long serve without maintenance in remote and difficult-to-reach regions with severe climate. The sources can well be put into operation without capital investments and without employing any skilled workers.

CATEG is a novel produce in Russia, while the like generators of Telan and Decap types have extensively been used in other countries since the early seventies. The Telan generators are manufactured by Teledyne Energy Systems Co. (USA) which is the world's leading producer thereof and have incorporated its daughter companies all over the globe [1].

As distinguished from other types of organic fuel-operated thermoelectric generators, CATEG generates heat by oxidizing a fuel on catalyst surface in a sealed catalytic chamber, rather than by open burning the fuel in a gas burner. Therefore, the CATEG operations prove to be highly stable and resistant to any atmospheric factors (the open-flame gas burners have to be extra shielded against high wind loads). The catalysis proper can proceed within a certain (and sometimes very broad) temperature range, so the process will not be stopped even by short-term interruptions in fuel supply. In case fuels do not contain catalytic poisons, the catalyst service life under continuous operations can reach years and even decades.

Of course, the performance (operation stability included) of CATEG is defined also by the particular type of thermoelectric converter used to generate electric power. Thus, two principal units of CATEG, i.e. thermocouple battery and catalytic chamber, define the CATEG actual technical data and operation characteristics.

Fig.1 is the lay-out diagram of CATEG design. The CATEG-90/24 generator prototype of 90 W electric power output at a 24 V load, which is now the basic model, was designed after manufacturing some CATEG modifications of lower power outputs.

Table 1 shows the technical data of the CATEG modifica-

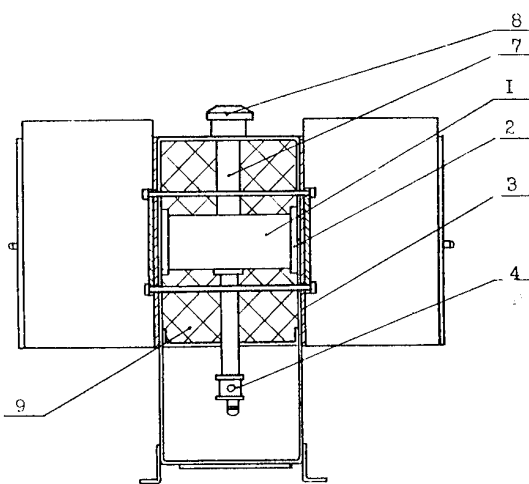


Figure 1: The CATEG principle scheme.

- 1 - Catalytic chamber
- 2 - Thermocouple battery
- 3 - Radiator
- 4 - Injector
- 7 - Exhaust tube
- 8 - Cover
- 9 - Heat insulation

Table 1: Basic CATEG prototypes

Type	Technical data				
	El. power W	Rated voltage V	Stabi- lized voltage V	Fuel (methane) consumption m <sup>3</sup> /hour	Electric equipment
KITT-15/12	15	12	12	0.6-0.75	With or without voltage stabilizer
KITT-15/12-AE	15	12	-	0.6-0.75	Automatic ignition system, battery unit, electromagnetic valve
CATEG-30/24	30	24(12)	24-29	1.2-1.5	Voltage stabilizer
CATEG-60/24	60	24	24-29	2.4-3.0	Voltage stabilizer
CATEG-90/24	90	24	24-29	3.6-4.5	Voltage stabilizer

tions designed.

Fig.2 is a picture of one of the pioneer prototypes of CATEG of 15 W electric power at 12 V that was tentatively named KITT-15/12 to reflect the now obsolete terminology.

The model was equipped with an automatic actuation system and with an electromagnetic valve for disengaging from gas line and was tested for a year as an autonomous electric power source for navigation marks and beacon lights on the base of the Head Office of Navigation and Oceanography at Oranienbaum [2].

The ignition system is started by an external signal which simultaneously opens the electromagnetic fuel valve. If necessary, remote starting by radio signal is feasible.

Platinum deposited on aluminum oxide grains was used as catalyst. As regards the completeness of oxidizing the hydrocarbon fuels, the contents of CO, NO, aldehydes, and other incomplete combustion products in exhaust gases, the CATEG catalyst performance effectiveness was estimated by experts from Neste Co. (Finland) who tested the KITT-15/12 generator [3]. The specific CO content in exhaust gas is below the norms prescribed to domestic gas appliances.

Since the optimal catalysis process proceeds at a temperature much below the open burning (below 400 °C [4], the thermoelectric converter was made of the bismuth telluride alloys that exhibit the highest effectiveness in a 20-350 °C interval [5].

The principal present-day consumers of CATEGs are the plants of GAZPROM Russian Joint-Stock Co. that employ the power sources of the kind in the systems of cathode protection and telemechanics of gas mains. Depending of the equipment type, the electric power of electric power plants must range from 300 to 1000 W and higher. Therefore the CATEG-90/24 of a 90 W electric power output at 24 V was selected to be the basic module.

The CATEG-90/24 is equipped with a voltage stabilizer that permits the stabilized voltage output to be adjusted from 24 to 29 V.

The CATEGs of too high power (above 100 W) are inexpedient to design because they are difficult in transportation and assembly.

The CATEG-90/24 weight-dimension characteristics permit improvised tools to be used in cargo handling and in assembly. (This is of particular importance in the far-northern regions). In the case of high power consumption, complex power plants can be assembled out of individual generators. The power plants of electric power of hundreds of W comprise not only the necessary set of CATEGs, but also the specialized assem-

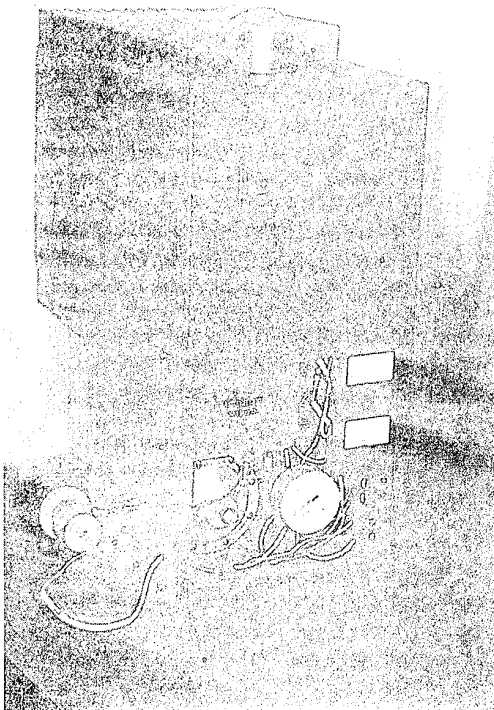


Figure 2: KITT-15/12-A

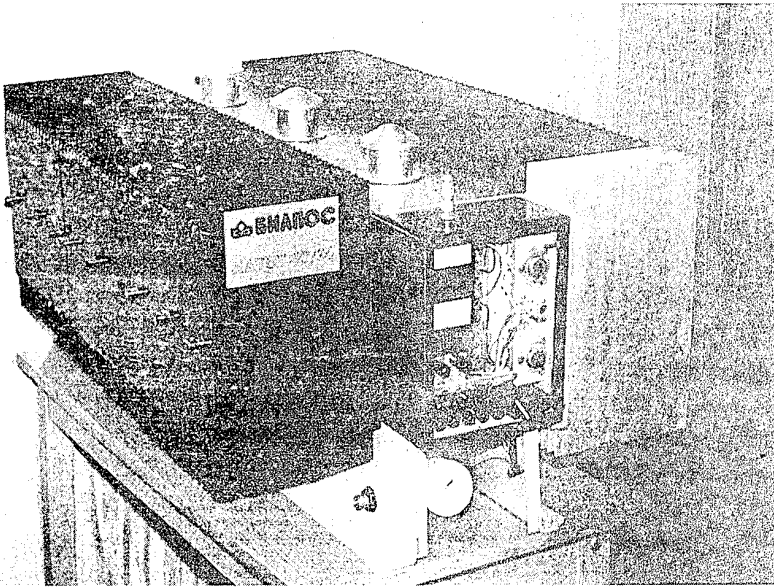


Figure 3: The picture of CATEG-90/24

bly construction with protective roofs or blockmodules and gas preparation system (for reduction and heating during cold seasons).

The catalytic thermoelectric generators can be used as separate power sources. If necessity arises, however, large complex power plants can readily be assembled out of different types of power sources that will supplement each other.

We designed and calculated a 30 W<sub>el</sub> autonomous complex power plant that includes a CATEG generator, a cell battery unit, and a solar battery. The CATEG - battery complex proves to be particularly promising. The battery power is consumed under peak loads (transmission, recording data, etc.) and is replenished by CATEG during the intervals between the peak loads. In such a way, the CATEG - battery complex involves generators of much lower power compared with the peak loads.

It should be noted in conclusion that the CATEG-270/24 power plant based on three CATEG-90/24 generators of a 270 W total electric power at 24 V is being tested to feed the cathode protection systems at the Ilych production site of the Vuktyl gas pipeline of SEVERGAZPROM Production Association.

The CATEG-270/24 total continuous service life has reached 1.5 year. The power plant has shown stable performance throughout the test service period, including the fall-winter seasons of severe service conditions in far-northern regions.

Basing on the results of designing and testing the CATEG-270/24, the experts from the SeverNIPIGAZ Engineering Design Institute have developed the type design of a 1 kW electric power plant that may be used for the diverse purposes of the GAZPROM enterprises.

has been designed for being used in the remote and difficult-to-reach regions.

2. The CATEG prototypes have been full-scale tested to suit the purposes of the Head Office of Navigation and Oceanography of Russia and the SEVERGAZPROM Production Association. The generator Has also been subjected to complex tests by experts from Neste Co. (Finland).

3. The tests have confirmed that CATEG can be completed with different pieces of equipment (electromagnetic valve, battery unit, etc.) and electronics (adjustable voltage stabilizer, automated actuation system).

4. The CATEG type design has been developed that can be used as a basis to building-block design the generators with but minor modifications capable of producing 15-90 W electric power.

5. In cooperation with the SEVERGAZPROM Production Association, a CATEG-90/24-based up-to 1 kW power plant type design has been developed for servicing the telemechanic systems of gas pipelines.

#### References

- [1] TELAN thermoelectric generators for producing electric power in the regions located far from power transmission lines, Review, VNIIGAZ, Moscow, 1973.
- [2] Report on automatic start and stop test of the experimental KITT-15/12 prototype, July 12, 1992.
- [3] Results of testing KITT, a combined heat and electricity generator using gas fuel, December 9, 1992, Neste Oy, Technology Center, P.O.B. 310.
- [4] M.B.Ravich, Surface Flame-Free Burning, USSR Acad.Sci. Publ. House, Moscow.
- [5] L.I.Anatychuk, Thermocouples and Thermoelectric Devices, Handbook, Kiev, 1979.

#### Conclusions

1. A promising autonomous catalytic thermoelectric generator (CATEG), which transforms thermal energy of low-temperature catalytic oxidation of gas fuel into electric power,

**APPLICATION OF SILICON GERMANIUM  
THERMOELECTRIC DEVICES FOR  
ELECTRICAL POWER PRODUCTION IN SPACE**

James F. Braun  
Lockheed Martin Astro Space  
720 Vandenberg Road  
Building B - Room 29B12  
King of Prussia, PA 19406 USA  
Phone: 1-610-354-3437  
Fax: 1-610-354-1184  
E-Mail: [jim.braun@den.mmc.com](mailto:jim.braun@den.mmc.com)

The application of silicon germanium (SiGe) based thermoelectric devices to provide electrical power to spacecraft is reviewed. Details of the SiGe thermoelectric unicouple and radioisotope thermoelectric generator (RTG) that represent the current generation of "flight qualified" designs are discussed. Flight performance data from ongoing missions are provided with an examination of degradation effects and the capability of RTGs to meet power requirements for long term missions in excess of ten years. The unique manufacturing processes and resources required for the fabrication of thermoelectric devices are presented. Finally, future space applications of thermoelectrics are explored with a review of the significant accomplishments achieved on advanced technology programs.

#### **Introduction**

The use of thermoelectrics to power space missions has a distinguished heritage in the U.S. space program. Specifically, power sources termed radioisotope thermoelectric generators (RTGs), have been used on 21 missions as reliable, continuous sources of electrical power. Table 1 provides the U.S. history of the use of RTGs in space [1, 2]. The selection of RTGs is ideal for power applications requiring high reliability since the heat produced through the decay of the radioisotope fuel is converted directly into electricity by the thermoelectric portion

of the generator. Earlier missions employing RTGs such as the Apollo lunar missions (1969-1972) and the Viking Mars Landers I and II (1975), used primarily lead telluride (PbTe) based thermoelectric materials. The specific power of lead telluride RTGs, ranged from 1.5 to 3.0 W/kg. More recent RTG designs have employed silicon germanium (SiGe) as the basic thermoelectric material. Improved specific power ranging from nearly 4.0 to 5.1 W/kg is obtained with the SiGe based RTGs, in which conversion is accomplished by a thermoelectric device known as a unicouple. As shown in Table 1, the SiGe unicouple was

**Table 1. History of U.S. RTG Space Missions**

Spacecraft/ Mission	RTG Type	Primary Thermoelectric Material	Specific Power W/kg	Nominal Initial Power (W <sub>0</sub> )	Launch Date (yr)	Mission Type
Transit 4a & 4b	SNAP-3B	PbTe	1.48	2.7	61	Navigational
Transit 5BN1 & N2	SNAP-9A	PbTe	2.20	25	63	Navigational
Nimbus III	SNAP-19B	PbTe	2.1	28	69	Meteorological
Apollo 12-17	SNAP-27	PbTe	2.34	73	69-72	Lunar
Triad	Transit	PbTe	2.6	35	72	Navigational
Pioneer 10 and 11	SNAP-19	PbTe	3.0	41	72 & 73	Planetary
Viking Lander I & II	SNAP-19	PbTe	3.0	41	75	Mars Lander
LES 8 & 9	MHW-RTG	SiGe *	3.94	154	76	Communications
Voyager 1 & 2	MHW-RTG	SiGe *	3.94	154	77	Planetary
Galileo	GPHS-RTG	SiGe *	5.14	296	89	Planetary (Jupiter)
Ulysses (ESA Mission)	GPHS-RTG	SiGe *	5.14	296	90	Planetary (Solar)
Cassini (Future)	GPHS-RTG	SiGe *	5.14	296	97 (Planned)	Planetary (Saturn)

\* MHW and GPHS RTGs both employ the SiGe unicouple.

first used in the multi-hundred watt (MHW) RTGs for the acclaimed Voyager missions and also in the general purpose heat source (GPHS) RTGs for the Galileo and Ulysses missions. The upcoming Cassini mission to explore the Saturnian system will also rely on the SiGe unicouple/GPHS-RTG design.

### SiGe Unicouple

Since the mid 1970s, the SiGe unicouple has been the preferred flight qualified thermoelectric device for space based RTGs. Advances in thermoelectric technology have occurred in the past two decades, but the rigorous qualification program needed for space applications has not been fully completed for more recent designs. Advanced thermoelectric technology as related to providing the next generation of thermoelectric power sources is discussed later in this paper. Flight qualification of the SiGe unicouple has been achieved through extensive testing which has included thermal performance and vibration testing of an RTG assembly. Furthermore, the SiGe unicouple has demonstrated successful performance in space with the RTGs from the LES, Voyager, Galileo and Ulysses missions.

The SiGe unicouple, with dimensional data, is provided in Figure 1 [3]. The GPHS-RTG which employs 572 unicouples and produces nearly 300 W<sub>e</sub> of power is illustrated in Figure 2. The heat collector at the hot side of the unicouple is the SiMo hot shoe which is 85/15 weight percent Si/Mo. The hot shoe is made from two halves; one doped N-type and the other P-type. The N and P SiGe thermoelectric couple legs are bonded to correspond-

ing halves of the hot shoe. The N-leg and hot shoe element are doped with phosphorus (~0.6 at% P), and the P-leg and hot shoe element are doped with boron (~0.24 at% B). The unicouple SiGe materials are described as coarse grain with an average grain size of 25 µm. Each thermoelectric leg is comprised of two sections termed the pellet and the segment. The pellet is 84 percent of the leg length and is nominally 78 at% silicon. The segment material is 63.5 at% silicon. While the 78 at% Si pellet provides better thermoelectric performance, the reduced silicon content in the segment compensates for the mismatch in coefficient of thermal expansion between the SiGe pellet and the tungsten cold shoe.

During RTG operation in space the unicouples function in a vacuum environment at a nominal hot shoe temperature of 1308K, giving a hot junction temperature of 1273K and a cold junction temperature of 573K across the legs. To prevent sublimation of silicon under these conditions a silicon nitride coating (typical thickness of 0.5 - 1.5 µm) is applied by chemical vapor deposition (CVD) to the pellet and hot shoe surfaces. An effective silicon nitride coating is crucial to device reliability.

Work on an advanced material task experimentally determined the figure-of-merit for the 78/22 SiGe unicouple pellet material [4]. For the N pellet material  $Z_n = 0.76 \times 10^{-3} \text{ K}^{-1}$  and for the P pellet material  $Z_p = 0.52 \times 10^{-3} \text{ K}^{-1}$ . These values represent the integrated average for measurements made over the 573K - 1273K temperature range.

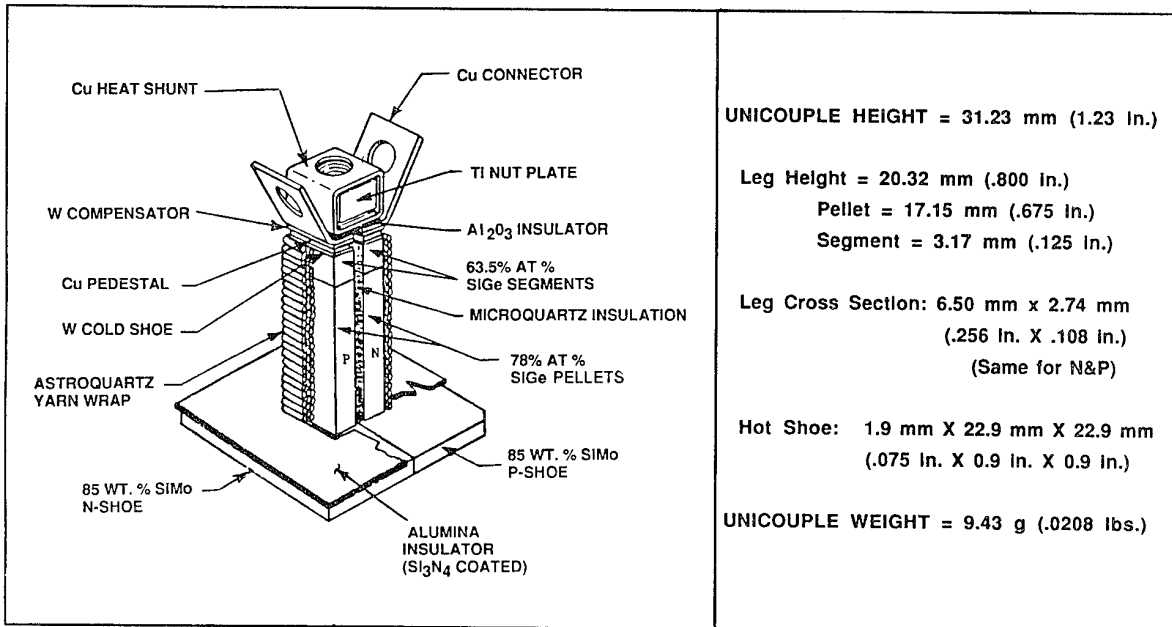


Fig. 1. SiGe Unicouple

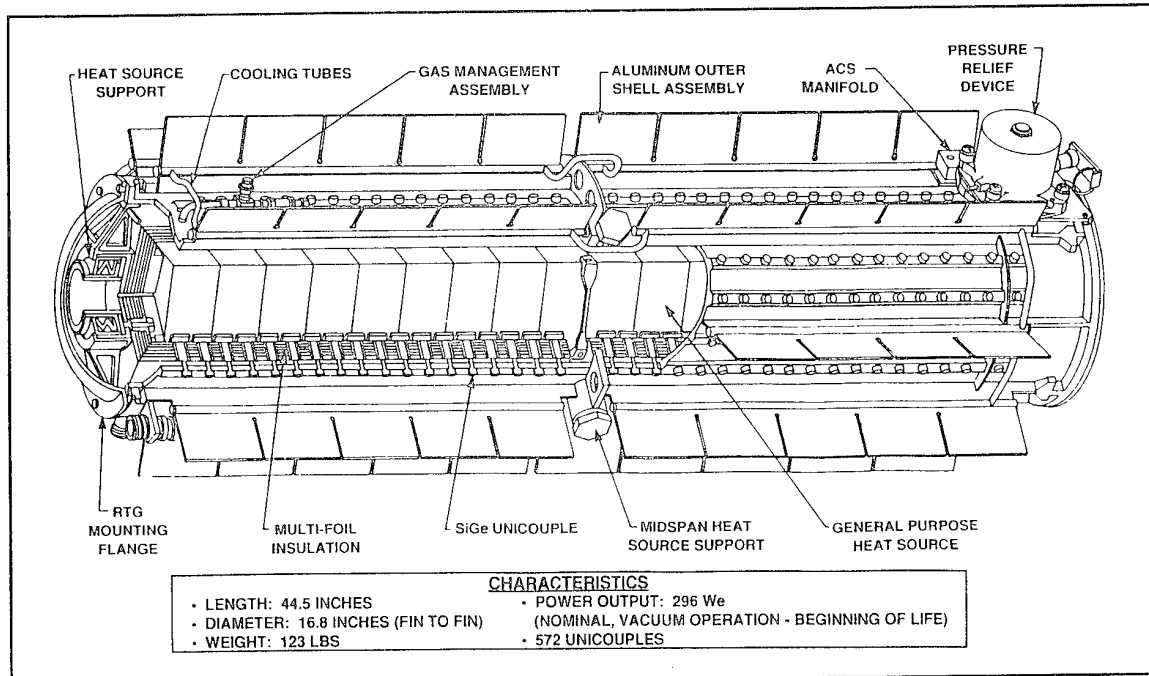


Fig. 2. GPHS RTG

The cold end of the unicouple, termed the cold stack assembly, provides the means to mechanically attach the unicouple to the converter structure. The cold stack also includes: the electrical connector extensions which allow the interconnection of the unicouples in the power circuit; and an insulator which isolates the thermoelectric circuit from the balance of the RTG assembly.

#### Unicouple Fabrication

The unicouple assembly is manufactured at the Lockheed Martin Astro Space facility in Valley Forge, Pennsylvania. This facility maintains the unique resources needed to process thermoelectric materials and assemble thermoelectric devices, ranging from the established unicouple design to advanced prototype configurations. An overview of the unicouple fabrication process is shown in Figure 3. Key attributes of the processing steps, highlighting the specialized equipment and skilled staff necessary for the manufacture of unicouples, are identified in Table 2. For the Cassini Mission, the unicouple production line was restarted in 1992 and nearly 2500 unicouples were produced in the subsequent three year span.

#### Unicouple Performance – Module Tests

During each program production cycle, small scale module tests are conducted [5, 6]. The modules are configured to simultaneously test eighteen (18) unicouples in a simulated RTG environment, with a twofold purpose. First the proper thermoelectric performance of the unicouple can be assessed. Second the effectiveness of the silicon nitride coating can be evaluated. Approximately twenty modules were tested during

the MHW-RTG program, and nine modules were tested during the GPHS-RTG program. The Cassini program has placed three modules on test. The modules can be operated at the nominal hot shoe temperature of 1308K, or the hot shoe temperature can be increased to 1408K to allow an accelerated evaluation of the silicon nitride coating effectiveness.

For the Cassini program, two of the three modules (designated as 18-10 and 18-11) were placed on test at the accelerated condition of 1408K hot shoe temperature. These tests were continued in excess of 10,000 hours which is approximately equivalent to six times the amount of thermal/vacuum exposure that the unicouples would endure in the sixteen year Cassini mission. Electrical monitoring of these two modules showed no power degradation related to silicon sublimation, and the performance of these modules was similar to test results from previous programs. To put these results into perspective, experimental module testing (circa 1975) with uncoated unicouples showed indications of failure after only 300 hours of testing. Thus, for the Cassini mission, excellent performance of the coating has been demonstrated.

The third Cassini module (designated as 18-12) was operated at the nominal 1308K hot shoe temperature. Figure 4 shows the power factor ratio (power at specified time/initial power) for module 18-12 in comparison to GPHS program module 18-7. Acceptable unicouple performance is demonstrated with agreement between the two modules and with module 18-12 showing a power reduction of only ~5% after 6000 hours.

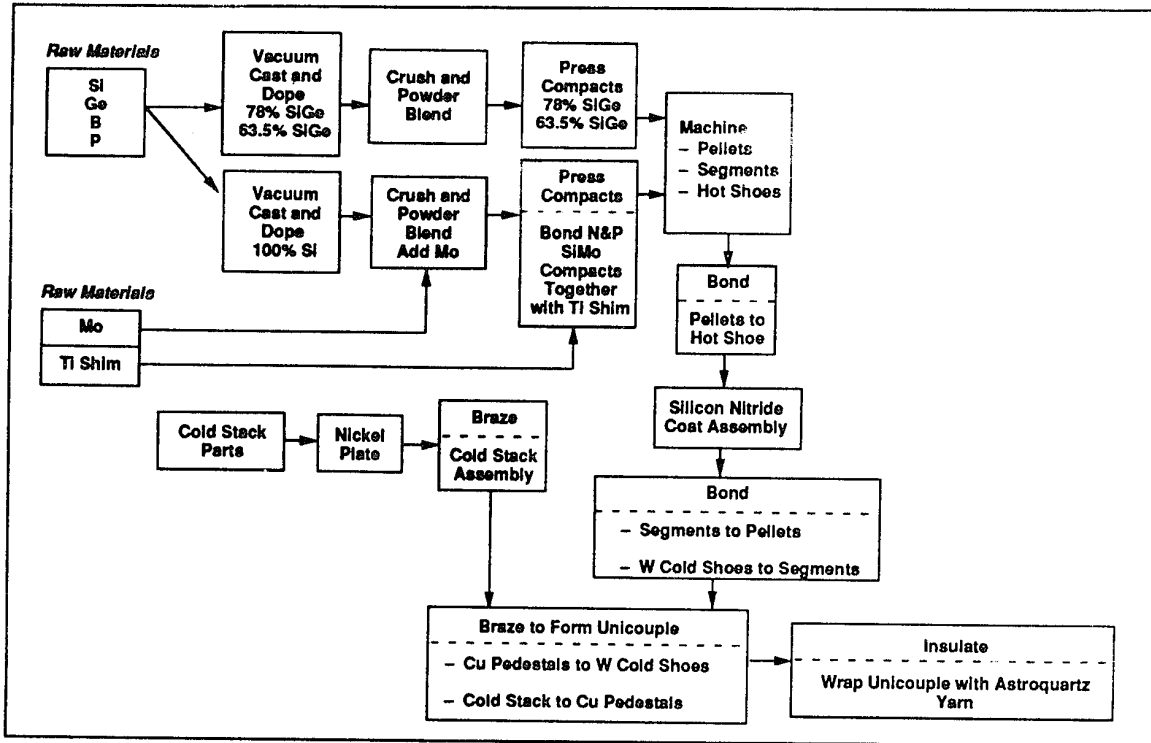


Fig. 3. Overview of Unicouple Assembly Process

#### Unicouple Performance – Flight Telemetry

RTG performance data from ongoing missions provide a valuable source by which unicouple performance can be examined [7, 8]. A plot of all SiGe unicouple RTG data, including the GPHS-RTG program qualification unit, is shown on Figure 5. In evaluating this RTG performance data, it is important to distinguish between the power loss associated with reduction in fuel thermal power from the power loss associated with unicouple degradation. The decay of the radioisotope fuel is a well understood phenomenon, therefore the total power loss can be apportioned between fuel decay and unicouple related degradation as shown in Table 3. As time of operation progresses, fuel decay accounts for an increasing portion of the decrease in RTG power. Testing and operational experience have shown that after about 50,000 hours unicouple behavior is relatively stable. Flight telemetry data provide positive proof of the ability of the SiGe unicouple to satisfy mission power requirements well in excess of ten years.

#### SiGe Advanced Technology and Future Space Applications

Numerous activities have been completed, are underway, or are being proposed to produce the next generation of higher performance thermoelectric systems. Development work has addressed both improved material performance and device configurations. With regard to exploring future flight power systems, the advanced technology efforts which have matured to the phase of device fabrication and test are pertinent to this discussion.

As part of the Modular RTG (MOD-RTG) program the multicouple thermoelectric device, shown in Figure 6, was developed [9]. The multicouple consists of 40 thermoelectric legs each coated with a silicon nitride/silicon dioxide ( $\text{Si}_3\text{N}_4/\text{SiO}_2$ ) barrier coating to suppress migration of the thermoelectric materials at operating conditions. Each leg is separated by a high temperature insulating glass. The legs are electrically connected in series through the use of SiMo hot shoes and tungsten cold contacts. The N-legs are composed of fine-grain silicon germanium-gallium phosphide (SiGe-GaP) and the P-legs are fine-grain SiGe. The performance goal for the multicouple is 2.5 W, at 3.5 V<sub>dc</sub> with hot/cold junction temperatures at 1273K/573K. The MOD-RTG multicouple configuration offers a potential 45% increase in specific power over the GPHS-RTG. The multicouple development effort is presently on hold due to funding constraints. Previously, however, thermal performance life testing on numerous multicouples had been completed with successive design improvements made to correct electrical degradation characteristics. Further development work, followed by confirmation of device reliability through long term life testing, is necessary to qualify the multicouple for flight use.

Building on the multicouple concept, a high power thermoelectric cell, illustrated in Figure 7 was developed for the SP-100 reactor system [10]. Design and assembly of this cell required advancements in compliant structure, insulator, and bonding/brazing technologies. The successful development of compliant pads and high voltage insulators were key accomplishments that enabled the cell to be conductively coupled to the heat source and

**Table 2. Key Attributes of the Unicouple Manufacturing Process**

Process	Key Attributes
• Vacuum Casting of Raw Materials	<ul style="list-style-type: none"> <li>- Vacuum Environment</li> <li>- Temperature Range: 1620 to 1820K</li> </ul>
• Crushing and Powder Blending of Vacuum Cast Ingots	<ul style="list-style-type: none"> <li>- Produce Powders in the 1 to 200 <math>\mu\text{m}</math> Particle Size Range</li> </ul>
• Vacuum Hot Pressing of Powders into a Compact	<ul style="list-style-type: none"> <li>- Vacuum Environment with Final Stage Gas Cooling</li> <li>- Temperature Range: 1570 to 1720K</li> <li>- Pressing Force Range: 620 to 845 kN (140 to 190 kbf)</li> </ul>
• Machining of Compacts into Thermolectric Parts (Pellets, Segments, and Hot Shoes)	<ul style="list-style-type: none"> <li>- Precision Wafering and Slicing Equipment, Tolerances Controlled to Below .025 mm (.001")</li> </ul>
• Bonding of Pellets to Hot Shoes and Segments to Pellets	<ul style="list-style-type: none"> <li>- Vacuum Environment with Final Stage Gas Cooling</li> <li>- Temperature Range: 1470 to 1620K with temperature controlled to <math>\pm 5\text{K}</math>.</li> </ul>
• Silicon Nitride Coating of Thermolectric Materials	<ul style="list-style-type: none"> <li>- Chemical Vapor Deposition Furnaces</li> <li>- Process Control Measurement <ul style="list-style-type: none"> <li>• Chlorine Content via X-Ray Fluorescence Spectrometry</li> <li>• Thickness via Metallurgical Examination</li> <li>• High Temperature/Vacuum Weight Loss Test</li> </ul> </li> </ul>
• Brazing of Cold Stack and Unicouple Assembly	<ul style="list-style-type: none"> <li>- Hydrogen Cover Gas Environment</li> <li>- Temperature Range: 1060 to 1090K</li> </ul>
• Insulation of Unicouple Assembly	<ul style="list-style-type: none"> <li>- Automated Yarn Wrapping</li> </ul>

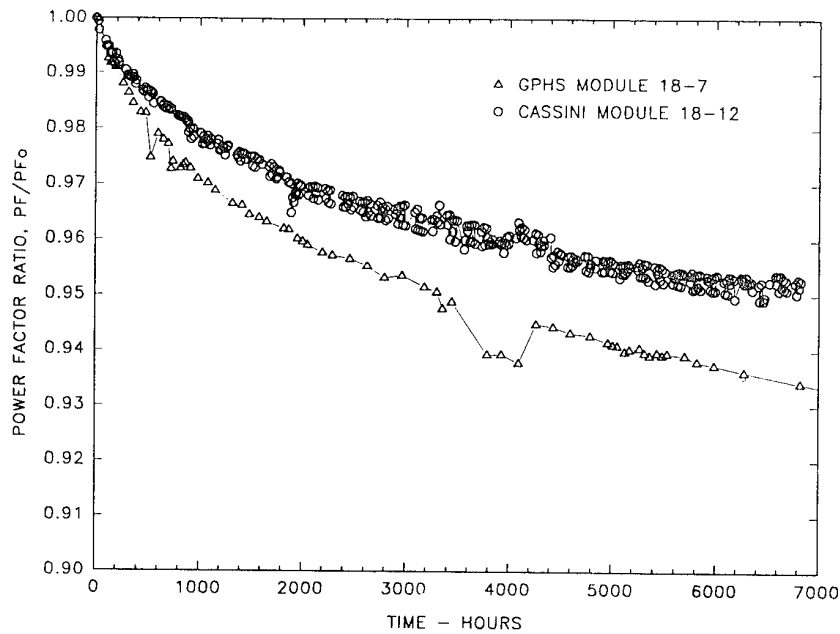
sink. The flight system design goal for the SP-100 cell, using advanced SiGe-GaP materials, is to provide 13 W<sub>e</sub> per device. As a substantial achievement towards this goal, prototype cells employing SiGe material have been fabricated and have produced nearly 9 W<sub>e</sub> of power during testing (hot/cold junction temperatures of 1273K/873K).

#### Summary

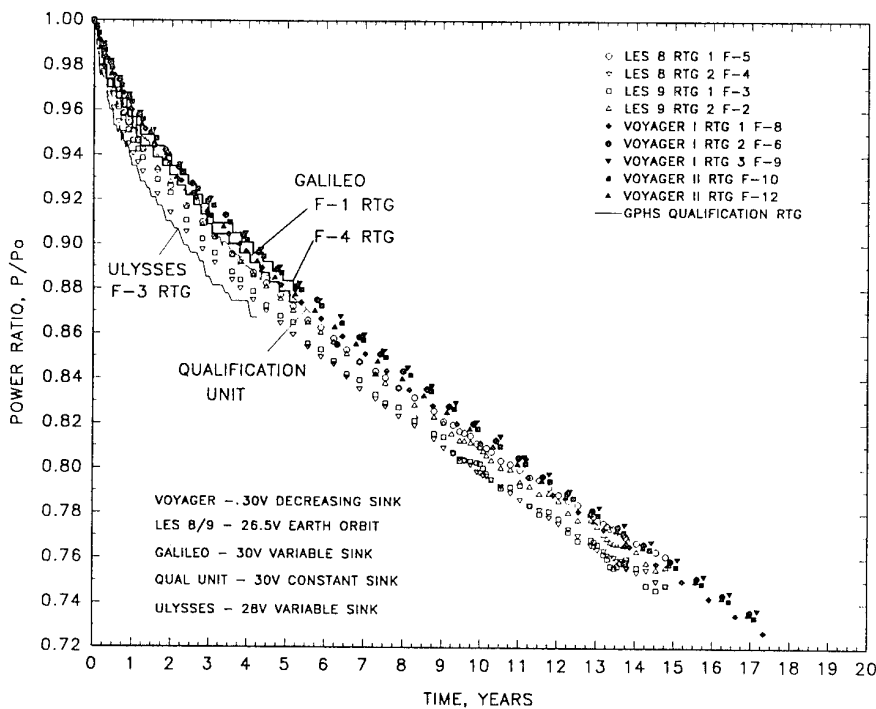
The SiGe unicouple, which is the premier flight qualified thermolectric device in use today, has demonstrated outstanding performance and reliability. The unicouple and the accompanying RTG technology, have enabled and continue to enable space missions in excess of ten years duration. Development efforts have demonstrated that improvements in thermoelectric performance beyond that of the unicouple are achievable. The unique resources to fabricate the unicouple and to conduct advanced thermoelectric work are maintained through U.S. Department of Energy support at the Lockheed Martin Astro Space facility in Valley Forge, Pennsylvania (U.S.A.).

#### References

- [1] M.S. Smith, "Radioisotope Thermal Generators as Spacecraft Power Sources," U.S. Congressional Library, February 1988, CRS Report 88-111 SPR.
- [2] G.L. Bennett, et al., "U.S. Radioisotope Thermoelectric Generator Space Operating Experience," *Proceedings of the 18th Intersociety Energy Conversion Engineering Conference*, August 1983.
- [3] "Final Report for the General Purpose Heat Source - Radioisotope Thermoelectric Generator Program," GESP-7209, General Electric Company (now Lockheed Martin Astro Space), Philadelphia, Pennsylvania, February 1991.
- [4] S. Loughin, J.F. Nakahara, D.X. Centurioni, B.A. Cook, and J.H. Harringa (1995), "Fabrication of Improved SiGe Alloys for an 18 Couple Module Test," *12th Symposium on Space Nuclear Power and Propulsion*, AIP Conference Proceedings 324, January 1995, Part Two pp. 779-784.
- [5] C.E. Kelly and P.M. Klee, "Cassini RTGs - Small Scale Module Tests," *Proceedings. 29th Intersociety Energy Conversion Engineering Conference*, Monterey, CA, 7-12 August 1994. Part 1 pp. 554-558.
- [6] C.E. Kelly and P.M. Klee, "Cassini RTGs Small Scale Module Tests - Part Two," to be presented at the 30th Intersociety Energy Conversion Engineering Conference, Orlando, FL, 31 July - 4 August 1995.



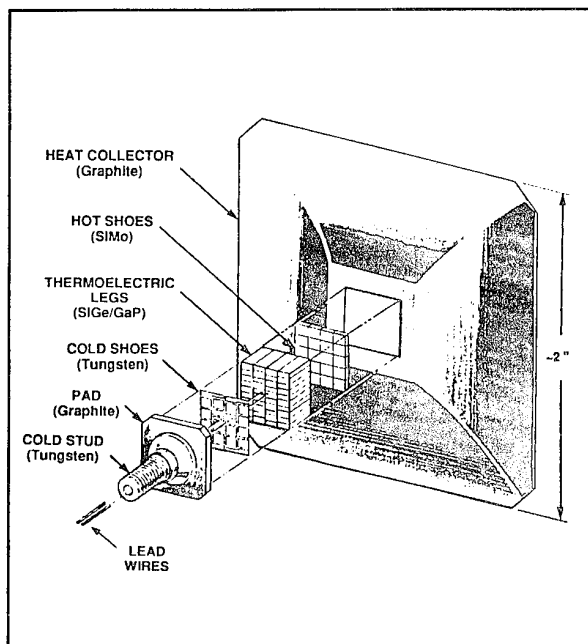
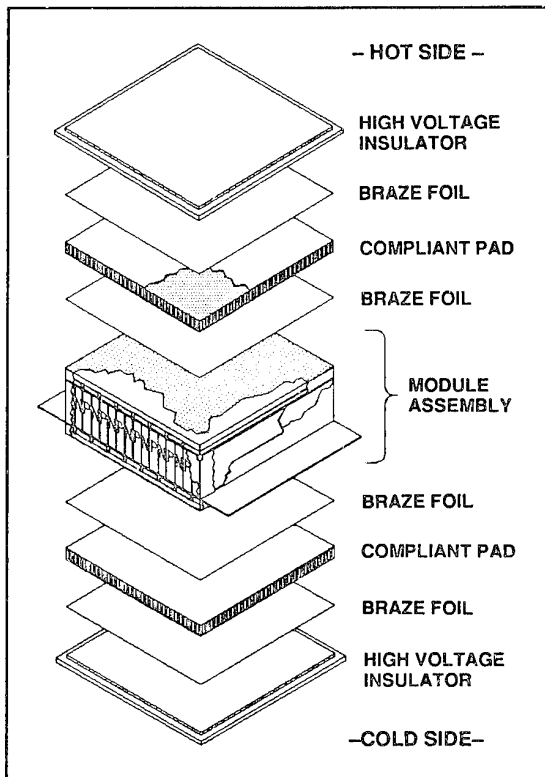
**Fig. 4. Modules 18-12 (Cassini) and 18-7 (GPHS) Power Factor Ratio Versus Time (1308K Operation)**



**Fig. 5. SiGe Unicouple RTG Power Factor as a Function of Mission Life**

**Table 3. Apportionment of RTG Power Losses throughout Mission Life**

Time	.57	1.14	2.28	5.7	11.4	15
Hours	5000	10000	20000	50000	100000	131400
Total Decrease in RTG Power	3%	5%	7.5%	13%	21%	25%
Power Decrease Due to Reduction in Fuel Thermal Power	0.8%	1.5%	3%	7.1%	14%	18%
Power Decrease Due to Unicouple Related Degradation	2.2%	3.5%	4.5%	5.9%	7%	7%

**Fig. 6. MOD-RTG Multicouple Thermoelectric Device****Fig. 7. SP-100 High Power Thermoelectric Cell**

- [7] R.J. Hemler and C.E. Kelly, "Flight Performance of Galileo and Ulysses RTGs," *Tenth Symposium Space Nuclear Power and Propulsion*, Albuquerque, NM, AIP Conference Proceedings 217, January 1993, Part One pp. 333-336.
- [8] G.L. Bennett, R.J. Hemler, and A. Schock, "Development and Use of the Galileo and Ulysses Power Sources," *45th Congress of the International Astronautical Federation*, Jerusalem, Israel, 9-14 October 1994.
- [9] R.F. Hartman and J.R. Peterson, "Status of Modular RTG Development," *Proceedings of the Seventh Symposium on Space Nuclear Power Systems*, January 1990, Part Two pp. 1074-1077.
- [10] D.N. Matteo, et al, "Recent Achievements in Conductivity Coupled Thermoelectric Cell Technology for the SP-100 Program," *Ninth Symposium on Space Nuclear Power Systems*, AIP Conference Proceedings 246, January 1992, Part One pp. 343-352.

# COMPARISON OF THERMOELECTRIC SPACE POWER SYSTEM WITH ALTERNATIVE CONVERSION OPTIONS

Alfred Schock

Orbital Sciences Corporation  
20301 Century Blvd., Germantown, MD, 20874, U.S.A.

## **Summary**

The paper compares the performance and maturity of alternative radioisotope power system options for an illustrative space mission, Pluto Express. During the past year the author has conducted detailed design studies and optimizations of power systems based on thermoelectric, thermophotovoltaic (TPV), and Stirling converters for the U.S. Department of Energy (DOE). All system options were based on General Purpose Heat Source (GPHS) modules previously developed and safety-qualified by DOE for various NASA and ESA missions (Galileo, Ulysses, Cassini). The system designs generated by Orbital Sciences Corporation (OSC) for DOE include the integration of the alternative conversion systems with those heat source modules and with a suitable radiator for heat rejection.

The thermoelectric option was based on SiGe unicouples successfully flown on the LES-8/9, Voyager, Galileo, and Ulysses missions, and slated for use on the upcoming Cassini mission. The paper compares the effect of standard American fuel, higher-enrichment Russian fuel, and American fuel originally produced for an unused Galileo spare generator that has been undergoing isotopic decay for almost 20 years. For the latter case, it describes a novel technique that can significantly increase the generator's EOM power.

The Stirling engine option was based on a derivative of a small (11-watt) free-piston Stirling engine and linear alternator with a measured efficiency of 18.5%, which has been successfully endurance-tested for over 17,000 hours to date. In the OSC-generated system design, the heat source is coupled to four engines and alternators, any three of which could deliver the desired design power (75 w) if the fourth should fail. The paper presents results of detailed analyses showing the effect of radiator geometry on system mass and performance before and after an engine and heat pipe failure.

Finally, the TPV option is based on gallium antimonide photovoltaic cells covered with spectrally selective infra-red filters. The cells and filters do not contact the hot heat source, but operate essentially at room temperature, which requires large, light-weight radiators described in the paper. The TPV analyses were based on measured spectral values of the filter's reflectivity and of the cell's quantum efficiency, and on projected improved values of those parameters. The paper describes an ongoing experimental program to determine to what extent those projected performance improvement parameters can in fact be achieved. The TPV technology is less mature than the thermoelectric unicouples with their demonstrated endurance, but offers the opportunity for greatly enhanced performance in a system without moving parts.

## **Introduction**

This paper deals with radioisotope power systems for space missions to locations where sunlight is inadequate for practical solar power systems. Although the paper is being presented at the International Conference on Thermoelectrics, only part of the paper deals with thermoelectric systems, and the rest deals with alternative power conversion systems.

Thermoelectric space power systems are by far the most mature and flight-proven, having demonstrated excellent reliability and long-term performance stability on previous space missions. But they are very inefficient (typically 7%), which increases the fuel requirement and cost for a specified power output. Since cost and mass are critical factors for presently planned space missions, there is great interest in developing advanced power systems with substantially higher conversion efficiencies.

There are three advanced power system options that offer the possibility of tripling the efficiency of present thermoelectric systems: TPV (thermophotovoltaic) generators, Stirling engines (free-piston, with linear alternators), and AMTEC (Alkali Metal Thermal to Electric Converters). The purpose of this paper is to make the thermoelectric community aware of these alternatives, and to apprise them of their development status and projected system performance compared to thermoelectric systems.

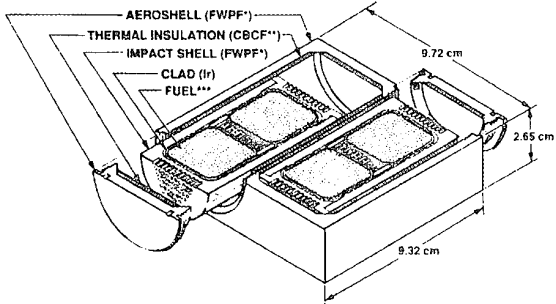
To make that comparison, the author will utilize the results of radioisotope power system design studies based on thermoelectric [1,2,3], TPV [4,5,6,7], and Stirling engines [8,9] which OSC recently conducted for DOE. (The author has started a fourth study based on AMTEC, but its results are not yet available.)

All of the above studies were for systems to power a robotic mission to the planet Pluto and its moon Charon, the only unexplored planet in the solar system [10,11,12]. The required power output, including contingencies and margin, specified by JPL (Jet Propulsion Laboratory), is for ~75 watts at the end of the 8.2-year mission.

All of the studied system designs were based on the same General Purpose Heat Source (GPHS) modules [13], which have been successfully used on other space missions after undergoing stringent safety analyses and tests. As shown in Figure 1, each GPHS module contains four 62.5 watt(t)  $\text{PuO}_2$  fuel pellets encapsulated in iridium-alloy clads. The remaining module components are graphitic and are designed to protect the integrity of the iridium clads in case of accidents before, during, and after launch.

There are two impact shells and one aeroshell made of fine-weave pierced fabric (FWPF), a very tough high-temperature three-dimensional carbon-carbon composite. The aeroshell would serve as an ablator in the unlikely event of inadvertent atmospheric reentry, and the impact shells would help to prevent

breach of the clads during subsequent Earth impact. Between the impact shells and the aeroshell is a high-temperature thermal insulator consisting of a low-density composite of carbon-bonded carbon fibers (CBCF), to prevent overheating of the clads during the reentry heat pulse and overcooling and embrittlement of the clads during the subsequent subsonic atmospheric descent before earth impact.



\*Fine-Weave Pierced Fabric, a 90%-dense 3D carbon-carbon composite  
\*\*Carbon-Bonded Carbon Fibers, a 10%-dense high-temperature insulator  
\*\*\*62.5-watt  $^{238}\text{PuO}_2$  pellet

Figure 1. GPHS-General Purpose Heat Source Module (250 Watts) Sectioned at Mid-Plane.

### Thermoelectric System Study

**Heat Source.** A previous study [3] of Radioisotope Thermoelectric Generators (RTGs) for the Pluto mission which the author published in 1993 had assumed a nominal thermal power of 250-watts per GPHS module at the beginning of the mission (BOM). A subsequent study [1] published in 1994 examined three specific fuel options:

- recently imported Russian fuel, yielding a BOM thermal power of 254 W/module,
- fuel made at the end of the Department of Energy's current production run for the Cassini mission, yielding a thermal power of 231 W/module at the time of the Pluto launch,
- and fuel from the F5 RTG, which was fabricated in 1982 as a spare for the 1989-launched Galileo mission, and which will yield a thermal power of 220 W/module at the time of the Pluto launch.

For each of these fuel options, JPL had requested that OSC analyze RTGs with 5, 6, and 7 heat source modules.

**Thermoelectric Unicouples.** The 1994 study was based on unicouple designs that are identical to those used in RTGs flown on the LES 8/9, Voyager, Galileo, and Ulysses missions and are slated for launch on the Cassini mission [14]. These unicouples have demonstrated exceptional reliability and endurance. They have operated in space for up to 17 years, always far beyond their original design goal.

As shown in Figure 2, each unicouple contains an n-doped and a p-doped SiGe leg, which are joined together by a SiMo hot-shoe to form the couple. The hot-shoe also serves as a heat collector to concentrate the heat which the heat source radiates across a vacuum gap. There is no contact between the heat source and the thermoelectric couples. The cold ends of the thermoelectric legs are bonded to electrical and thermal

conductors and to mechanical mounting hardware. The gap between the two legs is filled with quartz fibers, and their periphery is wrapped with quartz yarn.

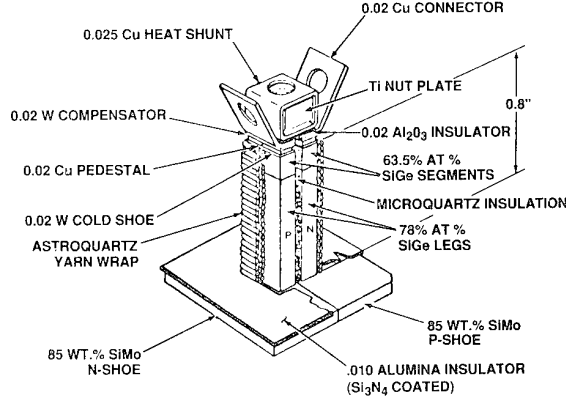


Figure 2. Unicouple.

**RTG Options.** Figure 3 shows cross-sectional views of an RTG with 5 heat source modules and 10 rings of 16 unicouples. This is consistent with previously flown RTGs in which there were 2 unicouple rings per heat source module [14]. As shown, the unicouples are embedded in multifoil thermal insulation, and are mounted on the inside of the finned RTG housing. There is no contact between the spring-loaded heat source stack and the cantilevered unicouples. All heat transfer is by radiation to the unicouples' hot shoes. Series-parallel connections between unicouples are in the space between the thermal insulation and the housing. The generated power emerges through a vacuum feedthrough. The 5-module RTG has a mass of 15.8 kg.

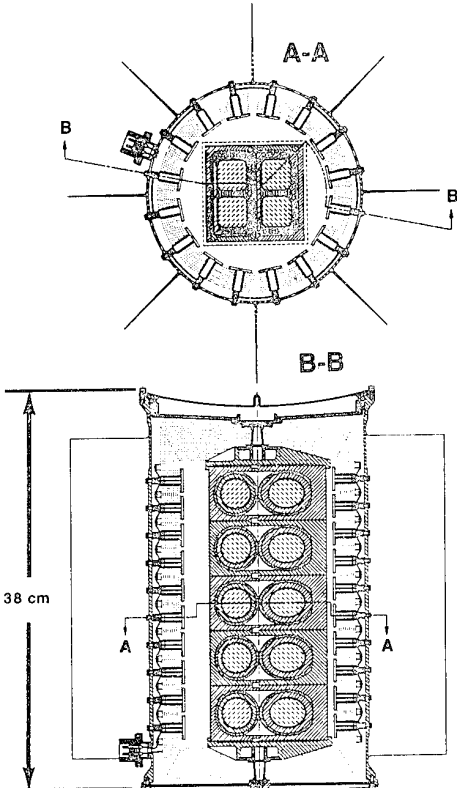


Figure 3. Cross-Sectional View of RTG with 5 Heat Source Modules.

Similar designs of RTGs with 6 and 7 heat source modules and respectively with 12 and 14 unicouple rings are depicted in Figure 4. These had respective heights of 43.7 and 49.0 cm, and respective masses of 18.1 and 20.4 kg.

Each of these designs was analyzed for the three previously mentioned fuel options. (Note: For the Galileo Spare option, only RTGs with 5 and 6 heat source modules were analyzed. The F5 spare unit contains 18 heat source modules, which only allows a maximum of 6 modules for the Pluto mission's two flight units and one spare RTG.)

The eight designs were subjected to detailed, coupled thermal and electrical analyses. The analyses employed previously published methodologies to compute the RTG's BOM performance [15] and EOM performance [16]. The salient results of those analyses are summarized in Table 1.

Fuller results are displayed in Figure 5, which shows the output power history of each option from beginning to end of mission.

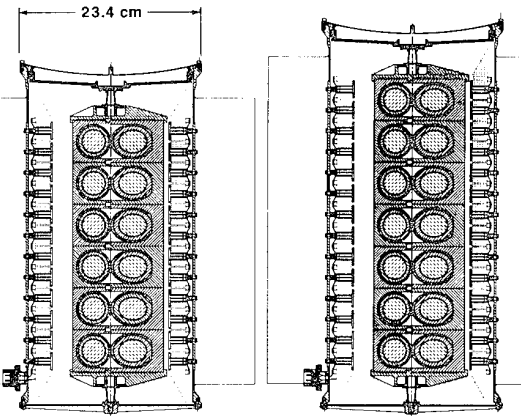


Figure 4. Cross-Sectional View of RTGs with 6 and 7 Heat Source Modules.

**Comparison with Pluto Power Demand.** The next step is to compare the predicted power profiles for the various cases with JPL's stipulated power demand schedule. As seen, the mission consists of an 8-year pre-encounter phase with a weekly 4-hour downlink period and several 30-minute prepropulsive and propulsive maneuvers, a 30-day encounter phase with daily 16 hours of data gathering and 8 hours of data transmission, followed by a 6-week post-encounter cruise with full-time data transmission. For each activity, the table lists the breakdown of the power demand and the total demand with a 20% contingency allowance plus a 10% margin, which is JPL's stipulated power goal. As will be seen, the most critical demands are the last of the prepropulsive maneuvers and the last of the weekly downlinks before encounter, and the data transmissions after encounter.

Table 1. Effect of Fuel Option and Number of Heat Source Modules on Performance of RTG.

Fuel Option	Russian			U.S. (Cassini)			GLL Spare (F5)	
Pu-238 Enrichment, %	87.7			79.7			82.6	
Thermal Watts per Module BOM (Jan 2000) EOM (Mar 2008)	254 236			231 216			220 206	
Heat Source Modules RTG Mass, kg Optimum RTG Voltage	5 15.8 19	6 18.1 23	7 20.4 27	5 15.8 17	6 18.1 21	7 20.4 25	5 15.8 16	6 18.1 20
Hot-Junction Temp., °C BOM EOM	992 948	1003 959	1012 970	916 875	930 889	940 899	878 839	893 854
Cold-Junction Temp., °C BOM EOM	254 245	262 253	234 226	240 231	247 238	253 244	233 224	240 231
Efficiency, % BOM EOM	7.1 6.1	7.2 6.2	7.3 6.1	6.5 5.9	6.6 5.9	6.7 6.0	6.2 5.7	6.3 5.7
Power Output, Watts(e) BOM EOM	90 73	109 88	129 102	75 64	91 77	108 90	68 59	83 71

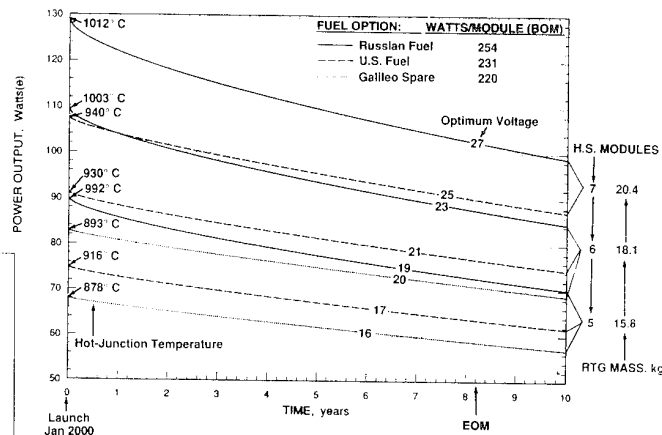


Figure 5. Effect of Fuel Option and Number of Heat Source Modules on Power Profile and Mass of RTG for Pluto Mission.

Table 2. JPL's 1994 Baseline Power Demand Schedule for PFF (2/18/94).

Mission Phase	Pre-Encounter			Encounter		Post-Encounter 6 weeks
	8 years			30 days		
Duration	1	2	3	6	6'	7
Mode #						
Activity Time	164 hr/wk	4 hr/wk	20x30 min	16 hr/day	8 hr/day	24 hr/day
Activity	Cruise	Downlink	PrePropulsive Maneuvres	Data Gathering	Data Transmission	
Power (Watts)						
Telecommunication	9.0	24.0	9.0	8.0	24.0	
Power Conditioning	12.2	14.7	15.1	13.5	14.4	
Attitude Control	9.7	9.7	9.9	16.0	9.7	
Data Processing	13.6	8.6	8.6	8.6	13.6	
Propulsion	0.4	0.4	16.9	0.4	0.4	
Thermal Control	1.0	1.0	1.0	1.0	1.0	
Science	1.0	1.0	1.0	6.0	0.0	
Total Power Demand incl. 20% contingency incl. 10% margin	46.8 56.2 61.8	59.3 71.2 8.3	61.4 73.7 81.1	53.4 64.1 70.5	58.1 69.7 76.7	
Energy Demand, kW hr	4216	110	1	34	96	

For the three fuel options, Figures 6a and b compares these critical power demands with the predicted power profiles for RTGs with 5 and 6 heat source modules. As shown, for an RTG with 5 heat source modules none of the fuel options meets JPL's 10% margin goal, while an RTG with six heat source modules more than meets the JPL goal with Russian fuel, almost meets it with U.S. (Cassini) fuel, but still falls considerably short of meeting JPL's 10% margin goal with the depleted fuel from the aged Galileo spare (F5) RTG.

The failure of the aged fuel to meet the JPL's power demand goal was disappointing, because a sufficient number of heat source modules with that fuel already exist, and their use could result in significant cost savings for the severely cost-constrained Pluto mission. Therefore, the author undertook a study to determine whether the RTG design could be modified (without increasing its mass) to meet the mission's EOM power demand goal [2].

**Design Modification.** A simple solution for increasing the RTG's power output is suggested by comparison of the upper and lower curves of Figure 6b. It is clear that the RTG with Galileo spare fuel yields a lower electrical output not only because its thermal power is lower but also because its efficiency is significantly lower. Its efficiency is lower because its hot-junction temperature is much lower, because of the depleted fuel's reduced thermal power.

Nothing can be done about the depleted fuel's lower thermal power, but something can be done about the RTG's lower hot-junction temperature. Note that the high-enrichment Russian fuel yields a BOM hot-junction temperature of 1003°C, which is about the limit of experience on previous flight RTGs. (Accelerated life tests have been conducted at higher temperatures.) As shown, the same RTG with depleted fuel has a BOM hot-junction temperature of only 893°C, which accounts for its much lower efficiency (6.3% versus 7.2%).

Clearly, the way to raise the RTG's efficiency is to raise its hot-junction temperatures. Can this be done without increasing the thermal power? Yes, by reducing the thermal conductance of the thermopile.

One way of reducing the thermopile's conductance is to lower the conductance of each thermoelectric leg, by increasing its length and/or reducing its cross-sectional area. But that would require revising the unicouple design and repeating lengthy qualification tests, clearly a very undesirable strategy considering how much effort has gone into perfecting the fabrication of the present unicouples and demonstrating their longevity. A much better strategy is to leave the unicouple design unchanged, but reduce the number of unicouples in the RTG.

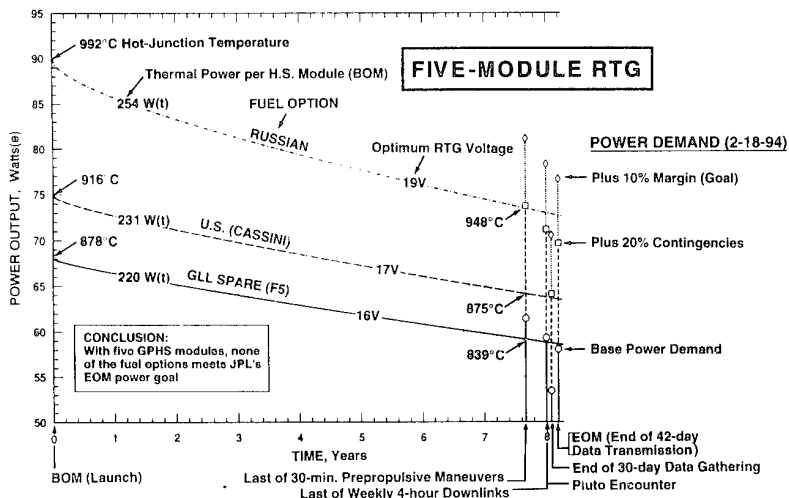


Figure 6a. Effect of Fuel Option on 5-Module RTG, Power Output Versus Demand.

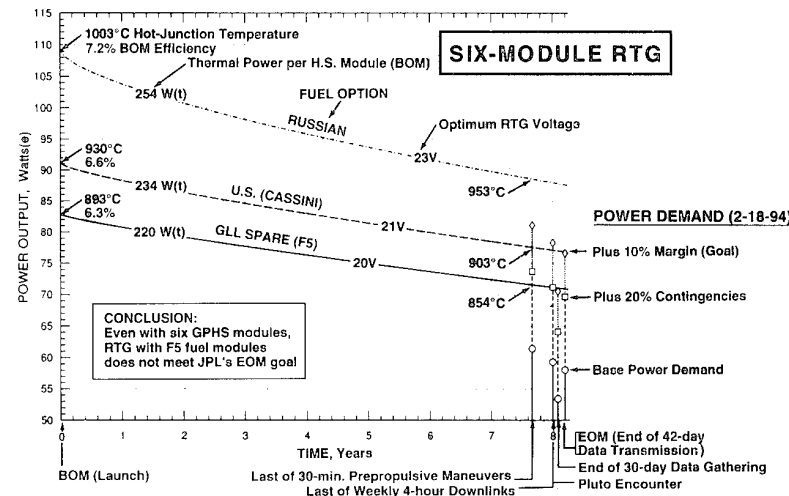
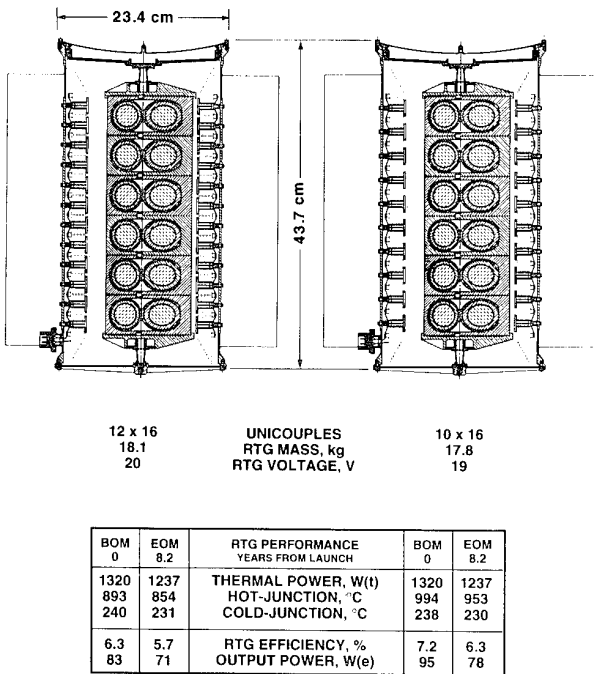


Figure 6b. Effect of Fuel Option for 6-Module RTG, Power Output Versus Demand.

This strategy is illustrated in Figure 7, which compares the standard six-module RTG with one in which the number of unicouple rings has been reduced from 12 to 10. As shown at the bottom of the figure, this raises the BOM hot-junction temperature from 893°C to 994°C (still within the established 1000°C limit), and raises the BOM efficiency from 6.3% to 7.2%.

In Figure 7 the reduced number of couple rings have been spread out over the full length of the heat source stack. This only requires the relatively trivial change of lengthening the axial series connectors between adjacent couple rings. Alternatively, we have analyzed two cases in which the spacing between couple rings is kept the same, by deleting the couple ring at each end or by omitting two couple rings at the center of the RTG. Surprisingly, all three alternatives gave essentially identical results.



**Figure 7.** Effect of Reduced Number of Standard Unicouples on Pluto RTG with 6 GPHS Modules from GLL Spare (F5).

Figure 8 shows the effect of varying the number of couple rings on the RTG's power profile during the 8.2-year mission, and compares those profiles with JPL's stipulated power demand goals. As can be seen, RTGs with 12 and 11 coupled rings do not provide the stipulated 10% margin, but the 10-ring RTG meets that goal after encounter and only misses it by ~3% during the final prepropulsive maneuvers.

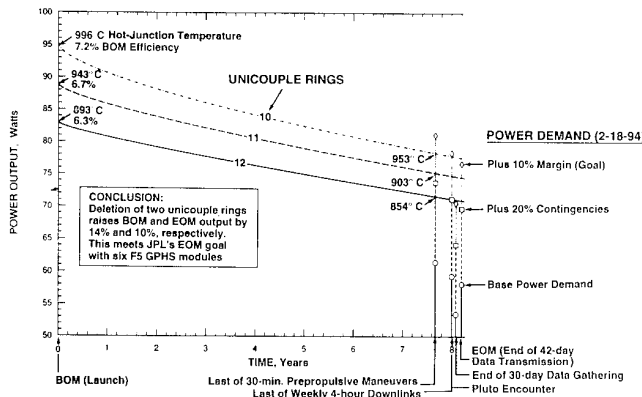


**Figure 8.** Effect of Number of 16-Unicouple Rings on Pluto RTG with 6 GLL-Spare GPHS Modules.

The figure shows that deleting two couple rings raises the BOM output by 14% and the EOM output by 10%. The reason for the smaller improvement at EOM is that part of the BOM gain is subsequently lost due to greater degradation rates at the higher hot-junction temperatures.

It may be wondered, if this is so effective why stop at 10 rings? Why not go to nine and achieve even greater improvement? We did analyze a 9-ring design, but found it to be self-defeating. Going to nine rings led to a large increase in BOM power, but the consequent rise in hot-junction temperature and degradation rate actually resulted in a lower EOM power than the ten-ring RTG. Therefore, for a six-module RTG with the depleted fuel, the design with ten unicouple rings appears to be optimum and was assumed in subsequent studies.

### Stirling System Study

**Introduction.** In October 1993 the author published a paper [8] presenting the results of a design study for a 75-watt(e) Radioisotope Stirling Power System, for possible application to the Pluto mission. That study was based on free-piston Stirling engine and linear alternator designs generated by MTI (Mechanical Technology, Inc.). The 75-watt MTI design was a derivative of a much larger (13 kwe) engine and alternator that they had developed and tested for NASA's LeRC [17,18]. Clearly, such a derivative would require a major extrapolation (downsizing) from what has actually been built and tested. Subsequently, STC (Stirling Technology Company) has developed and endurance tested a much smaller (11-watt) free-piston engine and alternator, for a terrestrial application, [19].

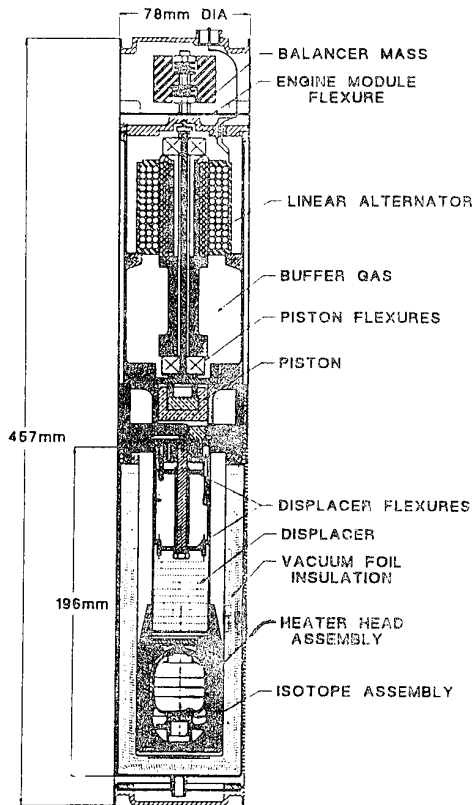


**Figure 9** STC's 11-Watt Engine and Alternator.

Low-power Stirling systems are practical because Stirling engines, unlike other dynamic systems, can retain their high efficiency at low power levels. Thus far, the STC engine and alternator depicted in Figure 9 have operated autonomously and stably for over 17,000 hours, at a measured efficiency of 18.5%.

Clearly, it would require much less extrapolation to go to a 75-watt system from 11 watts than from 13 kilowatts. Therefore, the Department of Energy asked OSC, to perform a similar study of a ~75-watt space power system based on derivatives of STC's 11-watt engine and alternator [19].

**STC Subcontract.** To support the above system study, OSC extended a subcontract to STC to design and analyze derivatives of their 11-watt engine and alternator. Specifically, they were asked to design engines for two system options. Each option employed a heat source with a thermal power of 500 watts BOM and 468 watts at the end of an 8.2-year Pluto mission.

In one system option the heat source was thermally coupled to two engines, and in the other it was coupled to four engines. In both cases, the engines were to be sized to enable the system to produce full design power (75 W EOM) after failure of one engine. Such redundancy is deemed essential to achieve acceptable reliability of dynamic power systems.

The engine and alternator designs generated by STC under the OSC subcontract for the two system options are depicted in Figure 9, and their predicted EOM performance, with and without an engine failure, are summarized below:

**Table 3.** Engine and Alternator Characteristics (STC).

	2-Engine Option	4-Engine Option
Engines Failed	0	1
Engines Operating	2	1
Power Output, watts DC		
Per Engine	62.5	124
Total	125	124
Conversion Efficiency, %	27	26
Mass, kg		
Per Engine	6.5	1.6
Total	13.4	6.7

There were two principal reasons why OSC asked STC for a four-engine design option in addition to the two-engine option. It was felt that the four small engines were closer in size to STC's previously demonstrated 11-watt engine, and therefore would require less development. Specifically, the 11-watt engine had not employed any matrix regenerators, and it was hoped that this would also be possible in the case of the four-engine configuration. But STC's analytical results showed that omitting the regenerator matrix was not practical. Even for the smaller engines, a regenerator matrix is required for efficient operation of the 75-watt system [20].

However, STC's subcontracted study (1994) did reveal that, contrary to our expectations, the mass of the four small engines and alternators, in spite of their lower efficiency, were much lower than that of the two large engines. This would not be true if there were no redundancy requirement. But with the redundancy requirement, the two engines must each be capable of producing 100% of the system's design power, whereas the four engines each need only be able to produce 33% of design power. Thus, a 75-watt output can be redundantly met with two 75-watt engines or with four 25-watt engines. As a result, STC found that the four small engines and alternators had only half the mass of the two large engines, as shown in Table 3. This was one of the most significant findings of the OSC-sponsored STC study. Because of the large mass difference, the OSC system design is based on the four-engine option, in spite of its somewhat lower conversion efficiency.

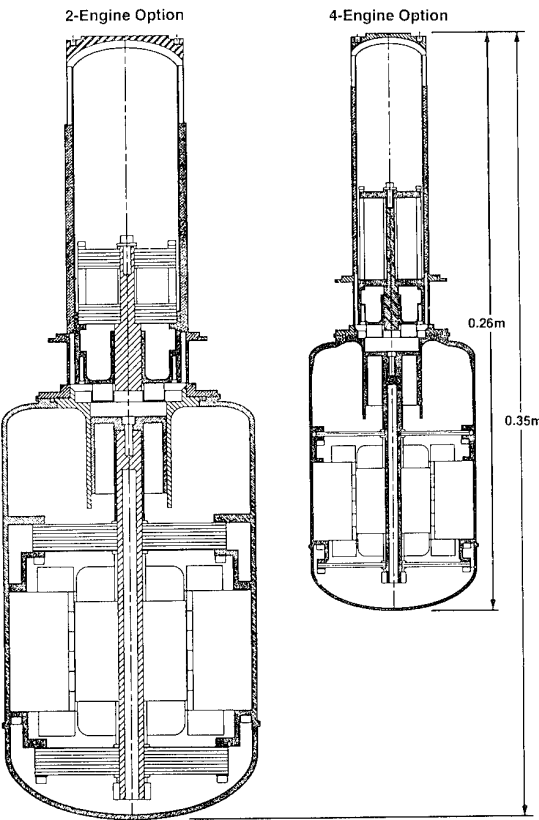


**Figure 10.** STC Engine and Alternator Designs.

**System Design and Assembly.** The OSC-generated design and assembly sequence of the Stirling power system [9] were based on two main ground rules: no single-point failures, which means that the system can continue to operate at or near full power after failure of one engine/alternator or one radiator heatpipe; and postponement of fueling as late as possible in the assembly sequence to minimize the need for glove box operations.

Figure 11 shows the four small engines being inserted into the four ports of the heat source housing. It also shows an inner hot-frame, which is wrapped with multifoil thermal insulation and inserted into that housing, where it is supported by the hot ends of the four engines. That frame serves to collect the heat emitted by the heat source and deliver it to the engines' hot ends, and also serves as the structural support of the heat source. The four engines' hot sections are then wrapped in multifoil thermal insulation and inserted into the housing ports.

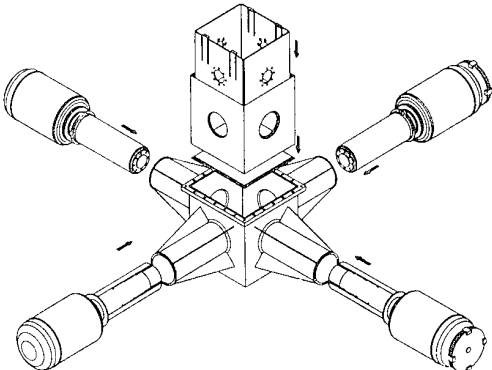


**Figure 11.** Engines, Housing, and Hot Frame.

Before insertion of the heat source into the housing, a segmented radiator is attached to the engines' cold ends. The radiator consists of four quadrants, one of which is shown in exploded view in Figure 12. As seen, it consists of an aluminum honeycomb core with an embedded copper/water heatpipe. The honeycomb core is covered with aluminum skins, which in turn are covered with high-conductivity graphitized carbon-carbon skins. The latter material, developed by NASA's LeRC, has excellent thermal conductivity at a relatively low density [21].

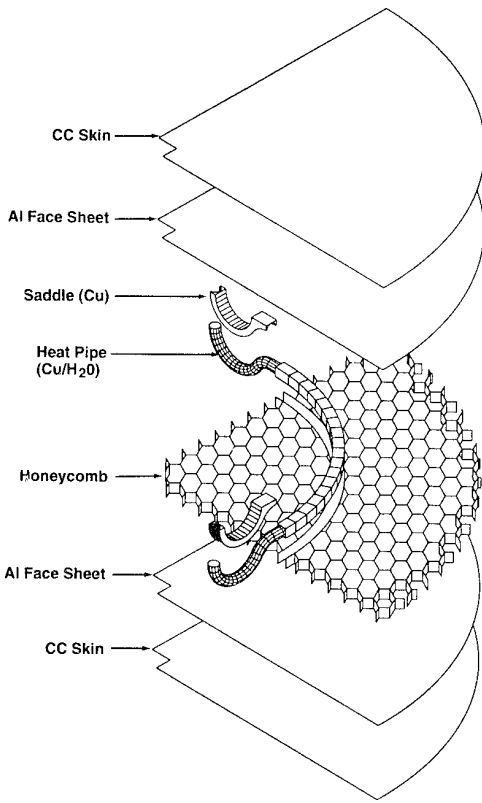


Figure 12. Exploded View of Radiator Quadrant.

Each quadrant's heatpipe follows a quarter-circular path, and has two semi-circular ends which are brazed to copper saddles. Those saddles are then bonded to the heat rejection zones of the two engines that adjoin the quadrant. Thus, each of the four engines is cooled by two radiator quadrants, and each quadrant is connected to two engines. As shown in Figure 13, the bonded assembly forms a planar double-sided radiator. The figure also depicts the two GPHS modules ready for insertion into the insulated housing. This operation must be carried out in a glove box, *e.g.*, by using a vacuum tool to pick up the GPHS modules. The glove box is filled with an inert cover gas.

Finally Figure 14 shows the assembly after insertion of the heat source modules, ready for closure by the multifoil-lined top cover of the housing. Final sealing, except for a gas management valve, is by O-ring or by welding.

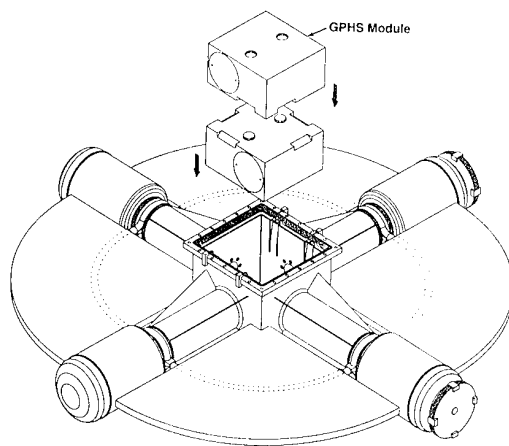


Figure 13. Insertion of Heat Source into Housing

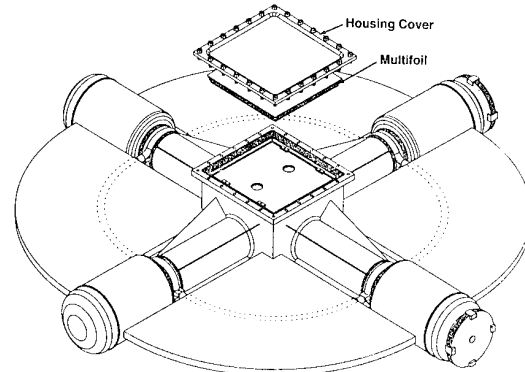


Figure 14 . Closure of Fueled Generator.

**System Analysis.** There are two basic system design variables: the size of the radiator quadrants, and the thickness of their carbon-carbon face sheets. Increasing either variable increases the system's power output and conversion efficiency, but also its mass. Thus, there is a trade-off between system performance versus mass, and the purpose of the system analyses is to quantify that trade-off.

OSC did not perform an independent assessment of the Stirling engine's and linear alternator's performance but used predictions furnished by STC [20], since those predictions were based on the same analytical methods they had used to design and successfully predict the measured performance of their 11-watt engine. The performance predictions which STC supplied to OSC had been based on an 80°C heat rejection temperature. In addition, STC had furnished data on the effect of varying the rejection temperature on the engine's power output. That data was inserted into OSC's detailed (465-node) thermal analysis to determine the effect of a range of radiator sizes and graphite skin thicknesses on heat rejection temperature, system mass, EOM power output and system efficiency, and specific power (after conversion of the alternator's AC output to 28 volts DC).

For an illustrative radiator radius of 35 cm, the effect of graphite skin thickness on system performance is shown in Figure 15. As can be seen, the specific power maximizes at a graphite thickness of 0.405 mm. This graphite thickness yields a generator mass of 13.2 kg, an 88°C heat rejection temperature, a 108-watt EOM output at 28V, a 23% system efficiency, and an 8.3 W/kg specific power. For thinner graphite skins, the system's specific power diminishes because of increased temperature drops in the radiator, leading to decreased power outputs and efficiencies. For thicker graphite skins, the engines' heat rejection temperature decreases and their efficiency increases, but the system's specific power diminishes because the increase in system power and efficiency is not enough to compensate for the increased mass of the radiator face sheets.

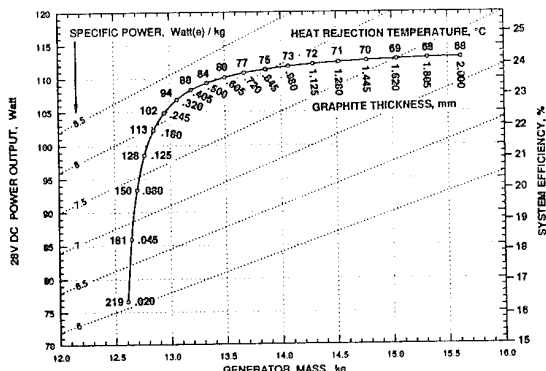


Figure 15. Effect of Graphite Thickness On EOM Performance of Generator with 35 cm Radiator.

Similar analyses were performed for seven radiator radii, ranging from 19 to 43 cm, with the results displayed by the seven curves of Figure 15. The graphite skin thickness is the implicit variable in each curve. The envelope tangent to those curves represents the highest power output for a given mass, or the lowest mass for a given EOM power. As shown, the specific power maximizes with a 39 cm radiator radius and a graphite skin thickness yielding a 13.5 kg generator mass. This results in a heat rejection temperature of 75°C, an EOM output of 112 watts, a system efficiency of 24%, and a specific power of 8.3 w/kg.

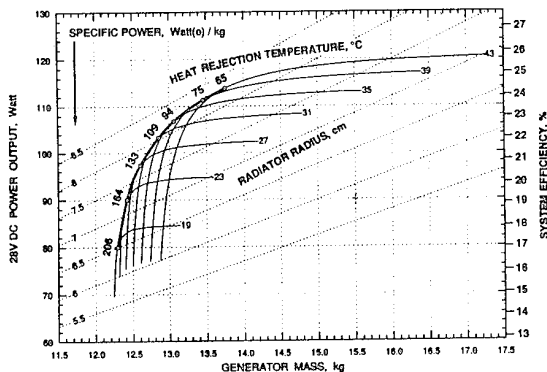


Figure 16. Effect of Radiator Size on EOM Performance of Unfailed System.

The results presented thus far were all for the failure-free system, with all four engines and four heatpipes operational. Figure 17 shows corresponding results after one engine failure, and Figure 18 shows similar results after one heatpipe failure.

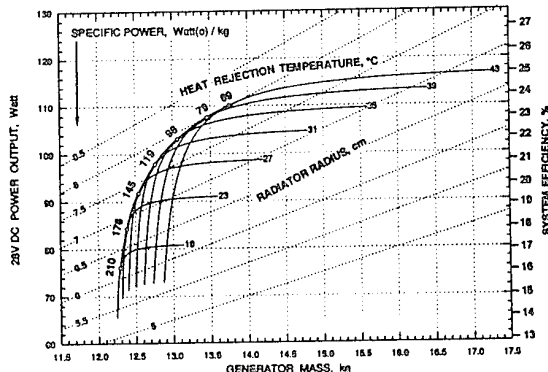


Figure 17. EOM Performance of System with Failed Engine.

As shown in Figure 17, the failure of one engine has only a minor effect on system performance, because the alternators' electronic control systems will automatically adjust the stroke of the unfailed engines to raise their output by 33%, thus maintaining design power.

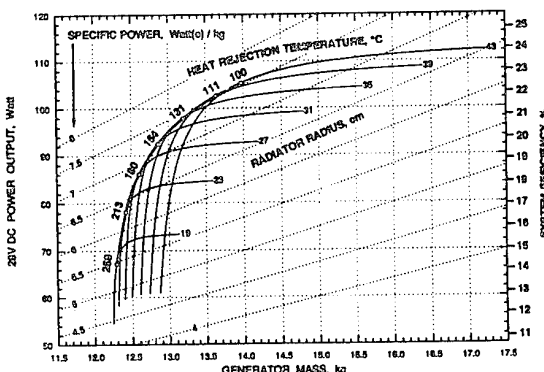


Figure 18. EOM Performance of System with Failed Heatpipes.

Figure 18 shows that the failure of one heatpipe would cause a significant drop in the system's power output, and is therefore the controlling case. But that effect could be avoided by installing two redundant heatpipes per radiator quadrant, although that would result in a small increase of the system's mass.

As shown in Figure 17, the EOM specific power of the system with one failed engine maximizes at 8 w/kg with a radiator of 39 cm radius. As shown, that results in a generator mass of 13.5 kg and a heat rejection temperature of 79°C, and yields an EOM system efficiency of 23% and output power of 108 watts at 28 VDC.

But that 108-watt output is well above the Pluto mission's 75-watt EOM goal, which itself contains allowances for 20% contingencies plus 10% margins. As shown, Pluto's 75-watt EOM goal can be met (actually exceeded) with a substantially smaller generator having a 23-cm radiator radius and weighing 12.4 kg. Such a radiator would result in a heat rejection temperature of 176°C at the engines' cold ends, and yield a

system efficiency of 18% and EOM power of 84 watts at 28 VDC. A cross-sectional overview of that smaller system is depicted in Figure 19, and Table 4 presents its mass breakdown.

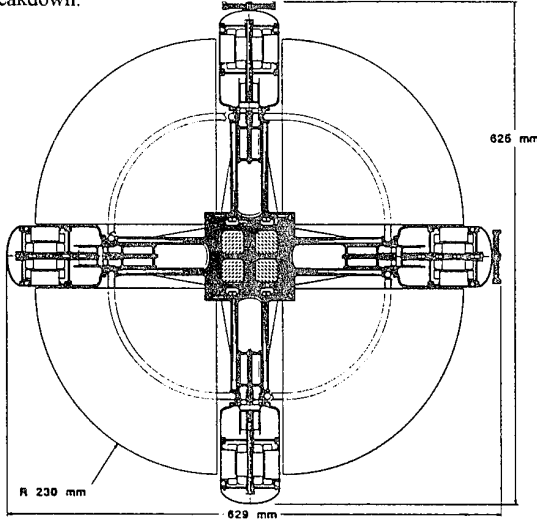


Figure 19. System Cross-Section.

Table 4. Stirling System Mass Summary.

Components	kg
Heat Source - 2 GPHS	2.894
Heat Collector (Mo)	0.609
Multifoil Insulation (Mo/ZrO <sub>2</sub> )	0.441
Housing & Cover Plate (Al)	0.768
Stirling Engine & Alternator (4)	7.067
Radiator (Al/C/C)	0.570
Fasteners & Hardware	0.035
<b>TOTAL</b>	<b>12.384</b>

### Thermophotovoltaic System Study

**System Design.** This subsection briefly reviews the design of the power system (consisting of a radioisotope heat source, TPV converter, heat rejection radiator) and its integration with the Pluto spacecraft. These were described more fully in other papers [6,7]. Optical, thermal and electrical analyses and optimization of the integrated system are discussed in subsequent sections.

The RTPV generator design is based on the use of two GPHS modules, which would be a two-thirds reduction from the six modules used in the RTG design for the Pluto mission [1].

As shown in Figure 20, the two GPHS modules are enclosed in a common molybdenum canister. The inside of the canister's end caps is lined with iridium as a reaction barrier between the graphite and molybdenum, and the outside of its side walls is coated with tungsten to minimize sublimation. To reduce the temperatures in the heat source, the inside of the canister's side walls are roughened to raise their effective total emissivity to 0.60. So is the walls' outside, for reasons explained in previous papers [5,6,7].

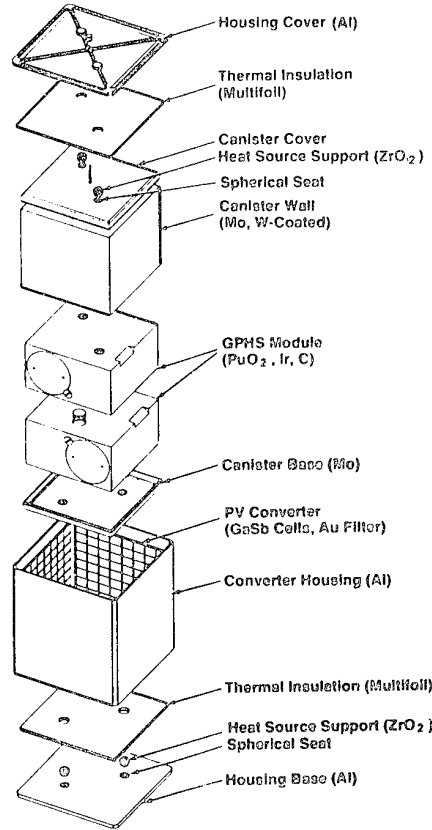


Figure 20. Exploded View of Converter.

Figure 20 presents an exploded view of the two-module heat source and of the thermophotovoltaic converter, and lists their components' construction materials. As indicated, the canister's two end faces are thermally insulated by a multifoil assembly, consisting of 60 layers of 0.008 mm Mo foils separated by ZrO<sub>2</sub> spacer particles, similar to those used in previous thermoelectric converters. Our analysis showed that only 2.2% of the thermal power is lost through the multifoil insulation.

As indicated in Figure 20, each of the canister's four side faces radiates heat to a photovoltaic array of 8x8 closely spaced gallium antimonide cells, slightly over 1 cm<sup>2</sup> each. The canister side walls and planar arrays of filtered PV cells are parallel to each other and closely spaced to provide a good view factor for radiative interchange. The spacing between the PV cells is the minimum necessary for the desired series-parallel connections. The cells on each face are bonded to a BeO substrate, which in turn is bonded to the generator's aluminum side wall.

Each of the four cell arrays is covered with a spectrally selective infra-red filter [22,23], to permit the transmission of those wavelengths which can be efficiently converted to electricity by the PV cells, and the reflection of those wavelengths that cannot. Much of the reflected radiation is absorbed by the heat source canister, which then re-emits it with a full spectral distribution. Thus, the unused reflected energy is conserved, which reduces the energy to be supplied by the radioisotope heat source and greatly increases the efficiency of the generator. Hence, the selective filter is a vital element of this RTPV system.

Each of the generator's four PV cell arrays is covered with a resonant gold filter. The filter consists of a continuous thin gold film deposited on a transparent substrate (e.g., sapphire), about 10 cm x 10 cm, containing over two hundred million submicronic holes per  $\text{cm}^2$  in its active regions (i.e., opposite each PV cells). The size, spacing, and geometry of the hole pattern determines the performance of the resonant filters.

Since the heat source modules are contained in a monolithic canister, unlike the stack of unsupported modules used in preceding RTGs [24], there is no need for a complex axial preload mechanism to hold the stack together during launch vibration. As indicated in Figure 20, each of the canister's two end faces is supported by a pair of diagonally opposed low-conductivity zirconia balls. The diagonal locations at the two end faces are orthogonal to each other. The zirconia balls penetrate through the multifoil thermal insulation, and are seated in spherical indentations on the outside of the canister end caps, and on the inside of the generator housing end caps. Thus, they provide both axial and lateral support to the heat source. For the dimensions shown, our analysis showed that only 0.5% of the heat source's thermal power is lost through the zirconia support balls. Hence, over 97% of the generated heat arrives at the converter.

The converter's 256 PV cells are arrayed in a series-parallel matrix. At each horizontal level, the cells are parallel-connected in groups of four, and these groups of parallel cells are series-connected to groups in adjacent horizontal levels. Thus, each generator side has two series-parallel networks of 8x4 cells, and the generator's eight networks are connected in series with each other to form a 64x4 series-parallel network, for a total output of approximately 28 volts.

**Heat Rejection System.** The RTPV needs much larger radiator fins than typical RTGs, because they must operate at much lower heat rejection temperatures to achieve their high efficiencies. The optimum dimensions, i.e., the dimensions that maximize the system's specific power, were determined by detailed analyses described later. Detailed analyses are warranted because the radiators are the biggest mass component of the RTPV system.

Figure 21 shows an exploded view of the generator and of one of the four radiator fins, with typical dimensions. As shown, there is a large trapezoidal fin bonded to each side of the converter housing. The exploded fin view shows a central core consisting of an aluminum honeycomb with two embedded  $\text{Al}/\text{NH}_3$  heat pipes. To each face of the honeycomb core, two skins are bonded: an inner skin of aluminum which has minimal thickness over most of its length, but is thickened near the fin root to provide increased structural strength for resisting bending moments during launch; and an outer skin consisting of a graphitized carbon-carbon composite to provide high thermal conductance in the fiber direction. The graphite fibers are oriented in the vertical direction, normal to the heat pipes' axes. In that direction they have a thermal conductivity twice that of copper, at about one fourth its density [21]. They serve to distribute the heat from the heat pipes over the width of the fin. They also provide the fin with high-emissivity surfaces.

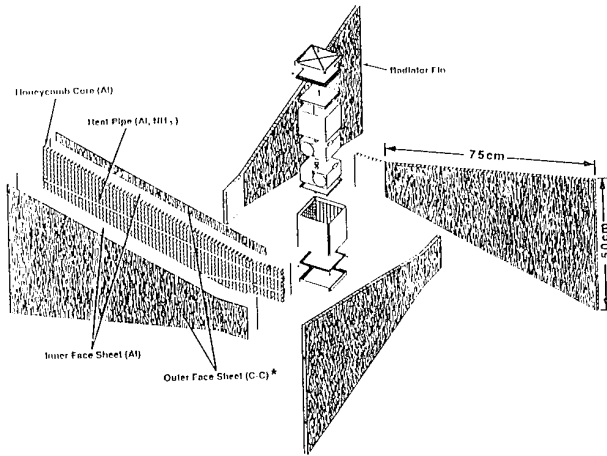


Figure 21. Exploded View of RTPV Generator and of Radiator Fin.

Finally, we need to examine whether these large fin sizes could really be accommodated on JPL's Pluto spacecraft design, which is shown in Figure 22. An earlier design had located the high-gain antenna at the top of the spacecraft, but this has now been moved to the side as shown. This frees up the space on top for mounting the optimized RTPV generator with its 75 cm-long fins. As shown, when the generator is rotated 45 degrees about its axis, its fins clear the antenna.

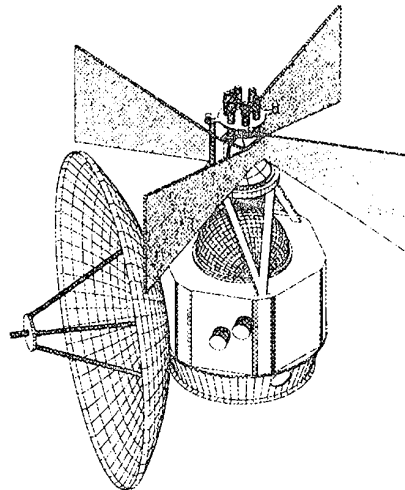


Figure 22. Optimized RTPV Generator Mounted on Top of Pluto Spacecraft.

**Alternative Arrangement.** An alternative design arrangement to minimize system mass, suggested by A. Newhouse, is depicted in Figure 23. It calls for merging the RTPV radiator with the parabolic high-gain antenna of the Pluto spacecraft. Both of these components employ carbon-carbon face sheets, stiffened respectively by aluminum heat-pipes and ribs.

As indicated, the radiator's high-conductivity fibers would be oriented in a circumferential direction, normal to its eight heat pipes. Merging the radiator and antenna would eliminate the need for the radiator's aluminum honeycomb and face sheets, since the radiator would be supported by the antenna's stiffening ribs, and since a parabolic dish is inherently much stiffer than a cantilevered planar fin. As will be shown, this arrangement - if feasible - would substantially raise the specific power of the RTPV system.

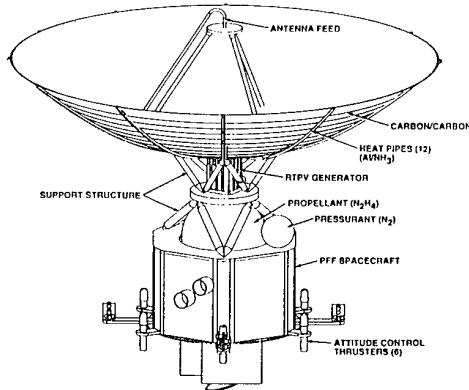


Figure 23. RTPV Generator and Pluto Spacecraft with Common Radiator/Antenna.

**Effect of Filter and Cell Improvements.** As described in detail in previous publications [5,6,7], analysis of the RTPV generator requires three sets of wavelength-dependent data: the emissivity of the heat source canister, the quantum efficiency of the PV cell, and the reflectivity of the IR filter. For the latter two, OSC's previous study employed measured and projected performance models supplied to us by Boeing (now EDTEK) personnel in 1993 [5]. The effect of those models is depicted in Figure 24, which presents plots of the converter's output power density versus input heat flux for the projected and measured filter and cell performance models (for an illustrative 0°C cell temperature). The figure also shows lines of constant conversion efficiency and the effect of heat flux on source temperature. As can be seen, for a given heat flux the projected filter and cell models yield much higher conversion efficiencies than the measured models. Therefore, OSC initiated a subcontract at EDTEK to develop improved filters and cells, and to demonstrate what performance improvements can actually be achieved.

In Figure 24 the differences between the first and second curves and between the third and fourth curves represent the effect of projected cell improvements; and the differences between the first and third curves and between the second and fourth curves represent the effect of projected filter improvements. Clearly, the efficiency gain produced by the projected filter improvement is much greater than that yielded by the projected cell improvement. Therefore, OSC requested that EDTEK give higher priority to filter improvement than to cell improvement.

The EDTEK subcontract started in the fall of 1994, and several of the filters made to date (May 1995) demonstrate very encouraging improvement over the filter measured in 1993. Their performance has closed 75% of the gap between the 1993 measured and projected performances. This enhances our confidence in achieving the projected performance levels in EDTEK's continuing filter and cell improvement studies [25].

**Parametric System Analysis and Optimization.** Analysis of the power system, including its heat rejection system, requires coupled optical, thermal, and electrical analyses. These analyses were described in detail in previous reports [5,6,7], were carried out by means of a thermal analysis code (SINDA [26]) that had been modified by OSC, and by a standard thermal radiation code (SSPTA [27]). For the former we constructed a 197-node model, and for the latter a model consisting of 496 surfaces.

In the coupled analysis, the heat generation rate is known, but the heat source surface temperature and cell temperature are not. Therefore, the analysis must be carried out iteratively. In each iteration, the two thermal codes compute a new set of canister and cell temperatures, which are used as inputs in the next iteration. This iterative procedure is repeated until the modified code converges on a consistent solution.

For a fixed heat source thermal power and converter design, the only other system design parameters are the size of the radiator fins and the thickness of the high-conductivity carbon-carbon face sheets (see Figure 21). Increasing either of those parameters will lower the cell temperature, which increases the power output and efficiency. But this benefit is obtained at the cost of increased system mass. Thus, the system design requires a trade-off between system mass and performance (efficiency, power output). The goal of the optimization study is to determine the radiator dimensions which maximize the power system's specific power. As was explained in detail in the previous papers [5,6], the mass of the radiator fins includes an allowance for thickening the aluminum honeycomb skins near the fin roots, to enable the cantilevered fins to withstand the bending moments during launch vibration.

**Effect of Graphite Skin Thickness.** Let us first examine the effect of varying the graphite skin thickness on system characteristics for a set of illustrative radiator fin dimensions. For a 75 cm root-to-tip fin length, a 50 cm tip height, a 9.5 mm honeycomb thickness, a 0.076 mm aluminum skin thickness, and a converter with 90% active cell area, the effect of varying the graphite skin thickness from 0 to 0.76 mm is illustrated in Figure 25. The figure shows the effect of graphite skin thickness on system mass, cell temperature, output power, system efficiency, and specific power. In each of the three figures, the solid curve represents results based on measured values of SCAN-A filter transmittance and cell quantum efficiency, the dotted curve is based of SCAN-A filter and

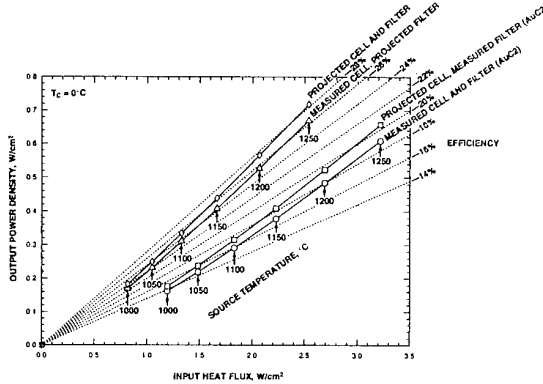


Figure 24. Effect of Projected Cell and Filter Improvements on Conversion Efficiency for Same Heat Flux.

projected cell performance, and the dashed curve is based on projected values of the two.

As shown in Figure 25, for each performance model the initial addition of the graphite skins lowers the cell temperature which increases the output power and efficiency significantly, but after adding a surprisingly small thickness (typically 0.15 mm) further additions of graphite only increase the mass with little further increase of power or efficiency.

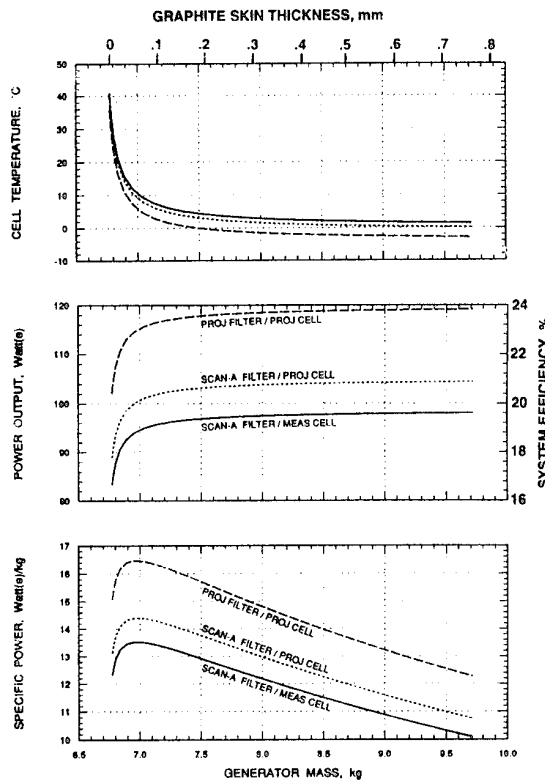


Figure 25. Effect of Graphite Skin Thickness.

**Effect of Radiator Fin Dimensions.** Similar analyses were carried out for fin lengths ranging from 50 to 100 cm and for fin tip heights of 30 and 50 cm. The results for all cases showed similar trends, confirming the previous conclusion that the specific power of the design is maximized at a graphite skin thickness around 0.15 mm. With thicker graphite skin, the increase in power output is quite small and is outweighed by the increased graphite mass.

The results of the parametric design studies are displayed in Figure 26 and 27. Both figures show curves representing the results of thermal, electrical, and mass analyses for fin lengths ranging from 50 to 100 cm and fin tip heights ranging from 30 to 50 cm, with the graphite skin thickness as the implicit variable within each curve. Each point on each curve is the result of an iterative solution of the coupled thermal and electrical analyses, using the modified thermal analysis code described earlier. All curves assume aluminum skins varying from 0.08 mm at the fin tip to whatever is needed near the fin root to survive a 40-g launch load without exceeding the allowable stress limit.

Figure 26 shows plots of cell temperature versus generator mass. For each fin size, the upper curve is based on the measured (SCAN-A) filter transmittance and the projected PV quantum efficiency model, and the lower curve is for the projected filter and cell characteristics. As can be seen, the larger fins lead to very low cell temperatures, but at substantially higher masses.

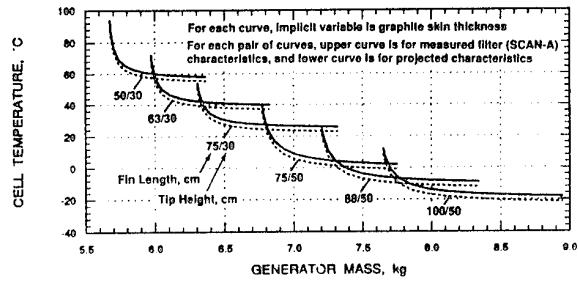


Figure 26. Effect of Fin Dimensions on Cell Temperature.

The trade-offs between mass and performance for the measured and projected filters are summarized in Figure 27. For each fin size, it presents curves of output power and system efficiency versus generator mass, with graphite skin thickness as the implicit variable. It also shows diagonal lines of constant specific power, which identify the fin dimensions that maximize the generator's specific power.

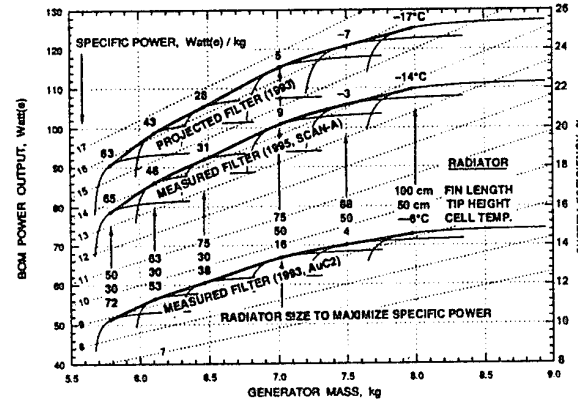


Figure 27. Effect of Filter on System Performance for Various Radiator Sizes.

For each filter and cell performance model, the figure shows a family of performance curves for different fin dimensions and a tangent envelope curve, with indicated cell temperatures at their point of tangency. For each performance model, the corresponding envelope curve represents the highest specific power that can be achieved by optimizing the system's radiator geometry. For every point on the envelope, there is some combination of fin length, fin tip height, and graphite skin thickness that will achieve the indicated performance.

Comparison of the three envelopes shows that EDTEK's improved filter (SCAN-A) has already succeeded in closing ~75% of the performance gap between their 1993 measured and projected filters.

As seen in Figure 27, for all three performance models the system's specific power is maximized with a 75 cm fin length and 50 cm fin height. But note that this optimum is quite broad. As illustrated in Table 5, major deviations from the optimum design result in only modest reductions in specific power. Thus, the designer has wide latitude in trading off power and efficiency versus mass and size to meet specific mission goals.

For example, for the projected filter and cell performance, the BOM power could be raised from 115 watts to 125 watts by lengthening the fins from 75 cm to 100 cm. As shown, this would increase the generator's mass from 7.0 to 8.0 kg, but would only decrease its specific power from 16.4 to 15.7 w/kg. Conversely, if desired the generator mass could be reduced from 7.0 kg to 5.8 kg by reducing the fin size. As shown, this would reduce the BOM power from 115 watts to 90 watts, but would only lower the generator's specific power from 16.4 to 15.6 w/kg.

**Table 5.** Effect of Off-Optimum Design on RTPV Performance.

Goal	Low Mass	Max Sp Power	High Power
Fin Length, cm	50	75	100
Fin Tip Height, cm	30	50	50
Cell Temperature, °C	63	5	-17
Power (BOM), Watt	90	115	125
Efficiency (BOM), %	18.1	23.1	25.0
System Mass, kg	5.8	7.0	8.0
Specific Power, W/kg	15.6	16.4	15.7

Even better performance may be achievable by employing the combined radiator/antenna scheme depicted in Figure 23. Comparative results for trapezoidal fins (dashed lines) and parabolic fins (solid curves) are depicted in Figure 28. There are two performance curves for each geometry. In each case, the lower curve is for the measured filter, and the upper curve is for the projected filter. As can be seen, the parabolic combined filter/radiator yields much higher performance than the previous trapezoidal radiators. In fact, the performance of the system with a parabolic radiator and the measured filter is actually better than that of a system with trapezoidal radiators and the projected filter.

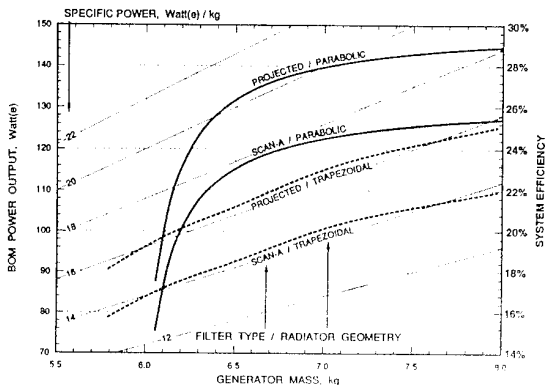


**Figure 28.** Effect of Radiator Geometry and Filter on System Performance.

## CONCLUSION

Finally, the performance of the three system options are compared in Figures 29 and 30. These were obtained by combining Figure 28 for the RTPV option with the envelope of Figure 16 for the Stirling option and with the three RTG point design results (for BOM and Russian fuel) from Table 1. Figure 29 compares the system efficiency of the three options and Figure 30 compares their power output and specific power.

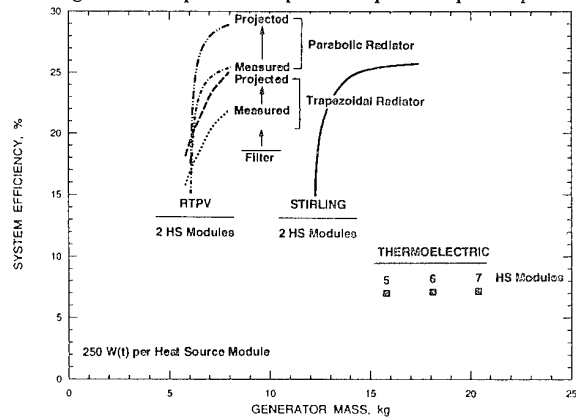


**Figure 29.** Comparative System Efficiency of Three Options.

As can be seen, both of the advanced-technology options (RTPV and Stirling) have much higher system efficiencies than the thermoelectric option, with consequent reduction in the number of heat source modules. In fact the efficiency of the Stirling system is as great as that of the thermophotovoltaic system with trapezoidal radiator fins, but its mass is more than twice as high, though not as high as that of the thermoelectric system.

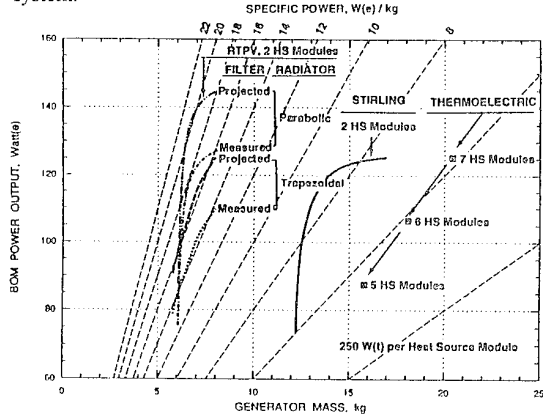


**Figure 30.** Comparative Power Output and Specific Power of Three Options.

Finally, Figure 30 shows that the RTPV system offers a much higher specific power than the Stirling system at its current state of technology. The high mass of the Stirling system is primarily due to the massiveness of the linear alternator's magnetic components. STC has design concepts for greatly reducing the mass of those components, but those concepts are still unproven and were not used in the OSC study.

The main conclusion is that the advanced conversion technologies, reportedly including AMTEC, promise much higher specific powers and system efficiencies than the far more mature silicon-germanium thermoelectric systems. That is why DOE and NASA are pursuing the development of those technologies. If one or more of those technologies are successfully developed, thermoelectric systems will clearly require a step change rather than marginal improvements to be competitive.

Acknowledgment. The author takes pleasure in acknowledging the contributions of his OSC colleagues C. Or and V. Kumar to the above studies, and the continuing encouragement of his DOE sponsors.

#### References

- [1] Schock, A., and C. T. Or, "Effect of Fuel and Design Options on RTG Performance Versus PPF Power Demand," *Proc. of the 29th Intersociety Energy Conversion Engineering Conference*, held in Monterey, CA, 7-12 August 1994.
- [2] Schock, A., C. T. Or, and V. Kumar, "Design Modifications for Increasing the BOM and EOM Power Output and Reducing the Size and Mass of RTG for the Pluto Mission," *Proc. of the 29th Intersociety Energy Conversion Engineering Conference*, held in Monterey, CA, 7-12 August 1994.
- [3] Schock, A., "RTG Options for Pluto Fast Flyby Mission," IAF-93-R.1.425a, 44th Congress of the International Astronautical Federation, Graz, Austria, 16-22 Oct 1993.
- [4] Schock, A. and V. Kumar, "Radioisotope Thermophotovoltaic System Design and its Application to an Illustrative Space Mission," *Proc. of the NREL Conference on Thermophotovoltaic Generation of Electricity*, held at Copper Mountain, Colorado, July 1994, published by the American Institute of Physics.
- [5] Schock, A., M. Mukunda, T. Or, and G. Summers, "Analysis, Optimization, and Assessment of Radioisotope Thermophotovoltaic System Design for an Illustrative Space Mission," *Proc. of the NREL Conference on Thermophotovoltaic Generation of Electricity*, held at Copper Mountain, Colorado, July 1994, published by the American Institute of Physics.
- [6] Schock, A., et. al. "Design, Analysis, and Optimization of a Radioisotope Thermophotovoltaic (RTPV) Generator, and its Applicability to an Illustrative Space Mission," 45th Congress of the International Astronautical Federation, Jerusalem, 9-14 October 1994.
- [7] Schock, A., C. Or, and M. Mukunda, "Effect of Expanded Integration Limits and of Measured Infrared Filter Improvements on Performance of RTPV System," to be presented at the 2nd NREL Conference on Thermophotovoltaic Generation of Electricity, in Colorado Springs, Colorado, July 1995.
- [8] Schock, A., "RSG Options for Pluto Fast Flyby Mission," IAF-93-R.1.425b, 44th Congress of the International Astronautical Federation, Graz, Austria, 16-22 Oct 1993.
- [9] Schock, A. Or, C.T., and V. Kumar, "Radioisotope Power System Based on Derivative of Existing Stirling Engine," IECEC-95-159, to be presented at the 30th Intersociety Energy Conversion Engineering Conference, in Orlando, Florida, August 1995.
- [10] Stern, Allen, "The Pluto Reconnaissance Flyby Mission," in Trans. of the American Geo-physical Union, Vol. 74#7, pp 73, 76-78.
- [11] Staehle, R.L., et. al., "Pluto Mission Progress Report: Lower Mass and Flight Time through Advanced Technology Insertion," IAF-93-Q.5.410, 44th Congress of the International Astronautical Federation, Graz Austria, 16-22 October 1993.
- [12] Staehle, R.L., et. al., "Pluto Mission Development Status," presented at IAA International Conference on Low-Cost Planetary Missions, Laurel, MD, 12-15 April 1994.
- [13] Schock, A., "Design Evolution and Verification of the General-Purpose Heat Source," #809203, *Proc. of 15th Intersociety Energy Conversion Engineering Conference*, held in Seattle, WA, 18-22 August 1980.
- [14] Schock, A. and H. Sookiazian, "Design Optimization of RTG for Solar-Polar Mission," #799307, *Proc. of 14th Intersociety Energy Conversion Engineering Conference*, held in Boston, MA, 1979.
- [15] Schock, A., "Thermal and Electrical Analysis of Mars Rover RTGs," *Proc. of the 24th Intersociety Energy Conversion Engineering Conference*, held in Washington, D.C., 6-11 Aug 1989.
- [16] Schock, A., "Closed-Form Solution for the Effect of Fuel Decay and Thermoelectric Degradation on Output of SiGe RTGs," *Proc. of the 26th Intersociety Energy Conversion Engineering Conference*, held in Boston, MA, 4-9 August 1991.
- [17] Dochat, G. And J. Dudenhoefer, "Performance Results of Stirling Power Converter," *Proc. of the 11th Symposium on Space Nuclear Power Systems*, CONF-9450101, M.S. El-Genk and M.D. Hoover, eds., American Institute of Physics, New York, AIP Conference Proc. No. 301, 1: 457-464, 1994.
- [18] Dochat, G.R. and J.E. Dudenhoefer, "Stirling Technology Development Status," *Proc. of the 10th Symposium on Space Nuclear Power Systems*, CONF-930103, M.S. El-Genk and M.D. Hoover, eds., American Institute of Physics, New York, AIP Conference Proc. No 271, 2: 1039-1044, 1993.
- [19] Ross, Brad, Garth L. Tingey, and Gerald C. Sorenson, "Isotope Powered Stirling Generator for Terrestrial Applications," *Proc. of the 12th Symposium on Space Nuclear Power and Propulsion*, M.S. El-Genk, ed., American Institute of Physics, New York, AIP Conference No. 324, 1: 95-110, 1995.
- [20] Stirling Technology Company, "Evaluation of Stirling Converters using STC Technology for Pluto Fast Flyby Mission," STC Report No. 9426, December 1994.
- [21] Denham, H.B., et. al. "NASA Advanced Radiator C-C Thin Development," *Proc. of the 11th Symposium on Space Nuclear Power Systems*, CONF-940101, M.S. El-Genk and M.D. Hoover, eds., American Institute of Physics, New York, AIP Conference No. 301, 3: 1119-1127, 1994.
- [22] Chase, S.T. and R.D. Joseph, "Resonant Array Bandpass Filters for the Far Infrared," Applied Optics, Vol. 22, No. 11, 1 June 1983, pp 1775-1779.
- [23] Kogler, Kent J. and Rickey G. Pastor, "Infrared Filters Fabricated from Submicron Loop Antenna Arrays," Applied Optics, Vol. 27, No. 1, 1 Jan 1988, pp 18-19.
- [24] Schock, A., "Use of Modular Heat Source Stack in RTGs," #799305, *Proc. of 14th Intersociety Energy Conversion Engineering Conference*, held in Boston, MA, 1979.
- [25] Horne, W. E., M. D. Morgan, and V. S. Sundaram, "IR Filters for TPV Converter Module," to be presented at the 2nd NREL Conference on Thermophotovoltaic Generation of Electricity, in Colorado Springs, CO, July 1995.
- [26] Gaski, J., SINDA (System Improved Numerical Differencing Analyzed), version 1.315 from Network Analysis Associate, Fountain Valley, CA, 1987.
- [27] Little, A.D., SSPTA (Simplified Space Payload Thermal Analyzer), version 3.0/VAX, for NASA/Goddard, by Arthur D. Little Inc., Cambridge, MA, 1986.

## ELABORATION OF NEW CONCEPT ON CREATION OF TRANSPORT NUCLEAR REACTOR - THERMOELECTRIC GENERATOR

N.D.Marchuk

*Institute for Nuclear Research, National Ukrainian Academy of Sciences  
Kiev, 252022, 47, pr.Nauki, Ukraine*

The possibility of creation of so-called "built-in" NR-TEG power system has been considered. The complex of theoretical and experimental investigations of nuclear irradiation influence (thermal and fast nuclear reactor neutrons and modeling space irradiation including) on its physical properties has been performed to meet the resource requirements in the severe conditions of the outer space and nuclear reactor irradiation. The methods of prediction and improvement materials radiation stability have been elaborated. The method of "in-pile" material parameters regeneration has been also experimentally verified. From the effectiveness point of view the optimal "built-in" NR-TEG power range is from 50 to 500 kWe.

### **Introduction**

The main reason of enforced attention to methods of direct thermal energy transformation is occurrence of new specific areas of electrical energy sources application. That is requiring combination of such qualities, as compactness, high reliability, long life and autonomy, high specific power of the generating system, profitability and absence of necessity in constant maintenance service. To areas of such devices application first of all concern development of space and global ocean exploration. The advantages of thermoelectrical way of thermal energy transformation are caused by successes achieved in the last years in the field of solid state physics and semiconductor thermoelectric materials technology. In comparison with other types of direct energy transformation devices, in particular, with thermoionic, thermoelectric generators (TEG) have already being tested more than 50 years at various levels of power under different conditions of operation.

The development of increased power TEG is possible only on the basis of the nuclear reactor (NR) practically of a unique source of energy, by use of which the power is not limited.

The nuclear reactor - thermoelectric generator (NR-TEG) have beside of properties, putting forward them in number the most perspective for transport objects. To these properties concern:

- static character of the electric power reception and source of heat, independent from external conditions;
- absence of mechanisms with rotating parts, extended pipelines under pressure, phase conversions of working body - that raise reliability of device and reduce its acoustic field;
- compactness of installation, simplicity of regulation and service, opportunity of long work without service.

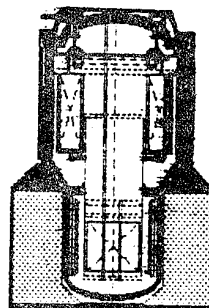
There are several NR-TEGs, at creation of which various physical principles were realized. They are "Romashka" (former USSR) [1], SNAP-10A (USA) and well-known perspective American SP-100 of increased power. In "Romashka", the heat generated in the active core of the fast neutrons reactor was transferred to the thermoelectric battery, located on an outside surface of berillium reflector. In American project SP-100 a new principle of conjunction NR with TEG has been used - transport of heat from active core by high-temperature lithium filled heat pipes [2,3]. Besides that, some other so-called "taken-out" types of NR-TEG exist, when the heat from the active core of the nuclear reactor is taken out by means of the heat-carrier and TEG is placed outside of active core on tubes with the circulating heat-carrier (for example, "Gamma" installation). However, as result of accounts has shown, power of such installations is essentially limited by the level of 50 kWe.

The purpose of the TEG specific characteristics increasing can be solved by modelling of the thermoelectric materials parameters

and scheme-technological decision of NR-TEG as a whole. One of the possible ways is use of so-called "built-in" NR TEG scheme when TEG is placing in active core with direct thermal contact with nuclear fuel. It excludes the heat losses connected with heat transfer and transport of the heat (fuel element - thermo bearer - hot solders of thermoelements) and hence power tension of device is increasing essentially.

The "built-in" NR-TEG (Fig.1) offers opportunities of more complete use of the nuclear reactor thermal potential, application middle and high-temperature materials for thermoelectric batteries up to 1500K. It is obvious, that the "built-in" system profitability will be higher, than "taken out", especially, if to use "taken out" TEG as the second cascade.

Fig.1.Possible configuration of "built-in" NR-TEG.



Carried out theoretical accounts have shown the usefulness of "built-in" type of NR-TEG for levels of power from 50 to 500 kWe.

Naturally, that in such a way the increase of the specific power characteristics is reached by the price of uranium load increase due to entering into the active core of the thermoelectrical, insulating and constructional materials. Besides there is the whole number of additional questions of technology, radiation stability, physical-chemical compatibility of TEG materials and active core materials. Therefore research of the possibility of operation of thermoelectric converter in the active core it is necessary to study as behaviour of separate NR-TEG subsystems, and their compatibility under irradiation. Thus major problems are:

- research of speed of physical properties change of elements, subsystems and thermoelectric converter as a whole under operation in active core conditions;
- investigation of thermoannealing modes, degree and multiplicity of induced radiation defects;
- estimation of acceleration of irreversible degradation connected with diffusion of doping impurities and basic matrix elements;

-estimation of compatibility of TEG elements (basic of which are semiconductor thermoelectric materials) and elements of the active core of the nuclear reactor.

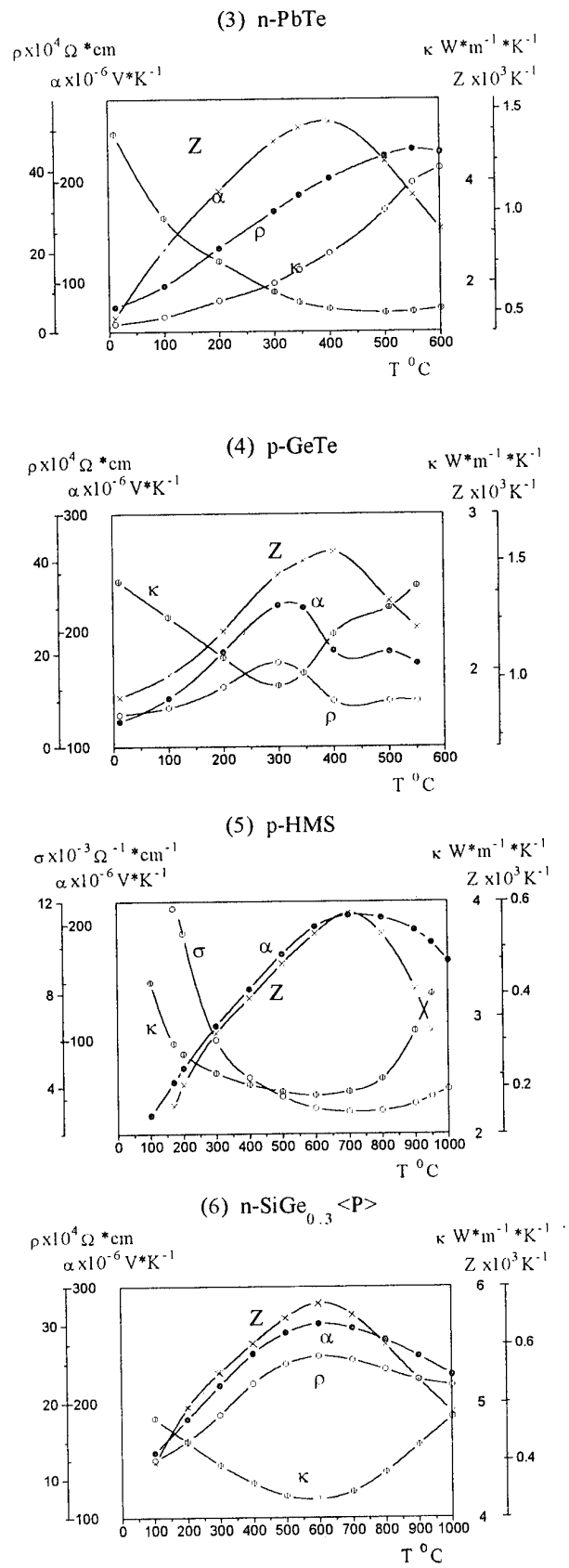
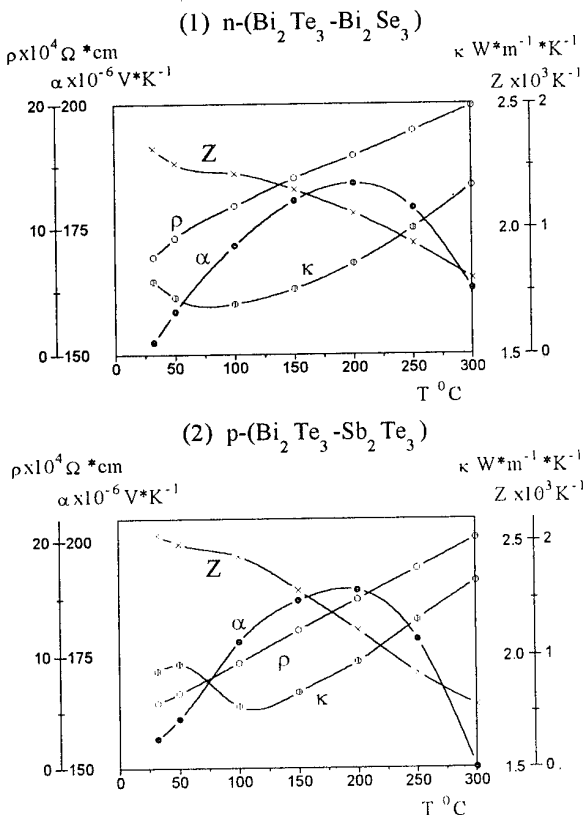
Since the radiation solid state physics has not yet sufficient predictive force now, it is necessary to investigate experimentally behaviour of separate subsystems and elements in the field of nuclear radiation in diverse precisely set external conditions (temperature, temperature gradient, content of gas environment, load level, regimes of heating, cooling, annealing etc.). And the external conditions for subsystems should match other requirements of optimum operation of all NR-TEG system. That means certain sequence and interrelation of tests of subsystems and device as a whole.

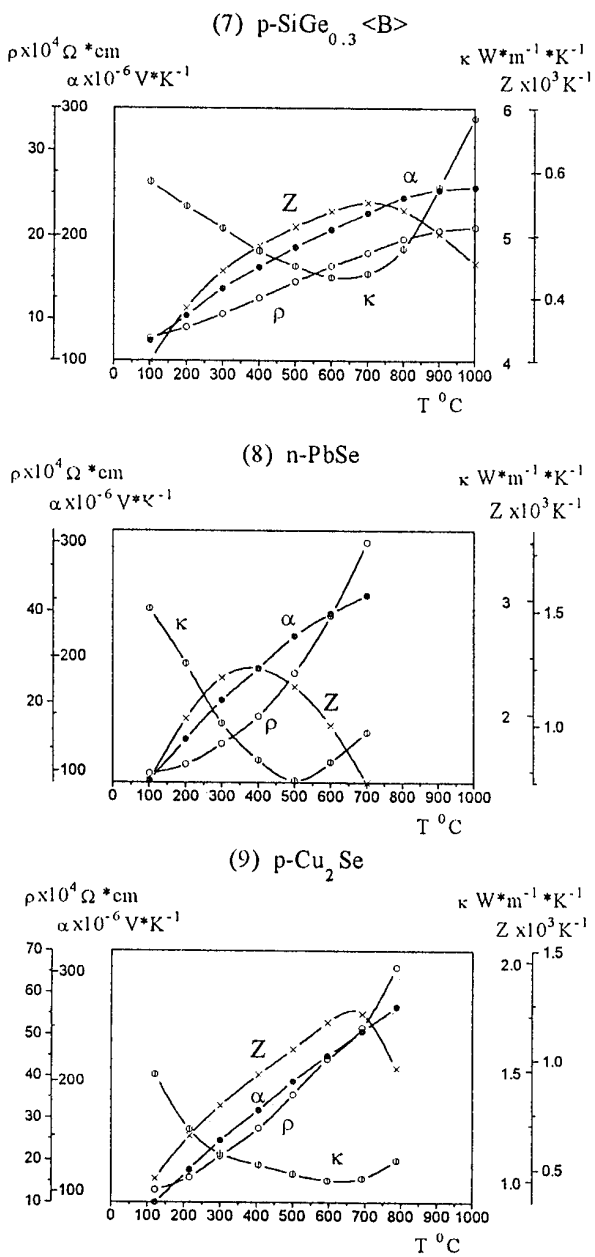
### 1.Thermoelectric materials.

At the first stage of work well-known thermoelectric materials of middle and high-temperature ranges of operation on the basis of lead and germanium chalcogenides ( $\text{PbTe}$ ,  $\text{GeTe}$ ,  $\text{PbSe}$ ) and their solid solutions, self-doped p- $\text{Cu}_{2-\delta}\text{Se}$  and cadmium-doped p- $\text{Cu}_2\text{Se}$ , some materials based on 3-d transition metal higher silicides (p- $\text{MnSi}_{1.71-1.75}$ -higher manganese silicide (HMS), n-, p- $\text{FeSi}_2$ ,  $\text{CrSi}_2$ ), and also n-, p- $\text{SiGe}_{0.3}$  doped with phosphorus and boron were investigated. Temperature dependence of main thermoelectrical parameters of these materials are shown on Fig.2, where:

$\alpha$  - the Seebeck coefficient,  $\sigma$  - electrical conductivity,  $\rho$  - specific electrical resistivity,  $\kappa$  - thermal conductivity,  $Z = \alpha^2 \sigma / \kappa$  - figure of merit,  $ZT$  - the dimensionless figure of merit,  $\alpha^2 \sigma = \alpha^2 / \rho$  - the electrical power factor.

Fig.2. Temperature dependencies of the main thermoelectric parameters for several materials.





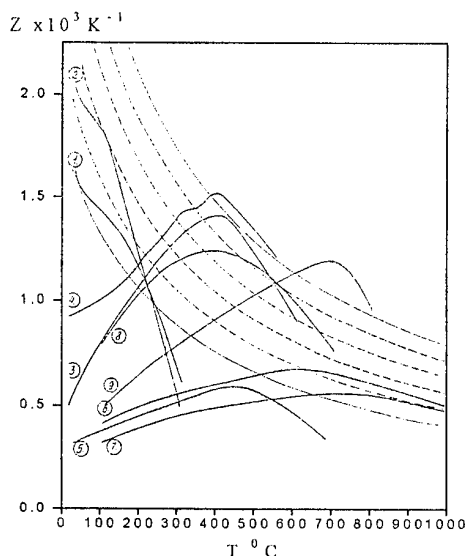
Along with R&D in the field of technology of semiconductor thermoelectric materials, directed on improving of their thermoelectrical parameters, accounts and analysis of nuclear reactions with thermal neutrons for all elements of basic matrixes of semiconductor thermoelectric materials, doping and probable uncontrollable impurities have been carried out.

After completion of reactor and post-reactor experiments the technological researches have developed in the main following directions:

- specification of composition of high-temperature silicon-germanium alloys,
- search of composition of the most effective p-type thermoelectric materials based on HMS by combined doping (Mo, W, Ge, Al),
- development of technology of new radiation-proof materials n- and p-types of conductivity based on solid solutions of HMS and transitive elements of Fe group,

-development of technology of new effective materials of n-type conductivity on the basis of Mn-Al-Si system,  
-R&D of new technological methods (extrusion and mechanical activation).

Fig.3. Figures of merit for some investigated materials.



## 2. Technique and instrumental providing of reactor and post-reactor experiments.

The irradiation of experimental specimens of thermoelectric materials was made in the active core of the water-water nuclear reactor WWR-M10 (thermal power 10MW) in "dry" vertical channels of the active core. The samples were installed in special physical ampoules (PA) of several types.

In PA1 samples were irradiated in non-gradient regime, that let to exclude diffusion process in materials. PA 2-4 let to carry out regimes ΔT=const and ΔT=var both for middle- and high-temperature ranges materials. The heating of samples to working temperatures in PAs was reached, basically, at the expense of radiation energy release in elements of ampoule. The electroheating elements built in PAs serve only for correction of temperature regime of tests in limits ±100°C from chosen average temperature. Terms of exposition of physical ampoules in the active core of the nuclear reactor exceeded one year.

The special measuring-metrological system let to supervise the density of flux and fluence of thermal and fast neutrons, but also to carry out remote measurements of ρ, σ, α, κ directly in the active core of the reactor during irradiation. Designs of PAs let to make irradiation and measurement of specimens parameters in the temperature range (150-750)°C. The energy spectrum of neutrons in PAs and irradiating channels was constantly supervised. Obtained information was accumulated in the computer IBM - PC/AT and then was analyzed with use of the various software packages.

Part of the samples was irradiated in "wet" vertical channels at fixed temperature (40-80)°C.

Isochronic thermal annealing of the samples after irradiation (the part of so-called post-reactor experiment) was carried out in "hot chambers" of the reactor in the interval (300-1200)K in argon atmosphere by steps 50°C during 20 minutes.

Installations for remote measurements in "hot chambers" of temperature dependencies of κ(T), Hall effect on alternating

electrical current and magnetic field, installation for mechanical properties research, special cryostats for optical properties research of high-radioactive irradiated materials in the temperature interval (4-1200)K were also developed. The second class of irradiating devices were looped thermoelectric channels with nuclear heating (Fig.4).

Fig.4. Design of LTC1 (part of channel in the active core is shown separately)

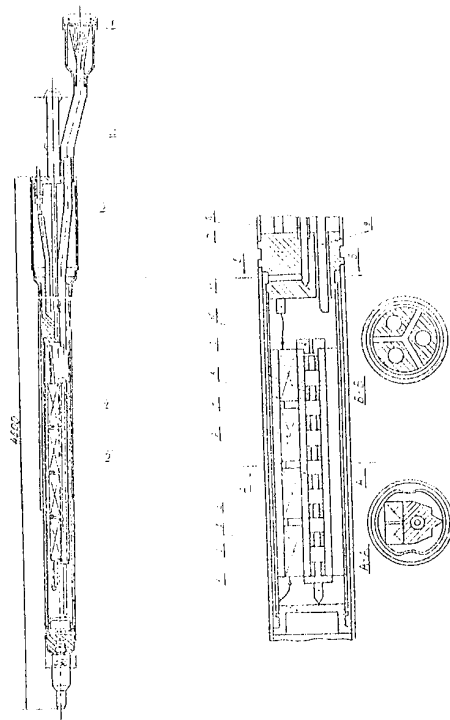


Table 1. The main mechanisms of energy losses for nuclear particles of reactor spectrum.

Particle, energy	Mechanism of energy losses	Some qualitative performance
$\gamma$ -quanta $\gamma$ -emission of reactor	1. Photoeffect 2. Compton effect 3. Electron-positron pairs generation	1. Photocurrent prevails at $E > 1 \text{ MeV}$ . 2. Probability of Compton effect increases with increasing charge number, energy of Compton electron can be close to $E$ - energy of $\gamma$ -quantum. 3. Electron-positron pairs generation is started from $E = 1.02 \text{ MeV}$ . Compton effect prevails photoeffect and pair generation for $\gamma$ -emission of reactor and material with small charge number (Si and Ge). Vacancies and interstitialities (V and I) are produced under internal irradiation of crystal by Compton electron, photoelectron, components of electron-positron pairs. Cross-section of interaction is $10^{-19} \text{ cm}^2$ .
Thermal neutron 0.025 eV	Inelastic interaction with atomic nuclei, nuclear reactions with producing high energy products	Both the simplest defects (V and I due to $\gamma$ -background and producing of light reaction products) and complex clusters of defects.
Fast neutron 100 keV	Elastic scattering on the atomic nuclei	Different defects of structure are produced, defects like clusters of defects predominate.

The designs of looped channels provided the tests possibility of thermoelectric modules and batteries in regimes close to operating: large values of temperature differences (up to 300-500° C) and operating electrical currents (up to several dozens A). The main technical characteristics of the thermoelectric converter

researched during irradiation ( $U$  - output voltage,  $R_x$  - differential resistance,  $W$  - specific electrical power) are the integrated characteristics, therefore in channel design with asymmetry placing of thermoelectric modules and nuclear fuel concerning longitudinal axis of the type channel LTC1 were stipulated 25 additional thermocouples, providing the control condition of the thermoelectric modules, thermoelectric materials, separate thermoelements and insulations also.

The looped thermoelectric channel LTC2 represented the model of "built-in" thermoelectric converter element with symmetric placing of nuclear fuel, carrying out hot junction heating up to 850°C (in regime of "vacuum" thermal annealing up to 1000°C). The temperature of cold ends of batteries was supported at the level 500-550°C by means of auto-manual control of heat-removal by pressure change in helium gap between LTC2 and hot loop-I of the nuclear reactor.

The thermoelectric converter of LTC2 consisted of four modules in which different middle- and high-temperature thermoelectric materials (p-Cu<sub>2</sub>Se, n-PbTe, p-(PbTe-GeTe), p-(GeTe-Bi<sub>2</sub>Te<sub>3</sub>), p-HMS) were used. Thus n- and  $\delta$ -branch of thermoelectric batteries were commutated for different LTC1s as follows: n-SiGe - p-SiGe, n-SiGe - p-Cu<sub>2</sub>Se, n-SiGe - p-SiGe<<sup>11</sup>B>, n-SiGe - p-SiGe<<sup>10</sup>B>, n-PbTe - p-(GeTe+PbTe), n-PbTe - p-(GeTe+Bi<sub>2</sub>Te<sub>3</sub>), n-SiGe - p-HMS.

The tests were carried out on constant level of thermal power of the nuclear reactor 7.5MW, thus the flux density of fast and thermal neutrons was  $5 \cdot 10^{13} \text{ n} \cdot \text{cm}^{-2}$ . Output on constant thermal power of 7.5MW was carried out by steps on (1-1.5) MW. The superfluous pressure in comparison to atmospheric in helium gap during irradiation was supported at the level 1.4 atmosphere, the pressure helium in a cavity of the converter was 0.4 atmospheres. During reactor experiment the offered method of in-reactor regeneration (restoration of parameters of the thermoelectric converter) was experimentally approved. The regeneration of parameters was carried out by means of short-term thermal annealing of entered radiation defects directly in the active core and could be carried out by two ways:

-increase of thermal power of the reactor in the range 7.5-10 MW, thus temperature of cold junctions raises owing to additional radiation heating;

"vacuum" thermal annealing on lowered thermal power of (1.5-2)MW; at that the pressure of helium gap was equal  $(1-2) \cdot 10^{-2}$  torr.

The results of reactor tests of physical ampoules and channels are submitted below.

### 3. Radiation physics of thermoelectric materials.

3.1. Interaction of nuclear radiations with semiconductor thermoelectric materials.

The passage of high-energy particles and quanta through substance is accompanied by exchange of energy and momenta between them and atoms and electrons of substance.

The energy transferred to atoms and electrons of substance results in displacement of atoms from their equilibrium positions and redistribution of electrons between energy levels of substance.

Table 2. Transmutational doping of some thermoelectric materials

Si <sub>0.7</sub> Ge <sub>0.3</sub>					
Isotop	Content of isotop, %	$\sigma \cdot 10^{24} \text{cm}^2$	T <sub>1/2</sub>	Product	Atomic concentration, cm <sup>-3</sup>
					10 <sup>20</sup>
30Si	3.12	0.11	2.62 h	<sup>31</sup> P-n	1.45·10 <sup>16</sup>
70Ge	20.55	3.42	11.4 days	<sup>71</sup> Ge-p	1.0·10 <sup>18</sup>
74Ge	36.74	0.25	82 min	<sup>75</sup> As-n	1.3·10 <sup>17</sup>
76Ge	7.67	0.13	12 h	<sup>77</sup> Se-n	1.43·10 <sup>16</sup>
10B(10 <sup>20</sup> cm <sup>-3</sup> )	19.8	3838	12 h	<sup>7</sup> Li	7.6·10 <sup>18</sup>
31P(10 <sup>20</sup> cm <sup>-3</sup> )	100	0.19	14.28 d	<sup>32</sup> S	1.9·10 <sup>15</sup>
Isotop	Atomic concentration, cm <sup>-3</sup> for $\Phi, \text{n} \cdot \text{cm}^{-2}$			Product	
	10 <sup>20</sup>	10 <sup>21</sup>			
PbTe					
204Pb	1.34·10 <sup>16</sup>	1.34·10 <sup>17</sup>		<sup>205</sup> Te	
208Pb	4.29·10 <sup>14</sup>	4.29·10 <sup>15</sup>		<sup>209</sup> Bi	
120Te	8.52·10 <sup>16</sup>	8.52·10 <sup>17</sup>		<sup>121</sup> Sb	
126Te	2.75·10 <sup>17</sup>	2.75·10 <sup>18</sup>		<sup>127</sup> T	
128Te	5.65·10 <sup>16</sup>	5.65·10 <sup>17</sup>		<sup>129</sup> T	
130Te	1.04·10 <sup>17</sup>	1.04·10 <sup>18</sup>		<sup>131</sup> Xe	
PbSe					
204Pb	1.71·10 <sup>16</sup>	1.71·10 <sup>17</sup>		<sup>205</sup> Te	
208Pb	5.48·10 <sup>14</sup>	5.48·10 <sup>15</sup>		<sup>209</sup> Bi	
74Se	3.95·10 <sup>17</sup>	3.95·10 <sup>18</sup>		<sup>75</sup> As	
78Se	1.64·10 <sup>17</sup>	1.64·10 <sup>18</sup>		<sup>79</sup> Br	
80Se	4.64·10 <sup>17</sup>	4.64·10 <sup>18</sup>		<sup>81</sup> Br	
82Se	8.67·10 <sup>15</sup>	8.67·10 <sup>16</sup>		<sup>83</sup> Kr	
PbS					
204Pb	2.02·10 <sup>16</sup>	2.02·10 <sup>17</sup>		<sup>205</sup> Te	
208Pb	6.48·10 <sup>14</sup>	6.48·10 <sup>15</sup>		<sup>209</sup> Bi	
34S	2.26·10 <sup>16</sup>	2.26·10 <sup>17</sup>		<sup>35</sup> Cl	
36S	4.91·10 <sup>13</sup>	4.91·10 <sup>14</sup>		<sup>35</sup> Cl	
GeTe					
70Ge	1.31·10 <sup>15</sup>	1.31·10 <sup>16</sup>		<sup>71</sup> Ce	
74Ge	1.71·10 <sup>17</sup>	1.71·10 <sup>18</sup>		<sup>75</sup> As	
76Ge	1.86·10 <sup>16</sup>	1.86·10 <sup>17</sup>		<sup>77</sup> Se	
120Te	1.16·10 <sup>17</sup>	1.16·10 <sup>18</sup>		<sup>121</sup> Sb	
126Te	2.79·10 <sup>17</sup>	2.79·10 <sup>18</sup>		<sup>127</sup> I	
128Te	7.70·10 <sup>16</sup>	7.70·10 <sup>17</sup>		<sup>129</sup> I	
130Te	1.42·10 <sup>17</sup>	1.42·10 <sup>18</sup>		<sup>131</sup> Xe	
Cu <sub>2</sub> Se					
63Cu	4.70·10 <sup>18</sup>	4.70·10 <sup>19</sup>		<sup>64</sup> Zn	
	7.66·10 <sup>18</sup>	7.66·10 <sup>19</sup>		<sup>64</sup> Ni	
65Cu	2.21·10 <sup>18</sup>	2.21·10 <sup>19</sup>		<sup>66</sup> Zn	
74Se	4.49·10 <sup>17</sup>	4.49·10 <sup>18</sup>		<sup>75</sup> As	
80Se	5.25·10 <sup>17</sup>	5.25·10 <sup>18</sup>		<sup>81</sup> Br	
82Se	9.86·10 <sup>15</sup>	9.86·10 <sup>16</sup>		<sup>83</sup> Kr	

There is no any universal formula for determination of number and space distribution caused electron excitation and lattice

defects in crystal. Accounts of cross-section, distribution of energy transferred to crystal by nuclear radiation and subsequent relaxation of primary excitations are actually known. The significant part of results is received by means of numerical accounts and can not be analytically distributed.

The value and mechanisms of energy losses of particles, which radiate the crystal, depend from their type and energy.

In Table 1 the main mechanisms of energy losses for nuclear particles of reactor spectrum are given.

The chemical impurity (doping and non-controllable), present in semiconductors, actively cooperate with primary radiation defects,

that results in formation of various complexes of radiation defects (point and clusters of defects) with chemical impurity, redistribution of clusters during thermal annealing [4]. The main contribution in radiation defects at irradiation of a semiconductor thermoelectric materials in the active core of nuclear reactor is brought by neutrons.

### 3.2. Nuclear reactions with thermal neutrons for semiconductor thermoelectric materials.

In accordance the general scheme of nuclear reactions, the primary products ( $n,\gamma$ )-reactions with thermal neutrons represent nuclei  $A+1_ZX$  on one atomic unit more heavily initial. It is the heavier isotop than that or next element of Periodical System. If these isotops are available in a natural mix of isotops of irradiated material and are non-radioactive, appropriate nuclear conversions result only in change of initial concentration of stable isotops in irradiated substance, not creating of impurity of the next elements of Periodical System.

If primary products of ( $n,\gamma$ ) reactions - are radioactive isotops, they undergo (in one or several stages) subsequent radioactive decay.

The analysis of all possible nuclear reactions lets to predict for each material a set entered in such a way electrically active impurity and their relative activity.

Concentration of  $i$ -impurity is:  $N_i = N_0 \cdot K_i \cdot \sigma_i \cdot \varphi \cdot t$ , where:  $N_0$  - concentration of initial mix of isotops;  $K_i$  and  $\sigma_i$  - the relative contents and cross-section of  $i$ -isotop;  $\varphi$  - the neutron flux density;  $t$  - time of irradiation.

The possibility of physical properties change with the help of impurity, entered by the method of nuclear doping at irradiation by neutrons is proved for a number of semiconductors: Ge, Si, CdS, InSb, GaAs.

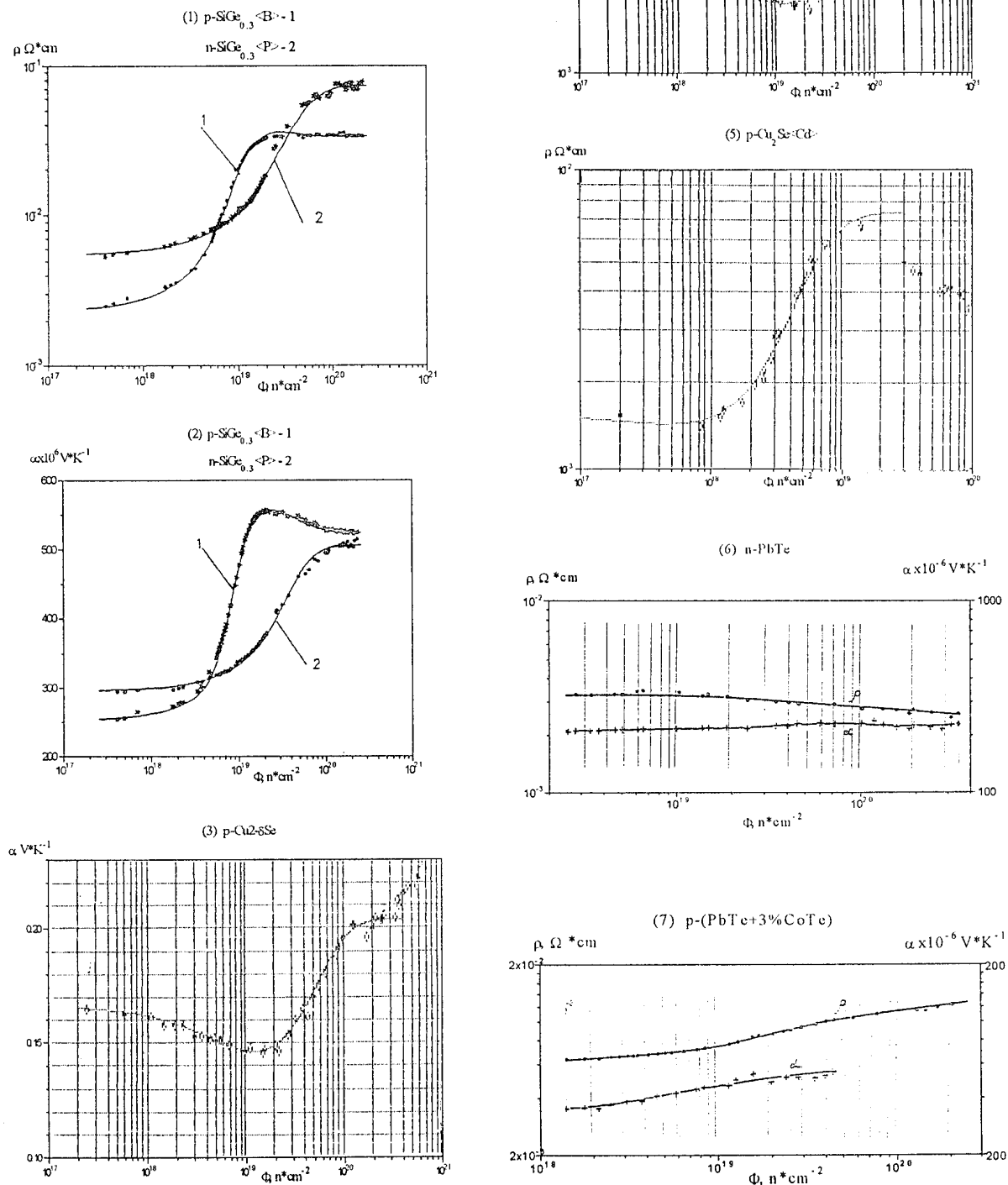
For semiconductor thermoelectric materials the specified questions were not studied. It is necessary to note, that their study is complicated by high concentration of unknown non-controllable impurity, but also practical application polycrystalline and pressed materials.

Results of account of transmutational change of elements (basic matrix and main doping) of semiconductor thermoelectric materials of middle- and high-temperature ranges for two meanings of neutrons fluence are given below.

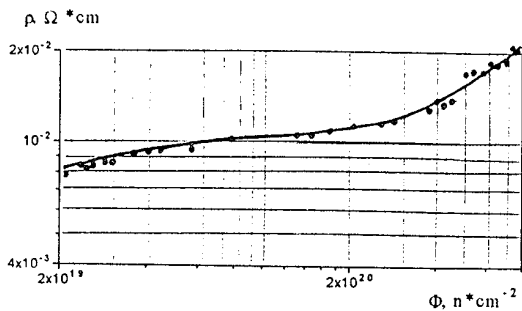
3.3 Doze dependence of  $\alpha$ ,  $\sigma$ ,  $\rho$  for main types of thermoelectric materials.

In Fig.5 the doze dependence of main thermoelectric parameters for materials of middle- and high-temperature ranges of application are submitted. The exposition of materials was carried out to the maximum possible doses of nuclear reactor irradiation with purpose to look after the behaviour of their main physical properties.

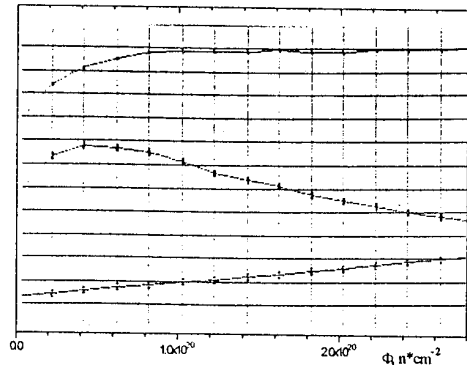
Fig.5. Doze dependencies of  $\rho$  and  $\alpha$  for some thermoelectric materials.



(8) p-(PbTe+3%CoTe)



(9) p-HMS



### 3.4 Research of radiation defects in thermoelectric materials by the thermal annealing method.

The thermal processing (annealing) is one of technological methods of radiation defects removal. If the concentration of defects in solids exceeds equilibrium for given temperature, under appropriate conditions the defects interact with each other to reduce free energy of the crystal. The processes of solids properties regeneration by means of step increase of temperature during fixed time (10-30 min) are known as isochronic annealing. It is easy to describe annealing of defects with the help of equations, similar those applied in chemical kinetics. Then the annealing speed of defects concentration can be written as:

$$\frac{dN_d}{dt} = -A \cdot F(N_d) \cdot \exp\left(-\frac{E_a}{kT}\right),$$

Usually the function  $F(N_d) = N_d^q$ , where  $q$  - is known as the reaction order;  $E_a$  - energy of annealing activation;  $A$  - constant, which at  $q=1$  serves as "frequent" factor ( $A=v$ ).

Now to research of annealing processes in thermoelectric materials the special attention is given. Formation of defects in the neutron field is investigated at increased temperatures. It is known, that reactor neutrons at increased temperatures create clusters of defects.

Local spacing of point defects in clusters imposes the peculiarities on annealing process for different types of thermoelectric materials.

The linear character of relative change of defects concentration as a function of temperature in a half-logarithmic dimension testifies

about annealing kinetics of the first order. One-stage and multiple annealing was experimentally observed.

Such multi-stage annealing is caused by localization of defects spacing in clusters.

In the table 3 the temperature intervals of thermal annealing of radiation defects (simple defects and clusters of defects) are given.

Table 3. Temperature intervals of annealing of radiation defects in thermoelectric materials.

Material	Temperature of irradiation	Fluence, n·cm⁻²	Temperature interval of annealing simple defects	Temperature interval of annealing clusters of defects
n-PbTe	70	$1.44 \cdot 10^{20}$	100-150 250-300	400-550
p-Ge <sub>0.9</sub> Pb <sub>0.1</sub> Te	300	$9.2 \cdot 10^{19}$	-	300-500
p-GeTe	70	$1.44 \cdot 10^{20}$	180-240	300-350
n-PbSe	70	$3.0 \cdot 10^{20}$	-	300-550
p-PbSe	70	$3.0 \cdot 10^{20}$	100-250	280-480
p-PbSe	320	$3.2 \cdot 10^{20}$	-	200-350
p-Cu <sub>2-δ</sub> Se	400	$4.48 \cdot 10^{20}$	-	300-550
p-Cu <sub>2</sub> Se	350	$3.0 \cdot 10^{20}$	200-270	-
p-HMS	70	$3.0 \cdot 10^{20}$	-	200-500
p-HMS	310	$2.73 \cdot 10^{20}$	-	400-600
n-SiGe <sub>0.3</sub>	250	$1.54 \cdot 10^{20}$	350-400	400-700
p-SiGe <sub>0.3</sub>	200	$1.08 \cdot 10^{20}$	350-400	450-750

### 3.5. The analysis of results of thermoelectric materials tests.

The describing of  $\rho(\Phi)$  and  $\alpha(\Phi)$  in the frame of effective medium theory was given for n-, p-SiGe<sub>0.3</sub> solid alloys in [5,6] and p-Cu<sub>2-δ</sub>Se, p-Cu<sub>2</sub>Se compounds in [7].

As was shown, defect clusters surround with electric and deformation fields interact with boron and phosphorus participation during of neutron irradiation is very actually in connection with the problem of radiation firmness of high temperature materials.

Electric and deformation fields, which arose around defect clusters, not promote in defect deduction only but interact with impurity later. It was shown, that lithium losing from conducting matrix is proportional to density of introduced defect clusters and copper precipitation leads to growing of hole concentration in Cu<sub>2</sub>Se, moreover it is electrically non-active in clusters.

Thus defect cluster can be a gutter for poor-diffusion dopant in during irradiation at high temperature. That is why we supposed phosphorus both in nature precipitation in own defects in the beginning of irradiation in temperature ~400°C and under future precipitation in clusters will lose its electric activity.

As follows from calculations, carrier concentrations in conducting matrix and defect clusters are changing during irradiation. It seems to us, it was conditioned by deduction of boron (which saved its negative charge) in electric field of cluster.

As follows from experimental dependencies  $\rho(\Phi)$  and  $\alpha(\Phi)$  for Cu<sub>2</sub>Se, it is visible that the thermoelectric material has high radiation stability up to meanings of fast reactor neutrons fluence  $(2-3) \cdot 10^{20} \text{n} \cdot \text{cm}^{-2}$ . In this range the changes of  $\rho$  and  $\alpha$  are those, that the electric power factor  $\alpha^2/\rho$  is not lower than initial value for a non-irradiated material.

As doses are higher than  $(4-5) \cdot 10^{20} \text{n} \cdot \text{cm}^{-2}$  deterioration of thermoelectrical properties of materials begins, however even at dose  $10^{21} \text{n} \cdot \text{cm}^{-2}$   $\alpha^2/\rho$  saves the meaning not below (80-85)% of initial value.

The results of irradiation experiments on middle-temperature thermoelectric materials of PbTe, n- and p-types of conductivity,

made by the method of extrusion (directed pressing) are submitted.

This pair of materials causes the special interest, as it is possible to expect their high physical-chemical and thermal-mechanical compatibility, that it is very important for manufacturing of the thermoelectric module. The irradiation was carried out at temperature 500°C. For n-PbTe slow decrease of  $\rho$  in all investigated interval of irradiation dozes up to  $5 \cdot 10^{20} \text{n} \cdot \text{cm}^{-2}$  was observed.  $\alpha$  with growth of doze was increased. Thus n-PbTe is thermoelectric material having high radiation stability of main physical properties under influence of reactor irradiation. Its characteristics under influence of irradiation in investigated dozes interval up to  $(4-5) \cdot 10^{20} \text{n} \cdot \text{cm}^{-2}$  are even improved.

The material of p-type based on PbTe, has good radiation stability in the dozes interval up to  $5 \cdot 10^{20} \text{n} \cdot \text{cm}^{-2}$  too. With increase of doze  $\rho$  and  $\alpha$  monotonously grow but the electric power factor grow in all investigated interval of doze up to  $5 \cdot 10^{20} \text{n} \cdot \text{cm}^{-2}$ .

The study of doze dependence for this material was continued up to  $3 \cdot 10^{21} \text{n} \cdot \text{cm}^{-2}$ .

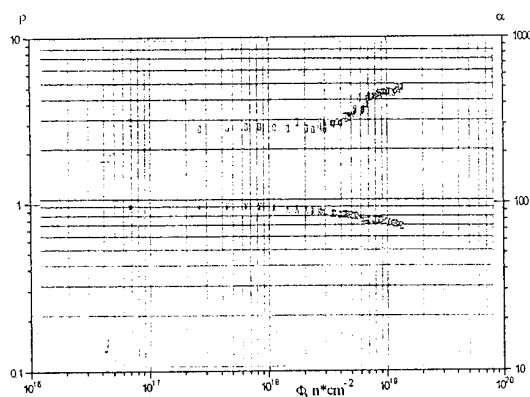
The doze dependencies of thermoelectric parameters other middle-temperature materials based on PbTe and GeTe were also investigated.

The results of experimental research of radiation stability of p-HMS polycrystalline samples are submitted on Fig.5.9. Doze dependence of  $\rho$  has practically linear character in all investigated dozes interval (the ratio value of  $\rho_{\Phi}$  to initial meanings  $\rho_0$  is equal 2.1-2.4).

The temperatures of an exposition were a little bit below than those meanings (400-450)°C, which should be recommended to operating from condition of maximum value of Z for non-irradiated material.

$\alpha$  for irradiated HMS in accordance with growth of doze grows, leaving by saturation at dozes of the order  $(1.0-1.2) \cdot 10^{20} \text{n} \cdot \text{cm}^{-2}$ . The electric power factor G from dozes of irradiation depends not monotonously: in the dozes interval of  $(3-5) \cdot 10^{19} \text{n} \cdot \text{cm}^{-2}$ ,  $\alpha^2 \sigma$  essentially increases in comparison with initial value (up to 40%) and than slow decreases and at  $2 \cdot 10^{20} \text{n} \cdot \text{cm}^{-2}$  reaches  $(\alpha^2 \sigma)_0$  for non-irradiated HMS.

Fig.6.Result of reactor test of thermoelectric module based on n-, p-PbTe consisting of LTC1/6.



#### 4.Reactor tests of LTC1,2 and prognosis theoretical estimations.

During resource reactor tests of looped thermoelectric channels temperature test specifications of thermoelectric modules were continuously supervised, thus the change of temperatures not

exceeded 4.5 % from of average meaning. In result of spent cycles of thermal regeneration of the thermoelectric battery parameters by means of "vacuum" annealing and annialing by increase of thermal power of the nuclear reactor complete restoration of the thermoelectric converter power parameters was established practically (Fig.6-8).

Fig.7.Result of reactor tests of p-SiGe<sub>0.3</sub><B> in thermoelectric module of LTC1/4.

Thermal annealing regimes: 1-870°C, 2-910°C.

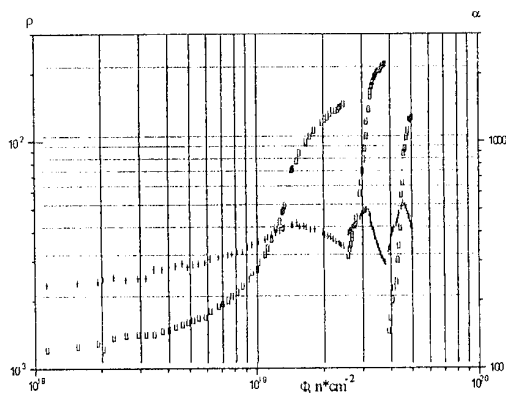
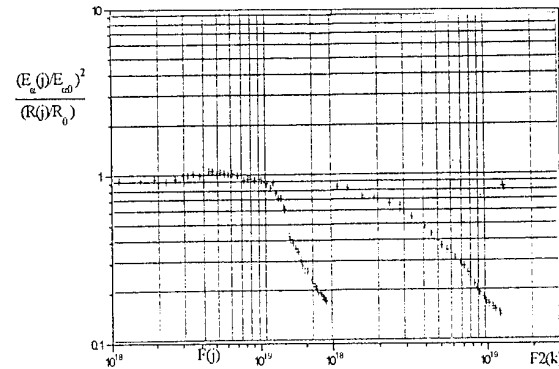


Fig.8. Result of reactor test of thermoelectric module in LTC1/4 (regeneration of the electric power factor by thermal annealing).



Some cycles of annealing were spent and is established, that the limiting factor, for example for n-SiGe<sub>0.3</sub><P> - p-SiGe<sub>0.3</sub>< B>, are p-branches of the thermoelectric battery. The volt-ampere characteristics of thermoelectric modules remained linear as during irradiation, and after carried out cycles of thermal annialing. As was marked above, designs of research LTC1 let simultaneously with the control of power parameters of the thermoelectric battery during irradiation to carry out research of influence of irradiation and annealing on the electrophysical properties of thermoelectric, insulational and commutation materials. On Fig.7 doze dependence of resistance R and thermopower of p-SiGe<sub>0.3</sub>< B> in thermoelectric module is given. In Fig.9 the scheme of mathematical model for the element of of the energy generating channel at symmetric heat exchange is submitted. Here: 1 - nuclear fuel; 2,13 - thermal conductors; 3,12 - electrical insulations; 5,10 branch of thermoelements; 14 - external shell.

Fig.9. Mathematical model for calculation of symmetrical heat transfer in LTC2.

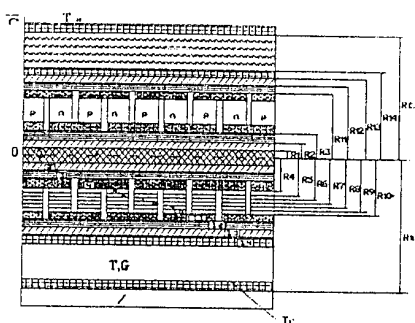
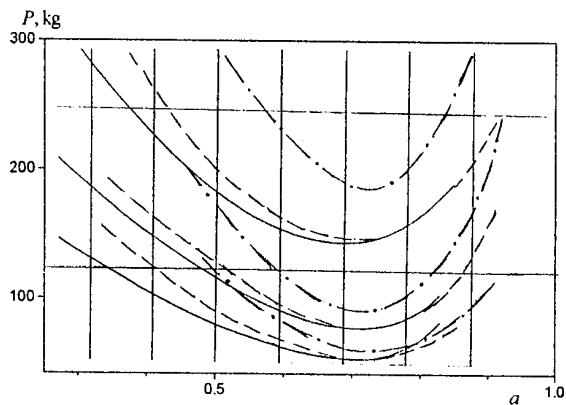


Fig.10. Calculated  $^{235}\text{U}$  load dependence from water gauge in cavity for NR-TEG power levels of 100, 200, 500 kWe at heat-carrier temperature 100, 200, 300°C.



As follows from the results of neutron-physical and thermo-physical calculations of active cores of NR-TEG (Fig.10), resulted data let us from large variety of possible variants of the active core of the water-water nuclear reactor - thermoelectric converter with "built-in" TEG to allocate some optimized elementary cell of the energy generating channel, containing realistic thermoelectric materials and constructive elements, the main characteristics of which poorly depend from powers of the reactor and temperature of the heat-carrier. Revealed in result of series of accounts presence such universal cell of the active core has let to concentrate efforts on given stages of technology development on creation of NR-TEG.

#### References.

1. М.Д.Миллионников. Проблемы энергетики будущего. В кн. "Наука и человечество", М.: Знание, 1964, с.370-377.
2. D.M.Rowe. United States Thermoelectric Activities in Space. Proc. VIII ICT, 1979, Nancy, France, pp.133-142.
3. G.Stapfer, W.Carroll. Thermoelectric Power Conversion for SP-100. Proc. VIII ICT, 1979, Nancy, France, pp.143-147.
4. Вопросы радиационной технологии полупроводников - п/ред. Смирнова Л.С. Изд."Наука", СО АН ССР, Новосибирск, 1980, 280 с.

5.N.D.Marchuk. Radiation Defects Built-up Kinetics and Thermal Stability in P-SiGe<sub>0.3</sub> under Reactor Irradiation, Proc. VIII Int.Conf. of Energy Conversion, 1979, Nancy, France, pp.91-95.

6.N.D.Marchuk, A.P.Dolgolenko. Defect Clusters Influence on Redistribution of Doping Impurities in N- and P-SiGe<sub>0.3</sub> under Reactor Irradiation, Proc. XII ICT, 1993, Yokohama, Japan, pp.66-68.

7.N.D.Marchuk, M.V.Basov, A.P.Dolgolenko. Radiation Defect study in the P-type Copper Selenide, Proc. XII ICT, 1993, Yokohama, Japan, pp.76-81.

## THERMOELECTRIC BATTERIES FOR LOW-POWERED RADIONUCLEIDE THERMOGENERATORS (RTG) WITH LONG SERVICE LIFE IN SPACE

L.I. Anatychuk<sup>1</sup>, B.N. Demchuk<sup>1</sup>, A.A. Pustovalov<sup>1</sup>, O.I. Makhorin<sup>2</sup>, V.N. Zhabin<sup>2</sup>

<sup>1</sup>*Institute of Thermoelectricity, Chernovtsy, 274000, General Post Office, box 86, Ukraine*

<sup>2</sup>*Scientific-production enterprise "Biapos" 117334, Moscow, Leninsky Prospect, 38, korp.6, Russia*

The paper stated about the main results of semiconductor thermoelectric batteries (STEB) "Angel-1" of increased power modified on the results of STEB "Angel" design early made for RTG "Angel" (project Mars-94). With preservation of RTG overall dimensions its electric power together with STEB "Angel" in the rated operating condition was 250 mW under voltage of 15 V.

### Introduction

Use of radionucleide sources energy (RSE) for space investigations is sensible only when the use of other sources is absolutely inefficient or impossible for a given research program fulfillment. This depends on the fact that the use of RSE for space investigations enlarges essentially the cost of project as a whole both due to high cost of radionucleide sources themselves and to the necessity of large volume of investigations and tests fulfillment by provision their nuclear safety under standard service and in the case of abnormal situation arising. Nevertheless there is a number of problems connected with far space research where the use of RNES is required. This includes projects connected with investigations of Solar system planets such as Mars, Jupiter, Pluto and asteroids, comets or polar regions of Sun.

The present report presents the information related to semiconductor thermoelectric batteries development (STEB) for low power radionucleide thermoelectric generators (RTG) on plutonium-238 used in small autonomous stations (SAS) of the international project Mars 94/96 (RTG "Angel"). Such RTGs can be used in other projects where it is required small energy consumption and the necessity of maintenance of standard temperature condition.

Due to the postpone of the expedition terms to Mars from October 1994 till November 1996 it was accepted expedient to modify the formerly developed STEB "Angel" within the project Mars-94 in an effect to electric power and efficiency increase of RTG "Angel" preserving its structure, mass and dimension parameters and other operational parameters.

### Peculiarities of STEB development for low-power RTG of space purpose

In relation to the fact that STEB development has the target-oriented character (for RTG "Angel" of the project Mars 94/96) let us consider the peculiarities of STEB for low power RTG development oriented oneself at the requirements laid the groundwork for RTG "Angel"

design. Following the adopted concept it was required to develop RTG with small mass and dimension parameters and electric power output no less than 100 mW at a voltage of 15 V. The upper nominal value of RHU thermal power must not exceed 8.7 W. Those requirements defined as it was showed earlier [1], the choice in favour of a single stage STEB based on low-temperature alloys of BiTe having the best efficiency in the temperature range up to 300 °C. The necessity of high output voltage provision (15 V) at relatively low electric power (100 mW) and temperature gradient (100 - 120 °C) along the operating material resulted in the choice of STEB micromodule structure [2]. The principle requirement under RTG development was the maintenance of RTG normal operation at the given electric power level not only after MAS landing on Mars surface but during the whole period of its operation in the Marsian conditions (no less than 3 years and a half).

Table 1 showed the main parameters of STEB "Angel" developed for RTG "Angel" and for STEB of STEB "Angel-1 improved structure .

Table 1

Parameter	Type of STEB		
	Angel by the request	effective value	Angel-1
Electric power, mW	100	150	250
Temperature gradient, °C	180	130	140
Operation temperature at NKY, °C	200	170	165
Electric resistance, kOhm	1700	1200	850
Load voltage, V	15	15	15
Number of elements	1600	1600	1600
Elements cross-section, mm	0.35×0.35	0.5×0.5	0.6×0.6
Dimensions, mm			

- height	19	19.5	22
- width	17	23	25
- thickness	18	23	25
Mass, g	70	60	75
Service life, years	10	10	10

Alloys of (BiSb)Te, p-type, and Bi(TeSe), n-type, produced by the extrusion method were used as starting materials for STEB "Angel" development as in the case of the first modification of STEB "Angel".

### Experimental modification of STEB

Experimental modification of STEB "Angel" was made within full-scale breadboards and prototypes of RTG "Angel". The accelerated tests were carried out according to the specially elaborated methods at the conditions imitating different types of external exposures on RTG at the terrestrial storage and transportation, at the flight by the Earth-Mars trajectory, at the landing on the Mars surface and operation in the Martian conditions.

During the experimental modification the technological process of development was adjusted to improve its technical characteristics and to prolong service life and reliability.

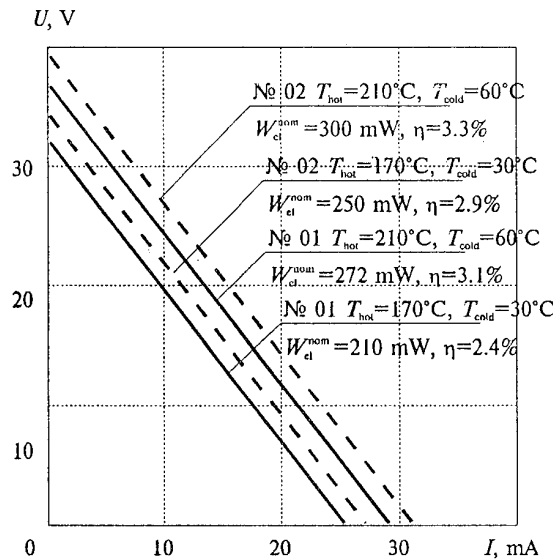
During STEB "Angel-1" structure modification it was found out, investigated and corrected the negative effects of thermal stresses arising in STEB during its operation within RTG and affecting its time stability of output electric parameters. This was accomplished by optimization of thermoelement leg dimensions, use of more perfect thermal resistance adhesive and epoxy compounds, melting temperature increase of commutation solders and use of other structure designs ensuring decrease of thermal stresses effect as to cross-section of STEB.

Experimental test of service life and operation reliability of STEB specimens within RTG "Angel" full-scale breadboards was carried out in permanent thermal conditions and in thermocycling conditions. Permanent thermal condition imitated STEB operating conditions within RTG at operation temperature increase in 1.3 times. Tests duration in the permanent thermal conditions was no less than a month and a half.

RTG operating conditions on the Mars surface were imitated more strictly in the thermocycling conditions (temperature of heat receiving junctions was changed from 130 to 205 °C) considering season and daily temperature changes in the most unfavourable as to climate conditions regions of SAS landing on the Mars surface. Limiting temperature conditions of STEB within RTG capacity for operation were determined experimentally during 6 - 10 hours. These limits were 240 °C by the operating temperature and 100 °C by the environment temperature.

Fig.1 shows volt-ampere characteristics of RTG breadboards STEB "Angel-1" № 01, 02.

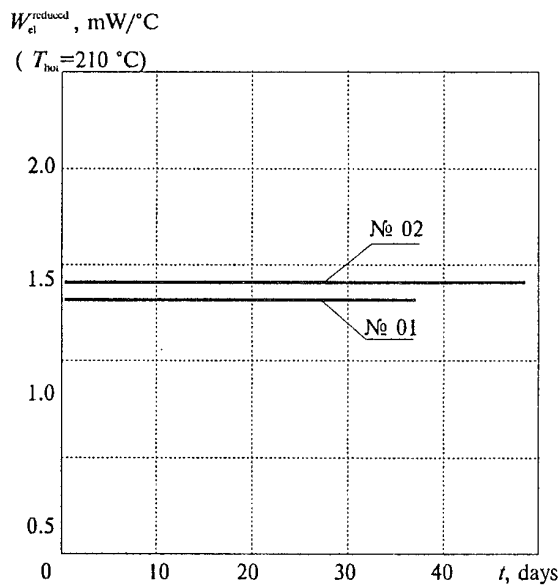
Fig.1. Volt-ampere characteristics of RTG with STEB "Angel-1" №№ 01, 02 at different ambient temperatures.



### Test results

Test results of STEB "Angel-1" are given in Fig. 2, 3. Fig.2 shows temporary change of output electric power value of STEB "Angel-1" full-scale specimens within RTG. The value, equals to its starting electric power ratio to the operating temperature difference, was the STEB reduced electric power value.

Fig.2. The relation between STEB "Angel-1" №№ 01, 02 as a part of RTG reduced electric power  
 $W_{el}^{reduced} = \frac{W_{el}^{nom}}{T_h - T_c}$  and continuous operation time at increased ambient temperature ( $T_c \approx 70^\circ C$ ).



In spite of more strict STEB test conditions than real operating conditions within RTG, STEB "Angel-1" output electric power was not changed during a month and a half continuous test period.

Test results of STEB "Angel-1" within RTG in the thermocycling conditions are given in Fig. 3.

STEB "Angel-1" test conditions in the thermocycling regime imitate RTG operating conditions within SAS on the Mars surface, cycle number determines RTG operating time in real conditions. STEB electric power value stability at its thermocycling within RTG confirms the achievement of required resource characteristics of STEB and tells about the efficiency of technical designs adopted during its modification.

*Fig.3. The relation between STEB "Angel-1" №№ 01, 02 as a part of RTG reduced electric power*

$$W_{el}^{reduced} = \frac{W_{el}^{nom}}{T_h - T_c} \quad \text{and number of thermocycles.}$$

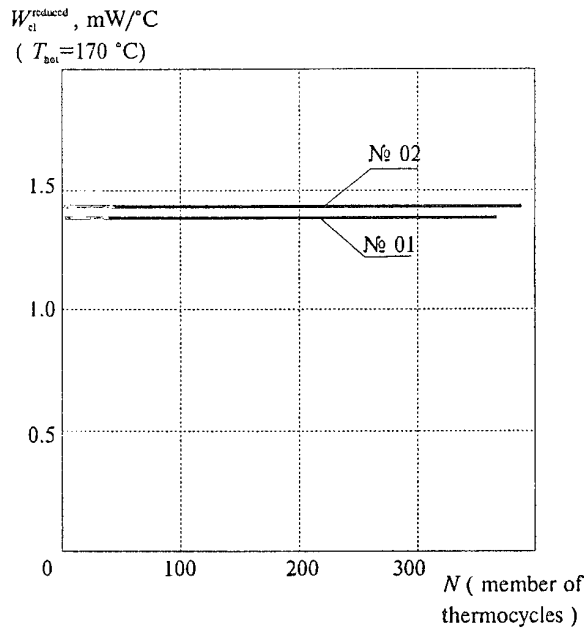


Table 2 shows the main characteristics of developed RTG with STEB models "Angel" and "Angel-1" according to the Mars 94/96 project in comparison with similar RTGs which are developed according to the "Power Stick" Program [3,4].

Table 2

Parameter	Type of RTG			
	Russia		USA	
	Angel	Angel-1	Option C	Option B
Electric power, mW	150	250	305	22
Voltage, V	15	15	5	5

RHU thermal power, W	8.7	8.7	6	1
STEB materials	BiTe	BiTe	BiTe	BiTe
Dimensions, mm	19×23×23	22×25×25	30×24×24	15×7×7
Cross-section, mm	0.5×0.5	0.6×0.6	0.94×0.94	0.21×0.2
Hot junctions temperature, °C	170	165	200	130
Efficiency	2	2.9	5.1	2.2
Dimension of RTG, mm	Ø=85 h=125	Ø=85 h=125	Ø=130 h=105	Ø=85 h=80
Mass, kg	0.50	0.53	0.86	0.37
Specific electric parameters, W/kg	0.34	0.47	0.36	0.06
W/m³	322	450	225	7

From the Table one can see that RTG "Angel-1" is more close to RTG "Option C" by its parameters. To our mind the most efficiency of RTG "Option C" than RTG "Angel-1" was achieved mainly by hot junction temperature forcing which was 200 °C and by use of the more perfect (fiber-vacuum) insulation. However, durable stability of module type STEB in vacuum under these temperatures is rather problematical and the information confirming the service life is absent in the work [4].

### Conclusions

1. The structure and technology of STEB development conventionally named "Angel-1" having better technical and operation characteristics than STEB "Angel" with retaining the RTG "Angel" structure and dimensions has been modified .

2. STEB "Angel-1" tests conducted within RTG in the nominal condition ( $T_{op}=165$  °C) showed that at temperature difference  $T=140$  °C its electric power is no less than 250 mW at output voltage 15 V.

3. STEB "Angel-1" tests within RTG conducted at more strict thermal exposures (increased operating temperature, multiple thermocycling, increased environment temperature and the like) confirmed stability of its operation in these conditions without changing starting electric parameters.

4. Analysis of the obtained results enable to make a conclusion on the expediency of RTG "Angel-1" use in small self-sufficient stations of the Mars 94/96 project and to recommend such RTG for electro-heat provision for other prolonged space expeditions as a basic module.

**References**

- [1]. Lazarenko Yu.V., Pustovalov A.A., Shapovalov V.P. Compact nuclear sources of electric power, 1992, Moscow, Energoizdat.
- [2]. Demchuk B.N., Luste O.J. Certificate N1145858 (USSR). Method of thermoelectric battery assembly. *Discovery. Inventions.* 1985, N 10.
- [3]. Chmielewski Artur B., Richard Ewell. "The Powerstick" in Proc. of 29th Intersociety Energy Conversion Engineering Conference, Monterey, CA, August, 1994, 1:311.
- [4]. Schock, A.C. Or Analysis of "mini-generator" with 6 W thermal source structure parameters. Report at the 12th Simposium of Space nuclear installations and engenes, Albukerk, Nm, January, 1995.

## THERMOELECTRIC METAL BASE MODULE

T.L.Lushkina, A.M.Blagorodov, V.I.Dubov

*"IMPULS" Joint-Stock Company, Moscow, 129626, Russia*

The thermoelectric metal base module (TM) production process is developed. The produced TMs were tested and investigated. As showed this study and digital simulation the use of metal base allows to increase effective heat transfers thermal conductivity by 1.5-2 times depending upon thermal conductivity of the material through which the heat is being removed at the hot side of the module. Owing to metal base the processing becomes easier and construction flexibility increases.

The application of metal base in TM became possible only after the problem of fabrication of metal substrate with dielectric layer was solved. The dielectric layer possesses of the complex of unique features such as porouslessness, excellent isolation parameters (specific resistance of insulating layer  $10^{16}$  Ohm $\cdot$ cm, breakdown voltage 400 V/mkm), high adhesiveness (more than 2000 N/sq.cm), operating temperature up to 400 °C, increased chemical resistivity in aggressive environment.

In order to increase the efficiency of thermoelectric module operation its design (construction) and know-how are worked out using the metal base instead of ordinary ceramic one.

Such a design makes it possible to rise the effective factor thermal conductivity base which results in increase of intensity of heat removal from the hot and cold sides of the module.

The advantage of the thermoelectric module as to the design of its cooler is evident, namely:

1. It is easy to solder the metal base to the heat sink. In this case, having a high thermal conductivity of the bases, the thermal resistance at the thermocouple boundaries - metal base-heat sink will be minimum, i.e. about (0.1 to 0.01) °K/W cm<sup>2</sup>, which considerably increases the cooler efficiency when using thermoelectric module-to-heat sink clamp through heat-conducting paste. The thermal resistance of the heat contact will amount to (0.5 to 1) °K/W cm<sup>2</sup> at specific thermal flows, amounting to (3 to 4) W cm<sup>-2</sup>. The parasitic drop of temperatures between the thermoelectric module hot surface and the heat-conducting surface may be equal to 5 °C in case of using the clamping contact.

2. The geometric sizes and configuration of metal bases may be more various than those of ceramic.
3. The possibility appears to create a new type of thermoelectric modules which combine in themselves the series-connected thermocouples and aluminium heat sinks for the heat liberated from thermocouple hot joints. This makes it possible to avoid problems of the heat contact of the thermoelectric module hot side with the heat sink and simplifies the cooler design.

As to the construction, the base is composed of aluminium alloy AMr, 0.8 mm thickness, and a thin dielectric layer, 10 mkm thickness. The main problem was in creating the reliable electric-insulation layer. The technology worked out by our company allowed to make a dielectric layer (coat), which possesses the combination of unique properties namely: density, high adhesion to the aluminium base (2600 N/cm<sup>2</sup>), high adhesion of applied conducting coats to the dielectric coat (2000 N/cm<sup>2</sup>), stability to aggressive media and thermal stability up to 400 °C (including in vacuum).

Determined is a cooperative thermophysical characteristics of the plates made of polycore ( $Al_2O_3$  - 99.8%) and aluminium with a dielectric layer.

An aluminium plate coated with a thin dielectric layer is not a solid material and has no thermal conductivity factor value in a common sense. We can talk about "effective" factor of thermal conductivity  $\lambda_{et}$ , which will depend on the heating mode. For the stationary mode,  $\lambda_{et}$  is defined from a simple expression, which is easily obtained from the Fourier law:

$$\lambda_{et} = \frac{\lambda_1 \lambda_2 (\Delta_1 + \Delta_2)}{\lambda_2 \Delta_1 + \lambda_1 \Delta_2}$$

where:  $\lambda_1, \lambda_2, \Delta_1, \Delta_2$  - thermal conductivities and thickness values of the first and second layers.

In order to compare the thermal conductivity of the plates made of  $\text{Al}_2\text{O}_3$  and Al with the dielectric layers, we determined value  $\lambda_{et}$  at their contact with a thick ( $\Delta=10$  mm) layer of the standard material with a known thermal conductivity. The standard material simulated the heat sink, the intensity of which may be characterized by the value of its thermal conductivity  $\lambda_{et}$ .

Value  $\lambda_{et}$  was defined by the contact method with a help of instrument QTM-D2 (error is  $\pm 5\%$ ) where the constant power point source is used.

The results of measurements showed that aluminium plate with a dielectric layer has the thermal conductivity efficiency 1.5 to 2 times higher than that of plate made of  $\text{Al}_2\text{O}_3$  at  $\lambda_{et}$  equal to 0.21 and 1.21 Kcal/m·h·deg.

We compiled a mathematic model of thermal mass-exchange process for the selected construction of the cooler, consisting of a thermoelectric modules and heat sinks. The model takes into account the transfer of heat due to the molecular thermal conductivity with sources and drains of heat and connection. The radiative transfer of heat is inconsiderable due to small values of temperatures both inside the module and in heat sink zones.

The general equation is as follows:

$$\bar{S}(x) C(x, T) \gamma(x, T) \frac{\partial T}{\partial t} = \frac{\partial}{\partial x} \bar{S}(x) \lambda(T, x) \frac{\partial T}{\partial x} + \bar{S}(x) W(x) + P(x) \cdot \alpha (T_r - T)$$

where:

$\bar{S}(x)$  - the ratio of the normal cross-section area to the base area,  $S_0 = 16 \cdot 10^4 \text{ m}^2$ ;

$C, \gamma, \lambda$  - specific heat capacity, density and thermal conductivity of structure materials;

$T$  - temperature;

$x$  - linear coordinate;

$t$  - time;

$W$  - volumetric heat source;

$$P_{(x)} = \frac{P_1}{S_0},$$

where:

$P_1$  - normal cross-section perimeter;

$\alpha$  - heat exchange factor;

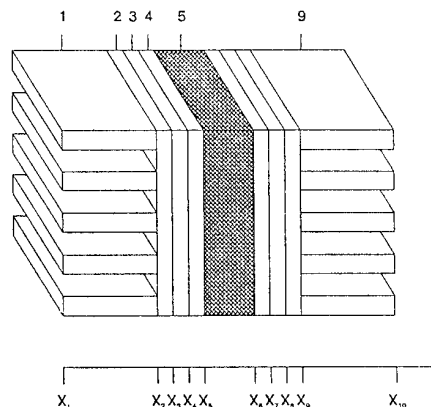
$T_r$  - air temperature (time function);

$I_i$  - thickness of  $i$ -layer.

On the bases of the analyses of the carried out calculations, it is evident to recommend the manufacture of thermoelectric module bases from the materials, possessing the maximum heat conductivity factor, i.e. that means the effective factor of heat conductivity.

Our selected aluminium-to-thin-layer dielectric base structure is sufficient, since even the replacement by the hypothecial one with the infinite factor of heat conductivity reduces the gas temperature less than by  $1^\circ$  as calculations showed.

Fig. 1 Construction Diagram



1, 9 - "cold" and "hot" sinks

2 - plate

3 - dielectric layer

4 - current bridge

5 - semiconductor bodies of  $\text{Bi}_2\text{Te}_3$

## EVAPORATING COOLING OF THE ELEMENTS OF THE THERMO-ELECTRIC HEAT PUMPS

G.L. Serebriany

Prived Individual Enterprise "COMFORT", Moscow, Russia

The calculation method and the testing results of the thermo-electric heat pumps (THP) with a water-evaporating cooling effect are presented.

The mathematical model of the diffusional and convective heat-masstransfer in the streams of wet air ventilating hot and cool THP radiators are worked out. The comparative analysis of the direct (by irrigating) and indirect evaporating cooling is given. The results of the realization of the experimental cooling devices are demonstrated.

The evaporating cooling of the THP heat-strained elements being an effective mean of its energetic characteristics improving, can be realized in the devices of direct or indirect action: the system of the hot radiator irrigation using wet porous plates contacting with its elements; or placed in radiators front and gathered into the blocks of the adiabatic air-cooler.

The calculation peculiarity is relayed to THP with a direct evaporating cooling as it demands to take into account interdependences of the load characteristics and the process of the heat-masstransfer in the radiators. The generalised model of the THP with ventilated hot and cool radiators. When evaporating and water condensing on their surfaces (Fig 1,2) is based on the equation of the heat balance, where the expressions of the heat streams density when diffusional evaporating or condensing are based on the admission of the equality of the thickness of the heat and diffusional boundary layers: when the values of vapor contenance is really little:

$$\begin{aligned} q_H &= \frac{r\alpha_H}{c} (Y_{FH} - Y_H) - \alpha_H (T_H - T_{FH}) = \\ &= k_{FH} (T_{RH} - T_{FH}) = \\ &= \frac{K}{F_H} \times \frac{T_{RC} - B_0 T_{RH} + U_0}{\xi_0}, \quad (1) \end{aligned}$$

$$\begin{aligned} q_C &= \frac{r\alpha_C}{c} (Y_C - Y_{FC}) + \alpha_C (T_C - T_{RC}) = \\ &= k_{FC} (T_{FC} - T_{RC}) = \\ &= \frac{K}{F_C} \times \frac{A_0 T_{RC} - T_{RH} - V_0}{\xi_0}. \quad (2) \end{aligned}$$

When applying the present model to the effective radiators assuring the little temperature hods, we can calculate

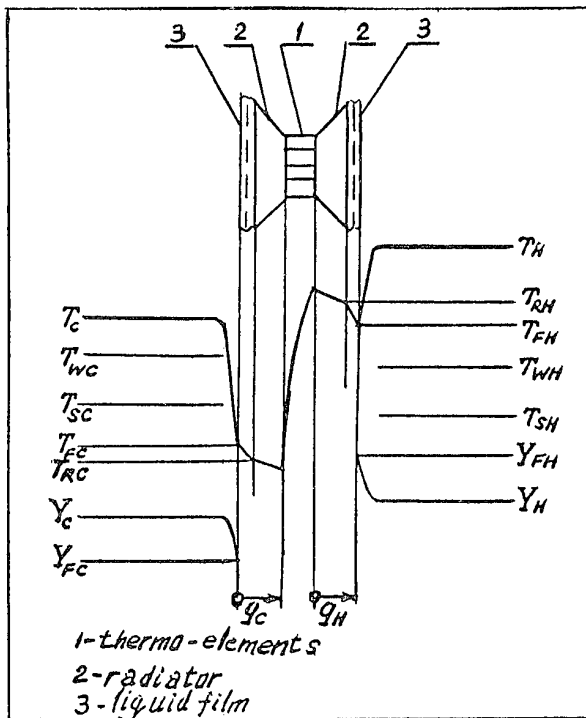
$$\frac{Y_F - Y}{T_F - T_S} = \frac{dY}{dT_S}, \quad (3)$$

and use a linear approximation

$$Y = M + NT_S, \quad (4)$$

correct within the small (5-10 K) limits of change  $T_S$ .

Fig.1 The scheme of heat-masstransfer



In the presence of the phase transformations on the hot and cool sides, we have the linear dependencies of the THP load characteristics from the air temperatures  $T_{WH}$ ,  $T_{WC}$  on wet thermometer:

$$Q_H = K \frac{T_{WC} - BT_{WH} + U}{\xi}, \quad (5)$$

$$Q_C = K \frac{AT_{WC} - T_{WH} - V}{\xi}. \quad (6)$$

The coefficients  $B$ ,  $U$ ,  $A$ ,  $V$ ,  $\xi$  are opened in accordance to  $B_0$ ,  $U_0$ ,  $A_0$ ,  $V_0$ ,  $\xi_0$  with the change of the inter-resistances  $\beta_0$  by the summary ones:

$$\beta_H = \beta_{H0} + \beta_{HR}; \beta_C = \beta_{C0} + \beta_{CR}.$$

$$\beta_{HR} = K(F_H k_H)^{-1}, \beta_{CR} = K(F_C k_C)^{-1},$$

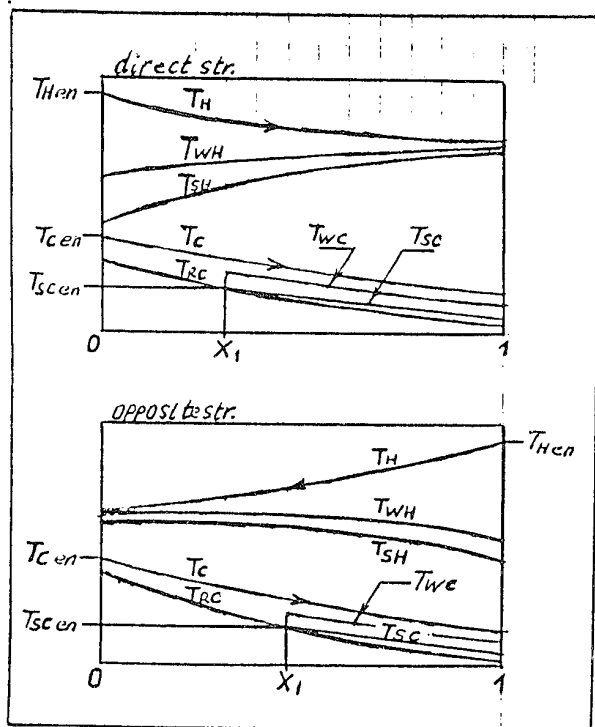
$$k_{H,C} = \left[ \frac{1}{k_{FH,C}} + \frac{1}{\alpha_{H,C}(1+\gamma_{H,C})} \right]^{-1},$$

$$\gamma_H = \frac{dY}{dT_{SH}} = \frac{rN_H}{c} = \text{const},$$

$$\gamma_C = \frac{dY}{dT_{SC}} = \frac{rN_C}{c} = \text{const}.$$

$$T_{WH,C} = \frac{T_{H,C} + \gamma_{H,C} T_{SH,C}}{1 + \gamma_{H,C}}. (7)$$

Fig. 2 Longitudinal temperature distribution of the ventilating streams. The resistance of film of liquid is insignificantly little



The system of differential equations of the energy transfer in the streams of wet air:

$$-\frac{dI_C}{dX} = Q_C(T_{WC}, T_{WH}); (8)$$

$$\pm \frac{dI_H}{dX} = Q_H(T_{WC}, T_{WH}) - (9)$$

- for direct and opposite streamflows.  
Accordingly I, Tw we have:

$$\begin{aligned} \frac{dY}{dX} &= W \left( \frac{dT}{dX} + \frac{r}{c} \frac{dY}{dT_s} \frac{dT_s}{dX} \right) = \\ &= W(1+\gamma) \frac{dT_w}{dX}. (10) \end{aligned}$$

Expressions (10), (5), (6) permit the differential description of the process of energy transfer by linear equations (8) and (9). Without formal difference from equations [1] for one-phase streams, that reflect the  $T_{C(X)}$  and  $T_{H(X)}$  changes. The essential difference is: the change of the streams temperatures  $T_{C(X)}$  and  $T_{H(X)}$  by their temperatures  $T_{WC(X)}$  and  $T_{WH(X)}$  on wet thermometer; water equivalents  $W_{C,H}$  - by their equivalent values

$$W_{*C,H} = W_{C,H}(1 + \gamma_{C,H});$$

coefficients  $\alpha_{C,H}$  by their equivalent values

$$\alpha_{*C,H} = \alpha_{C,H}(1 + \gamma_{C,H}).$$

When excluding the influence of the thin liquid film or wet porous covering on the hot side ( $k_{FH}^{-1} = 0$ ); and all the more-on the cool side when drop condensating ( $k_{FC}^{-1} = 0$ ):

$$k_{H,C} = \alpha_{*H,C}.$$

For calculation of the distribution  $T_{C,H(X)}$  and  $T_{SC,H(X)}$  for known (found from (8) and (9))  $T_{WC,H(X)}$  we must determine the liaison  $T_s = f(T)$ . In this case, in contrast to (8) and (9) we'll represent the separate description of the processes of longitudinal heat- and masstransfer:

$$-W_H \frac{dT_H}{dX} = \alpha_H F_H (T_H - T_{FH}), (11)$$

$$\frac{W_H}{c} \times \frac{dY_H}{dX} = \frac{\alpha_H}{c} F_H (Y_{FH} - Y_H) > 0; (12)$$

and

$$-W_C \frac{dT_C}{dX} = \alpha_C F_C (T_C - T_{FC}) < 0, (13)$$

$$-\frac{W_C}{c} \times \frac{dY_C}{dX} = \frac{\alpha_C}{c} (Y_C - Y_{FC}) < 0. (14)$$

When admitting (3), (4) the equations (12), (14) have a form similar to (11), (13):

$$W_H \frac{dT_{SH}}{dX} = \alpha_H F_H (T_{FH} - T_{SH}), (12a)$$

$$-W_C \frac{dT_{SC}}{dX} = \alpha_C F_C (T_{SC} - T_{FC}). (14a)$$

Thanks to this  $T_F$  is excluded and we have:

$$\theta_{H(X_H)} = \theta_{Hen} \times \exp\left(-\frac{\alpha_H F_H}{W_H} X_H\right), \quad (15)$$

$$T_{min} = \frac{T_{WH} + V}{A}; \quad (24)$$

$$\theta_{C(X)} = \theta_{Cen} \times \exp\left(-\frac{\alpha_C F_C}{W_C} X\right); \quad (16)$$

$$\theta = T - T_s; \theta_{en} = (T - T_s)_{en};$$

when the direct streamflow  $X_H=X$  and the opposite one -  $X_{H1}=1-X$ .

Use (7), we have:

$$T_{SH(X)} = T_{WH(X)} - \frac{\theta_{Hen}}{1+\gamma_H} \times \exp\left(-\frac{\alpha_H F_H}{W_H} X_H\right), \quad (17)$$

$$T_{H(X)} = T_{WH(X)} + \frac{\gamma_H}{1+\gamma_H} \theta_{Hen} \times$$

$$\times \exp\left(-\frac{\alpha_H F_H}{W_H} X_H\right), \quad (18)$$

$$T_{SC(X)} = T_{WC(X)} - \frac{\theta_{Cen}}{1+\gamma_C} \times \exp\left(-\frac{\alpha_C F_C}{W_C} X\right), \quad (19)$$

$$T_{C(X)} = T_{WC(X)} + \frac{\gamma_C}{1+\gamma_C} \theta_{Cen} \times$$

$$\times \exp\left(-\frac{\alpha_C F_C}{W_C} X\right). \quad (20)$$

Condensation of moisture from the stream of cooled air (Fig.2) take place when  $T_{RC}<T_{Sc}$  and can be partial ( $0 < X_1 < 1$ ) or full ( $X_1 \leq 0$ ). The necessary condition of condensation: the surface temperature of the cool radiator on the exit is less than the air saturation temperature on the radiator entrance

$$T_{RCex} < T_{SCen}; \quad (21)$$

the condensation of the total area  $F_C$ :

$$T_{RCen} \leq T_{SCen}. \quad (22)$$

The temperatures  $T_{RCex}$  and  $T_{RCen}$  are calculated for "dry" heat balance ( $\gamma_C = 0$ ) as functions  $T_{Cex}$ ,  $T_{WH(x=1)}$  and  $T_{Cen}$ ,  $T_{WH(x=0)}$ :

$$T_{RC} = \frac{T_c - T_{min}}{1+\kappa} + T_{min}, \quad (23)$$

$$\kappa = \frac{AK(\alpha_C F_C)^{-1}}{1+\beta_H + \beta_{C0} + \sqrt{(\beta_{C0} - \beta_H - \nu\beta_{C0}\beta_H)}}.$$

When realizing the condition (21) and the breaching (22) the coordinate  $X_1$  of the condensation area beginning is found from extreme condition

$$T_{RC(X_1)} = T_{SCen}, \quad (25)$$

when using (23) and (24) including  $T_{C(x1)}$  and  $T_{WH(x1)}$ . These functions' kind depends on the streamflow direction and is found from [1]. As a result we have a non-evident of dependency

$$X_1 = f(T_{Cen}, T_{SCen}, T_{WHen}),$$

that permits to calculate the THP energetic parameters, the intensity of evaporation and condensation.

From (18) it follows that, the hot radiator ventilating air can cool or get warm when moving; this is defined by symbol  $\frac{dT_H}{dX}$  and explicated by "evaporating capacity" of hot edges. So, if the THP heat-productivity is insufficient for water evaporation, this deficit is compensated by air cooling, accordingly under condition:

$$K \frac{T_{C*} - BT_{WH} + U}{\xi} < \frac{\alpha_H F_H}{W_H} \times \frac{\gamma_H}{1+\gamma_H} \times \\ \times \theta_{Hen} \times \exp\left(-\frac{\alpha_H F_H}{W_H} X\right);$$

$T_{C*} = T_c$  when  $\gamma_C = 0$  (dry section) and  $T_{C*} = T_{WC}$  when  $\gamma_C \neq 0$  (wet section).

The difficulty of the direct evaporation cooling system realization is explained by the overloading of the ventilating channels with porous plates. In this connections, the scheme of the preliminary air cooling in front of radiator is more convenient for an adiabatic device. Therefore this method of indirect cooling of radiator has an energetic demerits, evaluated by comparative analysis.

As a base of comparison let's review the THP with intermediate heat-bearer on the hot edges, permitting to remove a hot radiator to avoid an undesirable diffusional transfer of vapor into the area of cooled air. The intermediate heat-bearer can be represented by a closed liquid contour, assuring the "planned" hot edges temperatures, that simplifies a calculating scheme.

The comparison of direct and indirect evaporating cooling is reduced to evaluation of influence of hot radiator thermic resistance ( $\beta_{HR}$ ) on the THP cooling productivity.

$$Q_{C(\beta_{HR})} = \frac{Q_{C_{\max}} - KV^2 \beta_{HR} \left( T_{C^*} + \frac{1-0,5V}{Z} \right) \xi_1^{-1}}{\xi_1 + B \beta_{HR}}; \quad (26)$$

$$Q_{C_{\max}} = Q_{C(\beta_{HR}=0)} = K \frac{A_1 T_{C^*} - T_{H^{*en}} - V_1}{\xi_1};$$

$A_1, V_1, \xi_1$  - are the  $\beta_{H0}$  functions; on the section "hot edges - intermediate heat-bearer".  $T_{H^{*en}}$  - conventional air temperature on the entrance to hot radiator; for direct evaporating cooling  $T_{H^{*en}}=T_{WHen}$ , and for indirect one  $T_{H^{*en}}=T_{HVex}$  - on the exit from adiabatic evaporating air-cooler. When the effectiveness of the last one is maximum ( $E_V \rightarrow 1$ )

$$T_{HVex}=T_{WHen}$$

and the values  $Q_C$  of two schemes are different only at the expense of values  $\beta_{HR}$ .

For indirect cooling of radiator

$$\beta_{HR1} = \frac{K(W_{H1})^{-1}}{1 - \exp \left[ \frac{-\alpha_{H1} F_{H1} (W_{H1})^{-1}}{1 + \omega_1} \right]}, \quad (27)$$

and for direct one

$$\beta_{HR2} = \frac{K(W_{H2})^{-1} (1 + \gamma_H)^{-1}}{1 - \exp \left[ \frac{-\alpha_{H2} F_{H2} (W_{H2})^{-1}}{1 + \left( \frac{\alpha_{H2}}{k_F} + \omega_2 \right) (1 + \gamma_H)} \right]}, \quad (28)$$

$$\omega = (\alpha_H F_H) R_i.$$

The advantage of the direct evaporating cooling is obvious at the expense of large values  $\gamma_H$ : e.g. when  $T_{SH}=300$  K  $\gamma_H = 3,85$ .

Equality of the cooling effect of both schemes is assured by more complicated construction of the indirect evaporating devices: increased dimensions and air debit. The advantages evaluating the direct cooling by the value

$$\Phi = \frac{(\alpha_H F_H)_2}{(\alpha_H F_H)_1},$$

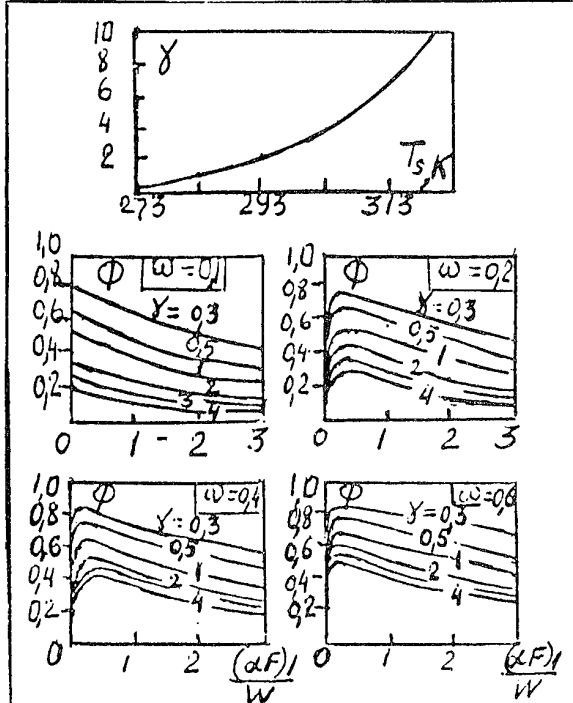
when  $\frac{\alpha_{H2}}{k_F} \ll \omega_2, W_{H1} = W_{H2} = W$  and  $\omega_1 = \omega_2 = \omega$

are presented on Fig. 3. From condition  $\beta_{HR1} = \beta_{HR2}$  it follows:

$$\Phi = \frac{1 + \omega(1 + \gamma_H)}{\mu} \ln \frac{1 + \gamma_H}{\gamma_H + \exp \left( \frac{-\mu}{1 + \omega} \right)}; \quad (29)$$

$$\mu = \frac{(\alpha_H F_H)_1}{W_H}.$$

Fig.3 Direct evaporating cooling advantages: economy of "convective conductivity" of radiator



The possibility of substantial decrease of the value  $\alpha_H F_H$  is evident, e.g. of 67% when  $\gamma_H = 2, \omega = 0.2, \mu = 1$ . This fact gives a possibility to make a convective surface with a greater equivalent diameter (of 75%) or to minimise to three times the radiator's dimensions. The decrease of  $\alpha_H F_H$  leads to reduction of irrigating demands. So, the heat stream for water evaporation in the direct cooling device is:

$$Q_{V1} = W_H \gamma_H (T_{SHex} - T_{SHen}) = \frac{\gamma_H}{1 + \gamma_H} \times \\ \times \left\{ Q_H + \theta_{Hen} W_H \left[ 1 - \exp \left( -\frac{\alpha_H F_H}{W_H} \right) \right] \right\}. \quad (30)$$

For an adiabatic air cooler the indirect cooling device, when  $E_V \rightarrow 1$  is:

$$Q_{V2} = \frac{\gamma_H}{1 + \gamma_H} \theta_{Hen} W_H. \quad (31)$$

When  $\alpha_H F_H \ll W_H$ , we can obtain

$$\frac{T_{WHen} - T_{WHex}}{\theta_{Hen}} + \frac{\alpha_H F_H}{W_H} = \frac{Q_{V1}}{Q_{V2}} < 1.$$

the decrease of debit of evaporated water.

The calculation of the device with intermediate heat-bearer are made when  $T_{WH} = T_{WHen} \neq f(x)$ , that's truth for schemes without intermediate heat-bearer when a big value  $W_H$ . The existence of the coordinate  $X_1$  of the condensation beginning in the limits  $0 \leq X_1 \leq 1$  accordingly to (23), (24) corresponds to the boundaries

$$\aleph \leq \frac{T_{Cen} - T_{SCen}}{T_{SCen} - T_{min}} \leq (1+\aleph) \exp \frac{K_c}{W_c} - 1. \quad (32)$$

$$K_c = K \frac{A}{\xi} = \frac{\aleph}{1+\aleph} \alpha_c F_c$$

(when  $\gamma_c = 0$ ).

In contrast to (24), here

$$T_{min} = \frac{T_{WHen} + V}{A}$$

is constant. The disturb of the left part of the system inequality (32) corresponds to water condensation on the whole surface  $F_c$ ; and in (19), (20):

$$T_{WC(X)} = T_{WCen} - (T_{WCen} - T_{min}) \times \\ \times \left[ 1 - \exp \left( - \frac{K_c}{W_c} \times \frac{1+\aleph}{1+\aleph+\gamma_c} X \right) \right]. \quad (33)$$

When the right part of the system inequality (32) is disturbed  $\gamma_c = 0$  and

$$T_{C(X)} = T_{Cen} - (T_{Cen} - T_{min}) \left[ 1 - \exp \left( - \frac{K_c}{W_c} X \right) \right]. \quad (34)$$

When accomolishing the conditions (32) and (25), using (23):

$$T_{C1(X)} \equiv T_{C(X1)} = (T_{SCen} - T_{min})(1+\aleph) + T_{min}. \quad (35)$$

From (34):

$$T_{C1} = T_{Cen} - (T_{Cen} - T_{min}) \left[ 1 - \exp \left( - \frac{K_c}{W_c} X_1 \right) \right]. \quad (36)$$

As results

$$X_1 = \frac{W_c}{K_c} \ln \frac{\Delta}{1+\aleph}; \quad (37)$$

$$\Delta = \frac{T_{Cen} - T_{min}}{T_{SCen} - T_{min}}.$$

From (37) it follows: with increasing of the air relative humidity on the radiator entrance (decreasing of the disparity  $T_{Cen}-T_{SCen}$ ) and with decreasing of the limit  $T_{min}$  of the thermoelectric cooling the value  $X_1$  decreases - water condensation surface increases. This fact is contributed by: the increasing of the thermo-conductivity  $K$  of the battery, decreasing of the convective heat yield intensity (when  $W_c > K_c$ ), of thermic resistances  $\beta_{C0}, \beta_H$  and air debit  $W_c$ .

On the section of condensation ( $X_1 < X < 1$ ) the temperature of cooled air on wet thermometer included in (19), (20), is found as

$$T_{WC(X)} = T_{WC(X1)} - [T_{WC(X1)} - T_{min}] \times$$

$$\times \left\{ 1 - \left[ \frac{\Delta}{1+\aleph} \exp \left( - \frac{K_c}{W_c} X \right) \right]^{\frac{1+\aleph}{1+\aleph+\gamma_c}} \right\}. \quad (38)$$

In accordance with (7)

$$T_{WC(X1)} = \frac{T_{C1} + \gamma_c T_{SCen}}{1 + \gamma_c},$$

$T_{C1}$  - from (35).

The calculation of the heat-masstransfer processes on this section is reduced to calculation of resulting cooling of the air stream in the radiator:

$$\delta T_{WC} = T_{WCen(X=X1)} - T_{WCex(X=1)} = \\ = [T_{WC(X=X1)} - T_{min}] E_W, \quad (39)$$

$$\delta T_{SC} = T_{SCen(0 \leq X \leq X1)} - T_{SCex(X=1)} = \\ = (T_{SCen} - T_{min}) E_s, \quad (40)$$

$$\delta T_C = T_{C1(X=X1)} - T_{Cex(X=1)} = \\ = [T_{SCen(X=0)} - T_{min}] E_C. \quad (41)$$

The coefficients of the cooling effectiveness:

$$E_W = 1 - \left[ \frac{\Delta}{1+\aleph} \exp \left( - \frac{K_c}{W_c} \right) \right]^{\frac{1+\aleph}{1+\aleph+\gamma_c}}, \quad (42)$$

$$E_s = E_W - \frac{\aleph}{1+\gamma_c} \left[ 1 - E_W - \exp \left( - \frac{\alpha_c F_c}{W_c} \right) \right], \quad (43)$$

$$E_C = \frac{E_w(1+\gamma_c + \aleph) + \gamma_c \aleph \left[ 1 - \exp\left(-\frac{\alpha_c F_c}{W_c}\right) \right]}{\Delta(1+\aleph_c)} \quad (44)$$

On the "dry" section ( $0 < X < X_1$ ):

$$\delta T_{Cdr} = T_{Cen(X=0)} - T_{C1(X=X_1)} =$$

$$= [T_{Cen(X=0)} - T_{min}] E_{Cdr}, \quad (45)$$

$$E_{Cdr} = 1 - \frac{1+\aleph}{\Delta} = 1 - \exp\left(-\frac{K_c}{W_c}\right). \quad (46)$$

The values of the cool productivity on the "dry" and "wet" sections:

$$Q_{Cdr} = W_c \delta T_{Cdr},$$

$$Q_{CW} = W_c (1+\gamma_c) \delta T_{WC}.$$

The middle integral temperatures:

$$T_{Cdr} = \frac{Q_{Cdr}}{K_c X_1} + T_{min},$$

$$T_{WC} = \frac{Q_{CW}}{K_c (1-X_1)} \times \frac{1+\aleph + \gamma_c}{(1+\aleph)(1+\gamma_c)} + T_{min}.$$

The expression of the THP heat productivity:

$$Q_{Hdr} = \frac{K_c}{A} X_1 (T_{Cdr} - B_{dr} T_{Hen} + U_{dr}),$$

$$Q_{HW} = \frac{(1+\aleph)(1+\gamma_c)}{1+\aleph + \gamma_c} K_c \frac{1-X_1}{A} \times$$

$$\times (T_{WC} - B_w T_{Hen} + U_w);$$

$T_{Hen} = T_{WHen}$  when  $\gamma_H \neq 0$  and  $T_{Hen} = T_{Hen}$  for the case of elimination of the evaporating cooling ( $\gamma_H = 0$ ).  $B_{dr}$ ,  $U_{dr}$  are calculated when  $\gamma_c = 0$ ;  $B_w$ ,  $U_w$  - when  $\gamma_c \neq 0$ .

Consumed electric power:

$$P_{dr} = Q_{Hdr} - Q_{Cdr};$$

$$P_w = Q_{HW} - Q_{CW}.$$

Water condensation intensity (kg/h):

$$G_C = \frac{W_c \gamma_c \delta T_{SC}}{r}.$$

Evaporation intensity:

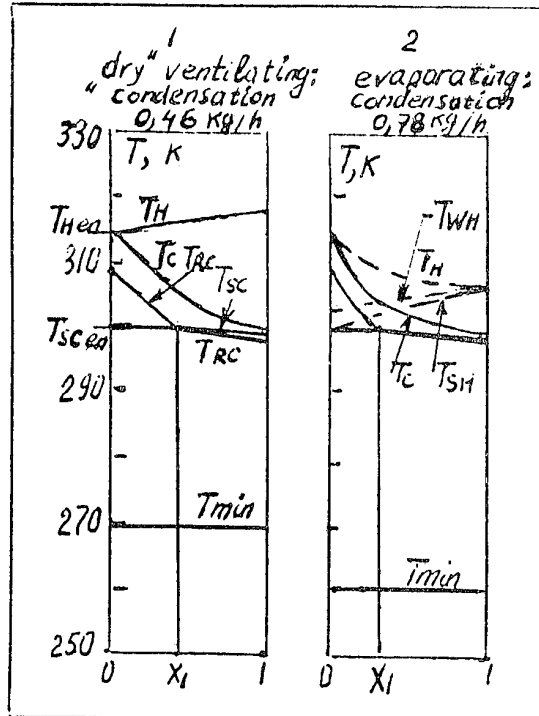
$$G_V = \frac{\gamma_H W_H}{r} (T_{SHen} - T_{Hen}) =$$

$$= \frac{Q_{Hdr} + Q_{HW} + W_H (T_{Hen} - T_{Hex})}{r} = \frac{\gamma_H}{r(1+\gamma_H)} \times$$

$$\times \left\{ \begin{array}{l} Q_{Hdr} + Q_{HW} + (T_{Hen} - T_{SHen}) \times \\ \times W_H \left[ 1 - \exp\left(-\frac{\alpha_H F_H}{W_H}\right) \right] \end{array} \right\}$$

The Fig.4 shows the results of calculation of the thermo-electric air-cooler with next parameters:  $K=39$  W/K;  $Z=2,56 \cdot 10^{-3}$  K<sup>-1</sup>;  $\beta_H=0,22$ =const for regimes 1 and 2 of "dry" and evaporating cooling of hot radiator;  $\beta_{C0}=0,1$ ;  $\nu=0,22$ ;  $\alpha_c F_c=330$  W/K;  $\alpha_H F_H=800$  W/K;  $W_{H1}=700$  W/K;  $W_{H2}=144$  W/K;  $T_{Cen}=T_{Hen}=313$  K;  $T_{SCen}=T_{SHen}=300$  K; relative humidity 52,7%;  $W_c=60$  W/K.

Fig.4 Comparison of the calculation results for the "dry" ventilating and evaporating cooling schemes

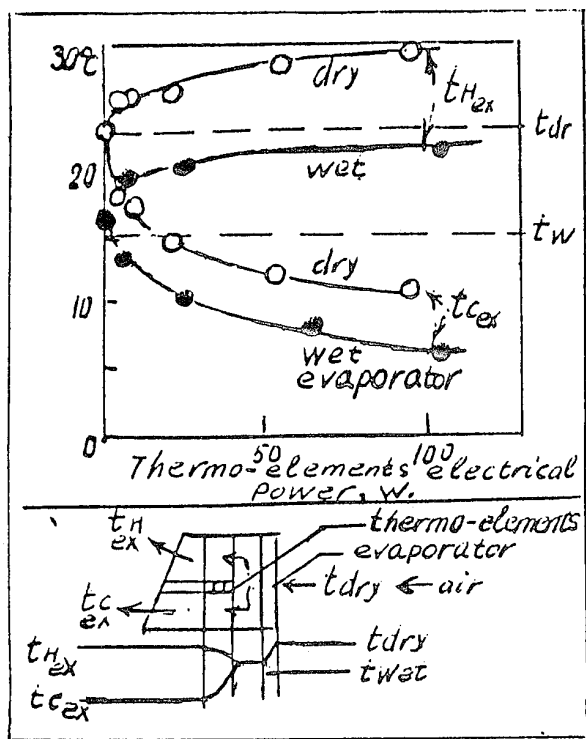


The advantages of the evaporating cooling of hot radiator: cool productivity is increased to 22%; consumed electric power is decreased to 9,7%; the drying effect (intensity of water condensation) is increased to 67,7%; the air of hot radiator is cooled to 6,6 K (additional cooling effect); when eliminating the evaporating cooling the air stream is heated to 3,37 K; the demand of ventilating air is decreased to 4,86 times. Insignificant  $T_{SC}$  decrease and  $T_{SH}$  increase and the small temperature heads " $T_{RH}-T_{SH}$ " and " $T_{SC}-T_{RC}$ " within the admissions are confirmed (3), (4). The intensity of water evaporation is 4,84 kg/h.

Construction difficulties of the organization of water transport to the hot radiator surface due to capillary effect are justified for cooler of great capacity. For small cooling devices-refrigerators, ice-makers, drink-coolers - the use of the adiabatic evaporating nozzle representing an element of indirect cooling system is justified.

The testing results of the above-mentioned experimental devices are shown on Fig. 5, 6, 7, 8, 9.

Fig. 5 THP combined with water evaporation cooler



On Fig. 5 we can observe the characteristics of THP combined with an evaporating cooler: in front of hot and cool radiators where the air is cooled an wetted by an evaporating nozzle. The air temperatures on exit of hot and cool radiators when moistening the nozzle are decreased accordingly to 7 and 4 K.

The Fig. 6 represents the testing results of the thermo-electric ice-maker: the advantages of evaporating air stream cooling in front of radiator are increased depending on the temperature  $T_{SUR}$  growth of surrounding air. When  $T_{SUR}=308$  K the productivity of the ice-maker increased to 60%.

The Fig. 7 demonstrates the advantages of the evaporating cooling by dynamic characteristics of the ice-maker: the time of one portion of ice preparation (70 g) is reduced twice.

The Fig. 8 represents the static characteristics of a refrigerator with capacity of 4-5 l: thanks to air cooling in front of hot radiator and the thermo-isolation surface [2] the temperature depth of the cooling is increased to 5-7 K.

The Fig. 9 represents a dynamic characteristic of a drink-cooler (capacity 0,33 l): advantages of evaporating cooling become evident when a great depth of cooling: the time of cooling from 298 to 273 K is reduced to 1,5 times, and to 288 K - to 1,4 times. The intensity of water evaporation is 0,08 - 0,1 kg/h.

Fig. 6 Productivity of the great thermoelectric ice-maker with evaporating cooling

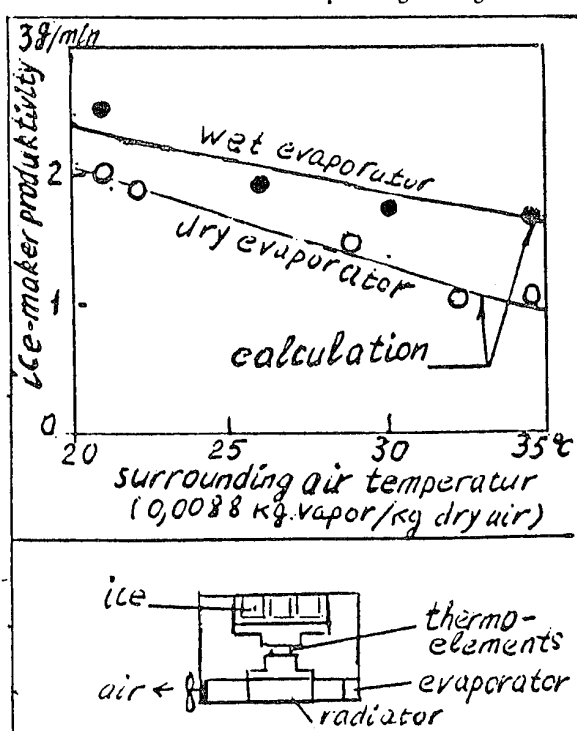


Fig. 7 Dynamic characteristics of the small ice-maker with "dry" and evaporating cooling

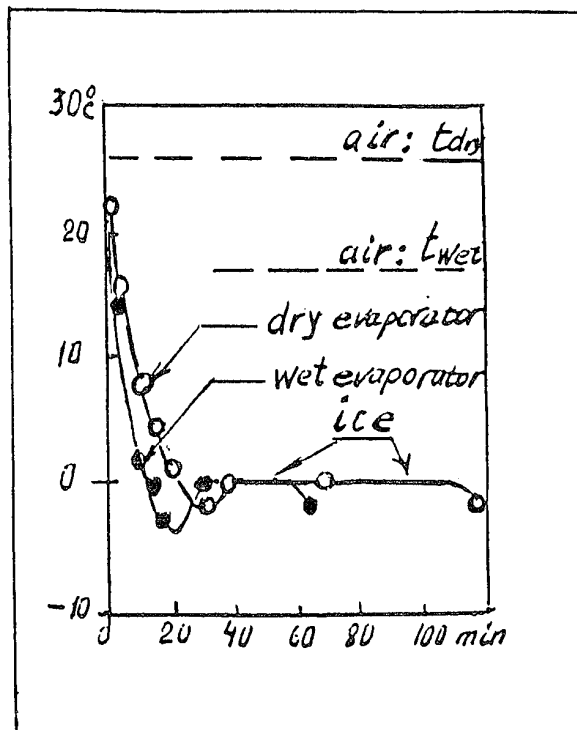


Fig. 8 Characteristics of thermo-electric refrigerators

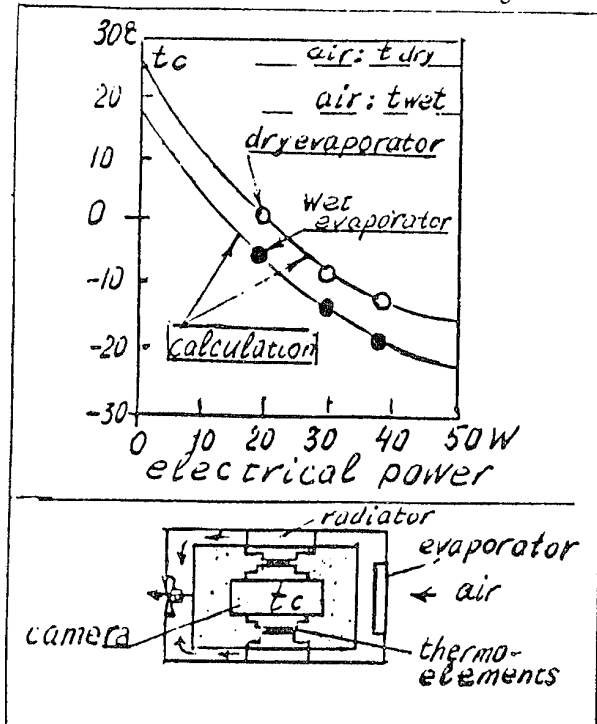
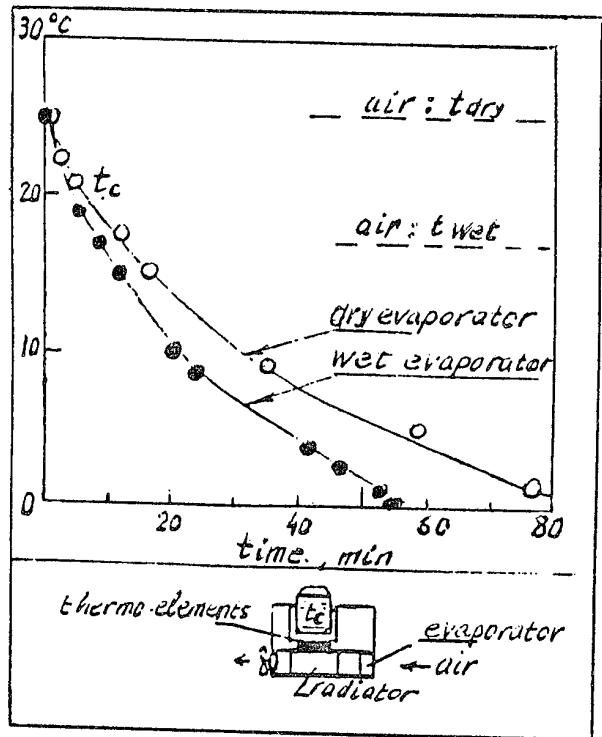


Fig. 9. Dynamic characteristics of the drink-coolers.



## SYMBOLS

$T_{RH}$ ,  $T_{FH}$ ,  $T_H$ ,  $T_{SH}$ ;  $Y_H$ ,  $Y_{FH}$  and  $T_{RC}$ ,  $T_{FC}$ ,  $T_C$ ,  $T_{SC}$ ;  $Y_C$ ,  $Y_{FC}$  - temperatures of wet radiator surface, outward surface of a liquid film, air, air saturation water vapor, K; specific weight contenance of the water saturated vapors when the temperature is  $T_S$ , the same ones when the temperature is  $T_F$ , kg vapor/kg dry air-accordingly on the sides of hot and cool THP radiators;  $T_{WH}$  and  $T_{WC}$  - temperatures of air on wet thermometer;  $q_H$  and  $q_C$  - densities of the heat streams on the radiators' convective

surfaces,  $\text{Wh/m}^2$ ;  $Q_H$  and  $Q_C$  - accordingly heat- and cool productivities of the THP, W;  $\alpha$  - average, taking account an effectiveness of radiator elements, value of heat yield coefficient;  $k_F$  - heat transfer coefficient through a liquid film or wet porous covering,  $\text{W/m}^2\text{K}$ ;  $c$  - specific weight heat of wet air,  $\text{Wh/kg}\text{K}$ ;  $K$  - heat conductivity of thermo-elements battery,  $\text{W/K}$ ;

$\xi_0 = 1 + \beta_{C0} + \beta_{H0} + \nu(\beta_{C0} - \beta_{H0} - \nu\beta_{C0}\beta_{H0})$ ;  
 $\beta_{C0}$  and  $\beta_{H0}$  - non-measured thermic resistances of the sections "cool film surface  $F_C$  - cool edges" and "hot edges - hot film surface  $F_H$ ";

$$\beta_{C,H0} = KR_{C,H};$$

$R_{C,H}$  - thermic resistance of the above-mentioned sections,  $\text{W/K}$ ;  $R_i$  - thermic resistance of the section "liquid intermediate heat-bearer - surface  $F_{RH}$  of the hot radiator";  $\nu$  - non-measured density of the electrical current;

$$A_0 = 1 + \gamma(1 - \nu\beta_{H0}); B_0 = 1 - \nu(1 + \nu\beta_{C0});$$

$$V_0 = 0,5\nu^2 Z^{-1} [1 + (2 - \nu)\beta_{H0}];$$

$$U_0 = 0,5\nu^2 Z^{-1} [1 + (2 + \nu)\beta_{C0}];$$

$Z$  - parameter of the thermo-elements battery high quality,  $\text{K}^{-1}$ ;  $W_{C,H}$  - water equivalents of the ventilating air,  $\text{W/K}$ ;

$$I = \left( T + \frac{r}{c} Y \right) W -$$

heat-contenance of the wet air, W;  $r$  - specific weight of heat evaporating or condensing,  $\text{Wh/kg}$ ;  
 $X$  - non-measured coordinate.

## REFERENCES

- [1]. М.А. Каганов, М.Р. Привин, Термоэлектрические тепловые насосы. М.-Л. 1970, 176 с.
- [2]. Г.Л. Серебряный. Термоэлектрический холодильник с испарительным охлаждением изоляции. // В кн.: Теплофизические вопросы преобразования энергии. Киев, Наукова Думка, 1979, с. 100-107.

# EXAMPLE OF APPLICATION OF THERMOELECTRIC COOLER WITH HIGH $T_c$ SUPERCONDUCTING ELEMENTS

N.A. Sidorenko

*Institute for Problems in Mechanics,  
prospect Vernadskogo 101, PO 117526, Moscow, RUSSIA*

Construction and main characteristics of combined cryocooler for long wave photodetector arrays with thermo stabilization level at 70K are presented, where magneto-thermoelectric battery with high  $T_c$  superconducting passive branches serves as the last cooling stage.

## 1. Introduction

Application of passive high  $T_c$  superconducting (HTSC) branches together with n-type Bi-Sb semiconducting branches gives opportunity to extend effective thermoelectric (TE) cooling to cryogenic temperatures:  $60K < T < T_c$  [1-5].

Previously [6] the main requirements were formulated to obtain high figure of merit of TE couples with passive HTSC branches and possible construction of single stage magneto-thermoelectric (MTE) coolers was described.

Present report is a continuation of previous one [6] and aimed to give an example of benefit obtained by application of MTE cooler with HTSC branches.

Construction of combined cryostat for long wavelength GaAs quantum well photodetector arrays with thermo stabilization level at 70K is presented, where single stage MTE battery with HTSC passive branches serves as the last cooling stage. Cryogenic bath filled with liquid nitrogen is used to get supporting pre-cooling of MTE stage.

## 2. Materials for cryogenic MTE cooler branches

Considering both TE and mechanical properties of Bi-Sb alloys, obtained by various kinds of technique, it was shown previously [3,5,6] that n-type Bi-Sb single crystals, containing 9-12 at.% of Sb and grown by Czochralski method with additional annealing, are the best known TE materials to build up effective and reliable TE or MTE cooler operating at temperatures below 150K.

In previous experiments [3,4,6] maximum temperature difference was obtained for thermocouples with passive HTSC YBaCuO film branches and thermoelectrically active n-type branches made of Bi-Sb single crystals with 11.5-12 at.% of Sb content. But taking into account results of previous mechanical strength investigations [3] it is preferably to use Bi-Sb single crystals with 8.5-9.5 at.% of Sb content. And what is more it is considerably easier to grow perfect and large single crystals containing 8.5-9.5 at.% of Sb content than containing 11.5-12 at.% of Sb content. So  $\text{Bi}_{0.91}\text{Sb}_{0.09}$  single crystal was used to prepare n-type branches of single stage cryogenic MTE cooler with operating temperatures in the interval (65-80)K.

Properties of TE material that need to calculate geometric configuration of one stage MTE cooler ensuring requested cooler parameters were measured previously. Temperature

dependence of MTE figure of merit  $Z_{33}(T)$ , Seebeck coefficient  $S_{33}(T)$ , electrical resistivity  $r_{33}(T)$  and thermal conductivity  $k_{33}(T)$  in the trigonal direction of used Bi-Sb single crystals are presented in Fig.1. All these properties were measured independently (with accuracy 2-5%) at temperatures 60-120K in the presence of permanent magnetic field 500-550 Gauss directed along bisectrix crystal axis  $\langle\bar{1}21\rangle$ .

In order to get possibility to use all passive HTSC film branches deposited on single substrate, the constitution of single stage MTE battery was chosen as a row of thermo couples, connected electrically in series -see Fig.2.

The aggregate of passive HTSC branches consists of 6 parallel stripes of YBaCuO (1-2-3 HTSC phase with  $T_c=90-91\text{K}$ ) films deposited on (001) strontium titanate ( $\text{SrTiO}_3$ ) substrate. HTSC films were covered (in situ) with protective Au layer also insuring good electric contact between current leads and HTSC material with  $(0.8-1.4)\cdot 10^{-4}$  Ohm-mm<sup>2</sup> of contact resistance at 77K. The thickness of HTSC layers is 0.4-0.5  $\mu\text{m}$ , the substrate thickness is 0.3 mm. The width of each stripe is 2 mm, the length is 15 mm and distance between stripes is 0.1mm. Dimensions of superconducting area are limited by dimensions of available substrate and by characteristics of used film deposition set-up.

HTSC films were obtained by laser sputtering method which insures critical current density of thick films  $j_c>5\cdot 10^6\text{A/cm}^2$  at 77K. Thermal conductivity of HTSC film substrate  $k_S=(18-20)\text{ W}\cdot\text{m}^{-1}\text{K}^{-1}$  at 77-80K.

SmCo permanent magnets are used to get approximately 500 Gauss of transverse magnetic field.

## 3. Characteristics and application of single stage MTE cryocooler

The required characteristics of MTE cooler are:

- total refrigerating capacity  $Q_0 = 70-80\text{mW}$ ,
- refrigerating temperature level or cold side temperature

$T_{\text{cold}}=70\text{K}$ ,

- hot side temperature  $T_{\text{hot}}=77-78\text{K}$ ,
- direct electric current  $I<5.5\text{A}$ .

Dimensions of Bi-Sb branches were calculated in accordance with measured TE material properties (see Fig.1)

and properties of superconducting branches to meet required MTE cooler parameters.

The following assumptions were used to carry out such calculations:

1) the values of  $r_{33}(T)$ ,  $S_{33}(T)$  and  $k_{33}(T)$  are changed for absolute values of their averages ( $r_{33}$ ,  $S_{33}$  and  $k_{33}$  correspondingly) over temperature interval 70-80K,

2) the value of  $Q_o = N \cdot q_o$ , where  $N$  is a number of MTE cooler thermocouples ( $N=6$  in our case) and  $q_o$  is an average value (over a number of thermocouples) of refrigerating capacity of single thermocouple,

3) the value of  $q_o$  is considered as the sum:

$$q_o = q_p - (0.5 \cdot q_{J,n} + q_{J,c}) - (q_{h,n} + q_{h,SC}) \quad (1)$$

where:

$q_p = S_{33} \cdot T_{cold} \cdot I$  is a Peltier heat absorbed by cold thermo couple junction;

$q_{J,n} = r_{33} \cdot I^2 \cdot (L_n / A_n)$  is a Joule heat emitted by n-type Bi-Sb branch, where  $L_n$  and  $A_n$  are the length and cross section area of Bi-Sb branch correspondingly;

$q_{J,c} = R_c \cdot I^2$  is a contact Joule heat and  $R_c$  is a total contact resistance of junction between Bi-Sb branch and HTSC branch through copper bus-bar, the measured value  $R_c = (2-2.5) \cdot 10^{-4}$  Ohm;

$q_{h,n} = k_{33} \cdot (T_{hot} - T_{cold}) \cdot (A_n / L_n)$  is a heat flow to cold junction due to thermal conduction of n-type branch;

$q_{h,SC} = k_S \cdot (T_{hot} - T_{cold}) \cdot (A_{SC} / L_{SC})$  is a heat flow to cold junction due to thermal conduction of HTSC branch, where  $L_{SC}$  and  $A_{SC}$  are the length and cross section area of HTSC branch correspondingly;

4) the MTE cooler energy consumption  $W = N \cdot w$ , where  $w$  is an average value of energy consumption of single thermocouple;

5) the value of  $w$  is considered as the sum:

$$w = q_{J,n} + 2 \cdot q_{J,c} + S_{33} \cdot (T_{hot} - T_{cold}) \cdot I \quad (2)$$

6) efficiency of MTE cooler is characterized by coefficient of performance (COP) that can be expressed as:

$$COP = q_o / w \quad (3)$$

The aim of calculation procedure is to get maximum value of thermocouple refrigerating capacity  $q_o$  on the basis of previously measured properties of TE and HTSC materials and the following set of thermocouple characteristics:  $T_{cold} = 70K$ ,  $T_{hot} = 78K$ ,  $A_n = 5mm^2$ ,  $A_{SC} = 0.6mm^2$ ,  $L_{SC} = 15mm$ ,  $I < 5.5A$ .

The values of electric current  $I$  and length of Bi-Sb branch  $L_n$  are variables.

Maximum value of  $q_o = 12mW$  is achieved if  $I = 5.2A$  and  $L_n = 4mm$ . In this case COP = 0.16.

Refrigerating surface of the whole MTE cooler is  $13 \times 13 mm^2$ . Plates of permanent magnets are mounted parallel to row of Bi-Sb branches.

MTE battery with magnets are placed in copper frame to protect battery from external mechanic damage and heat radiation - see Fig.4, where general appearance of actual MTE cooler is shown.

The MTE cooler is aimed to use as the last cooling stage of combined cryostat for long wavelength GaAs quantum well photodetector arrays. Fig.3 shows the scheme of the combined cryostat with MTE cooler and Fig.5 shows MTE cooler placing in the actual combined cryostat.

The whole combined cryostat insures refrigerating capacity  $Q_o = 70mW$  at 70K of cold temperature level. The liquid nitrogen stock (250mL) insures 2 hours of continuous operation of MTE cooler. Combined cryostat has following dimensions: diameter 90 mm, height 230mm, weight 3.5 kg.

#### 4. Conclusions

The available recent technologies of

- 1) Bi-Sb single crystal growth by Czochralski method,
- 2) YBaCuO high  $T_c$  superconducting films preparation by laser sputtering method,

3) assembling of thermocouples aggregate with YBaCuO superconducting film passive branches allow to build up cryogenic MTE coolers which are effective and reliable at temperatures 65-90K.

Combination of single stage cryogenic MTE cooler with small liquid nitrogen bath allows to build up portable, simple and inexpensive hybrid cooling system for infrared radiation receiver.

#### 5. References

- [1]. Goldsmid H.J., Copinathan K.K., Matthews D. et al, High  $T_c$  super-conductors as a passive thermoelements, *J. of Phys.(D)*, 1988, v.21, pp.344-348.
- [2]. Kuznetsov V.D., Vedernikov M.V., Dittman A.V. et al, Effective thermo-element with thermoelectrically passive HTSC leg, *Superconductivity: Physics, Chemistry and Technology*, 1991, v.4, pp.616-625 (in Russian).
- [3]. Dashevskii Z.M., Sidorenko N.A. et al, Cryogenic thermo electric coolers with passive superconducting branches, *Supercond. Sci. and Technol.* 1992, vol.5, p.690-693.
- [4]. Mosolov A.B. and Sidorenko N.A., Application of high  $T_c$  superconducting materials in cryogenic Peltier coolers, *Cryogenics* 1992, vol.32, ICEC Suppl., p. 36-39.
- [5] N.A. Sidorenko, Thermoelectric materials for Peltier cryogenic cooler, *Cryogenics*, 1992, v.32, ICEC Suppl., p.40-43.
- [6]. N.A. Sidorenko, Prospects of High  $T_c$  Superconductors in Thermoelectric Cooling, *Proc. of the 13-th Int. Conf. on Thermoelectrics*, August 30 -September 1, 1994. Kansas City, Missouri, USA, p.191-194.

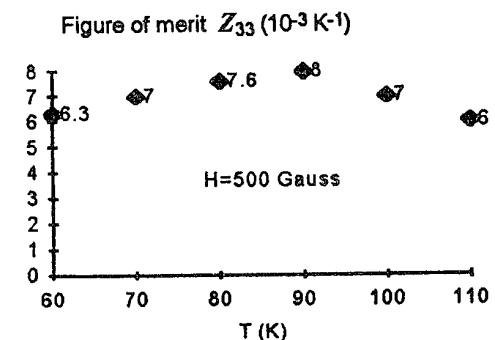
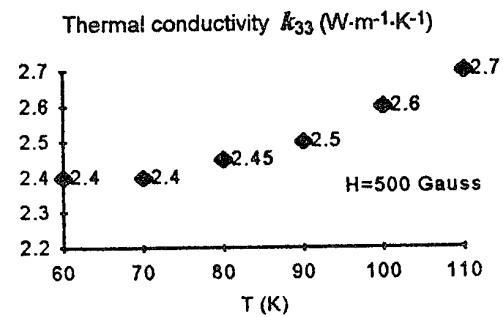
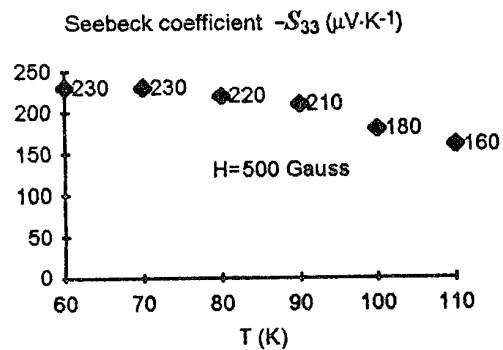
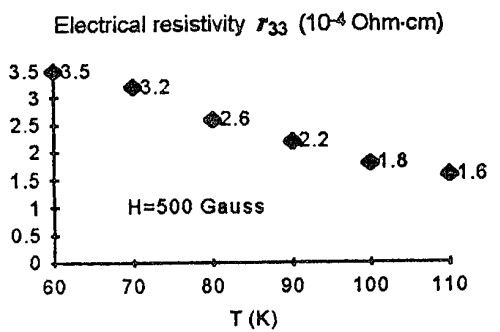


Fig.1. Thermoelectric properties of Bi-Sb n-type branches of MTE cooler in transverse magnetic field.

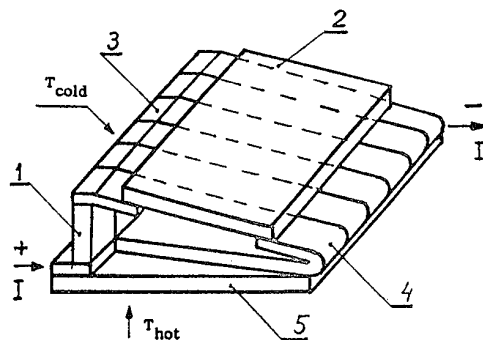


Fig.2. Scheme of constitution of single stage MTE cooling battery as an row of thermocouples with film HTSC passive branches: 1 -row of Bi-Sb n-type branches, 2 -row of HTSC film stripes deposited on single substrate, 3 -battery cold side, 4 -row of copper bus leads at battery hot side, 5 -metallized BeO plate. Permanent magnets are not shown.

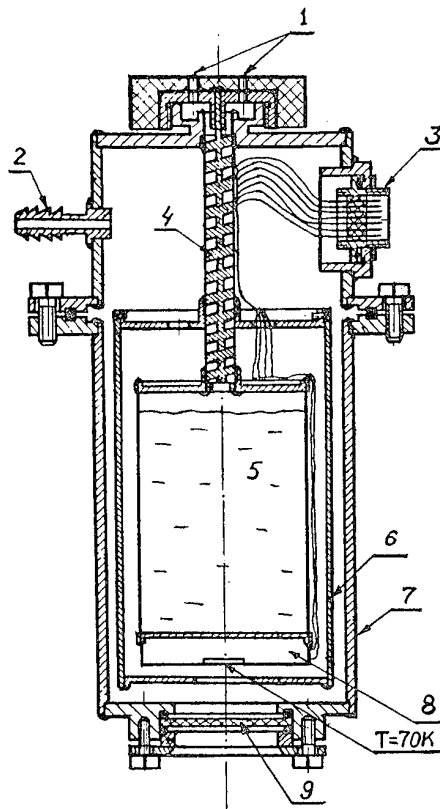
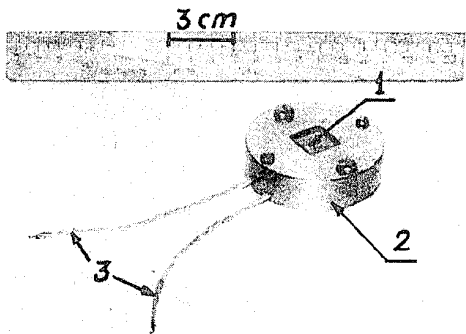
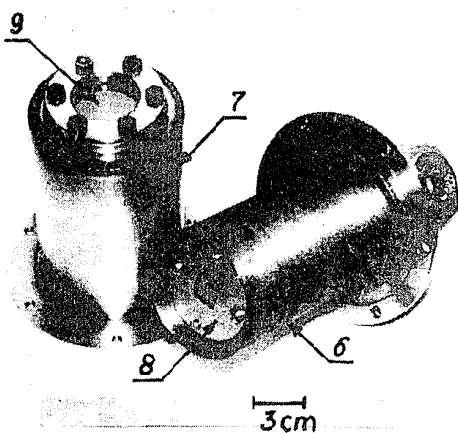


Fig.3. Total scheme of the cryostat: 1 -output of gaseous nitrogen, 2 -vacuum pump line, 3 -electric "input-output", 4 -nitrogen, 5 -liquid nitrogen, 6 -heat screen, 7 -stainless frame, 8 -MTE cooler, 9 -infrared window.



**Fig.4.** General appearance of MTE cooler: 1 -refrigerating surface ( $13 \times 13 \text{ mm}^2$  at 70K) of the MTE cooler; 2 -MTE cooler copper frame at temperature 77-78K; 3 -MTE cooler leads.



**Fig.5.** MTE cooler placing in the cryostat: 6 -heat screen, 7 -stainless frame, 8 -MTE cooler, 9 -infrared window (item numbers correspond to Fig.3).

#### Acknowledgments

This work was performed under grant N 92094 of Russian State program "High Tc Superconductivity". The perfect YBaCuO superconducting films were manufactured in the Institute of Applied Physics (Niznii Novgorod, Russia). The author would like to help Mr. A.V. Medvedev for assistance in manufacture of infrared window and metallic parts of cryostat at "Rostov Plant for Optics and Mechanics" (Rostov, Russia).

# A generalized procedure to study multistage thermoelectric cooler operated in the regime of maximum energy efficiency.

Galperin V.L.

MGNPP "OSTERM", St. Petersburg, Russia

The paper presents findings from an analytical investigation of multistage thermoelectric coolers operated in the regime of maximum energy efficiency. A criterial equations has been obtained permitting to define the conditions of attaining the maximum coefficient of performance in thermoelectric and combined multistage coolers. The relationships describing their main characteristics are given.

## Towards the Problem of Equality of Stage Coefficients of Performance

Among the main challenges in designing efficient multistage cooling systems is definition of operations conditions for each of the stages in terms of power- efficiency of the whole system. Most frequently the starting point is the generally accept idea of equality of stage coefficients of performance [1-5], even though, as is shown in [6], this may not be true for a number of cases. Consider the problem in greater detail.

It is a matter of general experience [7] the maximum coefficient of performance in a multistage thermoelectric cooler is obtainable with the minimum function

$$\mu_0 = \prod_{i=1}^N \mu_i , \quad (1)$$

defined with the set of equations

$$\frac{d(\mu_i \mu_{i+1})}{dT_i} = 0 , \quad (2)$$

$$\text{where } \mu_i = 1 + \frac{1}{\varepsilon_i} = \frac{M_i T_i - T_{i-1}}{M_i T_i - T_i} \quad (3)$$

$\varepsilon_i$  - coefficient of performance of the i-th stage;  $M_i = \sqrt{1 + 0.5 Z_i \bar{T}_i}$  - universal thermocouple characteristic of the i-th stage;  $T_i$  - intermediate temperature between the i-th and (i+1)th stage;  $\bar{T}_i$  - mean temperature of the i-th stage;

$Z_i$  - figure of merit of i-th stage units.

$$\frac{\mu_i}{\mu_{i+1}} = \frac{T_{i+1} M_i - T_{i-1} M_{i+1} + T_i \left( \frac{dM_i}{dT_i} T_{i+1} - \frac{dM_{i+1}}{dT_i} T_{i-1} \right)}{T_{i+1} M_{i+1} - T_{i-1} M_i - T_i \left( \frac{dM_{i+1}}{dT_i} T_{i+1} - \frac{dM_i}{dT_i} T_{i-1} \right)} - T_i^2 \left( M_{i+1} \frac{dM_i}{dT_i} - M_i \frac{dM_{i+1}}{dT_i} \right) , \quad (6)$$

This is just the generalized criterial equation permitting definition of the relationship of stage energy characteristics. Let us examine the relationship obtained. Assuming that  $M_i = M_{i+1} = \text{const}$ , we will gain the familiar equation  $\mu_i / \mu_{i+1} = 1$ , i.e. the exact equality of coefficients of performance  $\varepsilon_i$ . If, however, we hold that each stage  $M_i$  is

Since the function  $\mu_i$  and  $\mu_{i+1}$  in the temperature interval  $(T_{i+1}/M_{i+1}, T_i M_i)$  are intermittent and can be differentiated, the function  $\ln(\mu_i \mu_{i+1})$  has its minimum at the same point that the product  $(\mu_i \mu_{i+1})$  so that to examine the expression (1) instead of the set of equations (2) one need only to analyze the system of equations

$$\frac{d(\ln \mu_i \mu_{i+1})}{dT_i} = 0 , \quad (4)$$

By substituting in it the expressions for  $\mu_i$  and  $\mu_{i+1}$  from (3), and differentiating, we obtain

$$\begin{aligned} & M_i + \frac{dM_i}{dT_i} T_i - \frac{dM_i}{dT_i} T_{i-1} - 1 \\ & \frac{M_i T_i - T_{i-1}}{M_i T_{i-1} - T_i} + \frac{dM_{i+1}}{dT_i} T_{i+1} - 1 \\ & \frac{dM_{i+1}}{dT_i} T_{i+1} - 1 - \frac{M_{i+1} + \frac{dM_{i+1}}{dT_i} T_i}{M_{i+1} T_{i+1} - T_i} = 0 \end{aligned} , \quad (5)$$

On appropriate rearrangements (5), allowing for (3), we find that

temperature independent, that is,  $dM_i/dT_i = 0$ , but  $M_i \neq M_{i+1}$ , we will become the equation -

$$\frac{\mu_i}{\mu_{i+1}} = \frac{T_{i+1} M_i - T_{i-1} M_{i+1}}{T_{i+1} M_{i+1} - T_{i-1} M_i} . \quad (7)$$

Application of the equation (7) is advisable when the nature of the relationship  $M(T)$  is unknown, with only  $M_i$  values given. In this case the relationship  $\mu_i / \mu_{i+1}$  cannot be equal to

unity. Let us then examine the actual temperature dependence  $M(T)$  which for tertiary alloys Bi-Sb-Te in the interval (120-330) K can be represented [2] the form

$$M_i = a(\bar{T}_i)^b \quad (8)$$

Graphic representation of the function in the same source indicates that the  $M(T)$  dependence can — with sufficient accuracy — be described by the linear function

$$M_i = d\bar{T}_i + c \quad (9)$$

$$\frac{\mu_i}{\mu_{i+1}} = \frac{T_{i+1}M_i - T_{i-1}M_{i+1} + \frac{dM_i}{dT_i}[T_i(T_i - T_{i-1}) - T_i^2(M_{i+1} - M_i)]}{T_{i+1}M_{i+1} - T_{i-1}M_i - \frac{dM_i}{dT_i}[T_i(T_i - T_{i-1}) + T_{i+1}T_{i-1}(M_{i+1} - M_i)]} \quad (11)$$

Analysis of the relationship [8] brings to the approximate equation  $\mu_i/\mu_{i+1} = 1$  accurate to 1% and, consequently, to the actual equality of stage coefficients of performance  $\varepsilon_i$  as well.

The most substantial physical reasons for the equality of stage coefficients of performance allowing for the actual temperature dependence  $M(T)$  are the invariable and modest derivative

$\frac{dM}{dT}$  and the negligible difference between arithmetical and geometrical mean temperatures of stage sides ( $T_{i+1}, T_{i-1}$ ), eventually determined by temperature behavior and efficient value of thermoelectric materials, and also by operating temperature range.

An important consequence of our investigations was the invariable function

$$f(T_{i+1,i-1}; M_{i+1,i}) = \frac{T_{i+1}M_i - T_{i-1}M_{i+1}}{T_{i+1}M_{i+1} - T_{i-1}M_i} \quad (12)$$

for thermocouples with temperature-optimized parameters  $a = 0.312$ ,  $b = 0.259$ , which are in line with coefficients  $d = 1.5 \cdot 10^{-3}$  and  $c = 0.93$ .

From the expression (9) it follows that the equation

$$\frac{dM_i}{dT_i} = \frac{dM_{i+1}}{dT_{i+1}} \quad (10)$$

with account for which the equation (6) can be rearranged in the form

where the right-hand part of (11) goes over with  $\frac{dM_i}{dT_i} = 0$

This is easily demonstrated by examining in the interval from 1 to 2 the function

$$f(x) = \frac{x^2 - x^b}{x^{2+b} - 1} \quad (13)$$

derived from (12) using the  $M(T)$  dependence (8) and inserting the variable  $x = \sqrt{T_{i+1}/T_{i-1}}$ . The value of the function is only governed by the form of temperature dependence  $M$ -characteristic, remaining intact irrespective of thermocouple operating temperature difference. Thus for example, with  $M = 0.312 \cdot \bar{T}^{0.259}$ ,  $f(x) = 0.77$ . Another consequence was that the suggested approach to optimization of multistage thermoelectric coolers could be extended to a variety of combined cooling systems. In this case the criterial equation (6) will take the form as follows:

$$\frac{\mu_i}{\mu_{i+1}} = \frac{T_{i-1}\eta_{i+1}(1 - \eta_i) - T_i[T_{i-1}\eta_{i+1}^2(\eta_i/\eta_{i+1})^i - \eta_{i+1}^i(T_i - T_{i-1})]}{T_{i-1}\eta_i(1 - \eta_{i+1}) + T_{i-1}[T_i\eta_{i+1}^2(\eta_i/\eta_{i+1})^i + \eta_i^i(T_{i+1} - T_i)]} \quad (14)$$

where  $\eta_i$  - degree of thermodynamic sophistication of the  $i$ -th stage [9, 10]. This also does not make readily apparent the equality of stage coefficients of performance, whose relationships are determined by examinations of the right-hand side of the expression (14) in each particular case.

### A Workable Model for Multistage Thermoelectric Coolers.

Consideration of actual temperature dependence of  $M$  and  $Z$  parameters comes up with an optimal division of interstage temperatures, slightly differing from theoretical distribution

$T_i = T_0 \left( \frac{T_N}{T_0} \right)^{i/N}$  for the case  $M_i = \text{const}$ . According to

[11], the true value of intermediate temperatures can be represented as

$$T_i = T_0 t^i (1 + \alpha_i) \quad (15)$$

where  $t = \left( \frac{T_N}{T_0} \right)^{1/N}$ ,  $N$  - number of stage in a thermoelectric cooler,

$$\alpha_i = -\frac{t^2 - 1}{t} \frac{1}{N} \left[ (N - i) \sum_{m=1}^{m=i} m M_{m+1,m} + i \sum_{m=i+1}^{m=n} (n - m) M_{m+1,m} \right], \quad (16)$$

$$M_{m+1,m} = \frac{M_{m+1} - M_m}{M_{m+1} M_m - 1};$$

Entering the function

$$f_i^{(N)}(M_i) = \frac{1}{N} \left[ (N - i) \sum_{m=1}^{m=i} m M_{m+1,m} + i \sum_{m=i+1}^{m=n} (n - m) M_{m+1,m} \right] \quad (17)$$

we represent temperature distribution (15) in the form

$$T_i = T_0 t^i \left[ 1 - \frac{t^2 - 1}{t} f_i^{(N)}(M_i) \right] \quad (18)$$

Using  $f_i^{(N)}(M_i)$ , one can obtain expressions for the coefficient of performance, maximum temperature dependence, equivalent

thermoelectric efficiency of multistage thermoelectric coolers. They are given in the table of basic characteristics of multistage thermoelectric modules, along with similar expressions without allowance for temperature dependence of thermocouple parameters.

Table 1. Basic Characteristics of Multistage Thermoelectric Modules.

Without account of temperature dependencies of thermocouple parameters	Accounting for temperature dependencies of thermocouple parameters
$T_i = T_0 t^i, \quad t = \left( \frac{T_N}{T_0} \right)^{1/N}$ $\varepsilon_0 = \left[ \left( \frac{M_1 t - 1}{M_1 - t} \right)^N - 1 \right]^{-1}$ $Z^{(N)} = \frac{2 \left[ \left( 1 + \frac{Z_1 T_0}{2} \right)^N - 1 \right]}{T_0}$	$T_i = T_0 t^i \left[ 1 - \frac{t^2 - 1}{t} f_i^{(N)}(M_i) \right]$ $\varepsilon_0 = \left\{ \left[ \frac{\left[ t - f_i^{(N)}(M_i)(t^2 - 1) \right] M_1 - 1}{M_i - [t - f_i^{(N)}(M_i)(t^2 - 1)]} \right]^N - 1 \right\}$ $Z^{(N)} = \frac{2 \left\{ 1 + \frac{Z_1 T_0}{2} + f_i^{(N)}(M_i) \frac{\left( 1 + \frac{Z_1 T_0}{2} \right)^2}{1 - 2f_i^{(N)}(M_i) \left( 1 + \frac{Z_1 T_0}{2} \right)} \right\}^N - 1}{T_0}$

Comparison of expressions given in the right- and left-hand sides of the table demonstrates that account of temperature dependencies is taken by the function  $f_i^{(N)}(M_i)$  specified by the relationship (17). The function  $f_i^{(N)}(M_i)$  is a matrix setting into correspondence the theoretical and practicable models for a multistage thermoelectric module. It is easily comprehended that in the case  $f_i^{(N)}(M_i) = 0, (M_i = \text{const})$  all right-hand formulae go into corresponding left-hand ones.

The matrix  $f_i^{(N)}(M_i)$  is composed of  $(N-1)$  lines, each being the sum of  $(N-1)$  items describing characteristics stages, with the most important contribution to the intermediate temperature  $T_i$  made by the item with number  $i$ , related to the  $i$ -th and  $(i+1)$ -th stages. The lines with numbers  $i$  and  $(i-1)$  have the same coefficients with functions  $M_{i+1,i}$  but in the reverse order. Thus knowledge of  $N/2$  first lines will permit automatic writing of the sum for the remaining lines. The matrix characteristics are readily perceived in the case of the 7-stage thermoelectric module.

$$f_i^{(7)}(M_i) = \frac{1}{7} \begin{vmatrix} 6M_{21} + 5M_{32} + 4M_{43} + 3M_{54} + 2M_{65} + M_{76} \\ 5M_{21} + 10M_{32} + 8M_{43} + 6M_{54} + 4M_{65} + 2M_{76} \\ 4M_{21} + 8M_{32} + 12M_{43} + 9M_{54} + 6M_{65} + 3M_{76} \\ 3M_{21} + 6M_{32} + 9M_{43} + 12M_{54} + 8M_{65} + 4M_{76} \\ 2M_{21} + 4M_{32} + 6M_{43} + 8M_{54} + 10M_{65} + 5M_{76} \\ M_{21} + 2M_{32} + 3M_{43} + 4M_{54} + 5M_{65} + 6M_{76} \end{vmatrix} \quad (19)$$

Analysis of the expressions given in the table indicates that accounting for actual temperature dependence of thermocouple parameters by the function  $f_i^{(N)}(M_i)$  makes it possible to select the interstage temperatures (18) ensuring the most favorable operating conditions for each stage in terms of improving the coefficient of performance in the whole

thermoelectric module, rational stage selection, resulting in improved equivalent thermoelectric efficiency and consequent extension of maximum permissible temperature difference. Evaluation of seven- [12] and eight-stage [13,14] thermoelectric modules using the expressions revealed that energy consumption could be reduced by 25- 30 %.

### **Conclusions.**

A criterial equation has been obtained, to optimize multistage thermoelectric and combined coolers operated in the regime of maximum energy efficiency, accounting for temperature dependencies of thermoelectric material parameters. It follows from the equation that the generally accept criterion in the form of equality of stage coefficients of performance is not a universal but rather a specific case related to individual temperature dependencies of semi-conducting materials involved.

A procedure to define the parameters of multistage cooler has been developed, using a matrix permitting conversion from the theoretical (neglecting temperature dependencies) to a workable (allowing for temperature dependencies) model for a thermoelectric module. The procedure is applicable with all materials used in the stages, ensuring the best possible implementation of their potentials, a significant improvement in energy efficiency of cooling devices, particularly with temperature differences approaching the maximum.

### **References**

1. E.A.Kolenko. Thermoelectric cooling devices.- L.: Nauka, 1967.- P. 15.
2. A.L.Vainer. Multistage thermoelectric sources of cold.- M.: Sovetskoe radio, 1976.
3. E.V.Osipov. Solid- state cryogenics.- Kiev: Naukova Dumka, 1977.
4. C.L.Feldman, Sh.F.Martin, W.A.Meconty. Optimization of cascaded Peltier cooler/ ASHRAE J.- 1965.-V. 7.-N4.- P. 78-81.
5. A.R.Foster. Two- stage thermoelectric refrigeration/ ASHRAE J.- 1965.- V. 70.- P. 312-317.
6. N.V.Kukhar. On requirements for a maximum coefficient of performance in a multistage thermoelectric cooler/ Teplovye protsessy v MGD i Termoelektricheskikh generatorakh.- Kiev: Naukova Dumka, 1982.- P. 124-128.
7. A.I.Burshtein. Physical principles in designing semiconductor thermoelectric devices.- M.: Fizmatgiz, 1962.- 135 p.
8. V.L. Galperin. Towards the problem of equality of stage coefficient of performance in multistage thermoelectric modules operated in the regime of maximum efficiency/ Fiz. zhurnal.- 1983.-V. XLV.- N 4.- P. 667.
9. Naer, V.K. Garachuk. Theoretical foundations of thermoelectric cooling.- Odessa, 1982.
10. V.A.Naer. Intermediate temperature measurements in multistage and combined cooling devices/ Proc. All-Union sci.- eng. conf. "Sovershenstvovanie protsessov mashin i apparatov kholodilnoi i kriogennoi tekhniki i konditsionirovaniya vozdukh".- Tashkent, 1977.- P. 37-38.
11. V.L.Galperin. Extreme temperature sequence and economic feasibility the multistage thermoelectric module/ Fizika i tekhnika poluprovodnikov.- 1976.- V. 10.- N 8.- P. 1540-1542.
12. Alekseev, A.P. Vakhonina, K.P. Stafeev, Iu.P. Khorunzhin. A seven- stage thermoelectric cooler/ Kholodil'naia tekhnika.- 1977.- N 8.- P. 20-23.
13. R.J.Buist. Effective application of thermoelectric heat pumps/ Proc. 14-th Intern.-sos. Energy Couvers, Eng. Conf.- Boston.- 1979.- V.2.- P. 1850- 1853.
14. Buist, J. Fendon. Proc. Electro- Optical Systems Design Conf.- New York.-1972.- Sept.- 12-14.

# NON-STEADY COOLING PROCESSES IN PULSED-MODE THERMOELECTRIC DEVICES

V.L.Galperin

MGNPP "OSTERM", St.Petersburg, Russia

The paper discusses problems of non-steady cooling with thermoelectric modules operated in pulsed mode. Formulae suitable for engineering design have been obtained, describing the relationships of temperature differences on cold junctions and those between optimal current and time. The paper presents finding from experimental studies of thermoelectric coolers and a fast- acting device built around them.

## **Introduction**

A key element in the solution of many problems of thermoelectric cooling is appraising potentials of thermocouples in cooling the subjects in short time periods before they attain a steady state. These operating conditions are prevalent with electronic- and medical engineering products, information recorders and processors. The data obtained from a series of investigations [1-4] contributed to a deeper insight in the physical meaning of non-steady cooling processes, while their practical application in engineering design has been highly problematic. The traditional solution of conductivity equation results in cumbersome numerical analytical procedures, and multiple approximations and assumptions- to disagreements with experimental data.

## **Design model**

This paper presents analytical expressions to describe time relationships of thermoelectric cooler parameters with short- time pulse duration, resting on the assumption that maximum cooling effect is dependent on the preservation of quantities like: The amount of Joule heat released in a thermocouple in the pulse time, i.e.

$$I_{p_0}^2 R \tau_p = \text{const} \quad (1)$$

The thermoelectric power required to overcome the Seebeck voltage, i.e.

$$\alpha I_{p_0} \Delta T_{p_{\max}} = \text{const}, \quad (2)$$

where  $I_{p_0}$  - optimal current required to attain maximum temperature difference  $\Delta T_{p_{\max}}$  in the thermocouple in the pulse time  $\tau_p$ ;  $R$  - thermocouple electric resistance;  $\alpha$  - Seebeck voltage.

The assumption of Joule heat preservation accords well with precision solutions of non-steady problem [3,4] also furnishing the optimal relationship  $I_{p_0} \sqrt{\tau_p} = \text{const}$  for maximum temperature lowering our choice of the other constant quantity is an energy parameters related to purely thermoelectric surface effects (as distinct from Joule heat) and time-independent.

Representing entry into steady-state operation in the form of a pulsed process with parameters  $I_o$ ,  $\tau_o$ ,  $\Delta T_{p_{\max}}$  and starting from the terms (1) and (2), we become the following equations

$$I_{p_0}^2 \tau_p = I_o^2 \tau_o \quad (3)$$

$$I_{p_0}^2 \Delta T_{p_{\max}} = I_o^2 \Delta T_{\max} \quad (4)$$

where  $I_o$  - optimal current in the steady-state mode;  $\tau_o$  - time constant;  $\Delta T_{\max}$  - maximum temperature difference in steady-state thermocouple, allowing determination of  $I_{p_0}$  and  $\Delta T_{p_{\max}}$

$$I_{p_0} = I_o \sqrt{\frac{\tau_o}{\tau_p}} \quad (5)$$

$$\Delta T_{p_{\max}} = \Delta T_{\max} \sqrt{\frac{\tau_p}{\tau_o}} \quad (6)$$

From the familiar steady- state condition for the cold side of thermocouple without thermal load

$$\alpha I T_0 - 0.5 I^2 R - \kappa \Delta T = 0 \quad (7)$$

The expression for temperature difference  $\Delta T$ , on some simple rearrangements, can be represented as

$$\Delta T = \Delta T_{\max} \left( -\left( I/I_o \right)^2 + 2I/I_o \right) \quad (8)$$

Reasoning that it must be true for the pulsed mode as well, we will write it as

$$\Delta T_p = \Delta T_{p_{\max}} \left( -\left( I_p/I_{p_0} \right)^2 + 2I_p/I_{p_0} \right) \quad (9)$$

where  $\Delta T$  - the temperature difference corresponding to pulse current  $I_p$ .

Substituting  $I_{p_0}$  from (5) and  $\Delta T_{p_{\max}}$  from (6) in (9), we will come up with the equation for the dynamism of the cooling process

$$\Delta T(\tau) = \Delta T_{\max} \left( -\left( I^2 \tau^{3/2} / I_o^2 \tau_o^{3/2} \right) + 2 \left( I \tau / I_o \tau_o \right) \right). \quad (10)$$

The nature of time and current dependencies in this expression is in complete agreement with reported solutions of a similar problem [3,4], which is another evidence in favor of our proposals.

Using the expressions (5), (6), (10), we can work out operating and optimal parameters of thermoelectric coolers in non- steady modes with  $\tau < \tau_o$ , defining their potential temperature — lowering range during the course of one pulse. The expressions are simple and convenient in practice as first they permit analytical calculations, and second, only manipulate quantities like  $\Delta T_{\max}$  and optimal current  $I_o$ ,  $\tau_o$ . The maximum

temperature difference  $\Delta T_{\max}$  and optimal current  $I_o$  are universal and generally known characteristics of the steady mode. The time constant  $\tau_o$  determines the pace of entry to the steady-state and is primarily dependent on proper thermal capacities of the thermocouple, connecting plate and the subject to be cooled, and conditions of heat exchange with the environment. The quantity  $\tau_o$  can be found by mathematics means [3,5], and where this is a problem - experimentally.

### Experiment

Experimental investigations in the dynamics of cold-side behavior were performed on microcoolers 1, 2, 3 mm high with connecting plates 0.05 mm thick and without any special thermal insulation. Heat from hot junctions was removed by forced airing. All the measurements were taken with precision thermocouples using oscillographic memory.

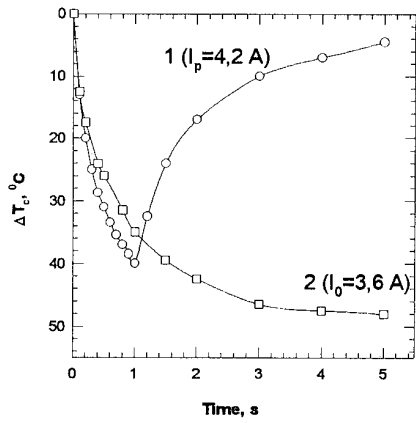


Fig. 1. Oscillograms for cold-side temperature variations with pulsed treatment (1) and entry to steady-state operation (2)

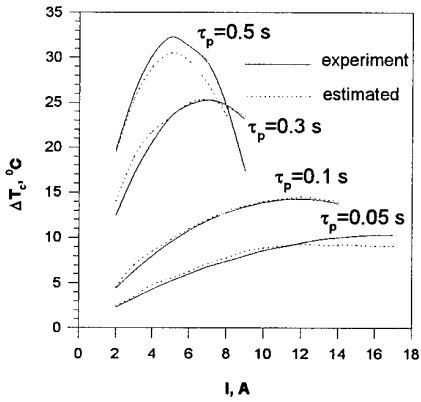


Fig. 2. Cold-side temperature difference / current relationships with different power-pulse lengths.

Comparison of oscillographs illustrated in Fig.1 indicates a greater lowering of temperature with pulsed-mode cooling than with an ordinary entry to steady-state operation during the same time. The time constant  $\tau_o$  can be derived from the term  $\Delta T = 0.632 \Delta T_{st}$ , running to 1.1 sec for a thermocouple of  $h = 2$  mm.

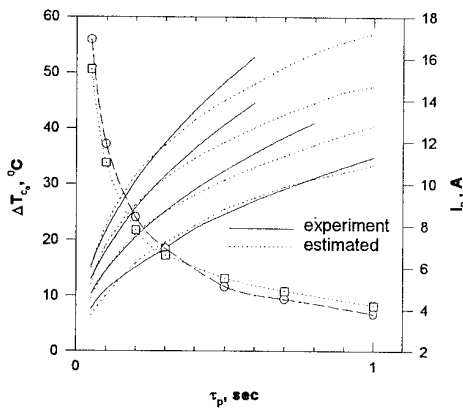


Fig. 3. Dependencies of cold-side maximum temperature difference and optimal current on power pulse lengths.

Fig. 2 shows cold-side temperature difference / current relationships for different power pulse duration. With decreased pulse duration, the curve maximum is shifted toward greater currents, the curves becoming more linear.

Fig. 3 gives the dependencies of maximum temperature differences on cold side and optimal current on powerpulse duration, and Figs 4, 5 - on thermocouple heights and hotside temperatures.

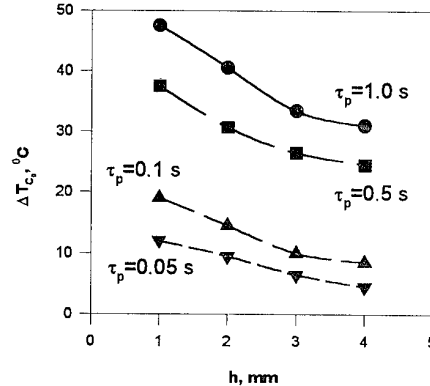
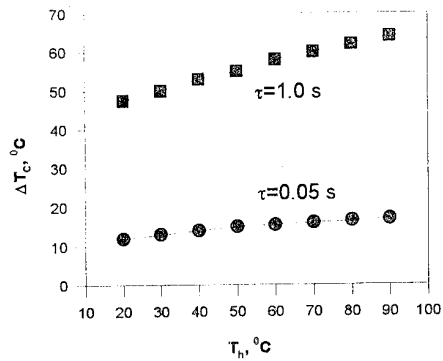


Fig. 4. Cold-side maximum temperature difference / thermocouple height relationships with different power-pulse lengths.



**Fig. 5. Cold-side maximum temperature difference / hot-side temperature relationships with different power-pulse lengths.**

In plotting design graphs, the presence of outside heat accumulation  $Q_0$  was accounted for by replacing  $\Delta T_{\max}$  with  $\Delta T_{st} = \Delta T_{\max} - Q_0/K$ , with  $\tau_0$  found experimentally. As can be expected, the best agreement of the results was observed with the time  $\tau_p < 0.5 \tau_0$ , that is, significantly shorter than required to attain the steady state. Lowering the thermocouple height results in decreased inertia, increasing the optimal current. With short pulse duration, hot-side temperature has little or no effect on temperature variations on the cold side.

#### Frequency operating mode

On the procedure discussed above, we designed a fast-acting thermoelectric cooler to process the optical information recorded on thermosensitive material [6,7]. Data erasure was to be performed with cooling pulses of the length  $\tau_p = 0.08 \dots 0.5$  sec and operating frequency from 1 to 10 Hz.

Frequency operation differs essentially from the unit operating mode, as the heat released in 1 sec in the former case  $I_{p_0}^2 R \tau_p f$  ( $f$  – number of pulses per sec) has no time to disperse in the intervals between pulses, causing pronounced overheating in the heat sink and thus affecting operation at large. To avoid this, requires appropriate selection of cooling pulse parameters. We make use of the formulae (5) and (10) to this end, obtaining the expressions for optimal current  $I_f$  and maximum temperature difference  $\Delta T_f$  in the frequency mode

$$I_f = I_0 \sqrt{\frac{\tau_0}{\tau_p f}} \quad (11)$$

$$\Delta T_f = \Delta T_{p_{\max}} \left( -\frac{1}{f} + \frac{2}{\sqrt{f}} \right) \quad (12)$$

With frequency of 10 Hz we gained a stable erasure quality approaching 100% ( $\Delta T_f = 12 \div 15^\circ\text{C}$ , see Fig.3), previously only possible with unit pulses of the lengths  $\tau_p \sim 1$  sec.

#### Conclusions

Findings from the investigations permit — within the accuracy of engineering practice- analytical treatment of thermocouple characteristics required for effective lowering of temperature in

short time periods with unit- and pulsed operation. The suggested design model fits the experimental data well and is useable for a variety of fast-acting thermoelectric cooling devices, including multistage.

#### References

1. L.S.Stilbans, N.A.Fedorovich. Thermoelectric coolers operated in the non- steady mode/ Zh. Tekh. Fiz.- 1958.- XXVIII.- N 3.- P. 489-492.
2. P.E.Gray. Approximate dynamic response calculation for thermoelectric Peltier- effect devices/ Solid state electronics.- 1963.- V. 6.- N 4.
3. M.A.Kaganov, M.R.Privin. Thermoelectric heat pums.- L.: Energiya, 1970.- P. 78.
4. E.K.Iordanishvili, V.P.Babin. Non- steady processes in thermoelectric and thermomagnetic energy- transformation systems.- M.: Nauka, 1983.- P. 105.
5. E.G.Pokornyi, A.G.Shcherbina. Calculation for semiconductor cooling devices.- L.: Nauka, 1969.- P. 102.
6. V.L.Galperin, I.A.Khakhaev, F.A.Chudnovskii, E.B.Shadrin. Control of metal semi- conductor phase transition by a fast-acting thermoelectric cooler / Zh. Tekh. Fiz.- 1991.- V. 61.- N 10.- P. 194- 196.
7. V.L.Galperin, I.A.Khakhaev, F.A.Chudnovskii, E.B.Shadrin. Control of metal semiconductor phase transition by a fast-acting thermoelectric cooler - II/ Pis'ma Zh. Tekh. Fiz.- 1992.- V. 18.- N 10.- P. 74- 78.

## Optimization Of The Thermoelectric Air Chillers Construction.

A.A. Aivazov, Y.I. Stern, K.B. Makhratchev

Moscow Institute Of Electronic Engineering, 103498, Russia  
Terif, Ltd

This paper describes the problem solution of thermoelectric module characteristics optimization. Both the analogy and differences between hydraulic and thermal pumps have been considered. The results of computer modeling and stand test are given and differences discussed.

### **Introduction**

The projection methodology of thermoelectric thermostabilizing and cooling systems was oriented to the production of extremely low temperatures in minimum time as a rule. Thus the thermoelectric modules were supposed to work in the mode of maximum cooling productivity. At low device power and corresponding thermal loads this situation was quite justified and didn't give any problems to the users working with such types of devices. An engineer as a rule oriented himself with respect to the necessary stabilization temperature and possible thermal loads. But as soon as we come to more powerful devices the user is not satisfied any longer with the effect itself of this or that stabilization temperature attainment, he is anxious of the fact if the devices is enough efficient as a thermal machine. In other words the question on the relation between supplied power to the device and the amount of heat which this device gives off per time unit is of great interest. The efficiency reserves of similar devices particularly air chillers were associated with thermoelectric efficiency increase of the used active materials. It is certain to be an important factor but our experience of design, investigation and maintenance of comparatively powerful cooling systems shows that their energy efficiency can be increased both at the expense of target - oriented changes of thermoelectric module construction and during introduction of corresponding correlations into the principles of the whole device design.

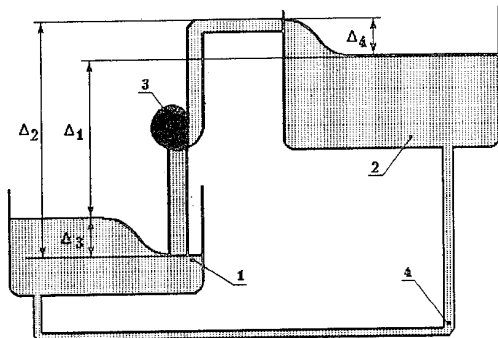
### **Hydraulic and thermal pumps**

The errors in the design usually occur at the formation stage of technical maintenance conditions and requirements to

thermoelectric chillers. These errors can occur with the customer by virtue of operation specificity misunderstanding of thermoelectric thermal pumps. Errors occur with the designer of similar devices too if the construction optimization is not performed and optimal maintenance mode of proper selected electric modules is not provided. In this connection the analogy between hydraulic and thermal pumps seems to be rather attractive and useful. The sequential use of this analogy permitted the customer of the device to formulate clearly that they require from the future device. On the other side the designers in the limits of clearly formulated task can perform the process of the whole construction optimization and its separate parts.

The diagrams illustrating the mentioned system are given in fig 1 and 2. It is obvious that as a hydraulic pump (fig1) transfers liquid as a thermal pump (fig2) transfers energy from a reservoir with a lower level into a reservoir with a higher one.

In the first case an usual mark corresponds to the level by height and in the second - by temperature. The first conclusion is obvious both for the customer and designer. To decrease artificially minimally the necessary low temperature level is quite senseless and there is no doubt that it is injurious to the effective work of the device. The device designed for lower temperature achievement "in store" might not work effectively under softer conditions. Artificially increased differences favour additional liquid leakages or unwanted thermal flows from the hot seal to the cold one. Thus, heat as water has to be increased from the level which is optimal from the point of view of the final effect of device work in whole.



1. Input reservoir.
  2. Output reservoir.
  3. Pump.
  4. Leakage path.
- $\Delta_1$  Required from pump height difference.  
 $\Delta_2$  Height difference, at which pump is really operate.  
 $\Delta_3$  Level drop at input  
 $\Delta_4$  Level drop at output

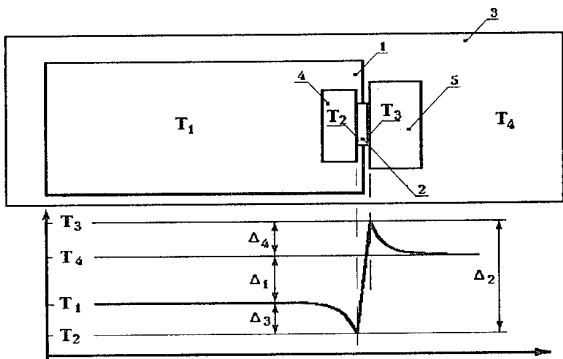
Fig 1 Hydraulic pump

If we speak about air chillers this level corresponds either to the comfortable temperature level in the given room or vehicle or corresponds to the necessary technological temperature in fridges or industrial equipment. As for the upper level we mean the ambient temperature which is usually given to the customer in the form of some range where the designer has to orient to the upper boundary.

To continue the analogy we should pay attention to some possible differences between two pump types as well as to the difference under conditions of their work connected with physical peculiarities of the transfer object. The matter is in the following: "thermal liquid" is differed by increased viscosity that results in large unwanted differences during the device operation process. These unwanted differences correspond to  $\Delta_3$  and  $\Delta_4$  values (fig2). Being utmost low for lowviscous liquids of water type they can be increased in case of more viscous types as glycerine one. Thus if in the general case:

$$\Delta_2 = \Delta_1 + \Delta_3 + \Delta_4$$

and for lowviscous liquids  $\Delta_3 \approx 0$ ,  $\Delta_4 \approx 0$ ,  $\Delta_1 \approx \Delta_2$ , then we can't ignore the values which are equivalent  $\Delta_3$  and  $\Delta_4$  respectively for thermal pumps. In other words by virtue of "thermal" liquid specificity unwanted differences  $\Delta_3$  and  $\Delta_4$  can turn out to be comparable and even higher the necessary difference  $\Delta_1$ .



1. Cooling object.
  2. Thermoelectric heat pump.
  3. Ambient.
  4. Cold side heat exchanger.
  5. Hot side heat exchanger.
- $\Delta_1$  Required from chiller temperature difference.  
 $\Delta_2$  Temperature difference, at which chiller is really operate.  
 $\Delta_3$  Temperature drop at input  
 $\Delta_4$  Temperature drop at output

Fig 2 Heat pump

Thus in designing of thermoelectric air chillers thermoelectric modules should be oriented to work under conditions when value  $\Delta_2$  will be substantially higher than  $\Delta_1$ . By the way our tests of chiller with rated power of 600 W on the stand by volume 1 m<sup>3</sup> (heat leakage about 19 W/K) gave the following results:

$$\Delta_1 = 11.4 \text{ K}$$

$$\Delta_2 = 32.5 \text{ K}$$

$$\Delta_3 = 6.4 \text{ K}$$

$$\Delta_4 = 14.7 \text{ K}$$

Thus to cool air volume in a camera partially isolated from the environment per 10 K it is necessary to use modules working effectively during differences of about 30 K. There is no doubt that values  $\Delta_3$  and  $\Delta_4$  are variable values and depend on the construction and maintenance conditions of the whole device but by virtue of their importance it is necessary to define them at the design stage either by the simulation method or by natural testings of real device layout. It is obvious that by their physical situ  $\Delta_3$  and  $\Delta_4$  characterize the thermoexchange efficiency relatively on radiators as well as cold and hot seals of thermoelements. There is no doubt that all designers wish to decrease these values but the experience shows that using standard cooling methods of these radiators - air or liquid it is very difficult to reduce sum  $\Delta_3 + \Delta_4$  less than 20 K. In this connection it is advisable to optimize thermoelectric module

construction to it work in air chillers under conditions by  $\Delta_2$  close to the mentioned value. Modules of Melcor's set and similar ones are known to be oriented to substantially larger temperature differences. This fact is considered to be very important.

### Theory and experiment

The cooling productivity of semielement in thermoelectric module can be approximately described as:

$$Q_c = \alpha I T_c - \kappa \frac{S}{L} (T_h - T_c) - \frac{1}{2} I^2 R \quad (1)$$

Here are:

$Q_c$	Cooling power
$\alpha$	Seebeck coefficient
$I$	Rated current
$R$	Semielement resistant
$\kappa$	Thermal conductivity of the semielement
$T_h$	Temperature of hot seal
$T_c$	Temperature of cold seal
$\Delta T$	Temperature difference across thermocouple $\Delta T = T_h - T_c$
$S$	Cross-sectional area of semielement
$L$	Length of the semielement

Let's consider the function:

$$F = \kappa \frac{S}{L} \Delta T - \frac{1}{2} I^2 R \quad (2)$$

This function by its meaning describes cool productivity losses due to thermal conduction of semielement (the first addent) and Joule effect (the second addent). Taking into account that semielement resistance:

$$R = \rho \frac{L}{S} \quad (3)$$

where  $\rho$  - resistivity of semielement material, we'll have :

$$F = \kappa \frac{S}{L} \Delta T - \frac{I^2 \rho \cdot L}{2S} \quad (4)$$

It is obvious that at the increase of semielement height the first addent decrease while the second increases. Thus the optimal value  $l$  corresponds to the function minimum  $F$ . For this purpose let's take the functional derivative (4):

$$F' = -\frac{\kappa S \Delta T}{L^2} + \frac{I^2 \rho}{2S} \quad (5)$$

At the extremum point functional derivative equals to zero and we obtain:

$$\frac{\kappa S \Delta T}{L^2} = \frac{I^2 \rho}{2S} \quad (6)$$

Let's define at what value  $\Delta T$  the minimum loses are observed. Thus we'll find  $\Delta T$  from expression (6):

$$\Delta T_m = \frac{I^2 L^2 \rho}{2 \kappa S^2} \quad (7)$$

If typical physical characteristics of thermoelectric materials and recommended working currents are substituted to expression (7) calculated values will turn out to be more than 30°K, which corresponds to real conditions of module work. If temperature difference on the module is less, then the main contribution into losses are brought at the expense of Joule effect, but if the difference is large then the losses prevail at the expense of heat conduction. This follows from the expression structure (2).

So, thermoelectric modules in air chillers are used at decreased temperature differences and to increase their efficiency we can follow by three ways:

1. Decrease of working currents
2. Decrease of semielements height
3. Increase of semielement cross-section

The first way is evident but it should be taken into account that it decreases integral cool productivity of a separate module and this results in the increase of the general number of modules what is not always economically justified. The problem solution of loss minimization by the second way was suggested in work [1], but their considerations too optimistically estimated the possibilities of heat removal from hot and cool seals of the modules and as a result they came to the conclusion that module constructions should be optimized for work under conditions of  $\Delta T = 10 - 15$  K. Such modules as seen from the mentioned above analogy are not able to cool air inside the closed volume per 10 K in comparison with environment. Besides too low dependence modules at typical sections, module branches will require the optimal branch height of 0.8 mm. The technological problems need no commentaries which will accompany the creation of such modules.

In this connection we decided to perform optimization of thermoelectric modules by increasing the cross-section of semielement. For this purpose theoretical calculations of the cooling coefficient for different modules types and experimental investigations of module (CP type on the stand)

have been done. Cooling productivity and cooling coefficient for fixed parameters were calculated using the special program. The program fills in the table in which the meaning of cooling coefficient corresponded to each combination (rated current - side of squared semielement section). The obtained table can be used for the choice of optimal current in the maximum coefficient mode of cooling productivity. Cooling power were calculated using equation (1). Cooling performance were calculated as following:

$$\varepsilon = \frac{Q_c}{I^2 R + \alpha \cdot I \Delta T} \quad (8)$$

Where  $Q_c$  - cooling power

$I$  - rated current

$R$  - module resistant

$\alpha$  - Seebeck coefficient

$\Delta T$  - Temperature difference across the module

Fig. 3 illustrates schematically a measurement method we used at stand tests.

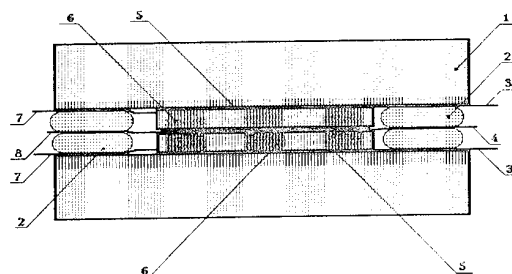


Fig 3 Measurement system

We used 2 modules with cold seals opposite each other to decrease thermal leakages from ambient. Film sensors on the basis of Ni foil were used to measure the temperature. We placed a heating element consisting of two film resistors made on the ceramic substrate by Cr vacuum deposition. This construction provides uniform heating of cold thermoelement seals. The analog of Melcor's CP-1.4-127-045L was used for stand tests and simulation.

Comparisons of theoretical and experimental results are given in table 1. Experimental values of optimal current in the

mode of maximum efficiency are seen to be systematically lower of the suggested theories. For  $\Delta T=20$  K discrepancy reaches 17%, for  $\Delta T=40$  K discrepancy is less than 9%. Thus calculations using relation 1 can be considered to be approximate by virtue of the fact that this relation doesn't take into account temperature dependence of thermoelectric properties of the material. It's also important that  $\alpha$ ,  $\kappa$ ,  $\rho$  were measured at average temperature about 20°C, but modules were tested at average temperature across the semielement 2.5 °C - 3.5°C.

$\Delta T, ^\circ C$	$T_a^{exp}, ^\circ C$	$T_a^{pr}, ^\circ C$	$I_o^{exp}, A$	$I_o^{pr}, A$	$\varepsilon_o^{pr}$	$\varepsilon_o^{exp}$
20	+2.5	20	<1.8	2.1	107%	>114%
30	+3.5	20	3.4	3.1	55%	56%
40	0	20	4.5	4.1	29%	26%

$\Delta T$  Temperature difference across the module  
 $T_a^{exp}$  Average temperature across the module  
 $T_a^{pr}$  Average temperature across the module, assumed in program  
 $I_o^{exp}$  Optimal current, obtained by experiment  
 $I_o^{pr}$  Optimal current, obtained by program  
 $\varepsilon_o^{pr}$  Cooling performance, program results  
 $\varepsilon_o^{exp}$  Cooling performance, experimental results

Table 1 Comparison program and experimental result

On the other hand as follows from table 1 the estimations of cooling coefficient correlate with the experiment results.

## Summary

The optimization ways of thermoelectric module and air chillers construction have been considered on the basis of the analog between hydraulic and heat pumps. Thermoelectric modules, commercially available for a present time, are to work with low efficiency at  $\Delta T$  about 30 K because they are oriented to work at relatively high temperature difference, more than required in typically air chillers. Experimental investigations confirmed theoretical researches and orient the designers of thermoelectric modules to module production with larger section at the fixed semielement height.

## References

- [1]. Rokusaboroh Sakai, Proposal For Electronic Air Conditioning Systems Using Semiconductor Thermo-Electric Conversion, XIII ICT, 1994, pp. 511-515.

## NEW APPROACH TO THERMOELECTRIC AIR-COOLED SUBUNIT CONFIGURATION

A.B. Sulin

*Research Institute of Industrial and Marine Medicine,  
St.Petersburg, 196143, Russia*

This report presents the results of the research TE heat pump, based on two-phase thermosiphone principle for its air heat exchangers. The space-saving configuration was reached by means of heat flows directions change in the unit.

### Introduction

The variety of thermoelectric device structural schemes is determined by mutual arrangement of thermoelements (modules) and heat exchangers. Customary the direction of heat flow is normal to the modules surfaces.

Let us consider the main schemes [1,2].

Fig.1 Scheme with large heat exchangers

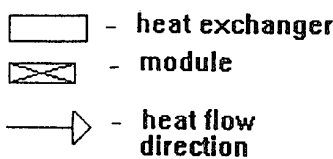
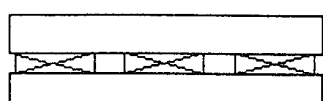


Fig. 2 Scheme with one heat exchanger per module

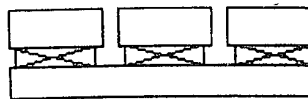


Fig. 3 Scheme with individual heat exchangers

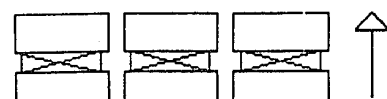
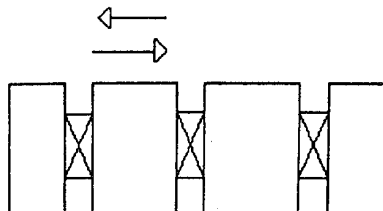


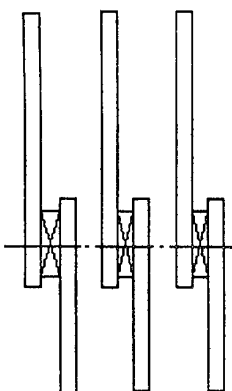
Fig. 4 Scheme with one heat exchanger per two modules



### Alternative scheme

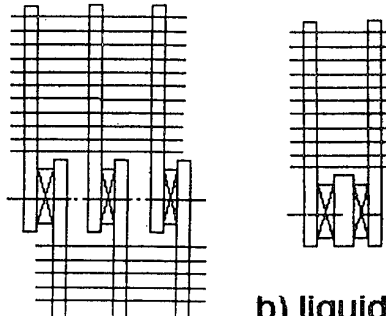
Alteration of heat flows directions for the parallel ones to the modules surfaces, enables to increase the space-saving configuration of the unit, in case the heat exchangers will be effective enough.

Fig. 5 Alternative scheme



However, the low coefficient of heat transfer of all-metal heat exchangers, assembled according to fig. 5, does not make it possible to achieve high indices over the results of our investigations. We achieved the significant decrease of heat exchangers thermal resistance by employment of two-phase thermosyphon principle. (Here we will make reference to the employment of thermosiphons in thermoelectric generators [3].)

Fig. 6. Thermosiphon-type TE unit configuration



a) air - air

b) liquid - air

In fig. 6 there has been shown the TE unit arrangement with employment of individual heat exchangers as thermosiphons, developed by us.

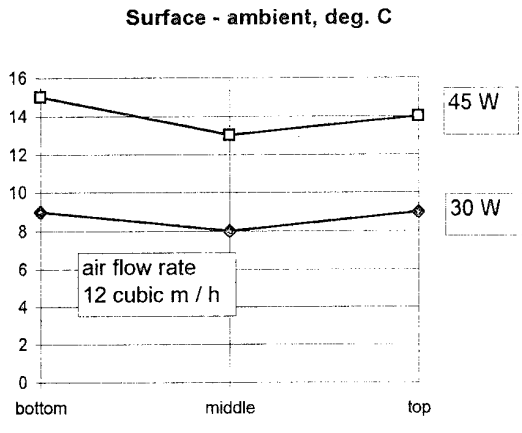
Further we will adduce the main results of these heat exchangers testing in cooling and heating modes.

#### The experimental study of heat exchangers

##### Heating mode

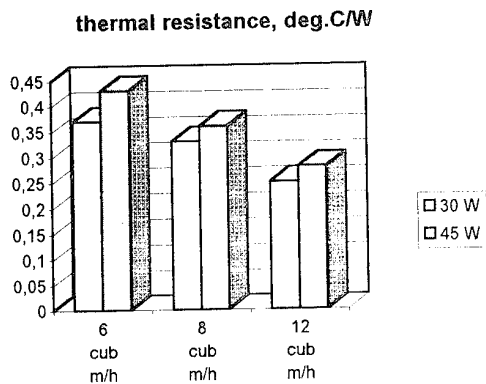
The plane thermosiphon with heat exchange surfaces dimensions  $100 * 70$  mm was studied. The heat exchange area was increased in 5 times by fining. Blowing rate was changed from 6 to 12 m<sup>3</sup>/h, heat load - from 20 to 45 W. In fig. 7 there are quoted temperature fields of heat exchanger.

Fig. 7 Temperature fields



In fig. 8 there are shown the heat exchanger's thermal resistance values.

Fig. 8 Thermal resistance

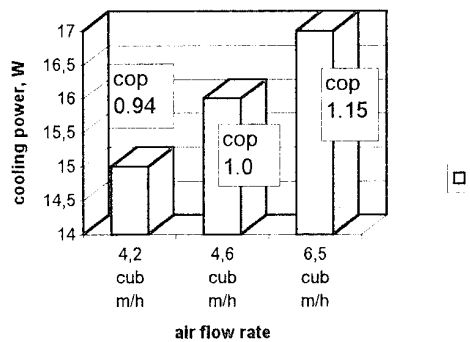


##### Cooling mode

There was studied the plane thermosyphon with heat exchange surfaces dimensions  $70 * 70$  mm by blowing rate from 4,2 to 8 m<sup>3</sup>/h. Cooling was carried out by Melcor-type TE module, on the warm side of which dissipation of heat was provided, corresponding to the work of the thermosyphon in heating mode.

Here we adduce results of module's cooling power and coefficient of performance measurements.

Fig. 9 Cooling mode's performance



#### Results

Here we adduce characteristics of air-air TE heat pump of 12 modules, assembled with employment of individual heat exchangers-thermosiphons in conformity with worked up scheme.

Cooling power, W	200
Electrical power, W	180
Blowing rate, m <sup>3</sup> /h :	
cold side	70
warm side	100
Overall dimensions, mm	210*80*250(H)
Weight, kg	2,5

#### References

- [1]. J.G.Stockholm, Future prospects in thermoelectric cooling systems, 12th International Conference on Thermoelectrics, Yokohama, 1993, pp.389-394.
- [2]. J.G. Stockholm and P.M. Schicklin, Industrial thermoelectric cooling and electricity generation between 200K and 500K, 1st European Conference on Thermoelectrics, Cardiff, 1987, pp. 235-262.
- [3]. R. Sawano and I. Higashi, An experimental evaluation of the thermoelectric generator with thermosiphon, 12 th International Conference on Thermoelectrics, Yokohama, 1993, pp. 471-472.

## THERMOELECTRIC FIN

I.V.Zorin

*A.F.Ioffe Physical-Techical Institute, 194021, St.Petersburg, Russia*

The paper considers the processes in a thermoelement with branches as cross-directed wedges, which are combined on the long side and have junctions of the opposite sign on the short sides. The thermoelement works as a fin transmitting the heat between the long lateral and short butt sides.

Using very sensitive elements, it is necessary to effectively reject its internal heat liberations. If an element is not thick, for example, made as a thin film, the most effective heat rejection will be in perpendicular direction to its thick side.

In many cases so cooling element must be placed in a narrow clearance between the walls of an instrument or between lateral sides of analogous elements and using of circulating heat-carrier for cooling is not desirable.

In these cases the lateral side with of the cooling element (Fig. 1) combines with lateral side of fin with good heat contact. Owing to high thermo-conductivity of the material of fin, the heat transfers from its lateral side to the bases. The bases of fin combined to external system of heat rejection which is located aside of the edges of cooling element.

However because of spreading of the heat along thus a fin, the temperature difference along its length occurs that causes increasing of

the temperature of parts of cooling element accordingly to their distance from the base of fin.

If the internal heat liberation of the element changes from the maximum till zero, the temperature of its farest parts will change by the same value and the temperature of extreme parts of the element could be almost constant if precise thermostating of fin base is available.

As a result the possible accuracy of the element thermostating is limited by temperature liberation along the length of the fin. To reduce temperature liberation by thickening of fin could be impossible because of undesirability of increasing the sizes in that direction.

To eliminate that defect of the heat rejection could be made by Peltier effect using instead of fin a thermoelement of special construction with one junction directed along the lateral side (Fig.2). In this thermoelement the branches 1 and 2 of the opposite sign made as cross-directed wedges, which are combined on the long lateral side and have junctions of the opposite sign on the short sides. The last ones combined to external system of heat rejection and electroisolated from it if necessary.

Going through the branches the current gradually passes from one branch to another and causes an even absorption or liberation of Peltier heat in the long-side junction and income (or outcome) of this one from vacant lateral side of branches. Thus the thermo-element works as a fin transmitting the heat between the long lateral and short butt sides.

The construction of the thermoelement with one junction on the lateral sides of branches, two another junctions on the butt sides of branches and uniform motion of current from one branch to another is suggested in [1].

Let us consider the processes which take place in thermoelectric fin.

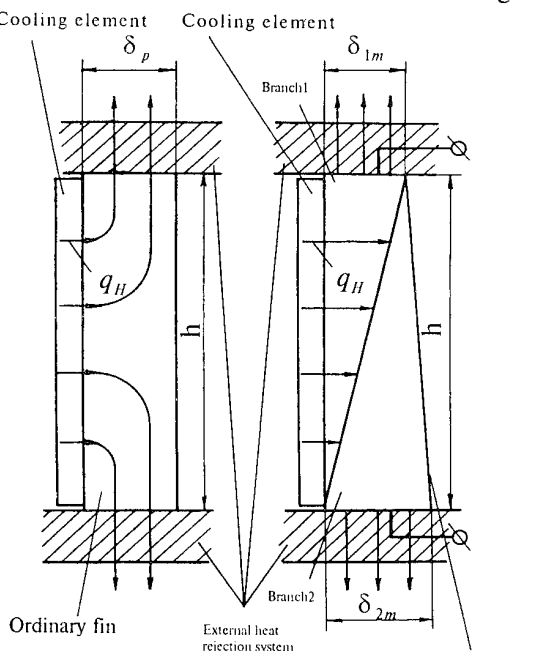


Fig.1

Fig.2

If the branches 1 and 2 (Fig.1) in thermoelectric fin are made of materials with differing electro-conductivities  $\sigma_1$  and  $\sigma_2$ , then to provide the uniform motion of current through the junction of these branches, it would be necessary that its cross-sections ratio  $F_1$  and  $F_2$  in any place of the current way would be inversely proportional to their electro-conductivities.

If the branches have the same width and variable on the length thicknesses  $\delta_1$  and  $\delta_2$ , taking into consideration that  $F = \delta * b$ , the ratio

$$\frac{F_1}{F_2} = \frac{\delta_1}{\delta_2} = \frac{\sigma_1}{\sigma_2} \quad (1)$$

realises. Thus the branches should be made as wedges with maximal thicknesses  $\delta_{1m}$  and  $\delta_{2m}$  at their base.

To prevent the shorting of longitudinal and cross-junctions, it has to be there a small layer of branch material between them. As the changing of these sizes is insignificant, we will consider hence the total length of thermoelement in current direction to be equal to maximal length  $h$  of branch in this direction.

As it is desirable to have a minimal temperature difference in cooling element by changing of its internal heat liberation, let us take the temperature difference between junctions of the thermoelectrical fin to be equal to zero.

For having the minimal instrument thickness, the thickness of branches is taken significant less than its length  $h$ . Then the influence of the heat transfer to short junction of branches onto the total heat balance could be neglected accurately enough.

Then the cold-productivity of thermoelectric fin will be:

$$Q_0 = \bar{\alpha} IT - I^2 R_\Sigma \quad (2)$$

where  $\bar{\alpha}$  - total coefficient of thermo-electromotive force of both branches,

$I$  - current intensity,

$T$  - the temperature of thermoabsorbing junction,

$R_\Sigma$  - total resistance of thermoelectric fin.

From the case  $\frac{\partial Q_0}{\partial I} = 0$ , the current

creating maximal cold-productivity:

$$I_{Q_{0m}} = \frac{\bar{\alpha} I}{2 R_\Sigma} \quad (3)$$

Maximal cold-productivity of thermoelectric fin after using equation (3) in (2) will be:

$$Q_{0m} = \frac{\bar{\alpha}^2 T^2}{4 R_\Sigma}$$

(4) Thus, both maximal cold-productivity as the current creating it in thermoelectric fin are two times less than ones in ordinary thermoelements. Because the summary of elementar parts conductivities in any place of branch lenght must be constant, the total resistance of both branches can be expressed with the conductivity of one branch:

$$R_\Sigma = \frac{h}{\sigma_1 b \delta_{1m}} \quad (5)$$

Maximal specific cold-productivity concerned to unit of lateral square of branch 1 of thermoelectric fin from equation (4) and using (5) is:

$$q_{om} = \frac{Q_{0m}}{hb} = \frac{\bar{\alpha}^2 \sigma_1 T^2 \delta_{1m}}{4 h^2} \quad (6)$$

Maximal density of Joule heat liberation caused by going the current in the branches, using equations (3) and (5) is:

$$q_{Jm} = \frac{I_{Q_{0m}}^2 R_\Sigma}{hb} = \frac{\bar{\alpha}^2 \sigma_1 T^2 \delta_{1m}}{4 h^2} \quad (7)$$

As shown in (7), it is numerically equal to the maximal specific cold-productivity.

The flow of heat from cooling element with density  $q_H$ , which is going across the branch 1 to heat-absorbing junction, causes to the temperature difference in this branch which is as high as the branch thick. Exceptional part is that nearest to short heat-absorbing junction, where the temperature is falling back because of an additional heat refection to that junction direction. That additional cross-directed heat refection influence to heat transfer could be estimated analogously with the influence of fin butt which, as known, can be taken into consideration by adding the calculated length of one-side-working fin with its thickness. Then in the case of  $h \gg b$ , maximal precise value of temperature difference across the branch will be insignificant less than one determined without that influence.

In connection with this it could be accurately enough taken a maximal temperature difference on the maximal thickness of the branch :

$$\Delta t_{1m} = \left( q_H + \frac{q_{J_m}}{2} \right) \frac{\delta_{1m}}{\kappa_1} \quad (8)$$

where  $\kappa_1$  - specific heat-conductivity of the material of branch 1.

Because  $q_{0m} = q_{J_m} = q_H$ , then

$$\Delta t_{1m} = \frac{1.5q_H\delta_{1m}}{\kappa_1} \quad (9)$$

Let us compare the maximal temperature difference in ordinary fin having the same heat rejection in two directions (Fig.1), the same length and thickness equal to medium thickness of thermoelectric fin which is with using equation (1) is:

$$\delta_p = \frac{\delta_{1m} + \delta_{2m}}{2} = \frac{\delta_{1m}}{2} \left( 1 + \frac{\sigma_1}{\sigma_2} \right) \quad (10)$$

Because of insignificance of temperature difference along the fin thickness relating that along length, the heat transfer of uniform heat liberation to its bases can be considered as one-dimensional process which is analogous to the well-known case of heat-conductivity in the wall with uniform internal heat liberations and heat rejection to both of its sides of wall [2]. Then rejecting the heat liberations with density  $q_H$  by fin with using its heat-conductivity, the temperature difference between the middle of the fin and its bases, using (10), will be expressed:

$$\Delta t_p = \frac{q_H h^2}{4\kappa_p \delta_p} = \frac{q_H h^2}{2\kappa_p \delta_{1m} (1 + \sigma_1/\sigma_2)} \quad (11)$$

where  $\kappa_p$  - specific heat conductivity of fin material. The ratio of temperature differences in ordinary and thermoelectric fins is:

$$\frac{\Delta t_p}{\Delta t_{1m}} = \frac{\frac{\kappa_1}{\kappa_p} \left( \frac{h}{\delta_{1m}} \right)^2}{3(1 + \sigma_1/\sigma_2)} \quad (12)$$

As shown in (12), the less the fin thickness under the given height, the better advantage in temperature differences when applying a thermoelectrical fin.

As minimal temperature difference and maximal density of heat rejection in ordinary fin is achieved at maximal specific heat conductivity, the most preferable material for it is copper.

The advantage in reducing the temperature difference for thermoelectric fin, as follows from equation (12), as much as  $\kappa_1$  is higher and closer to  $\kappa_p$ . In the same time, as follows from equation (9), as  $\kappa_1$  higher, as the cold-productivity the bigger under the same  $\Delta t_{1m}$  could be developed by thermoelectric fin. In connection with this, the most preferable material for branch 1 is copper too.

As follows from equation (6), the cold-productivity of thermoelectric fin the bigger, as  $\bar{\alpha}_p^2 \sigma_1$  the bigger, but copper, in spite of its high electro-conductivity, has a low coefficient of thermo-electro-motive force. That is why to obtain large  $\bar{\alpha}_p$  when making the second branch it is necessary to choose a material with high coefficient of thermo-electro-motive force. However, materials with high coefficient of thermo-electro-motive force have the electro-conductivity the significant less than that one copper has.

As shown in equation (12), that is educating the ratio  $\sigma_1/\sigma_2$  and causes reducing of advantage in temperature difference for thermoelectric fin.

Because of that reason, it would be most preferable to use as material for second branch the metal alloys which permitting to receive  $\bar{\alpha}_p$  big enough with minimal differences in  $\sigma_1$  and  $\sigma_2$ .

When comparing ordinary fin made of copper and thermoelectric fin having one branch ( closest to the cooling object ) made of copper too and the second branch made of cobalt with  $\sigma_1/\sigma_2 \approx 5$ , for  $h/\delta_{1m} = 150$  the thermoelectric fin will have the advantage in temperature difference  $\Delta t_p/\Delta t_{1m} = 1250$ .

Thus concerning to ordinary fin, thermoelectric fin provides a several orders decreasing of temperature difference between the middle and the edges of combined to the lateral side of fin of an elemend with uniform internal heat liberation and also provides increasing of the possible accuracy of thermostating of this element under the changing of its heat liberation from maximum to zero.

References:

- [1].Voronin A.N., Zorin I.V. Thermo rejection. Author's Certificate of the USSR No 240064.
- [2]. "Heat- and mass-exchange. Technical experiment on heat".-M.: Energoizdat, 1982.- 512 p.

# Preliminary thermoelectric cooling of cryogenic flux in microcryogenic vessel systems

Uryupin O.N.<sup>1</sup>, Bondarenko M.G.<sup>2</sup>, Grabov V.M.<sup>2</sup>, Ovchinnikov S.G.<sup>3</sup>

<sup>1</sup> A.F.Ioffe Physical-Technical Institute, St. Petersburg, Russia

<sup>2</sup> Herzen Russian State Pedagogical University, St. Petersburg, Russia

<sup>3</sup> Microcryogenmach, Omsk, Russia.

Preliminary thermoelectric cooling of a cryogen gas flux in a Joule-Thompson microcryogenic vessel systems was used. Two-cascade thermoelectric coolers have been developed for decrease of the coolant temperature approximately by 60 K. This has been ensured to increase a continuous operating time of the systems by 60-80% for the systems with the different heat pumping capacity.

## Introduction

At present, cooling and thermostatting of the objects at the temperature level approximately 80 K is carried out by means of the vessel Joule-Thompson effect microcryogenic systems (VMS J-T). However, an open-VMS J-T has the limited operating time and the considerable mass [1].

The thermoelectric coolers (TC) are characterized of the substantially smaller dimensions and mass and the considerably larger time of the continuous operation with respect to the VMS J-T. However, the achievement of the cooling levels up to 80 K by means of (TC) is the difficult problem.

That is why the development of the microcryogenic techniques for such cooling levels was determined by the modernization of the VMS J-T, increase of the working pressure of the filling and by the application of the mixed coolants [1, 2]. However, the level of the perfection of the conventionally executed VMS J-T corresponds to the technical limit, and non-standard approaches are required for the further improvement of their characteristics.

The influence of preliminary thermoelectric precooling upon the continuous operating time of the VMS J-T was considered in this work.

## The calculation of the influence of coolant precooling upon the characteristics of the self-regulating VMS J-T

An analysis of the temperature dependence of the isothermal Joule-Thompson effect shows that the temperature decrease by each 10 K increases isothermal Joule-Thompson effect by 10 approximately for such coolants as nitrogen, air, argon.

The continuous operation time of self-regulating VMS J-T determines according to [2]:

$$t_T = \frac{V}{RTQ_u} \cdot A \quad (1)$$

where  $V$  - vessel volume;  $Q_u$  - useful heat pumping capacity;  $T$  - environment temperature;  $R$  - gas constant ;  $A$  - integral:

$$A = \int_{P_r/Z_r}^{P_f/Z_f} \Delta i_T \cdot \eta_T \cdot d\frac{P}{Z}$$

$\Delta i_T$  - isothermal Joule-Thompson effect;  $P_r$ ,  $P_f$  - the initial pressure and the pressure when the system can not ensure the object temperature of 80 K.  $Z_r$ ,  $Z_f$  - corresponding coefficients

of coolant compressibility;  $n = Q_u/Q_p$  - operating ratio of available heat pumping capacity.

The decrease of coolant temperature can improve three parameters: the coolant Joule-Thompson effect, operating ratio of available heat pumping capacity and the pressure when the system can not ensure the object temperature of 80 K. Equation (1) shows, that the continuous operation time of VMS J-T with preliminary thermoelectric cooling can increase.

In order to compare of the continuous VMS J-T operation time with precooling and the conventional VMS J-T we shall assume, that both systems operate at identical conditions and their useful heat pumping capacity is identical at the maximum pressure when the system can not ensure the object temperature of 80 K.

Then the required relation of the continuous VMS J-T operation time is determined by the relation of integral values 0 and 1, which relate to the conventional VMS J-T and VMS J-T with the thermoelectric precooling:

$$\frac{t_1}{t_0} = \frac{A_1}{A_0} \quad (2)$$

The calculation results showed that the continuous VMS J-T operation time with coolant precooling depends actually on the change of coolant Joule-Thompson effect, the operating ratio of available heat pumping capacity and on the pressure when the system can not ensure the object temperature of 80 K. This time is determined by relation (3).

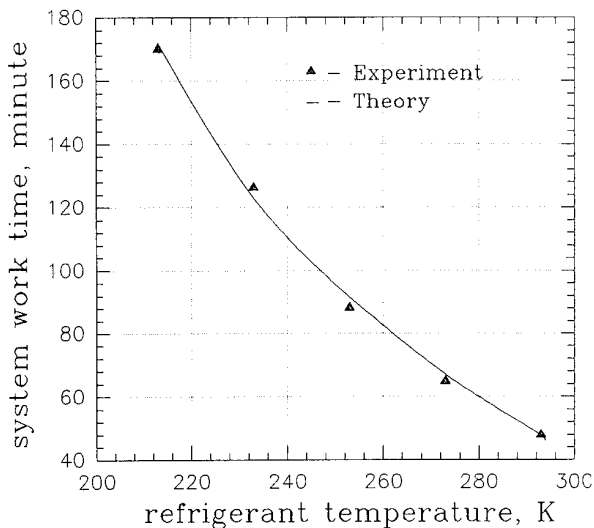
$$t_1 = t_0 \frac{A_1}{A_0} \quad (3)$$

The calculation dependence of operating time of VMS J-T, which operates with nitrogen is shown in Fig.1.

## Development and test of hybrid VMS J-T systems with the preliminary thermoelectric cooling of coolant

The one and two-stages thermoelectric coolant precoolers have been developed for the experimental determination of the influence of preliminary thermoelectric cooling on the duration of VMS J-T operation. Experimental investigations of mock-ups with hybrid self-regulating VMS J-T with heat pumping capacity of 1 and 10 W on the temperature level 80 K were carried out with nitrogen at the environment temperature 293 K, filling pressure - 35 MPa and vessel volumes of 0.72 and 5.0 liters accordingly.

Figure 1: Dependence of system work time on refrigerant temperature



## References

- [1] Fonyakov S.A., Ovshinnikov S.G., Ermakov V.M., Gavrin E.A., Ulibina L.P. Peculiarities of calculation of relative mass of the vessel Joule-Thompson microcryogenic systems *Himishes-koe i neftianoe machinostroenie* 1989. N.7. P.14-16. (in Russian).
- [2] Merkel N.D., Fischer E.A. Design and experimental determination of optimum pressure of filling of the vessel systems with self-regulating microcooling *Himischeckoe i neftianoe machinostroenie* 1988. N.8 C.13-16. (in Russian).

Table 1: The experimental data work mock-up

Heat pumping capacity	P,W	1	10
Object temperature	T, K	80	80
Work time without Coolant precooling	$t_0$ , min	49	58
Work time with Coolant precooling	$t_1$ , min	80.5	92.5
Times ratio	$t_1/t_0$	1.8	1.6

The results of those investigations are shown in the table.

In the table you can see that the increase of VMS J-T operating time due to application of preliminary thermoelectric coolant precooling are equal practically to the calculated values on Fig.1.

## Conclusion

The theoretically demonstrated opportunity of principle of the preliminary coolant precooling for increase of the operating time of the continuous self-regulating VMS J-T with various heat pumping capacity was confirmed by these experimental investigations.

The calculating dependence of VMS J-T operating time on the coolant temperature was received. The results of calculations are confirmed experimentally.

The thermoelectric coolers for the preliminary coolant precooling of self-regulating VMS J-T with heat pumping capacity of 1 and 10 W have been created.

The experimental investigations of the mock-ups of the VMS J-T with the preliminary coolant thermoelectric precooling were carried out. The continuous operating time of such hybrid systems is 1.8-1.6 times as great as that for conventional VMS J-T under equal other conditions.

## OPTIMAL FUNCTIONS OF MAGNETIC FIELD FOR THE PELTIER COOLERS

L.I.Anatychuk, L.N.Vikhor

*Institute of Thermoelectricity, Chernovtsy, 274000, General Post Office, box 86, Ukraine*

Methods of optimal control are used in the present work for search of the best magnetic field function of the Peltier stage cooler. The possibility of low-temperature coolers coefficient of performance increase by the use of optimally nonuniform magnetic field is demonstrated.

### Introduction

Reaching of the best thermoelectric cooling module characteristics is connected with solution and practical adoption of optimizing problems results. In our papers [1,2,3] we give a number of examples confirmed the concept of further progress in thermoelectricity by the change from optimal numbers to optimal functions.

Problems of optimal functions in thermoelectricity search were analyzed in [1]. There are about 120 such problems in thermoelectric cooling. Only nine of them have been solved for today. That is why Institute of Thermoelectricity (Ukraine) conducts researches in this approach.

The present paper continues a series of papers on the optimal control theory methods research for the optimal functions search and for their use at low temperature stage coolers design.

It is possible to provide the best parameters of the Peltier cooling modules in steady-state condition by two optimal functions. The first is the dependence of current carrier concentration along thermoelement leg height on coordinate. Search problem solution of such dependence for maximum temperature difference or thermoelement coefficient of performance achievement is given in [1]. It was found that cooling efficiency of the inhomogeneous thermoelement from *Bi-Te* based materials can be improved by 20-25% depending on temperature difference.

In low-temperature region it is expedient to use alloys based on *Bi-Sb* as *n*-type leg of thermoelements. It is connected with large thermoelectric figure of merit of these alloys which sharply increases with the effect of external magnetic field. In this connection cooling efficiency in low temperature region can be increased by the second optimal function. It is the magnetic field strength dependence on a leg coordinate.

The possibility of thermoelectric cooling parameters improvement in a separate magnetothermoelectric stage of the Peltier cooler is demonstrated in [2]. It is shown that the use of optimal nonuniform effect on the *n*-type leg from *Bi-Sb* results in coefficient of performance rise up to 20% depending on temperature difference in the stage.

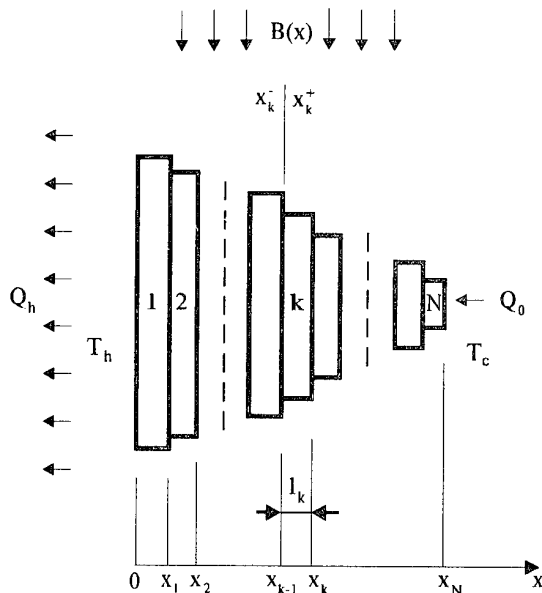
The problem of optimal control by magnetic field strength value in [3] is extended over optional stage number. It has found magnetic field optimum distribution for a multi-stage cooler where each stage has its own strength of magnetic field. Within each stage the magnetic field is uniform. It was shown that in case of temperature differences in 60-70 degrees the coefficient of performance gain reached 40-50% as compared with optimal uniform magnetic field.

The results having been obtained in [2] and [3] have lead to propounding of a novel, more complicated optimizing problem. It reduces to the problem of magnetic field strength optimal function search for the Peltier multi-stage cooler with *n*-type legs of *Bi-Sb*.

### Problem Formulation

The scheme of the optimal control problem by magnetic field strength value for *N*-stage cooler is shown in Fig.1. Magnetic field of *B* strength that can be the function of *x* coordinate is perpendicular to the current direction. The starting data for optimization include heat pumping capacity of a cooler  $Q_0$ , cooling temperature  $T_c$ , hot surface temperature  $T_h$ .

Fig.1. A model of *N*-stage thermoelectric cooler.



The object of the research is the determination of the magnetic field  $B(x)$  best function and the best power function for each stage.

The model also takes into account contact resistance values  $r_0$ , interstage temperature differences  $\delta T$  and heat exchange with environment at heat-transfer coefficient  $\alpha_T$ .

Temperature dependences of thermo-e.m.f. coefficient  $\alpha$ , electric conductivity  $\sigma$  and thermal conductivity  $\kappa$  are the given parameters as well as  $\alpha$ ,  $\sigma$ ,  $\kappa$  dependences on magnetic field strength.

Hence the problem covers rather completely all necessary parameters of a material, a cooler and its operation conditions.

Temperature  $T(x)$  and specific heat fluxes  $q(x)$  distributions in thermoelement legs are determined by the system of  $4N$ -differential equations in the form of

$$\left. \begin{aligned} \frac{dT}{dx} &= -\frac{\alpha i_k}{\kappa} T - \frac{i_k}{\kappa} q, \\ \frac{dq}{dx} &= \frac{\alpha^2 i_k}{\kappa} T + \frac{\alpha i_k}{\kappa} q + \frac{i_k}{\sigma}, \end{aligned} \right\}_{n,p} \quad k = 1, \dots, N \quad (1)$$

Here  $\alpha$ ,  $\sigma$  and  $\kappa$  for  $p$ -type leg are the functions of temperature, and for  $n$ -type they are functions of both temperature and magnetic field strength. This assumption is justified, since  $p$ -type leg is made of *Bi-Te* based material, its properties have weak dependence on magnetic field, and  $n$ -type leg is made of *Bi-Sb* based material, parameters of which have strong dependence on the field.

Boundary conditions for these equations are written as the temperature equalities between stages with regard to interstage temperature losses and have the form

$$\begin{aligned} T_n(0^+) &= T_p(0^+) = T_h, \quad T_n(x_N^-) = T_p(x_N^-) = T_c \\ T_n(x_k^+) &= T_p(x_k^+), \quad T_n(x_k^-) = T_p(x_k^-), \\ T_n(x_k^+) &= T_n(x_k^-) + \delta T, \end{aligned} \quad (2)$$

where positions of points  $x_k$ ,  $k=1, N$  are not fixed.

It is necessary to find such conditions when coefficient of performance reaches its maximum under given cooling value. In the optimal control theory language the problem is reduced to the functional minimum determination

$$J = \sum_{k=1}^N (\ln q_1^k - \ln q_0^k). \quad (3)$$

Specific heat fluxes on the junctions are determined by expressions

$$\begin{aligned} q_0^k &= \sum_{n,p} \left[ q(x_k^-) + i_k r_0 + \frac{\alpha_T}{i_k} (T_h - T(x_k^-)) \right], \\ q_1^k &= \sum_{n,p} (q(x_{k-1}^+) - i_k r_0). \end{aligned} \quad (4)$$

They depend on current densities controlled parameters  $i_{n,p}^k$  and magnetic field strength function  $B(x)$ .

The solution of the assigned optimal problem is given by the Portnyagin's maximum principle [4]. According to this principle the following conditions must be fulfilled for the minimum  $J$ :

1. Current densities in stages must satisfy the equalities

$$-\frac{\partial J}{\partial i_{n,p}^k} + \int_{x_{k-1}^+}^{x_k^-} \frac{\partial H^k(\psi, T, q, i_n^k, i_p^k)}{\partial i_{n,p}^k} dx = 0, \quad (5)$$

where the Hamilton function  $H^k$  has the form

$$H^k = \sum_{n,p} (\psi_1 f_1^k + \psi_2 f_2^k), \quad (6)$$

$(f_1^k, f_2^k)_{n,p}$  - are the right-hand terms of the equations (1),  $\psi = (\psi_1, \psi_2)_{n,p}$  - is the pulse vector [1].

2. Coordinates of junction points  $x_k$  satisfy the equalities

$$H^k(x_k^-) = H^{k+1}(x_k^+), \quad k = 1, \dots, N-1. \quad (7)$$

3. Optimal function of the magnetic field strength must satisfy the condition

$$\begin{aligned} H_n^k(\psi(x), T(x), q(x), B(x), i) &= \\ &= \max_{B \in G_B} H_n^k(\psi(x), T(x), q(x), B, i) \end{aligned} \quad (8)$$

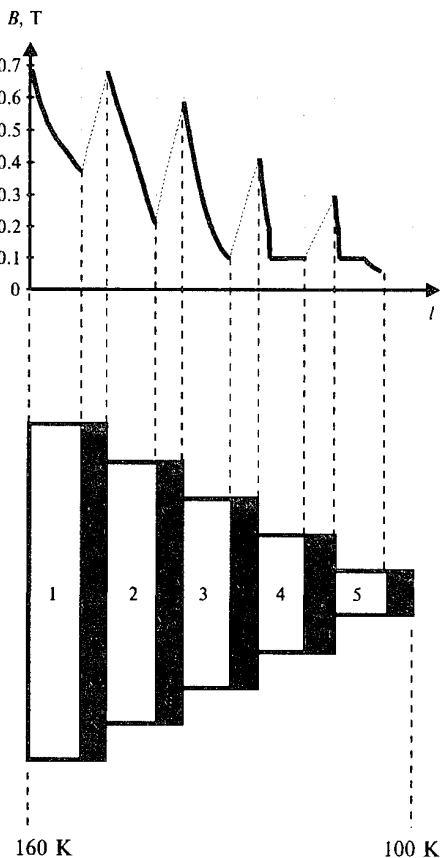
This problem solution was realized by the numerical method of successive approximations. The computer program has been developed which enables to determine the optimal function of the magnetic field nonuniformity and to use it for the determination of the stage best power functions and parameters of the Peltier magneto-thermoelectric coolers.

#### Discussion of results

The developed program was used for the calculations of multi-stage coolers providing cooling level of  $130-90K$  at  $T_h=160K$ . Experimental dependences of *Bi-Sb* alloy properties on the temperature and the magnetic field strength value given in [2] were used in calculations.

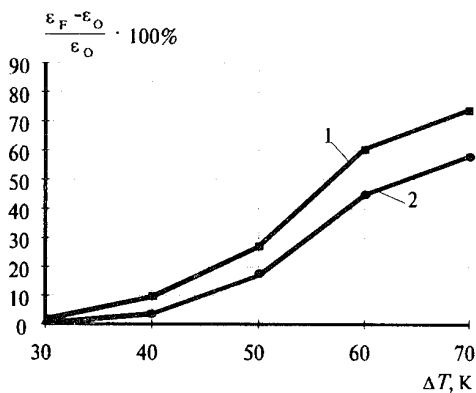
Fig.2 shows the example of one of the magnetic field optimal functions derived for 5-stage cooler at temperature difference of 60 degrees. These function forms are totally defined by material property dependence on

*Fig.2. Optimal function of the magnetic field for 5-stage cooler.*



magnetic field strength and temperature. Stage cooler energy efficiency increase with use of nonuniform magnetic field as compared with the best uniform one is given on the Fig.3.

*Fig.3. Relative deviation of COP with use of the magnetic field optimal function (curve 1) or optimal distribution of the field along the stages (curve 2)  $\varepsilon_F$  against its value at optimum uniform field  $\varepsilon_o$  on temperature difference in stage TEC at  $T_h=160K$ .*



Two curves are shown there. The curve 1 gives the gain in the coefficient of performance depending on the temperature difference on a cooler with use of the nonuniform magnetic field optimum function. The curve 2 is given for comparison. This is the similar dependence with use of the magnetic field optimum distribution between the stages that has been got in [3]. One can see that the greater cooling value the larger the gain in the coefficient of performance due to the nonuniform magnetic field effect. It is apparent that the effect is greater with use of the magnetic field optimal functions. The gain reaches 75% at the temperature differences of 60-70. It is highly essential for low-temperature coolers.

The obtained results lead to the statement of more complicated problem of optimal control in thermoelectricity. It reduces to the combination of optimal nonuniform effect by the magnetic field with optimally inhomogeneous structure of thermoelectric material. This problem is the subject of our further researches.

#### References

- [1]. L.I.Anatychuk, V.A.Semenyuk. Optimal Control by the Thermoelectric Material and Devices Properties. Chernovtsy, 1992, p.264.
- [2]. Anatychuk L.I., Vikhor L.N., Ivanov G.A. The Optimal Control Theory for Thermoelectric Cooler Design, in Proceedings for Twelfth International Conference on Thermoelectrics, Japan, Nov., pp.412-415.
- [3]. Anatychuk L.I., Vikhor L.N. Study On Cooler Design In Magnetic Field For Low Themperature Cascades, in Proceedings of the Thirteenth International Conference on Thermoelectrics, Cansas, Aug., 1994.
- [4]. Pontryagin L.S., Boltyansky V.G., Gamkrelidse R.V., Mischenko E.F. Mathematical Theory of Optimal Processes, M., Nauka, 1976 , p.392

## THERMOELECTRIC MICROCALORIMETRY OF BIOLOGICAL OBJECTS

Anatychuk L.I., Demchuk B.N., Luste O.J.

*Institute of Thermoelectricity, Ukraine*

Biology along with thermochemistry is a vast field for the use of microcalorimetry which represents today a highly developed trend of thermal measurement technique in the range from milliwatt to nanowatt.

Admittedly, thermoelectric methods in microcalorimetry have a number of advantages compared to other methods of measuring thermal production. Possibilities of thermoelectricity use in caloremetry were reported by Hart and Hirst [1] at one of the previous International Conferences on thermoelectricity. This paper indicates the possible microcalorimetry use in biology and medicine and gives examples of this use based on microcalorimetric sensors and microcalorimeters in the Institute of Thermoelectricity (Ukraine).

Biological processes occurring at various levels from a molecule to ecological system - are notable for high values of specific heat release compared to many physical and chemical processes. Therefore, the first calorimetric studies made by Lavoisier 200 years ago were based on biological objects. Since then biologists have repeatedly turned to calorimetry, but it was not until the recent decades that thermal process study became possible on molecular and cellular levels.

The strength of calorimetry as a method of biological studies lies in its universality which can be attributed to the fact that practically all biological processes are accompanied by thermal ones. Therefore, today microcalorimetry is increasingly used combined with the conservative and the newest methods of biological process study.

The beginning of modern phase of biological calorimetry can be traced back to the series of papers by E.Calvet and A.Prat [2] who firmly established microcalorimetry as the method of biological studies and determined its most important trends for a long period of time.

There trends are as follows:

thermodynamics of biological processes; thermochemistry and kinetics of biochemical reactions; biopolymer and biological macromolecule studies;

certain theoretical and applied research in microbiology (classification and identification of microorganisms, processes of growth and metabolism, choice of optimum culture media, analysis of sterilization efficiency, effect of antimicrobial preparations, etc.) and hematology;

study of thermal production and thermal control of animals and their organs;

physiology of plants, their seeds and organs, some problems of photosynthesis;

industrial microbiology and food production (heat release in the process, antibiotic producer activity, bacterial infection control, etc.);

medicine (diagnosis, choice of individual treatment methods, efficiency of medical preparations, etc.).

The emerging nonlinear thermodynamics of irreversible processes and self-organization theory operating both with quantity and adequacy of information will, admittedly, rely upon the microcalorimetric data.

The use of microcalorimetry for studying thermodynamics and kinetics of biochemical reactions virtually embraces all the sections of biochemistry and is adequate for determination of thermodynamic parameters, equilibrium constants, biopolymer molecular mass, heat capacity, enzyme activity, energy structural parameters of proteins, nucleic acids and other biopolymers. One of the most relevant fields of biological microcalorimetry is connected with studying intramolecular biopolymer transformations.

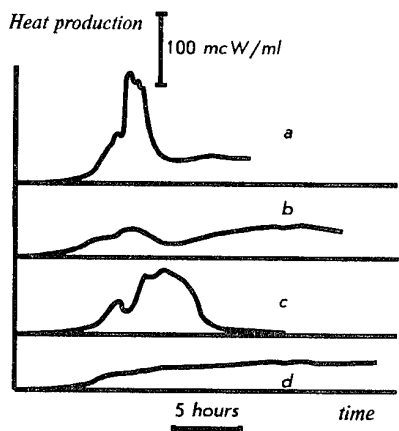
In the Institute of Thermoelectricity (Ukraine) there have been developed new types of microcalorimetric sensors which served the basis for biological purpose microcalorimeters. The typical parameters are listed in the Table.

Table. Parameters of biological microcalorimeters.

Parameters	Units	Parameter values
Temperature range	°C	0-100
Speed of response	s	0.1-200
Sensitivity	mcW	0.01-10
Measured power	mcW	0.1-10000
Number of cells		1-4
Working volume of cell	cm <sup>3</sup>	1-10

Microbiology is one of the best developed fields of microcalorimetry use, inasmuch as microorganisms have sufficient heat release level of the order of  $10^{14}$  -  $10^{-10}$  W calculating on one cell. Calorimetric studies of microorganisms have been conducted since the middle of the last century. E.Calvet and A.Prat [2] were the first to use microcalorimetry for studying microorganism cultures and proved that thermographs reflected specific features of each microorganism type. This thermograph type specificity later allowed to raise the idea of microorganism identification and classification according to the profile of heat release curve as function of time in the process of growth (Fig.1.). It is seen from the figure that under standard conditions each microorganism type has its unique curve profile.

Fig.1. Thermographs of microorganism cultures at 37°C: a - *E.coli* 355, b - *Bac. subtilis* 177; c - *St. aureus* 209; d - *C.albicans* 688.



Microorganisms change their thermograph profile depending in temperature, culture medium composition, the effect of toxic substances and antibiotics. At the present time microbiology has at its disposal a rich collection of thermographs for a large number of types. The best studied is thermal production of *E. coli*. The thermographs shown in Fig. 2-5 give the idea about the relative value of heat release and the character of changes in the colon bacillus heat production occurring at various stages of growth.

Fig.2. *E. coli* 355 thermograph profile as function of temperature: a - 39.8°C; b - 36.8°C; c - 32.3°C; d - 23.5°C; e - 20.5°C.

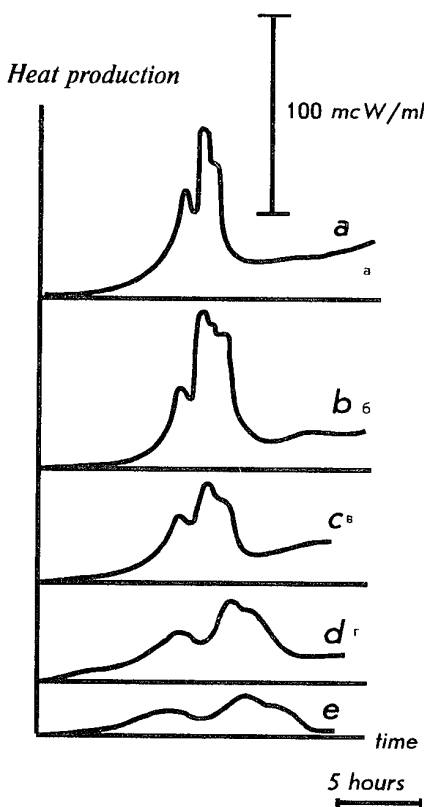


Fig.3. *E.coli* 355 thermographs at various glucos concentrations: a - 1%; b - 0.8%; c - 0.1%; dashed curve - standard medium.

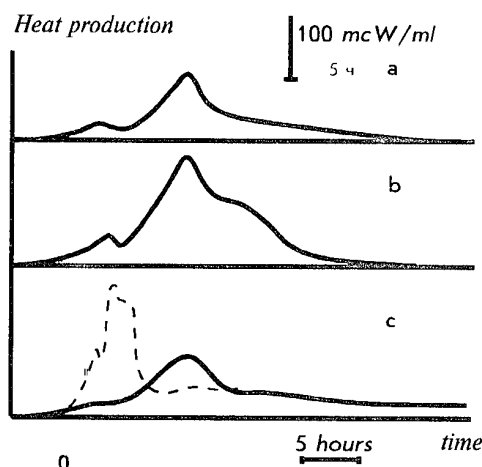


Fig.4. *E.coli* 355 thermograph profile as function o initial cell concentration.

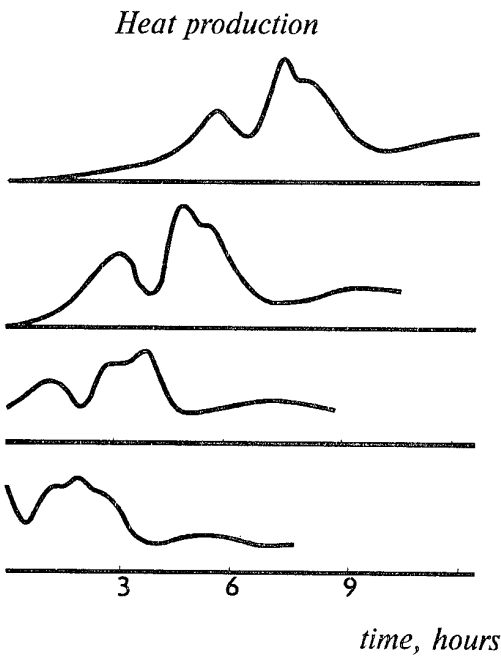
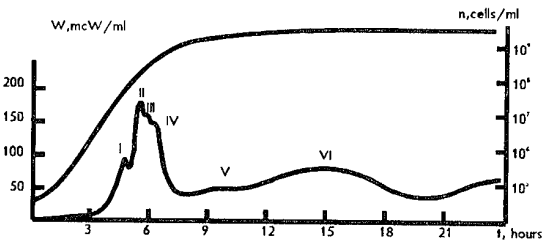
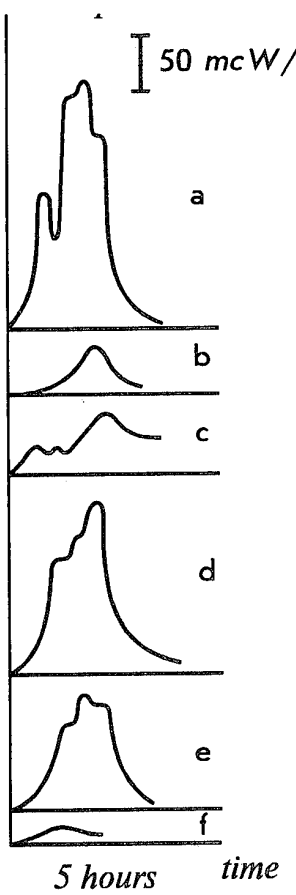


Fig.5. Thermograph and growth curve of *E. coli* 35 during 24 hour - test.



*Fig.6. St. aureus 209 thermographs for various decametoxine concentrations:*



In recent years microcalorimetric methods have been increasingly used in theoretical medicine and clinical practice. A valuable experience has been accumulated in the use of microcalorimetry for making analyses, studying pathogenic bacteria, blood and tissue cells, definition of medical preparation efficiency. These works are carried out on the biochemical level, the level of cells, tissues and individual organs.

Chemical and biochemical analyses in clinical practice are critical for the diagnosis of illnesses and control of medical treatment results. Conservative analysis methods are efficient enough but their number is insufficient to work on a cellular level. Therefore, microcalorimetry of microorganisms and cells is of great interest for medicine.

Among the analytical methods one should emphasize the use of microcalorimetry on a biochemical level to determine activity of enzymes. The thermograph shift is directly proportional to the thermal effect typical of enzyme activity. The accuracy of calorimetric definitions corresponds to the level of traditional methods.

Microcalorimeter methods are also effective for studying such complicated chain of processes as plasma coagulation and allow to determine time of coagulation with the error of the order of 3 sec.

Discussed methods of microorganism studies are adequate for solving a series of medical problems. They include diagnosis based on microcalorimetric identification of microorganisms and determination of bacterial infection. Experience shows that during several hours it is possible to determine the difference between the levels of bacteria concentration  $10^4 \dots 10^5$  cells/ml. Compared to chemical tests of bacterial infection and identification of pathogenic organisms.

Microcalorimetry also allows to use antibiotic action kinetics [4] to find the optimum (minimum) therapeutic doses (Fig.6).

Heat release measurements provide valuable information about the processes of antibiotic biosynthesis and other processes in microbiological industry.

Microcalorimetry proved itself to be a method of blood cell study and diagnosis in clinical hematology.

Valuable information has been obtained concerning energy expenditure of surviving organs which is of interest to transplantation science.

The list of possible biological and medical microcalorimetry applications testifies to the large potential opportunities of further introduction of microcalorimetric methods into there fields.

#### REFERENCES

1. R.M.Hart, M.W.Hirst, Thermoelectric devices and calorimetry, Proc. III Internat. Conf. on Thermoelectr. Energy Conver., Univ. Texas at Arlington, pp.113-116, 1980.
2. E.Calvet, H.Prat, Microcalorimetrie, Masson et Cie, Paris, 1956.
3. L.I.Anatychuk, O.J.Luste, Microcalorimetry, High School Publishers, Lviv, 1981 (in Russian).
4. B.N.Demchuk, G.K.Palij, Antibiotics, 1976, No. 3, pp.222-226 (in Russian).

## MICROCALORIMETER FOR CHEMICAL CURRENT SOURCES

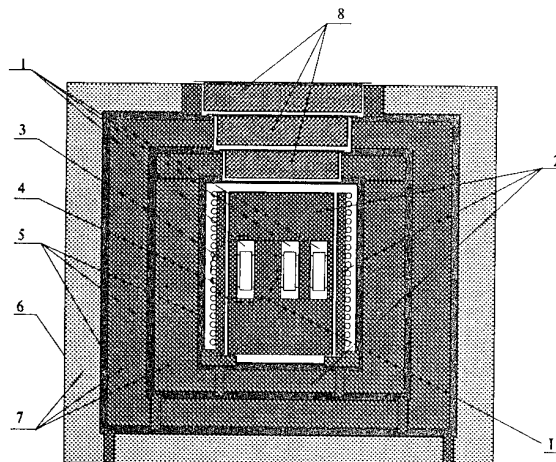
N.V.Gavriluk, B.N.Demchuk, N.S.Petrenko, Yu.S.Khmelevskaya

*Institute of Thermoelectricity, Chernovtsy, 274000, General Post Office, box 86, Ukraine*

Calorimetric complex for determination of chemical current sources self-discharge thermal energy is proposed. It consists of multi-cell microcalorimeter with separable thermal blocks and the control block provided signal measurements, their processing as well as the temperature regime of the thermostat. The microcalorimeter structure, its parameters and thermal measurements results are given.

There is a wide group of control-measuring devices and electronic equipment, the only supply source of which is chemical current sources (CCS). Along with such valuable qualities as small size, relatively high energy density and low cost, chemical current sources has disadvantages including electrical parameters dependence on environment effects, limited service life and problem in determination of power capacity current value. The advent of chemical current sources with improved parameters on the base on *Li* compounds and their use made the quality control problem that defines mainly by their power capacity very actual. Existing methods of power capacity determination by current measurement on the load discharge the sources and it appears the necessity in CCS quality assessments by other more effective methods than the direct current measurements on the load. It is also known that real CCSs are characterized by self-discharge currents the value of which greatly effects on their service life along with the load current. Even during storage (outside load current absence) the enlarged self-discharge current encourages CCS untimely aging. As the processes occurring in chemical energy conversion are accompanied by heat release depend on source power capacity and self-discharge current, use of microcalorimetry could determine CCS quality by the nondestructive control method.

*Fig. 1. Structure of the microcalorimeter.*



For this purpose microcalorimetric complex has been developed. It consists of multi-cell microcalorimeter itself with separate thermal blocks for CCS of three different sizes and the control block providing signals from calorimetric cells measurement, their processing, and the required temperature setting of the thermal block. Fig 1 shows the calorimeter structure, the base of which is mass compound aluminium block 2 with eleven measuring cells 1. Mass thermal block is places into thick-wall shell 3 with a heater 4. The shell 3 is surrounded by the radiation shields of a passive thermostat 5 and outer housing 6 the space between them is filled by basalt fibre 7. Removing covers 8 of the passive thermostat and removing top part of the thermal block are provided for the cells access. The arrangement of cells in the central part of the thermal block is shown in fig.2. For thermal symmetry "working" cells are arranged along two concentric circles with a "test" cell in the center. A cell structure is given in fig.3.

*Fig.2. Arrangement of measuring cells in the thermal block.*

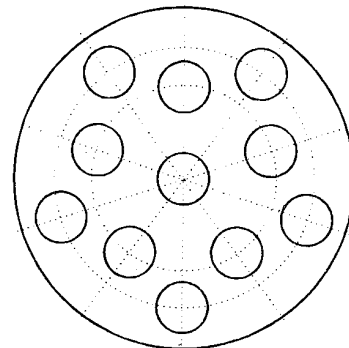
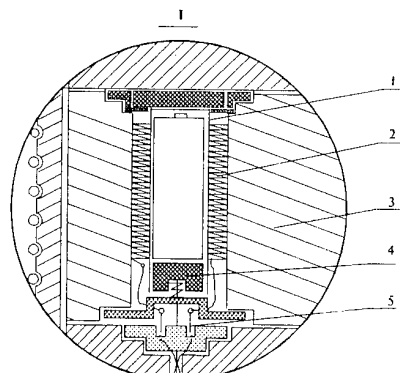


*Fig.3. Structure of a measuring cell.*



**Literature**

A measuring cell consists of reaction chamber 1 centered on the block space by covers of thermal insulation material. Thermobattery 2 has contacts by "hot" junctions with outside surface of the reaction chamber and by "cold" ones with inside surface of the thermal block 3 central part cavity. For easy CCS removal from the reaction chamber a push out unit 4 is provided. Electric section connector 5 permits quick replacement of the thermal block removal part.

Signals from the measuring cells put at the input commutator and amplifier that located under the outside shell of the microcalorimeter case for the external magnetic field pickups suppression. The enhanced signal of a given differential couple of cells through the cable puts at the control block. The control block consists of a thermoregulator unit and information processing unit. The information processing unit is made on the base of microprocessor KR580VM80 and permits to get the measurement results in form of thermo-e.m.f. signal, thermal flow power value or total heat release for a definite period and to calibrate and to exchange of information with external computer.

The tentative measurements of current sources self-discharge heat release of A373 type showed that power level is about 40-60 mW. In the case of 100 kOhm outside load connection to CCS its heat release is increased by a factor of two.

At present calorimetric measurements for statistic data set are carried out for CCS quality determination method development.

*Parameters of microcalorimetric complex*

Dynamic range of measurements 1 mcW	10 mW
Threshold sensitivity, no worth than	1 mcW
Constant time of measuring cells, no more than	300 s
Active thermostatting range	35-70°C
Number of thermal separate blocks a microcalorimetric cell size corresponds to CCS sizes of A316, A343, A373 types	3
Number of cells in each thermal block	11
Overall dimensions of a microcalorimeter, mm	1000×1000×1100
Mass of the microcalorimeter, no more than	110 kg
Overall dimensions of a control block, mm	480×480×140
Mass of a control block, no more than	10 kg

1. E.S.Takeuchi, S.M.Meyer, C.F.Holmes. Assessment of capacity loss in low-rate lithium/bromine chloride cells by microcalorimetry and long-term discharge. *J. Electrochem.Soc.*, 1990 137, N 6, pp. 1665-1670.
2. V.S.Donepujt, A.M.Sibbald, W.A.Adams. *Electrochemical calorimetry and lithium cells. J. Electrichem. Soc.*, 1989, 136, N3, p.109.
3. T.Iwamaru, O.Kajii, J.Uetant. Measurement of self-discharge rate of lithium/thionyl chloride battery by microcalorimeter. "3 jnt.meet lithium batteries, Kyoto, 27-30 May, 1986, Exteuded abstr." *S.J.*, 1986, pp. 52-55.

## THERMOELECTRIC COOLING OF SEMICONDUCTOR LASERS UNDER EXTREME TEMPERATURE CONDITIONS

V.A.Semeniouk, T.V.Pilipenko

*Thermion Company, Odessa 270009, Ukraine*

The results of the development of thermoelectric cooling devices (TCD) for cooling semiconductor lasers and light-emitting diodes at high ambient temperatures are given. The particular case of TCD application as a part of fiber-optic module, used for the research of Earth deep boreholes, where the temperature can reach 180 °C, is discussed in detail.

### **Introduction**

In many cases there appears the necessity to use semiconductor lasers under conditions of increased ambient temperature, at the same time great guaranteed life and high stability of light emission parameters are to be provided. Such conditions arise, for example, when lasers are used for borehole surveying with the aim of transferring information from deep Earth boreholes. The main problems arising in this case are connected with the increase of temperature which can reach 180 °C at the depth of 10000 m. The most important parameters of injection lasers such as frequency, mode composition, emission power, threshold characteristics, COP of laser transformation, degradation processes velocity greatly depend on temperature [1]. At temperatures close to 180 °C the operation of most injection lasers is impossible at all due to heat break-down of the laser generation. At the same time the peculiarity of the application field under consideration is such that the replace of defective products is impossible or extremely unprofitable and the breakage of even one laser is a catastrophic event. Thus the application of lasers under extreme temperature conditions requires their cooling to safe temperatures.

The results of the development of TCD for fiber-optic module used as a part of a borehole device while researching the Earth deep boreholes are given below. The researches were carried out in two directions: development of TCD for the borehole temperature  $T_e = 120$  °C with the laser temperature  $T_o$  being kept not higher than 40 °C, and determining the maximum temperature  $T_e$  at which it is still possible to maintain the laser temperature at the level of 60 °C in a standard borehole device. The research involved the following steps:

- heat sink optimisation;
- estimation of heat load at the object of cooling;
- choice of semiconductor materials and accurate study of temperature dependence of their thermoelectric properties;
- TE cooler optimization;
- technology development;
- TCD construction development;
- TCD testing;
- estimation of possibilities to develop TCD for increased temperature level.

The researches were carried out in the above mentioned order and each completed stage was the basis for the optimal solutions at the next step. Restrictions connected with the peculiarities of the borehole device construction and its operational conditions were taken into account.

### **Particular restrictions**

There is no doubt that the given temperature differences can be achieved in principle with the help of modern TE coolers. However in the case under consideration the problem becomes much more difficult because of the necessity to build-in TCD to the standard housing of borehole device. The borehole device is made in the form of a tube with the inner diameter of only 37.8 mm. Inside this cylinder it is necessary to place TCD consisting of TE cooler and the heat sink in the form of a hollow cylinder, providing the heat transfer to the housing of the borehole device. The object of cooling (semiconductor laser sealed in a cylinder casing of 11 mm diameter and 25 mm length) must be placed in the heat sink cavity. The annular clearance between the casing and the heat sink doesn't exceed 10 mm. Thus, the object to be cooled is surrounded by superheated jacket and the insulating clearance is very small. In this connection, the heat load applied to the object of cooling proves to be considerable even in using such an efficient thermal insulation as TSMK on the basis of porous silicon.

Besides, according to the assembly conditions there must be provided an cylinder air clearance not less than 0.2 mm between the TCD heat sink and the housing of the borehole device, which greatly increases the thermal resistance on the hot side of the TE cooler.

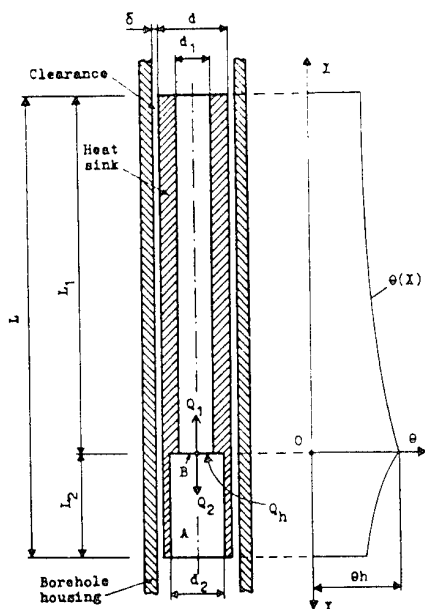
The next difficulty is that the most efficient TE materials on the basis of bismuth telluride show ambipolar conductivity in the temperature range under consideration which results in a sharp reduction of their thermoelectric quality. Therefore to develop a TE cooler with acceptable characteristics it is necessary to carry out optimal doping of semiconductor materials for the temperature range from 60 to 180 °C.

Thus, to solve the problem it is necessary to estimate and implement the limit characteristics of all TCD elements.

### **Heat sink optimization**

Schematic of the heat sink is given in Figure 1. The heat sink is made in the form of a tube with the diameter of 37.6 mm and the length of 260 mm installed with a clearance inside the borehole device housing. In the lower part of the heat sink there is a hole of 32 mm diameter (cavity A) for putting in the thermoelectric unit, laser emitter and thermal insulation. The upper part is made more thick-walled (inner diameter is 18 mm) to increase longitudinal heat conduction. Heat from coolers is transferred to surface B.

Fig. 1 To the estimation of heat sink thermal resistance



Let us consider the problem of optimal placing the TE unit inside the heat sink of such a construction. For the case of an equal-walled cylindrical heat sink the placing in the tube centre is an optimal version, as in this case the thermal resistance of the heat sink is minimal. In a more general case, when separate sections of the tube have different thickness, the problem of optimal placing the heat source requires additional research. The purpose is to find such a relation of lengths of separate tube sections which minimizes the temperature rise at the place of heat source location.

The following model has been used for solving this problem. The outer heat sink diameter  $d$ , its total length  $L$  and diameters of the upper and lower holes  $d_1$  and  $d_2$  ( $d_1 < d_2$ ) are fixed. The TE unit is considered as the concentrated heat source of  $Q_h$  power. Heat transfer on the end faces of the heat sink is not taken into consideration. There is thermal resistance in the form of annular air clearance of  $\delta$  thickness between the heat sink and the housing of the borehole device. The temperature of the borehole device housing is constant and equal to the ambient temperature  $T_e$ . The thermal conductivity of the heat sink is rather high, so the radial sections of the heat sink can be taken as isothermal (one dimensional model of heat dissipation).

One can easily see, that for each part of the tube the model discussed is reduced to the classical problem of heat conduction of a rod with constant cross section, transferring heat into the surroundings with temperature  $T_e$ . The known solution for the case of free convection has the form [2]

$$Q = mF\Theta_h th(mL) \quad (1)$$

where

$$m = \sqrt{\frac{\alpha P}{\lambda F}} \quad (2)$$

$Q$  - heat flow at the rod base;

$\alpha$  - heat transfer coefficient;

$$\Theta_h = T_h - T_e$$

$T_h$  - temperature at the rod base;

$L$  - rod length;

$F$  - rod cross section area,

$P$  - rod perimenter;

$\lambda$  - thermal conductivity of the rod

For the discussed case of heat conduction through the air clearance we have an identical solution with substitution of  $\alpha$  by equivalent ratio  $\lambda_a/\delta$ , where  $\lambda_a$  is thermal conductivity of air. The change concerns only the formula for  $m$  parameter which now takes the form:

$$m = \sqrt{\frac{\lambda_a P}{\lambda F \delta}} \quad (3)$$

Writing down relations of the form (1) for upper and lower parts of heat sink and adding them up termwise, we shall find

$$\Theta_h = \frac{Q_h}{\lambda} \cdot \left[ F_1 m_1 th(m_1 L_1) + F_2 m_2 th(m_2 L_2) \right]^{-1} \quad (4)$$

and then define the heat sink thermal resistance  $R_h = \Theta_h/Q_h$  as follows

$$R_h = [\lambda F_1 m_1 th(m_1 L_1) + \lambda F_2 m_2 th(m_2 L_2)]^{-1} \quad (5)$$

The solution of the problem of the heat source optimal location is reduced to the search of minimum  $R_h$  as a function of  $L_1$ . Supposing in (5)  $dR_h/dL_1 = 0$  and taking into account the equality  $L_2 = L - L_1$  we find an optimal condition of the form:

$$m_1 L_1 = m_2 L_2 \quad (6)$$

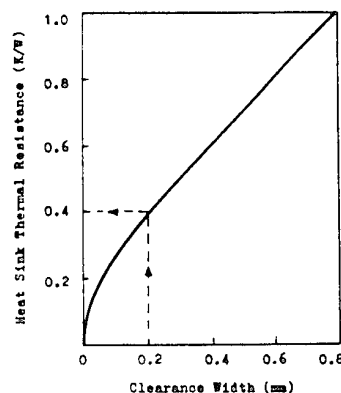
or

$$\frac{L_1}{L_2} = \sqrt{\frac{F_1}{F_2}} \quad (7)$$

It is interesting to note that the condition (6) corresponds to equality of thermal resistances of the heat sink separate parts, as well as the equality of excess temperatures at its ends.

For the case under consideration ( $d=37.6$  mm,  $d_1=18$  mm,  $d_2=32$  mm) we find from condition (7)  $L_1/L_2=1.68$ , which gives, with  $L$  value of 260 mm,  $L_1=160$  mm and  $L_2=100$  mm. Figure 2 shows the dependence of the minimum  $R_h$  value on the clearance calculated with the help of relationship (5) at optimal  $L_1$  and

Fig. 2 Dependence of thermal resistance at the hot side of TE cooler on the width of heat sink-to-housing clearance



$L_2$ . It is seen that at  $\delta = 0.2$  mm the minimum thermal resistance is 0.4 K/W. With the increase of the clearance width superheat increases nearly proportionally, indicating that the contribution of the air clearance thermal resistance is prevalent.

To conclude this section we shall note that in the minimum region the dependence of  $R_h$  on  $L$  is sloping enough so the heat source shift by 20-30 mm to both sides from established optimum is admissible without significant increase of superheat.

### Heat load identification

Heat load  $Q_o$  on the TE cooler consists of the laser's own heat dissipation  $Q_i$  and heat gains from the environment  $Q_e$ . The latter are defined by the borehole device construction, they considerably depend on mutual arrangement of separate TCD parts and cannot be estimated theoretically with sufficient accuracy. In this connection the experimental estimation of heat load was carried out on a TCD model. The idea of the method is to establish in a TCD model a standard TE cooler with known heat load characteristic  $Q_c(\Delta T)$ , and, on obtaining a definite temperature of the laser, to use it as a control point for determining the heat load with its subsequent recalculation for specified temperature conditions. In recalculating the linear dependence of  $Q_e$  on temperature difference  $\Delta T = T_h - T_o$  was taken into account.

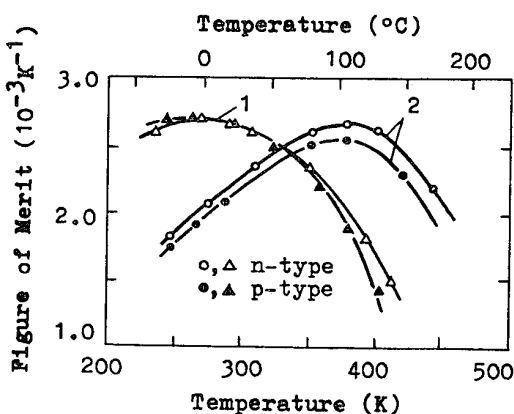
The value  $Q_e$  obtained in such a way for  $T_o = 40$  °C,  $T_e = 120$  °C was 1.73 W and hence the total heat load  $Q_o$  with the laser's heat dissipation 0.2 W taken into account equals 1.93 W.

### Thermoelectric materials

It is impossible to calculate exactly the TE cooler parameters without the knowledge of temperature dependence of semiconductor materials thermoelectric properties in the temperature range under consideration.

For the TCD on borehole temperature to 120 °C were chosen semiconductor materials obtained by extrusion method. Its figure of merit  $Z$ , calculated by the results of kinetic coefficients measurements in the temperature range from 0 to 150 °C is given in Figure 3 (relationships 1). It is seen that materials of both types of

Fig. 3 Temperature dependence of thermoelectric figure of merit for extruded TE materials (1) and Czochralski grown single crystals (2).



conductivity have thermoelectric efficiency high enough at temperatures up to 100 °C. However, at higher temperatures their thermoelectric figure of merit drops sharply, indicating that the ambipolar diffusion becomes rather significant.

### TE cooler optimization

The above mentioned results of preliminary researches together with specified temperature conditions give a complete set of input data for the cooler optimization. The operation with maximum COP, which corresponds to the minimum heat sink superheating, is chosen as a design condition. The optimization was carried out using the technique described in works [3-5]. There were used experimental data on the temperature dependence of kinetic coefficients for extruded semiconductor materials. According to the calculations for one-cascade version the necessary power exceeds 22 W, which is not acceptable considering specified heat removal limitation. In this connection a two-cascade construction of a cooler was accepted. Its design characteristics (Table 1) provide the attainment of the specified operating conditions ( $T_o = 40$  °C at  $T_e = 120$  °C,  $Q_o = 2$  W,  $R_h = 0.4$  K/W) with minimum power consumption.

Table 1. Design characteristics of TE cooler for TCD on borehole temperature 120 °C

Parameter	numerical value
Number of thermoelectric legs:	
high-temperature cascade	236
low-temperature cascade	112
Dimensions of TE legs, mm:	
cross section	0.6x0.6
height	0.8
Optimal current, A	0.8
Voltage, V	13.9

### Technology

Theoretical optimization and reasonable designing alone do not solve the problem of developing a TCD for extreme temperature conditions. The decisive factor is the technical possibility to realize adopted design which supposes efficient technology availability.

Technical characteristics of TE cooler must correspond to conditions of its operation. To avoid the damage of the cooler the melting temperature of solders used must be considerably higher than the specified heat sink temperature. TE leg junctions must be protected from the penetration of a commutation material. The cooler's parameters should not vary considerably under the conditions of long operation at high temperatures.

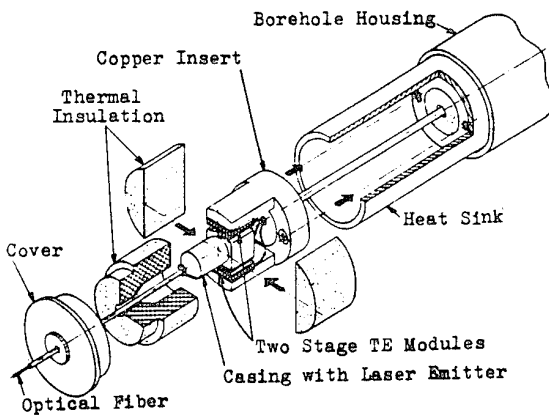
The technology of TE legs commutation providing stable reproduction of contact resistance at the level of  $(1-2) \cdot 10^{-6} \Omega \cdot \text{cm}^2$  was developed. It allows one to use relatively short TE legs with increased cooling capacity without a significant reduction of the attainable temperature difference. At the same time the antidiiffusion protection of contacts and possibility to use a wide variety of standard solders are provided.

In making cascade coolers the solder with melting point of 240 °C was used. Coolers were soldered to other parts of the TCD construction with the help of tin-lead solder, so the safe operation of the assembly was provided up to the temperature of 180 °C.

### TCD construction

The TCD construction is given in Figure 4. The main parts of TCD are the TE cooler, the casing with a laser emitter, the heat sink and the thermal insulation.

Fig. 4 TCD construction



The TE cooler is made of two similar two-cascade modules MK 118-56(0.8), placed symmetrically on both sides of the laser's casing. Their construction characteristics are given below:

hot side dimensions, mm	-	12x12
cold side dimensions, mm	-	8x8
height, mm	-	3.8
number of TE legs in cascades	-	118 and 56.

The modules are collected into a single unit with the help of a cylindrical copper insert. A borehole device contains a set of ten TCDs installed coaxially in the single cylindrical housing.

### Test results

Ten TCD samples for thermostating semiconductor laser emitters ILPN 203-1 are made on the basis of developed cooling modules. When testing the samples were installed in a borehole device model whose temperature was kept by a thermostat at the level of 120 °C.

Experimental results are given in Table 2. Calculated data are given ibidem for comparison.

Table 2. Comparison of calculated parameters with test results

TCD Parameter	Calculated value	Experimental values range for ten samples
Housing temperature, °C	120	120
Laser temperature, °C	40	40
Heat sink temperature, °C	124.6	124 - 127
Optimal current, A	0.8	0.78 - 0.80
Voltage, V	13.9	14.0 - 14.6
Power, W	11.1	10.9 - 11.7

It is seen that the accepted method of research provides practically complete coincidence of theoretical prediction with experimental results.

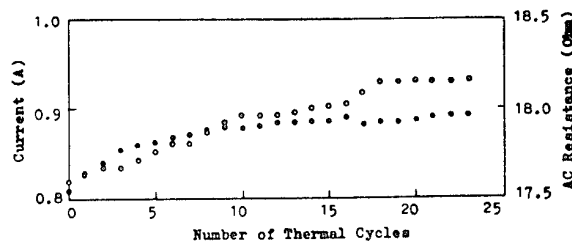
The most important characteristic of a borehole device is reliability and stability of its parameters. In this connection safe operation tests of the TCD in the housing of the borehole device were undertaken at  $T_e = 120$  °C.

Tests were carried out in thermal cycling mode by turning TE cooler on and off (16 hour's operation, 8 hour's interval). There were 23 cycles in all with total duration of 558 hours, out of them 368 hours of running.

By the end of safe operation tests the TCD retained the serviceability and its parameters met the specified requirements. However, during the whole period of testing a slight drift of cooler's parameters was observed (Figure 5). Electrical resistance increased insignificantly (not more than by 2%). For all that the greatest rate

Fig. 5 The change of TE cooler parameters when testing in thermal cycle operation:

- - AC resistance;
- - Current needed to maintain the laser at 40 °C.



of increasing took place in the first ten cycles, later on the cooler's resistance remained practically unchanged. A sharper increase (by 15%) was observed for the feed current, which is necessary to maintain the laser specified temperature  $T_o = 40$  °C.

### Operation at higher temperatures

Two reasons hinder one to develop a TCD on higher temperatures: heat load on the cooler increases and at the same time its thermoelectric characteristics become worse. The temperature level of 120 °C is critical for extruded materials used in the present work. The further temperature increase causes a sharp reduction of their thermoelectric efficiency, indicating that the material is becoming intrinsic. As a result the thermal conductivity increases considerably due to ambipolar diffusion, thermo-EMF decreases and hence thermoelectric figure of merit reduces catastrophically.

In this connection Czochralski grown single crystals of solid solutions of Bi and Sb chalcogenides with Z parameter maximum shifted to about 100 °C (Figure 3, relationships 2) were used to develop TCD on extremely high temperatures.

As it was in the previous case, the cooler is made in the form of two similar two-cascade modules, each one containing 52 TE legs in the low-temperature cascade and 118 legs in the high-temperature cascade. Due to higher electrical conductivity the TE leg optimal height becomes 1.5 mm. As for the rest, the TCD construction is quite identical to the previous variant.

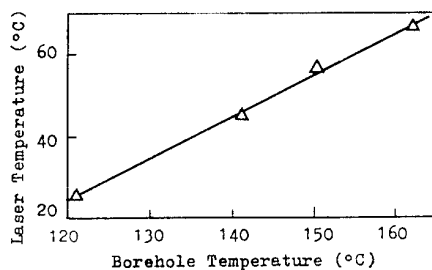
Testing results are given in Figure 6 in the form of  $T_o$  on  $T_e$  dependence. It is seen that the condition  $T_o < 40$  °C is valid up to  $T_e = 135$  °C. If the light-emitting diode ILPN 301-1, retaining serviceability at  $T_o = 60$  °C, is used instead of the laser emitter, the device operation is possible at borehole temperatures up to 155 °C.

Fig. 6 Dependence of the laser temperature on the borehole temperature when using TE cooler on single crystals

[3]. V.A.Semeniouk, Kaskadny termoelektrichesky okhладitel kak objekt optimalnogo upravleniya, Dep. v VINITI 30.03.84, No 1790-84, Dep. Annotatsiya V IFZh, 1984, v.47, No 2, pp.333-334.

[4]. V.A.Semeniouk, Nekotoriye obobscheniya teorii optimizatsii kaskadnikh termoelektricheskikh okhладiteley, IFZh, 1984, v.47, No.6, pp.977-988.

[5]. L.I.Anatychuk, V.A.Semeniouk, Optimalnoe upravlenie svoistvami termoelektricheskikh materialov i priborov, Chernovtsi, 1992, 264 p.



### Summary

The use of TE cooling provide safe operation of semiconductor lasers under extreme temperature conditions, in particular, when working-up deep boreholes of the Earth.

Particular difficulties of TCD development for such uses are caused by the necessity to build them into the standard housing of the borehole device. It defines an increased heat load on the cooler with rigid restrictions of its dimensions.

The attainable depth of cooling depends on the TE quality of applied semiconductor materials. When extruded materials are used it is possible to maintain the laser temperature at the level of 40 °C at the borehole temperature of 120 °C. The use of single crystals of solid solutions of bismuth and antimony chalcogenides optimally doped for the temperature level of about 100 °C makes it possible to raise this limit to 135 °C. For light-emitting diodes retaining their serviceability at  $T_o=60$  °C the device operation is possible at borehole temperatures up to 155 °C.

To provide acceptable resource of TCD operation at increased temperatures it is necessary to combine antidiffusion protection of contacts and the use of high-temperature solders. The developed technology provides thermal stability of coolers up to 240 °C and the stable reproduction of contact resistance at the level of  $(1-2) \cdot 10^{-6} \Omega \cdot \text{cm}^2$ .

### Acknowledgements

This work was carried out under a contract with the SKAIDULA joint-stock company. The authors would like to thank all the people that have been involved in the contract. We are also grateful to Drs. T.E. Svechnikova and L.D.Ivanova of the CRYSTALLIT Ltd. for supplying single crystals of solid solutions of Bi and Sb chalcogenides.

### References

- [1]. A.M.Lisenkova, I.S.Manek, Teplovoy rezhim raboty inzhektionnykh laserov (po dannym sovetskoy i zarubezhnoy pechati za 1968-1989 god) *Obzor po elektron tekhn.*, Ser 11, 1990, No.16, pp.1-55.
- [2] S.S.Kutateladze, Osnovy teorii teploobmena, Novosibirsk, 1970. 660 p.

# A NOVEL THERMALLY - DRIVEN THERMOELECTRIC HEAT PUMP

Yuji Nakahara, Atsushi Tsutsumi and Kunio Yoshida

*Department of Chemical System Engineering, The University of Tokyo, Tokyo 113, Japan*

A novel concept of a thermally-driven heat pump consisting of a combination of two different thermoelectric devices has been proposed. One thermoelectric device generates electricity from waste heat, the current thus generated being used by the other device to pump heat. The system of a thermally-driven thermoelectric heat pump has a simple structure and is compact because there is no need to integrate thermoelectric elements. The design and simulation of a car air-conditioning system using a thermally-driven thermoelectric heat pump have been carried out. To optimize the power density and energy efficiency, a new guideline for developing thermoelectric materials has been derived based on the heat transfer resistance. It has been found that the key to improving the output power density of thermoelectric device is to reduce the thermal conductivity.

## Introduction

Heat pumps, which can transform heat at low temperature to a higher temperature has aroused much interest because of its great potential for saving energy in industry. Practical heat pumps using thermoelectric devices are built with a number of elements in series electrically and in series and parallel thermally. Compared with conventional mechanical and chemical heat pumps, a thermoelectric heat pump made from the junction between n-type and p-type semiconductors has significant advantages:

- it is noiseless
- it is maintenance free
- it can be designed for a wide range of temperature by using appropriate combination of materials

However, there are several disadvantages including low conversion efficiency and high production cost. The high production cost is due to the complicated serial connections of the p-n junctions that enable the device to operate at a useful voltage and current. It is necessary to develop a system that can compensate for these disadvantages and be marketed commercially.

Here, a new thermoelectric heat pump concept is proposed, which is driven only by waste heat. The outline of the system is shown in Fig. 1. The system is a combination of two different thermoelectric devices. One thermoelectric device is used as a thermoelectric generator, which converts the waste heat into electricity. By introducing the generated DC electricity into the other thermoelectric device, heat can be pumped up from a low temperature source to a higher temperature and used for heating or cooling.

Since this system is driven by waste heat, the conversion efficiency of the system is not as important as if it were driven by

valuable energy. For a thermally-driven heat pump system, high output power density and compactness would be more important than the conversion efficiency. In a thermally-driven thermoelectric heat pump, the output power generated by one thermoelectric device is directly introduced into the other device. Therefore, there is no need to increase the voltage by serially connecting the p-n junctions. A simple layer of p-type or n-type thermoelectric material can be used as a generator device or heat pump device. This leads to a simple structure and compactness using an innovative yet inexpensive process of thermoelectrical material production.

For mechanical heat pump systems, the temperature in the condenser and the evaporator is constant. On the other hand, in thermoelectric heat pump systems the temperature decreases along the exothermic side of the thermoelectric film and increases along the endothermic side as shown in Fig. 2. This leads to relatively higher COP.

In addition, the heat source temperature which can be recovered by a mechanical heat pump depends on the boiling temperature of the working fluid. Therefore multi-stage arrangements which have different operating temperatures are required to utilize the waste heat over a wide range of temperature. On the other hand, thermoelectric heat pump systems can take advantage of the cascade utilization of waste heat because thermoelectric materials function over a wide temperature range.

In this paper, a conceptual design and simulation of a thermally-driven thermoelectric heat pump for a car air-conditioning system using commercial thermoelectric devices was carried out. The performance of thermoelectric devices for thermally-driven thermoelectric heat pumps considering film heat resistance between the heat source and device surface was then studied.

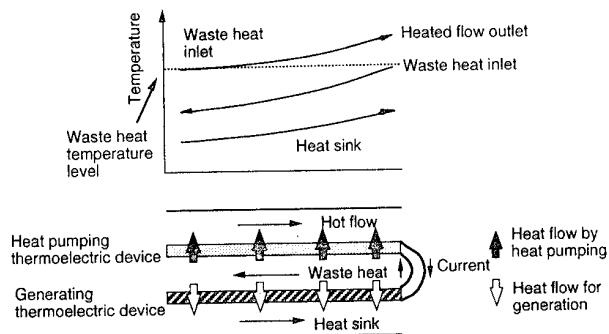


Figure 1 Conceptual diagram of a thermally-driven thermoelectric heat pump.

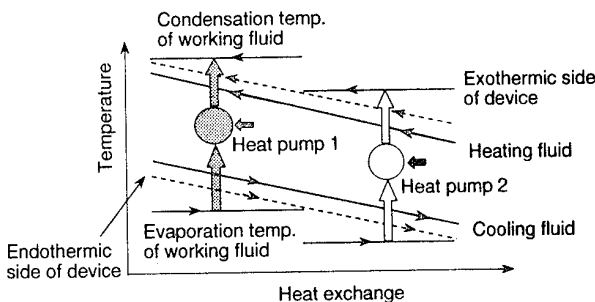


Figure 2 Temperature variation in a system of two-stage mechanical heat pumps and thermoelectric heat pumps.

### Car Air-Conditioning System

A thermoelectric heat pump for a car air cooling system driven by engine heat was simulated. The cooling load was designed to be 4kW, with a refrigerant temperature from 12°C to 7°C and a cooling water heat sink temperature of 47°C at the inlet. The engine exhaust temperature was assumed to a constant 530°C.

The schematic diagram of the system is shown in Fig. 3. Electricity is generated between the exhaust's high temperature and the cooling water by the generating module. This DC electricity is introduced into the cooling thermoelectric module which cools the refrigerant from 12°C to 7°C. The cooling water flows through the cooling module, then through the generating module, and is subsequently pumped back to the radiator.

The physical properties of the commercial thermoelectric device (FUJITAKA, TECI-12703) used for both generating modules and cooling modules are shown in Table 1.

The cross section of the duct for the heat source fluid was designed to be a rectangle 10mm x 50mm. For simplicity, the heat source fluid was assumed to be water, with a flow rate of 300 mL/s. The heat transfer coefficient was calculated as approximately 2000 W/K m<sup>2</sup> [1]. The simulation was carried out so that the thermal efficiency (ratio of cooling heat to inlet exhaust heat) would be maximized.

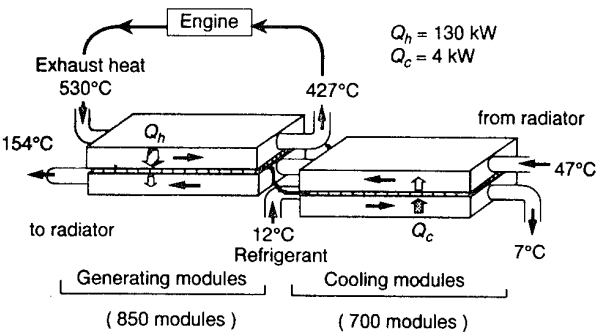


Figure 3 Car Air-Conditioning System using a thermally-driven thermoelectric heat pump.

Table 1 Physical properties of the device

Seebeck coefficient, $\alpha$	200 $\mu\text{V/K}$
Conductivity, $\sigma$	$1 \times 10^5 \text{ S/m}$
Thermal conductivity, $\kappa$	1.5 W/m K
Figure of merit, $Z$	0.0026 K <sup>-1</sup>

Table 2 Simulation results

Generation module	850 modules
Heat input (exhaust), $Q_h$	130 kW
Generated electricity, $P_g$	13 kW
Generation efficiency, $P_g / Q_h$	0.10
Heat transfer area, $A$	1.36 m <sup>2</sup>
Size .	40 cm x 40 cm x 26 cm
Cooling module	700 modules
Heat pump efficiency, $Q_c / P_g$	0.31
Heat transfer area, $A$	1.12 m <sup>2</sup>
Size	40 cm x 40 cm x 21 cm

The thickness of each module is 30 mm.

The results are shown in Table 2. The total thermal efficiency was  $\eta = 0.031$ . The size of the system designed was approximately a 50 cm cube, which is feasible.

### Theoretical Analysis of a Thermoelectric Device Considering Film Heat Resistance

Figure 4 shows the temperature profile of a thermoelectric device considering film heat resistance. Assuming that the heat transfer coefficient  $h$  is the same on both hot and cold sides of the thermoelectric device, the heat transfer rate across the surface of each side can be written as

$$Q_h = A h (T_h - T_{hj}) = \alpha T_{hj} I - \frac{rI^2}{2} + K \Delta T_j \quad (1)$$

$$Q_c = A h (T_{cj} - T_c) = \alpha T_{cj} I + \frac{rI^2}{2} + K \Delta T_j \quad (2)$$

By obtaining  $T_{hj}$  and  $T_{cj}$  from Eqs. 1 and 2, the temperature difference across the two sides of the thermoelectric device can be shown as

$$\Delta T_j = T_{hj} - T_{cj} = \frac{-(A h)^2 \Delta T + 2 A h \alpha I T_m + \alpha r I^3}{\alpha^2 I^2 - (A h)^2 - 2 A h K} \quad (3)$$

Assuming that the square of the dimensionless component  $(\frac{\alpha I}{A h})$  is

negligible because  $(\frac{\alpha I}{A h}) \ll 1$ , Eq. 3 is reduced to

$$\Delta T_j = \frac{\Delta T - 2 T_m (\frac{\alpha I}{A h})}{1 + 2 \frac{K}{A h}} \quad (4)$$

The power output is given by

$$P_g = Q_h - Q_c = \alpha \Delta T_j I - r I^2 \quad (5)$$

Substituting Eq. 4 into Eq. 5 gives

$$P_g = \frac{\alpha \Delta T I - J r I^2}{n} \quad (6)$$

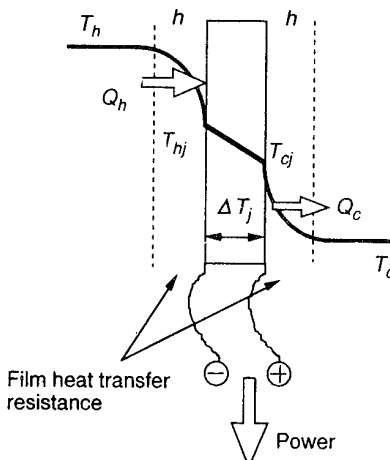


Figure 4 Heat flow and temperature profile considering film heat transfer resistance.

where

$$n = 1 + 2 \frac{\kappa}{L h}$$

$$J = 2 \kappa \frac{T_m Z + 1}{L h} + 1$$

Considering that  $P_g$  is a function of only  $I$ ,  $P_g$  has a maximum of

$$P_{g(\max)} = \frac{\Delta T^2}{4} \frac{A}{L} \frac{Z}{\left(1 + 2 \frac{\kappa}{L h}\right) \left(2 \frac{T_m Z + 1}{L h} + 1\right)} \quad (7)$$

To maximize the value of  $P_g$ , it is required to minimize component

$$L \left(1 + 2 \frac{\kappa}{L h}\right) \left(2 \frac{T_m Z + 1}{L h} + 1\right)$$

Taking  $L$  as a variable, this component can be minimized when  $L$  is

$$L_{opt} = 2 \frac{\kappa}{h} \sqrt{1 + T_m \frac{\alpha^2}{\kappa}} \quad (8)$$

Thus, there is an optimum device thickness to maximize the output power density. The optimum thickness is found to be proportional to the thermal conductivity and inversely proportional to the heat transfer coefficient.

From the point of view of material conservation and making the system light, it is desirable to make the thermoelectric device thin. Therefore, because  $Z$  is nearly constant, it is essential for the proper design of the thermoelectric heat pump to use thermoelectric materials with low thermal conductivity.

#### Measurements of $L_{opt}$

To confirm the validity of Eq. 8, maximum output power of a thermoelectric device was measured. Four p-type Si-Ge thermoelectric devices (9 mm x 10 mm) of 0.9, 1.1, 3 and 6 mm thickness were used. The thermoelectric properties are listed in Table 3.

The experimental apparatus is shown in Fig. 5. In/Ga alloy was applied to each side of the device and connected to a copper rod

Table 3 Thermoelectric properties of thermoelectric

Seebeck coefficient, $\alpha$	$140 \times 10^{-6}$ V/K
Conductivity, $\sigma$	$4.7 \times 10^4$ S/m
Thermal conductivity, $\kappa$	5.0 W/m K
Figure of merit, $Z$	$1.2 \times 10^{-3}$ K <sup>-1</sup>

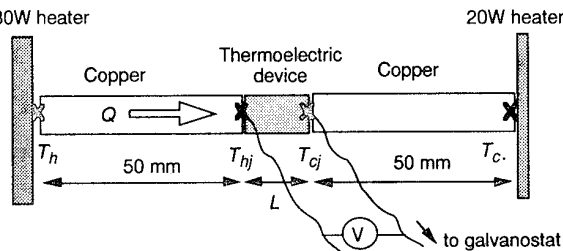


Figure 5 Experimental apparatus.

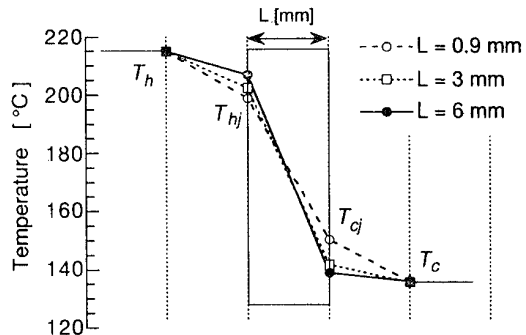


Figure 6 Temperature profile of thermoelectric device.

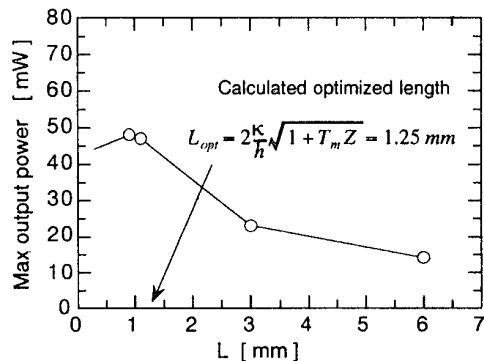


Figure 7 Maximum output power against device length.

of 10 mm OD and 50 mm in length. A plate heater was placed against each rod, and the temperature between the rod and heater was controlled to be constant by a CA thermocouple and temperature controller. Maintaining the hot and cold sides at  $T_h$  and  $T_c$ , respectively, the power output of the device was obtained from the voltage drop in the thermoelectric device measured galvanostatically using a galvanostat. The maximum power output was obtained by changing the current.

Figure 6 shows the result of the temperature profile. It can be seen that the temperature difference between each side of the thermoelectric device increases with increasing thickness of the device. The maximum output power was plotted against the thickness in Fig. 7. It can be seen that the maximum output power was maximum at the calculated optimized thermoelectric device thickness.

#### Theoretical Analysis of Conversion Efficiency

The conversion efficiency was calculated by considering the heat transfer resistance. For the sake of simplicity, it is assumed that the temperature difference on each side of the thermoelectric device was the same:

$$T_h - Thj = Tcj - Tc$$

$Thj$  can be then written as

$$Thj = T_c + \frac{1}{2}(\Delta T - \Delta T_j) = T_m - \frac{1}{2}\Delta T_j \quad (9)$$

The conversion efficiency can be defined as

$$\eta = \frac{P_g}{Q_h}$$

By substituting Eq. 9 into Eq. 1, combination of Eqs. 1 and 5 gives

$$\eta = \frac{P_g}{Q_h} = \frac{\alpha \Delta T I - J r I^2}{\alpha T_h I - J \frac{r I^2}{2} + K \Delta T} \quad (10)$$

By taking  $I$  as a variable, the maximum conversion efficiency is obtained as

$$\eta_{(\max)} = \frac{\Delta T}{T_h} \left( 1 - \frac{2T_m}{T_h \sqrt{1 + T_m Z / J + T_c}} \right) \quad (11)$$

Since  $Z/J$  is the only parameter other than temperature, a new figure of merit can be defined by

$$Z' = Z / J = \frac{\alpha^2 h}{\kappa \rho \left( 2 \frac{\kappa}{L} (T_m Z + 1) + h \right)} \quad (12)$$

For conventional thermoelectric devices the value of  $T_m Z$  can be assumed to be 1. Hence, Eq. 12 is reduced to

$$Z' = \frac{\alpha^2 h}{4 \kappa \rho \left( \frac{\kappa}{L} + \frac{h}{4} \right)} \quad (13)$$

For small  $L$ , Eq. 13 can be reduced to

$$Z' = \frac{\alpha^2 L h}{4 \kappa^2 \rho} \quad (14)$$

Thus,  $Z'$  is inversely proportional to  $\kappa^2$ . This means that the performance of thin thermoelectric device depends significantly on the value of  $\kappa$ .

## Conclusions

A new concept of a thermally-driven thermoelectric heat pump has been proposed, which is a combination of two different thermoelectric devices. One device is used as a thermoelectric generator, which converts the waste heat into electricity. By introducing the generated DC electricity into the other thermoelectric device, heat can be pumped up from a low temperature source to a higher temperature. Since there is no need to increase the voltage by serially connecting the p-type and n-type thermoelectric materials, the production cost can be low, which has hitherto been one of the major barriers against commercial marketing of a thermoelectric device.

Design and simulation for a car air-conditioning system using a thermally-driven thermoelectric heat pump was carried out in this study. It was estimated that a compact thermoelectric heat pump system of 50 cm cube could produce 4kW of cooling.

To optimize the power density and energy efficiency, a new guideline toward developing thermoelectric materials was derived based on the heat transfer resistance between the heat source and the thermoelectric device. It was found that the optimum thickness of a thermoelectric device is proportional to the thermal conductivity. This indicates that if a thin device is used in order to minimize the quantity of device material and make the device light, low thermal conductivity is desirable.

Regarding the conversion efficiency, a new figure of merit was introduced, which is inversely proportional to the square of thermal conductivity when designing the device under 1mm thick. The decrease in thermal conductivity has more influence than when film heat resistance between the heat source and device surface is not

considered. The key to utilizing this thermally-driven thermoelectric heat pump is to develop a inexpensive process that can produce low thermal conductivity thermoelectric materials.

## Acknowledgment

The authors acknowledge Professor K. Koumoto of Nagoya University and Professor K. Matsuzawa of Osaka University for their helpful discussions. The authors wish to thank NGK Insulators, Ltd. for their kind supply of Si-Ge thermoelectric devices.

## Nomenclature

$A$	device area, m <sup>2</sup>
$h$	heat transfer coefficient, W/K m <sup>2</sup>
$I$	current, A
$J$	parameter in Eq. 6
$K$	thermal conductance ( $= \kappa A/L$ ), W/K
$L$	device thickness, m
$L_{opt}$	optimum device thickness, m
$n$	parameter in Eq. 6
$P_g$	power output, W
$Q_c$	exothermic heat on cool side surface, W
$Q_h$	endothermic heat on hot side surface, W
$r$	resistance ( $= \rho L/A$ ), Ω/m <sup>2</sup>
$T_c$	Cool heat source temperature, K
$T_h$	Hot heat source temperature, K
$T_{cj}$	Cool side surface temperature, K
$T_{hj}$	Hot side surface temperature, K
$T_m$	average temperature of $T_h$ and $T_c$ , K
$T_{mj}$	average temperature of $T_{hj}$ and $T_{cj}$ , K
$Z$	Figure of merit ( $= \alpha^2 / \rho \kappa$ ), K <sup>-1</sup>
$Z'$	Figure of merit considering film heat resistance, K <sup>-1</sup>

## Greek symbols

$\alpha$	Seebeck coefficient, V/K
$\Delta T$	temperature difference of hot and cool heat source ( $= T_h - T_c$ ), K
$\Delta T_j$	temperature difference of hot and cool side of device ( $= T_{hj} - T_{cj}$ ), K
$\kappa$	thermal conductivity, W/K m
$\rho$	resistivity, Ω m
$\eta$	thermoelectric conversion efficiency ( $= P_g / Q_h$ ), -

## References

- [1] Kagakukougaku Kyousai, Kagakukougaku Binran, Tokyo, Japan, 1988, 334p.

# Thermoelectric regulation for electric cabinets

J.M. Redondo, J.M. Sanchez\*, I. Pascual\* & G. Noriega

*G.D.F. Departament de Física Aplicada. Universitat Politècnica de Catalunya. Barcelona.*

*\* BEROTZA, Pamplona, Navarra, Spain.*

We describe industrial applications of thermoelectric cooling using a numerical model of thermoelectric calculations for complex systems. The study of a thermoelectric system depends non-linearly on the heat transfer properties of both the hot and cold side, for example the efficiency of the Thermoelectric cells is highly dependent on the temperature gradients across the module. The effect of both internal and external turbulence on the heat exchangers has to be studied with care if a good design is to be developed. An example of practical applications are also presented, comparing the numerical predictions and the experimental behaviour of the prototype.

One of the main conclusions is that providing an optimal thermal balance on the hot side heavily outweighs increasing the number or power of thermoelectric modules in most applications.

## 1. Introduction

In the design of complex thermoelectric applications, it is very useful to have a detailed knowledge of the behaviour of the system before actually building a prototype. With this aim in view a series of computer programs have been coupled so as to give an interactive system of analysis.

The program works under an extensive menu of applications, ranging from the very simple, predesign of the thermoelectric application, to the more complex thermodynamic and hydrodynamic programs, which predict the temperature fields under different boundary conditions.

The main modules of the program, which takes advantage of the interactive capabilities of MCAD, using a symbolic algebraic system are: Predesign of system, including heat balance and design limitations. Calculation of effective power of Thermoelectric cells and minimum number of modules. Full iterative design of Conductive, Convective and Radiative heat losses. Calculations of Electric parameters for maximum C.O.P. and maximum cooling and Calculations of optimum insulation.

In the final stages of the design of the hot and cold heat exchangers, a more complicated program is used to investigate the following aspects: Transient behaviour. Effects of buoyancy and thermal equilibrium and Thermal control and stability. This has been used to design the standard TE forced air heat pump for electric cabinets, Figure 1.

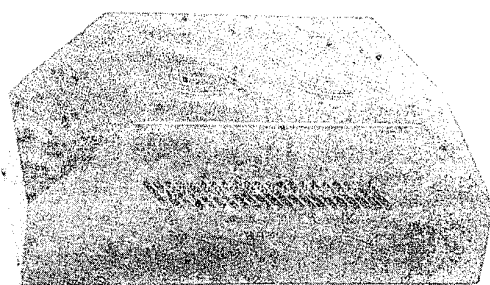


Figure 1:

In section 2 we show the capabilities of the model and in section 3 some details of the hydrodynamic codes are given. Some experimental results are given and finally the discussion

and conclusions are drawn.

## 2. Heat transfer modules used in the numerical model

For a detailed analysis of the heat exchanges in the application, which in turn will be used to estimate the number of TEC's needed in the application the Conduction, Convection and Radiative losses have to be calculated. In convection the following relation is used:  $Q = hA\Delta T$  where  $h$  is the *convective heat transfer coefficient* and  $A$  the area of exchange. The Nusselt number,  $Nu$ , relates the thermal loss by convection from a wall to the conductive losses by the same material across a length  $L$  so that the unit area flux is  $Q = h\Delta T$ , and  $Nu = \frac{hL}{\kappa}$ . The Stanton number determines the vertical heat flux at a fluid of specific heat  $c_p$  flowing at a speed  $v$  parallel to the wall with a difference of temperature  $\Delta T$ .  $St = \frac{q}{\rho c_p v \Delta T}$ .

The Prandtl number is:  $Pr = \nu/\kappa$  and  $Nu = Re \cdot St \cdot Pr$ . Grashof number is similar to Rayleigh's,

$$Gr = \frac{g\beta\Delta TL^3}{\nu^2}$$

and  $Gr = \frac{Ra}{Pr}$ .

Some of the empirical relationships used in the program are: For forced convection in a turbulent flow ( $Re \gg >$ )

$$Nu = 0.023Re^{0.8}Pr^{0.4}$$

For Laminar convection in tubes of diameter  $D$  and length  $L$

$$Nu = 1.62(RePr\frac{D}{L})^{1/3}$$

For Natural convection on a vertical wall:

$$Nu = 0.52Gr^{1/4}Pr^{1/4}$$

and for turbulent natural convection in gases ( $Re \gg >$ ):

$$Nu = 0.12Gr^{1/3}Pr^{1/3}$$

Radiation and Conduction losses are also calculated in a standard way Isachenko et. al (1979).

## 3. Cooling and energy conversion with thermoelectronic devices

Thermoelectric devices, developed since Seebeck and Peltier effects were discovered in 1822 and 1834, the advances of technology that make feasible the commercial uses of thermoelectric cooling has taken a long time. Some technical and

scientifical applications of thermoelectric cooling will be discussed below, for further references see De Groot(1968), Rowe and Bandary (1984). Thermoelectronic cooling has been feasible for many practical applications since the studies of Telkes in the 30's and of Ioffe in 1956, The new semiconductor materials allowed much higher efficiencies. Telkes used couples of PbS y ZnSb and Ioffe discovered the use of of PbTe y PbSe. Higher efficiencies are obtained with semiconductores of the n-type of PbTe and p-type BiTe-SbTe.

In a practical thermoelectric design, after the thermal loads have been calculated, the optimum Intensities and voltages may be found using the local heat balances between both sides of the TEC. The heat produced on the hot side  $p$  is  $Q_1^p = S T_1 I$  where  $T_1$  is the hot side temperature,  $S$  the Seebeck coefficient and  $I$  is the intensity of the electrical current.

Conversely the heat absorbed at the cold side is:  $Q_2 = S T_2 I$ , where  $T_2$  is the cold side temperature.

Assuming that Joule heating flows equally to both sides of the TEC, it can be written as:  $Q_j = 0.5 I^2 R$ , where  $R$  is the resistance of the semiconductors. The loss of heat by conduction across the TEC is:  $Q_c = \kappa (T_1 - T_2)$ , where  $\kappa$  is the thermal conductivity of the n and p materials taking account of the length and area.

The absorbed heat at the cold side is then:  $Q_{net} = Q_2^p - Q_j - Q_c$  and the hot side produced heat is:  $Q_d = Q_1^p + Q_j - Q_c$ . The electrical power, by the 1st Thermodynamic law must be then:  $P = Q_d - Q_{net} = S(T_1 - T_2) + I^2 R$

There are two basic ways of TEC behaviour, whithin a system, a) maximum heat transfer and b) maximum COP (Coeficient of Performance). The first way may be found by derivativing with respect to  $I$  and equating to zero, thus  $I_{max} = \frac{S T_e}{R}$ . The maximum temperature difference may be found substituting  $I_{max}$  in the expression of the net heat production.

$$\Delta T_{max} = (T_1 - T_2)_{max} = \frac{0.5 S^2 T_e^2}{R \kappa}.$$

The figure of merit is defined as:  $Z = \frac{S^2}{R \kappa}$ . For a system to work at maximum Coeficient of Performance, COP, it is necessary to maximize the rate between the net transported heat and the electric power.  $COP = \frac{Q_{net}}{P}$  which may be written as:

$$COP = \frac{S T_2 I - 0.5 R I^2 - \kappa (T_1 - T_2)}{R I^2 + S (T_1 - T_2)}.$$

We find  $COP_{max}$ , diferenciating with respect to the intensity, and equating to zero, this maximum corresponds to the intensity  $I_{cop}$  that may be expressed as  $I_{cop} = \frac{\kappa (T_1 - T_2)}{0.5 S (T_1 + T_2)} \cdot [(1 + 0.5 Z (T_1 + T_2))^{1/2} + 1]$ . Using  $I_{cop}$ , in the expresion of the COP, we find

$$COP_{max} = \frac{[1 + 0.5 Z (T_1 + T_2)]^{1/2} - T_1 / T_2}{[1 + 0.5 Z (T_1 + T_2)]^{1/2} + 1} \cdot \frac{T_2}{T_1 - T_2}.$$

This calculations are important for the correct design of a thermoelectric system, which may be ajusted to work either at maximum COP or at maximum cooling. The adjustment of working intensity depends on the use of the application. see Dominguez, et.al (1989,1991)

A detailed study of the transients is difficult, even in simplified models of the TEC, constant average properties of the modules, have to be obtained from the manufacturers, such as conductivities and resistances, they also vary with temperature. If we assume a constant temperature throughout the TEC, the basic differential equation is  $mc \frac{dT}{dt} = Q - Q_{net}$  where  $T$  is temperature,  $t$  is time,  $Q$  external heat and  $Q_C$

the heat pumped by the TEC,  $m$  the mass of the TEC and  $c$  the average especific heat of the TEC. Then

$$mc \frac{dT}{dt} = Q - (STI - \frac{1}{2} I^2 R - \kappa \Delta T)$$

Simplifying and separating the variables we may express the equation as

$$\frac{dT}{T - T_c} = \frac{SI + \kappa}{mc} dt$$

and integrating obtain

$$T = (T_0 - T_c) e^{-\frac{SI+\kappa}{mc} t} + T_c$$

The term  $\frac{mc}{SI+\kappa}$  is often called temporal constant, but we have to note that all terms are temperature dependent and will have fixed values only at fixed points at selected temperatures. The equations for the hot side temperature may be obtained in the same way. The temperature at estacionary state  $T_e$  is given by:

$$T_e = \frac{-Q_h + Q_j + \kappa \Delta T}{SI + \kappa} + T_c$$

and the transient temperature is

$$T = T_e (T_e - T_c) e^{-\frac{SI+\kappa}{mc} t} + T_c$$

All these ecuations are programmed in a TEC optimisation subroutine that may be used after the external heat balance has been calculated from the hydrodynamic and heat transfer modules of the program.

#### 4. Hydrodynamic calculations used in the numerical model

In order to acurately calculate the heat exchange under convective proceses in both the hot and cold sides of the TEC, more complicated finite difference programs may be used. The programs are written in FORTRAN which may be compiled in a PC, but for good grid resolution a larger computer, such as a VAX is needed. The most complicated heat transfer processes take place when buoyancy effects are important, and then it is usefull to define the Richardson number  $Ri = \frac{g \Delta \rho l}{\rho u'^2}$ , where  $g$  is la gravity,  $\Delta \rho$  the driving density difference,  $\rho$  the average density of the fluid,  $l$ , the integral scale of the turbulence and  $u'$  the r.m.s. velocity produced by turbulence. Other parameters described above are also important. next a brief description of the code, based in Rees(1987), Isachenko et.al(1979) is made. The detailed flow numerical model used in convective turbulent environments is Large Eddy Simulation (LES), where the Boussinesq time dependent equations are integrated in a twodimensional grid, as an example we show the u component equation:

$$\frac{\partial u}{\partial t} + u \frac{\partial u}{\partial x} + w \frac{\partial u}{\partial z} = - \frac{\partial p}{\partial x} + 2 \frac{\partial}{\partial x} \left( \nu \frac{\partial u}{\partial x} \right) + \frac{\partial}{\partial z} \left( \nu \frac{\partial u}{\partial z} + \nu \frac{\partial w}{\partial x} \right).$$

#### 5. Examples and Discussion

We have seen the various modules of Thermodynamics, Thermoelectricity and fluid dynamics, all of which define a complex application. For a set TEC, the limiting factors are due to heat exchange processes in the Hot and cold sides of the system. Turbulent flows are clearly more efficient, and a good preliminary knowledge of the flows is important. The effect of both internal and external turbulence on the heat exchangers has to be studied with care if a good design is to be developed. The thermal differences in the system due to buoyancy also need to be taken into account. The experiments were done

using an array of micro-temperature probes with a transversing mechanism that allows to calculate the evolution of the thermal profiles. In Figure 2 Hot side, cold side and ambient temperatures are shown. The study of a thermoelectric sys-

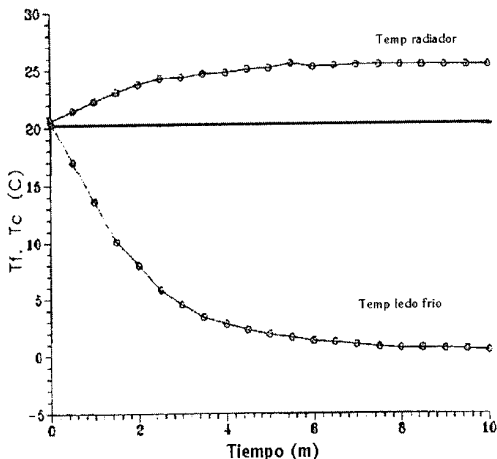


Figure 2:

tem depends non-linearly on the heat transfer properties of both the hot and cold side, for example the efficiency of the Thermoelectric cells is highly dependent on the temperature gradients across the module. For a large scale electric cabinet working at a power of 100 W in 25 °C ambient temperature, stable temperature of 18 °C is obtained after about 1000 s. see Figure 3 for the evolution of inner and outer fan temperatures of the cooler shown in Figure 1.

## 6. Conclusions

Providing an optimal thermal balance on the hot side heavily outweighs increasing the number or power of thermoelectric modules in most applications. Thermal control adjusting the flow characteristics of the hot side greatly simplifies most prototypes if the thermal control accuracy does not need to be better than 0.2 °C. A Predictive Integrative Derivative OMRON temperature controller was used to control the fan of the hot side radiators, after the initial oscillations of the predictive system, the stability of the interior temperature was good, in spite of the on-off mode of connection. Alternatively a ramp variable intensity or voltage regulator has been used with excellent stability results. The numerical model allows to predesign efficiently most thermoelectric systems, which a considerable reduction of experimental time, specially when the heat exchangers have to be custom built.

## References

- ISACHENKO, OSIPOVA Y SUKOMEL; "Transmision de calor". Marcombo, Boixeria editores (Barcelona, 1979).
- D. M. ROWE, C. M. BANDARI; "Modern termoelectrics". Ed. Holt Tecnology (Cardif, 1984).
- S. R. DE GROOT; "Termodinamica de los procesos irreversibles". Ed. Alhambra (1968).
- M. DOMINGUEZ, J. M. PINILLOS, P. GUTIERREZ; "Aportaciones al desarrollo del efecto Peltier en el campo del frío". Refrigeracion frial n.19 (junio 1991).
- M. DOMINGUEZ; "Analogia electrica con ordenador". Refrigeracion frial (septiembre 1989).
- M. DOMINGUEZ, P. D. SANZ, J. M. PINILLOS, P. GUTIERREZ; Patente Esp. n. 9000953. "Instalaciones frigorificas con tubos de calor y efecto Peltier para usos domesticos y comerciales". (1991).
- T. J. SEEBECK; "Magnetische Polarisation der Metalle und Erze durch Temperatur-Differenz". Abhandlungen der Deutschen Akademie der Wissenschaften zu Berlin (1822).
- J. C. PELTIER; "Nouvelles experiences sur la calorite des courans electriques". Annales de chimie LVI (1934).
- A. F. IOFFE; "Semiconductor Thermoelectric Cooling". Infosearch (1957).
- REES J.M. (1987) "The propagation of internal gravity waves in the stably stratified atmospheric boundary Layer" *Annales Geophysicae* 5 B 421-432.

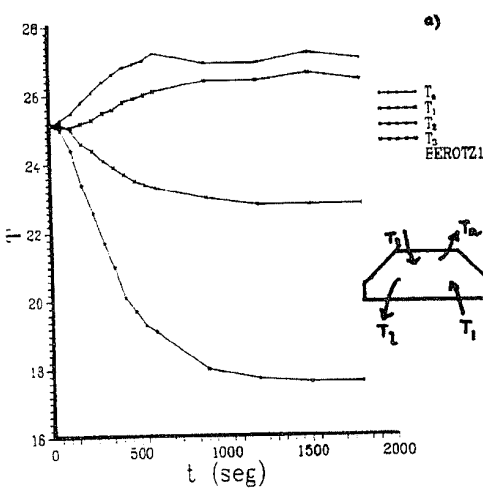


Figure 3:

## THE POTENTIAL FOR IMPROVED CYCLE EFFICIENCY BY COMBINING THERMOELECTRIC COOLERS WITH VAPOR COMPRESSION CYCLES IN HYBRID SYSTEMS

Hylan B. Lyon Jr. and James Bierschenk

Marlow Industries Inc.

10451 Vista Park Road, Dallas, TX 75238-1645, USA

This paper identifies the potential for improving the cycle efficiency of a "Throttle Cycle" system and Joule Thompson by the incorporation of thermoelectric devices in two specific locations within the cycle. The combined effect of a hybrid cycle using a vapor compression thermoelectric system is to increase the theoretical cycle efficiency. Bismuth Telluride alloy systems are proposed for the high temperature application (Top Cycle) and BiSb High Temperature Superconductor couples are proposed in the cold section (Bottom Cycle).

### Introduction

The hybridization of Vapor Phase Compression cycles and Thermo-electric Cycles is one pathway to the achievement of a low cost, reliable cryo-cooler with adequate capacity for several user communities. This paper addresses one analytical basis for this proposition.

### Review of basics

The thermal efficiency in the air-conditioning and refrigeration application fields are measured by several term. In this paper we propose the measure used in the thermoelectric field, which is the Coefficient of Performance

*Coefficient Of Performance =*

$$\frac{\text{Heat pumped}}{\text{Work required}} \quad (1)$$

$$COP = \frac{q}{W}$$

The limit of efficiency is defined by the Second Law of Thermodynamics<sup>1</sup>, and can be represented by the Carnot cycle<sup>2</sup>. This cycle consists of an isothermal expansion, an adiabatic expansion, an isothermal compression and an adiabatic compression.

The COP for a Carnot Cycle can be stated in terms of the  $T_h$  and  $T_c$  as:

$$COP_{\text{Carnot}} = \frac{T_c}{T_h - T_c} \quad (2)$$

In similar fashion the equations for COP from the thermodynamic literature can be stated as:

$$COP_{\text{Thermoelectric}} = \frac{1}{2} \left[ \frac{\Delta T_{\max}}{T_h - T_b} - 1 \right] \quad (3)$$

The term  $\Delta T_{\max}$  can be stated in terms of the material properties ZT and the maximum and minimum temperatures<sup>3</sup> as:

$$\Delta T_{\max} = (T_h + T_c) \left[ \frac{\sqrt{ZT + 1} - 1}{\sqrt{ZT + 1} + 1} \right] \quad (4)$$

It is interesting to note that when right hand term of equation 4 converges to unity, which would occur when ZT approaches infinity, that the COP for thermoelectrics converges to the COP for the Carnot cycle.

Historically, the Carnot cycle was used: to develop the statement of the second law of thermodynamics, to develop the concept of entropy and to demonstrate that entropy is a state variable.

The ZT of a thermoelectric device composed of a P-type and an N-type semiconductor was first given by the equation of Altenkirch<sup>4</sup>, and which today takes the form:

$$ZT = \frac{(\alpha_p - \alpha_n)^2 T}{[\sqrt{\rho_p \lambda_p} + \sqrt{\rho_n \lambda_n}]^2} \quad (5)$$

In the event of a high temperature superconductor, ( $T_c$  as high as 120 K are possible) used as the P-type leg below the transition temperature, the Seebeck coefficient will drop to zero along with  $\rho_p$ , leaving only the thermal conductivity  $\lambda_n$  as a contributing factor in the equation.

If one looks at a couple composed of an N-type thermoelement and an HTS leg operating below the  $T_c$  then one can describe the heat  $q$  pumped by this couple as:

$$q = \alpha_n T_{\text{cold}} J - \frac{1}{2} J^2 \rho_n \frac{l_n}{A_n} - \left[ \lambda_n \frac{A_n}{l_n} + \lambda_{\text{HTS}} \frac{A_{\text{HTS}}}{l_{\text{HTS}}} \right] \Delta T \quad (6)$$

Equation (6) implies that in the superconducting state the ZT can be written:

$$ZT = \frac{\alpha_n^2 T}{\rho_n \left( \lambda_n + \frac{l_n}{A_n} \frac{A_{\text{HTS}}}{l_{\text{HTS}}} \lambda_{\text{HTS}} \right)} \quad (8)$$

If one assumes that in the majority of cases  $l_n = l_{\text{HTS}}$  then:

$$ZT = \frac{\alpha_n^2 T}{\rho_n \left( \lambda_n + \frac{A_{HTS}}{A_n} \lambda_{HTS} \right)} \quad (8)$$

Thus we suggest that to optimize the thermoelectric performance of a couple composed of an N-type leg and an HTS leg, the thermal conductivity of the HTS and its cross sectional area should be minimized. Fortunately the thin film formats of the HTS materials can have very high current densities opening up a new horizon for these devices in addition to the past use of HTS as a leg of similar cross sectional area and length as the N-type material.

#### Multi-stage cycles

For the purposes of this paper we shall look at the improvements in overall cycle efficiency of real vapor compression cycles due to hybridization with thermoelectric devices. We shall arbitrarily defined by the following temperatures:

$$\begin{aligned} T_h &= 300 \text{ K} \\ T_{intermediate} &= 80 \text{ K} \\ T_c &= 72 \text{ K} \end{aligned} \quad (9)$$

The Carnot cycle cannot be improved upon by staging but "real" cycles can. We know the formula for the overall efficiency of a multi-stage cycle<sup>5</sup>:

$$COP = \left[ \left( 1 + \frac{1}{COP_1} \right) \left( 1 + \frac{1}{COP_2} \right) \cdots \left( 1 + \frac{1}{COP_n} \right) - 1 \right]^{-1} \quad (10)$$

#### Three Application Options

When the vapor compression cycle is operating far enough from Carnot efficiency, it is possible for three applications of thermoelectric cycles to yield a net gain. The first is where the thermoelectric device extracts heat from the gas between the compressor outlet and the expander chamber. The second is where the counter-flow heat transfer from the high pressure gas is accelerated to the returning gas utilizing a thermoelectric device as an augmenter. The third is used as a 2nd stage of the system. All of these can be accomplished with a net gain in overall efficiency. There are two known vapor compression systems where these situations occur. The Joule-Thompson cycle when approaching 77K and the mixed gas "Throttle" cycle.

#### Prior Art

Several others have recognized the potential of thermo-electric devices integrated into or used to augment the efficiency of a specific vapor compression cycle. These concepts are the basis of the proposal herein, namely that there are conditions under which it makes perfect sense for "competing technologies" to hybridize for the benefit of both.

#### Option One - The Top Cycle hybridized with a Joule Thomson Cycle

In 1989 a patent issued<sup>6</sup> concerning the augmentation of the Joule-Thompson cycle by using a plurality of thermoelectric devices for removing heat from the working fluid, this is a good example of the. By this process the power input to a closed loop J-T cycle was reduced by a factor of 4.5 bringing it nearly into power parity with Stirling cycles. Such cycles are proposed for nitrogen, neon and helium as working fluids. The pre-cooler in this device provides a fluid to the J-T expansion valve 100-200K cooler than at the outlet of the compressor. One watt of cooling at 77K results from providing 15 watts to the thermoelectric devices and 30 watts of power to the compressor. This yields a COP of 2.2% which is a very favorable efficiency. Carnot efficiency for this temperature difference would be:

$$COP_{Carnot} = \frac{77}{300 - 77} = 34.5\% \quad (11)$$

Thus we propose that the % Carnot efficiency of even this enhanced J-T cycle is so low that it is a candidate for enhancement through the application of the bottom thermoelectric cycle.

#### Option Two - The Counterflow Cycle

Later in the same year another patent was filed<sup>7</sup> which utilized the returning cold gas to chill the gas returning to the inlet to the expansion valve. The gas is still cold enough when effluxing from the return to cool the hot side of the thermoelectric devices.

#### Option One - The Top Cycle Hybridized with a Mixed Gas Throttle Cycle

The mixed gas throttle cycle<sup>8</sup> can be augmented to improve efficiency by using thermoelectrics at either the warm end or cold end of the mixed gas throttle cycle<sup>9</sup>. The concept of using thermoelectrics at the warm end of a throttle cycle heat exchanger provides opportunities to enhance the cooling power of mixtures by condensing a specific component or eliminating enthalpy imbalances that limit the available cooling. In a typical example, with 8 W of heat removed by thermoelectrics at the heat exchanger with a high pressure stream at 270K, overall cycle efficiency (including the increased power to the thermoelectrics) increased from 28% to 48% for a cycle cooling to 86 K.

Likewise, incorporating thermo-electrics on the cold end provides temperatures below those available by the throttle cycle alone as well as providing improved efficiency and temperature stability. A theoretical approach to modeling combined thermoelectric and vapor compression cycle systems was proposed by Anatychuk<sup>10</sup> in 1994. This however did not provide an easy practical method of evaluating when thermoelectrics should be used.

#### Option Three - A Closer Look at Bottom Cycle Feasibility

If we assume we have a throttle cycle for example, operating between a hot temperature of Th and a cold temperature Tc, when is it advantageous to add thermoelectrics on the bottom side (cold side) in order to improve cycle efficiency? If the initial cycle COP of the throttle cycle is COP<sub>TC</sub>, then we would want the combined hybrid (throttle cycle and TEC) cycle efficiency to be greater than COP<sub>TC</sub>. In other words:

72 K would need to be greater than

$$COP_{TC} <$$

$$\left[ \left( 1 + \frac{1}{COP_{newTC}} \right) \left( 1 + \frac{1}{COP_{TE}} \right) - 1 \right]^{-1} \quad (12)$$

If we solve for COP<sub>TE</sub> to determine what COP is needed from the TECs in order to realize a net improvement in overall system COP, we find that:

$$COP_{TE} > COP_{TC} \frac{COP_{newTC} + 1}{COP_{newTC} - COP_{TC}} \quad (13)$$

where COP<sub>TC</sub> is the initial cycle efficiency and COP<sub>newTC</sub> is the new COP of the cycle operating at reduced DeltaT since the TEC now is "carrying" a portion of the overall DeltaT.

There are three situations which can exist within a vapor compression cycle which need to be considered.

#### Near to Carnot Efficiency

If the vapor phase compression cycle efficiency is near the Carnot efficiency, then incorporating a thermoelectric cooler operating at much less than Carnot efficiency to carry a portion of the system DeltaT, would obviously reduce the overall system efficiency. Thus this case is not a case where thermoelectrics would be utilized.

#### Constant Carnot Efficiency

If vapor phase compression cycle is operating in a region where COP is fairly insensitive to the DeltaT, then the term in the denominator in equation 13 will become quite small. This will result in very high COP<sub>TE</sub> needed in order to provide a system COP improvement. This case occurs if the COP of the cycle is approximately the same whether it is pumping to 80 K or 75 K for example. This too is not a case where thermoelectrics should be incorporated.

#### Changing Carnot Efficiency

The only case, therefore, where thermo-electrics added to the bottom cycle of the mixed gas throttle cycle, Stirling cycle or any other vapor phase compression cycle would be when the reduction in DeltaT for the cycle has a significant impact in cycle performance. In this case the term in the denominator of equation 13 becomes large resulting in a reasonable COP<sub>TE</sub> needed to provide a net improvement in system COP. This case provides an ideal example of where thermoelectrics can be utilized to improve overall cycle efficiency. This is best illustrated in the following example.

#### Sample Calculations for Thermo-electrics in Bottom Cycles

Consider a mixed gas throttle cycle operating from 300 K to 72 K. At these temperatures, the mixed gas throttle cycle operates at a very low COP, around .0007 or 0.2% of Carnot. If the throttle cycle were to operate at 78 K instead of 72, the COP would increase to around .0054 or 1.5% Carnot. Using equation 13, we find that the COP of the thermoelectrics operating between 78 and

$$COP_{TE} > .0007 \frac{.0054 + 1}{.0054 - .0007} \quad (14)$$

$$COP_{TE} > 0.15$$

in order to realize a net increase in system cycle COP. Anticipated COPs for BiSb n-type thermoelectric material coupled with thin film high temperature superconductor passive leg should be in the .4 to .8 range for this temperature differential. Thus, in this case, significant improvements in system COP can be realized by incorporating thermoelectrics on the bottom end of the mixed gas throttle cycle.

To carry this example one step further, we might ask what is the desired portion of the overall DeltaT that the thermoelectric cooler should carry in order to maximize the system COP. Neglecting the interface contact resistances and thermal conduction losses of the high temperature superconductor, Figure 1 illustrates the potential COP improvement for both single crystal BiSb and with existing powder formats of BiSb. For the pressed and sintered powder formats of BiSb coupled with a thin film HTS, the optimum inner stage temperature is 78 K resulting in an overall hybrid system COP of around .0016 (1.5% Carnot). This is almost a 130% improvement in system COP without thermoelectrics operating over the same temperature range.

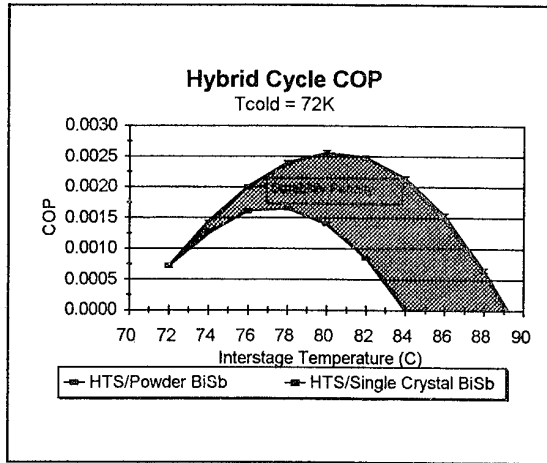


Figure 1

The more efficient single crystal BiSb coupled with a thin film HTS provides even greater COP improvements. The optimum inner stage temperature is 80 K with a system COP of .0026 (2.1% Carnot). This equates to a 250% improvement in cycle COP. The difference between the two lines represents the durability penalty suffered by the more rugged pressed and sintered powder formats of the BiSb material.

### Conclusions

The hybridization of vapor phase compression cycles and thermoelectric cycles is one path to producing more efficient, reliable cryo-cooling solutions. Three different applications of thermoelectrics in these vapor phase compression systems can be utilized to improve overall cycle efficiency.

Significant improvements in cycle efficiency can be realized for systems having vapor phase compression cycles operating near their maximum DeltaT as in the mixed gas throttle cycle presented. Additional work is required in order to realize the full benefit available from these hybrid systems. This work should be focused on:

- 1) reducing the durability penalty suffered in the powder formats of BiSb,
- 2) optimizing the BiSb/HTS device fabrication techniques incorporating thin film HTS to minimize the thermal conduction losses through the HTS
- 3) optimizing the Vapor Compression cycle performance to utilize this new cycle efficiency to improve reliability (life cycle costs), reduce acquisition costs and increase energy efficiency.

### References

- (1).S. Carnot, "Reflexions sur la puissance motrice du feu," Chez Bachelier Libraire, Paris 1824
- (2).G.N. Lewis, M. Randall, revised by K. Pitzer, L. Brewer, "Thermodynamics", McGraw Hill, New York, 1961
- (3).B.M. Gol'tsman, B.A. Kudinov, I.A. Smirnov, "Thermoelectric Semiconductor Materials based upon  $\text{Bi}_2\text{Te}_3$ ", Nauka, Moscow, 1972 ( U.S. Translation)
- (4).E. Altenkirch, 1911 *Phys. Z.*, **12**, 920
- (5).H.J. Goldsmid, "Electronic Refrigeration", Pion Limited, London 1986
- (6).B.A. Benedict, J.E. Lester, D.D. Lineberger U.S. Patent #4,825,667, May 2, 1989
- (7).U. Hingst, U.S. Patent #4,993,230, Feb. 19, 1991
- (8).R. C. Longsworth, M.J. Bojarski, L.A. Klusmier, "80 K Closed Cycle Throttle Cycle Refrigerator", presented at the International Cryocooler Conference, Vail CO., June 1994
- (9).H.B. Lyon, J. Bierschenk, R. Longsworth "Hybrid Throttle, Cycle and Thermoelectric Coolers for Cryocooling and Other Applications" in *Proceedings of the 1995 IRIA Specialty Group on Passive Sensors*, Dallas, TX 13-15 March 1995
- (10).L.I. Anatychuk, V.V. Raxinkov, L.N. Vikhor, "Combined Cooler Design by Optimal Control Theory Method", International Thermoelectric Society Symposium, 1994.

## SINGLE STAGE THERMOELECTRIC COOLERS WITH TEMPERATURE DIFFERENCE OF 80 K

V.A.Semeniouk<sup>1</sup>, T.E.Svechnikova, L.D.Ivanova<sup>2</sup>

<sup>1</sup>*Thermion Company, Odessa, 270009, Ukraine*

<sup>2</sup>*A.A.Baykov Institute of Metallurgy RAS, Moscow, 117334, Russia*

This paper represents the results of practical embodiment of the idea to improve a thermoelectric cooler (TEC) performance by using inhomogeneous TE materials. The limit performance of a TEC with segmented and inhomogeneous TE legs is predicted and reproduced in miniature single stage TE coolers, having  $\Delta T_{\max}$  value in the region of 80 K.

### Introduction

One of the promising possibilities of increasing the range of attainable temperatures for single stage TECs is the use of inhomogeneous thermoelements in which the so-called distributed Peltier effect occurs [1]. The distribution of thermo-EMF along the axis of such TE element is essential which absolute value must be reducing from the hot junction to the cold one. The Peltier heat is absorbed then not only at the cold junction but in the volume of a TE leg, which results in the additional temperature reduction as compared with a standard homogeneous thermocouple [2].

This paper gives the results of practical implementation of this idea in batch production of TE microcoolers. The problems connected with the development of such TECs are discussed, including design theory, technology, manufacturing and characterization of TE materials with proper thermoelectric parameters. The practical limits for performance of TE modules having segmented thermoelements and TE legs with distributed inhomogeneity are discussed.

### Selection of TE materials

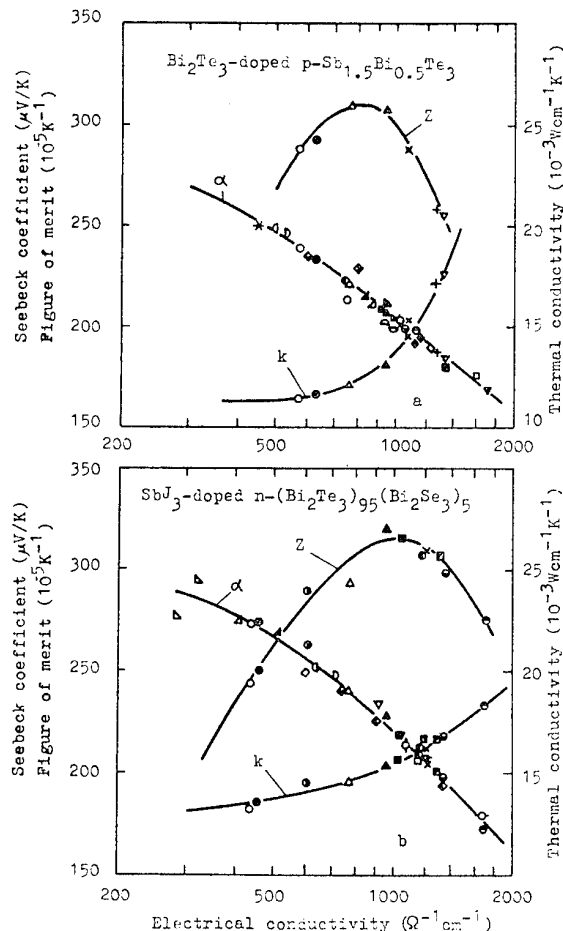
To develop efficient inhomogeneous TE elements it is necessary to obtain thermoelectric materials having rather high TE figure of merit in a wide range of Seebeck coefficient. The Czochralski method of pulling from a melt with feeding from a liquid phase was used to produce such materials. The following two advantages of this method are the most important for such applications:

1. The possibility of obtaining perfect single crystals with high figure of merit.
2. The possibility to monitor single crystals properties in the process of growing and to control them according to the specified program.

This method was used for growing homogeneous and inhomogeneous single crystals of bismuth and antimony chalcogenides with the Seebeck coefficient from 170 to 290  $\mu\text{V/K}$ . These materials properties are given in Figure 1 as the dependences of Seebeck coefficient  $\alpha$ , thermal conductivity  $\kappa$ , and figure of merit  $Z$  on electrical conductivity  $\sigma$ . The corresponding variation of the parameters was achieved by the change of the basic composition, doping impurity concentration, as well as by the relevant choice of technological parameters of growing process. With  $\text{SbJ}_3$ -doped n-type materials of the composition  $(\text{Bi}_2\text{Te}_3)_{95}(\text{Bi}_2\text{Se}_3)_5$  the maximum of TE figure of merit of  $(3.1-3.2) \cdot 10^{-3}\text{K}^{-1}$  level is achieved in the range of  $\sigma$  value of  $1000-1100 \Omega^{-1}\text{cm}^{-1}$ . With

$\text{Bi}_2\text{Te}_3$ -doped p-type materials of the composition  $\text{Sb}_{1.5}\text{Bi}_{0.5}\text{Te}_3$ , maximal  $Z$  value is of the same order, but its location is shifted to the reduced  $\sigma$  values ( $800-850 \Omega^{-1}\text{cm}^{-1}$ ).

Fig. 1 Interconnection of TE parameters in Czochralski grown single crystals of solid solutions of Bi and Sb chalcogenides (the solid lines represent polynomial approximation of the experimental data by least-squares technique)



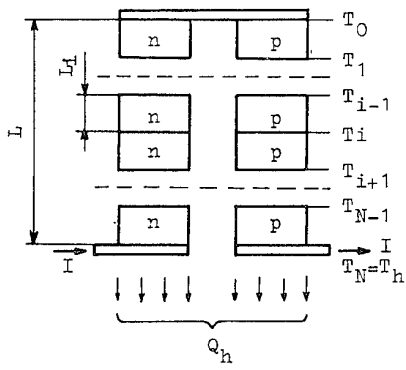
One should note the sloping character of the  $Z(\sigma)$  maximum for Czochralski grown single crystals, which makes it possible to change their parameters in a wide range, without considerable reduction of thermoelectric figure of merit. For instance, as it follows from Figure 1b, the  $Z$  value not less than  $2.8 \cdot 10^{-3} \text{ K}^{-1}$  can be retained for n-type materials in the  $\sigma$  range from 600 to  $1740 \Omega^{-1} \text{ cm}^{-1}$ . The corresponding variation of Seebeck coefficient is from 173 to  $257 \mu\text{V/K}$ , which can serve the basis for the development of an efficient inhomogeneous TE leg.

### Best segmented thermoelement

A zone-inhomogeneous TE element consisting of separate homogeneous segments is a particular variant of inhomogeneous thermoelement. In this TE element the Peltier heat is absorbed not only at the cold junction but at the joints of adjacent segments, which leads to additional temperature lowering as compared with TE elements of usual configuration.

Limit performance estimation. The question arises, what the limit efficiency of a segmented TE element can be achieved when using Czochralski grown single crystals having parameters presented in Figure 1. Let us consider TE element model with the specified height  $L$  containing  $N$  segments in each leg (Figure 2). At the hot junctions the temperature  $T_h$  is fixed, the rest surface of legs being adiabatically insulated. We designate the sequence of junction temperatures as  $T_i$ ,  $i=0, \dots, N$ , heat absorbed by a segment as  $Q_{0i}$ ,  $i=1, \dots, N$ , and heat rejected from a segment as  $Q_{1i}$ ,  $i=1, \dots, N$ . TE properties of separate segments can be varied but not arbitrarily, their interrelation defined by Figure 1 must be taken into account. Let us put the following problem: what must the properties of segments materials, their lengths  $L_i$ ,  $i=1, \dots, N-1$  and feeding current  $I$  be for achieving the minimal cold junction temperature  $T_0$ .

Fig. 2 Schematic illustration of a segmented TE couple



The complete system of restrictions in this optimal problem should include a set of heat balance equations at contacts

$$Q_{1i}^{n,p} = Q_{0i+1}^{n,p}, \quad i=1, \dots, N-1, \quad (1)$$

$$Q_0^n + Q_0^p = 0, \quad (2)$$

equality

$$T_0^n = T_0^p, \quad (3)$$

as well as relations of the form

$$\alpha = \alpha(\sigma), \quad \kappa = \kappa(\sigma), \quad (4)$$

reflecting the TE parameters interconnection, were the relations (4) must be defined for materials of both type conductivities.

If the temperature dependence of kinetic coefficients is neglected, relations for heat fluxes in Eq. (1) and (2) can be given in the form

$$Q_{0i} = \alpha_i I T_{i-1} - \frac{1}{2} I^2 \frac{L_i}{S\sigma_i} \left( 1 + \frac{2r_c\sigma_i}{L_i} \right) - \frac{\kappa_i S}{L_i} (T_i - T_{i-1}), \quad (5)$$

$$Q_{1i} = \alpha_i I T_i + \frac{1}{2} I^2 \frac{L_i}{S\sigma_i} \left( 1 + \frac{2r_c\sigma_i}{L_i} \right) - \frac{\kappa_i S}{L_i} (T_i - T_{i-1}), \quad (6)$$

where  $r_c$  is the electrical contact resistance,  $S$  is the cross-section of TE leg.

Together with Eq. (4)-(6) the relations (1)-(3) give the system of  $2N$  linear equations with regard to  $2N$  unknown temperatures  $T_i^{n,p}$ ,  $i=0, \dots, N-1$ . It is clear that for each set of  $I$ ,  $L_i^{n,p}$ ,  $\sigma_i^{n,p}$  parameters this system uniquely defines intermediate temperatures  $T_i$  and the desired functional  $T_0$ . It is necessary to find such a combination of these parameters, which the following condition

$$T_0(I; (L_1, \dots, L_{N-1})^{n,p}; (\sigma_1, \dots, \sigma_N)^{n,p}) = \min \quad (7)$$

corresponds to, the restrictions (1)-(6) being satisfied. Thus, the matter is about a problem of non-linear programming with complicated system of restrictions.

The solution of this problem for different  $N$  was carried out numerically. For the sake of simplicity the equalities of  $L_i^n = L_i^p = L$ ,  $i=1, \dots, N$  were assumed. As dependences (4) the polynomials, approximating experimental data, are used.

Table 1 gives calculation results for two-segment TE element at  $r_c=0$ . The set of TE parameters given provides the achievement of limit performance of two-segment TE element when using single crystals whose properties are given in Figure 1. The largest temperature difference of 83 K is provided when the lower (high temperature) segment length is 1/3 of the total leg length. For comparison, the Table 1 gives the data for a TE couple with homogeneous legs having maximal thermoelectric figure of merit. It is seen that the use of two-segment legs allows the increase of  $\Delta T_{\max}$  by 5 K. Calculations also show that for three and more segments the expected additional  $\Delta T_{\max}$  increase will not exceed 2.5-3 K.

Table 1. Calculated optimal parameters of two-segment and homogeneous TE elements, based on Czochralski grown single crystals

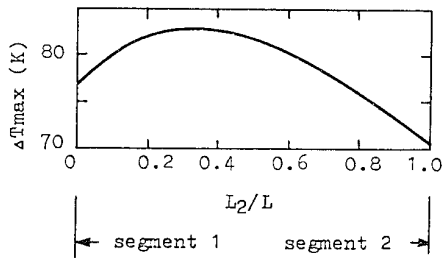
Model of TE couple	Type of TE leg	$\frac{\alpha_1}{\alpha_2}$ ( $\mu\text{V/K}$ )	$\frac{\sigma_1}{\sigma_2}$ ( $\Omega^{-1} \text{cm}^{-1}$ )	$\frac{\kappa_1 \cdot 10^3}{\kappa_2 \cdot 10^3}$ (W/cmK)	$\frac{Z_1 \cdot 10^3}{Z_2 \cdot 10^3}$ ( $\text{K}^{-1}$ )	$\Delta T_{\max}$
Optimal two-segment	n	202.0	1259.0	16.6	3.10	83.0
		268.1	487.8	13.7	2.55	
	p	201.7	1032.0	14.2	2.95	
		245.3	516.0	11.4	2.73	
Optimal homogeneous	n	227.7	925.3	15.3	3.14	78.3
	p	214.8	854.5	12.7	3.10	

It is interesting to note that materials for the upper part of segmented leg must have unexpectedly high  $\alpha$  value (of the order of 200  $\mu\text{V/K}$ ), which approves the result obtained recently in paper [3],

where the similar analysis was carried out using the method of microscopic description of kinetic coefficients interconnection in semiconductor materials. Taking into account some reduction of  $\alpha$  value with temperature we can state that in the low temperature part of a segmented thermocouple the usual semiconductor materials with a charge carrier concentration near its optimal level must be used. So, if one needs the maximal effect of additional temperature reduction it must be achieved by the use of materials with relatively high values of  $\alpha$  in the lower part of the thermocouple. These requirements being not satisfied, it is one of the reasons why the temperature differences exceeding possibilities of the best homogeneous thermocouples were not obtained in previous experiments.

It is of great interest to find how much the deviation of segment geometrical parameters from their optimal values affects the  $\Delta T_{\max}$  value. Figure 3 shows the dependence of  $\Delta T_{\max}$  on the ratio of  $L_2/L$ . The calculations were made with fixed segment parameters, given in Table 1. It is seen that the advantage of a segmented thermocouple as compared with homogeneous one is retained rather high even in the case when the deviation from optimal segment lengths relationship is considerable. This justifies the model accepted here, according to which n-type and p-type legs of separate section have the same length.

Fig. 3 Influence of deviation from optimal  $L_2$  value



Additional electrical resistance in the zone of intermediate contacts is an disadvantage of segmented TE couples. As the result, with the increase of  $r_c$  the advantages of a segmented TE couple can be lost. This is clearly shown in Figure 4, from which it follows that the use of segmented legs is reasonable at  $r_c$  of the  $10^{-6} \Omega \text{cm}^2$  order. At  $r_c=10^{-5} \Omega \text{cm}^2$  and higher the expected result does not justify the complication of technology.

Let us consider now the question of maximum performance of two-segment TE couple operating as a cooler at  $T_0 > T_{\min}$ . At fixed dimensions and specified physical parameters of segments the problem is reduced to the search of COP maximum as a function of feeding current

$$\text{COP} = \frac{Q_c}{Q_h - Q_c}, \quad (8)$$

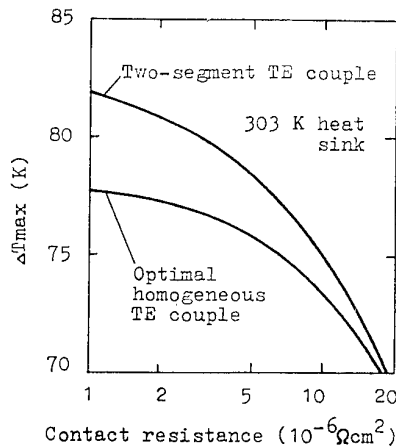
where  $Q_c$  - is the cooling capacity,  $Q_h = Q_{IN}^n + Q_{IN}^p$  - the heat transferred to heat sink.

The correction of the initial model for the problem under consideration concerns only equality (2), which becomes now of the form

$$Q_0^n + Q_0^p = Q_c. \quad (9)$$

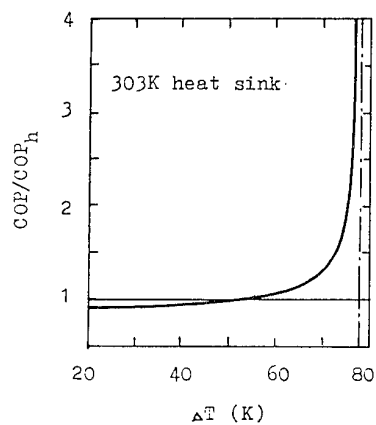
As for the rest, the system of restrictions (1)-(6) keeps unchanged.

Fig. 4 Dependence of maximal temperature difference on contact resistance



Results of calculations are given in Figure 5 in the form of ratio COP/COP<sub>h</sub> versus temperature difference where COP<sub>h</sub> is a performance of optimal homogeneous TE couple. It is seen, that the use of segmented thermocouples is reasonable at elevated  $\Delta T$  values, especially near  $\Delta T_{\max}$  when their advantage as compared with homogeneous ones is greatly increasing. At moderate temperature differences, on the contrary, the gain is relatively small, and at  $\Delta T < 50$  K segmented TE couples lose a little in performance as compared with homogeneous ones.

Fig. 5 Ratio of the COP for two-segment TE couple to the COP for optimal homogeneous one vs. temperature difference



Fabrication and testing. Development of semiconductor single crystals with a wide range of TE properties made it possible to fabricate miniature two-segment cooling modules having increased temperature differences. The promising technology was elaborated

which consists of two steps, the first one being the manufacturing a double layered semiconductor plates with the same type conductivity whose Seebeck coefficients are different. The second step is in rectangular cutting the plates, which gives a lot of segmented TE legs of needed cross-section. So, if the materials with required properties are available, the technology is not much more complicated than the one for manufacturing standard TE coolers.

Experimental research and technology perfection were carried out on miniature two-segment TECs identical to standard coolers of MOM series (Figure 6). Properties of single crystals used in separate segments, are given in Table 2. Two-segment legs of  $0.6 \times 0.6$  mm in cross-section and 1.5 mm in length were made of these materials. The height of the lower (high temperature) segment was 0.5 mm in TE legs of both type conductivity. In spite of marked deviation of the used single crystals parameters from optimal ones, the temperature differences from 79 to 81 K were obtained using such TE legs, which is 4-6 K higher than those for standard modules of MOM series [4]. Figure 7 gives the test results for one of two-segment coolers consisting of 16 TE legs. The test results for homogeneous thermocouples composed of segment 1 and segment 2 single crystals are also given here for comparison. It is seen that the temperature differences achieved exceed significantly  $\Delta T_{\max}$  values for initial homogeneous materials.

Fig. 6 Modified TE modules of MOM series

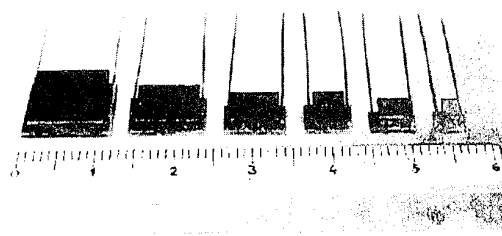


Fig. 7 Dependence of temperature differences on electrical current for two-segment TE module and for separate segments

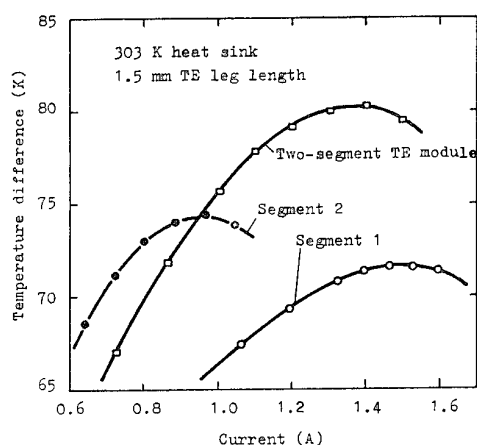


Table 2. Tested  $\Delta T_{\max}$  values for the modules with two-segment TE legs and TE properties of the single crystals used in separate segments

Type of TE leg	Segment	No	$\alpha$ ( $\mu\text{V/K}$ )	$\sigma$ ( $\Omega^{-1}\text{cm}^{-1}$ )	$K \cdot 10^3$ (W/cmK)	$Z \cdot 10^3$ ( $\text{K}^{-1}$ )	$\Delta T_{\max}$ (K)
n	1	186	1504	17.5	2.97	79-81	
	2	253	640	14.3	2.88		
p	1	188	1261	17.2	2.59	79-81	
	2	235	629	11.8	2.95		

It should be noted, that the results obtained practically coincide with calculated  $\Delta T_{\max}$  value for specified TE modules (80.3 K) and are rather close to the predicted limit temperature difference. This confirms the validity of theoretical approach and is an evidence of the efficiency of developed technology.

Prospects of practical application. It is natural to discuss whether such results have practical interest. In our opinion the application of segmented thermocouples is justified when cascading is not acceptable (for example, on conditions of miniaturization or speed of response), and the temperature difference is close to maximal or exceeds the possibility of a single stage cooler. Another promising field of application of segmented thermocouples is low temperature cascade coolers in which separate cascades operate near the limit temperature difference. It is well known today that performance of these devices can be repeatedly increased even at relatively small growth of Z parameter. This fact stated for the first time in paper [5] was many times confirmed later both theoretically and in practice [6]. It should be noted that the temperature difference of 83 K predicted for a single cascade corresponds to increasing in Z parameter by 12-15 %. Therefore the authors associate with this trend of research the hopes to highly increase the performance of low temperature cascade TECs and to widen the temperature limits of TE cooling.

#### The best inhomogeneous thermoelement

Theoretical prediction. At  $N \rightarrow \infty$  a segmented thermoelement is transformed into the system with continuously distributed inhomogeneity which is characterized by a maximal permissible performance. Variational problem concerning the best distribution of thermoelectric parameters along such a TE element was solved in [6] for bismuth-telluride-based semiconductor materials using the method of microscopic description of kinetic coefficients. The predicted limit temperature difference was about 90 K. In this paper the problem was being solved for single crystals of bismuth and antimony chalcogenides whose TE parameters interconnection is graphically represented in Figure 1. The method of optimal control theory was used. The obtained result amounts 87 K, which is rather close to the one predicted on the basis of kinetic theory.

Fabrication and test results. To check theoretical predictions the authors made repeated attempts to develop inhomogeneous TE single crystals with properties distribution close to the optimal one. Czochralski method of pulling from the melt with feeding from the liquid phase was used. Single and multi-point sections of continuous inhomogeneity from 0.1 to several mm in length along single crystals axis were produced through the growth process using variation of operating parameters and change of the feeding melt composition. The variations of thermo-EMF from 180 to 240  $\mu\text{V/K}$  and from 160 to 235  $\mu\text{V/K}$  were achieved in single crystals of n- and

p-type respectively. The sections of inhomogeneity were used for the production of inhomogeneous TE legs and TE couples on their basis.

Numerous testings of such TE couples proved that the distributed Peltier effect leads to significant temperature reduction but the result obtained appeared to be noticeably lower than the one theoretically predicted. Temperature differences of the order of 80 K were obtained which coincides practically with the result for two-segment TE couples. The fact that the limit temperature difference was not achieved is explained mainly by difficulties to get the sections with high  $\alpha$  values. Thus the further researches must be carried out in this field.

### Conclusion

Czochralski method of pulling from a melt with feeding from a liquid phase makes it possible to obtain single crystals of Bi and Sb chalcogenides retaining rather high TE figure of merit in a wide range of Seebeck coefficient variation. It provides the basis for manufacturing TECs with segmented and inhomogeneous legs having improved performance.

Single stage thermoelectric modules with two-segment TE legs, having  $\Delta T_{\max}$  up to 83 K can be produced from these single crystals, using rather simple technology. Materials with Seebeck coefficient value of 240-270  $\mu\text{V/K}$  must be used in the high temperature segment, while in low temperature one the use of standard materials with  $\alpha$  value of 200-210  $\mu\text{V/K}$  gives the best results.

The use of three and more segments is unreasonable as the expected increase in  $\Delta T_{\max}$  does not exceed 2.5-3 K, which cannot justify a significant complication of technology. High electrical contacts quality is the vital factor for segmented TECs performance. Contact resistance not more than  $10^{-6} \Omega\text{cm}^2$  is extremely desirable. At  $r_c=10^{-5} \Omega\text{cm}^2$  and higher the effect of additional cooling is almost suppressed by Joule heat dissipation at intermediate contact.

The absence of intermediate contacts in a thermoelement with continuously distributed inhomogeneity makes this one very attractive as an object of further research.

Modules developed have the advantage of improved performance. The possibility to obtain larger temperature lowering and increased COP makes them desirable for the application in single and multi-stage configurations.

### References

- [1]. C.A.Domenicali, Stationary temperature distribution in an electrically heated conductor, *J.Appl.Phys.*, 1954, v. 25, No. 10, pp. 1310-1311.
- [2]. Peltier thermoelectric couple with non-homogeneous elements, Brit. patent specification No. 1200384, 1970.
- [3]. V.A.Semeniuk, Vybor poluprovodnikovykh materialov dlya sostavnykh termopar, *Izv. Vuzov SSSR-Energetika*, 1976, No. 2, pp. 146-151.
- [4]. V.A.Semeniuk, T.E.Svechnikova, L.D.Ivanova, Miniature thermoelectric coolers on single crystals of solid solutions of bismuth and antimony chalcogenides, The 13th Int. Conf. on Thermoelectrics, Cansas City, august 1994.
- [5]. R.J. Buist, Low power 145 Kelvin thermoelectric cooler, *Electro-Opt. Syst. Des. Conf. Proc. of Technical Program*, N.Y., September 1972.
- [6]. L.I.Anatychuk, V.A.Semeniuk, Optimal control of properties of thermoelectric materials and devices, Chernovtsy, 1992, 264 p.

## MOCVD Growth Of $\text{Bi}_2\text{Te}_3$ and Related Materials and their Superlattice-Structures for High-ZT Thermoelectric Cooling Devices

R. Venkatasubramanian, T. S. Colpitts, D. Malta, and M. Mantini  
Research Triangle Institute, Research Triangle Park, NC 27709, USA.

### ABSTRACT

In this paper we describe the use of superlattice structures in  $\text{Bi}_2\text{Te}_3$ ,  $\text{Sb}_2\text{Te}_3$ , and  $\text{Bi}_2\text{Se}_3$  materials to improve the figure-of-merit (ZT) of thermoelectric refrigeration in the temperature range 100-300K. Considerable decrease in lattice thermal conductivity is predicted with the use of periodic superlattice structures due to structure-shifts that can cause enhanced phonon-scattering at the superlattice interfaces, with little effect on electrical conductivity. At RTI, we have recently begun work on the development of metallorganic chemical vapor deposition (MOCVD) of  $\text{Bi}_2\text{Te}_3$  and related materials for the evaluation of superlattice-structures. The initial growth of  $\text{Bi}_2\text{Te}_3$  films has been carried out on single-crystal sapphire substrates. X-ray photoemission spectroscopy (XPS) data of these thin films have been compared with those of commercially available, bulk single-crystalline  $\text{Bi}_2\text{Te}_3$  (with a few % of Se) substrates. Preliminary analysis indicates that the stoichiometry of the epitaxial films, i.e., the ratio of Bi to Te, is similar to that of the bulk substrate. Low-energy electron diffraction (LEED) data indicates that the  $\text{Bi}_2\text{Te}_3$  films on single-crystal sapphire substrates are epitaxial. X-ray diffraction data indicates that the  $\text{Bi}_2\text{Te}_3$  film is single-crystalline. Thus these initial results represent the first demonstration of single-crystal, hetero-epitaxial  $\text{Bi}_2\text{Te}_3$  films on sapphire substrates by MOCVD.

### INTRODUCTION

Efficient thermoelectric (TE) cooling devices based on high figure-of-merit (ZT) semiconductors such as  $\text{Bi}_2\text{Te}_3$  and its isomorphous alloys are highly desirable for several applications. The TE cooling devices available today employ 1960's semiconductor materials (bulk-polycrystalline, sintered  $\text{Bi}_2\text{Te}_3$  and its alloys with  $\text{Sb}_2\text{Te}_3$  and  $\text{Bi}_2\text{Se}_3$ ) technology and are not significantly different in performance than three decades ago. The TE materials parameter, determining the performance, is the figure-of-merit ZT at temperature T. The ZT of such materials have remained at 0.8 to 1.0. The goal of our work is to apply the 1990's semiconductor materials technology, specifically the use of thin-film deposition techniques like MOCVD, artificially-structured materials like superlattices and quantum-wells, towards achieving vastly-improved ZT values. If a ZT of around 5.0 can be achieved at 300K, implying a five-fold improvement over existing materials' figure-of-merit, the solid-state refrigeration systems would become competitive with present-day, CFC-based, dynamic refrigeration systems.

### THEORETICAL BACKGROUND

The motivation behind the use of superlattice structures as high performance thermoelectric materials stems from results on the reduction of lattice thermal conductivity using solid solution alloying in the  $\text{Bi}_2\text{Te}_3$  -  $\text{Sb}_2\text{Te}_3$  -  $\text{Sb}_2\text{Te}_3$  system. Thermal conductivity of solid solution alloys of various semiconductors, for example in the  $\text{Bi}_2\text{Te}_3$ - $\text{Sb}_2\text{Te}_3$  system [1], have been investigated. The lattice thermal conductivity of the  $\text{Bi}_2\text{Te}_3$ - $\text{Sb}_2\text{Te}_3$  system, on solid solution alloying, indicates a minimum thermal conductivity of around  $0.004 \text{ W cm}^{-1} \text{ deg}^{-1}$  at a ~ 50% alloy composition [2]. The significant decrease in the lattice thermal conductivity of the solid solution alloy  $\text{Bi}_2\text{Te}_3$ - $\text{Sb}_2\text{Te}_3$  is thought to be due to the lattice perturbations [1] or lattice distortions [2]. These perturbations are effective in phonon scattering, thereby impeding the flow of heat and thus offering lower lattice thermal conductivity. The wavelength of phonons contributing to thermal conductivity is much smaller than that of free carriers. Thus, the distortion of the lattice resulting from substitution of an isoelectronic impurity, such as Se for Te in  $\text{Bi}_2\text{Te}_3$ , should cause greater scattering of phonons than that of charge carriers [2]. Hence, the lattice component of thermal conductivity can be reduced without seriously affecting the electrical properties of the alloy.

Phonon scattering by the lattice distortions from introduction of isoelectronic impurities is less temperature dependent than normal lattice scattering [3]. While the thermal conductivity of  $\text{Bi}_2\text{Te}_3$  increases with decreasing temperature below 310K, the thermal conductivity of the  $\text{Bi}_2(\text{Se}_{0.1}\text{Te}_{0.9})_3$  alloy is relatively independent of temperature. In turn, Z for the alloy is stable down to ~200K. Similarly, it may be noted that boundary or interface scattering, if dominant in phonon-scattering processes in thermoelectric materials/structures, is also likely to be efficient at cryogenic temperatures in lowering thermal conductivity.

The idea is to utilize lattice perturbations at the superlattice interfaces to enhance phonon scattering rates. Efficient phonon scattering occurs when adjacent atoms in a lattice vary appreciably in mass and size. Thus the introduction of periodic structure shifts with a periodicity of ~ 25-50 Å should enable the scattering of phonons whose mean free path is about the same length.

The concept of "confined" phonons or lattice vibrations, depending on the AlAs-GaAs superlattice structure with a periodicity of ~ 20 - 50 Å, has also been experimentally observed utilizing Raman spectroscopy [4]. The term "confined" phonons implies non-propagating phonons, in turn lower thermal

conduction due to phonons. There has been one reported experimental study [5] on the lattice thermal conductivity in AlAs/GaAs superlattice structures. The epitaxial growth of AlAs/GaAs superlattice structure is well established and it is a good measure of the potential reduction possible in thermal conductivity through interfacial phonon scattering. In this work, a monotonic reduction in lattice thermal conductivity has been observed with the reduction in superlattice dimension. Going from a superlattice period of  $\sim 200 \text{ \AA}$  to about  $50 \text{ \AA}$ , the author [5] has observed a 2.5-fold reduction in thermal conductivity. Unfortunately, this work did not extend the superlattice-period down to about  $\sim 10 \text{ \AA}$ , which the epitaxial deposition technique is capable of, to explore for further reduction in lattice thermal conductivity.

The concept of using superlattices to decrease lattice thermal conductivity, utilizing the periodic interfaces to enhance phonon scattering and also the periodic atomic mass and size fluctuations in the superlattice to enhance disorder scattering, has been proposed by Venkatasubramanian [6] and suggested by Harman [7]. In addition, Venkatasubramanian presented preliminary modeling results on reduced lattice thermal conductivity in  $\text{Bi}_2\text{Te}_3$ - $\text{Sb}_2\text{Te}_3$  superlattice structures [6].

The estimation of time constant for phonon scattering at superlattice interfaces is similar to the calculation of relaxation time due to phonon scattering by grain boundaries in SiGe alloys [8]. The relaxation time due to scattering by superlattice interfaces, to a reasonably good approximation, is given by  $L/v_s$  where  $L$  is the one-dimensional superlattice period ( $\sim 20 - 50 \text{ \AA}$ ), a length similar to the linear crystal or grain-dimension and  $V_s$  is velocity of sound in the material. We assume a superlattice of equal thickness for  $\text{Bi}_2\text{Te}_3$  and  $\text{Sb}_2\text{Te}_3$  layers, as indicated in Fig. 1, and compare this with an alloy of 50 percent  $\text{Bi}_2\text{Te}_3$  - 50 percent  $\text{Sb}_2\text{Te}_3$ .

In addition to phonon scattering at the superlattice interfaces, we need to consider disorder scattering due to atomic mass and size differences in the  $\text{Bi}_2\text{Te}_3$ - $\text{Sb}_2\text{Te}_3$  system. The disorder scattering can be represented by a time constant

$$\tau_{\text{dis}}^{-1} = \frac{\Gamma V_s}{4\pi} \Omega_o \left( \frac{\omega}{V_s} \right)^4$$

where  $\omega$  is the phonon frequency,  $\Omega_o$  is the volume per atom.  $\Gamma$  is the disorder parameter [8] related to the mass differences between various atoms that comprise the superlattice. The velocity of sound is assumed comparable in both the  $\text{Bi}_2\text{Te}_3$  and the  $\text{Sb}_2\text{Te}_3$  materials. The calculated thermal conductivity as a function of superlattice dimension in the  $\text{Bi}_2\text{Te}_3$ - $\text{Sb}_2\text{Te}_3$  system is shown in Fig. 2. There is a reduction of lattice thermal conductivity by a factor of about 4.8 for a superlattice dimension of  $\sim 25 \text{ \AA}$  compared to the bulk value in the solid solution alloy  $(\text{Bi}_{0.5}\text{Sb}_{0.5})_2\text{Te}_3$  [1]. In the alloy only disorder scattering is present, and no interface scattering occurs.

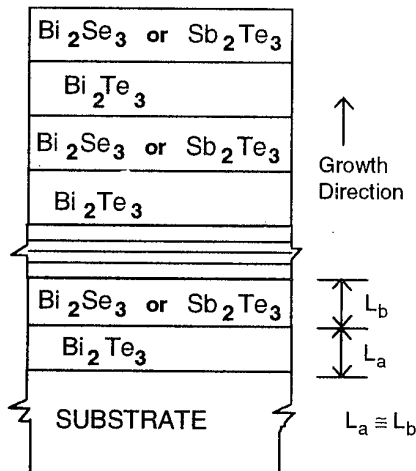


Fig. 1 Schematic cross-section of a  $\text{Bi}_2\text{Te}_3$ - $\text{Bi}_2\text{Se}_3$  or  $\text{Bi}_2\text{Te}_3$ - $\text{Sb}_2\text{Te}_3$  superlattice structure.

The reduction in lattice thermal conductivity in the  $\text{Bi}_2\text{Te}_3$ - $\text{Sb}_2\text{Te}_3$  superlattice system, compared to a bulk alloy of 50 percent  $\text{Bi}_2\text{Te}_3$  and 50 percent  $\text{Sb}_2\text{Te}_3$ , will directly translate into an improved ZT. This will be the case if the electronic component of thermal conductivity still remains low compared to the lattice thermal conductivity in the superlattice material system. The key, therefore, to maximize ZT values in the  $\text{Bi}_2\text{Te}_3$  -  $\text{Sb}_2\text{Te}_3$  superlattice material system with lower lattice thermal conductivity, is to reduce the free carrier concentration from near-degenerate conditions. The values of ZT are plotted as a function of superlattice dimension for various free carrier concentration at a temperatures of 300K in Fig. 3. Initial modeling results indicate that the use of lower free carrier concentration ( $\sim 10^{18} \text{ cm}^{-3}$  instead of  $\sim 10^{19} \text{ cm}^{-3}$ ) will enable the use of superlattice structures to achieve ZT values of  $\sim 7.5$  at 300K,  $\sim 4.7$  at 200K, and  $\sim 1.9$  at 100K.

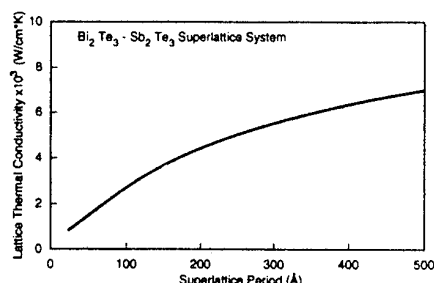


Fig. 2 Estimated lattice thermal conductivity of the  $\text{Bi}_2\text{Te}_3$ - $\text{Sb}_2\text{Te}_3$  as a function of the superlattice period.

Seebeck coefficients at the optimum doping levels and operating temperature for the overall maximization of ZT values.

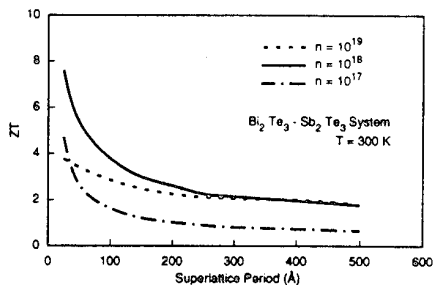


Fig. 3 ZT values obtainable at 300K, as a function of superlattice dimension for free carrier concentrations of  $10^{17}$ ,  $10^{18}$  and  $10^{19} \text{ cm}^{-3}$  in each of the  $\text{Bi}_2\text{Te}_3$  and  $\text{Sb}_2\text{Te}_3$  layers.

Important for superlattice structures involving layers of alternate materials such as  $\text{Bi}_2\text{Te}_3\text{-Sb}_2\text{Te}_3$  and  $\text{Bi}_2\text{Te}_3\text{-Bi}_2\text{Se}_3$ , is the carrier transport across the energy barriers that may exist at these heterojunction interfaces. Assuming one-dimensional periodicity, the location of quantized states with respect to the conduction and valence band minima, in short-period superlattice structures for which quantum-effects have to be considered, can be computed.

The energy displacements from the band minima have to be considered along with the doping levels and the heterojunction band offsets [9] that exist at the interface of two-layered materials to estimate the net potential barrier to carrier transport across the superlattice interface. We assume that the doping (free-carrier) levels will be essentially constant through the superlattice (along the direction of carrier transport). There is no previous study on the heterojunction band offset characteristics in the  $\text{Bi}_2\text{Te}_3\text{-Sb}_2\text{Te}_3$  system or the  $\text{Bi}_2\text{Te}_3\text{-Bi}_2\text{Se}_3$  system. As a first order approximation, we can assume that the bandgap difference in the two materials will split equally between the conduction and valence bands. These band offsets, along with the distribution of thermal energy of free carriers ( $kT/q$  to  $3kT/q$ ) at 300K, are shown in Fig. 4. It is clear that the average thermal energy values of free carriers are comparable to the band offset values. This is true for both n- and p-type doping conditions. The estimated weak quantum-confinement of carriers will only lead to a small increase in Seebeck coefficients, as per the calculations of Hicks and Dresselhaus [10], and, therefore, has not been considered in the predicted increase in ZT values in Fig. 3.

The choice of the superlattice material system for the n-type and the p-type sections of the thermoelement will depend on which superlattice material system ( $\text{Bi}_2\text{Te}_3$  -  $\text{Sb}_2\text{Te}_3$  or  $\text{Bi}_2\text{Te}_3$  -  $\text{Bi}_2\text{Se}_3$ ) offers the lowest thermal conductivity, the optimum electron (hole) transport properties, and, importantly, the highest

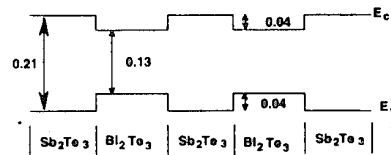


Fig. 4 Band diagram of the  $\text{Bi}_2\text{Te}_3\text{-Sb}_2\text{Te}_3$  and  $\text{Bi}_2\text{Te}_3\text{-Bi}_2\text{Se}_3$  Hetero-interfaces

#### THIN-FILM SUPERLATTICE TE DEVICE STRUCTURE

Epitaxial techniques like MOCVD, while being capable of synthesizing superlattice structures, are suited for producing thin layers and structures, typically  $\sim 5$  to  $10 \mu\text{m}$  thick. This is the result of smaller growth rates. However, practical thermoelectric elements require 250- to 1000- $\mu\text{m}$ -thick layers in the direction of heat flow, i.e., along the thermal gradient. Therefore, a key to utilizing the thin-film superlattice structures as high-performance thermoelectric elements is to devise an approach to process the thin-films ( $\sim 5$  to  $10 \mu\text{m}$ ) into a thermoelement with effective lengths of  $\sim 250$  to  $1000 \mu\text{m}$ . To achieve this, we have proposed a planar thin-film device-processing technology called monolithically interconnected, superlattice structured thermoelement (MISST) for each of the n-type and p-type segments of a typical thermoelectric couple. The schematic of a TE refrigeration device employing thin-film superlattice structures, using such a MISST concept, is compared with a conventional TE refrigeration device in Fig.5. Standard microelectronic processing is all that is required to fabricate these thermoelements.

## EXPERIMENTAL RESULTS AND DISCUSSION

We have installed a state-of-the-art MOCVD system, capable of growing the above mentioned thermoelectric materials under a variety of growth conditions, such as growth pressures ranging from 760 to 50 Torr, cooled or non-cooled reactor vessel, etc. The initial growth of  $\text{Bi}_2\text{Te}_3$  films has been carried out on single-crystal sapphire substrates. We have obtained specular morphology of  $\text{Bi}_2\text{Te}_3$  layers on sapphire substrates, although with noticeable crystallographic defects as observed under a scanning electron microscope (SEM). Fig. 6 indicates an SEM surface topography of a  $\text{Bi}_2\text{Te}_3$  film on single-crystal sapphire substrate.

X-ray photoemission spectroscopy (XPS) data of these thin films have been compared with those of commercially available, bulk single-crystalline  $\text{Bi}_2\text{Te}_3$  (containing a few % of Se) substrates. Preliminary analysis indicates that the stoichiometry of the epitaxial films, i.e., the ratio of Bi to Te, is about comparable with that of the bulk substrate. The x-ray photoemission lines used include the  $4f_{7/2}$  line of Bi with an atomic sensitivity factor (A.S.F.) of 2.8 and the  $3d_{5/2}$  line of Te with an atomic sensitivity factor of 4.0. A more detailed understanding of the XPS spectra of  $\text{Bi}_2\text{Te}_3$  films, in comparison to bulk substrates, is in progress. Low-energy electron diffraction (LEED), with electron energies in the range of 100-250 eV, is very useful for the analysis of thin hetero-epitaxial films. The LEED data of the  $\text{Bi}_2\text{Te}_3$  film on sapphire is shown in Fig. 7. The regularly-spaced circular spots can be correlated with the lattice spacing in the sample. It may be worth noting that, in amorphous and polycrystalline samples, the regular LEED spots would be absent and instead streaks and/or uniform intensity across the film would be observed. LEED studies were carried out on  $\text{Bi}_2\text{Te}_3$  films grown on sapphire substrates, by transferring the sample (after growth) from the MOCVD system to a high-vacuum chamber. Thus the samples were exposed to the ambient and therefore some surface oxidation of the sample is likely. In spite of this possibility, the quality of the LEED data on the  $\text{Bi}_2\text{Te}_3$  film on single-crystal sapphire substrate is good.

The  $\text{Bi}_2\text{Te}_3$  films on single-crystal sapphire substrates were also evaluated by single-crystal x-ray diffraction technique, using the Cu-K $\alpha$  lines. The x-ray diffracted intensity versus  $2\theta$  is shown in Fig. 8. The  $2\theta$  reflection associated with (00015) planes of the sapphire substrate is observable at  $42.1^\circ$ . The K $_{\alpha 1}$  and K $_{\alpha 2}$  lines of the substrate are clearly resolved. The  $2\theta$  reflection from the  $\text{Bi}_2\text{Te}_3$  film occurs at  $45^\circ$ . In addition to this reflection from the film, no other reflections were observable in the scanned range of  $30$ - $50^\circ$ , suggesting that the film is single-crystalline. The  $2\theta$  reflection corresponds to a lattice constant of  $4.467 \text{ \AA}^0$ , perpendicular to the growth direction. This is within 2% of the "a" lattice constant reported for bulk single-crystal  $\text{Bi}_2\text{Te}_3$  materials. It is also worth pointing out that we do expect to grow the materials, from energy considerations, along the "a" direction of  $\text{Bi}_2\text{Te}_3$ . The closeness of the estimated lattice constant supports the XPS data on stoichiometry of  $\text{Bi}_2\text{Te}_3$  films.

## CONCLUSIONS

In summary, we have proposed the use of superlattice structures to improve the figure-of-merit (ZT) of thermoelectric refrigeration. Considerable decrease in lattice thermal conductivity is predicted with the superlattice structures due to structure-shifts that can lower thermal conductivity through phonon scattering. Modeling calculations on the dimensions of superlattice structures and their doping levels on ZT values are presented. For a practical utilization of these superlattice structures in thermoelectric elements, we have proposed a planar technology called monolithically-interconnected, superlattice-structured thermoelement (MISST) for each of the n-type and p-type segments of a typical thermoelectric couple. We have also presented the first demonstration of single-crystal  $\text{Bi}_2\text{Te}_3$  hetero-epitaxial films on sapphire substrates. Work is in progress towards the characterization of electrical and thermal properties of these thin films and the growth of other isomorphs ( $\text{Sb}_2\text{Te}_3$  and  $\text{Bi}_2\text{Se}_3$ ) towards the fabrication of superlattice structures.

## ACKNOWLEDGMENTS

The MOCVD growth effort and characterization of films are as a result of a subcontract from Office of Naval Research. This support is hereby acknowledged.

## REFERENCES

1. F. D. Rosi and E.G. Ramberg, "Evaluation and Properties of Materials for Thermoelectric Applications", in Thermoelectricity, Edited by P. H. Egli, John Wiley and Sons, NY, 1960.
2. P. Egli, "Criteria for Materials Development", in Thermoelectricity, Edited by P. Egli, John Wiley & Sons, New York, 1960.
3. G. E. Smith and R. Wolfe, J. Appl. Phys., **33**, 841 (1962).
4. B. Jusserand and D. Paquet, "Confined and Propagative Vibrations in Superlattices", in Heterojunctions and Semiconductor Superlattices, Edited by G. Allan, G. Bastard, N. Boccato, M. Launois and M. Voos, Springer Verlag, 1986.
5. T. Yao, Appl. Phys. Lett., **51**, 1798 (1987).
6. R. Venkatasubramanian et. al., "Organometallic Epitaxy of  $\text{Bi}_2\text{Te}_3$  and Related Materials and the Development of Planar, Monolithically-Interconnected, Superlattice-Structured, High-Efficiency Thermoelectric Elements", Presented at 1<sup>st</sup> National Thermogenic Cooler Workshop, Sept. 17, 1992, Fort Belvoir, VA
7. T. C. Harman, "PbTeSe/BiSb Short-Period Superlattice as a New Thermoelectric Cooler Material", Presented at the 1<sup>st</sup>

National Thermogenic Cooler Workshop, Sept. 17, 1992, Fort Belvoir, VA.

8. D. M. Rowe and C. M. Bhandari, Modern Thermoelectrics, Reston Publishing Co., Reston, Virginia, 1983.

9. A. G. Milnes and D. L. Feucht, Heterojunctions and Metal-Semiconductor Junctions, Academic Press, New York, 1972.

10. L. D. Hicks and M. Dresselhaus, "The Effect of Quantum Well Structures on the Thermoelectric Figure of Merit", Phys. Rev. B, 47, 12727 (1993).

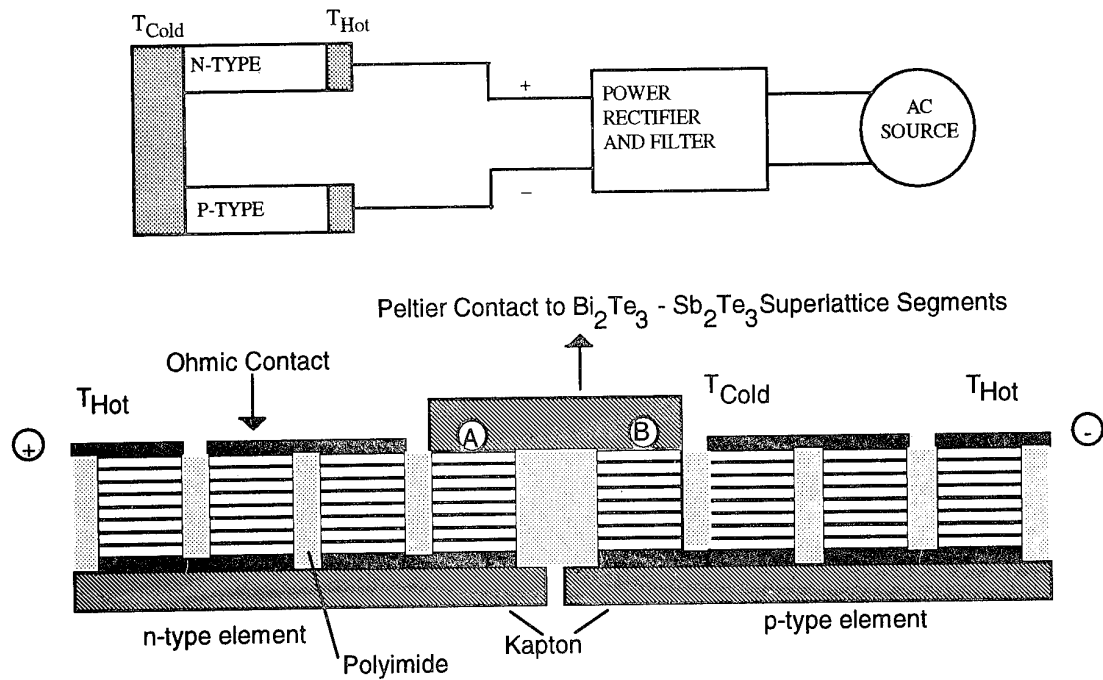


Fig. 5 Schematic of a thin-film TE refrigerator utilizing the MISST concept.

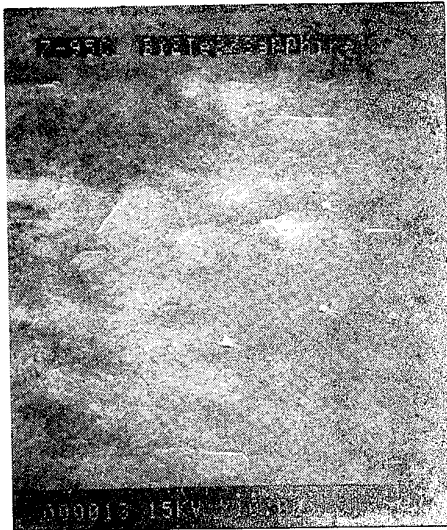


Fig. 6 SEM topography of a  $\text{Bi}_2\text{Te}_3$  heteroepitaxial film on single-crystal sapphire substrate.

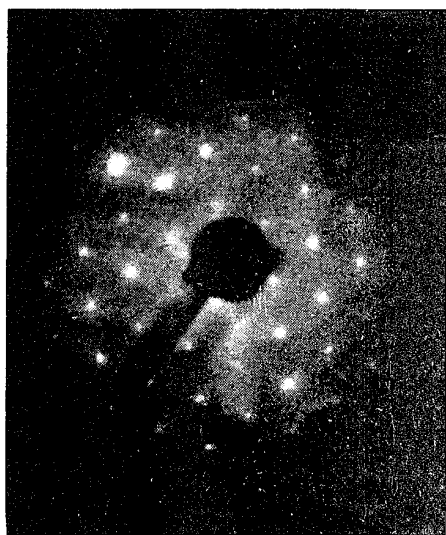
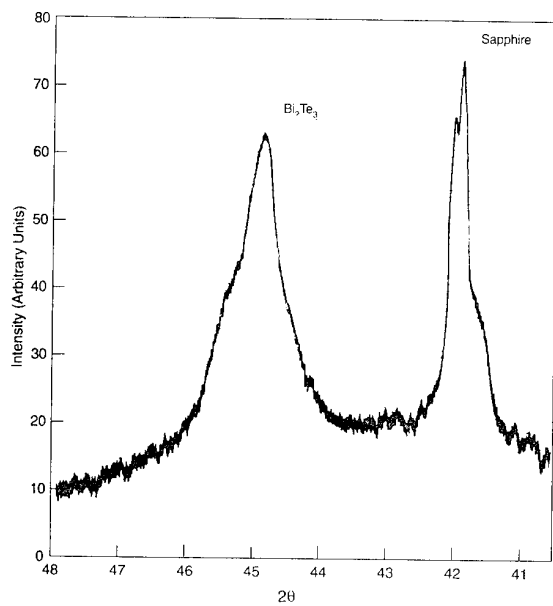


Fig. 7 LEED data obtained on a  $\text{Bi}_2\text{Te}_3$  hetero-epitaxial film on sapphire, using  $\sim 250$  eV electrons.



diffraction scan obtained from a  $\text{Bi}_2\text{Te}_3$  film on single-crystal sapphire substrate.

## Author Index

---



---

**A**

- Abaidulina T.G. 56  
 Abdullaev M.A. 198  
 Acharya H.N. 178, 185, 189  
 Aivazov A.A. 125, 449  
 Alekseeva G.T. 72, 75, 193  
 Aloke Kumar Das 178  
 Anatychuk L.I. 7, 295, 319,  
     341, 344, 369,  
     372, 424, 461,  
     464  
 Anukhin A.I. 65, 125  
 Arai H. 245  
 Aruga A. 222, 269  
 Ašhmontas S.P. 334

**B**

- Babin V.P. 338  
 Ball C.A.B. 305  
 Barbee T.W.Jr. 283  
 Bauer E. 354  
 Belya A.D. 37, 119  
 Bierschenk J. 481  
 Blagorodov A.M. 428  
 Bochegov V.I. 314, 315  
 Bodnaruc V.I. 341  
 Bogomolov V.N. 280  
 Boikov Yu.A. 174  
 Bondarenco M.G. 52, 115, 469  
 Borshchevsky A. 231  
 Braun James F. 394  
 Brehme S. 259  
 Bublik V.T. 33  
 Buist R.J. 301  
 Bulat L.P. 310, 367  
 Burkov A.T. 206, 259, 354

**C**

- Caillat Th. 231  
 Cassart M. 96  
 Chatterjee S. 178, 185, 189  
 Chizhevskaya S.N. 42  
 Cho Y.W. 104  
 Choi J.S. 130  
 Choudhary R.N.P. 178, 189  
 Cohn J.L. 240  
 Colpitts T.S. 490

**D**

- Danilov V.A. 174  
 Dauscher A. 96  
 Demchuk B.N. 424, 464, 467  
 Derjagina I.M. 174  
 Dietrich Th. 13  
 Donoval D. 331  
 Dubov V.I. 428

**E**

- Eguchi K. 245  
 Ehrlich A.C. 240  
 Engo I. 382  
 Evseev V.A. 166, 168

**F**

- Fano V. 182  
 Farmer J.C. 283  
 Fedorov M.I. 210, 215, 254  
 Fishchuk I.I. 324  
 Fleurial J.-P. 231  
 Foreman R.J. 283  
 Frolov A.M. 33  
 Fujimaki T. 24  
 Fujimoto S. 222, 269  
 Fukuda K. 100, 135

**G**

- Gadjieva R.M. 198  
 Gaiperin V.L. 442, 446  
 Gao W.X. 151  
 Gasenkova I.V. 29  
 Gavril'yuk N.V. 467  
 Gillespie D.J. 240  
 Gladun C. 206, 259  
 Glasov V.M. 49  
 Goldsmid H.J. 16  
 Gorodetskyi S.M. 338  
 Grabov V.M. 52, 85, 115,  
     469  
 Gribanova O.S. 174  
 Gritsai V.V. 380  
 Gromko E.D. 380  
 Gubanok I.I. 391  
 Gurevich Yu.G. 316, 331  
 Gurieva E.A. 193, 254  
 Gusev V.V. 391

**H**

- Ha H.P. 104, 130  
 Heinrich A. 206, 259  
 Higa M. 354  
 Hino M. 382  
 Horak J. 45  
 Hyun D.B. 104, 130

**I**

- Ido H. 140  
 Ido M. 100  
 Imaizumi H. 100, 135  
 Inoue M. 151  
 Ishii T. 100, 135  
 Ivanov G.A. 115  
 Ivanova L.D. 13, 60, 485

**J**

- Jang Kyung-Wook 108  
 Jesser W.A. 249, 305  
 Jouravlev O. 33  
 Jung B.Y. 130

**K**

- Kagan V.D. 78  
 Kagawa Sh. 382  
 Kaliazin A.E. 210  
 Kamisako K. 24, 264  
 Kaneko T. 140  
 Karatajev V.V. 33  
 Khabrenko A.A. 349  
 Khasbulatov A.M. 198  
 Khmelevskaya Yu.S. 467  
 Khochlachov P.P. 198  
 Kibayashi Y. 135  
 Kim Il-Ho 145  
 Kishimoto K. 227, 274  
 Kogo M. 140  
 Kolgunov D.A. 85  
 Konstantinov P.P. 72, 75, 193  
 Korzhuev M.A. 42, 201  
 Kosyachenko S.V. 319  
 Koyanagi T. 274  
 Ktitorov S.A. 210  
 Kuboki M. 140  
 Kulakova E.A. 42  
 Kulbachinskii V.A. 45, 151  
 Kurdyukov D.A. 280  
 Kutaisov V.A. 20, 72, 75  
 Kuznetsov A.V. 7  
 Kuznetsov G.D. 166, 168

**L**

- Lange H. 259  
 Laptev A.V. 201  
 Lavrukhan V.K. 391  
 Lee Dong-Hi 108, 145  
 Lenoir B. 96  
 Letiuchenko S.D. 7  
 Liaschenok V.I. 112  
 Logvinov G.N. 316  
 Lošťák P. 45, 88  
 Luk'yanova L.N. 20, 72, 75  
 Lushkina T.L. 428  
 Luste O.J. 344, 464  
 Lyon H.B. Jr. 16, 481

**M**

- Maddux J. 305  
 Magomedova I.Kh. 198  
 Makhorin O.I. 424  
 Makhratchov K.B. 449  
 Maksimova N.M. 10, 42

Malkovitch B.Sh.	163		Tochitsky E.I.	29
Malta D.	490		Tomm Y.	259
Mantini M.	490		Toyoda F.	135
Marchuk N.D.	217, 324, 415	R	Tritt T.M.	236, 240
Masumoto T.	140	Racko J.	331	
Matsubara K.	227, 274	Ravich Yu.I.	75, 96, 280	
Matsuura K.	382, 386	Razinkov V.V.	349, 351, 380	
Meletti G.	182	Red'ko N.A.	78, 82	
Melnichuk S.V.	319	Redondo J.M.	478	
Mikhailovsky V.Ja.	376	Reinshaus P.	10, 13	
Miki T.	227, 274	Resel R.	354	
Min Byong-Gue	145	Rowe D.M.	156, 159, 288, 291, 357, 386	
Min G.	156, 159, 288, 291, 357	Rybkin N.N.	391	
Miyakawa T.	222, 269	Rykov S.A..	60	
Morelli D.T.	236	S		
Morimoto J.	222, 269	Sagalova T.B.	33	
Müller E.	1	Samoilovich L.A.	280	
N		Samoilovich S.M.	280	
Nagamoto Y.	274	Sanchez J.M.	478	
Nakagawa Y.	140	Sasaki M.	151	
Nakahara Y.	474	Sato R.	140	
Nakama T.	354	Sawade Y.	264	
Naletov V.L.	115	Scherrer H.	96	
Navrátil J.	88, 92	Schock A.	401	
Nebera L.P.	391	Schumann J.	206	
Negishi H.	151	Semeniouk V.A.	469, 485	
Nemov S.A.	56, 60	Serebryaniy G.L.	430	
Nikolayev Yu.V.	369	Sha'nigrahi S.R.	189	
Nolas G.S.	236, 240	S'iche īrin A.A.	351	
Noriega G.	478	Shauerbina L.A.	341	
Novotny R.	92	Sher E.M.	277	
O		Shevchukovich Ya.A.	349	
Oh T.S.	130	Shim J.D.	104, 130	
Ohta T.	24, 264	Sidorenko N.A.	363, 438	
Ohtaki M.	245	Singh A.K.	189	
Okamoto Y.	222, 269	Skipidarov S.Ya.	65, 125	
Onodera A.	100	Skolozdra R.V.	217	
Opyr L.A.	330	Slack G.A.	236, 240	
Ordin S.V.	212	Sokolov O.B.	65, 125	
Ortalli I.	182	Solomkin F.Yu.	215	
Osvensky V.B.	33	Soutorshin V.N.	363	
Ovchinnikov S.G.	469	Stadnyk Y.V.	217	
Ovsjanov V.M.	315	Starý Z.	88, 92	
P		Stern Y.I.	449	
Pascual I.	478	Strekopytova N.I.	112	
Pervozvansky S.V.	344, 351	Strutinskaya L.T.	376	
Petrenko N.S.	467	Sulin A.B.	453	
Pilipenko T.V.	469	Summers L.J.	283	
Pischke W.	206	Süßmann H.	1, 10, 13	
Plecháček T.	88, 92	Suvorova N.A.	171	
Podgorbunskih S.A.	315	Sužiedelis A.	334	
Polystanskiy Yu.G.	166, 168	Svechnikova T.E.	10, 42, 56, 485	
Ponomarev Y.G.	119	T		
Poyarkov K.B.	49	Tamaki N.	100	
Pozela K.	182	Tan Z.S.	249	
Prokof'eva L.V.	193, 254	Tanaka T.	24, 264	
Prokofiev A.V.	280	Tanji Y.	140	
Pustovalov A.A.	391, 424	Tashiro H.	269	
		Teraoka Y.	227	
		Titov O.Yu.	316	